Lecture Notes in Electrical Engineering 437

Jiadong Sun
Jingnan Liu
Yuanxi Yang
Shiwei Fan
Wenxian Yu
Editors

China Satellite Navigation Conference (CSNC) 2017 Proceedings: Volume I

Springer

Lecture Notes in Electrical Engineering

Volume 437

About this Series

"Lecture Notes in Electrical Engineering (LNEE)" is a book series which reports the latest research and developments in Electrical Engineering, namely:

- Communication, Networks, and Information Theory
- Computer Engineering
- Signal, Image, Speech and Information Processing
- Circuits and Systems
- Bioengineering

LNEE publishes authored monographs and contributed volumes which present cutting edge research information as well as new perspectives on classical fields, while maintaining Springer's high standards of academic excellence. Also considered for publication are lecture materials, proceedings, and other related materials of exceptionally high quality and interest. The subject matter should be original and timely, reporting the latest research and developments in all areas of electrical engineering.

The audience for the books in LNEE consists of advanced level students, researchers, and industry professionals working at the forefront of their fields. Much like Springer's other Lecture Notes series, LNEE will be distributed through Springer's print and electronic publishing channels.

More information about this series at http://www.springer.com/series/7818

Jiadong Sun · Jingnan Liu · Yuanxi Yang
Shiwei Fan · Wenxian Yu
Editors

China Satellite Navigation Conference (CSNC) 2017 Proceedings: Volume I

Springer

Editors
Jiadong Sun
Academician of CAS
China Aerospace Science and Technology Corporation
Beijing
China

Jingnan Liu
Wuhan University
Wuhan
China

Yuanxi Yang
National Administration of GNSS and Applications
Beijing
China

Shiwei Fan
China Satellite Navigation Office
Beijing
China

Wenxian Yu
Shanghai Jiao Tong University
Shanghai
China

ISSN 1876-1100 ISSN 1876-1119 (electronic)
Lecture Notes in Electrical Engineering
ISBN 978-981-10-4587-5 ISBN 978-981-10-4588-2 (eBook)
DOI 10.1007/978-981-10-4588-2

Library of Congress Control Number: 2017937524

Printed on acid-free paper

This Springer imprint is published by Springer Nature
The registered company is Springer Nature Singapore Pte Ltd.
The registered company address is: 152 Beach Road, #21-01/04 Gateway East, Singapore 189721, Singapore

Preface

BeiDou Navigation Satellite System (BDS) is China's global navigation satellite system which has been developed independently. BDS is similar in principle to global positioning system (GPS) and compatible with other global satellite navigation systems (GNSS) worldwide. The BDS will provide highly reliable and precise positioning, navigation and timing (PNT) services as well as short-message communication for all users under all-weather, all-time and worldwide conditions.

China Satellite Navigation Conference (CSNC) is an open platform for academic exchanges in the field of satellite navigation. It aims to encourage technological innovation, accelerate GNSS engineering and boost the development of the satellite navigation industry in China and in the world.

The 8th China Satellite Navigation Conference (CSNC 2017) is held during May 23–25, 2017, Shanghai, China. The theme of CSNC2017 is Positioning, Connecting All, including technical seminars, academic exchanges, forums, exhibitions and lectures. The main topics are as follows:

Conference Topics

S01 Satellite Navigation Technology
S02 Navigation and Location Service
S03 Satellite Navigation Signals and Signal Processing
S04 Satellite Orbit and Satellite Clock Error
S05 Precise Positioning Technology
S06 Atomic Clock and Time-frequency Technology
S07 Satellite Navigation Augmentation Technology
S08 Test and Assessment Technology
S09 User Terminal Technology
S10 Multi-source Fusion Navigation Technology
S11 PNT New Concept, New Methods and New Technology
S12 Policies and Regulations, Standards and Intellectual Properties

The proceedings (Lecture Notes in Electrical Engineering) have 188 papers in twelve topics of the conference, which were selected through a strict peer-review process from 599 papers presented at CSNC2017. In addition, another 272 papers were selected as the electronic proceedings of CSNC2017, which are also indexed by "China Proceedings of Conferences Full-text Database (CPCD)" of CNKI and Wan Fang Data.

We thank the contribution of each author and extend our gratitude to 249 referees and 48 session chairmen who are listed as members of editorial board. The assistance of CNSC2017 organizing committees and the Springer editorial office is highly appreciated.

Beijing, China — Jiadong Sun
Wuhan, China — Jingnan Liu
Beijing, China — Yuanxi Yang
Beijing, China — Shiwei Fan
Shanghai, China — Wenxian Yu

Editorial Board

Topic: S5: Precise Positioning Technology

Qile Zhao, Wuhan University
Jianwen Li, Information Engineering University
Songshu Li, Shanghai Astronomical Observatory, Chinese Academy of Sciences
Feng Yanming, Queensland University of Technology Brisbane, Australia

Topic: S6: Atomic Clock and Time-frequency Technology

Lianshan Gao, The 203th Research Institute of China Aerospace Science & Industry Corporation
Chunhao Han, Beijing Satellite Navigation Center
Xiaohui Li, National Time Service Center, Chinese Academy of Sciences
Rochat Pascal, Spectratime & T4Science

Topic: S7: Satellite Navigation Augmentation Technology

Junlin Zhang, OLinkStar Co., Ltd., China
Jinping Chen, Beijing Satellite Navigation Center
Rui Li, Beihang University
Shaojun Feng, Imperial College London

Topic: S8: Test and Assessment Technology

Xiaolin Jia, Xi'an Institute of Surveying and Mapping
Jun Yang, National University of Defense Technology
Jianping Cao, Air Force Equipment Research Institute
Yang Gao, University of Calgary, Canada

Topic: S9: User Terminal Technology

Haibo He, Beijing Satellite Navigation Center
Baowang Lian, Northwestern Polytechnical University
Hong Li, Tsinghua University
Yong Li, University of New South Wales, Australia

Topic: S10: Multi-source Fusion Navigation Technology

Zhongliang Deng, Beijing University of Posts and Telecommunications
Hong Yuan, Academy of Opto-electronics, Chinese Academy of Sciences
Yongbin Zhou, National University of Defense Technology
Jinling Wang, University of New South Wales, Australia

Topic: S11: PNT New Concept, New Methods and New Technology

Mingquan Lu, Tsinghua University
Wei Wang, The 20th Research Institute of China Electronics Technology Group Corporation
Yin Xu, Academy of Opto-Electronics, Chinese Academy of Sciences
Xiangzhen Li, Chungnam National University, Korea

Topic: S12: Policies and Regulations, Standards and Intellectual Properties

Scientific Committee and Organizing Committee

The 8th China Satellite Navigation Conference (CSNC 2017)

Scientific Committee

Chairman
Jiadong Sun, China Aerospace Science and Technology Corporation

Vice-Chairman
Rongjun Shen, China
Jisheng Li, China
Qisheng Sui, China
Changfei Yang, China
Zuhong Li, China Academy of Space Technology
Shusen Tan, Beijing Satellite Navigation Center, China

Executive Chairman
Jingnan Liu, Wuhan University
Yuanxi Yang, China National Administration of GNSS and Applications
Shiwei Fan, China

Committee Members: (By Surnames Stroke Order)
Xiancheng Ding, China Electronics Technology Group Corporation
Qingjun Bu, China
Liheng Wang, China Aerospace Science and Technology Corporation
Yuzhu Wang, Shanghai Institute of Optics and Fine Mechanics, Chinese Academy of Sciences
Guoxiang Ai, National Astronomical Observatories, Chinese Academy of Sciences
Shuhua Ye, Shanghai Astronomical Observatories, Chinese Academy of Sciences
Zhaowen Zhuang, National University of Defense Technology
Qifeng Xu, PLA Information Engineering University

Houze Xu, Institute of Geodesy and Geophysics, Chinese Academy of Sciences
Guirong Min, China Academy of Space Technology
Xixiang Zhang, China Electronics Technology Group Corporation
Lvqian Zhang, China Aerospace Science and Technology Corporation
Junyong Chen, National Administration of Surveying, Mapping and Geoinformation
Benyao Fan, China Academy of Space Technology
Dongjin Luo, China
Guohong Xia, China Aerospace Science & Industry Corporation
Chong Cao, China Research Institute of Radio Wave Propagation (CETC 22)
Faren Qi, China Academy of Space Technology
Sili Liang, China Aerospace Science and Technology Corporation
Shancheng Tu, China Academy of Space Technology
Rongsheng Su, China
Zhipeng Tong, China Electronics Technology Group Corporation
Ziqing Wei, Xi'an Institute of Surveying and Mapping

Organizing Committee

Secretary General
Haitao Wu, Navigation Headquarters, Chinese Academy of Sciences

Vice-Secretary General
Weina Hao, Navigation Headquarters, Chinese Academy of Sciences

Under Secretary
Wenhai Jiao, China Satellite Navigation Office Engineering Center
Zhao Wenjun, Beijing Satellite Navigation Center
Wenxian Yu, Shanghai Jiao Tong University
Wang Bo, Academic Exchange Center of China Satellite Navigation Office

Members: (In Surname Stroke Order)
Qun Ding, The 20th Research Institute of China Electronics Technology Group Corporation
Miao Yu, China Academy of Space Technology
Li Wang, International Cooperation Research Center, China Satellite Navigation Engineering Office
Liu Peiling, Shanghai Jiao tong University
Ying Liu, China Satellite Navigation Office Engineering Center
Lu Mingquan, Tsinghua University
Xiuwan Chen, Peking University
Ouyang Guangzhou, Academy of Opto-Electronics, Chinese Academy of Sciences
Zhao Qile, Wuhan University

Xiangan Zhao, China Defense Science and Technology Information Center
Gang Hu, Beijing Unicore Communications, Inc.
Min Shui, National Remote Sensing Centre of China

Contents

Part I
Satellite Navigation Technology

Theoretical Study for Bare Soil Freeze/Thaw Process Detection Using GNSS-R/MR

Xuerui Wu, Shuanggen Jin, Yuanting Li and Yanfang Dong

Abstract GNSS-R remote sensing has emerged as a new promising remote sensing technique in the past two decades. It has gained wide attention at home and abroad. In essential, GNSS-R is a bistatic radar, the signals got by the GNSS-R receiver is delay Doppler map. Different from the specially designed receivers, the geodetic quality GPS receiver can be used to remotely sense the near surface soil moisture, vegetation growth and snow depth, i.e. GNSS-Multipath reflectometry (GNSS-MR). Three metrics, i.e. effective reflector height, phase and amplitude, are employed for retrieval. As for the applications of space-borne/air-borne GNSS-R or ground based GNSS-IR techniques, they include soil moisture, vegetation growth and snow depth retrieval. This paper has extended the bare soil freeze/thaw process detection, the theoretical fundamentals is that when the soil frozen/thawn process occurs, there is a big difference for the soil permittivity, which will result in the difference of reflectivities. The dielectric mixing models are employed for the calculations of the frozen/thawn soil permittivities, which are the inputs for the reflectivity models, the coherent scattering model and the random surface scattering models are employed for the calculation of specular scattering reflectivities and the diffuse scattering reflectivities, respectively. When the soil freeze/thaw process has occurred, the corresponding GPS multipath changes and the variations of delay Doppler map are simulated. The theoretical simulations indicate that the big dif-

X. Wu (✉) · S. Jin
Shanghai Astronomical Observatory, Chinese Academy of Sciences,
80 Nandan Road, Shanghai 200030, China
e-mail: xrwu@shao.ac.cn

X. Wu · S. Jin
Key Laboratory of Planetary Sciences, Shanghai Astronomical
Observatory, Chinese Academy of Sciences, Shanghai 200030, China

Y. Li
China Transport Telecommunications
and Information Center, Beijing, China

Y. Dong
Institute of Earthquake Science, China Earthquake
Administration, Beijing 100036, China

J. Sun et al. (eds.), *China Satellite Navigation Conference (CSNC) 2017 Proceedings: Volume I*, Lecture Notes in Electrical Engineering 437,
DOI 10.1007/978-981-10-4588-2_1

ference of permittivity will result in the apparent changes of GPS multipath observables and delay Doppler map. It has been demonstrated in theory that the bare soil freeze/thaw process can be detected by the GNSS-R or GNSS-MR techniques.

Keywords GNSS-R/MR · Multipath observables · Delay Doppler map · Soil freeze/thaw process

1 Introduction

About 35% of the land surface are covered by seasonal and permanent frozen soil, they are mainly distributed in high latitude and altitude area. The transformation of soil freeze/thaw process in the land is repeated every year with seasons and they are highly related to the human life, this process strongly affects the land-atmosphere energy exchange, the near surface runoff and carbon cycle et.cl. as for the phase change of liquid water in soil, this process strongly influences the exchange of the near surface radiative energy, evapotranspiration process and the intensity of surface runoff. Meanwhile, this process is a sensitive indicator of the climate change, therefore, the efficiently monitoring the soil freeze/thaw process and its related physical parameters seem very significantly important. The commonly used space-borne observations can improve the spatial resolution, while its time resolution cannot satisfy the scientific requirements.

GNSS-R is an efficient remote sensing technique with the advantages of low cost, small power, wide coverage and high spatial/temporal resolution. The scientific objectives of GNSS-R are to realize the space-borne observations. UK DMC (UK Disaster Monitoring Constellation mission) is the first space-borne mission, which has successfully received the reflected signals from global ocean, land surface and ice surface [1]. In recent years, this technique has gained more attention. Both America and European countries have launched several GNSS-R satellites. ESA has raised the PARIS demonstration satellite, i.e. PARIS IoD, its aim is for the meso-scale altimetric feasibility study [2]. In 2011, ESA has put forward the GEROS-ISS (GNSS Reflectometry, Radio Occultation and Scatterometry onboard the International Space Station) mission, which is used for the climate study [3]. TechDemoSat-1 has launched in July, 2014 and carried a GNSS-R sensor [4]. While CYGNSS mission of NASA, which launched in Dec 12th of 2016, has carried eight small satellites, their main scientific objectives are for the cyclone detection [5].

GNSS-R is essentially a bisatic radar, the received signals are delay Doppler maps. The applications for space-borne GNSS-R are remotely sense soil moisture, vegetation growth and snow depth.

Different from the specially designed GNSS-R receiver, the geodetic quality GPS receiver can be used for land geophysical parameters detection. Three metrics

are employed for retrievals, i.e. effective reflector height, phase and amplitude. Data analysis by PBO GPS sites has found that there is a linear relationship between soil moisture and the phase [6]; experimental data of PBO and SNOTEL has shown that the relationship between effective reflector height and snow depth is between 0.7 and 0.9 [7]; when the vegetation wet weight is below 1.5 kg m^2, amplitude is an efficient parameter for vegetation amount monitoring [8].

This paper has extended the applications of GNSS-R/GNSS-MR to bare soil freeze/thaw process detection. In the following section, the effects of freeze/thaw soil process on delay Doppler map and GPS multipath observables are presented.

2 Theoretical Models

2.1 Dielectric Permittivity Models

According to the electromagnetic properties, wet soil is composed of air, solid particles, free water and bound water [9, 10].

$$\varepsilon_m^\alpha = \sum_i V_i \varepsilon_i^\alpha \tag{1}$$

where α is the shape factor, ε_i is the ith material permittivity, Vi is its volume. As for the frozen soil, ice is added.

$$\varepsilon^\alpha = V_s \varepsilon_s^\alpha + V_a \varepsilon_a^\alpha + V_{fw} \varepsilon_{fw}^\alpha + V_{bw} \varepsilon_{bw}^\alpha + m_{vi} \varepsilon_i^\alpha \tag{2}$$

Subscripts s, a, fw, bw, i refers to solid soil, air, free water, bound water and ice.

2.2 Surface Reflectivity Models

The coherent scattering part of soil is calculated by the Fresnel reflectivity by taking surface roughness factor into consideration [11].

As for the random roughness soil surface, the interaction between navigation signals and bare soil surface is related to the scattering of random rough surface, the corresponding scattering models have been carried out over the past two decades. The commonly used scattering models include the KA (Kirchhoff Approach) model, SPM (Small Perturbation Method) model, IEM (Integrated Equation Model) model. The lately developed AIEM (Advanced Integrated Equation Model) model is employed for the diffuse scattering calculations [12].

2.3 The Forward GPS Multipath Model

A fully polarimetric GPS multipath simulator has been developed by Nievinski and Larson, this simulator has taken the GPS polarimetric response, antenna and surface responses into consideration [13].

$$\mathrm{P_d} = P_d^R G_d^R W_d^2 \tag{3}$$

$$\mathrm{P}_r = P_d^R |XSW_r|^2 \tag{4}$$

P represent the electric magnetic power, G is the antenna responses, W represents Woodward ambiguity function, subscripts d and r are the direct and reflected components, respectively, X is the coupled coefficients of surface and antenna.

$$\mathrm{X^R} = \mathrm{R^s}\sqrt{G_r^R}\exp\left(i\Phi_r^R\right) \tag{5}$$

$$\mathrm{X}^L = \mathrm{R}^X\sqrt{G_r^L}\exp\left(i\Phi_r^L\right) \tag{6}$$

Subscripts R and L represent RHCP and LHCP polarization. Φ is the interferometric phase, $\mathrm{R^s}$ and $\mathrm{R^X}$ are the same polarization and cross polarization reflectivity, they are the linear combinations of H pol and V pol.

2.4 The Fully Polarimetric Delay Doppler Map for Freeze/Thaw Soil

In essence, the fully polarimetric delay Doppler map for freeze/thaw soil is the integral form of bistatic radar equation [14].

$$Y_s\left(\hat{\tau},\hat{f}\right) = \frac{T_I^2 P_T \lambda^2}{(4\pi)^3}\iint_A \frac{G_T \sigma^0 G_R}{R_R^2 R_T^2}\Lambda^2(\hat{\tau}-\tau)\sin c^2\left(\hat{f}-f\right)dA \tag{7}$$

Y_s: the received GPS reflected power, which is the function of delay $\hat{\tau}$ and frequency; P_T: the GPS transmitted power; G_T: antenna gain of transmitter; G_R: antenna gain of receiver; R_R: the distance between receiver and the surface reflected point; R_T: the distance between transmitter and the surface specular reflected point; λ: wavelength; T_I: the coherent integral time; σ^0: the frozen soil bistatic radar cross section; $\Lambda(\hat{\tau}-\tau)$: GPS correlation function, $\hat{\tau}$, τ are the delay of replica signal and

incident signals; $\sin c^2(\hat{f}-f)$: Doppler filter function, $\hat{f}, f$ are the frequency of replica signal and incident signals; A: the effective scattering area, nearing the glisten zone; dA: integral area in A.

3 Theoretical Simulations

3.1 Permittivity for Frozen and Thawn Soil

The mixture dielectric models are employed for the simulation of frozen soil and thawn soil. Soil temperature is changed from −20 to 20 °C, the corresponding changes of permittivity (real part and imaginary part) are simulated in Fig. 1.

From the simulations, it can be seen, as for soil temperature below 0°, the permittivity (both the real part and the imaginary part) increase as the soil temperature; when the soil temperature is above 0°, it decreases as the soil temperature increases. When the soil temperature increase from below 0° to above 0°, there is an abrupt change for the soil permittivity. In the vicinity of 0°, when the soil temperature increase from below 0° to above 0°, the difference between real part is about 10, while the difference between imaginary part is about 2.

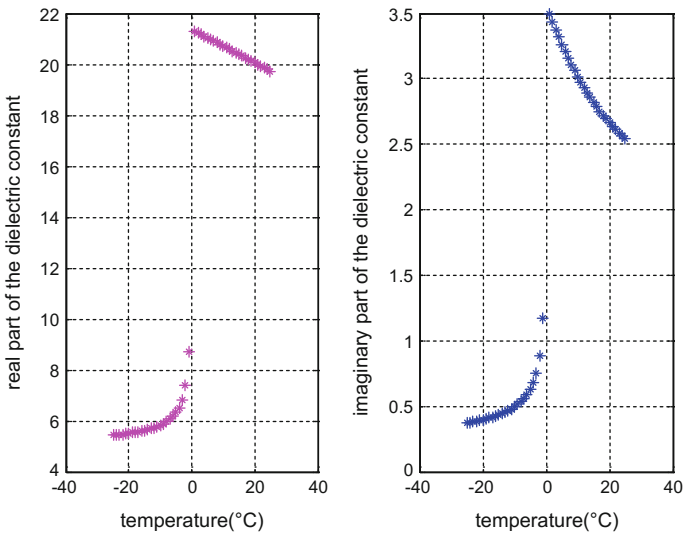

Fig. 1 Real part (*left*) and imaginary part (*right*) of the permittivities versus soil temperature

3.2 *Surface Reflectivity Simulations*

As shown in Fig. 2, as the soil temperature changes from −0.5 to 0.5 °C, there are differences (about 2–5 dB) for VV, RR and VR polarizations (when the elevation angle is greater than 10°). For VV/VR pol, the Brewster angle is observed through the notches in the plots, the frozen soil has larger reflectivity than thawn soil before the elevation angle approaches to the Brewster angle and the trend is just opposite after the Brewster angle. If the soil temperature is fixed, the Fresnel reflectivity at VV/VR pol decreases as the elevation angle increases (before the Brewster angle). However, the reflectivity at VV and VR pol increases after the elevation angle becomes larger than the Brewster angle.

When the direct signal of the navigation satellite is incident to the surface, not only the coherent scattering at the specular direction but also the diffuse scattering can be received. Here, the AIEM model is employed to get the diffuse scattering properties. We use the permittivity model to calculate the soil permittivity, which is

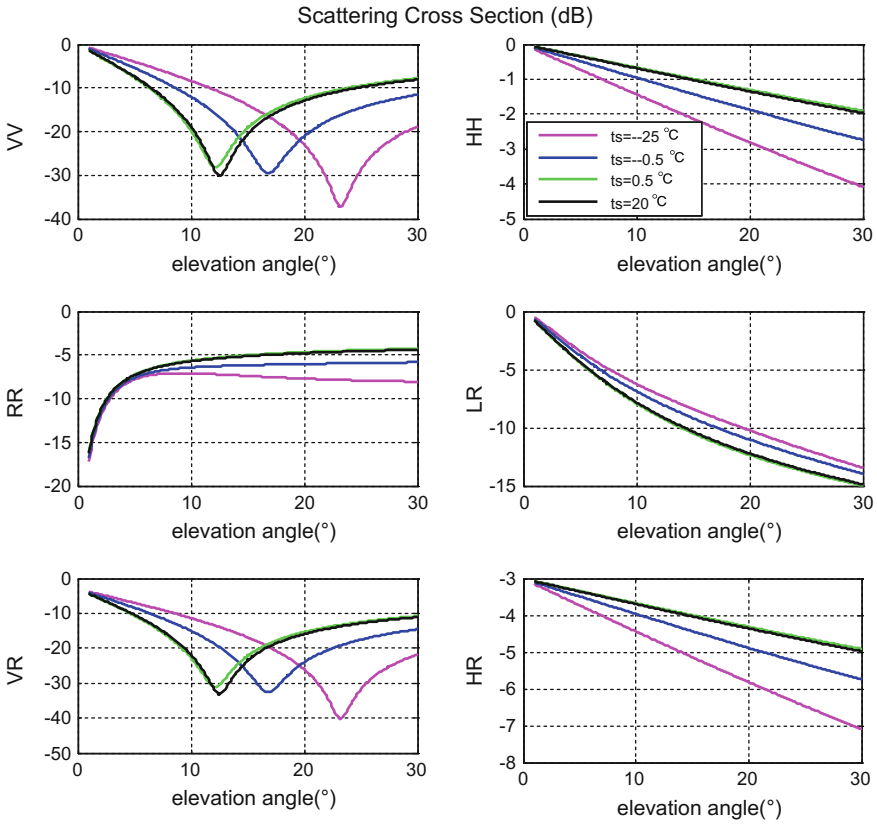

Fig. 2 Coherent scattering at XR polarizations for different soil temperatures

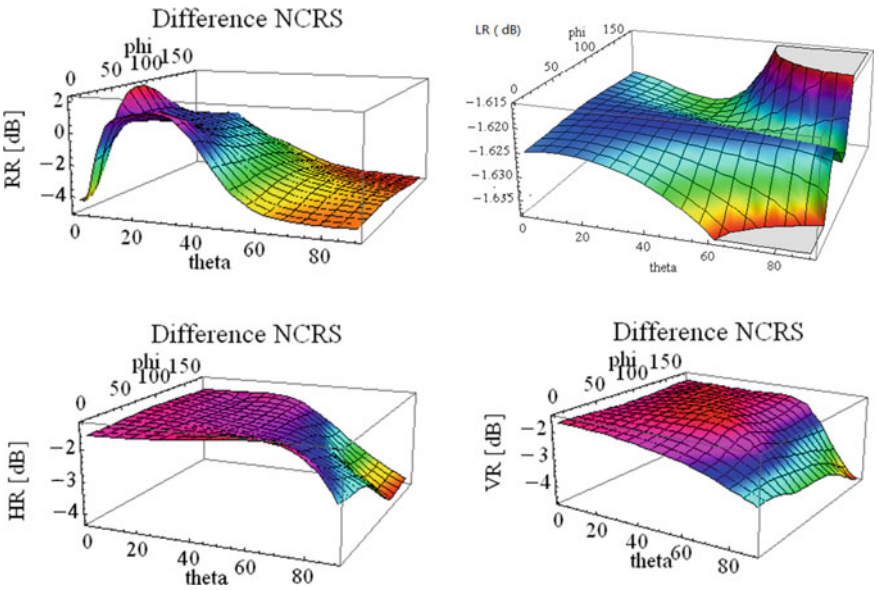

Fig. 3 Diffuse scattering differences (RR, LR, VR and HR pol) as for 1 °C soil temperature differences (from −0.5 to 0.5 °C). The incident azimuth angle is 30°, while the incident zenith angle phi is zero. Theta and phi are the scattering azimuth and zenith angle, respectively

a function of the soil temperature, and then put the permittivity as one of the inputs into the AIEM model. As the soil changes from −0.5 °C to above 0.5 °C, diffuse scattering differences for RR, LR, VR and HR pol are presented in Fig. 3. The soil temperature changes by 1 °C will cause about 4 dB NCRS differences for RR, VR and HR pol, while the scattering difference for LR pol is smaller, about −1.6 dB. From our simulations, it is thought that LR polarization is less sensitive to soil temperature.

3.3 Delay Doppler Map Difference

When the soil changes from frozen state to thawn state or vice versa, there is a big difference for the soil permittivity and this is the fundamental for detection. Table 1 has shown when the soil temperature changes from −1 to 1 °C, the changes for the real part and imaginary part of the permittivity are from 8.7 to 21.3 and from 1.2 to 3.5, respectively.

Table 1 Real part and imaginary part of the permittivity

Ts (°C)	Real part	Imaginary part
−1	8.70793	1.16876
+1	21.27701	3.49827

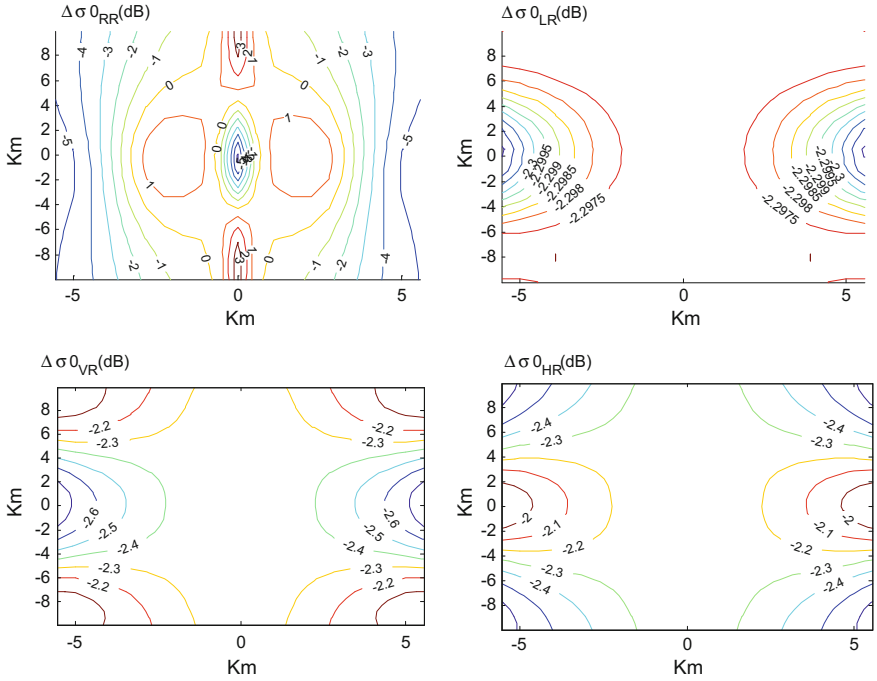

Fig. 4 Frozen/thawn soil reflectivity differences for different polarization

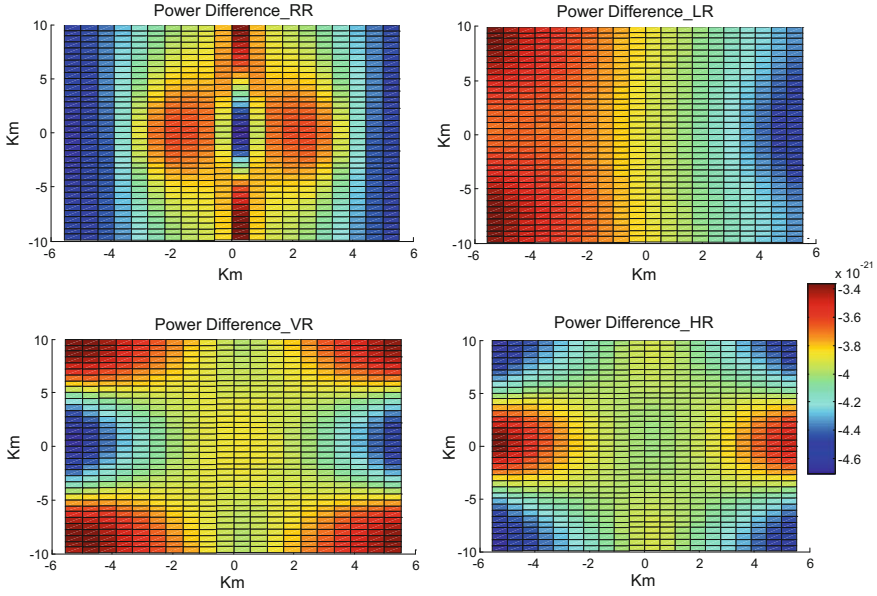

Fig. 5 Frozen/thawn soil delay Doppler map difference for different polarizaitons

When the soil has changed from frozen state to thawn state, the corresponding variations of the bistatic scattering cross section at different polarizations are shown in Fig. 4. The delay Doppler map difference at different polarizations are presented in Fig. 5, apparent changes can be observed. Therefore, it has been verified that the feasibility of bare soil freeze/thaw process detection using GNSS-R/GNSS-IR techniques.

4 Conclusions

GNSS-R and GNSS-MR has emerged as a new promising remote sensing technique in recent years. This paper has extended its applications from soil moisture, vegetation growth and snow depth to bare soil freeze/thaw process detection. Theoretical simulations indicate that as the soil freeze/thaw process occurred, there is big difference for soil permittivity, which will result in the apparent difference of coherent scattering and diffuse scattering properties. As for GNSS-MR remote sensing, these difference will lead to the variations of GPS multipath observables. They correspond to the difference of delay Doppler map. Therefore, this paper has demonstrated in theory the feasibility of soil freeze/thaw process detection.

Acknowledgements This research is supported by the Natural Science Foundation of National Natural Science Foundation of China (NSFC) Project (Grant Nos. 41501384 and 41304002).

References

1. Gleason ST, Hodgart S, Yiping S, Gommenginger C, Mack-in S, Adjrad M, Unwin M (2005) Detection and processing of bi-statically reflected GPS signals from low Earth orbit for the purpose of ocean remote sensing. IEEE Trans Geosci Remote Sens 43(6):1229–1241
2. Martin-Neira M, D'Addio S, Buck C, Floury N, Prieto-Cerdeira R (2011) The PARIS ocean altimeter in-orbit demonstrator. IEEE Trans Geosci Remote Sens 49(6):2209–2237
3. Carreno-Luengo H, Camps A, Perez-Ramos I, Forte G, On-rubia R, Diez R (2013) 3Cat-2: a P (Y) and C/A GNSS-R experimental nano-satellite mission. In: Proceedings of IEEE international geoscience remote sensing symposium, Melbourne, Australia, pp 843–846
4. Unwin M, Duncan S, Jales P, Blunt P, Brenchley M (2014) Implementing GNSS reflectometry in space on the TechDemoSat-1 mission. In Proc. Institute Navigation
5. Ruf CS, Gleason S, Jelenak Z, Katzberg S, Ridley A, Rose R, Scherrer J, Zavorotny V (2012) The CYGNSS nanosatellite constellation hurricane mission. In: Proceedings of IEEE international geoscience remote sensing symposium, Munich, Germany, pp 214–216
6. Chew CC, Small EE, Larson KM, Zavorotny VU (2014) Effects of near-surface soil moisture on GPS snr data: development of a retrieval algorithm for soil moisture. IEEE Trans Geosci Remote Sens 52(1):537–543
7. Mccreight JL, Small EE, Larson KM (2014) Snow depth, density, and SWE estimates derived from GPS reflection data: validation in the western U. S. Water Resour Res 50(8):6892–6909

8. Chew CC, Small EE, Larson KM, Zavorotny VU (2015) Vegetation sensing using GPS-interferometric reflectometry: theoretical effects of canopy parameters on signal-to-noise ratio data. IEEE Trans Geosci Remote Sens 53(5):2755–2764
9. Dobson MC, Ulaby FT, Hallikainen MT, El-Rayes MA (1985) Microwave dielectric behavior of wet soil—Part II: dielectric mixing models. IEEE Trans Geosci Remote Sens, GE-23 (1):35–46
10. Zhang L, Shi J, Zhang Z, Zhao K (2003) The estimation of dielectric constant of frozen soil-water mixture at microwave bands. In: Geoscience and remote sensing symposium, 2003. IGARSS'03. Proceedings. 2003 IEEE International, vol 4, pp 2903–2905. IEEE
11. Fung A, Eom H (1983) Coherent scattering of a spherical wave from an irregular surface. IEEE Trans Antennas Propag 31(1):68–72
12. Chen KS, Wu TD, Tsang L, Li Q, Shi J, Fung AK (2003) Emission of rough surfaces calculated by the integral equation method with comparison to three-dimensional moment method simulations. IEEE Trans Geosci Remote Sens 41(1):90–101
13. Nievinski FG, Larson KM (2014) Forward modeling of GPS multipath for near-surface reflectometry and positioning applications. GPS Solutions 18(2):309–322
14. Zavorotny VU, Voronovich AG (2000) Scattering of GPS signals from the ocean with wind remote sensing application. IEEE Trans Geosci Remote Sens 38(2):951–964

The Application of BDS/GPS/GLONASS Data Fusion in FAST Measurement

Benning Song, Lichun Zhu, Dongjun Yu and Hui Yuan

Abstract Five-hundred-meter Aperture Spherical Radio Telescope (FAST) is a Chinese mega-science project to build the largest and most sensitive single dish radio telescope in the world. To achieve precise positioning of FAST feed cabin, we need all-weather, large-span and high-precision real-time dynamic measurements. The coarse-adjusting measurement of the FAST feed support, uses RTK (Real Time Kinematic) with the fusion of BDS/GPS/GLONASS. This paper introduces the RTK measurement program of FAST feed support coarse-adjusting system. Combined with the measured data, it indicates the importance of BDS/GPS/GLONASS data fusion. We also use total station to evaluate the accuracy of RTK measurement. The results show that the accuracy of RTK with fusion of BDS/GPS/GLONASS meets the technical requirements, which can guarantee the normal observation and safe operation of FAST.

Keywords FAST · RTK · BDS · Data fusion · Application

1 Introduction

FAST is a Chinese mega-science project to build the largest and most sensitive single dish radio telescope in the world. It is designed independently by our scientists. The site of FAST is located in Qiannan, Guizhou province. Compared with the existing international giant single-dish radio telescope, there are three main innovations:

1. the karst depression used as the site, which is large to host the 500-m and deep to allow a zenith angle of 40°;

B. Song (✉) · L. Zhu · D. Yu · H. Yuan
National Astronomical Observatories, Chinese Academy of Sciences,
Beijing 100012, China
e-mail: bnsong@nao.cas.cn

J. Sun et al. (eds.), *China Satellite Navigation Conference (CSNC) 2017 Proceedings: Volume I*, Lecture Notes in Electrical Engineering 437,
DOI 10.1007/978-981-10-4588-2_2

2. the active main reflector correcting for spherical aberration on the ground to achieve a full polarization and a wide band without involving complex feed systems;
3. the light-weight feed cabin driven by cables and servomechanism plus a parallel robot as a secondary adjustable system to move with high precision.

Six suspension cables are driven and supported by six towers and capstans, which are uniformly distributed on a circle with a diameter of 600 m. Feed cabin is dragged by these suspension cables, which makes it to be able to move within a 206 m diameter meter range in the altitude of 150 m. Based on the astronomical plan and measurement feedback, we operate the feed cabin and reflectors synchronously to achieve the high the high accuracy astronomical track movement. Figure 1 shows the FAST panorama and optical geometry.

Main structure of FAST is moving when we observe, and there is no solid connection between the reflector and the feed cabin. Therefore, the large-span, high-sampling rate and high-precision real-time dynamic positioning, is the key to successful construct FAST feed with no support of platform.

The BeiDou Navigation Satellite System (BDS) is a global satellite navigation system designed and developed by China. The BDS was officially put into operation in December 27, 2012. It already has the ability of independent RTK positioning with double frequency. Researches show that, the fixed rate and the reliability of fuzzy degree solution are remarkably improved by the combination of BDS and GPS. In the case of short baseline, the accuracy of the dynamic positioning measured by carrier phase differential, is improved over 20% by the combination of BDS/GPS than the single GPS. The satellite navigation and positioning system can provide all-weather and real-time 3D coordinates of the vector, and it has the characteristics of non-accumulation of error, high sampling rate and so on. Using RTK measurement technique with multi satellite fusion, we can achieve the accuracy of horizontal ±10 mm and vertical ±20 mm.

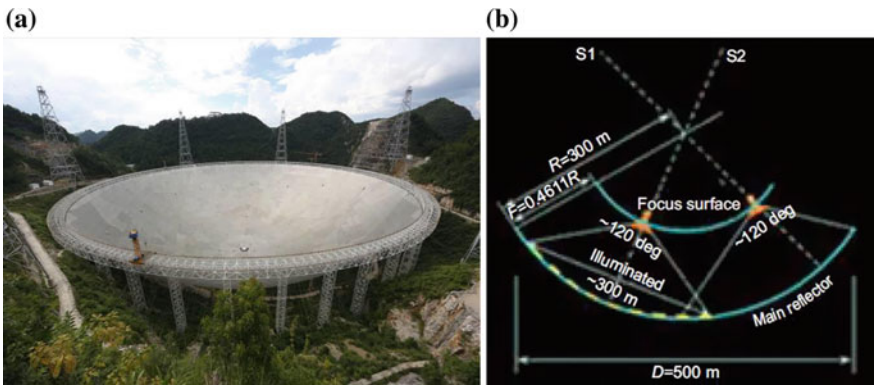

Fig. 1 FAST panorama (**a**) and optical geometry (**b**)

This paper introduces the RTK measurement of FAST feed support coarse-adjusting system. Combined with the measured data, it indicates the importance of BDS in the fusion.

2 The RTK Measurement of FAST Feed Support Coarse-Adjusting System

The FAST feed cabin system has no platform support and is composed by the three-tier adjustment agencies in series (Fig. 2): star frame, AB axes and Stewart fine-adjusting platform. Star frame is dragged by cables to achieve coarse position determination. AB axes mechanical structure is designed to determine the coarse attitude determination. Stewart fine-adjusting platform system is for the precise adjustment of the position and attitude.

2.1 Technical Specifications and Requirements

As the feedback source of the feed support control system, the feed support measurement system includes two parts: coarse-adjusting system and fine-adjusting system. The technical specifications and requirements of the feed support measurement system is:

1. Coarse-adjusting system:
   Location accuracy: ±17 mm;
   Measurement frequency: 5 Hz;

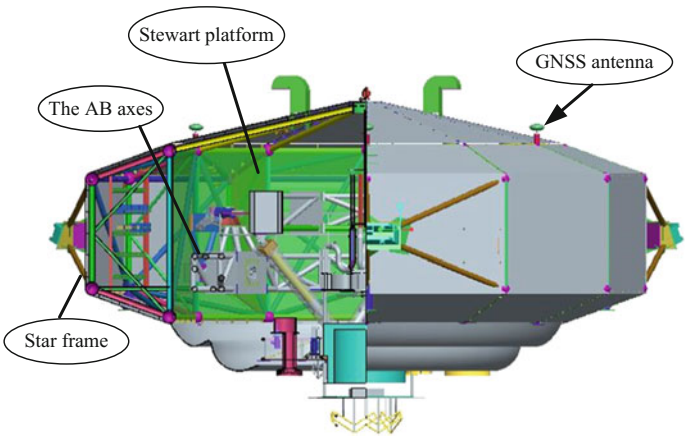

Fig. 2 The main structure of the feed cabin

2. Fine-adjusting system:
   Location accuracy: ±3 mm;
   Measurement frequency: 5 Hz;

In order to meet the requirements, coarse-adjusting system measurement uses RTK and total station measurement (Fig. 3). The RTK measurement can guarantee the safe operation of FAST when the total station cannot work, such as rain, fog and other inclement weather. In addition, the RTK measurement data can be used to verify whether the total station lost target or target confusion, and drive the total station pointing to the correct target.

2.2 RTK Measurement

1. RTK base station is installed on the surrounding mountain peak with a wide view.
2. The GNSS antennas of RTK rover stations are installed at the top of star frame, and its receivers are inside the feed cabin. The antennas are connected to the receivers through the filter.
3. The difference data of the base station is transmitted to the rover station receiver in real time by the optical fiber.
4. The serial server collects the measurement data obtained by rover station, and sends them to the measurement server.

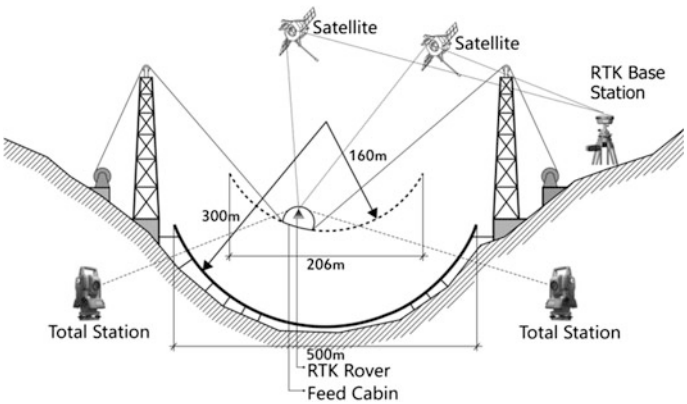

Fig. 3 FAST feed support coarse-adjusting measurement

2.3 Position and Attitude Solution

First of all, to establish the FAST measurement and control coordinate system: the center of the reflector sphere is the origin of the coordinate; the vertical direction is the positive direction of Z axis; the north direction is the x axis, and the y axis direction is determined by the right-hand rule. The following coordinate data are the coordinates in the FAST measurement and control coordinate system.

Based on the calibrated coordinates of GNSS antennas, TPS targets and AB axes center in the initial state of feed cabin, we establish the local Cartesian coordinate system where the origin G1 and $\overrightarrow{G1G2}$ is x-axis. The unit matrix of local coordinate system $\mathrm{M} = [\overrightarrow{x'}\,\overrightarrow{y'}\,\overrightarrow{z'}]$ can be obtained in the initial state as the following:

$$\begin{cases} \overrightarrow{x'} = \dfrac{\overrightarrow{G1G2}}{\left|\overrightarrow{G1G2}\right|} \\ \overrightarrow{z'} = \dfrac{\overrightarrow{G1G2}\times\overrightarrow{G1G3}}{\left|\overrightarrow{G1G2}\times\overrightarrow{G1G3}\right|} \\ \overrightarrow{y'} = \overrightarrow{x'} \times \overrightarrow{z'} \end{cases} \tag{1}$$

Similarly, by the GNSS measurement, we can calculate the unit matrix of local coordinate system $\mathrm{N} = [\vec{x}\,\vec{y}\,\vec{z}]'$ at any time. Then, the attitude K of the star frame in the global coordinate can be obtained as:

$$\mathrm{K} = \mathrm{M} * N^{-1} \tag{2}$$

The real-time position of AB axes center O_{ab} is:

$$[\mathrm{x'y'z'}]' = \mathrm{K} * \overrightarrow{G1O_{ab}}' + [x_{G1}y_{G1}z_{G1}]' \tag{3}$$

3 The Importance of BDS/GPS/GLONASS Data Fusion

Because FAST is located in the Karst depression, the surrounding mountains and the reflectors can cause a lot of problems, if we only use the common GPS + GLONASS RTK measurement model. The number of available satellites decreases, and multipath effects happen in the raise and fall of feed cabin. These can affect the RTK measurement accuracy. Therefore, to improve, the RTK measurement accuracy, we need to add more high-precision and high-reliability visible satellites. Based on the rapid development of the BeiDou navigation and positioning system and its regional positioning advantages in China, we proposed to use the RTK measurement of BDS/GPS/GLONASS data fusion. Figures 5 and 6 show

that the static RTK measurement data from GPS + GLONASS and BDS + GPS + GLONASS at the lowest point. The collecting time is respectively 16 and 24 h, and the measured frequency is 5 Hz (Fig. 4).

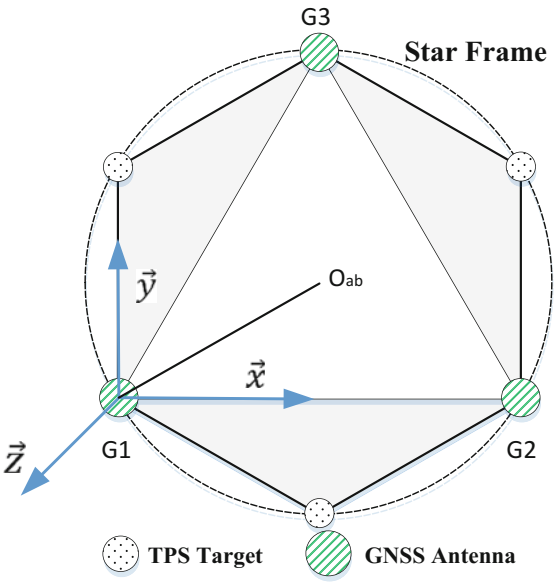

Fig. 4 Layout of GNSS antenna and TPS target

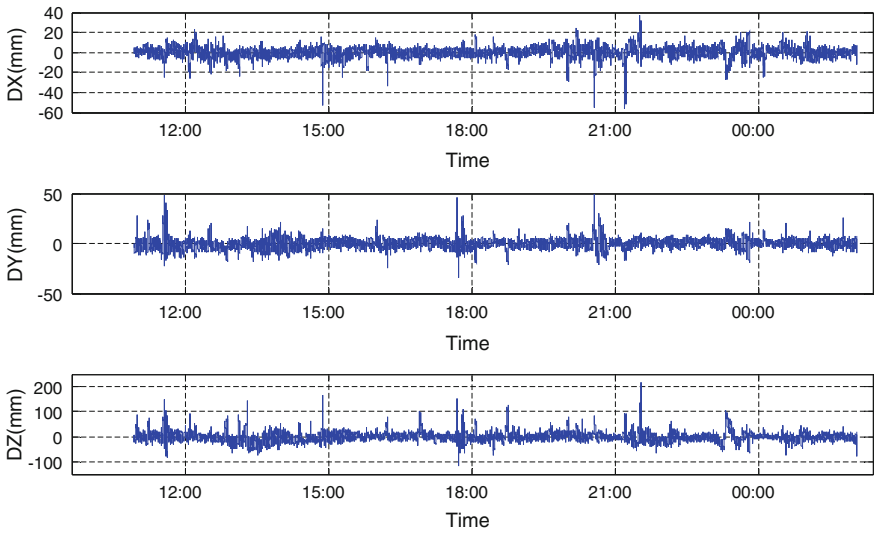

Fig. 5 Deviation of the GPS + GLONASS measured data (the lowest point)

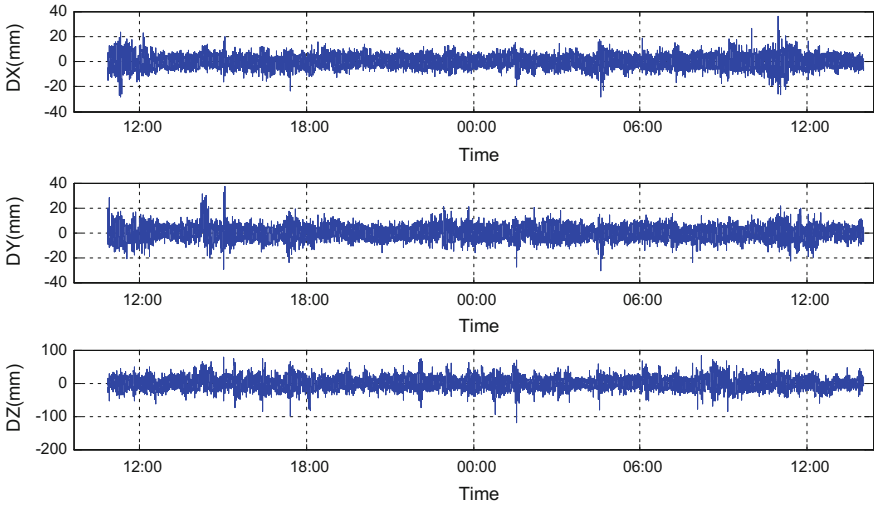

Fig. 6 Deviation of the BDS + GPS + GLONASS measured data (the lowest point)

The improvement of combining BDS are

1. RMS decreases in all directions: horizontal direction from 5 mm reduced to 3.6 mm; elevation direction from 18 mm reduced to 12 mm.
2. The range of data becomes smaller: horizontal direction from 50 mm reduced to 40 mm; elevation direction from 230 mm reduced to 120 mm.

Figure 7 shows the number of BDS/GPS/GLONASS available satellites at the lowest point (24 h). The minimum number of GPS and GLONASS available

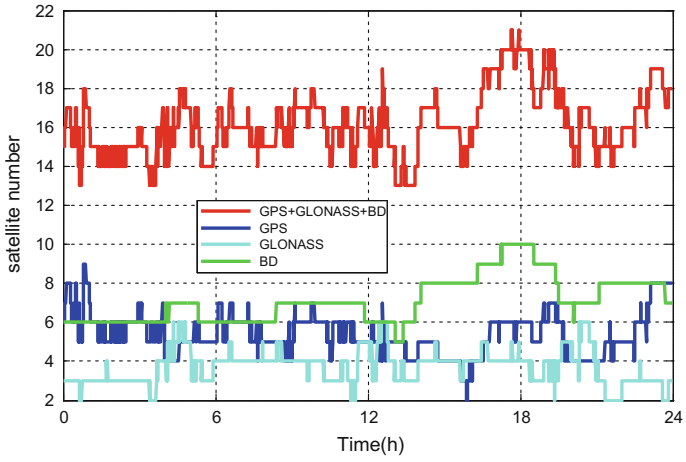

Fig. 7 The number of available satellites at the lowest point

Table 1 Comparative the RMS of measurements before and after the added BDS (mm)

	X_RMS	Y_RMS	Z_RMS
GPS + GLONASS	5	4.6	18.8
BD + GPS + GLONASS	3.6	4	12.9

satellites is two. At this time, only using the single satellite GPS, GLONASS, or double satellite GPS + GLONASS RTK measurement will not obtain the fixed solution. The minimum number of BeiDou satellite is five, which makes it available to obtain a fixed solution. However, the BDS + GPS + GLONASS fusion RTK will get more stable and reliable measurement data to ensure the safety during the raise and fall of feed cabin (Table 1).

4 Analysis of RTK Measurement Accuracy

The measurement accuracy of total station is 0.6 mm + 1 ppm, higher than RTK accuracy. By comparing total station and RTK measurement data on the trajectory of feed cabin, we can analyze RTK accuracy.

Select the data measured on January 4, 2016 as a comparison. Figure 8 shows the trajectory of AB axes center (the movement speed is 24 mm/s).

The total station data is considered as the true value, to compare with RTK data. Figure 9 shows the deviation of RTK measurement data in the horizontal direction and elevation direction.

As can be seen from Fig. 9, when the speed of feed cabin goes up to 24 mm/s, except for some bad points. The deviation range of RTK measurement data is ±10 mm in the horizontal direction and ±20 mm in elevation direction.

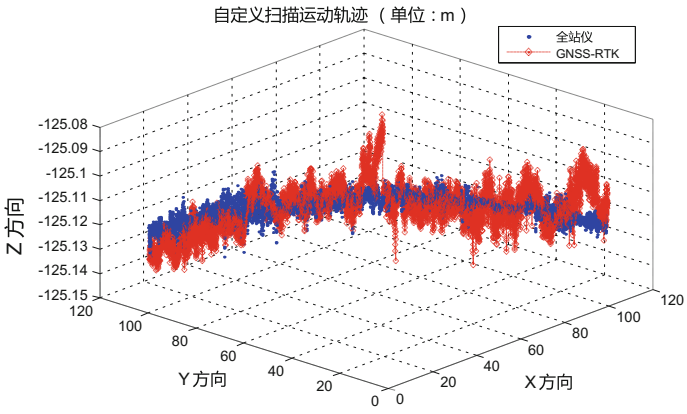

Fig. 8 The trajectory of AB axis center

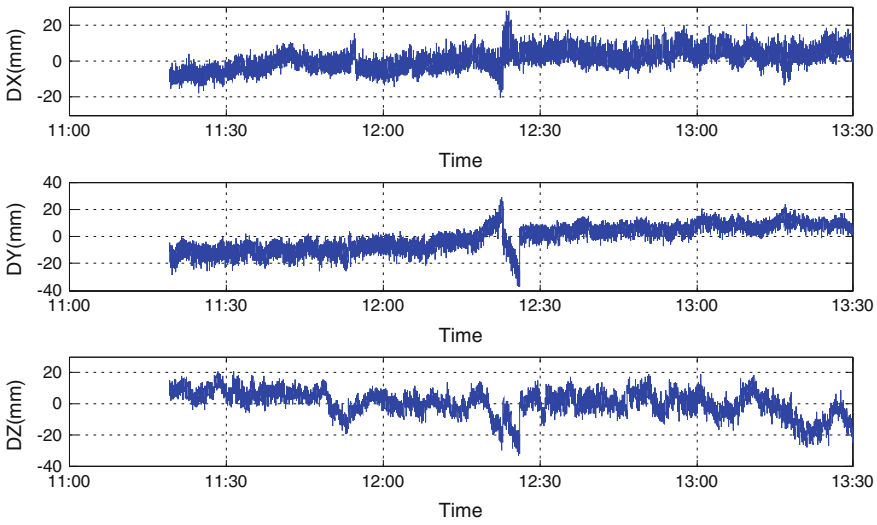

Fig. 9 Deviation of measured data

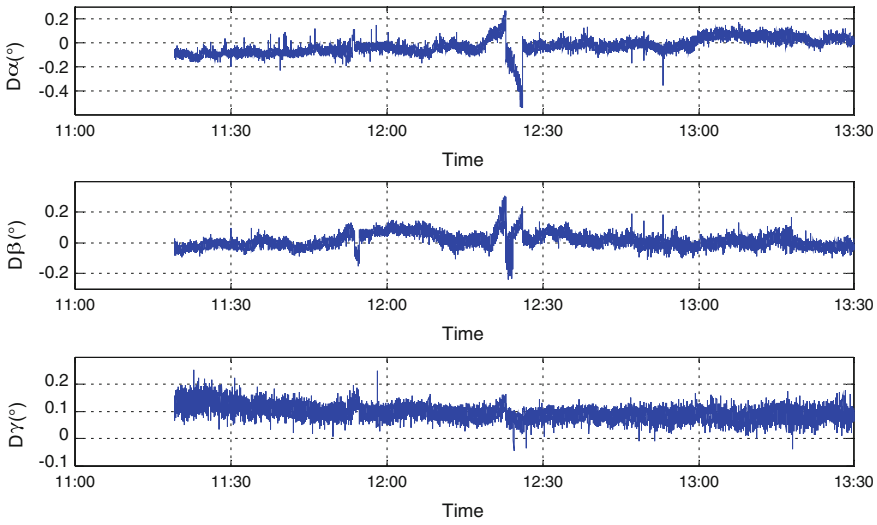

Fig. 10 Deviation of attitude angle

Pre-analysis shows that, the reason why this the bad points jumped away from the average, is that the location of the feed compartment near the surrounding mountains at that time. The deviation range of spin angle is ±0.1° (in Fig. 10). The RMS of RTK measurement data is in Table 2.

Table 2 RMS of RTK measurement data(mm)

	X	Y	Z
RMS	3.8818	5.5179	7.5990

The above data show the measurement accuracy of fusion RTK. In actual astronomical observation, the running speed of feed cabin is 11 mm/s. With the reduction of the speed (24–11 mm/s), the measurement accuracy of fusion RTK will be improved. Therefore, the accuracy of BDS/GPS/GLONASS fusion RTK measurement meets technical requirements, and it can guarantee the normal observation and safe operation of FAST.

5 Summary and Conclusions

Taking positioning advantage of the BeiDou satellite navigation system in China, we combine this BDS with GPS and GLONASS satellite navigation and positioning system, to do the RTK measurement. It can reach location accuracy of the feed cabin (≤ 17 mm)for astronomical observation, and guarantee the safe operation of FAST when the total station cannot work, such as rain, fog and other inclement weather. In the future, we will adopt the method of filtering to improve measurement accuracy and stability of fusion RTK.

In addition, the successful application of fusion RTK measurement in FAST, provides an effective solution for the real-time dynamic positioning of all weather and high precision for the upcoming large astronomical telescopes.

Acknowledgements This work is supported by China National Science Foundation of China (No: 11273001,11503048,11373001).

References

1. Nan RD, Li HX (2014) Progress of FAST in science, technique and instrument (in Chinese). Sci Sin-Phys Mech Astron 44:1063–1074. doi:10.1360/SSPMA2014-00153
2. Yang YX, Li JL, Wang AB et al (2014) Preliminary assessment of the navigation and positioning performance of BeiDou regional navigation satellite system. Sci China: Earth Sci 57:144–152. doi:10.1007/s11430-013-4769-0
3. Li HF, Dang YM et al (2014) Research on model and performance of BDS/GPS/GLONASS multi-mode fusion positioning. Bull Surveying Mapp (9):1–5. doi:10.13474/j.cnki.11-2246.2014.0280

Research on BDS/GPS Combined Single-Epoch Attitude Determination Performance

Kang Zhang and Jinming Hao

Abstract With the continuous development of science and technology, the attitude precise determination of the carriers is of important practical value as to whether in the military, civilian or commercial aspects. The attitude determination using satellite navigation system has the advantages of short initialization time, no accumulation of errors, low cost, light and flexible, and so on, and it is becoming a hotspot in the field of satellite navigation. With the rapid development and improvement of Beidou global satellite navigation system, the attitude determination by combining BDS and GPS can multiply the number of satellites, effectively improve the geometric structure of satellite space, which can greatly enhance the performance of carrier attitude determination with GNSS in complex environment. In this paper, the theory and algorithm of BDS/GPS combination single-epoch attitude determination are studied. The mathematical model of BDS/GPS combination single-epoch attitude determination is constructed and the related program is worked out. Through static experiment and dynamic sports-car experiment, the accuracy stability and reliability of BDS/GPS combination single-epoch attitude determination are analyzed and validated in complex observation environments with a serious block. The experimental results show that the BDS/GPS combination can still remain the accuracy of yaw 0.1°, pitch and roll 0.2°, and the success rate of attitude 100%, and the BDS/GPS combination can effectively improve the accuracy and usability of attitude determination with BDS or GPS single-system in complex environment with a serious block.

Keywords BDS/GPS combination · Single-epoch · Attitude determination · Accuracy

K. Zhang (✉)
Beijing Satellite Navigation Center, Beijing 100094, China
e-mail: 289147188@qq.com

J. Hao
College of Navigation and Aerospace Engineering,
Information Engineering University, Zhengzhou 450001, China

J. Sun et al. (eds.), *China Satellite Navigation Conference (CSNC) 2017 Proceedings: Volume I*, Lecture Notes in Electrical Engineering 437,
DOI 10.1007/978-981-10-4588-2_3

1 Instruction

There are advantages of convenience, low-cost, no accumulation of errors and so on of the carrier attitude determination with the use of the Global Navigation Satellite System (GNSS) [1]. At present, the US Global Positioning System (GPS) has been provided with all-weather, all-round navigation, positioning, timing, speed measurement and other services [2], and China's Beidou satellite navigation system (BDS) is developing rapidly from regional system to global system [3]. The carrier attitude determination through BDS/GPS combined can multiply the number of satellites and improve the geometrical structure of satellite [4], which greatly enhances the performance of attitude determination based on GNSS, which is superior to single system especially in complex environment.

Presently, the algorithms and techniques of attitude determination based on pseudorange and carrier phase observer of GPS are relatively mature, which can provide high accuracy and reliability of attitude determination [5]. Li [6] had studied on related algorithms and techniques of GPS attitude determination in detail. Teunissen et al. [7] tested the GNSS single-frequency carrier phase attitude determination method by land, sea and air carrier experiments, and verified the accuracy and usability of GNSS single-frequency attitude determination. It is mainly focused on algorithms and theoretical research of GPS/BDS combined attitude determination. In this paper, the mathematical model of BDS/GPS combined single-epoch attitude determination is constructed, based on related theory and algorithms, and the accuracy and usability of which under complex observation environment, such as urban buildings and trees shelter, is studied emphatically through experiments.

2 Mathematic Model of BDS/GPS Combined Single-Epoch Attitude Determination

The three attitude angles of the carrier (yaw, pitch, and roll) can be determined in real time using the baseline vectors, which between the antennas fixed on a rigid carrier (no less 2 antennas) are accurately determined through the carrier phase difference. In this section, the theory and algorithms of BDS/GPS combined attitude determination are analyzed.

2.1 Unification of BDS/GPS Combined Space-Time Reference

The uniformity of the space-time observational data must be considered for the attitude determination of combining different satellite navigation systems. In this paper, the BDS space-time datum is unified to that of GPS.

The time reference of BDS is named BDT, and that of GPS is GPST, whose basic units are both based on the International System of Units (SI) seconds, rather than doing leap second processing. Their time origin is 0 o'clock on January 6th, 1980(UTC) and o'clock on January 1 st, 2006(UTC) separately. The BDT is 14 s slower than the GPST due to 14 times of UTC leap seconds during these two moments.

Here,

$$BDT = GPST - 14^s \tag{1}$$

CGCS2000 coordinate system and WGS-84 coordinate system, which is respectively used in BDS and GPS, can be regarded as consistent regarding of the definition and implementation of the two coordinate systems. In practical applications, the difference between CGCS2000 and WGS-84 can be ignored as the ultra-short baseline is applied in the carrier attitude determination [8, 9].

2.2 Construction of BDS/GPS Combined Observation Equation

In the process of attitude determination, because of ultra-short baseline, the short baseline double difference model is used to eliminate the most common errors such as atmospheric delay error, clock error, orbit error, and so on [2]. BDS and GPS are combined to first form a single-difference observation between two stations in the same epoch on the same satellite, and then the difference of the single-difference observations of two different satellites is done. It should be pointed out that the double difference method within the same system is adopted in this paper [5], that is, BDS and GPS respectively select the reference satellite when doing difference, and only between the same frequency, so as to guarantee the integer characteristic of double difference ambiguity.

Assuming that the receiver antenna A in the carrier plane is the base station and the antenna B is the rover. The number of BDS and GPS common-sighted satellites respectively observed simultaneously are m and n. The i_R-th satellite of BDS and the i_G-th satellite of GPS are respectively selected as the reference satellite within the system. Then the pseudo-range and carrier phase double-difference observation equation of BDS/GPS combined can be classified as:

$$\begin{cases} \nabla\Delta P_{A,B}^{i_R,j_R}(t) = \nabla\Delta\rho_{A,B}^{i_R,j_R} \\ \nabla\Delta P_{A,B}^{i_G,j_G}(t) = \nabla\Delta\rho_{A,B}^{i_G,j_G} \\ \lambda^R\nabla\Delta\phi_{A,B}^{i_R,j_R} = \nabla\Delta\rho_{A,B}^{i_R,j_R} - \lambda^R\nabla\Delta N_{A,B}^{i_R,j_R} \\ \lambda^G\nabla\Delta\phi_{A,B}^{i_G,j_G} = \nabla\Delta\rho_{A,B}^{i_G,j_G} - \lambda^G\nabla\Delta N_{A,B}^{i_G,j_G} \end{cases} \tag{2}$$

where, i and j indicate the satellite number, subscript R and G indicate BDS and GPS, and $\nabla\Delta$ is the double difference operator.P means pseudo-range observation, ϕ means carrier phase observation, ρ is the distance from satellite to ground, N is carrier phase ambiguity, and λ represents the carrier wavelength.

According to the above double-difference observation equation, the baseline vector AB composed of the receiver antenna A and the antenna B on the carrier plane can be obtained by adding the known baseline length constraint LAMBDA algorithm [9].

2.3 Calculation of BDS/GPS Combined Attitude Parameter

Suppose there are three BDS/GPS dual-mode antennas A, B and C fixed on the plane of a rigid motion carrier, in which the base line AB composed of the antenna A and B pointing in the carrier's heading direction, while the baseline AC composed of the antenna A and C pointing to the right side, and the baseline AB and the baseline AC are perpendicular to each other, as shown in Fig. 1.

The coordinate of the baseline vector AB in the ECEF $\begin{bmatrix}\Delta x_1 & \Delta y_1 & \Delta z_1\end{bmatrix}^T$ is converted to that in the local horizontal coordinate system $\begin{bmatrix}\Delta e_1 & \Delta n_1 & \Delta u_1\end{bmatrix}^T$. Then the yaw angle and pitch angle of the carrier on the current epoch can be obtained by solving Eqs. (3) and (4).

$$\theta_y = \arctan(\Delta e_1/\Delta n_1) \tag{3}$$

$$\theta_p = \arctan\left(\Delta u_1/\sqrt{\Delta e_1 \times \Delta e_1 + \Delta n_1 \times \Delta n_1}\right) \tag{4}$$

Then, the coordinate of the baseline vector AC in the local horizontal coordinate system $\begin{bmatrix}\Delta e_2 & \Delta n_2 & \Delta u_2\end{bmatrix}^T$ is sequentially rotated the angle of θ_y around the U-axis

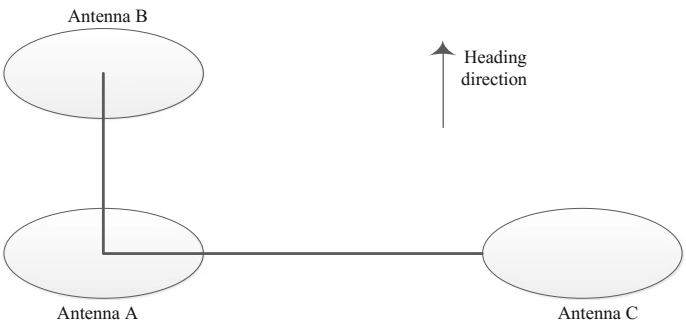

Fig. 1 Antenna configuration

and θ_p around the E-axis of the local horizontal coordinate system to obtain the coordinate $[\Delta e_{22} \quad \Delta n_{22} \quad \Delta u_{22}]^T$, finally, the roll angle of the carrier can be obtained by solving Eq. (5).

$$\theta_r = -\arctan(u_{22}/e_{22}) \tag{5}$$

3 Experiment and Analysis

In theory, BDS/GPS combined will be better than the single system in terms of the satellite space configuration, resulting in a more accurate baseline solution, thus a more accurate attitude solution. In order to study the accuracy and reliability of BDS single-system attitude determination and the advantages of BDS/GPS combined attitude determination compared with single-system, static and dynamic car experiments are carried out and analyzed. In the static experiment, the attitude measurement results of every 5° cut-off angle from 15° to 50° are analyzed and compared, and the dynamic car experiment is carried out under complex observation environment such as city buildings and trees shelter.

Because the short baseline double difference observation equation is applied, the correction of other error terms is neglected, the broadcast ephemeris is used, and the addition of known baseline length constraint LAMBDA algorithm by single epoch processing mode is used to fix the integer ambiguity, using the ratio value to test the correctness and availability of ambiguity integer solution (ratio = 2.0). Regardless of the static experiment or dynamic car experiment, the antenna configuration on the carrier plane is shown in Fig. 1, the Trimble R7 receivers are used with the data sampling rate setting to 1 s.

3.1 Static Experiment

The ultra-short baseline observations on the roof of a Beijing satellite experimental building on September 11th, 2016 are used in the static experiment. The observation lasts about 90 min. The length of the baseline AB is 2.958 m, and the length of the baseline AC is 4.011 m.

In this paper, the three schemes of BDS single system, GPS single system and BDS/GPS combined are carried out to solve the carrier's attitude in 7 cases with cut-off angles of 15°, 20°, 25°, 30°, 35°, 40° and 45° respectively. The RMS of the three attitude angles of the three schemes at different cut-off angles are shown in Fig. 2.

The detailed RMS statistics of the three attitude angles at different cut-off angles are shown in Table 1. It can be seen from Fig. 2 and Table 1 that with the increase of the cut-off angle, the error of BDS or GPS single-system attitude determination is bigger and bigger, while BDS/GPS combined can always guarantee RMS 0.1° of the yaw angle, RMS 0.2° of the pitch angle and roll angle.

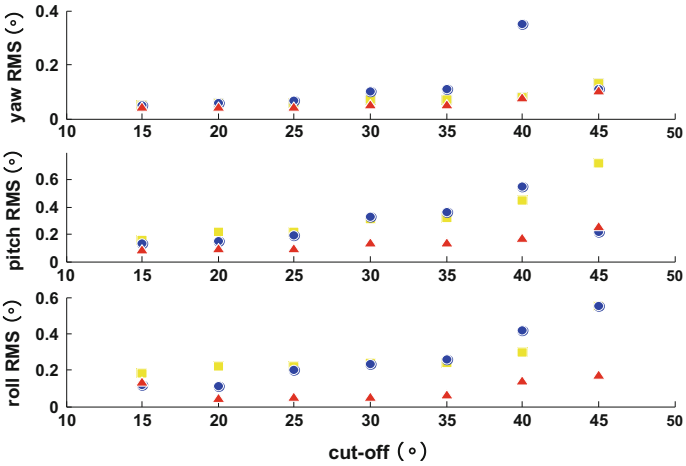

Fig. 2 Attitude at different cut-off

Table 1 RMS of attitude at different cut-off (°)

Cut-off		15°	20°	25°	30°	35°	40°	45°
Yaw	BDS	0.05	0.06	0.06	0.07	0.07	0.08	0.13
	GPS	0.05	0.06	0.07	0.1	0.11	0.35	0.11
	BDS/GPS	0.04	0.04	0.04	0.05	0.05	0.08	0.1
Pitch	BDS	0.16	0.22	0.22	0.31	0.32	0.45	0.72
	GPS	0.13	0.15	0.19	0.33	0.35	0.55	0.22
	BDS/GPS	0.08	0.09	0.09	0.13	0.13	0.17	0.25
Roll	BDS	0.18	0.22	0.22	0.24	0.24	0.3	0.55
	GPS	0.12	0.11	0.2	0.23	0.26	0.42	0.55
	BDS/GPS	0.13	0.04	0.05	0.05	0.06	0.14	0.17

The attitude resolution of the current epoch is considered successful when at least two baselines among the three baselines AB, AC and BC have obtained the fixed ambiguity solution (ratio = 2.0). The comparison of the success rate of attitude output of BDS or GPS single system and BDS/GPS combined at different cut-off angles is shown in Fig. 3.

It can be seen that in the case of low cut-off, BDS and GPS single system can achieve high attitude output success rate because of the large number of visible satellites. However, when the cut-off increases to 35°, the attitude output success rate of single-system drops sharply, while BDS/GPS combined can still keep the attitude output success rate at 100%. It is shown that BDS/GPS combined can guarantee the reliability of attitude determination compared with BDS or GPS single system.

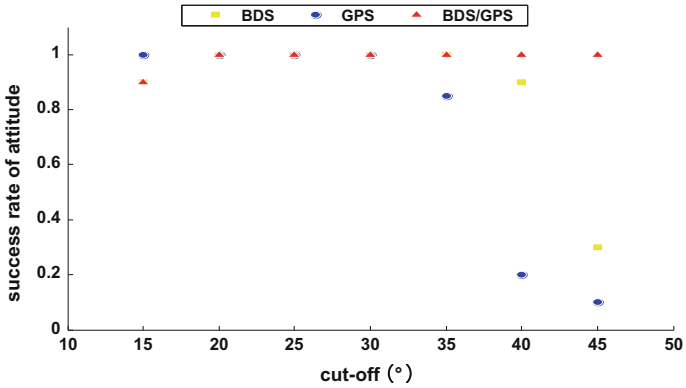

Fig. 3 Success rate of attitude at different cut-off

3.2 Dynamic Experiment

In order to further analyze the accuracy stability and reliability of BDS/GPS combined attitude determination in the dynamic environment of urban high-rise buildings and trees shelter, the sports car experiment in a certain urban area of Beijing is designed and carried out on November 18th, 2016 in this paper, with the car speed of about 30 km/h, lasting about 30 min. During the course of the sports car, the Trimble receiver antennas are fixed on the roof plane of the car, the length of baseline AB is 1.866 m and the length of baseline AC is 1.052 m. In addition, a set of Trimble vehicle positioning and attitude determination system (POS LV 220. Applanix) is also placed on the car, used as the reference value of BDS/GPS attitude determination results.

The results of the attitude determination of BDS and BDS/GPS combined are shown in Fig. 4.

The results of the single-epoch attitude error of BDS single system and BDS/GPS combined are summarized in Table 2. It can be seen that in the dynamic sports car, the BDS single system can obtain yaw accuracy of about 0.2°, pitch angle and roll angle of about 0.6°, while the corresponding attitude errors of BDS/GPS combined are respectively reduced to 0.142°, 0.442° and 0.319°. The results show that the stability and reliability of attitude determination can be effectively improved by the combination of BDS and GPS compared to BDS single system.

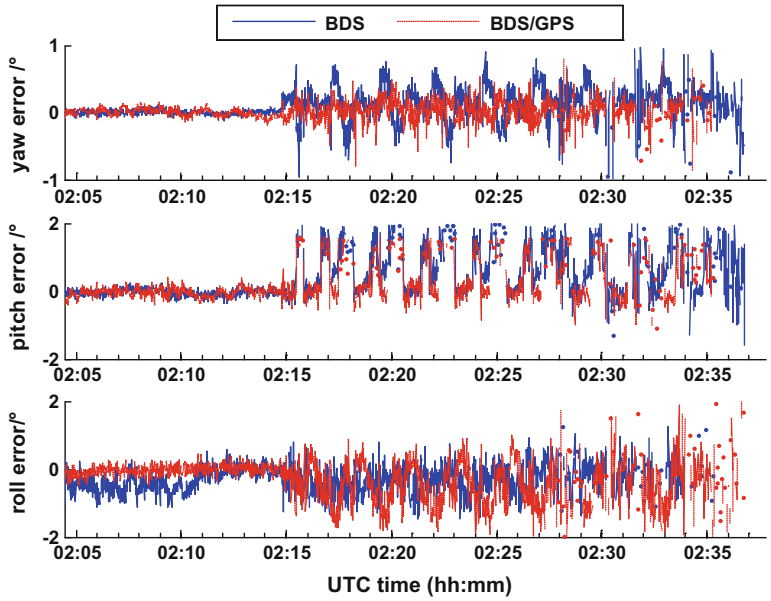

Fig. 4 BDS and BDS/GPS single-epoch attitude error

Table 2 Single-epoch attitude error statistics (°)

Attitude	BDS		BDS/GPS	
	MAX	RMS	MAX	RMS
Yaw	0.95	0.254	0.949	0.142
Pitch	1.999	0.665	1.512	0.442
Roll	2.012	0.599	1.489	0.319

4 Conclusions

In this paper, the theory and algorithm of single-epoch attitude determination of BDS/GPS combined are studied, and the mathematical model of BDS/GPS combined single-epoch attitude determination is constructed. The accuracy and success rate of single-epoch attitude determination of BDS or GPS single system and BDS/GPS combined at different cut-off angles are analyzed and compared in the static experiment, and the dynamic car experiment is set up in the case of severe occlusion in the city to further study the accuracy stability and reliability of BDS/GPS combined single-epoch attitude determination. The following conclusions are drawn:

1. With the increase of the cut-off, the error of BDS or GPS single-system attitude determination is bigger and bigger, while BDS/GPS combined can always guarantee RMS 0.1° of the yaw angle, RMS 0.2° of the pitch angle and roll angle.
2. When the cut-off increases to 35°, the attitude output success rate of single-system drops sharply, while BDS/GPS combined can still keep the attitude output success rate at 100%.
3. The dynamic experiment shows that the stability and reliability of attitude determination can be effectively improved by BDS/GPS combined compared to BDS or GPS single system. So BDS/GPS combined is particularly suitable for attitude determination under urban and other serious occlusion environments.

References

1. Li K, Yang L, Chai L, Ding A, Guo Z (2014) GNSS Positioning theory. Coal Industry Press
2. Hao J, Lv Z (2015) Theory and method of satellite positioning. People's Liberation Army Press
3. Wang B, Miao L, Wang S, Jun Shen (2009) A constrained LAMBDA method for GPS attitude determination. GPS Solutions 13(2):97–107
4. Li H, Dang Y, Li M et al (2013) Research on spatio tempora unification of BDS/GPS/GLONASS multi-mode fusion navigation and positioning. J Geodesy Geodyn 33 (4):73–78
5. Tang W, Deng C, Gao L (2013) Preliminary results of single epoch baseline solution based on Beidou navigation satellite system. Geomat Inf Sci Wuhan Univ 38(8)
6. Li J (2004) Research on GPS attitude measurement and related technologies. PLA Information Engineering University
7. Teunissen P, Giorgi G, Buist P (2011) Testing of a new single-frequency GNSS carrier phase attitude determination method: land, ship and aircraft experiments. GPS Solut 15(1):15–28
8. Wang B, Miao L, Wang S, Jun Shen (2009) A constrained LAMBDA method for GPS attitude determination. GPS Solutions 13(2):97–107
9. Giorgi G (2011) GNSS carrier phase-based attitude determination: estimation and applications. Delft University of Technology, TU Delft

Calculating High Frequency Earth Rotation Parameters Using GPS Observations and Precision Analysis

Xuexi Liu, Erhu Wei and Lingxuan Wang

Abstract The earth rotation parameters (ERP) have a strong correlation with the migration and movement of earth materials, extraterrestrial world gravity and the load deformation of solid earth. On the other hand, ERP is a very important parameter when converting the earth reference system to the celestial reference system. But the International Earth Rotation Service(IERS) and International GNSS Service(IGS) only release one ERP per day which cannot satisfy the user who need the high frequency of ERP. However, there are amounts of Global Positioning System(GPS) data which can be used to estimate ERP with high time resolution and long time span. Based on this, global uniformly distributed 40 IGS stations are selected to estimate ERP by using the data of the Day of Year(DOY) from 1 to 180 of 2015 with Bernese soft 5.0. In the first part, 24 h resolution of ERP is estimated. The precision of polar motion x_p, y_p can be achieved at the precision 0.289, 0.245 mas while the precision of UT1-UTC can be achieved at 0.0342 ms which are made a difference with the results of IGS. In the last part of the paper, the 2 h resolution of ERP are estimated and high frequency time series are got. The precision of high frequency polar motion x_p, y_p can be achieved at the precision 0.754, 0.688 mas and the precision of high frequency UT1-UTC can be achieved at 0.1050 ms which are made a difference with the results of IGS at UTC 12:00. The high frequency results have lower precision and stability compared with 24 h

X. Liu (✉) · E. Wei · L. Wang
School of Geodesy and Geomatics,
Wuhan University, Wuhan 430079, Hubei, China
e-mail: liuxuexixuzhou@126.com

E. Wei
e-mail: ehwei@whu.edu.cn

L. Wang
e-mail: geo_wlx@163.com

E. Wei
Key Laboratory of Geospace Environment and Geodesy,
Ministry of Education, Wuhan 430079, Hubei, China

J. Sun et al. (eds.), *China Satellite Navigation Conference (CSNC) 2017 Proceedings: Volume I*, Lecture Notes in Electrical Engineering 437,
DOI 10.1007/978-981-10-4588-2_4

resolution results, but still in the acceptable range. Both the results of 24 h resolution and high frequency series have different degrees of systematic deviation. The research above can provide a reference for calculating ERP using BeiDou observations.

Keywords Earth rotation parameter · GPS · High frequency · Precision analysis

1 Introduction

The Earth Orientation Parameters (EOP) include the Earth Rotation Parameters (ERP), precession and nutation in which the ERP refers to the polar motion and the length of day (LOD). The ERP have a strong correlation with the migration and movement of earth materials, extraterrestrial world gravity and the load deformation of solid earth [1]. On the other hand, ERP is a very important parameter when converting the earth reference system to the celestial reference system and also plays an significant role in spacecraft precise orbit determination and autonomous navigation [2, 3].

Nowadays, there are multiple space geodesy methods to determinate the ERP. The main technical means are VLBI(Very Long Baseline Interferometry), SLR(Satellite Laser Ranging), LLR (Lunar Laser Ranging), GPS and so on. In which GPS is a vital method to determinate ERP, because there are amounts of GPS data which can be used to estimate ERP with high time resolution, long time span and low cost [4]. Many application areas need high frequency variations. But most of the IERS and IGS ERP series, such as IERS C04 and Bulletin A (rapid prediction ERP series) do not contain high frequency variations because they are smoothed by Vondrak filtering. Based on this, this paper calculates high frequency variations by GPS in order to make a contribution to space geodesy parameters [5, 6]. At the same time, this paper is also hoped to provide a reference for the calculation of ERP by BeiDou.

2 The Principle of GPS Calculation ERP

Generally, coordinates of the receiver are given in the international terrestrial reference system (ITRF). But when calculating the distance vector ρ between satellite and receiver, the position vectors of satellite and receiver are usually converted to the same international celestial reference frame (ICRF). So it is necessary to convert the reference system of receivers from ITRF to ICRF. The vector $\vec{R}(t_i)$ in ICRF can be expressed by the position vector $\vec{R}_0^i$ in ITRF as:

$$\vec{R}(t_i) = PNSW\vec{R}_0^i \tag{1}$$

where P, N, S and W are the matrix of precession, nutation, earth rotation and polar motion, respectively.

In this paper, the double difference model is used to calculate the ERP. And the estimated parameters are the coordinates of the stations, the satellite coordinates, the ERP and the neutral atmospheric delay. The GPS carrier phase observations can be expressed as a function model by the estimated parameters as:

$$L = M(t, X_{SP}, X_T, X_N, X_{erp}, X_{atm}) \tag{2}$$

where M represents the function model of the observations and estimated parameters; t, X_{SP}, X_T, X_N, X_{atm} are time parameters, the initial orbital and perturbation parameters (radiation pressure model), the station coordinates, the phase ambiguity parameters, the atmosphere delay parameters respectively. X_{erp} is ERP which includes the polar motion parameters x_p, y_p and the LOD parameters D_R [7, 8]. The formula (2) can be linearized as:

$$L = C_0 + \frac{\partial M}{\partial X_{SP}}\delta X_{SP} + \frac{\partial M}{\partial X_T}\delta X_T + \frac{\partial M}{\partial X_N}\delta X_N + \frac{\partial M}{\partial X_{erp}}\delta X_{erp} + \frac{\partial M}{\partial X_{atm}}\delta X_{atm} + \varepsilon \tag{3}$$

where C_0, ε are the approximate values calculated by initial ERP and observation noise respectively [9].

The transformation matrix of the polar motion in x and y directions are divided into:

$$\frac{\partial R_1}{\partial x_p} = PNS\frac{\partial W}{\partial x_p}R_t(t) = PNS\begin{bmatrix} -z \\ 0 \\ x \end{bmatrix} \tag{4}$$

$$\frac{\partial R_1}{\partial y_p} = PNS\frac{\partial W}{\partial y_p}R_t(t) = PNS\begin{bmatrix} -x_p y \\ x_p x + z \\ -y \end{bmatrix} \tag{5}$$

where R_1 is the position vector in the inertial coordinate system; x_p, y_p are the component in x and y directions; D_R is the first order change rate of UT1-UTC (changes in length of day). Therefore:

$$\frac{\partial R_1}{\partial D_R} = \frac{\partial R_1}{\partial \theta_g}\frac{\partial \theta_g}{\partial D_R} \tag{6}$$

$$\frac{\partial R_1}{\partial \theta_g} = PN \frac{\partial S}{\partial \theta_g} W^T = PNSW \begin{bmatrix} -y - y_p z \\ x - x_p z \\ y_p x + x_p y \end{bmatrix} \tag{7}$$

$$\frac{\partial \theta_g}{\partial D_R} = 2\pi(1+k) \frac{\partial UT1}{\partial D_R} = 2\pi(1+k)(t - t_0) \tag{8}$$

$$\frac{\partial R_1}{\partial \dot{D}_R} = \frac{\partial R_1}{\partial D_R}(t - t_0) \tag{9}$$

$$\theta_g = GAST = 2\pi[GMST(UT0) + (1+k)UT1] + \Delta\varphi \ \cos\varepsilon \tag{10}$$

where GAST is Greenwich Apparent Sidereal Time (GAST); GMST is Greenwich mean sidereal time (GMST); $\Delta\varphi$ is nutation in longitude; ε is obliquity respectively.

Supposing there are m stations observing n satellites, the partial derivative can be inserted into the observation equation:

$$\underset{m\times j,1}{v} = \underset{m\times j,3}{B}\ \underset{3\times 1}{x} - \underset{m\times j,1}{l}, \qquad \underset{m\times j, m\times j}{P} \tag{11}$$

In the formula above:

$$\underset{m\times j,t}{B} = \begin{pmatrix} \frac{\partial M_1}{\partial X_{sp}} & \frac{\partial M_1}{\partial X_T} & \cdots & \frac{\partial M_1}{\partial X_{atm}} \\ \vdots & & & \vdots \\ \frac{\partial M_i}{\partial X_{sp}} & \frac{\partial M_i}{\partial X_T} & \cdots & \frac{\partial M_i}{\partial X_{atm}} \\ \vdots & & & \vdots \\ \frac{\partial M_n}{\partial X_{sp}} & \frac{\partial M_n}{\partial X_T} & \cdots & \frac{\partial M_n}{\partial X_{atm}} \end{pmatrix},$$

$$\underset{m\times j,1}{l} = \begin{pmatrix} L_1 - M_1(X_0) + \varepsilon_1 \\ \vdots \\ L_i - M_i(X_0) + \varepsilon_i \\ \vdots \\ L_n - M_n(X_0) + \varepsilon_n \end{pmatrix}, \ \underset{m\times j,1}{v} = \begin{pmatrix} v_1 \\ \vdots \\ v_i \\ \vdots \\ v_n \end{pmatrix}, \ \underset{t,1}{x} = \begin{pmatrix} \delta X_{sp} \\ \delta X_T \\ \delta X_N \\ \delta X_{erp} \\ \delta X_{atm} \end{pmatrix}$$

The ERP can be estimated by using least square method and its precision evaluation formulas are as follows:

$$X = (B^T PB)^{-1}(B^T Pl) = \left(\sum_{i=1}^{i=k} B_i^T P_i B_i\right)^{-1} \sum_{i=1}^{i=k} B_i^T P_i l_i \tag{12}$$

$$Q = \sigma_0^2 \left(\sum_{i=1}^{i=k} B_i^T P_i B_i\right)^{-1}, \ \sigma_0^2 = \frac{V^T V}{n-t} \tag{13}$$

where $(n-t), V, \sigma_0$ and Q are freedom, residual, variance of unit weight and coefficient matrix respectively in the formula above. Through the above calculation, the earth rotation parameters can be calculated using GPS observations.

3 Data Processing and Analysis

3.1 Choose Most Appropriate Station Numbers

In this paper, Bernese soft 5.0 is used for data processing. The paper focus on the calculating of ERP, thus, the parameters of the pole motion are loose constraint. The constraint value of polar motion is 3 mas while the change rate of polar motion is 0.3 mas/d. The absolutely strong constrained value of UT1 is 0.00002, while the loose constraint of the change rate of UT1 is 0.02 s/d. The constraint values of 6 orbital elements are 0.01, including a, e, i, n, w, M. The values of 9 solar pressure parameters are set to 0.01. The other parameters are strong constrained. In addition, some other models were used, including the IERS2000 sub-daily polar motion model, the gravity model EGM96, the IAU 2000 Nutation model, the OT_CSRC ocean tide file and the FES2004 Ocean loading correction.

Because of the limitation of computer hardware resource, the more of the number of stations, the much of computation time exponentially. Firstly, the experiment is done to explore the most appropriate number of stations. In the process of solution, the number of IGS stations is increased from 10 to 90, and the increment interval is about 10. The relationship between the number of station and the precision of ERP is shown in Fig. 1. The results show that the precision of ERP estimated by 40 sites can meet the requirements [10]. Continue increasing the number of stations, the precision of the ERP increases a little, but the time increases exponentially.

So, in the estimation experiments, about 40 sites are selected to estimate ERP. There are three main reasons for the selection. First of all, these stations are core sites of International Terrestrial Reference Frame. Second, the mean square errors of coordinates of the sites are less than 1 mm, while the mean square errors of velocity of the sites are less than 0.2 mm per year. Finally all the stations satisfy a

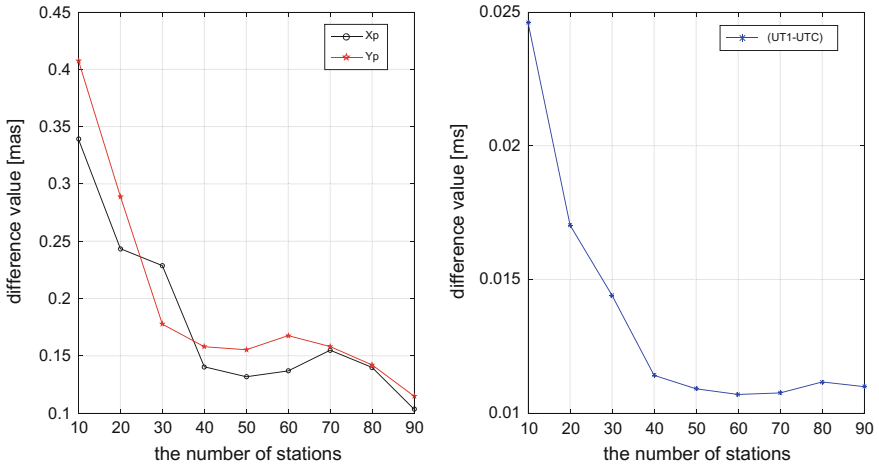

Fig. 1 The relationship between the number of station and the precision of ERP

Fig. 2 The 40 sites selected to estimate ERP

uniform distribution with stable and high quality observations [11]. The distribution of these stations is shown in Fig. 2.

3.2 Estimate ERP with a Frequency of 24 h

Secondly, the experiments of estimating ERP at UTC 12:00:00 every day for 180 days since 2015/01/01 are done in this paper. In order to analysis the precision

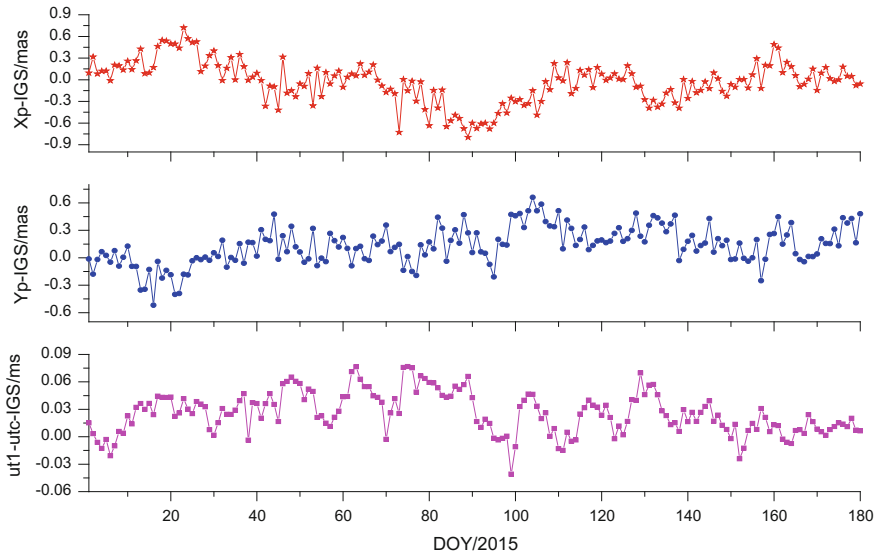

Fig. 3 The absolute difference between estimated results and IGS published values with a frequency of 24 h

Table 1 The statistical results of the absolute difference between estimated results and IGS published values with a frequency of 24 h

	Polar motion x_p (mas)	Polar motion y_p (mas)	UT1-UTC (ms)
Average absolute value	0.218	0.193	0.0281
Max value	0.721	0.660	0.0768
Min value	−0.798	−0.519	−0.0408
RMS	0.289	0.245	0.0342
STD	0.040	0.059	0.0069

of the results, the ERP series are compared to IGS published values [12, 13]. The absolute values of the difference between the calculating results and IGS published values are shown as the Fig. 3. Meanwhile, the statistical results about polar motion and UT1-UTC are illustrated in Table 1.

Fig. 3 and Table 1 show that most of the difference between polar motion x_p and the IGS published values are between positive and negative 0.4 mas and the RMS (Root Mean Square) is 0.289 mas which exists some systematic deviations. Most of the difference between polar motion y_p and the IGS published values are between positive and negative 0.45 mas and the RMS is 0.245 mas which also exists some systematic deviations. Most of the difference between UT1-UTC and the IGS published values are between positive and negative 0.045 ms and the RMS is 0.0342 ms

which also exists some systematic deviations. From the results, conclusions can be come to that the calculation method of ERP is reliable and the precision can meet the requirement.

3.3 Estimate ERP with a Frequency of 2 h

Finally, the experiment of estimating ERP with a frequency of 2 h for 180 days since 2015/01/01 which use the same strategy with Sects. 3.1 and 3.2 are done in this paper. The high frequency values of 2 h about polar motion and UT1-UTC are shown as the Figs. 4 and 5.

Because IGS only gives one solution per day (at UTC 12:00:00), so only the difference for 180 days at the same time (UTC 12:00:00) between IGS values and our results are shown in Fig. 6 and the statistical results are shown in Table 2.

From Fig. 6 and Table 2 we can see that the average absolute difference between high frequency of polar motion x_p at UTC 12:00:00 and IGS values is 0.597 mas, the maximum value is 1.680 mas while the minimum value is −2.740 mas and the RMS is 0.754 mas. The average absolute difference between high frequency of polar motion y_p at UTC 12:00:00 and IGS values is 0.569 mas, the maximum value is 1.939 mas while the minimum value is −1.472 mas and the RMS is 0.688 mas. The average absolute difference between high frequency of UT1-UTC at UTC 12:00:00 and IGS values is 0.075 ms, the maximum value is 0.4493 ms while the

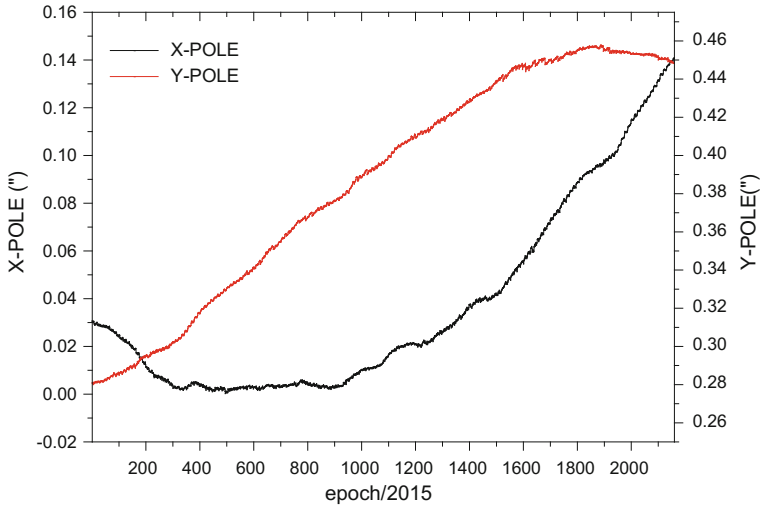

Fig. 4 The results of polar motion x_p, y_p with a frequency of 2 h

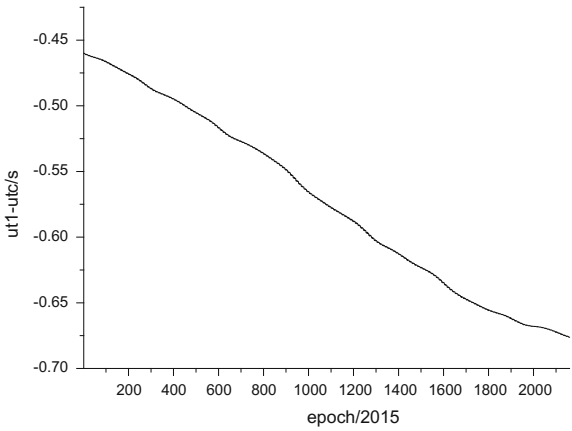

Fig. 5 The results of UT1-UTC with a frequency of 2 h

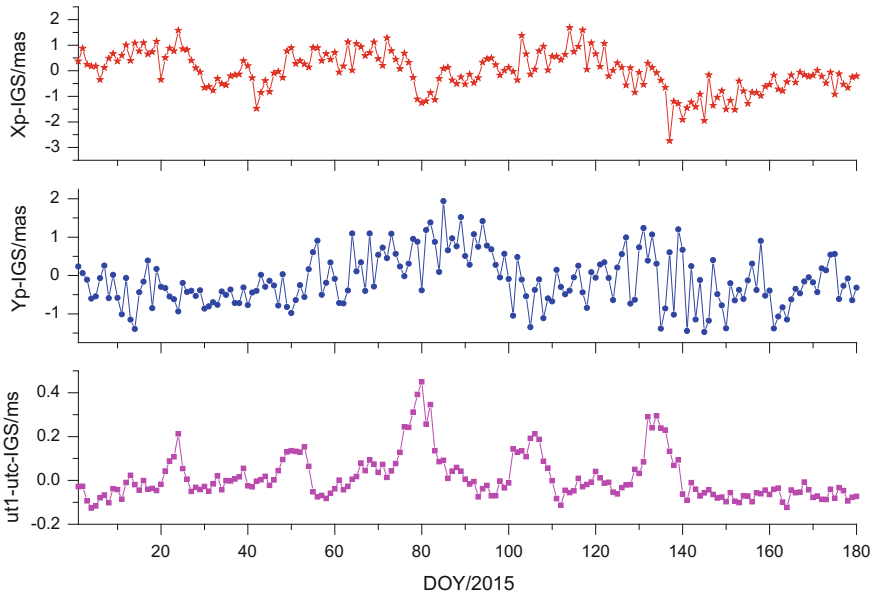

Fig. 6 The absolute difference between estimated results and IGS published values with a frequency of 2 h

minimum value is −0.1258 ms and the RMS is 0.1050 ms. In the results we can also see that the polar motion x_p and the UT1-UTC exist obvious systematic deviations while the polar motion y_p exist little systematic deviations.

According to Table 1 and Fig. 3, we can see that the precision of polar motion with a frequency of 2 h has declined compared to the frequency of 24 h but still

Table 2 The statistical results of the absolute difference between estimated results and IGS published value with a frequency of 2 h at UTC 12:00:00

	Polar motion x_p (mas)	Polar motion y_p (mas)	UT1-UTC (ms)
Average absolute value	0.597	0.569	0.075
Max	1.680	1.939	0.4493
Min	−2.740	−1.472	−0.1258
RMS	0.754	0.688	0.1050
STD	0.040	0.059	0.0699

stable while the precision and stability of UT1-UTC both declined due to the shortening of the observation time. However, the precision of high frequency ERP is in the permitted range [14].

4 Conclusion

GPS is one of the most vital data sources in geodesy and also one of the most important technical means to determinate ERP. Furthermore, we can estimate ERP with high time resolution by GPS. This paper does research on estimating high frequency ERP by GPS. Based on the research above and the real time processing, some conclusion can be come to:

1. 40 IGS stations is the most appropriate number to estimate ERP with the station uniformly distributed, because when the number of stations are over 40, the precision of ERP improved a little while the calculating time improved exponentially.
2. The results show that the precision of polar motion x_p,y_p, UT1-UTC can be 0.289, 0.245 mas and 0.0342 ms respectively with a frequency of 24 h.
3. From the high frequency time series we can see that the precision of polar motion x_p, y_p, UT1-UTC can be 0.754, 0.688 mas and 0.1050 ms respectively with a frequency of 2 h. The precision of high frequency ERP is in the permitted range for the user who need high time resolution ERP series but not high accuracy.

In addition, there remains some problems need to be solved, such as how to calculate ERP with more satellite navigation systems, how to eliminate the system error and improve the precision and stability of the solution. This will be the focus of the next research.

References

1. Wei E, Yan W, Jin S et al (2013) Improvement of Earth orientation parameters estimate with Chang'E-1 ΔVLBI observations. J Geodyn 72:46–52
2. Wei E, Jin S, Zhang Q et al (2013) Autonomous navigation of Mars probe using X-ray pulsars: modeling and results. Adv Space Res 51(5):849–857
3. Panafidina N, Hugentobler U, Seitz M (2015) Interaction between subdaily Earth rotation parameters and GPS orbits. Egu Gen Assembly 15.
4. Li Z, Wei E, et al (2010) Space Geodesy
5. Rothacher M et al (2001) High-frequency variations in Earth rotation from global positioning system data. J Geophys Res: Solid Earth (1978–2012) 106.B7:13711–13738
6. Zhu S, Zhao M (1986) A simplified algorithm for the joint solution of multi-techniques of ERP. Ann Shanghai Observatory Acad Sin 8
7. Wei E (2013) On the high-frequency ERPs with GPS observations. Wuhan Daxue Xuebao 38 (7):818–821
8. Xu GC (2007) GPS: theory, algorithms, and applications. Springer Verlag Berlin Heidelberg
9. Dach R, Hugentobler U, Fridez P, Meindl M (2007) Bernese GPS software version 5.0. Astronomical Institute, University of Bern, p 640
10. Yang ZHK, Yang XH, Li ZHG et al (2010) Estimation of Earth rotation parameters by GPS observations. J Time Freq 33(001):69–76 (Chinese)
11. Wang Q, Dang Y, Xu T (2013) The method of Earth rotation parameter determination using GNSS observations and precision analysis. China Satellite Navigation Conference (CSNC) 2013 Proceedings. Springer Berlin Heidelberg, pp 247–256
12. Wei E, Wan L, Jin S et al (2014) Estimation of ERP with combined observations of GNSS and SLR. Geomatics Inform Sci Wuhan Univ 39(5):581–585
13. Herring TA, Dong D (1994) Measurement of diurnal and semidiurnal rotational variations and tidal parameters of Earth. J Geophys Res: Solid Earth (1978–2012) 99.B9:18051–18071
14. Haas Rüdiger, Wünsch Johann (2006) Sub-diurnal earth rotation variations from the VLBI CONT02 campaign. J Geodyn 41(1):94–99
15. Bizouard C, Gambis D (2009) The combined solution C04 for Earth orientation parameters consistent with international terrestrial reference frame 2005. Geodetic reference frames. Springer Berlin Heidelberg, pp 265–270

A Comparative Analysis of Relative Positioning Methods for BDS/GPS in Three Different Fields of Combination

Lingchuan Wan, Guanwen Huang, Rui Tu, Juqing Zhang and Junqiang Han

Abstract In this contribution, we study the models of BDS/GPS combined in three different fields relative positioning, which contain field of coordinate estimates, field of normal equations and that of observation equations. The precision of coordinate solution, differences and similarities in different fields are discussed. On the condition of single epoch and static sequential Least-squares calculation, combination of normal equation field and that of observation equation field are with equivalence, while on the condition of dynamic calculation, the combination of observations equation field is more rigorous than that of normal equation field, and the Ratio rate of the integer ambiguity estimates is higher. Based on the data from measured short-baseline, we verify inference given in the contribution by experiment and analyze through calculation on single epoch, sequential Least-squares and dynamic.

Keywords GNSS · Combined positioning · Relative positioning · Combination fields · Ratio

1 Introduction

China's Beidou Satellite Navigation System (BDS) has been provided with continuous positioning, navigation and timing service for the Asia-Pacific region. BDS/GPS dual-system combined positioning significantly increase the number of

L. Wan (✉) · G. Huang (✉) · J. Zhang · J. Han
College of Geology Engineering and Geomantic, Chang'an University,
710054 Xi'an, Shaanxi, China
e-mail: 739797497@qq.com

G. Huang
e-mail: huang830928@163.com

R. Tu
National Time Service Center, Chinese Academy of Sciences,
710600 Xi'an, Shaanxi, China
e-mail: turui-2004@126.com

J. Sun et al. (eds.), *China Satellite Navigation Conference (CSNC) 2017 Proceedings: Volume I*, Lecture Notes in Electrical Engineering 437,
DOI 10.1007/978-981-10-4588-2_5

visible satellites, improve the geometric distribution of satellite structure, thereby improving the reliability and availability of coordinate estimates [1]. BDS/GPS combined positioning has become a hot research topic nowadays. Some scholars, such as Wei et al. [2], Gao et al. [3], Zang [4], Huang et al. [5] and Li et al. [6], have proved that the dual-system BDS/GPS combined positioning has better performance and accuracy than that of single system, and the satellite visibility and precision factor (DOP) of the BDS/GPS dual system have been also analyzed theoretically and empirically. However, no similarities and differences between different combined fields have been studied. In this contribution, three relative positioning models of BDS/GPS combined positioning in different fields are presented. The correlation and difference between the combination of normal equation field and that of observation equation field are analyzed. Finally, we, based on the measured short baseline data, proved the inference about similarity and difference between two kinds of combined fields, in normal equation field and observation equation, in relative positioning. Simultaneously, the performance and precision of the relative positioning methods in different fields are given, which provides a reference for high-precision combined BDS/GPS relative positioning method optimization.

2 BDS/GPS Combined Relative Positioning Function Model

2.1 GNSS Relative Positioning Function Model

High precision GNSS relative positioning is based on carrier phase and pseud-orange double-difference (DD) observations. Relative positioning eliminates errors associated with satellites and receivers, and the observed noise and unmodeled errors are negligible [7], When the baseline is short, the tropospheric delay and ionospheric delay parameters are also negligible due to the strong correlation of the atmosphere. The parameters, to be estimated, are only the coordinate and double-difference integer ambiguities. In the short baseline GNSS dynamic measurement, the error equation is expressed as

$$\boldsymbol{V} = \boldsymbol{Ab} + \boldsymbol{Ba} - \boldsymbol{l}, \boldsymbol{P} \tag{1}$$

where $\boldsymbol{a}$ and $\boldsymbol{b}$ respectively consist of ambiguities parameters, which are known to be integers, and coordinates parameters, A and B are the coordinate parameter coefficient matrix and that of the ambiguity parameters.

One simply discards the integer constraints on the ambiguities and performs standard least-squares adjustment with (1) to obtain the float solution.

$$\begin{bmatrix} \hat{\boldsymbol{b}} \\ \hat{\boldsymbol{a}} \end{bmatrix} = \begin{bmatrix} \boldsymbol{A}^T\boldsymbol{P}\boldsymbol{A} & \boldsymbol{A}^T\boldsymbol{P}\boldsymbol{B} \\ \boldsymbol{B}^T\boldsymbol{P}\boldsymbol{A} & \boldsymbol{B}^T\boldsymbol{P}\boldsymbol{B} \end{bmatrix}^{-1} \begin{bmatrix} \boldsymbol{A}^T\boldsymbol{P}\boldsymbol{l} \\ \boldsymbol{B}^T\boldsymbol{P}\boldsymbol{l} \end{bmatrix} \tag{2}$$

For the number of observation satellites is $\boldsymbol{n}+1$, the number of carrier double-difference observations is Correspondingly $\boldsymbol{n}$, the number of parameters to be estimated is $\boldsymbol{n}+3$. In order to avoid the rank loss of the coefficient matrix, one usually introduce pseudo-range observations

$$\boldsymbol{B}_{2n,n} = \begin{bmatrix} 0_{n,n} \\ \boldsymbol{B}'_{n,n} \end{bmatrix}, \quad \boldsymbol{B}'_{n,n} = \begin{bmatrix} \boldsymbol{\lambda} & 0 & 0 \\ 0 & \ddots & 0 \\ 0 & 0 & \boldsymbol{\lambda} \end{bmatrix} \tag{3}$$

where $\mathbf{0}$ represents the zero matrix and λ is the wavelength, subscript $\boldsymbol{n}$ represents the number of rows and columns of the matrix. The accuracy corresponding to the estimates is expressed as:

$$\boldsymbol{Q} = \begin{bmatrix} \boldsymbol{Q}_{\hat{b}\hat{b}} & \boldsymbol{Q}_{\hat{b}\hat{a}} \\ \boldsymbol{Q}_{\hat{a}\hat{b}} & \boldsymbol{Q}_{\hat{a}\hat{a}} \end{bmatrix} = \begin{bmatrix} \boldsymbol{A}^T\boldsymbol{P}\boldsymbol{A} & \boldsymbol{A}^T\boldsymbol{P}\boldsymbol{B} \\ \boldsymbol{B}^T\boldsymbol{P}\boldsymbol{A} & \boldsymbol{B}^T\boldsymbol{P}\boldsymbol{B} \end{bmatrix}^{-1} \tag{4}$$

High Precision relative GNSS positioning based on short-baseline data, is possible, when reliable Estimates of the integer double difference ambiguities can be Determined [8]. The ambiguity floating point estimate $\hat{a}$ and combining it with (4) to convert it to an integer estimates $\check{a}$ by Integer Least Squares Adjustment:

$$\Omega(\check{\boldsymbol{a}}) = (\hat{\boldsymbol{a}} - \check{\boldsymbol{a}})^T \boldsymbol{Q}_{\hat{a}\hat{a}}^{-1} (\hat{\boldsymbol{a}} - \check{\boldsymbol{a}}) = \boldsymbol{min} \tag{5}$$

And the ambiguities estimates are evaluated by the ratio:

$$\boldsymbol{Ratio} = \frac{\boldsymbol{\Omega}_{sec}}{\boldsymbol{\Omega}_{min}} > \mathrm{C} \tag{6}$$

where $\boldsymbol{\Omega}_{\mathbf{sec}}$ and $\boldsymbol{\Omega}_{\mathbf{min}}$ are the second and smallest residuals of the estimated integer ambiguities, $\mathbf{C}$ is the test threshold. This process is usually referred to as the 'ambiguity fixed'. In this contribution, we use the LAMBDA algorithm to fix the ambiguities [8]. That is, the ambiguity integer evaluation function can be expressed as

$$\check{\boldsymbol{a}} = \boldsymbol{LAMBDA}(\hat{a}, \boldsymbol{Q}_{\hat{a}\hat{a}}) \tag{7}$$

Once the integer ambiguities ă are computed, with (2)–(5) and

$$\check{\boldsymbol{b}} = \hat{\boldsymbol{b}} - \boldsymbol{Q}_{\hat{b}\hat{a}} \boldsymbol{Q}_{\hat{a}\hat{a}}^{-1} (\hat{\boldsymbol{a}} - \check{\boldsymbol{a}}) \tag{8}$$

to correct the 'float' coordinates estimates $\hat{b}$ to obtain the fixed coordinates estimates solution $\check{b}$, and its accuracy

$$\boldsymbol{Q}_{\check{b}\check{b}} = \boldsymbol{Q}_{\hat{b}\hat{b}} - \boldsymbol{Q}_{\hat{b}\hat{a}}\boldsymbol{Q}_{\hat{a}\hat{a}}^{-1}\boldsymbol{Q}_{\hat{a}\hat{b}} \tag{9}$$

2.2 BDS/GPS Combined in Coordinate Estimates Field Relative Positioning Function Model

Equations (2)–(8) are used to obtain BDS coordinate fixed solution $\check{b}_B$ and GPS coordinate fixed solution $\check{b}_G$. When $\check{b}_B$ and $\check{b}_G$ are averaged, we obtain the coordinate solution of BDS/GPS combined in coordinate estimates field positioning, and its accuracy

$$\check{\boldsymbol{b}}_{\boldsymbol{Cor}} = \left(\left(\hat{\boldsymbol{b}}_{\boldsymbol{B}} + \hat{\boldsymbol{b}}_{\boldsymbol{G}}\right) - \boldsymbol{Q}_{\hat{b}_B\hat{a}_B}\boldsymbol{Q}_{\hat{a}_B\hat{a}_B}^{-1}(\hat{\boldsymbol{a}}_{\boldsymbol{B}} - \check{\boldsymbol{a}}_{\boldsymbol{B}}) - \boldsymbol{Q}_{\hat{b}_G\hat{a}_G}\boldsymbol{Q}_{\hat{a}_G\hat{a}_G}^{-1}(\hat{\boldsymbol{a}}_{\boldsymbol{G}} - \check{\boldsymbol{a}}_{\boldsymbol{G}})\right)/2 \tag{10}$$

$$\boldsymbol{Q}_{\check{b}_{Cor}\check{b}_{Cor}} = \left(\left(\boldsymbol{Q}_{\hat{b}_B\hat{b}_B} + \boldsymbol{Q}_{\hat{b}_G\hat{b}_G}\right) - \boldsymbol{Q}_{\hat{b}_B\hat{a}_B}\boldsymbol{Q}_{\hat{a}_B\hat{a}_B}^{-1}\boldsymbol{Q}_{\hat{a}_B\hat{b}_B} - \boldsymbol{Q}_{\hat{b}_G\hat{a}_G}\boldsymbol{Q}_{\hat{a}_G\hat{a}_G}^{-1}\boldsymbol{Q}_{\hat{a}_G\hat{b}_G}\right)/2 \tag{11}$$

The subscript ***Cor*** represents the combined in coordinate estimate field.

2.3 BDS/GPS Combined in Normal Equation Field Relative Positioning Function Model

The normal equations of BDS and GPS positioning in single system are obtained from (2), and then extend them to obtain the normal equation of BDS/GPS combined in the normal equation field positioning. The corresponding float solution

$$\begin{bmatrix} \hat{\boldsymbol{b}}_{\boldsymbol{r}} \\ \hat{\boldsymbol{a}}_{\boldsymbol{B}}^{\boldsymbol{r}} \\ \hat{\boldsymbol{a}}_{\boldsymbol{G}}^{\boldsymbol{r}} \end{bmatrix} = \begin{bmatrix} \boldsymbol{N}_{\hat{b}_r\hat{b}_r} & \boldsymbol{N}_{\hat{b}_r\hat{a}_B^r} & \boldsymbol{N}_{\hat{b}_r\hat{a}_G^r} \\ \boldsymbol{N}_{\hat{a}_B^r\hat{b}_r} & \boldsymbol{N}_{\hat{a}_B^r\hat{a}_B^r} & \boldsymbol{N}_{\hat{a}_B^r\hat{a}_G^r} \\ \boldsymbol{N}_{\hat{a}\hat{b}_r} & \boldsymbol{N}_{\hat{a}_G^r\hat{a}_B^r} & \boldsymbol{N}_{\hat{a}_G^r\hat{a}_G^r} \end{bmatrix}^{-1} \begin{bmatrix} \boldsymbol{W}_1^{\boldsymbol{r}} \\ \boldsymbol{W}_2^{\boldsymbol{r}} \\ \boldsymbol{W}_3^{\boldsymbol{r}} \end{bmatrix} \tag{12}$$

where superscript ***r*** represents the combination of the normal equation field, subscripts ***B*** and ***G*** represent BDS and GPS respectively, notice

$$\begin{cases} N_{\hat{b}_r\hat{b}_r} = A_B^T P_B A_B + A_G^T P_G P_G \\ N_{\hat{b}_r\hat{a}_B^r} = A_B^T P_B B_B, N_{\hat{b}_r\hat{a}_G^r} = A_G^T P_G B_G \\ N_{\hat{a}_B^r\hat{a}_B^r} = B_B^T P_B B_B, N_{\hat{a}_G^r\hat{a}_G^r} = A_B^T P_B B_B \\ W_1^r = A_B^T P_B l_B + A_G^T P_G l_G \\ W_2^r = B_B^T P_B l_B, W_3^r = B_G^T P_G l_G \end{cases} \tag{13}$$

and covariance matrix

$$\begin{bmatrix} Q_{\hat{b}_r\hat{b}_r} & Q_{\hat{b}_r\hat{a}_B^r} & Q_{\hat{b}_r\hat{a}_G^r} \\ Q_{\hat{a}_B^r\hat{b}_r} & Q_{\hat{a}_B^r\hat{a}_B^r} & Q_{\hat{a}_B^r\hat{a}_G^r} \\ Q_{\hat{a}_G^r\hat{b}_r} & Q_{\hat{a}_G^r\hat{a}_B^r} & Q_{\hat{a}_G^r\hat{a}_G^r} \end{bmatrix} = \begin{bmatrix} N_{\hat{b}_r\hat{b}_r} & N_{\hat{b}_r\hat{a}_B^r} & N_{\hat{b}_r\hat{a}_G^r} \\ N_{\hat{a}_B^r\hat{b}_r} & N_{\hat{a}_B^r\hat{a}_B^r} & \hat{a}_{\hat{a}_B^r\hat{a}_G^r} \\ N_{\hat{a}_G^r\hat{b}_r} & N_{\hat{a}_G^r\hat{a}_B^r} & N_{\hat{a}_G^r\hat{a}_G^r} \end{bmatrix}^{-1} \tag{14}$$

Abbreviate them as

$$\hat{a}_r = \left[\hat{a}_B^r, \hat{a}_G^r\right]^T, \quad Q_{\hat{a}_r\hat{a}_r} = \begin{bmatrix} Q_{\hat{a}_B^r\hat{a}_B^r} & Q_{\hat{a}_B^r\hat{a}_G^r} \\ Q_{\hat{a}_G^r\hat{a}_B^r} & Q_{\hat{a}_G^r\hat{a}_G^r} \end{bmatrix}$$

With (7)–(8), we obtain the fixed solution of coordinate parameters and its accuracy of BDS/GPS combined in the normal equation field relative positioning

$$\check{b}_r = \left(\hat{b}_r - Q_{\hat{b}_r\hat{a}_r} Q_{\hat{a}_r\hat{a}_r}^{-1} (\hat{a}_r - \check{a}_r)\right) \tag{15}$$

$$Q_{\check{b}_r\check{b}_r} = Q_{\hat{b}_r\hat{b}_r} - Q_{\hat{b}_r\hat{a}_r} Q_{\hat{a}_r\hat{a}_r}^{-1} Q_{\hat{a}_r\hat{b}_r} \tag{16}$$

where

$$Q_{\hat{b}_r\hat{a}_r} = \begin{bmatrix} Q_{\hat{b}_B\hat{a}_B} & Q_{\hat{b}_G\hat{a}_G} \end{bmatrix}$$

2.4 BDS/GPS Combined in Observation Equation Field Relative Positioning Function Model

We earned the observation equations of both BDS and GPS, and the combined error equation is obtained:

$$V = A_C b_C + B_C a_B + C_C a_G - l_C, \quad P_C \tag{17}$$

where, Matrix A, B, C are coefficient matrices of coordinate, BDS ambiguities parameters and GPS ambiguities parameters coefficient matrix. The subscript c

represents combined in the observation equation field. We perform standard least-squares adjustment with (18) to obtain float solution

$$\begin{bmatrix} \hat{\boldsymbol{b}}_c \\ \hat{\boldsymbol{a}}_B^c \\ \hat{\boldsymbol{a}}_G^c \end{bmatrix} = \begin{bmatrix} \boldsymbol{A}_c^T \boldsymbol{P}_c \boldsymbol{A}_c & \boldsymbol{A}_c^T \boldsymbol{P}_c \boldsymbol{B}_c & \boldsymbol{A}_c^T \boldsymbol{P}_c \boldsymbol{C}_c \\ \boldsymbol{B}_c^T \boldsymbol{P}_c \boldsymbol{A}_c & \boldsymbol{B}_c^T \boldsymbol{P}_c \boldsymbol{B}_c & \boldsymbol{B}_c^T \boldsymbol{P}_c \boldsymbol{C}_c \\ \boldsymbol{C}_c^T \boldsymbol{P}_c \boldsymbol{A}_c & \boldsymbol{C}_c^T \boldsymbol{P}_c \boldsymbol{B}_c & \boldsymbol{C}_c^T \boldsymbol{P}_c \boldsymbol{C}_c \end{bmatrix}^{-1} \begin{bmatrix} \boldsymbol{W}_1^c \\ \boldsymbol{W}_2^c \\ \boldsymbol{W}_3^c \end{bmatrix} \tag{18}$$

abbreviated as

$$\begin{bmatrix} \hat{\boldsymbol{b}}_c \\ \hat{\boldsymbol{a}}_B^c \\ \hat{\boldsymbol{a}}_G^c \end{bmatrix} = \begin{bmatrix} \boldsymbol{N}_{\hat{b}_c \hat{b}_c} & \boldsymbol{N}_{\hat{b}_c \hat{a}_B^c} & \boldsymbol{N}_{\hat{b}_c \hat{a}_G^c} \\ \boldsymbol{N}_{\hat{a}_B^c \hat{b}_c} & \boldsymbol{N}_{\hat{a}_B^c \hat{a}_B^c} & \boldsymbol{N}_{\hat{a}_B^c \hat{a}_G^c} \\ \boldsymbol{N}_{\hat{a}_G^c \hat{b}_c} & \boldsymbol{N}_{\hat{a}_G^c \hat{a}_B^c} & \boldsymbol{N}_{\hat{a}_G^c \hat{a}_G^c} \end{bmatrix}^{-1} \begin{bmatrix} \boldsymbol{W}_1^c \\ \boldsymbol{W}_2^c \\ \boldsymbol{W}_3^c \end{bmatrix}$$

where both superscript $\boldsymbol{r}$ and subscript $\boldsymbol{r}$ represent the combined in the normal equation field, subscripts $\boldsymbol{B}$ and $\boldsymbol{G}$ represent BDS and GPS respectively, and covariance matrix of the float solution

$$\begin{bmatrix} \boldsymbol{Q}_{\hat{b}_c \hat{b}_c} & \boldsymbol{Q}_{\hat{b}_c \hat{a}_B^c} & \boldsymbol{Q}_{\hat{b}_c \hat{a}_G^c} \\ \boldsymbol{Q}_{\hat{b}_c \hat{a}_B^c} & \boldsymbol{Q}_{\hat{a}_B^c \hat{a}_B^c} & \boldsymbol{Q}_{\hat{a}_B^c \hat{a}_G^c} \\ \boldsymbol{Q}_{\hat{b}_c \hat{a}_G^c} & \boldsymbol{Q}_{\hat{a}_G^c \hat{a}_B^c} & \boldsymbol{Q}_{\hat{a}_G^c \hat{a}_G^c} \end{bmatrix} = \begin{bmatrix} \boldsymbol{N}_{\hat{b}_c \hat{b}_c} & \boldsymbol{N}_{\hat{b}_c \hat{a}_B^c} & \boldsymbol{N}_{\hat{b}_c \hat{a}_G^c} \\ \boldsymbol{N}_{\hat{a}_B^c \hat{b}_c} & \boldsymbol{N}_{\hat{a}_B^c \hat{a}_B^c} & \boldsymbol{N}_{\hat{a}_B^c \hat{a}_G^c} \\ \boldsymbol{N}_{\hat{a}_G^c \hat{b}_c} & \boldsymbol{N}_{\hat{a}_G^c \hat{a}_B^c} & \boldsymbol{N}_{\hat{a}_G^c \hat{a}_G^c} \end{bmatrix}^{-1} \tag{19}$$

Abbreviate as

$$\hat{\boldsymbol{a}}_c = \left[\hat{\boldsymbol{a}}_B^c \hat{\boldsymbol{a}}_B^c\right]^T, \quad \boldsymbol{Q}_{\hat{a}_c \hat{a}_c} = \begin{bmatrix} \boldsymbol{Q}_{\hat{a}_B^c \hat{a}_B^c} & \boldsymbol{Q}_{\hat{a}_B^c \hat{a}_G^c} \\ \boldsymbol{Q}_{\hat{a}_G^c \hat{a}_B^c} & \boldsymbol{Q}_{\hat{a}_G^c \hat{a}_G^c} \end{bmatrix} \tag{20}$$

With (7)–(8), we obtain the fixed solution of coordinate parameters and its accuracy

$$\check{\boldsymbol{b}}_c = \left(\hat{\boldsymbol{b}}_c - \boldsymbol{Q}_{\hat{b}_c \hat{a}_c} \boldsymbol{Q}_{\hat{a}_c \hat{a}_c}^{-1} (\hat{\boldsymbol{a}}_c - \check{\boldsymbol{a}}_c)\right) \tag{21}$$

$$\boldsymbol{Q}_{\check{b}_c \check{b}_c} = \boldsymbol{Q}_{\hat{b}_c \hat{b}_c} - \boldsymbol{Q}_{\hat{b}_c \hat{a}_c} \boldsymbol{Q}_{\hat{a}_c \hat{a}_c}^{-1} \boldsymbol{Q}_{\hat{a}_c \hat{b}_c} \tag{22}$$

where

$$\boldsymbol{Q}_{\hat{b}_c \hat{a}_c} = \begin{bmatrix} \boldsymbol{Q}_{\hat{b}_c \hat{a}_B} & \boldsymbol{Q}_{\hat{b}_c \hat{a}_G} \end{bmatrix}$$

3 Analysis of BDS/GPS Combined in Different Fields Relative Positioning

3.1 Analysis of Single Epoch Solving

Let the numbers of BDS, GPS carrier (pseudorange) double difference observations were $\boldsymbol{n}$, $\boldsymbol{m}$. Notice (19) with (2), (3), (13) and (14)

$$\boldsymbol{A_C} = \begin{bmatrix} \boldsymbol{A_B} \\ \boldsymbol{A_G} \end{bmatrix}, \boldsymbol{B_C} = \begin{bmatrix} 0_{n,n} \\ 0_{m,n} \\ \boldsymbol{B}'_{n,n} \\ 0_{m,n} \end{bmatrix}, \boldsymbol{C_C} = \begin{bmatrix} 0_{n,n} \\ 0_{m,n} \\ 0_{n,n} \\ \boldsymbol{C}'_{m,n} \end{bmatrix}, \boldsymbol{l_c} = \begin{bmatrix} \boldsymbol{l_B} \\ \boldsymbol{l_G} \end{bmatrix} \tag{23}$$

We abbreviate (12) and (18) as

$$\begin{cases} \boldsymbol{N_c}\hat{\boldsymbol{X}} = \boldsymbol{W_c} \\ \boldsymbol{N_r}\hat{\boldsymbol{X}} = \boldsymbol{W_r} \end{cases} \tag{24}$$

Take (23) into (19), it can be concluded that

$$\begin{cases} \boldsymbol{N_c} = \boldsymbol{N_r} \\ \boldsymbol{W_c} = \boldsymbol{W_r} \end{cases} \tag{25}$$

where $\boldsymbol{r}$ and $\boldsymbol{c}$ mean combination of the normal equation field and the observation equation field, respectively.

BDS/GPS combined, in observation equation field and in normal equation field combination, relative positioning solving in single epoch, is equivalent, earn the same coordinates, ambiguity float solution and its accuracy. With (16), (17) and (22), (23), we can also obtain the same coordinates and ambiguity fixed solution

$$\begin{cases} \hat{\boldsymbol{a}}_{\boldsymbol{c}} = \hat{\boldsymbol{a}}_{\boldsymbol{r}} \\ \hat{\boldsymbol{a}}_{\boldsymbol{c}} = \hat{\boldsymbol{a}}_{\boldsymbol{r}} \end{cases} \tag{26}$$

3.2 Analysis of Static Sequential Least Squares Solving

Sequential Least Squares correlates each group of two or more sets of observations, without taking into account the observations from the previous stage, but using the results of previous adjustments to achieve the same effect as the overall adjustment.

According to the principle of sequential least squares adjustment, with a total of k epochs metrical observations and error equations [9, 10]:

$$\boldsymbol{L} = \begin{bmatrix} \boldsymbol{L}_k \\ \vdots \\ \boldsymbol{L}_1 \end{bmatrix}, \begin{cases} \boldsymbol{V}_k = \boldsymbol{A}_k - \boldsymbol{l}_k \\ \vdots \\ \boldsymbol{V}_1 = \boldsymbol{A}_1 - \boldsymbol{l}_1 \end{cases} \tag{27}$$

The parameters of the current epoch are estimated by combining the parameters solution from the previous stage. When the parameters remain unchanged, the normal equation can be expressed as

$$\left(\sum_{i=0}^{k} \boldsymbol{N}_i\right)\boldsymbol{X} = \sum_{i=0}^{k} \boldsymbol{W}_i \tag{28}$$

In the GNSS positioning, if there is no cycle jump, satellite lift and reference star change, the single system normal equation is:

$$\left(\sum_{i=0}^{k} \begin{bmatrix} \boldsymbol{N}_{\hat{b}\hat{b}} & \boldsymbol{N}_{\hat{b}\hat{a}} \\ \boldsymbol{N}_{\hat{a}\hat{b}} & \boldsymbol{N}_{\hat{b}\hat{b}} \end{bmatrix}_i\right)\boldsymbol{X} = \sum_{i=0}^{k} \begin{bmatrix} \boldsymbol{W}_{1,i} \\ \boldsymbol{W}_{2,i} \end{bmatrix} \tag{29}$$

Even if the parameter member is changeable, the Sequential Least Squares still be trivial when we do some elementary transformation.

From (13), we obtain the normal equation on Sequential Least Squares of each system to obtain the combined solution

$$\left(\sum_{i=0}^{k} \begin{bmatrix} \boldsymbol{N}^r_{\hat{b}\hat{b},i} & \boldsymbol{N}^r_{\hat{b}\hat{a}_B,i} & \boldsymbol{N}^r_{\hat{b}\hat{a}_G,i} \\ \boldsymbol{N}^r_{\hat{a}_B\hat{b},i} & \boldsymbol{N}^r_{\hat{a}_B\hat{a}_B,i} & \boldsymbol{N}^r_{\hat{a}_B\hat{a}_G,i} \\ \boldsymbol{N}^r_{\hat{b}\hat{a}_G,i} & \boldsymbol{N}^r_{\hat{a}_G\hat{a}_B,i} & \boldsymbol{N}^r_{\hat{a}_G\hat{a}_G,i} \end{bmatrix}\right) \begin{bmatrix} \hat{\boldsymbol{b}} \\ \hat{\boldsymbol{a}}_B \\ \hat{\boldsymbol{a}}_G \end{bmatrix} = \sum_{i=0}^{k} \begin{bmatrix} \boldsymbol{w}^r_{1,i} \\ \boldsymbol{w}^r_{2,i} \\ \boldsymbol{w}^r_{3,i} \end{bmatrix} \tag{30}$$

With (23) and (5)–(8), it can be seen that the normal equations combined in normal equation field are still equivalent with that of combined in observation equation field, and the estimated values of parameters are the same:

$$\begin{cases} \check{\boldsymbol{b}}_{c,i} = \check{\boldsymbol{b}}_{r,i} \\ \check{\boldsymbol{a}}_{c,i} = \check{\boldsymbol{a}}_{r,i} \end{cases} \tag{31}$$

where $\boldsymbol{r}$, $\boldsymbol{c}$ get the same meaning in (26), $\boldsymbol{i}$ for the epoch.

3.3 Analysis of Dynamic Sequential Least Squares Solving

BDS/GPS relative positioning in the dynamic conditions can still be solved in sequential least squares adjustment to earn parameter floating solution [11]. The coordinate parameters relatively to be local parameters, the coordinate parameter

estimates from previous stage epoch do not appear in the next epoch. One should reduce the coefficient of coordinate before the next epoch.

From the analysis in 3.2, the method of combined in normal equation field earned normal equation in sequential least squares of each system individually. And then extent them to obtain the normal equation of the current epoch in BDS/GPS combined in normal equation field to solve the estimated parameters, but without retain the coefficient of coordinate.

The dual-system normal equation in dynamic condition can be expressed as:

$$\begin{bmatrix} N^{r}_{\hat{a}\hat{a},k} & N^{r}_{\hat{b}\hat{a}_B,k} & N^{r}_{\hat{b}\hat{a}_G,k} \\ N^{r}_{\hat{a}_B\hat{b},k} & N^{'}_{\hat{a}^r_B\hat{a}^r_B,k} & N^{'}_{\hat{a}^r_B\hat{a}^r_G,k} \\ N^{r}_{\hat{b}\hat{a}_G,k} & N^{'}_{\hat{a}^r_G\hat{a}^r_B,k} & N^{'}_{\hat{a}^r_G\hat{a}^r_G,k} \end{bmatrix} \begin{bmatrix} \hat{b} \\ \hat{a}_B \\ \hat{a}_G \end{bmatrix} = \sum_{i=0}^{k} \begin{bmatrix} w^{r}_{1,k} \\ W^{'}_{2} \\ W^{'}_{3} \end{bmatrix} \tag{32}$$

where, $N^{r}_{\hat{b}\hat{b},k}, N^{r}_{\hat{b}\hat{a}_B,k}, N^{r}_{\hat{b}\hat{a}_G,k}, w^{r}_{1,k}$ with the same mean as (13), notice

$$\begin{aligned} N^{'}_{\hat{a}^r_B\hat{a}^r_B,k} &= \sum_{i=0}^{k} N^{B}_{\hat{a}_B\hat{a}_B,i} - \sum_{i=0}^{k-1}\left\{ N^{B}_{\hat{b}\hat{a}_B,i}\left[N^{B}_{\hat{b}\hat{b},i}\right]^{-1} N^{B}_{\hat{a}_B\hat{b},i}\right\}, \\ N^{'}_{\hat{a}^r_G\hat{a}^r_G,k} &= \sum_{i=0}^{k} N^{G}_{\hat{a}_G\hat{a}_G,i} - \sum_{i=0}^{k-1}\left\{ N^{G}_{\hat{b}\hat{a}_G,i}\left[N^{G}_{\hat{b}\hat{b},i}\right]^{-1} N^{G}_{\hat{a}_G\hat{b},i}\right\} \end{aligned} \tag{33}$$

$$\begin{aligned} W^{'}_{2} &= \sum_{i=0}^{k}\left[w^{B}_{2,i}\right] - \sum_{i=0}^{k-1}\left\{ w^{B}_{2,i}\left[N^{B}_{\hat{b}\hat{b},i}\right]^{-1} N^{B}_{\hat{a}_B\hat{b},i}\right\}, \\ W^{'}_{3} &= \sum_{i=0}^{k}\left[w^{G}_{3,i}\right] - \sum_{i=0}^{k-1}\left\{ w^{G}_{3,i}\left[N^{G}_{\hat{b}\hat{b},i}\right]^{-1} N^{G}_{\hat{a}_B\hat{b},i}\right\} \end{aligned} \tag{34}$$

Superscript B, G, respectively, refer to BDS or GPS. Through the method of combination of observation equation field, there is a normal equation

$$\begin{bmatrix} N^{c}_{\hat{b}\hat{b},k} & N^{c}_{\hat{b}\hat{a}_B,k} & N^{c}_{\hat{b}\hat{a}_G,k} \\ N^{c}_{\hat{a}_B\hat{b},k} & N^{''}_{\hat{a}^c_B\hat{a}^c_B,k} & N^{''}_{\hat{a}^c_B\hat{a}^c_G,k} \\ N^{c}_{\hat{b}\hat{a}_G,k} & N^{''}_{\hat{a}^c_G\hat{a}^c_B,k} & N^{''}_{\hat{a}^c_G\hat{a}^c_G,k} \end{bmatrix} \begin{bmatrix} \hat{b} \\ \hat{a}_B \\ \hat{a}_G \end{bmatrix} = \sum_{i=0}^{k} \begin{bmatrix} w^{c}_{1,k} \\ W^{''}_{2} \\ W^{''}_{3} \end{bmatrix} \tag{35}$$

where

$$\begin{aligned} N^{''}_{\hat{a}^c_B\hat{a}^c_B,k} &= \sum_{i=0}^{k} N_{\hat{a}^c_B\hat{a}^c_B,i} - \sum_{i=0}^{k-1}\left\{ N_{\hat{b}_c\hat{a}^c_B,i}\left[N_{\hat{b}_c\hat{b}_c,i}\right]^{-1} N_{\hat{a}^c_B\hat{b}_c,i}\right\}, \\ N^{''}_{\hat{a}^c_B\hat{a}^c_G,k} &= \sum_{i=0}^{k} N_{\hat{a}^c_B\hat{a}^c_G,i} - \sum_{i=0}^{k-1}\left\{ N_{\hat{b}_c\hat{a}^c_B,i}\left[N_{\hat{b}_c\hat{b}_c,i}\right]^{-1} N_{\hat{a}^c_G\hat{b}_c,i}\right\} \end{aligned} \tag{36}$$

$$\begin{aligned} N''_{\hat{a}_G^c\hat{a}_G^c,k} &= \sum_{i=0}^{k} N_{\hat{a}_G^c\hat{a}_G^c,i} - \sum_{i=0}^{k-1}\left\{ N_{\hat{b}_c\hat{a}_G^c,i}\left[N_{\hat{b}_c\hat{b}_c,i}\right]^{-1} N_{\hat{a}_G^c\hat{b}_c,i}\right\}, \\ N''_{\hat{a}_G^c\hat{a}_B^c,k} &= \sum_{i=0}^{k} N_{\hat{a}_G^c\hat{a}_B^c,i} - \sum_{i=0}^{k-1}\left\{ N_{\hat{b}_c\hat{a}_G^c,i}\left[N_{\hat{b}_c\hat{b}_c,i}\right]^{-1} N_{\hat{a}_B^c\hat{b}_c,i}\right\} \end{aligned} \tag{37}$$

$$\begin{aligned} W''_2 &= \sum_{i=0}^{k} W^c_{2,i} - \sum_{i=0}^{k-1}\left\{ W^c_{2,i}\left[N_{\hat{b}_c\hat{b}_c,i}\right]^{-1} N_{\hat{a}_B^c\hat{b}_c,i}\right\}, \\ W''_3 &= \sum_{i=0}^{k} W^c_{3,i} - \sum_{i=0}^{k-1}\left\{ W^c_{3,i}\left[N_{\hat{b}_c\hat{b}_c,i}\right]^{-1} N_{\hat{a}_G^c\hat{b}_c,i}\right\} \end{aligned} \tag{38}$$

Substituting (14) and (19) into (32)–(38), we learn that (32) and (35), respectively, using the combination of normal equation field and that of observation equation field on condition of dynamic sequential least-squares solution, are not uniform.

Simultaneously, with

$$\left\|A_i^T P_i A_i\right\|_{m1} < \left\|A_{c,i}^T P_{c,i} A_{c,i}\right\|_{m1} \tag{39}$$

where $\left\|A_i^T P_i A_i\right\|_{m1}$ mean matrix m1 norm. With (28)–(38), In the case of the optimal solution of the integer ambiguity estimates and the optimal solution is the same, we have

$$\boldsymbol{\Omega}_r < \boldsymbol{\Omega}_c \tag{40}$$

With (7), we come to the conclusion:

$$\boldsymbol{Ratio}_r < \boldsymbol{Ratio}_c \tag{41}$$

Equations (39)–(41) show that on the condition of dynamic calculation, the ratio of the integer ambiguity estimates of the observation equation field combination is better than that of the normal equation field combination.

4 Exemplification

Data had been received by GPS/BDS receiver for static observation acquisition, the baseline of 1 km on August 29, 2016. Interval 1 s, observation time 1 h, the satellite height cut-off angle of 7°. Received 12 BDS satellites, GPS satellites 8.

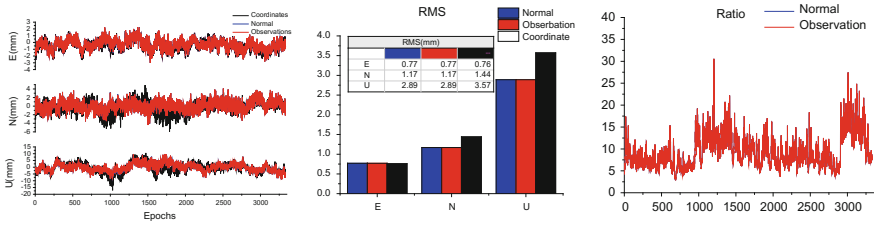

Fig. 1 The contrast of the error sequences and the ratio rates of single epoch calculation in the three different combinations

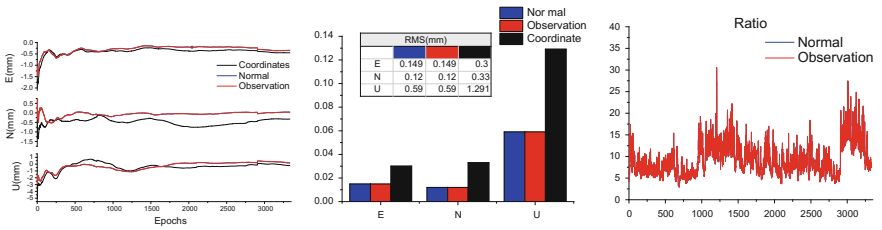

Fig. 2 The contrast of the error sequences and the ratio rates of sequential least-squares calculation in the three different combinations

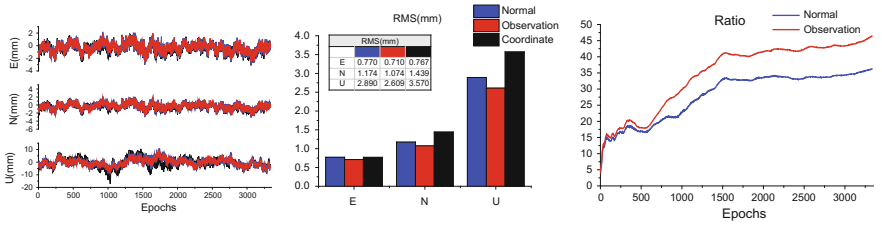

Fig. 3 The contrast of the error sequences and the ratio rates of dynamic sequential least-squares calculation in the three different combinations

We used, respectively, single epoch, static sequential least squares adjustment, and sequential least squares on condition of dynamic, with LAMBDA algorithm to fix ambiguities. Counted deviation in E, U, N direction, ***RMS*** and ***RATIO*** for each method, combined in different field. Both Deviation and ***RMS*** in mm. The results of the calculation mode are shown in Figs. 1, 2 and 3

4.1 Single Epoch Solving

4.1.1 Static Sequential Least Squares Solving

It can be seen from Figs. 1 and 2 that the result of combination, both of normal equation field and observation equation field, are the same, RMS and Ratio are the same, which validate the inferences made in 3.1 and 3.2 that BDS/GPS combined, both in normal equation field and observation equation field, relative positioning Equations of the combination of the equation field and the observation equation field on the conditions of single-epoch solving and sequential least-squares solution. The accuracy of the result is better than that of the coordinate estimation method.

4.2 Analysis of Dynamic Sequential Least Squares Solving

It can be demonstrated from Fig. 3 that, on the condition of dynamic sequential least squares solution, BDS/GPS combined, in normal equation field and in observation equation field, coordinate estimates, RMS and RATIO show a difference, Both RMS and RATIO of combination of observation equation field, contrast to that of combined in normal equation field, express the Optimality. Which verify the inference in 3.3.

5 Conclusion

In this contribution, We based on the BDS/GPS combined positioning in different fields and its analysis, the following conclusions can be obtained through the precise processing of the measured data:

(1) In the short baseline case, the plane error of BDS/GPS combined, in different field, positioning method in different solution are better than 1 cm. When single epoch solving, The combination of the normal equation field and the observation equation field are better than 2 cm on elevation direction, and that of the combination of the coordinate estimates field is about 3 cm, coordinate evaluation range combination is about 3 cm. On the condition of static sequential least squares solving, the error of combination of each field are better than 0.5 cm; on elevation direction, On the dynamic sequential least square solving, the combination error of the equation is better than 1 cm, the estimation of the method equation is better than 2 cm, the coordinate estimation combination is better than 3 cm.

(2) The results of observation field combination show the highest precision and the Ratio value of ambiguity integer estimate is higher than that of the equation field combination. The residuals of the combination of the coordinate estimates field are still relatively large, and the accuracy is lower than that of other combinations.
(3) On the condition of dynamic sequential least—squares solving, when decrease the coordinate parameters, between epochs, of the normal equation field combination method, The information between ambiguities of different system and coordinate solution, estimated from combined positioning, is not taken into account, Therefore, the combination of the observation equation field is more stringent than the normal equation field combination. Simultaneously, In the single epoch solving and static sequential least squares, the two are equivalent.

Acknowledgements This research is supported by the state key development program "collaborative precision positioning technology" (Project No. 2016YFB0501804), funded and supported by the National Natural Science Foundation (Project No.: 41504006416740 34), Chinese Academy of Sciences 100 and cutting-edge technology research plan (project number: QYZDB-SSW-DQC028) funding. At the same time, this paper also obtained the National Natural Science Fund Project (41304033); the two generation of navigation major project of construction and operation maintenance center (GFZX0301040308); the natural science foundation of Shaanxi province (2016JQ4011) funded project.

References

1. Yuanxi Y (2010) Progress, contribution and challenges of compass/Beidou satellite navigation system. Acts Geodaetlca et Canographica Sinico. 39(1):P1–P6
2. Wei Z (2008) China geodetic coordinate system 2000 and its comparison with WGS84. J Geodesy Geodynmics 28(5):P1–P5
3. Gao X, Guo J, Cheng P et al (2012) Fusion positioning of BeiDou/GPS based on spatio temporal system unification. Acta Geodaetica et Cartographica Sinica, 41(5):P743–748
4. Zang N (2015), A study on the algorithms of BDS and GNSS precise point positioning. Chang'an University, China
5. Huang G, Yang Y, Zhang Q et al (2013) GNSS precise point positioning algorithm based on parameter equivalent reduction principle. The 4th China satellite navigation conference (CSNC), pp 449–469
6. Li X (2014), Research on the algorithm of integrated positioning and the preliminary results based on BeiDou/GPS. The 5th China satellite navigation conference (CSNC)
7. Zhang Q, Li G (2005) GPS measuring principle and application. Science Press
8. Teunissen PJG (1995) The least-squares ambiguity decorrelation adjustment: a method for fast GPS integer ambiguity estimates. J Geodesy 70(1):P65–P82
9. (2009) Wuhan university adjustment error theory and measurement of foundation. Wuhan University Press
10. Huang GW (2008) GPS precise point positioning and high precision GPS baseline net adjustment research and its software implementation. Chang 'an University
11. Yang Y, He H (2005) Sequential least squares estimator for solving ambiguity of kinematic GPS phase measurement. Geomatic Sci Eng 2005(1):P1–4

Deformation Monitoring and Precision Analysis Based on BDS/GPS Dual System Combination

Lei Ren, Tianhe Xu, Qingsong Ai and Yuguo Yang

Abstract To test the accuracy and reliability of BDS/GPS dual system combination in geological hazard monitoring, the key technologies of BDS and GPS dual mode fusion relative positioning are analyzed. Through the processing and analysis of the measured deformation monitoring network data, the results show that. The precision of dual frequency BDS/GPS combined deformation monitoring is better than those of GPS and BDS single system. The positioning accuracy in horizontal direction is better than 2 mm, vertical direction is better than 3 mm. A new robust moving average method is proposed for smooth filtering of dual system combined deformation monitoring sequences. This method has good ability to resist outliers, and can make the deformation sequences smoothly. On the basis of combined positioning, the daily drift velocity of each monitoring station is estimated. The accuracy and reliability of BDS/GPS dual system combined positioning are further confirmed and analyzed, which shows a promising application of BDS in deformation monitoring field.

Keywords Combined BDS/GPS positioning · Deformation monitoring · Smoothing filter · Drift velocity

L. Ren · Q. Ai · Y. Yang
School of Geology Engineering and Surveying, Chang an University,
Xi an, Shanxi, China, No. 126, Yanta Road, Xi'an, China
e-mail: renchd009@163.com

T. Xu (✉)
Institute of Space Science, Shandong University,
Weihai, Shandong, China
e-mail: thxugfz@163.com

T. Xu
State Key Laboratory of Geo-Information Engineering,
Xi'an, Shanxi, China

J. Sun et al. (eds.), *China Satellite Navigation Conference (CSNC) 2017 Proceedings: Volume I*, Lecture Notes in Electrical Engineering 437,
DOI 10.1007/978-981-10-4588-2_6

1 Introduction

Beidou satellite navigation system (BDS) as a global satellite navigation system developed by China independently, has provided uninterrupted navigation and timing services to the Asia Pacific region on 2012 formally [1]. Since the BDS has been in service, the application of satellite navigation in China has made great progress in theoretical research, technical improvements, equipment manufacturing and application services.

As China's vast territory, complex and diverse topography, the natural geological disasters resulting in the loss of property happens with increasing frequency. In deformation monitoring, GNSS with its simple operation, all-weather observation, without indivisibility and other characteristics shows incomparable advantages over other methods [2]. The accurate and reliable positioning results by GNSS are closely related to adequate observation redundancy. The station measurement is often restricted by the environment, which affects the geometry of the visible satellite [3]. BDS has the characteristics of different satellite constellation, even if the next generation BDS is not completed, the number of BDS satellites in China is better than other systems such as GPS [4]. In addition, BDS and other GNSS compatibility and interoperability allows users to simultaneously use multiple system observation data, which can greatly improve the observation redundancy [5].

At present, the BDS pseudo-range and carrier-phase measurement accuracies have been at the same level as GPS [6]. The pseudo-range and carrier-phase measurement accuracies are about 33 cm and 2 mm respectively [7]. In addition, due to BDS data coding and the development of relevant standards, there is a certain similarity with GPS system, it can make a good combination and supplement in the constellation composition [8, 9]. In this paper, after reviewing the dual system combined relative positioning model, the feasibility of BDS/GPS dual system combined positioning application in deformation monitoring is analyzed. The accuracy and reliability of dual system combined positioning is verified using the real examples. A new robust moving average method is proposed for smooth filtering of displacement sequences. Finally, the high precision positioning results were used to analyze the drift velocity of the monitoring structure, which further proved the advantages of dual system positioning in deformation monitoring.

1.1 BDS and GPS Space and Time Datum Unification

1.1.1 Space Datum Unification

BDS uses the CGCS2000 geodetic coordinate system, while the GPS uses the WGS84 coordinate system. Although there are differences between the two coordinate systems, the definition of each parameter is almost the same, including origin, scale and evolution of ellipsoid [10]. At the same time the reference ellipsoid

flattening constants f used in the two coordinate systems are only slightly different. The geodetic coordinate anomalies caused by the difference of f can be calculated as follows:

$$dL = 0 \tag{1}$$

$$dB = \frac{M\left[2 - (2f - f^2)\sin^2 B\right]}{(1 - f)} \sin B \cos B \, df \tag{2}$$

$$dH = \frac{M}{1 - f}\left[1 - (2f - f^2)\sin^2 B\right] \sin^2 B \, df \tag{3}$$

where M is the radius of curvature of the meridian and df is the difference of the flattening rate. From the above equation, it can be seen that the difference of f does not cause the longitude change of the earth, and the latitude and height is influenced by the f change. In addition, the df will cause normal gravity difference of ellipsoid, which will affect the accuracy of geoid. However, the magnitude of this effect is small, and it can be ignored for short baseline measurement.

1.1.2 Time Datum Unification

BDS and GPS systems have their own time reference. BDT is used for the BDS time system, and GPST for the GPS time system [11]. This two systems have a certain similarity in the definition, illustrated by that they are both atomic time system, second as the basic unit of time scale, continuous accumulation and no leap seconds. The origin definition of two systems times is different. GPST time origin is January 6, 1980, UTC 00:00:00, and BDT time origin is January 1, 2006, UTC 00:00:00 [12]. There is a difference of 1356 weeks between this two systems, and also a 14 s time difference caused by UTC.

The conversion formula between BDT and GPST is:

$$BDT = GPST + \Delta t_{GPS} \tag{4}$$

$$\Delta t_{GPS} = A_{1GPS} + A_{2GPS} \times t_{BDT} \tag{5}$$

where t_{BDT} is the conversion time of BDS, A_{1GPS} and A_{2GPS} are the synchronization parameters of BDT relative to GPST. In this paper, the time difference between this two systems is eliminated in the double difference positioning.

1.1.3 Differences in Satellite Broadcasting Position Calculation

The constellation of BDS consists of three types, geostationary orbit satellite (GEO), inclined orbit synchronous satellite (IGSO), medium and high orbit satellite

(MEO). BDS has some differences with GPS in the calculation of the broadcasting position of satellites. The broadcasting position of IGSO satellites and MEO satellites are similar to that of GPS satellites. Due to the orbit of GEO satellite is stationary relative to the earth, the broadcasting position of GEO satellites need to be calculated by a certain coordinate rotation. The rotation calculation mainly influences the longitude and coordinates of ascending node.

1.2 Combined Positioning Model and Smoothing Filtering

1.2.1 Relative Positioning Model of Dual System Combination

To improve the accuracy of positioning, we often use the method of calculating single difference between stations and double difference between satellites in GNSS data processing strategy. Since double difference mode can eliminate the orbit error, the receiver and satellite clock error, it can greatly weaken the ionospheric delay and the phase ambiguity with integer characteristic is retained after the double difference processing [13]. In the relative positioning, carrier-phase double difference can get millimeter level of positioning accuracy. BDS/GPS combined carrier-phase double difference positioning model is presented.

The observation equation of the carrier phase double-difference model can be simply written as

$$\nabla\Delta\varphi = \left(\varphi_2^i - \varphi_1^i\right) - \left(\varphi_2^j - \varphi_1^j\right) \tag{6}$$

where $\nabla\Delta$ is the double-difference operator, i the reference satellite, j the non-reference satellite, 1 the base station, and 2 the rover station.

It can be further written as

$$\lambda\nabla\Delta\varphi = \nabla\Delta\rho + \lambda\nabla\Delta N - \nabla\Delta I + \nabla\Delta T + \varepsilon_{\nabla\Delta\Phi} \tag{7}$$

where λ is the carrier wavelength, φ the carrier phase observation, ρ the inter-satellite geometric distance, N the integer ambiguity, I the ionospheric delay error, T the tropospheric delay error, ε_Φ the carrier phase random noise and others error.

The linearization can be obtained as

$$\begin{aligned}\lambda\nabla\Delta\varphi = &\begin{bmatrix} -\nabla l_2^{ij} & -\nabla m_2^{ij} & -\nabla n_2^{ij} \end{bmatrix} \begin{bmatrix} dx_2 \\ dy_2 \\ dz_2 \end{bmatrix} - \lambda\nabla\Delta N + \rho_2^i \\ &- \rho_1^i - \rho_2^j + \rho_1^j + \nabla\Delta I - \nabla\Delta T + \varepsilon_{\nabla\Delta\Phi}\end{aligned} \tag{8}$$

Assuming that n + 1 GPS satellite and m + 1 BDS satellites are observed in a single epoch, the double-difference error equation is obtained

$$v_{n+m} = \begin{bmatrix} A_{(n+m)\times 3} & B_{(n+m)\times(n+m)} \end{bmatrix} \begin{bmatrix} dX_{3\times 1} \\ \nabla\Delta N_{(n+m)\times 1} \end{bmatrix} + L_{(n+m)\times 1} \tag{9}$$

where

$$v_{n+m} = \left[v_G^1, \cdots, v_G^n, v_B^1, \cdots v_B^m\right]^{\mathrm{T}}$$

$$A_{(n+m)\times 3} = \begin{bmatrix} -\nabla l_G^1 - \nabla m_G^1 - \nabla n_G^1 \\ \cdots\cdots\cdots \\ -\nabla l_G^n - \nabla m_G^n - \nabla n_G^n \\ -\nabla l_B^1 - \nabla m_B^1 - \nabla n_B^1 \\ \cdots\cdots\cdots \\ -\nabla l_G^m - \nabla m_G^m - \nabla n_G^m \end{bmatrix}$$

$$B_{(n+m)\times(n+m)} = \begin{bmatrix} diag(-\lambda_G)_{n\times n} & 0 \\ 0 & diag(-\lambda_B)_{m\times m} \end{bmatrix}$$

$$L = [\rho_2^i - \rho_1^i - \rho_2^j + \rho_1^j + \nabla\Delta I - \nabla\Delta T + \varepsilon_{\nabla\Delta\Phi}]$$

1.2.2 Smoothing Filter for Deformation Monitoring Sequence

It is usually considered that the displacement of each direction is smooth in a certain range for the structure of slow deformation geological disaster. GNSS deformation monitoring is easy to be affected by errors such as atmospheric residual delay and receiver noise, which makes the monitoring displacement sequence contain noise or even outliers. it is necessary to smooth the monitoring sequence to reduce the influence of noise. On the basis of the weighted moving average method [14], this paper proposed a new robust weighted moving average method.

The original weighted moving average model can be expressed as

$$\hat{y}_n = \frac{\sum_{j=0}^{m-1} \omega_j y_{n-j}}{\sum_{j=0}^{m-1} \omega_j} \tag{10}$$

where $\widehat{y}_n$ is the moving average corresponding to the n-th data point, ω_j is the weight corresponding to the j-th data point, and m is the window size in the moving average model.

In the process of smoothing filter, the epoch weight is calculated by the equivalent weight function. It is divided into three sections: if the error is small, the weight takes its original one; if the error is large but not significant, the weight is reduced by a robust factor; and if the error is abnormal, the weight sets to zero.

The equivalent weight function can be expressed as [15]

$$\omega_i = \begin{cases} p_i, & |v_i| < k_0 \\ p_i \cdot \frac{k_0}{|v_i|}\frac{(k_1-|v_i|)^2}{(k_1-k_0)^2}, & k_0 < |v_i| < \omega_n S_x \\ 0, & |v_i| \geq \omega_n S_x \end{cases} \tag{11}$$

The weight function used in this paper is improved on the basis of IGG III equivalent weight function, in which p_i is the original weight; and k_0, k_1 is the empirical value; after a large number of experimental verification, k_0 generally takes 1–1.5; k_1 takes 2.5–3. Anomalies are detected according to the Chauvenet criteria with the formula as follows:

$$|v_i| > \omega_n S_x \tag{12}$$

Among them:

$$\omega_n = 1 + 0.4\ln(n),\ S_x = \sqrt{\frac{\sum_{i=1}^{n}(x_i - \bar{x})^2}{n-1}}$$

where $|v_i|$ is the error absolute value, ω_n is the Schoeller coefficient, S_x is the standard deviation, and n is the number of epochs. If the error absolute value is greater than the product of the Shawell coefficient and the standard deviation, it is identified as outlier at this epoch.

1.3 Data Processing and Results Analysis

To analyze the accuracy of BDS/GPS dual system combined positioning, and verify the feasibility and stability in the deformation monitoring, the monitoring data were collected from the monitoring network of Yang Chang Wan in Ningxia province of China. This monitoring network used BDS/GPS dual-system and dual-frequency receivers for data acquisition. Ten GNSS stations were installed in this network, in which the base station was GD36. The distribution of the stations is shown in Fig. 1, and the observation time is from November 12, 2015 to November 19, 2015 (Day of year (doy) is from 316 to 323).

1.3.1 Data Quality Analysis

The distribution of all the monitoring stations is more centralized, and processing baselines are all within 2 km, so receiving satellites are basically the same in the same time period. In this paper, we select the observation file of 5 s sampling

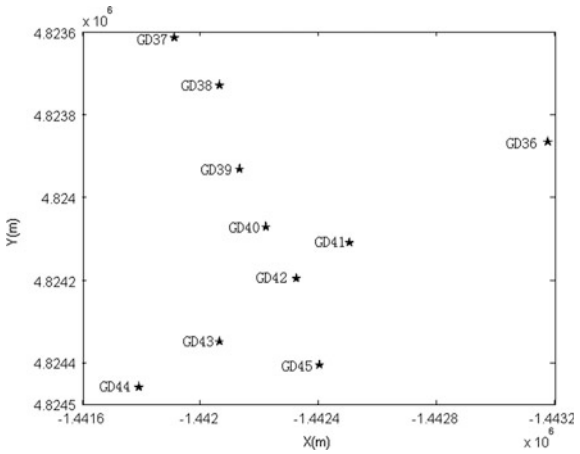

Fig. 1 The distribution of stations

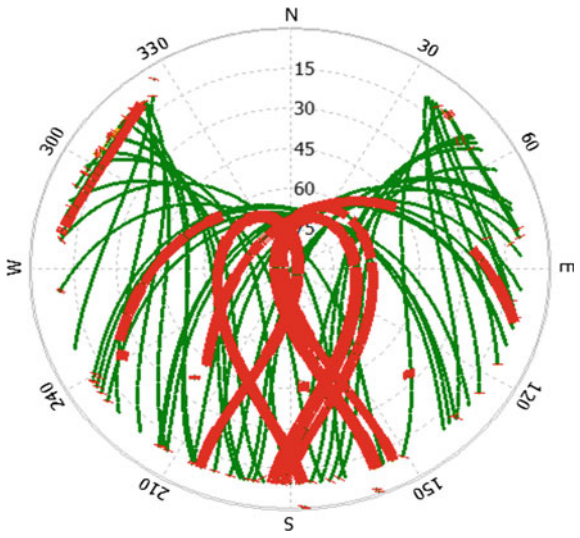

Fig. 2 Satellite sky map of GD36

interval of GD36 station to analyze the available satellites and PDOP value of each navigation satellite system. The analysis period is doy of 316.

Figure 2 is the satellite sky map of GD36 station, where the red line is BDS satellite trajectory and the green line is GPS satellite trajectory. It can be seen that the satellite cutoff height angle are set to 10° for data acquisition. During the monitoring period, about 70° below the altitude of the satellite is blocked in the north, and the rest of satellites distribution is uniform and more complete.

Figure 3 shows the number of visible satellites epoch-by-epoch. The number of visible satellite is about 16–20 for BDS/GPS dual system, 7–10 for GPS and 8–11 for BDS. Number of BDS satellites between adjacent epochs almost remained at

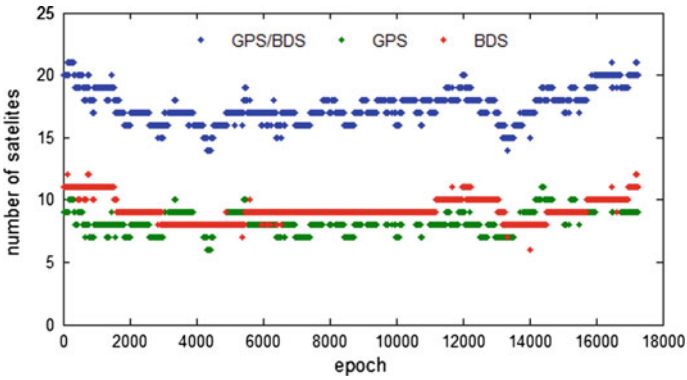

Fig. 3 The number of visible satellite

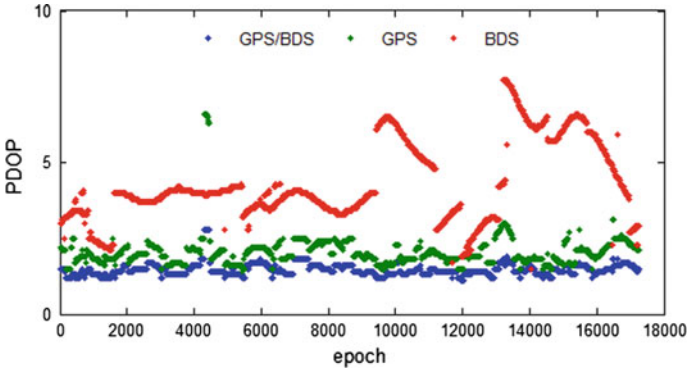

Fig. 4 PDOP in single epoch

about 9, while that of GPS satellites varied more frequent among different epochs. The number of visible satellites increases obviously when combining BDS/GPS dual system. Although there is some fluctuation, the overall number is obviously superior to single system, which greatly improves the observation redundancy.

Figure 4 is the distribution of PDOP values of each system in the observation period. The PDOP value of BDS/GPS dual system is much less than that of GPS and BDS single system, and the average value is about 1.5. It can be verified that dual system combination positioning can significantly improve the spatial distribution of satellite. The average value of GPS is about 2 and changes smoothly. Due to the influence of GEO satellite, BDS is not well distributed, and its PDOP average is about 4.3 and lower than that of GPS.

1.3.2 Positioning Accuracy Analysis

Three schemes GPS single system, BDS single system and BDS/GPS dual system combination are performed for positioning validation. We select the stable point of GD38 to analyze the positioning accuracy of all schemes. It avoids the influence of periodic items and displacement trend on positioning accuracy in this section.

The data processing mode is dual frequency relative positioning, and the troposphere correction model adopts Saastamoinen model, the ionospheric correction uses broadcast ephemeris correction. Kalman filter is used for parameter estimation. After deleting the epochs of convergence, the positioning errors are shown in Fig. 5. The standard deviation (STD) and mean (AVE) statistics of error time series are given in Table 1.

The positioning accuracy of BDS is the same level as that of GPS in the short baseline measurement, the direction of E and N is better than 2 mm; that of U is better than 5 mm. The accuracy of E direction is better than that of N direction, which is mainly because that BDS has not yet completed the global system. The combined positioning accuracy of BDS/GPS dual system is better than those of GPS and BDS in all directions, which fully proves the high accuracy and reliability of dual system combined positioning. The combination of BDS/GPS positioning

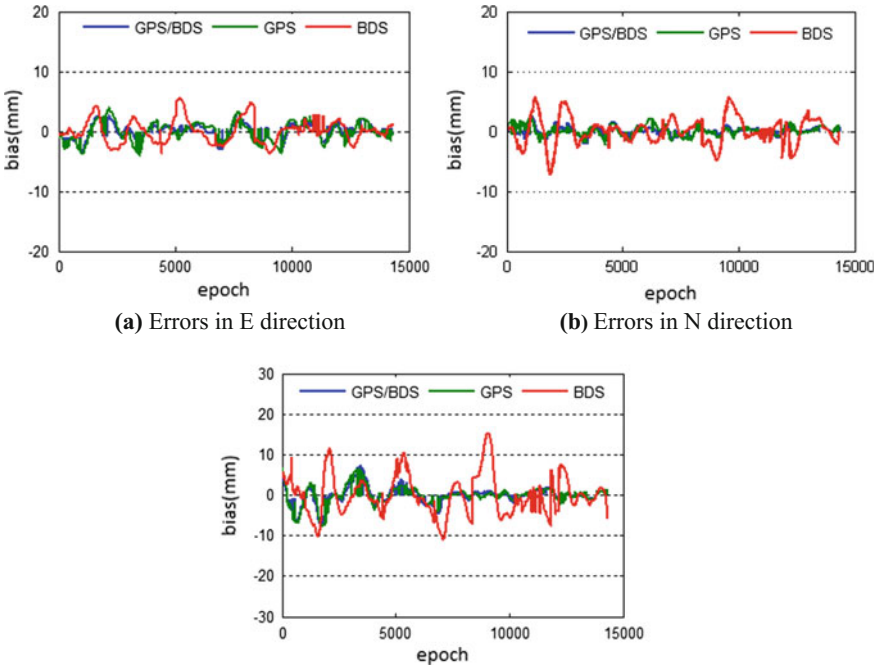

(a) Errors in E direction

(b) Errors in N direction

(c) Errors in U direction

Fig. 5 Errors of GD38 station for doy of 316

Table 1 Accuracy statistics of relative positioning

	STD			AVE		
	BDS/GPS	GPS	BDS	BDS/GPS	GPS	BDS
E (mm)	1.39	1.66	1.54	1.14	1.38	1.48
N (mm)	0.73	0.97	2.01	0.57	0.70	1.77
U (mm)	2.33	2.61	4.77	1.54	1.57	3.84

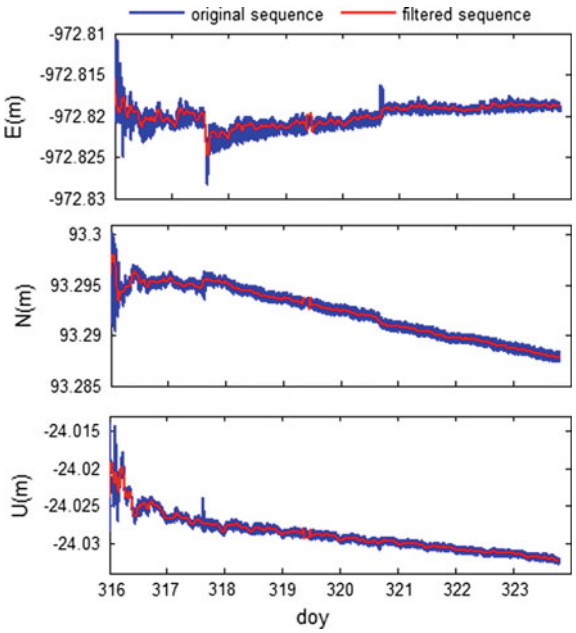

Fig. 6 Smoothing filter for monitoring sequence

can enhance the observation redundancy and overcome the shortcomings of possible low data quality of single system.

1.3.3 Smoothing Filter for Monitoring Sequence

Figure 6 shows dual system combined monitoring sequence of GD40 station. BDS/GPS positioning can accurately describe the displacement of this station in each direction after a convergence procedure in initial time. The sequence has some outliers, the whole sequence changes are relatively stable and no jump. The sequence become more smoothly when it is filtered by robust weighted moving average of GD40 station. The results show that the proposed method can effectively improve the monitoring accuracy.

Table 2 Accuracy evaluation of smoothing filter

Between system RMS (mm)	Weighted moving average method RMS (mm)	Robust weighted moving average method RMS (mm)	Improvement rate (%)
1.47	1.44	0.91	38
1.51	1.27	1.13	25
2.53	2.15	1.94	23

Table 3 Estimation of daily drift velocity

Station	E (mm/day)	N (mm/day)	U (mm/day)
GD37	0.08	0.09	0.21
GD38	0.05	0.01	−0.30
GD39	0.31	−0.29	−0.41
GD40	0.02	−0.87	−0.96
GD41	−1.80	−5.11	−8.91
GD42	0.12	−2.44	−4.86
GD43	0.87	−0.52	−0.77
GD44	0.30	0.02	−0.44
GD45	0.11	0.36	−0.01

To confirm the validity and reliability of the proposed method further, we use the GPS system solution processed by Bernese5.2 software as a reference to calculate the residual sequence. The RMS values are shown in Table 2. Compared with the ordinary weighted moving average method, the proposed method can improve the accuracy of the monitoring results and better control the influence of outliers.

1.3.4 Analysis of Station Drift Velocity

Based on the combined positioning of dual system, we take the station coordinates obtained by BDS/GPS combined solution as quasi-observations with variance information to estimated the daily drift velocity of each station by using the dynamic Kalman filter.

The drift velocity of each station can be seen in Table 3. The average drift velocity of GD41 station was greater than 1 mm in all directions, while the drift velocity even reached −8.91 mm/day in U direction. Combined with the monitoring results to those provided by the relevant department, it is verified that the displacement and velocity estimating obtained by BDS/GPS combination positioning are in good agreement with the actual situation, which can provide displacement prediction for the follow-on monitoring in this area.

1.4 Conclusions

The combination of BDS/GPS dual system can significantly improve the number of visible satellites and enhance the observation redundancy. For dual frequency relative positioning of short baseline(less than 2 km), the positioning accuracy of BDS in the direction of E and N is better than 2 mm, and 5 mm in U direction. The precision of BDS/GPS dual system combined positioning is better than those of GPS and BDS single system in all directions. The positioning accuracy is better than 2 mm in horizontal, and 3 mm in vetical. The robust weighted moving average method can be used to smooth the monitoring sequence for the deformation geological disaster effectively. But the size of moving window is experiential and need to be studied further. The combination of BDS/GPS positioning can be used for estimating station drift velocity. With the development of BDS, fusion positioning combining BDS and other GNSS systems can get more accurate positioning results and expand its applications in more broad fields.

Acknowledgements This work was supported by the National Natural Science Foundation of China (41574013) and the National Key Research and Development Program (2016YFB0501701).

References

1. China satellite navigation system management office (2012) "Beidou" satellite navigation system development report [J]. Int Space 4:6–11 (In Chinese)
2. Yugang Xiao, Weiping Jiang, Hua Chen et al (2016) Reserach and realization of deformation monitoring algorithm with millimeter level precision based on Beidou navigation satellite system [J]. Acta Geodaetica Cartogr Sin 45(1):16–21 (In Chinese)
3. Zhenzhong Peng, Qianxia LI, Zhiqiu XU, Bo YANG, Linyuan XIA (2016) Beidou and GPS integrated high precision positioning and monitoring analysis of bridges [J]. Trop Geogr 36(4):717–726 (In Chinese)
4. Qiang Shi, Wujiao Dai, Guoxiang Yang et al (2016) Test on precision of combined single-frequency GPS/BDS deformation monitoring system [J]. Eng Surv 44(3):69–74 (In Chinese)
5. Yuanxi Yang (2010) Progress, contribution and challenge of Beidou satellite navigation system[J]. J Surv Mapp 39(1):1–6 (In Chinese)
6. Li Wang, Qin Zhang, Lihong Fan et al (2015) Test and result analysis of Beidou/GPS fusion static relative positioning for high precision ground subsidence monitoring [J]. J Eng Geol 23(1):119–125 (In Chinese)
7. Yang Y, Li J, et al (2014) Preliminary evaluation of the basic navigation and positioning performance of Beidou satellite navigation system [J]. China Sci Earth Sci 1:72–81 (In Chinese)
8. Lou Y, Gong X, Gu S, et al (2016) BDS/GPS mixed double differential RTK positioning method and result analysis [J]. J Geodesy Geodyn 36(1):1–5 (In Chinese)
9. Deng C, Tang W, Liu J et al (2014) Reliable single-epoch ambiguity resolution for short baselines using combined GPS/Beidou system [J]. GPS Solutions 18(3):375–386
10. Zhang C, Wang SD, Dang Y, et al () Relative positioning model and accuracy analysis of BDS/GPS combined system [J]. Surv Mapp Sci 39(10) (In Chinese)

11. Tang W, Deng C, Gao epoch-by-epoch, Dimitris A (2013) Beidou baseline and preliminary results of algorithm [J]. J Wuhan Univ (Inform Sci Ed) 38(8):897–901 (In Chinese)
12. Han C, Yang Y, Cai Z (2011) Beidou navigation satellite system and its time scales [J]. Metrologia 48(4):S213–S218(6)
13. Teunissen PJG, Odolinski R, Odijk D (2014) Instantaneous Beidou+GPS RTK positioning with high cut-off elevation angles [J]. J Geodesy 88(4):335–350
14. Guangchun Li, Wujiao Dai, Fanhe Zeng (2016) Robust moving average in GPS automatic monitoring data processing applications [J]. J Geodesy Geodyn 36(1):85–88 (In Chinese)
15. Yang Y (1994) Principle of equivalent weight: robust least squares solution of parameter adjustment model [J]. Bullet Surv Mapp (6):33–35+29 (In Chinese)

The Research on Nonlinear Attitude Determination Method of GNSS Multi-antenna Attitude Measurement

Yuan Tian, Lifen Sui, Bing Wang, Qing Dai, Yijun Tian and Tian Zeng

Abstract GNSS multiple antenna attitude measurement possesses three attitude determination methods, direct solution, nonlinear least squares method and linear least squares method. Normal nonlinear least squares method on attitude estimate realizes linearization of observation equation with additive euler angle error being the parameter, of which the calculation is largely increased and accuracy can be further enhanced. Hence, nonlinear least squares methods respectively based on additive quaternion error, multiplicative euler angle error and multiplicative quaternion error are derived, and detailed calculation procedures and least squares solutions are respectively presented. Finally a simulation experiment is designed to compare and analyze the direct solution, linear least squares method and 4 types of nonlinear least squares method. Conclusions are as follows: (1) direct solution possesses short calculation time consumption, only being available to degree-level navigation application due to low accuracy; (2) the least squares method whose accuracy is higher than direct solution by more than 60%, reaching to 30′, and single epoch time consumption is just a little more than direct solution, is available to minute-level navigation application; (3) nonlinear least squares method based on multiplicative error is relatively the best.

Keywords GNSS multi-antenna attitude measurement · Attitude determination method · Nonlinear least squares · Additive attitude error · Multiplicative attitude error

Y. Tian (✉) · L. Sui · Q. Dai · Y. Tian · T. Zeng
Information Engineering University, Zhengzhou 450001, China
e-mail: tyuan1247@qq.com

B. Wang
Beijing Satellite Navigation Center, Beijing 100094, China

J. Sun et al. (eds.), *China Satellite Navigation Conference (CSNC) 2017 Proceedings: Volume I*, Lecture Notes in Electrical Engineering 437,
DOI 10.1007/978-981-10-4588-2_7

1 Introduction

Attitude measurement system is a significant component of dynamic navigation system. Traditional attitude measurement system, Inertial Navigation System (INS), has many limitations of error rapidly increasing with time going by, long initial calibration time consumption and hard controlled accuracy and high cost [1, 2], which largely restrict its application. Global Navigation Satellite System (GNSS) can provide high-accuracy navigation, positioning and time service. Besides, GNSS multi-antenna attitude measurement system which providing real-time minute-level attitude information, compared with INS, is widely applied in navigation and aviation, road and dam measurement due to the merits of low cost, high real time, small volume, light weight, easy fixation and short initialization time consumption.

Recent years, research related to GNSS multi-antenna attitude measurement mainly focus on velocity and accuracy improvement of integer ambiguity fixation [3, 4], and several fruitful searching algorithm have been presented. Also some scholars studied the influences from antenna layout, antenna number, baseline length and observed satellite number on attitude measurement accuracy [5, 6], drawing several conclusions that better antenna layout, longer baseline length and more antennas and observed satellites lead to higher attitude accuracy. Currently the integer ambiguity fixation methods are relatively mature and such factors mentioned above are always limited in practical situation, therefore attitude calculation methods with higher accuracy is necessary. Direct solution and nonlinear least squares method [7], two frequently-used methods, are contrasted in [8] which drawing a conclusion that nonlinear least squares method is better than direct solution. Note that normal nonlinear least squares method realizes linearization of observation equation with additive euler angle error being the parameter, of which the calculation is largely increased. In [9] an Attitude Matrix Element Solution (AMES) is presented, avoiding the linearization of observation equation.

In this paper, based on nonlinear least squares method the other three linearization methods of observation equation are researched. We respectively regard additive quaternion error, multiplicative euler angle error and multiplicative quaternion error as parameter to implement linearization, after that the attitude calculation formulas under different linearization methods are derived. Finally, direct solution, linear least squares method and 4 types of nonlinear least squares method are compared in detail.

2 Direct Solution

Direct solution needs at least two baselines (three GPS antennas) to calculate the attitude. Let the position of master antenna being the origin of Body Frame System [7] (BFS, B), and install the first baseline $\mathbf{b}_1$ along the vertical axis of body frame, then baseline vector is $\mathbf{b}_1^B = [0 \quad b_1 \quad 0]^T$. The angle between $\mathbf{b}_1$ and the second

baseline $\mathbf{b}_2$ which can be installed randomly is α, hence $\mathbf{b}_2^B = [\, b_2 \sin\alpha \quad b_2 \cos\alpha \quad 0\,]^T$, where b_1 and b_2 denote baseline length. Supposing that $\mathbf{b}_1^L$ and $\mathbf{b}_2^L$ are the two baselines in Local Level System [7] (LLS, L), then according to the transformation relation of the first baseline— $\mathbf{b}_1^L = \mathbf{R}\mathbf{b}_1^B$—we can calculate the yaw (ψ) and pitch (θ), where $\mathbf{R}$ denotes the direction cosine matrix. Formulas are as follows:

$$\mathbf{R} = \begin{bmatrix} C_\psi C_\gamma - S_\psi S_\theta S_\gamma & -S_\psi C_\theta & C_\psi S_\gamma + S_\psi S_\theta C_\gamma \\ S_\psi C_\gamma + C_\psi S_\theta S_\gamma & C_\psi C_\theta & S_\psi S_\gamma - C_\psi S_\theta C_\gamma \\ -C_\theta S_\gamma & S_\theta & C_\theta C_\gamma \end{bmatrix} \tag{1}$$

$$\psi = -\arctan\left(\frac{b_{1,x}^L}{b_{1,y}^L}\right) \tag{2}$$

$$\theta = \arctan\left(\frac{b_{1,z}^L}{\sqrt{(b_{1,x}^L)^2 + (b_{1,y}^L)^2}}\right) \tag{3}$$

In order to calculate the roll (γ), we rotate $\mathbf{b}_2^L$ with yaw and pitch to get $(\mathbf{b}_2^L)'$,

$$(\mathbf{b}_2^L)' = \begin{bmatrix} 1 & 0 & 0 \\ 0 & \cos\theta & \sin\theta \\ 0 & -\sin\theta & \cos\theta \end{bmatrix} \begin{bmatrix} \cos\psi & \sin\psi & 0 \\ -\sin\psi & \cos\psi & 0 \\ 0 & 0 & 1 \end{bmatrix} \mathbf{b}_2^L \tag{4}$$

then γ can be calculated as follows:

$$\gamma = -\arctan\left(\frac{(b_{2,z}^L)'}{(b_{2,x}^L)'}\right) \tag{5}$$

3 Nonlinear Least Squares Method

3.1 *Least Squares Based on Additive Euler Angle Error*

The baseline vectors in the two coordinate systems are related as follows:

$$\mathbf{B}^{\mathrm{L}} = \mathbf{R}\mathbf{B}^{\mathrm{B}} \tag{6}$$

where $\mathbf{B}^{\mathrm{L}} = [\, \mathbf{b}_1^{\mathrm{L}} \quad \mathbf{b}_2^{\mathrm{L}} \quad \ldots \quad \mathbf{b}_m^{\mathrm{L}}\,]$, $\mathbf{B}^{\mathrm{B}} = [\, \mathbf{b}_1^{\mathrm{B}} \quad \mathbf{b}_2^{\mathrm{B}} \quad \ldots \quad \mathbf{b}_m^{\mathrm{B}}\,]$, m denotes baseline number and $\mathbf{R}$ denotes direction cosine matrix. In normal nonlinear least squares, with $\mathbf{R}$ being always expressed as the form of euler angle shown in (1) and (6) becomes a nonlinear observation equation related to euler angle and need linearization.

Define additive euler angle error as $\Delta\hat{\mathbf{e}} = [\Delta\hat{\psi} \quad \Delta\hat{\gamma} \quad \Delta\hat{\theta}]^T$ that satisfies $\mathbf{e} = \mathbf{e}_0 + \Delta\hat{\mathbf{e}}$, where $\mathbf{e}$ denotes the true euler angles and $\mathbf{e}_0$ denotes the approximate ones. Then the linearization of (6) can be implemented with $\Delta\hat{\mathbf{e}}$ being its parameter, after that the error equation of the ith baseline reads:

$$\mathbf{V}_i = \mathbf{A}_i\hat{\mathbf{X}} - \mathbf{L}_i = \mathbf{A}_i\Delta\hat{\mathbf{e}} - \left(\mathbf{b}_i^{\mathrm{L}} - \mathbf{R}_0\mathbf{b}_i^{\mathrm{B}}\right) \tag{7}$$

where $\mathbf{A}_i = \left[\frac{\partial \mathbf{R}}{\partial \psi}\mathbf{b}_i^{\mathrm{B}} \quad \frac{\partial \mathbf{R}}{\partial \gamma}\mathbf{b}_i^{\mathrm{B}} \quad \frac{\partial \mathbf{R}}{\partial \theta}\mathbf{b}_i^{\mathrm{B}}\right]$, and $\mathbf{R}_0$ denotes the initial direction cosine matrix. Combining all baselines' error equation together, we can obtain the least squares solution based on additive euler angle error as:

$$\begin{gathered}\Delta\hat{\mathbf{e}} = \begin{bmatrix}\Delta\hat{\psi}\\ \Delta\hat{\gamma}\\ \Delta\hat{\theta}\end{bmatrix} = \left(\sum_{i=1}^{m}\mathbf{A}_i^{\mathrm{T}}\mathbf{P}_i\mathbf{A}_i\right)^{-1}\left(\sum_{i=1}^{m}\mathbf{A}_i^{\mathrm{T}}\mathbf{P}_i\mathbf{L}_i\right)\\ \mathbf{P}_i = \left(\mathbf{Q}_{b_i^{\mathrm{L}}} + \mathbf{R}_0^{\mathrm{T}}\mathbf{Q}_{b_i^{\mathrm{B}}}\mathbf{R}_0\right)^{-1}\end{gathered} \tag{8}$$

where $\mathbf{Q}_{b_i^{\mathrm{L}}}$ and $\mathbf{Q}_{b_i^{\mathrm{B}}}$ respectively denote the inverse weight matrix of baselines in LLS and BFS. With $\Delta\hat{\mathbf{e}}$ obtained, the estimate value of attitude can be calculated by $\mathbf{e} = \mathbf{e}_0 + \Delta\hat{\mathbf{e}}$.

3.2 Least Squares Based on Additive Quaternion Error

Except for euler angle, carrier's attitude can also be expressed by quaternion [10]. Due to this matrix $\mathbf{R}$ in (6) can be expressed as:

$$\mathbf{R}(\mathbf{q}) = \begin{bmatrix} q_0^2+q_1^2-q_2^2-q_3^2 & 2(q_1q_2-q_0q_3) & 2(q_1q_3+q_0q_2)\\ 2(q_1q_2+q_0q_3) & q_0^2-q_1^2+q_2^2-q_3^2 & 2(q_2q_3-q_0q_1)\\ 2(q_1q_3-q_0q_2) & 2(q_2q_3+q_0q_1) & q_0^2-q_1^2-q_2^2+q_3^2\end{bmatrix} \tag{9}$$

Define additive quaternion error as $\Delta\mathbf{q}$ which satisfies $\mathbf{q} = \mathbf{q}_0 + \Delta\mathbf{q}$, where $\mathbf{q}$ denotes the true quaternion and $\mathbf{q}_0$ denotes the approximate value. Then based on $\Delta\mathbf{q}$ we implement the linearization of (6) by using Taylor expansion at $\mathbf{q}_0 = [q_0 \quad q_1 \quad q_2 \quad q_3]$. After that the error equation of the ith baseline in quaternion form reads:

$$\mathbf{V}_i = \mathbf{A}(\mathbf{q})_i\hat{\mathbf{X}} - \mathbf{L}_i = \mathbf{A}(\mathbf{q})_i\Delta\hat{\mathbf{q}} - \left(\mathbf{b}_i^{\mathrm{L}} - \mathbf{R}(\mathbf{q}_0)\mathbf{b}_i^{\mathrm{B}}\right) \tag{10}$$

$$\mathbf{A}(\mathbf{q})_i = \left[\frac{\partial \mathbf{R}(\mathbf{q})}{\partial q_0}\mathbf{b}_i^{B} \quad \frac{\partial \mathbf{R}(\mathbf{q})}{\partial q_1}\mathbf{b}_i^{B} \quad \frac{\partial \mathbf{R}(\mathbf{q})}{\partial q_2}\mathbf{b}_i^{B} \quad \frac{\partial \mathbf{R}(\mathbf{q})}{\partial q_3}\mathbf{b}_i^{B}\right] \tag{11}$$

According to this equation we can obtain the least squares solution of $\Delta\hat{\mathbf{q}}$, further the estimate value of quaternion by $\hat{\mathbf{q}} = \mathbf{q}_0 + \Delta\hat{\mathbf{q}}$. After normalization of $\hat{\mathbf{q}}$ and calculation of direction cosine matrix $\mathbf{R}(\mathbf{q})$ by (9), attitude angle can be easily determined [10].

3.3 Least Squares Based on Multiplicative Euler Angle Error

According to vectorization theorem, vectorization of (6) is realized as follows:

$$vec\mathbf{B}^{\mathrm{L}} = \left((\mathbf{B}^{\mathrm{B}})^{\mathrm{T}} \otimes \mathbf{I}_3\right) vec\mathbf{R} + vec\mathbf{V} \tag{12}$$

The true direction cosine matrix $\mathbf{R}(\mathbf{e})$ and the estimated direction cosine matrix $\mathbf{R}(\hat{\mathbf{e}})$ which expressed by euler angle are related as follows:

$$\mathbf{R}(\mathbf{e}) = \mathbf{R}(\Delta\mathbf{e})\mathbf{R}(\hat{\mathbf{e}}) \tag{13}$$

Here we define $\Delta\mathbf{e}$ as multiplicative euler angle error, also named the misaligned angle of the platform. Since $\Delta\mathbf{e}$ is a small value, so it approximately equal to the euler error of yaw, roll and pitch [11], then such relationships exist:

$$\mathbf{R}(\Delta\mathbf{e}) \approx [\mathbf{I} + (\Delta\mathbf{e}\times)] \tag{14}$$

$$(\Delta\mathbf{e}\times) = \begin{bmatrix} 0 & -\Delta\psi & \Delta\gamma \\ \Delta\psi & 0 & -\Delta\theta \\ -\Delta\gamma & \Delta\theta & 0 \end{bmatrix} \tag{15}$$

Apply (14)–(13), and execute vectorization to it:

$$vec\mathbf{R}(\mathbf{e}) = vec\mathbf{R}(\hat{\mathbf{e}}) + \left(\mathbf{R}^T(\hat{\mathbf{e}}) \otimes \mathbf{I}_3\right) vec[\Delta\mathbf{e}\times] \tag{16}$$

Afterwards applying (16)–(12), we can obtain such an equation:

$$vec\mathbf{V} = \left((\mathbf{B}^{\mathrm{B}})^{\mathrm{T}} \otimes \mathbf{I}_3\right)\left(\mathbf{R}^T(\hat{\mathbf{e}}) \otimes \mathbf{I}_3\right) vec[\Delta\mathbf{e}\times] - vec\left(\mathbf{B}^{\mathrm{L}} - \mathbf{R}(\hat{\mathbf{e}})\mathbf{B}^{\mathrm{B}}\right) \tag{17}$$

This equation's parameter is $vec[\Delta\mathbf{e}\times]$. In order to get the equation based on $\Delta\mathbf{e}$, we need to use $\Delta\mathbf{e} = [\,\Delta\psi \quad \Delta\gamma \quad \Delta\theta\,]^T$ to express $vec[\Delta\mathbf{e}\times]$ as follows:

$$vec[\Delta\mathbf{e}\times] = \mathbf{\Pi}^T\Delta\mathbf{e} \tag{18}$$

$$\mathbf{\Pi} = \begin{bmatrix} 0 & 1 & 0 & -1 & 0 & 0 & 0 & 0 & 0 \\ 0 & 0 & -1 & 0 & 0 & 0 & 1 & 0 & 0 \\ 0 & 0 & 0 & 0 & 0 & 1 & 0 & -1 & 0 \end{bmatrix} \tag{19}$$

According to the three equations above, the least squares solution $\Delta\hat{\mathbf{e}}$ can be described as:

$$\mathbf{N} = \left(\left((\mathbf{B}^{\mathrm{B}})^{\mathrm{T}} \otimes \mathbf{I}_3\right)\left(\mathbf{R}^T(\hat{\mathbf{e}}) \otimes \mathbf{I}_3\right)\mathbf{\Pi}^T\right)^{\mathrm{T}} \mathbf{Q}_{B^{\mathrm{L}}}^{-1} \left(\left((\mathbf{B}^{\mathrm{B}})^{\mathrm{T}} \otimes \mathbf{I}_3\right)\left(\mathbf{R}^T(\hat{\mathbf{e}}) \otimes \mathbf{I}_3\right)\mathbf{\Pi}^T\right) \tag{20}$$

$$\mathbf{U} = \left(\left((\mathbf{B}^{\mathrm{B}})^{\mathrm{T}} \otimes \mathbf{I}_3\right)\left(\mathbf{R}^T(\hat{\mathbf{e}}) \otimes \mathbf{I}_3\right)\mathbf{\Pi}^T\right)^{\mathrm{T}} \mathbf{Q}_{B^{\mathrm{L}}}^{-1} vec\left(\mathbf{B}^{\mathrm{L}} - \mathbf{R}(\hat{\mathbf{e}})\mathbf{B}^{\mathrm{B}}\right) \tag{21}$$

$$\Delta\hat{\mathbf{e}} = \mathbf{N}^{-1}\mathbf{U} \tag{22}$$

3.4 Least Squares Based on Multiplicative Quaternion e Error

Transform (13) to quaternion form as:

$$\mathbf{R}(\mathbf{q}) = \mathbf{R}(\Delta\mathbf{q})\mathbf{R}(\hat{\mathbf{q}}) \tag{23}$$

$$\Delta\mathbf{q} = [\,\Delta q_0 \quad \Delta\bar{\mathbf{q}}\,]^T \tag{24}$$

where $\Delta\bar{\mathbf{q}} = (\,q_1 \quad q_2 \quad q_3\,)^T$; the direction cosine matrix and quaternion are related as follows:

$$\mathbf{R}(\Delta\mathbf{q}) = (\Delta q_0^2 - \|\Delta\bar{\mathbf{q}}\|)\mathbf{I}_3 + 2\Delta q_0[\Delta\bar{\mathbf{q}}\times] + 2\Delta\bar{\mathbf{q}}\Delta\bar{\mathbf{q}}^{\mathrm{T}} \tag{25}$$

For quaternion error being a small value, we consider that $\Delta q_0 \approx 1$, $\|\Delta\bar{\mathbf{q}}\| \approx 0$, $\Delta\bar{\mathbf{q}}\Delta\bar{\mathbf{q}}^{\mathrm{T}} \approx 0$ and apply these to (25), which transformed as:

$$\mathbf{R}(\Delta\mathbf{q}) = \mathbf{I}_3 + 2[\Delta\bar{\mathbf{q}}\times] \tag{26}$$

$$[\bar{\mathbf{q}}\times] = \begin{bmatrix} 0 & -q_3 & q_2 \\ q_3 & 0 & -q_1 \\ -q_2 & q_1 & 0 \end{bmatrix} \tag{27}$$

Subsequent derivation steps being similar to last chapter, we don't present any more, directly giving out the least squares solution of $\Delta\bar{\mathbf{q}}$ as follows:

$$\mathbf{N} = \left(2\left((\mathbf{B}^{\mathrm{B}})^{\mathrm{T}} \otimes \mathbf{I}_3\right)\left(\mathbf{R}^{T}(\hat{\mathbf{q}}) \otimes \mathbf{I}_3\right)\mathbf{\Pi}^{\mathrm{T}}\right)^{\mathbf{T}}\mathbf{P}\left(2\left((\mathbf{B}^{\mathrm{B}})^{\mathrm{T}} \otimes \mathbf{I}_3\right)\left(\mathbf{R}^{T}(\hat{\mathbf{q}}) \otimes \mathbf{I}_3\right)\mathbf{\Pi}^{\mathrm{T}}\right) \tag{28}$$

$$\mathbf{U} = \left(2\left((\mathbf{B}^{\mathrm{B}})^{\mathrm{T}} \otimes \mathbf{I}_3\right)\left(\mathbf{R}^{T}(\hat{\mathbf{q}}) \otimes \mathbf{I}_3\right)\mathbf{\Pi}^{\mathrm{T}}\right)^{\mathbf{T}}\mathbf{P}vec\left(\mathbf{B}^{\mathrm{L}} - \mathbf{R}(\hat{\mathbf{q}})\mathbf{B}^{\mathrm{B}}\right) \tag{29}$$

$$\Delta\bar{\mathbf{q}} = \mathbf{N}^{-1}\mathbf{U} \tag{30}$$

Δq_0 can be calculated by normalization of quaternion: $\Delta q_0 = \sqrt{1 - \Delta\bar{\mathbf{q}}^{T}\Delta\bar{\mathbf{q}}}$.

4 Experiment and Analysis

A simulation experiment is designed. Satellite trajectory in coarse accuracy can be calculated by utilizing practical almanac of GPS satellites that downloaded from *navcen.usug.gov*. Meanwhile all antennas' WGS-84 coordinates can be obtained according to antenna position in BFS and attitude angle given before. After that, appropriate simulated random noise, as observation noise, is added to the distance that calculated by satellite position and antenna position to realize the simulation of carrier phase observation information. Simulation parameter settings are shown in Table 1.

Based on such settings, a set of simulated data is produced. Note that an angular change rate is given to simulate the dynamic change of attitude, and integer ambiguities are given. After that we determinate the attitude by six methods as follows:

1. Direct solution (DS);
2. Linear least squares: attitude matrix element solution (AMES) [9];
3. Nonlinear least squares: based on additive euler angle error (LS-AE), additive quaternion error, (LS-AQ), multiplicative euler angle error (LS-ME) and multiplicative quaternion error (LS-MQ).

Table 1 Simulation parameter settings

Parameter name	Parameter settings
Sampling time	2008-01-22 22:05-22:48
Master antenna position	50°E, 3°N, altitude 200 m
Observation noise (pseudo range/carrier phase)	0.2/0.01 m
Epoch/epoch interval	2000/0.5 s
Elevation mask angle	15°
Baseline vector	$b_1 = [0 \quad 2 \quad 0]^{\mathrm{T}}$ $b_2 = [1 \quad 1 \quad 0]^{\mathrm{T}}$ $b_3 = [1 \quad 1 \quad 2]^{\mathrm{T}}$
Initial attitude	$(\psi, \gamma, \theta) = (30°, 5°, 10°)$

Experiment results are shown in following figures and tables. Figures 1, 2 and 3 present the result comparison between direct solution, linear least squares method and nonlinear least squares method, note that nonlinear least squares method selects LS-AE. As is shown in these three figures, DS's accuracy is the lowest, only the

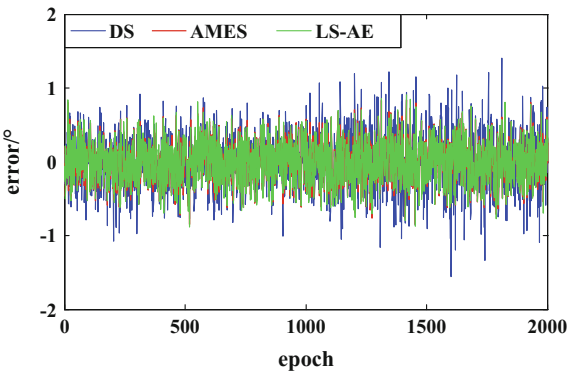

Fig. 1 Yaw error of DS, AMES and LS-AE

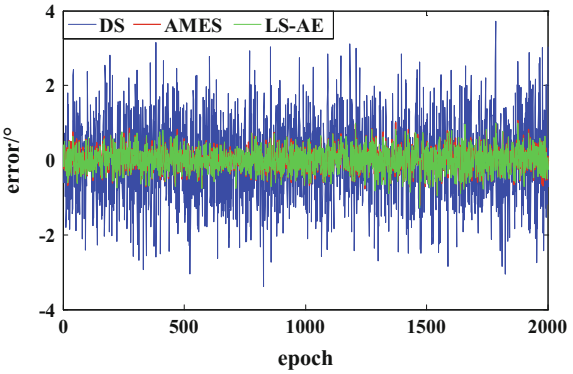

Fig. 2 Roll error of DS, AMES and LS-AE

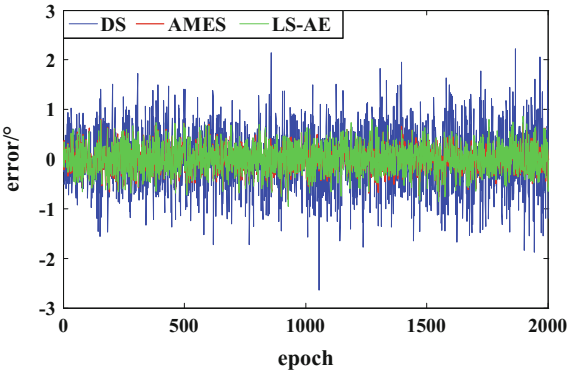

Fig. 3 Pitch error of DS, AMES and LS-AE

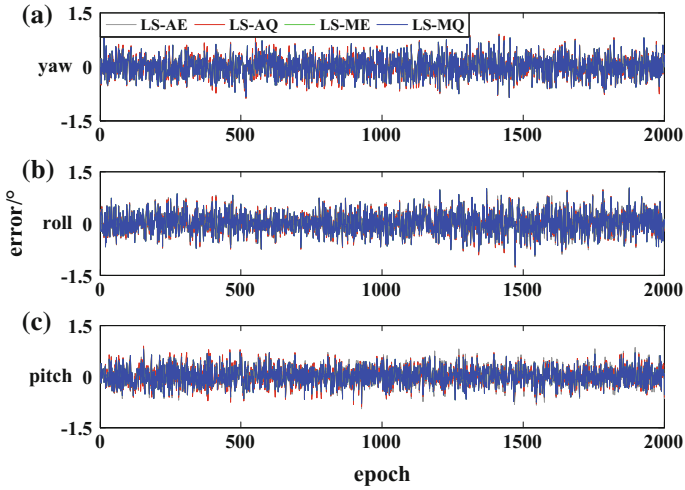

Fig. 4 Error of four types of nonlinear least squares method

yaw barely remaining at minute-level accuracy, while the error of roll and pitch fluctuating remarkably are both more than 1°. The accuracy of linear least squares method and nonlinear least squares method, almost the same, is largely improved compared with direct solution. Three angles' accuracies, smooth and steady, are all superior to 0.5°. Hence, for minute-level required navigation applications, the least squares method should be chosen rather than direct solution.

The result comparison of 4 different types of nonlinear least squares method are presented in Fig. 4, where (a), (b) and (c) respectively present the error of yaw, roll and pitch. As is shown, there are few differences between 4 methods, methods based on multiplicative error being slightly better than that based on additive error. In order to obtain more obvious contrast result, the statistic of mean error, root mean square error (RMS) and single epoch time consumption (STC) of all six methods are presented as shown in Table 2.

According to Table 2 following conclusions can be obtained:

1. The accuracy of DS, RMS exceeding 1°, is the lowest. And the error of roll is almost twice to three times as large as that of yaw and pitch due to the vertical baseline coordinate which is used on calculation of roll and always within low accuracy. However, single epoch time consumption of DS, simple and needless to iterate, is the shortest.
2. The accuracy of least squares method which is superior to 0.5°is improved more than 60% compared with direct solution, and three angles' accuracy are approximate. While for the reason of relatively complex algorithm and iteration, single epoch time consumption multiply increases.
3. The accuracy of LS-AE is the lowest compared with other nonlinear least squares methods, and its linearization procedure is of large amount of

Table 2 Error statistic of six methods/°

Method	Attitude	Mean	RMS	Attitude RMS	STC/s
DS	Yaw	0.2925	0.3721	1.2867	0.0006
	Roll	0.8551	1.0721		
	Pitch	0.4742	0.6064		
LS-AE	Yaw	0.2199	0.2734	0.4901	0.0021
	Roll	0.2370	0.2988		
	Pitch	0.2211	0.2760		
LS-AQ	Yaw	0.2216	0.2760	0.4837	0.0014
	Roll	0.2342	0.2952		
	Pitch	0.2122	0.2658		
LS-ME	Yaw	0.2173	0.2698	0.4711	0.0011
	Roll	0.2323	0.2933		
	Pitch	0.2024	0.2513		
LS-MQ	Yaw	0.2173	0.2698	0.4711	0.0011
	Roll	0.2323	0.2933		
	Pitch	0.2024	0.2513		
AMES	Yaw	0.2173	0.2699	0.4717	0.0011
	Roll	0.2324	0.2942		
	Pitch	0.2023	0.2513		

calculation, which leads to relatively the longest single epoch time consumption. The accuracy of LS-AQ is improved by over 26″, and simplified linearization procedure leads to shorter time consumption. The methods based on multiplicative error whose accuracy and time consumption are almost the same are both better than that based on additive error, with accuracy improved by 45″.

4. There are almost no differences between the results of AMES and nonlinear least squares methods based on multiplicative error.

5 Conclusions

Direct solution possesses short calculation time consumption, but only available to degree-level navigation application due to low accuracy. The least squares method whose accuracy is higher than direct solution by more than 60%, reaching to 30′, and single epoch time consumption being just a little more than direct solution, is available to minute-level navigation application. The nonlinear least squares method based on multiplicative error is especially the best.

Acknowledgements We greatly appreciate the support of the national natural science foundation of China (41274016 and 41674016).

References

1. Park C, Kim I, InJee G, Lee JG (1997) An error analysis of GPS compass [C]. SICE'97. In Proceedings of the 36th SICE annual conference, international session papers, 1997, 1037–1042
2. Xu J, Z T, Bian H (2004) Review on GPS attitude determination [J]. J Nav Univ Eng 15 (3):18–20
3. Zhijian Liu, Yi Liu (2005) Algorithm of a real-time attitude system using non-dedicated GPS receivers [J]. Acta Geod Cartogr Sin 34(3):213–217
4. Giorgi G, Teunissen PJG (2010) Carrier phase GNSS attitude determination with the multivariate constrained LAMBDA method [J], pp 1–12
5. Yuanjun G (2011) Research on GPS attitude determination algorithm and antenna configuration [D]. Harbin Engineering University
6. Yong Wang, Xiubin Zhao, Chunlei Pang et al (2014) Antenna configuration and accuracy analysis of GNSS attitude determination system [J]. Comput Measur Control 22(9): 3024–3027
7. Dai Z, Knedlik S, Loffeld O (2009) A MATLAB toolbox for attitude determination with GPS multi-antenna systems [J]. GPS Solutions 13(3):241–248
8. Zhang F, Chai Y, Chai H et al (2016) Analysis on precision of two attitude determination methods using GNSS multi-antenna data [J]. J Chin Inertial Technol 24(1):30–35
9. Li Y, Murata M (2002) New approach to attitude determination using global positioning system carrier phase measurements [J]. J Guid Control Dyn 25(1):130–136
10. Yu G (2015) GNSS/INS integrated system model refining and position & attitude determination using carrier phase [J]. Acta Geod et Cartogr Sin 44(11):1295–1295
11. Titterton D, Weston J (2004) Strapdown inertial navigation technology, 2nd edition [M]. The IEE, UK, pp 3–21

Estimation and Evaluation of the Precipitable Water Vapor from GNSS PPP in Asia Region

Zhimin Liu, Yangyang Li, Fei Li and Jinyun Guo

Abstract Water vapor is one of the main atmospheric parameters, which has important reference value for climate research, weather forecast, weather monitoring and so on. BDS and GALILEO not only can realize high precision orbit determination and user positioning, but also can be an effectively sensor for satellite meteorology. The rapid development and improvement of BDS and GALILEO, which provide an opportunity to estimate a more high-resolution, precise solution of zenith wet delay (ZWD) and precipitable water vapor (PWV). In this paper, the observation from MGEX stations over Asia regional are processed respectively by GPS-only and GPS/BDS/GALILEO combining precise point positioning (PPP), and ZWD and PWV are retrieved by PPP method. The performance of the estimated ZWD and PWV was tested and verified by GGOS (Global Geodetic Observing System) and radiosonde data. The result shows that the ZWD solutions estimated from PPP agree with GGOS solution very well. Compared with the MAE and RMS of GPS, the results of GPS/BDS/GALILEO decrease by 0.6, 0.5 cm, respectively. The correlation coefficient increases 0.027–0.031. The correlation coefficient between PPP and radiosonde is above 0.9, which shows that they have reached a high level of convergence. The MEAN, RMS value of GPS/BDS/GALILEO is about 1 mm less than GPS. The correlation coefficient increases 0.023–0.034, which further proves that BDS and GALILEO can improve the estimation accuracy of PWV. Then we are sure that BDS and GALILEO will bring great benefits of ZWD and PWV.

Keywords Precipitable water vapor · Precise point positioning · Zenith wet delays · Weighted mean temperature

Z. Liu · Y. Li (✉) · F. Li · J. Guo
College of Geomatics, Shandong University of Science and Technology, Qingdao 266590, China
e-mail: liyang1416@126.com

J. Sun et al. (eds.), *China Satellite Navigation Conference (CSNC) 2017 Proceedings: Volume I*, Lecture Notes in Electrical Engineering 437,
DOI 10.1007/978-981-10-4588-2_8

1 Introduction

Water vapor is a highly instability component of atmospheric. It plays important roles in the transfer of energy and global climate change, which is one of crucial characterized meteorological parameters in weather forecast and atmospheric research applications [1]. A good knowledge of the spatiotemporal characteristics of water vapor will be needed for the improvement of weather forecast. Radiosonde is one of the traditional technique to obtain precipitable water vapor (PWV) observation, which has a long observation history. The algorithm using radiosonde data to retrieve PWV is relatively straightforward. However, the operational radiosonde stations commonly only measure water vapor twice a day because of high operational costs and heavy workload. It produces at most two measurements every day. Subject to the low spatio-temporal resolution and the low geographic density of radiosonde stations, PWV obtained from radiosonde becomes more and more unable to satisfy with the request of short-term weather forecast.

GPS has the advantages of low equipment costs, all-weather continually operating and high spatio-temporal resolutions, which provides a completely new method for high-accuracy exploration and real time continuous monitoring of the earth's atmosphere. Through PPP technique, the accurate coordinate, velocity and zenith tropospheric delay (ZTD) can be obtained directly [2]. Therefore, the research of PWV using PPP technique is of important theoretical significance and practical value. Accompanied by the rapid development and improvement of multi-constellation Global Navigation Satellite System (GNSS), the world of satellite navigation is undergoing dramatic changes. When four systems (GPS/GLONASS/BDS/GALILEO) are fully deployed over the next few years, there will be about 120 satellites available for navigation and positioning. When the time comes, for both scientific and engineering applications, Multi-GNSS will bring great opportunities and challenges [3].

Multi-GNSS Experiment (MGEX) has been started by the International GNSS Service (IGS) to obtain and analyze data and products from four satellite systems [4]. Accordingly, a new tracking network of MGEX tracking GPS and one of GLONASS, BDS, GALILEO, or QZSS satellites has been deployed over the past few years. In view of the improved spatial distribution of observations, the ZTD estimation in particular will get benefit from the rapid increases of the ground-based stations, furthermore for improving weather nowcast even monitoring extreme weather. On account of more observable satellites and more reliable geometry, multi-GNSS processing will help to stabilize and better the ZTD and PWV solution. Li et al. [5] investigated the BDS for PWV estimation by using BDS observations, the study showed that the PWV results obtained from the BDS observations can reach the same precision level as PWV from GPS and BDS is ready for the high precision meteorological applications. Li et al. [6] found that accuracy of several millimeters for the multi-GNSS-based ZTD estimates with high reliability is achievable, which would be beneficial for meteorological applications.

In this paper, we investigate the ZWD and PWV estimated from GPS only and combining GPS/BDS/GALILEO observations by using PPP technique. The observations from MGEX stations distributed over the Asia regional are processed to retrieve two different ZWD/PWV solutions: GPS-alone, and GPS/BDS/GALILEO combined solution. Then, we compare its results with the Global Geodetic Observing System (GGOS)-derived ZWD and radiosonde-derived PWV. The performance of solutions from only GPS observations is analysed and assessed, and the significant benefit of combining BDS, GALILEO with GPS data to estimate ZWD/PWV is also further evaluated.

2 Estimation of ZWD and PWV

Generally, the first order ionospheric delay can be eliminated by the linear combination of ionospheric free using dual-frequency pseudorange and carrier-phase observations in PPP processing. Since the influence of higher-order ionospheric (HOI) on PPP is at millimeter level [7], the HOI is neglected in this paper. The observation equations are usually written as [6]:

$$P_3 = \rho + c(dt - dT) + T + \varepsilon_{P3} \tag{1}$$

$$L_3 = \rho + c(dt - dT) + T + \lambda N + \varepsilon_{L3} \tag{2}$$

where P_3 is the first order ionosphere free code pseudorange combinations, L_3 is the first order ionosphere free carrier-phase combinations, ρ is the geometrical range between satellite and receiver, c is the speed of light in vacuum, dt is the receiver clock errors, dT is the satellite clock errors, T is the tropospheric delay, λ_3 is the wavelength of the ionosphere-free carrier-phase combinations, N_3 is the unknown carrier-phase ambiguity of the ionosphere-free carrier-phase combination, ε_{P3} and ε_{L3} are the other error sources for pseudorange and carrier-phase, respectively.

Due to each satellite system uses individual time reference, the inter system biases (ISB) should be carefully treated in processing multi-GNSS data. The GPS, BDS and GALILEO ionosphere free combinations considered ISB of both pseudorange and carrier-phase can be expressed as:

$$\begin{cases} P_3^G = \rho^G + c(dt - dT^G) + T^G + \varepsilon_{P3}^G \\ L_3^G = \rho^G + c(dt - dT^G) + T^G + \lambda_3^G N_3^G + \varepsilon_{L3}^G \end{cases} \tag{3}$$

$$\begin{cases} P_3^C = \rho^C + c(dt - dT^C) + T^C + ISB^C + \varepsilon_{P3}^C \\ L_3^C = \rho^C + c(dt - dT^C) + T^C + ISB^C + \lambda_3^C N_3^C + \varepsilon_{L3}^C \end{cases} \tag{4}$$

$$\begin{cases} P_3^E = \rho^E + c(dt - dT^E) + T^E + ISB^E + \varepsilon_{P3}^E \\ L_3^E = \rho^E + c(dt - dT^E) + T^E + ISB^E + \lambda_3^E N_3^E + \varepsilon_{L3}^E \end{cases} \tag{5}$$

where indices G, C, and E refer to the GPS, BDS and GALILEO satellites, respectively. ISB is the inter-system bias.

In consideration of the homogeneity and inhomogeneity characteristic of the troposphere delay, the complete model for the slant troposphere total delay T can be modeled by hydrostatic, wet delay and the horizontal gradient with their individual mapping functions:

$$T_R^S = Mf_h \cdot ZHD + Mf_w \cdot ZWD + Mf_G(el) \cdot (G_{NS} \cdot \cos(az) + G_{WE} \cdot \sin(az)) \quad (6)$$

$$mf_G(el) = 1/[\sin(el) \cdot \tan(el) + 0.0032] \quad (7)$$

where Mf_h and Mf_w are mapping functions of the hydrostatic and wet delay, respectively (here Vienna Mapping Function (VMF1)), el and az is the elevation and azimuth angles of the individual satellite. Zenith hydrostatic delay (ZHD) can be accurately corrected using empirical correction models. However, as high temporal variability and instability, ZWD is difficult to calculate with enough accuracy. Thus, ZWD in the process filter is treated as an unknown parameter. $Mf_G(el)$ is the horizontal gradient mapping function, G_{NS} and G_{WE} are the horizontal gradient components in North-South and West-East directions, respectively.

ZWD derived from PPP are converted to the PWV by using the relation [8],

$$PWV = \Pi \cdot ZWD \quad (8)$$

$$\Pi = 10^6/\left[\rho_w R_v\left[(k_3/T_m) + k_2'\right]\right] \quad (9)$$

where Π is the conversion factor, $\rho_w = 10^3\,\mathrm{kg/m^3}$ is the water density, $R_v = 461.50\,\mathrm{J\,K^{-1}\,kg^{-1}}$ is the specific constant of gas, $k_3 = 377600\,(\mathrm{K^2\,hPa^{-1}})$ and k_2'=16.52 $(\mathrm{K\,hPa^{-1}})$ are the refractivity constants of atmospheric, and T_m is the weighted mean temperature of the atmosphere which varies in space and in time. The uncertainty in Π is decided by the uncertainty in T_m, which can be accurately calculated with the vertical profiles of water vapor and temperature. Only if the station with external meteorological data are available, this method can be applied. However, these meteorological data are usually difficult to be obtained at the high temporality and spatiality resolution and also are usually not available at ground based GNSS stations. Thus T_m value is often computed using alternative technique.

In this study, we used the global T_m grid model of the Global Geodesy Observation System (GGOS), which provides T_m globally on 2° × 2.5° grids every 6 h. The T_m grid is estimated from the meteorological data provided by European Centre for Medium-Range Weather Forecasts (ECMWF). Yao et al. [9] showed that compared with radiosonde and COSMIC data, the mean error of the PWV can be less than 1% when using the T_m interpolated from GGOS.

3 Experiment and Analysis

3.1 Experimental Data and Processing Strategies

In order to assess the performance of ZWD/PWV estimated from the multi-GNSS PPP processing, the online GAPS (GNSS Analysis and Positioning Software) was used. The MGEX observations from the Asia regional are investigated and analyzed using the online PPP tool technique. Multi-GNSS observations collected at the 5 MGEX stations (Fig. 1) had been downloaded from the IGS website from DOY180 of 2016 (June 28, 2016) to DOY210 of 2016 (July 28, 2016). The cut-off elevation angle of satellite is set as 10°. Horizontal gradients with Chen and Herring gradient mapping function is applied to the gradient model. ZWD and gradients are estimated as a random walk. GPS orbit and clock error products adopted the IGS final precise product. BDS/GALILEO orbit and clock error products adopted the CODE final precise product. The antenna phase center offset (PCO) of BDS and GALILEO satellites are just simply corrected with the IGS MGEX standard [4]. Since the PCO or phase center variation (PCV) of the receiver for BDS and GALILEO signals are not available currently, they are not considered in this paper.

3.2 ZWD Comparisons Between PPP and GGOS

In this section, we analysis and assess the performance of the ZWD estimated from the PPP processing and evaluate the benefit of adding BDS and GALILEO for

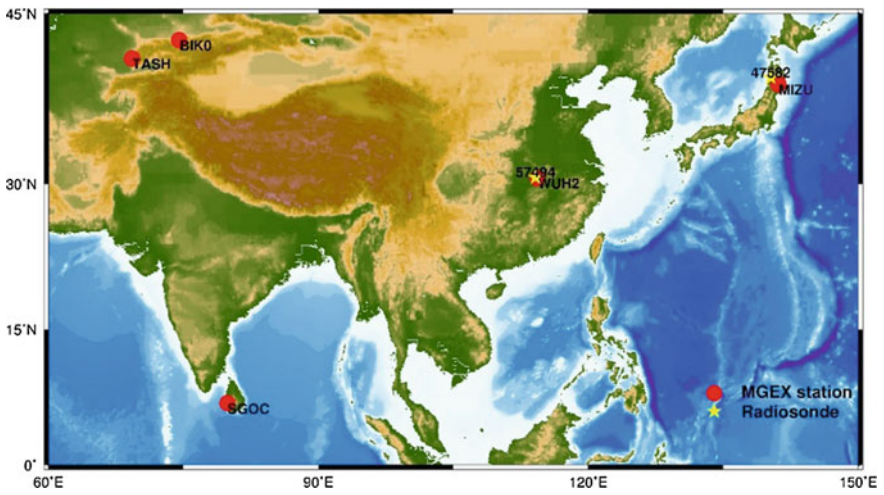

Fig. 1 Distribution of the selected MGEX stations and radiosondes

ZWD retrieval, the ZWD series derived from PPP are compared with that from GGOS solution with time resolution of 6 h interval. ZWD values at common epochs to avoid interpolation are taken into account for the solution comparison. Figure 2 shows the ZWD time series at stations BIK0 and SGOC from DOY180 to DOY210 of 2016. It can be seen that, in general, the value of ZWD is about 0–0.4 m, and the diurnal variation is less than 10 cm. The scatter plots of ZWD between the two solutions at station BIK0 and SGOC are displayed in Fig. 3. It can be seen from Fig. 3 that the ZWD result of PPP agree quite well with the result of GGOS. The correlation coefficient is more than 0.8, implying high correlation between the PPP ZWD and GGOS ZWD. The correlation coefficient of GPS/BDS/GALILEO compared to GPS-only increases by 0.027–0.031, which show that BDS and GALILEO can significantly increase the reliability and accuracy of ZWD. As we can see from Fig. 1, the station SGOC is at low latitude coastal areas, and affected by tropical climate and marine climate. The change of ZWD is more drastically compared to the mid latitude inland station BIK0, which lead to that there is a larger deviation of the ZWD solution between PPP and GGOS.

Figure 4 presents the MEAN and RMS of ZWD comparison between PPP and GGOS solutions at the abovementioned MGEX stations. The MEAN and RMS of ZWD comparison between PPP and GGOS is less than 2.5 cm, showing that the ZWD can be captured accurately by PPP estimates. It can be noticed from Fig. 4 that the MEAN of ZWD differences ranges from 1.0 to 2.2 cm, indicating that there is no apparent systematic bias between PPP and GGOS. The RMS is between 1.2 and 2.3 cm, which show that the reliability and stability of the result. The MEAN and RMS of ZWD solution derived from GPS/BDS/GALILEO is respectively 0.6, 0.5 cm smaller than the GPS-only solution, which indicates a potential benefit for ZWD estimated from PPP with the contribution of adding BDS and GALILEO satellites.

3.3 *Validations with Radiosondes*

In order to evaluate the stability and accuracy of PWV, the PWV series obtained from PPP method are compared with radiosonde data. Figure 5 shows the PWV

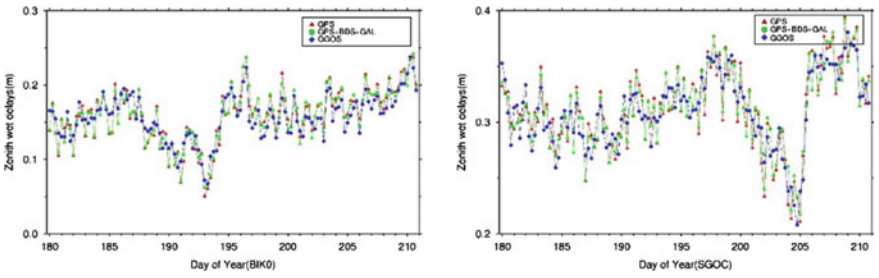

Fig. 2 ZWD derived from PPP and GGOS solutions at station BIK0 and SGOC

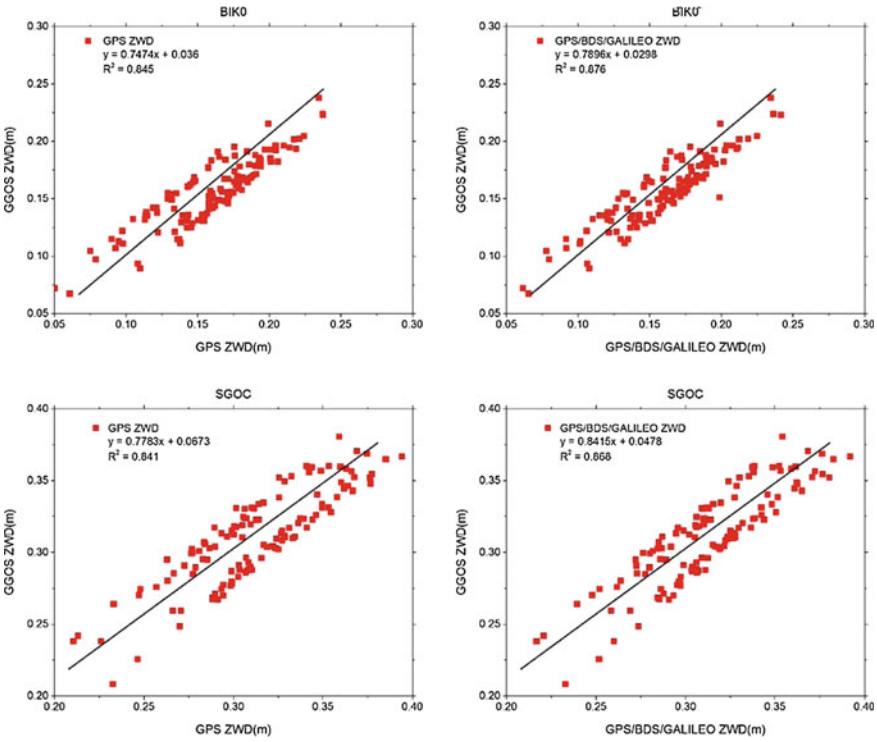

Fig. 3 Scatter plot of ZWD between PPP and GGOS at station BIK0 and SGOC

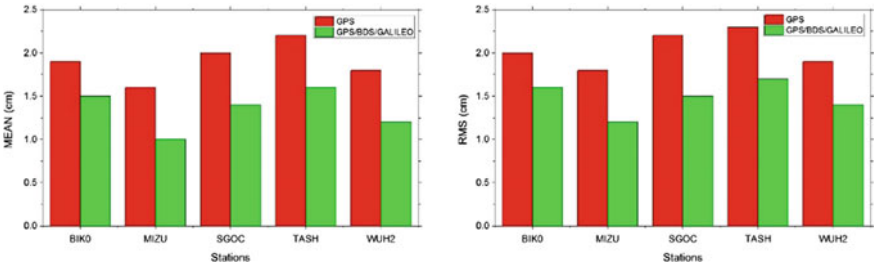

Fig. 4 MEAN and RMS of ZWD differences

solutions retrieved from PPP and nearby radiosonde solution at station MIZU (140.10°E, 39.71°N) and station WUH2 (114.13°E, 30.61°N), where nearby radiosonde launch sites are available (Fig. 1). PWV retrieved from radiosonde is sampled every 12 or 24 h, which are considered for the comparison at the common epochs. We can see from Fig. 5 that the PWV obtained from the PPP agrees well with radiosonde. The accuracy level of PWV differences is at few millimeters and

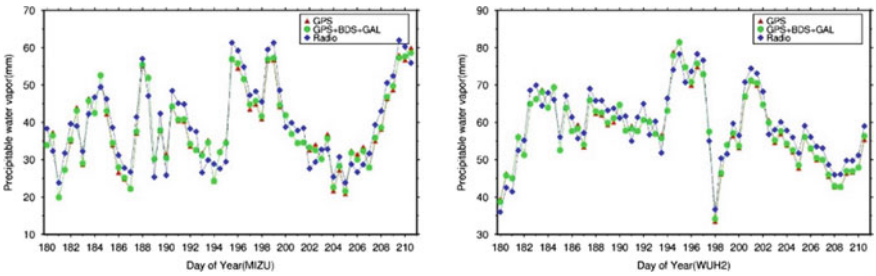

Fig. 5 PWV derived from PPP and radiosonde solutions at station MIZU and WUH2

the MEAN and RMS between the two solutions are about 4 mm. Compared to the station WUH2, the station MIZU is affected by the maritime climate, so that the change interval of PWV is more significant. The variation of PWV value at station WUH2 during days of year (DOY) 193–195 and 197–198 of 2016 reach to 30 mm, which is related to the heavy rainfall around the station area. So the variation of PWV can provide a certain reference for forecasting heavy rainfall. The scatter plots of PWV between the PPP and radiosonde at station MIZU and WUH2 are shown in Fig. 6. It can be also seen that the GPS PWV and GPS/BDS/GALILEO PWV all show good agreement with the radiosonde, and there are no apparent systematic biases between PPP and radiosonde solutions. Compared to the GPS only, the correlation coefficient of GPS/BDS/GALILEO increases by 0.023–0.034. Due to the radiosonde stations nearby MIZU is relatively farther than the station WUH2 and the dispersion of the data increases, which results in the correlation coefficient is smaller.

Figure 7 gives the MEAN and RMS of the PWV comparison for the GPS only, and GPS/BDS/GALILEO combined solutions with respect to the radiosonde solutions. The PWV solution of the GPS/BDS/GALILEO shows show a full of consistency with that of the GPS only. The MEAN of GPS-only solution is 3.0 and 3.6 mm, and the RMS of GPS/BDS/GALILEO is 3.3 and 3.8 mm, respectively. Furthermore, the PWV differences of the GPS/BDS/GALILEO combined solution are smaller, where the MEAN is 2.3 and 3.1 mm and the RMS of the differences are 2.5 and 3.2 mm, respectively. Therefore, the GPS/BDS/GALILEO combined can improve the accuracy of PWV compared to the GPS only. However, the accuracy level of PWV is limited by the accuracy of the PCO and PCV models of satellite and receiver antennas. So the accuracy of PWV in this paper is not significantly improved. Further work is still required to improve the PCO and PCV models, especially for BDS and GALILEO.

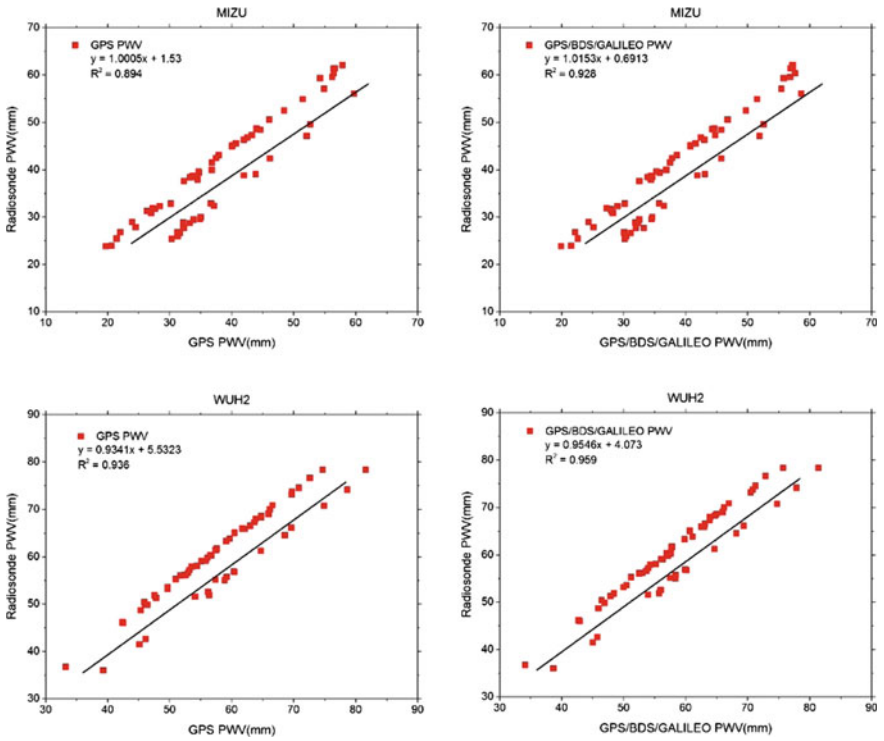

Fig. 6 Scatter plot of PWV between PPP and radiosonde solutions at station MIZU and WUH2

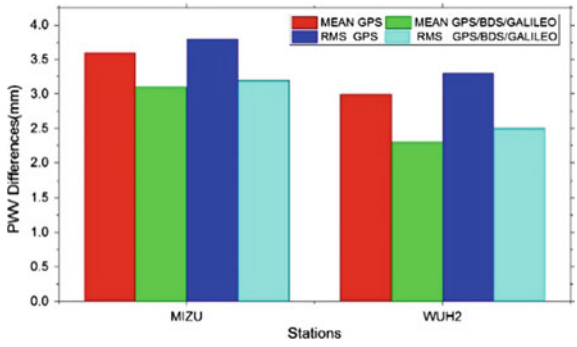

Fig. 7 MEAN and RMS of PWV differences

4 Conclusions

In this paper, we study the solution of ZWD/PWV retrieval from multi-GNSS, and the estimated ZWD and PWV were compared with GGOS and radiosonde as independent validations. The relationship between the horizontal gradient and PWV

was further analyzed. BDS, GALILEO and GPS data of 5 MGEX stations from Asia regional for the seventh month of the year 2016 using the PPP technique were processed. The performance of the ZWD/PWV estimates derived from PPP and the contribution of combining GPS/BDS/GALILEO was analyzed and assessed.

The results show that the correlation coefficient between PPP and GGOS solutions is more than 0.8, which imply that the ZWD derived from PPP show good consistency with the GGOS ZWD. The MEAN and RMS of GPS/BDS/GALILEO is 0.6, 0.5 cm smaller than the GPS only, respectively. The correlation coefficient of GPS/BDS/GALILEO increases by 0.027–0.031, which further confirms that BDS and GALILEO can significantly improve the accuracy of ZWD. For validation, PWV estimates of the GPS/BDS/GALILEO and GPS-only, show good agreement with the PWV derived from radiosonde. The MEAN of PWV comparison between the GPS only solution and the radiosonde solution is around 3.1–3.6 mm, and 3.0–3.8 mm for the RMS. The PWV comparison are smaller than the GPS/BDS/GALILEO combined solution, for which the MEAN ranges from 2.3 to 3.1 mm, and 2.5–3.2 mm for the RMS. Compared to the GPS-only PWV, The correlation coefficient of GPS/BDS/GALILEO increases by 0.023–0.034. Therefore, it is confirmed that BDS and GALILEO can contribute to meteorological applications, and more accurate ZWD/PWV solution can be obtained in PPP mode with BDS and GALILEO. Furthermore, the variation of PWV is at mm level, so the HOI should be considered in further studies.

Acknowledgements We would like to acknowledge IGS for MGEX data supporting and precise products. We thank IGRA for providing the radiosonde data and GGOS for providing grids of Tm. We also thank the online PPP software service systems GAPS. This research was supported by National Natural Science Foundation of China (41374009) and the Public Science and Technology Research Funds Projects of Surveying and mapping (201512034).

References

1. Rocken C, Ware R, Hove TV et al (1993) Sensing atmospheric water vapor with the global positioning system. Geophys Res Lett 20(23):2631–2634
2. Zumberge JF, Heflin MB, Jefferson DC et al (1997) Precise point positioning for the efficient and robust analysis of GPS data from large networks. J Geophy Res Solid Earth 102(B3): 5005–5017
3. Li X, Zhang X, Ren X et al (2015) Precise positioning with current multi-constellation global navigation satellite systems: GPS, GLONASS. Galileo and BeiDou, Scientific Reports 5
4. Montenbruck O, Steigenberger P, Khachikyan R et al (2014) IGS-MGEX: preparing the ground for multi-constellation GNSS science. Espace 9(1):42–49
5. Li M, Li W, Shi C et al (2015) Assessment of precipitable water vapor derived from ground-based BeiDou observations with precise point positioning approach. Adv Space Res 55 (1):150–162
6. Li X, Dick G, Lu C et al (2015) Multi-GNSS meteorology: real-time retrieving of atmospheric water vapor from BeiDou, Galileo, GLONASS, and GPS Observations. IEEE Trans Geosci Remote Sens 53(12):6385–6393

7. Liu Z, Li Y, Guo J et al (2016) Influence of higher-order ionospheric delay correction on GPS precise orbit determination and precise positioning. Geodesy Geodyn 7(5):369–376
8. Askne J, Nordius H (1987) Estimation of tropospheric delay for microwaves from surface weather data. Radio Sci 22(3):379–386
9. Yao YB, Zhang B, Yue SQ et al (2013) Global empirical model for mapping zenith wet delays onto precipitable water. J Geodesy 87(5):439–448

Correlation Analysis Among GPS-SNR, Precipitation and GPS-PWV

Min Mao, Li Wang, Shuangcheng Zhang, Xiaolei Wang and Peng Hu

Abstract Because of the increase of water vapor content in the atmosphere or precipitation, the satellite signal prones to multipath effect, which leads to the changes of signal-to-noise ratio(SNR). Therefore, this paper mainly focuses on the correlation among GPS-SNR, precipitation and GPS-PWV. In order to analyze the correlation among GPS-PWV, GPS-SNR and the actual precipitation, this article inverse the foundation GPS atmospheric water vapor (GPS-PWV), and then use the GPS signal to noise ratio(GPS-SNR) for Lomb_Scargle analysis of SNR power spectrum, finally using the actual precipitation data measured by sensors for comparison by using the plate boundary observation program (PBO) GPS network observation data of 62D (doy 153–214). The preliminary results show that the precipitation, GPS-PWV and GPS-SNR has a good relationship in the time distribution. Furthermore, the various parameters of GPS-SNR (A, F, $\psi 0$) rapidly change with the content of GPS-PWV increase or precipitation.

Keywords GPS inversion · Signal to noise ratio · GPS water vapor · Precipitation

M. Mao (✉)
College of Geology Engineering and Geomantic, Chang'an University,
Xi'an 10054, Shanxi, China
e-mail: maomin1220@163.com

L. Wang (✉)
Key Laboratory of Western Chian's Mineral Resources and Geological Engineering,
Ministry of Education, Xi'an 10054, Shanxi, China
e-mail: wangli@chd.edu.cn

S. Zhang · X. Wang · P. Hu
State Key Laboratory of Geographic Information Engineering,
Xi'an 10054, Shanxi, China

J. Sun et al. (eds.), *China Satellite Navigation Conference (CSNC) 2017 Proceedings: Volume I*, Lecture Notes in Electrical Engineering 437,
DOI 10.1007/978-981-10-4588-2_9

1 Introduction

Signal to noise ratio (SNR), a kind of accessary observation value of the common measurement receiver, is a value that represents the received signal strength of receiver antenna [1]. It is mainly affected by the antenna gain parameters, the state of the correlator and the multipath effect. As the GPS antenna gain pattern is generally designed that the higher the incident angle, the greater the gain, and the receiver noise power is small. Therefore, the multipath effect becomes the dominant factor when the satellite altitude angle is low [2]. When the water vapor content in the atmosphere increases or the precipitation occurs, the satellite signals are prone to multipath effects. And when this happens, the satellite signal quality (observation accuracy) will be reduced, the SNR value will also change. In the high precision GPS measurement, multipath signal is a factor that must be considered. Therefore, the research on SNR is very important.

At present, the research of GPS signal to noise ratio (GPS-SNR) mainly includes data quality analysis, GPS-SNR inversion and analysis of influencing factors of GPS-SNR. For most users, the use of GPS-SNR to analyze the quality of observation data is more commonly used, and the larger the SNR value, the better the quality of the data. With the rapid development of global navigation and positioning system (GNSS), it is a new research field to use SNR to inverse the environmental parameters around the station. In this field, some scholars put forward to the GPS-MR technology based on the observations of signal-to-noise. By using the multi path reflection component of SNR, the snow surface, sea level, vegetation cover and other surface onvironment were monitored, and a series of results were obtained [3–7]. At home and abroad, the study of the first two types of GPS-SNR has been basically improved, but there is little research on the correlation between GPS-SNR and its influencing factors.

Based on the plate boundary observation program (PBO) GPS network observation data of 62D (doy 153–214) and actual precipitation on data. This article inverse the foundation GPS atmospheric water vapor (GPS-PWV) constant, and then use the GPS signal to noise ratio (GPS-SNR) for Lomb_Scargle analysis of SNR power spectrum, finally use the actual precipitation data measured by sensors as comparison. And based on the existing research results, this paper explores the variation of precipitation, GPS-PWV and GPS-SNR at P015 and P026 stations.

2 Technical Methods

In general, total zenith tropospheric delay (ZTD) of GPS is calculated by the Saastamoinen model, and the content of GPS-PWV is inversed by the wet delay (ZWD), which isolated from ZTD in the tropospheric zenith. GPS-SNR power spectrum is analyzed by Lomb_Scargle spectrum analysis.

2.1 Inversion Principle of Foundation GPS-PWV

When the GPS satellite signals pass through the atmosphere, it will be affected by the atmospheric refraction delay Where ZTD is equal to the sum of ZWD and the tropospheric zenith hydrostatic delay (ZHD). In view of the water vapor in the atmosphere is active, GPS meteorology is usually the first to get ZTD of stations over through data processing, then High precision ZHD value is obtained by using delay model, and then ZWD was isolated from ZTD, finally convert ZWD to PWV. This paper uses Saastamoinen model to calculate ZHD as follows:

$$\begin{aligned} \mathrm{ZHD} &= 2.2768 \times \frac{\mathrm{p_0}}{\mathrm{f}(\varphi, \mathrm{h})} \\ \mathrm{f}(\varphi, \mathrm{h}) &= 1 - 0.00266\cos 2\varphi - 0.00028\,\mathrm{h} \end{aligned} \tag{1}$$

Formula: P_0 for the ground pressure (mbar), φ for the latitude of the earth (degree), h for the geodetic height (km), $f(\varphi, h)$ for the result of the earth's rotation caused by changes in the acceleration of gravity correction [8].

ZWD is obtained indirectly by the difference between ZTD and ZHD:

$$\mathrm{ZWD} = \mathrm{ZTD} - \mathrm{ZHD} \tag{2}$$

ZWD can be converted into atmospheric water vapor:

$$\mathrm{PWV} = \mathrm{ZWD} \cdot \Pi \tag{3}$$

Formula: Π for water vapor conversion coefficient, which is called the dimensionless scaling factor. It can be expressed as:

$$\Pi = \frac{10^6}{\rho_w R_v \left[(k_3/T_m) + k_2'\right]} \tag{4}$$

Formula: ρ_w for the liquid water density, T_m for atmospheric weighted average temperature, K_2', K_3 for the atmospheric refractive index.

2.2 Power Spectrum Analysis Based on GPS-SNR Observations

The signal received by the GPS receiver antenna is a direct signal and a composite signal reflected by the ground surface. In order to effectively suppress the multipath observation error introduced by the surface reflection, the relationship between the amplitude of the direct signal and the reflected signal is as follows [1]:

$$A_d \gg A_m \tag{5}$$

Formula: Direct signal A_d determines the overall trend of the composite signal, which is equivalent to the overall trend of the signal. Among them, the reflected signal A_m is a local periodic oscillation, which is mainly due to the low altitude angle multi-path effect. The relationship between SNR and signal amplitude is as follows [9]:

$$SNR^2 = A_c^2 = A_d^2 + A_m^2 + 2A_dA_m \cos\lambda \tag{6}$$

Formula: A_c is the amplitude of the synthetic signal, and the cos λ is the Cosine of angle between the direct signal and the reflected signal.

In order to obtain the information of GPS multipath variation caused by surface reflection in SNR, the multipath effect should be separated from the SNR observations. The results show that the SNR trend term is parabolic, which can be fitted and separated by quadratic polynomial. Therefore, the amplitude of the reflected signal can be expressed as:

$$A_m = A\cos\left(\frac{4\pi h}{\lambda}\sin E + \psi_0\right) \tag{7}$$

Formula: λ for a carrier wavelength, E for the satellite elevation angle, H for the vertical reflection distance, ψ_0 for the phase shift constant associated with reflecting surface. The formula is simplified to the standard cosine function expression associated with frequency as:

$$A_m = A\cos(2\pi f \sin E + \psi_0) \tag{8}$$

Lomb-Scargle spectrum analysis can be used to obtain the corresponding characteristic parameters [10], so as to study the relationship between the characteristic parameters and precipitation.

3 Data Processing and Analysis

In order to explore the variation of precipitation, GPS-PWV and GPS-SNR, this article carries on the related inversion by using the plate boundary observation program (PBO) GPS network observation data of 62D (doy 153–214) at P015 and P026 stations where the environment is easy to be monitored, and the observation data is complete and has the actual precipitation data.

3.1 Relationship Between Precipitation and GPS-PWV

At present, the research on the correlation between GPS-PWV and precipitation have been relatively perfect. Bevis and Businger put forward the principle of using ground-based GPS to detect the atmospheric water vapor content [11, 12]. Li et al. [13] think that there was a close relationship between water vapor content and precipitation. Cui et al. [14] think that the precipitation process has a good correspondence with the high value area of GPS-PWV. Li, Cao et al. [15, 16] studied and show that there is a good relationship between precipitation and the rapid increase of GPS-PWV. Wang et al. [17] think that GPS-PWV can be used as one indicator of Short-term Precipitation Forecast.

To analyze the correlation between GPS-PWV and precipitation at P015 and P026 stations, this paper mainly uses high precision GPS data processing software GAMIT to calculate the baseline results file (O−), and joint the meteorological data of observation station to calculate the GPS-PWV, then compares and analyzes the actual precipitation data measured by sensor and GPS-PWV. In Figs. 1 and 2, the light blue line represents the atmospheric water vapor content, and the dark blue line represents the actual precipitation.

As is shown in Figs. 1 and 2, the increase of GPS-PWV has a good positive correlation with the formation of precipitation, and the each increase of GPS-PWV corresponds to a precipitation process, and most of the precipitation occurs in the peak period of GPS-PWV sequence. On the 10th and 57th day of Fig. 1, the 38th day of Fig. 2, there is a significant decrease in the content of GPS-PWV in precipitation of single day. From the comparison of 24th–27th, 47th–55th, 60th–62th days of Fig. 1 and 6th–10th, 23th–35th, 47th–50th, 54th–57th, 61th–62th days of Fig. 2, content of GPS-PWV has no significant decrease after precipitation, which is associated with the occurrence of multi day continuous precipitation.

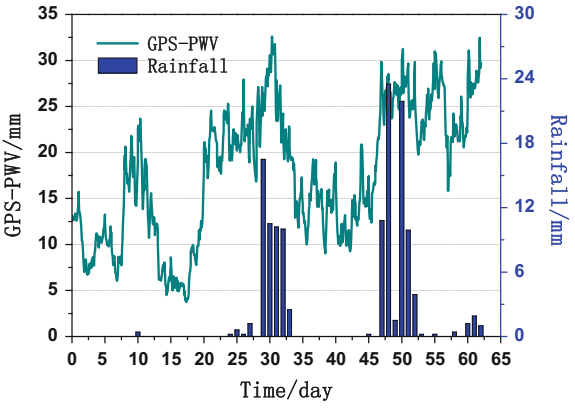

Fig. 1 Relationship between GPS-PWV and actual precipitation at P015

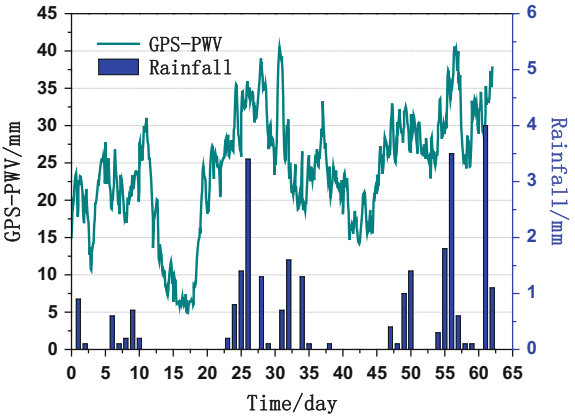

Fig. 2 Relationship between GPS-PWV and actual precipitation at P026

Based on the correlation analysis between GPS-PWV and precipitation, it can provide an important guarantee for the study of the correlation among precipitation, GPS-PWV and GPS-SNR.

3.2 Changes Research of Precipitation and GPS-SNR

31 satellites are used per day, and the GPS-SNR data are processed as follows [1]:

1. According to the geographical environment around the station and satellite sky map, the experimental target satellite is selected;
2. Calculate the height angle of each satellite and extract the SNR data at low elevation (5°–30°);
3. The quadratic fitting method is used to remove the direct signal component which is the tendency of the synthesized signal, i.e. the trend term, consequently obtain the information sequence representing of the reflected signal;
4. The Lomb-Scargle spectrum analysis method is used to process the information sequence, and the corresponding characteristic parameters are obtained.

Figures 3 and 4 analyze the relationship between precipitation and GPS-SNR parameters. The black line shows the variation of amplitude of the GPS-SNR

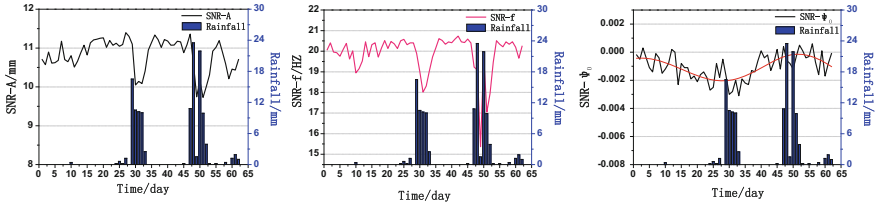

Fig. 3 Relationship between characteristic parameter of GPS-SNR and precipitation at P015

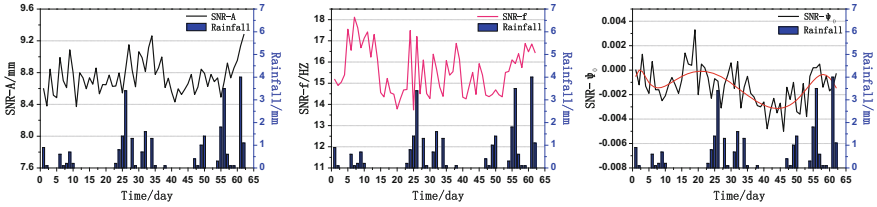

Fig. 4 Relationship between characteristic parameter of GPS-SNR and precipitation at P026

characteristic parameter. The purple line indicates the frequency change. The red line indicates the phase change of After Gaussian fitting, and the dark blue line represents the actual precipitation:

As is shown in Figs. 3 and 4:

1. The precipitation has a good correspondence with the amplitude (SNR-A) of the information sequence based on GPS-SNR, and the precipitation process corresponds to the rapid change of SNR-A, which is slightly ahead of SNR-A's rapid change.
2. The precipitation has a good correspondence with the frequency (SNR-f) of the information sequence based on GPS-SNR, and the precipitation process corresponds to the rapid change of SNR-f, which is slightly ahead of SNR-f's rapid change.
3. Direct observation from the figure founds that precipitation and phase (SNR-ψ_0), based on information sequence of GPS-SNR, were not significantly related; but the Gauss fitting of SNR-ψ_0 shows that precipitation usually occurs in the fitting band peaks and trough stages.

3.3 Study on the Changes of GPS-PWV, Precipitation and GPS-SNR

In order to further analyze the relationship among precipitation, GPS-PWV and GPS-SNR, the comparison map (Figs. 5 and 6) of GPS-PWV, GPS-SNR characteristic parameters and precipitation was drawn at P015 and P026 stations, and has been explored its intrinsic relation and the change rule. In the Figures, the horizontal axis represents the number of days, and the vertical axis represents the parameters, and the light blue line represents the atmospheric water vapor content, and black, purple and red lines represent the various parameters of the GPS-SNR respectively. The dark blue line represents the actual precipitation:

The following conclusions can be drawn in conjunction with Figs. 5 and 6:

1. The increase of GPS-PWV content in the atmosphere is always accompanied by the occurrence of precipitation.

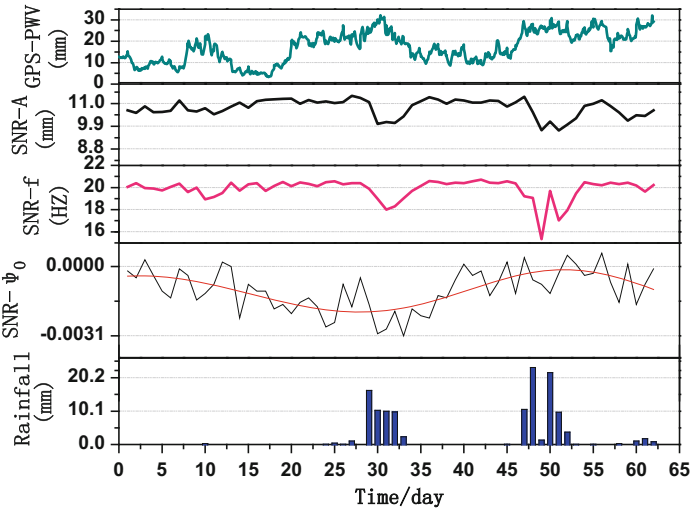

Fig. 5 Comparative analysis of various parameters (P015)

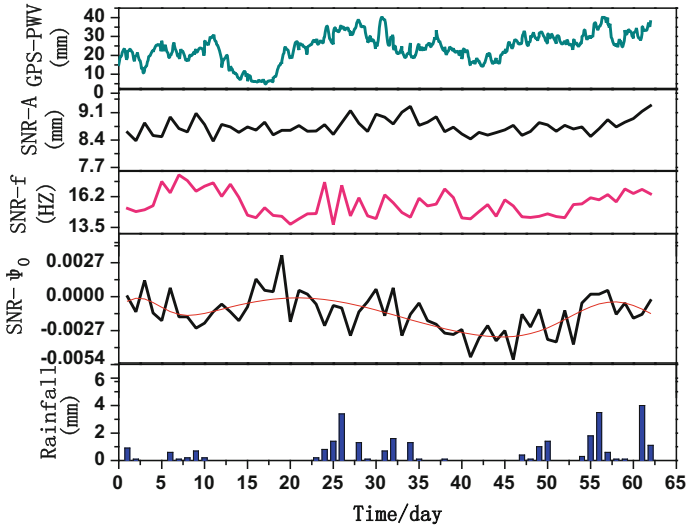

Fig. 6 Comparative analysis of various parameters (P026)

2. When the precipitation process occurs, the amplitude and frequency of GPS-SNR signal sequence change drastically, and the phase change reaches the peak or trough of the fitting sequence.

3. When the GPS-PWV content in the atmosphere increases, the amplitude and frequency of GPS-SNR signal sequence change dramatically, and the phase change reaches the peak or trough of the fitting sequence. It indicates that the satellite signal is prone to multipath effect.
4. There is also a good correspondence of the various characteristic parameters of GPS-SNR signal sequence.

4 Conclusions

SNR is the ratio of the carrier signal strength and noise intensity of the receiver, which is very easy to be affected by multi-path. Therefore, it is of great significance to study the change rule of precipitation, GPS-PWV and GPS-SNR for the research and application of SNR. In this paper, the correlations among GPS-PWV, GPS-SNR and precipitation are analyzed by using the observational data and the actual precipitation data at P015 and P026 stations. The results show: GPS-PWV, GPS-SNR and precipitation have a good correlation in temporal distribution; The increase of GPS-PWV content usually leads to the change of precipitation and GPS-SNR; The occurrence of precipitation process will directly cause the change of GPS-SNR. However, in this paper, only P015 and P026 stations are chosen to do the analysis. In order to better analyze the change rules of precipitation, GPS-PWV and GPS-SNR, it is necessary to verify the reliability of the conclusion through longer time and more regional data. Furthermore, GPS-SNR is affected by many factors, that it needs more comprehensive consideration in the actual application.

Acknowledgements The authors would like to thank the Grand Projects of the Beidou-2 System (GFZX0301040308), The project of National Natural Science Foundation of China (41104019, 41504006, 41604001) and Central University Research Funds (310826151050) for their support. The authors would like to thank the United States NSF, USGS and NASA jointly launched the earth lens (Earthscope) plans for providing GPS data and the GPS Reflections Research Group of the US PBO H2O team for providing reference and experimental data. And thanks to the editors and anonymous referees provide for the valuable comments and suggestions in this paper.

References

1. Zhang S, Dai K, Liu K, et al (2016) Research of GPS-MR on snow depth monitoring. Prog in Geophys 31(4):1879–1884
2. Ao M, Zhu J, Hu Y et al (2015) Comparative experiments on soil moisture monitoring with GPS SNR observations. Geomatics Inf Sci Wuhan Univ 40(1):117–120
3. Larson KM, Small EE, Gutmann E et al (2008) Using GPS multipath to measure soil moisture fluctuations: initial results. GPS Solutions 12(3):173–177
4. Small EE, Larson KM, Braun JJ (2010) Sensing vegetation growth with reflected GPS signals. Geophys Res Lett 37(12):245–269

5. Larson KM, Gutmann ED, Zavorotny et al (2009) Can we measure snow depth with GPS receiver Geophys Res Lett 36(17):153–159
6. Gutmann ED, Larson KM, Williams MW et al (2012) Snow measurement by GPS interferometric reflectometry: an evaluation at niwot ridge, colorado. Hydrol Process 26 (19):2951–2961
7. Wu J, Yang R (2012) Measurement of water surface height by using GPS receiver. Geodetic Earth Dyn 32(6):135–138
8. Saastamoinen J (1973) Contributions to the theory of atmospheric Refraction. Bulletin Geodesique 105:279–298
9. Bilich A, Larson KM (2007) Mapping the GPS multipath environment using the signal-to-noise ratio(SNR). Radio Sci 43(6):3442–3446
10. Xu B, Yng T, Tan B et al (2011) The simulate study of signal detection based on Lomb-Scargle Algorithm. Nuclectron Detect Technol 31(6):702–705
11. Bevis M, Businger S, Chiswell SR et al (1994) GPS moteorology: mapping zenith wet delays onto precipitable water. J Appl Meteorol 33(3):379–386
12. Bevis M, Businger S, Herring TA et al (1992) GPS meteorology: romote sensing of atmospheric water vapor using the global positioning system. J of Geophys Res Atmos 97 (D14):15787–15801
13. Xu L, Xu B, Hu X et al (2001) Test and study of the earth-based GPS tecor remote sensing of atmospheric precipitable water. Q J of Appl Meteorol 12(1):61–69
14. Li-na CUI, Yu-guang SHI, Cai-xia CUI et al (2011) Relationship between GPS precipitable water vapor and precipitation in taklimakan desert. Environ Sci Technol 24(1):22–25
15. Qingchuan Li, Chaolin Zhang, Yanli Chu et al (2007) Applications of precipitable water vapor monitored by ground-based GPS to analyzing heavy rain event. Meteorol Mon 33 (6):51–58
16. Cao Y, Fang Z, Xia Q (2005) Relationship between GPS precipitable water and precipitation. Q J of Appl Meteorol 16(1):54–59
17. Wang Y, He R, Yang B et al (2010) Study of comparisons between GPS precipitable water vapor and rainfall. Sci of Studying and Mapp 35(5):80–82

The Determination of Plumb-Line Deviation by Adopting GNSS/ Leveling Method in Super Long Tunnel Break-Through Measurement

Ji Ma, Zhiqiang Yang and Guofeng Ji

Abstract In the long tunnel connection surveying, GNSS technology is generally used to measure the ground azimuth and transmit benchmark to the underground. Constrained by topographic conditions and other special factors, it shows a great difference between the height of ground control point and entrance point, and the tunnel break-through accuracy is affected by the plumb-line deviation. The gravity anomalies measurement and astronomical measurement are the common ways to calculate the plumb-line deviation correction. Although there are many local model algorithm of plumb-line deviation, the model parameters are not easy to obtain, and the calculation accuracy is hard to guarantee. The GNSS relative positioning and orientation technology can easily obtain the distance between two base lines, azimuth and geodetic height difference; the normal height difference between two base lines can be obtained by leveling or trigonometric leveling method. Hence in the small area and the region of linear change, it is an ideal way to use GNSS/leveling method to calculate the plumb-line deviation. In view of the fact that there is a great difference between the height of ground control point and entrance point in Hanjiang-to-Weihe river water diversion Qinlig Mountains Long Tunnel Project, the authors analyzed the influence of plumb-line deviation on the long tunnel through error, calculated the plumb-line deviation by adopting GNSS/leveling method, the results were compared by the global gravity model (GGMplus) calculation. The example results show the superiority of GNSS/leveling method, it is applicable to calculate the influence value of through error which affected by the plumb-line deviation, and optimized the reliability of the break-through error estimation.

Keywords GNSS/leveling · GGMplus model · Plumb-line deviation · Super long tunnel · Break-through error

J. Ma (✉) · Z. Yang · G. Ji
School of Geological Engineering and Surveying, Chang'an University, Xi'an, China
e-mail: 125667397@qq.com

J. Sun et al. (eds.), *China Satellite Navigation Conference (CSNC) 2017 Proceedings: Volume I*, Lecture Notes in Electrical Engineering 437,
DOI 10.1007/978-981-10-4588-2_10

1 Introduction

In the process of tunnel connection surveying, due to the high relative positioning accuracy, the GNSS technology is used to measure the ground control point for azimuth transmission. However, field observation data belong to the plumb-line system, but GPS results are belong to the normal system. The plumb-line deviation which is the angle between the plumb line and the corresponding ellipsoid surface normal, has a great influence on the projective calculation of the surveying results [1, 2]. It is generally between 3″ and 5″, the maximum can reach 20″–30″ in China. The influence of plumb-line deviation on the break-through error (BE) depends on the initial azimuth error (IAE) affected by the plumb-line deviation, the altitude angle and azimuth on the observed directions [3]. Limited by terrain factors, the height differences between GPS control points and entrance point are very large, building a tunnel in the high mountains and lofty hills need to consider the influence of plumb-line deviation.

Method of plumb-line deviation determination generally including gravity measurement method, astrogeodetic method, earth gravity model method and GNSS/leveling method, etc. [4–6]. Among them, gravity measurement method is to determine the plumb-line deviation by the gravity anomaly data based on the Stokes function approximation technique, this method is affected by the accuracy and resolution of gravity anomaly. Ning [7] used the gravity data to determine the plumb-line deviation of the WGS84 ellipsoid system in mainland China, the overall accuracy is better than 1.5″. Astrogeodetic method is to determine the plumb direction by measuring the astronomical latitude and longitude of ground point, and then to calculate the geodetic latitude and longitude on the reference ellipsoid to determine the normal direction [8]. Earth gravity model method [9, 10] is to calculate the plumb-line deviation by the gravity model coefficients, this method is affected by the accuracy and resolution of the model, and the accuracy of different regional models are different. GNSS/leveling method [11] is to acquire the height anomaly value to calculate the plumb-line deviation by adopting GNSS and leveling technology.

Gravity measurement method and astrogeodetic method can obtain higher accuracy results, but the solution processes are more complex. Obviously, for the tunnel measurement, it is not necessary to obtain the plumb-line deviation in a very high accuracy. Therefore, GNSS/leveling method and earth gravity model method are the better methods to obtain the plumb-line deviation for the tunnel measurement. In order to reduce the influence of plumb-line deviation on the BE, and to ensure super long tunnel get through. This paper adopt GNSS/ leveling method and earth gravity model method to the plumb-line deviation of ground control point, and analyze the effect of plumb-line deviation on BE in the long tunnel. Take a long tunnel project (Hanjiang-to-Weihe River Water Diversion in Qinling Mountains 5#–6# Tunnel Project) as an example, the author calculated the influence value of plumb-line deviation on IAE and BE, and the experimental results of two methods are compared and analyzed.

2 The Calculation Method of Plumb-Line Deviation

2.1 GNSS/Leveling Method

The GNSS relative positioning and orientation method can obtain the baseline vectors and difference of ellipsoidal height between GNSS points. The normal height difference between the baselines can be obtained through leveling or trigonometric leveling method, in the small area and the region of linear variation, this method is a better way to determine the plumb-line deviation.

The relationship between ellipsoidal height and normal height is $H = H_r + \xi$, when using GNSS to measure the baseline [12]:

$$\Delta H = \Delta H_r + \Delta\xi \tag{1}$$

where H is ellipsoidal height, H_r is normal height, ξ is height anomaly, ΔH is the difference of ellipsoidal height between GNSS points, ΔH_r is the difference of normal height between GNSS points, $\Delta\xi$ is the height anomaly between GNSS points.

ΔH can be obtained by GNSS differential positioning technology, ΔH_r can be obtained by leveling or trigonometric leveling method, so $\Delta\xi$ can be calculated by Formula (1):

$$\Delta\xi = -\frac{\delta_A + \delta_B}{2} S_{AB} - \frac{\left[(g-\gamma)_A + (g-\gamma)_B\right]}{2} h_{AB} \tag{2}$$

where δ_A, δ_B are the components of the astro-geodetic plumb-line deviation in the direction of AB; S_{AB} is the baseline length; h_{AB} is the height difference between point A and B; $(g-\gamma)_A, (g-\gamma)_B$ are the gravity anomaly correction terms of point A and B [13].

When $(g-\gamma) \leq 50\ mg$, the impact of the second items can be ignored in general, if $\delta_A = \delta_B = \delta$, δ can be calculated by:

$$\delta = -\frac{\Delta\xi}{S_{AB}} \tag{3}$$

where δ is the component of plumb-line in any observation direction. Suppose the component of plumb-line deviation in the baseline direction is δ_A, δ_B, they can be calculated by:

$$\left.\begin{aligned} \delta_1 &= \xi \cos\ \alpha_1 + \eta\ \sin\ \alpha_1 \\ \delta_2 &= \xi \cos\ \alpha_2 + \eta\ \sin\ \alpha_2 \end{aligned}\right\} \tag{4}$$

Solving the equation set:

$$\left.\begin{aligned}\xi &= \frac{\delta_1 \sin\,\alpha_2 - \delta_2 \sin\,\alpha_1}{\sin(\alpha_2 - \alpha_1)} \\ \eta &= \frac{\delta_1 \cos\,\alpha_2 - \delta_2 \cos\,\alpha_1}{\sin(\alpha_1 - \alpha_2)}\end{aligned}\right\} \tag{5}$$

The NS component ξ and EW component η of plumb-line deviation can be calculated by Formula (5). From Formula (3), the calculation accuracy of plumb-line deviation is affected by GNSS altimetry accuracy, leveling accuracy and baseline length. Because of leveling accuracy achieve sub-millimeter level, the error is negligible. Based on the law of error propagation error, the error of plumb-line deviation is:

$$m_\delta = \pm\frac{\sqrt{2}\rho}{S_{AB}} m_{H_{GNSS}} \tag{6}$$

where, $m_{H_{GNSS}}$ is the GNSS altimetry accuracy. In general, $m_{H_{GNSS}}$ can achieve millimeter level by using GNSS post-differential technology, assuming $m_{H_{GNSS}} = 5\,\text{mm}$, when the baseline length is greater than 500 m, the accuracy of plumb-line deviation will be better than 3″.

From Formula (5), it can be seen that the accuracy of ξ and η are obviously affected by the angle between baselines. Based on the law of error propagation error, the error of plumb-line deviation component is:

$$\begin{aligned} m_\zeta &= \pm\frac{\sqrt{\sin^2\alpha_2 + \sin^2\alpha_1}}{\sin(\alpha_2 - \alpha_1)} m_\delta = K_1 m_\delta \\ m_\eta &= \pm\frac{\sqrt{\cos^2\alpha_2 + \cos^2\alpha_1}}{\sin(\alpha_1 - \alpha_2)} m_\delta = K_2 m_\delta \end{aligned} \tag{7}$$

where, K_1 and K_2 is the influence coefficient of two baseline angle of plumb-line deviation NS component and EW component. Therefore we should pay special attention to the angle between the two baselines.

2.2 *Earth Gravity Model Method*

With the increasing precision of global gravity field model, the plumb-line deviation on the earth's surface can be calculated by the Global Gravity Model plus (GGMplus) [14]. In Asia, the accuracy of plumb-line deviation can reach 5″. This model consists of the Technical University of Munich and Curtin University jointly developed, using the GRACE satellite tracking data, satellite altimetry data and ground gravity data, the spatial resolution reached 7.2″, the accuracy has

significantly improved in compared with Earth Gravitational Model 2008 (EGM2008) [16, 17].

The plumb-line deviation can be calculated by GGMplus:

$$\begin{aligned}\xi &= \frac{GM}{\gamma a^2}\sum_{n=0}^{N}\left(\frac{a}{r}\right)^n\sum_{m=0}^{n}\left(\bar{C}_{nm}\cos m\lambda + \bar{S}_{nm}\sin m\lambda\right)\frac{d\bar{P}_{nm}(\cos\theta)}{d\theta}\\ \eta &= \frac{GM}{\gamma a^2\sin\theta}\sum_{n=0}^{N}\left(\frac{a}{r}\right)^n\sum_{m=0}^{n}\left(-\bar{C}_{nm}\sin m\lambda + \bar{S}_{nm}\cos m\lambda\right)\bar{P}_{nm}(\cos\theta)\end{aligned} \tag{8}$$

where, r is radius, θ is geocentric colatitude, λ is longitude, G is universal gravitational constant, M is the mass of the earth, γ is the normal gravity, a is the mean radius of the earth's equator, $\bar{C}_{nm}$, $\bar{S}_{nm}$ are the Stockes coefficient of n-th order and m-th degree, for GGMplus model n = 2190, m = 5, $\bar{P}_{nm}$ is 4π standardized Legendre function.

3 Influence of the Plumb-Line Deviation on BE

After the NS component and the EW component of plumb-line deviation has been calculated, now consider the influence of the plumb-line deviation on BE. Based on the theory of geodesy, we can calculate the observation direction difference between normal benchmark and vertical benchmark [18].

$$\Delta L_{ji} = (-\xi_j \sin A_{ji} + \eta_j \cos A_{ji})\tan\alpha_{ji} \tag{9}$$

where ξ_j is the NS component of plumb-line deviation of point j, η_j is the EW component of plumb-line deviation of point j, A_{ji} is azimuth, α_{ji} is altitude angle.

For the angle β_j, the deviation value of β_j affected by plumb-line deviation is $\Delta\beta_j$:

$$\begin{aligned}\Delta\beta_j = &(-\xi_j \sin A_{jk} + \eta_j \cos A_{jk})\tan\alpha_{jk}\\ &-(-\xi_j \sin A_{ji} + \eta_j \cos A_{ji})\tan\alpha_{ji}\end{aligned} \tag{10}$$

The relationship between the two angles is $\beta_N \approx \beta_V + \Delta\beta$

Where β_N is β_j in normal benchmark, β_V is β_j in vertical benchmark, $\Delta\beta$ is the difference between normal benchmark and vertical benchmark.

According to Formulas (9) and (10), it can be seen that when the altitude of two points is basically equal, $\alpha \approx 0$, the effect of plumb-line deviation on the observation direction $\Delta L \approx 0$. When i, j, k are basically on the same altitude surface, $\alpha_{ji} \approx 0$ and $\alpha_{jk} \approx 0$. Owing to the underground traverse is straight type, $\Delta\beta \approx 0$. Thus the underground traverse survey itself was little affected by the plumb-line deviation. But when the ground GPS side connects to the underground traverse, if

the height differences between GPS control points and entrance points (as well as the height differences between GPS control points themselves) are very large, the transmission of initial orientation will be affected by the plumb-line deviation, thereby increasing the BE.

3.1 *Influence of the Plumb-Line Deviation at the Two Entrances of the Tunnel*

As shown in Fig. 1, A and B are the GPS control points, point 1 and 2 are underground traverse point. Where AB is initial orientation side, we can measure the direction of A1 to determine point $1, 2, \ldots$, extending to the break-through surface.

Influence of the plumb-line deviation on BE is reflected in two aspects [19]: β_A and β_1, according to Formula (10):

$$\begin{aligned}\Delta\beta_A &= \Delta L_{A1} - \Delta L_{AB} \\ &= (-\xi_A \sin A_{A1} + \eta_A \cos A_{A1})\tan\alpha_{A1} \\ &\quad - (-\xi_A \sin A_{AB} + \eta_A \cos A_{AB})\tan\alpha_{AB}\end{aligned} \tag{11}$$

In the same way, β_1 can be calculated by:

$$\begin{aligned}\Delta\beta_1 &= \Delta L_{12} - \Delta L_{1A} \\ &= (-\xi_1 \sin A_{12} + \eta_1 \cos A_{12})\tan\alpha_{12} \\ &\quad - (-\xi_1 \sin A_{1A} + \eta_1 \cos A_{1A})\tan\alpha_{1A}\end{aligned} \tag{12}$$

where AB, CD are GPS baselines, point $1, 2, \ldots, N$ are underground traverse points, β_i is traverse angle. In local area, the plumb-line deviation value of each control point can be treated as the same, $\Delta L_{A1} = \Delta L_{1A}$. Since the altitude of underground

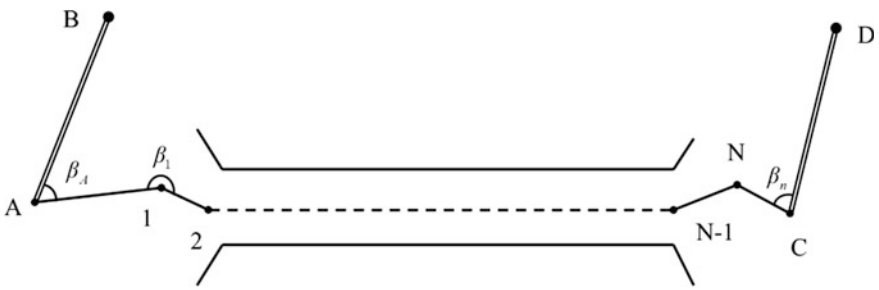

Fig. 1 The transmission of GPS baseline in the underground traverse

traverse point 1 and 2 is basically equal, $\alpha_{12} \approx 0$, so $\Delta L_{12} \approx 0$, the total effect of plumb-line deviation value on the observation direction is Δ:

$$\begin{aligned} \Delta &= \Delta\beta_A + \Delta\beta_1 \\ &= \Delta L_{A1} - \Delta L_{AB} - \Delta L_{1A} + \Delta L_{12} = -\Delta L_{AB} \end{aligned} \tag{13}$$

Influence of initial observation direction error on the BE is Δ_L:

$$\Delta_L = \frac{|\Delta L_{AB}|S}{\rho} \tag{14}$$

where, S is vertical distance from point A to break-through surface. If the altitudes of GPS control points at the two entrances of the tunnel are basically equal, BE will be little affected by the plumb-line deviation.

3.2 *Influence of the Plumb-Line Deviation in the Inclined Shaft*

As shown in Fig. 2, A and B are the GPS control points at the pithead, point E is the junction point of inclined shaft bottom and main tunnel. For the angle i − j − k of straight traverse in the inclined shaft:

$$\begin{aligned} A_{ji} &= A_{jk} + 180^\circ \\ \sin A_{ji} &= \sin(A_{jk} + 180^\circ) = -\sin A_{jk} \\ \cos A_{ji} &= \cos(A_{jk} + 180^\circ) = -\cos A_{jk} \end{aligned} \tag{15}$$

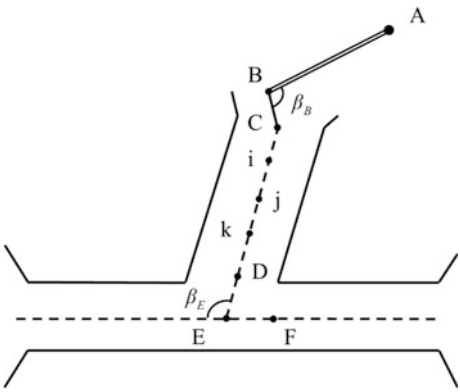

Fig. 2 The transmission of GPS baseline in the inclined shaft

According to Formula (10):

$$\Delta\beta_j = (-\xi_j \sin A_{jk} + \eta_j \cos A_{jk})(\tan \alpha_{jk} + \tan \alpha_{ji}) \tag{16}$$

If the slope of inclined shaft is uniform, $\alpha_{ji} \approx -\alpha_{jk}$, and $\Delta\beta_j \approx 0$. At the bottom of the inclined shaft, since the altitude of underground traverse point E and F is equal, $\alpha_{EF} \approx 0$, $\Delta L_{EF} \approx 0$. At the entrance of the inclined shaft, if the altitudes of GPS control points A and B are basically equal, $\alpha_{BA} \approx 0$, and $\Delta L_{BA} \approx 0$

$$\begin{aligned} \Delta\beta_B &= \Delta L_{BC} - \Delta L_{BA} \approx \Delta L_{BC} \\ \Delta\beta_E &= \Delta L_{ED} - \Delta L_{EF} \approx \Delta L_{ED} \end{aligned} \tag{17}$$

Assuming the plumb-line deviation value of points B and E are the same, $\alpha_{ED} \approx -\alpha_{BC}$, the total effect of plumb-line deviation value on the observation direction is Δ:

$$\Delta = (-\xi \sin A_{BC} + \eta \cos A_{BC})(\tan \alpha_{BC} + \tan \alpha_{ED}) \approx 0 \tag{18}$$

In summary, if the slope of inclined shaft is uniform, and the altitudes of GPS control points at the entrances are basically equal, BE will be little affected by the plumb-line deviation.

3.3 The Total Influence Value of Plumb-Line Deviation on BE

Due to the plumb-line deviation is system error; it is non-random and not equivalent to the mean error. It can only be combined with break-through limit error. For safety's sake, BE can be estimated according to the most unfavorable conditions. Therefore, consider the influence of plumb-line deviation, BE estimation is:

$$\begin{aligned} \Delta_L &= 2\sqrt{m_U^2 + m_G^2} + \Delta_V \\ \Delta_V &= \Delta_I + \Delta_O = \left(\frac{|\Delta L|S}{\rho}\right)_I + \left(\frac{|\Delta L|S}{\rho}\right)_O \end{aligned} \tag{19}$$

where ΔL is the correction for plumb-line deviation of the coordinate azimuth, m_U and m_G is the influence value of underground and ground controls measurement errors on BE, Δ_I and Δ_O is the influence value of the plumb-line deviation on BE at the two entrances of branch tunnel, Δ_V is the influence of plumb-line deviation on total break-through error (TBE), S is vertical distance from GPS control point to break-through surface.

4 Example and Analyses

Now, take a long tunnel project (Hanjiang-to-Weihe River Water Diversion in Qinling Mountains 5#–6# Tunnel Project) as an example, we calculated the plumb-line deviation by GNSS/leveling method and GGMplus model method, and determine the influence value of the plumb-line deviation on BE.

4.1 Project Overview

Hanjiang-to-Weihe River Water Diversion in Qinling Mountains Tunnel total length 97 km, across the central Shaanxi area and the southern Shaanxi area, connect the Yangtze River and the Yellow River. This tunnel has a characteristic of super long, deep-buried, complicated geological condition, high geotemperature and high geostress. As shown in Fig. 3, the two branch tunnels are both inclined shaft excavation, where 5# branch tunnel length 4.5 km, 6# branch tunnel length 2.5 km, main tunnel length 10 km.

As shown in Figs. 4 and 5, the black line represents the visibility between the control Points. Due to the limitation of terrain, the height differences between GPS control points and entrance points are very large, and some GPS baselines lengths are very short. Therefore, it is necessary to consider the influence of the plumb-line deviation on the BE.

4.1.1 Calculation Result

Based on the GNSS/leveling method and GGMplus model method, we calculated the plumb-line deviation of GPS control point. Consider the spatial resolution of GGMplus model is 7.2″, the regional plumb-line deviation of two branch tunnel can

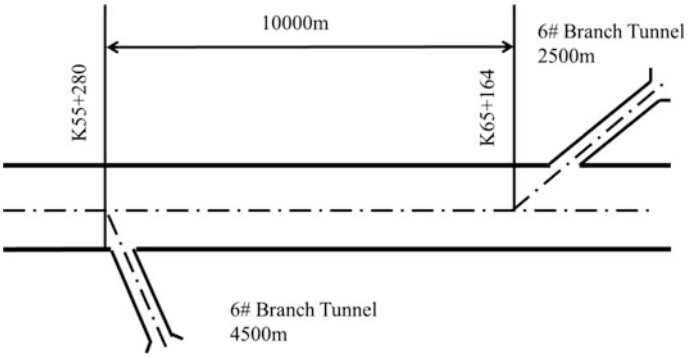

Fig. 3 5#–6# branch tunnel breakthrough schematic

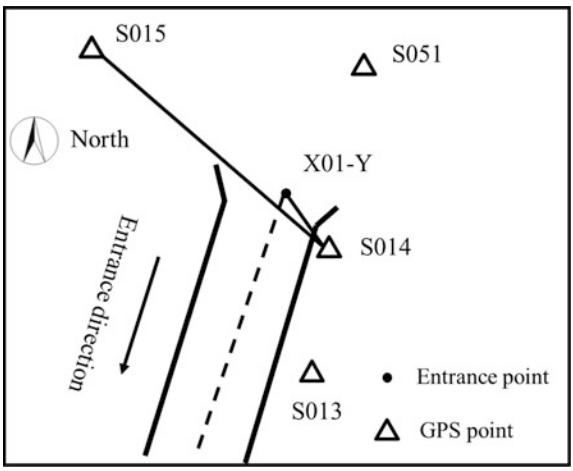

Fig. 4 GPS points of 5# branch tunnel

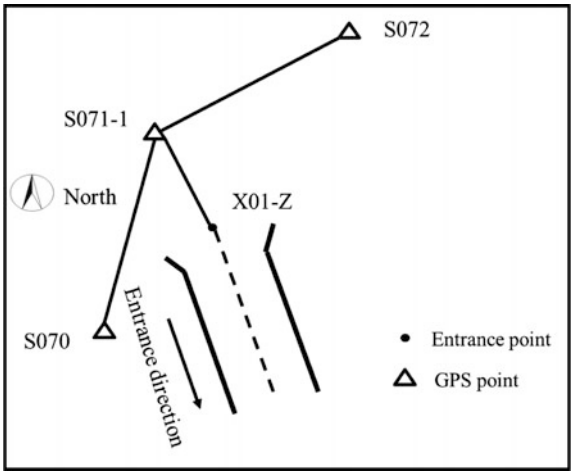

Fig. 5 GPS points of 6# branch tunnel

be determined. For the GNSS/leveling method, the accuracy of the NS component ξ and EW component η are determined by the horizontal angle of the GNSS baseline. As shown in Table 1.

From Table 1, the result shows that the maximum deviation of two methods is 4.5″, hence these two methods have good accuracy and coincide with each other. For the GGMplus model, the accuracy of plumb-line deviation can reach 5″ in Asia. For GNSS/leveling method, each control point results have little difference. However, the calculation accuracy is quite different. According to the Formula (7), the accuracy of the NS component and EW component are related to the horizontal angle of the GNSS baselines, and the influence rule is shown in Figs. 6 and 7. Where, the X axis, Y axis, respectively, shows the two GNSS baselines azimuths, Z axis shows the size of the influence coefficient K.

Table 1 Calculation result of the plumb-line deviation

GPS control points	GGMplus		GNSS/leveling			
	$\xi('')$	$\eta('')$	$\xi('')$	Accuracy ($''$)	$\eta('')$	Accuracy ($''$)
S014	16.08	−3.43	13.12	1.08	−0.73	3.39
S013			13.17	0.66	−0.60	3.93
S015			13.33	1.02	−0.19	2.36
S051			13.04	0.96	−0.25	2.10
S072	18.01	−3.94	13.42	2.04	−0.12	5.95
S071-1			13.42	1.04	−0.12	4.12
S070			13.42	1.07	−0.13	6.40

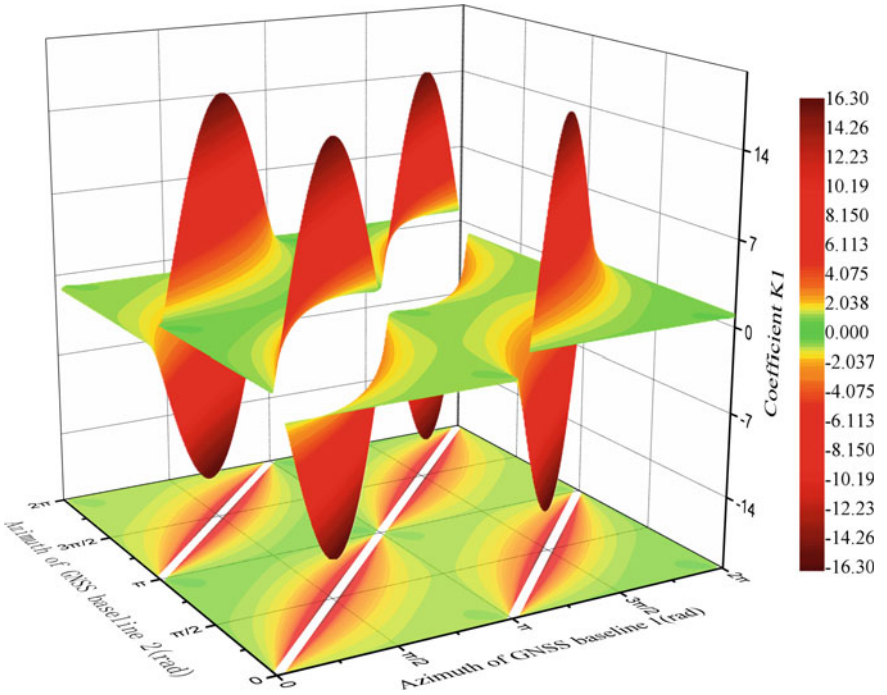

Fig. 6 Influence coefficient of two baselines horizontal angle of NS component

As shown in Figs. 6 and 7, with the decreasing of the angle of the two baselines, the influence coefficient increases gradually. When the two baseline angle is close to 90°, the influence coefficient is small, as shown in the green area. When the baseline angle is less than 60°, the influence coefficient is large, the accuracy of plumb-line deviation component will decrease, as shown in the red area. For this project, using GNSS/leveling method, the accuracy of NS components are higher than EW components. This is due to the long tunnel construction along the

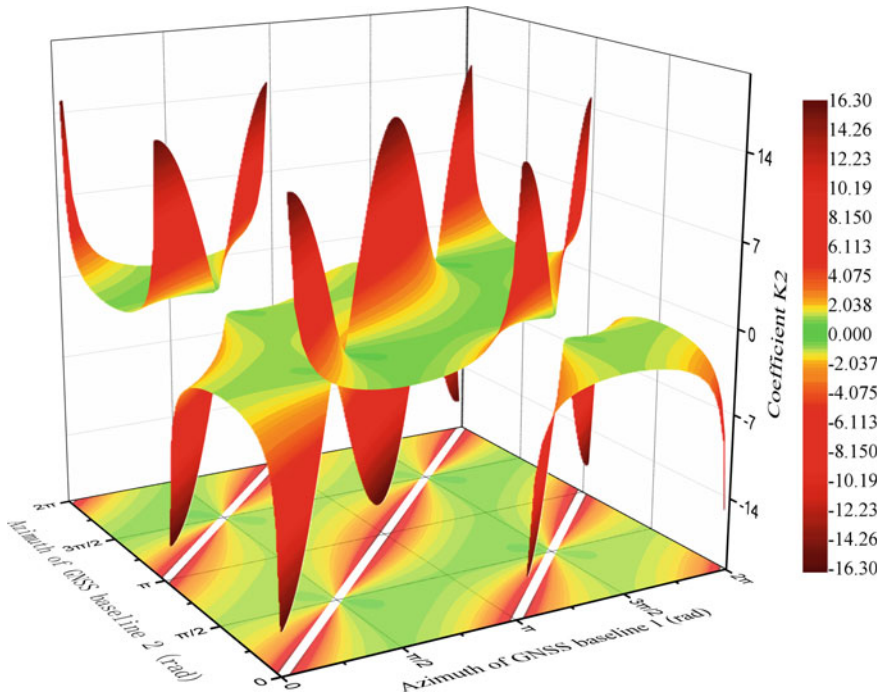

Fig. 7 Influence coefficient of two baselines horizontal angle of EW component

north-south direction, the GPS baselines are almost in north-south direction (which azimuths are about 180°), and the GPS baselines of east-west direction are less, hence the baseline azimuths are mostly distributed in the central area of Figs. 6 and 7, which lead to high accuracy of NS components and poor accuracy of EW components.

Now, we calculate the plumb-line deviation effect on initial azimuth value. In local area, the plumb-line deviation value of each control point and each underground traverse point can be treated as the same. Next, combined with underground traverse data, we calculated the influence of plumb-line deviation on IAE and BE. As shown in Tables 2 and 3.

From Tables 2 and 3, the results show that there are obvious differences in the influence of plumb-line deviation on IAE and BE when we choose difference initial orientation plan. Once the plumb-line deviation is determined, according to the Formula (10), the influence of plumb-line deviation on the BE depends on the IAE affected by the altitude angle of initial orientation and entrance orientation. Take S015 → S014 → X01-Z in the 5# branch tunnel as an example, the influence rule of altitude angle of initial orientation and entrance orientation on IAE is shown in Fig. 8. Where, the X axis shows the altitude angle of entrance orientation, Y axis shows the altitude angle of initial orientation, Z axis shows the influence of plumb-line deviation on IAE.

Table 2 Influence of plumb-line deviation on IAE and BE (5# branch tunnel)

Plan	Initial orientation	Altitude angle ° ′ ″	Entrance orientation	Altitude angle ° ′ ″	GNSS/leveling		GGMplus	
					IAE (″)	BE (mm)	IAE (″)	BE (mm)
1	S015 → S014	0 10 36	S014 → X01-Z	−41 43 36	−5.47	119.36	−4.78	104.20
2	S051 → S014	−16 14 23			−4.24	92.49	−2.55	55.64
3	S013 → S014	2 51 56			−5.38	117.41	−4.53	98.92
4	S014 → S013	−2 51 56	S013 → X01-Z	−2 20 52	0.16	3.43	0.44	9.53
5	S015 → S013	−1 43 05			0.01	0.07	0.19	4.23
6	S051 → S013	−6 47 37			0.37	8.14	0.88	19.27
7	S014 → S015	−0 10 36	S015 → X01-Z	−8 54 35	1.18	25.75	1.00	21.85
8	S013 → S015	−1 43 05			1.09	23.88	1.00	21.84
9	S051 → S015	−12 29 06			3.89	84.82	4.02	87.61
10	S014 → S051	16 14 23	S051 → X01-Z	−32 19 28	−3.06	66.74	−4.62	100.82
11	S013 → S051	6 47 37			−3.89	84.96	−6.16	134.36
12	S015 → S051	12 29 06			−1.50	32.83	−3.83	83.62

Table 3 Influence of plumb-line deviation on IAE and BE (6# branch tunnel)

Plan	Initial orientation	Altitude angle ° ′ ″	Entrance orientation	Altitude angle ° ′ ″	GNSS/leveling		GGMplus	
					IAE (″)	BE (mm)	IAE (″)	BE (mm)
1	S071-1 → S072	−3 23 32	S072 → 01-Y	−2 36 35	−0.63	38.42	−1.23	74.56
2	S070 → S072	−3 40 23			−0.46	28.09	−1.04	63.05
3	S072 → S071-1	3 23 32	S071-1 → X01-Y	−18 27 32	−0.60	36.36	−2.26	137.09
4	S070 → S071-1	−3 43 27			−0.23	14.11	−1.82	110.23
5	S071-1 → S070	3 43 27	S070 → X01-Y	−15 41 05	0.18	11.05	1.06	63.99
6	S072 → S070	3 40 23			−0.01	0.87	0.80	48.65

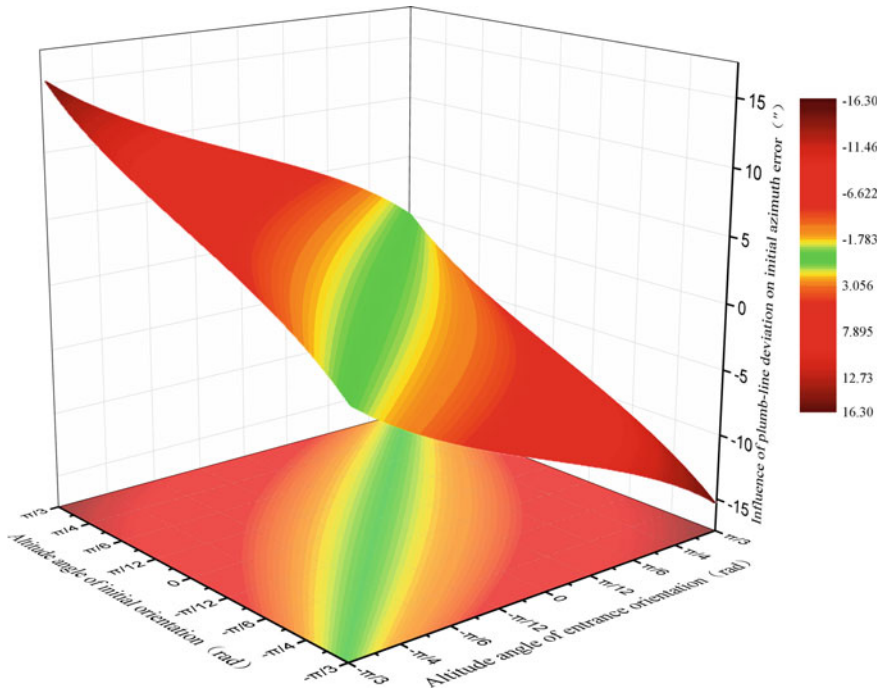

Fig. 8 Influence of altitude angle of initial orientation and entrance orientation on IAE

As shown in Fig. 8, when the altitude angle of entrance orientation equal to the initial orientation (or they are both close to 0°), the influence of plumb-line deviation on IAE is very small, as shown in the green area. It was proved that the plumb-line deviation has little influence on IAE in uniform inclined shaft and flat main tunnel.

However, with the increase of the altitude angle difference between the initial orientation and entrance orientation, IAE increases gradually, as shown in the red area. For the entrance orientation S014 → X01-Z, the altitude angle was more than 40°, influence of plumb-line deviation on IAE reached −5.47″, which had a great influence on BE. The larger the height differences between GNSS control points and entrance points (as well as the height differences between GNSS control points themselves), the greater BE.

Therefore, in order to reduce the influence of plumb-line deviation, it is necessary to make the GNSS control points and entrance points at the same elevation. If cannot meet the conditions in difficult areas, we'd better calculate the influence of plumb-line deviation on IAE and BE, and choose the plan which IAE is minimal.

Figures 9 and 10 show the effects of different initial orientation plans on IAE and BE of 5# branch tunnel and 6# branch tunnel by using GGMplus method and GNSS/leveling method.

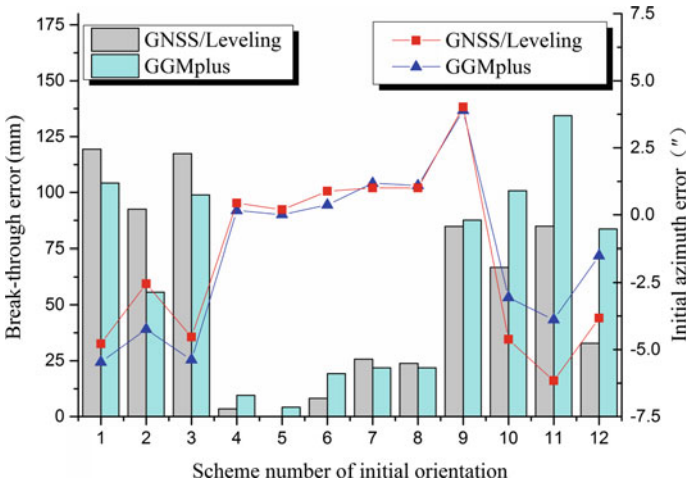

Fig. 9 Effects of different plans on IAE and BE of 5# branch tunnel

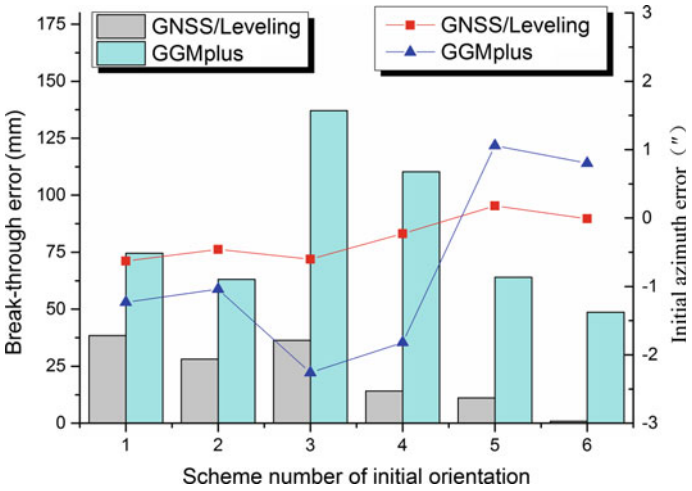

Fig. 10 Effects of different plans on IAE and BE of 6# branch tunnel

Consider the GPS control points distribution at the two entrances of branch tunnel, the influence of plumb-line deviation on total break-through error (TBE) under different initial orientation plan as shown in Table 4.

For 5# branch tunnel, Selecting NGPS015 → NGPS013 as initial orientation side had the least influence on BE, and NGPS015 → NGPS013 would have the largest effect. For 6# branch tunnel, Selecting GPS072 → GPS070 as initial

Table 4 influence of plumb-line deviation on TBE under different plans

Plan	Initial orientation side of 5# branch tunnel	Initial orientation side of 6# branch tunnel	TBE(mm)	
			GGMplus model	GNSS/leveling
Plan A	S015 → S013	S072 → S070	48.83	0.87
Plan B	S015 → S014	S072 → S071-1	172.20	125.39

orientation side had the least influence, and GPS072 → GPS071-1 would have the largest effect. To summarize, Plan A represents the selection scheme of initial orientation side which TBE is minimum, and Plan B represents the selection scheme of initial orientation side which TBE is maximum.

5 Conclusions and Discussion

From the above findings, the following conclusions can be drawn:

1. The accuracy of GNSS/leveling method to determinate the plumb-line deviation depends on the GNSS vertical positioning accuracy and baseline length. If we want to calculate the NS (EW) component of plumb-line deviation by GNSS/leveling method, we should pay special attention to the angle between the two baselines. In theory, 90° is the best. Limited by terrain, it should not be less than 60°. Otherwise, the calculation accuracy of plumb-line deviation will decrease.
2. In the case of this super long tunnel project, the result shows that the maximum deviation of GNSS/leveling method and GGMplus model method is 4.5″, so these two methods have good accuracy and coincide with each other. The accuracy is enough to meet the need for analysis of BE.
3. Owing to the influence of plumb-line deviation on the IAE depends on the altitude angle and azimuth on the observed directions, when we layout GNSS control point, it is necessary to make the control points at the same elevation, and the length of initial orientation side should more than 500 m as much as possible. If it cannot meet the requirements in difficult areas, according to the described methods in this paper, the influence of plumb-line deviation value can be estimated for selecting the optimal plan of initial orientation.
4. In practical work, limited by the poor visibility conditions of control points, selection of the initial orientation side may not be the optimum. For security reasons, we can calculate the maximum influence value of plumb-line deviation; and regard it as the BE estimation value. For Hanjiang-to-Weihe River Water Diversion in Qinling Mountains 5#–6# Tunnel Project, the maximum influence of plumb-line deviation on BE is 172 mm. Combined with the underground traverse error, the TBE estimated value is 307 mm.

In order to further improve the break-through accuracy to meet the design requirements, it is suggested to layout new GNSS control points, consider moving the entrance point to the outside of entrance and increasing the visibility conditions, as far as possible to maintain the elevation of GNSS control points and entrance point are basically equal, to reduce the influence of plumb-line deviation on BE.

Acknowledgements This research was partially supported by the National Natural Science Fund (No. 41504001) and Fundamental Research Funds for the Central Universities (No. 310826 175016). And I would like to express my sincere heartfelt thanks to Hanjiang-to-Weihe River Valley Water Diversion Project Construction Co. Ltd Shaanxi Province and China Railway First Survey& Design Institute Group Co., Ltd for the data support.

References

1. Zhang Y, Zhang X (2016) Determination and accuracy analysis of vertical deflection. J Geodesy Geody 36(5):395–399
2. Yuefeng LI, Xingbin DING (2008) Progress in studying plumb line variations. Prog Geophys 23(6):1736–1745
3. Lu B, Fan D, Xiong Y et al (1998) Influence of Plum-line deflection on tunneling error. Geotech Invest Surv 3:56–59
4. Sun F, Wu X, Zhang C (2005) Fast determination of the vertical deflection and its precision analysis of any point on the land and sea in China. Geomatics Info Sci Wuhan Univ 30(1):42–50
5. Soler T, Carlson JAE, Evans AG (1989) Determination of vertical deflections using the global positioning system and geodetic leveling. Geophys Re Lett 16(7):695–698
6. Tse CM, Iz HB (2013) Deflection of the vertical components from GPS and precise leveling measurements in Hong Kong. Am Soc Civil Eng 132(3):97–100
7. Jinsheng NING, Chunxi GUO, Bin WANG et al (2006) Refined determination of vertical delfection in china mainland area. Geomatics Info Sci Wuhan Univ 31(12):1035–1038
8. Zheng W, Xu H, Zhong M et al (2010) Progress and present status of research on earth's gravitational field models. J Geodesy Geodyn 30(4):83–91
9. Yang H (2011) Gravity field model in the application of engineering control network. Cheng du: Southwest Jiaotong University
10. Wei D, Zhang X, Feng D (2009) Local quasi-geoid determination basedon EGM2008 Model. Surv Mapp Geol Miner Resour 25(3):17–18
11. Ceylan A (2010) Determination of the deflection of vertical component via GPS and leveling measurement: a case study of a GPS test network in Konya, Turkey. Sci Res Essays 4(12):1038–1438
12. Jianzhong Li (1999) Determining components of vertical deflections using GPS. Eng Surv Mapp 8(2):34–37
13. Aisheng Wang (2002) Using GPS and leveling to calculate the deviation of vertical line. Bull Surv Mapp 2:17–20
14. Junyu Chen (2014) Study on the methods of refining the quasi-geoid based on GGMplus model. Northeastern University, Shenyang
15. Zhang C, Guo C, Chen J et al (2009) EGM 2008 and its application analysis in Chinese mainland. Acta Geodaetica et Cartographica Sinica 38(4):283–289

16. Yang J, Zhang X, Zhang F et al (2012) On the accuracy of EGM2008 earth gravitational model in Chinese Mainland. Prog Geophys 27(4):1298–1306
17. Hirt C, Kuhn M, Claessens S et al (2014) Study on the Earth's short-scale gravity field using the ERTM2160 gravity model. Comput Geosci 73:71–80
18. Wentong WANG, Zhang X (2006) Study on influence of plumb line deflection on transverse break-through survey of tunnels. Tunnel Construction 26(6):17–19

BDS/GPS High Precision Railway Deformation Monitoring Software Design and Verification

Rongpan Xu, Zhaoying Liu, Zhaofeng Gao, Daquan Tang and Yingying Zhang

Abstract Based on double-difference model of Beidou and GPS data fusion processing algorithm, this paper presents a set of high precision baseline processing scheme and develops deformation monitoring software adapted to railway. Based on the software, the displacement platform set on a mobile robot is utilized to simulate railway subsidence, time series of coordinate differences are provided and the accuracy of different length baselines is analyzed. The experiment shows that calculated values coincide well with the true values among the time series of displacement platform. For baselines of 35.3 and 551.2 m, the plane accuracy is better than 1 mm while the vertical accuracy is better than 1.5 mm. And when the baseline is 5095.4 m in length, the plane and vertical accuracy drops to 2 mm. The software is capable of monitoring minimum deformation of 2 mm in plane or 3 mm in vertical to meet the demand of railway industry monitoring accuracy.

Keywords GPS/BDS · Railway deformation monitoring · Time series · Accuracy

1 Introduction

At present, China is in the expanding of its rail network, and to 2020, the railway mileage will reach 150,000 km, thus a strong demand for railway safety monitoring is created. Current monitoring methods mainly depend on the layout of the CPI, CPII, CPIII control points along the railway, using artificial operation manner such as total station and level, which brings high maintenance cost and difficulties to realize real-time or near real-time monitoring. An automated monitoring technology of high precision is in urgent need.

R. Xu (✉) · Z. Liu · Z. Gao · D. Tang · Y. Zhang
North Information Control Research Academy Group CO.LTD,
Nanjing 210000, China
e-mail: xurongpan@163.com

J. Sun et al. (eds.), *China Satellite Navigation Conference (CSNC) 2017 Proceedings: Volume I*, Lecture Notes in Electrical Engineering 437,
DOI 10.1007/978-981-10-4588-2_11

Global Navigation Satellite System (GNSS), with its characteristics of all weather, real time, high precision, no need visibility between sites, is widely studied and successfully applied to deformation monitoring such as the bridges, dams and tall buildings. Early researches were mainly undertaken around GPS. Chen [1] considered a variety of error corrections through GPS data processing, realizing the vertical ground movement monitoring instead of the traditional measurement method. Li made use of GPS technologies to study the feasibility of the dam deformation monitoring, the results showed that with appropriate control measures, GPS positioning accuracy could meet the requirements of dam deformation monitoring accuracy [2]. Huang et al. combined GPS with wavelet analysis technology, implemented high-rise building and bridge monitoring and accelerated the popularization and application of GPS in deformation monitoring [3, 4]. At the end of 2012, Beidou satellite navigation systems with independent property rights of China started to provide services to the Asia-Pacific region, deformation monitoring gradually developed to the multi-frequency and multi-mode GNSS high-precision monitoring. Studies have shown that the use of GNSS for earth and rock fill dam monitoring can achieve the precision of 3 mm in plane and 4 mm in height, and has higher reliability relative to a single system [5]. If the GNSS positioning technology is applied in railway subsidence monitoring, instead of traditional artificial measuring way, not only monitoring can be done fast and continuously, and the dependence on CPI, CPII, CPIII control points can be reduced, thus maintenance costs can be reduced greatly.

Based on the double difference model, this paper aimed at railway deformation characteristics and studied the Beidou, GPS data fusion processing algorithms. A set of baseline processing scheme with high precision is proposed, and subsidence monitoring system suitable for railway is developed, including the original data receiving and storage, data decoding, baseline calculating, coordinate transformation, deformation data storage, display system and alarm system, etc. To verify the analysis, the article designs a set of complete experiment scheme to test baselines of different lengths respectively, undertake error statistics and discuss the availability of GNSS in the measurement of the railway.

2 Data Processing Algorithms

2.1 Unity of Time and Coordinate Reference Frame

Beidou adopts China Geodetic Coordinate System 2000 (CGCS2000) while GPS adopts WGS-84 Coordinate System. Literature [6] points out that CGCS2000 and WGS84 (G1150) is compatible by comparing CGCS2000 and WGS84, and within the scope of the precision of the coordinate system implementation, CGCS2000 and WGS84 coordinate (G1150) coordinates are consistent. For short baseline relative

positioning, the GNSS systems choose separate reference satellite to difference, so the effects of different coordinate benchmarks can be eliminated [7]. In this paper, during calculating the baseline and forming double difference observation values, BDS and GPS choose separate reference satellites, so the conversion of coordinates is not necessary.

As to time system, Beidou uses Beidou Time (BDT) and GPS uses GPS Time (GPST). Both belong to the atomic time, but the different starting points should be considered during the data processing [8]. As many documents have described, it is no longer discussed here.

2.2 Data Processing Strategy

Double difference observation model parameter settings are shown in Table 1. (1) Noise of carrier phase observation values B1 or L1 is the 1/3 of non-ionospheric combination observations LC. Therefore, for a short baseline, parameter estimation uses B1 and L1 [9]. (2) Because of the characteristics of BDS itself, according to the experience, setting the GPS and Beidou observation weight to 1.5:1 in data fusion is helpful to improve the calculating accuracy. (3) Stochastic model is determined by satellite elevation, when elevation is less than 15°, the satellite observations are given up. (4) Minimum public time 600 s refers to that only when the synchronized continuous observation time of monitoring station and base station is longer than the

Table 1 Observation model

Parameters	Models	Priori constraints
Observations	BDS adopts B1 and GPS adopts L1. Weight of GPS&BDS observations is set to 1.5:1 by experience	L1 0.01 circle, P1 1.0 m
Cut-off elevation	15°	
Processing interval	30 s	
Minimum public time	600 s	
Duration	14,400 s	
Satellite orbit	BDS and GPS adopt orbits calculated with their broadcast ephemeris	
Satellite clock errors	BDS and GPS adopt clock errors calculated with their broadcast ephemeris	
Receiver clock offsets	Estimated	300 m
Station coordinates	Estimated	Random process noise 10 m
Antenna phase error	PCO, PCV parameters provided by igs08.atx	
Ambiguity	Fixed(ratio set to 3)	
Ionospheric correction	Eliminated by double difference	
Troposphere correction	Eliminated by double difference	

600 s, this observation data is valid. (5) Length of time is set to 4 h, that is 14400 s. (6) BDS and GPS adopt their own broadcast ephemeris. (7) For short baselines, error has very good spatial correlation. Most errors can be eliminated after double difference, so no additional parameter estimation of station ionosphere, zenith tropospheric delay is needed. (8) Ignore the earth tide, tidal correction model.

2.3 Data Processing Flow

Figure 1 is the data processing flow diagram. It consists of three containers:

(1) Container I is data cleaning process. The process includes: reading observations and broadcast ephemeris; Extracting header file coordinates or SPP results to initialize moving station and base station coordinates; Calculating the triple difference results; Cycle slip detecting and repairing of triple difference residual method; Triple difference results output. After a cycle of 10 times, the three difference solution coordinates are gradually elaborated. Cycle slip is detected again and the epoch of cycle slip is identified.
(2) Container II is float solution solving process. First by using the precise coordinates of triple difference solutions, re-linearization the equations are undertaken and double difference observations between stations and satellites are formed. Secondly, in the judgment of each epoch, add data satisfying the quality control to the normal equation. Finally, after iterating through all the epochs, output float solution through the least squares parameter estimation.
(3) Container III is fixed solution solving process. After obtaining the float solution, the LAMBDA search algorithm is used to fix ambiguity and output fixed solution. For medium and long baselines, to improve the correctness of ambiguity calculation, before calculating the double difference observation value ambiguity, wide lane, narrow lane ambiguity should be solved first.

3 Railway Subsidence Simulation Experiment and Analysis

3.1 Experimental Design

(1) Experiment one

To verify the core algorithm of the deformation monitoring system, that is the reliability and accuracy of the baseline solution, this paper carried out a large

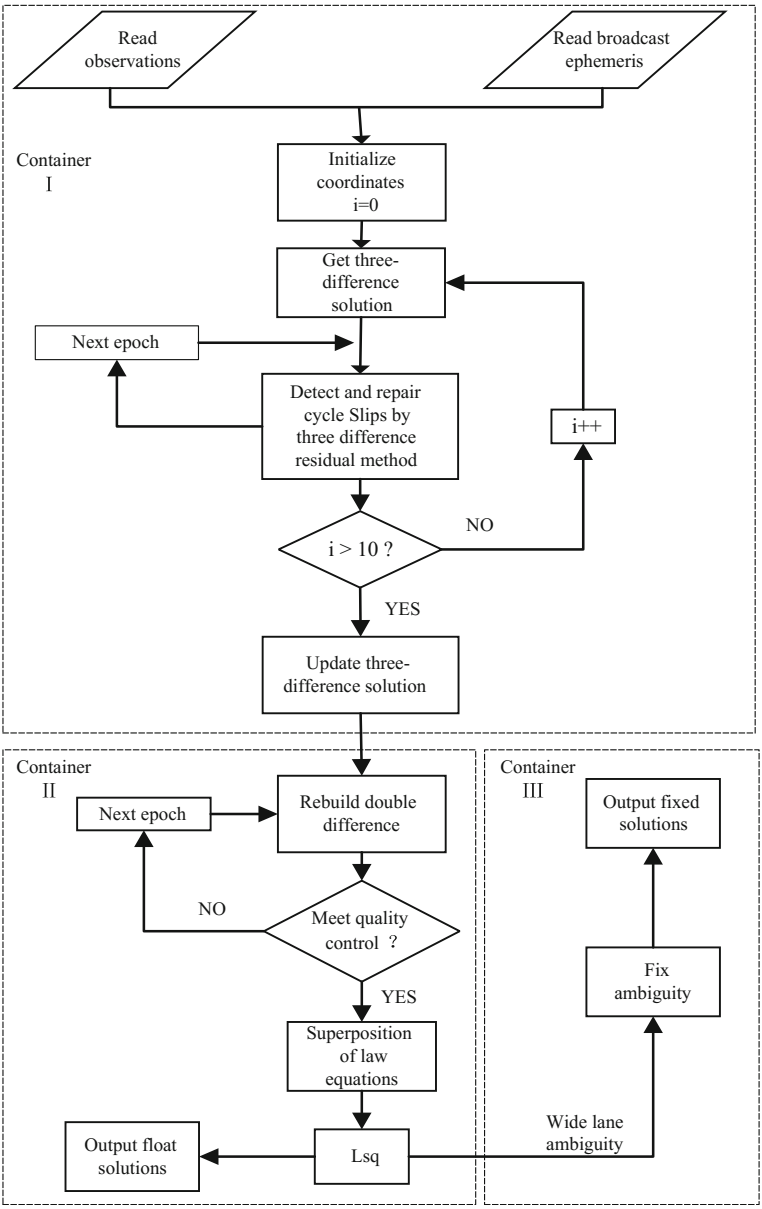

Fig. 1 Data processing flow

Table 2 Point movement records

Sequence number	Date and time	Displacement (mm)		
		E	N	U
1	2016.08.16 08:00	0	0	0
2	2016.08.17 08:00	−2	0	0
3	2016.08.18 08:00	−4	0	0
4	2016.08.19 08:00	−2	0	−5
5	2016.08.22 08:00	0	0	0
6	2016.08.24 08:00	0	0	−5
7	2016.08.25 08:00	0	0	−10
8	2016.08.26 08:00	0	0	−5
9	2016.08.29 08:00	0	0	0
10	2016.09.02 16:00	0	0	0

number of railway subsidence simulation experiments. Observation stations are laid out on the stable pier as base station while observation stations placed on a mobile robot (displacement platform) act as a monitoring station. Baseline length is 35.3 m. The mobile robot can be controlled externally and its precision is 0.01 mm, so its movement error can be ignored and the mobile results can be considered as true values. Both station uses Unicore UR380 receiver and Unicore antenna (HXCGS488A). During the experiment, from August 16, 2016 to September 2, continuous observation for 24 h was undertaken. Table 2 is moving records of the displacement platform during the experiment.

The two-axis displacement platform has two movable axes, around the two axes the platform can move in two-dimensional planes, including moving up and down and back and forth. Therefore, in the process of the experiment, the robot movement is only in the vertical and east and west direction. Considering the characteristic that accuracy of GNSS system is better in plane monitoring than in vertical, during the experiment, the platform moves 5 mm in vertical at a time when moves every 2 mm in plane. East, up movement is positive when negative value means movement in the opposite direction, relative to the reset state. For instance, (0, 0, 0) means the reset state. (−2, 0, −5) mean 2 mm to the west and 5 mm down. During the experiment, the subsidence and rise of the platform are continuous in order to test the system monitoring results of continuous deformation in the same direction.

(2) Experiment two

Using the same receiver and antenna with experiment one and selecting of two observation piers 551.2 m away from each other, static continuous observations are undertaken for 4 periods. Each period is 4 h, and the antenna is not moved between periods.

(3) Experiment three

Like experiment two, the baseline is extended to 5095.4 m, and then a statistical accuracy is obtained.

3.2 *Time Sequence of Coordinate Difference of Displacement Platform*

Figure 2 is coordinate time series of displacement platform in east, north and up direction of experiment 1 (During the experiment 2, experiment 3 monitoring observation piers are immovable, so only period differences and precision statistics are undertaken in Sect. 3.3). For comparative analysis, black refers to real displacements and red refers to calculated values. Calculation method is, during reset of the displacement platform to (0, 0, 0), using 24 h observation data to calculate the baseline as a reference between the base station and the displacement platform, calculating a result every 4 h, and comparing the results with the reference. Due to the displacement of the mobile platform starts around 8 o'clock in the morning, therefore, the result of four hours after the moving platform, such as calculation of 8–12 o'clock, is taken as a result of the 8 o'clock.

By comparing the calculated value and true value of the east-west direction in the figure, we can see that when the displacement platform moves westward to the 2 mm, the monitoring system can tell the change. When the displacement platform moves westward to 4 mm, the change is more easily found for the monitoring system. Subsequently, the displacement platform has experienced two call backs in

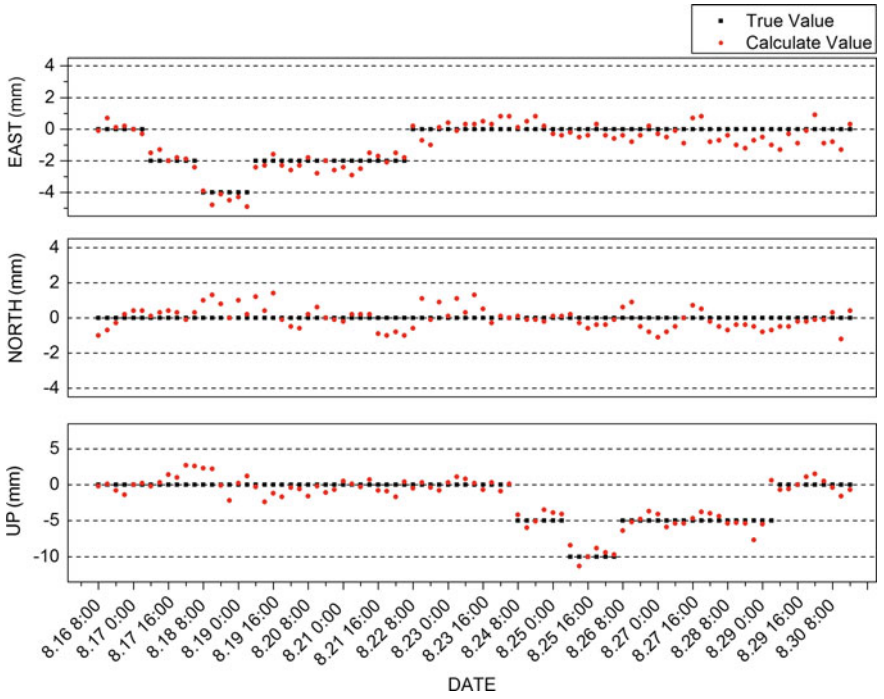

Fig. 2 Time sequence of displacement platform coordinate difference

turn, 2 mm each time, to make the plane back to the reset state. It can be found in the process that calculated results vary with the true values within ±1 mm of the true value. The good compliance between calculated results and the true value illustrate the reliability of the monitoring system.

During the experiment, the displacement platform is not moving in the north-south direction, at this time, the calculated value is random fluctuations ±1 mm around the true value. In a few periods it is in the ±2 mm, but on the whole it still can reflect the situation of monitoring points in this fixed direction.

Monitoring precision in vertical is the key problem of railway subsidence monitoring. As can be seen from the figure, from August 16, 2016 to August 24th in vertical it has not moved, at this time, the calculated values are in random fluctuations in the range of +2 mm around the true value. Then, the displacement platform moves downward gradually, 5 mm each time, afterwards it moves twice upward, each time 5 mm. During the process calculated values still change around the true values, and according to the calculated values whether the displacement platform increase or decrease can be significantly distinguished, thus the monitoring system has good effect.

3.3 Monitoring Accuracy Analysis

Table 3 shows the maximum, minimum, average value and standard deviation of experiment one corresponding to the different displacement platform moving values respectively. In plane direction, when the displacement platform moves 0, 2, 4 mm, the maximum and minimum values are limited to within ±2 mm around the true value. In vertical, when the displacement platform moves 0, 5, 10 mm, from the standard deviation it can be seen that the accuracy is slightly worse than that in the plane direction, but the maximum and minimum value is still within ±3 mm around the true value.

For quantitative analysis, the true values of the corresponding time period are subtracted from the calculated results to obtain deviation from the true value and undertake accuracy statistics, which can be seen in Table 4. It can be seen that

Table 3 Comparison between actual displacements of the platform and calculated results (mm)

Direction	Displacement	Calculated result			
		Maximum	Minimum	Average	Standard deviation
East	0	0.9	−1.3	−0.2	0.5
	−2	−1.3	−2.9	−2.1	0.4
	−4	−3.9	−4.9	−4.4	0.4
North	0	1.4	−1.2	0.0	0.6
Up	0	2.7	−2.4	−0.1	1.3
	−5	−3.5	−7.7	−5.0	1.0
	−10	−8.4	−11.3	−9.6	1.0

Table 4 RMS accuracy statistics of displacement platform (mm)

East	North	Up
0.5	0.6	1.2
Plane: 0.8		

accuracy in plane direction is higher, better than 1 mm. It is slightly worse in vertical, reaching 1.2 mm.

The accuracy of RMS is given in Table 4, combined with maximum, minimum value and true value deviation analysis in Table 3, the realized monitoring system can monitor the deformation of the minimum 2 mm in plane direction and 3 mm in vertical.

Table 5 is the statistics of deviations from the average values and RMS in very period of 551.2 and 5095.4 m baselines in experiment two and three. As can be seen, for short baseline about 500 m, the deviations between periods in plane direction have been kept within 2 mm and in vertical within 3 mm. When the baseline increases to 5 km, the horizontal and vertical deviations between period increases, especially in the vertical direction the error is significant. The possible reason is that, with the longer of the baseline, ionosphere and troposphere error after double difference still has part of the residual, resulting in reduced accuracy, while in the vertical direction the accuracy affected more significantly.

Figure 3 shows accuracy comparison of the three baselines. It can be seen when the baseline increases from 35.3 to 551.2 m, since the baseline is still short, each error is well eliminated by double difference. In the horizontal and vertical direction the accuracy is not significantly affected. Within the plane direction the accuracy is better than 1 mm, and in the elevation direction accuracy is better than 1.5 mm. When the baseline increases to 5095.4 m, the accuracy in plane and elevation direction decreases, but still stays within 2 mm. Thus, in the railway monitoring, within the allowable range of accuracy, the distance between the reference stations can be appropriately expanded to save costs. In each baseline results, the east is better than the north direction. The reason may be related to the constellation structure of Beidou, consistent with the description of the literature [10].

Table 5 Baseline deviations and RMS statistics (mm)

Periods	551.2 m			5095.4 m		
	East	North	Up	East	North	Up
1	−0.5	0.3	−0.8	0.3	0.0	0.4
2	−0.3	1.1	−0.3	0.6	−1.6	−2.2
3	0.6	0.8	1.7	−1.5	1.8	−0.8
4	0.4	−0.5	1.2	0.5	−0.1	2.5
RMS	0.5	0.7	1.2	1.0	1.4	2.0
	Plane: 0.9			Plane: 1.7		

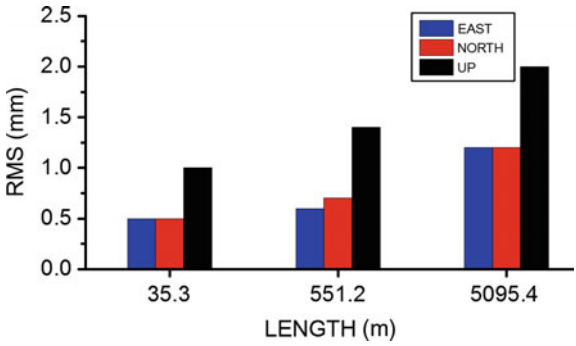

Fig. 3 Accuracy comparison of each baseline in the three directions

4 Conclusions

In this paper, the availability of Beidou and GPS hybrid system in high-precision railway subsidence monitoring is analyzed, and a reasonable data processing strategy and processing flow are developed. Through a large number of experimental analyses, the following conclusions can be obtained: (1) For a baseline within 500 m, accuracy of 1 mm in plane and 1.5 mm in vertical can be achieved, while a minimum rail track deformation of 2 mm in plane or subsidence of 3 mm in vertical can be monitored; (2) When the baseline reaches 5 km, the accuracy decreases in plane and vertical, but still can reach 2 mm. Therefore in the application in railway monitoring, under the premise of meeting the accuracy requirements, the number of base stations can be reduced appropriately to save the cost.

References

1. Chen Y (1989) Monitoring ground vertical motion with GPS. Geotech Invest Surv 5:61–64
2. Li Z, Liu Z, Wang Z (1996) Study on monitoring dam deformation with GPS positioning. Wuhan Univ Hydr Elec Eng (6):26–29
3. Huang S, Yang B, You X (2009) Applications of GPS dynamic geometric deformation monitoring system to Sutong bridge. Geomat Inf Sci Wuhan Univ 34(9):1072–1075
4. Huang S, Liu J, Liu X (2003) Deformation analysis based on wavelet and its application in dynamic monitoring for high-rise buildings. Acta Geodetica et Cartographica Sinica 32(2):153–157
5. Zhang W, Li T, Gong C, et al (2016) Real-time deformation monitoring by GNSS technology on earth and rock filled dam. In: Proceedings of the seventh China satellite navigation academic annual meeting—S01 Beidou/GNSS application technology, p. 5
6. Wei Z (2008) China geodetic coordinate system 2000 and its comparison with WGS84. J Geod Geodynam 28(5):1–5
7. Yang Y, Lu M, Han C (2016) Some notes on interoperability of GNSS. Acta Geodaetica et Cartographica Sinica, 45(3):253–259. doi:10.11947/j.AGCS.2016.20150653

8. Li H, Dang Y, Bei J (2013) Research on spatio temporary unification of BDS/GPS/GLONASS multi-mode fusion navigation and positioning. J Geod Geodynam 33 (4):73–78
9. Jiang W, Liu H, Zhou X, et al (2012) Analysis of long-term deformation of reservoir using continuous GPS observations. Acta Geodaetica et Cartographica Sinica 41(5):682–689
10. He HB, Li J, Yang Y et al (2014) Performance assessment of single-and dual-frequency BeiDou-GPS single-epoch kinematic positioning. GPS Solut 18(3):393–403

Application Performance Analysis of Three GNSS Precise Positioning Technology in Landslide Monitoring

Guanwu Huang, Yuan Du, Lumin Meng, Guanwen Huang, Jin Wang and Junqiang Han

Abstract In this paper, the accuracy and applicability of GNSS PPP (Precise Point Positioning), RTK (Real Time Kinematic) and static baseline positioning based on landslide monitoring are presented with compared the characteristics of different methods. The performance of BeiDou, GPS and BDS/GPS modes is demonstrated by using the real experiment data from a large loess landslide and simulated slow deformation test. It is show that for the integrated GPS/BeiDou, the precision of PPP, RTK, and Static baseline solutions are better than 6 cm, 6 and 3 mm respectively. The accuracy of those is significantly improved with the BeiDou/GPS case. These results reveal that the technology of RTK, PPP, and Static baseline can be used for the real-time monitoring, deformation datum recovery and periodic deformation monitoring respectively.

Keywords GNSS · BDS/GPS RTK · Landslide · Real-time monitoring

1 Introduction

China is one of the countries which have most serious geological disasters in the world, and the disasters are numerous. There are thousands of deaths and property losses of up to 10 billion every year in china [1]. Therefore, it is of great significance to carry out real-time monitoring and forecasting of landslide disaster. The key of monitoring and forecasting is the issues of accuracy, real-time and reliability

G. Huang · L. Meng
College of Mapping Science and Technology, Xi'an University of Science and Tecnology, Xi'an, Shanxi, China
e-mail: 294149365@qq.com

Y. Du (✉) · G. Huang · J. Wang · J. Han
College of Geology Engineering and Geomantic, Chang'an University, Xi'an, Shanxi, China
e-mail: du719801522@126.com

J. Sun et al. (eds.), *China Satellite Navigation Conference (CSNC) 2017 Proceedings: Volume I*, Lecture Notes in Electrical Engineering 437,
DOI 10.1007/978-981-10-4588-2_12

[2]. The research shows that the process of the formation and evolution of the landslide can be divided into 4 stages: initial, uniform, accelerated, and rapid deformation stage [3–5].

For the different stages, the three methods are used according the active condition. As a commonly used high-precision positioning technology, it is applied to the landslide monitoring with its advantages, for instance, low efficiency limits and good automation [7–12].

Chinese BeiDou navigation satellite system (BDS) has launched 20 satellites, of which 15 satellites are in operation. Therefore, the performance of BDS is widely promising [6]. The characteristics and application of the three positioning methods (PPP, RTK, and Static baseline) are demonstrated with three modes of GPS-only, BDS-only, and GPS/BDS. For the landslide monitoring, the applicability and precision of those technology are also been summarized.

2 Mathematical Model

In this section, the principle and characteristics of the three positioning methods: PPP, RTK, Static baseline are compared. In GNSS relative positioning, the method using the carrier phase is a double difference positioning technology with a high accuracy, which used to process the original observation. For the continuous observing, it can be obtained enough redundant data to improve the accuracy based on the fixed of receiver position. As relative positioning, the number of station is two at least, at the same time, and the directly results are the components of the E, N, and U direction [13].

As for the relative positioning of GNSS, the position of at least one point must be known. Then the baseline vector can be computed by using the satellite position and observation. After obtaining the values of baseline vectors, the coordinate values can be computed by the way of three dimensional constraint network adjustments or three dimensional joint network adjustments. Finally, for the different periods, the deformation values of monitoring stations can be obtained. The technology of static baseline with a high precision and a poor real-time performance can be applied for the periodic landslide monitoring as a post-processing case.

RTK is a real-time double difference positioning technique based on carrier phase measurement. The principle is that a receiver is placed on the base station for continuous observation of all visible satellites, and the original or computed observations will be sent to the rover station through real data link at the same time. For the rover station, the accuracy of three-dimensional coordinates can be reached to the level of centimeter in real time [13].

RTK is a real-time positioning technique based double difference mode with the precision of slightly worse than the static baseline case. With the function of communication work normally, it can be realized the single-epoch solution, as a effective method for landslide monitoring.

Table 1 Application of landslide stage and monitoring methods

Stage	Static baseline	RTK	PPP
Slow (<2 mm/d)	✓	×	×
Uniform (<4 mm/d)	✓	×	×
Accelerated (<10 mm/d)	×	✓	×
Sharp (>10 mm/d)	×	✓	✓

PPP is a positioning technology, using the precise satellite orbit and satellite clock offset computed from GNSS observations of several ground tracking stations, processing the observations of the phase and pseudo from a single-receiver, which can get the high precise position of ITRF frame coordinate [13]. At present, there are a number of institutions which can provide the products of real-time precise orbit determination and clock offset in the world. As a real technology, it is widely used with the precision of centimeter level.

The PPP technique can be used to deal with the observations of non-difference pseudo range and carrier phase from a single GNSS receiver. It can achieve a precision of millimeter to centimeter level in static and centimeter to decimeter level in kinematic positioning respectively and with a result of absolute coordinates under the framework of the ITRF or WGS84. Compared to the static baseline and RTK technology, it didn't rely on the stability of the reference station as a supplement method.

The landslide deformation can be divided into four stages: slow, uniform, accelerated and rapid deformation stage. With the high accuracy, the static baseline case can be applied for the slow and uniform stage while it can be used to check the correct of the landslide monitoring results. As a method of periodic monitoring, it used to give a general solution, which needs much longer observation time (generally more than 2 h). Therefore, there are some limitations in the application of real-time landslide monitoring. When the landslide enters the dangerous period (the acceleration and the sharp deformation stage), needing to carry on the real-time monitoring, the RTK technology was chosen. For a real-time solution, compared to PPP case, the accuracy and reliability of RTK are much higher. But the RTK technology needs stable data from the reference station. Under the challenging environment and the reference station destroyed in the period of rapid deformation, the PPP technology can take the advantages of single-station solution without reference station. The application of different methods for landslide monitoring is shown in Table 1.

3 Exemplification

3.1 Accuracy Test of PPP Solution in Landslide Monitoring

In order to evaluate the performance of applicability and accuracy of PPP case for landslide monitoring, the observations were acquired from a large loess landslide, a

real-time data of 4 h on PS-1 site of in Xian yang City, Shanxi Province in August 28, 2016 with the sampling rate of 1 s. With choosing the precise orbit and the precise clock error, three experiment schemes were designed to evaluate the performance of kinematic positioning: scheme 1—kinematic PPP of single GPS, scheme 2—kinematic PPP of single BeiDou, scheme 3—kinematic PPP of the integrated BeiDou/GPS.

The position errors of the three solutions in east (E), north (N) and up (U) directions for schemes 1, 2 and 3 are illustrated in Figs. 1, 2 and 3 respectively. The statistic values of the three schemes in the average accuracy and convergence time are shown in Fig. 4, Tables 2 and 3 respectively.

It can be seen from Figs. 1, 2, 3 and 4 that: the accuracy and convergence time of scheme three is best. Tables 2 and 3 show that the precision and convergence time of scheme three is better than the others. The positioning error of BeiDou

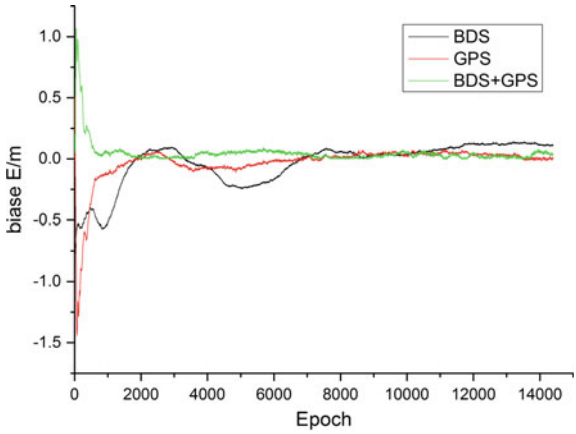

Fig. 1 Positioning errors of E direction

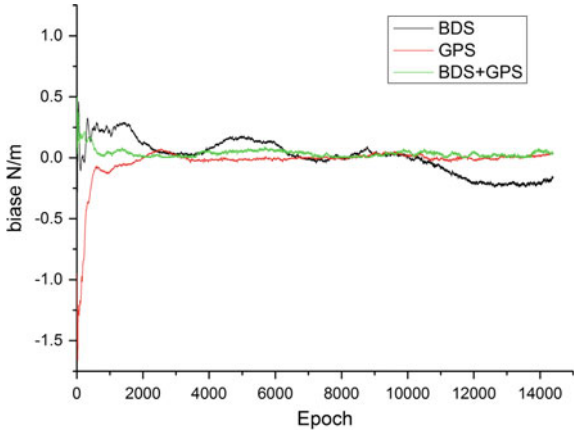

Fig. 2 Positioning errors of N direction

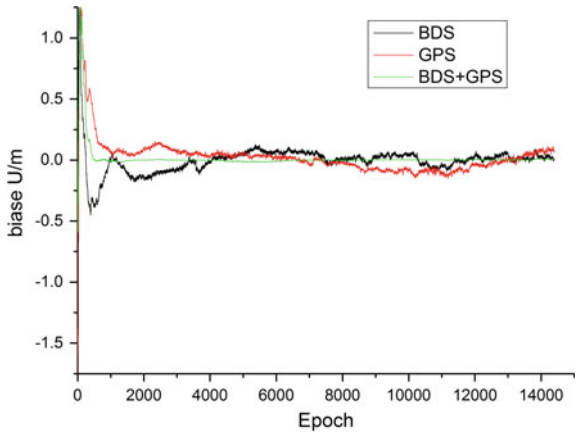

Fig. 3 Positioning errors of U direction

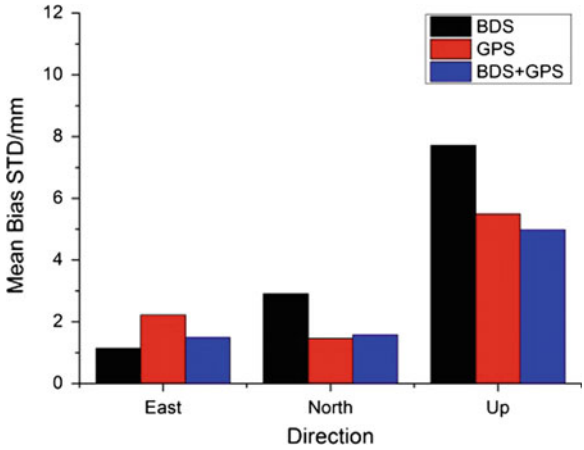

Fig. 4 The statistic positioning errors

Table 2 Average STD values of site PS-1

STD (cm)	Scheme one	Scheme two	Scheme three
E	12.8	6.7	2.3
N	11.0	4.5	2.5
U	6.6	8.3	4.4
Plane	16.9	8.1	3.4
Location	18.1	11.6	5.6

Table 3 Average convergence time for site PS-1

Convergence time (cm)	Scheme one	Scheme two	Scheme three
<20	25 min	10 min	5 min
<15	–	19 min	10 min
<10	–	–	23 min

system is slightly worse than the GPS system. The positioning accuracy of BeiDou/GPS is the best, and is about centimeter level.

3.2 *The Accuracy Test of RTK Solution in Landslide Monitoring*

Using the real data collected by the PS-1 and JS-1 points of landslide, the performance of three experiment schemes are evaluated with the sampling rate of 1 s. The length of baseline is 278 m. As the PS-1 point for the rover station and JS-1 for the reference station, the RTK positioning solution is used. With the broadcast ephemeris, three experiment schemes were designed to evaluate the performance of kinematic positioning: scheme 1—RTK of GPS-only, scheme 2—RTK of BeiDou -only, scheme 3—RTK of the combined BeiDou/GPS.

The position errors of the three solutions in east (E), north (N) and up (U) directions for schemes 1, 2 and 3 are illustrated in Figs. 5, 6 and 7 respectively. Figure 8 and Table 4 shows the statistic average values of the three schemes.

From Figs. 5, 6, 7 and 8 respectively. Figure 8, it can be seen the accuracy of three schemes in the three directions is millimeters level. The accuracy and reliability of scheme three are the best. The results show the positioning accuracy of BeiDou is comparable to the GPS while the precision of BeiDou/GPS constellation is the best. The improvement from the combined BeiDou/GPS becomes more significant with much more available satellites.

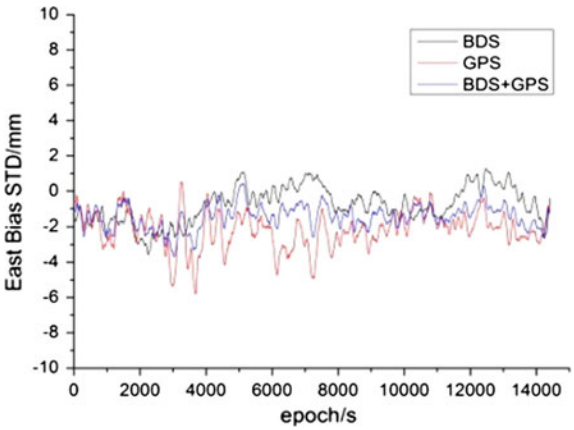

Fig. 5 Positioning errors of E direction

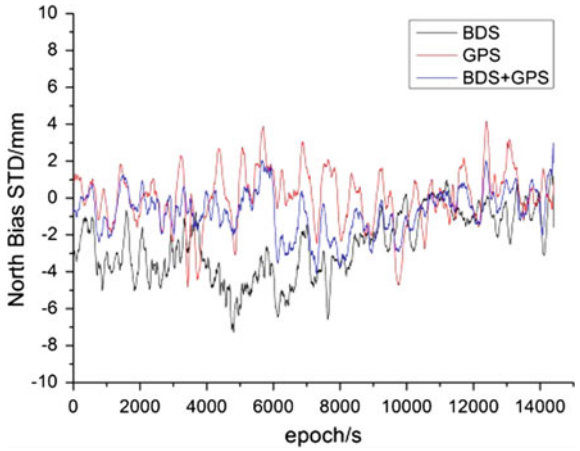

Fig. 6 Positioning errors of N direction

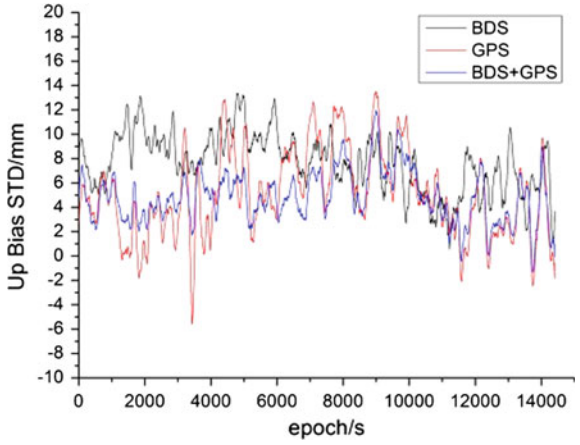

Fig. 7 Positioning errors of U direction

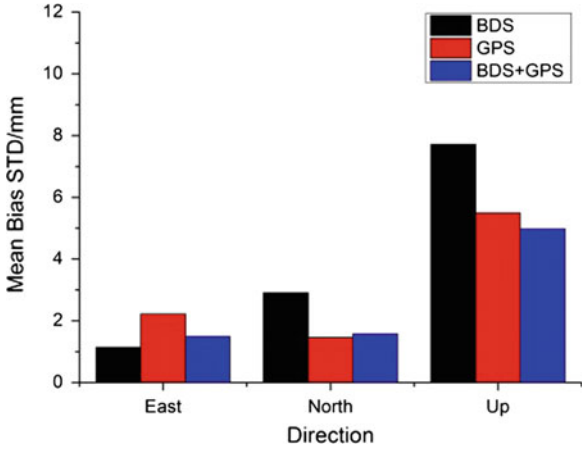

Fig. 8 The statistic STD errors

Table 4 Average STD values of site PS-1

STD (mm)	Scheme one	Scheme two	Scheme three
E	1.1	2.2	1.5
N	2.9	1.5	1.6
U	7.7	5.5	5.0
Plane	3.1	2.7	2.2
Location	8.3	6.1	5.5

3.3 The Accuracy Test of Baseline Positioning Technology in Landslide Monitoring

Utilizing the observations acquired from Sect. 3.2, the applicability and accuracy of static baseline positioning technology for landslide monitoring are evaluated with the sampling rate of 1 s. The length of baseline is 278 m. As the PS-1 point for the rover station and JS-1 for the base station. With the broadcast ephemeris, three experiment schemes were designed to evaluate the performance of kinematic positioning: scheme 1—Static baseline positioning of GPS-only, scheme 2—Static baseline positioning of BeiDou-only, scheme 3—Static baseline positioning of the combined BeiDou/GPS.

The position errors of the three solutions in east (E), north (N) and up (U) directions for schemes 1, 2 and 3 are illustrated in Fig. 9 respectively. Table 5 shows the result of the three schemes.

It can be seen from Table 5 that the positioning accuracy of the three schemes is millimeter. The results show that the values of scheme one is smaller the millimeter in the E direction with the smaller values of scheme two than the millimeter in N and U direction, while the values of the scheme three in the u direction is smaller millimeter. The three experiment schemes specified by BeiDou-only, GPS-only and the combined BeiDou/GPS were the same accuracy, which are better than 5 mm with the short baseline.

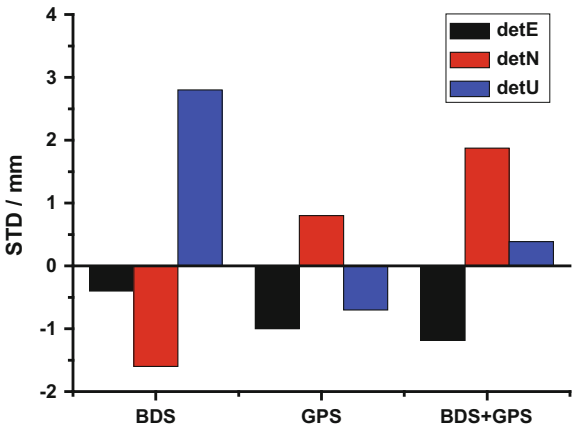

Fig. 9 Difference of baseline components derived from three schemes

Table 5 Difference of baseline components

STD (mm)	Scheme one	Scheme two	Scheme three
E	−0.4	−1	−1.2
N	−1.6	0.8	1.9
U	2.8	−0.7	0.4
Location	3.2	1.5	2.3

3.4 Experimental Test of Slow Change Mode Based on PPP and RTK Positioning Technology

The performance of sensitivity and accuracy by PPP and RTK positioning case, using the mode of the combined BeiDou/GPS are evaluated with the sampling rate of 1 s. A simulation experiment was carried out in the roof of an office building. The base receiver was installed on a place of GPS continuously operating reference station and the rover receiver was mounted on a temporary erection. The length of baseline is about 30 m. During the experiment, fixing the base receiver, the rover receiver was installed on an instrument platform. The platform can be moved on two mutual vertical of guide and the amount of movement can be accurately measured by a scale ruler with a precision of 1 mm, regarded as a correct value. With placing two guide rails to the E, N direction respectively, the values of the artificially movement in the rover case can be measured. Compared the measured deformation by two methods with the correct values, the sensitivity and accuracy of the two methods can be evaluated respectively with 1 s sampling internal. Two experiment schemes were designed to evaluate the performance of kinematic positioning: scheme 1—PPP of the integrated BeiDou/GPS, scheme 2—RTK of the integrated BeiDou/GPS.

Figures 10 and 11 show the positioning error of the two schemes in E and N directions about the rover receiver. The results can be seen from Tables 5 and 6 which was compared to the true values.

The results of Figs. 10, 11 and Tables 6, 7 derived from scheme 1 and scheme 2 can effectively reflect the real movement of the rover station in the E, N directions.

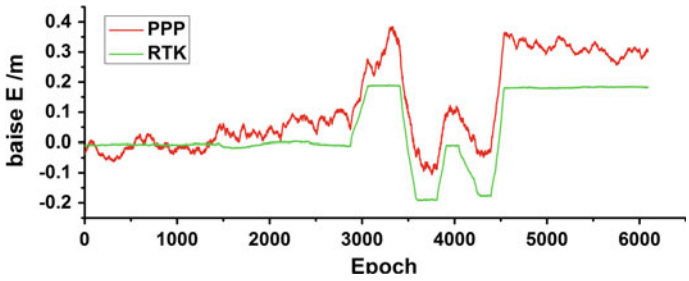

Fig. 10 Residual sequence of rover station in E direction

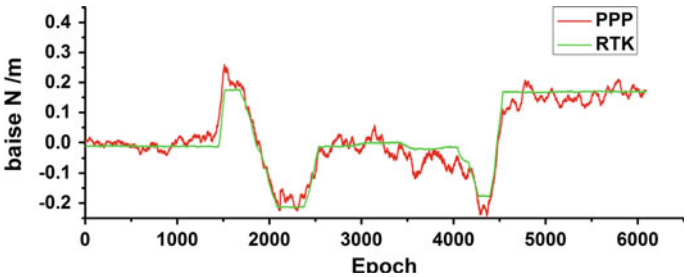

Fig. 11 Residual sequence of rover station in N direction

Table 6 Difference between the platform adjustments and the estimated results (mm)

Order	E (true)	Scheme one	Scheme two
1	+195	+294	+196
2	−375	−458	−376
3	+170	+191	+168
4	−150	−134	−149
5	+350	+380	+350

Table 7 Difference between the platform adjustments and the estimated results (mm)

Order	N (true)	Scheme one	Scheme two
1	+180	+200	+180
2	−380	−386	−382
3	+200	+185	+200
4	−165	−214	−163
5	+345	+345	+344

Comparing the scheme 1, the accuracy of scheme 2 is better than 3 mm with more reliability and sensitivity in the real-time monitoring of landslide.

4 Conclusions

BeiDou navigation satellite system, as one of the 4 global navigation satellite system, had been fully deployed for its region constellation in the end of 2012. We evaluated the performance of the three positioning methods of PPP, RTK, Static baseline solutions for the GPS-only, BeiDou-only, the integrated BeiDou/GPS with real kinematic data. The following conclusion can be drawn:

(1) The three positioning technology are suitable for the landslide monitoring with a high precision. With the initialization of PPP and RTK technique, the accuracy of them can reach centimeter and millimeter respectively, while the precision of post-processing static baseline solution is better than 5 mm.

(2) The results of three positioning cases in different modes show that the BeiDou/GPS can significantly enhance reliability and accuracy of RTK, PPP, solutions. The dual-system performance is comparable to single-system in the static baseline case, with a precision of mm level. In practical, the dual-system can overcome the problem of the lack of visible satellites, and improve the reliability, with the better geometric configuration of the satellite.
(3) Comparing the results from the simulation experimental of PPP and RTK technology, the RTK mode can be illustrated effectively than PPP, with a positioning accuracy of millimeter, which can be applied for the stage of the uniform and accelerated in landslide monitoring.
(4) In practical, according the different stage of the landslide, the methods can be set respectively. In the stable stage, the static baseline method can be used to periodically. In the stage of the acceleration and rapid, RTK can be used for effective monitoring method. Under the condition of the base station destroyed, PPP technology will be taken the advantages of single station computing without reference as a supplement method.

Acknowledgements The authors are very grateful to three anonymous reviewers for their patient and constructive suggestions in improving our manuscript. This research is supported by the state key development program "collaborative precision positioning technology" (Project No. 2016YFB0501804), funded and supported by the National Natural Science Foundation (Project No.: 4150400641674034), Chinese Academy of Sciences 100 and cutting-edge technology research plan (project number: QYZDB-SSW-DQC028) funding. At the same time, this paper also obtained the National Natural Science Fund Project (41304033); the two generation of navigation major project of construction and operation maintenance center "(GFZX0301040308)"; the natural science foundation of Shaanxi province (2016JQ4011) funded project.

References

1. Yin Y (2004) Initial study on the hazard-relief strategy of geological hazard in China. Chin J Geol Hazard Control 15(2):1–7
2. Wang S (1999) Landslide monitoring and forecasting of the Three Gorges. Geological Press, Beijing
3. Xu Q, Tang M, Xu K, et al (2008) Research on space-time evolution laws and early warning-prediction. Chin J Rock Mech Eng 27(6):1104–1112
4. Zeng Y (2008) Study on forecast and prediction of large scale and sudden landslide hazard. Chengdu University of Technology, Chengdu
5. Qin S, Wang S (2006) Advances in research on nonlinear evolutional mechanisms and process of in stabilization of planar-slip slope. Earth Environ 33(3):75–82
6. Ning J, Yao Y, Zhang X (2013) Review of the development of global satellite navigation system. J Navig Position 1(1):3–8
7. Wang L, Zhang Q, et al (2014) Experiment results and analysis of landslide monitoring by using GPS PPP technology. Rock Soil Mech 35(7):2118–2124
8. Wang L, Zhang Q, et al (2011) Dynamic and real time deformation monitoring of landslide with GPS-RTK technology. J Eng Geol 19(2):193–198

9. Malt JP, Macquarie O, Calais E (2002) The use of global positioning system techniques for the continuous monitoring of landslides: application to the Super-sauze earth flow. Geomorphology 43(1–2):33–54
10. Zhen Guozhong G, Xu J, Ma F et al (1998) GPS Monitoring of slope deformation in Jinchuan open pit mine. J Eng Geol 6(3):282–288
11. Xu S, Cheng W, Huang X et al (2003) The investigation of the landslides monitoring in the Three Gorges reservoir region by applying GPS. J Hydr Eng 6:114–118
12. Guo J, Yang J, Ding Z, et al (2004) GPS Application in landslide monitoring. J Geomech 10(1):65–70
13. Huang D, Zhang Q, Zhang X, et al (2015) The theory of navigation satellite. Wuhan University Press, Wuhan

GPS Signal to Noise Ratio Analysis and Using for Real-Time Tide Monitoring

Kai Liu, Shuang-cheng Zhang, Qianyi Wang, Qin Zhang, Jing-jiang Zhang and Yang Nan

Abstract As a new remote sensing method, GPS-MR technology is gradually used for surface environmental monitoring. In this paper, the characteristics of GPS signal-to-noise ratio (SNR) are analyzed at first. Secondly, the basic principle of GPS-MR monitoring tidal level is introduced, and finally the GPS-MR tide level experiment is analyzed by using SNR at different frequencies. In this paper, the dual-frequency observation data of the GPS tracking station SC02 near Friday Harbor in Washington State are used to analyze. The measured GPS data are compared with the measured data of Friday Harbor harbor tide station 359 m apart from SC02 station. The mean square error is about 10 cm, the correlation coefficient is better than 0.98. The experimental results show that the signal-to-noise ratio of the L1 and L2 bands can both be used to monitor the tide level by GPS-MR and further increasing the observation data of GPS-MR monitoring tide level.

Keywords GNSS · GNSS multipath reflectometry · SNR · Sea level variations · Tide guage

1 Introduction

Global climate change has led to significant melting of ice in the two-tiered and sub-boreal regions, and the melting of fresh water into the sea makes the sea level rising. It is predicted that up to 332 million people living in coastal and low-lying areas in the 21st century will be directly affected by floods due to sea-level rise. In addition, as rising sea levels compress the living space of these people, this will lead to millions of people migrating [1]. Therefore, we need continuous real-time monitoring the sea level rising which threat to human society, to master the trend of

K. Liu · S. Zhang (✉) · Q. Wang · Q. Zhang · Y. Nan
College of Geology Engineering and Geomantic, Chang'an University, Xi'an, China
e-mail: shuangcheng369@vip.163.com

J. Zhang
Institute of Urban Meteorology, CMA, Beijing 100089, China

J. Sun et al. (eds.), *China Satellite Navigation Conference (CSNC) 2017 Proceedings: Volume I*, Lecture Notes in Electrical Engineering 437,
DOI 10.1007/978-981-10-4588-2_13

tide change. And the emergence of GNSS-MR (GNSS Multipath Reflectometry, GNSS-MR) technology is to provide a new tidal monitoring means. A geodetic GNSS receiver is installed on the coast, and GNSS (Global Navigation Satellite System, GNSS) signal-to-noise ratio analysis is carried out on the reflected signal which carried the characteristic information of the surface, and then can get the change of sea level height, and finally achieve the real-time monitoring of tide level.

Many foreign scholars have carried out research on the key technologies of using GNSS-MR to detect tide change by using the GNSS observation station deployed in the coastal areas, and obtained the gratifying research results, and Chinese scholars have also carried on the related research and analysis in succession. Anderson [2] first proposed that the SNR observations after interfering with direct and reflected signals can be used for measurements of sea surface height variations, and got result with an RMS of 12 cm. Larson et al. [3–5] proposed and developed the GPS-MR technique, which utilizes multi-path reflection components of SNR observations to monitor the surface environment that causes multipath errors such as snow depth, tide level, soil moisture, vegetation change and volcanic activity, and obtained a series of extremely valuable research and application. Larson et al. [6] applied the GNSS-MR technique to an area where the tide diurnal variation was 7 m. Nakashima and Heki [7] used GPS-MR technology based on the SNR to detect sea level change, and got the result of RMS (root mean square, RMS) for 27 cm. Löfgren et al. [8] used the modified LSP(Lomb-Scargle spectrum) spectrum analysis to invert the sea surface tide of five GNSS stations in different environments around the world and found while the improved method was applied to the stations with large daily variation of tide level, the result was obviously superior to the simple LSP spectrum analysis method. In addition, Löfgren et al. also make a harmonic analysis of the tidal changes of the GNSS-MR inversions and the amplitude and phase obtained are in good agreement with those of the tide gauge stations. Löfgren and Haas [9] used the GPS and GLONASS-based multi-mode multi-frequency SNR to invert the tide changes and compared the results with the tidal changes in the GNSS-R technique based on phase delay. Wu and Yang [10] carried out the research on the static lake height measurement by using SNR observations of GPS. The results are in good agreement with the measured water level data. Under good conditions, the standard deviation of the static lake height is ± 3 cm. Zhang et al. [11] introduced the basic theory of tidal monitoring using GNSS-MR technology, and combined with the station SC02 and nearby tide guage to verify, they got the results of the mean error of 0.091 m and the correlation coefficient of 0.99.

GNSS-MR research is mainly based on a single frequency at home and abroad. In this paper, the characteristics of GPS signal-to-noise ratio (SNR) are introduced. Combined with the measured GPS data, the tidal level inversion based on SNR of L1 band and L2 band is performed respectively and the accuracy of the two bands for inversion of tide level is analyzed by compared with tide guage data. We hope it could provide reference for the real-time tide level monitoring of GNSS-MR.

2 Characteristic Analysis of GPS SNR

The SNR measurement in GPS is a measure of the magnitude of the signal received by the receiver antenna. The research results show that the variation of SNR is mainly affected by satellite signal transmission power, antenna gain, satellite-to-receiver distance and multipath effect [12]. At high altitude, the SNR is effectively improved by the large antenna gain; while in the low elevation angle, SNR decreased more serious due to the decrease of antenna gain and the multipath effect (see the red box in Fig. 1 area). It can be seen that the GPS multi-path reflection directly affects the GPS signal-to-noise ratio at the low elevation angle. Therefore, the surface environment parameters that cause GPS multipath reflection can be obtained by studying SNR sequences at low elevation angles.

Figure 1 shows the elevation angle, SNR and multipath relationship of the PRN05 satellite received by the North American SC02 station at 309 days in 2013, and from the top to bottom are the change of multipath, SNR, SNR residual sequence of the de-trend term, and the elevation angle with time. It can be seen clearly from Fig. 1 that the multipath and signal-to-noise ratio both change as the elevation angle changes. At the low elevation angle, the multi-path effect is serious

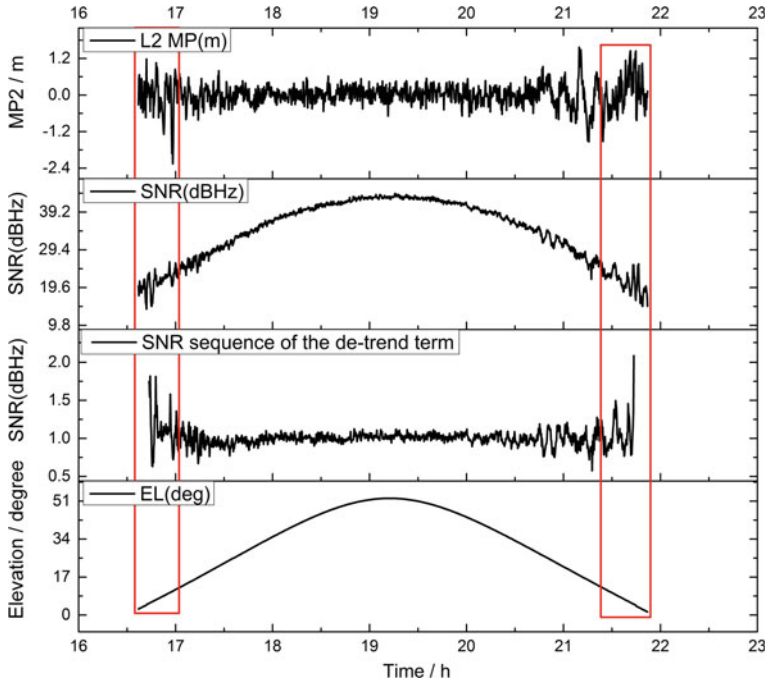

Fig. 1 Relationship of elevation angle, SNR, and multipath

due to the observation environment and so on, and the signal to noise ratio also be violent fluctuations for this. When the elevation angle is increased, the influence of multipath is reduced, and the signal-to-noise ratio is also relatively stable.

3 The Principle of GPS SNR for Tidal Level Monitoring

GPS multipath has become the main source of error which restricts high precision positioning. GPS multipath generation is mainly related to the structure and dielectric parameters of the reflector, and GPS multipath effect is everywhere. When the GPS station is located near the sea surface, the GPS receiver receives the composite signal which actually composed with direct signal and the signal reflected from sea surface (see Fig. 2).

Figure 2 is a schematic diagram of monitoring the change of tide level by using GPS-MR technology. In the figure, h is the vertical distance from the center of the antenna phase to the sea surface, which is called the vertical reflection distance in this paper and θ is the angle between the direct signal and the sea surface. In Fig. 2, the GPS receiver receives the composite signal which actually composed with direct signal and the signal reflected from sea surface, set the amplitudes of the direct and reflected signals be A_d and A_m, respectively. For the geodetic GPS receiver antenna, the amplitude of the direct signal and the reflected signal in the following relationship:

$$A_d \gg A_m \tag{1}$$

The SNR observation is the additional observation data of the geodetic GPS receiver. The SNR and the signal amplitude have the following relationship:

$$SNR = A_c^2 = A_d^2 + A_m^2 + 2A_dA_m \cos\theta \tag{2}$$

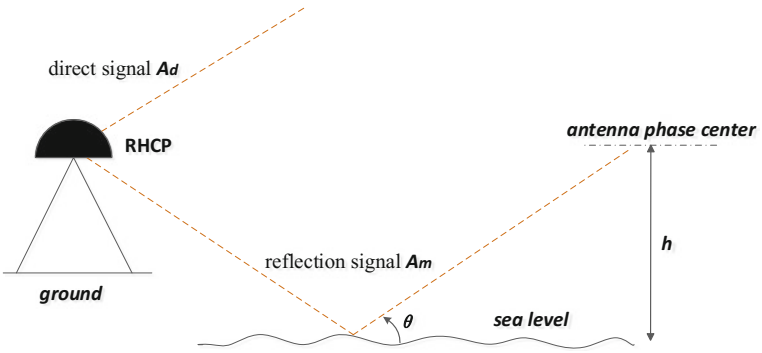

Fig. 2 Schematic diagram of GPS-MR monitoring of tide changes

where A_c is the amplitude of the synthesized signal and $\cos\theta$ is the cosine value of the angle between the direct signal and the reflected signal.

In order to obtain the GPS multi-path change information caused by the ground reflection in the SNR, the reflected signal should be extracted from the mixed signal. The SNR global trend term is parabolic and can be fitted by quadratic polynomials. By fitting the SNR sequence and then removing the trend term from the original sequence, the SNR residual sequence can be obtained.

The amplitude of the multipath reflected signal in the sequence of low-altitude residuals can be expressed as [4, 5]:

$$A_m = A\cos\left(\frac{4\pi h}{\lambda}\sin E + \phi\right) \tag{3}$$

In the formula (3), λ is the carrier wavelength, E is the satellite elevation angle, h is the vertical reflection distance, if $t = \sin E$, $f = \frac{2h}{\lambda}$, formula (3) can be reduced to a standard cosine function expression:

$$A_m = A\cos(2\pi ft + \phi) \tag{4}$$

In formula (4), the frequency f contains the vertical reflection distance parameter h in Fig. 2, if we do the spectral analysis of (4), we can obtain the frequency, and then the vertical distance h from the antenna phase center to the sea surface can be obtained. $\sin E$ is a known quantity varying with elevation angle, but sin E is not sampled at equal intervals, so that $\sin E$ residual sequence can not guarantee the whole cycle truncation. Because the fast Fourier transform (FFT) cannot solve the non-equal interval sampling problem [13], Lomb-Scargle spectral analysis method (referred to as L-S spectral analysis) can be used here.

The frequency f of GPS multi-path reflected signal A_m can be obtained by L-S spectrum analysis of SNR residual sequence, and the vertical reflection distance h can be obtained by $y = 2h/\lambda$. And then convert the h to the sea surface height changes, as a result, the monitoring of tide level is realized by SNR observation [11].

4 Application of SNR in Tide Level Monitoring

In order to verify the validity of the theory of GPS-MR based on SNR of different band, this paper uses the observation data of GPS continuous operation tracking station SC02, which is located at the seaside, to carry out the experimental analysis on L1 band and L2 band. The station SC02 belongs to the PBO network. The station is located in Washington State's Friday Harbor port, and built adjacent to the sea, so this station could receive GNSS reflection signal from the sea surface in a large space. Figure 3 is the SC02 site receiver placement map and observation environment. The SC02 station is equipped with a TRIMBLE NETR9 dual-frequency geodetic receiver and a choke coil antenna (TRM59800.80) with a

Fig. 3 SC02 station observation environment

radome (SCIT). In order to verify the accuracy of GPS-MR monitoring tide level, in this paper, the tidal data of Friday Harbor tide station 359 meters away from SC02 station are used as reference for comparative analysis.

In order to make use of the GPS data of different time span to carry on the experimental analysis, this article carries on the contrast experiment analysis by using the SC02 station's GPS data of one day, one week and one month respectively.

4.1 Selection of GPS Effective Satellites

In this paper, SNR data of 15 Hz sampling rate at 309th day of 2013 in SC02 station are collected and analyzed by GPS-MR. All satellites tracked by the SCO2 station on 309th day are shown in Fig. 4a below. Since the monitoring of the tide level based on the GPS tracking station can only use GPS satellite signals with low elevation angles reflected from the sea surface (see Fig. 4b), the altitude angle range for extracting the SNR observations is 5°–12° and the azimuth interval is 90°–150°.

In Fig. 4, the horizontal axis and the vertical axis represent the components of the distance to the station in the east and north directions respectively, and the concentric circles represent the satellite elevation angles corresponding to the reflection points. Figure 4a shows the trajectory of the reflected points of all the satellite signals received at the station. Figure 4b shows the trajectory of the reflected points of the effective satellite signals received at the station.

4.2 GPS-MR Experimental Data Processing

The experimental data of one day (the first day of the year), one week (the first day to the seventh day of the year) and one month (the first day to the thirty-one day of

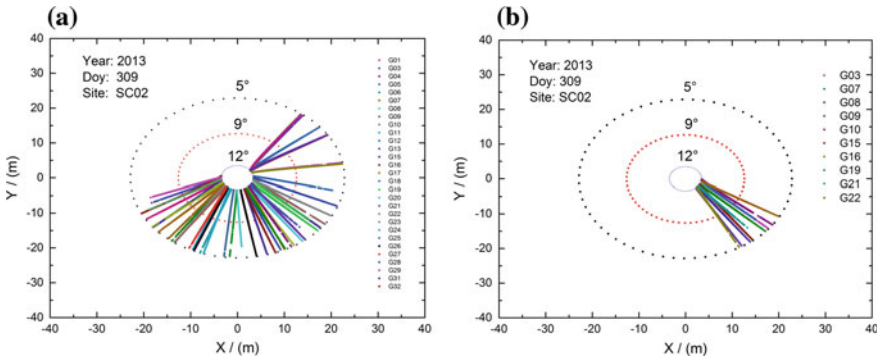

Fig. 4 **a** Satellite trajectories for full arcs and **b** satellite trajectories for effective arcs

the year) were processed respectively, and the vertical distance h from the center of the antenna phase to the sea level can be obtained by L-S spectral analysis. In order to verify the accuracy of the GPS-MR technique to monitor the change of tide level, the corresponding observational data of Friday Harbor tide station are obtained and the results are unified to the Mean Lower Low Water. The comparison results are shown in Figs. 5, 6, 7, and 8.

Figures 5, 6, 7, and 8 show the GPS time along the horizontal axis and the sea surface height relative to the mean low tide plane. The black dots represent the measured sea surface height at the six-minute sampling rate acquired by the tide gauge. The red and the blue points respectively represent the sea surface height detected by GPS-MR based on the SNR of the L1 band and L2 band. The data of Friday Harbor tide station are interpolated to obtain the tide value corresponding to the GPS-MR inversion result. The results of the experiment are compared with the tide gauge data. The standard deviations of daily inversion results which based on

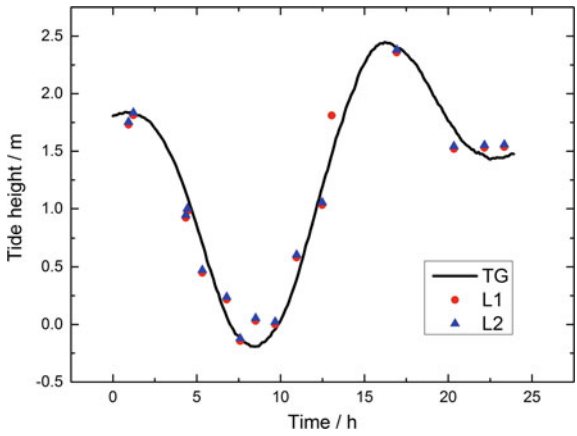

Fig. 5 Comparison of daily tide results obtained by tide station and GPS-MR (L1 and L2)

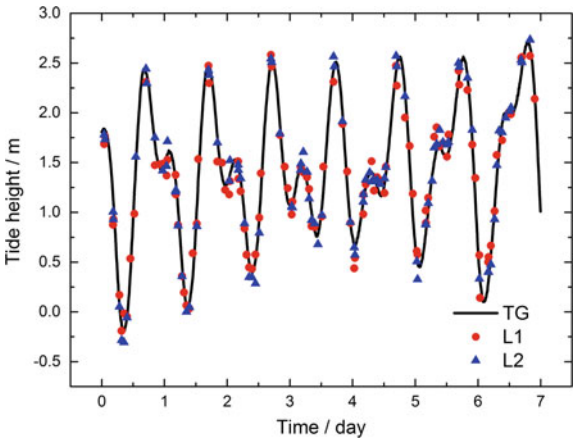

Fig. 6 Comparison of weekly tide results obtained by tide station and GPS-MR (L1 and L2)

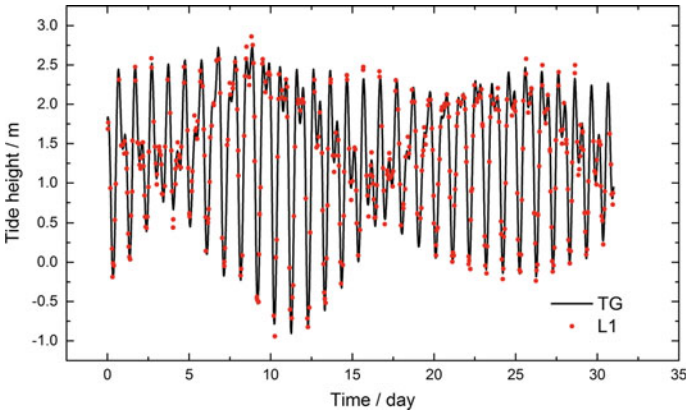

Fig. 7 Comparison of monthly tide results obtained by tide station and GPS-MR (L1)

the L1 and L2 bands are 0.12 and 0.10 m, the correlation coefficients are 0.98 and 0.98 respectively. The standard deviations of weekly inversion results were 0.11 and 0.10 m, respectively, with correlation coefficients of 0.98 and 0.99. The standard deviations of monthly inversion results were 0.10 and 0.11 m, respectively, and the correlation coefficients were 0.99 and 0.99, respectively. Due to limited space, only the monthly correlation coefficient graph between the inversion results based on measured data and the tide gauge station is given in Fig. 9:

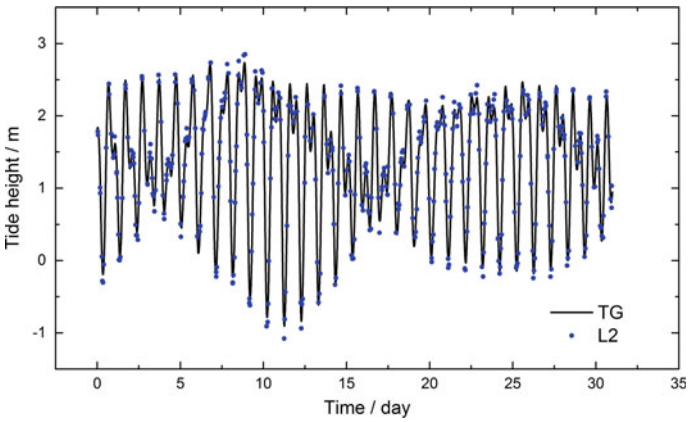

Fig. 8 Comparison of monthly tide results obtained by tide station and GPS-MR (L2)

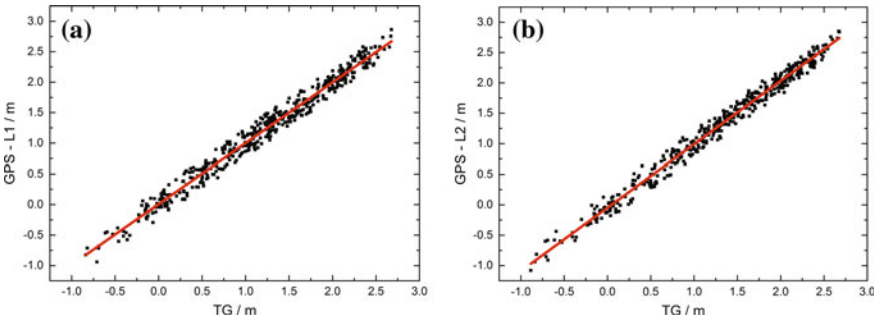

Fig. 9 **a** Correlation analysis of monthly GPS-L1 results with tide observatory and **b** correlation analysis of monthly GPS-L2 results with tide observatory

4.3 Analysis of GPS-MR Experiment Results

By inverting the real-time data of SC02 station and comparing with the data of Friday Harbor tide station, the following preliminary analysis results are obtained:

1. By processing the measured data of GPS and comparing the inversion results with tide gauge data, it is found that the results are consistent with each other and it confirms the reliability of the GPS-MR algorithm and demonstrates its feasibility in real-time tide monitoring.
2. The sea surface height obtained by GPS-MR coincided with the corresponding tide gauge data, the standard deviation was about 10 cm, and the correlation coefficient was better than 0.98. It indicates the GPS-MR technique can be used to monitor the tide level, and the GPS-MR technique can reflect the periodic change of the tide level and the trend of the whole tide by processing the long-term observation data.

3. We process experiments on the L1 and L2 bands, and get the standard deviation about 10 cm, it indicates that the two frequency bands both can be applied to real-time monitoring of the tide.
4. It is worth noting that the shore-based GPS stations can only use the GPS reflected signal from the sea, for example, the inversion results of one day is only 16, which is limited by the number of effective satellites. With the development of GNSS, there will be more and more effective satellites, as a result, the density of inversion results will be greatly improved and the accuracy will be correspondingly promoted.
5. The selected tide station and the GPS station are located 359 m away from each other, because they are not together, it may cause some errors in the results. At the same time, the rough sea surface, the height of the shore-based GPS antenna and the GPS signal frequency may also have some impact on the detection results. In order to reduce the error, we should select the GPS station located at the same location as the tide gauge station and obtain the high frequency experiment data of synchronous observation.

5 Conclusion

Facing the situation that sea level rises year by year and continues to erode coastal areas, the emergence of GPS-MR technology greatly meets the demand of people to carry out a wide range monitoring of real-time tidal level changes. By using the SNR observations, GPS-MR technology transforms the multi-path signal which has been seen as noise into a valuable useful signal, which provides a new technique for tide level monitoring. In this paper, by processing the SNR sequences of L1 band and L2 band, the accuracy of the results is about 10 cm and the correlation coefficients are both better than 0.98. It proves that the different frequencies of GPS signals can be applied to real-time monitoring of tidal level. Using the SNR observation to monitor the change of tide level is based on geodetic GPS receiver, which can effectively extend the application field of shore-based CORS network. Although there are some problems such as insufficient effective satellites, limited azimuth, and GNSS signal frequency in the current research, with the further research and the development of GNSS, it is believed that the accuracy of GPS-MR monitoring will be greatly improved. GPS-MR technology can not only get the absolute change in tidal level, but also can obtain GPS station three-dimensional crustal deformation, which could finally accurately assess the changes in tidal level and sea level rise [11].

Acknowledgements Thanks to the United States NSF, USGS and NASA jointly launched the earth lens (Earthscope) plans to authorize the use of GPS data, thanks to the GPS Reflections Research Group of the United States PBO H2O provides reference and experimental data. This work was supported by the National Science Foundation of China (41104019, 41274004, and GFZX03010403080). Thanks to the editors and anonymous referees provide for the valuable comments and suggestions in this paper!

References

1. Watkins K, Ugaz C, Carvajal L et al (2007/2008) Human development report 2007/2008—fighting climate change: human solidarity in a divided world. Palgrave Macmillan, New York, USA, for United Nations Development Programme
2. Anderson KD (2000) Determination of water level and tides using interferometric observations of GPS signals. J Atmos Oceanic Technol 17(8):1118–1127
3. Larson KM, Small EE, Gutmann E, Bilich A, Axelrad P, Braun J (2008) Using GPS multipath to measure soil moisture fluctuations: initial results. GPS Solutions 12(3):173–177
4. Larson Kristine M, Small Eric E, Gutmann Ethan D et al (2008) Use of GPS receivers as a soil moisture network for water cycle studies[J]. Geophys Res Lett 35(24):1–5
5. Larson KM, Gutmann ED, Zavorotny VU et al (2009) Can we measure snow depth with GPS receivers? Geophys Res Lett 36(17):1–5
6. Larson KM, Ray RD, Nievinski FG et al (2013) The accidental tide gauge: a GPS reflection case study from Kachemak Bay, Alaska. IEEE Geosci Remote Sens Lett 10(5):1200–1204
7. Nakashima Y, Heki K (2013) GPS tide gauges using multipath signatures. J Geodetic Soc Jpn 59(4):157–162
8. Löfgren JS, Haas R, Scherneck HG (2014) Sea level time series and ocean tide analysis from multipath signals at five GPS sites in different parts of the world. J Geodyn 80:66–80
9. Löfgren JS, Haas R (2014) Sea level measurements using multi-frequency GPS and GLONASS observations[J]. Eurasip J Adv Signal Process 2014(1):1–13
10. Wu J, Yang R (2012). Measuring water surface height by using reflected signal of geodetic-quality GPS receiver. J Geodesy Geodyn 32(6):135–138
11. Nan Y, Zhang SC, Zhang Q et al (2015) Preliminary results of sea level change monitoring with GNSS-MR. Sci Surveying Mapp 40(12):125–129
12. Bilich A, Larson KM, Axelrad P (2004) Observations of signal-to-noise ratios (SNR) at geodetic GPS site CASA: implications for phase multipath. Proc Centre Eur Geodyn Seismol 23:77–83
13. Bin XU, Yang T, Tan BH et al (2011) The simulate study of signal detection based on Lomb-Scargle algorithm. Nucl Electron Detect Technol 31(6):702–705

Ship Detection and Data Processing by Using Shore-Based GNSS-R

Chaoqun Gao, Dongkai Yang, Yunlong Zhu, Xuejing Qiu and Lei Yang

Abstract The use of GNSS-R technology to detect surface ships is a new application in this field. Aiming at the blurring problem of mirror image and diffuse scattering component in sea surface electromagnetic field, this paper combines the sea surface two-scale model to generate the regional sea surface with different wind speed, and analyzes the variation of scattering coefficient caused by mirror image and diffuse scattering component when satellite signal incident angle changes. Based on the difference of dielectric constants between the metal structures on the ship surface and seawater under L-band signal, the scattering signal power was analyzed, and the first domestic ship detection experiment in Yingkou port of Liaoning province was carried out. By processing the reflected signal SNR (signal-to-noise ratio) and dielectric constants, the ship characteristic has been found obviously, and the feasibility of using the shore-based GNSS-R technology to detect close-sea ship is verified.

Keywords Shore-based · GNSS-R · Sea surface · Ship · Two-scale model · Dielectric constant

C. Gao · D. Yang · Y. Zhu (✉)
School of Electronics and Information Engineering, Beihang University,
Xue Yuan Road 37, HaiDian District, Beijing, China
e-mail: inca_zyl@126.com

X. Qiu
School of Information Engineering,
China University of Geosciences, Beijing 100083, China

L. Yang
No. 95927 Troops of PLA, Cangzhou 061000, China

J. Sun et al. (eds.), *China Satellite Navigation Conference (CSNC) 2017 Proceedings: Volume I*, Lecture Notes in Electrical Engineering 437,
DOI 10.1007/978-981-10-4588-2_14

1 Introduction

In 2013, the United States NASA uses L-band in the heavy rain area has better penetration advantages [1], through CYGNSS (The Cyclone Global Navigation Satellite system) to receive the surface of the sea surface reflected signal, monitoring and early warning of tropical cyclone path [2]. The hurricane weather forecast model and the forward scattering model were used to generate the power-delay waveform, and the sea-level hurricane wind speed was derived to show the great potential of CYGNSS in typhoon forecasting [3]. In [4, 5] Gleason used CYGNSS to receive GPS L1 and L2 signals for the correction of wind speed, which laid the theoretical foundation for the analysis of sea surface scattering field. In 2014, Riccardo completed 10 cm dry soil buried metal objects detection by analysis of the GNSS reflection signal SNR [6]. At the same time, Wu Nan in the China's ship research and design center analyzed RCS impact of the ship's main structure by using computational electromagnetics and computer graphics [7], In 2015, Clarizia validated the advantages of using GPS backscatter to detect sea targets through simulation [8], which supported the theoretical development of using GNSS-R to detect surface ships.

However, there is no analysis on the blurring problem between the mirror image and the diffuse scattering component in the sea surface electromagnetic field by the different signal excitation condition. In this paper, the sea surface two-scale model is used to generate regional sea surface with different wind speed. The change of scattering coefficient caused by mirror image and diffuse scattering component at different sea state and incident angle is analyzed when satellite signal incident angle changes. In order to verify the feasibility of the ship detection by using GNSS-R, an experiment was set up in Yingkou Port, LiaoNing Province, through the analysis of its dielectric constant.

2 Analysis of Electromagnetic Scattering

Under the influence of wind, the sea surface has random rough surface, and the electromagnetic scattering characteristic are complicated, which can be divided into two kinds of scale waves by the two-scale model (TSM) [9], the large-scale gravity wave and the small-scale tensional wave. The large-scale wave-induced sea surface mirror image component is solved using the Kirchhoff Geometric Optics Approximation Model (KA-GO) model and the small-scale wave-induced diffuse scattering component is solved by the Small Perturbation Method (SPM) [10, 11].

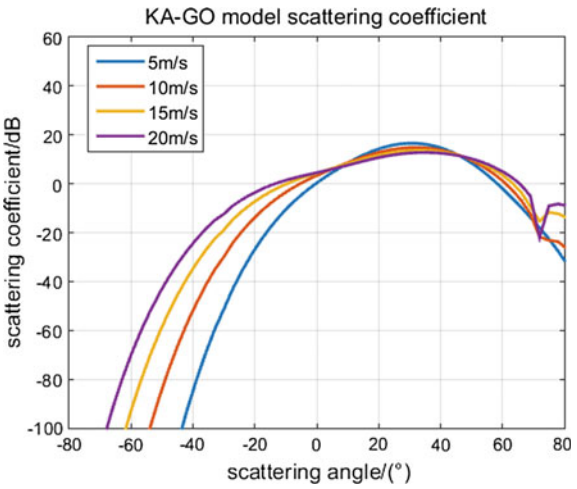

Fig. 1 Curve: analysis of mirror component scattering coefficient

2.1 Analysis of the Mirror Image Component Scattering

Using the KA-GO model, the scattering coefficients are simulated at wind speeds of 5, 10, 15 and 20 m/s. In the simulation, the incident angle is 30°, and the scattering angle is taken as −90 to 90°, which is shown in Fig. 1. When the scattering angle is negative, it indicates the scattering type is back scattering. When the scattering angle is positive, it indicates that the type is forward scattering, and the polarization mode is HH.

The maximum scattering coefficient is near the scattering angle of 30°, which is shown in Fig. 1. From the Fig. 1, it can be seen that: (1) The scattering energy is the strongest when the scattering angle is equal to the incident angle; (2) As the scattering angle deviates from the incident angle, the scattering energy decreases rapidly; (3) The increase of wind speed will influence the sea surface roughness, so the mirror image component and its scattering coefficient are weakened.

2.2 Analysis of Diffuse Scattering Component

In the case of different wind speed and scattering angle, the SPM model is used to simulate the sea surface scattering coefficient, and the simulation conditions are not changed, which is shown in Fig. 2. From the Fig. 2, it can be seen that: (1) The diffuse scattering energy is the strongest when the scattering angle is near 0, which is indicating the vertical direction; (2) When the scattering angle increases, the scattering energy reduces gradually; (3) When the wind speed increases, the diffuse component increases.

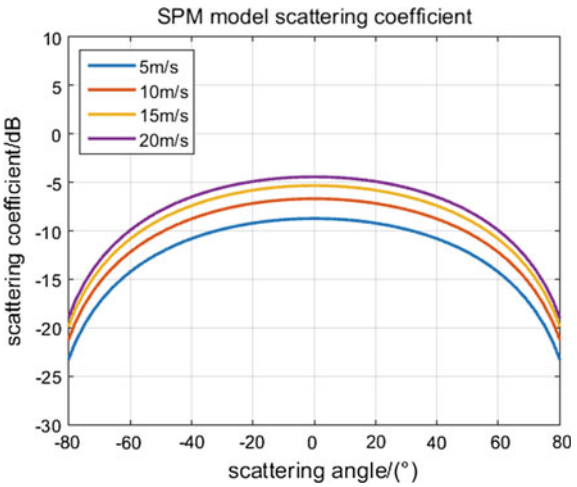

Fig. 2 Curve: analysis of diffuse component scattering coefficient

2.3 *Two-Scale Scattering Model*

The two-scale model is the superposition of the KA-GO model and the SPM model, and the scattering coefficient analysis is shown in Fig. 3. It can be seen that: (1) When the scattering angle is equal to the incident angle, the scattering coefficient is the maximum; (2) When the scattering angle deviates from the incident angle, the scattering coefficient decreases, but there is still some scattering energy in the other direction due to the diffuse scattering component; (3) When the wind speed increases, the scattering component of mirror decreases and the diffuse scattering component increases.

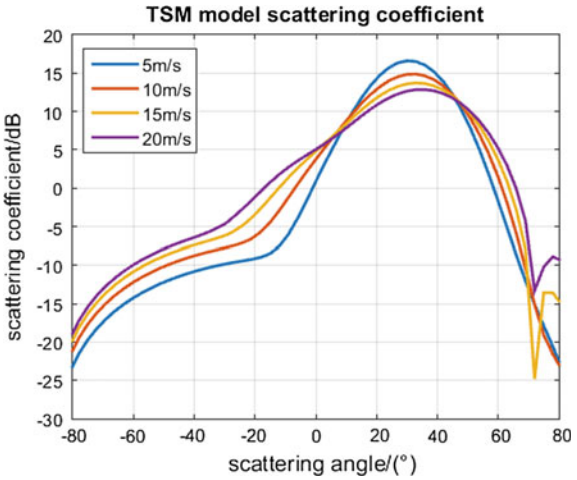

Fig. 3 Curve: analysis of two scale model scattering coefficient

3 Analysis of the Reflected Signal Characteristic

3.1 Reflection Coefficient

On the metal surface of ship, the scattering type of L-band signal excitation source is mainly divided into plane scattering, specular scattering and edge diffraction. The ship's scattering medium is the mental, and sea surface scattering medium is mainly the sea water.

GNSS is the right-handed circular polarization signal, when the signal encounters reflection, the reflected signal strength is mainly determined by the reflection coefficient, according to Fresnel reflection law, the reflection coefficient can be expressed as:

$$\Re_{VV} = \frac{\varepsilon \sin\theta - \sqrt{\varepsilon - \cos^2\theta}}{\varepsilon \sin\theta + \sqrt{\varepsilon - \cos^2\theta}} \tag{1}$$

$$\Re_{HH} = \frac{\sin\theta - \sqrt{\varepsilon - \cos^2\theta}}{\sin\theta + \sqrt{\varepsilon - \cos^2\theta}} \tag{2}$$

$$\Re_{LR} = \Re_{RL} = \frac{1}{2}(\Re_{VV} - \Re_{HH}) \tag{3}$$

$$\Re_{RR} = \Re_{LL} = \frac{1}{2}(\Re_{VV} + \Re_{HH}) \tag{4}$$

where the subscripts V and H denote the vertical and horizontal polarization, L and R denote the left and right circular polarization, and ε is the dielectric constant. The dielectric constant of seawater, fresh water, metal are 69, 80, 2×10^8.

The relationship between the Fresnel reflection coefficient and the satellite elevation angle is shown in Fig. 4, and the range of the elevation angle is from 0 to 90°.

From Fig. 4, it can be seen that: (1) The left-hand component of seawater increases with the satellite elevation angle, and it changes quickly when the elevation angle is less than 35°, and stabilizes after more than 35°, but the change of right-hand component is reversed; (2) For metal, the right-hand component is very small, and the signal energy can be considered completely reflected, and the reflected signal is the left-handed polarization; (3) The reflectivity of metals and seawater on the L-band signal is quite different, the reflection ability of the metal signal is stronger, and the greater the satellite height angle, the more obvious difference, which can be used to distinguish ship and seawater.

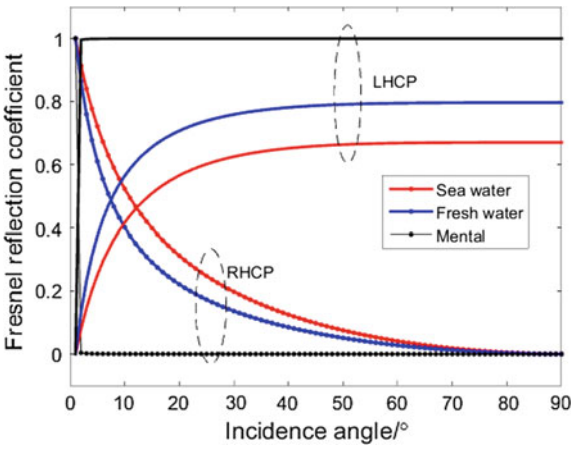

Fig. 4 Analysis of seawater, freshwater and metal scattering coefficient

When GNSS-R is used to analyze the scattering surface characteristics, Based on the correlation power, the scattering coefficient can be expressed as:

$$\Re_{RL} = \frac{|Y_R|^2}{|Y_D|^2} \tag{5}$$

where Y_D and Y_R are the correlation power of the direct and reflected signal, which can be obtained by performing the coherent and non-coherent accumulation operation of in-phase and quadrature component data. Considering the formula (1–5), the relationship between the dielectric constant of scattering surface and the power can be expressed as:

$$\frac{|Y_R|^2}{|Y_D|^2} = \frac{(\varepsilon - 1)^2 \sin^2\theta(\varepsilon - \cos^2\theta)}{\left(\varepsilon \sin\theta + \sqrt{\varepsilon - \cos^2\theta}\right)^2 \left(\sin\theta + \sqrt{\varepsilon - \cos^2\theta}\right)^2} \tag{6}$$

3.2 *Analysis of the Scattering Signal Power*

The detection of ship by GNSS-R is based on the reflection coefficient difference between the ship metal structure and sea water. By analyzing the differences in reflected signal power, it is possible to monitor the presence of ships in the coverage area.

In the sea remote sensing application, the sea surface is divided into different regions based on the iso-doppler line and iso-delay line [12]. The reflected signal power is a function of delay τ and doppler frequency f, which can be expressed as:

$$P_R = \frac{P_T \lambda^2}{(4\pi)^3} \iint_A \frac{G_T(x_s, y_s) G_T(x_s, y_s) W^2(\tau, f, x_s, y_s) \sigma_0(x_s, y_s)}{R_T(x_s, y_s)^2 R_R(x_s, y_s)^2} d^2 r \tag{7}$$

$$W = |S(x_s, y_s; f)|^2 \Lambda^2(x_s, y_s; \tau) \tag{8}$$

where P_T is the satellite transmit power, λ is the signal wavelength, R_R, R_T are the distance from the sea-surface scattering point to the satellite and GNSS-R receiver, G_T, G_R are the transmitted and received antenna gain, x_s, y_s are the spatial coordinate of the scattering point, Λ is the autocorrelation function, σ_0 is the sea surface RCS, and A is the coverage area of reflected signal.

The coverage area of a single GNSS-R receiving platform is determined by the height, the beam angle of the antenna, and the view angle. As shown in Fig. 5, α is the beam angle of the antenna, β is the view angle, and h is the height of the

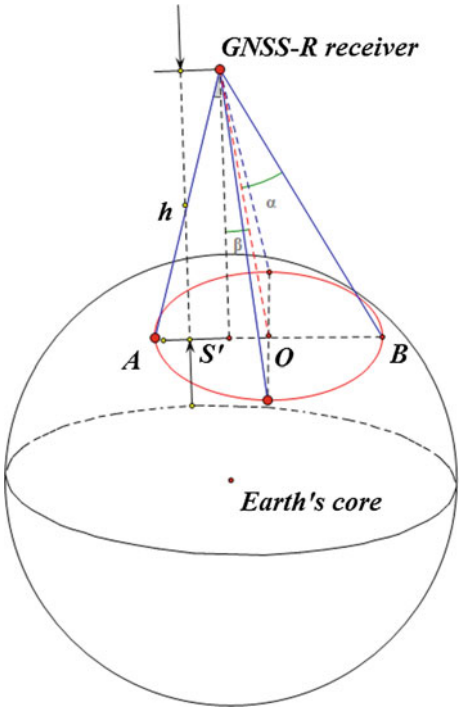

Fig. 5 GNSS-R platform geometry diagram

receiving platform. When the view angle is zero, the receiving area of the platform is "spherical crown" shape, and its coverage area can be expressed as:

$$A = 2\pi R^2(1 - \cos(\alpha + \arcsin(\frac{R+h}{R}\sin\alpha))) \tag{9}$$

As shown in formula 7, the total scattered signal power can be obtained by integrating the power of all scattered points in the coverage area. When the scattering points are concentrated in the area where the sea surface target is located, the scattered signal power can be expressed as:

$$P_{\text{target}} = \frac{P_T G_T(x_t, y_t) G_R(x_t, y_t) W^2(\tau_t, f_t, x_t, y_t)\sigma(x_t, y_t)}{(4\pi)^3 R_T^2(x_t, y_t) R_R^2(x_t, y_t)} \tag{10}$$

$$\sigma(x_t, y_t) = \frac{12\pi l^4}{\lambda^2} \tag{11}$$

where the subscript l is the edge size of ship.

Because the reflection coefficient of metal is much larger than that of sea water, assuming the wind speed is 5 m/s and the scattering signal can be completely received, the simulation analysis of reflected signal power has been done by combining with the double-scale model, which is shown in Fig. 6.

It can be seen from Fig. 6 that when there is no ship in the sea, the scattering medium is mainly the seawater, and its two-dimensional correlation power is mainly related to the change of wind speed. When the ship appears, the scattering medium is mainly metal, and the reflection coefficient increases, so that the two-dimensional correlation power suddenly becomes larger, resulting in "peak" situation.

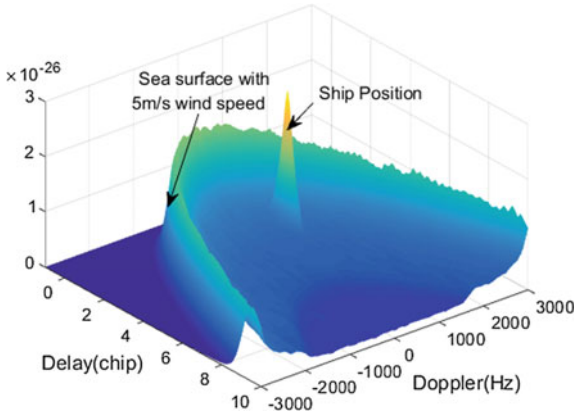

Fig. 6 Analysis of 2D delay Doppler correlation power

4 Data Processing

4.1 Experimental Scene

In order to verify the feasibility of GNSS-R to detect ships, the relevant experiments were designed.

- Experimental position: Yingkou Port, Liaoning Province, State Oceanic Administration, Ocean Environmental Monitoring Station, 5th Floor, roof (122.09°, 40.28°).
- Experimental equipment: four-channel navigation signal acquisition device, 3 dB RCHP (Right Hand Circular Polarized) antenna, 12 dB LCHP (Right Hand Circular Polarized) antenna, which is shown in Fig. 7.
- Experimental time: March 26, 2016 7:33.

4.2 Data Processing

The 100s data is processed by Matlab software. The satellite acquisition results of the direct and reflection channels are shown in the Fig. 8. The acquisition satellites PRN of the direct channel are 5, 13, 15, 18, 20, 21, 24, and the reflection channel are 5, 18, 29.

It can be seen from Fig. 8 that: (1) The elevation angle of PRN 29 is low and RHCP antenna is placed horizontally, so the antenna can not receive its direct

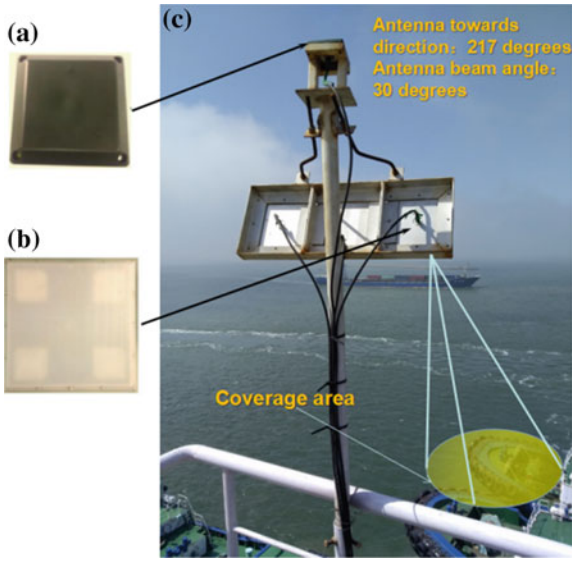

Fig. 7 Diagram of equipment structure. **a** RHCP; **b** LHCP; **c** Antenna installation

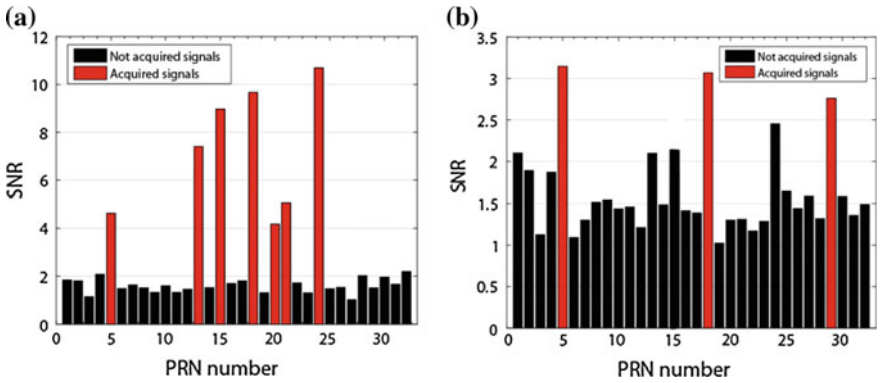

Fig. 8 Satellite acquisition results. **a** Direct channel. **b** Reflection channel

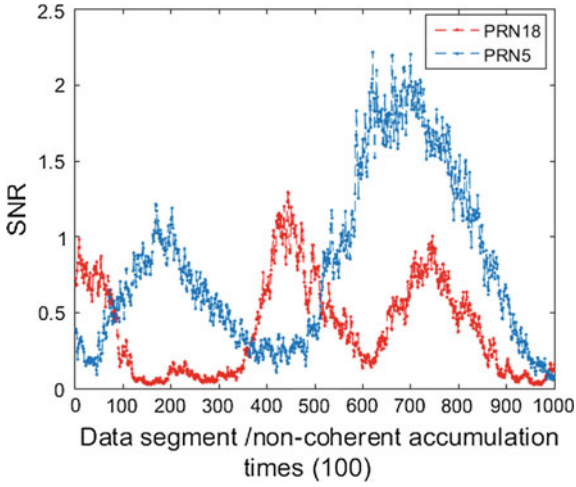

Fig. 9 SNR analysis of the reflected channel

signal. LHCP antenna is placed downward, the scattering signal from the coverage area can be received; (2) The PRN 5/18 can both be acquired in direct and reflection channel. According to the antenna orientation, the scattering type is backscattering and the scattering signal is mainly from the ship.

In the processing, the coherent time is 1 ms and the number of non-coherent accumulations is 100 times. The reflected signal SNR and dielectric constant are analyzed (due to the large dielectric constant of the metal, when the dielectric constant is greater than 500, it will be taken 500 by using threshold cutoff), and its processing results are shown in Figs. 9 and 10.

It can be seen from Figs. 9 and 10 that the reflected signal SNR fluctuates obviously. The reasons are as follows: (1) The influence of the device itself, but its effect is relatively stable; (2) The intensity of reflected signal increases, due to the change of the scattering medium in the coverage area; (3) By combining the

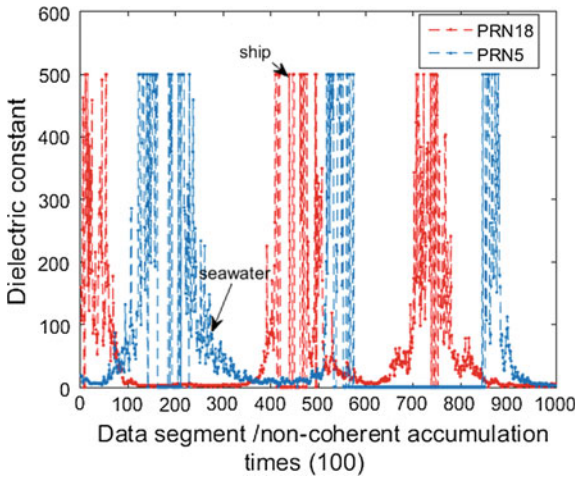

Fig. 10 Analysis of dielectric constant of reflected surface

satellite skyplot and the ship orientation in the coverage area, the reflected signals are mainly from the ship deck and superstructure and the scattering medium is mainly metal, thus the dielectric constant increases.

The inversion results of the dielectric constants vary between the empirical values of dielectric constant between the seawater and the metal, the reasons are as follows: (1) The covering area contains a part of sea water, due to sea surface ups and downs, causing gravity waves and tension waves of the sea changes at all times, the scattering type and scattering coefficient also changes at all times; (2) The fluctuation of sea surface affects the ship stability, which can change the incident; (3) When the incident angle changes, the scattering coefficient changes due to the ship scattering type and scattering structure; (4) The presence of non-metallic objects such as tires and anti-collision devices on the deck, which creates a complex scattering medium in the coverage area;

5 Conclusion

In the paper, the scattering field theory of GNSS-R sea target detection is completed and the experimental data are processed. The results show that: (1) When the sea surface wind speed increases, the roughness increases, resulting in the reduction of its mirror scattering components and the increase of its diffuse scattering component; (2) The reflection coefficient between sea water and the metal structure on the ship's surface is stable when the elevation angle is less than 35°. When the ship appears, the reflected signal power value will be significantly different; (3) By the inversion of the dielectric constant, the obvious characteristics of the ship can be found.

In the future, the theoretical research in the field will be perfected, which is laying the foundation for the application of GNSS-R in detecting the ships.

References

1. Ruf C, Unwin M, Dickinson J, et al (2013) CYGNSS: enabling the future of hurricane prediction. IEEE Geosci Remote Sens Mag 1:52
2. Ruf CS. Gleason S et al (2012) The CYGNSS nanosatellite constellation hurricane mission. In: IEEE international geoscience & remote sensing symposium
3. Rose R, Ruf C et al (2015) The CYGNSS flight segment; mainstream science on a micro-budget. In: IEEE aerospace conference
4. Rose D, Vincent M, Rose R et al (2013) The CYGNSS ground segment; innovative mission operations concepts to support a micro-satellite constellation. In: IEEE aerospace conference
5. Shoer J, Singh L, Henderson T (2015) Conical scanning approach for sun pointing on the CYGNSS microsatellite. IEEE
6. Notarpietro R, Salvatore M Detection of buried objects using reflected GNSS signals. EURASIP J Adv Signal Process
7. Nan W, Huang S (2008) Analysis of radar scattering characteristic of large ship on surface. Equip Environ Eng 5:1
8. Clarizia M-P, Ruf C (2005) Target detection using GPS signals of opportunity. In: 18th international conference on information fusion, Washington, DC, 6–9 July 2015
9. Trinks I et al (2016) Efficient mapping of agricultural soils using a novel electromagnetic measurement system. EGU General Assembly 2016, held 17–22 April 2016 in Vienna Austria, p 2622
10. Schiavulli D (2015) GNSS-R wind-dependent polarimetric signature over the ocean. IEEE Geosci Remote Sens Lett 12(12)
11. Emadi A, Afrakhte H (2016) A reference current perturbation method for islanding detection of a multi-inverter system. Electr Power Syst Res 132:47–55
12. Rodriguez-Alvarez N, Garrison L (2016) Generalized linear observables for ocean wind from calibrated GNSS-R DelayDoppler maps. IEEE Trans Geosci Remote Sens 54(2)

Characteristic of GPS SNR and It's Application for Snow Depth Monitoring Analysis

Ning Zhang, Shuangcheng Zhang, Yuefan He, Qin Zhang, Xiaojuan Zhang and Tianhe Wan

Abstract With the continuous construction of GNSS and the continuous improvement of GNSS reflection signal theory, GNSS-MR technology based on signal-to-noise ratio has gradually become an emerging field of GNSS for surface environmental monitoring. Based on the detailed analysis of the GPS signal-to-noise ratio (SNR) characteristics, this paper givens the GPS-MR technique based on SNR observation is proposed to detect the snow depth basic principle and calculation flow. In order to verify the effectiveness of SNR based on different frequencies for snow depth detection, this paper compares and analyzes the differences between L1C/A and L2P signals. On the basis of the above results, the GPS data of the AB33 station from 2011 to 2014 for four consecutive years were analyzed and compared with the snow depth of meteorological sensors. The experimental results show that the SNR-based GPS-MR algorithm can effectively obtain the snow depth from the GPS data, and the inversion result of L1C/A signal coincides well with the snow depth detection value of meteorological sensor, and it can detect the snow depth more effectively. GNSS-MR technology not only makes full use of the signal-to-noise ratio information, but also provides potential development space for GNSS technology for surface environment monitoring.

Keywords SNR (signal-to-noise ratio) · L1C/A · L2P · GNSS-MR (GNSS multipath reflectometry) · Snow depth detection

N. Zhang · S. Zhang (✉) · Y. He · Q. Zhang
College of Geology Engineering and Geomantic, Chang'an University, Xi'an, China
e-mail: shuangcheng369@vip.163.com

X. Zhang · T. Wan
Xinjiang Altai Meteorological Bureau, Altai, China

J. Sun et al. (eds.), *China Satellite Navigation Conference (CSNC) 2017 Proceedings: Volume I*, Lecture Notes in Electrical Engineering 437,
DOI 10.1007/978-981-10-4588-2_15

1 Introduction

Snow is one of the most important components in the hydrological system, which impacts the water cycle and atmospheric circulation, at the same time snow is also an important freshwater resource [1, 2]. Fresh water comes from snowmelt feeds one sixth of the world population [3]. Through mentoring the snow status, we can learn the amount of fresh water stored in snow by understanding the state of the snow. However, it is difficult to monitor the variations of snow because of the high spatial and temporal variability. Manual and automated techniques are the main ground-based measurement [4]. Manual measurements have high precision to measure the depth of snow, but they are lack of high time resolution and they waste more time and energy. Compared with manual measurement, sonar measurement and radiation measurement has high time resolution but lack of spatial information of GPS site [4]. Due to physical reflectivity and polarization characteristics of snow surfaces with GPS-reflected signals, GPS-Reflectometry (GPS-R) can be used to monitor snow depth variations [5, 6]. GPS-R technology has the advantages of low cost, low power consumption and high temporal resolution [7], Based on this, in the ocean and lake altimetry, sea surface wind speed, soil moisture and other fields have been widely studied and applied, but it's hardware equipment is very strict, must use the left-hand circular polarization and right-handed circular polarization two antennas Combined together to receive the reflected signal and direct signal can be effectively received and processed. For today's users generally use conventional measurement type GPS receiver is undoubtedly extremely restrictive. Then, Professor Larson innovatively proposed GPS—MR technology. Such as snowfall [8], soil moisture [9], vegetation index [10], sea level change [11], volcanic activity and other surface environmental parameters using the SNR measurements recorded by conventional GPS receivers Inversion. It has advantages that converging large area, high time resolution, all-weather, real-time, automation and making full use of existing GNSS monitoring stations provides a new and powerful sensor for the meteorological department [12]. So that the technology will also replace the traditional method of snow depth measurement and become the current GPS in the field of remote sensing one of the latest research.

Because GPS L2C signal has a higher SNR strength when compared to L1C/A and L2P signals, previous studies, e.g., Larson et al. and Larson and Nievinski, mainly used L2C SNR data to retrieve snow depth but did not evaluate and validate the estimations from the L2P signal [7]. In 2016, Larson used L1C/A and L2C signals to estimate snow depth, and the results showed that the difference was about 3 cm [13]. In addition, the first Block IIR-M GPS satellite with broadcasting L2C signal was launched in 2005, Because of short operational time, the old-configuration GPS receivers cannot track the L2C signal. Most of the current measurement GPS receivers can only receive L1C/A and L2P signal data. In this paper, based on the existing research results, the inversion estimation of snow depth using L1C/A and L2P signal SNR data is carried out, and compared with the

observed snow depth of meteorological station, And further verify the effectiveness of GPS-MR technology in snow depth detection.

2 Theory and Methods

2.1 Characteristics Analysis of SNR

The SNR is the ratio of the received carrier signal strength to the noise strength. Most receivers denote SNR as C/N_0 in decibels dB-Hz. GPS SNR observations are a measure of the magnitude of the signal received by the receiver's antenna. The research show that the variation of SNR is mainly affected by satellite signal transmission power, antenna gain, receiver state and multipath effect [14]. Figure 1 shows the SNR and multipath effects vary with satellite elevation of the SNR10 satellite of doy 200 in 2013 at AB33 station. Under the condition of high elevation angle, the SNR is effectively improved by the large antenna gain. On the other hand, it is obvious from the figure that the multipath effect is relatively good, distribution is relatively stable, SNR is affected by multipath effect is very small; While in the low altitude conditions, the antenna gain is reduced, On the other hand, as shown in Fig. 1, the degree of multi-path effect dispersion is large, Distribution

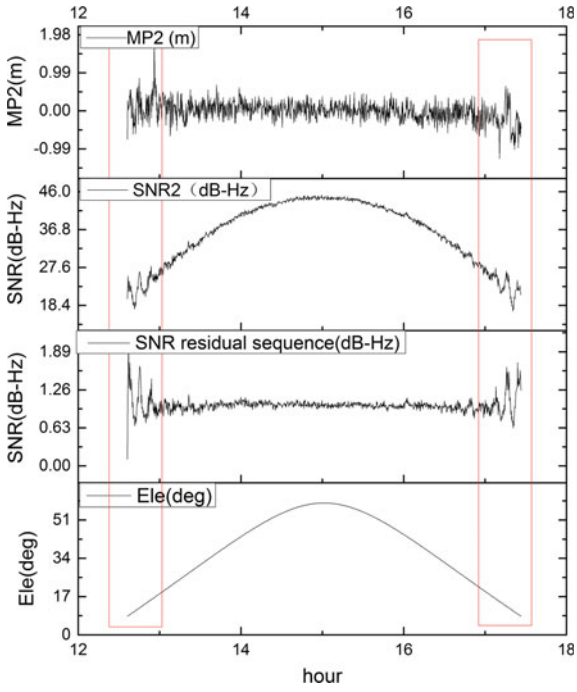

Fig. 1 Multi-path signal-to-noise ratio with elevation angle changes

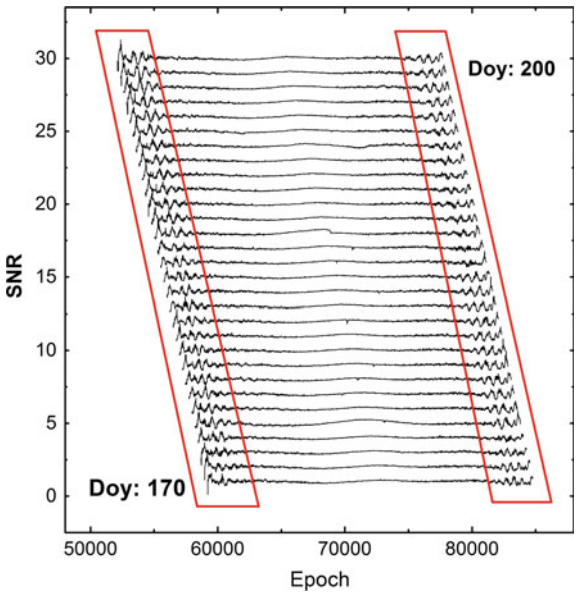

Fig. 2 PNR 10 satellite residual sequence

instability seriously affected the low-altitude angle of the SNR, making it fluctuated large, and, the multipath effect makes the SNR drop more serious.

Figure 2 shows the SNR trend variation of the PRN 10 satellite from 170 to 200 days in 2011 at AB33 station with a sampling rate of 15 s. It can be seen from the figure that the SNR fluctuates greatly at the low elevation angle, which is mainly affected by the multipath effect of the low elevation angle. As the satellite continues to rise, the multipath effect decreases gradually. It can be seen that the SNR is seriously affected by multipath at low elevation angles. Therefore, the SNR is often used to evaluate multipath and multipath error modeling. In contrast, GPS multipath reflection will directly affect the GPS signal to noise ratio, so by SNR spectrum analysis can be obtained to cause GPS multi-path reflection of the surface environmental parameters, namely GPS-MR technology. At the same time, from Fig. 2 can also be seen as the GPS satellite cycle is 11:58 min, so the signal to noise ratio per day will appear about 4 min ahead of the offset.

2.2 Algorithm and Theory

GPS multi-path has become the main error source which restricts high-precision positioning. The generation of GPS multipath is mainly related to the structure and medium parameters of reflector. GPS multipath effect everywhere, GPS receiver to receive the signal is actually a direct signal and the surface of different media after the reflection of the composite signal. Figure 3 shows the Schematic of GPS-MR Snow depth detection [15].

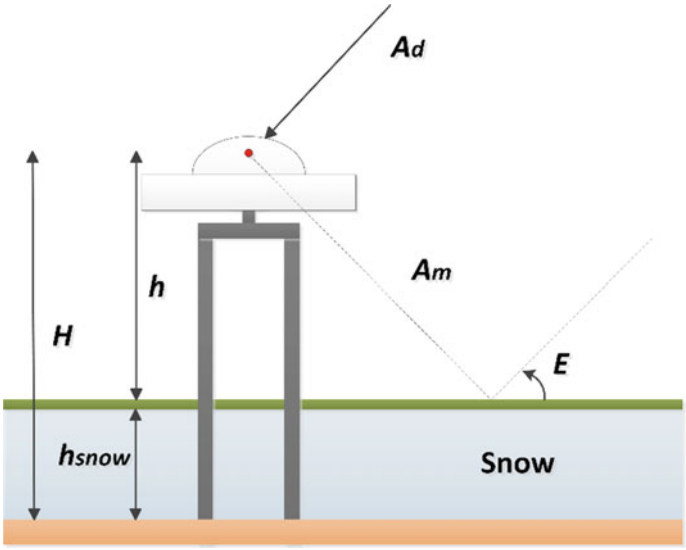

Fig. 3 Schematic of GPS-MR snow depth detection

The height of antenna is H, It is the distance from receiver antenna phase center to soil surface. h is for the distance from receiver antenna phase center to snow surface, and it is called vertical reflection distance in the following paper. h_{snow} is for the thickness of snow, E is for the angle between signals and snow surface, A_d, A_m are for the amplitude of the direct and reflected signal respectively.

Set in Fig. 3 the residual sequence of reflected signal amplitude can be expressed as [16]:

$$A_m = A\cos\left(\frac{4\pi h}{\lambda}\sin E + \phi\right) \tag{1}$$

λ is for carrier wavelength. E is for satellite elevation angle. h is the vertical reflection distance. if set $t = \sin E$, $f = \frac{2h}{\lambda}$, Then the above equation can be simplified as the standard cosine function expressions:

$$A_m = A\cos(2\pi ft + \phi) \tag{2}$$

In Eq. (2) the frequency f contains the vertical reflection distance parameter h in Fig. 1, on the type Lomb-Scargle spectrum analysis, can obtain the frequency f, And get the vertical reflection distance by $f = 2h/\lambda$; Then the snow thickness can be calculated by $h_{snow} = H - h$. Thus, the snow depth is measured by GPS-MR technology.

Based on the above principle of GPS—MR for snow depth detecting technology, the processes can be summarized as shown in Fig. 4:

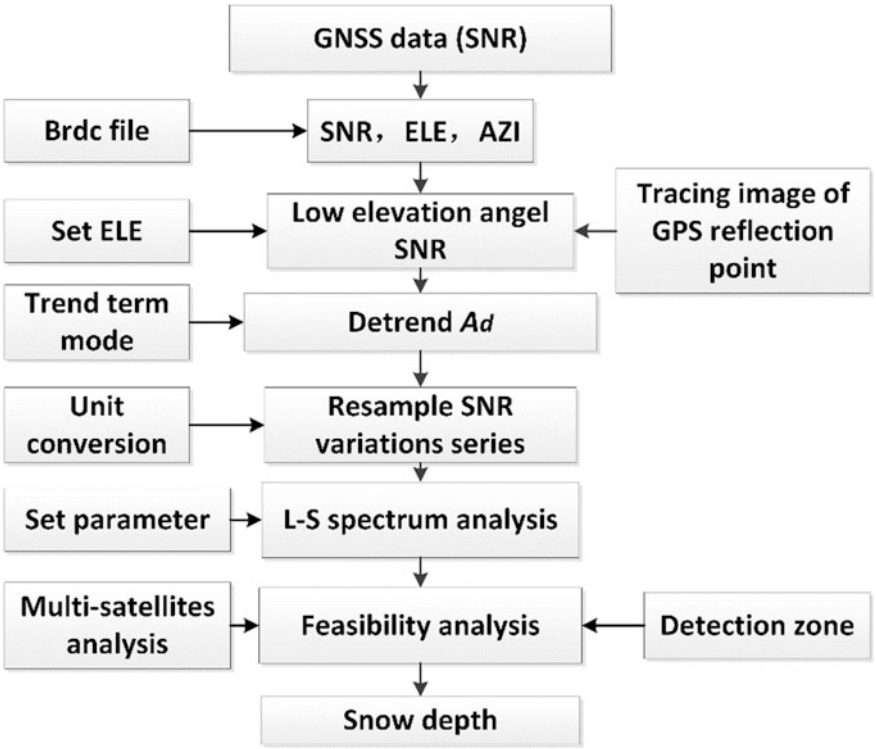

Fig. 4 Flow graph of GPS-MR for snow depth

Table 1 Comparison of L1C/A and L2P signals

GPS signal	Wavelength (m)	Frequency (MHz)	Chipping rate (Mchip/s)	Code length (Chip)	Min received (dBW)
L1C/A	0.19	154 × 10.23	1.023	1023	−158.5
L2P	0.244	120 × 10.23	10.23	6.187×10^{22}	−164.5

2.3 SNR Analysis of L1C/A and L2P

Most of the current Measurement type receiver can only receive L1C/A and L2P signal data, In order to analyze the difference of snow depth detection between L1C/A and L2P SNR, first of all must compare the differences between L1C/A and L2P signals themselves, their modulations are compared in Table 1 [7].

The SNR is the ratio of the signal power to the noise power, so the minimum power is the most important difference. Because the signal is reflected by a part of the energy absorbed by the reflective surface and the right-handed circular polarization antenna is also reflected on the reflected wave suppression, so when the

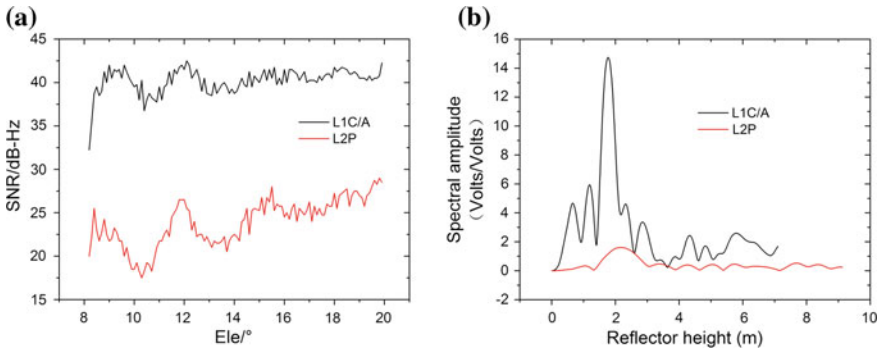

Fig. 5 **a** L1C/A and L2P SNR. **b** L1C/A and L2P spectrum analysis

reflected wave is received by the GPS receiver in addition to the existence of phase delay, the signal strength is generally reduced. Therefore, the minimum received power determines the SNR of L1C/A and L2P signals. Due to the presence of more low power signals in the L2P signal, the L2P signal SNR is about 15 dB weaker compared to L1C/A (Fig. 5a). Figure 5a shows the comparison of the SNR of L1C/A and L2P signals at the same low elevation. From Fig. 5a, it can be seen that the energy of L2P signal-to-noise is weaker than L1C/A. Figure 5b gives a Lomb-Scargle spectrum analysis of the low-elevation L1C/A and L2P SNR residuals for the same satellite. The abscissa represents the reflection height h, and the ordinate represents the spectral amplitude. It can be seen from the figure that the spectral amplitude of the spectral analysis of the SNR residual sequence of the L2P signal is significantly weaker than that of L1C/A.

3 Analysis of Examples

In order to further verify the validity of the GPS-MR detection theory and the difference of SNR between SNR of L1C/A and L2P signals, this paper selects AB33 station in PBO network (only L1C/A and L2P Signal) from 2011 to 2014 for four consecutive years of GPS data for example analysis. AB33 station is located in the United States Alaska, with an average elevation of 335.0 m, relatively open around the station, the winter snow covered by long-term. AB33 station was built in 2006, Receiver has been used TRIMBLE NETRS, and antenna is used TRIMBLE29659.00 (Radome is SCIT). Figure 6 shows the observation environment of AB33 station in different seasons.

In order to verify the accuracy of the detection of snow depth L1C/A and L2P signal, we provides GPS inversion of snow depth value provided by the PBO H2O task group in America and the snow depth value of meteorological observation stations provided by SNOTEL near AB33 as a reference for comparison. Then we analyze the correlation between them.

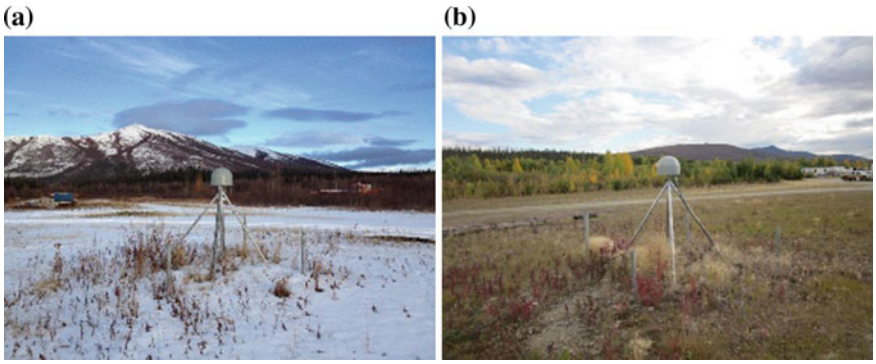

Fig. 6 Environment around the AB33 station. **a** Winter environment. **b**. Summer environment

Figure 7a shows the comparison among the inversion of snow depth based on the L1C/A SNR and the snow depth in practice measured by the SNOTEL station and the GPS inversion of snow depth value provided by the PBO H2O task group for four consecutive years from 2011 to 2014 in the AB33. Figure 7b shows the comparison among the inversion of snow depth value based on the L2P SNR and the snow depth in practice measured by the SNOTEL station and the GPS inversion of snow depth value provided by the PBO H2O task group for four consecutive years from 2011 to 2014 in the AB33. In Fig. 7, the horizontal axis represents the year, the vertical axis represents the snow depth value, the black square represents the snow depth value based on L1C/A and L2P signal-to-noise ratio, the red dot represents the GPS inversion depth value provided by PBO H2O, The solid blue line indicates the measured snow depth provided by the meteorological observatory SNOTEL. According to the statistical analysis, the correlation between the inversion of snow depth value based on the SNR of L2P and L1C/A and the value of snow depth in practice provided by meteorological observation station SNOTEL were 0.98 and 0.90. Meanwhile, the correlation between the inversion of snow depth value based on the SNR of L2P and L1C/A and GPS inversion of snow depth value provided by PBO H2O were greater than the 0.95.

Combined with Fig. 7 and the analysis theory in this paper, the following conclusions can be drawn as follows:

1. GPS-MR algorithm based on SNR can effectively obtain the depth of snow.
2. Figure 7 results show that the GPS-MR inversion of snow depth based on the SNR of L1C/A and L2P is highly consistent with the value of snow depth in practice provided by SNOTEL station in the overall trend. The results further verify the effectiveness of GPS-MR technology based on SNR in the snow depth detection.
3. Figure 7 results show that the inversion snow depth value based on the SNR of L1C/A and L2P is more consistent with the value of snow depth in practice

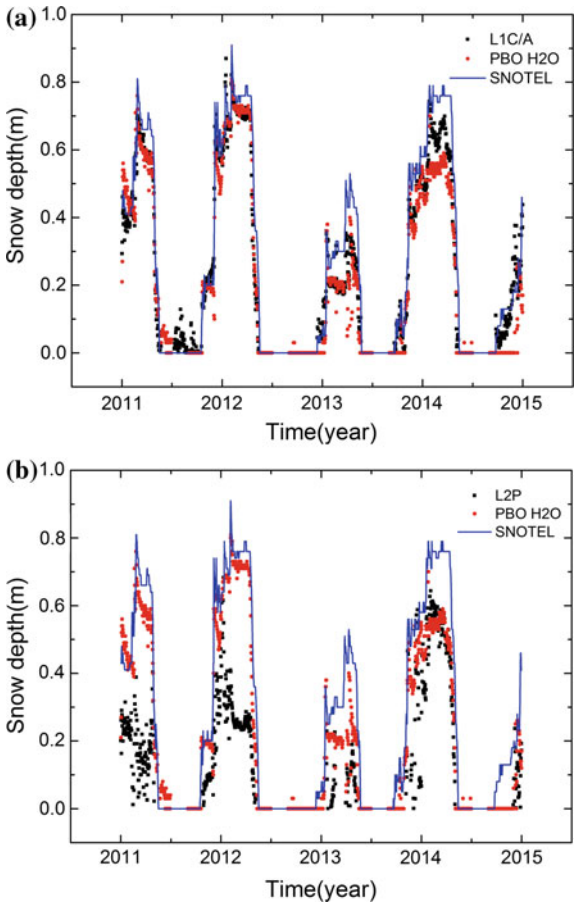

Fig. 7 **a** L1C/A snow depth contrasts with SNOTEL and PBO H2O. **b** L2P snow depth contrasts with SNOTEL and PBO H2O

provided by SNOTEL station compared with the SNR of L2P which indicates that the SNR based on L1C/A can more effectively detect the depth of snow.

4. The inversion of snow thickness based on the different frequency SNR of GPS is much larger deviation than that measured in practice by SNOTEL station, which is mainly due to the AB33 station is far away from the SNOTEL station rather than the co-located station.

4 Conclusion

Snow depth detection is of great significance to global water resources and climate and environmental science research. Based on GPS signal-to-noise ratio Characteristic and SNR based GPS-MR detection of snow depth of the basic theory,

estimation of snow depth using GPS measured data, and GPS-MR snow depth inversion results based on L1C/A and L2P SNR were compared. The SNR snow depth inversion result of L1C/A signal is more accurate than GPS-MR snow depth inversion of SNR of L2P signal, and it can effectively estimate the snow depth, the results further verify the effectiveness of GPS-MR technology based on SNR in the snow depth detection. The preliminary experimental results are also affected by many factors, need to be studied and solved in depth.

GPS-MR technology uses SNR observations to convert the multi-path signals that have been noise into useful signals. Based on the traditional geodetic GPS receivers, SNR observations can be used to detect snow depth, which can effectively save costs. And expand the application field of CORS network, and then play an important role of GNSS in global environmental change monitoring.

Acknowledgements Thanks to the United States NSF, USGS and NASA who launched the Earthscope and authorized the use of GPS data (http://www.earthscope.org). Thanks to the PBO H2O research group to provide reference resources (http://xenon.colorado.edu/portal/). Thanks to the NRCS to provide measured snow depth data (http://www.wcc.nrcs.usda.gov/). This work was supported by the National Science Foundation of China (41104019, 41274005, and GFZX0301040308). Heartfelt thanks to the editors and anonymous referee experts provide valuable opinions and suggestions for this article!

References

1. Cohen J, Entekhabi D (1999) Eurasian snow cover variability and Northern Hemisphere climate predictability. Geophys Res Lett 26:345–348
2. Walsh JE (1984) Snow cover and atmospheric variability: changes in the snow covering the earth's surface affect both daily weather and long-term climate. Am Sci 72:50–57
3. Beniston M (2003) Climatic change in mountain regions: a review of possible impacts. In: Climate variability and change in high elevation regions: past, present & future. Springer, Dordrecht, pp 5–31
4. Gutmann ED, Larson KM, Williams MW, Nievinski FG, Zavorotny V (2012) Snow measurement by GPS interferometric reflectometry: an evaluation at Niwot Ridge, Colorado. Hydrol Process 26:2951–2961
5. Najibi N, Jin SG (2013) Physical reflectivity and polarization characteristics for snow and ice-covered surfaces interacting with GPS signals. Remote Sens 5:4006–4030
6. Najibi N, Jin SG, Wu X (2015) Validating the variability of snow accumulating and melting from GPS reflected signals: forward modeling. IEEE Trans Antennas Propag 63:2646–2654
7. Jin S, Qian X, Kutoglu H (2016) Snow depth variations estimated from GPS-reflectometry: a case study in Alaska from L2P SNR data. Remote Sens 8(1)
8. Larson KM, Gutmann ED, Zavorotny VU, et al (2009) Can we measure snow depth with GPS receivers? Geophys Res Lett 36(17). doi:10.1029/2009GL039430
9. Larson KM, Small EE, Gutmann ED, et al (2008) Use of GPS receivers as a soil moisture network for water cycle studies. Geophys Res Lett 35(24). doi:10.1029/2008GL036013
10. Small EE, Larson KM, Braun JJ (2010) Sensing vegetation growth with reflected GPS signals. Geophys Res Lett 37(12). doi:10.1029/2010GL042951
11. Larson KM, Löfgren JS, Haas R (2013) Coastal sea level measurements using a single geodetic GPS receiver. Adv Space Res 51(8):1301–1310

12. Dai K, Zhang Q, Zhang S, et al (2016) Preliminary research on snow depth monitoring with GPS SNR[M]. In: China Satellite Navigation Conference (CSNC) 2016 proceedings, vol I. Springer, Singapore
13. Larson KM, Small EE (2016) Estimation of snow depth using L1 GPS signal-to-noise ratio data. IEEE J Sel Topics Appl Earth Obs Remote Sens 1–7
14. Bilich A, Larson KM, Axelrad P (2004) Observations of signal-to-noise ratios (SNR) at geodetic GPS site CASA: implications for phase multipath. Proc Centre Eur Geodyn Seismol 23:77–83
15. Zhang S, Dai K, Liu K, et al (2016) Application of GPS-MR technology in snow thickness monitoring. Prog Geophys 31(4):1879–1884
16. Larson KM, Small EE, Gutmann E, Bilich A, Axelrad P, Braun J (2008) Using GPS multipath to measure soil moisture fluctuations: initial results. GPS Solut 12(3):173–177

A Fast Algorithm of GNSS-R Signal Processing Based on DBZP

Lin Han, Yansong Meng, Yanguang Wang and Xingyuan Han

Abstract An important observation of GNSS-R is Delay-Doppler mapping (DDM). According to the requirement of GNSS-R signal real-time processing, a fast processing algorithm of GNSS-R signal based on double block zero padding (DBZP) and frequency domain rotation transformation is proposed for DDM generation. The reflected data is blocked and then correlated, which avoids the FFT calculation with too long points. The block and zero padding operations not only guarantee the full search of the pseudo code phase, but also avoid the repetitive calculation. In the frequency domain, the correlation results at different Doppler frequencies are approximated by the rotation transformation method, which avoids a large number of carrier multiplication operations and effectively reduces the computational burden. The computational burden and computational loss of parallel code phase correlation algorithm and fast algorithm are analyzed. Finally, the UK-DMC satellite-borne reflected data are processed by two algorithms and the simulation time-consuming and processing results were compared. The results show that the fast algorithm greatly shortens the DDM generation time and the loss of the processing result is small.

Keywords GNSS-R · GNSS reflected signal processing · DBZP · Fast algorithm · DDM

1 Introduction

GNSS-R is a new kind of remote sensing technology that uses GNSS navigation signal as the illumination source to extract the features of the reflect surface or detect the moving target [1]. Compared with traditional radar remote sensing

L. Han (✉) · Y. Meng · Y. Wang · X. Han
Institute of Satellite Navigation & ISL Technology,
Academy of Space Electrical Information Technology, Xi'an 710100, China
e-mail: 13152078791@163.com

J. Sun et al. (eds.), *China Satellite Navigation Conference (CSNC) 2017 Proceedings: Volume I*, Lecture Notes in Electrical Engineering 437,
DOI 10.1007/978-981-10-4588-2_16

methods, the advantages of GNSS-R technology are rich in GNSS signal resources, wide coverage and high temporal resolution.

GNSS-R has been widely used in sea surface height measurement [2, 3], sea surface wind retrieval [4], sea ice detection [5], soil moisture detection [6], etc. ESA and SSTL are working on the development of spaceborne GNSS-R receiver. NASA has successfully launched CY-GNSS satellites for hurricane observation. The GNSS-R technology has been included in the guidelines for the development of on-board payloads, and the GNSS-R-based small satellite program has been proposed by the Chinese authorities. The target also points to typhoon observations and forecasts disaster weather [7]. In order to achieve the purpose of disaster early warning, and because of the receiver storage space constraints, the future spaceborne receiver must have the ability to on board real-time signal processing.

An important observable of GNSS-R is delay Doppler mapping (DDM). Considering the generating of DDM, this paper proposes a fast coherent integration algorithm for GNSS-R signals based on Double Block Zero Padding (DBZP). The fast algorithm based on DBZP blocks the reflection data and avoids the FFT calculation with too long points. The rotation transformation method is used to approximate the correlation value at different Doppler frequency points to avoid a large number of carrier multiplication operations.

In this paper, we first analyse the computational burden and processing loss of the parallel coherent phase integral algorithm and the fast coherent integration algorithm based on DBZP. Then the UK-DMC on-board reflected data was processed by this two coherent integration algorithms and simulation results were compared.

2 Traditional GNSS-R Signal Processing Algorithm

2.1 GNSS-R Signal Model

The GNSS reflected signal is the sum of the scattered signals on all the elements of the reflect surface and can be expressed as below:

$$r(t) = \iint_{\rho} A_{\rho} \cdot c(t-\tau_{\rho}) \cdot d(t-\tau_{\rho}) \exp\left(-j2\pi\left(f-f_{\rho}\right)t\right) d^2\rho + n(t) \tag{2.1}$$

In this equation, A_ρ is the amplitude of the signal, c is the pseudo-random code, d is the data code, τ and f are the time delay and Doppler frequency on the scattering surface element, and $n(t)$ is the Gaussian white noise (Fig. 1).

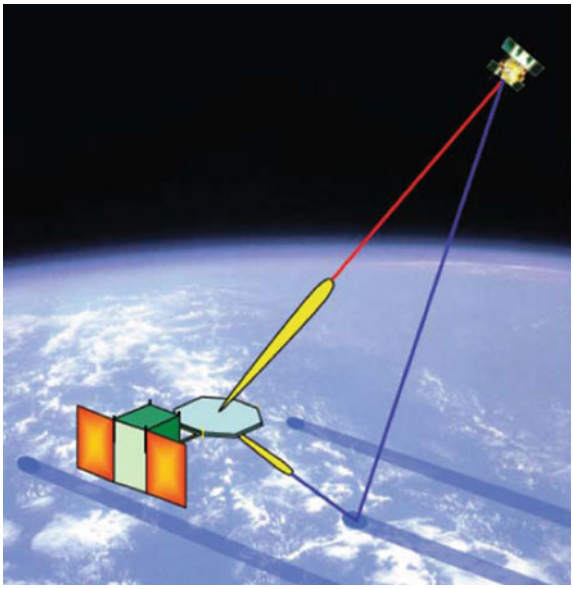

Fig. 1 Overview of remote sensing geometry of GNSS-R: PARIS-IoD concept [8]

2.2 *Parallel Code Phase Coherent Integration Method*

When DDM is generated, the reflected signal is first coherently integrated. Parallel code phase correlation algorithm is a commonly used method for the acquisition of navigation signals. The convolution is implemented in the frequency domain using FFT and IFFT, and the correlation results at all code phases are calculated at one time (Fig. 2).

First, the input reflected signal is multiplied by the local carrier, and the local pseudo-random code is subjected to the following N-point correlation convolution.

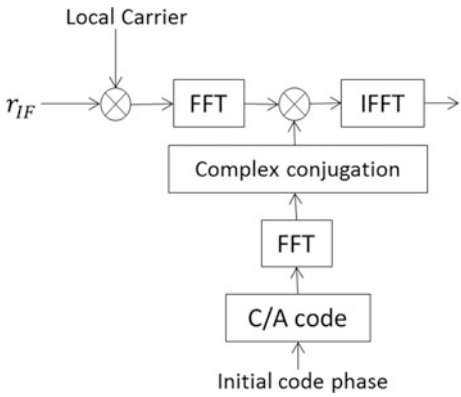

Fig. 2 Parallel code phase correlation algorithm

$$R = \frac{1}{N}\mathcal{F}^{-1}\{\mathrm{conj}\{\mathcal{F}\{c_n\}\} \cdot \mathcal{F}\{r_n\}\} \tag{2.2}$$

The parallel code phase algorithm significantly reduces the computational burden compared with directly correlation. Usually we only care about about dozens of chips on DDM. However the parallel code phase algorithm calculates the correlation result in all code phases, so the computational efficiency is limited.

3 A Fast Algorithm of GNSS-R Signal Processing Based on DBZP

3.1 Description of the Algorithm

The fast coherent integration algorithm proposed in this paper is based on the DBZP correlation algorithm and the frequency domain rotation transformation. The block and zero padding operations in the DBZP algorithm not only ensure the searching of the pseudo code phase, but also avoid the repetitive calculation (Fig. 3).

First, according to the Doppler frequency characteristic of the reflected signal and the required resolution of the DDM, set up the Doppler frequency range *Fd*, the frequency rotation transformation step *Fn* and the Doppler frequency resolution *Fm*. Fd must be an integral multiple of *Fn* and *Fn* must be an odd multiple of *Fm*. Conduct (*Fd*/*Fn*) cycles in operation, the main steps of each cycle are as follows:

Step one: The IF reflected signal is multiplied by a local carrier of the frequency at a Doppler frequency step point to obtain a baseband reflected signal.

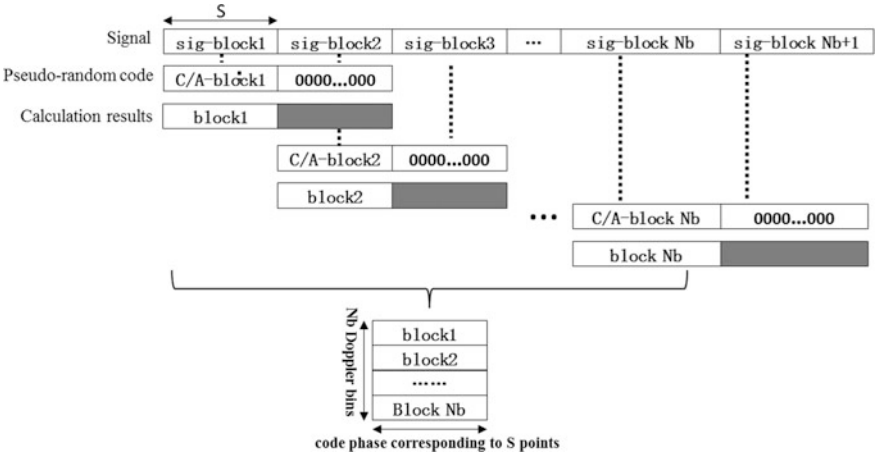

Fig. 3 DBZP correlation algorithm

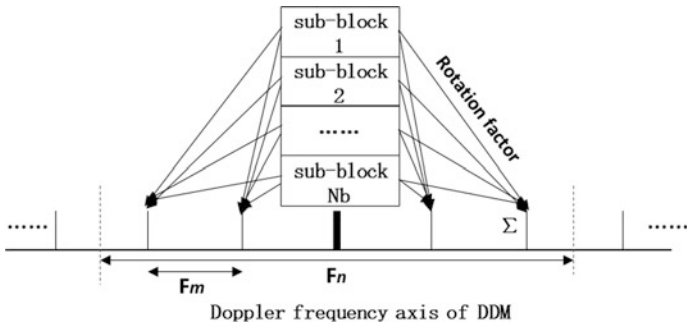

Fig. 4 Frequency domain rotation transformation

Step two: The baseband reflected signal of *Ti* millisecond, *N* sampling points is divided into *Nb* sub-blocks of length *S*, and the adjacent two sub-blocks are combined into a $2 \times S$ double-block. The last sub-block is combined with an extra block of size *S*, which is obtained from the equivalent samples over the *Ti* millisecond range.
Step three: The local pseudo-random code of *Ti* milliseconds is processed in the same way, and each sub-block is zero padded to a $2 \times S$ double-block.
Step four: Use the FFT to do the correlation computation of corresponding two-blocks, and only save the previous *S* sampling points of the correlation result, and get the correlation result matrix of $Nb \times S$.
Step five: The obtained *Nb* group of results are multiplied by the corresponding e-based rotation factors and summed to obtain the correlation results of *S* sampling points at (*Fn*/*Fm*) Doppler frequency points. $t(i)$ in rotation factors represent the time of the results sub-block (Fig. 4).

$$R_i = \sum_{i=1}^{N_b} S_i \cdot \exp(-j2\pi f_e \cdot t(i)) \tag{3.1}$$

S samples correlation results correspond to the correlation results on $S \times fc/fs$ chips. By analyzing the reflected signal, we set the local pseudo code initial phase to get the appropriate code phase interval of DDM's delay axis.

3.2 Computational Burden Analysis

For N-point complex Fourier transforms or inverse Fourier transforms, the operations include $(N/2) \cdot log\ 2\ (N)$ complex multiplications and $N \cdot log\ 2\ (N)$ complex additions. In MATLAB, a correlation operation with *N* points consists of two times

Table 1 The computational burden of the two algorithms

Algorithm	Complex additions	Complex multiplications
PCPS	11.296×10^5	6.2478×10^5
Fast algorithm based on DBZP	4.2477×10^5	2.5138×10^5
Improvement factor	2.6593	2.4854

FFT and one time IFFT with N points. That is, $N + 3\ (N/2) \cdot log\ 2\ (N)$ complex multiplications and $3N \cdot log\ 2\ (N)$ complex additions.

Using the parallel code phase correlation method to generate the correlation results on a Doppler frequency needs to carry out a local carrier multiplication and an N-point correlation. To obtain (Fn/Fm) groups of results on several Doppler frequency, the complex multiplication calculation amount is $(N/N + 3) \cdot (log\ 2\ (N))$ and the complex additions calculation amount is $(Fn/Fm) \times (3N \cdot log\ 2\ (N))$.

As described in the previous section, one cycle of the fast algorithm include (Fn/Fm) groups correlation results, consists of a Nb times 2S-length correlation and one time carrier multiplication, and (Fn/Fm) times rotation transformation. So the complex multiplication calculation amount is $Nb(2S + 2S + 3S \cdot log2(2S)) + (Fn/Fm) \times (S \times Nb)$, and the complex additions calculation amount is $Nb\ (3 \times 2S \cdot log\ 2(2S)) + (Nb - 1) \times (S \times Nb)$.

Taking into account the simulation parameters of the UK-DMC data, the computational burden of the two algorithms are listed in Table 1:

3.3 Computational Loss Analysis

Within 1 ms coherent integration time, the probability of the navigation data change is very small, so we can ignore its impact. The coherent integration results of the reflected signal can be expressed as [9]:

$$\begin{aligned} R(\widehat{\tau},\widehat{f}) = {} & A_s \times T_I \times \Lambda(\widehat{\tau} - \tau) \\ & \times \operatorname{sinc}\left(\left(\widehat{f} - f\right)T_I\right) \cdot \mathrm{e}^{j2\pi\left(\widehat{f}-f\right)T_I} \times \mathrm{e}^{j\phi} \end{aligned} \tag{3.2}$$

The coherent integration process acts as a band-pass filter, and the magnitude of the coherent integration result is related to a function of frequency error [10]:

$$S(\widehat{f} - f) = \operatorname{sinc}\left(\left(\widehat{f} - f\right)T_I\right) \cdot \mathrm{e}^{j2\pi\left(\widehat{f}-f\right)T_I} \tag{3.3}$$

So the total power after the integration can be expressed as:

$$Y(\widehat{\tau},\widehat{f}) = P_s \times T_I^2 \times \Lambda^2(\widehat{\tau} - \tau) \times S^2(\widehat{f} - f) \tag{3.4}$$

The coherent integration results on $\widehat{f_1}$ was approximated by rotating the results on $\widehat{f_2}$, as the equation below:

$$\begin{aligned} & R(\widehat{\tau},\widehat{f_2}) \cdot \mathrm{e}^{-j2\pi\left(\widehat{f_2}-\widehat{f_1}\right)t_n} \\ & = A_s \times T_I \times \Lambda(\widehat{\tau}-\tau) \times \mathrm{sinc}\left(\left(\widehat{f_2}-f\right)T_I\right) \cdot \mathrm{e}^{j2\pi\left(\widehat{f_1}-\widehat{f}\right)t_n} \\ & = R(\widehat{\tau},\widehat{f_1}) \cdot \frac{\mathrm{sinc}\left(\left(\widehat{f_2}-f\right)T_I\right)}{\mathrm{sinc}\left(\left(\widehat{f_1}-f\right)T_I\right)} \end{aligned} \tag{3.5}$$

In DDM, the output of a delay-Doppler point is the sum of the results of the components of the reflected signal on all the surface facets. The ratio of the correlation power after the fast algorithm to the traditional algorithm is:

$$\eta(\widehat{\tau},\widehat{f_1},\widehat{f_2}) = \frac{\sum_{i=1}^{M} Y_i(\widehat{\tau},\widehat{f_1}) \cdot \frac{\mathrm{sinc}^2\left(\left(\widehat{f_2}-f_i\right)T_I\right)}{\mathrm{sinc}^2\left(\left(\widehat{f_1}-f_i\right)T_I\right)}}{\sum_{i=1}^{M} Y_i(\widehat{\tau},\widehat{f_1})} \tag{3.6}$$

As can be seen from the equation above, the factors that affect the fast algorithm computational loss are delay, $\widehat{f_1}$, $\widehat{f_2}$, the scattering characteristics of the surface and the coherent integration time. The shorter the coherent integration time is, the less the computational loss of the fast algorithm. If the difference in the reflected signal power between adjacent delay-Doppler ranges is ignored, the correlation power loss can be approximated as:

$$\eta(\widehat{f_1},\widehat{f_2}) = \mathrm{sinc}^2\left(\left(\widehat{f_2}-\widehat{f_1}\right)T_I\right) \tag{3.7}$$

In the following simulation, the difference between $\widehat{f_1}$ and $\widehat{f_2}$ is 100 and 200 Hz. From the equation above, the loss due to the frequency difference is about 0.1434 to 0.5792 dB.

4 Simulation and Verification

4.1 Simulation Parameters

The simulation in this paper uses the C/A code data at the L1 frequency of the 22th GPS satellite collected by United Kingdom's Disaster Monitoring Constellation (UK-DMC) at 07:54:53 on November 16, 2004 in Hawaiian waters. The Doppler frequency at the specular point is 10.5 kHz and the Doppler frequency range is ±5 kHz. The sampling rate is about 5.714 MHz. For the convenience, calculate

Table 2 Simulation parameters

T_i	$T_{in\text{-}coh}$	F_{sp}	F_d	F_n	F_m	N_b	S
1 ms (N = 6000)	500 ms/1000 ms	10.5 kHz	±5 kHz	500 Hz	100 Hz	6	1000

Table 3 The PC platform used for the experiment

Processor	Intel(R) Core(TM) i3 CPU M 370 @ 2.40 GHz (4 CPUs), ~2.4 GHz
Memory	2048 MB RAM
Display card	ATI mobility Radeon HD 4500 series

$N = 6000$ points as one time's coherent integration, corresponding to 1 ms coherent integration time.

The computer platform used in the simulation is LENOVO 0578A64 computer, its parameter is shown in Tables 2 and 3.

4.2 Simulation Results

4.2.1 Time-Consuming

The two algorithms are simulated with the non-coherent integration time being 500 and 1000 ms. The fast algorithm needs 0.0056 s to complete the calculation cycle of one Doppler step (Table 4).

The processing time of fast algorithm based on DBZP is about 3.8 times faster than the parallel code phase correlation algorithm. The shorten times of the processing time is not equal to the theoretical analysis of the computational burden, since the actual simulation time-consuming depends not only on the algorithm design, but also on the input data size, compiler, processor speed and code optimization, etc.

4.2.2 Computational Loss

The DDM results of parallel code phase correlation algorithm and fast algorithm are shown in Fig. 5.

Table 4 Time-consuming of two algorithms

Algorithms	$T_{in\text{-}coh}$ = 500 ms	$T_{in\text{-}coh}$ = 1000 ms
PCPS	60.5745 s	118.8823 s
Fast algorithm based on DBZP	229.1010 s	454.1872 s
Improvement factor	3.7821	3.8205

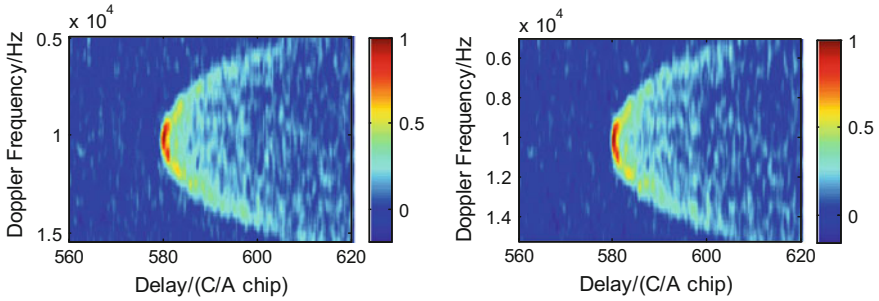

Fig. 5 Delay-Doppler mapping. *Left* the parallel code phase correlation algorithm; *Right* the fast algorithm based on DBZP

As can be seen from the figure, the fast algorithm generates a small distortion of the DDM in the glistening zone. The processing results at most of the Doppler frequency points are approximated by the frequency domain rotation transformation, which is equivalent to smoothing the amplitude of the DDM on the same time delay. When the non-coherent integration time is 1000 ms, the peak amplitude of the DM in central Doppler frequency is changed from 0.5919 to 0.5748. That is, the peak power loss is 0.2546 dB (Fig. 6).

The peak signal-to-noise ratio is defined as:

$$\mathrm{SNR}_p = \frac{Y_{peak} - \overline{N}}{RMS\left(N - \overline{N}\right)} \tag{4.1}$$

In the formula, Y_{peak} is the peak power, $\overline{N}$ is the mean background noise. The peak signal-to-noise ratio reflects how much the useful signal exceeds the noise in DM (Table 5).

Fig. 6 Delay mapping. *Black line* the parallel code phase correlation algorithm; *blue line* the fast algorithm based on DBZP

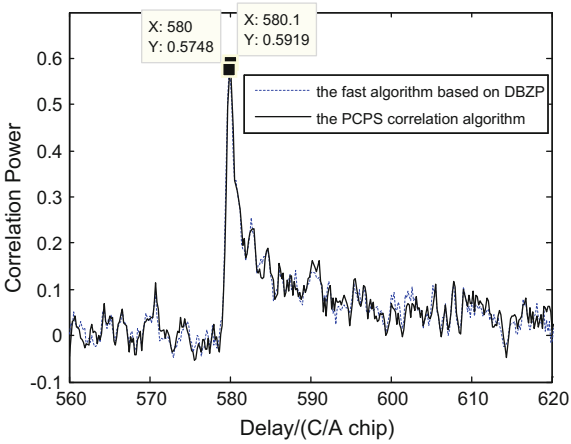

Table 5 Peak signal-to-noise ratio of DM in central Doppler frequency

Algorithms	$T_{in\text{-}coh}$ = 500 ms	$T_{in\text{-}coh}$ = 1000 ms
PCPS (dB)	11.3112	13.2554
Fast algorithm based on DBZP (dB)	11.1481	12.9645
SNRp loss (dB)	0.1631	0.2909

When the in-coherent integration time are 500 ms and 1000 ms, the peak signal-to-noise ratio of the parallel code phase correlation algorithms are 11.3112 and 13.2554 dB, while for the fast algorithm they are 11.1481 and 12.9645 dB. The SNRp loss is 0.1631 and 0.2909 dB respectively. The peak signal-to-noise ratio increases with the in-coherent integration time, and the simulation results of the fast algorithm are basically the same as the previous theoretical analysis.

5 Conclusion

The development trend of GNSS-R is on-board real-time processing and space multi-source reflected signal receiver system. Based on the analysis of the UK-DMC reflected data, it is proved that the proposed fast algorithm based on DBZP has a 2.6-fold reduction in computational burden compared with the parallel code phase correlation algorithm, and the actual DDM generation time is shortened 3.8 times. At the same time, the fast algorithm has some processing loss. When the in-coherent integration time is 1000 ms, the correlation peak power loss of the DM is 0.2546 dB at the central Doppler frequency, and the peak signal-to-noise ratio losses are 0.1631 and 0.2909 dB when the accumulation time are 500 and 1000 ms respectively.

References

1. Yang D, Zhang Q (2012) GNSS reflected signal processing: fundamentals and applications. Publish House of Electronics Industry, Beijing [in Chinese]
2. Hajj GA, Zuffada C (2003) Theoretical description of a bistatic system for ocean altimetry using the GPS signal. Radio Sci 38(5):10–1
3. Martin-Neira M, D'Addio S, Buck C et al (2011) The PARIS Ocean altimeter in-orbit demonstrator. IEEE Trans Geosci Remote Sens 49(6):2209–2237
4. Zavorotny VU, Voronovich AG (2000) Scattering of GPS signals from the ocean with wind remote sensing application. IEEE Trans Geosci Remote Sens 38(2):951–964
5. Gleason S (2010) Towards sea ice remote sensing with space detected GPS signals: demonstration of technical feasibility and initial consistency check using low resolution sea ice information. Remote Sens 2(8):2017–2039
6. Rodriguez-Alvarez N, Bosch-Lluis X, Camps A et al (2009) Soil moisture retrieval using GNSS-R techniques: experimental results over a bare soil field. IEEE Trans Geosci Remote Sens 47(11):3616–3624

7. Huang L, Wei W (2013) The development of exogenous-aided remote sensing radar technology. The 30th Annual Meeting of Chinese Meteorological Society, Nanjing [in Chinese]
8. Martin-Neira M, D'Addio S, Buck C, et al (2009) The PARIS in-orbit demonstrator. Geoscience and remote sensing symposium, 2009 IEEE international, Igarss, pp II-322–II-325
9. Gleason S (2006) Remote sensing of ocean, ice and land surfaces using bistatically scattered GNSS signals from low earth orbit. University of Surrey
10. Gang X (2013) Principles of GNSS: GPS, GLONASS, and Galileo. Publishing House of Electronics Industry, Beijing [in Chinese]

Model Establishment and Analysis of Weighted Mean Temperature in the Region of Guilin

Zixin Chen, Junyu Li, Lilong Liu, Guiren Luo and Xuqi Mo

Abstract Compared to conventional vapour detection instruments, new means of GPS water vapor detecting with high temporal and spatial resolution, without calibration, low cost, suitable for wide range of promotion. And then GPS water vapor detecting play a positive role in the surviving of heavy rain, hail and other severe weather. Inversion of atmospheric water vapor using GPS accurately (GPS-PWV) needs to have accurate the Weighted Mean Temperature (Tm), literature studies have shown Tm that precise calculations need to establish local optimization model. On May 8, 2016, the world tourist destinations Yangshuo has sustained heavy rain, flood was once the county seat of West Street, the main street flooded, which greatly threaten people's personal and property safety, serious impact on the local tourism industry, causing huge economic losses. Therefore, accurately predicting GPS-PWV in Guilin region and predicted rainfall becomes more important, and to accurately compute GPS-PWV it is necessary to establish the region's weighted average model. This Guilin weighted average atmospheric temperature model establishment and analysis research has scientific significance and practical value. The mainly research contents and results are: weighted average temperature model was established for Guilin. Sounding using radiosonde station in Guilin region 2010–2015 data, set up a monthly, quarterly and annual single station

Z. Chen (✉) · J. Li · L. Liu · G. Luo · X. Mo
College of Geomatics and Geoinformation,
Guilin University of Technology, 541006 Guilin, China
e-mail: 972231204@qq.com

J. Li
e-mail: yl_lijunyu@163.com

L. Liu
e-mail: hn_liulilong@163.com

G. Luo
e-mail: 1015562772@qq.com

X. Mo
e-mail: 760634990@qq.com

J. Sun et al. (eds.), *China Satellite Navigation Conference (CSNC) 2017 Proceedings: Volume I*, Lecture Notes in Electrical Engineering 437,
DOI 10.1007/978-981-10-4588-2_17

(Tm) model, and comparison with the existing (Tm) models. Results showed that, compared to this Tm model and the traditional Tm model accuracy is significantly improved, the BIAS of the model for −2.1670, MAE for 2.1670, RMSD for 1.4721, the models used in GPS-PWV can meet the requirements of GPS meteorology inversion of atmospheric water vapor.

Keywords Rainfall · GPS water vapor detecting · Atmospheric water vapour · The average temperature

1 Introduction

Water vapor is the basic conditions of precipitation, its temporal and spatial distribution and by the latent heat of phase change directly affects the development of the vertical stability of the atmosphere and weather systems, resulting in strong convective weather, rain, even heavy rain and hail. As an important atmospheric greenhouse gas and system is an important part of the Earth's atmosphere, water vapor in the small and medium-scale disaster weather (mostly rain) plays an important role in monitoring, forecasting, and small and medium-scale disaster weather (horizontal scale at about 100 km) life-cycle is often only a few hours, or even less. Compared to conventional vapour detection instruments, new means of GPS water vapor detecting with high temporal and spatial resolution, without calibration, low cost, suitable for wide range of promotion and other characteristics of heavy rain, hail and other severe weather monitoring has a positive role, have received increasing attention in the water vapor observation system.

In GPS inversion atmospheric precipitation (PWV) in the process of need zenith tropospheric zenith delay (done) from the dry separation delay (ZHD), minus the day set the statics of delay caused by the atmosphere, get the zenith wet delay (ZWD), ZWD multiplied by a conversion factor (generally through the establishment of local weighted draw temperature model or the atmosphere can be achieved by constant (K = 0.15) precipitation PWV. Many scholars in our country using ground-based GPS to carry out the amount of atmospheric water vapor remote sensing research, especially the weighted average atmospheric temperature, the Weighted Mean Temperature model research. However, in view of the guilin area weighted average temperature of the model establishment and analysis has not been implemented. Use of guilin sounding station sounding data from 2010 to 2014, analysis and modeling of guilin region, in order to get higher accuracy of the weighted average temperature, better meet the requirements of GPS meteorology inversion of atmospheric water vapor.

Has a large number of studies have shown that, to obtain a more accurate PWV, need to establish local weighted average temperature optimization model. Due to the famous Bevis [1] model was originally sounding stations derived from parts of

the northern hemisphere, this model is only applicable to particular regions (27°N–65°N), therefore, a number of studies according to the applied area local weighted average temperature model is established, in order to obtain accurate GPS PWV. For example, by using the radiosonde station sounding data for 8 years in Hong Kong, a $T_{m(HK)}$ model applicable to the region, author's research showed that the differences between the $T_{m(HK)}$ and $T_{m(B)}$ in the 3–8 K range [2]. Similarly, through studying the relation between station altitude and weighted average temperature, some scholars has established the apply to the whole mainland China ($T_{m(CHN)}$) model. Study results show that when the station from several meters to thousands of meters above sea level change, ($T_{m(CHN)}$) with the difference between $T_{m(B)}$—8 and 10 k [3]. Qin et al. [4], such as related to the temperature, pressure and humidity is established the Weighted Mean Temperature model, the model is suitable for the qing hai-tibet plateau area. In addition, in order to avoid the error of the meteorological data, such as pressure, temperature, impact, Sheng and Lin [5] also studied the PWV obtained by fitting the linear relationship between done get PWV method.

Due to China's vast territory, east-west, north and south to span is large, complex and varied topography, climate type variable, the existing the Weighted Mean Temperature model is the use of a wide range of distribution of the country's established sounding station observation data, it is difficult to promote to remote areas, and the existing local T_m model and away from the low latitudes, China, for example, guilin in guangxi region. Even if currently the most widely used $T_{m(B)}$ = 70.2 K + 0.72T_s (K) Bevis model, is used in the United States 27–65°N 13 sounding station data of 8718 samples to establish, root mean square error is 4.74 K. Because the Weighted Mean Temperature has as latitude, season, and the changing characteristics of geographical position, therefore to establish the Weighted Mean Temperature nationwide model is applied to different areas, inevitably affected by other parts of the error is also increases. In addition, the accuracy of the Weighted Mean Temperature model of the specific region in Guilin area needs to be further verified. Therefore, it is necessary to analyze and validate the existing model to establish a new Weighted Mean Temperature model in Guilin area.

In order to change analysis of Guilin area of the Weighted Mean Temperature, this paper selects the Guilin area of 2010–2015 radiosonde data was used to build a T_m model of the local area, and compared with the existing models.

2 Affiliating Scale Average Temperature

The formula for calculating the affiliating scale average temperature can be expressed as:

$$T_m = \frac{\int (P_v/T)dz}{\int (P_v/T^2)dz} \tag{2.1}$$

The actual calculation, the sounding data provided from the ground to the heights of T_i temperature and vapor pressure of $P_{w,i}$, it will be the type of discretization can be obtained after the following formulas:

$$T_m = \frac{\sum_{i=0}^{i=n-1} \frac{\overline{P}_{w,i}}{\overline{T}_i}(h_{i+1} - h_i)}{\sum_{i=0}^{i=n-1} \frac{\overline{P}_{w,i}}{\overline{T^2}_i}(h_{i+1} - h_i)} \tag{2.2}$$

In the formula, $\overline{P}_{w,i}$ and $\overline{T}_i$ respectively from the height of h_i to h_{i+1} high average vapor pressure and average temperature, $\overline{P}_{w,i} = \frac{1}{2}(P_{w,i+1} + P_{w,i})$; $\overline{T}_i = \frac{1}{2}(T_{i+1} + T_i)$.

The type 2 can accurately calculate the weighted draw temperature. However, in the practical application is not possible in each GPS station and radiosonde data. According to Bevis research, the Weighted Mean Temperature can be obtained by ground temperature calculation

$$T_m = a + b \cdot T \tag{2.3}$$

Formula, the coefficient a, b can be obtained using the least squares method

The Weighted Mean Temperature model based on ground temperature can be widely used in mid latitude region through linear regression Bevis:

$$T_{m(B)} = 70.2\,\mathrm{K} + 0.72T_s\,(\mathrm{K}) \tag{2.4}$$

Because the Weighted Mean Temperature by latitude, seasonal and topographic factors, while the Bevis model is suitable for mid latitudes (27–65°N). Many studies show that a local weighted average temperature model in GPS PWV inversion process can obtain higher accuracy. In order to obtain a more suitable T_m model China area, Sheng et al. [6] on the basis of the Bevis model was obtained with the correct altitude related error model after:

$$T_{m(CHN2)} = \begin{cases} T_m = T_{m(B)} + 5.1, & h < 200\,\mathrm{m} \\ T_m = T_{m(B)} + 3.0, & 200\,\mathrm{m} \le h < 500\,\mathrm{m} \\ T_m = T_{m(B)} + 2.1, & 500\,\mathrm{m} \le h < 1500\,\mathrm{m} \\ T_m = T_{m(B)}, & 1500\,\mathrm{m} \le h < 3000\,\mathrm{m} \\ T_m = T_{m(B)} - 6.6, & h \ge 3000\,\mathrm{m} \end{cases} \tag{2.5}$$

As can be seen from the above, the model through the analysis of Bevis formula in different elevation of the residual error on the basis of the elevation subsection formula correction.

3 Existing Local Tm Model

Single station and regional the Weighted Mean Temperature model are given in table Bevis model and some applicable to China area. This paper is comparative analysis of T_m model and Bevis model is established by using station data in the Guilin area of sounding.

4 Establishment and Comparative Analysis of the Weighted Mean Temperature Model in Guilin Area

The Guilin area sounding data during 2010–2014 to establish a regional T_m model, and compared with the existing models. Figures 1, 2, 3, 4 and 5 shows the Guilin radiosonde station T_m changes T_s and surface temperature 2010–2014.

Through the research and analysis of data for 2010–2014 and Guilin radiosonde stations, following the establishment of the local T_m model:

$$T_m = 102.1122518\,\mathrm{K} + 0.6151567 T_s\,(\mathrm{K})$$

In the Weighted Mean Temperature model, calculated 2010–2014 radiosonde station falls within the accuracy of the data, fitting 2015 Guilin sounding data, gaining 2015 Guilin sounding data line with precision. Mean deviation (BIAS), root mean square error deviation (RMSD), and mean absolute deviation (MAE) are used as indicators to evaluate the accuracy of the model.

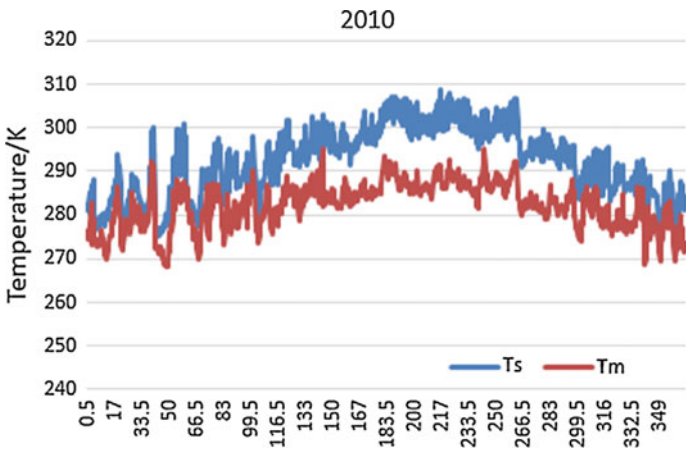

Fig. 1 Guilin change 2010 Tm and ground temperature sounding station

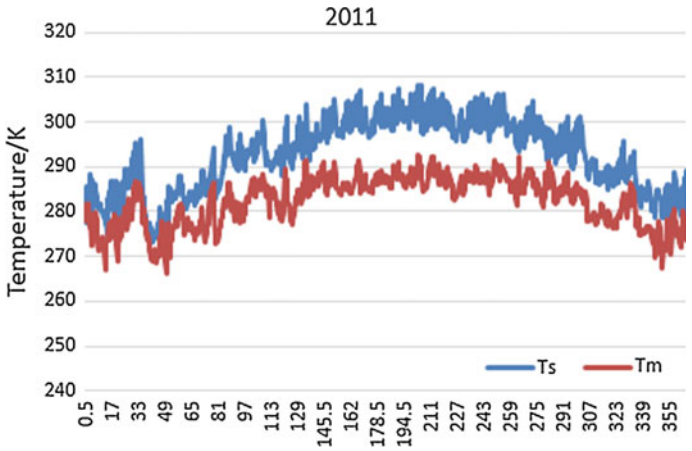

Fig. 2 Guilin change 2011 Tm and ground temperature sounding station

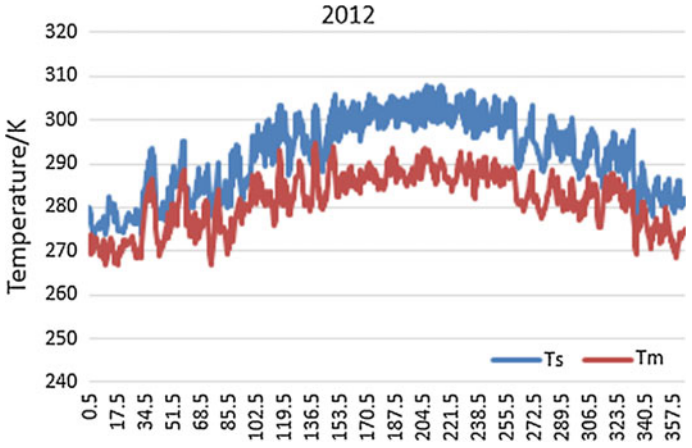

Fig. 3 Guilin change 2012 Tm and ground temperature sounding station

Table 1 shows the accuracy of regression model for years local sounding data obtained in the area, RMSD was less than 3 K. However, the accuracy of Bevis model in the region is different, when the sounding data using this model to fit the RMS for 2015 is 7.974349365 K. It can be seen from Table 2 that the Weighted Mean Temperature average deviation, mean absolute deviation and root mean square error deviation of the Weighted Mean Temperature fitting by the Weighted Mean Temperature model in Guilin area are smaller than those calculated by Bevis model. From Table 3, we can conclude that in the Guilin area by using the local

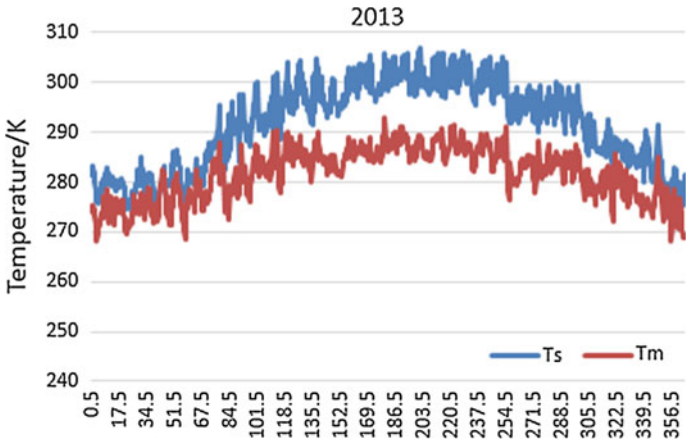

Fig. 4 Guilin change 2013 Tm and ground temperature sounding station

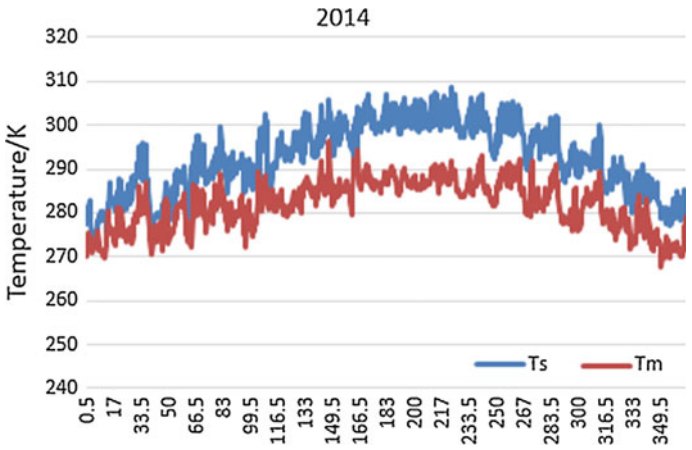

Fig. 5 Guilin change 2014 Tm and ground temperature sounding station

Weighted Mean Temperature model of local sounding data the accuracy is higher than the accuracy of the Bevis model.

In addition, we are extracting 2015, such as hail, heavy rain and other inclement weather the weighted average temperature data, calculated on the basis of the BIAS in the local model for −0.160721894 K, RMSD for 1.074360365 K, MAE for 1.283149772 K, Compared with the 2015 year outside in line with precision, which is very small, it can be seen that even in complicated weather conditions, we created the weighted average model with high precision.

Table 1 Existing local Tm model

Model	Affiliating scale average temperature
Bevis et al. [1, 7]	$T_{m(B)} = 70.2\,\mathrm{K} + 0.72T_s\,(\mathrm{K})$
Wang et al. [8]	$T_{m(CHN1)} = 53.244\,\mathrm{K} + 0.783T_s\,(\mathrm{K})$
Sheng and Lin [3]	$T_{m(CHN2)} = \begin{cases} T_m = T_{m(B)} + 5.1, & h < 200\,\mathrm{m} \\ T_m = T_{m(B)} + 3.0, & 500\,\mathrm{m} \le h < 1500\,\mathrm{m} \\ T_m = T_{m(B)} + 2.1, & 500\,\mathrm{m} \le h < 1500\ \mathrm{m} \\ T_m = T_{m(B)}, & 1500\,\mathrm{m} \le h < 3000\,\mathrm{m} \\ T_m = T_{m(B)} - 6.6, & h \ge 3000\,\mathrm{m} \end{cases}$
Chen et al. [2]	$T_{m(HK)} = 106.7\,\mathrm{K} + 0.605T_s\,(\mathrm{K})$

Table 2 Accuracy comparison in 2010–2014 years

	2010	2011	2012	2013	2014
BIAS	−0.25853	−0.14113	0.20949	−0.05969	0.24935
MAE	1.92758	1.71858	1.96186	1.67706	1.91175
RMSD	2.46395	2.21082	2.53594	2.14792	2.41459

Table 3 2015 accuracy comparison between local model and Bevis model

	BIAS	MAE	RMSD
Local model	0.029221572	1.818370377	2.352513978
Bevis	7.568872368	7.568872368	7.974349365

5 Conclusion

Through the analysis of Guilin 1020–2014 radiosonde station data, establishment of Guilin's weighted average temperature of the atmosphere model, concluded as follows:

By using the local Guilin radiosonde data established the accuracy of the Weighted Mean Temperature model than the Bevis model with high precision. Although the mathematical expression of Bevis model is simple and widely used in many areas, it is necessary to establish a more suitable local T_m model to obtain higher accuracy GPS in low latitude regions in China. In addition, the model is applied to the inversion of GPS-PWV can reach GPS meteorology water vapor retrieval requirements.

Acknowledgements This research was supported by National Natural Science Foundation of China (Grant No.41664002).

References

1. Bevis M, Bnsinger S, Herring TA et al (1992) GPS Meteorology: remote sensing of atmospheric water vapor using the global positioning system. J Geophys Res 97:15787–15801
2. Chen YQ, Liu YX, Wang XY et al (2007) Some key technologies of real time GPS water vapor monitoring system in Hongkong. J Surv Mapp 36(1):9–12
3. Sheng JY, Lin TL (2009) Verification and analysis of water vapor weighted mean temperature regression formula. J Wuhan Univ Inf Sci Ed 34(6):741–744
4. Qin J, Yang K, Koike T et al (2012) Evaluation of AIRS precipitable water vapor against ground-based gps measurements over the tibetan plateau and its surroundings. J Meteorol Soc Jpn 90:87–98
5. Sheng JY, Lin TL (2008) Study on precipitable water temperature without ground pressure data. Geodesy Geodyn 28(5):34–38
6. Sheng JY, Lin TL (2012) Use selected the right fitting solution GPS water vapor tomography. J Wuhan Univ Inf Science Ed 37(2):183–186
7. Bevis M, Businger S, Chiswell S et al (1994) GPS meteorology: mapping zenith wet delays onto precipitable water. J Appl Meteorol 33(3):379–386
8. Wang XY, Dai ZQ, Cao YC et al (2011) Tm statistical analysis of GPS weighted mean temperature in China. J Wuhan Univ Inf Sci Ed 36(4):412–416

GNSS-R Ocean Altitude Detection Technology Based on Carrier Phase Assistant

Liang Kan, Meng Li, Junbo Han, Juanjuan Dong, Linfei He, Kangning Zhang, Yingna Liu and Dingcheng Tang

Abstract GNSS-R is a new branch of GNSS which has been developed since the 1990s. It can be applied to remote sensing exploration of marine environment and remote sensing of terrestrial environment. GNSS-R has many advantages over other remote sensing techniques, such as remote sensing, Low cost, low power consumption, high spatial and temporal resolution, and many other advantages of the project can be detected. GNSS-R marine remote sensing detection technology mainly through high-gain reflection antenna to receive the GNSS reflection signal from the sea to complete the marine environmental detection, the reflected signal carries changes in signal waveforms, changes in polarization characteristics, amplitude, phase, and frequency. In this paper, a GNSS-R ocean height detection technique based on carrier phase assistant was introduced. The conventional channel accomplishes the initial acquisition of the signal and outputs the original DDM pattern by the time delay-Doppler mapping correlator, DDM diagram can be used to complete the inversion of the wind field, etc., while the DDM map contains the reflected signal doppler, time delay information, the accuracy of doppler and time delay was determined by the DDM Doppler interval and the time interval. The processor can process the time delay of the reflected signal to obtain a roughly phase and doppler information. The closed-loop acquisition and tracking of the signal was completed by the time information and doppler information obtained by the reflection. By calculating the direct and reflection channel carrier phase, pseudo-range difference for the sea surface height inversion. In order to verify the inversion accuracy of the system, in this paper, the ground-based test and flight test was carried out using the self-research phased-array GNSS-R ocean reflection receiver system. The experimental data showed that the inversion error of sea surface height was better than 10 cm.

Keywords GNSS-R · Marine remote sensing · Carrier phase assistant · Flight test

L. Kan (✉) · M. Li · J. Han · J. Dong · L. He · K. Zhang · Y. Liu · D. Tang
Space Star Technology Co., Ltd., Beijing 100086, China
e-mail: kllara@163.com

J. Sun et al. (eds.), *China Satellite Navigation Conference (CSNC) 2017 Proceedings: Volume I*, Lecture Notes in Electrical Engineering 437,
DOI 10.1007/978-981-10-4588-2_18

1 Introduction

GNSS-R is a new branch of GNSS which has been developed since the 1990s. It can be applied to remote sensing exploration of marine environment and remote sensing of terrestrial environment. GNSS-R has many advantages over other remote sensing techniques, such as remote sensing, Low cost, low power consumption, high spatial resolution, and many other advantages [1–3].

As shown in Figs. 1 and 2 for the GNSS-R detection system diagram. The GNSS-R detection system is mounted on LEO, GNSS-R detection system consists of GNSS-R receiver, pre-amplifier, positioning antenna, GNSS-R reflector antenna. Positioning antenna to receive from the zenith direction of the navigation constellation signal to complete the satellite's own positioning, orbit function, The GNSS-R reflector antenna is a high-gain phased-array antenna that receives GNSS reflected signals from the ocean for the detection of the marine environment [4].

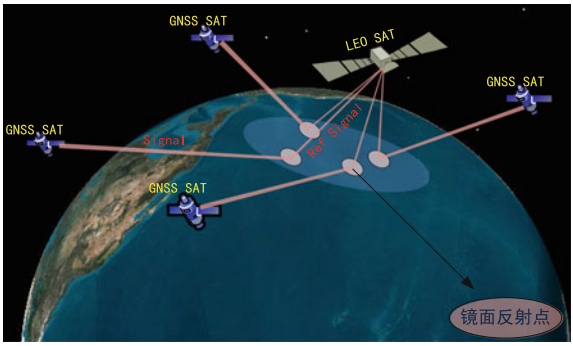

Fig. 1 GNSS-R detection schematic

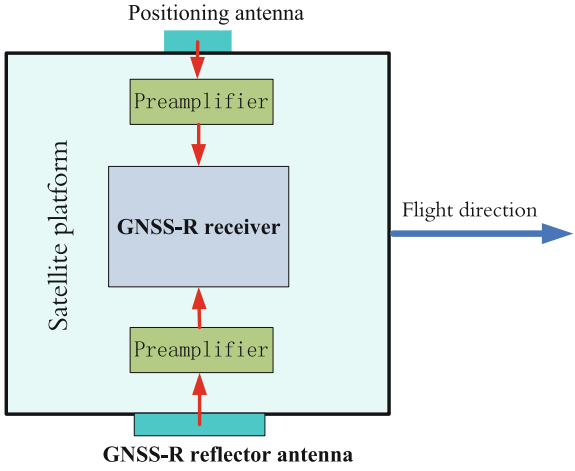

Fig. 2 GNSS-R receiver system

2 Principles of GNSS-R Ocean Detection Technology

2.1 Inversion of Sea Surface Height

The principle of GNSS-R for inversion of sea surface height is shown in Fig. 3. The receiver completes the prediction of the location and reflection events of the receiver by receiving a direct signal from the zenith, By receiving the ephemeris information of each navigation star and the earth model to complete the prediction of the GNSS-R reflection event. As shown in Fig. 3, by calculating the GPS satellite surface reflection signal and the direct signal arrival time difference to calculate the distance, in order to achieve the altimeter. The relationship between the path difference and the receiver height as shown in Fig. 3, the arrival time of the direct signal can be calculated by the positioning information. The distance is the pseudorange value after subtracting the clock error and ionospheric delay. The time difference of the reflected signal is obtained by the peak value of the accumulated amount in the DDM diagram.

Where: R represents the receiver position, R ‘represents the receiver under the sea surface of the mirror, ε for the satellite elevation angle, S for the mirror point. Suppose the path difference is, according to the diagram, the following relations are obtained:

$$\Delta\rho = 2h \sin(\varepsilon) \tag{1}$$

When the GNSS-R is used to invert the sea surface height, the error is mainly caused by atmospheric delay error, scattering delay error and random noise caused by various error sources (mainly including Multi-path error, clock error, signal processing error and receiver thermal noise, etc.), antenna installation error. The

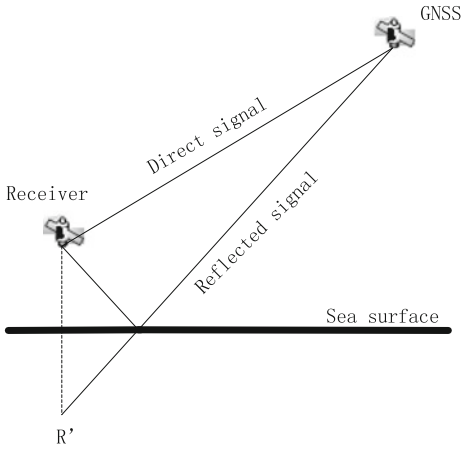

Fig. 3 GNSS-R altimetry diagram

main words in all headings (even run-in headings) begin with a capital letter. Articles, conjunctions and prepositions are the only words which should begin with a lower case letter.

1. Atmospheric delay error: the error caused by the signal through the atmosphere including the incident and reflect the error caused by two parts of the path.
2. Scattering delay error: mainly due to the roughness of the sea caused, but also with the sea breeze.
3. Random noise error: including multi-path error, clock error, signal processing error and the receiver thermal noise.
4. Antenna installation error: Since the positioning antenna and the sea anti-antenna is not installed in the same position, positioning antenna installed in the top of the satellite, and sea anti-antenna installed in the bottom, so this installation also brings additional path to the measurement.

Taking into account the above errors, the equation for the altimeter becomes:

$$\Delta\rho = 2h\ \sin(\varepsilon) + \rho_{atm} + \Delta h\ \sin(\varepsilon) + \rho_n \tag{2}$$

2.2 *Inverse Principle of GNSS—R Sea Level Based on Carrier Phase*

In Sect. 2.1, the principle of GNSS-R sea surface height inversion is introduced. It can be seen from Sect. 2.1 that the most important condition of the altimetry is to calculate the pseudorange value of the direct signal and the pseudorange value of the reflected channel. And the accuracy of the earth model determines the inversion accuracy of the system. The pseudorange value of the direct signal and the pseudorange value of the reflected channel are the most important measurement error. Clock error, random noise error and installation error can be eliminated by the calibration and resolution of the ground, so how to get the high precision direct signal and the pseudorange value of the reflected signal determines the inversion accuracy of the system.

As shown in Fig. 4, the GNSS-R sea surface height is based on carrier assistance. Direct path pseudorange values can be obtained by double difference method, can eliminate the error caused by the ionospheric delay, direct measurement error can be controlled at the cm level. The carrier phase measurement error of the direct channel is about 2 mm by conventional methods such as Kalman filtering. Therefore, how to solve the high-precision pseudo-range value of the reflected signal determines the altimeter error.

Conventional reflection signal processing is done by reflecting the channel, that is, through the time delay—Doppler array correlator to complete the reflection signal acquisition. DDM diagram can output the time delay, Doppler delay and reflected signal energy of the reflected signal. Due to the hardware resources and the code rate,

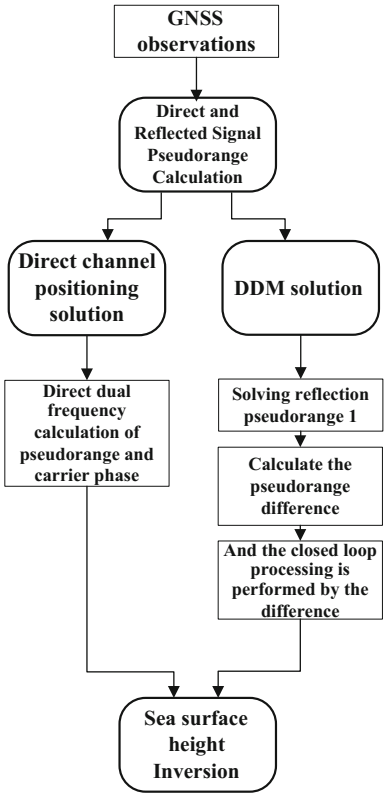

Fig. 4 Inversion flow chart

the error of the time delay dimension in the DDM diagram is large. The time interval is inversely proportional to the time coverage. Taking the time interval of 1/128 chip as an example, the measurement error of the reflection channel at this time interval is about 2 m, which is far from the requirement of cm-level measurement.

In this paper, we propose a carrier-aided-based altimetry method. As shown in Fig. 4, DDM acquisition is performed using conventional measurement channels. We can obtain the pseudorange values of the reflected channel roughly by DDM. We can calculate the error terms of the system by calculating the difference between the pseudoranges of the direct path and the reflected path. At this point we can take the difference as a known amount and enter the value into the closed-loop processing channel. The closed-loop processing channel can be finely captured and tracked near the pseudo-range value, and increases the gain of the signal by increasing the coherent accumulation time and the non-coherent accumulation time. And through the carrier-aided pseudorange in the form of the reflected signal to complete the precise capture. Output direct path carrier pseudorange information, reflection channel carrier pseudorange information. And the difference between the direct pseudorange and the reflected pseudorange is calculated by doing the difference, and then the inversion of the sea surface height is completed.

3 Experimental Verification

3.1 Floor-Based Test Validation

In order to verify the algorithm's inversion accuracy, we conducted a number of floor-based tests in September 2015–October, as shown in Figs. 5 and 6 for the floor-based test equipment connection. The positioning antenna is installed at the edge of the roof, vertically upward, receiving the positioning signal from the zenith. The sea anti-antenna is fixed on the bracket and installed at an angle of 25° with the wall. Receive the reflected signal from the floor below.

Figures 7 and 8 shows the satellite DDM of No. 5 and No. 13.

As shown in Figs. 7 and 8 for the DDM diagram. We will get the original measurement of the carrier-assisted way to complete the measurement of the floor.

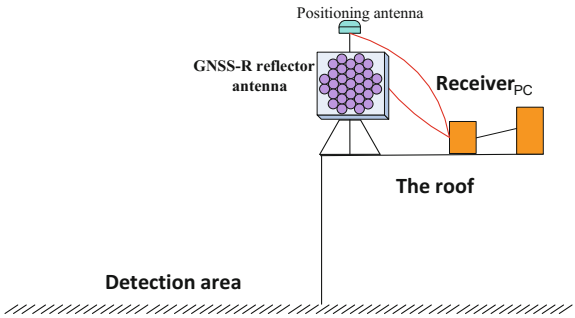

Fig. 5 Floor-based test equipment connection diagram

Fig. 6 Antenna detection field of view

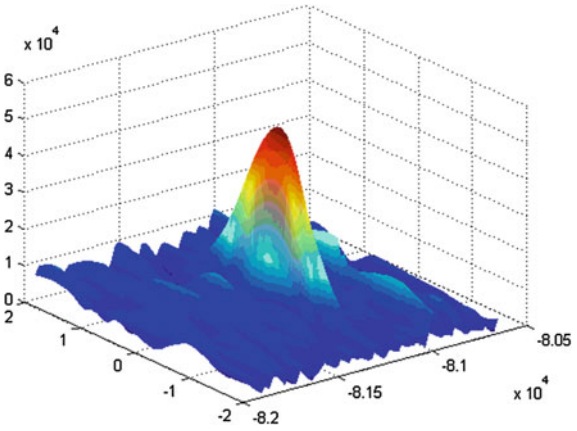

Fig. 7 DDM diagram of the 5 prn

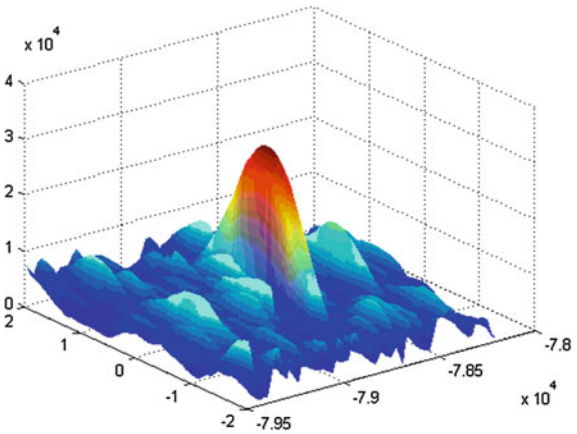

Fig. 8 DDM diagram of the 13 prn

The calibration of the antenna and the calibration of the system measurement error are completed before the test. And use these calibrated parameters as the system error parameters for subsequent inversion. Table 1 shows the results of calibrating the antenna installation error and the system clock error. We will be one day to get the 35 groups of raw measurement data processing. The self-coincidence accuracy is 35 sets of error between the measured data. As can be seen from Table 1, the use of carrier-assisted way to get the floor measurement error is better than 5 cm. Within the test accuracy of better than 3 cm.

Table 1 Inversion accuracy comparison results

Type of data	The amount of data	Building height	RMS	Precision
GNSS-R reflected signal	35	34.385 m	34.344 m	0.027 m

3.2 *Flight Test Validation*

In order to verify the algorithm's inversion accuracy, we conducted three flight tests in Tianjin Bohai Bay from November to December, 2015. The flight test was carried on a 12-glide transport aircraft, as shown in Fig. 9.

The phased-array GNSS-R antenna was used in the flight test. The positioning antenna was installed on the top of the airplane. The phased-array antenna was installed at the bottom of the airplane. The first flight test flight was 1.2 km.

Figures 10 and 11 shows the DDM of the 29th and 15th satellites obtained during the flight.

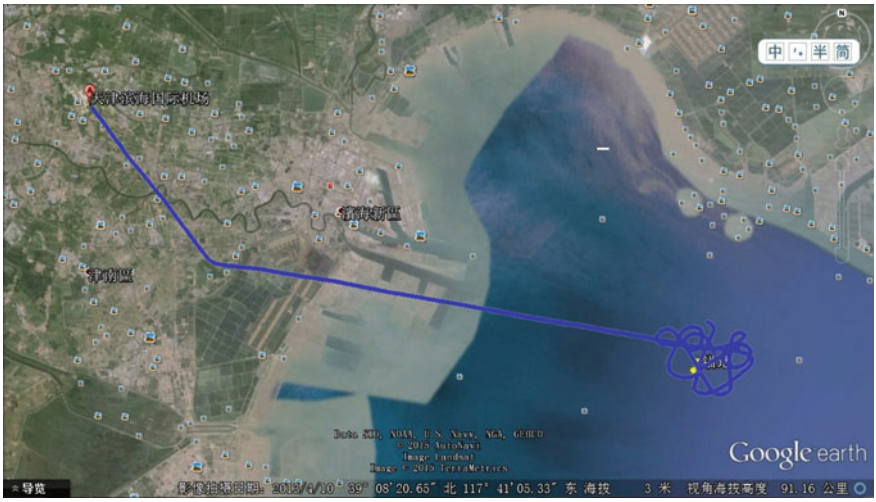

Fig. 9 Route map

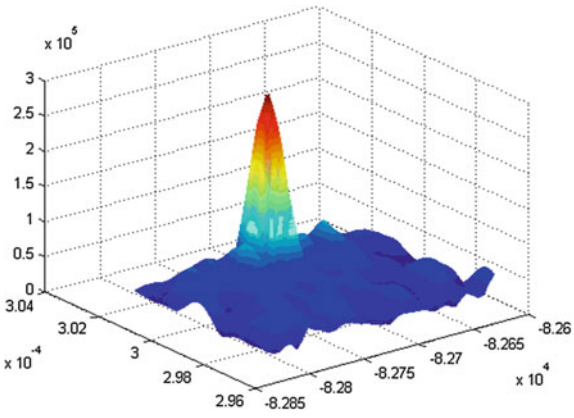

Fig. 10 DDM diagram of the 29 prn

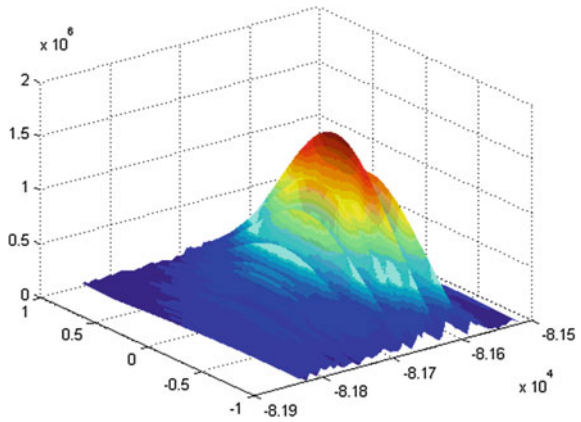

Fig. 11 DDM diagram of the 15 prn

Table 2 Inversion accuracy comparison results

Type of data	Prn	Precision (cm)
GNSS-R reflected signal	15	3.7
GNSS-R reflected signal	9	6.8
GNSS-R reflected signal	3	4.5
GNSS-R reflected signal	13	12.4
GNSS-R reflected signal	7	7.5
GNSS-R reflected signal	21	2.2
GNSS-R reflected signal	17	8.3

The part of the data obtained from the first flight test is processed. Since the flight height of the aircraft is uncertain, the results of the processing are self-consistent. The resulting inversion results are self-consistent with the altitude values of the airplane. The height of the aircraft is obtained by the positioning channel, and the output frequency is 1 Hz. The reflection channel can be used to retrieve the sea surface height of the reflection event, and the accuracy of the inversion can be obtained. As shown in Table 2 for the inversion accuracy, can be seen from the table part of the events of the height difference is greater.

The total measurement error is cm-level and meet the requirements.

4 Summary

GNSS-R technology is a new branch of GNSS which has been developed since 1990s. It can be applied to remote sensing detection of marine environment and remote sensing of land environment. The conventional processing method is limited by the hardware, code rate and other reasons can not be a higher accuracy of the inversion. In this paper, a method based on carrier phase aids is proposed, which

can acquire the pseudorange values of the reflected channels by the channel DDM. The error term of the system can be obtained by calculating the difference between the pseudorange values of the direct channel and the reflected channel. By increasing the coherent accumulation time, the non-coherent accumulation time increases the gain of the signal. And through the carrier-aided pseudorange in the form of the reflected signal to complete the precise capture. Output direct path carrier pseudorange information, reflection channel carrier pseudorange information. And the difference between the direct pseudorange and the reflected pseudorange is calculated by doing the difference, and then the inversion of the sea surface height is completed.

In order to verify the accuracy of the algorithm, we use the self-study of the GNSS-R ocean reflex receiver system in September to December 2015 during a number of floor-based validation and flight verification. From the results of floor-based can be seen, the various conditions of building-based stability, measurement error is small, measuring the height value is better than 5 cm. The aircraft flight test due to the weather, aircraft attitude, jitter and other reasons, resulting in a larger measurement error of the system. But the total error is better than 10 cm, can meet the requirements of the use, and do a theoretical support and experimental verification for the subsequent spaceborne detection.

References

1. Clarizia MP, Bisceglie MD, Galdi C et al (2009) Delay super resolution for GNSS-R. In: Geoscience and remote sensing symposium, 2009 IEEE international, IGARSS, pp V-134–V-137
2. Valencia E, Camps A, Marchan-Hern Andez JF et al (2010) Experimental determination of the sea correlation time using GNSS-R coherent data. Geosci Remote Sens Lett 7(4):675–679
3. Semmling M, Schön S, Beckheinrich J et al (2014) Carrier phase altimetry using Zeppelin based GNSS-R observations and water gauge reference data. In: EGU general assembly conference. EGU general assembly conference abstracts, vol 16, p 11787
4. Martin-Neira M, Caparrini M, Font-Rossello J et al (2001) The PARIS concept: an experimental demonstration of sea surface altimetry using GPS reflected signals. IEEE Trans Geosci Remote Sens 39(1):142–150

Characteristics of Coordinate Time Series of Shenzhen Continuously Operating Reference Stations

Shuguang Wu, Guigen Nie and Haiyang Li

Abstract Based on the coordinate time series from Shenzhen CORS (Continuously Operating Reference Stations) during a period from 2010 to 2015, the algorithm of PCA (Principal Component Analysis) is employed in this paper to remove the CME (Common Mode Error) contained in the original series. After that, the optimal noise models of all stations' components are determined by means of computing the MLE (Maximum Likelihood Estimation) values of selective noise combinations. Meanwhile, impacts of different surface mass loadings to station displacement are computed, including atmospheric pressure, non-tidal ocean, snow and soil moisture, which partly accounts for the existence of CME. The results of these experiments show that the SNR (Signal Noise Ratio) of the original time series can be improved by 2 or 3 times after the employment of PCA, and the filtered series shows a noise characteristic of flick noise and white noise. When the colored noise is to be considered, the velocity uncertainties is 3–9 times as large as that of white noise. Surface mass loadings as a whole, is one of the sources of CME. After the deducting the impact of CME, construction and depiction of horizontal velocity field of Shenzhen area is presented in the paper.

Keywords Coordinate time series · Principal component analysis · Maximum likelihood estimation · Noise model · Surface mass loading · Horizontal velocity field

1 Introduction

Over the past 20 years, global stations of International GNSS Service (IGS) and Continuously Operating Reference Stations (CORS) of different levels have accumulated a large amount of GPS observation data, which provides a valuable data

S. Wu · G. Nie (✉) · H. Li
Global Navigation Satellite System Research Centre,
Wuhan University, Wuhan, Hubei, China
e-mail: ggnie@whu.edu.cn

J. Sun et al. (eds.), *China Satellite Navigation Conference (CSNC) 2017 Proceedings: Volume I*, Lecture Notes in Electrical Engineering 437,
DOI 10.1007/978-981-10-4588-2_19

base for geodesy and geodynamics research. By studying characteristics of coordinate time series from regional reference stations, it not only helps to understand the influence of various geophysical phenomena on the position of reference stations, but also modify kinds of error models to further improve the accuracy of reference stations [1].

In fact, various type of noises are common in GPS observation data, including time-independent white noise and time-dependent colored noises [2–4]. After data processing, these noises pass to coordinate time series. Nilolaidis [5] analyzed many GPS stations around the world and drew a conclusion that the noise in coordinate time series is closer to a superposition of white noise (WN) and flick noise (FN). Ignorance of this point, the results of velocity estimates based on the assumption of only white noise contain a certain deviation [6]. Consequently, taking the influence of colored noise into account is particularly important.

Based on observation data of five CORS stations in Shenzhen for nearly 6 years, this paper uses PANDA software to acquire single-day coordinate time series according to the PPP model of this software. Then the algorithm of PCA (Principal Component Analysis) is employed to remove the CME (Common Mode Error) contained in the original sequence. MLE (Maximum Likelihood Estimation) values of selective noise combinations are computed and then the optimal noise models of all stations' components are determined. Meanwhile, impacts of different surface mass loadings to displacement of each station is calculated, which partly accounts for the existence of CME. Finally, construction and depiction of horizontal velocity field in Shenzhen area is presented in the paper.

2 Coordinate Calculation

Since the establishment of the IGS organization, the accuracy of satellite precision orbit and clock error products has been improved, providing a reliable data foundation for accurate positioning in non-differential precision positioning. The PPP method based on non-differenced positioning model can deal with a single station, which not only avoids the problem of selecting the reference stations, but also has the advantage that the positioning results of different stations are irrelevant [7–9].

In this paper, the PPP module of PANDA software is used to calculate the coordinate time series of CORS reference stations in Shenzhen. The data used are: ① observation file: SZCORS reference stations 6-year observation files (data in Dapeng and Longgang begin in March 2012 because of hardware upgrading of the two stations); ② ephemeris files: broadcast ephemeris and IGS precision ephemeris; ③ clock errors: IGS precision clock errors. The corrections of various error models include phase winding, tropospheric model, relativistic effect, tide and so on. The least squares method is used to estimate the parameters of reference station coordinates, receiver clock errors, troposphere and non-differential ambiguities.

The original single-day coordinate sequences of SZCORS stations under the framework of ITRF2008 are obtained. It is shown that the original coordinate

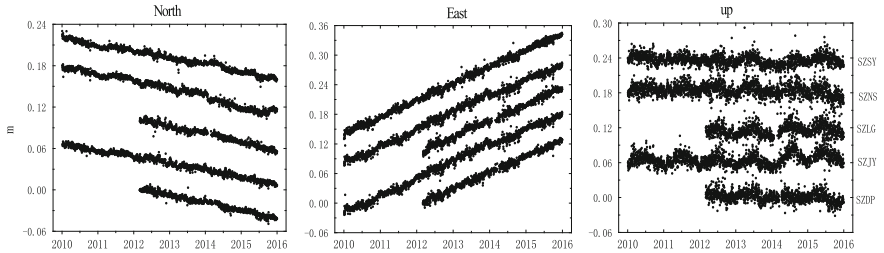

Fig. 1 Original coordinate time series of stations

sequences of these reference stations are highly correlated in time and space, as shown in Fig. 1. Because the larger common deformation characteristics of the area covers smaller deformation characteristics of internal network, it has an unneglectable influence on the study of position stability and the velocity field of the reference stations. It is common practice to eliminate the Common Mode Error (CME) by region filtering [5] to improve the SNR of the coordinate sequence. In this paper, the spatial filtering technique proposed by Dong et al. [12] is used to calculate the CME and remove it by principal component analysis.

3 Principal Component Analysis

Principal component analysis (PCA) provides just such a tool. It can decompose the network time series into a series of principal component mode. Each mode consists of a common temporal function and related different spatial responses. According to the first few principal components, the time-related characteristics of the regional network can be presented to maximum. It is applied to GPS network time series analysis to perform spatial regional filtering to remove CME [13].

For a regional network daily station coordinate time series with n stations and spanning m days, any component (north, east or vertical) from coordinate time series of a single station in network can be described as $X(t_i, x_j)(i = 1, 2, \ldots, m \text{ and } j = 1, 2, \ldots, n)$. The PCA method can decompose $X(t_i, x_j)$ into mutually orthogonal eigenvectors and corresponding time functions [12]

$$X(t_i, x_j) = \sum_{k=1}^{n} a_k(t_i) v_k(x_j) \tag{1}$$

$a_k(t_i)$ is called the kth principal component (PC) of matrix X, and $v_k(x_j)$ is its corresponding eigenvector. The decomposition results of PCA method are arranged according to the power contribution of each principal component. The first principal component is the one-dimensional variable with the most information of the whole network, usually reflecting the common change characteristics of the whole

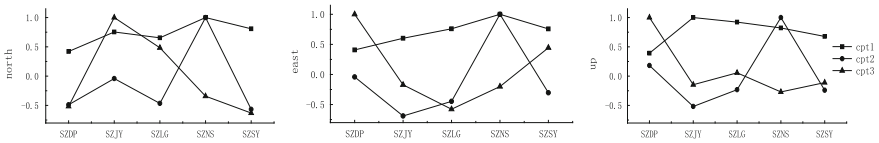

Fig. 2 Top three special eigenvectors of SZCORS coordinate time series

network. The latter components have lesser information of the whole network, as they often reflect the change characteristics of the reference station itself. The eigenvectors corresponding to these principal components reflect the spatial distribution of these temporal changes.

At first, in this paper the weighted least squares method is used to analyze the original coordinate sequences, deducting the linear term and point mutation term (caused by various tectonic and non-tectonic movements), while preserving the periodic term. Then, PCA is carried out on the newly-made coordinate series, and the spatial vectors of principal components shown in Fig. 2 is obtained. The result shows that the first principal component has a more uniform pattern of spatial distribution. The contribution rates of the first principal component to the components of the coordinate sequence are 57.03, 52.02 and 51.84% respectively, the second principal components, 20.24, 19.52, 19.88% and the third, 9.94, 10.53 and 13.10% respectively. In contrast to reference [1], the contribution rates of the first principal component obtained in this paper is 50–60%, which is relatively low. In order to reflect the common deformation of the area as full as possible, the first three principal components are defined as the CME of the whole regional network, that is

$$\varepsilon_i(t_i) = \sum_{k=1}^{3} a_k(t_i) \sum_{k=1}^{n} v_k(x_j)/n \tag{2}$$

Figure 3 shows the calculated CME sequence, we can see that the in vertical and north component is more obvious. The annual periodicity signal in vertical component is strong, while it is not obvious in east component. Filtered sequence can be acquired by deducing CME from the original coordinate sequence. In order to ensure the good effect of filtering, we can repeat the steps in this section with the filtered sequence, generally with 4 times iteration [1]. The signal-to-noise ratio (SNR) of three components of the coordinate sequences are increased by 3, 2.52

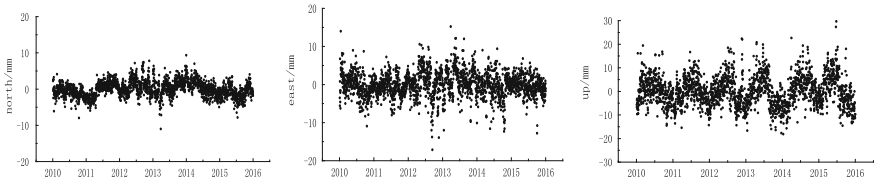

Fig. 3 Time series of common mode errors

and 2.96 times, respectively. Before filtering, the mean RMS error of all reference stations are 3, 4.92 and 9.36 mm, and after filtering they are 1, 1.95 and 3.16 mm.

4 Surface Mass Load Correction

Earth deformation obtained by GPS observations usually contains the influence of crustal non-structural deformation which can be divided into two categories. The first category is tidal deformation, including ocean tide, polar tide and solid tide; the second is the surface load changes caused by mass transfer of atmosphere and water of various states, including air, non-tidal, soil water and snow. By quantitatively calculating the influence of various non-structural deformation and correcting it, GPS method can reflect the deformation details of the earth more accurately and improve the monitoring accuracy of crustal deformation. When calculating the time series of reference stations using PANDA, the IERS03 standard model has been used to correct the influence of the solid tide and polar tide errors. The FES2004 model has been used to remove the influence of ocean tide load. However, the effect of all kinds of surface mass loading is not corrected, so it is necessary to obtain these model errors and make corresponding corrections.

The elastic deformation of the earth caused by the surface mass load is usually calculated by the Green function method [14, 15]. The method uses the surface load function $q\ (\varphi,\ \lambda)$ to estimate the surface radial elastic deformation $u\ (\varphi,\ \lambda)$. The load function $q\ (\varphi,\ \lambda)$ is developed into a sequence of spherical harmonic functions,

$$q(\varphi,\lambda) = \sum q_n(\varphi,\lambda) \tag{3}$$

$$q_n(\varphi,\lambda) = \sum [qc_{n,m}(\varphi,\lambda)\cos(m\lambda) + qs_{n,m}(\varphi,\lambda)\sin(m\lambda)]P_{n,m}(\sin\varphi) \tag{4}$$

where $\varphi,\ \lambda$ are latitude and longitude, $qc_{n,m}(\varphi,\ \lambda)$ and $qs_{n,m}(\varphi,\ \lambda)$ are Stokes coefficients of load expansion, $P_{n,m}$ is Legendre function. At this time, the surface radial deformation $u\ (\varphi,\ \lambda)$ corresponding to the surface load $q\ (\varphi,\ \lambda)$ can be expressed as

$$u(\varphi,\lambda) = \frac{3}{\rho_e}\sum_{n=0}^{\infty}\frac{h'_n}{2n+1}q_n(\varphi,\lambda) \tag{5}$$

in which ρ_e is the average density of the earth, and h'_n is the load Love function [15].

When calculating the surface mass loading in this paper, the NCEP-DOE reanalysis data[1] are used to calculate the atmospheric loading, with 6 h temporal

[1] http://www.esrl.noaa.gov/psd/cgi-bin/db_search/DBListFiles.pl?did=61&tid=53752&vid=4267.

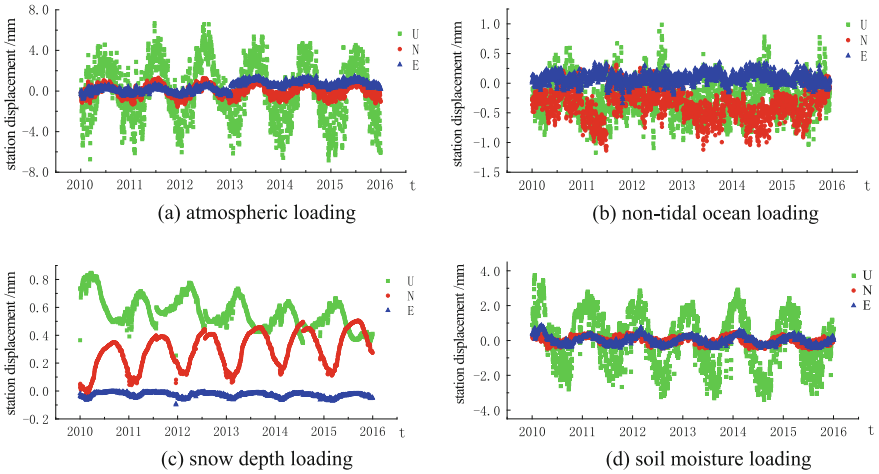

Fig. 4 Daily displacement of SZSY in U, N, E directions influenced by different surface mass loadings

resolution and 2.5° × 2.5° spatial resolution. The non-tidal ocean loading use the NOPP-ECCO ocean bottom pressure model[2] with 12 h temporal resolution and 1° × (0.3° ~ 1°) spatial resolution. The soil moisture[3] and snow loading data[4] are also from NCEP-DOM which the temporal resolution was 24 h and the spatial resolution was 1.865° × 1.884°. Based on the method of Green Function, QOCA software is used to calculate the station displacement under the influence of the above-mentioned four types of surface loadings in SZCORS stations. Figure 4 is the one-day displacement time series in U, N and E directions of Shiyan station.

The differences of surface mass loading among SZCORS stations are very small, which are below 0.1 mm of the four kinds of loading corrections. From the calculation results in Fig. 4 and other stations, it can be seen that different types of surface mass loading have the greatest influence on U direction, compared with their effect on N and E. The displacements on U direction are about 2–5 times as large as N and E, and show different periodic characteristics. As for Shenzhen, the influence of atmospheric loading on the station displacement is the largest, causing 5–8 mm station displacement on U direction. The second is the soil moisture load, and its impact on U direction is 3–4 mm. The non-tidal ocean loading and snow depth loading are smaller, causing station displacement of less than 1 mm.

Figure 5 is the average of the sum of the four kinds of surface mass loadings. It can be seen that the displacement of the reference station caused by surface mass

[2]http://ecco.jpl.nasa.gov/thredds/catalog/ecco_KalmanFilter/catalog.html.

[3]http://www.esrl.noaa.gov/psd/cgibin/db_search/DBListFiles.pl?did=59&tid=53820&vid=4281.

[4]http://www.esrl.noaa.gov/psd/cgi-bin/db_search/DBListFiles.pl?did=59&tid=53820&vid=4309.

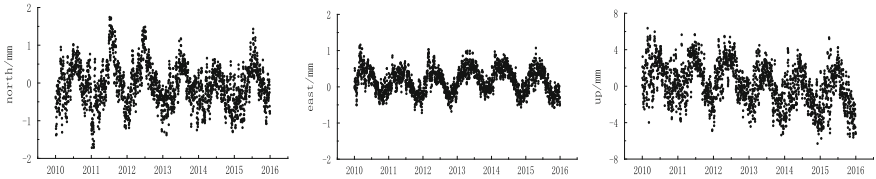

Fig. 5 Average values of five stations' mass loadings

loadings shows obvious characteristics of annual periodicity in N, E and U directions. The amount of displacement in horizontal directions is within 2 mm and vertical displacement is about 4–8 mm, with difference of around 14 mm between its maximum and minimum. In order to explore the causes of CME, we can see that there is a strong correlation between CME and the surface mass loading by comparing the vertical series in Figs. 3 and 5. It indicates that the various surface mass loadings are among the factors that cause the CME of vertical sequence. However, due to the different amplitudes of the annual periodicity, the surface mass load cannot fully explain the causes of CME. Other influencing factors such as satellite orbit error, definition of reference frame, and single station noises [16] have yet to be further explored.

5 Determination of the Optimal Noise Model

Spectral analysis and maximum likelihood estimation (MLE) are two common methods of noise analysis for coordinate sequences. Spectral analysis requires uniform sampling of the data and relies on spectral averaging, unable to estimate the spectral components using data of the longest period of time. MLE not only simultaneously estimates noise types, periodic amplitudes, stations velocities and their uncertainty but also avoids the above limitations of spectral analysis, which makes it be considered as the most accurate noise analysis method [17, 18]. Firstly, we establish the following function model for the single-day solution sequence of the coordinate components of each station.

$$\begin{aligned} y(t_i) &= a + bt_i + c\sin(2\pi t_i) + d\cos(2\pi t_i) + e\sin(4\pi t_i) \\ &\quad + f\cos(4\pi t_i) + \sum_{j=1}^{n_i} g_i H\left(t_i - T_{hj}\right) + v_i \end{aligned} \tag{6}$$

The covariance matrix C can express several random noise processes such as white noise (WH), variable white noise (VW), flicker noise (FN), random walk noise (RW), power law noise (PL), Gauss-Markov noise (GM) and so on, as well as various combinations among them. After the principal component spatial filtering to remove the CME, this paper analyzes the combinations of these noises to determine

the optimal noise model. In this paper, eight noise combinations including WH, WH + FN, WH + RW, WH + FN + RW, WH + PL, WH + GM, WH + RW + GM and VW + FN are selected. CATS software is used to calculate the MLE values of the selected noise combinations before and after CME correction. The results are shown in Tables 1 and 2.

It should be noted that in order to ensure the accurate judgment of the optimal noise model, the size of the MLE value cannot be used as the criterion simply because the MLE value tends to increase as the noise model contains more unknown parameters. According to Langbein's conservative estimation criterion [17, 22], the MLE values of WH + FN and WH + RW are calculated respectively, and the larger one is chosen as the null hypothesis. Then, the MLE values of WH + PL, WH + FN + RW, WH + GM are compared with the null hypothesis respectively. If the MLE difference is greater than 2.6, the null hypothesis is rejected and the new model is considered to be superior. Otherwise, the null hypothesis is accepted. If WH + PL, WH + FN + RW and WH + GM are all better than null hypothesis, the model with the biggest MLE value is chosen as the better model. In this way, the optimal noise model is found. Here, the threshold of WH + PL, WH + FN + RW and WH + GM are set to 2.6 and WH + RW + GM is set to 5.2. Table 3 lists the optimal noise model for each component of SZCORS stations before and after CME correction.

From Table 3, it can be concluded that: (1) The noise model of coordinate sequences in the regional reference stations is diversified, and the N, E, U components also have diversified characteristics; (2) The noise types of the 15 coordinate components of the 5 reference stations are mainly WH + FN and WH + GM before CME correction, and the noise is mainly WH + FN after CME correction. In the optimal noise models, the proportion of WH + FN model increases from 40 to 73.3%, which is consistent with the literature [17]; (3), there are different numbers of stations that the optimal noise turned to WH + FN, all five stations on U component and four stations on E component, while two stations on N component. Therefore, after CME corrections, optimal noise on U component is more uniform than that on N and E.

6 Analysis of Velocity and Its Uncertainty

Table 4 shows the velocities and uncertainties of each reference station based on WH + FN and WH. It can be seen that the horizontal velocity error estimated by the WH + FN is less than 0.4 mm and the vertical velocity error is less than 0.5 mm. By comparing the results, it is found that the velocity error calculated with colored noise is three to nine times larger than that obtained by considering white noise only. This conclusion is consistent with the results of many scholars [1, 17, 18, 20, 22]. The white noise assumption in traditional geodetic data processing is flawed

Table 1 MLE values of Shenzhen reference stations before CME correction

Name	Component	WH	WH + FN	WH + RW	WH + FN + RW	WH + PL	WH + GM	WH + RW + GM
SZDP	N	−3065.29	−2902.26	−2925.17	−2902.26	−2901.61	−2903.83	−2902.92
	E	−3833.67	−3719.10	−3732.07	−3719.10	−3719.07	−3707.86	−3707.86
	U	−4616.13	−4537.75	−4560.68	−4537.75	−4535.49	−4534.16	−4534.16
SZJY	N	−5107.86	−4553.88	−4607.03	−4553.88	−4552.94	−4563.41	−4554.16
	E	−6052.88	−5828.59	−5849.20	−5828.59	−5828.59	−5820.61	−5820.61
	U	−7449.61	−7158.85	−7204.97	−7158.85	−7154.66	−7172.53	−7154.21
SZLG	N	−3118.91	−2877.49	−2894.94	−2877.49	−2877.43	−2878.90	−2876.56
	E	−3889.49	−3776.58	−3786.53	−3776.58	−3776.56	−3771.19	−3771.19
	U	−4611.03	−4550.60	−4574.60	−4550.60	−4546.25	−4545.52	−4544.99
SZNS	N	−5575.26	−4588.59	−4618.88	−4585.62	−4586.11	−4606.29	−4585.87
	E	−6557.28	−6112.75	−6129.56	−6112.75	−6112.25	−6116.27	−6112.01
	U	−7792.71	−7607.97	−7646.13	−7607.97	−7603.95	−7611.51	−7606.94
SZSY	N	−5231.32	−4580.78	−4615.66	−4580.74	−4580.38	−4598.30	−4582.38
	E	−6094.44	−5965.56	−6003.50	−5965.56	−5957.24	−5954.61	−5954.61
	U	−7275.13	−7007.11	−7036.49	−7007.11	−7006.59	−7017.97	−7007.90

Table 2 MLE values of Shenzhen reference stations after CME correction

Name	Component	WH	WH + FN	WH + RW	WH + FN + RW	WH + PL	WH + GM	WH + RW + GM	VW + FN
SZDP	N	−2531.54	−2480.23	−2507.53	−2480.23	−2473.13	−2470.26	−2470.26	−2480.23
	E	−2819.33	−2801.20	−2807.79	−2801.20	−2799.42	−2800.45	−2800.45	−2801.20
	U	−1948.08	−1935.83	−1940.83	−1935.83	−1933.83	−1934.18	−1934.35	−1935.83
SZJY	N	−2543.54	−2424.51	−2439.40	−2424.51	−2423.70	−2432.81	−2422.80	−2424.51
	E	−4750.56	−4619.07	−4631.71	−4619.07	−4619.06	−4619.11	−4619.11	−4771.14
	U	−5708.22	−5677.10	−5683.08	−5677.10	−5676.98	−5677.68	−5677.39	−5677.15
SZLG	N	−2171.28	−2144.86	−2154.62	−2144.86	−2142.34	−2143.92	−2143.59	−2144.86
	E	−2996.17	−2921.17	−2929.11	−2921.17	−2921.15	−2923.77	−2922.01	−3003.62
	U	−3939.89	−3926.38	−3931.51	−3926.38	−3924.68	−3925.72	−3925.54	−4035.18
SZNS	N	196.66	267.52	249.40	267.52	270.19	264.92	268.58	267.52
	E	−1725.76	−1591.02	−1603.62	−1591.02	−1591.02	−1590.90	−1590.90	−1738.83
	U	−1563.22	−1538.08	−1542.60	−1538.08	−1537.84	−1539.71	−1537.89	−1746.99
SZSY	N	−2913.45	−2774.37	−2810.68	−2774.37	−2768.88	−2774.27	−2770.40	−2774.38
	E	−4768.37	−4734.36	−4747.12	−4734.36	−4732.37	−4731.67	−4731.67	−4896.51
	U	−6410.30	−6249.15	−6264.48	−6249.15	−6248.90	−6255.54	−6248.84	−6369.09

Table 3 The optimal noise model of each component before and after CME correction

Name	N		E		U	
	Before	After	Before	After	Before	After
SZDP	WH + FN	WH + GM	WH + GM	WH + FN	WH + GM	WH + FN
SZJY	WH + FN	WH + FN	WH + GM	WH + FN	WH + PL	WH + FN
SZLG	WH + FN	WH + FN	WH + GM	WH + FN	WH + GM	WH + FN
SZNS	WH + FN + RW	WH + PL	WH + FN	WH + FN	WH + PL	WH + FN
SZSY	WH + FN	WH + PL	WH + GM	WH + GM	WH + FN	WH + FN

Table 4 The contrast of stations' velocities and their uncertainties between WH + FN and WH models

Name	N		E		U	
	WH + FN	WH	WH + FN	WH	WH + FN	WH
SZDP	−10.90 ± 0.302	−11.23 ± 0.039	33.17 ± 0.195	32.88 ± 0.048	−2.00 ± 0.090	−1.88 ± 0.025
SZJY	−9.98 ± 0.066	−9.82 ± 0.010	34.44 ± 0.194	34.66 ± 0.029	1.07 ± 0.188	1.33 ± 0.045
SZLG	−11.84 ± 0.154	−11.80 ± 0.033	33.69 ± 0.342	33.15 ± 0.062	1.18 ± 0.483	2.26 ± 0.129
SZNS	−11.35 ± 0.017	−11.92 ± 0.003	33.21 ± 0.048	33.55 ± 0.007	−1.19 ± 0.024	−1.06 ± 0.007
SZSY	−10.24 ± 0.113	−9.82 ± 0.0120	33.84 ± 0.156	33.80 ± 0.030	−0.89 ± 0.458	−0.72 ± 0.065

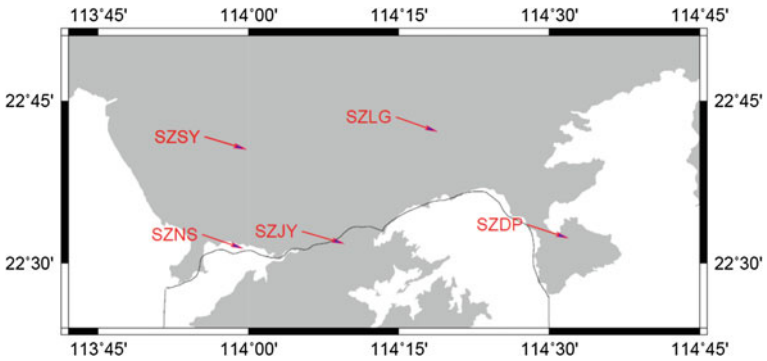

Fig. 6 The horizontal velocity field of Shenzhen CORS

when GPS observations are used to determine the velocity field and its error estimate. It is also necessary to consider the output of error estimates by data processing software in GPS time series analysis. As shown in Fig. 6, it can be seen that the Shenzhen area as a whole is moving at an average speed of 35.39 mm per year in a direction from 16°10′ to 19°22′ east to south.

7 Conclusions

Based on the observation data of CORS station in Shenzhen, the following conclusions are obtained.

(1) The original coordinate sequences of Shenzhen CORS stations have a high correlation in time and space, and the SNR of the three components (north, east and vertical) of the coordinate sequences are increased by 3, 2.52 and 2.96 times respectively after principal component spatial filtering.
(2) Regional CME has a strong correlation with the surface mass loadings, which indicates that all kinds of surface mass loadings are the factors that cause the vertical sequence of CME. However, due to the different amplitudes of the annual periodicity, the surface mass loading cannot fully explain the cause of CME.
(3) Noise models of the reference station coordinate sequence are diversified, and the N, E, U components also have different characteristics. The noise types of coordinate components are mainly WH + FN and WH + GM before CME correction, while the noise type is mainly WH + FN after CME correction, and the proportion of WH + FN increases from 40 to 73.3%. After CME corrections, optimal noise on U component is more uniform than that on N and E.
(4) The horizontal velocity error estimated by WH + FN model is less than 0.4 mm and the vertical velocity error is less than 0.5 mm. In general, CORS data can be used to construct the 3D velocity field of less than 0.5 mm per year. The velocity error calculated with colored noise is three to nine times larger than that obtained by considering white noise only. So the velocity estimation based on the white noise assumption will result in the deviation of the result. The influence of this deviation must be taken into account when constructing millimeter-scale velocity field.

Acknowledgements The 6-year CORS data provided by the Shenzhen Cadastral Surveying and Mapping Office; the precision ephemeris and clock error products provided by IGS; the helpful discussion with Prof. Dong Danan and Dr. He Xiaoxing in the calculation of surface loading correction; guidance and recommendations from Dr. Yuan Linguo in determining CME; CATS software and manuals from Dr. Simon D. P. Williams, as well as warm-hearted help from Guo Xiangxin and Zhou Boye, my sincere gratitude to all above!

References

1. Yuan L, Ding X, Chen W (2008) Characteristics of daily position time series from the Hong Kong GPS fiducial network. Chin J Geophys 05:1372–1384
2. Mao A, Harrison CGA, Dixon TH (1999) Niose in GPS coordinate time series. J Geophys Res 104(B2):2797–2816
3. Han Y,Fu Y (2003) Analysis of GPS time series of height component. Geomatics Inf Sci Wuhan Univ 28(4):425–428

4. Qiao Xuejun, Wang Qi, Wu Yun (2003) Time series characteristic of GPS fiducial stations in China. Geomatics Inf Sci Wuhan Univ 04:413–416
5. Nikolaidis R (2002) Observation of geodetic and seismic deformation with the global positioning system. University of California, San Diego
6. Liren H (2006) Noise properties in time series of coordinate component at GPS fiducial stations. J Geodesy Geodyn 02:31–33 + 38
7. Fang R (2010) High-Rate GPS data non-difference precise processing and its application on seismology. Wuhan University, Wuhan
8. Kejie C, Rongxin F, Min L et al (2011) Research on application of PANDA software to high frequency kinematic precise point positioning. J Geodesy Geodyn 31(4):132–134 + 143
9. Geng T, Zhao Q, Liu J et al (2007) Real-time precise point positioning based on PANDA software.Geomatics Inform Sci Wuhan Univ 32(4):312–315
10. Liu J, Ye S (2002) GPS precise point positioning using undifferenced phase observation. Geomatics Inform Sci Wuhan Univ 27(3):234–240
11. Zhao Q, Guo X, Li M et al (2016) Calculation of horizontal movement velocity field of chinese continent using PANDA software. J Geodesy Geodyn 36(4):338–342
12. Dong D, Fang P, Bock Y et al (2006) Spatiotemporal filtering using principal component analysis and Karhunen—Loeve expansion approaches for regional GPS network analysis. J Geophys Res Sol Ea 111(B3):B03405. doi:10.1029/2005JB003806
13. http://qoca.jpl.nasa.gov/tutor_base.html
14. Dong D, Fang P, Bock Y et al (2002) Anatomy of apparent seasonal variations from GPS-derived site position time series. J Geophys Res Sol Ea 107(B4):2075. doi:10.1029/2001JB000573
15. Farrell WE (1972) Deformation of earth by surface loads. Rev Geophys Space Ge 10(3):761
16. Tian Y (2011) Study on intermediate- and long-term errors in GPS position time series. Institute of Geology, China Earthquake Administration, Beijing
17. Li Z, Jiang W, Liu H et al (2012) Noise model establishment and analysis of IGS reference station coordinate time series inside china. Acta Geod Cartogr Sin 41(4):496–503
18. Zhang J, Bock Y, Johnson H et al (1997) Southern california permanent geodetic array: error analysis of daily estimates and site velocities. J Geophys Res 102(B8):18035–18055
19. Bock Y (2004) Environmental issues and monumentation. IGS workshop. Bern, l Mar 2004
20. Langbein J (2004) Noise in two-color electronic distance meter measurements revisited. J Geophys Res 109(B4):1–16
21. Williams SDP (2004) Error analysis of continuous GPS position time series. J Geophys Res 109(B3):412–430
22. Langbein J (2008) Noise in GPS displacement measurements from Southern California and Southern Nevada. J Geophys Res 113(B5):1–12

Voxel Nodes Model Parameterization for GPS Water Vapor Tomography

Nan Ding, Shubi Zhang, Xin Liu and Yili Xia

Abstract Water vapor is the basic parameter to describe atmospheric conditions and the content of it in the atmosphere is rare for water circulation system, but it is the most active element with quick space-time change. GPS tomography is a powerful way to provide high spatiotemporal resolution of water vapor density. In general, water vapor tomography utilizes slant wet delay information from ground-based GPS network to reconstruct the humidity field. Space at the zenith directions of ground-based GPS is discretized into voxel both at horizontal and vertical direction; setting up tomographic equations by slant delay observations can work out vapor parameter in voxel. In this paper, spatial structure model of humidity field is constructed by voxel nodes, and new parameterizations for acquiring data of water vapor in the troposphere by GPS are proposed based on inverse distance weighted (IDW) interpolation in horizontal and vertical interpolation function in vertical. Unlike the water vapor density is constant within a voxel; the density at a certain point is determined by new parameterizations. This algorithm avoids using horizontal constraint to smooth some voxels that not be crossed by satellite rays. Grouping and sorting access order scheme is introduced to minimize correlation between SWV observations. Three experimental schemes for GPS tomography are carried out using 7 days of Hong Kong Satellite Positioning Reference Station Network (SatRef). The results indicate that water vapor density derived from 4 nodes parameterization are most robust than 8 nodes and 12 nodes.

Keywords GPS water vapor tomography · Inverse distance weighted interpolation · Vertical interpolation function · Grouping and sorting access order

N. Ding (✉) · S. Zhang · X. Liu · Y. Xia
School of Environment Science & Spatial Informatics, CUMT,
1 Daxue Road, Xuzhou, China
e-mail: metdingnan@163.com

J. Sun et al. (eds.), *China Satellite Navigation Conference (CSNC) 2017 Proceedings: Volume I*, Lecture Notes in Electrical Engineering 437,
DOI 10.1007/978-981-10-4588-2_20

1 Introduction

Based on the GPS meteorology technique [2], two experiments promoted the development of GPS integrated water vapor (IWV) inversion: GPS/STORM [13] and the GPS–Winter Icing and Storms Project experiment [6]. Both experiments showed that GPS is a cost-effective and reliable means of continuously monitoring IWV with accuracies comparable to water vapor radiometer (WVR) and radiosonde (RS). However, the IWV is a measure of the total amount of water vapor above a certain station and it cannot provide the information on the spatial distribution of water vapor. In order to meet the demand, GNSS water vapor tomography [1, 3–5, 7, 10, 14–16, 19] came out as a promising method providing information on the four-dimensional distribution of the water vapor in the troposphere.

In this paper, a new parameterized approach instead of traditional constraints is introduced, which is based on IDW interpolation and vertical interpolation function. The new algorithm is investigated by the data of SatRef. The experiment mainly analyzes and discusses the influences of different numbers of voxel nodes on the results of GPS water vapor tomography. The question about some voxels may not be crossed by any signals is addressed by IDW interpolation.

2 Voxel Nodes Model Parameterization for GPS Tomography

The slant water vapor (SWV) is the integrated water vapor along the slant path. Specific GPS processing techniques provide this product as the observations for GPS tomography. Using SWV input data the tomography observations in the absolute humidity can be expressed by [1]:

$$SWV = \int_s H_s ds + RB \tag{1}$$

where Hs is the absolute humidity, s is the slant path, RB is the partial water vapor caused by ray bending. The second term is due to ray bending. However, the effect of this geometric water vapor, making much smaller contribution to SWV, can be neglected [8].

Voxel nodes model (VNM) parameterization assumes that troposphere is divided into a numbers of layers which constructed by neighboring parallel planes (see Fig. 1). The voxel nodes (blue points) are designed in each plane. SWV produced by one signal (red line) is discretely modeled by the value at points of intersection between straight line and planes.

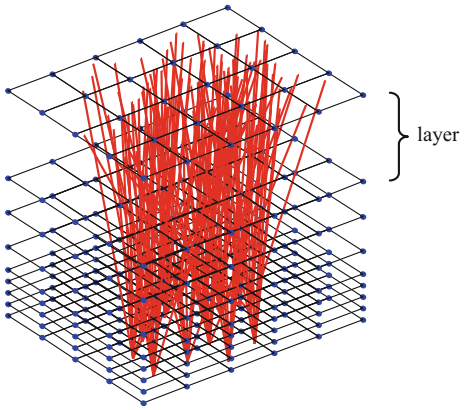

Fig. 1 Voxel nodes structure of GPS tomography model and the distribution of signal rays (*red line*) crossing the layers, the value of SWV divides into the value of water vapor at voxel nodes (*blue point*)

In the VNM parameterization, Eq. 1 is decomposed into sum of piecewise integration:

$$SWV = \sum_{i=1}^{n} \int_{s_i}^{s_{i+1}} H_s(i)ds \tag{2}$$

where n is the number of layer, Hs(i) is the absolute humidity in i-th of layer.

Piecewise integration in Eq. 2 can be addressed through Newton-Cotes formulae [11]. It is assumed that the value of piecewise integration defined on $[s_i, s_{i+1}]$ is known at equally spaced point p_1-p_5 (see Fig. 2). This allows the integral in Eq. 2 to be expressed as a weighted sum of the water vapor density at the voxel nodes. In this paper, the closed Newton–Cotes formula of degree 4 is utilized with water vapor density at the 5 equally spaced points. Point p_1 and p_5 in the plane i and (i + 1) respectively can be estimated by inverse distance weighted (IDW) interpolation. IDW parametrical method explicitly implements the assumption that the value of water vapor density that are close to one another are more alike than those that are farther away. The IDW interpolation can be given as

$$P_{IDW} = \begin{cases} \dfrac{\sum_{j=1}^{m} D(P,x_{node}^{j})^{-1} \cdot x_{node}^{j}}{\sum_{j=1}^{m} D(P,x_{node}^{j})^{-1}}, & \text{if } D(P,x_{node}^{j}) \neq 0 \text{ for all j} \\ x_{node}^{j}, & \text{if } D(P,x_{node}^{j}) = 0 \text{ for some j} \end{cases} \tag{3}$$

where $D(P,x_{node}^{j})$ is the distance between pierce point P_{IDW} and voxel node x_{node}^{j}, x_{node}^{j} is the value of water vapor at a certain voxel node, and m is the number of voxel node which is used for IDW interpolation. In the case of point p_2-p_4, correspondence between the value of equally spaced points and projection points would be defined by using vertical interpolation function (VIF) in the relatively

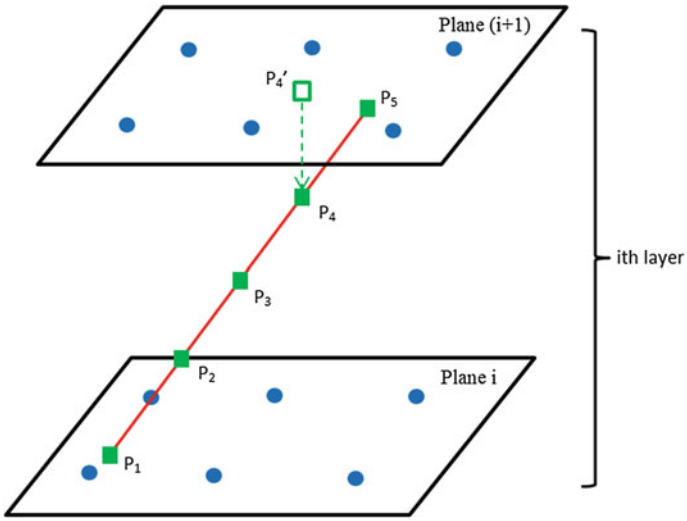

Fig. 2 Voxel nodes parameterized design based on the closed Newton–Cotes formula of degree 4 and interpolation. Voxel nodes (*blue points*) are used for equally spaced points (*green square*) interpolation. P'_4 (*green hollow square*) is projection point of P_4 in plane (i + 1)

nearby plane between plane i and (i + 1). VIF based on the exponential law [12, 17] can be expressed by the formula

$$P = P'_{IDW} e^{-Z/H} \tag{4}$$

where P is the water vapor density of the equally spaced points, P'_{IDW} is the water vapor density of projection points which can be expressed by Eq. (3), Z is the height between P and P'_{IDW}, H is the water vapor scale height, which can be calculated by Eq. (5) [18]

$$H = \frac{10W}{\rho_s} \tag{5}$$

where W is the vertical total water vapor content in g/m^2, ρ_s is the surface humidity in g/m^3. W can be obtained from PWV. Ground-based GPS network, for the purpose of meteorological monitoring, provides meteorological parameter, which can be used for calculating ρ_s.

However, grid points not used in any interpolation should not generally be avoided. In fact, this case often occurs in lower-level layers with the 4 nodes method, and occurs less often when many points are included in the interpolation. We also address "empty" grids using the inverse distance weighted (IDW) interpolation. The values of an "empty" grid are estimated by the "non-null" grids around it.

Based on Eqs. (2)–(4), the GPS tomography equations could be constructed

$$A \cdot X = b \tag{6}$$

where A is the coefficient matrix of GPS tomography model, b presents the SWV observations vector, X is the value of the humidity at all designing voxel nodes.

Algebraic reconstruction techniques (ART) have successfully been used to reconstruct the humidity field [1, 3]. An advantage of ART is that it has high numerical stability even under bad conditions and it is relatively easy to incorporate prior knowledge into the reconstruction process.

In our study, grouping and sorting access order [9] is used for improving the accuracy of inversion. It is desirable to order the SWV observations (SWVs) such that subsequently applied SWV are largely uncorrelated. This means that consecutively available SWVs must have significantly different values, because the value of SWV is determined by the azimuth and elevation angles of a signal. If the SWV in a set have similar values solved by ART, the results tend to move away from the desired solution, which delays convergence. To summarize, the principle of SWV access order is that in a subsequence of iterations, steps should be as independent as possible from the previous steps.

3 GPS Tomography Results

3.1 Tomography Strategy

SatRef is a local satellite positioning system covering the extent of Hong Kong. The network consists of 18 Continuously Operating Reference Stations (CORS) and 14 of them were used in this study. The area of investigation ranges from 113.749° to 114.474°E longitude and from 22.115° to 22.651°N latitude (Fig. 3a) with a height domain of 0–10,800 m (Fig. 3b). The horizontal and vertical station distributions are presented in Fig. 3a and Fig. 3b, respectively. The number of spatial voxel nodes (Fig. 3a) using for tomography are $6 \times 4 \times 10$ with a horizontal resolution of 0.145 (15 km). Non-uniform layers are adopted with the interval from 500 to 3800 m (Fig. 3b). We made the hypothesis that all the value of water vapor at any point in the plane is determined by a weighted average of the value at voxel nodes that closest the point. The experiments used for reconstruction of the humidity field covered a seven-day period from August 9–15, 2015 (day of year, DOY 221–227). Samples of GPS and surface meteorological data are obtained in 30 s intervals, with a temporal resolution of 30 min.

The data from Hong Kong network are processed with GAMIT software version 10.5. Based on number of voxel nodes are used for IDW interpolation points P, three sets of schemes are presented

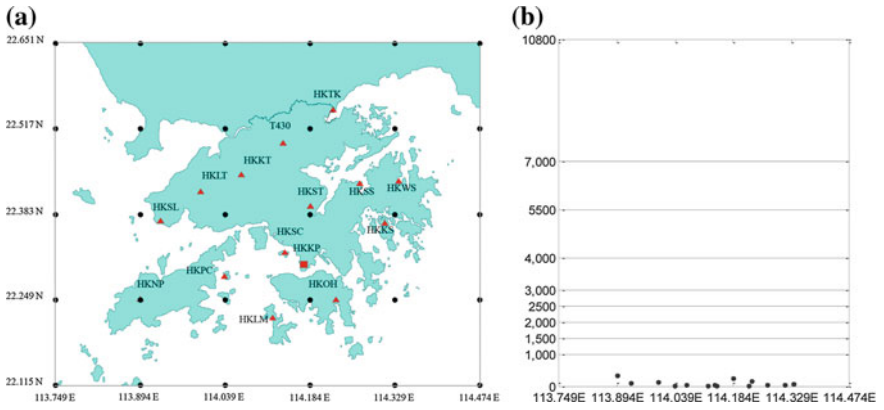

Fig. 3 **a** Distribution of the Hong Kong reference stations (*red triangle*) and the King's Park meteorological station (*red square*). The *gray wireframe* indicates the plane that contains voxel nodes (*black dot*) using in the tomographic processing. The study area was discretized into $6 \times 4 \times 10$ voxel nodes for the water vapor tomography. **b** The vertical structures of the voxel nodes model used in the tomographic processing

- 4 nodes: four voxel nodes (neighbors) from voxel nodes model will be used
- when calculating a water vapor value for the piercing point.
- 8 nodes: eight voxel nodes will be used when calculating a water vapor value for the piercing point.
- 12 nodes: twelve voxel nodes will be used when calculating a water vapor value for the piercing point.

3.2 Analysis of Total Statistics

Three kinds of solutions compare with radiosonde data (RS) in Hong Kong. Because of limited space, only a representative example at 2015–08–09 (DOY 221) UTC 0 and 12 is shown (see Fig. 4). It is clear that all of the water vapor profiles increasing height. At UTC 12, the variation of water vapor from radiosonde data presents disturbance instead of keeping smooth decrease. But the tomographic solutions keep consistent with changing trends of radiosonde data. In each plane (Fig. 3b), mean water vapor density in voxel nodes are computed. It indicates that the humidity with high spatial resolution (e.g. radiosonde) is difficult to retrieve because of the limited accuracy of tomography solution. It is difficult to judge which scheme is best suited for GPS water vapor tomography from the statistics of RMSE, IQR and BIAS data (Table 1). These methods have their advantages respectively; 4 nodes parametrization presents more accurate results than others from RMSE. The inter quartile range (IQR), to some extent, reflects the discreteness of datasets. Based on the value of IQR (Table 1) and scatter plots of water

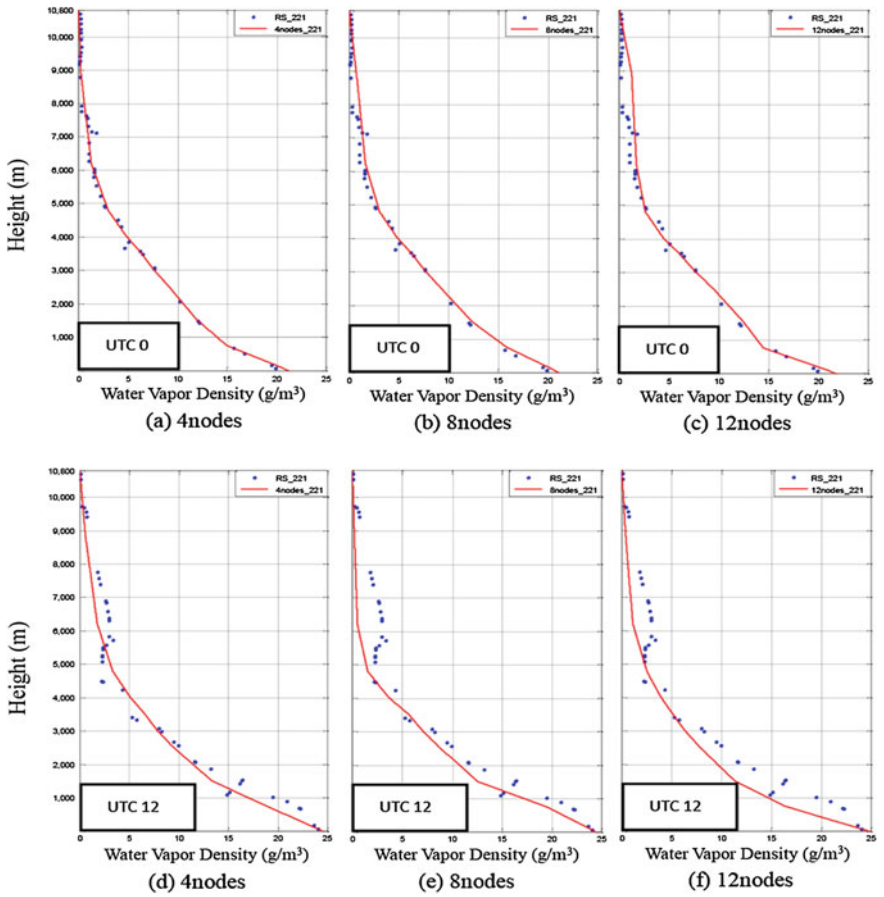

Fig. 4 Comparison of HKKP's radiosonde data (*blue dot*) with three sets of water vapor tomography schemes (*red lines*) at DOY 221 2015 UTC 0 and 12, respectively. (red lines) reconstructed by tomographic solutions accord with radiosonde data. At UTC 0, all profiles and the scatter of radiosonde data decrease exponentially with increasing height. However, at UTC 12, radiosonde data unable to keep smooth

vapor density (Fig. 5), it is clear to find that tomographic solutions computed by 4 nods and 8 nodes parameterizations more concentrated than 12 nodes.

However, compared with the first two methods, 12 nodes tomographic has a smallest negative bias (Table 1) with highest discretization. These statistical properties of the differences between three parametrizations and radiosonde data are also presented by box plots (Fig. 5d). It contains five characteristic values: the first and third quartiles (Q1 and Q3) at the bottom and top of the box, the second quartile (Q2) is located inside the box (the median) and the ends of the whiskers (upper and lower bound) at Q1 − 1.5(IQR) and Q3 + 1.5(IQR). In addition, whiskers are applied to detect outliers (cross in Fig. 5d). All of these are summarized in Table 1.

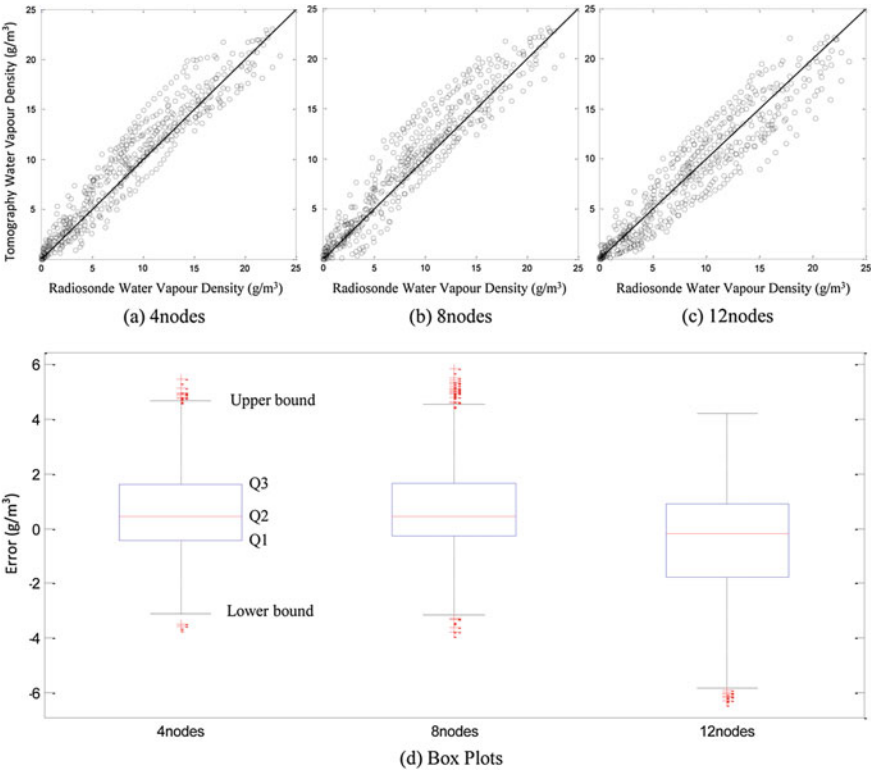

Fig. 5 Tomographic solutions compared with radiosonde data. **a**–**c** Scatter plots of water vapor density with 4 nodes, 8 nodes and 12 nodes parameterization and **d** Box plots of the difference between three parametrization methods and radiosonde data at UTC0 and UTC12 from August 9 to 15, 2015

Table 1 Statistics between three parameterizations and water vapor measurements constructed by HKKP's radiosonde data for 7 days (DOY 221–227) in 2015

Statistics	4 nodes	8 nodes	12 nodes
RMSE (g/m^3)	1.857	2.016	2.092
IQR (g/m^3)	1.948	2.048	2.702
BIAS (g/m^3)	0.65	0.742	−0.336
Q1	−0.42	−0.275	−1.792
Q2	0.436	0.458	−0.169
Q3	1.628	1.673	0.91
Upper bound	4.701	4.594	4.964
Lower bound	−3.4925	−3.196	−5.846
Number of outliers	16	34	8

IQR is the difference between Q3 and Q1 quartiles. It is important because IQR represents the spread of data and unlike total range, it is not be affected by outliers. Q2 is the measure of central tendency and in good accordance with the bias. Upper and lower bound can be used to identify outliers. The 12 nodes has the smallest number of outliers, but it also has maximum bounds. 4 nodes and 8 nodes have similar bounds. However, if we use the bounds of 4 nodes, the number of outliers is 34 and 58 in 8 nodes and 12 nodes respectively. So compare 4 nodes parametrization with others has relative minimal outliers

4 Conclusion and Outlook

In this paper, a new GPS tomographic parameterization approach is proposed in our study. This approach can reconstruct a humidity field without using horizontal constraint and avoid some voxels not be crossed by satellite rays. On the other side, instead of dividing the troposphere into several layers with identical height, the vertical structure of tomography model adopts non-uniform layers to satisfy inherent characteristics of water vapor distribution and to lower the effect of difference magnitude between the calculated tomographic results. In order to minimize correlation in projection access, grouping and sorting access order scheme is developed to order the SWV observations in such a way that subsequently applied values of SWVs are largely uncorrelated. Based on number of voxel nodes is selected for IDW interpolation, three schemes are designed to retrieve water vapor density in voxel node.

Results of Hong Kong tomographic experiments using GPS data from DOY 221–227, 2015 show that this proposed approach is validated for GPS tomography. We discuss and analyze 4 nodes, 8 nodes and 12 nodes parameterizations. The 4 nodes method has highest accuracy with perturbations of 1.857 g/m^3 compare to the two other methods regarding the overall dataset. However, due to the limitation of tomographic accuracy, mean water vapor density computed by GPS tomography is hard to retrieve humidity field with the high spatial resolution of radiosonde. From results of different statistical methods, we can draw a conclusion that 4 nodes parametrization has relative minimal outliers and the error caused by it more concentrated than others. It means that tomographic results derived from 4 nodes have a higher stability and reliability.

Further investigations are needed to improve the horizontal structure of humidity field by adjust node position in each layer to fit distribution of satellite rays. Flexible layout is the advantage of voxel nodes model. In the future, fusion of GNSS and external measurements from other sensors in GPS tomography system will be a prospective direction to enhance stability and reliability of water vapor tomography and to decrease intervals of tomography.

References

1. Bender M, Dick G, Ge M et al (2011) Development of a GNSS water vapor tomography system using algebraic reconstruction techniques. Adv Space Res 47:1704–1720
2. Bevis M, Businger S, Herring TA et al (1992) GPS meteorology: remote sensing of atmospheric water vapor using the global positioning system. J Geophys Res Atmos 97:15787–15801
3. Chen B, Liu Z (2014) Voxel-optimized regional water vapor tomography and comparison with radiosonde and numerical weather model. J Geodesy 88:691–703
4. Flores A, Ruffini G, Rius A (2000) 4D tropospheric tomography using GPS slant wet delays. Ann Geophys-Ger 18:223–234
5. Gradinarsky LP, Jarlemark P (2004) Ground-based GPS tomography of water vapor: analysis of simulated and real data. J Meteorol Soc Jpn 82:551–560
6. Gutman S, Chadwick R, Wolfe D et al. (1995) Toward an operational water vapor remote sensing system using the global positioning system. Environmental Sciences Div, USDOE Office of Energy Research, Washington, DC (United States)
7. Hirahara K (2000) Local GPS tropospheric tomography. Earth Planets Space 52:935–939
8. Ichikawa R, Kasahara M, Mannoji N et al (1995) Estimations of atmospheric excess path delay based on three-dimensional, numerical prediction model data. J Geodetic Soc Jpn 41:379–408
9. Nan D, Shubi Z (2016) Land-based GPS water vapor tomography with projection plane algorithm. Acta Geod et Cartographica Sin 45:895–903
10. Nilsson T, Gradinarsky L (2006) Water vapor tomography using GPS phase observations: simulation results. IEEE T Geosci Remote 44:2927–2941
11. Perler D, Geiger A, Hurter F (2011) 4D GPS water vapor tomography: new parameterized approaches. J Geodesy 85:539–550
12. Reitan CH (1963) Surface dew point and water vapor aloft. J Appl Meterology 2:776–779
13. Rocken C, Hove TV, Johnson J, Solheim F, Ware R, Bevis M, Chiswell S, Businger, S (1995) GPS/STORM-GPS sensing of atmospheric water vapor for meteorology. J Atmos Ocean Tech 12:468–478
14. Rohm W (2013) The ground GNSS tomography-unconstrained approach. Adv Space Res 51:501–513
15. Seko H, Shimada S, Nakamura H et al (2000) Three-dimensional distribution of water vapor estimated from tropospheric delay of GPS data in a mesoscale precipitation system of the Baiu front. Earth Planets Space 52:927–933
16. Song SL, Zhu WY, Ding JC et al (2006) 3D water-vapor tomography with Shanghai GPS network to improve forecasted moisture field. Chin Sci Bull 51:607–614
17. Tomasi C (1981) Determination of the total precipitable water by varying the intercept in reitan's relationship. J Appl Meterology 20:1058–1069
18. Tomasi C (1977) Precipitable water vapor in atmospheres characterized by temperature inversions. J Appl Meteorol 16:237–243
19. Yao YB, Zhao QZ, Zhang B (2016) A method to improve the utilization of GNSS observation for water vapor tomography. Ann Geophys-Ger 34:143–152

The Spatial Deformation Characteristic Analysis of CORS Stations: A Case Study of Tianjin CORS

Wei Wang, Zhong Jie Sheng, Qi Zhang, Yong Huang and Bastiaan van Loenen

Abstract The general processing procedure and models for CORS stations' spatial deformation characteristic analysis are presented in this paper. The soft threshold filtering formula is deduced, which is for the Daubechies wavelet denoising, by utilizing the variance–covariance of Tianjin CORS baselines solution. The methods and models are adopted for Tianjin CORS datasets processing and the numerical results are calculated: the maximum annual deformation rate in U direction is up to 40 mm/yr, the accumulated deformation in plane and height direction are up to 84 and 400 mm separately. Based on the analysis, the suggestive updating frequency for Tianjin Geoinformation Reference Frame which sustained by Tianjin CORS should be 3–4 years in plane and 1 year in height. The experience and models can also be referenced by any other city CORS.

Keywords CORS · Spatial deformation · Wavelet denoise · Soft threshold filter

1 Background

Currently most cities have established Continuous Operation Reference System (CORS), which plays an irreplaceable role in the city construction. Generally, in order to keep the stability of the CORS stations, the establishment of CORS must be obey the strict serials construction regulations. However, the CORS stations are inevitable to be unstable with time goes by because of the curst movement, the underwater exploitation as well as the skyscraper construction. The slow movement of the CORS stations will cause the Geoinformation Reference Frame which is the basic reference to all geoinformation collection to be spatial tortuosity and

W. Wang (✉) · Z.J. Sheng · Q. Zhang · Y. Huang
Tianjin Institute of Surveying and Mapping, Tianjin, China
e-mail: wangwei_sgg@163.com

B. van Loenen
Architecture and the Built Environment, TU Delft, Delft, The Netherlands

J. Sun et al. (eds.), *China Satellite Navigation Conference (CSNC) 2017 Proceedings: Volume I*, Lecture Notes in Electrical Engineering 437,
DOI 10.1007/978-981-10-4588-2_21

deformation. This results the collected geoinformation biases away from the true position since which is referenced by the Geoinformation Reference Frame [1].

In order to keep the stability and reliability of the CORS stations, it is feasible to analyse and model the spatial deformation by utilizing the long-time observation CORS datasets, and feedbacking the result to modify the Geoinformation Reference Frame. Many scholars have deeply researched the algorithms and methodology for GNSS time serials processing, such as Principal Component Analysis (PCA) [2] and wavelet analysis [3]. Those methods have also applied to national CORS datasets processing and achieved some suggestion conclusions [4].

This paper, taking Tianjin CORS as an example, studies the general processing methodology of the characteristics and spatial deformation of local CORS with almost ten-year collected data. The formula, which is used for the denoising soft threshold setting, was deduced by utilizing the variance–covariance of baseline processing results. By applying the general processing methodology and model, the spatial deformation characteristic of Tianjin CORS was obtained. Based on this results, the advised update frequency of Tianjin Geoinformation Reference Frame which maintained by Tianjin CORS was proposed. The methodology and models presented in this paper can also be referenced by any other city level CORS during its systematic maintenance.

2 The Models and Methods for the CORS Spatial Deformation Characteristic Analysis

In this section, we first introduce the general CORS datasets processing procedure and classify the procedure into five key points, and then deduce the soft threshold setting formula for Daubechies wavelet denoising by applying the variance–covariance value of baseline solution results, at last the time serials trend and detail analysis methods which used for Tianjin CORS datasets processing are briefly summarized.

2.1 General Methodology

The key points of the CORS spatial deformation characteristic analyzing focus on CORS data pre-processing, CORS network baseline processing, the reference point affirmation for the CORS network spatial deformation analyzing, CORS stations' time serials analysing and the whole CORS spatial deformation characteristic analysis. Those five key points covered the datasets pre-processing, datasets processing and results analysing and application. The CORS datasets pre-processing and baseline processing are normal steps which are no difference with the GNSS dataset processing. This paper mainly focuses on the soft threshold Daubechies

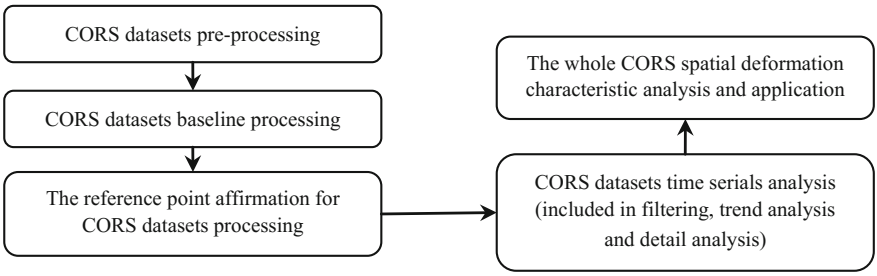

Fig. 1 The characteristic analysis flow chart of CORS station datasets processing

wavelet denoising processing and the CORS time serials analysing and processing. The general CORS datasets processing flow chart is as Fig. 1.

2.2 The Filtering for the CORS Time Serials Analysis

The filtering for the CORS time serials is adopted by soft threshold Daubechies wavelet denoising. Many researchers have deeply studied data filter methodologies, such as the robust filtering [5, 6] and the adaptive filtering [7, 8]. The wavelet analysing is widely adopted for GNSS time serials processing for that the wavelet can de-composite signal into multi-level details [9–11], the unwanted high frequency noise can be filter out and then the signal is reconstructed.

In this paper, Daubechies wavelet is adopted for Tianjin CORS time serials multi-level decomposition, utilizing transferred variance-covariance of the baseline solutions as the threshold to filter out the high frequency noise, then the signal is reconstructed. The basic theory of wavelet denoising will not be demonstrated in this paper because of the limitation of the paper length, instead the soft threshold setting formula for the wavelet filter is presented.

Considering the signal slowly change characteristic during the filter processing, the variance-covariance of the baseline processing results is used for the soft threshold setting by considering the interconnection of the different coordination systems' transformation.

Supposing the baseline processing variance–covariance in x, y and z direction is $D_{baseline}$, and $D_{baseline}$ can be denoted as:

$$D_{baseline} = \begin{bmatrix} \delta_x^2 & \delta_{xy} & \delta_{xz} \\ & \delta_y^2 & \delta_{yz} \\ & & \delta_z^2 \end{bmatrix} \tag{1}$$

Hereby, δ_x, δ_y and δ_z are the Root Mean Square in x, y and z directions separately. Using the differential formula to translate Earth Center Earth Fix (ECEF)

coordinate to Geodetic coordinate which will be used for the NEU coordination calculation:

$$\begin{bmatrix} dL \\ dB \\ dH \end{bmatrix} = C_{coefficent} \begin{bmatrix} dX \\ dY \\ dZ \end{bmatrix} \tag{2}$$

$$C_{coefficent} = \begin{bmatrix} -\frac{\sin L}{(N+H)\cos B} & \frac{\cos L}{(N+H)\cos B} & 0 \\ -\frac{\sin B \cos L}{M+H} & -\frac{\sin B \sin L}{M+H} & \frac{\cos B}{M+H} \\ \cos B \cos L & \cos B \sin L & \sin B \end{bmatrix} \tag{3}$$

Hereby, $[dL\ dB\ dH]^T$ and $[dX\ dY\ dZ]^T$ are the differential vector for geodetic coordination and ECEF coordination separately. N is the radius of curvature in prime vertical, M is the radius of curvature in meridian, H is the ellipsoid height.

According to Eq. (2), the ellipsoid variance-covariance value can be acquired from the transition. Supposing ellipsoid variance-covariance value is $D_{ellipsoid}$, it can be expressed as following by applying covariance propagation theory:

$$D_{ellipsoid} = C_{coefficent} D_{baseline} C_{coefficent}^T \tag{4}$$

Substitute $C_{coefficent}$ in Eq. (4) with (3):

$$D_{ellipsoid} = \begin{bmatrix} A & B & C \\ & D & E \\ & & F \end{bmatrix} \tag{5}$$

Here,

$$A = \left[\frac{\sin L}{(N+H)\cos B}\right]^2 \delta_x^2 - \frac{\sin L \cos L}{[(N+H)\cos B]^2}\delta_{xy} + \left[\frac{\cos L}{(N+H)\cos B}\right]^2 \delta_y^2 \tag{6}$$

$$\begin{aligned} B = {} & \frac{\sin B \sin L \cos L}{(M+H)(N+H)\cos B}\delta_x^2 + \frac{\sin B(\sin^2 L - \cos^2 L)}{(M+H)(N+H)\cos B}\delta_{xy} \\ & - \frac{\sin B \sin L \cos L}{(M+H)(N+H)\cos B}\delta_y^2 + \frac{\cos B \sin L}{(M+H)(N+H)\cos B}\delta_{xz} \\ & - \frac{\cos B \cos L}{(M+H)(N+H)\cos B}\delta_{yz} \end{aligned} \tag{7}$$

$$\begin{aligned} C = {} & -\frac{\cos L \sin L}{(N+H)}\delta_x^2 + \frac{\cos^2 L}{(N+H)}\delta_{xy} + \frac{\cos L \sin L}{(N+H)}\delta_y^2 \\ & - \frac{\sin B \sin L}{(N+H)\cos B}\delta_{xz} + \frac{\sin B \sin L}{(N+H)\cos B}\delta_{yz} \end{aligned} \tag{8}$$

$$D = \left[\frac{\sin B\ \cos L}{M+H}\right]^2 \delta_x^2 + \frac{2\sin^2 B\ \cos L\ \sin L}{(M+H)^2}\delta_{xy} - \frac{2\cos B\ \sin B\ \cos L}{(M+H)^2}\delta_{xz} + \left[\frac{\sin B\ \sin L}{M+H}\right]^2 \delta_y^2 - \frac{2\sin B\ \sin L\ \cos B}{(M+H)^2}\delta_{yz} + \left[\frac{\cos B}{(M+H)}\right]^2 \delta_z^2 \quad (9)$$

$$E = -\frac{\cos^2 L\ \cos B\ \sin B}{(M+H)}\delta_x^2 - \frac{2\sin B\ \sin L\ \cos B\ \cos L}{(M+H)}\delta_{xy} + \frac{\cos L(\cos^2 B - \sin^2 B)}{(M+H)}\delta_{xz} - \frac{\cos B\ \sin B\ \sin^2 L}{(M+H)}\delta_y^2 + \frac{(\cos^2 B - \sin^2 B)\sin L}{(M+H)}\delta_{yz} + \frac{\cos B\ \sin B}{(M+H)}\delta_z^2 \quad (10)$$

$$F = (\cos B\ \cos L)^2\delta_x^2 + (2\cos^2 B\ \cos L\ \sin L)\delta_{xy} + (2\cos B\ \cos L\ \sin B)\delta_{xz} + (\cos B\ \sin L)^2\delta_y^2 + (2\cos B\ \sin B\ \sin L)\delta_{yz} + (\sin^2 B)\delta_z^2 \quad (11)$$

The NEU coordination of CORS stations can be calculated by using the transformation form ellipsoid coordinate to NEU coordinate. The soft threshold in N, E, U direction used for the Daubechies wavelet denoising can be set as:

$$\begin{cases} N_{Threshold} = D \\ E_{Threshold} = A \\ U_{Threshold} = F \end{cases} \quad (12)$$

During the denoising process with Daubechies wavelet, all the high frequency parts beyond the soft threshold can be taken as the high frequency noise, which will be filtered out. The signal will be restored again by utilizing Daubechies wavelet in N, E and U directions after filtered.

2.3 The Trend and Detail Analysis of CORS Stations

With the filtered time serials by Daubechies soft threshold wavelet denoising method, the CORS stations' characteristics can be analysed. The characteristic analysing includes trend analysis and detail analysis. The trend analysis is used to find out the general spatial deformation model which can be used for forecasting and prediction the trend of the stations' movement in near future by linear and non-linear fitting method. And the detail analysis focuses on the hair-like signal's fluctuation which can be extracted from the CORS stations raw movement signal by taking the trend signal away. The fluctuation frequency of the detail signal can also be clear expressed by using the frequency spectrum analysing.

The trend analysis of Tianjin CORS stations' time serials adopted Chebyshev nine-order fitting polynomial, and the detail analysis was done by using Fast Fourier Transform method to detect the change frequency.

3 Tianjin CORS Case Study

Tianjin CORS has established in 2004. There were totally twelve stations with about 43 km average distance between stations. This paper adopts almost ten years' datasets of Tianjin CORS as the analysing case. the datasets time span is from Jan 1st 2006 to Sep 1st 2015.

3.1 The Reference Point Affirmation for Tianjin CORS Deformation Analysis

The six peripheral IGS stations named bjfs, daej, suwn, ulab, wuhn, yssk have been adopted for Tianjin CORS datasets baseline processing by using GAMIT 10.5 software firstly. The relatively stable CORS station will be taken as the reference station, which will be used for the other CORS stations datasets processing for their characteristic analysing, by judging its linear time serials characteristic in ITRF08 frame.

In order to get relative stable reference point for Tianjin CORS datasets analysis, JIXN station was selected for its' good stable geology which located in north Tianjin city. The JIXN station's stability was analyzed by Kalman filtering method with GLOBK software in ITRF08 frame datum by combining global isg1, igs2, and igs3 data together. The stability in N, E and U directions of JIXN station are demonstrated in Fig. 2.

From Fig. 2, JIXN station has near linear movement in N and E direction, this movement reflects the plate movement, and U direction is relatively stable because it only has 0.15 mm + 0.05 mm/yr annual movement rate. It is suitable to be taken as the reference station for Tianjin CORS stations spatial deformation movement analysis.

3.2 Time Serials Denoising and Fitting Analysis

Taking JIXN station as the reference, the other eleven stations in Tianjin CORS were filtered by the aforementioned Daubechies wavelet soft threshold filtering method. Limited by the length of this paper, only CH01 station filtered results are

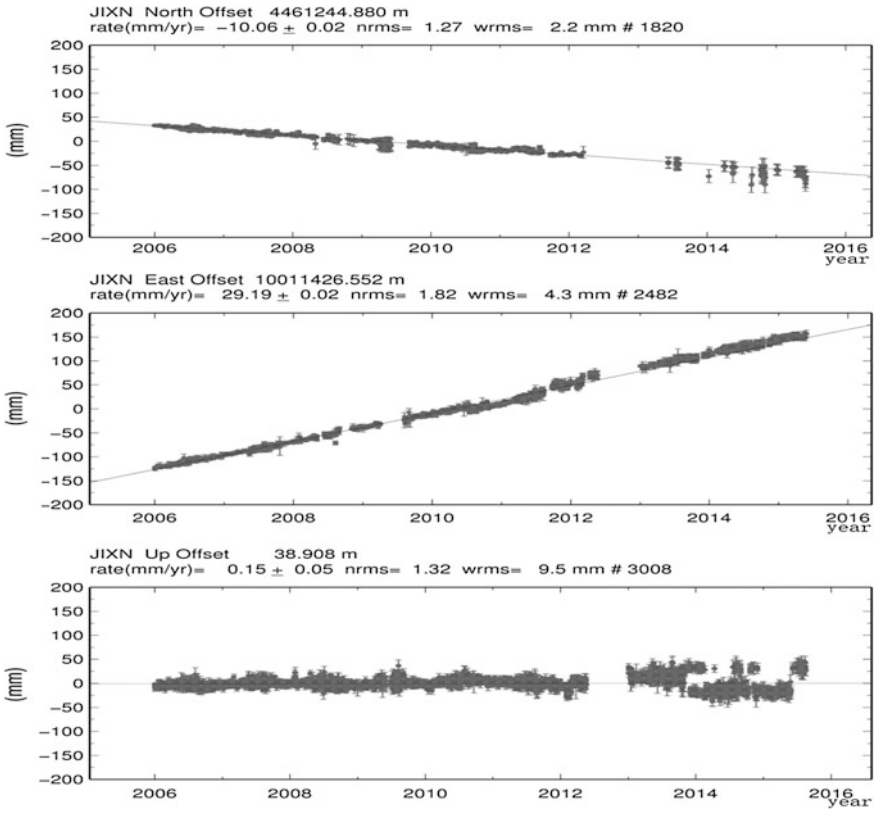

Fig. 2 The stability of JIXN station in NEU directions

demonstrated here, which mounted on the top of building of Tianjin institute of surveying and mapping. The results are shown in Figs. 3, 4, and 5.

As seen from Figs. 3, 4 and 5, the spicule points of the time serials were filtered out and the signal trends were kept very well. The filtered time serials can be used for trend analysis, and nine-order Chebyshev polynomial was adapted in this paper for the trend analysis.

3.3 The Spatial Deformation Characteristic Results

In order to display the value of Tianjin CORS stations' deformation, the eleven stations' annual deformation rate were calculated based on the filtered results, as well as the RMS of deformation rate. The results show in Table 1.

As demonstrated in Table 1, most stations' U direction annual movement were lager than E and N direction. Some annual movement even reached to 40 mm/yr.

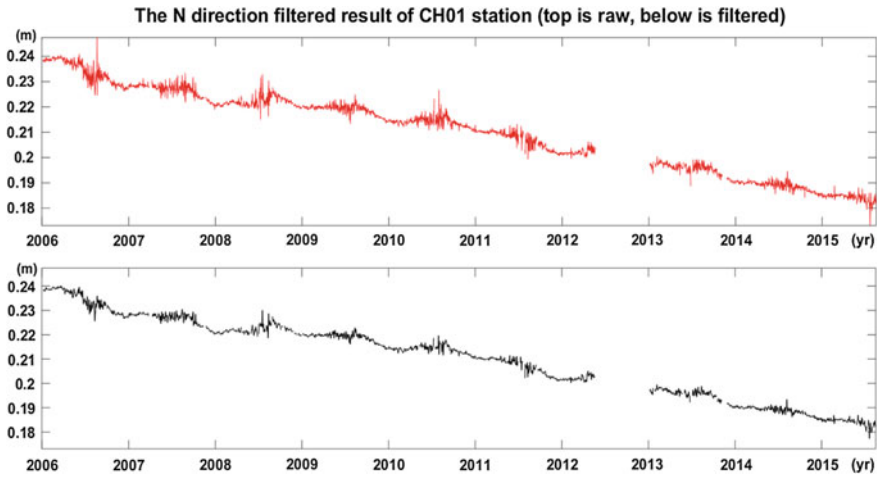

Fig. 3 CH01 station N direction before and after filtered

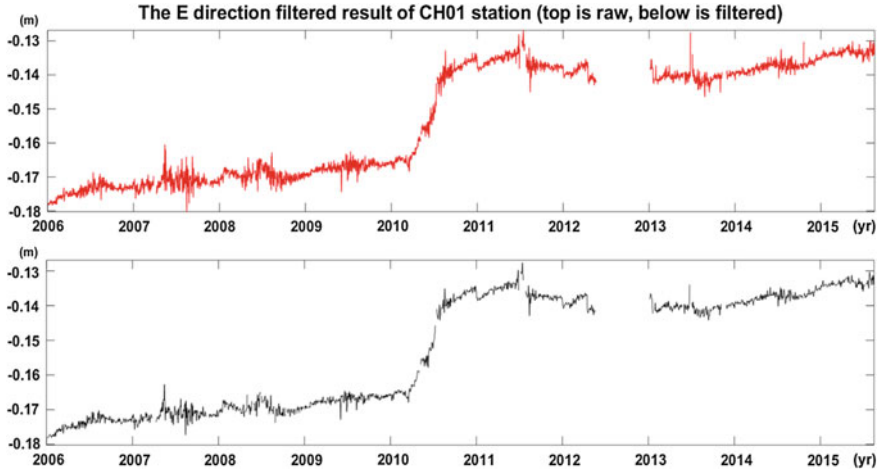

Fig. 4 CH01 station E direction before and after filtered

In N direction, all stations move towards South except SW01. We investigated the reason and found that some subsidence funnels lied in the North where was very near to SW01, and the funnels had larger subsidence rate than SW01, that's why SW01 moves toward North. In E direction, all stations move towards East except CH02, but the movement rate less than 1 mm/yr.

In order to directly illustrate the deformation characteristic of Tianjin CORS stations, a plane accumulated deformation graph and a vertical accumulated subsidence graph were drawn as shown in Fig. 6.

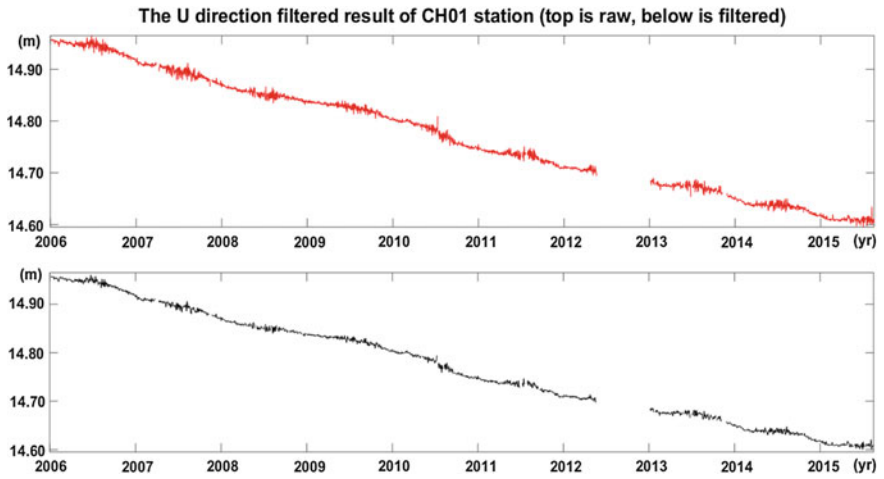

Fig. 5 CH01 station U direction before and after filtered

Table 1 Annual deformation rate of Tianjin CORS stations

Station name	N deformation rate		E deformation rate		U deformation rate	
	Annual rate (mm)	RMS (mm)	Annual rate (mm)	RMS (mm)	Annual rate (mm)	RMS (mm)
CH01	−5.2	0.7	7.3	0.7	−40.8	1.8
CH02	−3.8	0.7	−0.6	0.7	−3.5	2.8
DZ01	−4.1	0.7	2.0	0.7	−9.7	1.9
DZ02	−3.3	0.8	2.1	0.7	−19.1	2.6
KC01	−3.2	0.8	1.4	0.9	−17.8	1.8
KC02	−4.2	0.7	3.2	0.6	−29.0	1.8
KC03	−2.3	0.7	3.9	0.7	−29.7	1.8
SW01	3.1	1.2	1.3	0.7	−40.5	2.5
TJA1	−0.7	0.6	0.4	0.8	−8.8	2.3
TJA2	−3.8	0.8	1.8	0.6	−0.9	2.1
YC01[a]	−5.3	0.3	1.7	0.3	−19.8	0.8

[a]Represents the datasets was last till to the year 2011

As seen from the plane graph, all stations movement towards South–East except SW01, the reason why SW01 moves towards North–East explained above. The largest accumulated plane movement value is about 84 mm named CH01. We also see that all the stations had subsidence, the stations located in West had larger subsidence accumulated value than the East. The largest subsidence value is about 400 mm named CH01 and SW01.

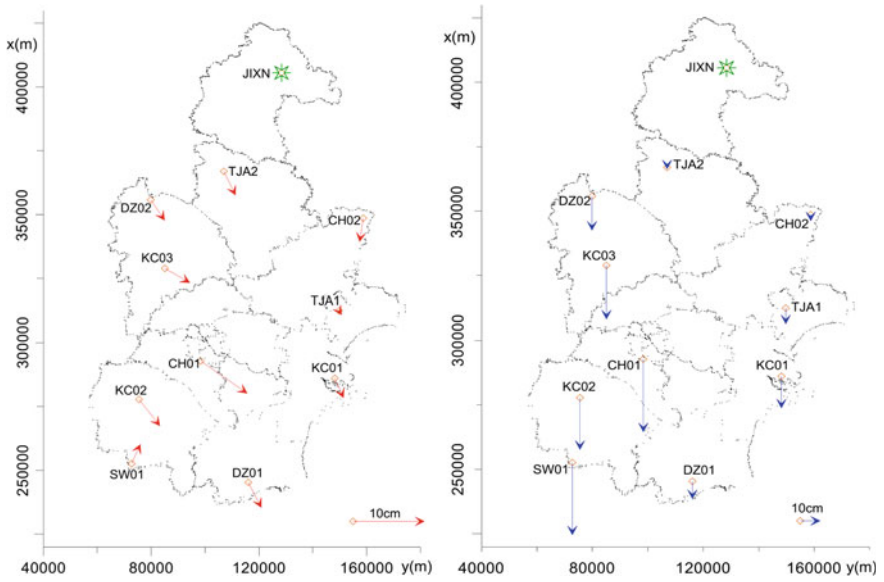

Fig. 6 Tianjin CORS stations accumulated deformation in plane (*left graph*) and accumulated subsidence in vertical (*right graph*)

According to the analysis, considering the tolerance error of engineering surveying, the Tianjin Geoinformation Reference Frame, which was sustained by Tianjin CORS, should be updated in every 3–4 years in plane, and the height should be updated every year.

4 Conclusion

The CORS spatial deformation analysis method and the general processing procedure are presented in this paper. This paper also focused on the deducing model of soft threshold wavelet denoising with the variance–covariance of CORS baseline solution. Those methods and models have been applied in Tianjin CORS time serials processing and some qualification results were calculated. From the analysis, there were about 84 mm maximum accumulated plane movement towards South–East, and about 400 mm maximum accumulated subsidence in height direction. All the stations' movement values were different. The results of the deformation also have been used for the updating of Tianjin Geoinformation Reference Frame which sustained by Tianjin CORS. The experience and data processing methods of Tianjin CORS can also be referenced by any other city CORS.

Acknowledgements This study is funded by Key Laboratory of Geo-informatics of State Bureau of Surveying and Mapping in 2016.

References

1. Liu J, Liu H, Zou R, Wei N (2009) Some thoughts on the establishment of nationwide continuously operating reference stations. Geomatics Inf Sci Wuhan Univ 34(11):1261–1284
2. Jiang ZH, Zhang P, Bei JZ, Li ZC (2012) Characteristics of the non-linear movement of CORS network in China based on the CGCS2000 frame. Chin J Geophys 55(3):841–850
3. Yang Y, Zhang J, Zhang L (2008) Variance component estimation based collocation and its application in GIS error fitting. Acta Geod Cartogr Sin 2:152–157
4. Zhang HJ (2013) Nonlinear time-varying study of GPS height time series of national CORS stations. Liaoning Technical University, China
5. Yang Y, Song L, Xu T (2002) Robust estimator for correlated observations based on bifactor equivalent weights. J Geodesy 76(6):353–358
6. Koch KR, Yang Y (1998) Robust Kalman filter for rank deficient observation models. J Geodesy 72(7):436–441
7. Yang Y, Gao W (2006) An optimal adaptive Kalman filter. J Geodesy 80(4):177–183
8. Yang Y, Ren X, Xu Y (2013) Main progress of adaptively robust filter with application in navigation. J Navig Positioning 1(1):9–15
9. Zhang Z, Zhu J, Kuang C, Zhang Y (2014) A hybrid filter method based on wavelet packet and its application. Geomatics Inf Sci Wuhan Univ 39(4):471–475
10. Feng B, Ge Y (2015) GPS baseline solution based on wavelet denoising. J Nanjing Tech Univ 37(3):79–84
11. Liu C, Gao J, Zhang J (2012) GPS baseline solution based on average sequence data method. Geomatics Inf Sci Wuhan Univ 37(4):445–449

Wide Area Beidou Foundation Enhanced Grid Space-Time Interlinked Science and Education Collaborative Experimental Service

A Science and Education Cooperative Experiment Demonstration Platform for the Wide-Area and Grid Enhanced China Beidou Satellite System

Jianping Xing, Zedong Wang, Zidong Wang, Zhao Wang, Shengli Wang and Tao Yang

Abstract The typical applications of future smart cities require an integrated system that performs multi-source spatiotemporal information collection, trusted information transmission, real-time big data fusion and precise electronic map display, which involves issues such as different standards, platforms and applications among different systems. To tackle these issues, taking the Internet of Things and Smart Campus as examples, a demonstration platform for collaborative science and education study is needed for exploratory research and education purpose. This paper proposes a next-generation network science and education experiment platform on the China educational network, using the wide-area grid-base enhanced Beidou GNSS system. It provides real-time positioning of mobile or static targets in scales of sub-meter and centimeter, as well as implements high-precision time calibration and real-time communication services. This study develops the

J. Xing (✉)
School of Microelectronics, Shandong University,
Shanda Nanlu 27, Jinan 250100, China
e-mail: sduxingjianping@163.com

Z. Wang · Z. Wang · Z. Wang
School of Information Science and Engineering, Shandong University,
Shanda Nanlu 27, Jinan 250100, China

S. Wang
Institute of Ocean Engineering, Shandong University of Science and Technology,
579 Qianwangang Road, Huangdao District, Qingdao, Shandong Province 266590, China

T. Yang
Shandong Star Beidou Information Technology Co., Ltd, Qilu Software Park,
Gaoxin District, Jinan City, Shandong Province 250000, China

J. Sun et al. (eds.), *China Satellite Navigation Conference (CSNC) 2017 Proceedings: Volume I*, Lecture Notes in Electrical Engineering 437,
DOI 10.1007/978-981-10-4588-2_22

BD + GPS positioning equipment and proposes an algorithm to combine the inertial navigation, network and database load balancing technology to achieve high concurrency, large data storage, processing and application access. The data collection experiments on mobile and static targets were conducted in Jinan, Qingdao and Weihai. The preliminary results show that the system can effectively solve the problem of real-time network processing for large-scale users and sub-meter level and centimeter-level positioning of mobile objects in Beidou foundation enhanced grid-based service science and education experiment system. This research provides an application basis for high-precision positioning in the coming big data era.

Keywords Beidou foundation enhanced · Grid services · Large-capacity concurrent · Next generation network · Science and education coordination

1 Introduction

In July 2016, the General Office of the CPC Central Committee and the General Office of the State Council jointly issued the "Outline of the Development Strategy of the National Informatization", and proposed to "enhance the capacity of space facilities, coordinate the construction and application of the Beidou satellite navigation system and advance the Beidou industrialization and going out". Accelerate the next generation of large-scale Internet deployment and commercial use.

The typical applications of the future smart cities [1] include the integrated system of multi-industry space-time information collection, reliable objects transmission, large data fusion processing and precise electronic map display, which involves many standards, technologies, data, platforms and applications, And the wisdom of the campus as an example, we need to build a clear and hierarchical technology line demonstration of science and education collaborative experimental platform to study and first verify the content [2].

In this paper, a platform for next-generation network science and education experiment is proposed, which is for Beidou GNSS ground-based enhanced grid-based time-space fusion service information processing with wide-area features for intelligent campus teaching, especially the three-dimensional, whole-process foundation, verification, system, innovative course, teaching material, experiment, training, competition and so on of moving target and large capacity concurrent application perception, transmission, storage, processing, display, control and service.

Based on the study of differential positioning of satellite signals, the Wide area Beidou foundation reinforced grid test platform is studied and constructed in this paper. It provides real-time sub-meter, centimetre-level positioning for mobile and static targets, as well as high-precision time integration and real-time integration of communication services. The research proposes a grid pseudo-range differential positioning strategy algorithm which provides a significant reduction in data center data processing burden. At the same time, the study uses network and database load balancing technology to achieve high concurrency, large data storage, processing

and application access. Combined with Jinan, Qingdao, Weihai and other off-campus experimental network to carry out a new energy vehicle network with moving targets, multi-source fixed target of the wisdom of the campus space-time information collection specific validation, and the information system planning and design, space and time to demonstrate the course system and experimental training system planning and design. It is indicated that the construction of the next-generation network on the educational network, the Beidou, enhances the grid-based space-time science and technology collaborative service platform, which can improve the utilization of existing resources and provide theory and application basis for high-precision positioning of the next-generation network large data age.

2 Wide-Area Beidou Reinforcement Grid-Based Space-Time Collaborative Experiment Service

2.1 Service Platform Design Principles

Beidou high-precision positioning system as the infrastructure of a smart city, intelligent campus, and the sound, light, heat, electricity, mechanics, chemistry, biology, location and other needs of information collected by the Internet of Things is a basic resource. According to the principles of resource reconstruction, on-demand use, and module configuration, through the large data technology and a series of intelligent combination of information technology to meet the needs of different professional and scientific experiments, for the next generation network, Beidou applications, the development of things to provide a unified test platform.

2.2 Service Platform Design

Wide-area Beidou enhanced grid-based space-time science and technology collaborative experimental service platform is the integration of the Beidou credible high-precision space-time information, multi-source information and education network resources. The development of large data resources based on "Internet +" mode can realize the information sharing among different subjects and experiments, and develop the data service model based on Big Data of Beidou.

Service platform from the top of the unified design, the formation of the perception layer, network layer, support layer and application layer 4-layer platform, especially the first three layers of effective integration and unity [3]. The structure of the service platform is shown below (Fig. 1).

The sensing layer is a kind of positioning terminal including the Beidou high-precision positioning base station, sensors such as acousto-optic heating and experiment terminal. It is responsible for collecting satellite navigation data and multi-source information, and parsing related protocols.

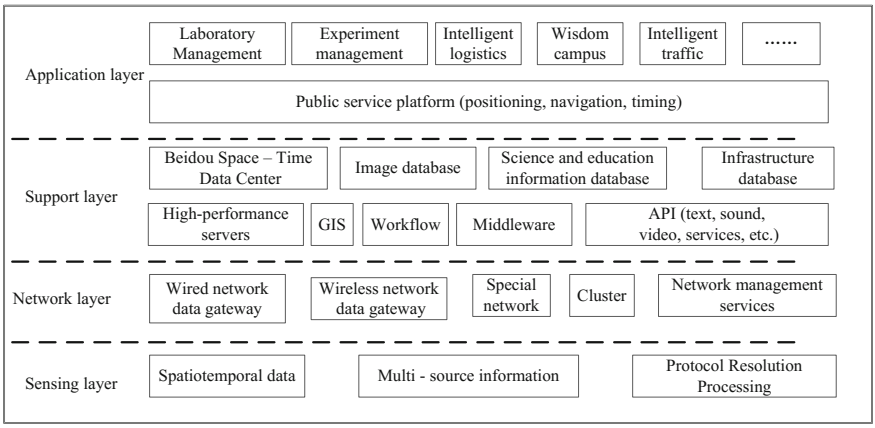

Fig. 1 Wide area Beidou enhanced grid space-time science and technology collaborative service platform structure

The network layer mainly provides the communication function for the realization of the service function, including the education network, the next generation network involved in the Internet, the wireless network, the cluster network and other means of transmission to realize the protocol conversion between the sensing layer and the network layer. The network layer also takes care of the management of the platform network.

The support layer provides the necessary flat storage, high-performance computing, mapping, workflow, middleware, and service APIs for the service platform.

In the application layer, the service platform will provide positioning, navigation, timing and other basic functions of the public service platform. The service platform has both software and hardware experimental platform, covering electronic design experiment, information data processing and other courses teaching content. On this basis, the professional users can organize their own basic experiment, the development of experiments, application and promotion of different levels of verification experiments.

2.3 Platform of Science and Education Cooperative Experiment Construction

The service platform uses the education network to build Beidou positioning reference base station in Jinan, Qingdao, Weihai, respectively. The network center is built in Jinan which serves as the entire service platform for network management; the sub network center is built in Qingdao, serving the local area network management.

Network Center is the core of the service platform, mainly running the internal network, data processing software, user monitoring software, databases, servers and

other components. The network center analyzes, divides, synchronizes, solves, generates and processes the data provided by the base station, and carries out data fusion or information integration according to the service requests made by the users. The system can be used for data collection [4, 5].

Based on the comprehensive consideration of the observation environment, communication environment and electromagnetic environment, the Beidou ground station of Jinan City is constructed at the top of information building of Shandong University Center Campus. Receiver with VNet6 high-precision GNSS receiver, set the receiver connected to the data center, and the receiver saves observation data of the latest week.

In the design of experimental devices, a variety of experimental system devices such as hand-held terminals and vehicle terminals are designed for the purpose of carrying out various experiments flexibly.

3 Key Technologies

3.1 Virtual Grid Pseudo-range Differential Localization Strategy

The virtual grid pseudo range differential positioning strategy divides the reference station area into several networks according to the distance or area, and interpolates the virtual observation values of the network points by interpolation method. Then, the data processing center selects the nearest grid point from the user terminal according to the probability coordinates uploaded by the user, and sends the virtual observation value of the network point to the user for pseudo range differential positioning.

Suppose the latitude and longitude coordinates of the three reference stations are $P_1(B_1, L_1)$, $P_2(B_2, L_2)$, $P_3(B_3, L_3)$, respectively. The observed data of the three reference stations are $\mathrm{Obs}_i(C_1^i, P_2^i, L_1^i, L_2^i, S_1^i, L_2^i)$, i indicates the reference station number, $i = 1, 2, 3$ the plane equations for the triangular elements formed by fitting the three reference station is:

$$Obs = f(B, L) = a_0 + a_1 B + a_2 L \tag{1}$$

Then, B, L is the latitude and longitude of each virtual observatory coefficient, a_0, a_1, a_2 are determined by Observed data from three reference stations, as shown in Eq. (2)

$$\begin{cases} Obs_1 = a_0 + a_1 B_1 + a_2 L_1 \\ Obs_2 = a_0 + a_1 B_2 + a_2 L_2 \\ Obs_3 = a_0 + a_1 B_3 + a_2 L_3 \end{cases} \tag{2}$$

Then, Obs_1, Obs_2, Obs_3 are observed data for the three reference stations. Solve Eq. (2) to obtain the coefficient a_0, a_1, a_2:

$$\begin{cases} a_1 = \frac{(L_1-L_3)(Obs_1-Obs_2)-(L_1-L_2)(Obs_1-Obs_3)}{(B_1-B_2)(L_1-L_3)-(B_1-B_3)(L_1-L_2)} \\ a_2 = \frac{(B_1-B_3)(Obs_1-Obs_2)-(B_1-B_2)(Obs_1-Obs_3)}{(B_1-B_3)(L_1-L_2)-(B_1-B_2)(L_1-L_3)} \\ a_0 = Obs_1 - a_1B_1 - a_2L_1 \end{cases} \tag{3}$$

Then, B, L is substituted into the Eq. (1) to get the virtual observation value of the virtual observing station C_1, P_2, L_1, L_2, S_1, S_2. In this way, the position of the virtual observatory closest to the user's location can be obtained:

$$\begin{cases} N_x = \left[\frac{X-X_{MIN}}{d}\right] \\ N_y = \left[\frac{Y-Y_{MIN}}{d}\right] \end{cases} \tag{4}$$

Among them, N_x, N_y are the line number and column number of the virtual observatory closest to the user's location in the network; [] Is rounded to the operator; X, Y are the probability positions coordinate of the user; X_{MIN}, Y_{MIN} are the coordinate precision and latitude minimum of each virtual observing station; d is the grid spacing.

The ground reinforcement area planning to reduce the data processing center for each terminal interpolation calculation of the burden of server computing to effectively address the large amount of user-oriented sub-level positioning problem for the future of high-precision positioning of the data age to provide solution. The following figure shows the test network, three sites in Jinan, Qingdao and Weihai have been used, the transfer system in the triangle area has been able to achieve sub-meter positioning (Fig. 2).

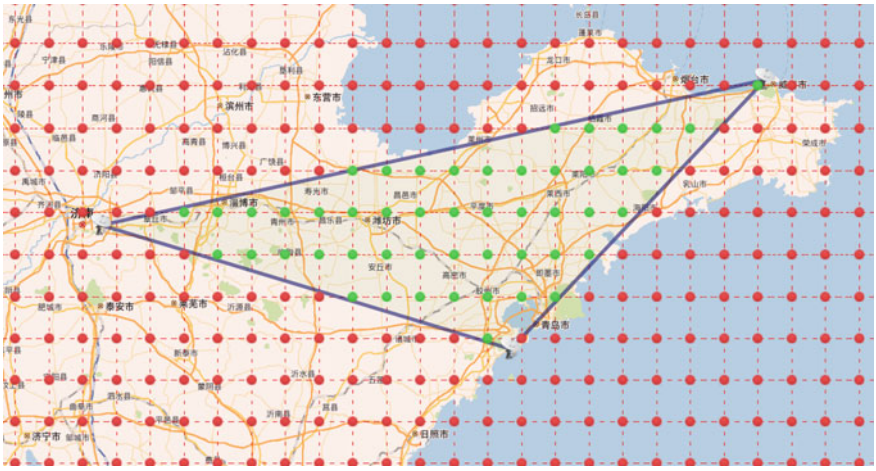

Fig. 2 Virtual grid pseudo-range differential positioning strategy test network

Fig. 3 Handheld locator made with board and the terminal fixed-point test (no differential mode accuracy of 5–10 m)

3.2 Low-Cost Integrated Navigation Terminal Board

In order to extend the use of the wide-area Beidou to enhance the use of grid-based space-time science and technology collaborative experimental service platform, an integrated navigation algorithm based on inertial navigation and Beidou enhanced loosely coupled to terminal card implementation is presented in this paper. The integrated navigation system can realize the complementarity of GNSS and inertial navigation systems, and achieve continuous, all-weather and high-precision navigation, and obtain better performance in accuracy and reliability than any navigation equipment. Using MPU9250 as IMU, the navigation terminal board can meet the high-precision positioning and low-cost requirements (Fig. 3).

3.3 High Concurrency, Large Data Storage, Processing and Application Access

The wide area Beidou enhanced grid space-time science and technology collaborative service platform faces Shandong province and even more wide area. There are a large number of intelligent terminals and platform interaction. In order to ensure the successful completion of the interaction process, the database uses load balancing technology, distributed processing technology, database data level division technology based on the data model, data partitioning technology based on the time, to fully utilize the storage and processing capacity of multiple databases to provide query, statistics and data mining services.

4 Wide Domain Beidou Enhanced Grid-Based Space-Time Science and Technology Co-experimental Service Applications

4.1 Teaching Experiment: Internet of Things

In the wide domain Beidou enhanced grid space-time science and technology cooperation in experimental teaching services in colleges and universities, a general model of universality is proposed, which forms a teaching chain of perception, transmission, storage, processing, control and service.

At the same time, according to the curriculum arrangement of colleges and universities, a teaching design of knowledge points: teaching, learning, training, examination, research and creation is put forward in this paper. From the reception of navigation satellite signals to the user to use the entire link, involving multi-disciplinary, multi-disciplinary knowledge, different links can be used as different courses of experimental teaching content, there are 17 courses, about 8 credit hours, which is equivalent to 4 standard courses (Table 1).

Wide Area Beidou enhanced grid space-time science and technology collaborative experimental service platform, in the data sources, network connections, application testing and other aspects of teaching for the curriculum to provide a variety of resources. So, it can lead the teaching model from the traditional teaching

Table 1 Space of physical information of knowledge points teaching table

Knowledge points	Hours	Knowledge points	Hours
Information system planning and design	4	Advanced programming techniques	10
Embedded software and hardware (case)	10	Electronic map production Electronic map production	6
Beidou navigation, enhanced	6	Network communication (case)	4
Database	8	Land information system	6
System software development (case)	4	APP software development	8
Software engineering	4	System integration (bidding, supervision)	6
Big data analysis and calculation	6	Project roadshow	4
Intellectual property	4	Testing and Reliability	2
Subtotal	96 h = 6 credits, 3 standard courses		
Practical innovation course design	2 credits		
Total	8 credits, 4 standard courses		

Table 2 Comparison of two kinds of teaching mode

Course	Traditional teaching mode	Project-based teaching mode
C language	1. Focus on sentences, grammar and other details of teaching 2. Adopt "concept, examples to explain, exercises" approach 3. "Teach" is the center	1. Focus on the complete project solution 2. Using the "ask questions, seek ways to broaden the knowledge, skills, problem-solving" approach 3. "Learn" is the center
Embedded development	1. From the curriculum itself, the lack of other professional point of view to consider curriculum design 2. Can not meet the learning needs of different professional background 3. Teaching experiments are basically basic confirmatory experiments	1. Comprehensive knowledge of all aspects of the project points 2. Different professionals according to different needs, design their own experiments 3. Task-driven, complete the entire project

model to project-oriented teaching, students in the actual project environment hands-on to enhance the understanding of knowledge points to improve the efficiency of curriculum teaching. C language and embedded development courses as an example, the comparison between the traditional teaching mode and the existing teaching mode is as follows (Table 2).

4.2 Scientific Research Experiment: Study on Public Traffic Signal Priority

"Bus priority", that is, on the right of way, the establishment of public transport priority rights to achieve priority to the development of public transport, to reduce the pressure on the purpose of urban roads [6]. The study of public traffic signal priority works on the wide-area Beidou enhanced grid-based space-time science and technology cooperative experimental service platform, sets up bus test field in the Shandong University Xinglong Hill campus, set the new energy Shandong University Beidou Space Test vehicle as the test terminal, and the vehicle is equipped with intelligent bus stop and sub-meter antenna system.

Beidou sub-meter lane-oriented bus priority system to sub-meter positioning accuracy, precise timing, reporting data per second, and the real-time calculation of the data collected per second analysis, solve problems with global and real-time policies. And, it has a strong Beidou backstage, can provide the necessary technical support to the "Governance Blocking " project of Jinan City (Fig. 4).

Fig. 4 Experimental vehicle and the intelligent stop device

5 Conclusion

On the basis of making full use of the resources of university education network, Wide-area Beidou enhanced grid-based space-time science and technology collaborative experimental service platform, can effectively solve the moving target sub-meter level and fixed target centimeter-level positioning of large users in real-time network processing problems, To support the innovation of teaching and diversification of scientific research projects carried out for the next generation of large data era of high-precision positioning to provide theoretical and application basis for the development of the Big Dipper and the Internet of Things to provide an open, unified experimental platform.

Acknowledgements The first author is grateful to the support of the Shandong Province independent innovation major project (Beidou high-precision positioning equipment industrialization, network service platform).

References

1. Arroub A, Zahi B, Sabir E et al (2016) A literature review on Smart Cities: Paradigms, opportunities and open problems [C]. International Conference on Wireless Networks and Mobile Communications. pp 180–186
2. Xiao WJ, Zhang FZ, He HX (2013) Application analysis of IOT based on Beidou navigation system. Adv Mater Res 718–720:2401–2408
3. Fan Q, Wang Q (2015) Performance comparison of web servers with different architectures: a case study using high concurrency workload. IEEE workshop on hot topics in web systems & technologies, pp 37–42
4. Kirkko-Jaakkola M, Saarimaki J, Soderholm S et al (2014) P3: a public precise positioning service based on a national GNSS network. In: International conference on localization and GNSS, IEEE, pp 1–5

5. Luo Y, Wu X, Meng X et al (2011) A distributed management system with high concurrency. In: Tenth international symposium on distributed computing and applications to business, engineering and science, IEEE, pp 74–77
6. Hounsell NB, Shrestha BP, D'Souza C (2012) Using automatic vehicle location (AVL) data for evaluation of bus priority at traffic signals. Road transport information and control, pp 1–6

Single-Antenna Attitude Determination Using GNSS for Low-Dynamic Carrier

Wen Chen, Chao Yu, Miaomiao Cai and Yaxuan Dong

Abstract Single-antenna pseudo-attitude determination method has the advantages of low cost and low space requirement, thus has got more and more attention by the field of high dynamic navigation. However, researches on its application to low-dynamic carriers have not been carried out. This paper discusses the feasibility of the pseudo-attitude determination method in low-dynamic application. Three kinds of errors of this method are summarized, and correction methods are also put forward. Vehicle experiment suggest that if we adopt reasonable threshold to mitigate the measurement error, and simultaneously use sudden change detection to eliminate the offset error, the GNSS single-antenna pseudo-attitude determination method can be used to measure the attitude of low speed carriers at m/s level. The standard deviation of the pseudo-azimuth angles is 3.7°, and that of the pseudo-pitch angle is 1.4°. This method has great practical significance for small carriers, which cannot accommodate multiple antennas. In addition, for the existing single-antenna carriers, this method can provide reliable attitude information without adding any equipment or making any device modifications, thus is of great application value and economic benefits.

Keywords Single-antenna · GNSS · Attitude determination · Low-dynamic

W. Chen · C. Yu (✉) · M. Cai · Y. Dong
Engineering Center of SHMEC for Space Information and GNSS, East China Normal University, 500 Dongchuan Rd., Shanghai 200241, China
e-mail: cyu@sist.ecnu.edu.cn

W. Chen · C. Yu
Shanghai Key Laboratory of Multidimensional Information Processing, East China Normal University, 500 Dongchuan Rd., Shanghai 200241, China

W. Chen · C. Yu
Key Laboratory of Geographic Information Science, Ministry of Education, East China Normal University, 500 Dongchuan Rd., Shanghai 200241, China

J. Sun et al. (eds.), *China Satellite Navigation Conference (CSNC) 2017 Proceedings: Volume I*, Lecture Notes in Electrical Engineering 437,
DOI 10.1007/978-981-10-4588-2_23

1 Introduction

Attitude determination is an important branch of GNSS applications. Compared with inertial navigation unit, GNSS attitude determination technology has many characteristics, such as low cost, and no initial correction or temporal accumulated error, thus becomes more and more attractive. Traditional GNSS attitude determination are mainly in multi-antenna mode, the attitude angles of carriers are obtained from the baseline vectors among two or more antennas deployed on the carrier. Multi-antenna attitude determination can get the real attitude, however, it needs to use several antennas, which increases the expense. In addition, for the carrier with limited space such as unmanned aerial vehicle (UAV), it also raises the difficulty of deploying the antennas.

To reduce the cost and meet the space requirement of special carriers, [1] proposed an attitude determination method using single-antenna. This method substitutes the carrier rotation angles with the trajectory rotation angles, thus called the pseudo-attitude determination method. Previous studies showed that this method can reach the precision requirements of high-dynamic carrier attitude measurement, such as UAV [2–5]. However, researches on its application to low-dynamic carriers (such as vehicles, ships) have not been carried out. In low-dynamic scenarios, the deviations of the pseudo-attitude angles from the real attitude angles may not be neglected. Solutions should be put forward to ensure the reliability of pseudo-attitude determination method. This paper summarizes three kinds of deviations between the pseudo-attitude angles and the real attitude angles in low-dynamic scenarios, and proposes corresponding correction methods for these deviations. Through vehicle experiments, the feasibility of the proposed scheme is verified. Pseudo-attitude determination method is of potentials to reduce the cost of GNSS attitude measurement for low-dynamic carriers, thus is very valuable to popularize GNSS application for civil use.

2 Single-Antenna Attitude Determination for Low-Dynamic Carriers

2.1 Pseudo-attitude Determination Method

Let the three components of GNSS antenna velocity relative to the earth in the local geographic coordinate are v_n,v_e,v_u. The pseudo-azimuth φ_s and pseudo-pitch angle θ_s are defined respectively as

$$\varphi_s = \arctan(v_e/v_n) \tag{1}$$

$$\theta_s = \arctan\left(v_u/\sqrt{v_e^2 + v_n^2}\right) \tag{2}$$

The pseudo-roll angle γ_s is calculated based on the acceleration. The acceleration a can be decomposed into a^t and a^n respectively along the radial and normal direction of the velocity v. Similarly, the acceleration of gravity g can also be decomposed into g^t and g^n respectively. Lifting acceleration l of an object may be considered as the summation of lift force and gravity, that is $l = a^n - g^n$. Simultaneously, utilizing g and v, we can construct the horizontal vector p, and let $p = g \times v = g^n \times v$, here $\times$ means vector multiplication. Thus, γ_s is defined as

$$\gamma_s = \arcsin[(l \cdot p)/(|l| \cdot |p|)] \tag{3}$$

2.2 Deviations from the Pseudo-attitude Angles to the Real Attitude Angles

Different from the traditional multi-antenna attitude measurement technique, the pseudo-attitude attitude determination method calculates the rotation angles of the carrier trajectory relative to the earth. Thus it inevitably contains some deviations comparing with the real attitude angles. These deviations can be divided into three categories.

2.2.1 Measurement Error

When the carrier moves slowly, the measurement error of velocity can cause large deviation of the pseudo-attitude angles. Taking the pseudo-azimuth angle as an example, when the measurement error is considered, the pseudo-azimuth angle can be written as

$$\varphi'_s = \arctan[(v_e + \varepsilon_e)/(v_n + \varepsilon_n)] \tag{4}$$

where ε_e and ε_n are velocity measurement errors in the east and north direction respectively. We can see that when the velocity component values (v_e and v_n) are small, the error terms (ε_e and ε_n) will lead to large measurement deviation of pseudo-azimuth angle. Similarly, the velocity measurement errors will also cause deviations of the pitch and roll angles. This type of error is called the measurement error in this paper.

2.2.2 Offset Error

When estimating the pseudo-attitude angles, we define the carrier velocity as the velocity of its geometric center, however, which we in fact measuring is the velocity of the antenna. The offset of the antenna position from the carrier

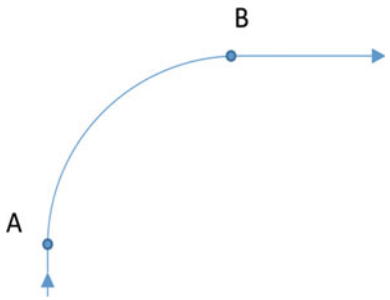

Fig. 1 The assumed trajectory of the carrier

geometric center will cause the deviation of pseudo-attitude angles. Assume the carrier firstly drives northward, then turns eastward (or turns right), and runs along the arc AB curve $(y = f(x) = \sqrt{r^2 - x^2})$ in an uniform speed. The assumed trajectory of the carrier is shown in Fig. 1.

Given the length of carrier is n meters, when the carrier runs along the arc AB, the coordinates of carrier head are,

$$\begin{aligned} x_1 &= x + n/2 \times \cos(\arctan(f'(x))); \\ y_1 &= y + n/2 \times \sin(\arctan(f'(x))) \end{aligned} \tag{5}$$

Also, the coordinates of the rear of carrier are,

$$\begin{aligned} x_2 &= x - n/2 \times \cos(\arctan(f'(x))); \\ y_2 &= y - n/2 \times \sin(\arctan(f'(x))) \end{aligned} \tag{6}$$

Suppose the radius of the quadrant trajectory is very small, let the range of x is -0.1–0 m, and $n = 5$. Figure 2 is the simulated trajectories of carrier center (black line), carrier head (red line), and carrier rear (blue line). It indicates that if the offset length is far greater than the radius of the quadrant trajectory, the deviation in azimuth angle caused by offset error will be close to 90° (red line) or −90° (blue line).

2.2.3 Lateral Error

Lateral error caused by crosswind has already been discussed in high-dynamic field. In heavy crosswind condition, the carrier will probably move laterally, which makes the carrier trajectory deviate from the scheduled route. Therefore, the calculated pseudo-azimuth angle based the trajectory will contain a sideslip angle caused by crosswind, and lead to the deviations from real azimuth angle [6]. In addition, the change of wind speed can also cause the error of pseudo-roll angle. In Eq. (3), the acceleration of wind speed is assumed to be zero. This assumption is only applicable to the situation that the change of wind speed is not significant.

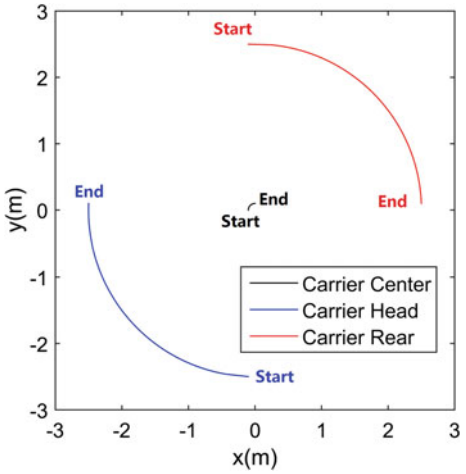

Fig. 2 Trajectories of different parts of carrier when it turns around

However, it will no longer valid when serious wind shear occurs or under non-coordinate flight (such as severe slip or yaw maneuver). In these conditions, pseudo-roll angle will deviate from real roll angle obviously [1]. This paper defines the error caused by crosswind as lateral error. The lateral error not only exists in high-dynamic application, but also in low-dynamic application (e.g. vehicle and ship), the sideslip of the vehicle and disturbances of crosswind and cross wave to the ship, for instance.

2.3 Single-Antenna Attitude Determination for Low-Dynamic Carriers

To correct the measurement error, speed threshold is used in this paper. If the vehicle speed is less than 10 cm/s, we do not measure the pseudo-attitude angle at the present epoch, but substitute it with that at the previous epoch.

To reduce the offset error, we can install the antenna as near as possible to the carrier center.

Since we found no obvious lateral error in the vehicle experiment mentioned in the next section, we do not go into details in this paper.

3 Experiments

Vehicle experiment is processed in two steps. First is to validate the feasibility of pseudo-attitude determination method in vehicle environment. Second is to test the strategies for correcting the measurement and offset errors. The test was carried out

Fig. 3 Antenna configurations in the vehicle experiment

in the campus of East China Normal University on March 23th, 2015. We deployed two antennas on the top of the vehicle with the baseline parallel to the principal axis (Fig. 3). The baseline length was about 1.75 m. Two antennas were connected with a multi-antenna synchronized GNSS receiver (Trimble BD982). The observations from antenna B were used to calculate pseudo-attitude angles (we let the antenna B obviously offset from the vehicle center to show the effect of offset error). The attitude results from dual-antenna were taken as the reference data. Figure 4 shows the vehicle's trajectory. It first stopped in point D for five minutes, then ran around the campus slowly for two laps (about 13 and 10 min respectively). The whole experiment lasted about 30 min The velocity of vehicle was estimated based on the ionofree combination of pseudorange and carrier phase observations using Kalman filter.

Figures 5 and 6 show respectively the pseudo-attitude results without correction and dual-antenna attitude measurements. Since the road in campus is almost flat, the roll angles are close to zero, we only demonstrate the results of azimuth angle and pitch angle. It is easy to find that, when the vehicle is static (at the beginning and end of the experiment), the pseudo-attitude measurements are disorderly, which are obviously wrong. These results are caused by the measurement error. In contrast, as the vehicle running (the speed is 2–3 m/s), the pseudo-azimuth and pseudo-pitch angles coincide with the results from dual-antenna very well.

Figure 7 shows the corrected results with speed threshold. It demonstrates that the disorderly results of static vehicle were eliminated. Since the vehicle was stationary at the beginning, there is no previous azimuth angle information, the pseudo-attitude angles are assumed to zero at first. From epoch 2996 to 3082, there is a sudden change of 180° in azimuth angle, which are inconsistent with the

Fig. 4 Trajectory of the vehicle

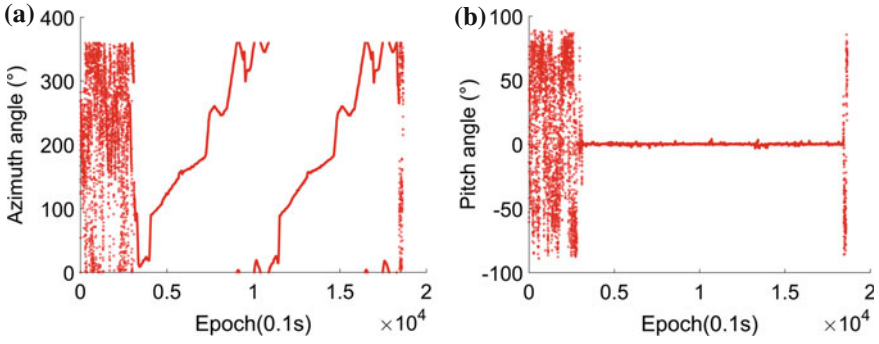

Fig. 5 Pseudo-attitude measurements **a** Azimuth angle **b** Pitch angle

azimuth trend. It is a mixed problem of two reasons. First, the vehicle was turning, but it drove slowly. We do not calculate the azimuth angle, but assign the value at the previous epoch to it (165° at epoch 2995) to mitigate the measurement error, which cause a deviation of 90° in azimuth angle. Second, the radius of the vehicle trajectory was very small. According to the case in Sect. 2.2.2, the offset error will also lead to a deviation of 90° in azimuth angle. And these two reasons will result a total deviation of 180° in azimuth angle. For this error, the strategy in the paper is to add (or minus) 180° to make the azimuth angles maintain consistent when the first sudden change occurs, and stop the operation of adding (or minus) 180° when the second sudden change occurs. Figure 8 shows the azimuth angle measurements

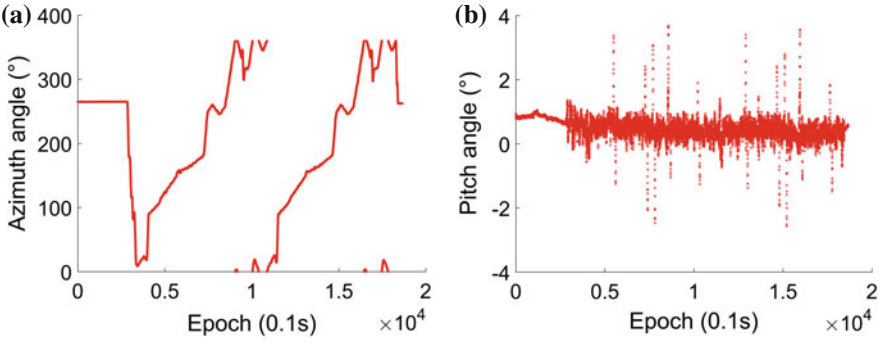

Fig. 6 Dual-antenna attitude measurements **a** Azimuth angle **b** Pitch angle

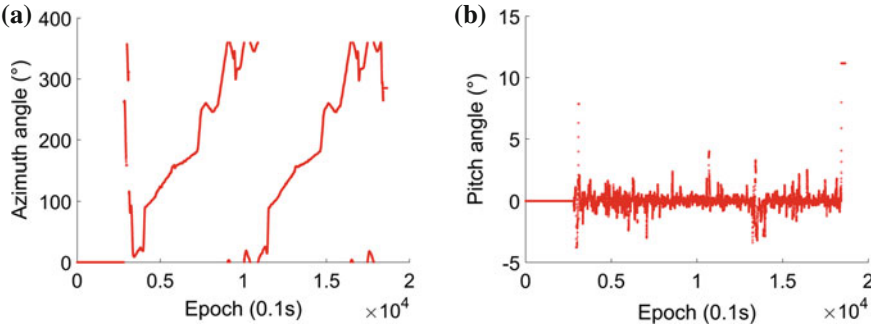

Fig. 7 Attitude measurements after measurement error correction **a** Azimuth angle **b** Pitch angle

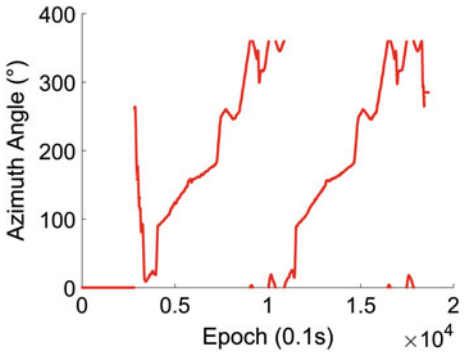

Fig. 8 Azimuth angle measurements after offset error correction

after the offset error correction, which essentially in agreement with the results from the dual-antenna measurements. Comparison results show that the standard deviation of pseudo-azimuth angles is 3.7°, and the standard deviation of pseudo-pitch angle is 1.4°.

4 Conclusions

This paper discussed and tested the feasibility of attitude determination using single-antenna GNSS receiver for low-dynamic carriers. Vehicle experiment results show that if we adopt reasonable threshold to correct the measurement error, and simultaneously use sudden change detection to eliminate the offset error, the GNSS single-antenna pseudo-attitude determination method can be used to measure the attitude of low speed carriers at m/s level. The measurement precision of azimuth angles and pitch angles can reach the level of less than 5°. This method has great practical significance for small carriers, which cannot accommodate multiple antennas. For the existing single-antenna carriers, this method can provide reliable attitude information without adding any equipment or making any device modifications, thus is of great application value and economic benefits.

Acknowledgements This work is sponsored by National Natural Science Foundation of China (No. 61,372,086, No. 61671264), the Science and Technology Commission of Shanghai (No. 13511500300, No. 15511101602).

References

1. Kornfeld RP, John HR, Deyst J (1998) Single-antenna GPS-based aircraft attitude determination. Navigation 45(1):51–60
2. Lee S, Lee T, Park S, Kee C (2013) Flight test results of UAV automatic control using a single-antenna GPS receiver. In: AIAA guidance, navigation, and control conference and exhibit
3. Cho A, Kim J, Lee S, Choi S (2007) Fully automatic taxiing, takeoff and landing of a UAV using a single-antenna GPS receiver only. Int Conf Control Autom Syst 41:821–825
4. Liu R, Zhang P, Zhang L (2009) Algorithm of pseudo-attitude determination based on single antenna GPS. J Civ Aviat Univ China 27(6):25–28
5. Zeng Q, Liu J, Zhang Q (2014) Attitude determination algorithm based on Bei Dou single-antenna. In: China satellite navigation conference
6. Wang Q, Li Q, Cheng N, Song J (2014) Counteracting crosswind control method for flying-wing UAV without sideslip sensors. J Tsinghua Univ (Sci Technol) 54(4):530–535

Differenced Measurements Between Satellites Applied on RTK PPP for Structure Monitoring

Xu Tang and XingXing Li

Abstract Double differenced (DD) GPS are widely used for civil structure monitoring. Errors, introduced by troposphere/ionosphere and orbit, could be significantly mitigated by the double differenced operator in short baseline applications. The distance between reference station and roving stations, as well as the instability of reference in nature disaster, limit the applications due to the failure of error sources mitigation. RTK PPP using for bridge deflection monitoring is investigated in this paper. Differenced ionosphere-free measurements are applied for avoiding estimating the receiver's clock error. GNSS data were gathered at 10 Hz with the antenna mounted on the Severn bridge on 18th March 2010. Bridge deformation results estimated by DD technology is used as truth against which the performance of satellite differenced RKT PPP is assessed. The study implies real time PPP, applying difference measurement between satellites, is competent for the suspension bridge deformation.

Keywords RTK PPP · Satellite difference measurement · Ionosphere-free linear combination measurement

1 Introduction

Vast majority of GPS bridge deflection monitoring studies, carried out in the past few decades, were using double differenced technology [1, 2, 5, 6, 11]. DD GPS can estimate centimeter level accuracy deflections with mitigating the troposphere

X. Tang (✉)
University of Nottingham Ningbo,
199 Taikang East Road, Ningbo 315100, Zhejiang, China
e-mail: Tang.GNSS@qq.com; Xu.Tang@nottingham.edu.cn

X. Li
School of Geodesy and Geomatics, Wuhan University,
129 Luoyu Road, Wuhan 430079, Hubei, China
e-mail: lxlq109121@gmail.com

J. Sun et al. (eds.), *China Satellite Navigation Conference (CSNC) 2017 Proceedings: Volume I*, Lecture Notes in Electrical Engineering 437,
DOI 10.1007/978-981-10-4588-2_24

and ionosphere error sources, as well as the clocks' errors both in satellite and receivers. In some circumstance, such as earthquake, power outage of reference station, the use of DD GPS is not possible. PPP is one alternative method for providing precise standalone position with the precise products, such as clock and orbital post-processed documentary. PPP is considered as the promising tools, has been applied in many applications, such as precise orbit determination of low orbital satellites [12]; coseismal displacement monitoring [4, 8]; real-time zenith tropospheric delay (ZTD) estimation for meteorology analysis [10]. Different from the DD operator eliminates/mitigates the most of error sources introduced from troposphere, ionosphere broadcasted ephemeris and clocks' errors, PPP applies the precise produces from IGS analysis centers, takes the receiver clock error and tropospheric ZTD as unknown parameters to estimate with the carrier phase ambiguity and positions. The residual errors which cannot be modeled and eliminated are called as un-calibrated fractional offsets (UFO). The un-calibrated fractional offsets are absorbed into the carrier phase ambiguities, further, destroyed the integer ambiguity property [3]. PPP can achieve centimeter level accuracy with approximate half an hour's convergence. The regional reference network is applied to augment the PPP resolution for the instantaneous ambiguity fixing [7, 9] for shortening the convergence time.

This paper employs the satellite-difference ionosphere-free measurement for the PPP extracting the bridge deflection movements epoch by epoch. DD results is used as truth against which the RTK PPP is applied in structure deflection monitoring assessment.

2 Methodology

2.1 Linear Combined Ionosphere-Free Equation

The linear combined carrier phase and code measurements for the RTK PPP model can be written as,

$$\varphi_{(i,j)} = \rho + (\delta T + \delta t) \cdot c + \delta_{orb} + N_{(i,j)} \cdot \lambda_{(i,j)} - \beta_{(i,j)} \cdot \frac{-40.3TEC}{f^2_{(i,j)}} + \delta_{trop} + \xi_{\varphi_{(i,j)}} + \left(B_{(i,j)} + b_{(i,j)}\right) \cdot \lambda_{(i,j)} \tag{1}$$

$$P_{(i,j)} = \rho + (\delta T + \delta t) \cdot c + \delta_{orb} + \left(D_{(i,j)} + d_{(i,j)}\right) + \beta_{(i,j)} \cdot \frac{-40.3TEC}{f^2_{(i,j)}} + \delta_{trop} + \xi_{P_{(i,j)}} \tag{2}$$

where, $\varphi_{(i,j)}$ and $P_{(i,j)}$ are the linear combined carrier phase and code measurements in the unit of meters, respectively. ρ is the geometric distance between the tracked satellite and receiver. δT and δt represent the clock errors of the tracked satellites and receiver, respectively. c is the speed of light in a vacuum. δ_{orb} is the satellite orbital error. TEC is the abbreviation of total electron content. $f_{(i,j)}$ is the frequency of linear combined carrier phase frequency. $N_{(i,j)}$ is the linear carrier phase combination ambiguity, satellite and receiver linear combined un-calibrated carrier phase delays in unit of cycles can be expressed as $B_{(i,j)} = i \cdot B_1 + j \cdot B_2$ and $b_{(i,j)} = i \cdot b_1 + j \cdot b_2$. The satellite and receiver linear combined code delays in unit of meters are $D_{(i,j)} = \frac{i \cdot f_1 \cdot D_1 + j \cdot f_2 \cdot D_2}{i \cdot f_1 + j \cdot f_2}$ and $d_{(i,j)} = \frac{i \cdot f_1 \cdot d_1 + j \cdot f_2 \cdot d_2}{i \cdot f_1 + j \cdot f_2}$, respectively. The first-order of combined measurements $\varphi_{(i,j)}$ and $P_{(i,j)}$ ionospheric linear coefficient is $\beta_{(i,j)} = (i/f_1 + j/f_2) \cdot f_{(i,j)}$. $\xi_{\varphi_{(i,j)}}$ and $\xi_{P_{(i,j)}}$ are linear combined carrier and code random noise. δ_{trop} is the tropospheric delay, including the zenith hydrostatic delay (ZHD) and zenith wet delay (ZWD). With the empirical model, the total slant tropospheric delay is given,

$$\delta_{trop} = M^h \cdot \delta_{ZHD} + M^w \cdot \delta_{ZHD} \tag{3}$$

where, M^h and M^w are corresponding mapping functions dependent on satellites' elevations. δ_{ZHD} and δ_{ZWD} denote ZHD and ZWD, respectively.

The linear combined carrier phase and code measurements can be expressed as,

$$\varphi_{(i,j)} = \frac{i \cdot f_1 \cdot \varphi_1 + j \cdot f_2 \cdot \varphi_2}{i \cdot f_1 + j \cdot f_2} \tag{4}$$

$$P_{(i,j)} = \frac{i \cdot f_1 \cdot P_1 + j \cdot f_2 \cdot P_2}{i \cdot f_1 + j \cdot f_2} \tag{5}$$

In order to keep the integer property of the carrier phase measurement, i and j could be arbitrary integer in the above equations, which means $i, j \in Z$. f, φ and P with subscript 1 and 2 represent L1/L2 frequency, phase measurement and code measurement, respectively. Linear carrier phase measurement wavelength is,

$$\lambda_{(i,j)} = \frac{c}{i \cdot f_1 + j \cdot f_2} \tag{6}$$

2.2 Kalman Filter for the Satellite Difference RTK PPP

Kalman filter is applied for estimate the unknown parameters including position, tropospheric delay, as well as the undifferenced ambiguities. Receiver clocker's error which estimated in traditional PPP is not taken considering here, as the

satellite differenced measurement absolutely eliminates this effect. Satellite difference RTK PPP's Kalman filter state can be expressed as,

$$x = [\,\delta x \quad \delta y \quad \delta z \quad \delta_{wet} \quad N_1 \quad \ldots \quad N_s\,]^T \tag{7}$$

where, δx δy and δz are the position corrections at the component of x y and z, respectively. δ_{wet} is the zenith wet delay (ZWD), reflects the levels of vapor in the atmosphere. N with the subscripts from 1 to s denotes the number of s tracked satellites' ambiguities.

The observation equation coefficient H is designed as,

$$H = \begin{bmatrix} l_1 & m_1 & n_1 & -1 & 0 & 0 & 0 & \ldots & 1 & \ldots & 0 \\ l_1 & m_1 & n_1 & 0 & 0 & 0 & 0 & \ldots & 1 & \ldots & 0 \\ l_2 & m_2 & n_2 & 0 & -1 & 0 & 0 & \ldots & 1 & \ldots & 0 \\ l_2 & m_2 & n_2 & 0 & 0 & 0 & 0 & \ldots & 1 & \ldots & 0 \\ & & & \vdots & & & & & \vdots & & \\ l_{(s-1)} & m_{(s-1)} & n_{(s-1)} & 0 & 0 & 0 & 0 & \ldots & 1 & \ldots & -1 \\ l_{(s-1)} & m_{(s-1)} & n_{(s-1)} & 0 & 0 & 0 & 0 & \ldots & 1 & \ldots & 0 \end{bmatrix} \tag{8}$$

where, l, m and n denote the unit vector from receiver to tracked satellites; the column, which elements are all 1, is the ambiguity coefficient of reference satellite. Reference satellite is chosen by the highest elevation within all tracked satellites.

3 Experiment–Severn Suspension Bridge, UK

Severn bridge connects Wales and England over the Severn bridge. Main span of the Severn bridge is 998 m, supported with two 136 m towers. The Severn bridge is equipped with anemometers and thermometers, as well as weight-in-motion (WIM) sensors on the Welsh side of bridge, which is 1.522 km away from the Beachley supporting towers. WIM sensors can record the weight of the vehicle, as well as its travelling direction and speeds, when vehicle travels over these WIM sensors. The traffic load on Severn bridge, at any time/any point, can be derived from the vehicles' weight, speed and the distance between vehicle and WIM sensors. It is important to note that this load traffic is derived with the assumption of all vehicles traveled over the bridge with some constant speeds which were recorded by the WIM sensors. This field work was carried out from 10 to 12 March 2010 and again on 18 March 2010. The study is focused on the dataset gathered on 18th. We attached 9 dual-frequency survey grade GPS/GLONASS receivers on the bridge. 4 of them located on the top of two pairs of towers with 20 Hz sampling rate, the rest of 5 receivers were mounted on the suspension cables with 10 Hz sampling rate. Two receivers were setup on the stable ground, respectively, for processing the data relatively with the survey points on the bridge. The relative results would be

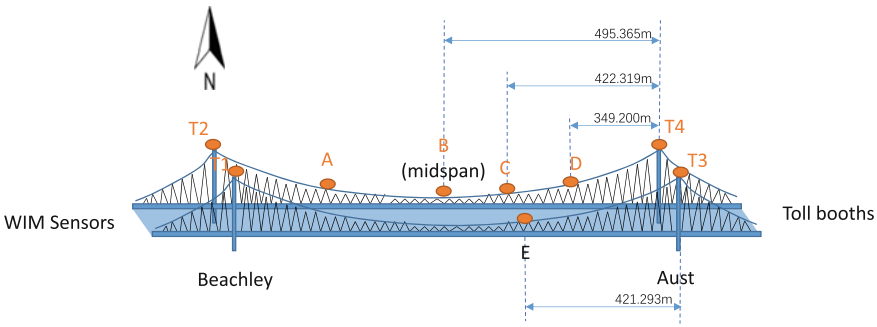

Fig. 1 Survey points on the Severn bridge, as well as the WIM sensors location

used as truth deflection against which the RTK PPP results are assessed. Figure 1 illustrates the configurations of survey points. Point A/B/C/D/E are mounted with GPS/GLONASS antennas. T1/T2 and T3/T2 are the surveying points on the supporting towers. This configuration allows us analyzing the synchronize movements of Towers with bridge deck.

4 Results

The vast amount of data is processed by both DD and satellite difference RTK PPP techniques. The DD technology has been well applied in many structures deflection monitoring. The DD deflections are treated as truth movements to assess the satellite difference RTK PPP results. This section also finds the synchronized movements between the towers, as well as the deck movement, the relationship between deflections and bridge weight loads.

Figure 2 illustrates the deflections of the supporting towers in the longitudinal direction. The pairs of supporting towers longitudinal deflections have an evident consistency. This is evident, in particular, between tower 03 and tower 04 results, as well as tower 1 and tower 2. Figure 2 also imply the satellite difference RTK PPP could be used for detecting small movements detection.

Figure 3 shows the DD vertical results, as well as the one of satellite difference RTK PPP results over 1 h. the satellite difference RTK PPP has strong consistency with the DD results, particularly the peaks exist in the two waveforms. It is necessary to notice there is gradually movement in satellite difference RTK PPP, evidently, but does not exist in DD results. This gradually position movement is derived from the ambiguity integer property destroyed, as well as the tropospheric delay residuals.

The traffic load is derived from the weight sensors data, 1.522 km away from the beachley supporting towers. Weight sensors could record the weight of vehicle and its heading direction when passing the bridge. The traffic weight load is calculated

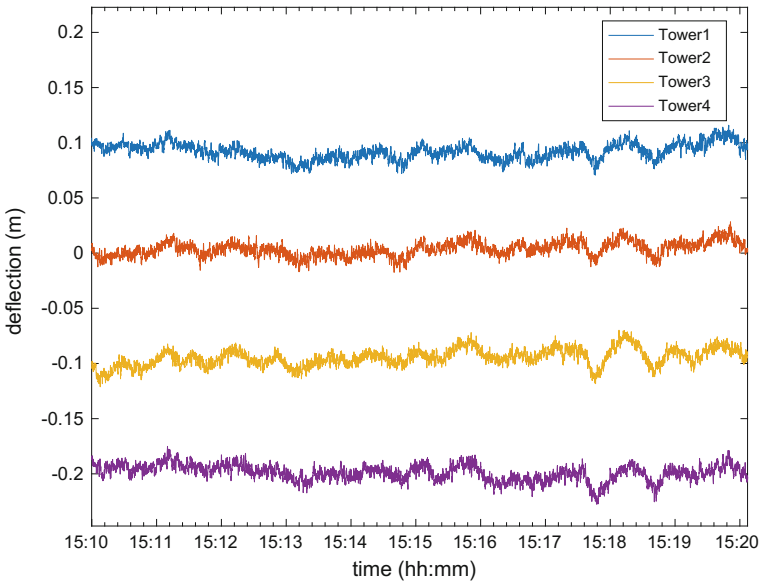

Fig. 2 Satellites difference RTK PPP deflections at 4 towers' survey points in longitudinal direction from 15:10 to 15:20

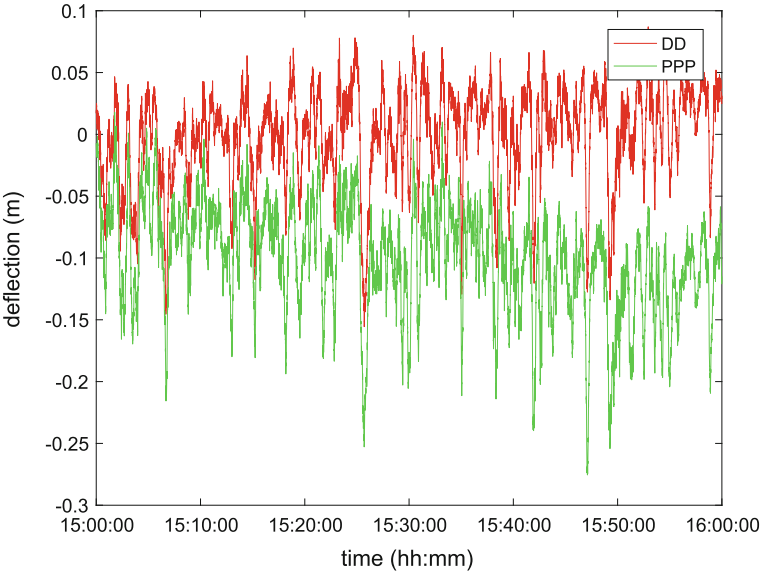

Fig. 3 Satellites difference RTK PPP and DD deflections in vertical direction at survey point B over 1 h

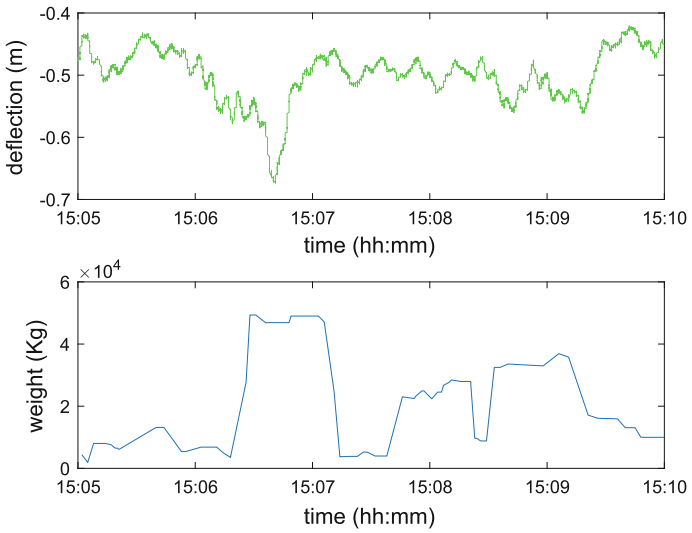

Fig. 4 Vertical deflection at survey point B (*top panel*) and the total load of traffic (*bottom panel*) on the north side of main span over 5 min

under the assumption of all the vehicle traveled over the bridge over a constantly speed which is recorded by the weight sensors. Figure 4 illustrates the relativity between bridge vertical movements at the suspension cable survey point and the traffic load over 5 min. In the bottom panel of Fig. 4 from 15:06 to 15:07, the bridge weight load is up to approximate 50 tons on the north-side of main span, with correspondingly large vertical deflection at location B.

5 Conclusion

Double differencing operator can mitigate the tropospheric and ionospheric delays, and eliminate the satellites and receiver's clock errors in GPS monitoring applications. Many previous researches used double differenced GPS techniques for detecting the movement of bridges, with very high accuracy. Real time PPP can provide the position without any reference station. In this paper, satellite difference RTK PPP is used for measuring the deflection of such a bridge without considering the receiver clock's error. Double difference movement results met agreement with the one of RTK PPP. Satellite difference RTK PPP can not only derive the bigger movements at survey point at suspension cable, but also the small movements on the supporting towers. Traffic dataset are used to assess the amplitude of movement. Real time satellite difference RTK PPP can derive the bigger movements while there is a heavy traffic.

Acknowledgements The work in this paper is supported by the Ningbo Science and Technology Bureau as Part of the Projects: Integration of GPS and BDS to monitor large bridge on real time (2016A610116) and Structural Health Monitoring of Infrastructure in the Logistics Cycle (2014A35008).

References

1. Ashkenazi V, Roberts GW (1997) Experimental monitoring of the Humber Bridge using GPS. In: Proceedings of the ICE-Civil Engineering. Thomas Telford
2. Brown CJ, Karuna R, Ashkenazi V, Roberts GW, Evans RA (1999) Monitoring of structures using the global positioning system. Proc Inst Civil Eng-Struct Build 134:97–105
3. Geng J, Meng X, Dodson AH, Ge M, Teferle FN (2010) Rapid re-convergences to ambiguity-fixed solutions in precise point positioning. J Geodesy 84:705–714
4. Guo B, Zhang X, Ren X, Li X (2015) High-precision coseismic displacement estimation with a single-frequency GPS receiver. Geophys J Int 202:612–623
5. Guo J, Dai LJ, Lu YC (2000) Study of method for realtime survey on humen bridge by GPS (RTK). Bull Surv Mapp 12:4–5
6. Huang S, Wu W, Li P (2005) GPS dynamic monitoring experiment and result analysis of long span cable stayed bridge. Geomat Inf Sci Wuhan Univ 30:999–1002
7. Li X, Ge M, Douša J, Wickert J (2013) Real-time precise point positioning regional augmentation for large GPS reference networks. GPS Sol 18:61–71
8. Li X, Ge M, Zhang Y, Wang R, Guo B, Klotz J, Wickert J, Schuh H (2013) High-rate coseismic displacements from tightly integrated processing of raw GPS and accelerometer data. Geophys J Int 195:612–624
9. Li X, Zhang X, Ge M (2010) Regional reference network augmented precise point positioning for instantaneous ambiguity resolution. J Geodesy 85:151–158
10. Lu CX, Li XX, Nilsson T, Ning T, Heinkelmann R, Ge MR, Glaser S, Schuh H (2015) Real-time retrieval of precipitable water vapor from GPS and BeiDou observations. J Geodesy 89:843–856
11. Roberts GW, Brown CJ, Tang X, Meng X, Ogundipe O (2014) A tale of five bridges; the use of GNSS for monitoring the deflections of bridges. J Appl Geodesy 8:241–264
12. Weinbach U, Schön S (2012) Improved GRACE kinematic orbit determination using GPS receiver clock modeling. GPS Sol 17:511–520

Research on Retrieval of PWV Based on PPP and NCEP/NCAR Global Reanalysis 1 Data

Zhilu Wu, Yanxiong Liu, Xiufeng He, Kai Guo, Lina He and Menghao Li

Abstract Aimed at lack of temperature and pressure data in retrieving Precipitable Water Vapor (PWV) from Precise Point Positioning (PPP), a Layer Interpolation Method (LIM) used the NCEP/NCAR layer reanalysis data is proposed. 14 IGS stations located at different altitudes are selected to validate the method with its meteorology files. The interpolated temperature and pressure values from the LIM and those from the classical Surface Interpolation Method (SIM) have been compared with the observed data, further for evaluating effect on the derived PWV. The experimental results show that (1) two interpolation methods perform well in pressure at the GPS sites below 2000 m with RMS 1.79 mbar (LIM) and 3.83 mbar (SIM), LIM is better than SIM. While the interpolated temperature values nearly have the same accuracy with RMS 3.63 K (LIM) and 3.69 K (SIM). (2) The LIM and the SIM exist the large pressure errors for the GPS site above 3000 m as LHAZ. The interpolated pressure error reach 8 mbar, which contributes 3 mm PWV error. While the accuracy is still better than the accuracy of PWV without meteorological data, especially for LIM with the improvement from 4.36 to 3.29 mm. (3) The derived PWV accuracy with interpolation data shows obvious positive correlation with the accuracy of the interpolated pressure data, while the accuracy of PWV has no correlation with temperature data, which means the accuracy of retrieving PWV is mainly effected by pressure. (4) The accuracy of the PWV retrieved with the interpolated meteorological data has no obvious coupling relation with altitude and latitude.

Keywords PPP · NCEP/NCAR reanalysis 1 data · Cubic hermite interpolation · IGS stations

Z. Wu (✉) · X. He · K. Guo · L. He
College of Earth Science and Engineering, Hohai University, Nan Jing, China
e-mail: wuzhilu@hhu.edu.cn

Z. Wu · Y. Liu · K. Guo · M. Li
First Institute of Oceanography, State Oceanic Administration, Qing Dao, China

J. Sun et al. (eds.), *China Satellite Navigation Conference (CSNC) 2017 Proceedings: Volume I*, Lecture Notes in Electrical Engineering 437,
DOI 10.1007/978-981-10-4588-2_25

1 Introduction

With the development of Precise Point Positioning (PPP) technology, the research on Precipitable Water Vapor (PWV) based on PPP is widely carried on. PPP technology has the advantage of no reference stations, no correlation between the stations, no distance limit, single receiver position process and so on, existing research shows that PPP derived Zenith Troposphere Delay (ZTD) has the same accuracy of network resolution [1] ZTD estimation based on the static PPP technology is relatively mature at present, the accuracy of PWV based on PPP and IGU product (International Unit/IGS fast forecast product) is 2–3 mm [2].

Meteorological data such as pressure and temperature of observation stations are necessary when retrieving PWV based on PPP. While in the actual observation, stations sometimes are not equipped with meteorological instruments, which cause the missing of meteorological data. Therefore, Meteorological data can only be calculated through equations from sea level, therefore, the accuracy of PWV will be effected. Research shows that the accuracy requirement for pressure has to be in the range of 1–2 mm to achieve roughly 1.5–3 mm accuracy in Zenith Hydrostatic Delay (ZHD) [3]. At present, many scholars at home and abroad put forward using the NCEP (U.S. National Centers for Environmental Prediction) reanalysis data to obtain meteorological data. NCEP data take variational data assimilation technology, fusing different kind of meteorological observation data. When stations lack of observation meteorological data, accuracy meteorological data can be obtained from NCEP reanalysis data. Schueler took experiment based on NCEP data, the results verified the possibilities of estimating the meteorological through weather models [3]; Wang obtained global PWV data based on IGS troposphere product and NCEP interpolation meteorological data [4]; Jade used 6 GPS stations of India, combined NCEP/CEAR data to inverse the PWV of India area [5].

Basing NCEP reanalysis data to interpolate data in the vertical direction mainly through empirical equations, but the changing of temperature and pressure in the vertical direction do not entirely follow the empirical equation, which bring the errors inevitably. In this paper, a method based on NCEP/NCAR hierarchical data is proposed, cubic Hermite interpolation is used to conduct Layer Interpolation Method (LIM). 14 global IGS stations are taken into consideration to carry the test, comparing with the result of Surface Interpolation Method (SIM) [4, 6, 7] and observation meteorological data. PPP retrieved PWV with observation data is taken as true value and compare the true value with the results with two different interpolation data and without meteorological data to evaluate the accuracy of interpolation method.

2 Meteorological Data Interpolation Method

2.1 Requirement of Meteorological Data in the Retrieval of PWV

To retrieve PWV from PPP contain three main steps: estimation of troposphere delay, atmospheric static delay estimation and conversion coefficient estimation [8]. In the paper, GPS ZHD is separated by models; GPS Zenith Wet Delay (ZWD) component is set as parameter to be estimated; mapping functions model use Nilell Mapping Function (NMF); taking into account the inhomogeneity of the water vapor distribution, the atmospheric horizontal gradient correction parameters are introduced [9].

SAAS model is used to estimate ZHD, troposphere weight average temperature T_m is obtained by BEVIS equation during the transformation factor estimation [10]. Therefore surface pressure and temperature data are necessary during the calculation of ZHD and T_m.

2.2 Method of Meteorology Data Interpolation

2.2.1 Surface Interpolation Method (SIM)

NECP/NCAR reanalysis 1 data is an important part of the meteorological data assimilation system, which is implemented by the U.S. National Weather Service in 1991 [6]. NCEP/NCAR can provide a resolution of 2.5° × 2.5° global grid analysis of meteorological data (144 × 73), data ranges 90N-90S, 0E-357.5E, updated per six hours. Based on near the surface (0.995 sigma layer) data, the main interpolation steps are as follow:

1. Find the longitude and latitude data of the nearest four grid points around target point S_0, calculate the height of four grid points S_i(i = 1, 2, 3, 4) at 0.995 sigma layer:

$$H_{0.995i} = H_{si} + R_d T_{0.995i} \ln(1/0.995)/g \quad (\mathrm{i} = 1, 2, 3, 4) \tag{1}$$

where $H_{0.995i}$, $T_{0.995i}$ are the height and temperature of S_i in 0.995 sigma layer respectively, H_{si} is the geodetic height of gird points S_i, R_d is dry air gas constant.

2. When interpolation in the vertical direction, first calculate the temperature T_{oi} and pressure P_{oi} of four points O_i(i = 1, 2, 3, 4) with the same height as target point S_0, which is achieved through iteration. When difference between H_s and $H_{0.995i}$ <20 m:

$$T_{oi} = T_{0.995i} + \beta(H_s - H_{0.995i}) \quad (\mathrm{i} = 1, 2, 3, 4) \tag{2}$$

$$T_m = (T_{0.995i} + T_{oi})/2 \quad (\mathrm{i} = 1, 2, 3, 4) \tag{3}$$

$$H_m = (H_o - H_{0.995i})/T_m \quad (\mathrm{i} = 1, 2, 3, 4) \tag{4}$$

$$P_{oi} = P_{0.995i}\mathrm{e}^{-g \cdot H_M / Rd} \quad (\mathrm{i} = 1, 2, 3, 4) \tag{5}$$

where β is the adiabatic lapse rate of temperature, $\beta = -5.930 - 0.0359$ $(T_{0.995i} - 273.15)$; H_m,T_m are intermediate variables. When the difference between H_s and $H_{0.995i}$ is larger than 20 m, H_m become:

$$\triangle z_i = \begin{cases} 20\ \mathrm{m}, H_S > H_{oi} \\ -20\ \mathrm{m}, H_S < H_{oi} \end{cases} \tag{6}$$

$$T_i = T_s + \beta \cdot \triangle z_i \tag{7}$$

$$H_m = \sum_{H_g}^{H_i} \frac{\triangle z_i}{(T_i + T_{i+1})/2} \tag{8}$$

3. Inverse Distance Weight (IDW) is used in the horizontal direction, the temperature and pressure of GPS station are obtained at UTC 0, 6, 12 and 18 h respectively.
4. When interpolation in the time domain, cubic spline interpolation is applied to interpolate the temperature and pressure of the target time.

2.2.2 Layer Interpolation Method (LIM)

NECP/NCAR reanalysis 1 data provides 17 pressure layer data in each grid point, which ranges from 1000 to 10 mbar. A new method based on pressure layer data is proposed in the paper, the steps are as follow:

(1) Find the longitude and latitude data of the nearest four grid points around target point S_0, get temperature and height data of first six pressure layer respectively, which are 1000, 925, 850, 700, 600 and 500 mbar.

(2) Interpolate pressure data by cubic Hemite interpolation, the pressure P_{oi} of nearest four grid points S_{oi} (i = 1, 2, 3, 4) at the same height as S_0 are obtained. Using cubic Hemite interpolation to interpolate temperature data and then temperature T_{oi} of corresponds to pressure P_{oi} are calculated.
(3) Using IDW to interpolate pressure and temperature in the horizontal direction, getting the pressure and temperature values of GPS station at standard time (UTC 0, 6, 12, 18 h).
(4) Basing the pressure and temperature values at standard time of GPS station, cubic spline interpolation is used to get the temperature and pressure at any time.

3 PPP PWV Estimation and Analysis of the Results

3.1 Selected GPS Stations

To validate the accuracy of LIM, 14 IGS stations with decreasing elevation are selected. The stations distribute uniformly with observation meteorological data from Day of Year (DOY) 300 to 306 in 2014, among which MDO1and ULAB are not provided with observation data, ZIMM lack of observation data at DOY 302 and 303, temperature data of ULAB is missing. Figure 1 give the distribution of all selected sites and detail information of GPS stations are in Table 1.

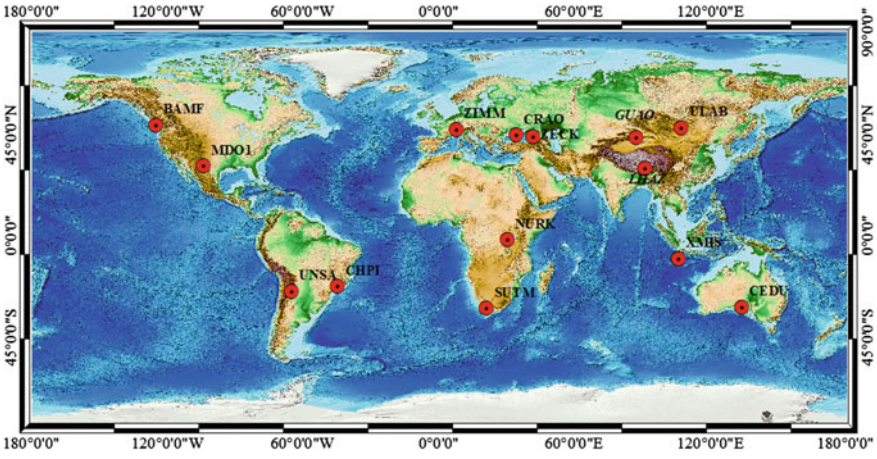

Fig. 1 Distribution of GPS stations

Table 1 GPS stations used in the analysis

Site code	B(°)	L(°)	H(m)	GPS observation time (DOY)	Meteorological data (DOY)
LHAZ	29.66	91.1	3622	300–306	300–306
GUAO	43.47	87.18	2049.2	300–306	300–306
MDO1	30.68	−104.01	2004.48	–	300–306
SUTM	−32.38	20.81	1797.6	300–306	300–306
ULAB	47.67	107.05	1611.7	–	Temperature data missing
NURK	−1.94	30.09	1485.3	300–306	300–306
UNSA	−24.73	−65.41	1257.8	300–306	300–306
ZECK	43.79	41.57	1166.8	300–306	300–306
ZIMM	46.88	7.47	956.7	302–303 missing	300–306
CHPI	−22.69	−44.99	617.42	300–306	300–306
CRAO	44.41	33.99	365.8	300–306	300–306
XMIS	−10.45	105.69	261.58	300–306	300–306
CEDU	−31.87	133.81	144.82	300–306	300–306
BAMF	48.84	−125.14	11.1	300–306	300–306

3.2 Accuracy Evaluation of Interpolated Meteorological Data

Meteorological data from LIM and SIM are obtained respectively and measured meteorological data are available in 14 GPS sites. Compare the interpolated meteorological data with the measured data to evaluate the accuracy of two different interpolation methods. The average bias and the standard deviation (STD) between interpolated values and measured values of temperature and pressure for DOY 300–306 in 2014 are given in Figs. 2a and 3a. The RMS between interpolated and measured are given in Figs. 2b and 3b.

From accuracy analysis figures (Figs. 2 and 3): (1) both LIM and SIM cannot interpolate pressure of LHAZ from Qinghai-Tibet plateau accurately, while other GPS sites perform well, the average difference RMS of LIM is 1.79 mbar and SIM is 3.83 mbar, the accuracy and reliability of LIM is better than LIM; (2) the accuracy of interpolation temperature values are the same, among which, the results of LIM in higher elevation are better and SIM is more suitable for lower elevation; (3) there is no obvious coupling relation between the accuracy of interpolated meteorological and the elevation.

3.3 Accuracy Evaluation of PPP PWV

With the aid of PPP software static module, using four different process strategies to retrieve PWV of 12 IGS stations from observation data: (1) with measured

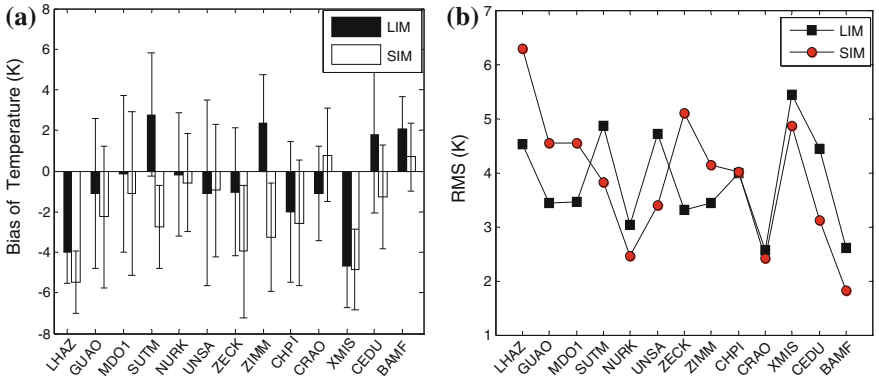

Fig. 2 Accuracy analysis of two interpolation methods in temperature at 13 sites: **a** average bias and the standard deviation between interpolated values and measured values, the *boxes* are the mean values of temperature and the *black lines* are STD which range around mean values; **b** RMS of interpolated values and measured values

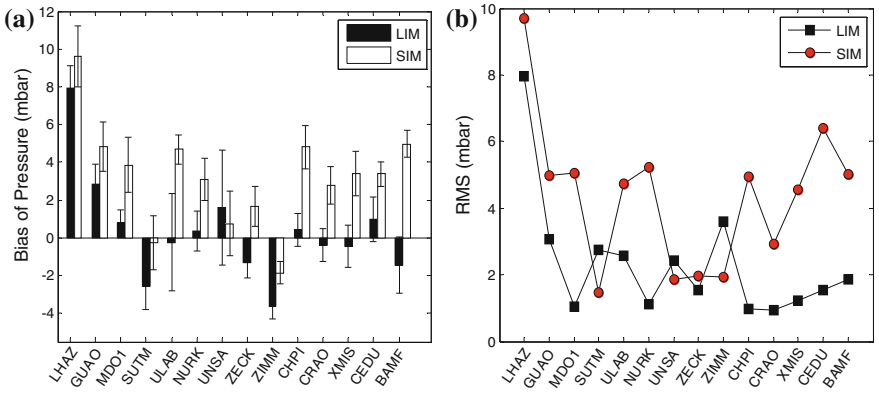

Fig. 3 Accuracy analysis of two interpolation methods in pressure at 14 sites: **a** average bias and the standard deviation between interpolated values and measured values, the *boxes* are the mean values of pressure and the *black lines* are STD which range around mean values; **b** RMS of interpolated values and measured values

meteorological data; (2) with meteorological data of LIM; (3) with meteorological data of SIM; (4) without meteorological data. When lack of meteorological data, PPP software calculates the meteorological data by equations from the sea level standard meteorological data. Retrieved PWV of strategy 1 is act as true value, compare the PWV from other process strategies with true value. Figure 4 (boxplot) give the correlation coefficients between true value and the PWV retrieved from

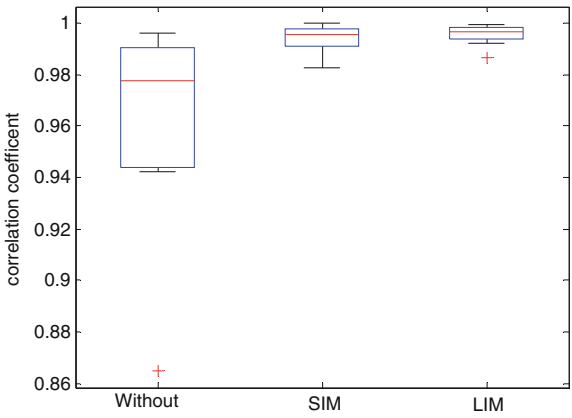

Fig. 4 Correlation coefficients between true values and the PWV retrieved from other three strategies, the *red lines* represent the middle value of correlation coefficients, the *blue boxes* range from upper and lower quartiles, *black lines* mean *top* and *bottom* edges, the *red crosses* are abnormal values

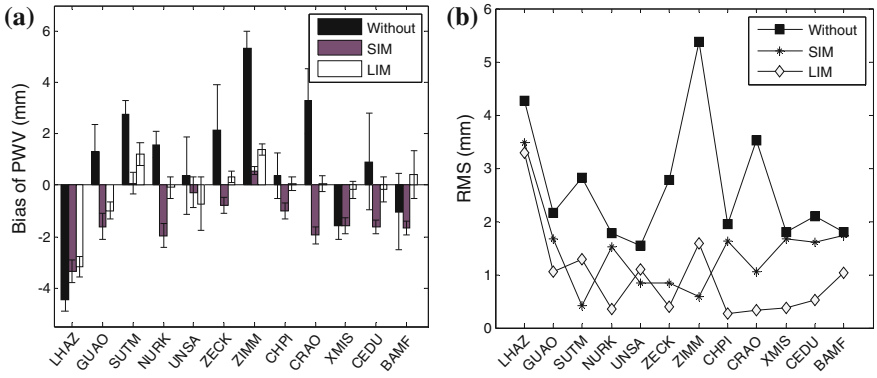

Fig. 5 Accuracy analysis of retrieved PWV with different strategies at 12 sites: **a** average bias and the standard deviation between true values and retrieved PWV with different strategies, the *boxes* are the mean values of PWV and the *black lines* are STD which range around mean values; **b** RMS between true values and the PWV from other three process strategies

other three strategies. The average bias and the standard deviation between true values and the PWV of other three strategies for DOY 300–306 in 2014 are shown in Fig. 5a. The RMS between true values and retrieved with different process strategies are given in Fig. 5b. Figure 6 shows the accuracy improvement by two different interpolation methods in 3D view (the differences between RMS of PWV without meteorological data and RMS of PWV with two different interpolation methods). Table 2 shows the RMS and STD between true values and the PWV from other three processing strategies.

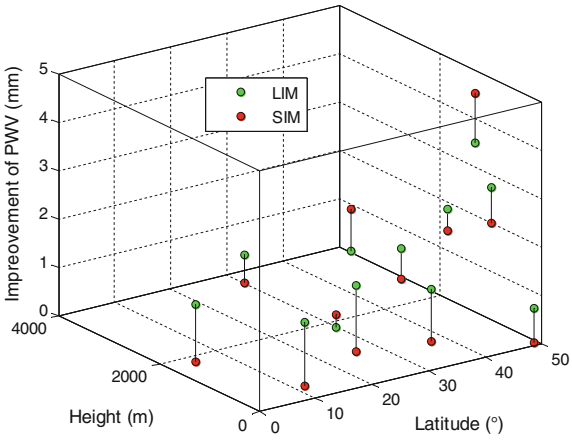

Fig. 6 Accuracy improvement by two interpolation methods in 3D view with latitude as X axis, height as Y axis, improvement of PWV as Z axis

Table 2 STD and RMS from different processing strategies (*Unit* mm)

Station code	STD			RMS		
	Without	SIM	LIM	Without	SIM	LIM
LHAZ	0.61	0.40	0.44	4.36	3.47	3.29
GUAO	1.05	0.35	0.51	2.17	1.67	1.04
SUTM	0.55	0.44	0.41	2.81	0.42	1.29
NURK	0.51	0.41	0.48	1.78	1.52	0.34
UNSA	1.49	0.83	0.59	1.54	0.84	1.10
ZECK	1.80	0.23	0.32	2.79	0.85	0.40
ZIMM	0.69	0.23	0.15	5.37	0.59	1.59
CHPI	0.87	0.27	0.31	1.95	1.63	0.27
CRAO	1.27	0.32	0.33	3.52	1.05	0.32
XMIS	0.51	0.34	0.32	1.79	1.68	0.38
CEDU	1.88	0.49	0.27	2.09	1.60	0.51
BAMF	1.47	0.93	0.26	1.79	1.64	1.03
Average	1.06	0.44	0.37	2.66	1.41	0.96

The analysis table and figures show that (1) the average correlation coefficients between the PWV retrieved without meteorological data and true value is 0.9537, the average correlation coefficients of SIM and LIM are 0.9940 and 0.9956, respectively. Results with interpolation meteorological data are better than the result without meteorological data, which demonstrates the PWV time series with interpolation data are more similar with the true value time series, LIM has higher coefficient. (2) The correction effect of two different interpolation methods are obvious at low altitude area (height < 2000 m), the RMS between true values and

PWV with interpolated data are only 1.15 mm (SIM) and 0.68 mm (LIM), respectively. While the accuracy of PWV without meteorological data is 2.51 mm, LIM shows higher accuracy. (3) The accuracy of interpolation methods are generally at high altitude area (LHAZ) (RMS all >3 mm), while the accuracy of PWV with interpolation data are still better than that without meteorological data with the accuracy of 4.36 mm (without), 3.47 mm (SIM) and 3.29 mm (LIM). (4) The trend of accuracy of retrieving PWV with interpolated data is in good agreement with interpolated pressure accuracy, which means the pressure play a more important role in the retrieval of PWV. (5) Retrieval accuracy of PPP PWV with interpolated data has no obvious correlation with attitude and elevation.

4 Conclusions and Suggestions

Pressure and temperature data are necessary in the retrieval of PWV, while the meteorological instruments are not equipped with in the actual observation, therefore the accuracy of retrieved PWV will be effected definitely. In this paper, an interpolation method based on pressure layer data is proposed, the results are compared with the results interpolated from the surface data. The results show that: (1) the accuracy of meteorological data from LIM of GPS station is better than that from SIM obviously, especially at low altitude area, therefore improve the accuracy of PWV; (2) the interpolation accuracy of temperature and pressure are unsatisfactory at altitude over 3000 m (such as LHAZ), which effect the accuracy of the retrieval of PWV. While the accuracy from SIM and LIM are still better than the PWV without meteorological data, especially for LIM with the improvement from 4.36 to 3.29 mm; (3) the trend of the accuracy of retrieved PPP PWV with interpolated meteorological data is in good agreement with the trend of the accuracy of interpolated pressure, which demonstrates pressure is the main effect factor of the retrieval of PPP PWV; (4) the accuracy of retrieved PPP PWV with interpolated data shows no obvious correlation with the height and latitude.

Though the results of this test are inspiring, there are still some problems need to be solved. The accuracy of LHAZ is poor, which need more observation data. The source of reference data is single, other data such as weather balloons need to be added in the future if they are available, which can make the result more objective and comprehensive.

Acknowledgements This research is supported by the National Natural Science Foundation of China (NSFC) (No: 41374044; 41404025)

References

1. Shuang Z, Yibin Y, Rui Z (2011) Research on calculation methods of zenith tropospheric delay. J Geodesy Geodyn 3:028
2. Shaoguang X, Yongliang X, Peng Li (2014) Effects of receiver and satellite clock error on dynamic atmospheric delay solution during PPP. J Geodesy Geodyn 34(3):86–90
3. Schueler T (2001) On ground based GPS tropospheric delay estimation. Dissertation for the Doctoral Degree. University der Bundeswehr Müchen, Neubiberg
4. Wang J, Zhang L, Dai A et al (2007) A near-global, 2-hourly data set of atmospheric precipitable water from ground-based GPS measurements. J Geophys Res Atmos 112(D11)
5. Jade S, Vijayan MSM (2008) GPS-based atmospheric precipitable water vapor estimation using meteorological parameters interpolated from NCEP global reanalysis data. J Geophys Res Atmos 113(D3)
6. Chang L, He X (2012) Regional precipitation forecast using GPS and NCEP. Scientia Sinica Phys Meth Astron 40(5):685–692
7. He X, Wang J (2013) Regional PWV estimation using interpolated surface meteorological data from NCEP CFSv2[C]//China Satellite navigation conference (CSNC) 2013 proceedings. Springer, Berlin Heidelberg, pp 229–238
8. Chen Y, Liu Y, Wang X et al (2007) GPS real-time estimation of precipitable water vapor-Hong Kong experiences. Acta Geod Cartogr Sin 36:9–12
9. Fan S (2013) Research on GPS marine water vapor inversion and three dimensional water vapor tomography. Wuhan University, Wuhan
10. Bevis M, Businger S, Chiswell S et al (1994) GPS meteorology: mapping zenith wet delays onto precipitable water. J Appl Meteorol 33(3):379–386

Determining the Reasonable Time Resolution of the Precise Satellite Clock Bias Products

Zhiping Liu, Dantong Zhu, Qianxin Wang and Jian Wang

Abstract The GPS precise satellite clock bias produced by IGS analysis centers is widely used; the time resolution is 5 s, 30 s, 5 min, and 15 min, respectively. However, the determination of the reasonable time resolution is lacking in theoretical and experimental research. On one hand, high time resolution can improve the data accuracy and reliability of post-processing applications. On the other hand, it could lead to a large quantity of data. Thus, both the accuracy and data quantity should be comprehensively considered. Firstly, this paper analyzed the variation of the precise satellite clock bias in detail using the epoch-differenced method and interval fitting method. Secondly, the periodicity of the 5-s GPS precise satellite clock bias was analyzed using spectrum analysis. Non-negative matrix factorization was then employed to extract the intrinsic feature dimension and determine the time resolution of the precise GPS satellite clock bias. Finally, it was suggested that the best time resolution is one minute. The results can also be used as reference for the BDS precise satellite clock bias.

Keywords GPS precise satellite clock bias · Time resolution · Epoch-differenced method · Interval fitting method · Spectrum analysis · Non-negative matrix factorization

1 Introduction

GPS satellite clock bias is one of the main sources of error for GPS high-precision navigation and positioning, timing, and other related applications [1–3]. At present, The available sampling intervals of existing GPS precise clock bias products (PCBPs) produced by the International GNSS Service (IGS) and other data analysis

Z. Liu (✉) · D. Zhu · Q. Wang · J. Wang
School of Environment Science and Spatial Informatics,
China University of Mining and Technology, Xuzhou 221116
People's Republic of China
e-mail: zhpliu@cumt.edu.cn

J. Sun et al. (eds.), *China Satellite Navigation Conference (CSNC) 2017 Proceedings: Volume I*, Lecture Notes in Electrical Engineering 437,
DOI 10.1007/978-981-10-4588-2_26

centers (such as CODE and JPL) are 5 s, 30 s, 5, and 15 min [4–6]. Clock bias time series products are complex curves because of the high frequency and diverse types of satellite clocks and the complex external environment and inherent physical characteristics [7]. To obtain the satellite clock bias synchronized with the observations sampling rate for post-processing applications, users have to carry out interpolations or fitting using various methods, such as the fractal algorithm [7], Chebyshev algorithm [8], or binomial regression algorithm [9].

The time resolution of the PCBPs affects the fitting accuracy of the clock bias [7]. During dynamic precise point positioning (PPP), the PCBPs with higher time resolutions provide better positioning accuracies and convergence rates [10, 11]. The higher the time resolution, the more reliable applied results are. However, the storage space of the data products has to be increased, which reduces the response rates during data processing, and vice versa [12]. Therefore, the reasonable time resolution of PCBPs should be selected after balancing the tradeoffs between error characteristics, accuracies, and data requirements.

In view of the aforementioned issues, the PCBP time resolution was the focus of this study, with the aim to determine the reasonable time resolution that complies with various requirements. First, the epoch-differenced and interval fitting methods were used to analyze the respective probability statistical characteristics of the epoch-differenced clock bias and the fitting residual errors for different time resolutions. Next, the PCBP periodicity was examined with the Lomb–Scargle (L–S) spectrum analysis method [13]. The time resolutions of the PCBPs were then studied based on feature extraction [14] and data compression [15] approaches of non-negative matrix factorization (NMF). Finally, the reasonable time resolution for PCBPs was arrived at through comprehensive studies using 5 s GPS PCBPs.

2 Analytical Method for Precise Clock Bias Time Series

2.1 Interval Fitting

Prior to interval fitting, first-order epoch differentiation was applied to PCBPs with different time resolutions. The key time resolution at which the error characteristics suddenly change can be generally determined using the histogram statistics of the epoch-differenced clock bias. For the in-depth analysis of the key time resolution, the interval fitting errors for the PCBPs with different key time resolutions were analyzed. This eventually led to the identification of the reasonable time resolution.

A clock-bias fitting model must be established to extract the interval fitting errors for PCBPs. Based on the inherent physical characteristics of satellite atomic clocks, the clock bias models frequently used are the second-order polynomial and first-order linear models. The specific equation is expressed as follows:

$$y(t_i) = \sum_{j=0}^{k} a_j (t_i - t_0)^j + \Delta \tag{1}$$

where $y(t_i)$ indicates the fitted clock bias at time t_i; t_0 is the reference epoch of the satellite clock bias; parameters a_0, a_1, a_2 of the model represent the deviation, drift, and drift rate at time t_0, respectively; Δ is the fitting error; $k = 2$ is the second-order polynomial model; and $k = 1$ is the linear fitting model.

To analyze the probability statistical characteristics of the clock bias with different time resolutions, The interval fitting method was used to calculate the fitting errors for different time resolutions. The node length of fitting interval was set as m, where $m = k + 2$. The clock bias time series was divided into equal intervals with the same number of nodes, then Eq. (1) was used for the interval fitting of the clock bias with different time resolutions. The parameters f the fitting model were then used to derive the 5-s sampling rate clock bias time series. The differences between this fitting result and that publicly released for 5-s PCBPs were then used to calculate the fitting errors.

2.2 *Lomb–Scargle Spectrum Analysis*

The precise satellite clock bias contains a linear trend term, which has to be removed prior to spectrum analysis of the precise clock bias. After elimination of the linear trend term, the precise clock bias time series was set as $x(n)$ and its normalized power spectrum function $P(\omega)$ is: [13]

$$\begin{aligned} P(\omega) &= \frac{1}{N\sigma^2} |X(\omega)|^2 \\ &= \frac{1}{N\sigma^2} \left| \sum_{n=0}^{N-1} x(n) e^{-j\omega n} \right|^2 \end{aligned} \tag{2}$$

where $\omega = 2\pi f$; $X(\omega)$ is the spectrum function of $x(n)$; σ^2 is the variance of $x(n)$; and N is the number of signal samples.

Equation (2) was used to decompose the clock bias time series $x(n)$ into a series of harmonic components in the time domain, leading to the frequency structure of the clock bias time series. However, it must be noted that the aforementioned power spectrum analysis method is implemented by the fast Fourier transformation (FFT), which requires that $x(n)$ is a uniform time series.

In reality, the clock bias time series is usually non-uniform due to missing data or non-uniformly sampling data. If the FFT method would still be used in this situation, false frequencies would likely be produced, resulting in unreliable

spectrum estimates. To effectively eliminate the false frequencies arising from missing data or non-uniformly sampling data, the L–S spectrum analysis method was used in this study because it is valid for non-uniform time series. The equation used to calculate $P_X(f)$, the normalized power spectrum of the L–S method, can be written as follows: [16]

$$P_X(f) = \frac{1}{2\sigma^2}\left\{\frac{[\sum \Delta x_t \cos 2\pi f(t-\tau)]^2}{\sum \cos^2 2\pi f(t-\tau)} + \frac{[\sum \Delta x_t \sin 2\pi f(t-\tau)]^2}{\sum \sin^2 2\pi f(t-\tau)}\right\} \tag{3}$$

where $\Delta x_t = x_t - \bar{x}$ and $x_t, \bar{x}, \sigma^2$ refer to the de-trended clock bias, the raw clock bias, mean value, and variance, respectively, and f, τ are the frequency and phase.

2.3 Non-negative Matrix Factorization Algorithm

Non-negative Matrix Factorization (NMF) is a matrix factorization algorithm for multivariate analysis where a matrix with reduced-rank is factorized into two matrices with the property that all three matrices have no negative elements. The basic principle is as follows: For a random non-negative matrix $\boldsymbol{A} \in \boldsymbol{R}_{+}^{\{m\times n\}}$, two matrices $\boldsymbol{W} \in \boldsymbol{R}_{+}^{\{m\times r\}}$ and $\boldsymbol{H} \in \boldsymbol{R}_{+}^{\{r\times n\}}$ are identified. Given that all elements of both matrices are non-negative, $\boldsymbol{A} \approx \boldsymbol{WH}$ has to be satisfied as far as possible.

If the noise matrix is assumed to be $\boldsymbol{E} \in \boldsymbol{R}_{+}^{\{m\times n\}}$, then the mathematical model of the NMF algorithm can be expressed as: [14]

$$\boldsymbol{E} = \boldsymbol{A} - \boldsymbol{WH} \tag{4}$$

Because the NMF algorithm is the reasonable approximation of the matrix $\boldsymbol{A}$, which is singular matrix with reduced-rank, the algorithm must be iterated under the constraint of a specific objective function to constantly approach the to-be- factorized matrix $\boldsymbol{A}$. Presently, the most widely used objective function is the Euclidean distance, which assumes that the noises comply with a normal distribution:

$$J(\boldsymbol{W},\boldsymbol{H}) = \frac{1}{2}\sum_{i,j}\left[\boldsymbol{A}_{ij} - (\boldsymbol{WH})_{ij}\right]^2 \tag{5}$$

In accordance with the principle of the gradient descent method, the learning rate matrices were set as $\boldsymbol{\lambda_W}, \boldsymbol{\lambda_H}$. This means that the iterative equations of the base matrix $\boldsymbol{W}$ and coefficient matrix $\boldsymbol{H}$ can be expressed as follows:

$$\begin{cases} \boldsymbol{W}_{ik} = \boldsymbol{W}_{ik} + \boldsymbol{\lambda}_{\boldsymbol{W}} \dfrac{\partial J(\boldsymbol{W}, \boldsymbol{H})}{\partial \boldsymbol{W}_{ik}} \\ \boldsymbol{H}_{kj} = \boldsymbol{H}_{kj} + \boldsymbol{\lambda}_{\boldsymbol{H}} \dfrac{\partial J(\boldsymbol{W}, \boldsymbol{H})}{\partial \boldsymbol{H}_{kj}} \end{cases} \tag{6}$$

$$\begin{cases} (\boldsymbol{\lambda}_{\boldsymbol{W}})_{ik} = \dfrac{\boldsymbol{W}_{ik}}{(\boldsymbol{W}\boldsymbol{H}\boldsymbol{H}^T)_{ik}} \\ (\boldsymbol{\lambda}_{\boldsymbol{H}})_{kj} = \dfrac{\boldsymbol{H}_{kj}}{(\boldsymbol{W}^T\boldsymbol{W}\boldsymbol{H})_{kj}} \end{cases} \tag{7}$$

3 Determining the Time Resolution of the Precise Clock Bias

3.1 Probability Statistics for the Epoch-Differenced Clock Bias

The PCBPs provided by the IGS analysis centers have a nominal accuracy with 0.1 ns and a highest time resolution of 5 s. Users can download these products based on user's corresponding application requirements. In this section, a first-order epoch-differenced clock bias time series was performed for different time resolutions. This helped to establish the relationship between the differential value of the clock bias and the nominal accuracy, thereby facilitating the study of the probability statistical characteristics for epoch-differenced clock bias time series with different time resolutions.

The experimental data were all-day PCBPs (5-s time resolution) from 31 GPS satellites released by the CODE analysis center. The data were accumulated in DOY 80 of year 2016 (Vernal Equinox Day). The clock bias time series are resampling with the time resolutions of 30 s, 1, 3, 5, and 10 min, and epoch differentiation was applied to these data. Next, the probabilities of the first-order differential values of the clock bias (absolute values) were calculated. The statistical results are shown in Fig. 1.

It can be seen from Fig. 1 that, regardless of time intervals, the epoch-differenced clock bias consistently exhibited the phenomenon of "small concentrations but large dispersions." However, the distribution range of the absolute values for the epoch-differenced clock bias gradually expanded with increasing time intervals, which demonstrated the clock bias features of different types of satellites. This was caused by the decrease in the temporal correlation within the clock bias time series as the time interval increased, leading to greater variations in the clock bias between adjacent epochs.

The distribution of epoch differences was similar when the time interval was less than 1 min. Most of the epoch-differenced clock bias values were also smaller than

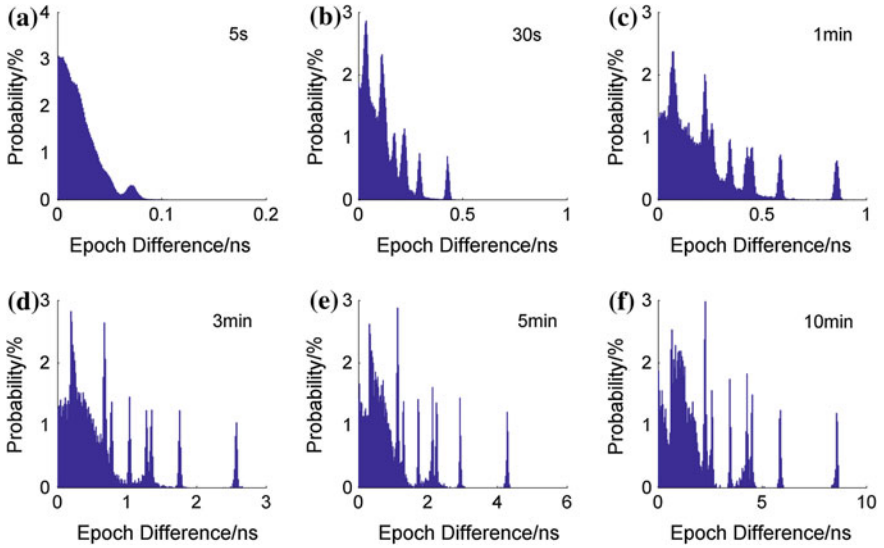

Fig. 1 The probability histogram of the epoch-differenced PCBPs

the nominal accuracy of PCBPs with the same resolution. The distribution of the epoch-differenced clock bias had greater differences when the time intervals were larger. In other words, greater accuracies were achieved when low-order polynomial fitting models were used for PCBPs with time resolutions of 1 min or less. In contrast, more complex methods such as high-order Chebyshev polynomials are required for PCBPs with longer time intervals to satisfy accuracy requirements.

3.2 Analyzing the Interval Fitting Errors of the Clock Bias

The interval fitting method explained in Sect. 2.1 was used to compare the fitting errors of the precise satellite clock bias for different time resolutions. The data used for the experiment were same to that stated in Sect. 3.1. The specific experimental schemes were as follows: a second-order polynomial model with an interval length of four nodes (Scheme A) and a linear model with an interval length of three nodes (Scheme B) were selected as the fitting models. Fitting was performed using the satellite precise clock bias with the time resolutions of 5 s, 1, 3, 5, and 10 min. The fitting models were then used to reconstruct the clock bias data with 5-s time resolution. The released PCBPs at 5-s resolution were then used as the standard values to compute the interval fitting errors (IFEs) for two schemes. The results are shown in Table 1.

Table 1 Results of the interval fitting errors

IFEs		<0.1 ns	0.1–0.2	0.2–0.3	0.3–0.4	>0.4 ns
Time intervals						
Scheme A	5 s	100	0	0	0	0
	30 s	99.68	0.32	0	0	0
	1 min	96.04	3.78	0.17	0.01	0
	3 min	80.99	15.36	3.04	0.52	0.10
	5 min	75.03	18.20	5.33	1.14	0.29
	10 min	69.48	19.68	7.57	2.38	0.89
Scheme B	5 s	100	0	0	0	0
	30 s	99.45	0.55	0.01	0	0
	1 min	95.33	4.40	0.24	0.02	0
	3 min	80.38	15.76	3.19	0.57	0.10
	5 min	74.76	18.46	5.33	1.17	0.29
	10 min	69.41	19.89	7.55	2.35	0.80

Table 1 shows that large differences existed in the distribution of fitting errors for different time resolutions in Scheme A. At 1 min or less, the time interval had a smaller impact on the distribution of fitting errors, with most of the errors being smaller than the 0.1-ns nominal accuracy of the PCBPs. However, the distribution range of the fitting errors expanded with increasing time intervals; when the latter was greater than 1 min, approximately 20–30% of the fitting errors exceeded 0.1 ns. This is due to the significant temporal correlation within the precise clock bias time series when the time interval was small. Consequently, the models had better fitting accuracies and the fitting errors were distributed in a smaller range. On the other hand, the temporal correlations of the clock bias data weakened as the time interval increased, leading to worse fitting accuracies and the gradual expansion in the distribution range of the fitting errors.

It was further noted that the fitting error distributions in Schemes A and B were quite similar, with a maximum difference in the interval distribution between the two of only 0.7%. This suggests that both fitting models achieved the same degree of accuracy for the corresponding fitting intervals. In addition, the turning point of the time resolution for the fitting errors was determined to be the 1-min time interval. At or below this time interval, the majority of the fitting errors were smaller than the nominal accuracy of 0.1 ns. However, the distribution of the fitting errors became more widespread and the ratio of errors smaller than 0.1 ns declined sharply once the time interval exceeded 1 min. These results indirectly showed the PCBPs with different time resolutions have different requirements on selecting a fitting method with reasonable complexities.

3.3 Spectrum Analysis of the Clock Bias

The 5-s time resolution data from 31 all-day GPS satellites accumulated in DOY 80 of year 2016 (Vernal Equinox Day) and released by the CODE analysis center were used to test the periodicity of the PCBPs. The products have a significant linear trend term, which was eliminated before the residual terms were used for L–S spectrum analysis.

Data processing was carried out as follows: (i) the clock bias data were linearly fitted to obtain $\{v_i\}$, which is the sequence of the residual clock bias errors after the linear trend had been eliminated; and (ii) the L–S method was used to carry out spectrum analysis of the residual clock bias $\{v_i\}$ to determine the amplitude corresponding to each frequency and analyze the periodic characteristics of the PCBPs.

For brevity, only the clock bias results for the typical satellites PRN1, PRN2, and PRN23 were shown. The clock bias data before and after the trend elimination are shown in Figs. 2, 3 and 4, while the results of the spectrum analysis are shown in Figs. 5, 6 and 7.

Figures 2a–4a show a notable linear trend of the clock bias time series for each of the three satellites PRN1, 2, and 23. This indicates the rationality of using polynomial models for the clock bias fitting. The L–S spectrum analysis neglecting the trend term can lead to false peaks, thereby affecting the accurate identification of periodic characteristics. Figures 2b–4b show the time series of residual clock bias contains notable long-period terms and complex short-period terms after removal of the trend term from the clock bias time series.

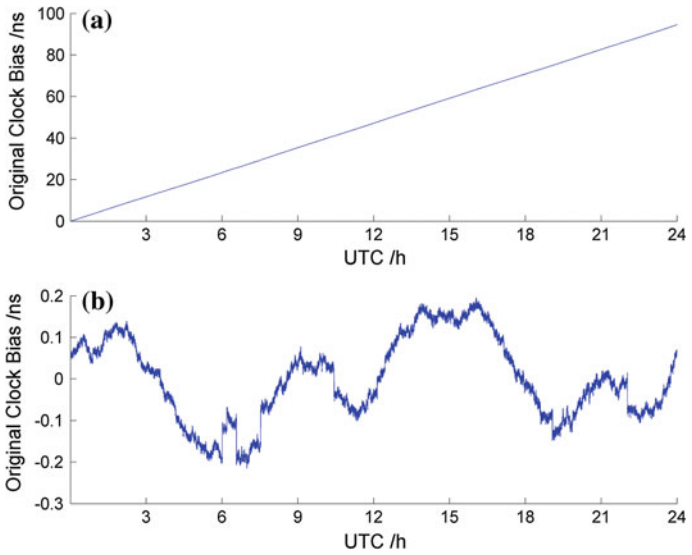

Fig. 2 Original and residual clock bias of PRN1

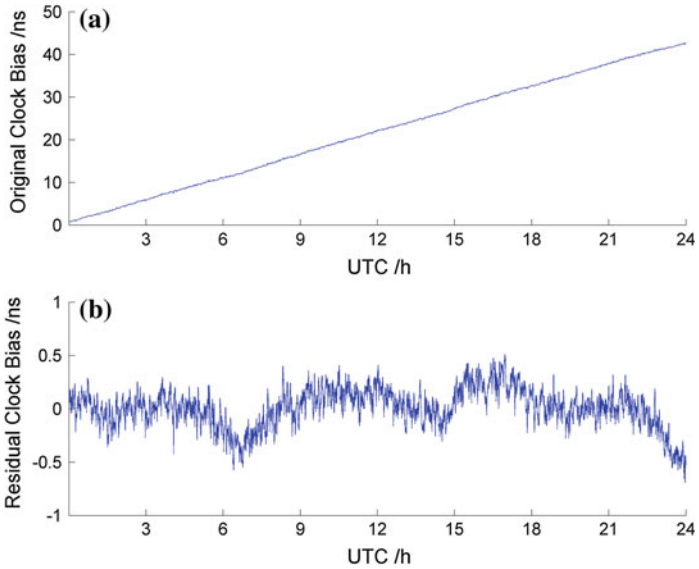

Fig. 3 Original and residual clock bias of PRN2

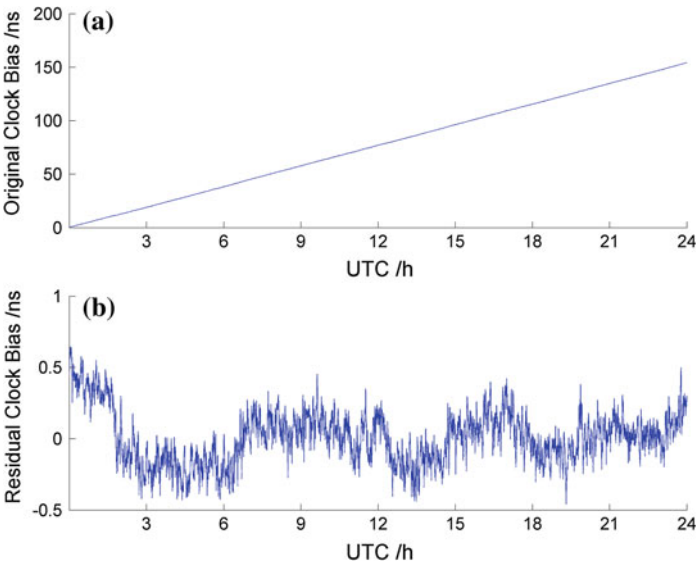

Fig. 4 Original and residual clock bias of PRN23

The spectrum analysis results for the residual clock bias are shown in Figs. 5, 6 and 7. The long periods at approximately 8 h similarly existed for PRN1, 2, and 23. Besides, most of the energy was concentrated in the low-frequency band (0.01 Hz

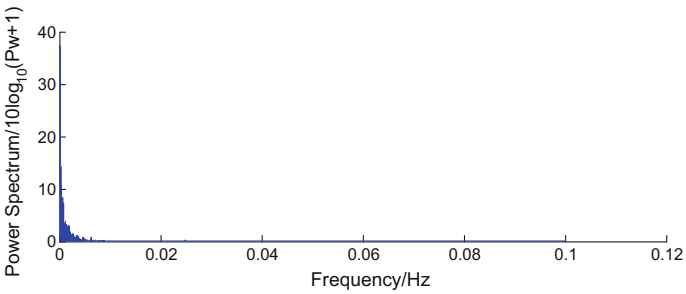

Fig. 5 Spectrum analysis for the residual clock bias of PRN1

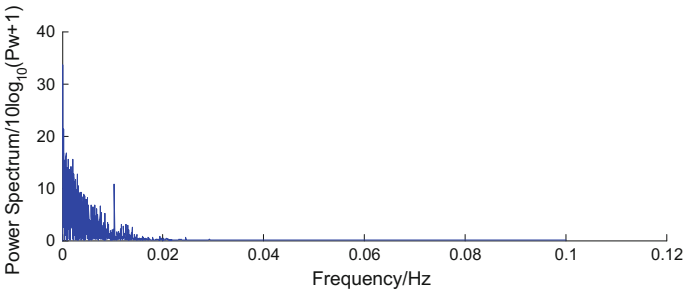

Fig. 6 Spectrum analysis for the residual clock bias of PRN2

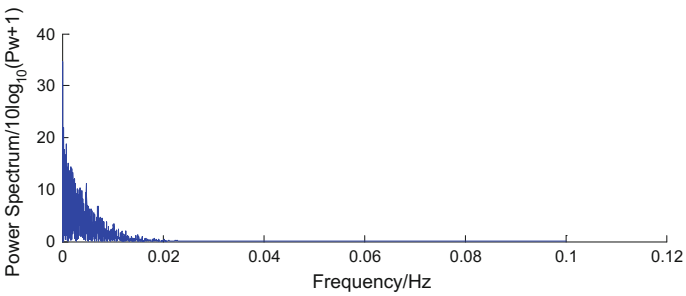

Fig. 7 Spectrum analysis for the residual clock bias of PRN23

and below). In contrast, the characteristics of the short periods were very complex. The typical time intervals for the short period of the three satellites were 250, 150, and 100 s, respectively. Based on the Nyquist sampling theorem [13], the theoretical time interval of the PCBPs should be approximately 50 s to retain complete information from the clock bias time series. Thus, the time interval with 60 s was recommended as reasonable time resolution for GPS PCBPs.

3.4 Non-negative Matrix Factorization of the Clock Bias

Under normal circumstances, it is assumed that the spatial feature (feature dimension r) is known when using the NMF method for feature extraction, and reduced-rank factorization with a feature dimension has to be carried out under the cut-off accuracy condition. Because the spatial feature of the satellite clock bias is uncertain, the feature dimensions were set in advance for this study. The NMF iterative convergence errors with the different feature dimensions for PCBPs of different time resolutions were compared. This way, the reasonable time resolution for the satellite clock bias could be determined.

The analysis in the previous section showed that the long period of the satellite clock bias time series was approximately 8 h. Hence, in this section, only PCBPs (5-s time resolution, 31 GPS satellites) of UTC 0–8 h accumulated in DOY 80 of year 2016 were selected for NMF algorithm. The specific data processing flow was as follows: (i) the sparsification of the time series for the clock bias with 5-s time resolution led to clock bias time series products with time resolutions of 10, 30 s, 1, 3, 5, 10 and 15 min; (ii) the feature dimensions selected were 5, 10, 15, 20, 25, and 30, respectively. The iteration stop condition includes the iterative convergence error and threshold of the error reduction rate were 0.12 ns and 1×10^{-7}, respectively. To ensure that the results have statistical significance, each feature dimension was calculated 50 times using NMF algorithm and (iii) the median values of the iterative convergence errors for each feature dimension were calculated for the aforementioned data. The statistical results are shown in Fig. 8.

Figure 8 shows that the NMF iterative convergence errors with different feature dimensions for different time resolutions differed substantially. Overall, the differences in the convergence errors were smaller when the time intervals were larger. There were even similarities at the individual level. The iterative convergence errors of the different feature dimensions became significantly different with increasing time resolutions, represented by the initial bifurcation of the iterative convergence error curves in Fig. 8.

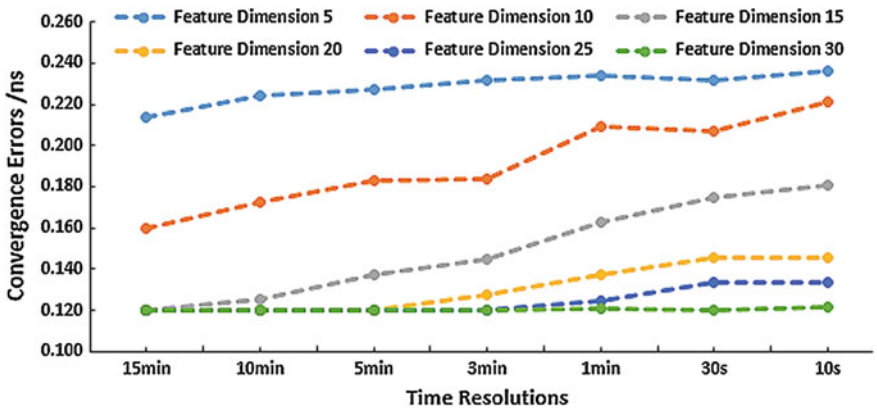

Fig. 8 The NMF results of multi-time resolution clock bias

This is due to the temporal features of the PCBPs, which were relatively low complexity when the time resolution was low. This means that fewer feature dimensions were needed to completely reflect their distribution. In the figure, this is shown by fewer differences between the convergence error curves of the feature dimensions. There were even cases of overlap. However, the temporal features became more complicated when the resolution increased and higher feature dimensions were needed for the proper expression of those characteristics. If the presetting number of feature dimensions was insufficient, the iterative convergence error increased. This explains the continuous bifurcations of the convergence error curves of the different feature dimensions when the resolution increased.

The analysis indicated that the mean error curves of the feature dimensions could not be properly differentiated when the time interval was greater than 1 min. This implies greater losses in the temporal features of the GPS PCBPs. On the other hand, the convergence error curves could be completely differentiated when the time interval was within 1 min and the temporal features of the GPS PCBPs were better retained. From the perspective of NMF iterative convergence errors, the GPS PCBPs with a time interval of 1 min retain the temporal features better. Thus, it is suggested that the IGS analysis centers should release GPS PCBPs with the time interval of 1 min.

4 Conclusions

(i) The impact of PCBPs time resolutions for high-precision post-processing applications on (a) the reliability of the results and (b) the response speed of data processing was pointed out and followed by further analysis related to the temporal features of PCBPs. These analyses were based on epoch-differenced, interval fitting, L–S spectrum analysis, and NMF algorithms.

(ii) The data of this study included the original 5-s single-day GPS PCBPs released by the CODE analysis center and resampled products with time resolutions of 30 s, 1, 3, 5, and 10 min. Based on the probabilistic statistics of the epoch-differenced clock bias, analysis of interval fitting errors, spectrum analysis of the clock bias, and NMF results, the 1-min interval was determined to be the reasonable time interval. At this time resolution, it is possible to achieve a good balance between the amount of clock bias data and retaining the temporal features of the GPS PCBPs.

Acknowledgements This work was supported by projects including the National Natural Science Foundation of China (No. 41204011, No. 41504032) and the National Key Research and Development Program of China (No. 2016YFC0803103).

References

1. Huang G, Zhang Q (2012) Real-time estimation of satellite clock offset using adaptively robust Kalman filter with classified adaptive factors. GPS Solutions 16(4):531–539
2. Xiangguag M, Yueqiang S, Qifei D et al (2016) Stability analysis of atomic clocks onboard the Beidou Satellites. J Geodesy Geodyn 36(7):574–576
3. Guo F, Zhang X (2014) Real-time clock jump compensation for precise point positioning. GPS Solutions 18(1):41–50
4. Wang K, Rothacher M (2013) Stochastic modeling of high-stability ground clocks in GPS analysis. J Geodesy 87(5):427–437
5. IGS (2016) The International GNSS Service [EB/OL]. http://www.igs.org/products/ Cited 15 Nov 2016
6. CODE (2016) Center of Orbit Determination of Europe [EB/OL]. ftp://ftp.un.ibe.ch/ciub/Code. Cited 15 Nov 2016
7. Zhiping L, Guangli G (2012) Fractal interpolation method for GPS precise satellite clock bias. J Astronaut 33(11):1623–1629
8. Xing W, Jingxiang G, Jian W et al (2015) Using sleek Chebyshev polynomial to fit the precise satellite coordinate and clock error. Bulletin Surveying Mapp 5(6–8):16
9. Zhang B, Jikun O, Yuan Y et al (2007) Fitting method for GPS satellite clock errors using wavelet and spectrum analysis. Geomatics Inf Sci Wuhan Univ 32(8):715–718
10. Xiaojing L, Fei G, Cuixian L et al (2010) Impacts of sampling rates of IGS satellite clock on convergence of precise point positioning. Geomatics Inf Sci Wuhan Univ 35(6):683–686
11. Xiaohong Z, Fei G, Xingxing L (2010) Impact of sample rate of IGS satellite clock on precise point positioning. Geomatics Inf Sci Wuhan Univ 35(2):152–155
12. Shi J, Xu C, Li Y, et al (2015) Impacts of real-time satellite clock errors on GPS precise point positioning-based troposphere zenith delay estimation. J Geodesy 89(8):747–756
13. Huang G, Zhang Q, Xu GC et al (2008) IGS precise satellite clock model fitting and its precision by using spectral analysis method. Geomatics Inf Sci Wuhan Univ 33(5):496–499
14. Zhan C, Li W, Ogunbona P (2012) Local representation of faces through extended NMF. Electron Lett 48(7):373–375
15. Rui S, Jun G (2009) Image hashing method via combination of NMF and PCA. J Electron Meas Instrum 23(5):52–57
16. Bin X, Baohua T, Yi C (2011) The simulate study of signal detection based on lomb-scargle algorithm. Nucl Electron Detect Technol 31(6):702–705

Part II
Navigation and Location Service

Pseudolite Cellular Network in Urban and Its High Precision Positioning Technology

Xingli Gan, Baoguo yu, Zhang Heng, Zhu Ruihui and Li Yaning

Abstract GNSS in urban was Easy to cause signal shielding effect, it is difficult to provide seamless positioning service, Firstly, the positioning cellular networks based on pseudolites was Proposed in the paper, the system composition, working principle and compatible signal was introduced, the innovation is put forward that the closed loop time synchronization technology based on the pseudolites navigation signal transmission network, and the digital time synchronizer was developed. The experimental tests was showed that time synchronization accuracy between pseudolites were better than 2 ns; Secondly, three network topology of pseudolite was put forward, such as star, ring and cellular structure. According to the principle of service area was biggest, quantity of pseudolites was less, GDOP and HDOP was least, it was proved that a kind of center-distribution cellular networks was optimal by the simulation analysis. Finally, The positioning performance testbed of Ye San Po for pseudolite cellular networks was build, it was showed that the pseudorange positioning accuracy was better than 5 m, carrier phase positioning accuracy was better than 20 cm, then the pseudolite cellular network could satisfy the high-precision positioning requirement of the urban.

Keywords Pseudolite · Cellular networks · Positioning · GNSS

It was funded by 2016 National Key Research Projects "indoor hybrid intelligent positioning and indoor GIS (2016YFB0502100)" and "Indoor wireless location technology based on ground station (2016YFB0502101)".

X. Gan (✉) · B. yu · Z. Heng · Z. Ruihui · L. Yaning
State Key Laboratory of Satellite Navigation System
and Equipment Technology, The 54th Research Institute
of China Electronics Technology Group Corporation, Hijiazhuang,
People's Republic of China
e-mail: ganxingli@163.com

J. Sun et al. (eds.), *China Satellite Navigation Conference (CSNC) 2017 Proceedings: Volume I*, Lecture Notes in Electrical Engineering 437,
DOI 10.1007/978-981-10-4588-2_27

1 Introduction

GNSS in urban was Easy to cause signal shielding effect, it is difficult to provide seamless positioning service, pseudolites become a hot research topic in the field of satellite navigation [1–8], such as LocataLite pseudolites in Australia, high precision positioning pseudolites of Space system company in Finland and Anchalee Puengnim in German etc. Ministry of Science and Technology of China carried out "indoor hybrid intelligent positioning and indoor GIS", BeiDou pseudolites positioning network was an important part of and important research direction.

Firstly, the components and synchronization technology of pseudolites networks was introduced in this paper; secondly, the network topology structure of pseudolites was designed according to the service area and GDOP/HDOP; Finally, the carrier phase difference algorithm of pseudolites positioning system was put forward, it was proved that carrier phase positioning accuracy was better than 20 cm, then the pseudolites cellular network could satisfy the high-precision positioning requirement of the urban.

2 GNSS Pseudolites Positioning Network in Urban

2.1 Composition of Pseudolites Positioning Network

The composition of Pseudolites positioning network was cellular network, as shown in Fig. 1a, the signal of pseudolites was transmit between sub cellular, achieve time synchronization of cellular network based on the closed-loop processing technology. Each sub cellular was including pseudolites, the positioning server and receiver, as shown in Fig. 1b.

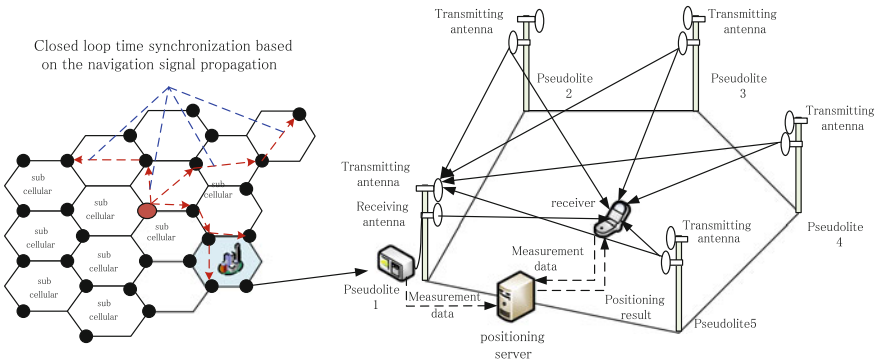

(a) pseudolites cellular network (b) Sub cellular of pseudolites

Fig. 1 The composition of pseudolites positioning network

Table 1 Signal parameters between pseudolites and Beidou/GPS

	GPS	Beidou	Pseudolites	
			GPS L1	Beidou B1
Frequency MHz	1575.42	1561.098	1575.42	1561.098
Spread spectrum code	1–32	1–32	33–37	33–37
Code rate	1.023 MHz	1.023 MHz	1.023 MHz	1.023 MHz
Code length	1 ms	1 ms	1 ms	1 ms
Data rate	50 bps	50 bps	50 bps	50 bps
Modulation method	BPSK	BPSK	Pulse +BPSK	Pulse +BPSK
Polarization mode	RHCP	RHCP	RHCP	RHCP

2.2 Compatible Signal of Pseudolites Network

In order to make the GNSS receiver or chips, can receive signal of pseudolite signal parameters as shown in Table 1, it can be seen that the center of the pseudolites signal frequency, code length and code rate, rate of information, same as the big dipper and GPS polarization modes, but pseudolites spread spectrum code using GNSS navigation control system interface file of PRN code extension code, pseudolite modulation method adopts "pulse + BPSK" method [9–13], so as to solve the problem of near-far effect. Pseudolites pulse plan was recommended by RTCM SC-104 committee, it was defined as pulse durationis 1/11 of code cycle.

3 Time Synchronization Based on Signal Propagation

Pseudolites to form network provide positioning services in urban space, primary problem is solving the problem of time synchronization. Figure 2 was the closed-loop time synchronization of pseudolites based on signal propagation, the

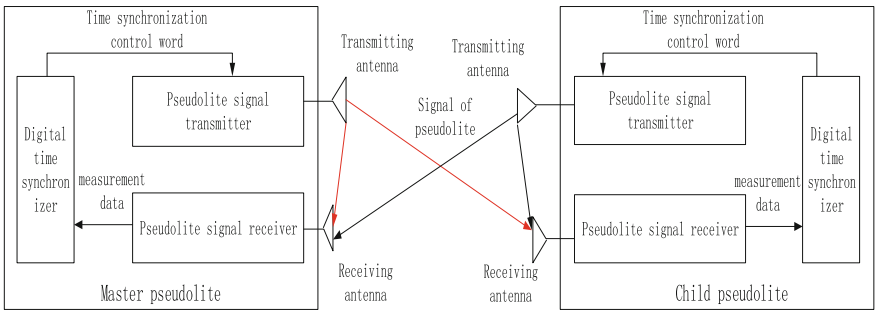

Fig. 2 Closed-loop time synchronization of pseudolites

measurement equation from receiver to master pseudolites was established as follow [14]:

$$\rho_{\mathrm{r}}^{\mathrm{m}} = P_{\mathrm{r}}^{\mathrm{m}} + c \times (dt_{\mathrm{r}} - dt^{\mathrm{m}}) \tag{1}$$

The measurement equation from receiver to child pseudolites:

$$\rho_{\mathrm{r}}^{\mathrm{c}} = P_{\mathrm{r}}^{\mathrm{c}} + c \times (dt_{\mathrm{r}} - dt^{\mathrm{c}}) \tag{2}$$

Because the coordinates of receiving antenna and transmitting antenna was known, the clock difference M between pseudolites was get through the formula (1) minus formula (2).

$$M = c \times (dt^{\mathrm{c}} - dt^{\mathrm{m}}) = (\rho_{\mathrm{r}}^{\mathrm{c}} - \rho_{\mathrm{r}}^{\mathrm{m}}) + (P_{\mathrm{r}}^{\mathrm{c}} - P_{\mathrm{r}}^{\mathrm{m}}) \tag{3}$$

The digital time synchronizer of Pseudolites would calculate the clock difference, and generate the time synchronization control word to the signal transmitter. When the time synchronization precision between Pseudolites was less than two seconds, it means that the networking was successful.

4 The Optimal Network Topology and Geometry Factor

4.1 Network Topology of Pseudolites

The network topology structure of Pseudolites was shown in Fig. 3, Network types including the star, ring and cellular, which according to the signal emission direction. Among them, the cellular network was the combination of star and ring network.

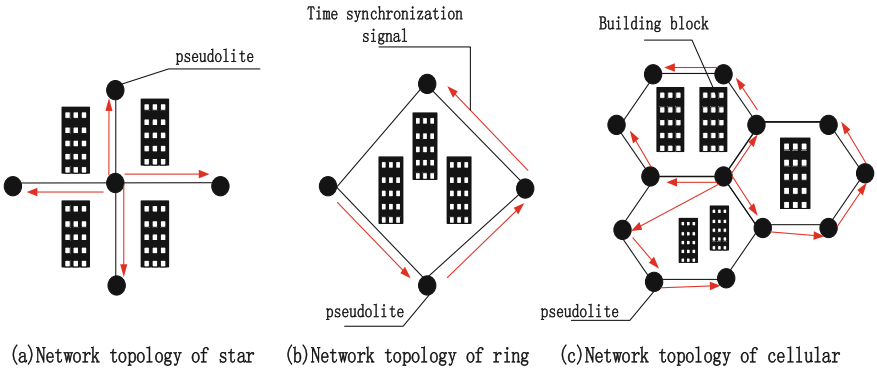

Fig. 3 The topology of pseudolites cellular networks

4.2 Geometric Precision Dilution of Optimal Network Topology

The principles of optimal pseudolites network: service area was biggest, pseudolites nodes were least and geometrical factors was minimum [15], then positioning error equation was:

$$\Delta X = (\mathbf{H}^T\mathbf{H})^{-1}\mathbf{H}^T\varepsilon \tag{4}$$

The covariance of positioning error equation was:

$$\mathrm{cov}(\Delta X) = \delta^2(\mathbf{H}^T\mathbf{H})^{-1} = \begin{bmatrix} g_{11} & g_{12} & g_{13} & g_{14} \\ g_{21} & g_{22} & g_{23} & g_{24} \\ g_{31} & g_{32} & g_{33} & g_{34} \\ g_{41} & g_{42} & g_{43} & g_{44} \end{bmatrix} \tag{5}$$

Geometric precision dilution (GDOP) was:

$$GDOP = \sqrt{(g_{11} + g_{22} + g_{33} + g_{44})} \tag{6}$$

Horizontal precision dilution (HDOP) was:

$$HDOP = \sqrt{(g_{11} + g_{22})} \tag{7}$$

The geometric relations between Pseudolites was shown in Fig. 4, considering the launch of power limitation, Pseudolites was located in the four vertices and center of the square area.

The GDOP and HDOP of pseudolites cellular networks (surrounding) was shown in Fig. 5. It can be seen that GDOP and HDOP of four pseudolites was very big in Fig. 5a, then pseudolites couldn't provide positioning service; When quantity is greater than four, With the increase of pseudolite number from Fig. 5b–e, GDOP and HDOP was decreased. When the number of pseudolites reached eight in Fig. 5e, the HDOP was minimum and the positioning area was biggest, its HDOP was less than two.

When one pseudolite was located in the center of the service area, the result of GDOP and HDOP as shown in Fig. 6, under the condition of same number pseudolites, the largest of GDOP was 40 in Fig. 6a, the largest of GDOP was 120 in Fig. 5c, the area in Fig. 6a (HDOP was less than (2) was greater than that in Fig. 5c. Therefore, the cellular network was optimized for urban, which was one in the center and five in the surrounding.

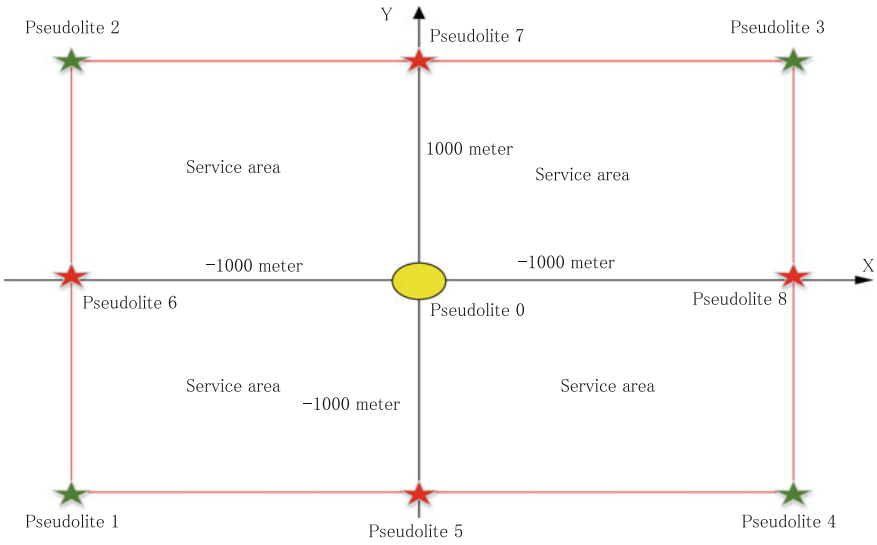

Fig. 4 The geometric relationships of pseudolite networks

4.3 High Precision Positioning of Pseudolite Cellular Networks

The carrier phase measurement equation from pseudolites to monitoring receiver [16] was

$$\lambda\phi^r = P^r + I + c(\delta t^r - \delta t^i) + N^r + \varepsilon^r \tag{8}$$

The carrier phase measurement equation of user receiver was:

$$\lambda\phi^u = P^u + I + c(\delta t^u - \delta t^i) + N^u + \varepsilon^u \tag{9}$$

where, ϕ^r and ϕ^u was the carrier phase measurements from receiver to pseudolite, P^r and P^u was the distance from receiver to pseudolite, δt^r and δt^u was bias of receiver clock, δt^i was bias of pseudolite clock, N^r and N^u was ambiguity, λ was wavelength of carrier, I was troposphere delay, ε^r and ε^u was Carrier phase measurement error.

the single difference measurement equation between Eqs. (8) and (9) was:

$$\lambda\Delta\phi^{ru} = \Delta P^{ru} + c(\delta t^{ru}) + N^{ru} + \varepsilon^{ru} \tag{10}$$

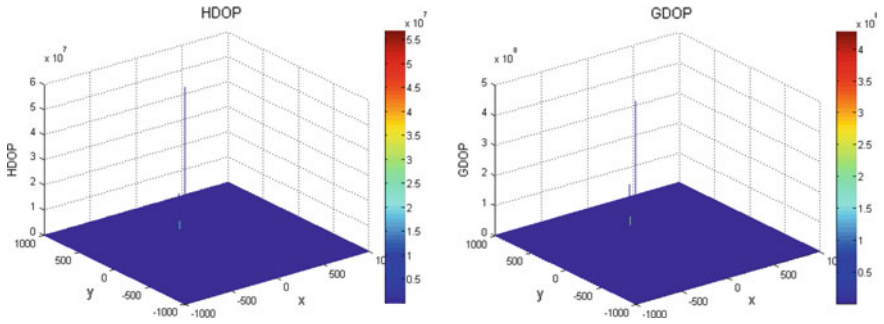

(a) GDOP and HDOP of pseudolites from 1 to 4

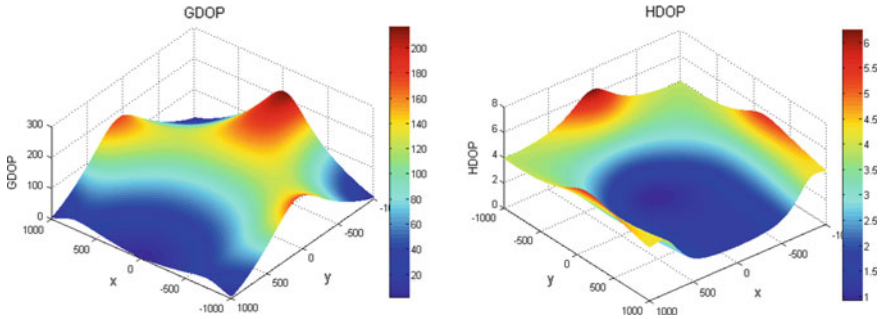

(b) GDOP and HDOP of pseudolites from 1 to 5

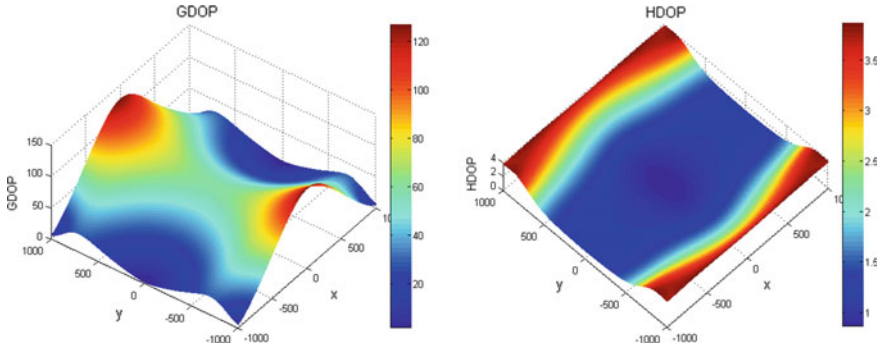

(c) GDOP and HDOP of pseudolites from 1 to 6

Fig. 5 GDOP and HDOP of pseudolites cellular networks

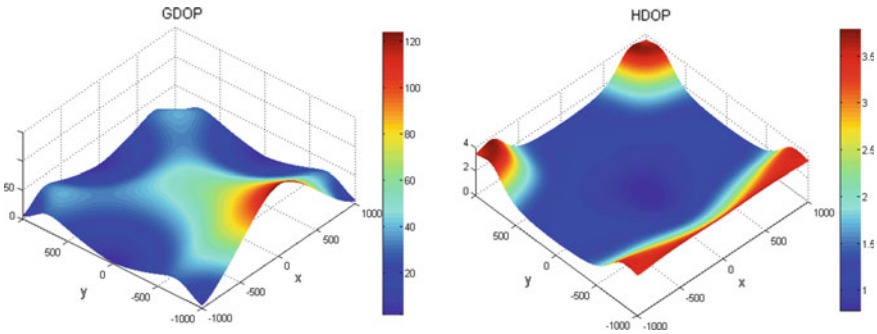

(d) GDOP and HDOP of pseudolites from 1 to 7

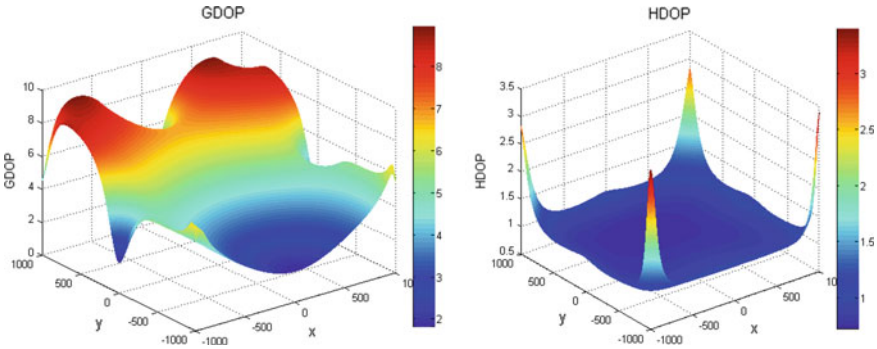

(e) GDOP and HDOP of pseudolites from 1 to 8

Fig. 5 (continued)

We could use the satellite navigation positioning method of carrier phase difference, then calculate the precise coordinates of receiver.

5 Positioning Accuracy Testing of Pseudolite Cellular Network

5.1 Positioning Accuracy Testbed of Pseudolites

The positioning precision testbed of Ye San Po for pseudolite cellular networks was build, such as Fig. 7, seven pseudolites were in the top of the hill, one was located in the center of the service area, the coordinate of transmitting antenna and receiving antenna was calibration in advance.

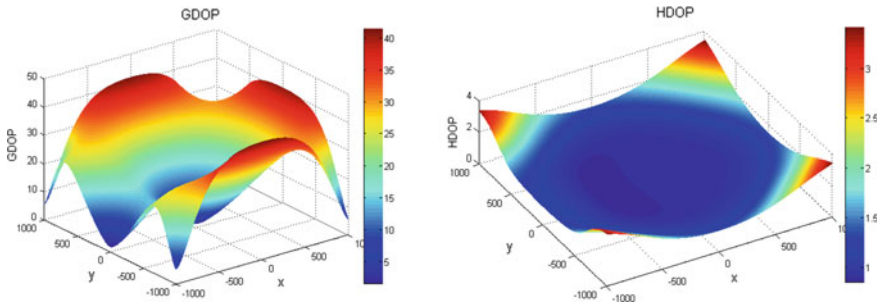

（a）GDOP and HDOP of pseudolites from 0 to 5

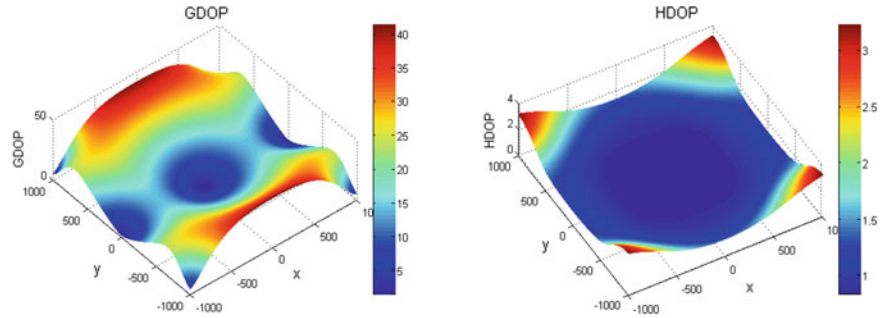

（b）GDOP and HDOP of pseudolites from 0 to 6

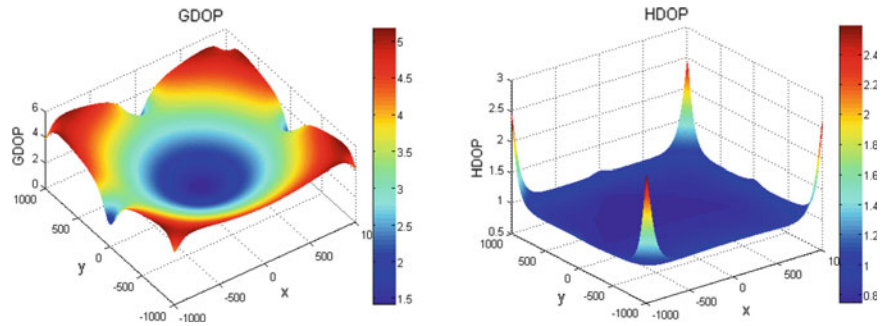

（c）GDOP and HDOP of pseudolites from 0 to 7

Fig. 6 GDOP and HDOP of pseudolites cellular networks (one in center)

5.2 Positioning Result of Pseudolites Cellular Networks

The positioning result for pseudolite pseudorange positioning was shown in Fig. 8, pseudolites receiver and trimble RTK receiver were placed in a test car. Through

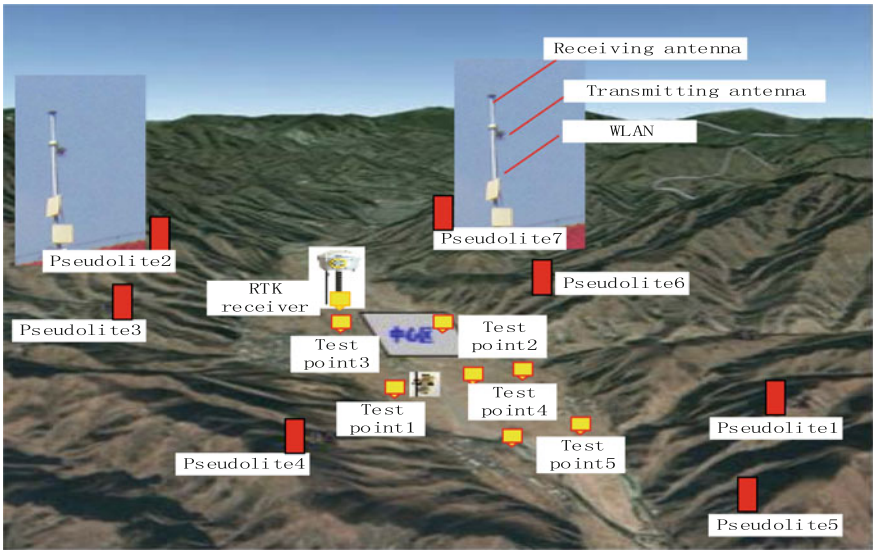

Fig. 7 The positioning testbed of pseudolites cellular networks

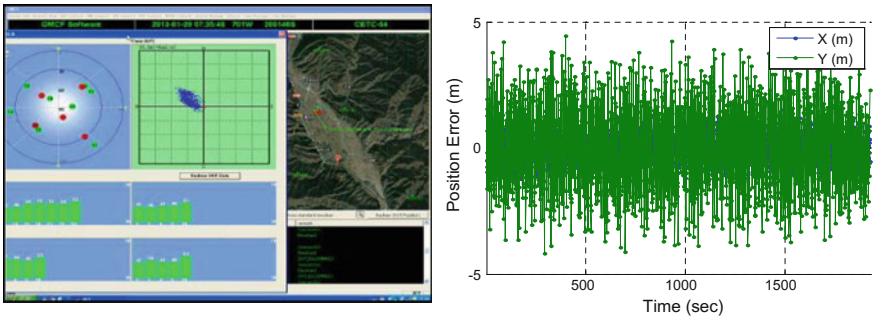

Fig. 8 Pseudorange accuracy testing of pseudolites cellular networks

the long time test, X axis and Y axis positioning error at about 2 m, and the level positioning error was less than 5 m.

The positioning result for pseudolite carrier phase differential positioning was shown in Fig. 9, and fifteen static test points were selected. Comparing each test point positioning results with the prior precise measurement results, it could be seen that pseudolite RTK positioning accuracy was better than 20 cm.

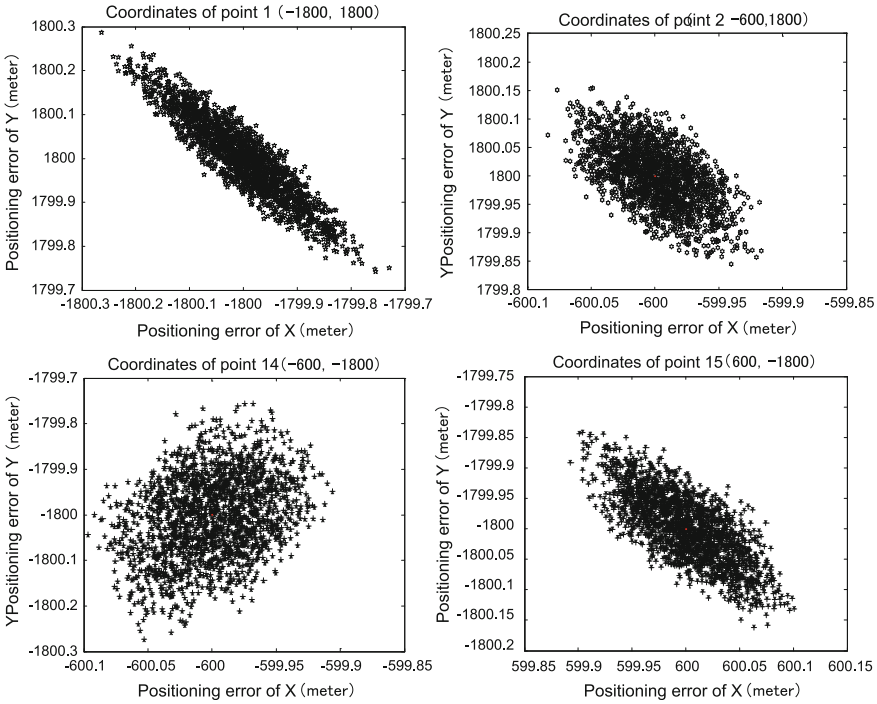

Fig. 9 RTK accuracy of pseudolite cellular networks

6 Conclusion

As the construction of National PNT System and Beidou Navigation System, GNSS pseudolites networks become an important supplement for the satellite navigation system, especially in urban location service applications. The pseudolites positioning system for urban, navigation signal, time synchronization, the optimization of network topology and high precision positioning Methods were studied. Finally, The positioning performance testbed of Ye San Po for pseudolite cellular networks was build, it was showed that the pseudorange positioning accuracy was better than 5 m, carrier phase positioning accuracy was better than 20 cm, then the pseudolite cellular network could satisfy the high-precision positioning requirement of the urban.

References

1. Japan Aerospace Exploration Agency, Interface Specifications for QZSS (IS-QZSS Ver.1.0). Available from the following site: http://www.gnss.co.jp/file/paper/null
2. GILT Study (2005) Core technology document for Pseudolites for enhanced availability. GILT-TRT-DD-15, GALILEO Initiative for Local Technologies, Alenia-Spazio, Thales, Indra
3. E Electronic Communications Committee, Compatibility studies between pseudolites and services in the frequency bands 1164–1215, 1215–1300 and 1559–1610 MHz, ECC Report 128. Available from the following site: http://www.cept.org/ecc
4. GPS.gov, Interface Specification IS-GPS-200. Available from the following site: http://www.gps.gov/technical/icwg/
5. Abt T-L, Soualle F (2005) Optimal pulsing schemes for GALILEO pseudolites signals. Paper presented at ION GNSS 2005, Long Beach, CA
6. Wang J (2000) Pseudolites applications in positioning and navigation: progress and problems. J GPS 1(1):P48–P56
7. Barnes J (2005) The integration of GPS and pseudolites for bridge monitoring. In: Sanso F (ed) A window on the future of geodesy, IAG Symp. 2005. vol 128, pp 83–88
8. Soon BHK (2003) Flight test results of precision approach and landing augmented by airport pseudolites. In: 16th International technical meeting of the satellite division of the U.S. Institute of Navigation, Portland, Oregan, USA, pp 2318–2325, 9–12 Sept 2003
9. Progri IF, Michalson WR (2007) Indoor geolocation using FCDMA pseudolites: signal structure and performance analysis. Navigation 54(3):241–256
10. Xingli G (2015) The development, test and application of new technology on Beidou/GPS dual-mode pseudolites. In: Proceedings of China satellite navigation conference (CSNC) 2015, vol I, pp 353–364
11. Cobb (1997) GPS pseudolites: theory, design, and applications. Stanford. Ph.D., 1997, pp 39–44
12. Ford T, Neumann J (1996) HAPPI—a high accuracy Pseudolites/GPS Positioning Integration. In: Proceedings of the 9th international technical meeting of the satellite division of the institute of navigation (ION GPS-96), 17–20 Sept 1996, Kansas City, Missouri, pp 1719–1728
13. Kalafus RM, van Dierendonck AJ Special committee 104 recommendations for differential GPS service. The U.S. Institute of Navigation, USA, pp 101–126
14. Choi, IK, Wang J, Han S (2000) Pseudolites: a new tool for surveyors, 2nd Trans Tasman Survey Congress, Queenstown, New Zealand, pp 141–149, 20–26 Aug 2000
15. Holden T (1997) Pseudolites augmented DGPS for land applications. In: 10th International technical meeting of the satellite division of the U.S. Inst. of Navigation GPS ION-97, Kansas City, Missouri, pp 1397–1403, 16–19 Sept 1997
16. Weiser M (1998) Development of a carrier and C/A-code based pseudolites system. In: 11th International technical meeting of the satellite division of the U.S. Institute of Navigation GPS ION-98, Nashville, Tennessee, pp 1465–1475, 15–18 Sept 1998

Performance Analysis for AP Selection Strategy

Xianghong Hua, Wei Zhang, Kegen Yu, Weining Qiu, Shoujian Zhang and Xin Chang

Abstract In recent years, received signal strength (RSS) based WiFi fingerprinting positioning technology has gradually become a research hotspot due to its ease of deployment and low cost implementation. However, the positioning accuracy of WiFi fingerprinting positioning based on RSS is affected by many factors. The quality of observed RSS is different among APs due to the complex and time varying indoor environment. Thus the selection of subset of optimal APs has a great influence on the RSS based WiFi fingerprinting positioning. This paper introduces three main AP selection algorithms: joint information gain (JIG) maximization based, mutual information (MI) minimization based and MaxMean (MM) based AP selection strategy, respectively. And the advantages and disadvantages of three different AP selection algorithms are compared and analyzed in this paper. At the same time, the influence of the number of subset of optimal APs and the number of RSS observations at the target point is comprehensively analyzed. Through the experiments, we found that: (1) for all the three algorithms, the positioning results tend to be stable when the number of real time RSS observations at the target point is more than 50; (2) with the given number of real time RSS observation at the target point, the position estimation accuracy change slowly with the increase of number of AP subset when the number of AP subset is more than 5; (3) given that the number of real-time RSS observations at the target point is 50 and the number of subset of optimal APs is 5, the position estimation accuracy of the AP selection strategy based on MI minimization is similar to the AP selection strategy based on MM, and both of them are better than the AP selection strategy based on the JIG maximization.

Keywords WiFi fingerprinting positioning · AP selection · Joint information gain · Mutual information · MaxMean

X. Hua (✉) · W. Zhang · K. Yu · W. Qiu · S. Zhang · X. Chang
School of Geodesy and Geomatics, Wuhan University, Wuhan, China
e-mail: xhhua@sgg.whu.edu.cn

J. Sun et al. (eds.), *China Satellite Navigation Conference (CSNC) 2017 Proceedings: Volume I*, Lecture Notes in Electrical Engineering 437,
DOI 10.1007/978-981-10-4588-2_28

1 Introduction

In recent years, Location Based Service (LBS) application in indoor environment is developing rapidly, which relates to people's work, study and life, such as employee tracking, self-service shopping, person positioning in emergency etc [1, 2]. Nowadays, the low cost, high precision indoor positioning solution becomes the key factor in the further development of LBS applications. Due to the widespread deployment of AP and universal popularity of smart mobile devices, RSS based WiFi fingerprinting positioning technology has gradually become a research hotspot for its ease of deployment and low cost characteristics [3, 4]. Due to the complexity of the indoor environment, the fading of signal which transmitted by AP is not only a function of distance, but also be affected by the multipath effect and Non Line of Sight (NLOS) [5, 6]. At the same time, the mutual interference between the APs may also distorted the RSS observations. Thus, in order to improve the accuracy of RSS based WiFi fingerprinting positioning algorithms, the subset of APs with better observation quality need to be selected for positioning estimation. AP selection is not only able to remove some APs which have poor data quality, but also reduce the signal space dimension and the computation load. Generally, there are two phases for RSS based WiFi fingerprinting positioning algorithm: the offline phase, fingerprinting database establishment on this phase; and online target positioning and tracking phase [7]. The JIG maximization based AP selection strategy was implemented at the offline phase, while the MI minimization based AP selection strategy and MM based AP selection strategy are implemented at the online phase. In order to figure out the influence of AP selection strategy on the WiFi fingerprinting positioning based on RSS, the basic principles of three main AP selection strategies are introduced in this paper, and the advantages and disadvantages of these selection strategies are also compared. Meanwhile, the performance of the three different AP selection strategies is evaluated using experimental results. In addition, both the lower bounds of the number of RSS observations during real-time sampling and the number of the subset of optimal APs are determined based on experimental results.

2 AP Selection Strategies

The purpose of the AP selection strategy is to select a certain number of APs from all available APs, which is usually called the subset of optimal APs. Only the selected subset of optimal APs is used to estimate target position, while other APs are excluded. Details of the three mentioned selection strategies are provided below.

2.1 AP Selection Based on the JIG Maximization

The JIG maximization based AP selection strategy, which measures the discriminant ability of subset of APs, selects the subset of APs with max JIG maximization as the subset of optimal APs. For RSS based WiFi fingerprinting positioning, the JIG of subset with N APs is calculated as following [8]:

$$\mathrm{JIG}(AP_1, AP_2, \ldots, AP_N) = \mathrm{H}(L) - \mathrm{H}(L|AP_1, AP_2, \ldots, AP_N) \quad (1)$$

Here, $\mathrm{JIG}(AP_1, AP_2, \ldots, AP_N)$ is the JIG of the N APs, $H(L)$ stands for the information entropy of calibration point, $\mathrm{H}(L|AP_1, AP_2, \ldots, AP_N)$ is the conditional entropy of the calibration point with information from N APs known, which can be calculated by a priori conditional probability.

2.2 AP Selection Based on the MI Minimization

The mutual interference between the APs is considered with the MI minimization based AP selection strategy, which uses MI as a measure of the correlation between the APs. The greater the MI is, the more redundant information is included in the selected subset of AP, and the smaller the MI is, the smaller the correlation between the selected APs exists and the stronger collective discrimination ability is obtainable. Han et al. [9] describes the detailed process of AP selection based on MI minimization.

2.3 AP Selection Based on the MM

RSS observation sequence associated with an AP typically fluctuates over time due to the dynamic indoor environment. The signal from an AP may be lost when the signal observation quality is too poor. AP selection strategy based on MM makes use of the fact that: the stronger the RSS of an AP is, the better the observation quality of the AP is, which means the signal is less affected by the dynamic changes of the environment, and better location estimation results can be obtained with these APs.

2.4 Performance Evaluation Index

The maximum error (MAXE), average distance error (ADE), root mean square (RMS), standard deviation (STD) and cumulative distribution function (CDF) are

leveraged for evaluation of positioning performance of WiFi fingerprinting positioning based on RSS. Let (x, y) stand for the real coordinates of target point and $(\hat{x}, \hat{y})$ be the estimated target point coordinates. Then the positional error (Euclidean distance between x, y and x, y) can be calculated as:

$$\delta = \sqrt{(x - \hat{x})^2 + (y - \hat{y})^2} \tag{2}$$

The ADE and RMS error are simply calculated as:

$$ADE = \frac{1}{n}\sum_{i=1}^{n} \delta_i, \quad RMS = \sqrt{\frac{1}{n}\sum_{i=1}^{n} \delta_i^2} \tag{3}$$

Here, n is the total number of target points.

3 Experiments and Analysis

To evaluate the influence of the number of RSS observations, the number of subset of optimal APs, and the AP selection strategy on the performance of the RSS based WiFi fingerprinting positioning three experiments were conducted in an office building. The weighted k-nearest neighbor (WKNN) algorithm is used for target position estimation. In the experiments, a millet smart phone is used for receiving AP signals and all APs deployed in the building are treated as valid signal transmitters. There are totally 6 calibration points and 18 target points in the positioning area, which are respectively represented by solid triangles and circles as shown in Fig. 1. The horizontal and vertical distance between two adjacent calibration points are four meters, while the horizontal and vertical distance between two adjacent target points are one meter. Here 180 epochs were observed at each calibration point. Since the scanning rate of WiFi signal used is one second, the scanning period of each calibration point is three minutes.

3.1 Analysis on Number of RSS Observations

The average of a sequence of consecutive RSS observations is used by the WKNN algorithm to reduce the influence of RSS fluctuation on position determination. Before analyzing the influence of AP different selection strategies on the position estimation, we first consider the influence of the insufficient number of RSS observations. In the experiments, the observation time ranges from 10 to 150s and increases by 10s each time. Three AP selection strategies are separately used to select the subset of optimal APs, and the number of subset of APs has a range of 4–8. Thus there are totally $15 \times 3 \times 5 = 225$ tests. Figures 2, 3 and 4 shows the

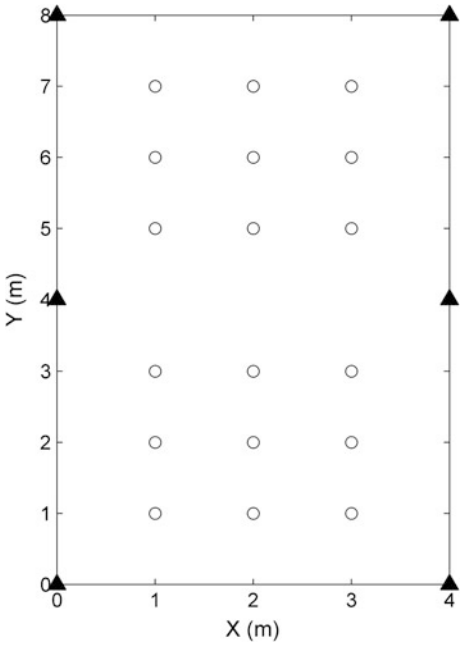

Fig. 1 Schematic diagram of calibration points and target points in the positioning area

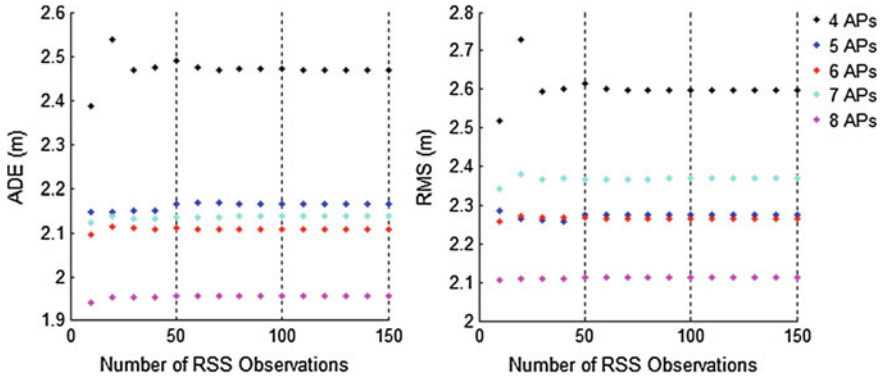

Fig. 2 Scatter diagram of ADE and RMS error of position estimation with JIG maximization based AP selection strategy

scatter diagram of ADE and RMS of position estimation using the three AP selection strategies, respectively. The horizontal axis represents the number of RSS observations at the target point. Each scatter point in ADE scatter diagram represents the average distance error of the 18 target points of the corresponding

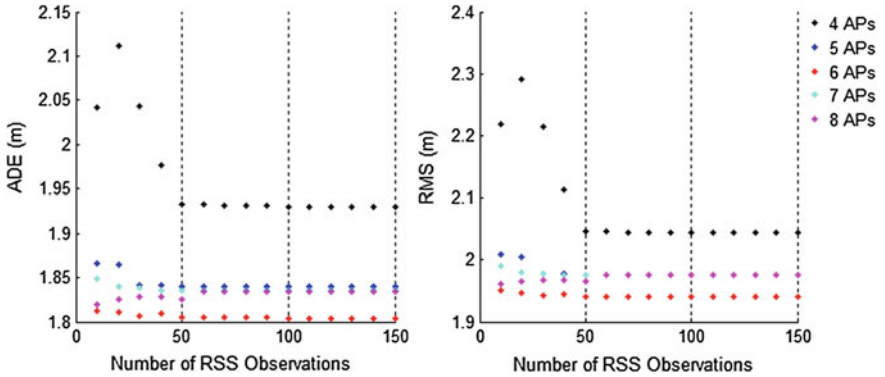

Fig. 3 Scatter diagram of ADE and RMS error of position estimation with MM minimization based AP selection strategy

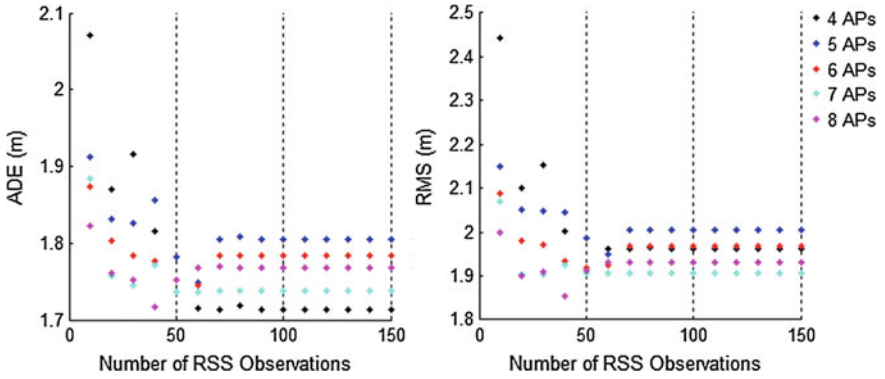

Fig. 4 Scatter diagram of ADE and RMS error of position estimation with MI based AP selection strategy

experiment, while scatter point in RMS scatter diagram represents the root mean square of the 18 target points of the corresponding experiment.

As shown in Figs. 2 and 3, both ADE and RMS error vary significantly when the number of RSS observations is less than 50. As the number of observations is greater than 50, the variation in both of them is very marginal.

Similar observations can be seen in Fig. 4. Both ADE and RMS error also change greatly when the number of RSS observations is less than 50. However, the ADE and RMS error still vary considerably when the number of the RSS observations goes from 50 to 70. As the number of observations increases from 70, they basically remain the same.

Overall, both ADE and RMS are insensitive to the variation in the number of APs when the number of APs is greater than a threshold for all the three AP selection strategies. And to reduce computational complexity without positioning

accuracy loss, the number of RSS observations should be set to be slightly greater than the threshold, 50 for JIG maximization based and MM based strategies, and 70 for the MI minimization based strategy.

3.2 Analysis on Number of Subset of Optimal APs

In order to analyze the influence of number of APs on the positional accuracy of WiFi fingerprinting positioning, the number of RSS observations is fixed at 50 according to the above analysis.

Table 1 shows the positional accuracy in terms of four different indexes, and the online device-dependent execution time caused by online AP selection. With JIG based AP selection strategy, the MAXE, ADE and RMS have a larger change when the number of subset of APs increases from 4 to 5. The same phenomenon appears again while the number of subset of APs increases from 6 to 7. However, for both MI based and MM based AP selection strategies, the MAXE, ADE and RMS have no significant change while the number of subset of APs ranges from 5 to 8, namely that the positioning performance is stable. The number of subset of APs has little effect on the STD through all of the three AP selection strategies. At the same time, in the MI minimization based AP selection strategy, the execution time increases with the increase of the number of subset of APs. In summary, the number of subset of APs should not be less than 5 to ensure the positional accuracy and positional reliability. It is reasonable to set the number of subset of APs to 5 when taking into account the online execution time.

Table 1 Statistical results when the number of RSS observations is 50

AP selection strategy	Number of APs	MAXE (m)	ADE (m)	RMS (m)	STD (m)	Time (ms)
JIG	4	3.90	2.49	2.61	0.81	–
	5	3.59	2.17	2.27	0.71	–
	6	3.57	2.11	2.27	0.85	–
	7	4.36	2.13	2.36	1.05	–
	8	3.28	1.96	2.11	0.82	–
MI	4	3.99	1.74	1.99	1.00	23.24
	5	3.44	1.78	1.99	0.90	26.85
	6	3.07	1.74	1.92	0.84	31.63
	7	3.11	1.74	1.91	0.81	34.19
	8	3.18	1.75	1.91	0.79	36.69
MM	4	2.97	1.93	2.05	0.69	1.50
	5	2.90	1.84	1.98	0.74	1.56
	6	2.91	1.81	1.94	0.73	1.44
	7	2.87	1.84	1.97	0.75	1.33
	8	2.89	1.83	1.96	0.75	1.71

Table 2 Statistical results when the number of RSS observations is 50 and the number of subset of APs is 5

AP selection strategy	MAXE (m)	ADE (m)	RMS (m)	STD (m)	Time (ms)
JIG	3.59	2.17	2.27	0.71	
MI	3.44	1.78	1.99	0.90	26.85
MM	2.90	1.84	1.98	0.74	1.56

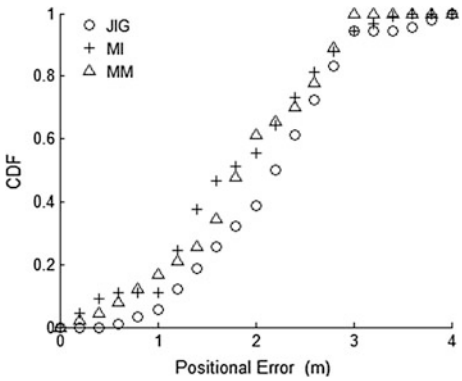

Fig. 5 CDF curves of different AP selection strategies

3.3 Effect of Difference AP Selection Strategies

From what have been discussed above, the number of RSS observations is fixed at 50 and the number of subset of APs is fixed at 5 when evaluating the influence of different AP selection strategies on the positional accuracy and positional reliability of WiFi fingerprinting positioning algorithm.

Table 2 shows the positional accuracy of WiFi fingerprinting positioning of the three different AP selection strategies. Also shown is the online execution time of the three strategies. It is clearly seen that the positional accuracy of both the MI minimization based and the MM based AP selection strategies is significantly better than that of the JIG based AP selection strategy. Furthermore, the MM based AP selection strategy is slightly better than the MI based on AP selection strategy by comparing the MAXE and the error STD. However, the online execution time of MM based selection strategy is significantly less than that of the MI minimization based AP selection strategy.

Figure 5 shows the CDF of the three AP selection strategies. The CDF curve of the MM based strategy is similar to that of the MI based strategy. However, the CDF curve of the JIG based strategy is significantly lower than the other two strategies, which means a lower positional accuracy. In a word, the MM based AP selection strategy is the best among the three AP selection strategies.

4 Conclusions

In this paper, several factors affecting the performance of RSS based WiFi fingerprinting positioning are discussed, including the number of RSS observations, the number of subset of APs and the AP selection strategies. In order to ensure a consistent positioning accuracy of a positioning algorithm such as the WKNN algorithm, the number of RSS observations at target point should be no less than 50 and the number of subset of APs should not be less than 5. These empirical values are applied to all of the three AP selection strategies. By using experimental results and comparing the effects of three different AP selection strategies on positional performance of WiFi fingerprinting positioning, we found that the AP selection strategy based on MM is the best among the three AP selection strategies.

Acknowledgements This research is sponsored by National Natural Science Foundation of China (41374011) and by the Key Laboratory for Digital Land and Resources of Jiangxi Province under Grant DLLJ201702.

References

1. Deng Z, Yu Y, Yuan X, Wan N, Yang L (2013) Situation and development tendency of indoor positioning. China Commun 10(3):42–55
2. Stojanović D, Stojanović N (2014) Indoor localization and tracking: methods, technologies and research challenges. Facta Univ Ser Autom Control Rob 13(1):57–72
3. Tsui AW, Chuang YH, Chu HH (2009) Unsupervised learning for solving RSS hardware variance problem in WiFi localization. Mobile Netw Appl 14(5):677–691
4. So J, Lee JY, Yoon CH, Park H (2013) An improved location estimation method for Wifi fingerprint-based indoor localization. Int J Softw Eng Appl 7(3):77–86
5. Wang J, Katabi D (2013) Dude, where's my card?: RFID positioning that works with multipath and non-line of sight. ACM SIGCOMM Comput Commun Rev 43(4):51–62
6. Yang C, Shao HR (2015) WiFi-based indoor positioning. IEEE Commun Mag 53(3):150–157
7. Zou H, Lu X, Jiang H, Xie L (2015) A fast and precise indoor localization algorithm based on an online sequential extreme learning machine. Sensors 15(1):1804–1824
8. Deng Z, Ma L, Xu Y (2011) Intelligent AP selection for indoor positioning in wireless local area network. In: International ICST conference on communications and networking in China. IEEE, Harbin, pp 257–261
9. Zou H, Luo Y, Lu X, Jiang H, Xie L (2015) A mutual information based online access point selection strategy for WiFi indoor localization. 2015 IEEE international conference on automation science and engineering (CASE). IEEE, Gothenburg, pp 180–185

Definition of Conversion and Allocation Model for GNSS Index Basing Navigation Performances

Mengli Wang, Jinping Chen, Yang Yang, Yuan Hong and Junyi Xu

Abstract Performance index assignment and demonstration is an important accordance for satellite navigation system, and it is necessary to direct and restrict each system's scheme design and project implement. Integrity and continuity are key service performance indexes, and if they are satisfied with user's requirement depending on the design of SIS fault and monitoring performance. Taking user's integrity and continuity performances as designing accordance, the conversion and distribution relationships among SIS fault times, mean fault probability, fault misdetection probability, fault alarming probability and hazardous probability are defined. Then calculation and analyzation are implemented aiming at Beidou system and its constellation characters. In the calculation, requirements of user's integrity and continuity adopt the ICAO standard. Beidou system monitoring performance index under different SIS fault level is analyzed. The research conclusions provide demonstration and design foundation if reliability index for Beidou global system.

Keywords Signal in space · Integrity monitoring · Fault times · Hazardous probability · Misdetection probability

1 Introduction

In general, GNSS navigation performances are evaluated by accuracy, integrity, continuity and usability, which are called "four properties". Precision refers to any point of the user position, speed and time deviation between the measurements and the true values. The main factors affecting the accuracy including constellation geometry, determination accuracy of satellite orbit and clock bias, atmospheric propagation delay correction error and receiver measurement error. Integrity is

M. Wang (✉) · J. Chen · Y. Yang · Y. Hong · J. Xu
Beijing Satellite Navigation Center, Beijing 100094, China
e-mail: compass2020@126.com

J. Sun et al. (eds.), *China Satellite Navigation Conference (CSNC) 2017 Proceedings: Volume I*, Lecture Notes in Electrical Engineering 437,
DOI 10.1007/978-981-10-4588-2_29

established on the basis of precision. It is defined as the timely warning ability when the user's navigation and positioning services to provide more than the permitted limits, and can't be competent for the requirements of the navigation task. The evaluation index of integrity includes warning time, risk probability and location error protection level. Continuity refers to the probability of performance within the stipulated time required to accomplish the function in the given conditions, continuity is based on the accuracy and integrity, so there are three kinds of continuity: the accuracy of the continuity, integrity and continuity of service. Usability refers to the time percentage of the system can provide available navigation service for users, and it is based on the accuracy, integrity and continuity. According to different user needs level, there are three kinds of availability, the accuracy of the availability, integrity and continuous availability. From the concept of time and space; availability can be divided into availability for a position at a certain time (instantaneous availability), availability for the same position in different time (single point availability) and availability for the entire service area in different time (service availability).

The accuracy, integrity, continuity and availability as the basic indicators of system performances, can meet the needs of users to sign depends on the geometrical distribution, user equivalent range error, spatial signal fault and performance monitoring design. This paper analyzes the conversion and distribution relationship between system indexes and navigation services indexes. According to the requirement of accuracy, integrity, continuity and availability in different flight phases specified by the international civil aviation organization, the design requirements of the system are analyzed. The research conclusions provide basis for the evaluation of the top level indicators of the GNSS system and the design of the subsystem.

2 Conversion and Distribution Model of Navigation Performances Index

The decomposition relationship of GNSS navigation performance index is shown in Fig. 1. The performance of spatial signal integrity monitoring is characterized by missing alarm rate and false alarm rate. The missing alarm rate is the probability that the system is not detected when the space signal is in fault, and the false alarm rate is the probability that the space signals are in good condition and the system is detected as a failure. The correct detection and fault occurs when no fault false alarm signal will cause the space out of service, and resulting in the observation geometry of poor user service interruption, which is continuous risk. Fault occurs without correct detection and signal space without fault, a comprehensive introduction of positioning signal space of random error and can't correctly detected abnormal, is integrity risk.

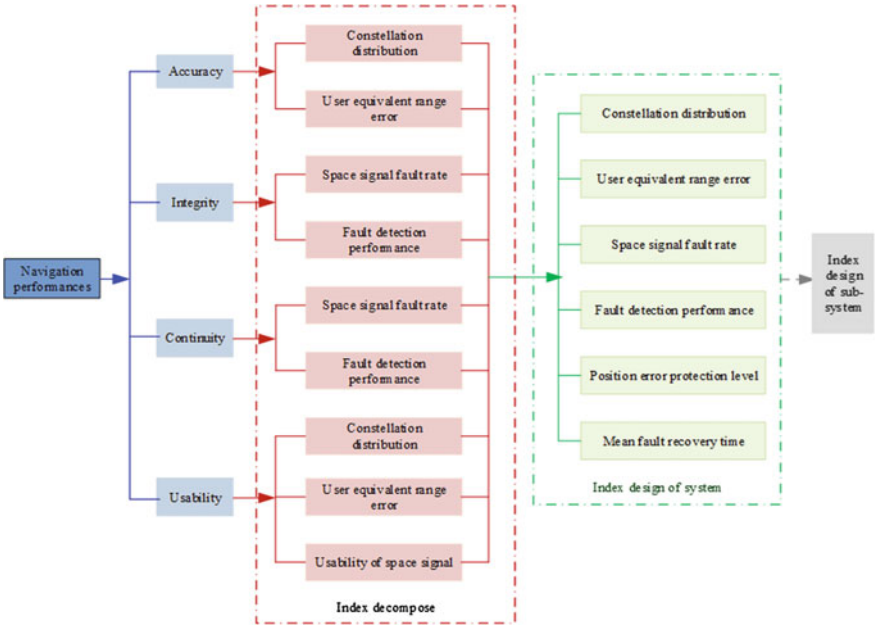

Fig. 1 Decomposition relationship of navigation performance index

2.1 Conversion Model of Positioning Accuracy Index

Positioning accuracy PE is resting with observation geometrical value DOP, user equivalent range error UERE and probability level Pr. Furthermore, it can be decomposed into horizontal and vertical positioning accuracy, which are labeled as HPE and VPE respectively. As follows:

$$PE = \kappa(P_r) \cdot \sigma_{UERE} \cdot PDOP, HPE = \kappa(P_r) \cdot \sigma_{UERE} \cdot HDOP,$$
$$VPE = \kappa(P_r) \cdot \sigma_{UERE} \cdot VDOP$$

Therein, $\kappa(P_r)$ is the corresponding fractile quantile.

Therefore, positioning accuracy index can be converted into constellation geometry and UERE index. When constellation distribution is determined, user positioning accuracy requirement can be converted as demand of UERE. As follows:

$$\sigma_{UERE} = PE/[PDOP \cdot \kappa(P_r)] \tag{1}$$

2.2 Conversion Model of Integrity Index

Integrity index includes alarming time, risk probability and positioning error protection level. Suppose that there is a fault signal (named as H1 hypothesis), there will be integrity risk when the fault is missed detection; Suppose that there is no fault signal (named as H0 hypothesis), there may be integrity risk caused by multi-signals' random errors. Therefore, the conversion model of integrity risk and signal fault detection performances is as following:

$$\begin{cases} \text{H1}: \sum_{i=1}^{n} P_{MD} \cdot P_{F,SIS} \le P_{IR|H1} \\ \text{H0}: \sum_{j=1}^{m} P_{ffmd} \cdot (1 - P_{F,SIS}) \le P_{IR|H0} \end{cases}$$

In the formula, $P_{F,SIS}$ is mean fault rate of one satellite signal; P_{MD} is missing detection rate in H1 hypothesis; P_{ffmd} is missing detection rate in H0 hypothesis; i is satellite serial number, n is satellite number participating in positioning; j is serial number of independent sample, m is independent sample number in the course of navigation time.

Integrity risk requirement is $P_{IR} = P_{IR|H1} + P_{IR|H0}$. So, calculation methods of missing detection rate for H1 hypothesis and H0 hypothesis are as followings [1]:

$$P_{MD} = P_{IR|H1}/(n \cdot P_{F,SIS}) \tag{2}$$

$$P_{ffmd} = P_{IR|H0}/[m \cdot (1 - P_{F,SIS})] \tag{3}$$

P_{MD} and P_{ffmd} are missing detection rate, which can be used for the calculation of $\kappa(P_r)$, and then for positioning error protection level [2, 3]. Without fault hypothesis, there are:

$$\begin{cases} HPL_{H0} = \kappa(P_{H,ffmd}) \cdot HDOP_{\max} \cdot \sigma_{UERE} \\ VPL_{H0} = \kappa(P_{V,ffmd}) \cdot VDOP_{\max} \cdot \sigma_{UERE} \end{cases} \tag{4}$$

With fault hypothesis, there are:

$$\begin{cases} HPL_{H1} = \kappa(P_{H,MD}) \cdot HDOP_{\max} \cdot \sigma_{UERE} \\ VPL_{H1} = \kappa(P_{V,MD}) \cdot VDOP_{\max} \cdot \sigma_{UERE} \end{cases} \tag{5}$$

Taking the minimum value between conditions of with and without fault as the positioning error protection level. That is:

$$\begin{cases} HPL = \min\{HPL_{H0}, HPL_{H1}\} \\ VPL = \min\{VPL_{H0}, VPL_{H1}\} \end{cases} \tag{6}$$

In the formula, $\kappa(P_{H,ffmd})$ and $\kappa(P_{V,ffmd})$ are fractile quantiles which are respectively corresponding with the P_{ffmd} of horizontal and vertical direction. $\kappa(P_{H,MD})$ and $\kappa(P_{V,MD})$ are fractile quantiles which are respectively corresponding with the P_{MD} of horizontal and vertical direction. Calculation of fractile quantile is determined by definition of positioning error probability distribution function. In general, horizontal and vertical positioning errors are assumed as normal distribution, and three-dimensional positioning error is assumed as root distribution.

Therefore, integrity risk probability can be converted into constraint requirements about signal fault probability $P_{F,SIS}$, fault detection performance P_{MD} and P_{ffmd}, and positioning error protection level. Furthermore, converted into design index requirements of ground system and satellite system.

2.3 Conversion Model of Continuity Index

The main continuity index is continuity risk probability. Supposing any signal is fault (H1 hypothesis), if the fault is detected correctly, there will be continuity risk; Supposing no signal is fault (H0 hypothesis), if the fault is detected mistakenly, there will be continuity risk. Therefore, the probability conversion model between continuity risk and signal detection performance is as following [4]:

$$\begin{cases} \text{H1}: \sum_{i=1}^{n} (1 - P_{MD}) \cdot P_{F,SIS} \le P_{CR|H1} \\ \text{H0}: \sum_{j=1}^{m} P_{FA} \cdot (1 - P_{F,SIS}) \le P_{CR|H0} \end{cases}$$

In the formula, P_{FA} is missing alarm rate of hypothetical inspect; i is satellite serial number, n is satellite number participating in positioning; j is serial number of independent sample, m is independent sample number in the course of navigation time.

Continuity risk requirement is $P_{CR} = P_{CR|H1} + P_{CR|H0}$. So, calculation methods of missing detection rate for H0 hypothesis is as followings:

$$P_{FA} = P_{CR|H0} / [m \cdot (1 - P_{F,SIS})] \tag{7}$$

Therefore, fault alarm probability P_{FA} without fault can be converted into constraint requirements about system fault monitoring ability.

2.4 Conversion Model of Usability Index

From the view of user demands, available positioning accuracy requires that position error protection level is less than the alarm limiting value. That is:

$$\begin{cases} HPL < HAL \\ VPL < VAL \end{cases} \tag{8}$$

On the other hand, from the view of system design, service usability can be converted into signal usability, and the signal usability determined by mean time of fault recovery MTTR and mean time of fault interval MTBF.

$$P_{av} = \frac{MTBF}{MTBF + MTTR} \tag{9}$$

There into, P_{av} is system usability index, MTBF is determined by signal fault rate $P_{F,SIS}$, and MTBF = satellite working time/total fault times.

Therefore, combining with formulas (4)–(9), user usability demands can be converted into system design requirements about UERE and mean fault recovery time.

3 Calculation Example Analysis of Navigation Performance Index Conversion

According to above conversion model calculation methods of GNSS navigation performance index, one example is offered here. In the example, the GNSS constellation is constituted of 24 MEO satellites, 3 IGSO satellites and 3 GEO satellites, and the 24 MEO satellites are distributed as Walker (24/8/3). With the constellation, the mean visible satellite numbers are 14, that is, the satellite number participating positioning is n = 14. DOP value of the constellation is shown in Table 1, and the cut-off angle is 10°.

Index requirements of GNSS navigation performances are according to the ICAO's regulations, which includes different flight phases [3]. Shown as Table 2.

Table 1 Analysis result of the constellation DOP value

DOP	PDOP	HDOP	VDOP
Maximum value	4.1	2.5	3.2
Minimum value	2.1	1.0	1.8
Mean value	3.2	2.0	2.5

Table 2 GNSS navigation performance requirements defined by ICAO

Flight phases	Accuracy (95%)		Integrity				Continuity risk probability
	Horizontal	Vertical	Alarming limit value		Alarming time	Integrity risk probability	
			Horizontal	Vertical			
Ocean area	3.7 km	N/A	7.4 km	N/A	5 min	1×10^{-7}/h	$10^{-4} \sim 10^{-8}$/h
Mainland	3.7 km	N/A	3.7 km	N/A	5 min	1×10^{-7}/h	$10^{-4} \sim 10^{-8}$/h
Terminal area	0.74 km	N/A	1.85 km	N/A	15 s	1×10^{-7}/h	$10^{-4} \sim 10^{-8}$/h
NPA	220 m	N/A	556 m	N/A	10 s	1×10^{-7}/h	$10^{-4} \sim 10^{-8}$/h
APV I	16 m	20 m	40 m	50 m	10 s	2×10^{-7}/P	8×10^{-6}/15 s
APV II	16 m	8 m	40 m	20 m	6 s	2×10^{-7}/P	8×10^{-6}/15 s
CAT I	16 m	6–4 m	40 m	15–10 m	6 s	2×10^{-7}/P	8×10^{-6}/15 s

Table 3 UERE analysis results of different flight phases calculated according to accuracy requirements

Flight phases	Accuracy (95%)		σ_{UERE} (m)		
	Horizontal	Vertical	Horizontal	Vertical	Minimum value
Ocean area	3.7 km	N/A	943.9	–	943.9
Mainland	3.7 km	N/A	943.9	–	943.9
Terminal area	0.74 km	N/A	188.8	–	188.8
NPA	220 m	N/A	56.1	–	56.1
APV I	16 m	20 m	4.1	4.1	4.1
APV II	16 m	8 m	4.1	1.6	1.6
CAT I	16 m	6–4 m	4.1	1.2–0.8	0.8

(1) Analysis of index UERE according to accuracy requirements

According to ICAO define of positioning accuracy requirements for different flight phases, the UERE analysis results for different flight phases are shown in Table 3. The analysis is basing on formula (1). Positioning errors obey normal distribution, and $\kappa(P_r) = 1.96$ on condition of 95% confidence probability. All DOPs value are mean.

It can be seen that different flight phases require different UERE value given constellation configuration. For positioning accuracy of class I precision approach, UERE value should less than 4.1 m. For positioning accuracy of class II precision approach, UERE value should less than 1.6 m. For positioning accuracy of CAT I, UERE value should less than 0.8 m. Basing on the analysis, the UERE index can be converted and distributed further, such as ephemeris error, satellite clock error, ionophoric correction error, user observation error, etc.

Table 4 Fault detection performance analysis results for different flight phases

Flight phases	$P_{F,SIS} = 1.0 \times 10^{-4}$/h			$P_{F,SIS} = 1.0 \times 10^{-3}$/h		
	P_{MD}	P_{ffmd}	P_{FA}	P_{MD}	P_{ffmd}	P_{FA}
Ocean area	6.9×10^{-5}	1.0×10^{-9}	1.0×10^{-6}	6.9×10^{-6}	1.0×10^{-9}	8.0×10^{-8}
Mainland	6.9×10^{-5}	1.0×10^{-9}	1.0×10^{-6}	6.9×10^{-6}	1.0×10^{-9}	8.0×10^{-8}
Terminal area	6.9×10^{-5}	1.0×10^{-9}	1.0×10^{-6}	6.9×10^{-6}	1.0×10^{-9}	8.0×10^{-8}
NPA	6.9×10^{-5}	1.0×10^{-9}	1.0×10^{-6}	6.9×10^{-6}	1.0×10^{-9}	8.0×10^{-8}
APV I	3.3×10^{-3}	2.0×10^{-9}	1.0×10^{-6}	3.3×10^{-4}	2.0×10^{-9}	8.0×10^{-8}
APV II	3.3×10^{-3}	2.0×10^{-9}	1.0×10^{-6}	3.3×10^{-4}	2.0×10^{-9}	8.0×10^{-8}
CAT I	3.3×10^{-3}	2.0×10^{-9}	1.0×10^{-6}	3.3×10^{-4}	2.0×10^{-9}	8.0×10^{-8}

(2) Analysis of fault detecting performances

According to ICAO define of integrity and continuity risk requirements for different flight phases, analysis results of missing detection probability and fault alarm probability are shown in Table 4. The analysis is basing on formulas (2), (3) and (7), and the signal fault probability value is different. In one-hour navigation phase, independent sample number m is 1, that is, m = 1 when navigation time is 15 s, 150 s or 1 h. Risk probability distribution under H0 and H1 hypothesis is as follows: the risk probability is 1% when there is no fault signal; when there is fault signals, the risk probability is $P_{F,SIS} = 1.0 \times 10^{-4}$/h or $P_{F,SIS} = 1.0 \times 10^{-3}$/h [5].

It can be seen that different signal fault condition needs different system monitoring ability. In the design of system index, the fault probability and fault monitoring performances should be overall considered according to system realization ability. On this basis, single signal fault probability can be distributed to sub-systems and task processing units further. Fault missing detection probability and fault alarming probability can be distributed to task processing units of integrity monitoring.

(3) Analysis of positioning error protection level

Analysis results of positioning error protection level for different flight phases is shown in Table 5. The analysis includes no fault and different fault probability conditions according to formulas (4)–(6). In the analysis, UERE = 0.8 m, the calculation conditions and fault detection performances of different signal fault probability are mentioned above.

It can be seen that position error protection levels are different under different signal faults. The probability of signal fault is lower, the requirement of position error protection level is higher. In application, if there is no signal fault, the position protection level can be calculated by fault missing detection quantile basing on no fault condition; if there are signal faults, the position protection level can be calculated by fault missing detection quantile basing on fault conditions.

Table 5 Positioning error protection level analysis results for different flight phases

Flight phases		Ocean area	Mainland	Terminal area	NPA	APV I	APV II	CAT I
No-fault hypothesis	$\kappa(P_{H,ffmd})$	6.1	6.1	6.1	6.1	6.0	6.0	6.0
	$\kappa(P_{V,ffmd})$	–	–	–	–	6.0	6.0	6.0
	HPL_{H0}	12.2	12.2	12.2	12.2	12.0	12.0	12.0
	VPL_{H0}	–	–	–	–	15.4	15.4	15.4
$P_{F,SIS}$ = 1.0×10^{-4}/h	$\kappa(P_{H,MD})$	3.8	3.8	3.8	3.8	2.9	2.9	2.9
	$\kappa(P_{V,MD})$	–	–	–	–	2.9	2.9	2.9
	HPL_{H1}	7.6	7.6	7.6	7.6	5.9	5.9	5.9
	VPL_{H1}	–	–	–	–	7.5	7.5	7.5
$P_{F,SIS}$ = 1.0×10^{-3}/h	$\kappa(P_{H,MD})$	4.5	4.5	4.5	4.5	3.6	3.6	3.6
	$\kappa(P_{V,MD})$	–	–	–	–	3.6	3.6	3.6
	HPL_{H1}	9.0	9.0	9.0	9.0	7.2	7.2	7.2
	VPL_{H1}	–	–	–	–	9.2	9.2	9.2
Minimum value	HPL	7.6	7.6	7.6	7.6	5.9	5.9	5.9
	VPL	–	–	–	–	7.5	7.5	7.5

Table 6 UERE analysis results of different flight phases calculated according to usability requirements

Flight phases	Alarming limit value		σ_{UERE} (m)		
	Horizontal	Vertical	Horizontal	Vertical	Minimum value
Ocean area	7.4 km	N/A	779.0	–	779.0
Mainland	3.7 km	N/A	389.4	–	389.4
Terminal area	1.85 km	N/A	194.8	–	194.8
NPA	556 m	N/A	58.6	–	58.6
APV I	40 m	50 m	5.6	5.4	5.4
APV II	40 m	20 m	5.6	2.2	2.2
CAT I	40 m	15–10 m	2.8	1.6–1.0	1.0

(4) Analysis of index UERE according to usability requirements

UERE analysis results for different flight phases with different alarming limit value are shown in Table 6. Integrity alarming limit value requirements of different flight phases agree with ICAO define. According to formulas (4), (5) and (8), all DOP values are the maximum values. Missing detection probability quantile value of different fault conditions according to Table 5, and $P_{F,SIS} = 1.0 \times 10^{-4}$/h.

To satisfy both UERE requirements of accuracy and usability in different flight phases, UERE value should be determined comprehensively by Tables 3 and 6. Taking the minimum value, so UERE = 0.8.

4 Conclusion and Application

System index distribution and demonstration is an important accordance, for it will guide and constraint each systems design and engineering implementation. Integrity and continuity are key system service indexes. And if they can satisfy users' requirements is determined by the index design of signal fault and detection. Establishing in users' requirements of integrity and continuity, this paper define the conversion and distribution relationship between system indexes and integrity and continuity risk probabilities. Therein, system indexes include signal fault times, mean fault probability, fault missing detection probability and fault alarming probability. Aiming at BDS constellation characteristics and according to ICAO definition on users' integrity and continuity requirements, signal integrity detection requirements with different signal fault are analyzed. The study can provide design basis for BDS index demonstration, especially for reliability indexes.

In the design of system index, indexes of signal fault probability and signal integrity monitoring are complement and constraint each other. They should be designed Synthetically according to the realization ability of each link. According to the signal fault level of BD regional system, if signal fault rate is 3 times every year, then single signal fault probability is 1.1×10^{-5}/h. Adapted to that, to satisfy the risk requirements of different flight phases, signal fault missing detection probability should be 6.2×10^{-4}, and fault alarming probability should be 1.0×10^{-6}. Where, the receiver autonomous integrity monitoring means isn't considered. Index of signal fault probability is designed and implemented by multiple links, including monitoring and receiving of initial data, navigation parameters calculation, navigation messages uplink, satellite data receiving and processing, satellite clock, down-link signal modulation and launch, system basic integrity monitoring. Index of signal integrity monitoring is designed and implemented by ground system.

References

1. Felix K, Carsten S, Gunter H (2010) Combined integrity of GPS and Galileo. Inside GNSS 52–63
2. Anon (2006) Annex 10 to the convention on international civil aviation, international standards and recommended practices (SARPs), volume I—radio navigation aids. In: International civil aviation organization (ICAO), Montreal, PQ, Canada, July 2006: ATT A-1-7

3. RTCA DO-229D. Minimum Operational Performance Standards for GPS/Wide Area Augmentation System Airborne Equipment [S]. Washington D.C. 2006
4. Jörg H et al (2004) The galileo integrity concept. In: Proceeding of ION GPS GNSS 2004
5. Karl K et al (2008) GPS III integrity concept. In: Proceeding of ION GNSS 2008, pp 16–19

Analysis of GPS for Monitoring Rain and Snow Weather

Xiaowei Hou, Shuangcheng Zhang, Zhengxun He, Qin Zang, Tianhe Wan and Xiaojuan Zhang

Abstract With the continuous improvement of the theory of the Ground-based GPS Meteorology and GPS-MR technology, and increases of the global GPS tracking station. Making the Ground-based GPS as a new kind of sensor in space weather monitoring plays an increasingly important role. This paper describes the basic principle of remote sensing water vapor using Ground-based GPS and the GPS-MR technology, then analyze the feasibility and validity of the experimental data. GPS observation data and meteorological files in P360 station of California PBO network in 2013 are used to obtain PWV by GAMIT and GPS-MR snow depths. Then compare it with the measurements and precipitation by SNOTEL station. By comparing the experimental data showing the strong correlation between PWV and precipitation, and the correlation between GPS-MR snow depths and measured snow depth is 0.97, RMSE is 0.12 m. The experimental results show that the Ground-based GPS not only can be used for monitoring the precipitation, continuous real-time, high time resolution, but also for continuous, real-time, high-resolution snow depth monitoring around the station in winter. Which further expanding the application of GPS in weather monitoring and forecasting.

Keywords GPS · Precipitable water vapor (PWV) · GPS-MR (multipath reflectometry) · Snow depth · Weather monitoring

X. Hou · S. Zhang (✉) · Z. He · Q. Zang
College of Geology Engineering and Geomantic, Chang'an University, Xi'an, China
e-mail: shuangcheng369@vip.163.com

T. Wan · X. Zhang
Xinjiang Altai Meteorological Bureau, Altai, China

J. Sun et al. (eds.), *China Satellite Navigation Conference (CSNC) 2017 Proceedings: Volume I*, Lecture Notes in Electrical Engineering 437,
DOI 10.1007/978-981-10-4588-2_30

1 Introduction

Water vapor can affect weather changes in many ways, affecting the balance of radiation, energy transport, cloud formation and precipitation, is one of the most important gas components in the atmosphere, but also it has a strong directive significance for small-scale disaster weather. Therefore monitoring of atmospheric water vapor content and its change timely and accurately is important. However, the time and space resolution of water vapor detection methods such as radiosonde, microwave radiometer or satellite remote sensing can't meet the requirements [1]. With the development of GPS and Ground-based GPS/MET, it provides a new way for water vapor information inversion because of its high precision, high temporal resolution, all-weather, real-time continuous and simple maintenance. Bevis of the United States proposed this principle that use of measurement GPS receiver inversion of water vapor theory [2]. On this basis, domestic scholars have also carried out relevant research, Li et al. [3] through the GPS remote sensing water vapor in Chengdu experiment proved the accuracy of GPS Precipitable Water Vapor (GPS/PWV) can reach 1–2 mm. And further uses GPS Slant Water Vapor (GPS/SWV) and its horizontal gradient information to reflect the three-dimensional structure of atmospheric refractive index distribution. Song et al. [4] show that the technology can be obtained in different directions of the water vapor changes in space information by analyzing the Shanghai GPS monitoring network data. CAO et al. [5–7] have greatly promoted the development of the GPS/MET to the application in the spatial algorithm study of water vapor distribution. At present, the research of GPS/MET mainly concentrates on the three-dimensional and four-dimensional inversion of water vapor and the combination with other disciplines. Fan et al. [8] took the Bohai Sea as the research area to research the marine PWV information and three-dimensional water vapor chromatography. Wang et al. [9] analysis the relation between atmospheric water vapor and PM2.5 during the Beijing haze, and found that the two have a good consistency.

Snow is one of the most important components in the hydrological system, which impacts the water cycle and atmospheric circulation. Current measurement techniques, such as manual, echo-based snow depth measurement and radiation measurement, are mainly based on ground measurement, have greatly limited the progress of this field due to their high cost, low temporal or spatial resolution. Since 1997, GPS Reflectometry (GPS-R) research using signal-to-noise information with multipath effects has been carried out jointly by the NASA Langley Research Center and the University of Colorado. GPS-R technology take advantage of GPS data obtained by receiving reflected signals and direct signals inversion of surface parameters is used for snow depth monitoring, but due to that need to use a special antenna device, limiting its wide range of applications [10, 11]. Larson et al. [12, 13] first innovatively proposed a GPS Multipath Reflectometry (GPS-MR) technique based on Signal-to-Noise Ratio (SNR), which is a method using an ordinary measurement GPS receiver can achieve snow depth monitoring. Domestic research started relatively late in this area. Dai et al. [14] described the GPS-MR theory and

its flow in detail, then gave the relationship between multipath and signal-to-noise ratio and proved the effectiveness of the technology in 2015. Jin et al. [15] used the US Panel Boundary Observations Program (PBO) observations show that L2P SNR data can be used to retrieve snow depth in 2016 make the theory of GPS-MR technology more complete. The above-mentioned scholars have made a preliminary study on the theory and application of GPS-MR theory. At present, with GPS, GLONASS modernization, BDS and Galileo and other global navigation systems developing rapidly, GNSS will greatly promote the GNSS-MR technology continues to improve, GNSS-MR technology is expected to be a powerful complement for the meteorological department in snow depth monitoring.

At present, there are few researches on the application of measurement GPS receiver in snow weather monitoring, this paper will combine with GPS/MET and GPS-MR technology to carry out rain and snow monitoring research. And the experimental data were used for validation analysis. With a view to provide a reference for the extensive development of GNSS for rain and snow weather monitoring.

2 Theory System of GPS for Rain and Snow Weather Monitoring

2.1 Principle of GPS/PWV Detection

Ground-based GPS Meteorology is an emerging interdisciplinary, the deep research on it has had the important influence on the space geodetic technology, atmospheric space structure, weather forecasting, climate change monitoring and other related fields. So its research and application are being carried out rapidly on a global scale. In recent years, China in the field of GPS/MET has also carried out extensive research work, and further promote it to provide public services. GPS/PWV detection technology is more mature, in order to save space, this article will not repeat its estimation method. Figure 1 shows the basic flow with GAMIT software [16, 17].

1. Calculation of Zenith Total Delay (ZTD) using GPS observations;
2. The Zenith Hydrostatic Delay (ZHD) is calculated by empirical model, and the Zenith Wet Delay (ZWD) is separated.
3. PWV values were calculated according to the transformation relationship between ZWD and PWV.

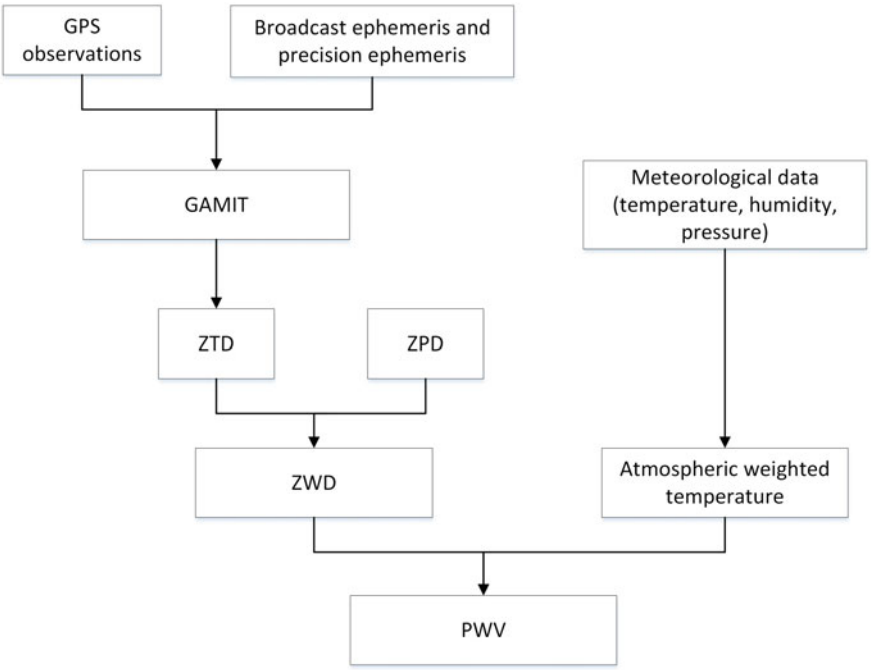

Fig. 1 Flow graph of using GPS to inverse PWV

2.2 *Principle of GPS-MR Technology*

The satellite signals (reflected waves) reflected by the terrestrial environment enter the receiver antenna and interfere with the direct signal (direct waves) coming directly from the satellite, causing the observed value to deviate from the true value that called Multipath Error (MP), MP will reduce the accuracy of positioning and baseline resolution. MP effects still exists when the satellite elevation angle is low to 5–20° even if it is suppressed by the choke antenna, GPS measurements using signal-to-noise ratio (SNR) to represents the ratio of signal strength to noise intensity, SNR will increase with the elevation of the satellite height due to multi-path changes, from the SNR value can be see the impact of MP intuitively [12]. Reference to Larson's s GPS-MR theory based on SNR [13]:

$$SNR \infty P_d + P_r + \sqrt{P_d P_r} \cos\ \varphi \tag{1}$$

In Eq. (1), P_d is the direct signal energy, P_r is the reflected signal energy, and φ is the angle between the direct signal and the reflected signal. In order to obtain the information MP changes caused by SNR, the MP needs to be separated from the received SNR observations. Because P_d and P_r in the numerical difference is large, the reflected signal energy can be through the formula method:

$$SNR(Volts/volts) = 10^{\frac{SNR(\mathrm{db-Hz})}{20}} \tag{2}$$

In order to remove the direct trend, a low-order polynomial is used to fit the SNR measurements. The residual sequence amplitude of the MP reflected signal after removal of the direct signal trend term can be expressed as:

$$dSNR = A\ \cos(4\pi H\lambda H^{-1}\sin E + \phi) \tag{3}$$

In the formula (3), A is the amplitude, H is the reflection height, λ is the GPS carrier wavelength, E is the satellite elevation angle and ϕ is the phase. The frequency can be obtained by Lomb-Scargle Spectral analysis. If the record $t = \sin E$, $f = \frac{2H}{\lambda}$ [18]. The vertical reflection distance can obtained by $f = 2H/\lambda$, and then the snow depth is obtained by the difference between the height of the station and the vertical distance of reflection $H_{snow} = H_{Station} - H$. Thus, the snow depth is measured by GPS-MR technology.

Based on the above principle of GPS-MR for snow depth detecting technology, the processes can be summarized as shown in Fig. 2 [14].

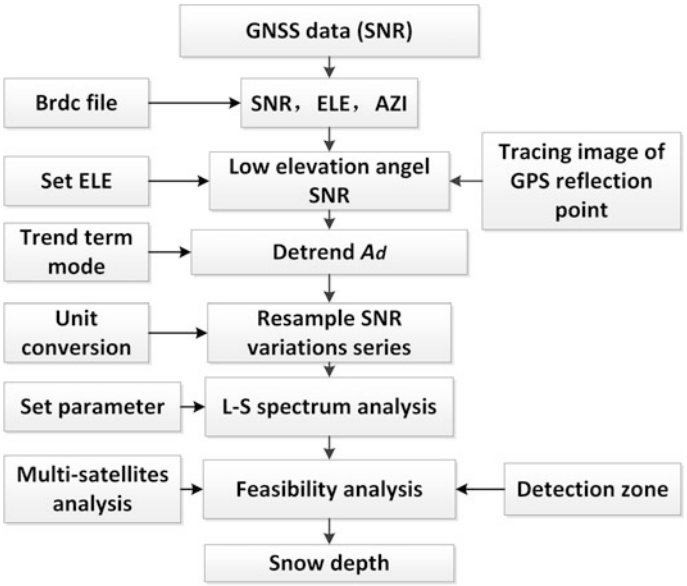

Fig. 2 Flow graph of GPS-MR for snow depth

3 Analysis of Examples

3.1 Data Source

In order to verify the feasibility and effectiveness of the GPS tracking station in the rain and snow weather monitoring, this paper use the P360 station of PBO to carry on the experimental analysis. P360 station is located in the United States Montana Island Park area, with an average altitude of 1857.861 m, around the site is empty, the maximum snowfall in winter up to 1.63 m, rainfall up to 38.2 mm in summer. P360 station was established in 2005, the receiver has been used TRIMBLE NETRS, antenna is used TRIMBLE29659.00 (Radome is SCIT). Figure 3 is the environment around the P360 station.

This paper collects the GPS data from the P360 station in 2013 for the experimental analysis. In order to obtain long time series and high precision GPS/PWV, five IGS stations that SASK, BREW, NIST, GOLD, PIE1 around the P360 station were measured based on GAMIT software. ZTD was estimated at 2 h intervals. Then combined it with meteorological observation data of P360 station to extract the PWV value. The measured snow depth (SNOTEL snow depth) around P360 is provided by the Natural Resources Defense Service (NRCS) of the US Department of Agriculture. Actual rainfall is collected by the site's Vaisala WXT520 sensor and the data acquisition unit for days.

3.2 Sample Results

In order to verify the effectiveness of ground-based GPS for rain and snow weather monitoring, this paper obtain the GPS/PWV and GPS-MR snow depth at P360 in 2013 and compares it with the measured precipitation and SNOTEL snow depth.

(a) Summer **(b)** Winter

Fig. 3 Environment around the P360 station

Due to snowfall in winter, the PWV in winter is lower than rainy season, so it can't clearly show the fluctuation value of winter PWV in one year scale. Therefore, in order to analysis of GPS-MR snow depth, PWV, SNOTEL snow depth more intuitive. So the relationship between them in Figs. 4 and 5 are given respectively. Figure 4 just shows a comparison of PWV and rainfall.

In Fig. 4, the horizontal axis represents the doy, the red broken line represents the GPS/PWV, and the blue represents the actual rainfall. It shows that there is a good correlation between the rainfall and the PWV in rainy season from doy 100 to doy 280, and the continuous increase or decrease of the PWV indicate the start or the end of the precipitation.

Figure 5 shows the comparison of GPS-MR snow depth, SNOTEL snow depth, and PWV from doy 001 to doy 070 in 2013. The horizontal axis represents the doy, the vertical axis represents the snow depth and the PWV. The red line represents the GPS PWV, the blue line represents the SNOTEL snow depth, and the cross mark represents the GPS-MR snow depth. From the Fig. 5 the following conclusion can be obtained:

1. The correlation coefficient between GPS-MR snow depth and SNOTEL snow depth is 0.97 and the root mean square error (RMSE) is 0.12 m. It is proved that GPS-MR based on SNR can be used in snow depth detection
2. The variation of PWV is related to the change of snow depth. When the PWV reaches its peak value and then speed descends, it corresponds to the snowfall. Such as PWV from 8 down to 2 mm from doy 110 to doy 140, snow depth from 0.6 to 0.8 m. It is concluded that the condensation of water vapor content to the surface reduce its PWV content, so the change of PWV can predict snowfall in winter.

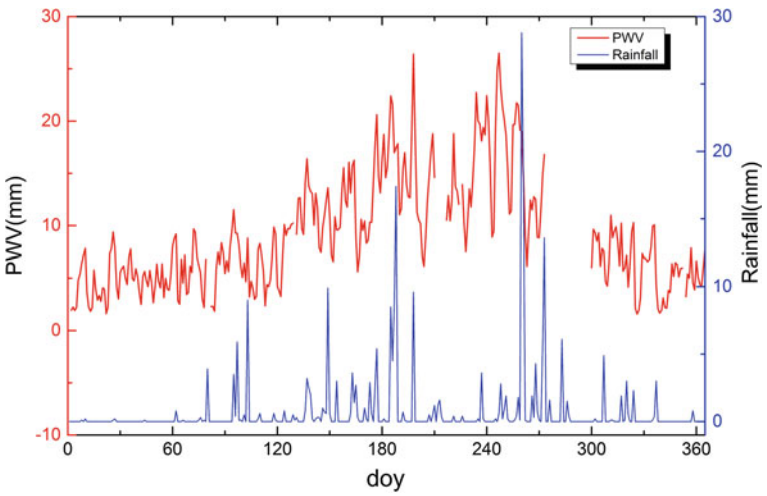

Fig. 4 Comparison of PWV and precipitation at P360

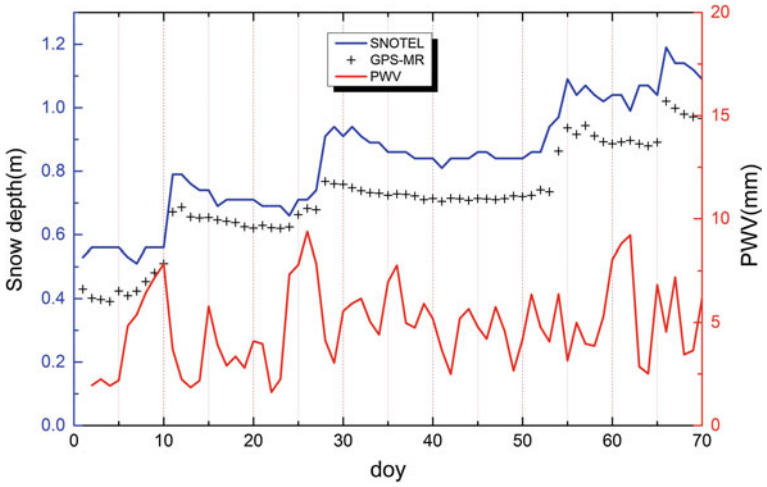

Fig. 5 Comparison of PWV and GPS-MR and SNOTEL snow depth recorder at P360

Combining with the analysis of Figs. 4 and 5 can be seen based on GPS/MET and GPS-MR can achieve high precision real-time rain and snow weather monitoring by GPS tracking station.

4 Conclusion

As the GPS-MR technology appears, making the measurement of GPS receiver can be used as a complement means of monitoring snow depth. In this paper, compared with the PWV, rainfall and GPS-MR snow depth at the P360 station of PBO network in 2013. Firstly, the GPS-MR snow depth is compared with the SNOTEL snow depth, the RMSE is 0.12 m, and the correlation coefficient is 0.97. Secondly, the comparison of the GPS/PWV and GPS-MR snow depth shows that the GPS tracking station can achieve long-term effective snow and rain weather monitoring. In the rainy season, precipitation is predicted by GPS/MET, and snow depth is forecasted by GPS-MR technique while predicting snowfall corresponding to PWV changes in the winter. The combination of the two techniques make GPS tracking station in rain and snow weather monitoring has a high application and practical value.

Acknowledgements Thanks to the United States NSF, USGS, and NASA who launched the Earthscope and authorized the use of GPS data. Thanks to the PBO H2O team to provide reference resources. Thanks to the NRCS to provide measured snow depth data and Rainfall measured data. Heartfelt thanks to the editors and anonymous referee experts provide valuable opinions and suggestions for this article.

Found Project The Nation Nature Science Foundation of China (41104019, 41274005, and GFZX0301040308).

References

1. Jiang G (2011) Study of the theory and application to realtime remote sensing using ground-based GPS. Chang'an University, Xi'an
2. Bevis M, Businger S, Herring TA et al (1992) GPS meteorology: remote sensing of atmospheric water vapor using the global positioning system. Chin J Geophys 97(D14): 15787–15801
3. Li G (2007) On the remote sensing PWV using ground-based GPS technique and application in meteorology. Southwest Jiaotong University, Si'chuan
4. Song S (2004) Sensing three dimensional water vapor structure with ground-based GPS network and the application in meteorology. Shanghai Astronomical Observatory, CAS
5. Cao Y, Chen Y et al (2006) Atmospheric water vapor by ground-based GPS survey profile method. Meteorol Sci Technol 03:241–245
6. Zhang S, Ye S, Wan R, Chen B (2008) Ct scan preliminary based on Kalman filter Tomographic moisture in wet refractive index distribution. Geomat Inf Sci Wuhan Univ 33(08):796–799
7. Bi Y, Yang G, Nie J (2010) GPS water vapor tomography method based on Kalman filter and its application. Plateau Meteorol 30(1):109–114
8. Fan S (2013) Research on GPS marine water vapor inversion and three dimensional water vapor tomography. Wuhan University, Wuhan
9. Wang Y, Wei D, Liu Y, Hu L (2014) Effects of for and haze weather on GPS Zenith tropospheric delay and precipitable water vapor. J Geod Geodyn 34(2):120–123
10. Wan W, Chen X, et al (2012) GPS reflectometry: a review of theories and empirical applications in ocean and land surfaces. Remote Sens Inf 27(3):112–117
11. Advances in GPS-R studies and key technologies. Geomat Inf Sci Wuhan Univ 32(11): 955–960 (2007)
12. Larson KM, Gutmann ED, Zavorotny VU, Braun JJ, Williams MW, Nievinski FG (2009) Can we measure snow depth with GPS receivers. Geophys Res Lett 17(1):1–5
13. Larson KM, Nievinski FG (2013) GPS snow sensing: results from the EarthScope plate boundary observatory. GPS Solut 17:41–52
14. Dai KY, Zhang SC, et al (2016) Preliminary research on snow depth monitoring with GPS SNR. In: China satellite navigation conference (CSNC) 2016 proceedings, vol I. Springer, Berlin, pp 71–84
15. Jin SG, Qian XD, et al (2016) Snow depth variations estimated from GPS-reflectometry: a case study in Alaska from L2P SNR data. Remote Sens 8(1)
16. Zhang S (2009) Research and application of remote sensing water vapor using ground-based GPS/Met. Wuhan University, Wuhan
17. Zhang Q, Li J et al (2005) GPS measurement principle & application. China Science Publishing & Media Ltd, Beijing
18. Xu B, Yang T, Tan B, et al (2011) The simulate study of detection based on Lomb-Scargle algorithm. Nucl Electron Detect Technol 31(6):702–705

Evolutionary Particle Filter for Indoor Navigation and Location

Jian Chen, Gang Ou, Ao Peng, Lingyu Chen, Lingxiang Zheng and Jianghong Shi

Abstract Indoor positioning technology can provide accurate location services for pedestrians. MEMS inertial sensors are inexpensive and small in size. Therefore, inertial navigation and positioning become popular research direction. The inertial sensor, which contains 3-axis accelerometer and 3-axis gyroscope, collects the acceleration and angular velocity information. The relative position of the pedestrian is calculated by integrating the acceleration and the angular velocity. The extended Kalman filter estimates attitude, angular velocity, position, velocity and acceleration system state errors. The system state error is updated when the foot touches the ground. Directional drift is the main problem of inertial navigation. Correcting heading by adding auxiliary basic information is one of the more common methods, such as GPS, geomagnetism, and Wi-Fi, but the additional basic information adds to the extra cost. We propose a novel algorithm based on the fact that pedestrians cannot cross the wall during walking. After the extended Kalman filter, the step size and the azimuth change are used as the observed state to establish the walking motion model. Considering the map information, the particle filter estimates the pedestrian position. For the particle impoverishment problem, the mutation operation of the genetic algorithm is used. A healthy male participates in the experiment. The results show an absolute error of 1.6 m.

J. Chen (✉) · G. Ou (✉) · A. Peng (✉) · L. Chen (✉) · L. Zheng (✉) · J. Shi (✉)
Xiamen University, Xiamen, China
e-mail: 914091855@qq.com

G. Ou
e-mail: ougangcs@gmail.com

A. Peng
e-mail: pa@xmu.edu.cn

L. Chen
e-mail: chenly@xmu.edu.cn

L. Zheng
e-mail: lxzheng@xmu.edu.cn

J. Shi
e-mail: shijh@xmu.edu.cn

J. Sun et al. (eds.), *China Satellite Navigation Conference (CSNC) 2017 Proceedings: Volume I*, Lecture Notes in Electrical Engineering 437,
DOI 10.1007/978-981-10-4588-2_31

Keywords Inertial navigation · Particle filter · Mapping information · Inertial sensors

1 Introduction

Due to the complex indoor environment, the satellite signal into the room has become quite weak, which leads to satellite signal positioning accuracy is relatively poor. However, pedestrians spend most of their time indoors, so indoor pedestrian positioning has attracted the attention of many academics and experts [1]. For large shopping malls, personal indoor navigation and positioning technology can provide accurate location services.

MEMS inertial sensors are small, inexpensive and suitable for integration into other consumer products. In the inertial navigation system, accelerometers and gyroscopes collect pedestrian accelerations and angular velocities. The relative position of pedestrian can be obtained by integrating the acceleration and angular velocity. The extended Kalman filter estimates the attitude, angular velocity, position, velocity and acceleration state errors. When the foot touches the ground, the system state errors are updated. Directional drift is an unavoidable problem in inertial positioning system. In order to reduce the directional drift, we present the use of map information to eliminate the directional error. The main contribution of this paper is that particle filter estimates the pedestrian location after the extended Kalman Filter is performed. In order to solve the particle impoverishment problem, mutation operation is adopted to improve the particle diversity. The main idea is that the particles are detected before they are resampled. If the particles lie outside the wall, the weights are set to zero. If the particles are in the wall, the weights are not changed. For the particles outside the wall, mutation operation is used. After mutation operation, the particles are back to the wall. In addition, the particle weights are updated.

In [2], Johann Borenstein developed a self-heuristic drift elimination algorithm for personal tracking systems. When the path of pedestrian walking is rectangular, the directions of pedestrian are divided into four main directions. The self-heuristic drift elimination algorithm forces pedestrians to approach the nearest main directions. In addition, dual low-pass filters and step-size resonators further improve the accuracy of inertial navigation systems. The non-main direction will deteriorate the navigation accuracy. The literature [3, 4] proposed improved self-heuristic elimination algorithm. Wi-Fi and inertial navigation systems have a strong highly complementary features, hybrid algorithm is proposed [5]. Hybrid algorithm is classified into two steps. In the first step, the initial direction and the initial position are obtained. In the second step, maximum likelihood algorithm calculates the rotation matrix. In [6], a reliable-enhanced particle filter is used to process the mobile magnetic field and inertial sensor data. A self-heuristic particle algorithm and a dynamic step-size algorithm are used to improve the positioning accuracy and improve the robustness of the basic particle filter. Based on the map matching

information and the inertial sensor data, the particle filter estimates the step size and the direction change [7]. If the particle crosses the wall, the weight is set to zero. The remaining particles are used to estimate the pedestrian position. The main problem of the algorithm is that the inertial sensor drifts are more and more over time. By several iterations, the particles in the wall will be fewer and fewer. Few particles will be very difficult to approximate the posterior distribution. In some extreme cases, it will lead to algorithm failure.

2 Extended Kalman Filter

The extended Kalman filter (EKF) is an effective estimation method [8, 9]. EKF can be used to estimate the nonlinear inertial navigation system. When the foot of a pedestrian touches the ground, the speed should be zero. The 15-element state error vector can be defined as:

$$\delta \mathbf{x}_k = \left[\delta \boldsymbol{\varphi}_k, \delta \boldsymbol{\omega}_k^b, \delta \mathbf{r}_k, \delta \mathbf{v}_k, \delta \mathbf{a}_k^b\right]^T \tag{1}$$

where $\delta \boldsymbol{\omega}_k^b$ and $\delta \mathbf{a}_k^b$ represent angular velocity and acceleration errors in the body coordinate system, respectively. $\delta \boldsymbol{\varphi}_k$,$\delta \mathbf{r}_k$ and $\delta \mathbf{v}_k$ represent the errors in attitude, position, and velocity, respectively. The subscript k represents the sampling time. For the inertial navigation system, the state transition model and the observation model are:

$$\delta \mathbf{x}_k = \mathbf{F}_{k-1} \delta \mathbf{x}_{k-1} + \boldsymbol{\omega}_{k-1} \tag{2}$$

$$\mathbf{z}_k = \mathbf{H} \delta \mathbf{x}_k + \mathbf{n}_k \tag{3}$$

where $\boldsymbol{\omega}_k$ and $\mathbf{n}_k$ are state transition noise and observation noise, respectively. The transition state vector $\mathbf{F}$ is:

$$\mathbf{F}_{k-1} = \begin{bmatrix} \mathbf{I}_{3*3} & -\Delta T * \mathbf{R}_{b2t} & \mathbf{O}_{3*3} & \mathbf{O}_{3*3} & \mathbf{O}_{3*3} \\ \mathbf{O}_{3*3} & \mathbf{I}_{3*3} & \mathbf{O}_{3*3} & \mathbf{O}_{3*3} & \mathbf{O}_{3*3} \\ \mathbf{O}_{3*3} & \mathbf{O}_{3*3} & \mathbf{I}_{3*3} & \Delta T * \mathbf{I}_{3*3} & \mathbf{O}_{3*3} \\ \Delta T * \mathbf{S}(\mathbf{f}^t) & \mathbf{O}_{3*3} & \mathbf{O}_{3*3} & \mathbf{I}_{3*3} & -\Delta T * \mathbf{R}_{b2t} \\ \mathbf{O}_{3*3} & \mathbf{O}_{3*3} & \mathbf{O}_{3*3} & \mathbf{O}_{3*3} & \mathbf{I}_{3*3} \end{bmatrix} \tag{4}$$

The observation vector $\mathbf{H}$ is defined as

$$\mathbf{H}_c = \begin{bmatrix} 0 & 0 & 0 \\ 0 & 0 & 0 \\ 0 & 0 & 1 \end{bmatrix} \tag{5}$$

$$\mathbf{H} = [\mathbf{H}_c, \mathbf{O}_{3*3}, \mathbf{O}_{3*3}, \mathbf{I}_{3*3}, \mathbf{O}_{3*3}] \tag{6}$$

Kalman filter update process includes state update and measurement update. When a pedestrian is walking, the state update is carried out. When the foot touches the ground, the measurement update starts to work. The process of extended Kalman filtering is shown in Fig. 1.

3 Particle Filter

Particle filter (PF) provides a relatively novel technique for estimating some highly nonlinear systems. Particle filter plays a very important role in many fields [10], such as target tracking, robot navigation, process monitoring. The particle filter system is defined as:

$$\mathbf{x}_k = f(\mathbf{x}_{k-1}) + \boldsymbol{\omega}_k \tag{7}$$

$$\mathbf{y}_k = h(\mathbf{x}_k) + \boldsymbol{\upsilon}_k \quad k = 1, 2\ldots \tag{8}$$

It is difficult to solve the analytic solution of the posterior distribution. Instead of solving the analytical solution, the approximate solution is well developed. Many particles approximate analytical solution. In order to resample the particles from posterior distribution, a resampling technique is proposed. The importance distribution is defined as:

$$q(\mathbf{x}_{0:k}|\mathbf{y}_{1:k}) = q(\mathbf{x}_{0:k-1}|\mathbf{y}_{1:k-1})q(\mathbf{x}_k|\mathbf{x}_{0:k-1}, \mathbf{y}_{1:k}) \tag{9}$$

The recursive importance weight for each particle is given by:

$$\begin{aligned} \omega_k^i &= \frac{p(\mathbf{x}_{0:k}|\mathbf{y}_{1:k})}{q(\mathbf{x}_{0:k}|\mathbf{y}_{1:k})} \\ &\propto \omega_{k-1}^i \frac{p(\mathbf{y}_k|\mathbf{x}_k^i)p(\mathbf{x}_k^i|\mathbf{x}_{k-1}^i)}{q(\mathbf{x}_k^i|\mathbf{x}_{0:k-1}^i, \mathbf{y}_{1:k})} \end{aligned} \tag{10}$$

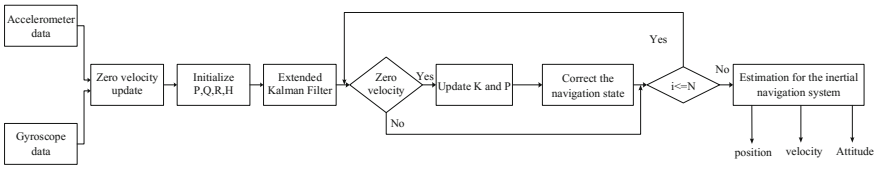

Fig. 1 The extended Kalman filter framework

where ω_k^i represents the importance weight. $\tilde{\omega}_k^i$ is the normalized weight. Thus, the posterior distribution is approximated by particles as:

$$p(\mathbf{x}_{0:k}|\mathbf{y}_{1:k}) \approx \sum_{i=1}^{N} \tilde{\omega}_k^i \delta(\mathbf{x}_{0:k} - \mathbf{x}_{0:k}^i) \tag{11}$$

4 A Direction Error Elimination Algorithm Based on Map Information

Assume that the step-size noise and direction-varying noise satisfactory a Gaussian distribution with zero mean [11]. Combined with the map information, we use particle filter to estimate the pedestrian location. State transition equations and measurement equations can be written as:

$$\begin{bmatrix} x_k \\ y_k \\ \psi_k \end{bmatrix} = \begin{bmatrix} x_{k-1} \\ y_{k-1} \\ \psi_{k-1} \end{bmatrix} + \begin{bmatrix} l_k & 0 & 0 \\ 0 & l_k & 0 \\ 0 & 0 & \delta\psi_k \end{bmatrix} \begin{bmatrix} \cos\psi_{k-1} \\ \sin\psi_{k-1} \\ 1 \end{bmatrix} \tag{12}$$

$$\begin{bmatrix} \hat{l}_k \\ \delta\hat{\psi}_k \end{bmatrix} = \begin{bmatrix} l_k \\ \delta\psi_k \end{bmatrix} + \begin{bmatrix} v_{lk} \\ v_{\psi k} \end{bmatrix} \tag{13}$$

where (x_k, y_k) represents the pedestrian position. ψ_k represents the pedestrian direction. $l_k = \sqrt{(x_k - x_{k-1})^2 + (y_k - y_{k-1})^2}$ and $\hat{l}_k$ represent the actual step size and the estimated step size, respectively. $\delta\psi_k = \psi_k - \psi_{k-1}$ and $\delta\hat{\psi}_k$ are the direction change and the estimated direction change, respectively. v_{lk} and $v_{\psi k}$ represent the step-size noise and the direction-changing noise, respectively.

In the resampling process, the particles that cross the wall are invalid. Their weights should be set to zero. If the invalid particles are too much, it will seriously affect the particle distribution. To mitigate the particle impoverishment problem, genetic algorithm with global search ability is integrated into particle filter, namely evolutionary particle filter (EPF). Before the particles are resampled, we can detect the validity of the particle. If the particle is in the wall, the mutation operation of the genetic algorithm does not work. If the particle lies outside the wall, the genetic operator begins to work. The mutation operator can be written as:

$$l_k^i = l_k^i + \beta_1 \tag{14}$$

$$\delta\psi_k^i = \delta\psi_k^i + \beta_2 \tag{15}$$

where β_1 and β_2 are random values in the mutation operation.

The main idea of mutation operation is to generate new particles. The new particles meet the requirements of map matching. In addition, the weight of the new particles is updated. After the mutation operator is performed, the particles have the opportunity to participate in the resampling process.

Before the mutation operation is performed, the weight of the particle filter is obtained by standard particle filter. After the mutation operation is performed, particles outside the wall will be updated. The update technique is as follows

$$w_k^i = \frac{1}{k-1}\sum_{n=1}^{k-1} w_n^i \tag{16}$$

The proposed algorithm is as follows:

1. Particle filter initialization
2. Calculate the weight of the particle
3. detect whether the particles outside the wall, if the particles are in the wall, the weight is not updated
4. If the particles are outside the wall, the mutation operation begins to modify the step size and the direction change
5. Update the particle weights using Eq. (16)
6. Resampling.

5 Experimental Results

Acceleration and angular velocity data are collected using an inertial sensor with 3-axis accelerometer and 3-axis gyroscope. The parameters of the inertial sensor are shown in Table 1. Inertial sensors are tied to the 29-year-old male's right ankle. To verify effectiveness of the evolutionary algorithm, pedestrians took part in walking experiments. Based on the map information, the calculated position cannot cross the wall. If the particle crosses the wall, the mutation operation is triggered.

Table 1 Performance of inertial sensors in IMU

	Accelerometer	Gyroscope
Axes	3	3
Full scale range	±2 m/s^2	±250 °/s
Cross-axis sensitivity	±2%	±2%
Nonlinearity	±0.5%	±0.1%
Max output data rate	500 Hz	8000 Hz
Total RMS noise	8 mg-rms	0.1 °/s-rms

5.1 Particle Weight Experiment

To illustrate that the mutation operation can increase the weight of the zero-weight particles, we select the fortieth step and the eightieth step as an example. The fortieth and eightieth particle weights are depicted in Figs. 2 and 3. In Fig. 2a, there are 2 particles with zero weight before mutation operation is performed. There are 0 particles with zero weight in Fig. 2b. In Fig. 3a, there are 46 particles with zero weight before mutation operation is performed. There is 1 particle with zero weight in Fig. 3b. The mutation operation increases the weight of zero-weight particles. As can be seen from the figures, there are a large number of particles with zero weight before the mutation operation. The zero-weight particles greatly reduced through the mutation operation.

5.2 Walking Experiment

To comprehensively evaluate effectiveness of the proposed algorithm, auxiliary particle filter (APF) [12] is presented for comparison. The particle impoverishment problem often occurs in the resampling process. In the particle weight experiment,

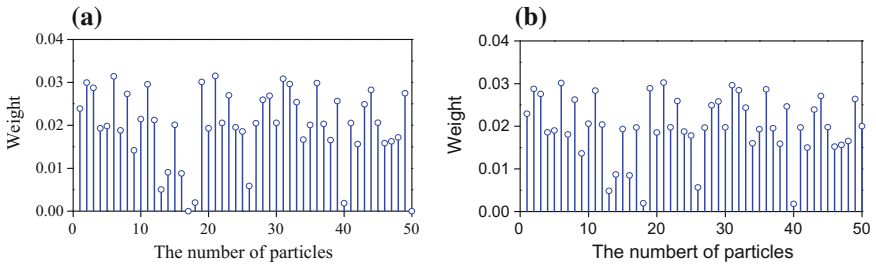

Fig. 2 **a** The fortieth step weights before mutation, **b** the fortieth step weights after mutation

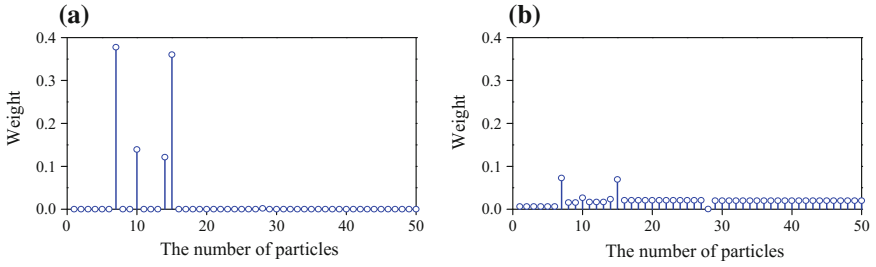

Fig. 3 **a** The eightieth step weights before mutation, **b** the eightieth step weights after mutation

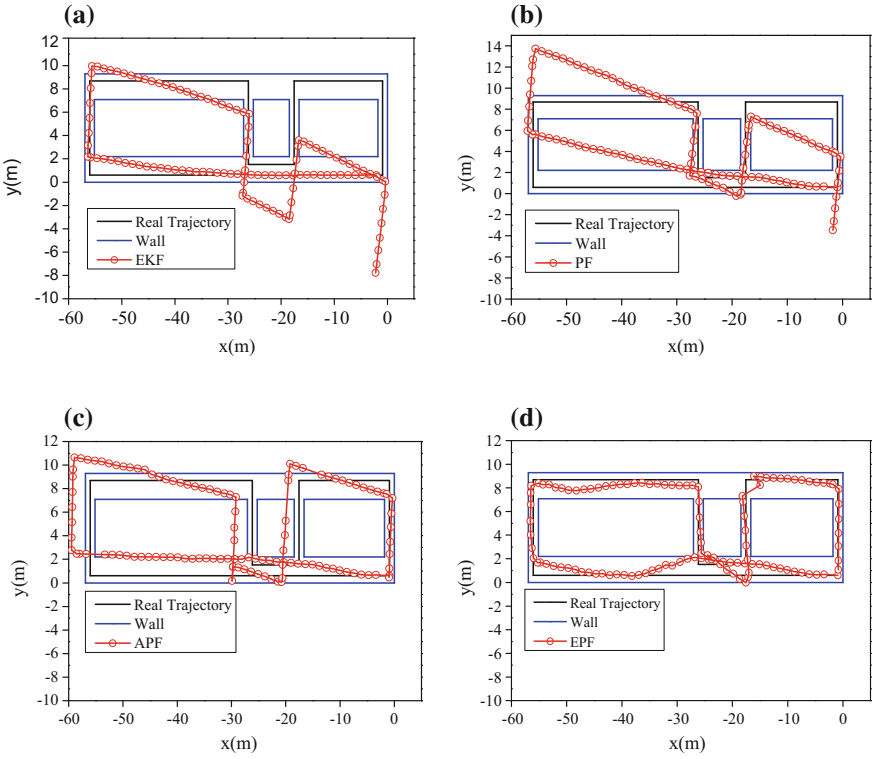

Fig. 4 **a** EKF trajectory, **b** PF trajectory, **c** APF trajectory, **d** EPF trajectory

the diversity of the particle is enriched by mutation operation. All particles have the opportunity to participate in resampling.

The results of the walking experiment are depicted in Fig. 4. In Fig. 4a, b, since EKF and PF do not use map information, the direction is prone to drift, which will lead to the misleading positioning error. In Fig. 4c, the auxiliary particle filter reduces the weight of particles outside the wall. The chance of the particles outside the wall is reduced to participate in resampling, so that the positioning accuracy is improved. Compared with APF, we let the weight of the particle outside the wall be zero and regenerate the new particle by mutation operation in Fig. 4d. In Fig. 4d, the position error of EPF is 1.6 m.

6 Conclusion

This paper presents a personal navigation system that integrates map information. PF is designed to estimate the pedestrian location. Considering the particle impoverishment problem, this paper proposes an evolutionary particle algorithm. The mutation operation of the genetic algorithm is used to modify the particles. The new particles are generated. In addition, the weights are updated. The proposed algorithm can effectively improve the positioning accuracy.

References

1. Barberis C, Andrea B, Giovanni M, Paolo M (2014) Experiencing indoor navigation on mobile devices. IT Prof 16(1):50–57. doi:10.1109/MITP.2013.54
2. Borenstein J, Ojeda L (2010) Heuristic drift elimination for personnel tracking systems. J Navig 63(04):591–606. doi:10.1017/S0373463310000184
3. Jiménez AR, Seco F, Zampella F, Prieto JC, Guevara J (2011) Improved heuristic drift elimination (iHDE) for pedestrian navigation in complex buildings. In: 2011 international conference on indoor positioning and indoor navigation (IPIN). doi:10.1109/IPIN.2011.6071923
4. Ju HJ, Lee MS, Park CG, Lee S, Park S (2014) Advanced heuristic drift elimination for indoor pedestrian navigation. In: 2014 International conference on indoor positioning and indoor navigation (IPIN). doi:10.1109/IPIN.2014.7275553
5. Chen LH, Wu EHK, Jin MH, Chen GH (2014) Intelligent fusion of Wi-Fi and inertial sensor-based positioning systems for indoor pedestrian navigation. IEEE Sens J 14(11):4034–4042. doi:10.1109/JSEN.2014.2330573
6. Xie H, Gu T, Tao X, Ye H, Lu J (2016) A reliability-augmented particle filter for magnetic fingerprinting based indoor localization on smartphone. IEEE Trans Mob Comput 15(8):1877–1892. doi:10.1109/TMC.2015.2480064
7. Perttula A, Leppäkoski H, Kirkko-Jaakkola M, Davidson P, Collin J, Takala J (2014) Distributed indoor positioning system with inertial measurements and map matching. IEEE Trans Instrum Meas 63(11):2682–2695. doi:10.1109/TIM.2014.2313951
8. Liu C, Shui P, Wei G, Li S (2014) Modified unscented Kalman filter using modified filter gain and variance scale factor for highly maneuvering target tracking. J Syst Eng Electron 25(3):380–385. doi:10.1109/JSEE.2014.00043
9. Loiola MB, Lopes RR, Romano JMT (2012) Modified Kalman filters for channel estimation in orthogonal space-time coded systems. IEEE Trans Signal Process 60(1):533–538. doi:10.1109/TSP.2011.2170682
10. Shenoy AV, Prakash J, Prasad V, Shah SL, McAuley KB (2013) Practical issues in state estimation using particle filters: case studies with polymer reactors. J Process Control 23(2):120–131. doi:10.1016/j.jprocont.2012.09.003
11. Woodman O, Harle R (2008) Pedestrian localisation for indoor environments. In: Presented at the proceedings of the 10th international conference on Ubiquitous computing, Seoul, Korea
12. Yu C, Lan H, Liu Z, El-Sheimy N, Yu F (2016) Indoor map aiding/map matching smartphone navigation using auxiliary particle filter. In: China satellite navigation conference (CSNC) 2016 proceedings, vol I. Springer. doi:10.1007/978-981-10-0934-1_29

An Indoor Three Dimensional Positioning Algorithm Based on Attitude Identification and Visible Light Propagation Model

Qu Wang, Haiyong Luo, Xile Gao, Jie Wei and Fang Zhao

Abstract With the continuous development of green lighting technology, the visible light based indoor localization has attracted much attention. The visible light based indoor positioning technology leverages the light propagation model to achieve target location. Compared with the radio localization technology, the visible light based indoor positioning can achieve higher localization accuracy with no electromagnetic interference. In this paper, an indoor three dimensional positioning algorithm based on attitude identification and visible light propagation model is proposed. This algorithm can accurately identify smartphone's attitude by integrated sensor of smartphone, distinguish different LED beacons by FFT algorithm, construct a position cost function base on visible light radiative decay model, applying a nonlinear optimizing method to acquire the optimal estimation of final location. Extensive experimental results demonstrate that the algorithm can effectively avoid the negative effects on smartphone's attitude angle dynamically change, has better locating accuracy and robustness, obtain a sub-meter level positioning accuracy.

Keywords Visible light · Indoor position · Attitude identification · Visible light radiative decay model · Sub-meter level positioning accuracy

Q. Wang (✉) · H. Luo · X. Gao
Institute of Computing Technology, Chinese Academy of Sciences,
Beijing 100190, China
e-mail: wangqu@ict.ac.cn

H. Luo
e-mail: yhluo@ict.ac.cn

X. Gao
e-mail: 13036111236@163.com

J. Wei · F. Zhao
Beijing University of Posts and Telecommunications, Beijing 100876, China
e-mail: 1019734138@qq.com

F. Zhao
e-mail: zfsse@bupt.edu.cn

J. Sun et al. (eds.), *China Satellite Navigation Conference (CSNC) 2017 Proceedings: Volume I*, Lecture Notes in Electrical Engineering 437,
DOI 10.1007/978-981-10-4588-2_32

1 Introduction

The critical demand for accurate localization for both indoor and outdoor is increasing day by day, such as asset and personnel tracking, anti-terrorism action, emergency rescue, exploration missions, etc. User can find out the target quickly by indoor positioning. Accurate positioning can help rescuers to find out the people quickly who need to be rescued in emergency circumstances. For the outdoor case, Global Positioning System (GPS) is well established, and has been widely used. Because the GPS needs a Line of Side (LOS) connection with the satellite to determine the position of a person or object. The GPS accuracy drops when it is used indoors, because of the signals from GPS satellites are blocked by walls or tall buildings [1, 2]. At the same time, GPS is associated with a host of higher power consumption, slow-response, and inefficiency problems.

For the indoor case, researcher proposed Many alternatives which be divided into two typically types. The one type leverage pre-deployed additional positioning infrastructure to realize precise positioning, such as radio frequency identification (RFID) [3], Ultra Wideband (UWB) [4], ultrasonic sensors [5], Bluetooth [6] and ZigBee [7]. The accuracy can be increased when the number of reference nodes (with known position) is increased but this leads to an increased installation and material cost, exclusively for positioning purposes. The ubiquitous of positioning system is restrained by the problem of difficult deployment and high equipment cost. The other type sample the signals fingerprint, then, to achieve user position by comparing the on-line signals fingerprint with the pre-generated signals fingerprint model, such as wireless local area networks (WLAN) [8] and magnetic [9, 10]. Wi-Fi-based communication systems suffer from multi-path propagation due to the environment and the signals can be received in nearby rooms. Signals fingerprint collection is time-consuming and labor-intensive, disk space is required for Signals fingerprint. These properties specific make it very difficult to realize accurate positioning. What's worse, positioning technology based on RF cannot use in the electromagnetic sensitive environment.

In recent years, lighting devices are undergoing a revolution transforming from fluorescent lamps or tubes to light emitting diodes (LEDs) because of the energy efficiency for the delivered light output, low costs and the long lifetime of the LED. Visible Light has the double functions of the dominant illumination source and indoor positioning. The Visible Light Positioning (VLP) systems can overcome several known problems with radio frequency (RF) based indoor positioning system. A receiver cannot receive signals from nearby rooms so the positioning algorithm will only use information that was transmitted inside the room in which it needs to calculate its position. Due to the local character of light, the Line of Sight (LoS) component of the signal will be present in most cases and the multi-path propagation, which becomes a problem in RF systems, will be negligible for VLC [11]. Comparing with the mentioned positioning technology, the VLP has the

advantage of good position accuracy, without the need of deploying additional positioning infrastructure, low deployment cost, strong anti-interference capacity, no electromagnetic interference, and no access authentication. Besides, the VLP system have been designed for the RF or electromagnetic sensitive area like hospital and air crafts, and the area without radio frequency signal coverage, such as tunnel and underground mine. The local character of VLP is the main reason why VLP is a good candidate for indoor positioning purposes.

The main contributions in this paper are that:

(1) This paper proposed an indoor high accuracy positioning algorithm with single LED which merely rotating the mobile device by a small angle several times. This method get localization by slightly changing the roll angle or pith angle four times instead of the measurements of multiple LEDS at same time and same position. To reduce the heading direction errors caused by the surrounding steel building materials, electrical equipment or other sensor noises, this paper leverage indoor paths and user's treading track to calibrate the heading direction. This method has desirable performance and stability in LED-beacon sparse environment, such as corridor, also has advantages of low costs.
(2) Achieving the cosine of incidence angle by the method of vector dot product, and the positioning algorithm support a three-dimensional positioning under various attitudes. Smartphone sense self-attitude by built-in accelerometer sensor and magnetic sensor, and the smartphone's normal vector is obtained. Combine with the light vector is determined by the coordinate of the sender-receiver (LED and smartphone), and point out from LED and into smartphone, the cosine of incidence angle of smartphone is obtained by the method of vector dot product between the smartphone's normal vector and the light vector. This method can effectively avoid the restriction of coplanar of irradiation ray, incidence ray and normal ray in incidence angle by using irradiation angle and smartphone attitude. So this positioning algorithm can support a pervasive three-dimensional positioning.

The remainder of this paper is organized as follows. In Sect. 2, the related work is introduced. The positioning algorithm is proposed in Sect. 3. The experimental results and analysis are given in Sect. 4. The conclusion of this paper is made in Sect. 5 finally.

2 Related Work

VLP system mostly use photodiodes at the receiver to detect the received signal strength (RSS) or the time difference of arrival (TDOA) of the incoming optical signals and then a position determination algorithm is developed to achieve the

unknown location coordinates of the receiver [12–16]. The algorithms developed in [12–14] are based on RSS measurements at the receiver. On the other hand, the algorithms proposed in [15, 16], use the TDOA of the received signals. Comparing with RSS-based VLP, the TDOA-based VLP can achieve better performance. The TDOA-based VLP need for accurate transmitter synchronization and cost of deployment will be a daunting task.

In [17], positioning approach based on attaching each LED with an identification, namely the LED-identification (LED-ID) technology is proposed. In [18], an improvement positioning method of LED-ID is proposed, which combines the location code and the RSS. In [19], an angular diversity approach is proposed, which provides location information without relying on signal intensity measurements, time-of-flight data or complex imaging approaches. In [20], an image approach is proposed, which solves unknown position by using the position information of the reference LEDs and the geometric relationship of the images on the image sensor.

Different from the aforementioned VLP methods, our proposed VLP method introduces single LED location and attitude identification, which can effectively avoid the negative effects on smartphone's attitude angle dynamically change, has better locating accuracy and robustness.

3 Three Dimensional Positioning Algorithm

The indoor three-dimensional positioning algorithm base on attitude identification and visible light radiative decay model include the position model and attitude identification. The position model is usually assumed to follow a Lambertian radiation pattern [21]. Terminal's position is obtained by at least three measurements using three distinct orientations of the terminal. The terminal's attitude is obtained by using the accelerometer sensor, compass and indoor paths.

3.1 Symbol Description

To illustrate the positioning algorithm in this paper, we define the symbol in Table 1.

3.2 Position Model

This paper establishes cost function of position algorithm by the widely used Lambertian radiation pattern. The theoretical received optical power of

Table 1 Symbol description

No.	Symbol	Meaning
1	$T_i = (x_i, y_i, z_i)$	The coordinate of the *ith* LED $(i = 1, \ldots, N)$
2	$R = (x, y, z)$	The coordinate of terminal
3	ϕ_i	The irradiance angle of the *ith* LED $(i = 1, \ldots, N)$
4	ψ_{ij}	The *jth* $(i = 1, \ldots, K)$ measurement of the incidence angle of the *ith* LED $(i = 1, \ldots, N)$
5	$\vec{n}_j = (a_j, b_j, c_j)$	The normal vector of the measurement plane of the *jth* $(i = 1, \ldots, K)$ measurement, $\left\|\vec{n}_{ij}\right\| = 1$
6	$\hat{P}_{ij}$	The practical received optical power of *jth* $(i = 1, \ldots, K)$ measurement of the *ith* LED $(i = 1, \ldots, N)$
7	P_{ij}	The theoretical received optical power of *jth* $(i = 1, \ldots, K)$ measurement of the *ith* LED $(i = 1, \ldots, N)$
8	$d_i = \sqrt{(x_i - x)^2 + (y_i - y)^2 + (z_i - z)^2}$	The Euclidean distance from terminal to the *ith* LED $(i = 1, \ldots, N)$
9	$\vec{l}_i = (x_i - x, y_i - y, z_i - z)$	The vector point out from smartphone and into the *ith* LED $(i = 1, \ldots, N)$, obvious $\left\|\vec{l}_i\right\| = d_i$
10	P_i^T	The transmitting power of the *ith* LED $(i = 1, \ldots, N)$
11	$\phi_{1/2}^i$	The half irradiance angle of the *ith* LED $(i = 1, \ldots, N)$
12	$\psi_{1/2}$	The half incidence angle

jth$(i = 1, \ldots, K)$ measurement of the *ith* LED $(i = 1, \ldots, N)$ is calculated as the (1), base on the Lambertian radiation pattern.

$$P_{ij} = P_i^T \frac{(m+1)A}{2\pi d_i^2} \cos^m(\phi_i) T(\psi_{ij}) g(\psi_{ij}) \cos^M(\psi_{ij}) \tag{1}$$

where Lambertian parameters $m_i = -\log 2/(\log(\cos(\phi_{1/2}^i)))$ and $M = -\log 2/(\log(\cos(\psi_{1/2})))$ is determined by the physical aspects of the LED and the photodiode. A is the effective area of the photodiode at the receiver. The $T(\psi_{ij})$ and $g(\psi_{ij})$ are the filter gain and concentrator gain, respectively. In this paper, we assume that no filter or concentrator is used at the receiver ($T(\psi) = g(\psi) = 1$).

Under measurement noise conditions, the experimental value deviate from theoretical value is found by measuring received optical power. In order to realize indoor precise positioning, this paper establish a positioning model as (2)

$$(x, y, z) = \min_{(x,y,z) \in R^3} \sum_{i=1}^{N} \sum_{j=1}^{K} [\hat{P}_{ij} - P_i^T \frac{(m+1)A}{2\pi d_i^2} \cos^m(\phi_i) \cos^M(\psi_{ij})]^2 \tag{2}$$

where

$$\begin{cases} \cos(\phi_i) = \frac{z_i - z}{d_i} \\ \cos(\psi_{ij}) = \frac{\vec{l}_i \cdot \vec{n}_{ij}}{|\vec{l}_i| * |\vec{n}_{ij}|} = \frac{a_j(x_i - x) + b_j(y_i - y) + c_j(z_j - z)}{d_i} \\ d_i = \sqrt{(x_i - x)^2 + (y_i - y)^2 + (z_i - z)^2} \end{cases}$$

The positioning model as (2) shown become an optimal problem of nonlinear function which only contain an unknown variable $R = (x, y, z)$, Many alternative nonlinear optimization algorithms have been proposed for solving the unknown position estimation. In this paper, the DFP quasi-Newton method [22] is applied to solve $R = (x, y, z)$. DFP has a higher efficiency computing capability and the time complexity is $O(n^2)$, due to a matrix without second partial derivatives are used to instead of the inverse matrix of the Hessian matrix in quasi-Newton method.

The cosine of incidence angle of smartphone is obtained by the method of vector dot product between the smartphone's normal vector and the light vector which point out from the Receiver R to Transmitter (LED). This method can effectively avoid the restriction of coplanar of irradiation ray, incidence ray and normal ray in solving incidence angle with geometric relations by using irradiation angle and smartphone attitude.

Where N = 1, the localization model in Eq. (2) becomes a single-point positioning problem. In simulation experiment, the positioning performance will be analyzed with different number of LED beacons and measurements which represents different LEDS assemblages in various indoor positioning scenarios. Extensive experiments demonstrate that this positioning model can fit various indoor scenarios and different beacon deployment scheme.

3.3 *Achieving the Normal Vector of Photosurface of Receiver*

The received power given by Eq. (1) depends on not only the distance, but also the irradiance and incidence angles.

The irradiance angle $\emptyset$ is determined by the receiver's position. If we fix the receiver's position and only change the receiver's attitude, the received power P is determined only by the incident angle ψ. The receiver's attitude (azimuth θ, pith ϕ and roll ψ) can be obtained by the built-in accelerometer sensor, and eventually, the incidence and irradiance angles is obtained also.

According to the definition of the attitude angle, the receiver frame is obtained by three times rotation of the East-North-Up reference frame that rotation round z, y and x-axis for ψ, θ and ϕ. For convenience, we use multiple coordinate frames to describe the process of rotation, including the "inertial frame," the "vehicle-1 frame," the "vehicle-2 frame," and the "body frame." The inertial frame axes are

Earth-fixed, and the body frame axes are aligned with the sensor. The vehicle-1 and vehicle-2 are intermediary frames used for convenience when illustrating the sequence of operations that take us from the inertial frame to the body frame of the sensor.

The yaw angular represents rotation about the inertial-frame z-axis by an angle ψ. The yaw rotation produces a new coordinate frame where the z-axis is aligned with the inertial frame and the x and y axes are rotated by the yaw angle ψ. We call this new coordinate frame the vehicle-1 frame. The rotation matrix for moving from the Inertial frame to the vehicle-1 frame is given by

$$R_I^{v_1}(\psi) = \begin{pmatrix} \cos(\psi) & \sin(\psi) & 0 \\ -\sin(\psi) & \cos(\psi) & 0 \\ 0 & 0 & 1 \end{pmatrix} \tag{3}$$

Pitch represents rotation about the vehicle-1 y-axis by an angle θ. The rotation matrix for moving from the vehicle-1 frame to the vehicle-2 frame is given by

$$R_{v_1}^{v_2}(\theta) = \begin{pmatrix} \cos(\theta) & 0 & -\sin(\theta) \\ 0 & 1 & 0 \\ \sin(\theta) & 0 & \cos(\theta) \end{pmatrix} \tag{4}$$

Roll represents rotation about the vehicle-2 x-axis by an angle ϕ. The rotation matrix for moving from the vehicle-2 frame to the body frame is given by

$$R_{v_2}^{B}(\phi) = \begin{pmatrix} 1 & 0 & 0 \\ 0 & \cos(\phi) & \sin(\phi) \\ 0 & -\sin(\phi) & \cos(\phi) \end{pmatrix} \tag{5}$$

The complete rotation matrix for moving from the inertial frame to the body frame is given by

$$R_I^B(\phi, \theta, \psi) = R_{v_2}^B(\phi) R_{v_1}^{v_2}(\theta) R_I^{v_1}(\psi) \tag{6}$$

The rotation matrix for moving the opposite direction from the body frame to the inertial frame—is given by

$$R_B^I(\phi, \theta, \psi) = R_I^{v_1}(-\psi) R_{v_1}^{v_2}(-\theta) R_{v_2}^{B}(-\phi) \tag{7}$$

In the body frame, the normal vector of smartphone plane $N_B = (001)^T$, and the normal vector of smartphone plane in the inertial frame is given by

$$\vec{n}_I = R_B^I(\phi, \theta, \psi)\vec{n}_B = \begin{pmatrix} s(\phi)s(\psi) + c(\phi)c(\psi)s(\theta) \\ c(\phi)s(\psi)s(\theta) - c(\psi)s(\theta) \\ c(\phi)c(\theta) \end{pmatrix} \tag{8}$$

3.4 Distinguishing Different LED Lamp by FFT

In localization with multiple LEDs scenario, in order to differentiate each LED which is driven by specific blinking frequency, VLP system requires a suitable multiple access technology to distinguish the signals of the different LEDs, such as frequency division multiple access (FDMA). Avoiding the ocular discomfort caused by low frequency, blinking frequency of LED lamp is designed more than 120 Hz.

In multi-LEDs area, the received power is the superposition of all the LEDs in the Line of Sight (LoS) area. The received power cannot be directly applied to calculate the position estimate of receiver, and a LED distinguish mechanism base on Fast Fourier Transform (FFT) is used to extract the RSSI of each LED from the superposition of all the LEDs.

The RSSI of each LED with specific blinking frequency is obtained from multi-frequency composite signal by performing a Fast Fourier Transform (FFT), as shown in (9).

$$X(k) = \sum_{n=0}^{N'-1} x(n) \mathrm{e}^{-j\frac{2\pi}{N'}kn} \tag{9}$$

where $x(n)(n = 0, \ldots, N' - 1)$ multi-frequency composite received power sampled by the terminal, N' is the number of sample.

The amplitude of FFT coefficient $X(k)$ divided by $N'/2$ Corresponding with the RSSI of $(k-1) * f_s/N'$(sample rate f_s is double times more than the maximum blinking frequency f of LED, according to the Nyquist theorem).

In order to avoid the flickering and distinguish signal of LED from ambient light such as sunlight and fluorescent light, the minimum blinking frequency more than 200 Hz.

The time domain and frequency domain signal of three LEDs with different frequency (420, 2000 and 4000 Hz) is shown in Fig. 1, it is easy to distinguish each LED by performing FFT.

4 Simulation Experiment and Performance Analysis

4.1 Simulation Environment

The proposed algorithm in this paper is evaluated by simulation method. The environment is a room whose size is 5 m × 5 m × 3 m. Four LED lamps with

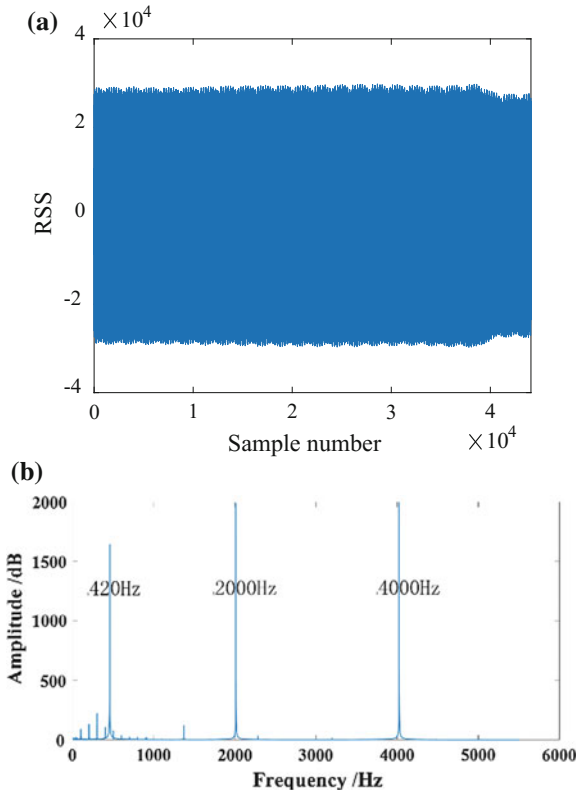

Fig. 1 The time domain and frequency domain signal of three LEDs with different frequency. **a** The time domain signal of three LEDs with different frequency. **b** The signal amplitude of three LEDs in frequency domain

different flicker frequencies were deployed in (0,0,3), (0,5,3), (5,0,3) and (5,5,3). The simulation area is evenly divided into 0.5 m * 0.5 m mesh, in order to get 121 test points. 100 experiments will be done at each test point. The positioning performance is calculated by the results of the experiments.

The Matlab 8.4 tool and a laptop (Windows 8.1, Intel core i5 CPU, 6 GBytes memory) are used in the simulation.

All the simulation data is produced with the Lambertian radiation model. And different SNR will be used to get reasonable noise. During the meantime, three Euler angle will also be changed because of the existence of noise which is defined as normal distribution noise, and the variance is different.

As a comparison, the algorithm in [23] is also implemented.

4.2 Location Performance

4.2.1 Positioning Performance Under Multiple LED Single Observation

The main work of this part is analysis the performance under the condition that the LED is deployed densely. We assume that all of the test points can receive the emitting light from three or more LEDs. There is no necessary for users to rotate the terminal. And the performance is showed in Fig. 2.

As we can see in this Fig. 2, with the increasing number of LED lights, the positioning accuracy increases. When the number of LED is 4, the average positioning error is 0.64 m. On the other hand, the SNR also influences the performance greatly. The smaller the SNR, the greater the error. When SNR is greater than 25, the positioning error tends to be stable.

The positioning error is also different because of the position of the terminal. As is showed in Fig. 3, the positioning error of margin area is greater than the central area. This is because the terminal can receive much more emitting light from LEDs in small incidence angles. This is similar to the impact of satellite positioning GDOP.

4.2.2 Positioning Performance Under Single LED Condition

As we all know, the deployment density of LEDs is relatively low in the corridor. In order to increase the positioning accuracy, we can use artificial participation way. Under the condition that the terminal position and heading angle (same as the path aisle direction) remain unchanged, slightly change the roll angle and pitch angle of the terminal, so as to obtain a plurality of observations.

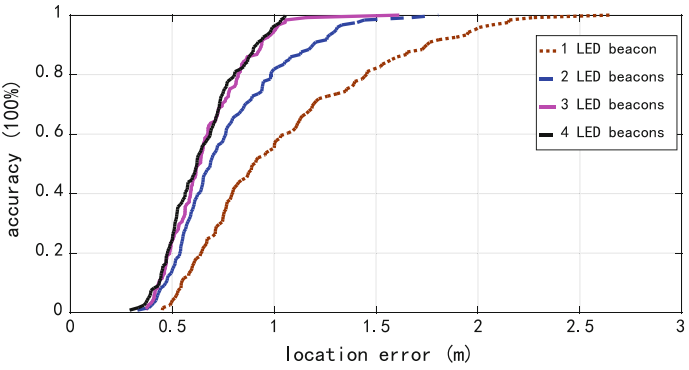

Fig. 2 Localization error under multiple LED single observation

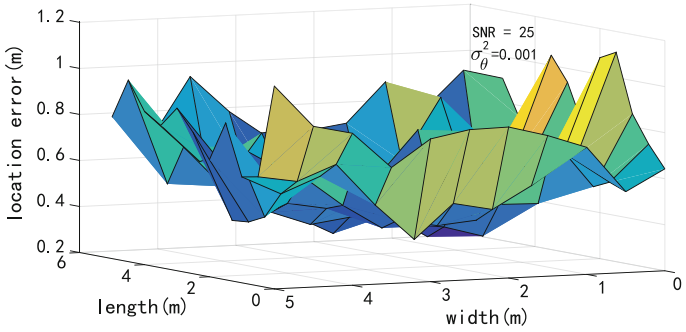

Fig. 3 Localization error under multiple LED and different position

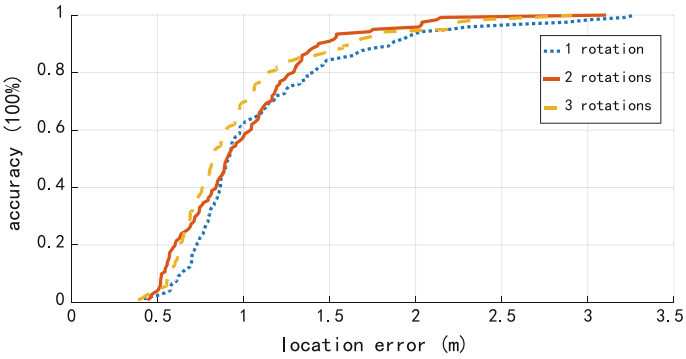

Fig. 4 Localization error under single LED with different rotation times

The Figs. 4 and 5 shows the positioning performance under the condition of single LED, and with the participation of users. It is obvious that the positioning error is increased when compare with the multiple LEDs. But it can still meet the requirements of indoor positioning. In addition, with the increase of rotation times, the positioning performance is improved. However, due to the accuracy of angles measured, further increase of the number of rotation, positioning performance improvement is not obvious (Figs. 5, 6 and 7).

4.2.3 Positioning Performance Under Multiple LEDs and Multiple Rotation

This part evaluates the positioning performance of multiple LEDs and multiple rotation.

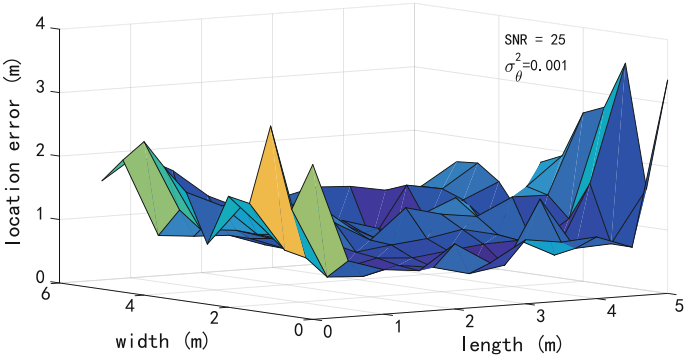

Fig. 5 Localization error under single LED and different position

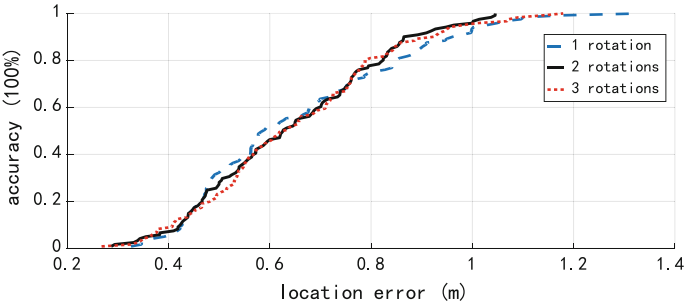

Fig. 6 Localization error under multiple LED with different rotation times

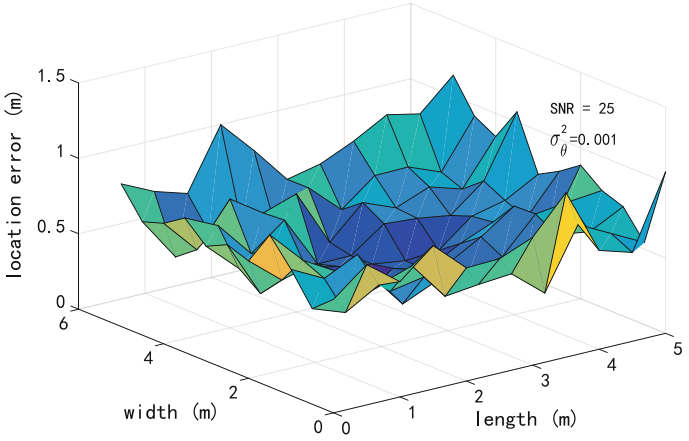

Fig. 7 Localization error of different position under multiple LED and rotation

Table 2 Operation time

LED number	Operation time/s
1 LED	9.61
2 LED	10.16
3 LED	12.41
4 LED	12.15

In our experiments, we define the position error as the Euclidean distances between the estimated position and the actual position. Figure 6 shows the cumulative distribution function (CDF) of localization errors in multiple LEDs and multiple rotation. The medium error is about 0.6 m.

As is showed in Fig. 7, we find that the positioning error of margin area is greater than the central area (the area surrounded by lamps).

4.2.4 Complexity

Table 2 lists the total computational time of the above algorithms be performed 1210 times (121 point and 10 times each point), the mean time of once positioning is less than 10 ms. The positioning algorithm is very high efficiency.

5 Conclusion

In this paper, by constructing a pervasive loss function, an indoor three dimensional positioning algorithm based on attitude identification and visible light propagation mode is proposed. It not only supports localization with multiple LEDs, but also supports localization with one single LED, which is fit for the sparse LED environments. By obtaining the cosine of incidence angle with the vector dot product of the terminal normal and the vector from the target to the LED beacon, this localization algorithm does not require the coplanar of the irradiation ray, incidence ray and normal ray, which is more pervasive in the three dimensional localization. Extensive simulation results demonstrate that the proposed algorithm can achieve sub-meter level positioning accuracy.

In the future, we will evaluate the algorithm in the real physical environments.

Acknowledgements This work was supported in part by the National Natural Science Foundation of China (61374214), the National Key Research and Development Program (2016YFB0502004), the International S&T Cooperation Program of China (2015DFG12520), and the Open Project of the Beijing Key Laboratory of Mobile Computing and Pervasive Device.

References

1. Al-Ammar MA, Alhadhrami S, Al-Salman A, Alarifi A, Al-Khalifa HS, Alnafessah A, Alsaleh M (2014) Comparative survey of indoor positioning technologies, techniques, and algorithms. In: International conference on cyberworlds (CW), 6–8 Oct 2014, pp 245–252
2. Al Nuaimi K, Kamel H (2011) A survey of indoor positioning systems and algorithms. In: International conference on innovations in information technology (IIT), 25–27 Apr 2011, pp 185–190
3. Ni LM, Liu Y, Lau YC, Patil AP (2004) LANDMARC: indoor location sensing using active RFID. ACM Wireless Netw 10(6):701–710
4. Monica S, Ferrari G (2015) UWB-based localization in large indoor scenarios: optimized placement of anchor nodes. IEEE Trans Aerosp Electron Syst 51(2):987–999
5. Schweinzer H, Syafrudin M (2010) LOSNUS: an ultrasonic system enabling high accuracy and secure TDoA locating of numerous devices. In: Proceedings of the IEEE 2010 international conference on indoor positioning and indoor navigation, pp 1–8
6. Zhuang Y, Yang J, Li Y, Qi L, El-Sheimy N (2016) Smartphone-based indoor localization with Bluetooth low energy beacons. Sensors 16(5):1–20
7. Lee S, Kim B, Kim H, Ha R, Cha H (2011) Inertial sensor-based indoor pedestrian localization with minimum 802.15.4a configuration. IEEE Trans Industr Inf 7(3):455–466
8. Liu H, Darabi H, Banerjee P, Liu J (2007) Survey of wireless indoor positioning techniques and systems. IEEE Trans Sys Man Cybernet C 37(6):1067–1080
9. Shu YC, Cheng B, Shen GB, Zhao F (2015) Magicol: indoor localization using pervasive magnetic field and opportunistic WiFi sensing. IEEE J Sel Areas Commun 33(7):1443–1457
10. Xie H, Gu T, Tao X, Ye H, Lu J (2014) A reliability augmented particle filter for magnetic fingerprinting based indoor localization on smartphone. IEEE Trans Mob Comput 13(9):1–14
11. Kim J, Lee K, Park H (2012) Power efficient visible light communication systems under dimming constraint. In: IEEE 23rd international symposium on personal indoor and mobile radio communications (PIMRC), 9–12 Sept 2012, pp 1968–1973
12. Zhang W, Kavehrad M (2012) A 2-D indoor localization system based on visible light LED. In: IEEE photonics society summer topical meeting series, Seattle, WA, pp 80–81
13. Hann S, Kim JH, Jung SY, Park CS (2010) White LED ceiling lights positioning systems for optical wireless indoor applications. In: 36th European conference exhibition on optical communication (ECOC), Torino, Italy, pp 1–3
14. Yang SH, Jeong EM, Kim DR et al (2013) Indoor three-dimensional location estimation based on LED visible light communication. Electron Lett 49(1):54–56
15. Jung SY, Hann S, Park CS (2011) TDOA-based optical wireless indoor localization using LED ceiling lamps. IEEE Trans Consum Electron 57(4):1592–1597
16. Panta K, Armstrong J (2012) Indoor localisation using white LEDs. Electron Lett 48(4):228–230
17. Lou P, Zhang H, Zhang X et al (2012) Fundamental analysis for indoor visible light positioning system. In: IEEE international conference on communications in china workshops, IEEE, pp 301–311
18. Hann S, Kim JH, Jung SY et al (2010) White LED ceiling lights positioning systems for optical wireless indoor applications. In: European conference and exhibition on optical communication, IEEE, pp 1–3
19. Taylor MT, Hranilovic S (2013) Angular diversity approach to indoor positioning using visible light. In: GLOBECOM Workshops, IEEE, pp 1093–1098
20. Rahman MS, Haque MM, Kim KD (2011) Indoor positioning by LED visible light communication and image sensors. Int J Electr Comp Eng 1(2):420–431
21. Barry JR (1994) Wireless infrared communications, vol 280. Springer, Berlin
22. Davidon WC (1991) Variable metric method for minimization. SIAM J Optim 1:1–17
23. Yasir M, Ho SW, Vellambi BN (2014) Indoor positioning system using visible light and accelerometer. J Lightwave Technol 32(19):3306–3316

An Indoor Positioning and Navigation Technique Based on Wi-Fi Fingerprint and Environment Information

Boxiong Han and Long Zhao

Abstract With the development of urbanization in recent years, the conditions for building the smart city gradually mature, the increase in large airports, shopping centers and office buildings makes indoor positioning and navigation services more important. The satellite signal in indoor environment is too weak to locate, while notebook computers, mobile phones and other intelligent terminals greatly increase, and Wi-Fi signals become more dense and extensive, which provide the material foundation for the development of indoor positioning technology. In order to solve the indoor positioning problem, we propose an indoor positioning and navigation technique based on Wi-Fi fingerprint and environment information. The user's intelligent terminal can detect the signal strength of each wireless access point and obtain the received signal strength indication (RSSI), then the specific location of the device can be calculated according to the indoor radio pass loss model and Wi-Fi signal strength fingerprint database composed by each node. The combination of k nearest neighbor (k-NN) algorithm and particle filter (PF) algorithm helps to improve the positioning accuracy and robust stability in the paper, and the combination of the Dijkstra algorithm and Wi-Fi fingerprint database based on reference nodes provides the optimal navigation route by calculating the shortest path from the start position to destination. Simulation experiment was carried out on the 4th floor of new main building of Beihang University, from which we obtain the location map and the navigation route map from the starting point to destination. The experiment result shows the efficiency and reliability of the algorithm.

Keywords Indoor positioning · Fingerprint · Wi-Fi · Received signal strength indication · Navigation

B. Han (✉) · L. Zhao (✉)
School of Automation Science and Electrical Engineering,
Beihang University, Beijing 100191, China
e-mail: boxiong_han@buaa.edu.cn

L. Zhao
e-mail: buaa_dnc@buaa.edu.cn

J. Sun et al. (eds.), *China Satellite Navigation Conference (CSNC) 2017 Proceedings: Volume I*, Lecture Notes in Electrical Engineering 437,
DOI 10.1007/978-981-10-4588-2_33

1 Introduction

Global Positioning System is widely used in the outdoor environment because of its high accuracy, wide coverage and convenience. However high buildings in the city make the satellite signal not strong enough to carry on in indoor environment. Meanwhile Wi-Fi equipment become very common in modern buildings, so it is necessary to develop the indoor positioning and navigation system based on Wi-Fi signals [1].

Nowadays positioning can be divided into two types: (1) Triangulation technique, the principle of triangulation technique is to measure the distance between the user and access points (APs) and get the user position according to geometric properties of triangles [2] including time of arrival (TOA) technique, time difference of arrival (TDOA) technique and angulation of arrival (AOA) technique [3–5]. (2) Fingerprint technique, the principle of the fingerprint technique is data matching, it can reduce the effects of environmental noise [6, 7], so it is commonly used in Bluetooth technique, radio frequency identification (RFID) technique, ZigBee and Wi-Fi technique [8–12]. In this paper, we focus on the fingerprint technique [13]. There are two phases in fingerprint technique, offline phase and online phase [14]. In offline phase, we collect Wi-Fi signal data from access points (APs) and build the fingerprint database [15, 16]; in online phase, we receive Wi-Fi signals online and get RSSI then use approximate matching algorithm to get the location information [17, 18]. There are many kinds of matching algorithms, such as k nearest neighbor (k-NN) algorithm, support vector machine (SVM) algorithm and artificial neural network (ANN) algorithm, k-means algorithm, however, these algorithms have poor positioning accuracy or low computational efficiency [19]. An indoor positioning algorithm based on PF and k-NN algorithm is proposed to improve the positioning accuracy and stability in this paper.

Indoor navigation service is equally important as indoor positioning. Airports, shopping centers, office buildings and other large building groups are increasing, in which there are many different areas, therefore, only knowing where the location is not enough, we also need to know the route to reach the destination, so indoor navigation should base on the structure of the building or environmental information [20]. In this paper, the Dijkstra algorithm is used to calculate the shortest route to a destination in a building. The Dijkstra algorithm solves the shortest path problem in a directed graph, which is used in computer networks to find the fastest way to communicate, as for indoor navigation it can be used to find the optimal path based on the building structure and fingerprint reference nodes [21].

This paper consists of four sections: Sect. 1 Introduction of indoor positioning and navigation technology; Sect. 2 The radio propagation model, the fingerprint technique, k-NN, PF and the Dijkstra's algorithm are described in detail; Sect. 3 Indoor positioning and navigation algorithms are demonstrated in the test venue on 4th floor of new main building, Beihang University; Sect. 4 Summary and discussion.

2 Methodology

2.1 Radio Path Loss Mode

When the radio signal is transmitted in the medium, the received signal strength indication (RSSI) will be in logarithmic attenuation with the increase of the distance from the receiving end [23]. According to the relationship between the distance and the signal strength in the radio signal path loss model, the distance between the receiver and the transmitter can be calculated, then the user's location can be estimated according to the principle of triangulation. The wireless signal path loss model is shown in Eq. (1).

$$PL(\text{dB}) = PL_{d_0}(\text{dBm}) - 10\gamma \log_{10}\left(\frac{d}{d_0}\right) - H \tag{1}$$

where PL(dB) is the power receiver measured in decibel, PL_{d_0} (dBm) is the RSSI value 1 m from APs, γ is path loss exponent, d is the distance between transmitter and receiver, d_0 is the unit distance, H is the sum of the power loss caused by environmental factors such as channel noise. γ is determined by the environment, people move and indoor arrangement effect the value of γ, the path loss exponent in different environments is shown in Table 1.

2.2 Fingerprint Technique

Wi-Fi fingerprint technique is a non-ranging method of positioning, it can reduce the impact of ambient noise, fingerprint database works like a map that combines location information and received signal strength. As shown in Fig. 1, the fingerprint technology is divided into two phases, first is the offline phase, signal reference nodes should be determined, then signal information of the Wi-Fi access point is collected at each point, finally the location coordinates (x, y) of the reference nodes, RSSI and service set identifier (SSID) of Wi-Fi routers make up the fingerprint database. The second part is the online phase, user compare the online received signal with the offline information from fingerprint database, then obtain the position by data matching algorithm; at the same time, the reference nodes of the fingerprint database also constitute the indoor route reference nodes used for indoor navigation service.

Table 1 Path loss exponent [22]

Condition	Path loss exponent
Downtown	3.7–6.5
Office	2–6
Free space	2
Outdoor	2.8

2.3 K Nearest Neighbor Algorithm

K nearest neighbor algorithm is used to match the online measured data with the information fingerprint database, then the position is classified to the best matching point, with the conditions of minimum Euclidean distance to estimate the position of the receiver. Euclidean distance is introduced as the reference quantity, the position of the receiver is estimated in the condition of minimum Euclidean distance.

$$d_i = \| rf_i - rs \| = \sqrt{\sum_{i=1}^{n} (rf_i - rs)^2} \tag{2}$$

In Eq. (2), d_i is the distance between the receiver and the reference nodes in the fingerprint database, rf_i is the RSSI of each reference nodes in the fingerprint database, rs is the RSSI of the receiver. The particle filter algorithm in the next section will explain how to improve the accuracy of the k-NN algorithm.

2.4 Particle Filter (PF)

Particle filter is based on Monte Carlo method and Bayesian framework, the basic idea of particle filter is to generate particles and calculate the weight of each particle, which should find important particles through resampling technology and

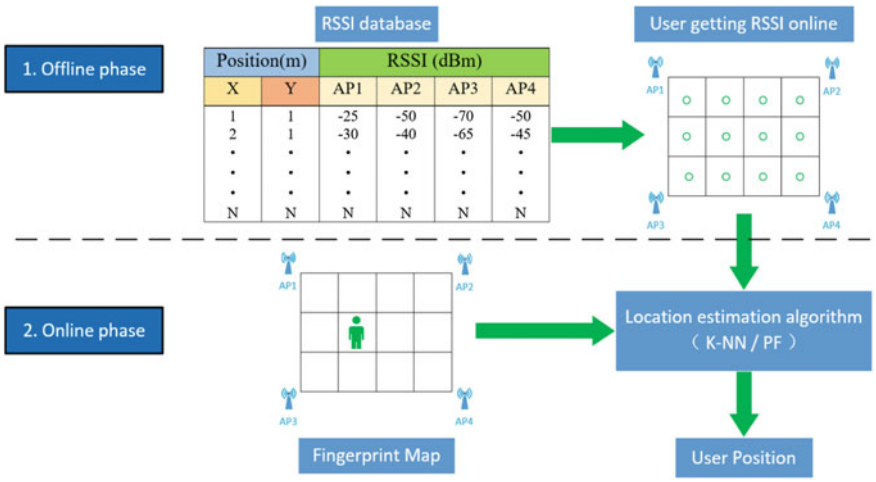

Fig. 1 Fingerprint technique

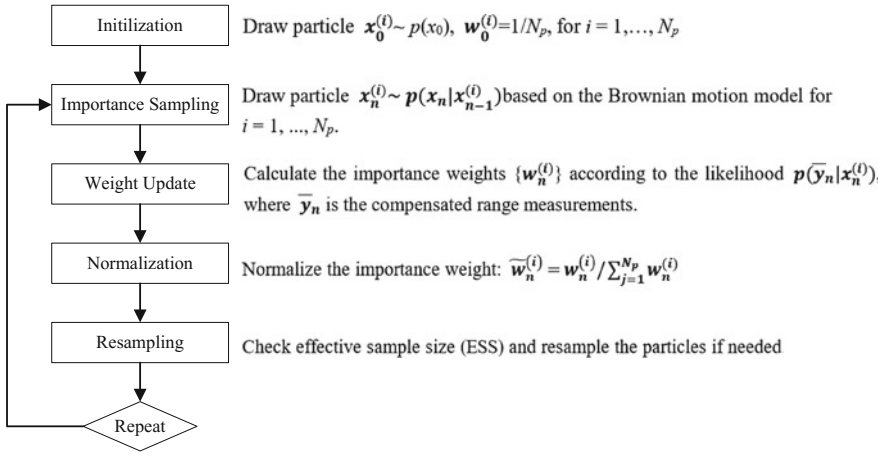

Fig. 2 PF algorithm

finally return the generated particles back [24]. Particle filter algorithm combined with k-NN algorithm can reduce the positioning error, the algorithm is shown in Fig. 2.

2.4.1 System Model

The principle of particle filter is to find a set of random samples spread in the state space to approximate the probability density function, then replace the integral operation of the sample mean, finally obtain the distribution of the state minimum variance. In this paper, we propose an indoor positioning system model based on dead reckoning model and particle filter.

As shown in Eqs. (3) and (4), x_k refers to the state vector, $x_k = [P_x\ P_y\ v_x\ v_y]^{\mathrm{T}}$, P_x and P_y are position of the user, v_x and v_y are velocity, Q is system noise, k is the time step and ΔT is the sample time.

$$\begin{bmatrix} P_{x_{k+1}} \\ P_{y_{k+1}} \\ v_{x_{k+1}} \\ v_{y_{k+1}} \end{bmatrix} = \begin{bmatrix} 1 & 0 & \Delta T & 0 \\ 0 & 1 & 0 & \Delta T \\ 0 & 0 & 1 & 0 \\ 0 & 0 & 0 & 1 \end{bmatrix} \begin{bmatrix} P_{x_k} \\ P_{y_k} \\ v_{x_k} \\ v_{y_k} \end{bmatrix} + Q \tag{3}$$

$$Q = \begin{bmatrix} \Delta T^2/2 & 0 & 0 & 0 \\ 0 & \Delta T^2/2 & 0 & 0 \\ 0 & 0 & \Delta T & 0 \\ 0 & 0 & 0 & \Delta T \end{bmatrix} \tag{4}$$

2.4.2 Measurement Update

For measurement update, we choose likelihood function to find the weight (P_w) between position of k-NN and each PF. z_{k_r} refers to the position from k-NN, z_{k_p} refers to the position from PF, and σ is variance of measurement, as shown in Eq. (5).

$$P_w = \frac{1}{\sqrt{2\pi\sigma}} \exp\left(-\frac{(z_{k_r} - z_{k_p})^2}{2\sigma^2}\right) \tag{5}$$

Next step is to normalize the importance weight of particle and use resampling technique to find the importance sample from P_{wk}, then generate next state x_{k+1} in PF equation, finally calculate the mean value of the particles to estimate the position of the receiver. Black circle points and yellow circles in Fig. 3 represent the particle distribution represent weight from likelihood function. For instance, the number 7 has the maximum weight at time k, around which algorithm will generate next particle at time k + 1. It shows that the weight of the particles determines the next state, which decides the position of the receiver.

2.5 *Dijkstra Algorithm*

Dijkstra algorithm is a popular algorithm in computer network, which is used to find the shortest path to improve communication efficiency [25]. The algorithm has high computational efficiency so the time occupied is short, and the principle is quite simple. As shown in Fig. 4a, according to Dijkstra algorithm, after

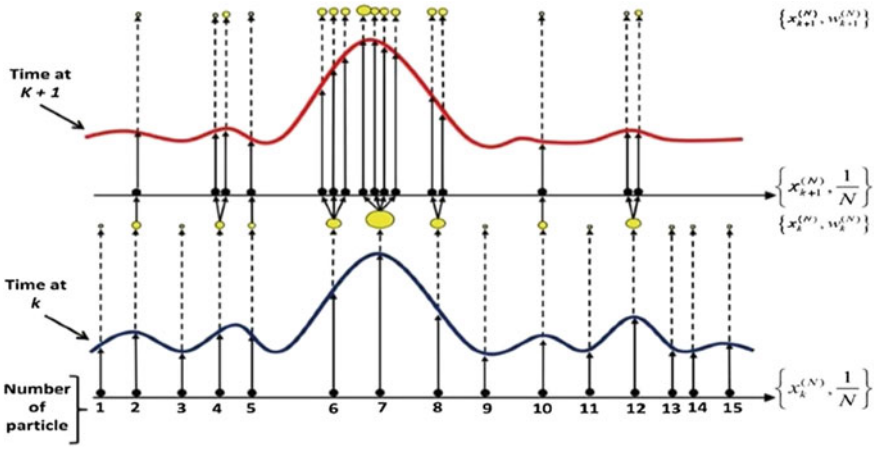

Fig. 3 Resampling technique

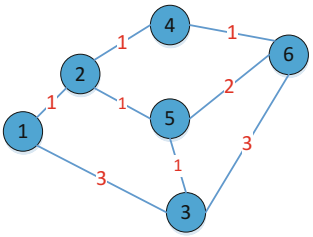

A. Fingerprint nodes

node	1	2	3	4	5	6
1	0	1	3	∞	∞	∞
2	1	0	∞	1	1	∞
3	3	∞	0	∞	1	3
4	∞	1	∞	0	∞	1
5	∞	1	1	∞	0	2
6	∞	∞	3	1	2	0

B. Link matrix

Fig. 4 Reference nodes and link matrix

determining the starting point and ending point, we extend from the starting point as the center and approach to the end node through each node in the path, the distance between connected nodes should be recorded and compared in order to get the shortest total distance and then make an optimum path planning.

According to Dijkstra algorithm and the indoor positioning algorithm, we build the link matrix based on the reference nodes from fingerprint database. As shown in Fig. 4b, if two reference nodes are connected directly, enter the right distance between them in the link matrix; if they are not directly connected, fill in the matrix at the corresponding space with ∞.

After establishing the link matrix, we need to define the start point (user's position) and the end point (destination), then calculate the distance to find the shortest path by using the link matrix.

As shown in Fig. 5, indoor positioning and navigation system proposed in this paper is divided into two steps, the first step is the indoor positioning based on fingerprint database, users get RSSI from indoor Wi-Fi APs and estimate the position by using k-NN algorithm based on fingerprint database. In this paper, we propose a positioning algorithm based on the combination of particle filter and k-NN algorithm to reduce the effect of ambient noise and improve the accuracy of positioning. The second step is indoor navigation based on the information of reference nodes in fingerprint database, Dijkstra algorithm is used in the paper to find the shortest distance between two points, which helps to make an optimum path planning from location to destination.

3 Experiment and Analysis

In order to verify the effectiveness and accuracy of the indoor positioning and navigation algorithm, we set up an experimental field on the 4th floor of the new main building in Beihang University and carry out the experiment. As shown in Fig. 6, there are 18 classrooms, 4 elevators, 2 emergency exits, 1 toilet, and some electrical facilities in the experimental field. First of all is to set the map and axis,

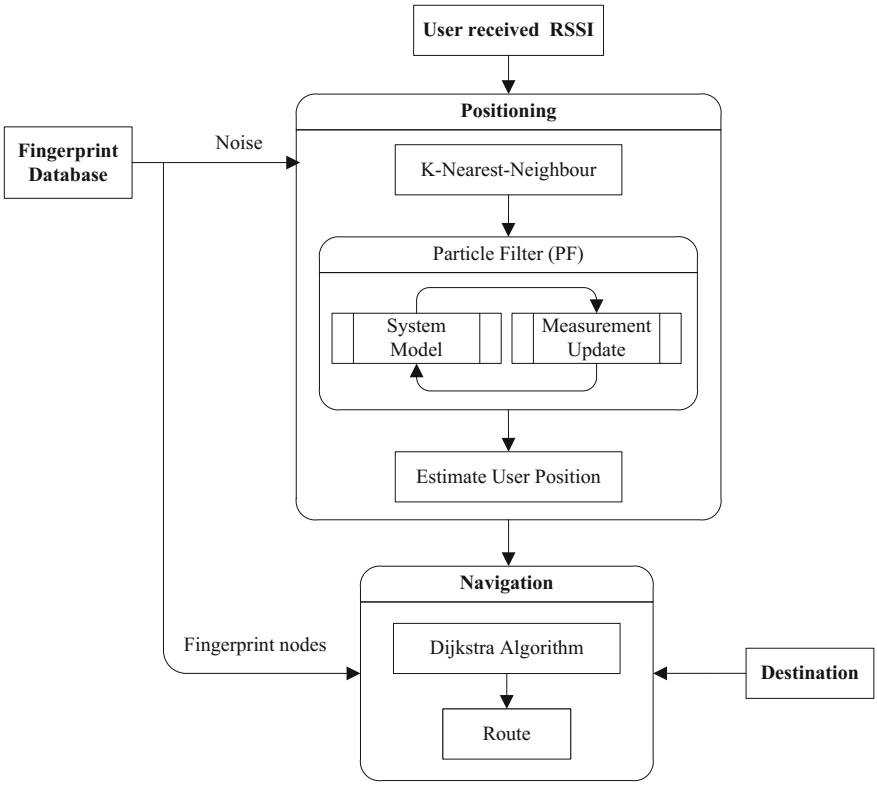

Fig. 5 Indoor positioning and navigation system

according to the experiment, we use the outside boundary of the 4th floor of new main building E to form a square, x and y axis is set as shown in Fig. 6, the unit distance is 1 m. There are 18 Wi-Fi access points (APs) in the classroom providing signals for the experiment, red dots in Fig. 6 indicate their position. Secondly, Eq. (1) which indicates the path loss model is used to generate RSSI of each AP. Considering the signal noise from personnel and wall floor in the experimental environment, we add a standard Gaussian white noise N (0, 3) in H of path loss model. Last is to establish the fingerprint database, blue dots indicate the reference notes as shown in Fig. 6 which are set evenly in the corridor with a distance of 2 m according to the principle of uniform distribution and setting special points. At the same time, there are two corridors which are 2 m wide, where the reference nodes are in the middle line, so the distance between the inflection point and adjacent point is 1 m. There are 73 reference nodes in total. The position coordinates of each node together with RSSI of each AP at the node form the fingerprint database.

In indoor navigation experiments, we assume that the user starts from the door of room E403 (Δ as shown in Fig. 6) and goes to water dispenser 1 (① as shown in Fig. 6) next to F407 or water dispenser 2 (② as shown in Fig. 6) next to F411, the

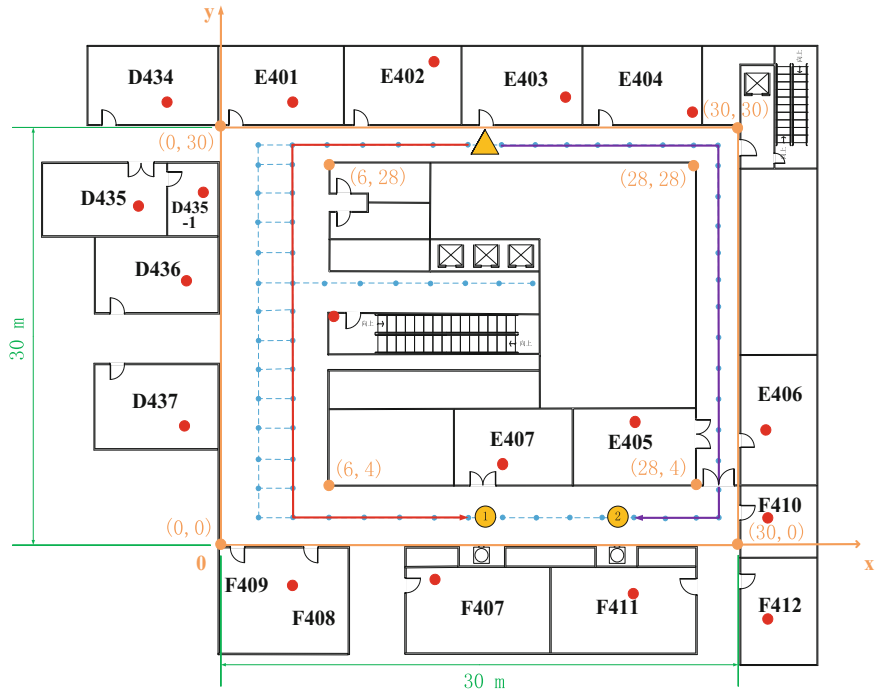

Fig. 6 Experimental field and the navigation route

shortest path is given by Dijkstra algorithm based on fingerprint reference nodes. Two reference nodes together with atan2 function are used to calculate the direction angle, angle result of atan2 varies in the area $[-\pi, \pi]$. For example we get angle 90° first, so 0° is right hand and 180° is left hand next. In order to make the result more accurate, we use the average of 10 experimental data as the shortest path time.

As shown in Fig. 6, we use Dijkstra algorithm to determine the path, finally we get the way through different corridors to the two water dispensers at different place. It is shorter to reach water dispenser 1 through the red line while it is shorter to reach water dispenser 2 through the purple line. This result is consistent with the actual walking route and the shortest path principle which illustrates the effectiveness and correctness of Dijkstra algorithm based on fingerprint reference nodes for indoor route planning. Table 2 shows the direction, distance, reference nodes and calculation time of each route.

In positioning path, we add Gaussian white noise N(0, 3) in Eq. (1) in accordance with the experimental environment, which is the same used in reference nodes of fingerprint database. According to the Dijkstra algorithm, the experiment is carried out in the red line as shown in Fig. 7, comparing the algorithm accuracy and robust stability of the k nearest neighbor algorithm, particle filter and unscented Kalman filter. Especially k nearest neighbor algorithm use three nodes for

Table 2 Route data

Route	Red	Purple
Route planning	△ E403 ← 10 m ↓ 25 m → 10 m ○ dispenser 1	△ E403 → 13 m ↓ 25 m ← 5 m ○ dispenser 2
Total distance (m)	45	43
Reference nodes	24	24
Calculation time	0.1215	0.1257

reference, particle filter and unscented Kalman filter algorithm are compared for their similar principle. The route to water dispenser 1 is chosen to test the accuracy and robustness of k-NN (Red line), PF (Blue line) and UKF (Green line), the result is shown in Fig. 8.

In experimental field, we need to use trial and error method to determine the initial data. According to Eq. (3), the initial conditions of particle filter is N = 30, variance of measurement $\sigma = 1.5$. The initial condition of the unscented Kalman filter is set as matrix $Q = \text{diag}\{1, 1, 1,1\} \times 10^1$ and $R = \text{diag}\{1, 1, 1, 1\} \times 10^2$. Figure 8 and Table 3 show the relative error between real route and the route calculated by each algorithm and show the time they spend to calculate, the relative error of PF algorithm is less than k nearest neighbor algorithm and unscented Kalman filtering algorithm, while the average error of each algorithm is still quite close which is around 1.6 m, but the maximum error value from PF algorithm and UKF algorithm is 1.5 m less than k-NN algorithm.

4 Summary and Discussion

In this paper, the theoretical analysis and algorithm research were carried out on the positioning and navigation technique in the indoor environment. The experimental field was built on the 4th floor of the new main building of Beihang University. In terms of positioning technique, the combination of k-nearest neighbor algorithm and particle filter algorithm can improve the positioning accuracy and track smoothness. For the navigation technique, the Dijkstra algorithm based on Wi-Fi fingerprint node can give us the best route in indoor environment. The experimental result shows that the shortest path from the starting point to the destination can be achieved by the Dijkstra algorithm, which is proved to be effective and practical by comparing the two different routes from E403 (the starting point) to two different water dispensers (destinations). For the positioning technique, the two better algorithms, k-nearest neighbor and particle filter, are combined to a certain weight by comparing the error and computational efficiency of k-nearest neighbor, particle filter and unscented Kalman filter algorithm. The experimental results show that the particle filter algorithm is better in error and computation time than unscented

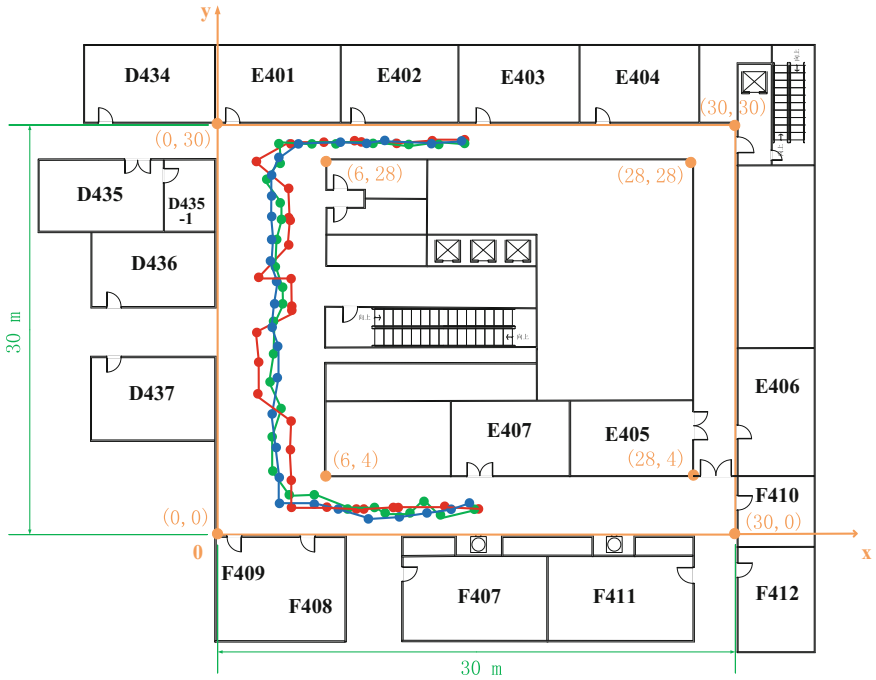

Fig. 7 Calculated trajectory

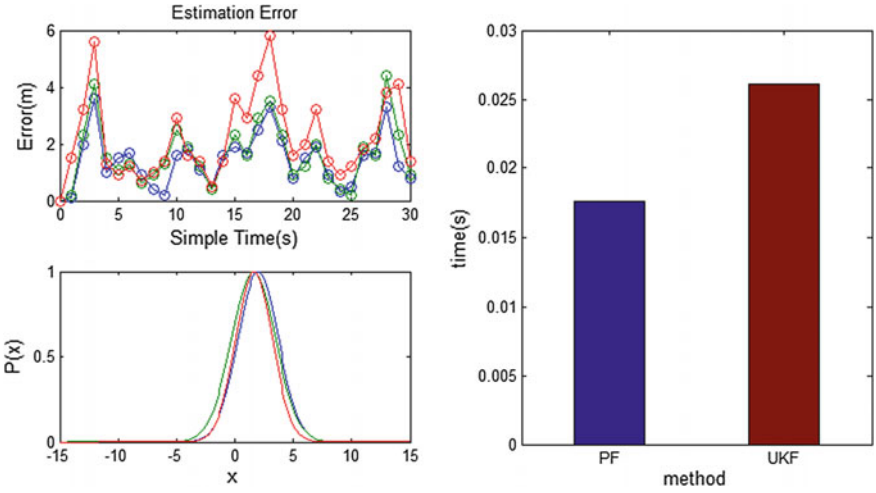

Fig. 8 Experimental error and calculation time

Table 3 Results of the three algorithms

Algorithm		k-NN	PF	UKF
Error	Min	0	0.0134	0
	Mean	1.5778	1.5346	1.6325
	Max	5.9863	4.3250	4.5023
Calculation time		–	0.0176	0.0261

Kalman filter algorithm though they are similar in principle, therefore we use the k nearest neighbor algorithm combined with the particle filter algorithm.

Then we will carry out further research work. As for positioning algorithm, we would analyze deeply on the weight between k-NN and PF to improve the positioning accuracy; as for indoor navigation, we would set a certain standard to remove the useless nodes which can further improve the efficiency of Dijkstra algorithm, and the computation time would reduce a lot.

Acknowledgements This project is supported by National Science and Technology Major Project of the Ministry of Science and Technology of China (Grants No. 2016YFB0502102, 2016YFB0502004), National Natural Science Foundation of China (Grant No. 41274038, 41574024), Beijing Natural Science Foundation (Grant No. 4162035) and Aeronautical Science Foundation of China. Thanks to the support above!

References

1. Kasantikul K, Xiu C, Yang D et al (2015) An enhanced technique for indoor navigation system based on WIFI-RSSI. In: Seventh international conference on ubiquitous and future networks. IEEE, pp 513–518
2. Khalil L, Waadt A, Bruck G et al (2014) Positioning framework for HAN 802.11n utilizing Kalman filter on received signal strength, pp 1172–1176
3. Roshanaei M, Maleki M (2009) Dynamic KNN: a novel locating method in HAN based on angle of arrival. In: IEEE symposium on industrial electronics and applications, Kuala Lumpur Malaysia, pp 722–726
4. Subhan F, Hasbullah H, Rozyyev A, Sheikh T (2011) Bakhsh, indoor positioning in Bluetooth networks using fingerprinting and lateration approach. In: International conference on information science and application (ICISA), pp 1–9
5. Phimmasean S, Chuenurajit T, Cherntonomwong P (2013) Indoor localization system based on fingerprint technique using RFID passive tag. In: 10th international conference on electrical engineering/electronics, computer, telecommunication and information technology (ECTI-CON), pp 1–6
6. Gunawan M, Li B, Gallagher T, Dempster AG, Retscher G (2012) A new method to generate and maintain a Wi-Fi fingerprinting database automatically by using RFID. In: International conference on indoor positioning and indoor navigation (IPIN), pp 1–6
7. Fink A, Beikirch H, Voss M et al (2010) RSSI-based indoor positioning using diversity and inertial navigation. In: International conference on indoor positioning and indoor navigation, pp 1–7
8. Li Y, Zhuang Y, Lan H et al (2015) A hybrid Wi-Fi/magnetic matching/PDR approach for indoor navigation with smartphone sensors. IEEE Commun Lett 20(1):169–172

9. Torteeka P, Chundi X (2014) Indoor positioning based on Wi-Fi fingerprint technique using fuzzy K-Nearest Neighbor. In: 4th international Bhurban conference on applied sciences and technology (IBCAST), pp 461–465, 518
10. Chen LH, Wu HK, Jin MH et al (2014) Intelligent fusion of Wi-Fi and inertial sensor-based positioning systems for indoor pedestrian navigation. Sens J IEEE 14(11):4034–4042
11. Del Mundo LB, Ansay RLD, Festin CAM, Ocampo RM (2011) A comparison of wireless fidelity (Wi-Fi) fingerprinting techniques. In: International conference on ICT convergence (JCTC), pp 20–25
12. Tian Z, Fang X, Zhou M et al (2015) Smartphone-based indoor integrated Wi-Fi/MEMS positioning algorithm in a multi-floor environment. Micromachines 6(3):347–363
13. Bai S, Wu T (2013) Analysis of K-Means algorithm on fingerprint based indoor localization system. In: 5th international symposium on microwave, antenna, propagation and EMC technologies for wireless communications (MAPE), pp 44–45
14. Duvallet F, Tews AD (2008) Wi-Fi position estimation in industrial environments using gaussian processes. In: IEEE/rsj international conference on intelligent robots and systems, pp 2216–2221
15. Kim I, Choi E, Oh H (2012) Indoor user tracking with particle filter. In: COGNITI VE 2012: the fourth international conference on advanced cognitive technologies and application, pp 59–62
16. Sakib SR, Quyum A, Andersson K, Synnes K, Korner U (2014) Improving Wi-Fi based indoor positioning using particle filter based on signal strength. In: IEEE ninth international conference on intelligent sensors, sensor networks and information processing (ISSNIP), pp 1–6
17. Lu H, Cao X, Jensen CS (2012) A foundation for efficient indoor distance-aware query processing. In: IEEE 28th international conference on data engineering, pp 438–449
18. Li D, Lee DL (2008) A lattice-based semantic location model for indoor navigation. In: 9th international conference on mobile data management, pp 17–24
19. Sriharee G (2013) Indoor navigation using semantic symbolic information. In: IEEE 16th international conference on computational science and engineering, pp 1167–1173
20. Juzoji H, Nakajima I, Kitano T (2011) A development of network topology of wireless packet communications for disaster situation with genetic algorithms or with Dijkstra's. In: IEEE international conference on communications, pp 1–4
21. Jiang JR, Huang HW, Liao JH, Chen SY (2014) Extending Dijkstra shortest path algorithm for software defined networking. In: 16th Asia-Pacific network operations and management symposium (APNOMS), pp 1–4
22. Yan Z, Jun Z (2010) Dijkstra's algorithm based robust optimization to airline network planning. In: International conference on mechanic automation and control engineering (MACE), pp 2783–2786
23. Chen Z (2013) Bayesian filtering: from Kalman filter to particle filter, and beyond. J Stat 182:1–69
24. Sun CJ, Kuo HY, Lin CE (2010) A sensor based indoor mobile localization and navigation using unscented Kalman filter. In: Position location and navigation symposium (PLANS), pp 327–331
25. Levchev P, Krishnan MN, Yu C et al (2014) Simultaneous fingerprinting and mapping for multimodal image and Wi-Fi indoor positioning. In: International conference on indoor positioning and indoor navigation. IEEE

Identification of LBS Deception for Smart Phone Based on the Speed Consistency

Da-peng Li, Ting Liu, Wei-na Hao, Bing Liu, Ling-chuan Zeng and Yan-kun Li

Abstract Although the LBS applications benefit the public, there are lawless users trying to make profit from LBS deception. A deception identification method for smart phone based on the speed consistency of sensors is presented in this paper. To mitigate the different characteristic of GNSS and MEMS sensors for speed measurement, which would bring much difficult to the direct comparison, the velocity peak interval probability distribution of smart phone sensors is used as the feature. Two-sample kolmogorov-smirnov test is applied for the statistical decision of LBS deception. Experimental results show that the proposed method can identify LBS deception correctly.

Keywords LBS · Deception · Smart phone · K-S test

1 Introduction

APPs supported by the LBS (location-based services) technique, such as travel, shopping, accommodation, has brought much convenience for consumers and penetrated into the lives of the people. However, LBS making the tremendous contribution for the national economic development at the same time, also bred many negative issues. Refer to two news events below to illustrate the current main problems of the LBS.

According to media reports [1], in the ride-hailing field, a taxi driver in Beijing gained coupons through false transportation, and took illegal profit about 30,000 CNY after several months. Similarly, in the takeaway field, a takeaway delivery platform staff made up a lot fake courier deliveries and gain the subsidies by positioning cheating [2].

D. Li (✉) · T. Liu · W. Hao · B. Liu · L. Zeng · Y. Li
Academy of Opto-Electronics, Chinese Academy of Sciences,
Beijing 100094, China
e-mail: lidapeng@aoe.ac.cn

J. Sun et al. (eds.), *China Satellite Navigation Conference (CSNC) 2017 Proceedings: Volume I*, Lecture Notes in Electrical Engineering 437,
DOI 10.1007/978-981-10-4588-2_34

Therefore, the behavior of unlawfully obtaining profits from LBS deception is a widespread problem. Unfortunately, the platform of LBS is still a lack of effective means to accurately determine the deception behavior.

2 The State-of-Art, Countermeasures and Challenges of LBS Deception of Smart Phone

2.1 The State-of-Art and the Countermeasures of LBS Deception

There are a lot of researches on LBS security, but mainly focus on the high quality user experience and the privacy information security [3, 4], and seldom on the anti-deception method for LBS. At the same time, GNSS as the main positioning means of LBS applications, is the main target of LBS deception. Therefore, we focus on the anti-spoof research status in the GNSS field.

Considering the service of GNSS positioning, there are two kinds of different threats: one is the suppression jamming; the other is the confusion jamming, usually called deception jamming. Suppression jamming is the biggest threat to satellite navigation signal, which could make the receiver cannot capture and track the satellite navigation signal correctly. Due to the limited coverage of the interference, found by the monitor departments of the state easily, and no economic benefits to pursuit, therefore the suppression jamming for the LBS deception is rare.

Relatively speaking, the possibility of deception jamming is much more likely to threat the LBS applications. Deception jamming can cheat by changing the time delay of signal received by the target receiver, which results in the position and clock error. But the technical difficulty and costs of implementation of this kind of jamming are too high for the situation of few users.

In summary, the suppression and deception interference of GNSS is not a new topic, scholars have carried out a widespread research, but due to the technical difficulty and cost considerations, there is no deception interference of navigation signal level for civilian smart phone users.

2.2 Challenges

The anti-deception technology has been developed for more than 20 years in the field of navigation, a variety of GNSS protection measures have been proposed in literatures. It is summarized as: the absolute power monitoring, signal power monitoring, Doppler detection, L1 and L2 cross-correlation detection, residual signal analysis [5, 6], ephemeris data verification, dual receiver code cross-correlation detection [7], receiver automatic integrity monitoring (RAIM) [8]

and inertial measurement unit (IMU) consistency checking, arrival time and angle detection [8, 9], message encryption [10, 11]. Unfortunately, these methods are almost impossible to run on the smart phone. This is because:

(1) The security of smartphone operating system is poor
Android system is completely open source, lawless users tamper with the GPS position information using the Android system leaks. What is more, some people develop the Android system simulator running on the PC platform and could virtualize the output of the built-in navigation positioning module of the smart phone directly;
(2) The navigation sensor of smart phone is hard to modify
The program of smartphone navigation module has been fixed, it is difficult to change the positioning algorithm. Some of the original navigation measurements, such as correlation peaks, Doppler, pseudorange, carrier phase, etc., cannot be obtained. It makes a large number of anti-deception algorithms failed which is based on the original navigation measurement;
(3) The sensor accuracy of smart phone is low
Because of the cost, compared with the special equipment such as navigation receiver, the navigation sensor accuracy on the smart phone is low. It usually has no high gain antenna, high sensitivity components, and professional calibration;
(4) The smartphone resource is limited
Considering the computation cost, power consumption and other issues, many complex algorithms couldn't perform on the smart phone platform. Some methods of signal detection and spectrum analysis are difficult to run in real time. Additionally, the storage and network resources of smart phone are limited, it is hard for users to endure the consuming of a lot of storage space and the net flow of Internet;

Thus, it is a challenging new task to realize the anti-deception of LBS on the smart phone in the face of the constraints above.

3 LBS Deception Identification Based on the Velocity Peak Interval Distribution and the K-S Test

Based on the above analysis, the identification of anti-deception for smart phone should fully use the internal smart phone sensor resources, such as MEMS, communication module, barometer, etc. In order to identify the behaviors of modification or falsification of the GPS output by some lawless users, a LBS deception recognition method for smart phone based on the speed consistency is proposed in this paper. Specifically, the speeds obtained from GPS and MEMS in the smart

phone are compared. If they are consistent, then there is no LBS deception, and vice versa. Unfortunately, the sensors of GPS and MEMS have different velocity sensitivity and temporal characteristics. Additionally affected by the asynchronization of the Android system processes, it is hard to compare the consistency directly.

Assuming the Y axis of the MEMS sensor in the smart phone is consistent with the direction of the vehicle, and the corresponding speed output is $Acc^{Phone}_{MEMS,y}$,

$$Acc^{Phone}_{MEMS,y}(t) = Acc^{True}(t) + AccBias^{Phone}_{MEMS,y} \tag{1}$$

where the Acc^{True} is the true vehicle acceleration, $AccBias^{Phone}_{MEMS,y}$ is the constant bias of the Y axis accelerator of the MEMS. After integration, the speed of the Y axis of the MEMS is estimated,

$$V^{Phone}_{MEMS,y}(t) = \int_0^t Acc^{True}(s)ds + AccBias^{Phone}_{MEMS,y} \cdot t \tag{2}$$

Similarly, assuming the output position of GPS in the ECEF coordinate system is $[x(t), y(t), z(t)]$, and the speed estimated by GPS for time t is

$$V^{Phone}_{GPS}(t) = \frac{\sqrt{(x(t) - x(t-\Delta t))^2 + (y(t) - y(t-\Delta t))^2 + (z(t) - z(t-\Delta t))^2}}{\Delta t} \tag{3}$$

where the Δt is the time interval of GPS output sampling.

Usually, the $V^{Phone}_{MEMS,y}(t)$ and $V^{Phone}_{GPS}(t)$ have different sample rates and sensitivities to the speed, moreover, there exists the accumulation error in the $V^{Phone}_{MEMS,y}(t)$, therefore, they couldn't be compared directly. Enlightened by the vicinity of the velocity peaks outputted from the $V^{Phone}_{MEMS,y}(t)$ and $V^{Phone}_{GPS}(t)$ when there is no deception, we regard the velocity peak interval as a random variable which follows some distribution. Then, the problem is turned into the test that if the velocity peak intervals outputted from the MEMS and GPS follow the same distribution.

The K-S test is named after the two Soviet mathematician Kolmogorov and Smirnov, which is based on the cumulative distribution function and test that if an empirical distribution follows some theory distribution or whether two empirical distributions have significant differences. Especially, two-sample K-S test becomes one of the most useful non-parametric test due to its sensitivity to the differences of position and shape parameters in the two-sample empirical distribution function.

Assuming $VPeakInterval^{Phone}_{MEMS,y}$ and $VPeakInterval^{Phone}_{GPS}$ are two samples of the independent population from two independent sensors.

Define the hypotheses,

- H0: There is no significant difference between the two distributions of the independent samples;
- H1: There is significant difference between the two distributions of the independent samples.

where [h, p, ks2stat] = kstest2($VPeakInterval^{Phone}_{MEMS,y}$, $VPeakInterval^{Phone}_{GPS}$), H = 1 indicates that K-S test rejects the null hypothesis in favor of the alternative hypothesis at the α significance level, p is the p-value of the hypothesis test, ks2stat is the value of the test statistic.

4 Experimental Verification

Using 2 sets of experimental data to verify the algorithm. The vehicle and smart phone for experiment are the ordinary taxi and HUAWEI smart phone. The phone is placed horizontally in the taxi. The coordinate system is shown in Fig. 1a, where the direction of Y axis and the vehicle are the same. The experiment time is around 16 clock in 2016.08.24 and 2016.09.05, as shown in Fig. 1b, c. Where the starting point and end point of the path in Fig. 1b is the same as that of Fig. 1c, but the driving path and the time of recording are different.

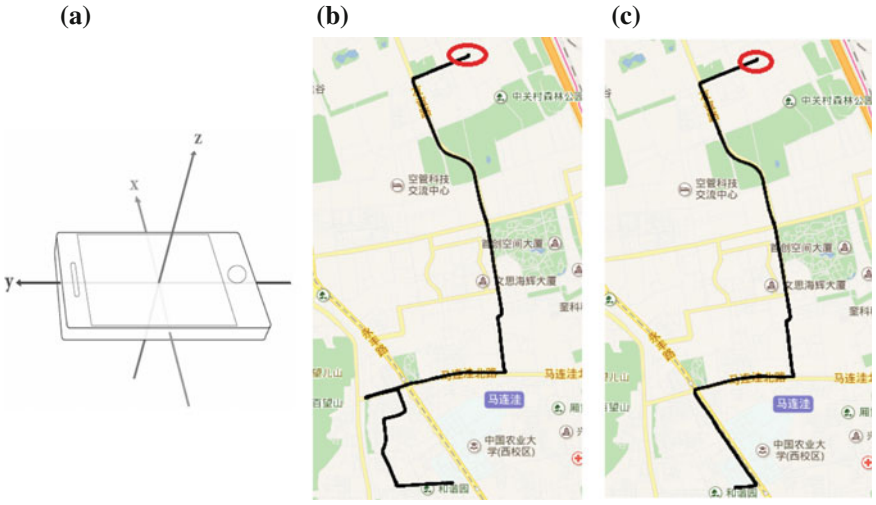

Fig. 1 Experiment illustration, **a** smartphone local coordinate system, **b** data 2016.08.24 16:05, **c** data 2016.09.05 15:45

4.1 Identification Without LBS Deception

Firstly, we verify the algorithm in the situation of no LBS deception. The speed estimated from GPS is obtained by the differential GPS position data of Fig. 1b and the DC component is removed. The speed estimated from accelerator of MEMS is obtained by the accumulated data of MEMS accelerometer of Y axis and the DC component is removed too. The speed curves estimated, and the corresponding peaks are as follows (Fig. 2).

As can be seen, the trends of the estimated speeds obtained by the GPS output positions and the MEMS accelerometer are roughly the same. However, there is a linear superposition trend in the speed estimated from accelerator data due to the accelerator cumulative error. In addition, there is a certain time delay caused by the Android system between the outputs of the GPS and the acceleration sensors, which makes it impossible to directly compare these two kinds of sensor outputs in the same physical quantity (speed). We will use the K-S test to identify the deception behavior, which is based on the statistics theory.

The probability distributions of the velocity peak intervals are obtained as follows (Fig. 3).

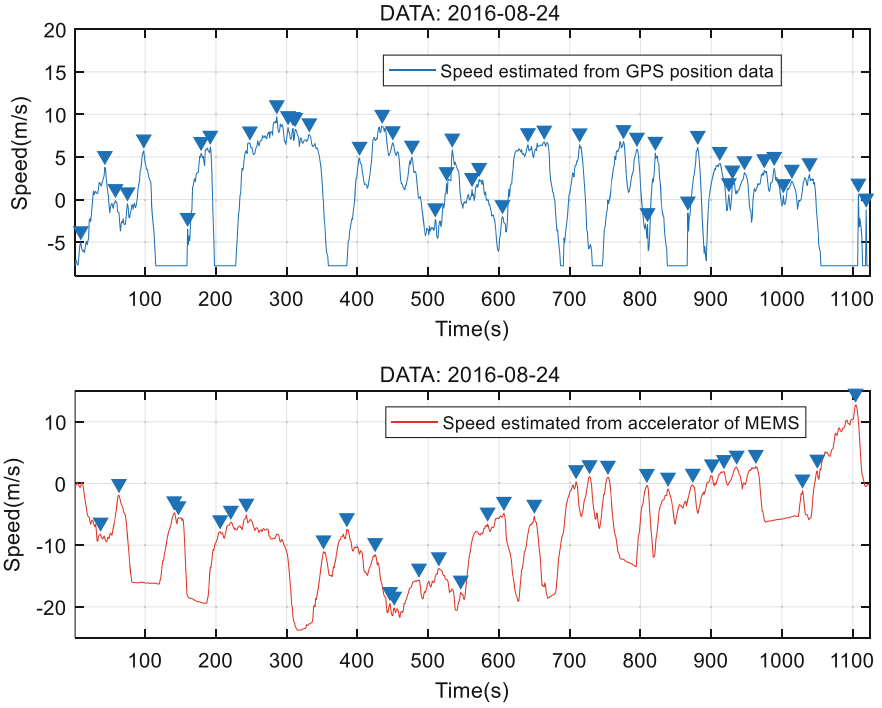

Fig. 2 The comparison of the speeds estimated from different sensors without LBS deception

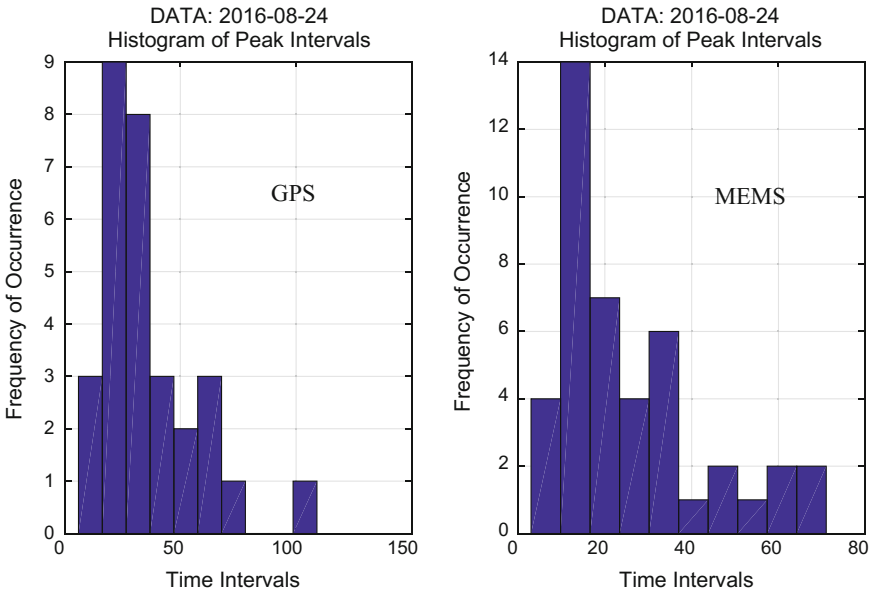

Fig. 3 The comparison of the distributions of velocity peak interval estimated from different sensors without LBS deception

Define the hypotheses,

H0: the distributions of velocity peak intervals obtained by the GPS and MEMS are the same;
H1: the distributions of velocity peak intervals obtained by the GPS and MEMS are not the same.

Finally, with the significance level alpha = 0.05, the two sample K-S test is used and the results are follows: h = 1, p = 0.0287, ks2stat = 0.3349. This shows that the hypothesis H0 can be accepted, that is, the distribution of velocity peak intervals obtained by GPS is the same as that obtained by the MEMS. It further shows that only a small probability of LBS deception exists.

4.2 Identification with LBS Deception

Usually, the lawless user directly makes the fake navigation path, however, this kind of deception is very easy to identify because the output of MEMS sensor of smart phone isn't consistent with that of GPS obviously. Here to increase the difficulty, we simulate the situation of the growth of navigation path maliciously by the lawless user for illegal economic profits. For example, instead of the real path data in Fig. 1c, the longer path in Fig. 1b is used. And they have the same starting

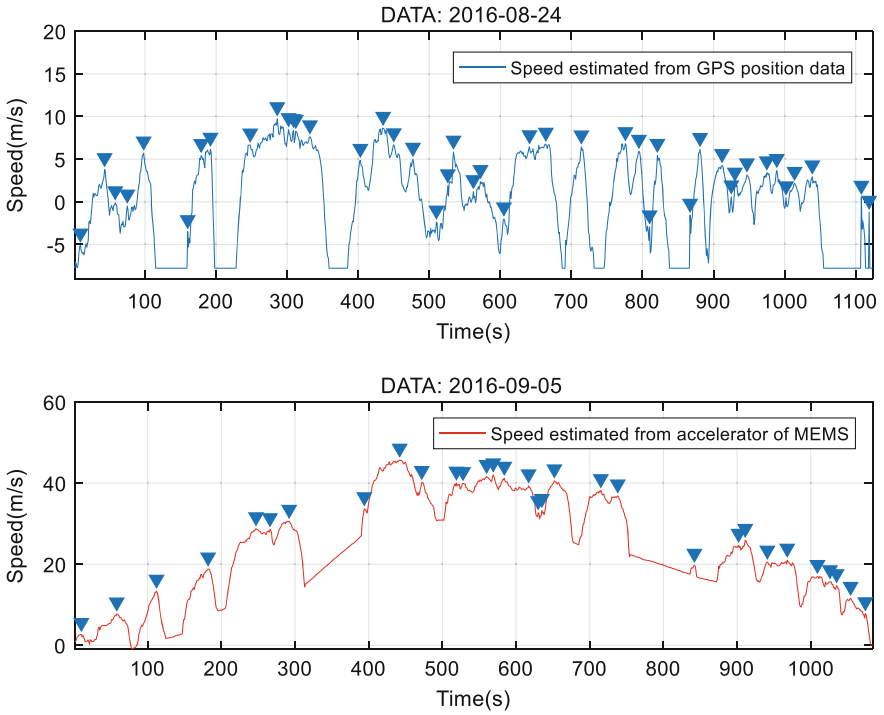

Fig. 4 The comparison of the speeds estimated from different sensors with LBS deception

and end points. The speed estimated from GPS is obtained by the differential GPS position data of Fig. 1b and the DC component is removed. The speed estimated from accelerator of MEMS is obtained by the accumulated data of MEMS accelerometer of Y axis and the DC component is removed too. The speed curves estimated, and the corresponding peaks are as follows (Fig. 4).

The probability distributions of the velocity peak intervals are obtained as follows (Fig. 5).

Define the hypotheses of H0 and H1 as above. Finally, with the significance level alpha = 0.05, the results obtained by the two sample K-S test are follows: h = 0, $p = 0.4112$, ks2stat = 0.2039. Furthermore, the null hypothesis could be rejected, which shows the distribution of velocity peak intervals obtained by GPS and MEMS does not follow the same distribution. There is a large probability of LBS deception existed.

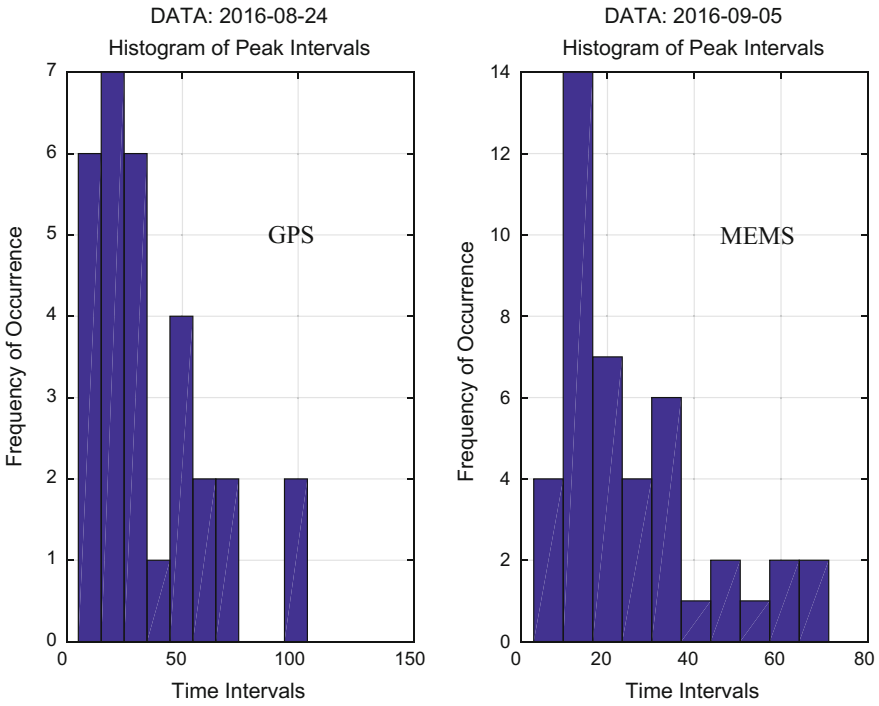

Fig. 5 The comparison of the distributions of velocity peak interval estimated from different sensors with LBS deception

5 Conclusion

Although many anti-jamming methods of navigation have been proposed by many scholars, the research hotspots are basically around the navigation receiver or other special equipments, and seldom consideration is given to the case of smart phone where the resources are limited. It makes the identification of LBS deception for smart phone become a promising and few people involved research direction. In this paper, under the constraints of the smart phone, the identification of LBS deception is achieved based on the speed information consistency of the sensors and the K-S test. It would help the healthy development of the LBS industry. In the future, more sensors will be considered to improve the security and reliability of LBS on smart phone.

References

1. Jian G. http://bjrb.bjd.com.cn/html/2015-10/10/content_317283.htm
2. Chengdu Economic Daily. http://sc.sina.com.cn/news/b/2016-03-14/detail-ifxqhmve9142025.shtml
3. Yi T et al (2013) Study of information security for location based services. Telecom Eng Tech Stand 2:38–42
4. Bo Q et al (2015) Review on location privacy protection research. J East China Normal Univ (Nat Sci) 5(9):14–27
5. Long H et al (2011) Anti-spoofing techniques for GNSS Receiver. Geomatics Inf Sci Wuhan Univ (Nat Sci) 11:1344–1347
6. Te H et al (2008) Assessing the spoofing threat development of a portable GPS civilian spoofer. In: Proceedings of the ION GNSS international technical meeting of the satellite division
7. Psiaki Ml et al (2011) Civilian GPS Spoofing detection based on dual receiver correlation of military signals. In: Proceedings of the institute of navigation GNSS, pp 20–23
8. Michelson WR et al (1995) Ensuring GPS navigation integrity using receiver autonomous integral monitoring. IEEE Aerosp Electron Syst Mag 10(10):31–34
9. Montgomery PY et al (2009) Receiver-autonomous spoofing detection: experimental results of a multi-antenna receiver defense against a portable civil GPS spoofer. In: Proceedings of the ION international technical meeting, pp 124–130
10. Wesson K et al (2012) Straight talk on anti-spoofing. GPS World 23(1):32–39
11. Chao T et al (2015) Research on GNSS civil navigation message encryption and authentication technology. Comput Simul 32(9)

iBeacon/WiFi Signal Characteristics Analysis for Indoor Positioning Using Mobile Phone

Ling Yang, Bofeng Li, Haojun Li and Yunzhong Shen

Abstract Mobile phone equipped with WiFi, Bluetooth, MEMS-IMU, and other sensors is a perfect platform to provide location based service for personal users. For positioning using wireless signals, the fingerprints of received signal strength (RSS) measurements from access points (APs) are typically used, which are called fingerprinting methods. The main characteristic of the fingerprint positioning technologies is to calculate the similarities between the observed RSS and the known RSS fingerprints. Compared with WiFi, the iBeacon APs are with lower cost, smaller size, and more flexible location, so it is much more suitable and economic for applications where enough WiFi APs are not available. In this paper, the RSS noise characteristics of iBeacon and WiFi signals are compared. The fingerprinting positioning performance by using iBeacon and WiFi RSS measurements are further presented and evaluated.

Keywords WiFi · iBeacon · Received signal strength · Fingerprint

1 Introduction

Accurate localization enables the system to provide location-based services, optimize network deployment, and improve the system's energy efficiency. Because of their locality, ubiquity, and low cost of deployment, radio frequency (RF)-based positioning techniques, typically based on WiFi, iBeacon, UWB, as well as the

L. Yang (✉) · B. Li · H. Li · Y. Shen
College of Surveying and Geo-Informatics,
Tongji University, Shanghai 200092, China
e-mail: ling_yangsy@163.com

L. Yang
Key Laboratory of Watershed Ecology and Geographical Environment
Monitoring NASG, Nanchang 330209, China

L. Yang
State Key Laboratory of Geodesy and Earth's Dynamics, Wuhan, China

J. Sun et al. (eds.), *China Satellite Navigation Conference (CSNC) 2017 Proceedings: Volume I*, Lecture Notes in Electrical Engineering 437,
DOI 10.1007/978-981-10-4588-2_35

mobile communication infrastructure, naturally arise as a set of methods of choice. With these wireless signals, indoor localization is done utilizing many different properties. Some techniques are based on such information as TOA (the time of arrival), TDOA (the time difference of arrival), and DOA (the direction of arrival). To mitigate the effects of the receiver's clock offset, multi-path and so on, multiple round-trip-time (RTT) is usually measured instead of TOA [6, 7]. While, there still exist some open problems in terms of large positioning latencies and the lack of scalability [4, 10]. Furthermore, the accurate coordinate of every access point (AP) must be provided in advance.

Compared with TOA, TDOA, DOA, the received signal strength (RSS) from the transmitter can be measured much easily. Therefore, several localization methodologies based on RSS measurements have been proposed and mainly classified into two groups of methods, trilateration and fingerprinting methods. In the trilateration approach a signal propagation model is used to convert the RSS to a distance measurement from AP to user device [1, 14]. With more than three APs, the mobile user's position can be determined in a manner similar to the traditional trilateration surveying method. While the accuracy of the distance estimated by direct RSS measurements severely decay in indoor environments, where signal are easily blocked by human bodies, walls or furniture, and so as to deteriorate the final positioning accuracy and stability [1]. The so-called fingerprinting method can achieve location with a few meters' accuracy in a typical building. Unlike the trilateration method, a fingerprint makes little use of the physical properties of the signals (e.g., various propagation models of such wireless signals). Instead it relies on the fundamental assumption that the RSS fingerprints vary continuously with location.

A fingerprint map associates each reference point (RP) to a characterization of the RSS of each AP visible at that location. Therefore it requires laborious human involvement in the training phase to build so-called fingerprint maps for each AP. In positioning phase, the RSS from visible APs are matched to the fingerprints to estimate the location. Typical matching algorithms include deterministic [5, 8] and probabilistic methods [12, 15]. Deterministic algorithms use a similarity metric to differentiate the online signal measurements and the fingerprint data. The target is located at the closest fingerprint location in signal space. Euclidean distance [5], or cosine similarity [8] have been implemented for signal comparison. Probabilistic algorithms are based on statistical inference between RSS measured during positioning phase and stored fingerprint. These algorithms find the target's location with the maximum likelihood by some probabilistic model reflecting the spatial RSS distribution [3, 18].

Although additional costs to the service provider are minimal based on existing network infrastructure (e.g. WiFi, mobile communication network), the iBeacon transmitter benefits from its low cost, portability, as well as easy maintainability, and can better fit for localization in specific environments where WiFi APs are not available or hard to set up such as underground parking, mine, subways and similar venues. In this paper, we mainly compare the performance of fingerprinting methods by using WiFi and iBeacon signals due to their different noise

characteristics. The paper is organized as follows. Firstly, the fundamental principle of fingerprinting positioning methods are introduced. Then the RSS noise characteristics of iBeacon and WiFi signals are analysed and compared. Next the fingerprinting positioning performance by using iBeacon and WiFi RSS measurements are presented and evaluated. Finally, the conclusion of the study are given.

2 Fingerprint-Based Positioning Principle

Fingerprint-based positioning methods utilize the attenuation property of the radio wave signal to estimate location of a mobile device. One common approach employs surveying of signal strength information in a particular area. This information forms a database describing the signal strength fingerprint of that area. The database is later used to determine the location of a mobile device by a particular pattern matching algorithm.

2.1 Propagation Model

The typical propagation model follows the distance power law [12, 19]:

$$RSS = A - 10 \cdot n \cdot \log_{10}(d) + \varepsilon \tag{1}$$

where *RSS* is the received signal strength in *dB* at a distance, *d*, from the transmitter; *A* is a constant depending on several factors: average fast and slow fading, transmitter gain, receiver gain, and the transmitter power. In practice, its value is usually known beforehand; *n* is the path loss exponent that depends highly on the specific channel environment presented between the transmitter and the mobile receiver. Usually, *n* can be assumed constant in an environment for a certain period of time [11]. ε is the shadow noise modeled as a Gaussian random variable with zero mean and, while standard deviation, σ_{RSS} depends on the characteristics of a specific multipath environment [16].

Expression (1) has been widely used to describe RSS values as a function of the distance between the transmitter and the receiver. Based on this formula, there are typically two classes of methods for location. One is to obtain the distance estimation from RSS values and then determine the receiver's location by trilateration method. The positioning accuracy of these methods mainly rely on determining the accurate value of *A* and *n*. The other class is the fingerprinting methods which rely on a fingerprint map with a table of signal strength receive at selected location (RPs) from the APs in the area of interest [3]. For fingerprinting methods, the variation of the RSS measurements is the crucial issue to limit the positioning accuracy. Usually, the RSS variance is explained as a result of multiplication of

large number of random attenuation factors in the radio channel [9]. The next section will analyze the RSS noise variation for WiFi and iBeacon signals.

2.2 Probabilistic Method for Positioning

In this work, we take use of the probabilistic models for the location estimation. For any given location l_i we can obtain a distribution $p(o_j/l_i)$, where o_j indicates the RSS value from the jth transmitter at the location l_i. By application of the Bayes rule, the so-called posterior distribution of the location can be obtained [15]:

$$p(l_i/o_j) = \frac{p(o_j/l_i)p(l_i)}{p(o_j)} = \frac{p(o_j/l_i)p(l_i)}{\sum_{l_k \in \boldsymbol{L}} p(o_j/l_k)p(l_k)} \tag{2}$$

where $p(l_*)$ is the prior probability of being at location l_*, and the summation goes over the set of possible location values, denoted by $\boldsymbol{L}$. The prior distribution of $p(l_*)$ principally should incorporate background information such as personal user profiles or implement tracking. It is proved that the assumption of $p(l_*)$ is only critical for environments where the number of APs deployed is limited and the heterogeneity of the environment is high [18]. A reasonable assumption by most of the current WLAN location determination systems is that all locations are equi-probable. In this case, $p(l_*) = 1/n$ and n is the number of the grid points in the fingerprint database. $p(o_j/l_i)$ is the likelihood function that means the probability of a certain RSS from the jth transmitter at the location l_i.

As can be seen from (2), the key issue in the probabilistic approach for positioning is to estimate the probability distributions of the measured signals o_j at different location l_i. It is usually estimated by a Gaussian distribution [2]:

$$p(o_j/l_i) = \frac{1}{\sqrt{2\pi}\sigma_{i,j}} e^{-\frac{(o_j-\mu_{i,j})^2}{2\sigma_{i,j}^2}} \quad i = 1, \ldots, n; j = 1, \ldots, m \tag{3}$$

where i is the indicator for each RP and j is the indicator for each AP. Each Gaussian distribution has a mean value μ and a standard deviation σ, which are calculated using sample data during the training and positioning phases.

Specifically, given a target RSS vector $\boldsymbol{o} = (o_1, \ldots, o_m)$ and m APs, the estimated location is the one which obtains the maximum value of the posterior probability [13]:

$$l^* = \arg\max_{\boldsymbol{L}} p(l/\boldsymbol{o}) \tag{4}$$

where $p(l/\boldsymbol{o})$ is the probability of the target at location l given signals $\boldsymbol{o}$. It can be further transformed into this form:

$$\arg\max_{\boldsymbol{L}} p(l/\boldsymbol{o}) = \arg\max_{\boldsymbol{L}} \left[\prod_{j=1}^{m} p(o_j/l) \right] \tag{5}$$

where $p(o_j/l)$ can be approximated by some parametric distributions including Gaussian distribution as (3).

3 RSS Noise Characteristics of iBeacon and WiFi Signals

Although the RSS measurement varies noticeably with the distance between the transmitter and the receiver, location accuracy using the RSS measurement still highly depends on the noisy characteristics of the signal. In this section, the noise characteristics of the RSS measurements from iBeacon and WiFi transmitters are analyzed.

Both iBeacon and WiFi signal strengths were performed. The iBeacon devices are low cost and power conserved, with longest service distance around 30 m. A battery of 1000 mAh can provide service for 66 days with a frequency of 10 Hz and for nearly 600 days with a frequency of 1 Hz (http://www.aprbrother.com/). The WiFi transmitters used were initially installed at each office, and may from different manufacturers. For experiments in this paper, data from six iBeacon APs and six WiFi APs were collected with a frequency of 10 Hz by a Huawei Rongyao 8 smartphone for positioning.

3.1 Sampling Rate

Firstly, the effects of reducing the sampling time N_s were analyzed with the APs mounted at the same distance to the mobile receiver. To reducing the influence of shadow fading, the data was firstly collected under stable environment at office Room 513 of College of Surveying and Geo-informatics, Tongji University. The sampling time N_s = 10 s, 20 s, 30 s and 40 s are tested. The cumulative distribution function (CDF) for two iBeacon APs are shown in Fig. 1. Signals from other four iBeacon APs show similar characteristics and therefore not presented here. It shows that the CDFs of the RSS are coincident when the sampling time spans increase from 10 to 40 s. While the variation amplitudes of the RSS may be larger than 20 dB, although they do not increase during longer sampling periods.

The RSS CDFs from two WiFi APs are shown in Fig. 2. Compared with the iBeacon signals RSS from the WiFi APs concentrate within a smaller interval. Similarly, RSS distributions obtained by different sampling time periods do not show significant differences. That means 10 s data would be enough to ensure the stability.

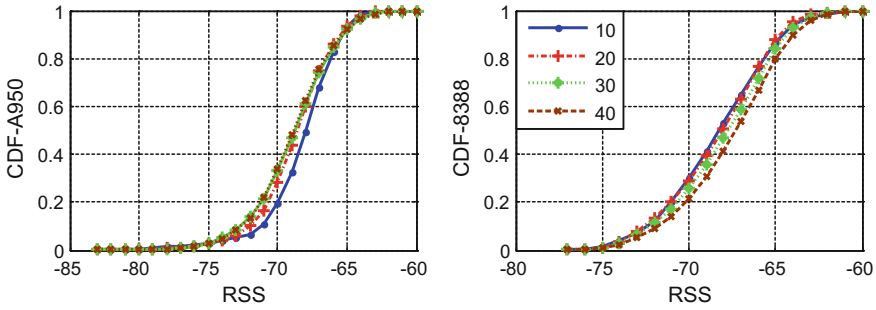

Fig. 1 CDF for iBeacon signals with different sampling time span

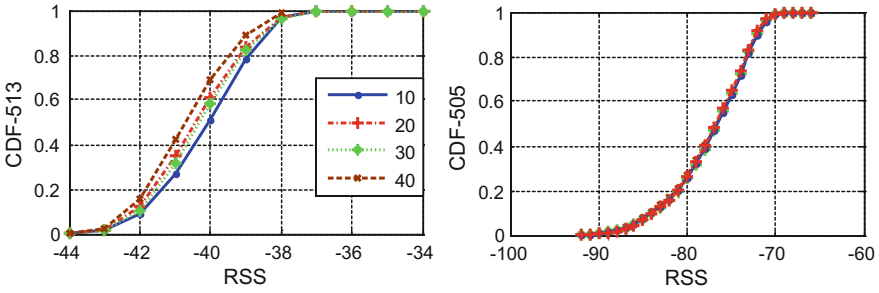

Fig. 2 CDF for WiFi signals with different sampling time span

For further comparison, the RSS deviation intervals for iBeacon and WiFi APs with 90% confidence level are shown in Table 1. It shows that the deviations for iBeacon signals reach 10 dB although the environment keeps stable. Comparably the fluctuations of WiFi signals are much gentle. To obtain a reliable evaluation, RSS from six iBeacon APs and six WiFi APs are collected during six time periods, and each period last for an hour with a sampling rate of 10 Hz. In general, the stability of WiFi signals are 50% better than the iBeacon signals. In next subsection, the positioning accuracy and reliability influenced by the data stability are analyzed and assessed.

3.2 RSS Tendency and Deviation

For fingerprinting methods, a database with RSS properties at each AP should be firstly built. The precision of the database largely depends on the divergences of the signal strength at different RPS. To analyze the RSS deviation characteristics for both WiFi and iBeacon signals at each RPs, the experiment were carried out at the 5th floor of the College of Surveying and Geo-informatics Building. Six iBeacon

Table 1 RSS deviation region with 90% confidence level (iBeacon APs: A930, 837E, A950, 8388; WiFi APs: R517, R513, R505, R506)

APs	Sampling time			
	10 s	20 s	30 s	40 s
A930	(−66, −58)	(−65, −58)	(−5, −59)	(−65, −58)
837E	(−69, −60)	(−68, −59)	(−68, −59)	(−67, −59)
A950	(−73, −64)	(−73, −64)	(−74, −64)	(−73, −64)
8388	(−73, −63)	(−73, −64)	(−73, −63)	(−73, −63)
R517	(−53, −49)	(−53, −49)	(−53, −48)	(−53, −48)
R513	(−42, −39)	(−42, −39)	(−42, −39)	(−42, −39)
R505	(−87, −71)	(−87, −71)	(−87, −72)	(−87, −72)
R506	(−87, −74)	(−87, −74)	(−88, −75)	(−88, −76)

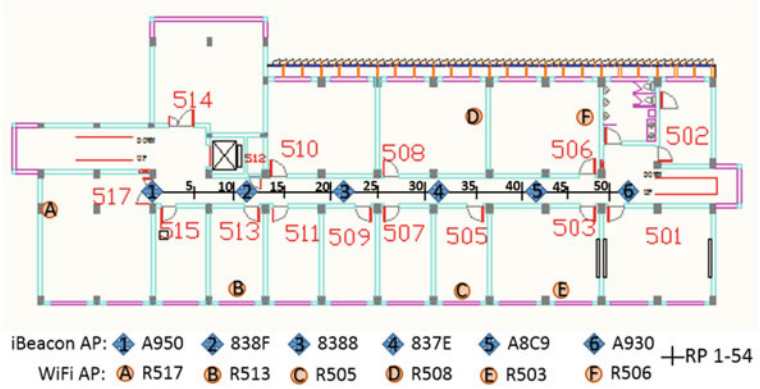

Fig. 3 Experiment layout with WiFi and iBeacon APs and RPs

and six WiFi transmitters covering the office area were used. During the training phase, 54 RPs with a grid size of 0.6 m were initially selected to form the fingerprint database. The building layout and the location of APs and RPs are shown in Fig. 3.

Figure 3 shows that the six iBeacon APs are uniformly distributed along the corridor, while the location of the WiFi APs are previously determined by the users at these offices. To analyze the RSS variations along with locations, the RSS values and standard deviations (STD) from different APs at each RP are shown in Fig. 4 for iBeacon signals and are shown in Fig. 5 for WiFi signals. In each figure, the red dot markers denote the mean value of RSS measured at the RP, the blue and green line with circle markers denote the RSS deviation interval, and the black line denotes the reciprocal of the distance from each RP to the AP.

In Fig. 4, RSS from 4 iBeacon APs are presented, with AP A950 and A930 mounted at the end of the corridor and AP 8388 and 837E mounted at the middle of the corridor. We can see that the RSS is proportional to the reciprocal of the distance between the AP and the RP. The AP 8388 was mounted above the RP 21,

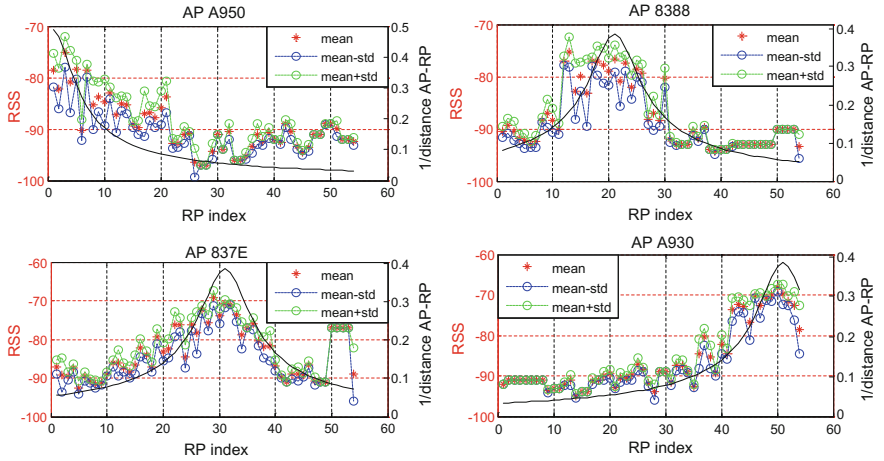

Fig. 4 RSS at each RP from iBeacon APs

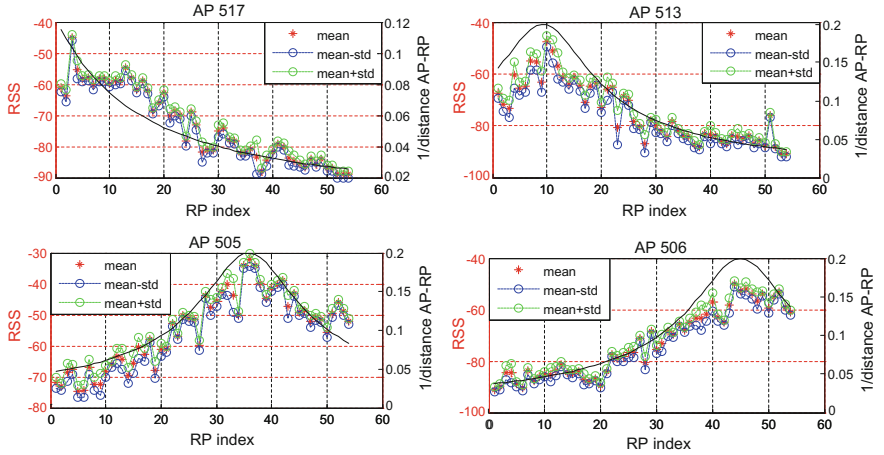

Fig. 5 RSS at each RP from WiFi APs

as a result the RSS value is the largest around the nearest locations. However, it also shows that the RSS mean and STD values between some of the two adjacent RPs do not show significant divergences. That unavoidably introduces positioning uncertainty among adjacent RPs, which actually indicates that denser RPs may not work for higher positioning accuracy. Therefore, the proper density of the fingerprint database should rely on the specific characteristics of the signal from different

Table 2 RSS mean and STD values of iBeacon/WiFi signals at 4 RPs (mean, STD)

AP	RP index			
	10th	20th	30th	40th
A950	(*−84, 4.48*)	(−86, 3.24)	(−91, 0)	(−92, 0)
8388	(−88, 2.32)	(*−79, 2.60*)	(−80, 1.79)	(−94, 0)
837E	(−89, 0.50)	(−83, 2.30)	(*−74, 1.91*)	(−87, 1.47)
A930	(−93, 0)	(−89, 1.03)	(−89, 0)	(*−82, 2.44*)
R517	(*−60 ,1*)	(−63, 1)	(−75, 2)	(−82, 1)
R513	(*−46, 2.2*)	(−72, 1.9)	(−80, 2.5)	(−83, 3.4)
R505	(−68, 1.9)	(−61, 2.1)	(−46, 1.5)	(*−41, 1.2*)
R506	(−85, 1)	(−89, 1)	(−76, 1.5)	(*−57, 3.5*)

types of APs. As shown in Fig. 4, it is concluded that a 0.6 m grid size seems to be over denser for the iBeacon transmitters we used. To shorten the expression, the similar results from AP 8388 and A8C9 are not given here.

Comparably, the RSS mean and STD values at each RPs from 4 WiFi APs are shown in Fig. 5. Similar properties as the iBeacon signals are shown in the figure. The closer the distance between the RP and the AP, the stronger the signal strength. While, the RSS interval bounded by the STD values shows that the WiFi signals are much more stable than the iBeacon signals, which means the signals divergences from WiFi APs among adjacent RPs are much more significant, so as to provide higher positioning accuracy. Also the RSS of WiFi signals are generally stronger than the iBeacon signals. The highest RSS for WiFi signals reaches −30 dB when the RP are closest to the AP, while for iBeacon signals the highest values are just around −60 dB. Generally, the RSS lower than −92 dB is considered as invalid. Therefore, the valid RSS region length of WiFi signals is double as that of iBeacon signals.

To further compare the deviation of the iBeacon and WiFi signals, the RSS mean and STD values at 4 RPs are listed in Table 2. The values with closest distance between the RP and AP are marked by italic. We can see that for iBeacon signals the distance not only influence the RSS measurements, but also influence the fluctuation of the signals at different RPs. Generally, the user can receive stronger signal if the distance to the AP is shorter, but the signal deviation is also enlarged, which means the stability of the signals decays as the receiver goes closer to the AP. For signals from AP A950, the RSS at the 10th RP is the highest while the STD is also the largest. For AP 8388 the closest RP is the 20th, and the RSS deviation at this point is also the largest. Similar conclusions can also be drawn from the data of other iBeacon APs. However, for WiFi signals the distance's impacts on the RSS STD are much smaller and do not show obvious significance. Totally, the STD value of RSS received at most WiFi RPs are around 2.

4 Positioning Performance Evaluation

Above analysis may indicate that under the same condition the positioning performance by using iBeacon signals would be worse than that of using WiFi signals. In this section, the positioning accuracy and stability are compared and evaluated. To estimate the positioning accuracy, 600 samples of iBeacon and WiFi RSS measurements are collected at each RP respectively. The mean values of the positioning errors at each AP are shown in Fig. 6, with dot line for the iBeacon and solid line for the WiFi signals. The cumulative distribution function (CDF) of the total position errors are shown in Fig. 7, also with dot line for the iBeacon and solid line for the WiFi signals.

Figure 6 shows that the positioning errors by using WiFi are generally smaller than the errors by using iBeacon APs. For iBeacon, the positioning errors are generally varied with the distances between the RPs to the APs. The positioning errors are usually larger at the points between two adjacent APs and reduce as the receiver moving close to one AP. While the WiFi positioning shows better stability

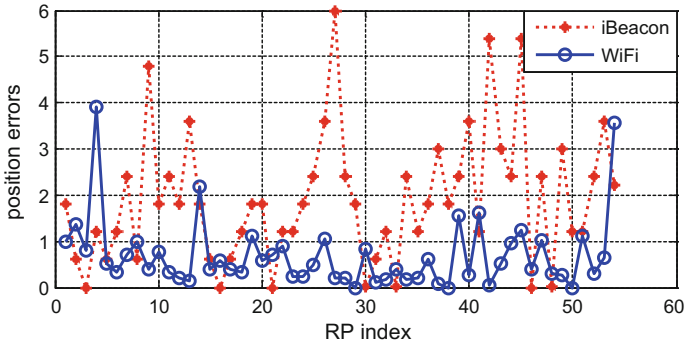

Fig. 6 Position errors on RPs using iBeacons/WiFi

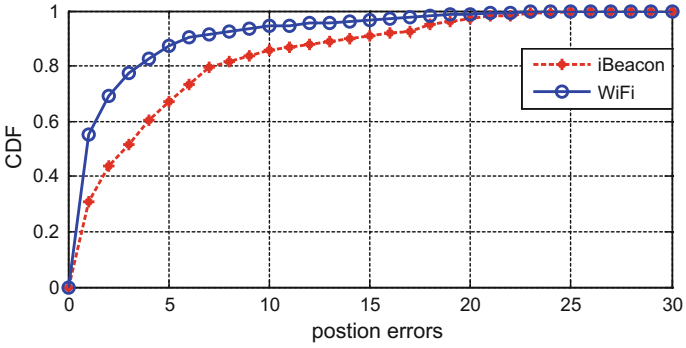

Fig. 7 CDF of the position errors

with comparable error magnitudes on each of the corridor RPs, except for slightly larger errors at some points which are near the two sides. Figure 7 further shows that 70% of the WiFi positioning errors are less than 2 m, while only 40% of the iBeacon positioning errors are within this threshold. When the error threshold enlarges to 5 m, the possibility for WiFi goes up to around 90% and the possibility for iBeacon is less than 70%. Generally, with the same number of APs used, the WiFi positioning accuracy and stability are better than the iBeacon we used here.

5 Conclusions

This paper presented the fingerprinting algorithms for indoor wireless positioning, typically using WiFi and iBeacon signals. The RSS noise characteristics of the iBeacon and WiFi signals are compared. Generally, the WiFi signals are much more stable compare with the iBeacon signals. In terms of the signal variation at a stationary point, the standard deviation of WiFi RSS shows little dependence on the distance between the receiver and the transmitter. While for iBeacon signals, the RSS standard deviation at the point closer to the transmitter is larger which further increases the positioning uncertainty. The evaluation of the positioning accuracy of iBeacon and WiFi are coincident with previous analysis. Generally, with the same number of APs, the WiFi positioning accuracy is higher than that of the iBeacon. The iBeacon devices used here are not specifically designed for positioning function and are without any beforehand calibration procedure. Further study will focus on the calibration algorithms and the improved fingerprinting algorithms for the iBeacon signals.

Acknowledgements This work is supported by the National Natural Science Funds of China (41504022), the Key Laboratory of Watershed Ecology and Geographical Environment Monitoring, NASG (WE2015001), the State Key Laboratory of Geodesy and Earth's Dynamics (SKLGED2016-3-3-E), and the Key Laboratory of Advanced Engineering Surveying of NASMG (TJES1501).

References

1. Akyildiz IF, Sun Z, Vuran MC (2009) Signal propagation techniques for wireless underground communication networks. Physical Communication 2(3):167–183
2. Bose A, Foh CH (2007) A practical path loss model for indoor WiFi positioning enhancement. International Conference on Information, Communications and Signal Processing
3. Chai X, Yang Q (2007) Reducing the calibration effort for probabilistic indoor location estimation. IEEE Transactions on Mobile Computing 6(6):649–662
4. Ciurana M, Barcelo-Arroyo F, Llombart M (2009) Improving the performance of TOA over wireless systems to track mobile targets. IEEE International Conference on Communications Workshops, 2009. ICC Workshops. 2009:1–6

5. Feng C, Au WSA, Valaee S et al (2012) Received-signal-strength-based indoor positioning using compressive sensing. IEEE Transactions on Mobile Computing 11(12):1983–1993
6. Günther A, Hoene C (2005) Measuring Round Trip Times to Determine the Distance Between WLAN Nodes. Springer 2005:768–779
7. Hoene C, Willmann J (2008) Four-way TOA and software-based trilateration of IEEE 802.11 devices. IEEE, International Symposium on Personal, Indoor and Mobile Radio Communications. 2008:1–6
8. He S, Chan SHG (2014) Sectjunction: wi-fi indoor localization based on junction of signal sectors. IEEE ICC 2014—Mobile and Wireless Networking Symposium. 2014:2605–2610
9. Laitinen H, Juurakko S, Lahti T et al (2007) Experimental evaluation of location methods based on signal-strength measurements. IEEE Transactions on Vehicular Technology, 56 (1):287–296
10. Llombart M, Ciurana M, Barcelo-Arroyo F (2008) On the scalability of a novel WLAN positioning system based on time of arrival measurements. The Workshop on Positioning, Navigation & Communication. 2008:15–21
11. Li X (2006) RSS-based location estimation with unknown pathloss model. IEEE Transactions on Wireless Communications 5(12):3626–3633
12. Mazuelas S, Bahillo A, Lorenzo RM et al (2009) Robust indoor positioning provided by real-time RSSI values in unmodified WLAN networks. IEEE J Selected Topics in Signal Processing 3(5):821–831
13. Mirowski P, Milioris D, Whiting P et al (2014) Probabilistic radio-frequency fingerprinting and localization on the run. Bell Labs Technical J 18(4):111–133
14. Motley AJ (1988) Personal communication radio coverage in buildings at 900 MHz and 1700 MHz. Electronics Letters 24(12):763–764
15. Roos T, Myllymäki P, Tirri H et al (2002) A probabilistic approach to WLAN user location estimation. International J Wireless Information Networks, 2002, 9(3):155–164
16. Salo J, Vuokko L, El-Sallabi H M et al (2007) An additive model as a physical basis for shadow fading. IEEE Transactions on Vehicular Technology 56(1):13–26
17. Wang H, Wang C, Wang JX et al (2014) Global characteristics of the second-order ionospheric delay error using inversion of electron density prfiles from COSMIC occultation data. Sci China-Phys Mech Astron 57: 365–374
18. Youssef MA, Agrawala A (2007) Analysis of the optimal strategy for WLAN location determination systems. International J Modelling Simulation 27(1):53–59
19. Zhuang Y, El-Sheimy N (2016) Tightly-Coupled Integration of WiFi and MEMS Sensors on Handheld Devices for Indoor Pedestrian Navigation. IEEE Sensors J 16(1)

Research on Signal Design Method of Pseudolite "Near-Far Effect" Based on TDMA Technique

Xu Liu

Abstract The Global Navigation Satellite System (GNSS) provides comprehensive and instantaneous positioning information for human life and production, causing huge changes in various industries and fields. However, in practical application, it is obvious that the accuracy of GNSS cannot meet all industry requirements. The integrity, reliability and continuity of GNSS are seriously affected by the satellite distribution. In some special locales, such as basement, indoors, open mines and tunnels, GNSS often cannot offer correct positioning information; furthermore, it doesn't function at all. The requirements of high accuracy and good reliability promote the proposition and development of pseudolite. There are many problems to be solved in pseudolite application, such as multipath effect, time synchronization and near-far effect. In this paper, we study how to solve the near-far effect. In short, the near-far effect is the large difference in the received signal power caused by the difference in the distance between the orbiting satellites, pseudolites and receivers. We choose TDMA technique to design pseudolite pulse signal, after analysing the existing three methods TDMA, FDMA and CDMA techniques' advantages and disadvantages. A 10% duty cycle hopping sequence pulse method is proposed by using RTCA and RTCM pulse mode for reference. In MATLAB simulation environment, the pulsed signal acquisition method based on the segmented FFT is used to achieve pulsed signal acquisition simulation in the case of different SNR (signal to noise ratio) of pseudolites. And then, the closed-loop delay based on the lead-lag half symbol and the three-order phase-locked loop (PLL) assisted by second-order frequency-locked loop (FLL) are used to achieve pulsed signal tracking simulation in the case of different SNR. The simulation results show that the design of pseudolite pulsed signal can overcome the near-far effect.

Keywords Pseudolite · Near-far effect · Pulse · Acquisition · Tracking

X. Liu (✉)
Beijing Satellite Navigation Center, Beijing, China
e-mail: liuxae@126.com

J. Sun et al. (eds.), *China Satellite Navigation Conference (CSNC) 2017 Proceedings: Volume I*, Lecture Notes in Electrical Engineering 437,
DOI 10.1007/978-981-10-4588-2_36

1 Introduction

Nowadays, global positioning and navigation systems such as GPS, GLONASS and Compass have played an increasingly important role in the measurement, geodesic and navigation industries. However, the availability, integrity and accuracy of GNSS are limited by the geometric layout of the satellite and the number of visible satellites. In some extreme environments such as canyons, tunnels, indoors and underground, the normal GNSS satellite positioning accuracy is very low, and may not even function. This problem can be solved by the introduction of pseudolite [2].

Pseudolite was proposed in 70s of the last century, of which essence is the ground signal transmitter. The application of pseudolite will enhance the availability, integrity, stability and measurement accuracy of the whole system. However, there are many problems existing in the development of the pseudolite, such as near-far effect, multipath effect and time synchronization. In this paper, we will explore how to solve the near-far effect of pseudolite by signal design.

2 Overview of the Near-Far Effect

Figure 1 shows a schematic diagram of the near-far effect. The near area means the signal strength of pseudolite is large enough to interfere with the GNSS signal within a certain distance. The far area signifies the pseudolite signal is weak and cannot be tracked. Therefore, the receiver's normal operating area should be in the middle of the near and far areas, which is able to receive both pseudolite signals and satellite signals [7].

Pseudolites can be applied to assist GNSS, or be used for positioning alone. Here are several commonly used methods to solve the near-far effect (taking GPS system for example):

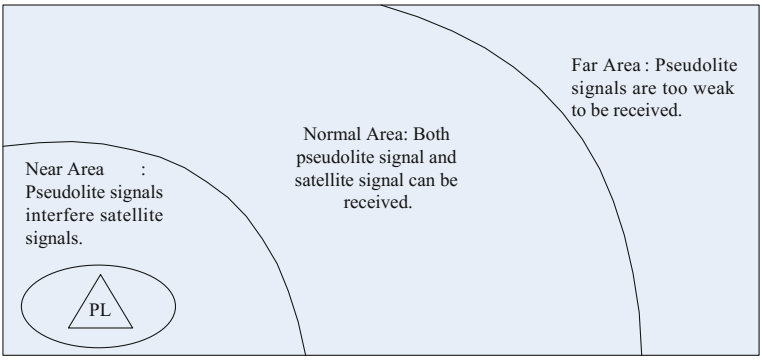

Fig. 1 Diagram: Near-far effect of pseudolite

(1) CDMA (Code Division Multiple Access) Technique

The C/A codes used in GPS signals are series of pseudo-random codes with good orthogonality. Different orbiting satellites are modulated by different C/A codes, and the orthogonality of codes can be used to separate signals. It is shown that the maximum orthogonality of the codes can be separated by 25 dB, which cannot meet the requirement of high dynamic range of pseudolites. Assuming a dynamic range of 60 dB, a pseudo-random code of 25 MHz or more is required [7]. This is a challenge for receiver compatibility, which will significantly increase the development cost of the receiver and is not easily implemented in hardware.

(2) FDMA (Frequency Division Multiple Access) Technique

After the signal is modulated by C/A code, it becomes a spreading spectrum signal, which occupies a large bandwidth. However, there are many frequency points which do not emit energy and are distributed on both sides of the carrier. The pseudolite can follow certain ways to emit signals in the higher and lower two zero jump. Different jump mode stands for different pseudolite, in order to eliminate or weaken near-far effect [2]. However, the GPS and the pseudolite signal enter the receiver through different channels, and the resulting inter-channel delay needs fine control, which will increase the cost of the receiver.

(3) TDMA (Time Division Multiple Access) Technique

TDMA technique is to divide the time into many time slots. These time slots do not affect each other, transmitting different signals on each one. This technique requires strict synchronization of time, otherwise it is likely to cause the signal confusion due to receiver's asynchronous signals [5].

The duty cycle is the ratio of the signal transmission time to the total transmission time. The use of low-duty-cycle pulses can reduce the interference of satellite signals. But the lower the duty cycle is, the greater the difficulty of the receiver to acquire and track will be. So we should weigh these two factors to choose the appropriate duty cycle [5]. Pseudolites use TDMA technique to transmit pulse signals. Different pseudolites are launched at different times, which can counteract the near-far effect, and the design cost gets very low.

Considering the cost and complexity of the development, the TDMA technique is very attractive and feasible in the three techniques. Therefore, this paper intends to use TDMA technique to design the pseudolite signal structure.

3 Signal Structure Design Based on TDMA

We need to consider the following parameters when TDMA technique is used to design the pseudolite signals:

(1) Spreading Code

The spreading code is the pseudo-random code used in the modulated signal. As in the case of pseudo-random codes in orbiting satellites, the autocorrelation and cross-correlation of the spreading codes are very important and need to be carefully chosen [6]. We select spreading code in GPS pseudo-random code family when we design GPS pseudolite.

(2) Pulse Duty Cycle

Pulse duty cycle is the most important parameter in pulse design.

(3) Pulse Position

If the position of the pulse in each cycle is the same, a new spectrum peak appears on the spectrum, and the receiver may erroneously lock to this spectral peak. Therefore, the location of the pulse needs to change randomly, which will reduce the probability of different pseudolite pulses' collision [1].

(4) Number of Pseudolites

In practical applications, there are many cases of simultaneous use of pseudo-lites. At this point the increase of duty cycle will lead to the decrease of the received power of orbiting satellite, and the pulses may also be a collision. The pulse duty cycle and the number of pseudolites are mutually constrained, which should weigh the consideration.

There are two kinds of pulse signal design schemes, RTCM [1] and RTCA [4]. Based on these two methods, this paper proposes a new pulse mode of 10% duty cycle, assuming up to 10 pseudolites used at the same time.

The used spreading code is the C/A code of 10.23 MHz, and the basic format of the pulse signal is the same as the orbit satellite signal. Each of the 10 base stations in the sub-network according to the design of the time hopping sequence, transmits signal in the corresponding time slot, which can ensure that each time slot only one base station transmit pulse signal.

In order to facilitate the rapid synchronization of the receiver and save storage space, ten time-hopping sequences can be obtained according to a 10×10 matrix, as shown in Table 1. The base station A1 corresponds to the first column, that is, 3, 9, 8, 5, 7, 6, 4, 2, 1, 10, then the 3rd, 9th,…, and 4th columns are sequentially taken out from the generation matrix and a length of 100 time-hopping sequence is obtained. The hopping sequences of the remaining base stations can be obtained in a same way.

When the pulse signal is transmitted, the pseudolites transmit signals according to the time slot number corresponding to the time hopping sequence. For example, in the first sub-frame, the base station A1 transmits a signal in the tenth slot, and the base station A2 transmits a signal in the ninth slot; in the second sub-frame, A1 transmits a signal in the eighth slot, A2 transmits the signal in the 10th time slot… And so on. The acquisition module of the receiver can be converted into a time slot

Table 1 Generating matrix of time hopping sequence

A1	A2	A3	A4	A5	A6	A7	A8	A9	A10
3	7	10	1	6	2	9	5	4	8
9	3	8	2	5	4	10	1	6	7
8	10	3	6	2	5	7	4	1	9
5	6	2	3	8	9	1	7	10	4
7	8	9	5	4	1	3	6	2	10
6	4	1	7	10	3	5	8	9	2
4	2	5	8	9	7	6	10	3	1
2	1	6	10	3	8	4	9	7	5
1	5	4	9	7	10	2	3	8	6
10	9	7	4	1	6	8	2	5	3

number according to the captured code phase, and the synchronization of the time hopping sequence is completed.

The rest of this paper will verify the feasibility of the signal designed above.

4 Simulation Analysis

4.1 Acquisition Method

The basic principle of signal acquisition is correlation. In this paper, the code phase parallel search is considered to improve the efficiency. Figure 2 is a module of segmented FFT pulse acquisition, where the segmented FFT acquisition method is summarized as follows [8]:

(1) Cache the data, and supply zero according to the length of the set segment, (if necessary), then perform FFT on each segment to get$\{Y_k\}$;
(2) Supply zero to the local pseudo-random code, perform FFT and take conjugate to get C^*;
(3) Calculate the result of $\{Y_kC^*\}$ and perform IFFT. Determine the threshold V_T in advance. It is proved that the pulse signal exists in the segment if $F^{-1}(Y_kC^*) \geq V_T$, and then the relative position of pulse is obtained according to the position of the peak.

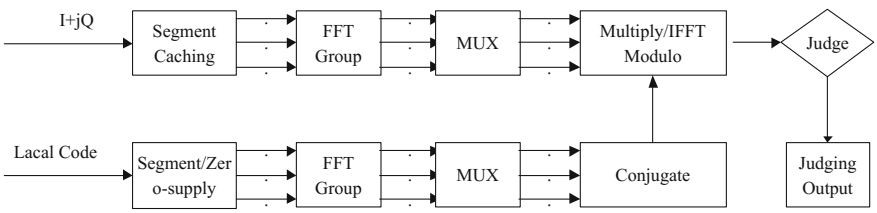

Fig. 2 Module: system result of standard experiment

4.2 Tracking Method

The code phase and carrier frequency of the pseudolite signal obtained by the acquisition will change due to external factors and need to be accurately determined by tracking. Tracking these two parameters requires code tracking loop and carrier tracking loop according to the principle of phase-locked loop (PLL). The code tracking loop adopts DLL (lead-lag delay locked loop), and the carrier tracking loop adopts third-order phase-locked loop assisted with second-order frequency-locked loop (PLL3FLL2) [3].

4.3 Simulation Parameters

The pseudolite signal duty cycle is 10%, the center frequency is 45.42 MHz, the code rate of C/A code is 10.23 MHz, and the sampling rate is 62 MHz. According to the time sequence of A1 and A2 of the base station in Table 1, the length of the signal segment is 10 ms.

4.4 Acquisition Simulation Examples

Simulation I: The signal-to-noise ratio (SNR) of a single pseudolite is −60 and −90 dB, Doppler frequency shift is 0, and the simulation results of a 10 ms signal are shown in Figs. 3 and 4. As can be seen from Fig. 4, a certain range of SNR decreasing will not affect the pulse acquisition.

Simulation II: The SNR of a signal pseudolite is −60 dB, Doppler frequency shift is 300–400 Hz and time-hopping sequence is set as the base station A2. The Doppler frequency shift is assumed to be 0, followed by the simulation I to perform acquisition and then do a local two-dimensional search in the vicinity and a certain width of the acquired code phases, which can improve the efficiency, and the results are shown in Fig. 5 and Table 2:

The actual Doppler frequency shift is 300–400 Hz, and the local search Doppler frequency shift average is 300 Hz, which can be used for accurate tracking. In the simulation, the step size is 250 Hz that can be reduced to improve the accuracy in practice.

Simulation III: The SNR difference of two pseudolites is 60 dB. Figure 6 shows the signals amplitude, Fig. 7 shows the result of acquisition of the No. 1 pseudolite (Al sequence), Fig. 8 shows the result of acquisition of the No. 2 pseudo-satellite (A2 sequence), and Fig. 9 shows the acquisition result of the A2 sequence using the improved method.

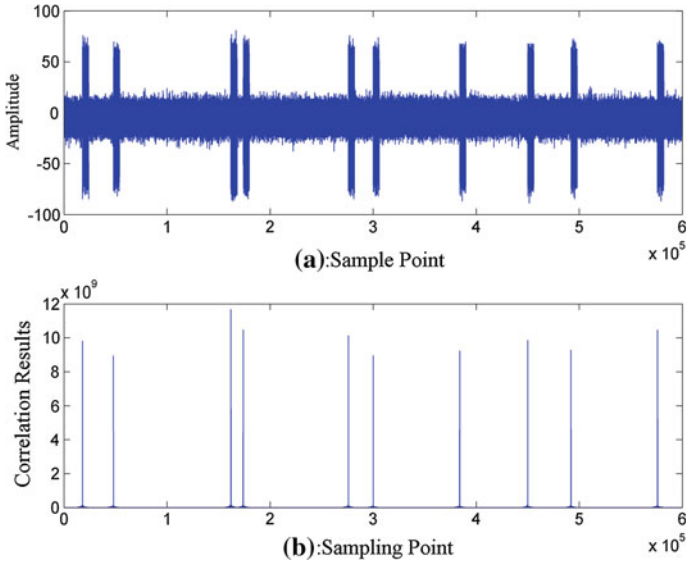

Fig. 3 **a** Single pseudolite pulse signal of SNR −60 dB. **b** Acquisition correlation results

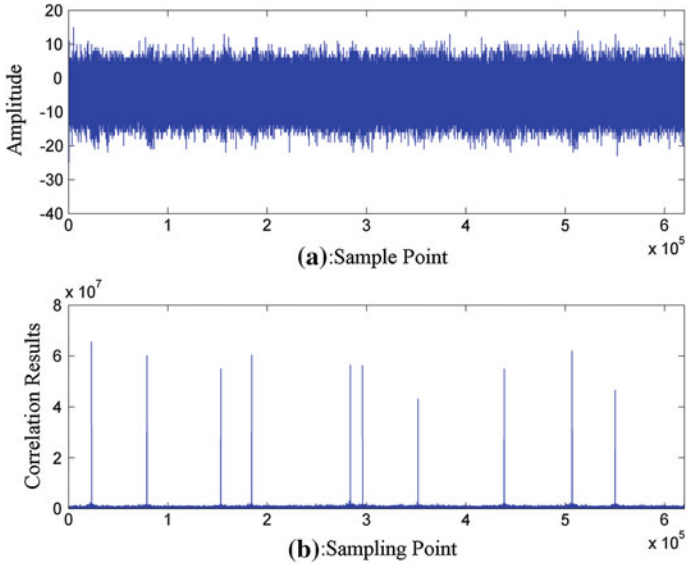

Fig. 4 **a** Single pseudolite pulse signal of SNR −90 dB. **b** Acquisition correlation results

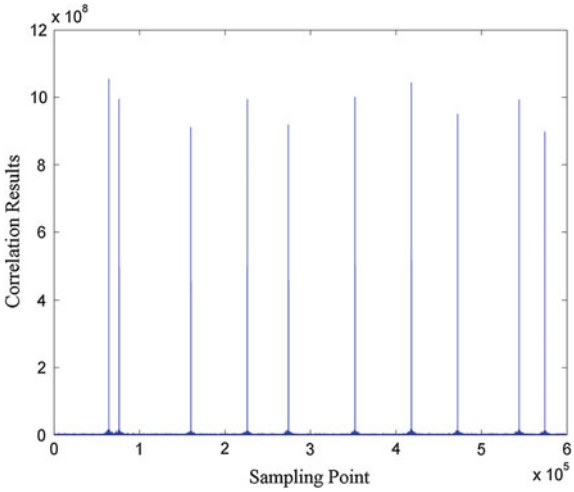

Fig. 5 Code phase searching result assuming zero doppler frequency

Table 2 Doppler frequency of pulses after local search (Unit: Hz)

Number	1	2	3	4	5	6	7	8	9	10
Frequency offset	250	250	250	500	500	250	250	250	250	250

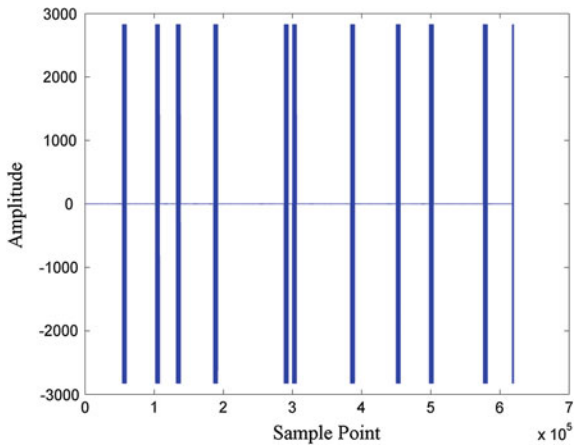

Fig. 6 Signals with 60 dB power difference

In order to overcome the interference caused by strong signal for weak signal, Fig. 9 sets the strong signal acquisitioned to zero in the corresponding time slot, and then acquisition the next signal, when the correlation peaks separate and weak signal is acquired successfully.

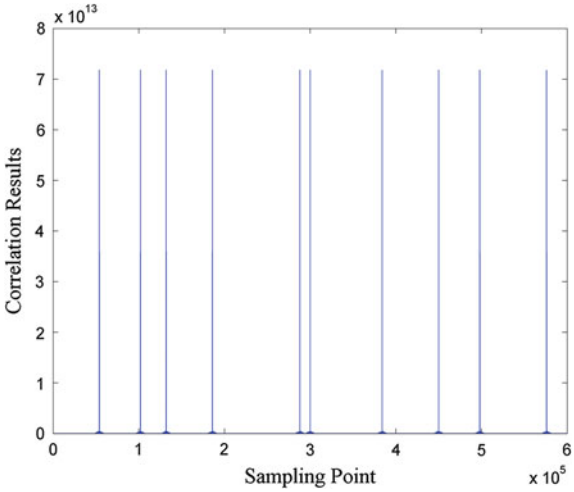

Fig. 7 PRN1 pseudolite signal acquisition result

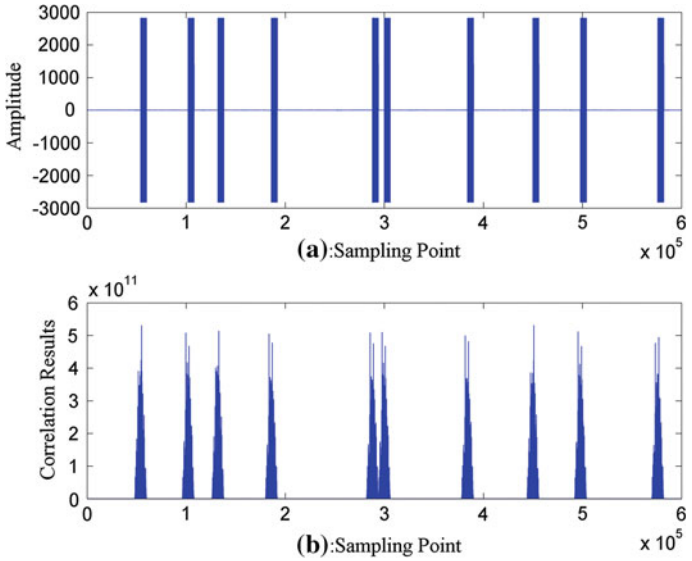

Fig. 8 PRN2 pseudolite signal acquisition result

4.5 Tracking Simulation Examples

Fast and accurate acquisition is the key to tracking. Due to the limitation of space, only the above-mentioned single pseudolite signal is tracked, and the method of

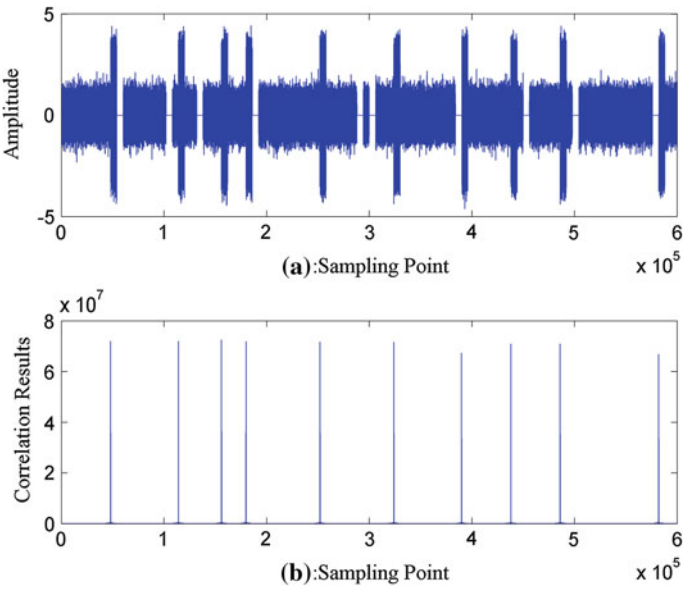

Fig. 9 **a** Weak signal after eliminating strong signals. **b** Signal acquisition result

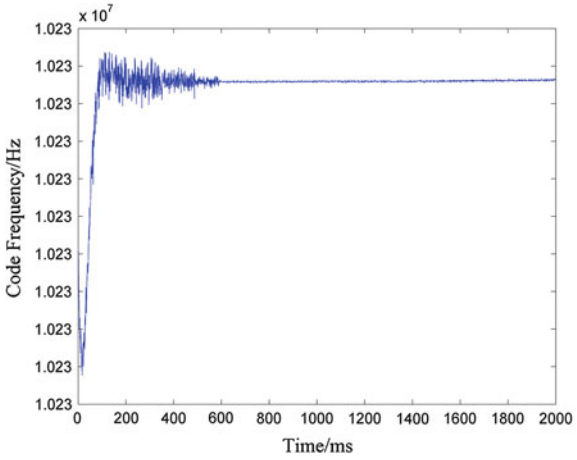

Fig. 10 Code phase acquisition result of single pseudolite signal (−60 dB)

tracking multiple pseudolite signals is similar. The simulation condition is the same as simulation one. The results are shown in Figs. 10, 11, 12 and 13.

This paper adopts the following tracking strategy: when entering the tracking stage, the carrier signal is tracked by PLL3FLL2 and then gradually stepped into the

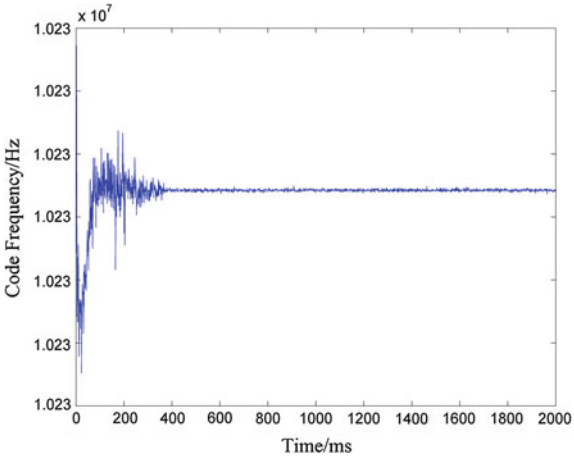

Fig. 11 Code phase acquisition result of single pseudolite signal (−90 dB)

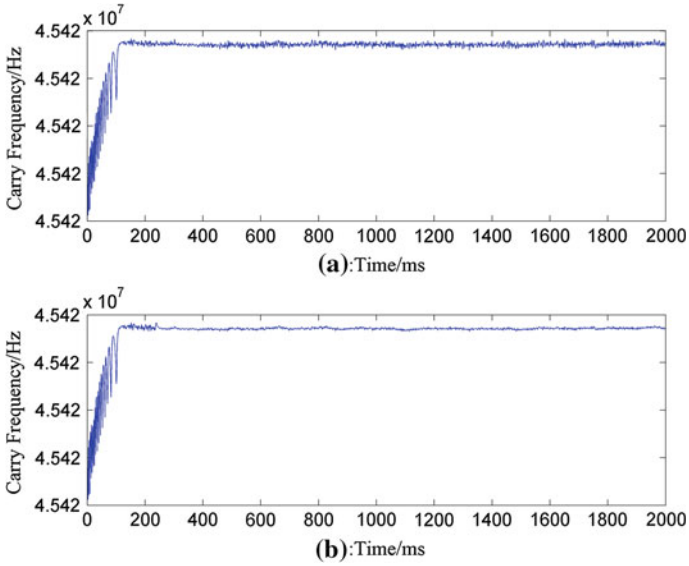

Fig. 12 SNR = −60 dB, **a** Carrier tracking using FLL2PLL3. **b** Carrier tracking using both FLL2PLL3 and PLL2

second-order PLL. Figures 12 and 13 show that this method can effectively improve the tracking accuracy. The above simulations show that the pulse pseudolite signal can be accurately tracked.

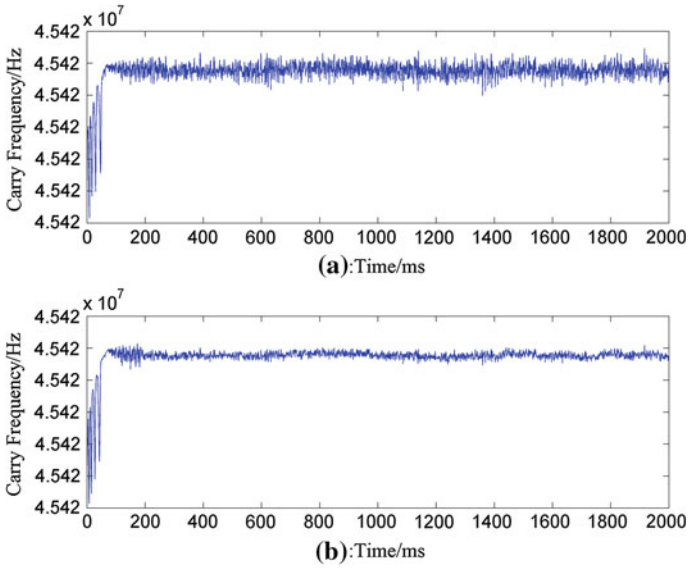

Fig. 13 SNR = −90 dB, **a** Carrier tracking using FLL2PLL3. **b** Carrier tracking using both FLL2PLL3 and PLL2

5 Conclusion

Through theoretical analysis, this paper presents a pulse signal design method based on TDMA, and analysis the signal acquisition and tracking performance. The results show that the designed pulse signal structure can be acquired and tracked effectively, which can be used to confront the near-far effect.

References

1. Abt TL, Soualle F, Martin S (2007) Optimal pulsing schemes for Galileo pseudolite signals. Positioning 1(12)
2. Cobb HS (1997) GPS pseudolites: theory, design, and applications. Stanford University
3. Gang X (2009) Understanding GPS principles and applications. Publishing House of Electronics Industry
4. Long Y, Jianhua Z, Yiyong H (2009) Signal design and validation of the near space local area auqmentation system. Radio Eng 04:32–39
5. Hongjun Y (2010) Analysis and research on the near-far effect of pseudolites. Radio Eng 06:31–33+61
6. Ye H, Yu B, Zhou B (2008) Study on optimal pulsing schemes for Galileo Pseudolite signals. Radio Eng 07:40–42+46

7. Zhang L, Wang J, Dai N (2007) Analysis and research on near-far effect of pseudolites based on TDMA technology. Comput Technol Develop 17(11):167–170. doi:10.3969/j.issn.1673-629X2007.11.048
8. Zhou B, Yu B, Luo W (2009) Pulsed pseudolite signal acquisition using segmented FFT. Trans Beijing Inst Technol 11:1006–1013

Precision Analysis of CNAV Broadcast Ephemeris and Its Impact on the User Positioning

Ahao Wang, Junping Chen and Jiexian Wang

Abstract GPS broadcast ephemeris error is an important factor affecting the real-time positioning accuracy. Since April 2014, the IGS provided two new broadcast ephemeris products, namely LNAV (Legacy Navigation Message) and CNAV (Civil Navigation Message). Compared with LNAV, CNAV was broadcasted only on Block IIR-M and IIF satellites. This paper introduces the parameters of satellite orbit calculation in CNAV, and algorithm of satellite orbits calculation is introduced by using CNAV broadcast ephemeris. CNAV satellite orbits and clocks of one year are calculated and evaluated by using the IGS precise products as reference. Results show that mean and RMS of CNAV orbits error is less than 0.4 and 2 m for all three components, respectively; RMS of 3D orbits error is about 3 m. RMS of CNAV satellite clock error is about 1.5 ns. CNAV SISRE is around 0.6 m. User pseudo-range positioning using CNAV shows similar performance as the LNAV.

Keywords CNAV broadcast ephemeris · LNAV broadcast ephemeris · Precise ephemeris · 3D orbit errors · Clock bias · SISRE · User positioning

A. Wang · J. Chen
Shanghai Astronomical Observatory, Chinese Academy of Sciences,
200030 Shanghai, China

A. Wang · J. Wang
College of Surveying and Geo-Informatics,Tong Ji University,
200092 Shanghai, China

J. Chen
School of Astronomy and Space Science, University of Chinese Acadamy of Sciences,
100049 Beijing, China

J. Chen (✉)
Shanghai Key Laboratory of Space Navigation and Positioning Techniques,
Shanghai Astronomical Observatory Chinese Academy of Sciences,
200030 Shanghai, China
e-mail: junping.chen@shao.ac.cn

J. Sun et al. (eds.), *China Satellite Navigation Conference (CSNC) 2017 Proceedings: Volume I*, Lecture Notes in Electrical Engineering 437,
DOI 10.1007/978-981-10-4588-2_37

1 Introduction

The GPS broadcast ephemeris is the basic of satellite navigation and positioning, its orbit errors and clock bias will directly affect the final stand-alone positioning. At present, the common ephemeris products have two kinds: one is the precise ephemeris by the IGS (International GNSS Service), the other is GPS (Global Positioning System) broadcast ephemeris, which is widely used in stand-alone real-time positioning. Though its precision is lower than former, it has the characteristics of real-time and easy to obtain. Several researches from 2002 to 2013 [1–4] have been conducted for the in-depth analysis of NAV (Navigation Message) ephemeris precision. With the implementation of the L-AII (Legacy Accuracy Improvement Initiative) program, the global station increases and the improvement of dynamic model in orbit prediction. The current precision of NAV broadcast ephemeris is less than 1.5 m, clock bias is about 8 ns, and its overall precision is increasing year by year.

The need for more flexibility and higher precision of the transmitted data fostered the development of a new CNAV (Civil Navigation Message) broadcast ephemeris from 28 April 2014, its broadcast time at intervals of two hours from 01:30:00 to 23:30:00, each ephemeris group contains 32 parameters. An initial CNAV test campaign was conducted from 15 to 29 June 2013, and [5] found RMS of 3D orbit errors is 88 cm for a few hour data set of three satellites. Steigenberger et al. [6] have conducted analysis of CNAV broadcast ephemeris precision from 2014 to 2015, its SISRE (signal-in-space range error) is about 0.6 m. This paper will introduce an algorithm of satellite orbits calculation using CNAV broadcast ephemeris, and CNAV satellite orbits and clocks of one year are calculated and evaluated by using the IGS precise products as reference. Finally, the performance of CNAV on user positioning is analyzed.

2 Analysis Strategy of CNAV Broadcast Ephemeris Error

2.1 CNAV Parameters

Daily CNAV + LNAV (Legacy Navigation Message) broadcast ephemeris are recorded in RINEX 3 navigation format and provided at ftp://cddis.gsfc.nasa.gov/gnss/data/campaign/mgex/daily/rinex3/20yy/cnav/brdxddd0.yyx, where ddd and yy denotes the day of year and two-digit year respectively [6]. Each group of CNAV broadcast ephemeris contains 32 parameters, satellite orbits and clocks are calculated using 20 parameters in Table 1.

Table 1 CNAV broadcast ephemeris parameters

a_{f0}	clock bias (seconds)	i_0	i0 (radians)
a_{f1}	clock drift (sec/sec)	ω	omega (radians)
a_{f2}	clock drift rate (sec/sec^2)	$\dot{\Omega}$	OMEGA DOT (radians/sec)
$\sqrt{A}$	sqrt(A) [sqrt(m)]	*iDot*	IDOT (radians/sec)
ΔA	aDot (meters/sec)	C_{rc}	Crc (meters)
Δn	Delta n (radians/sec)	C_{rs}	Crs (meters)
t_{op}	Time of ephemeris prediction (secs of week)	C_{uc}	Cuc (radians)
M_0	M0 (radians)	C_{us}	Cus (radians)
e	e Eccentricity	C_{ic}	Cic (radians)
Ω_0	OMEGA0 (radians)	C_{is}	Cis (radians)

2.2 Algorithm of Satellite Orbits and Clocks Calculation

The algorithm of satellite orbits and clocks calculation using CNAV broadcast ephemeris is described in the Ref. [5, 7]. Compared to LNAV, CNAV provides an extended orbit parameterization including a change rate for the semi-major axis and the mean motion as well as improved precision of the orbital elements. Different from the previous studies, we do not consider the change rate of mean motion. Detailed calculation procedure is shown in Table 2.

2.3 Evaluation Methods

IGS provide precise ephemeris at 15 min intervals,its orbit and clock precision is less than 2.5 cm and 0.075 ns respectively [8] and thus can be regarded as reference, the precise ephemeris of IGS is under the ITRF framework, which provided by IERS, while the CNAV uses the WGS-84 coordinate system. The deviation between the two systems is about 1–2 cm [2], compared with CNAV broadcast ephemeris error is much smaller and it can be neglected in comparison. Empirically derived satellite antenna z-offsets given in the Ref. [9] are applied in the comparison, as the IGS products refer to the center of mass of the satellites whereas the CNAV broadcast ephemeris refer to the mean antenna phase center [9]. Detailed satellite antenna offset correction algorithm in the Ref. [1]. The median of all satellite clock bias as a time benchmark is used to access accuracy of clock errors.

The data sampling of orbits and clocks comparison is 15 min. Satellite orbit errors, clock bias and SISRE are all calculated, the mean difference and RMS are calculated as follows:

Table 2 Algorithm of satellite orbits and clock bias

Calculation formula	Meaning
$t_{oe} = week\_in\_\sec(y, mon, d, h, \min, \sec)$	Time of reference epoch (week in seconds)
$t_k = t - t_{oe}$	Time difference
$A = (\sqrt{A})^2 + \Delta A^* t_k$	Semi-major axis
$n = \sqrt{GM/A^3} + \Delta n$	Mean angular velocity GM is Earth's gravitational constant
$M_k = M_0 + n \cdot t_k$	Mean anomaly
$E_k = M_k + e \cdot \sin E_k$	Eccentric anomaly
$\cos v_k = \frac{\cos E_k - e}{1 - e \cdot \cos E_k}$ $\sin v_k = \frac{\sqrt{1-e^2} \cdot \sin E_k}{1 - e \cdot \cos E_k}$	True anomaly
$\phi_k = v_k + \omega$	Latitude parameter
$\delta u_k = C_{us} \sin(2\phi_k) + C_{uc} \cos(2\phi_k)$ $\delta r_k = C_{rs} \sin(2\phi_k) + C_{rc} \cos(2\phi_k)$ $\delta i_k = C_{is} \sin(2\phi_k) + C_{ic} \cos(2\phi_k)$	Perturbation correction
$u_k = \phi_k + \delta u_k$	Corrected latitude parameter
$r_k = A(1 - e \cos E_k) + \delta r_k$	Corrected radius
$i_k = i_0 + \delta i_k + iDot \cdot t_k$	Corrected orbit inclination
$\Omega_k = \Omega_0 + (\dot{\Omega} - \dot{\Omega}_e)t_k - \dot{\Omega}_e t_{oe}$	Corrected longitude of ascending node
$x = r_k \cos(u_k)$ $y = r_k \sin(u_k)$	Coordinates in the orbit plane
$X_k = x \cdot \cos(\Omega_k) - y \cdot \cos(i_k) \cdot \sin(\Omega_k)$ $Y_k = x \cdot \sin(\Omega_k) + y \cdot \cos(i_k) \cdot \cos(\Omega_k)$ $Z_k = y_k \cdot \sin(i_k)$	Coordinates in the WGS-84
$dts = a_{f0} + a_{f1} \cdot t_k + a_{f2} \cdot t_k^2$	Clock bias

$$Mean = \frac{\sum V_i}{n}, \quad RMS = \sqrt{\frac{\sum V_i^2}{n}}$$

where n is the total number of epoch, V_i is the CNAV broadcast ephemeris error, $i = 1, 2, 3, \ldots, n$.

3 Analysis of CNAV Broadcast Ephemeris Error

All Block IIR-M and IIF satellites transmitting CNAV messages are specified in Table 3. Where the total numbers keep increased from 11 to 19 satellites with the modernization of the GPS system since 28 April 2014.

Table 3 Satellite capable of providing CNAV

CNAV start	PRN
2014-04-28	01, 05, 07, 12, 15, 17, 24, 25, 27, 29, 31
2014-05-30	30
2014-07-30	06
2015-02-23	03, 09
2015-09-17	08, 26
2016-05-05	10, 32

All CNAV broadcast ephemeris error is calculated from DOY(day of year) d001 to d310 in 2016, except for PRN 10 and PRN 32 satellites, which began to transmit CNAV from DOY 126. Outliers in orbit errors and clock bias exceeding a limit of 15 m and 30 ns respectively have been rejected in the following analysis. And the 'clean' ephemeris errors to evaluate CNAV broadcast ephemeris precision.

3.1 Analysis Precision of Orbit Errors

Using PRN09 satellite as an example, the orbit error curve of the CNAV broadcast ephemeris is present in Fig. 1, where X, Y and Z components are represent in red, green and blue respectively; the horizontal and vertical axis represents epoch numbers and errors (m) respectively. CNAV orbit error of the other 18 satellites basically fits this error curve.

All 19 satellites orbit errors are calculated for the whole year, except for PRN10 and PRN32, including mean and RMS errors in X, Y and Z components. The horizontal and vertical axis represents PRN and errors (m) respectively in Fig. 2. Results show that all satellites orbit errors is less than 0.4 m, the minimum mean orbit error is about 1 cm for the Z component of PRN09 and Y component of PRN15. The maximum orbit error is −0.37 m, appears in the Z component of PRN08. All RMSs of satellites orbit errors are less than 2 m. The minimum RMS orbit error is 1.43 m for the Z component of PRN09.

3D orbit errors are calculated by considering its errors in X, Y and Z components using the formula $\sigma = \sqrt{V_x^2 + V_y^2 + V_z^2}$. Mean and RMS of 3D orbit errors for all

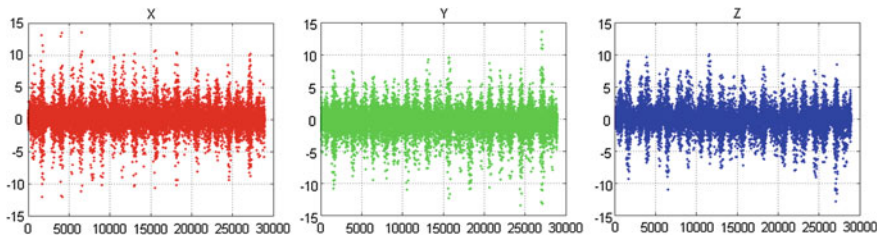

Fig. 1 Orbit error curve of the CNAV broadcast ephemeris of satellite PRN09 in a year

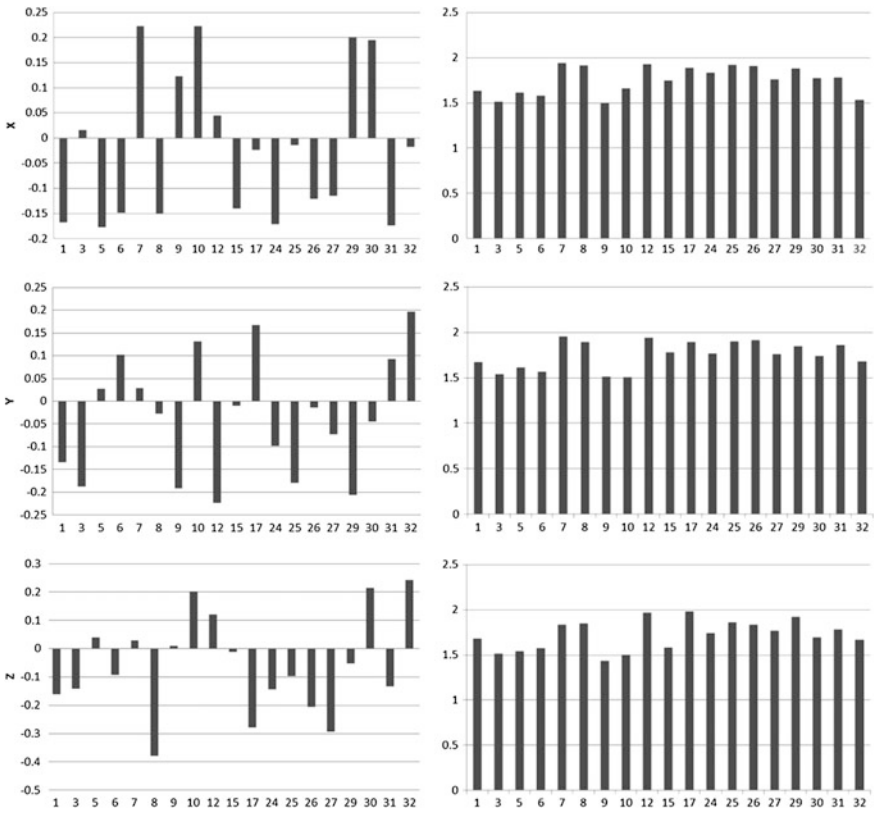

Fig. 2 Mean and RMS error of the CNAV broadcast ephemeris of 19 satellites in X, Y and Z components

satellites are present in Fig. 3. Red and blue represents mean and RMS respectively; the horizontal and vertical axis represents PRN and errors (m) respectively. In Fig. 3 the maximum and minimum mean value is 2.39 m of PRN12 and 1.79 m of PRN09, respectively. For the RMS statistics, the maximum and minimum RMS is 3.37 m of PRN12 and 2.57 m of PRN09.

3.2 Analysis Precision of Clock Bias

Satellites PRN06 and PRN17 are used as examples for the analysis of clock biases, Fig. 4 presents the clock bias curve of the CNAV broadcast ephemeris, where the horizontal and vertical axis represents epoch number and clock bias (ns) respectively. In Fig. 4 we see that the clock bias variation of PRN17 is larger, between −10 to 15 ns, while PRN06 satellite clock bias variation is between −3 to 4 ns. Most other satellites is similar to PRN06, the variation range of clock bias is less than 10 ns.

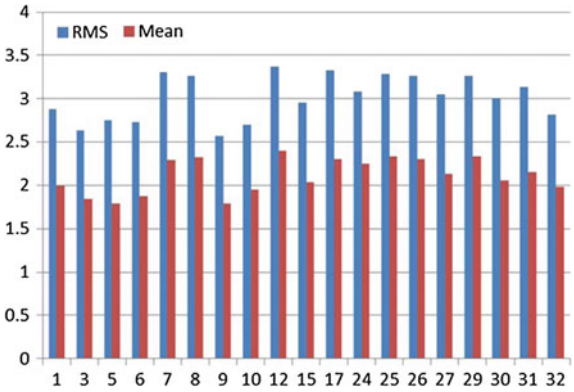

Fig. 3 3D orbit error of the CNAV broadcast ephemeris of 19 satellites

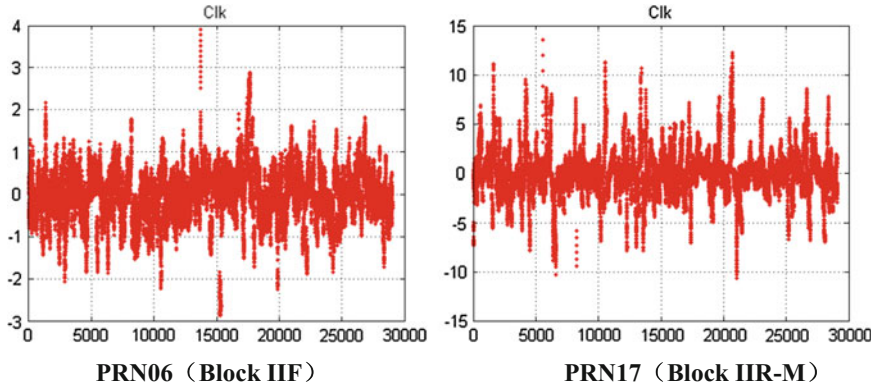

Fig. 4 Clock bias curve of the CNAV broadcast ephemeris of satellite PRN06 and PRN17 in a year

Figure 5 shows the mean and RMS of clock bias for all satellites, where we see that they are less than 0.6 and 2 ns respectively for most satellites. PRN08, PRN17, PRN24, PRN29 and PRN31 satellite clock bias have poor accuracy; Largest RMS is 4.3 ns of satellite PRN24.

3.3 SISRE Analysis

In order to calculate the CNAV SISRE, CNAV orbit errors in ECEF (Earth Centered Earth Fixed) are transformed into orbit coordinate system, and clock errors is converted to range by multiplying the speed of light. The detail algorithm of SISRE calculation is described in the Ref. [9]. All 19 satellites SISRE and SISRE

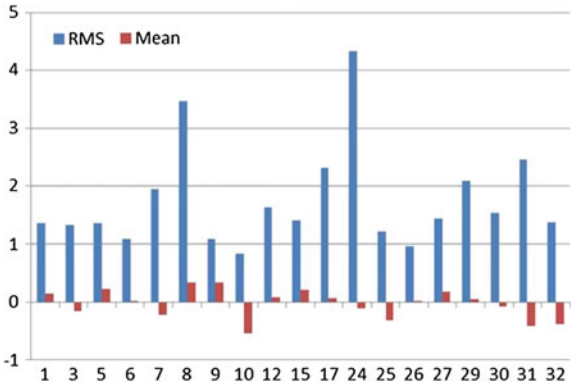

Fig. 5 Mean and RMS clock bias of the CNAV broadcast ephemeris of 19 satellites

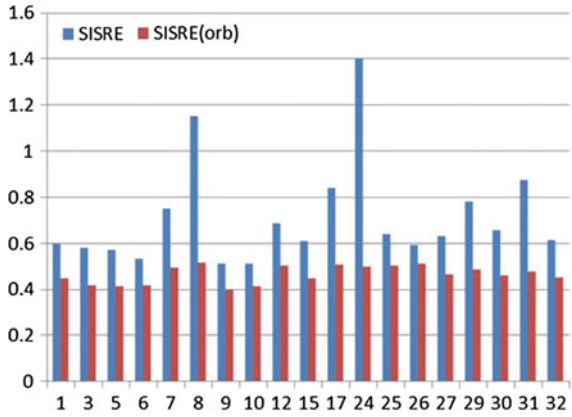

Fig. 6 SISRE and SISRE (orb) of the CNAV broadcast ephemeris of 19 satellites

(orb) are calculated for the whole year and present in Fig. 6, Red and blue represents SISRE (orb) and SISRE respectively; the horizontal and vertical axis represents PRN and SISRE values (m) respectively. In Fig. 6 we see that all satellites CNAV SISRE (orb) is about 0.4–0.5 m, while CNAV SISRE is between 0.5 and 1.4 m. The difference of CNAV SISRE for all satellites is mainly affected by the accuracy of clock bias. PRN08, PRN17, PRN 24, PRN 29 and PRN 31 satellites CNAV SISRE is about 0.8–1.4 m and significantly larger than other satellites. Most satellites CNAV SISRE is around 0.6 m.

4 Performance of CNAV Broadcast Ephemeris on User Positioning

PPP (precision point positioning) software developed by the Shanghai Astronomical Observatory is modified to add solution module for CNAV broadcast ephemeris. Specific corrections are as follows: dual frequency ionospheric-free,

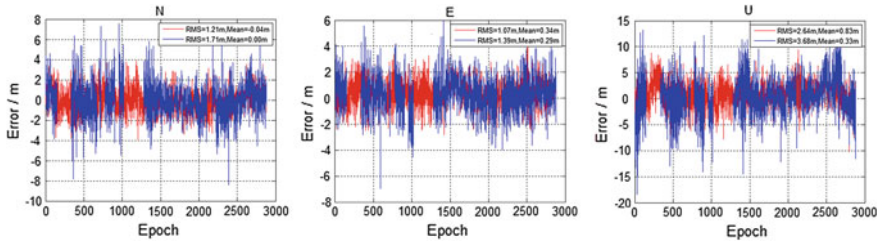

Fig. 7 Coordinate error curve

Table 4 Mean and RMS of coordinate error

Component	Mean_CNAV/m	Mean_LNAV/m	RMS_CNAV/m	RMS_LNAV/m
N	0.00	0.02	1.71	1.68
E	0.29	0.31	1.39	1.35
U	0.33	0.59	3.68	3.60

SAAS tropospheric model, relativity, earth rotation, antenna phase center and solid tide. CNAV and LNAV broadcast ephemeris are used to calculate user pseudo-range based positioning.

The data of the IGS station SHAO at shanghai with sampling of 30 s is used for coordinate calculation using LNAV and CNAV broadcast ephemeris for DOY 288 in 2016. Figure 7 compares the two solutions. Red and blue represents LNAV and CNAV respectively; the horizontal and vertical axis represents epoch numbers and errors (m) respectively.

The coordinate error curve based on two broadcast ephemeris are similar. The total number of CNAV results is less than LNAV, this is due to the fact that the CNAV is available on 19 satellites and less than 4 satellites could be tracked for some epoch. CNAV and LNAV uses 19 identical satellites to calculate user pseudo-range based positioning. Mean and RMS of coordinate error in N, E and U components is calculated in Table 4. CNAV shows similar performance as the LNAV.

5 Conclusions

CNAV satellite orbits and clocks of one year are calculated and evaluated by using the IGS precise products as reference, and the performance of CNAV on user positioning is analyzed in this paper. We have found the following conclusion:

(1) Orbit errors for all three components using CNAV show similar performance as the LNAV, its mean and RMS is less than 0.4 and 2 m respectively. For 3D orbit errors, the mean and RMS is about 2.4 m and 3.5 m respectively.

(2) Mean and RMS of clock bias of most CNAV satellites are about 0.6 and 1.5 ns respectively. PRN08, PRN17, PRN24, PRN29 and PRN31 satellite clock bias variation range is larger and less stable.
(3) CNAV SISRE (orb) for all satellites is about 0.4–0.5 m, and most satellites CNAV SISRE is around 0.6 m.
(4) User kinematic pseudo-range positioning using CNAV shows similar performance as the LNAV, but the solution fails in some epochs when less than 4 satellites could be simultaneously tracked.

Acknowledgements This paper is supported by the 100 Talents Programmer of The Chinese Academy of Sciences, the National High Technology Research and Development Program of China (Grant No. 2014AA123102), the National Natural Science Foundation of China (NSFC) (Grant No. 11273046, 11673050).

References

1. Zhenghang L, Wenwu D, Zhao L (2008) Error analysis of orbit determined by GPS broadcast ephemeris. J Geodesy Geodyn 01:50–54
2. Fei G, Xiaohong Z, Xingxing L (2009) Precision analysis on orbit and clock of GPS satellites broadcast ephemeris. Geomatics Inf Sci Wuhan Univ 05:589–592
3. Feizhou Z, Peng C, Zemin Y (2013) Analysis of GPS broadcast ephemeris error. Comput Meas Control 01:155–156
4. Xiaying W, Jinzhong B, Decheng Z (2014) Analysis of precision of position velocity and clock of GPS satellite broadcast ephemeris. J Geodesy Geodyn 03:164–168
5. Yin H, Morton Y, Carroll M et al (2014) Performance analysis of L2 and L5 CNAV broadcast ephemeris for orbit calculation In: Proceedings of the 2014 international technical meeting of the institute of navigation. San Diego, CA, pp 761–768
6. Steigenberger P, Montenbruck O, Hessels U (2015) Performance evaluation of the Early CNAV navigation message In: Proceedings of the 2015 international technical meeting of the institute of navigation. Laguna Cliffs Marriott, Dana Point, California, pp 155–163
7. Yaowen Z (2007) Study on GPS broadcasting ephemeris and precision evaluation of GPS broadcasting ephemeris. Chang'an University, Xi'an, pp 12–13
8. Yongjiu C (2015) The precision of GNSS broadcast ephemeris. Geomatics Spat Inf Technol 6:186–191
9. Montenbruck O, Steigenberger P, Hauschild A (2015) Broadcast versus precise ephemerides: a multi-GNSS perspective. GPS Solutions 02:321–333

Research on Path Loss and Multipath Propagation of Indoor Pseudolite Signal

Yaning Li, Baoguo Yu and Xingli Gan

Abstract The indoor positioning technology based on Beidou/GPS pseudolite can improve the indoor signal coverage and geometric configuration. Due to the mechanism of complex environment and navigation signal has not been solved, the stability, reliability and high precision of indoor positioning can not be ensured. Aiming at solving the problem like power attenuation and multipath fading in navigation pseudolite indoor propagation, based on the previous research on indoor communication model, detailed analysis of peculiarities of pseudolite signal and indoor environment is made firstly. Simulation experiments of the pseudolite signal propagation are performed by using ray-tracing method secondly, and then practice tests are performed in real condition. The results show that the corrected log-distance path loss model can accurately describe the path loss feature of pseudolite signal, the carrier phase positioning method can reduce the ranging error brought by multipath propagation.

Keywords Pseudolite · Path loss · Multipath propagation · Indoor positioning

1 The Introduction

The indoor environment is the place where people live and work, the public have strong demand of positioning and guiding in parking lots, shopping malls, airports and other places. Satellite navigation signal lost navigation service ability for shading effects in indoor spaces, with the advantages of convenient layout and compatible GNSS receiver hardware technology, Beidou navigation pseudolite can realize GNSS users to use a mobile terminal positioning module to receive the pseudolite signals indoors, then complete indoor navigation and location service. But indoor electromagnetic signal propagation scene is more complex than outdoor scene, which causes a lot of difficulties of indoor navigation signal measurement

Y. Li · B. Yu · X. Gan (✉)
Ann Arbor, China
e-mail: lemon_785287994@qq.com

J. Sun et al. (eds.), *China Satellite Navigation Conference (CSNC) 2017 Proceedings: Volume I*, Lecture Notes in Electrical Engineering 437,
DOI 10.1007/978-981-10-4588-2_38

and positioning information extraction. The transmission mechanism of cognition on indoor signal is the key problem to realize the indoor positioning.

Logarithmic path loss model, describes the relationship of signal propagation attenuation degree in the process of changing with the propagation distance, and predict the electromagnetic wave attenuation in the environment through statistical attenuation factor of different scenarios; The attenuation factor model that Seidel proposed is a model that describing the specific location within the building, the model put different kinds of wall and floor between the penetration loss into consideration, thus have better adaptability to the environment; After a summary of the experience of our predecessors' studies, IEEE802.15.3 puts forward the suggestion of uwb indoor channel model, the model represents the quantity of each diameter to signal envelope obey the lognormal distribution, determine the corresponding path loss model and the channel impulse response.

In general, most studies of indoor signal transmission model focus on the ultra broadband and communication signals, the pseudolite indoor positioning signal transmission mechanism and the research of indoor locating multipath error is relatively rare, based on the existing indoor signal transmission model, we can combine the feature of pseudolite signal system and the application environment, to analysis of pseudolite signal transmission attenuation and the multipath error suppression method.

2 Analysis of Indoor Pseudolite Signal Propagation Effect

2.1 Indoor Pseudolite Signal Propagation Characteristics

The features of indoor signal can be summarized as:

(1) In order to ensure compatibility with the existing terminal receiver, pseudolite using Beidou/GPS code sequences which are not used by the space satellite, thus wavelength is about 10 cm, less than the general size of obstacles, so the indoor pseudolite signal propagation forms mainly are direct wave and reflected wave.
(2) Due to the constant layout of indoor furniture and ignore the mobile personnel, we can think environment roughly constant, and generally not considered the doppler effect caused by the relative motion of a transmitter and a receiver.
(3) Due to the limited interior space scale, the velocity of electromagnetic radiation to the speed of light, led to the ray delay interval at receiver is very small, it is difficult to tell one from another, it is more meaningful to research multipath ray distribution.

Study on indoor electromagnetic wave propagation characteristics are calculated by statistics or the method of indoor wireless transmission channel was simulated and the simulation, so as to realize the indoor navigation signal propagation

prediction. Pseudolite signals is a narrow-band signal, still follow the rules of large scale path attenuation when travels in the indoor environment, and suitable for general statistical model, but as a result of the difference of indoor environment compared with outdoor environment, the transmission parameters need to be revised, accurate description of indoor propagation environment factors is the key to the accuracy of decision model.

2.2 Indoor Pseudolite Channel Modelling

Research shows that on the basis of free space attenuation formula, in outdoor and indoor environment, the average received signal power is a logarithmic attenuation with distance [6–8], without considering the cross-layer signal transmission, the log distance path loss model is a common indoor large-scale channel model:

$$P_d(\mathrm{dB}) = P_{d_0}(\mathrm{dB}) + n \times 10\log(\frac{d}{d_0}) + X_\sigma(\mathrm{dB}) \tag{1}$$

In order to more accurately describe the specific features of indoor environment, X_σ will now have new meaning, it indicates that the concrete environment condition, has relationship with the spatial coordinates of the noise. Pseudolite indoor path attenuation model is rewritten as follows:

$$P_d(\mathrm{dB}) = P_{d_0}(\mathrm{dB}) + n \times 10\log(\frac{d}{d_0}) + X_\sigma(x, y) \tag{2}$$

According to the size and location of the specific obstacles, to determine the scope and magnitude in order by precise calculation combined with environmental statistics method to realize accurate description of the real scene.

3 Simulation Analysis of Indoor Pseudolite Signal Propagation Effects

3.1 Pseudolite Signal Propagation Simulation of the General Environment

Simulation modelling of the scene office space scale is medium (15 m * 7 m * 3 m), barrier type and quantity is more, and pseudolite signal wavelength and the environment in the model size close, individual small obstacles should not ignore most of the diffracted wave's contribution to the received signal, but on the whole direct and reflection is still the main transmission phenomenon. Considering the height of the human handheld receivers, four receiver is set to 1 m high. Compute each ray

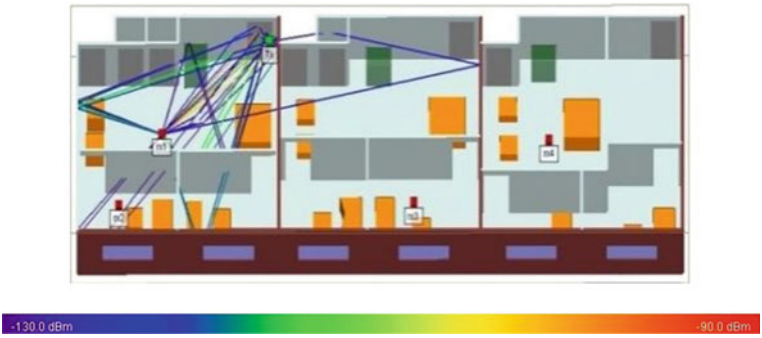

Fig. 1 General environmental signal propagation diagram

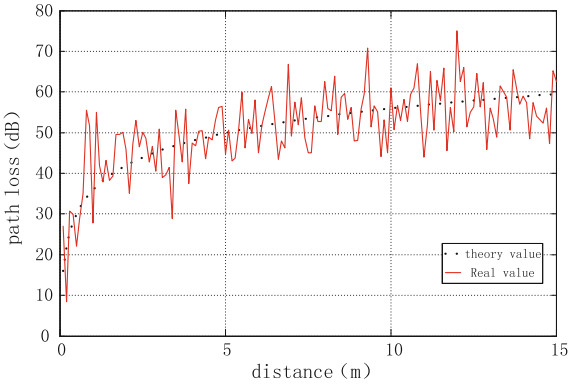

Fig. 2 *Curve* The general environment of path loss and transmission distance

propagation path using the ray tracing method, then get all direct arrive, reflection and transmission path, and every ray power size between pseudolite launch TX antenna and receiver RX1–RX2 (Fig. 1).

Smooth dotted line in Fig. 2 as log distance path loss model simulation curve of the attenuation factor n = 2.8, solid lines for office scenario simulation model of pseudolite signal power with distance attenuation relation curve, it can be seen that the traditional log distance path loss model is able to get a basic description and the large scale general indoor environment signal path loss.

3.2 Pseudolite Signal Propagation Simulation Barrier Environment

Due to receiver RX2, RX3 and ignore the distance between launch TX path, wall block caused the shadow covered, reaches the receiver generally experienced a transmission of signal of the communication process, so the signal attenuation is very severe.

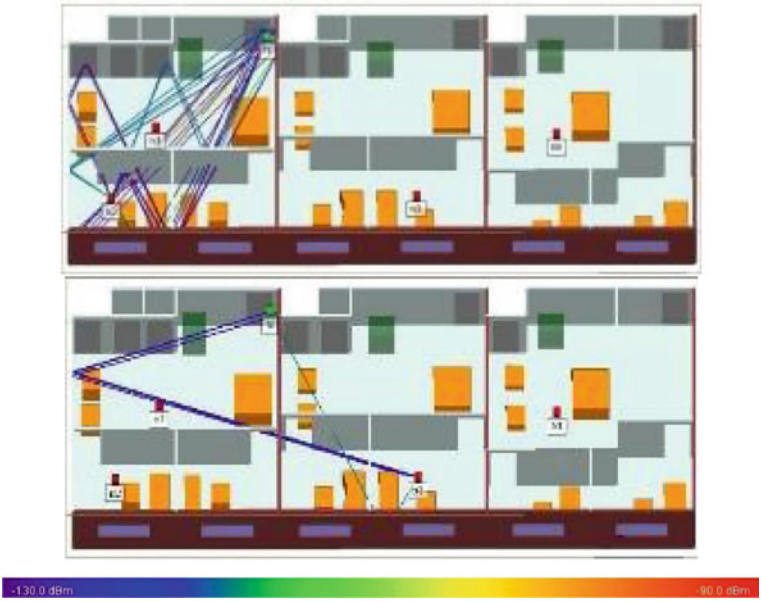

Fig. 3 Signal transmission schematic obstacle environment

The traditional log distance path loss model can't accurately describe the pseudolite signals transmission process, need to join the correction term.

$$X_\sigma(x, y) = A \cdot N(5, \sigma) \tag{3}$$

Figure 3 for obstacle environment model of pseudo satellite signal multipath transmission diagram, shown in figure out the pseudolite signals launch position, by the graph, you can see that with the increase of pseudolite signal propagation distance, signal attenuation degree increase gradually, but in the partition of the coordinates of the corresponding attenuation appeared a spurt, points out that with the signal of the wall effect, as shown in Fig. 4.

4 Related Experiments and Analysis

4.1 Test on Pseudolite Signal Power Attenuation Model

4.1.1 General Environment Experiment

Test scenarios is shown in Fig. 5, office space size is about 5.5 m * 6 m * 3 m, planar approximate square shape, simple furniture such as desks and chairs in office, the ceiling is made of gypsum board, the ground is relatively smooth wooden

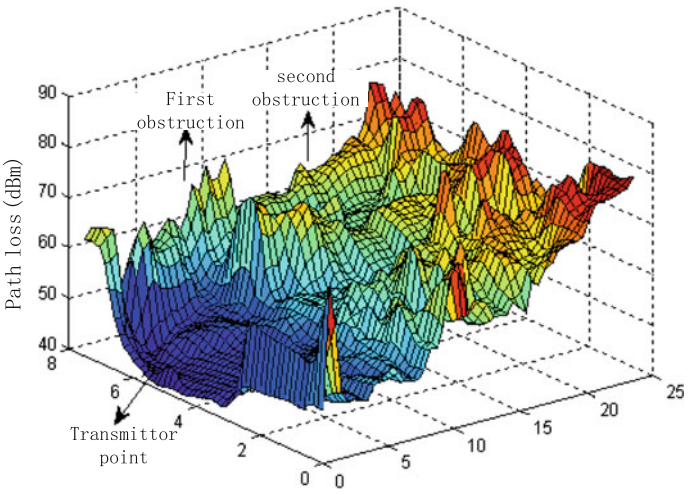

Fig. 4 Average path loss environment with propagation distance

Fig. 5 General office test environment

floor, the window is made of glass, indoor temperature constant, ignore people. In order to simplify the test difficulty and compatible with mobile phone positioning software, choose BD 3 star pseudo code as a pseudo satellite spread spectrum code, handheld smartphone by testing personnel in the specific test area actual measurement.

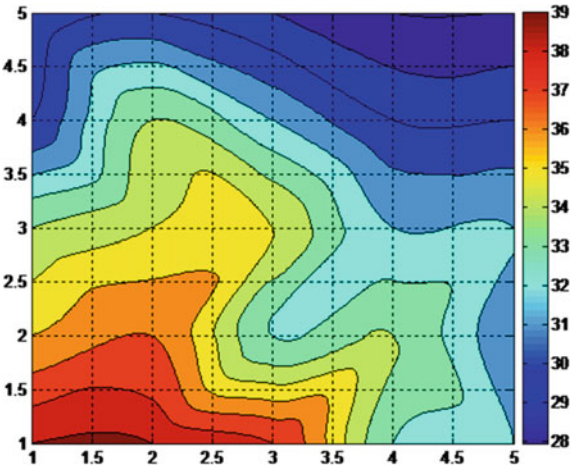

Fig. 6 Office environment pseudolite signals to arrive at the power distribution

The above experimental data from statistical smooth after receiving manic than relationship along with the change of spatial coordinates, as shown in Fig. 6, we can see the received signal power decreases with the increase of propagation distance.

In order to quantitatively describe the pseudolite signal power changes with the propagation distance, the relation between each test point data integration process after get the average received signal carrier manic ratio relation with the change of the propagation distance, as shown in Fig. 7.

In Fig. 7, theory curve for the attenuation factor in 2.7 log distance path loss curve, it can be seen that basic test curve and theoretical curve matching, namely traditional log distance path loss model can generally describe pseudolite signal power attenuation law office scene.

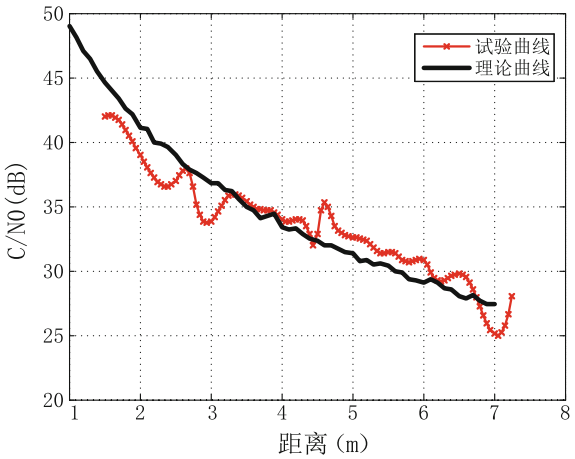

Fig. 7 Office scenario pseudolite signal power change

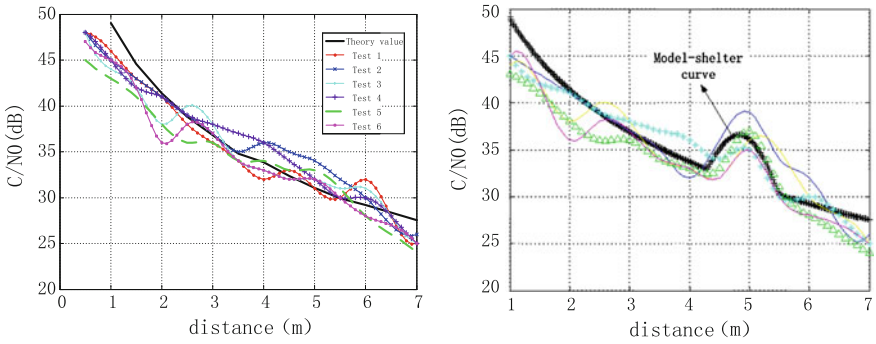

Fig. 8 Test results with/without obstacles environment

4.1.2 Obstacle Environment Experiment

As shown in Fig. 8, test scenario space size of about 10 m × 5 m × 3 m, on both sides of the aisle have two rows of bearing column, inside the hall office soft compartment and obstacles such as green plant pot, the ceiling is made of gypsum board, the ground is relatively smooth, indoor temperature constant, ignore people. The scenario to the mixture of barrier-free environment with obstacles environment scenarios, test environment as shown in Fig. 8.

Because of the limitation of test environment from 4.5 to 5.5 m in pseudo satellite launch area barrier pillars, keep out area serious multipath effect, will cause actual measurement and the deviation of traditional theoretical model.

Now obstacles in the environment path loss model is as follows:

$$P_d(\text{dB}) = P_{d_0}(\text{dB}) + 2.8 \times 10\log(\frac{d}{d_0}) + A \cdot N(5, [4, 6]) \tag{4}$$

By measuring the two indoor hall scene: there are obvious obstacles (pillars), and no obvious obstacles environment get mania of the received signal receiving device, the experimental results as shown in Fig. 8.

Figure 9 in implementing line is logarithmic curve model from loss, curves of the rest have six times the test data, it can be seen that under the condition of barrier-free, removal of individual big deviation, logarithmic accessible distance loss model can be a basic description signal of the scene in the spread of the large scale decline; Under the condition of the disabled, revised log distance path loss model can more accurately describe disabled and the large scale environment signal fading.

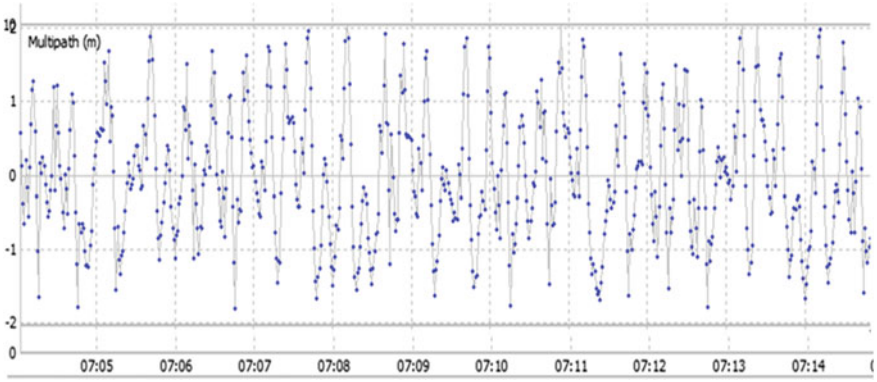

Fig. 9 Multipath office environment signal of the test results

4.2 Pseudo Satellite Signal Multipath Transmission Test

Pseudolite signal carrier phase multipath measurement for the whole week, the existence of ambiguity, difficult to adopt the pseudorange multipath measurement. Now adopts dual-frequency carrier phase multipath estimation method, the GPS L1 pseudolite to L2P carrier signal, so as to analyze multipath indoor carrier size. Is obtained by IGMAS data processing of GPS pseudolite signals of multipath situation as shown in the figure below.

Select testing office for testing two kinds of scene, Fig. 10 is a obstacle less general multipath environment test results, Fig. 11 is by the workbench, composed of multipath reflection area such as cabinet and Windows office environment test results. See general office environment by the picture of multipath RMS within 0.5 m in most of the time; Office environment of multipath RMS spend most of their time more than 1 m, ranging error is bigger.

Can use half wavelength apart ground base station antenna array carrier phase positioning technology, because of the same source, same path transmission and the

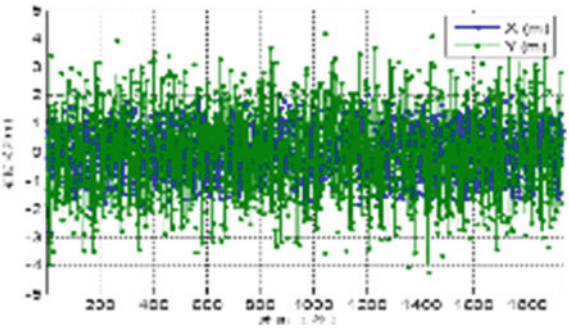

Fig. 10 Indoor pseudo satellite pseudorange positioning results

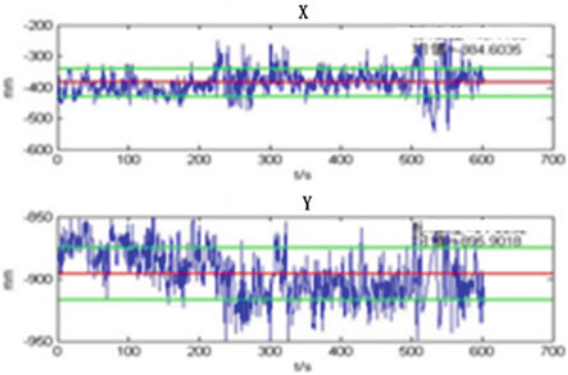

Fig. 11 Indoor pseudolite carrier phase positioning results

whole week of fuzzy degree of the same features, can be poor and whole week ambiguity, clock and multipath error such as irrelevant carrier phase difference measurement equation, achieving high accuracy indoor localization effect.

Through the pseudorange and carrier phase positioning results positioning results show that the indoor area of carrier phase on pseudo satellite positioning methods improve the positioning accuracy.

5 Conclusion

Through the analysis of classical communication indoor signal transmission model, combined with the feature of the practical application environment, the research of indoor field intensity distribution characteristics of the environment signal analysis method, analyzes the existing indoor propagation models and contrast, on the basis of the traditional log distance path loss model to join the correction term, by the method of ray tracing simulation and based on the real environment of experiment proved the availability of the model; In actual the signal of the multipath error measurement, based on carrier phase positioning method is proved by the simulation to enhance the feasibility of indoor positioning accuracy, support the establishment and application of pseudolite indoor positioning system.

References

1. Fluerasu A (2007) Study of multipath effects for the GNSS repeater based indoor positioning technique. In: ION GNSS 20th international technical meeting of the satellite division, pp 25–28
2. Liu Z (2013) Indoor and outdoor scenarios based on ray tracing algorithm of wireless channel prediction research. Xi'an University of Electronic Science and Technology, Xi'an, pp 39–50

3. Barnes J, Rizos C, Wang J (2003) High precision indoor and outdoor positioning using LocataNet. Positioning 25(12):96–102
4. Barnes J, Rizos C, Wang J (2004) Locata: a new positioning technology for high precision indoor and outdoor positioning. J Geophys Res 57(6):79–82
5. Barnes Joel, Rizos Chris, Kanli Mustafa et al (2004) Indoor industrial machine guidance using Locata: a pilot study at BlueScope Steel. J Geophys Res 5(7):56–58
6. Shaolun W (2012) Based on the ray tracing method of arbitrary shape tunnel field strength prediction method research. University of Electronic Science and Technology, Chengdu, pp 56–63
7. Saeidi C, Fard A, Hodjatkashani F (2012) Full three-dimensional radio wave propagation prediction model. Trans Antennas Propag 60(5):2462–2471
8. Galvan Tejada CE (2015) Multivariate or univariate model analysis for indoor location systems: a comparison. In: 2015 international conference on electronics, communications and computers, pp 116–120
9. Lopes RLF (2013) Empirical ARMA indoor propagation model for WLAN signals in 2.4 GHz. Electr Eng Post Graduation Program 8(12):1338–1341

The GNSS/Inertial Navigation Based Private Car Incentive Travel Information Platform

Zhao Wang, Jianping Xing, Qianli Yang, Shengli Wang and Zedong Wang

Abstract In this paper, a method is proposed to build a real-time massive vehicle big data collection platform, and develops BD GNSS sub-meter navigation and 4G communication systems for private cars. Through the analysis of real-time sparse distributed urban transportation network data, the road space-time congestion levels are graded and Chromaticity graph are modeled. A new type of urban traffic cars incentive mechanism is proposed to retrieve and process the private car traffic rule and statistic. The case studies were carried out in typical areas of Jinan City, including the information platform prototype design, time-space road jamming rule design and model construction, BD high-precision sub-meter road test and data comparison analysis.

Keywords Information terminal · Congestion classification · Private cars incentive mechanism

1 Project Background

With the rapid development of society, the urban traffic problems become increasingly serious. At present, most large and medium-sized cities in our country faces increased traffic congestion, road congestion, accidents and other traffic problems. These problems affect the life of urban residents, and restrict the development of cities and the economy. The surge in the number of private cars has

Z. Wang · J. Xing (✉) · Z. Wang
Shandong University, Shanda Nanlu 27, Jinan, China
e-mail: sduxingjianping@163.com

Q. Yang
Shandong TDT Digital S&T Co., Ltd, No. 554 Zhengfeng Road, Jinan City Environmental Science and Technology Park F South, 3018 Jinan, China

S. Wang
Shandong University of Science and Technology, 579 Qianwangang Road, Huangdao District, Qingdao, Shandong Province, China

J. Sun et al. (eds.), *China Satellite Navigation Conference (CSNC) 2017 Proceedings: Volume I*, Lecture Notes in Electrical Engineering 437,
DOI 10.1007/978-981-10-4588-2_39

contributed to the growing urban transport problems. With economic growth, China's vehicle ownership will further increase, urban traffic contradiction between demand and supply infrastructure will become more prominent.

Bus priority has become promising national development strategy, and public transport subsidies was identified as the main economic means in the bus priority policy. Since then, the size of public transport subsidies began to gradually expand by many cities, which laid a solid foundation for urban public transport development.

Although recent years, Chinese government issued a considerable amount of public transport subsidies, but it is still difficult to effectively mitigate traffic congestion. Given today's rapid development of market economy, introducing the incentive mechanism is promising to solve the traffic congestion problem. The so-called incentive mechanism refers to not to travel in high congested area or choosing a green travel mode, such as public transportation by giving cash reward, parking subsidy, bus CARDS based on on-demand use of public resources, such as vehicle insurance fees [1].

Public transport priority policies plus providing incentive mechanism, to encourage people to take public transport is potential to help to solve the traffic congestion, problems and promote the sustainable development of urban traffic.

2 Project Design

The system consists of two parts: a collection platform that can obtain real-time mass vehicle data accurately in both time and space, which is comprised of two parts, data center and management platform; The other one is Amish level based on BD navigation lanes and 4G communication coordinated universal application of information terminal installed on private cars. Due to the existence of more high buildings, tunnels and overpass signal occlusion, the BD GNSS system compatible with the inertial navigation will greatly enhance the usability and accuracy which is more appropriate for urban area [2].

As shown in Fig. 1, firstly, the management platform pre-set the congested areas, which are compared with the real-time GNSS collected car position data during the rush hour and congested areas. When the car terminal detected the vehicles entered the congestion zone in the rush hours, the car terminal reports the information via 4G network to the data center and management platform. The event verification module receives the car terminal reported vehicle GNSS space and time information, and then further verifies the real-time location of the vehicle to determine if the vehicle enters a congested area during a rush hour.

The management platform will calculate the reward amount and feed back to the car terminal, and store the information in the data center, by considering the frequency of the vehicles entering the congested areas, trip starting area and residential area during a fixed cycle.

3 Project System Architecture

As shown in Fig. 2, the system architecture is divided into three parts:

Car terminal installed on the vehicle, which include GNSS module, 4G communication module, LED module, encryption module, MCU module and storage module.

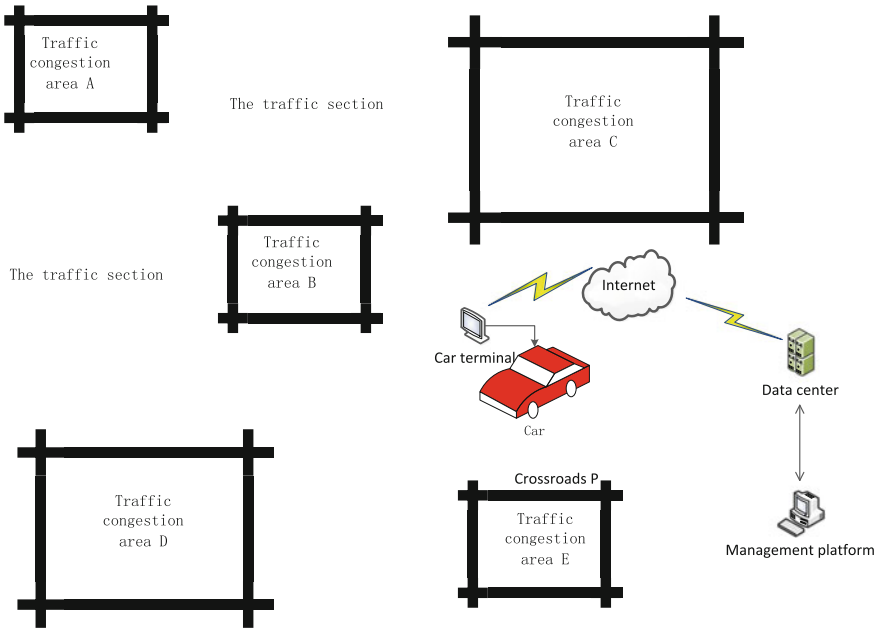

Fig. 1 Project design

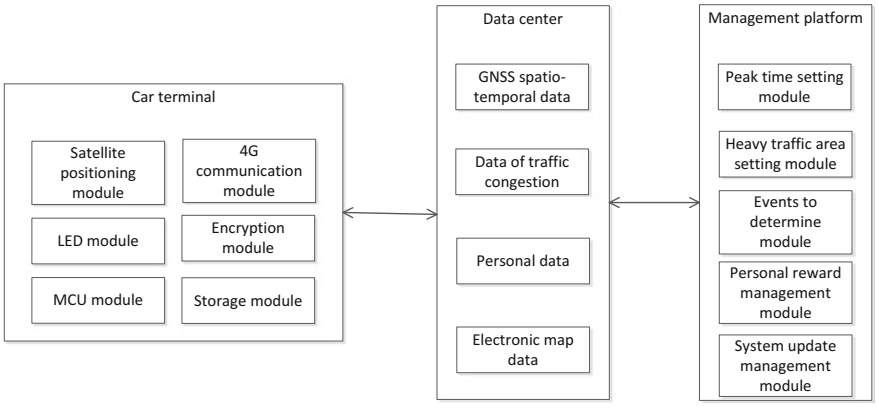

Fig. 2 System architecture diagram

Data center for storing all data traffic vehicles discriminant device information which is compatible with BD GNSS special spatio-temporal information, including GNSS spatio-temporal data, owner information, traffic data, personal data, and electronic map data [3].

Management platform comprises a peak time setting module, Heavy traffic area setting module, an Events to determine module, a personal reward management module and a System update management module [4].

3.1 Car Terminal

In the car terminal, GNSS module is used for acquisition of vehicle real-time GNSS information in time and space. The 4G communication module is used for wireless network communication. GNSS time and space information and vehicle information of the car terminal are uploaded to the data center using this module, and receive information management platform of the notice. The LED module is used for car terminal input and output. The Encryption module is used for translate GNSS information of vehicle and vehicle owner information, ensuring the security of the information. The MCU module is used for interaction and procession between different modules inside a car terminal. The storage module is used to store the electronic map data and system information which needs in the normal operation of car terminal.

3.2 Data Center

The data center is a distributed database which adopts the technology of big data. Different kinds of data information is stored in accordance with different levels of granularity respectively. It also provides a wealth of data analysis and demonstration, to ensure the security of the data and business system access.

3.3 Management Platform

In the management platform, Peak time setting module is used to specify a period for rush hour of the city.

Heavy traffic setting module is used in the electronic map, according to the corresponding geographic information data and logic, set road strip and close regional block to make virtual boundary, which is defined by heavy traffic area. Outside the virtual boundary is defined as the traffic section. This module can also remove, add or modify heavy traffic area.

Events to determine module receives the report of car terminal and determines whether the vehicles move into heavy traffic area in rush hours, by combining with information of license plate number and vehicle owners of residential address.

Personal reward management module collects the time, place and frequency data of vehicles moving into heavy traffic in rush hour traffic in a certain period. This module is used to influence individual's travel behaviour. It can modify people's reward accordingly and sent to the data center and the car terminal.

System update management module is responsible for the system settings, including changing rush hour and congestion zone, sending car terminal change, and updating the data in the car terminal.

4 System Working Process

As shown in Fig. 3, the system set rush hour time period to 07:00–9:30, 17:30–19:30, and scheduled five heavy traffic area. When the user open the car terminal, he/she must agree with BD GNSS spatio-temporal information city special discriminant system domain transportation vehicles, especially the agreement relating to personal information. After that he/she can login system by use vehicle license plate and car owner's identification information. This process is mainly through the car terminal touch screen information input and output.

After start up, the car terminal download the rush hour period, traffic congestion, and system information such as notice. When the vehicle cruising along the journey, the GNSS module receives real-time positioning signal BD system, and combines it with the inertial navigation generated the space-time location information. The car terminal compares the information data with the system setting information such as peak period and crowded area to determine whether the vehicle enters the traffic crowded area in the peak period.

When the car terminal initially determines that the car enters the traffic congestion area at the peak time, the car terminal uploads the encrypted vehicle GNSS data and the entering congestion area status information to the data center, and the event determination module further confirms the car terminal. When further confirmation is completed, it is possible to combine the picture and video information into the traffic congestion area from the non-traffic congestion area, and upload the information to the data center at the same time.

The events determination module in the management platform compares the GNSS time-space data, the traffic jam data and the owner's residence address information uploaded by the corresponding car terminal with the virtual boundary and the peak time period of the established traffic congestion area. If it is found that the GNSS spatio-temporal data is in the peak period and located in the geographical area of the congested area, and the owner's residential address is not in the traffic congestion zone, it is judged that the vehicle enters the traffic crowded area during the peak period. After the events determination module verifies that the vehicle enters the traffic congestion area during the peak period, the system will issue a system notification of "vehicle enters crowded area" to the car terminal.

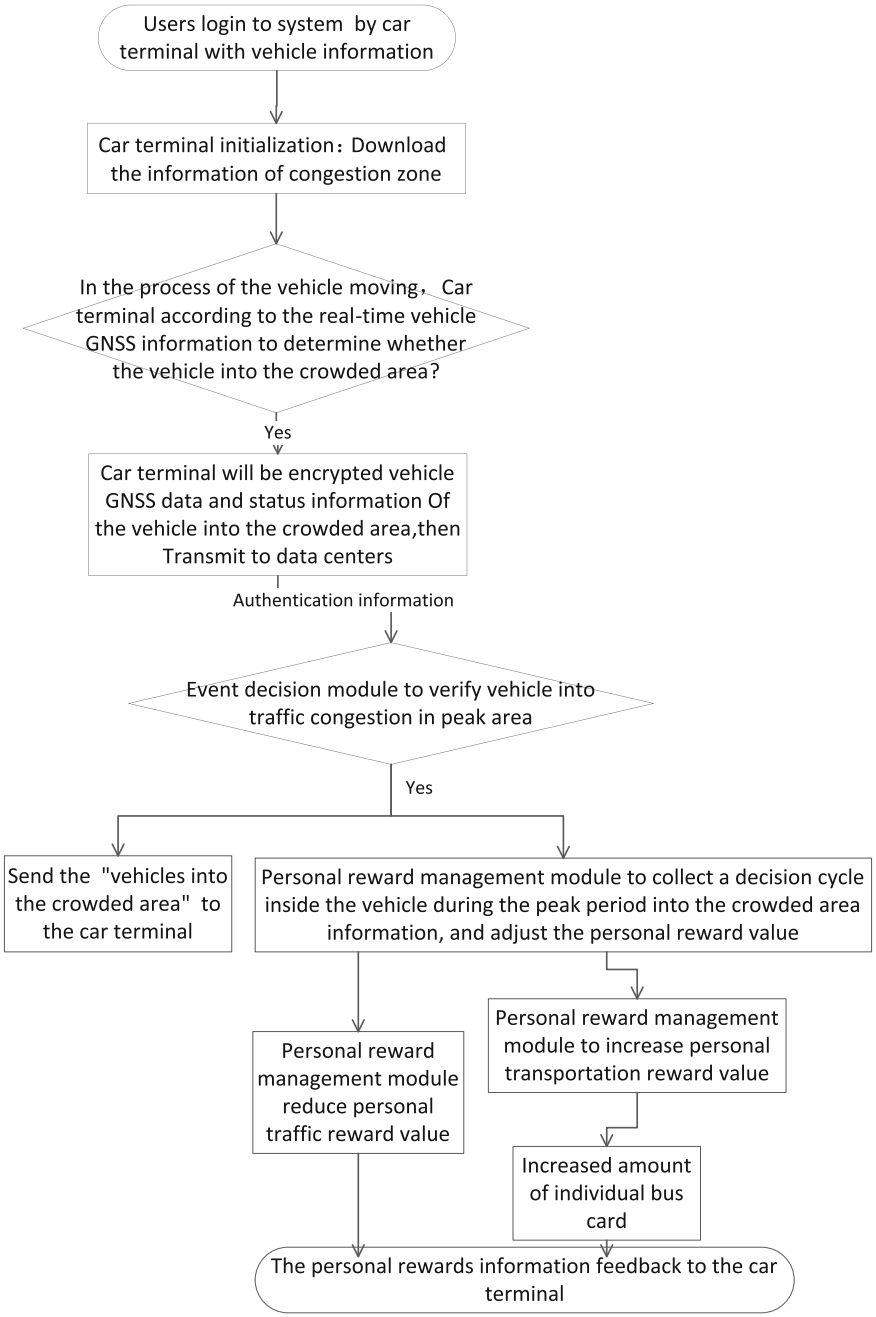

Fig. 3 System work flow chart

Table 1 Punishment rule table

Total time / Frequency (Times per week) / Penalty value (Yuan)	2H	4H	6H	8H	More than 10H
1	1	2	4	6	8
2	2	4	6	8	10
3	3	6	8	10	12
4	4	8	10	12	12
More than 5	5	10	12	12	12

In a reward decision cycle, the personal reward management module will pool the event decision module on the vehicle behavior of the decision results and the individual reward information values are changed accordingly. For example, if the personal credit determination period is set to one week, the personal reward management module increases reward information value of the vehicle owner who does not enter the city area in the peak period and increases the balance X yuan in the individual bus card. Personal reward management module for the peak period into the city of vehicles, according to the vehicle in the crowded area of the total length of time and the frequency of entering the city to reduce the corresponding N-yuan operation, the specific rules shown in Table 1. In the personal reward information value changes, as well as changes in individual bus card balance, the system will send a notification message to the vehicle terminal to the owners.

5 System Experimental Data Analysis

In the field of transportation, road traffic index is widely used to comprehensively evaluate the overall evaluation of road traffic quality. The road traffic index is calculated based on such indexes as motor speed and road saturation. The bigger the index is, the better the traffic quality. The evaluation criteria for different ranges of indices are shown in Table 2:

5.1 Traffic Comprehensive Index Model

The Traffic comprehensive index model:

Table 2 Traffic in different scope of index and evaluation standard

Index range	Level	Traffic conditions described
more than 80	Excellent	Traffic flow stability, the speed of normal traffic load level is reasonable
80–70	Well	Traffic is stability, the speed is normal, the traffic load level is relatively reasonable
70–60	Ordinary	Traffic in unstable state, the speed of the car began to abnormal, traffic load is high
60–45	Worse	Traffic often appear unstable state, the speed deviation from normal big, traffic load is too big
less than 45	Bad	Traffic is extremely stable, large speed deviation from normal, traffic jams

$$\mathrm{T}_{total} = \frac{\sum_{i=1}^{N} \omega_i T_i}{\sum_{i=1}^{N} \omega_i} \tag{1}$$

T_{total} Traffic comprehensive index;
T_i Trunk road, expressway traffic index;
ω_i Comprehensive index weighting factor;
N The total number of main road and fast track;

For the main road, fast track, road comprehensive index model [5]:

$$T_{road} = \begin{cases} \dfrac{\omega_v\left(1-\frac{\tau V}{V_f}\right)+\frac{\omega_k \mu K}{K_j}+\frac{\omega_q \gamma Q}{Q_m}+\frac{\omega_d \kappa D}{D_m}+\frac{\omega_a \eta A}{A_m}}{(\omega_v+\omega_k+\omega_q+\omega_d+\omega_a)} & K < K_m \\ \dfrac{\omega_v\left(1-\frac{\tau V}{V_f}\right)+\frac{\omega_k \mu K}{K_j}+\omega_q \rho \ell^{-\frac{\gamma^2 Q^2}{Q_m^2}}+\frac{\omega_d \kappa D}{D_m}+\frac{\omega_a \eta A}{A_m}}{(\omega_v+\omega_k+\omega_q+\omega_d+\omega_a)} & K \geq K_m \end{cases} \tag{2}$$

T_{road} Road composite index;
V_f Road speed;
V Average road speed;
K_j Worst - case traffic density;
K_m Maximum road traffic density;
K Road traffic flow density;
Q_m Maximum road traffic;
Q Road traffic flow;
D_m Maximum road delay time;
D Road traffic delay time;
A Number of road accidents;
A_m Maximum number of road accidents of the same type;
τ Meteorological factors, environmental factors, traffic order, policy factors for the speed of the regulatory factors;

μ	Meteorological factors, environmental factors, traffic order, policy factors for the traffic density of the regulatory factors;
γ	Meteorological factors, environmental factors, traffic order, policy factors such as traffic flow control factor;
κ	Meteorological factors, environmental factors, traffic order, policy factors such as the delay factor for traffic control;
η	Meteorological factors, environmental factors, traffic order, policy factors such as traffic control factors for the accident;
ρ	Traffic flow influence constant factor;
$\omega_v, \omega_k, \omega_q, \omega_d, \omega_a$	Factor weighting factor.

The average vehicle speed, traffic density, traffic flow and traffic delay time are the factors that determine the relative comprehensive index of the road. The influence is generally considered as a linear relationship. The average speed, traffic density, and traffic flow have the following relationship:

$$Q = VK \tag{(3)}$$

After the traffic density exceeds the maximum traffic density K_m, the exponential decay mode has an influence on the traffic index. It is shown that the exponential calculation should be based on the maximum value of the traffic flow density according to different formulas. In the model, the role of traffic accidents and other factors can be represented by a modified constant term, which over a period of time is an empirical constant.

The relevant variables and parameters of the above formula are:

The average road speed, the worst traffic density, the road traffic density, the road traffic flow, the road traffic delay time, the road accident black spot rate and the correlation constant factor need to be obtained through statistical analysis of the historical data. Regulatory factors also need to take into account a variety of factors under the premise of the historical data for statistical analysis model access.

The urban traffic comprehensive index is regarded as the relative number and can be processed by normalization. The range can be set in the range of easy to understand, such as 0–1, 1–10, 1–100, 1–1000, In this paper, the value range is 1–100.

5.2 Construction of Experimental Environment

After the system has been built, the data of the day traffic of Jinan section of the city center are selected as the template of the simulation verification data, and the data of the support data of the driver of the private car are obtained. The data are tabulated after finishing the questionnaire. The reference value is used to simulate the influence of the reference value to the road traffic comprehensive index (Table 3).

In the simulation process, some of the reference values in Eq. 2 are fixed, as shown in Table 4. Other values are real-time based on traffic conditions at the time, and the changes can be estimated as shown in Table 5.

Table 3 Survey data statistics

Period of time	Whether private car driver support incentive schemes		
	Support	No support	No matter
8:00–9:00	67	12	15
11:00–12:00	45	7	11
14:00–15:00	35	4	8
17:00–18:00	86	14	15
20:00–21:00	43	6	7
Statistics (%)	275 (73.3%)	43 (11.5%)	56 (15.2%)

Table 4 Constant parameter table

V_f	50 km/h	K_j	330/km
K_m	300/km	Q_m	1500/h
D_m	30 min	A_m	10
τ	0.5	μ	0.7
γ	0.4	κ	0.6
η	0.1	ω_v	45
ω_k	58	ω_q	63
ω_d	42	ω_a	23

Table 5 Parameters estimation table

Proportion of private car drivers	10%	20%	30%	40%	50%
V	5%↑	7%↑d	10%↑	14%↑	18%↑
K	3%↓	4%↓	6%↓	8%↓	11%↓
Q	2%↑	3%↑	4%↑	6%↑	7%↑
D	4 min↓	7 min↓	11 min↓	14 min↓	17 min↓
A	1.5↓	2.3↓	2.9↓	4.1↓	6.4↓
ρ	4.5	4.7	4.9	5.3	6.5

The reference traffic index curve can be derived according to the data changes in the table and road section data template using Eq. 2, as shown in Fig. 4. The blue dotted line is the original template curve. And the solid lines of other colors indicate the traffic index curves for incentive drivers with different proportions. It can be seen that the two composite traffic index becomes much significantly better as the ratio of incentive platform for private car drivers increases, specially for morning and evening traffic peaks.

The conclusions here are only for a section of the road. Future work will extend to the entire transport system. Congestion road transfer, and other issues related to determining the border areas are also interesting directions for further investigation.

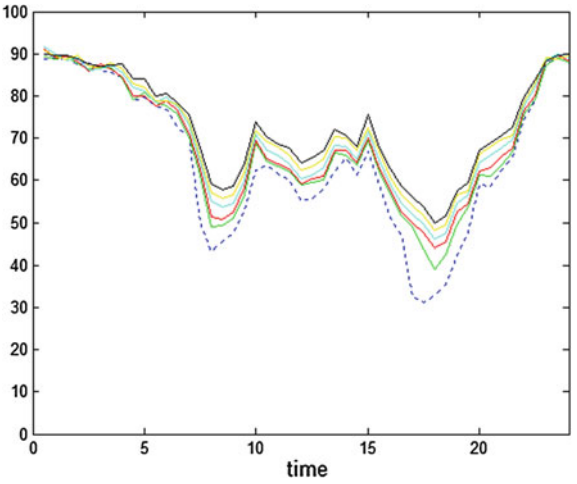

Fig. 4 Traffic composite index contrast figure

6 Conclusion

In this paper, a traffic incentive platform is proposed based on the BD GNSS and inertial navigation combination positioning system. It aims to unify private vehicle and public transport control to promote private car owners to use public transport during congested hours, increase the utilization of public transport, and ultimately mitigate traffic congestion problem in urban area, which is deem to be a win-win project planning.

The establishment of the platform has an outstanding social and economic benefits, such as it can provide private car owners with real-time traffic information to help them to plan their trips wisely which can help to form a good travel environment and improve residents' quality of life.

Acknowledgements The authors acknowledge the support from the Shandong Province independent innovation major project.

References

1. Yang Y (2010) Progress, contribution and challenges of compass/Beidou satellite navigation system. Acta Geodaetica Cartogr Sin 39(1):1–6
2. Chong C (2008) Global navigation satellite system (GNSS) and industrial development. Navigation and positioning technology progress and innovation expert forum
3. Min LI, Zhao Q, Shi C et al (2012) Precise orbit determination of BeiDou satellites by BeiDou/GPS data. Cuangzhou; CSNC2012
4. Li M (2011) Research on multi-GNSS precise orbit determination theory and application. Wuhan University, Wuhan, pp 1–11
5. Ji-zhen G (2004) Urban traffic index, travel index and mathematic model. J Transp Syst Eng Inf Technol 4(1):49–53

Research on the Next Generation of Emergency Positioning Signal Design and Ground Stations Receive Processing Based on GNSS

Henglin Chu, Tianqiao Zhang, Jiemin Shen, Hongbing Wang and Jingyuan Li

Abstract As typical representative of the emergency research and rescue signal in the field of Life Safety and Emergency Service, both the 2nd generation COSPAS-SARSAT beacon and the BeiDou System (BDS) locating report (or named RDSS) signal have been practiced for more than 20 years. These two systems with emergency positioning signals played significant social value and economic benefits, but also gradually exposed some issues, such as the high-power consumption for user terminal, low reliability and so on. The performance improvement plans of the two emergency service systems have been put on the agenda respectively, including the signal structure and the system architecture. Based on the next generation of satellite-based emergency positioning and reporting system, this paper presented the design of a highly reliable and low-power user signal/distress beacon system, as well as ground station processing methods. Firstly, the characteristics of the system frame and signal structure for the existing two kinds of emergency positioning system are introduced. Then, further discussions on the key element and corresponding scheme of the next generation emergency location signal, among the aspects of spreading sequence, channel encoding, frame structure, message arrangement, are expanded. At the same time, in order to minimize the power consumption of the user terminal and make full use of the uplink multi-coverage of the satellite-based positioning report system, a ground station diversity receiving user emergency positioning signal/distress beacon processing method is proposed. The ultimate purpose of this research is to improve the terminal power consumption, single detection probability and other key indicators of the next generation of emergency search and rescue application, to 2 W consumption, which is 5 W of the current user terminal supported by the two systems.

H. Chu · T. Zhang (✉) · J. Shen · H. Wang · J. Li
Beijing Satellite Navigation Center, Beijing 100094, China
e-mail: gary_85@163.com

J. Sun et al. (eds.), *China Satellite Navigation Conference (CSNC) 2017 Proceedings: Volume I*, Lecture Notes in Electrical Engineering 437,
DOI 10.1007/978-981-10-4588-2_40

Keywords Satellite-based search and rescue · Emergency location · Location report signal · Distress beacon · Diversity reception

1 Introduction

In recent years, global aviation safety accidents take place frequently and attract worldwide attention. Meanwhile, the aviation safety rescue capability is being explored. The development of the global satellite search and rescue system (SARSAT) has attracted much interest. Since COSPAS-SARSAT establishment, it has experienced two generations of signal system and three stages of development. At present, COSPAS-SARSAT has achieved high integration with GNSS, and with the rapid development of Galileo and other systems, the new generation system MEOSAR has begun to take shape [1], and more than 72 MEO navigation satellites is expected to carry MEOSAR repeater after 2025.

Chinese BeiDou Navigation Satellite System (BDS) is expected to have global full-service capability by 2020. It would also, like GPS, GLONLASS and Galileo, be equipped with the international common MEOSAR repeater, to become an important component of the global integrated SARSAT service framework. On the other hand, the RDSS service of BDS is also very suitable for emergency rescue applications with its special location reporting and communication ability. Through the literature [2] some information can be known that, BDS RDSS signal system has certain advantages in concurrent capacity, real-time, anti-jamming performance compared to MEOSAR, and could become a satellite search and rescue means with superior performance for further promotion of the application in the future.

For the user beacon, also called the inbound signal, whether the International COSPAS second-generation satellite search and rescue beacon or the Chinese BDS's Location Reporting Service (RDSS), the existing signal structure has been applied more than 20 years. The two emergency positioning services gradually exposed that the power consumption is too large, low reliability and other issues, while they played significant social value and economic benefits. Therefore, COSPAS and RDSS service performance improvement plan including signal system and system architecture have been put on the agenda. In this paper, the design of a high-reliability, low-power user inbound signal/beacon system and ground station processing scheme for a new generation of satellite-based emergency location and reporting system is presented [3]. Then, the key elements and corresponding schemes of the new emergency locating signal are discussed, such as frame structure, message arrangement, channel coding and so on. At the same time, in order to reduce the user terminal power consumption, improve uplink demodulation performance, and make full use of the uplink multi-coverage of the satellite-based positioning system, this paper proposes a data combination processing scheme for the ground station, and gives the performance analysis results.

2 Main Features and Optimal Design of Emergency Location Signals

At present, the number of satellites with MEOSAR repeater of the GNSS satellite navigation system is gradually increasing [4–6], and the system architecture is gradually improved. Through the detailed analysis of the international MEOSAR system and RDSS inbound service, we can see that there are a lot of common points in signal structure and system characteristics:

(1) Inbound return links are transparently forwarded on the satellite;
(2) Inbound return link is multiple coverage for the user;
(3) Inbound signal is a periodic short burst signal;
(4) Inbound signal frame structure can be divided into pilot segment, identity segment, message segment or sync segment, common segment, data segment three-segment frame structure;
(5) Inbound user power level is 5–10 W.

The procedure of signal processing and system framework of RDSS and MEOSAR emergency location reporting are shown in Fig. 1.

BDS RDSS inbound and MEOSAR emergency positioning beacons are periodic short burst signals, and the frame structure is similar as summarized and shown in Fig. 2.

In which, the pilot segment of MEOSAR beacon and the synchronization segment of RDSS inbound signal are all used to capture the inbound signal in the ground receiving system. The main information content of the identity segment of MEOSAR beacon segment or the common segment of the RDSS inbound signal includes the user ID, message structure type or the message length identifier.

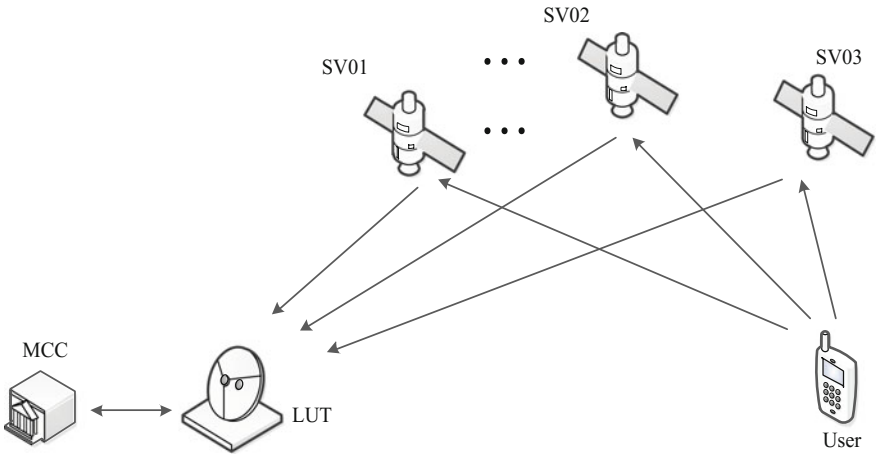

Fig. 1 MEOSAR/RDSS emergency location reporting system model

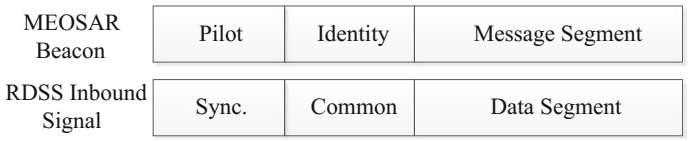

Fig. 2 MEOSAR/RDSS inbound frame structure

The message segment of the MEOSAR beacon and the data segment of the RDSS inbound signal carry the different message with specified format. During the actual use in the past 20 years, the two different inbound signals exposed two main problems: The first one is that the total terminal power is too large, and the second is that the inbound demodulation success rate was significantly affected when the user terminal is in shadow or poor attitude. To resolve the above problems, a new generation beacon optimal design ideas are presented as follows:

(1) Improving the spread spectrum performance by using a larger spreading ratio;
(2) Reducing the capture threshold by increasing the pilot/sync segment;
(3) Reducing the demodulation threshold of the common segment by reducing the data rate, simplify the field content, independent channel coding, and also adopting the better channel coding scheme in the message segment to improve the demodulation threshold;
(4) Allocating each segment information rate according to the constraint criterion that the sync segment capture threshold ≈ common segment demodulation threshold, and the common segment demodulation threshold is better than the data segment about 2 dB (Fig. 3).

Based on the above optimal design idea for the signal system, the analysis of MEOSAR beacon signal were conducted without changing the central frequency, data segment rate of 400 bps, satellite receiving G/T value and so on. The analysis results (as shown in Table 1) show that the level of user terminal can be reduced

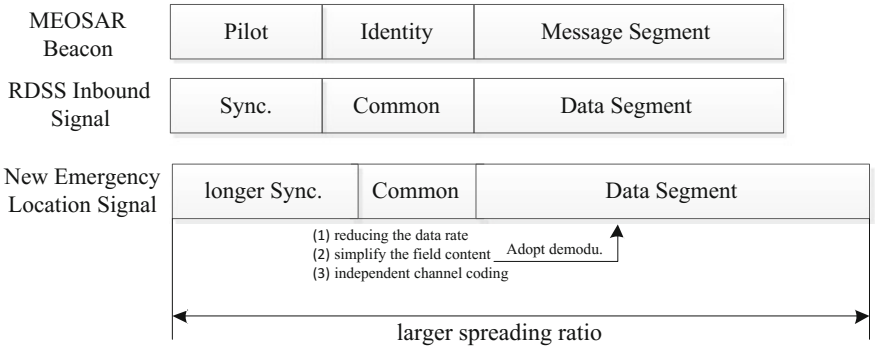

Fig. 3 Main optimization path for next generation emergency location signals

Table 1 Performance comparison of the new and old emergency positioning signals

Inbound uplink	Existing MEOSAR Beacon	New emergency positioning signals
Center frequency (MHz)	406	
Sat. distance (km)	26,000	
User transmit power (W)	5	2
Uplink trans. loss (dB)	−172.91	−172.91
Arrival power(dBW)	−165.92	−169.90
Sat. G/T(dB/K)	−17.7	−17.7
Total C/N0 (dBHz)	44.47	40.49
Common segment demodulation threshold (dBHz)	35.62 (400 bps, coded)	30.51 (200 bps, coded)
Common segment demodulation margin (dB)	8.85	9.98
Data segment demodulation threshold (dBHz)	35.62 (400 bps, coded)	32.52 (400 bps, coded)
Data segment demodulation margin (dB)	8.85	7.97

from the existing 5–2 W, and the demodulation performance of data segment can also be improved according to the segment processing solution as mentioned in the next section.

3 Ground Receiving Combine Processing Scheme and Performance Evaluation

The main premise of the new algorithm is that the emergency locating system such as MEOSAR or RDSS inbound has a very prominent feature: the inbound uplink has overlapping coverage of 2–4 or even more, and there are at least two approaches for the inbound signal power arriving at the ground station. The uplink multi-coverage feature of this system is mainly for the completion of positioning calculation [7–9], but on the point of communication, the large number of redundant information is a waste of channel resources. Meanwhile, a new generation of emergency positioning signal design will be dedicated to enhance the performance of common segment demodulation, and provide better condition for the joint data demodulation and receiving with different arrival times, different arrival location of.

The combine processing framework for a new generation of emergency positioning signal data segment is proposed as shown in Fig. 4.

Data segment combine processing is to complete the user inbound signal through different satellites, different beams in a certain time window to receive the identity of the pair, the data segment of the diversity and joint decoding work. The main processing flow is as follows:

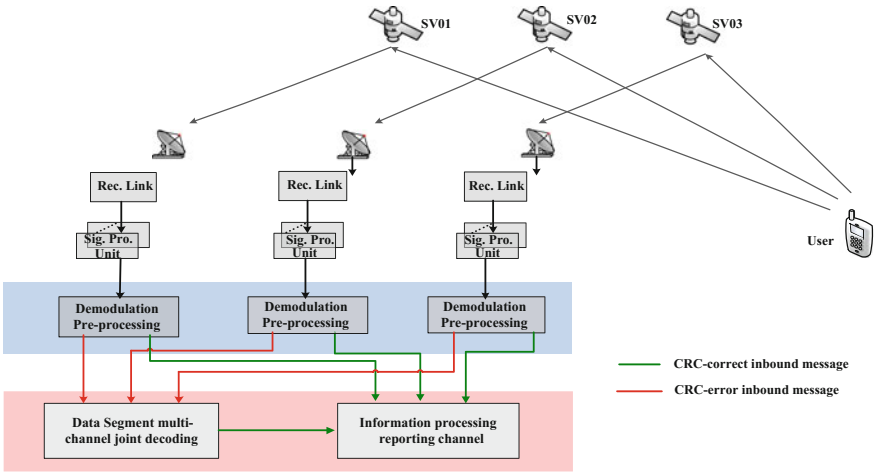

Fig. 4 Data segment synthesis solution

(1) The combine processing unit filters out all inbound messages of the same user by matching the user identification numbers within the set receiving time window;
(2) If the combine processing unit receives a CRC check correct indication in the receiving time window, it does not need to carry out the joint decoding processing, and sends the correct CRC check message to the information processing reporting channel;
(3) If CRC checksum for all inbound message of the same user are not correct, then it need to carry out the multiple joint decoding processing. Finally, the joint decoding unit sends the diversity processed inbound message to the information processing reporting channel.

For inbound data segment combine processing, in theory, when there are no pseudo-code and carrier frequency phase tracking errors, 2-way inbound signals with the same carrier-to-noise ratio are combined to achieve about 3 dB diversity gain.

In practice, when there is pseudo-code and carrier frequency phase tracking error, the diversity gain of the inbound signal depends on the tracking accuracy of single signal and the demodulation loss of single-channel signal. The main factors include pseudo-code phase error, carrier phase error. Next, we conduct the analysis of the two-channel diversity receiver gain problem based on the maximum-ratio combining algorithm, and focus on the diversity reception performance under pseudo-phase phase mismatch and carrier phase mismatch.

Assuming that the first signal carrier phase mismatch is φ_1, the second signal carrier phase mismatch is φ_2, and no other error factors, then the diversity gain is as follow:

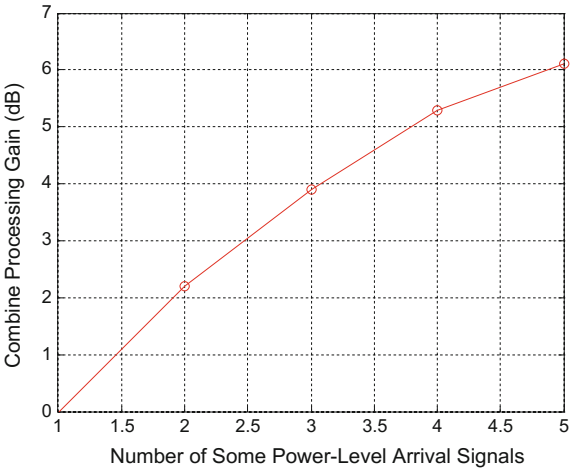

Fig. 5 Multiplexing diversity receive gain

$$G_0 = 10 \log 10\left(\frac{(\cos(\varphi_1) + \cos(\varphi_2))^2}{2}\right) \quad (1)$$

When the carrier-to-noise ratio is greater than 30 dBHz, the carrier phase tracking accuracy is less than 0.4, the corresponding demodulation loss is 0.8 dB, and the diversity gain is 2.2 dB.

For multi-channel simultaneous data segment combine processing, the diversity gain increases as the number of processing uplinks increases, and the increasing trend is shown in Fig. 5.

In summary, based on the existing international MEOSAR or RDSS service, the new generation of satellite-based emergency positioning signal system is optimized and the data segment fusion processing algorithm can be adopted. When there are two similar inbound arrival levels, the data segment is made to have a diversity gain of about 2.2 dB. Return to Table 1 data, with comparing the old and new emergency positioning report system, it can be seen that the new system of emergency positioning signals in the terminal power consumption has been about 3.9 dB decline, the system segment and data segment demodulation margin has been about 1.1 dB increase, the overall performance is very obvious.

4 Conclusion

In this paper, based on the analysis of the similar points between the international satellite search and rescue system MEOSAR and BDS RDSS inbound service, a new generation of emergency positioning inbound/beacon signal design is presented in terms of reducing the power consumption of the user terminal. At the same time, a data segment combine processing scheme in the ground system is

proposed to further improve the demodulation performance. On the whole, the new system inbound signal and fusion algorithm proposed in this paper can reduce the power consumption of emergency terminal to 2 W from the existing 5 W level, and improve the inbound demodulation margin by 1.1 dB. The overall system performance is improved by 5 dB. The results of this paper can provide reference for the optimization and upgrading of the next generation RDSS service and MEOSAR technology framework.

References

1. Gregoire Y, Petcu A, Calmettes T (2014) MEOSAR new GNSS role in search & rescue. Inside GNSS, pp 57–67
2. Zhang T, Wang H (2014) Comparative performance—analysis between BDS RDSS position report and the SARSAT service. Geomatics Sci Eng 34(6):74–78
3. Langley R (2011) The distress alerting satellite system. GPS World, pp 72–76
4. International Civil Aviation Organization (2006) Aeronautical telecommunications volume I radio navigation aids, 6th edn
5. Congress of the United States Congressional Budget Office (2011) The global positioning system for military user: current modernization plans and alternatives
6. Department of Defense of United States of America (2008) Global positioning system standard positioning service performance standard, 4th edn. http://pnt.gov/public/docs/2008/sp-sps2008.pdf
7. Yuanfeng L, Yan Z, Falin W (2010) Analysis of global availability for Beidou 2nd generation navigation system. Electron Meas Technol 33(7):15–18
8. Li G, Li J, Jiao W, Gui Q (2010) Analysis of PDOP availability of navigation constellation based on satellite service intermittence. Geomatics Info Sci Wuhan Univ 35(7):841–845
9. Zheng H, Li H, Yang Z (2011) The analysis of constellation availability for satellite navigation system. Aerosp Control 29(3):P87–94

Obstacle Avoidance Path Planning of Rotor UAV

Xiaodong Zhang, Xiangyang Hao, Guopeng Sun and Yali Xu

Abstract With the increasingly wide application of UAV in military, civil and other fields, autonomous navigation and obstacle avoidance of UAV has become a hot issue of study, and path planning is one of core technologies to realize it. Based on traditional path planning method cannot juggle global optimal and real-time obstacle avoidance effectively, this paper proposes a new path planning method fusing the global and the local,it uses genetic algorithm in global and artificial potential field method in local, then gets an optimal path to reach the destination safely. Through simulation experiment, this method has good real-time and reliability, meeting the requirements of autonomous navigation and obstacle avoidance.

Keywords Rotor UAV · Path planning · Artificial potential field · Genetic algorithm · Optimal path

1 Introduction

As UAV is finding wider and wider application in the field of military and civilian, UAV autonomous navigation and obstacle avoidance technology has become a hot research topic, and path planning in flight is one of the core technology of realizing autonomous navigation and obstacle avoidance.

According to the target range of UAV path planning, which can be divided into global path planning and local path planning [1]. From the state of the planning environment it is divided into static path planning and dynamic path planning [3].

X. Zhang (✉) · X. Hao · G. Sun · Y. Xu
Information Engineering University, Zhengzhou 450000, China
e-mail: 1228024443@qq.com

X. Zhang · X. Hao · G. Sun · Y. Xu
Beidou Navigation Technology Collaborative Innovation Center of Henan, Zhengzhou 450000, China

J. Sun et al. (eds.), *China Satellite Navigation Conference (CSNC) 2017 Proceedings: Volume I*, Lecture Notes in Electrical Engineering 437,
DOI 10.1007/978-981-10-4588-2_41

Common four UAV path planning methods are template matching method, artificial potential field method respectively, map building method and artificial intelligence method [4]. The principle of template matching method is simple and matching effect is good, but it can't find a matching path without enough template library [5]; The principle of artificial potential field method is simple and easy to control, but it often has local minimum points and the difficulty is the design of the gravitational field and the repulsive force field in a dynamic environment [6]; Map building method is straightforward and obstacle avoidance effect is good, but excessive amount of data leads to its bad real-time [7]; Artificial intelligence method improves the intelligence features of UAV and makes up for the shortcomings of other methods, but it can't complete the task alone in unknown environments [8]. In existing known methods, global planning method has a good effect on the known environment, but poor real-time performance in unknown environment; Local planning method can timely deal with random encounter obstacles, but the path planning is difficult to achieve the best in the whole environment, the traditional method of path planning is difficult to meet the needs of UAV autonomous navigation and autonomous obstacle avoidance.

Aiming at the problems of traditional path planning method, this paper proposes a path planning method fusing global path planning method and local path planning method. The idea is as follows: global path planning is carried out by genetic algorithm, and the sub-target node sequence arriving at the target point is generated. At the same time, local path planning is carried out by artificial potential field method to generate the smooth path between sub-targets. The advantage of this method is that it can generate global optimal path by using known information, deal with random obstacle in time and has better security and reliability.

2 Related Research

2.1 The Principle of Artificial Potential Field Method

Artificial potential field method is a virtual force field method proposed by Khatib. The basic idea is regarding the movement of UAV in the real environment as the movement of UAV in virtual force field. The target point attracts UAV and the obstacle exclude UAV, and vector sum of the two is the resultant force of UAV in the potential field, so as to control the direction of movement of UAV.

In order to facilitate the calculation, artificial potential field model is constructed and the obstacle is abstracted as circular model. As shown in Fig. 1d is the distance from UAV to the midpoint of obstacle, r2 is the dangerous distance that UAV will be dangerous when $d < r2$, r3 is safe distance that UAV will be safe when $d > r3$. To ensure safety, UAV can't enter the area of radius r2, so the following radius r2 circle for the obstacle area, $r2 < d < r3$ ring for the repulsion field area. UAV under the influence of gravity F_{att} is always subject to the target point in any area. UAV, is

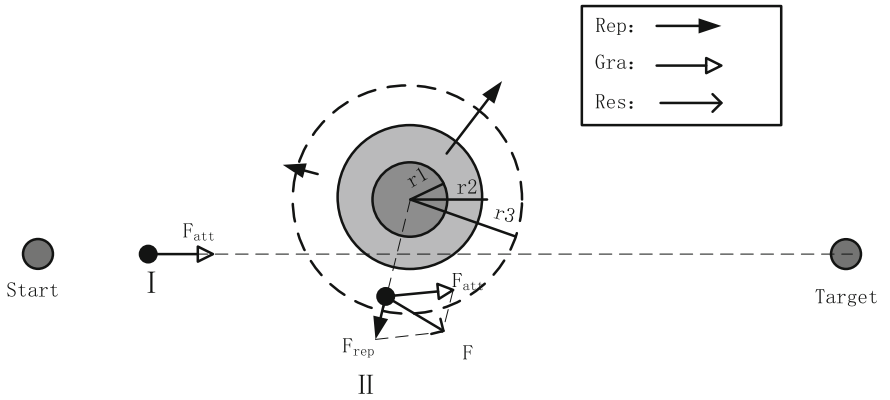

Fig. 1 Model of the artificial potential field method

affected by the repulsive F_{rep} in the obstruction area, repulsion can be seen as infinite in the obstruction area repulsion, so the UAV will not enter the obstacle area.

Artificial potential field method is simple and convenient for real-time control, and it is widely used in local path planning. According to its principle, we can see that the gravitational field has larger range of action, which can acts on any distance; the range of the repulsive force field is smaller, and when the distance from the UAV to the obstacle exceeds a certain range, it is not affected by the repulsive force field. Therefore, the artificial potential field method is suitable to solve the obstacle avoidance problem in the local space, but it lacks global information, easy to fall into the local minimum. In the actual path planning, it is prone to shock in front of obstacles, swings in the narrow channel, can't reach the target and so on. The local minimum is that UAV is subject to the gravitation as well as the repulsion in the artificial potential field. When there are many obstacles, UAV will be subject to multiple forces, which will be zero in a certain area or a point, at this time UAV will produce shock or stagnation. The more likely the obstacle is, the more likely it will be to generate local minimum points.

2.2 The Principle of Genetic Algorithm

Genetic algorithm (GA) is a kind of stochastic search method which is proposed by Professor J. Holland of the United States learning from evolution law of biology. The method is characterized by direct operation on the target, automatic acquisition of the search space, adaptive adjustment of the search direction, with good parallelism and global optimization capabilities, and is suitable for solving complex multi-objective problems, applied in multi-obstacle path planning. The basic operation steps of genetic algorithm are as follows:

1. Initialization: randomly generate the initial population;
2. Individual evaluation: assess individual fitness in the population;
3. Select the operation: select the operator on the population, according to the individual selection of chromosome fitness;
4. Crossover operations: the crossover operator on the population, resulting in a new sub-individual;
5. Mutation operation: the mutation operator on the population, the group of individual strings in the gene value changes;
6. Termination of judgment: if the termination conditions are met, then stop the calculation, otherwise return to the second step.

The key technology of genetic algorithm in path planning is chromosome coding. In a multi-obstacle environment, each individual code can represent a combination of multiple patterns without generating redundant dates. Genetic algorithm requires individual coding to operate with genetic operators easily and improve search efficiency. In this paper, redundant binary coding is used. Assuming that the number of obstructions is N, the number of chromosomes is $n = \log_2 N + 1$, and the representable state is $2n > N$, and $2n - N$ redundant states are represented by vacant bits.

3 Modeling of Path Planning

3.1 Obstacle Avoidance Path Planning Model for Single Obstacle

The problem of obstacle avoidance path planning for UAV can be considered as the best path from the starting point to the target point under the resultant forces of gravitation and repulsion. UAV direction always point to the direction of its force, namely the direction of the resultant forces of repulsion and gravity. Resultant forces only change the direction of the speed, but don't change the size of the speed. The obstacle avoidance path approach is described as follows:

1. Establish potential field model. According to the known information to determine the starting point coordinates $P_s(x_s, y_s)$, UAV flight speed v, the target point coordinates $P_e(x_e, y_e)$, the location of obstacles D and the force field range.
2. Path planning that does not cross the obstacle area. If the connection does not pass through the obstacle and repulsion field area from the starting point to the target point, then the connection is the optimal path, as shown in Fig. 2.
3. Path Planning Through Obstacle Repulsion Field. If the connection from the starting point to the target point passes through the repulsive force field but does not pass through the obstacle, then UAV only receives the gravitational force out of the repulsive force field, the repulsive force and the gravitational force in

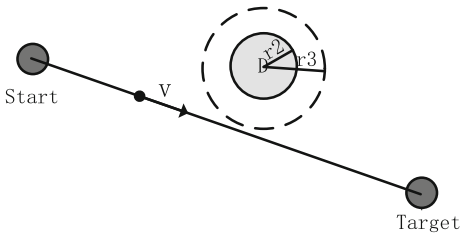

Fig. 2 The path not through obstacles

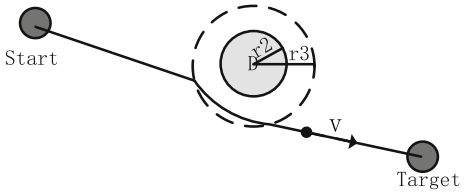

Fig. 3 The path through repulsive force field

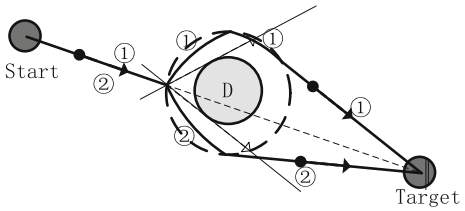

Fig. 4 The path through obstacles

the repulsive force field and finally reach the target point, as shown in Fig. 3. The direction of velocity in motion is always the same as the resultant force.

4. Path planning through obstructions. When the starting point to the target point of the connection through the obstacle, then the starting point to the target point of the first intersection of obstacles for the two tangents. In the repulsion field, the direction of gravitation is changed to the direction of two tangent lines respectively. After leaving the repulsive force field, the gravitational direction points to the target point again. UAV is subject to gravitational force out of the repulsive force field, gravitational and repulsive force in the repulsion field, and ultimately reach the target point, selecting the shorter as the optimal path, as shown in Fig. 4.

3.2 Obstacle Avoidance Path Planning Model with Multiple Obstacles

UAV flying in complex environments may encounter multiple obstacles. Solving the optimal obstacle avoidance path in a multi-obstacle environment is namely

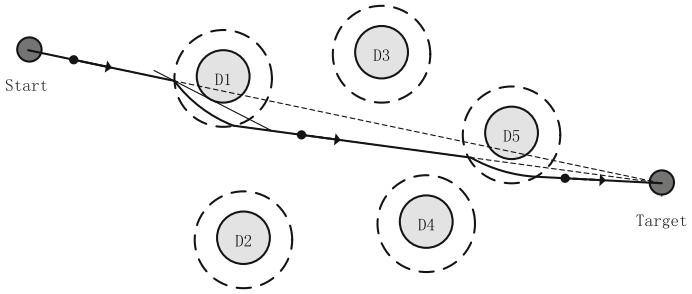

Fig. 5 The path through multi-obstacles

Table 1 Coding table for GA

Coding	000	001	010	011	100	101	110	111
Status	D_1	D_2	D_3	D_4	D_5	B	B	B

solving the shortest directional curve of avoiding the obstacles effectively that UAV flies from the starting point to the target point in the artificial potential field.

As shown in Fig. 5, there are five obstacles between the starting point and the target point. These obstacles were genetically coded and the number of known obstacles was N = 5, then the number of chromosomes n is $\log_2 5 + 1$ rounded, so n = 3, then $23 - 5 = 3$ redundant spaces. The code table is shown in Table 1.

The optimal path in Fig. 5 can be described as (D1, D5, blank, blank), and the corresponding chromosome is encoded as (000, 100, 101, 110). An optimal path can be encoded by a variety of chromosomes, which reflects the advantages of redundant binary chromosome coding can expand the search space, converging to the optimal solution quickly. After path order determined by the reciprocal of the selected path length as the fitness function, the whole path planning is transformed into the path planning of single obstacle. The obstacle avoidance path planning of single obstacle is shown in Sect. 3.1.

3.3 Real-Time Obstacle Avoidance Path Planning Model

Assuming that the UAV is flying in unknown environment, only the target and some obstructions are located. When a new obstacle is encountered, the path can only be planned in real time after the obstacle is found. The detection distance of UAV to the obstacle is R, and if a new obstacle is detected to enter UAV detection area, UAV can safely reached the target point by re-path planning. The steps of real-time obstacle avoidance path planning are as follows:

First, the coordinates P_s, P_e, the flight velocity v, and the initial obstacle course D, the obstacle radius r2, the repulsive field radius r3, and the UAV detection distance R is input to the start point and the target point.

Second, path planning according to the obstacle information in the method of Sect. 3.2, then fly forward following the current planning path.

Third, detect whether a new obstacle in the radius R within the flight process. If an obstacle is detected, the current position and the existing obstacle position are compared and the obstacle sequence is updated, and then the process returns to the second step. If no obstruction is detected, skip to the next step.

Fourth, if the UAV to fly to the target point, the algorithm ends.

4 Simulation

4.1 Simulation of Obstacle Avoidance Path Planning for Single Obstacle

UAV flight parameters is the starting point coordinates (60, 50) m, the target coordinates (540, −50) m, the flight speed of 2 m/s. Respectively, in the coordinates (130, −30), (140, −8), (140, 0) set radius of 10 m, repulsion radius of 20 m obstacles. Using the algorithm of Sect. 3.1, the simulation results show that the obstacle avoidance paths are shown in Figs. 6, 7 and 8 respectively.

In Fig. 6, connection from the starting point to the target point does not pass through the obstacle area, so the connection is the optimal path. In Fig. 7, the connection from the starting point to the midpoint passes through the repulsive field, but does not pass obstacle, the optimal path is obtained under the effect of the potential field. In Fig. 8, there are two routes, and a shorter route is selected as the optimal route.

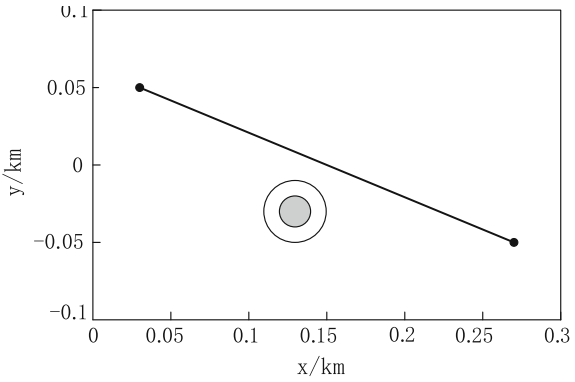

Fig. 6 Path of obstacle avoidance with the obstacle's center at (130, −30) m

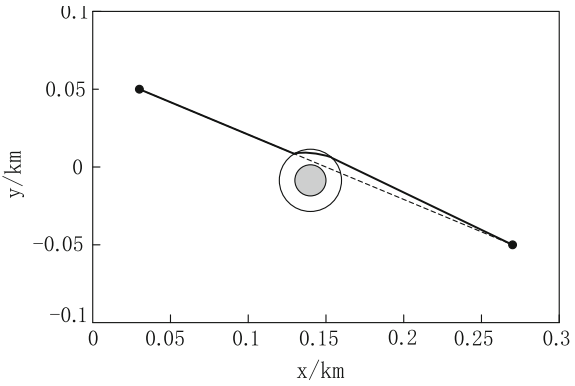

Fig. 7 Path of obstacle avoidance with the obstacle's center at (140, −8) m

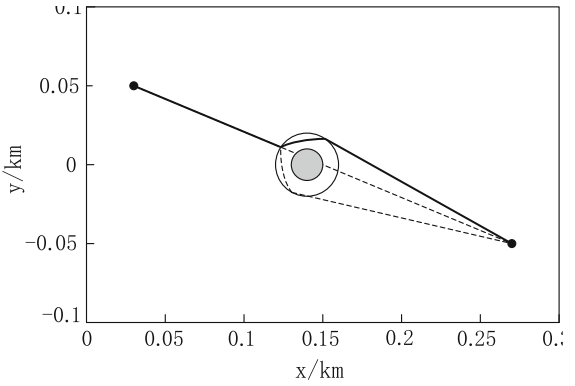

Fig. 8 Path of obstacle avoidance with the obstacle's center at (140, 0) m

4.2 Multi Obstacle Avoidance Path Planning Simulation

UAV flight parameters remain unchanged, setting up multiple obstacles in the flight area, obstacle parameters in Table 2, the obstacles for chromosome coding in Table 3. After the genetic algorithm and artificial potential field method, the obstacle avoidance path can be obtained as shown in Fig. 9.

In Fig. 9 there are four obstacles, three of which will affect UAV flight, one is not on the flight path. So the path planning only needs to avoid three obstacles.

Table 2 Lists of obstacle

Obstacle no.	D_1	D_2	D_3	D_4
Center coordinates/m	(70, 20)	(105, −15)	(175, 0)	(230, –25)
Obstacle radius/m	10	7.5	15	10
Repulsion radius/m	20	17.5	25	20

Table 3 Coding table of GA

Coding	000	001	010	011	100	101	110	111
Status	D_1	D_2	D_3	D_4	B	B	B	B

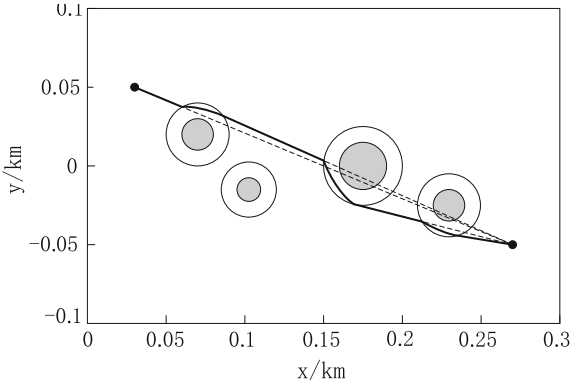

Fig. 9 Path of obstacle avoidance for multiple obstacles

4.3 Real-Time Obstacle Avoidance Path Planning and Simulation

UAV flight parameters remain unchanged, the detection range is 50 m, the flight path has a known obstacle and a number of unknown obstacles, then simulation experiments according to the algorithm of Sect. 3.3. UAV starting at t = 0, the simulation step is 0.1 s, the UAV flight path in the follow-up is shown in Figs. 10, 11 and 12.

At t = 0 s, the path planning based on the existing obstacle information is shown in Fig. 10. The first new obstacle was found when fly to t = 5.2 s, and the path was

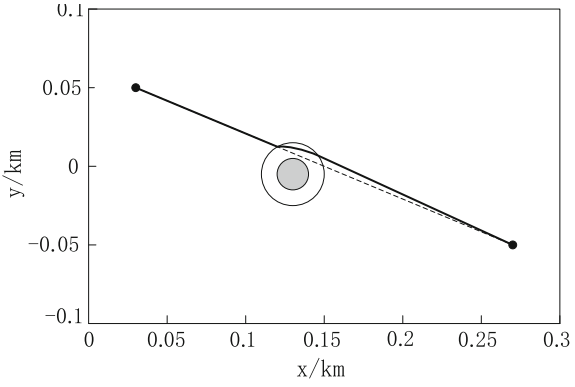

Fig. 10 Path of obstacle avoidance when t = 0 s

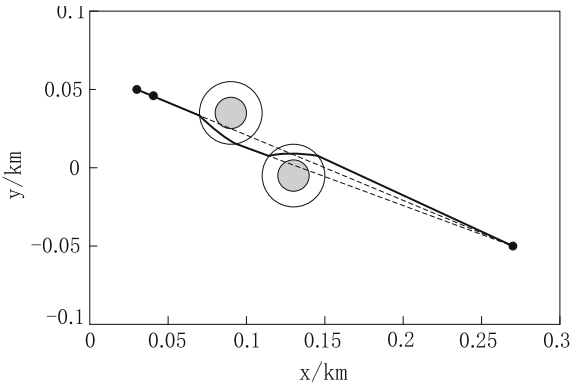

Fig. 11 Path of obstacle avoidance when t = 5.2 s

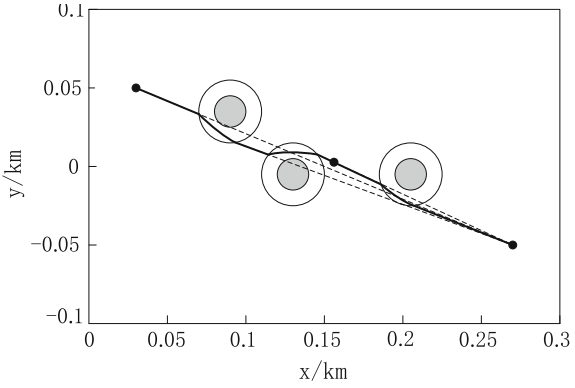

Fig. 12 Path of obstacle avoidance when t = 77.6 s

re-planned as shown in Fig. 11. After a new path to t = 77.6 s, the second new obstacle was found and the path was re-planned. As shown in Fig. 12, the UAV continued to fly on the new path until it reached the target.

5 Conclusion

This paper provides a path planning method fusing the global and the local, genetic algorithms for global planning, artificial potential field method for local planning, and get an optimal path arriving at the target point safely. The method not only can grasp the global optimal path, but also quickly deal with the sudden encounter of new obstacles. The path obtained by this method only has a small gap with the shortest path, but keeps the UAV and obstacle at a certain distance and improves the safety of the flight. Simulation results show that the proposed method can

effectively avoid the obstacle in real time, and obtain a safe and reliable optimal route with short travel time, which can fulfill the requirements of UAV autonomous navigation and obstacle avoidance.

References

1. Bao YQ, Li SM, Shen H (2009) Survey of local path planning of autonomous mobile robot. Transducer Microsyst Technol 28(9):1–4
2. Xu J (2009) The reserch of mobile robot path planning algorithm based on ant colony algorithm. Beijing University of Chemical Technology, China
3. Zhang GL, Hu XM, Chai JF (2011) Summary of path planning algorithm and its application. Mod Mach 5:86–90
4. Zhu DQ, Yan MZ (2010) Survey on technology of mobile robot path planning. Control Decis 25(7):961–967
5. Arleo A, Smeraldi F, Gerstner W (2004) Cognitive navigation based on non-uniform gabor space sampling, unsupervised growing networks, and reinforcement learning. IEEE Trans Neural Netw 15(3):639–652
6. Masoud AA (2009) Managing the dynamics of a harmonic potential field-guided robot in a cluttered environment. IEEE Trans Ind Electron 56(2):488–496
7. Cai CH, Ferrari S (2009) Information-driven sensor path planning by approximate cell decomposition. IEEE Trans Syst Man Cybern Part B Cybern 39(3):672–689
8. Zhu A, Yang SX (2006) A neural network approach to task assignment of multi-robots. IEEE Trans Neural Netw 17(5):1278–1287
9. Pereira FB (2009) Bio-inspired algorithms for the vehicle routing problem. Springer, Berlin

Orbit Analysis for Tiangong-2 Space Lab Under Different Perturbation Forces

Lina He, Wenli Wang and Zhilu Wu

Abstract Tiangong-2 is a space laboratory of China, which carries out various the Earth observations and space experiments. Controlling of the Tiangong-2 and completing these experiments rely on high precision orbit information. Hence, study on perturbed motion, which can be switched to analyze perturbation forces is the basis and core tasks. Firstly, in order to analyze the influence to the orbit by the perturb forces, initial orbit state is obtained by two line elements. Furthermore, several integral orbits are achieved under different perturb forces using numerical integration method, including the Earth potential perturbation, tides, three body perturbation, atmospheric drag perturbation, the solar radiation pressure and the Earth albedo. The experimental result shows that the atmospheric drag perturbation is one of the key factors to constraint the orbit accuracy and much more complex, due to the fact that Tiangong-2 is a low Earth orbit spacecraft. Moreover, atmospheric drag perturbation is discussed in details for comparing different upper atmosphere density models. And its orbit affect level is concluded, which is benefit for precise orbit determination.

Keywords Tiangong-2 · Perturbation force · Atmospheric drag · Gravity

L. He (✉) · W. Wang · Z. Wu
School of Earth Sciences and Engineering, Hohai University, Nanjing 211100, China
e-mail: hlnyh@hhu.edu.cn

W. Wang
e-mail: hhuwangwenli@163.com

Z. Wu
e-mail: wuzhilu@hhu.edu.cn

L. He
State Key Laboratory of Geo-Information Engineering, Xi'an 710054, China

J. Sun et al. (eds.), *China Satellite Navigation Conference (CSNC) 2017 Proceedings: Volume I*, Lecture Notes in Electrical Engineering 437,
DOI 10.1007/978-981-10-4588-2_42

1 Introduction

Thanks to the low orbit altitude, the LEO (Low Earth Orbit) spacecraft play a key role in kinds of scientific tasks, for example, high resolution observation, communications, target detection. The most famous low orbit spacecraft includes Shenzhou spaceship, Iridium star communication system, gravity satellites, space stations and so on. The latest launched space lab Tiangong-2, which carries out multi Earth observation and space experiments, realized high difficulty tasks like docked by Shenzhou-11 and experimental repairing on board. The design, control and operation of LEO rely on the deeply recognition for its orbit. The comprehensive of LEO motion is the basis for precise orbit determination and orbit keeping. However, in the space environment, LEO suffers from complex perturbations, especially atmospheric drag, which is the main factor to restrict the accuracy of the orbit prediction. At present, the atmosphere density models are empirical models with a limited accuracy [1]. Hence, the study on how these perturbations impact the LEO orbit including the earth non-spherical gravity and atmospheric drag is an important work.

Tiangong-2 space lab is the experimental target in this paper. Firstly, different perturbations are considered for obtaining three-day prediction orbits, using two body orbit combined with one kind of perturbation force, to analyze the influence of each perturbation force to Tiangong-2 orbit. The results show that as for the Tiangong-2, the largest impacts are from the earth non-spherical gravity and the atmospheric drag. Different degree and order of EGM96 gravity models are studied to investigate the sensitive of the gravity model. Using high precision orbit integration method to obtain several three-day orbits, in which different atmospheric density models with varying solar activity parameters are chosen to compare the orbit results. The rest of the paper is organized as follows, perturbation and impact on orbit are discussed in Sect. 2. In Sect. 3, the sensitive of the Earth non-spherical gravity model is analyzed and three types of atmospheric density models are investigated in Sect. 4. Finally, the conclusions are drawn in Sect. 5.

2 Perturbation Force Analysis for Tiangong-2

Supposing the Earth is a sphere with its mass distributed equally, a central gravitational field is formed. In this situation, only two bodies are required to be considered when neglecting other forces, one is the spacecraft, and the other is the Earth. However, the earth is not an ideal sphere, the motion of spacecraft is very complex since various perturbations. To solve the motion differential equation of spacecraft, analysis method and numerical method are common used. Analysis method can hardly meet high accuracy requirements. While as long as suitable step and order are given, numerical method can obtain solution with any high accuracy. In the high precision orbit integration, perturbation forces are considered including

Table 1 The initial condition of Tiangong-2

Spacecraft	Initial epoch	X (km)	Y (km)	Z (km)
Tiangong-2	2016275.0	4918.92	766.59	−4584.39
		VX (km/s)	VY (km/s)	VZ (km/s)
		−1.4984	7.5145	−0.3579

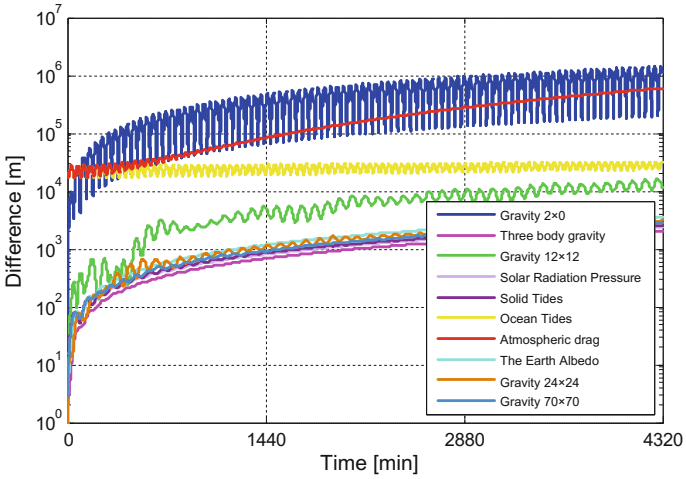

Fig. 1 The orbit analysis for Tiangong-2 space lab

the Earth non-spherical gravity potential, tides perturbation, three-body gravitation, the solar radiation pressure, atmospheric drag perturbation and the Earth albedo. These perturbations can be expressed as acceleration form, some of which are related to the parameters of spacecraft, for example, flat plate area, the mass, radiation area and so on.

Taking Tiangong-2 as an example, the orbit integration progress is explained. First of all, Tiangong-2 instant position and velocity are calculated in true equator mean equinox frame using Two Line Elements as the orbit initial conditions [2, 3]. The results are then transmitted to J2000 inertial coordinate frame, which are shown in Table 1. After that, the orbit initial conditions are input to Runge-Kutta-Fehiberg (RKF) integrator to obtain prediction orbit [4]. Then a reference orbit is calculated by two-body case. Each perturbation orbit is calculated under the condition of a two-body orbit combined with one kind of perturbation. The influence of perturbation is obtained by perturbation orbit comparing with two-body orbit. These perturbation forces are including the Earth non-spherical gravity potential with degree and order as 2×0, 12×12, 20×20, 70×70, three-body gravitation considering the sun and the moon, the ocean tide, the solid tide, the solar radiation pressure, the Earth albedo and the atmospheric drag. The three-dimension (3D) position difference between prediction orbit and two-body orbit are presented in Fig. 1.

Figure 1 shows the position difference between ten prediction orbits and the two-body orbit. The X axis denotes three-day arc of orbit, unit is minutes. The Y axis denotes the magnitude of position difference, using logarithmic coordinates with meter as its unit. It can be seen from Fig. 1, perturbation appears certain periodic characteristic. The period is accordance with cycle of operation, and the amplitude is different for each perturbation. In the perturbation, the largest one is the Earth non-spherical gravity potential, which reaches 10^6 m when predicting a three-day orbit. The second large perturbation is atmospheric drag, which is calculated by Jacchia Roberts density model. The atmospheric drag is the main key perturbation for low orbit spacecraft. Besides, the three-body perturbation from the sun and the moon is small because the orbit altitude is low.

3 The Sensitive of the Earth Non-spherical Gravity

For the purpose to investigate the sensitive of gravity model, orbits using EGM96 model with different degree and order are predicted. The complete EGM96 model is with degree and order as 70 × 70, which is considered to achieve reference orbit. The compared orbits contain five square ones, of which degree and order value are the same, and five non-square ones, of which the degree is 70 and the order is different. The comparison is shown in Fig. 2.

Results show that when using the Earth non-spherical gravity model with square degree and order, the orbit accuracies have no relationship with degree and order. Namely, when the degree and order is larger, the orbit is not always better. In this example, the largest difference of orbit with reference orbit is 16 × 16, the smallest

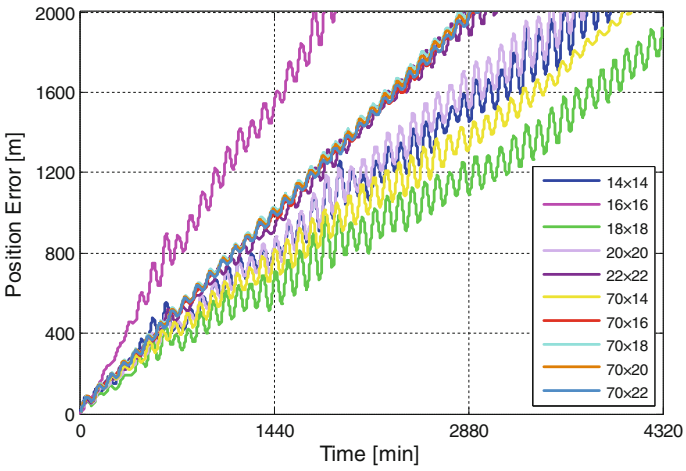

Fig. 2 The position difference between prediction orbit with reference orbit using different degree and order of the earth non-spherical gravity model

one is 18 × 18. As for non-square, when degree is 70 and the order is 22, 20, 18 and 16, respectively, the orbit accuracy is decreased in sequence.

Furthermore, the two predicted orbits with 16 × 16 and 18 × 18, one of which causing the largest position difference, the other is the smallest, are compared in radial, in-track, cross-track components, respectively, displayed in Figs. 3, 4, 5 and 6.

Due to the fact that in-track difference is much larger than radial and cross-track, the results are shown in different figures respectively. It can be seen from Figs. 3, 4, 5 and 6, the error mainly appears in the in-track component, which leads to the large error in 3D position difference. In the radial and cross-track component, the position difference almost at the same magnitude, while the in-track error of 18 × 18 is obviously less than that of 16 × 16. Hence, different degree and order impact much on the in-track component of orbit.

4 Atmospheric Drag Influence on Tiangong-2

Atmospheric drag is the second large perturbation force, next to the Earth non-spherical gravity for low orbit spacecraft. It is also a very complex one. Currently, the following acceleration is used for atmospheric drag [5],

$$\ddot{\mathbf{r}}^{atm-drag} = -\frac{1}{2} C_D \frac{A}{m} \rho v_r^2 \mathbf{e}_v \tag{1}$$

where A/m is the ratio of flat plate area to the mass of spacecraft; C_D is the damping coefficient, which is used to describe the damping relationship between atmosphere

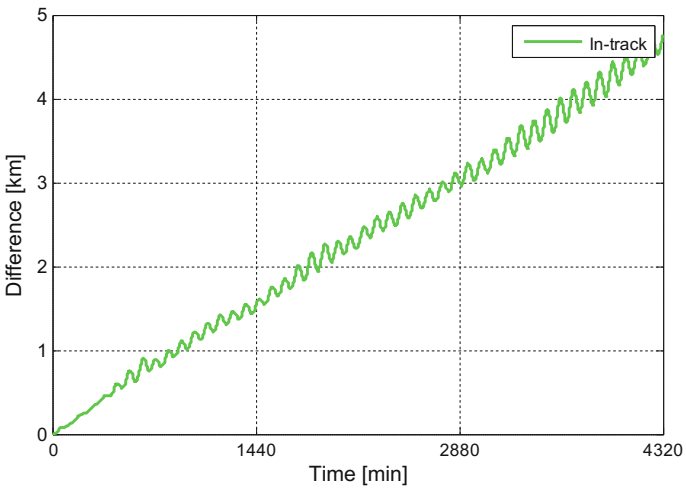

Fig. 3 In-track orbit comparison by 16 × 16 with 70 × 70 as reference, the unit is kilometer

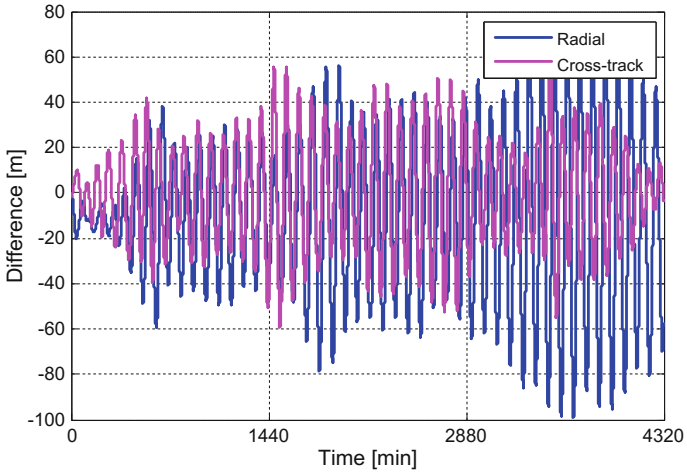

Fig. 4 Radial and cross-track components of orbit compared by 16 × 16 with 70 × 70 as reference, the unit is meter

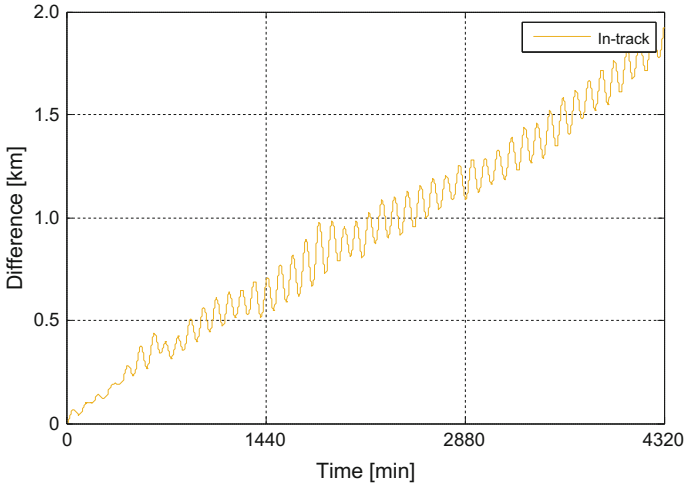

Fig. 5 In-track orbit comparison by 18 × 18 with 70 × 70 as reference, the unit is kilometer

and the surface materials of spacecraft; ρ is the atmospheric density. $v_r^2\mathbf{e}_v$ denotes the velocity vector of the mass center of spacecraft to atmosphere, its direction is matched with drag accelerate.

In the Eq. (1), the atmospheric density ρ is calculated by experiential density models. There are two kinds of the experiential density models, static model and time-varying model. The common used static model is Harris-Priester model, and the time-varying model contains CIRA series, Jacchia series and MSIS series.

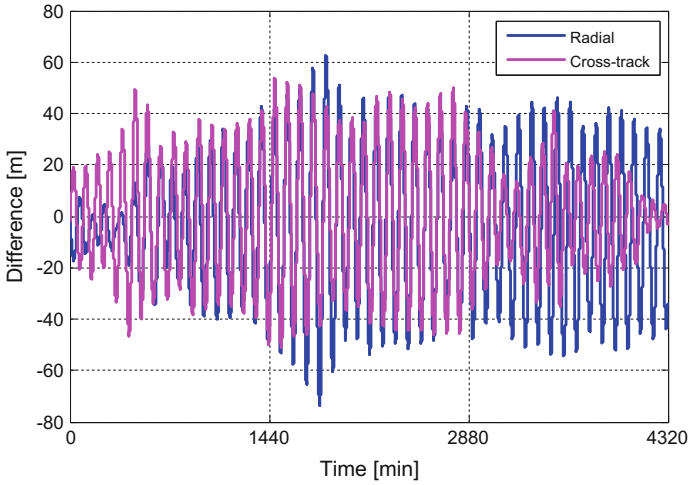

Fig. 6 Radial and cross-track components of orbit compared by 18 × 18 with 70 × 70 as reference, the unit is meter

Jacchia combines space position and environment factor, is the earliest three dimension density model. When modeling the atmosphere density, the solar active and geomagnetism are applied to solve exosphere temperature. Then, standard density is derived and modified with time considering the variance of density. In the process of density modeling, multi space environment parameters are involved, especially the solar activity and geomagnetism [6–9]. The solar activity is described by F10.7 cm solar flux.

In order to analyze different atmosphere model, high precise orbit prediction method is applied to propagate three-day orbit arc. The reference epoch is 2016284.0 with 10 s as integration step. The perturbation force are considered including the Earth non-spherical gravity, the solar radiation pressure, the three-body perturbation, tides, the Earth albedo and one kind of atmospheric drag. The orbit using Jacchia Roberts model is the reference one, the orbit difference of other models are displayed in Fig. 7. The Y axis denotes the position difference using logarithmic coordinate with meter as its unit, while X axis stands for the orbit prediction time, unit is minute.

It can be seen from Fig. 7, Jacchia 1960 occurs the largest position difference with reference model, the second one is 1976 Standard model and Harris-Priester model. The possible reason is these three models consider no solar activity and geomagnetism parameters. MSISE series models represent difference at the beginning 12 h. With the increasing of prediction time, the models are approaching to each other. CIRA1972 and Jacchia 1971 shows a decrease and then increase process. When predicting 12 h, the CIRA1972 is most close to Jacchia Roberts, while when predicting for 24 h, the Jacchia Roberts gets close to Jacchia 1971.

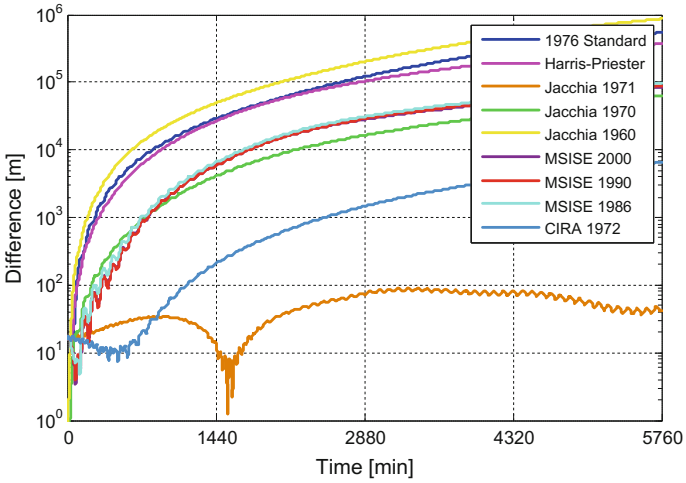

Fig. 7 Orbit position different between atmospheric density models

Table 2 The solar activity parameters

No.	Name	Description
1	3-h	3-h kp, daily F10.7 cm
2	3-h interpolate	3-h interpolation kp, daily F10.7 cm
3	3-h cubic spline	3-h cubic spline kp, daily F10.7 cm
4	Daily	Daily average kp, daily F10.7 cm
5	Last 81 day	Last 81 days average F10.7 cm

Table 3 3-hour solar activity K_p value

Epoch	Hour							
	00–03 h	03–06 h	06–09 h	09–12 h	12–15 h	15–18 h	18–21 h	21–24 h
2016284	33	27	23	10	10	27	30	7
2016285	0	0	7	10	3	0	3	7
2016286	7	3	7	3	3	10	17	30
2016287	23	30	43	47	47	63	63	50

Because that the atmospheric density model is strongly correlate with solar radiation flux F10.7 cm and geomagnetism, the experiment use different F10.7 cm and geomagnetism parameters as input for Jacchia Roberts model. The details for input parameters are shown in Table 2.

The solar radiation flux F10.7 cm and geomagnetism data are provide by NOAA. The reference epoch of Tiangong-2 is 2016284.0, and the parameters value are shown in Tables 3 and 4.

Table 4 The solar activity F10.7 cm value

Epoch	Type	
	Daily F10.7 cm	Last 81 days
2016284	101.6	87.7
2016285	98.8	87.8
2016286	97.2	87.9
2016287	94.8	88.0

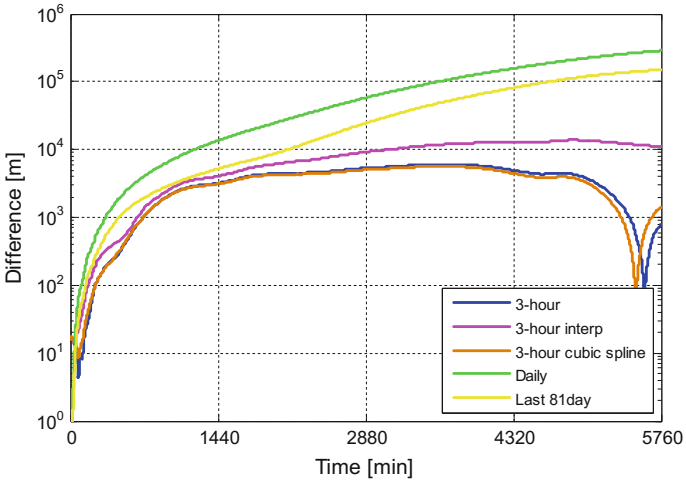

Fig. 8 The position error caused by different solar activity conditions

The daily F10.7 cm result is represented in green curve, which cause the largest position error of orbit, and the second large one is last 81 days F10.7 cm. As for three-hour geomagnetism, there are three methods for solution, including point data, interpolation for a smooth curve and cubic spline. Consequently, the cubic spline orbit and the point data are almost the same, which are less than the interpolation one (Fig. 8).

5 Conclusions

In this paper, Two Line Elements are employed to obtain Tiangong-2 initial conditions and its integration orbits are achieved for analysis based on the force models. To analyze orbit perturbation, "two body orbit combined with one kind of perturbation force" method is applied. The experimental results show that the largest two impacts are the Earth non-spherical gravity and the atmospheric drag.

Then, according to the different order of the Earth non-spherical gravity model, the truncation of model order on the orbit is analyzed. Furthermore, atmospheric drag is analyzed for comparing nine different atmospheric density models with reference model. For Jacchia Roberts model, the values of solar activity parameters are discussed in details. Overall, the atmospheric density model is very complex and one of the key factors in perturbation forces. In spite of this work is an analysis for Tiangong-2, it also has some reference on other spacecraft.

Acknowledgements This work is partially funded by the Program of National Natural Science Foundation of China (No. 41404025), and State Key Laboratory of GeoInformation Engineering (No. SKLGIE2014-M-2-2). It is also supported by the Fundamental Research Funds for the Central Universities (No. 2014B03314) and the Program of National Natural Science Foundation of China (No. 41374044).

References

1. Rong W, Zhi X, Li Q, Jianye L (2007) Analysis and research of micro satellite orbit perturbation based on the perturbative orbit model. Areospace Control 25(3):P66–P70
2. Vallado DA, Crawford P, Hujsak R (2006) Revisiting spacetrack no. 3. AIAA 2006-6753. In: AIAA/AAS astrodynamics specialist conference and exhibit, Keystone, Colorado
3. Kelso TS (2007) Validation of SGP4 and IS-GPS-200D against GPS precision ephemerides. In: AAS/AIAA space flight mechanics conference, San Diego
4. Liu L (2000) Orbit theory of spacecraft. National Defense Industry Press, Beijing
5. Montenbruck O, Gill E (2000) Satellite orbits models, methods and applications. Springer, Berlin
6. Wen S, Yan Y (2015) Atmosphere density modeling and prediction in low earth orbit based on ar model. Sci Tech Eng 15(6):104–108
7. Chen XX, Hu X, Xiao CY et al (2013) Correction method of the low earth orbital neutral density prediction based on the satellites data and NRLMSISE-00 model. Chin J Geophys 56(10):3246–3254
8. Wang P, Gong X, Xu Q (2013) Time-varying atmospheric model and its application to leo satellite autonomous orbit determination. J Geomatics Sci Tech 30(3):219–224
9. Hu W, Cheng W, Wang JX, Dang YM, Bai GX, Wang QX (2014) Global characteristics of the second-order ionospheric delay error using inversion of electron density profiles from cosmic occultation data. Sci China Phys Mech Astron 57(2):365–374

Research on Topological Map Building Based on Crowdsourcing Data

Xinzheng Lan, Ying Xu, Dongyan Wei and Hong Yuan

Abstract Topological map is the basis of navigation and can be used for positioning. At present, the acquisition of map mainly relies on manual or machine measurement, which is costly. And for indoor situation, re-measurements are needed when the topology of the building changes. Aiming at the above problems and fully considering the widely use of smart mobile phone terminals and applications, this paper proposes a method for establishing topological map based on crowdsourcing data. Through conducting similarity analysis and matching of magnetic field intensity and WLAN/Bluetooth signal in crowdsourcing data, this method establishes connections between crowdsourcing data, and then construct a topological map with the main features of road segments. Experimental analysis shows that the method proposed can realize the self-generation of topology of general buildings by using data collected by ordinary users.

Keywords Crowdsourcing data · Topological map · Road section matching

1 Introduction

Indoor topological map describes the indoor road network information, including the length and direction of paths and the connection between paths. It can be used to assist some indoor localization methods, such as Pedestrian Dead Reckoning (PDR), to improve their accuracy [1, 2]. At present, there are two main types of methods of building indoor topological maps, including accurate building methods

X. Lan
University of Chinese Academy of Sciences, Beijing 100049, China

X. Lan · Y. Xu (✉) · D. Wei · H. Yuan
Academy of Opto-Electronics, Chinese Academy of Sciences, Beijing 100049, China
e-mail: nadinexy@aoe.ac.cn

J. Sun et al. (eds.), *China Satellite Navigation Conference (CSNC) 2017 Proceedings: Volume I*, Lecture Notes in Electrical Engineering 437,
DOI 10.1007/978-981-10-4588-2_43

using floor plans or actual measurements, and SLAM (Simultaneous Localization And Mapping) methods applied to mobile robots. The former requires accurate floor plans or measurements in advance, which is not easy to obtain, and when the building's topology changes, re-measurement and rebuilding is needed [3]. The latter uses a camera or a laser radar to obtain the robot's ambient information, and generates topological maps based on Kalman filtering, particle filtering or other methods, combined with the movement information of the robot itself. This method is costly and has a strong dependence on the accuracy of movement information [4].

Due to the ferromagnetic nature of buildings' steel structure, there are abundant and long-term stable geomagnetic anomalies indoors, resulting in the specific magnetic field intensity in different locations [5, 6]. At the same time, in order to meet people's demand for wireless network connection and communication, wireless local area network (WLAN) and low-power Bluetooth (Bluetooth Low Energy, BLE) nodes are generally equipped in shopping malls, office buildings and other buildings. In different locations of these buildings, the accessible nodes and their signal strength is different. And from another perspective, the accessible nodes and their signal strength is similar in the same location.

Nowadays, the smart phone terminal has become widely popular. They are generally equipped with a WLAN module, a low-power Bluetooth communication module, a magnetometer and inertial sensors including an accelerometer, a gyroscope and a orientation sensor. These modules and sensors enable them to sense the ambient WLAN/BLE signals and magnetic field intensity, and to obtain the acceleration, angular velocity and azimuth relative to the north, which can be used to derive the motion state of pedestrians. In addition, the background running ability of smart phones makes the data of information above can be uploaded continuously in the background without affecting the user's normal operation on the phone.

Through the upload of applications running on user's smart phone, we can get signal strength data and inertial sensor data form different users, known as crowdsourcing data [7]. By analyzing the similarity of various types of signal strength in crowdsourcing data and taking into account the walking trajectories of pedestrians obtained from the inertial sensor data, we can correlate the signal strength information with the indoor paths so that an indoor topological map can be established accordingly. To this end, this paper designs a novel topological map structure, which is composed of "road segments" and "intersections", proposes a WLAN/BLE-aided road segment matching algorithm based on the feature points of magnetic field intensity sequence, and presents a topological map building system which adopts the above structure and matching algorithm to match and splice road segments, and to generate the indoor topological map that is conformed to the real scene provided exact coordinates of a certain road segment.

The paper is organized as follows. Section 2 outlines the architecture of the topological map building system and defines the novel topological map structure it adopts. Section 3 presents the algorithms used in the system in detail. Experiment and results are presented in Sects. 4 and 5 concludes this paper.

2 Topological Map Building System Design

2.1 Topological Map Structure

In order to realize the splicing and updating of the topological map, this paper define a topological map (denoted by M) as one that contains several "road segments" (denoted by R) and "intersections" (denoted by C), i.e.,

$$M = \{R_1, R_2, \ldots, R_k\} + \{C_1, C_2, C_3, \ldots, C_l\}$$

where k and l are the number of road segments and intersections in M, respectively.

The "road segment" in this paper refers to a path with no turning, combined with some properties of it, i.e.,

$$R = \{\text{length}, \text{ori}, pos_{m1}, mag_1, pos_{m2}, mag_2 \ldots pos_{mm}, mag_m, posn_1, wlan_1, ble_1, pos_{n2}, wlan_2, ble_2 \ldots pos_{nn}, wlan_n, ble_n\}$$

where "length" and ori are the length and the azimuth relative to the north of R respectively, and pos_{mi} and mag_i mean that the magnetic field intensity at the location which is on R and is pos_{mi} far from the starting point is mag_i. Similarly, pos_{nj} and $wlan_j/ble_j$ mean that there is a WLAN/BLE record at the location pos_{nj}. Each WLAN/BLE record contains the hardware address and signal strength of the WLAN/BLE nodes whose signal can be received. As shown in (Fig. 1), there is a road segment whose length is 20 m. And there are 7 WLAN/BLE records and a magnetic sequence forming by a large number of magnetic field intensity data collected on this road segment.

Fig. 1 An example of "road segment"

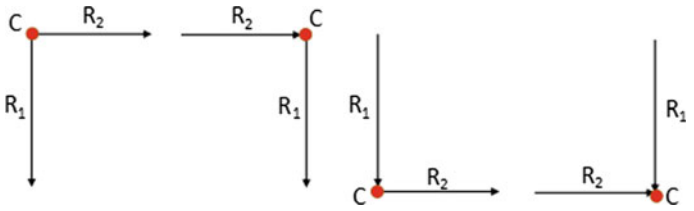

Fig. 2 Types of intersection

"Intersection" is used to record the connection relation between two road segments if they are connected, i.e.,

$$C = \{R_p, R_q, \text{type}, \text{angle}\}$$

where R_p and R_q are the two road segments C connects, "angle" is the needed rotation angle when rotating R_p to the same the orientation of R_q, whose range is (–180°, 180°), with positive value indicating counter clockwise rotation and negative indicating clockwise rotation, and "type" is one of four intersection types, namely type 1–4, indicating that C connects R'_p starting point and R_q starting point, R'_p starting point and R'_qs end point, R'_p end point and R_q starting point, R'_p end point and R_q end point, respectively, as shown in (Fig. 2). It should be noted that the "intersection" in this article describes the connection between only two road segments, and if there are three or more road segments connected at the same point, we use multiple intersections to record it.

Trough definitions of the topological map M above, the set of R provides the length and orientation of each road segments, and the set of C provides relative position between road segments. So when the coordinates of a road segment in M is determined, the coordinates of all other road segments can be calculated.

2.2 Architecture of Topological Map Building System

The topological map building system we present takes road segments data, which is collected by pedestrians' phone when walking in indoors, as input, and outputs the topological map of the indoor scene and the fingerprint on the paths of this topological map, where the fingerprint contains the magnetic field intensity and the received signal strength (RSS) of WLAN/BLE. As shown in Fig. 3, the system consists of three components: A. data selection and partition, B. road segment matching and splicing and C. coordinate generation. Component A is responsible for removing the invalid data from the crowdsourcing data received, partitioning paths to road segments and sending road segments data to B. Component B matches road segments sent by A, finds out the overlapping parts, and splices these road segments together according to these overlapping parts, forming a preliminary

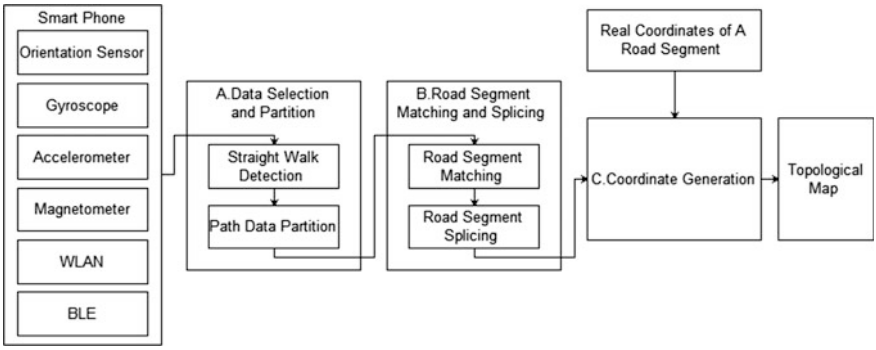

Fig. 3 Architecture of topological map building system

topological map. Given real coordinates of a road segment in the preliminary topological map, component C then calculate the coordinates of all other road segments and intersections, forming a topological map conforming to the real scene.

A. Data Selection and Partition

As mentioned in Sect. 2.1, the topological map of this paper takes the non-turning straight-line road segments as the basic units, but the crowdsourcing data may contain data of various kinds of walking trajectories. Therefore, this component extracts available data of straight-line road segments from collected data. In order to determine whether the walk is straight, it is needed to identify the attitude of the phone relative to the user.

Based on the analysis above, component A consists of two parts. The first part is to identify the phone's attitude and ensure that there is not significant change in the attitude of the phone relative to the user in the data collection process. Related research has been carried out in literature [8–10], concluding that the attitude of the mobile phone can be detected by analyzing the angular velocity data of gyroscope and the azimuth data of orientation sensor. The second part is to detect turning points, thereby partition the data to several road segments data according to the detection results. Research and experiment found that when the pedestrian walk straight and the attitude of the mobile phone changes little, the angular velocity reading given by the gyroscope mounted on the mobile phone fluctuates in the vicinity of zero and the absolute amplitude is relatively small. And when the pedestrian turns, the absolute amplitude of angular velocity will significantly increase and fall, corresponding to the start and end of the turn. In addition, the angular velocity value is positive when the turn is counterclockwise and negative if the turn is clockwise. Furthermore, the accuracy of gyroscopes currently equipped on smart phones is high in a short period of time, enabling them to be used to calculate the turning angle [11].

B. Road Segment Matching and Splicing

The magnetic field intensity sequence and the RSS of WLAN/BLE collected are similar when walking along the same road segment, which is manifested in two aspects. Firstly, the magnetic field intensity on a road segment is quite stable over a long period of time, and when pedestrians walk along the same road segment, the profiles formed by the magnetic field intensity sequence follow a similar pattern. Secondly, When the building is equipped with WLAN/BLE nodes, the detected nodes are similar in the same region although the received signal strength of the same nodes at different time may vary over a wide range at about 20 dBm due to the change of the indoor environment and the impact of multipath effect [12]. Therefore, it is possible to determine whether the pedestrian is in a particular region based on whether or not certain nodes' signals are received. According to the above principle, this paper proposes a WLAN/BLE-aided road segment matching algorithm based on the feature points of magnetic field intensity sequence to match the same road segments, through results of which the segments splicing and topological map building can be performed.

C. Coordinate Generation

In the process of splicing in component B, the length of road segments are derived from step detection and step length estimation utilizing the acceleration data given by the accelerometer mounted on phones. There have been many studies on step detection and step length estimation giving several available algorithms such as step detection algorithms based on peak detection, based on FFT, based on zero-crossing detection and step length estimation algorithms based on linear model and based on nonlinear model [13–15]. In this paper, we adopt the step detection algorithm based on peak detection [13] to count steps and adopt a fixed step length of 60 cm. However, there are errors inevitably when counting steps and estimating step length, resulting in the inaccurate estimated length of road segments. So in component B all road segments in the topological map are scaled to the same level according to matching results. Therefore, when given real coordinates of a road segment, component C can calculate the coordinates of all other road segments and intersections according to the scaling relation and connection between road segments.

3 Topological Map Building Algorithm

3.1 Path Data Partition Algorithm

Considering the characteristic of the angular velocity whose value increases and falls significantly when turning, we present a path data partition algorithm to partition a "path data" into several "road segments data" based on turning detection, where the "path data" means the inertial sensor data, magnetic field intensity data,

and RSS data of WLAN/BLE collected when walking on a path that may contain turns, and the "road segments data" means that of road segments as defined in Sect. 2.1.

As shown in Fig. 4, the algorithm first performs a moving averaging over the angular velocity data, and then searches out local maximum and local minimum points (which are turning points, namely "intersections" defined in Sect. 2.1) of it that exceed a certain threshold, which is 30°/s in this paper. Next, these turning points are used as partition points to "split out" several road segments. Finally, the turning angles between road segments are calculated by integrating the angular velocity, taking the first zero-crossing point before and after the turning point as the starting point and end point of the integration, respectively.

3.2 Road Segment Matching Algorithm

In this section, we study how to identify the overlapping part (if there is) of two road segments, namely, to match road segments.

Figure 5 shows three magnetic field intensity sequences collected on a road segment at different time. The horizontal axis is the distance to the road segment's starting point, and the vertical axis is the total magnetic field intensity. As shown in the figure, there are many variation characteristics in magnetic sequences of indoor road segments. Note that the three estimated lengths are different caused by estimation errors.

The magnetic sequence matching algorithms based on correlation analysis are the main matching algorithms of indoor localization based on magnetic field, including the cross correlation algorithm (COR), the correlation coefficient algorithm (CC), the product correlation algorithm (PROD), the normalized product correlation algorithm (NPROD) that emphasize the similarity, the absolute difference algorithm (AD), the mean absolute difference algorithm (MAD), the square difference algorithm (SD), the mean square difference algorithm (MSD) that emphasize the difference and the matching algorithm based on Hausdorff distance [16–18]. In algorithms mentioned above, the accuracy of the CC algorithm is very high. COR and PROD are poor in stability and accuracy. MAD, MSD and other algorithms that emphasize the difference may encounter difficulties when determining the threshold due to the different sensitivity of different magnetic field sensors. Note that these algorithms require the alignment of the two magnetic sequence to be matched. For example, for the there sequences that are different in length in (Fig. 5), if we directly calculate their correlation coefficient without stretch or shrink, then the correlation coefficients between sequence 1 and 2, 1 and 3, 2 and 3 are 0.9680, 0.7212 and 0.6914, respectively. But if we scale them to the same length, the results are 0.9753, 0.9779, 0.9843, indicating high similarity.

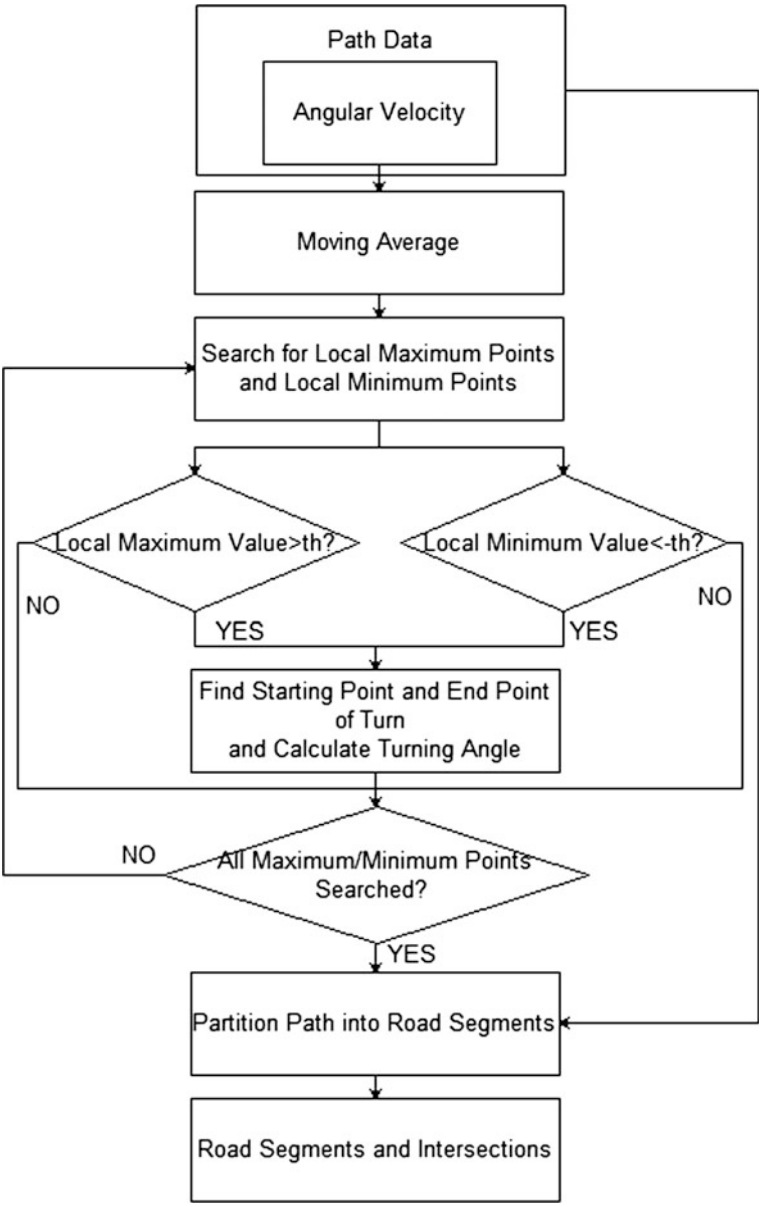

Fig. 4 Flow chart of the path data partition algorithm

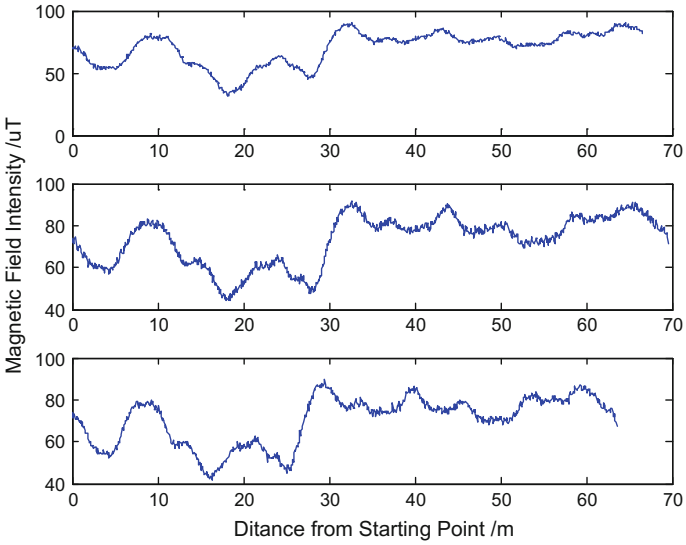

Fig. 5 Magnetic field intensity sequences collected on the same road segment at different time

To solve the above problems, we propose a WLAN/BLE-aided road segment matching algorithm based on the feature points of magnetic field intensity sequence. For the two road segments R_1 and R_2 to be matched, whose magnetic field intensity sequence are mag_1 and mag_2 and whose orientations are ori_1 and ori_2, respectively, the matching algorithm is described as follows.

1. Pre-judgment and Pretreatment.

If the difference between ori_1 and ori_2 is greater than 45°, then R_1 and R_2 are considered to be different road segments. Otherwise perform the local least squares linear fitting [19] on mag_1 and mag_2 to smooth them.

2. Feature Point Extraction

Extract peak points and trough points of mag_1 and mag_2 as feature points, which is denoted by FP_i(i = 1, 2, … k). The feature points for each sequence should meet the requirements that the peaks and the troughs appear alternately, and

$$\begin{cases} |\mathrm{mag}\,(FP_1) - \mathrm{mag}(1)| > thMagDiff \\ |\mathrm{mag}\,(FP_k) - \mathrm{mag}(len)| > thMagDiff \\ |\mathrm{mag}\,(FP_i) - \mathrm{mag}(FP_{i-1})| > thMagDiff,\ i = 2, 3, \ldots, \mathrm{k} \end{cases}$$

where mag(·) is the magnetic field intensity of this point, |·| means to take the absolute value, len is the length of the sequence, and thMagDiff is the minimum difference between adjacent peak and trough, which is set to 1uT in this paper.

The feature points extracted from mag_1 and mag_2 are denoted by FP_i^1 (i = 1, 2, … k_1) and FP_i^2 (i = 1, 2, … k_2), respectively.

3. Calculating the Scaling Ratio

Take two feature points FP_i^1 and FP_j^1 (i < j) from FP_1, and take two feature points FP_p^2 and FP_q^2 (p < q) from FP_2, then calculate the scaling ratio with

$$ratio = \frac{dis(FP_q^2) - dis(FP_p^2)}{dis(FP_j^1) - dis(FP_i^1)}$$

where dis(·) represents the distance from starting point. If FP_i^1 and FP_p^2 are the same point in space and so do FP_j^1 and FP_q^2, then the calculated result is the correct scaling ratio of R_1 and R_2. The distance estimation error mainly comes from the step length estimation error, and the step length of pedestrians generally ranges from 0.4 to 0.8 m, so the reasonable range of the calculated ratio is [0.5, 2]. Therefore, if the ratio is out of this range, then repeat this step using other feature points. And when the ratio is in the range, go to the next step.

4. Feature Point Alignment Judgment

Scale mag_2 with the ratio of step 3, taking FP_i^1 and FP_p^2 as alignment points (namely taking FP_p^2 as the scaling center), and the scaled mag_2 (denoted by mag_2') is obtained. Calculate the number of aligned feature points (denoted by g) between mag_1 and mag_2', where the judgment basis of alignment is

$$(\mathrm{dis}(FP_x^1) - dis(FP_i^1)) - (dis(FP_y^2) - dis(FP_p^2)) < thMaxDis$$

And when

$$\frac{g}{\min(k_1, k_2)} > thMinAlign$$

it is believed that the scaling ratio and the alignment points are correct, then the algorithm goes to the next step, otherwise back to the step 3. The threshold thMaxDis and thMinAlign are set to be 1 and 0.8 m, respectively in this paper.

5. Calculating the Correlation Coefficient

Calculate the correlation coefficient between mag_1 and mag_2' which is scaled in step 4.

$$cc = \frac{\sum_{m=1}^{n} (mag_{1m} - \overline{mag_1})(mag'_{2m} - \overline{mag'_2})}{\sqrt{\sum_{m=1}^{n} (mag_{1m} - \overline{mag_1})^2 \cdot \sum_{m=1}^{n} (mag'_{2m} - \overline{mag'_2})^2}}$$

Repeat steps 3–5, taking all possible combination of feature points in step 3, and obtain the maximum correlation coefficient (denoted by ccMax) derived from all

these repetition. If ccMax is larger than a specific threshold (denoted by thCC, which is set to be 0.9 in this paper), go to the next step, otherwise the conclusion that R_1 and R_2 are not matched is given.

6. Assist of WLAN/BLE

After scaling the road segment R_2 according to the final scaling ratio and scaling center given by step 5, we can extract the overlapping part (denoted by OP) of R_1 and R_2. At the starting point of OP, the number of the same WLAN/BLE nodes detected by both R_1 and R_2 is N_{s1}, and that of all nodes detected by R_1 or R_2 is N_{a1}. N_{s2} and N_{a2} are defined similarly except that the point is the end point of OP. When these four numbers satisfy

$$\begin{cases} N_{s1}/N_{a1} > thAPr \\ N_{s2}/N_{a2} > thAPr \end{cases}$$

where thAPr is 0.8 is this paper, it is believed that OP is indeed an overlapping part of R_1 and R_2, so the conclusion that R_1 and R_2 are matched is given.

3.3 Splicing, Updating and Coordinate Generation

The splicing and updating architecture of the topological map is shown in Fig. 6. For the path data that are continuously acquired, if there are overlapping segments between the incoming path data and the existing topological map, then the

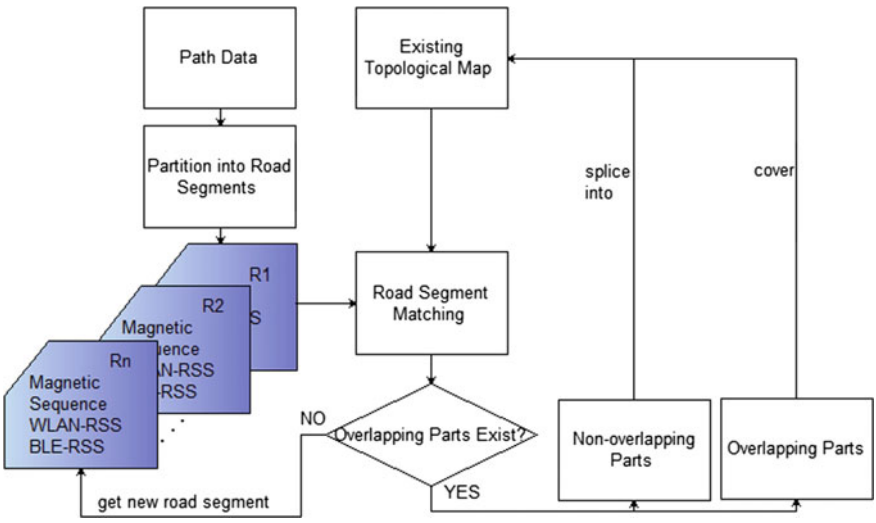

Fig. 6 Splicing and updating architecture of the topological map

overlapping segments are used to cover the existing one, and the other segments, which is new to this map, will be spliced into the map.

The splicing and updating of topological map is achieved by adding new intersections and altering existing intersections. As shown in Fig. 7, the topological map M before splicing can be represented as $M = \{R_1, R_2\} + \{C_1\}$, where $C_1 = \{R_1, R_2, 3, 90°\}$. And when the new road segment R_3 is matched with the existing road segment R_2, R_2 is covered by R_3, C_1 is altered correspondingly and the new intersection C_2 is added to M, forming a new topological map which is represented as $M = \{R_1, R_3, R_4\} + \{C_1, C_2\}$, where $C_1 = \{R_1, R_3, 3, 90°\}$ and $C_2 = \{R_3, R_4, 3, 90°\}$. Noted that the length of new road segments should be scaled according to the ratio given by matching results before being spliced into the existing map.

To fix the actual coordinates in the real world of the topological map, coordinates generation process based on breadth-first-search is performed, taking the road segment whose coordinates is fixed as the searching starting-point.

4 Tests and Analysis

The test was conducted at the underground garage of Academy of Opto-Electronics, Chinese Academy of Sciences. The size of this garage is around 60.43×100.68 m^2 and there are a number of WLAN and BLE nodes equipped in this area. The test were performed with Xiaomi Note smart phone. Data was collected along 5 paths with different walking speed, which consists of 18 road segments, as shown in Fig. 8. The inertial sensor data and the magnetic field intensity data are collected at a frequency of about 20 Hz, and the RSS of WLAN/BLE is collected at a frequency of 0.25 Hz.

4.1 Road Segment Partition Results

The results of turning detection and road segment partition are shown in Fig. 9 and Table 1. The partition algorithm based on turning detection detected all the turning

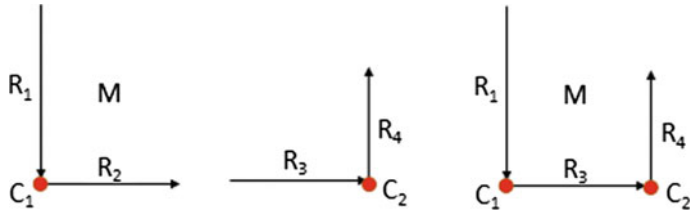

Fig. 7 An example of splicing and updating

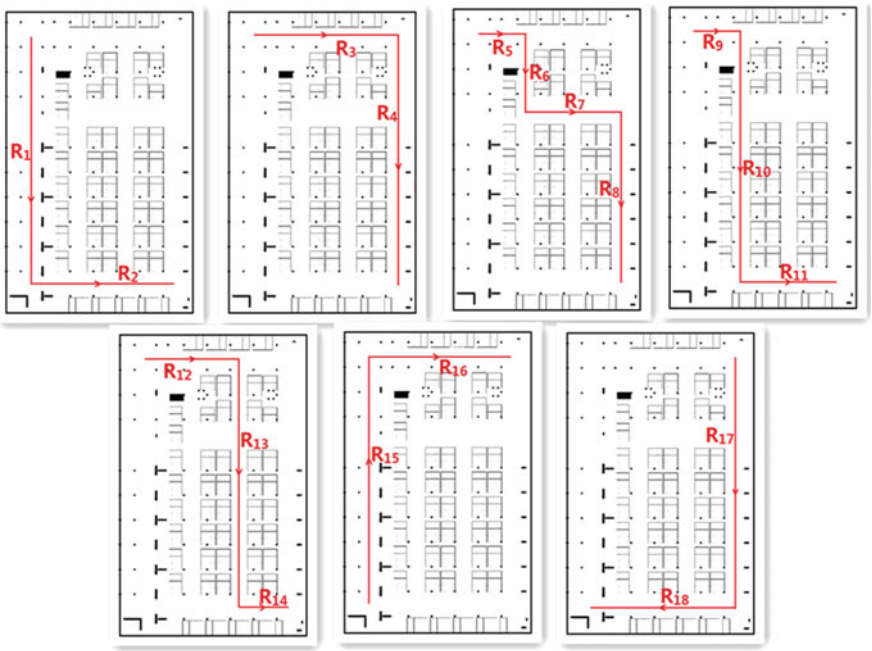

Fig. 8 Experimental site and walking paths

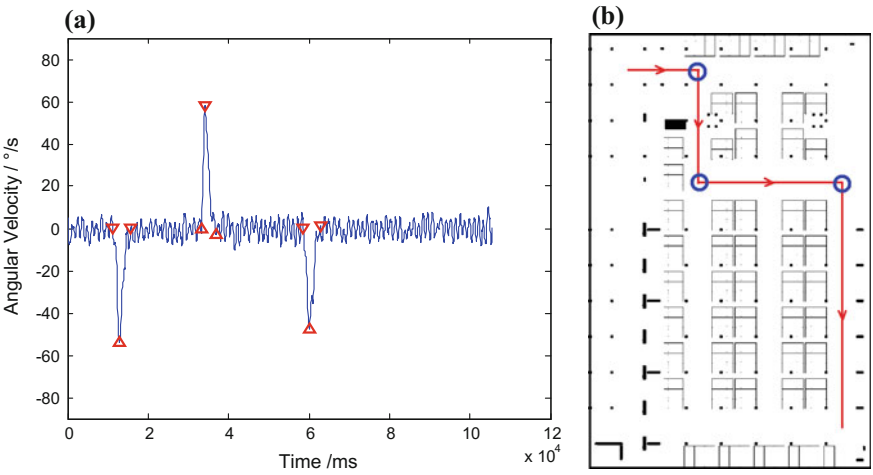

Fig. 9 **a** Turning detection results. **b** Partition results

Table 1 Intersections generated by the partition algorithm

Road segment 1	Road segment 2	Turning angle	Road segment 1	Road segment 2	Turning angle
R_1	R_2	89.20°	R_{10}	R_{11}	83.03°
R_3	R_4	−79.85°	R_{12}	R_{13}	−100.73°
R_5	R_6	−91.13°	R_{13}	R_{14}	86.85°
R_6	R_7	83.05°	R_{15}	R_{16}	−95.97°
R_7	R_8	−97.69°	R_{17}	R_{18}	−94.23°
R_9	R_{10}	−106.51°			

points and correctly partitioned these 5 polyline paths into 18 road segments, and obtained the connection relation between them represented by "intersections" as shown in Table 1. For right-angled turns in the paths, the error of calculated turning angle was within 10°. This error is caused by the insufficient precision of gyroscope and also the slight shaking of the phone and the change of attitude relative to human body.

4.2 Road Segment Matching Results

A total of $C_{18}^2 = 53$ matches was performed on all the 18 road segments, the match results of the matching algorithm without assistance of WLAN/BLE are show in Table 2. Note that "r" means that the two road segments' orientations are opposite, and the matching result is obtained by inverting one of the road segments before matching.

According to the facts, the results emphasised in bold in Table 2, namely "2–7", "7–16" and "12–14", are wrong, and all the other results are correct. In all 153 matches performed, there should be 21 pairs of matched road segments, and our matching algorithm recognized 16 of them, getting the recognition rate of 76.19%. And 145 of the 153 matching results given by our matching algorithm are correct, resulting in the correct rate of 94.77%. In 132 pairs of road segments that do not match, 3 wrong matching results are given, so the false recognition rate is 2.27%.

When the matching algorithm is aided by WLAN/BLE, all the mismatch results in Table 2 are filtered out, and the other matching results are consistent with Table 2, making the correct rate increased to 96.73% and the false recognition rate down to 0.

The algorithm also gives the ratio between the estimation of the same length estimated by the two matched road segments and the distance between starting points and end points of the two matched road segments. And the average estimated error of staring points and end points is 0.6745 m.

Table 2 Road sections matching results without assistance of WLAN/BLE

Road segment 1	Road segment 2	Scaling ratio	Distance between starting points (m)	Distance between end points (m)
1	17/r	0.9478	0.7085	0.5153
2	**7**	**0.8021**	**4.5615**	**14.0646**
2	11	0.9716	14.0012	0.6048
2	14	1.0335	26.9888	1.0586
2	16/r	0.9332	0.3542	0.8236
3	12	0.9395	0.1860	12.8973
3	18	0.9607	0.2365	0.4139
4	8	1.0123	22.5991	0.1948
4	15	0.9736	0.3247	0.9092
5	9	0.9691	0.2316	0.0571
5	18	0.9183	0.0565	26.3327
6	10	1.0008	0.000000	47.3880
7	**16/r**	**1.1863**	**6.4530**	**17.1079**
8	15	0.9620	22.1016	0.7683
11	14	1.0420	13.5709	0.3767
11	16/r	0.9725	14.9465	1.1205
12	**14**	**0.5947**	**10.1167**	**10.6757**
12	18	1.0237	0.5040	14.2377
14	16/r	0.9526	28.1975	1.4460

4.3 Topological Map Generation Result

Splice the road segments utilizing the generation method as presented in Sect. 3.3 according to the matching results in Sect. 4.2, the topological map is obtained. And after given the start and end coordinates of the road segment R_1 as (0, 0) and (0, −81.66), respectively, coordinates of all the other road segments and intersections are fixed, forming the topological map and the 3D-Magnetic field intensity fingerprint map as show in Fig. 10. Note that all the turning angles are incorporated into one of the nearest multiple of 90°, which is closest to the original turning angles.

As we can see in Fig. 10, the topological map generated by the building system proposed contains ten intersections, which are marked by red circles. In order to evaluate the accuracy and determine whether the generated map is conformed with the experimental site, we calculate the maximum distance error and the average distance error of these intersections. The distance error is calculated with

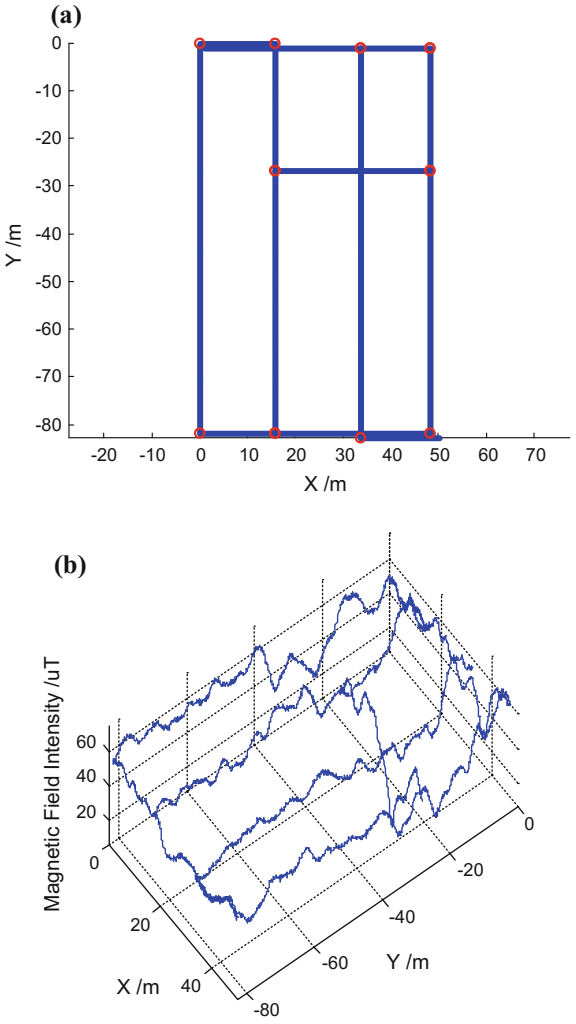

Fig. 10 **a** The topological map generated. **b** 3D magnetic field intensity map

$$\delta_i = \sqrt{(x_i - x_r)^2 + (y_i - y_r)^2}, \quad i = 1, 2, \ldots n$$

where n = 10, (x_i, y_i) is the generated coordinates and (x_r, y_r) is the real coordinates. The result is that the maximum distance error is 3.1284 m and the average distance error is 1.4175 m, illustrating that the generated topological map is basically conformed with the real scene.

5 Conclusions

In order to solve the problem that the topological map is not easy to obtain and update, this paper studies the topological map building method based on crowdsourcing data. A novel topological map building system and its splicing and updating architecture are designed based on and a new topological map structure, which is composed of road segments and intersections. The system takes data collected by pedestrians' smart mobile phones as input and gradually forms a topological map utilizing the path data partition algorithm based on turning detection and the WLAN/BLE-aided road segment matching algorithm based on the feature points of magnetic field intensity sequence we proposed. Experiments were conducted and the partition and matching results illustrated the good performance of above two algorithms. A topological map was generated and its accuracy was evaluated using the maximum distance error and the average distance error of intersections. The result shows that the generated topological map is basically conformed with the experimental site, illustrating the effectiveness of the topological map building method we proposed.

References

1. Lu Y, Wei D, Lai Q et al (2016) A context-recognition-aided PDR localization method based on the hidden markov model. Sens 16(12):2030
2. Yin H (2014) A research of indoor position and navigation using MEMS inertial measurement unit and topological map. University of Electronic Science and Technology of China
3. Guo X (2011) The study of topological map model and graph-database integration. Chang'an University, Xi'an, China
4. Wang N (2009) Research on topological map building for mobile robots. Shandong University, China
5. Li B, Gallagher T, Dempster AG et al (2012) How feasible is the use of magnetic field alone for indoor positioning. In: 2012 international conference on Indoor Positioning and Indoor Navigation (IPIN), IEEE, pp 1–9
6. Yang Y, Shi Z, Guan Z et al (2007) Application of geomagnetic field in navigation and Iocalization system. J Chin Inertial Technol 15(6):686–692
7. Rai A, Chintalapudi KK, Padmanabhan VN et al (2012) Zee: zero-effort crowdsourcing for indoor localization. In: Proceedings of the 18th annual international conference on mobile computing and networking, ACM, pp 293–304
8. Liu Y, Xiang G, Wang Y et al (2016) An improved pedestrian navigation algorithm. J Chongqing Univ Posts Telecommun (Nat Sci Ed) 2:015
9. Susi M, Renaudin V, Lachapelle G (2013) Motion mode recognition and step detection algorithms for mobile phone users. Sens 13(2):1539–1562
10. Zhang H, Yuan W, Shen Q et al (2015) A handheld inertial pedestrian navigation system with accurate step modes and device poses recognition. IEEE Sens J 15(3):1421–1429
11. Xie H (2016) An improved pedestrian navigation algorithm. J Chongqing Univ Posts Telecommun (Nat Sci Ed) 2:015
12. Yao TJ, Wei DY, Yuan H (2016) Research on the feedback correction-based fusion method for WLAN and PDR positioning. Chin J Sci instrum 2:446–453

13. Harle R (2013) A survey of indoor inertial positioning systems for pedestrians. IEEE Commun Surv Tutorials 15(3):1281–1293
14. Kim JW, Jang HJ, Hwang DH et al (2004) A step, stride and heading determination for the pedestrian navigation system. Positioning 1(08)
15. Alvarez D, González RC, López A et al (2006) Comparison of step length estimators from weareable accelerometer devices. Engineering in medicine and biology society, EMBS'06. In: 28th annual international conference of the IEEE, IEEE, pp 5964–5967
16. Deng C, Huang C, Zhao H et al (2012) Review of geomagnetic matching navigation algorithm. Sci Technol Eng 20(24):6125–6131
17. Guo C, Hu Z, Zhang S et al (2009) A survey of geomagnetic navigation. J Astronaut 30 (4):1314–1319
18. Kong Y, Lu H, Xu J et al (2011) Study of MAGCOM algorithm based on hausdorff distance. Tactical Missile Technol 4:26–29
19. Cleveland WS (1979) Robust locally weighted regression and smoothing scatterplots. J Am Stat Assoc 74(368):829–836

Part III
Test and Assessment Technology

High Precision Broadband Direct-Spread Signal Delay Control Based on Phase Controlled Waveform Hermite Interpolation

Xin Zhang, Ziqing Ye and Fenghua Mei

Abstract When generating simulation satellite navigation signal, the delay of the broadband direct-spread satellite navigation signal needs to be controlled with high precision. A widely used signal delay control method was changing the phase of the NCO which drives the signal generation. But the signal delay variation that less than a NCO system clock cycle can't be observed at every part of the signal at real time, when it control by the NCO method. The delay less than a NCO system clock cycle can only be observed by matching correlation. Therefore, this delay control can only be defined as an "average" delay control method, and it can't be calibrated by using simple time domain measurement method, which is wildly used for calibrating the delay control of the VFD (Variable Fraction Delay) filter method that consumes a large amount of hardware resources. A high precision delay control method for broadband direct-spread signal based on NCO phase controlled waveform Hermite interpolation is proposed, which achieves the same time domain measurement performance with the VFD filter method at the precision of 10 ps level, but consumes much more less hardware resources. At last, the testing results verify the validity of the theoretical method.

Keywords Simulator · Phase control · Hermite interpolation · Broadband direct-spread signal · Delay control

1 Introduction

As a high-precision test device, the high dynamic satellite navigation signal simulator plays a vital role in the testing of various receivers used by the military and civilian [1], and the high precision broadband direct-spread signal delay control technology is the critical for generating the dynamic delay of broadband navigation signal [2, 3]. Since the receiver pseudorange measurement accuracy usually reaches

X. Zhang (✉) · Z. Ye · F. Mei
Aviation Equipment Institute, Shanghai 200436, China
e-mail: marmy@163.com

J. Sun et al. (eds.), *China Satellite Navigation Conference (CSNC) 2017 Proceedings: Volume I*, Lecture Notes in Electrical Engineering 437,
DOI 10.1007/978-981-10-4588-2_44

the order of nanosecond, the delay control accuracy of broadband navigation signal generated by the high dynamic satellite navigation signal simulator needs to reach sub-nanosecond. For achieving this high control accuracy of the broadband signal, there are mainly two technology methods: NCO method and VFD Filter method.

The NCO method comes from Direct Digital Frequency Synthesis (DDFS) technology [4], and the delay of the broadband direct-spread signal is controlled by adjusting the phase of baseband signal generating clock, which is generated by the NCO. The theoretical analysis shows that the NCO method can achieve sufficient delay control accuracy while the NCO operating clock rate and the baseband baud rate are co-prime [5]. But NCO method has its disadvantages, mainly including the spurs introduced by the method [6], and the delay less than a NCO system clock cycle can't be observed in time domain measurement [7]. Especially the time domain observation problem, which makes the simulator using the NCO method can't calibrate bias delay in sub-nanosecond in time domain measurement [8].

In order to overcome the disadvantages of the NCO method, high precision delay control satellite navigation signal simulator based on VFD filter method was proposed by Yang Jun [9]. The principle of this delay control method is intuitive, and the delay results observed in both time domain measurement and correlation domain measurement are consistent. However, due to the variation and high precision of satellite navigation signal delay, the resource consumption of the VFD filter method is drastically increased relative to the NCO method. Although researches about how to simplify the implement structure and reduce the resource consumption has been done [10, 11], but the relative NCO method is still a big gap.

For conquering the problems of the two traditional method mentioned in this paper, the mathematic principle of controlling broadband signal delay directly by NCO phase is deduced, and then the definition of the finite state of the base-band signal waveform is introduced. Then, high precision broadband direct-spread signal delay control based on phase controlled waveform Hermite interpolation was proposed, and the implement structure and resource consumption are analyzed. At last, the validation and high precision of the proposed method was verified by the measurement data.

2 Principle of Controlling Broadband Signal Delay Directly by NCO Phase

For high precision delay control of broadband satellite navigation signal, ideal VFD filter can be equivalent to the digital realization process as shown in the upper half part of Fig. 1.

In the "Baseband signal Waveform generation" part, F_s is the system clock of VFD filter, and the clock cycle is T_s. M_0 is the times of the design delay control resolution relative to T_s, and it sets the "sampling" rate of the baseband signal in the filter to T_s/M_0. Then, the filtered signal waveform data is obtained at required

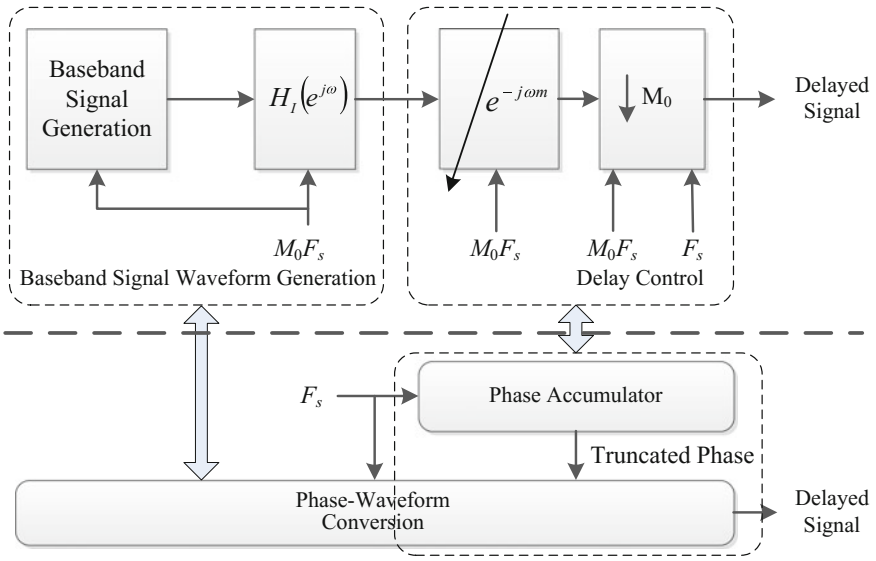

Fig. 1 Principle diagram of controlling signal delay by NCO phase

bandwidth. In the "Delay Control" part, the signal waveform is delayed by an integral multiple of T_s/M_0, and output after M_0 times down sampling. By changing the value of m in the "Delay Control" part, the delay of the output signal varies according to the resolution T_s/M_0.

The digital process shown in the upper half part of Fig. 1 is difficult to be realized directly, it can only be equivalently realized by various of VFD filter algorithm [9]. However, if the VFD filtering algorithm is not used, and the ideal VFD filtering process is reassembled and function switched, the principle of using the NCO phase to control the broadband signal delay can be obtained, as shown in the lower part of Fig. 1.

Set f_c as the baseband signal symbol rate, which is also the overflow frequency of the phase accumulator; $T_c = 1/f_c$ as the corresponding symbol duration; P as the phase accumulation modulo value; N_t as the phase accumulator truncation bit num, which determined the bit num input to the "Phase-Waveform Conversion" block.

So, if they satisfy

$$\Delta\tau = \frac{T_s}{M_0} = \frac{2^{N_t}}{P} T_c \tag{1}$$

The delay $\Delta\tau$ that corresponding to the least significant digital bit of truncated accumulator output, which input to phase-waveform conversion block, is equal to T_s/M_0. So, as the NCO phase accumulator value changes 2^{Nt}, the output baseband signal delay adjusts of T_s/M_0. Furthermore, considering $f_c = 1/T_c$ and Eq. (1), we have

$$f_c = \frac{1}{T_c} = \frac{M_0 2^{N_t}}{\mathrm{P}} \frac{1}{T_s} = \frac{\mathrm{FW}}{\mathrm{P}} f_s \tag{2}$$

It can be seen that when the frequency control word FW = $M_0 2^{Nt}$, the "Phase-Waveform Conversion" block outputs a signal sample point separated by M_0 points from the previous output, which is equivalent to the M_0 times down sampling function of the VFD filter process.

Based on the above analysis, the basic mathematical principles of using NCO phase control for broadband signal delay are presented. When it needs to change the signal delay for mT_s/M_0, simply change the phase value of the NCO phase accumulator. And it is obvious that the delay control performance is equivalent to the VFD filter method.

3 Definition of the Finite State of the Baseband Signal Waveform

The principle of the above description actually contains the hypothesis: "Phase Waveform Conversion" block saves all the possible baseband signal waveform, and it can output waveform sampling point according to the variation of the input phase. However, due to the baseband signal is not periodic, how to make this hypothesis be tenable is the key to the realization of the above principle.

Taking BPSK navigation signal as an example, ignoring writing the sampling clock cycle T_s/M_0, the band-limited signal generated by baseband signal waveform generation part can be expressed as

$$s(n) = D(n)C(n) * h_I(n) \tag{3}$$

where $h_I(n)$ is the impact response of baseband signal low-pass filter, $D(n)$ is navigation message or secondary code, $C(n)$ is pseudo random code. $D(n)$ and $C(n)$ only have two levels, +1 and −1. After the ideal baseband signal sampling sequence passing through $h_I(n)$, the signal waveform is not only non-periodic, but also no longer be a few discrete finite ideally value.

Although the filtered baseband signal is non-periodic and has complexity waveform changes, if $h_I(n)$ is a N_{M0} order FIR digital filter, the filter nth output signal sampling points only correlates to the current input and previously N_{M0} signal sampling points input. Due to the structure and characteristics of the FIR filter, the impact of each sampling point on the current output sampling point is determined by the value of the filter coefficients. This makes the baseband signal waveform can be defined in finite states, so that the phase waveform conversion block can generate any desired sampling point according to the small amount of necessary input.

The symbol duration of BPSK satellite navigation baseband signal is pseudo random code bit width T_c, and there are R baseband signal sampling points in symbol duration. When the ideal baseband signal is filtered by $h_I(n)$, only previous N_{M0} sampling points needs to be used for the current sampling point output of this code chip. For the ideal baseband signal, waveform of the whole chip is completely known, so the R sample points of the whole chip after passing through $h_I(n)$ can also be considered to be determined. Therefore, if previous q ideal baseband signal chip before the current chip can be known, and qT_c satisfies $qT_c \geq N_{M0}T_s/M_0$, the every point output of current chip, when passing through $h_I(n)$, comes from the q ideal baseband signal chip values and the current ideal baseband signal chip value. Moreover, the output value is selected from several finite waveform state. The number of state of an ideal BPSK baseband signal waveform of each chip is 2, respectively +1 and −1, and the +1 and −1 baseband signal waveform symmetry. Then, there are 2^q waveform states for every filter output baseband signal chip.

Taking the BeiDou2 B3I signal as an example, the B3I pseudo random code rate is 10.23 MHz, the bandwidth of filter $h_I(n)$ is 20.46 MHz, and the system clock f_s = 100 MHz. If the delay resolution $\Delta\tau$ = 0.1 ns, the phase accumulator modulus P = 5×10^{11}, then the truncated digit N_t calculated according to the Eq. (1) is non-integer value.

In order to make the N_t an integer, and the final delay resolution can satisfy the design requirements, an integer N_t can be set to make the designed delay resolution $\Delta\tau_D \ll \Delta\tau$. Select $N_t = 24$, then $\Delta\tau_D \approx 3.3$ ps, and the order of $h_I(n)$ is N_{M0} = 25,093. It is easy to know that q = 1 can satisfy the design requirements, and the corresponding filtered BPSK baseband signal waveform has 2 states, as shown in Fig. 2.

All the baseband signal waveforms, which is output from low-pass filter $h_I(n)$, can be completely and accurately obtained by combining the 2 waveform states, as shown in Fig. 3.

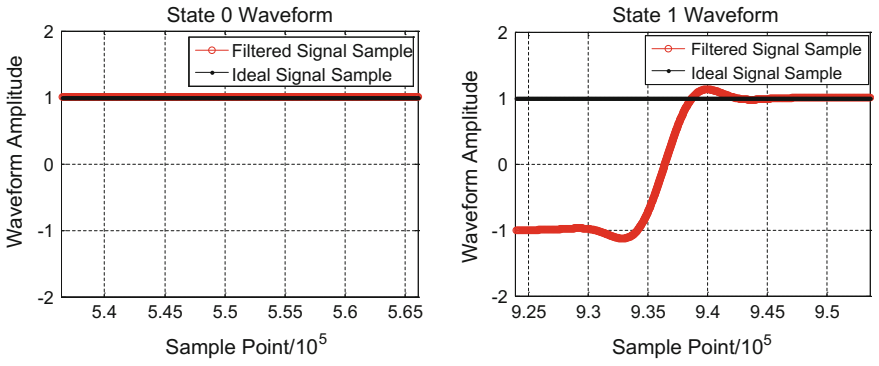

Fig. 2 Two waveform states of BPSK signal

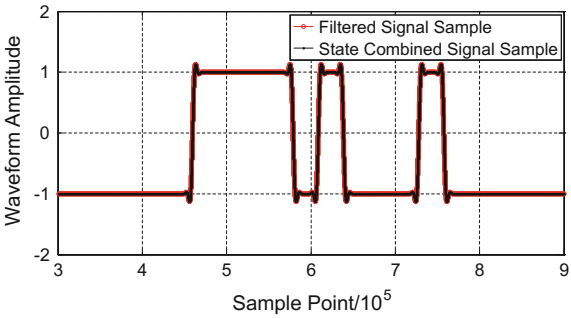

Fig. 3 The waveform composed of finite state of the filtered signal waveform and the direct filtered signal waveform

4 The Implementation of Delay Control Phase Controlled Hermite Waveform Interpolation

4.1 The Implementation Structure

According to the principle of the proposed mathematic principle and definition of the finite state of the baseband signal waveform, the NCO phase control high precision delay implementation structure is designed, as shown in Fig. 4.

As it shows in Fig. 4, NCO is not only output the clock which drives the baseband signal generation, but also output the truncated accumulator phase, which

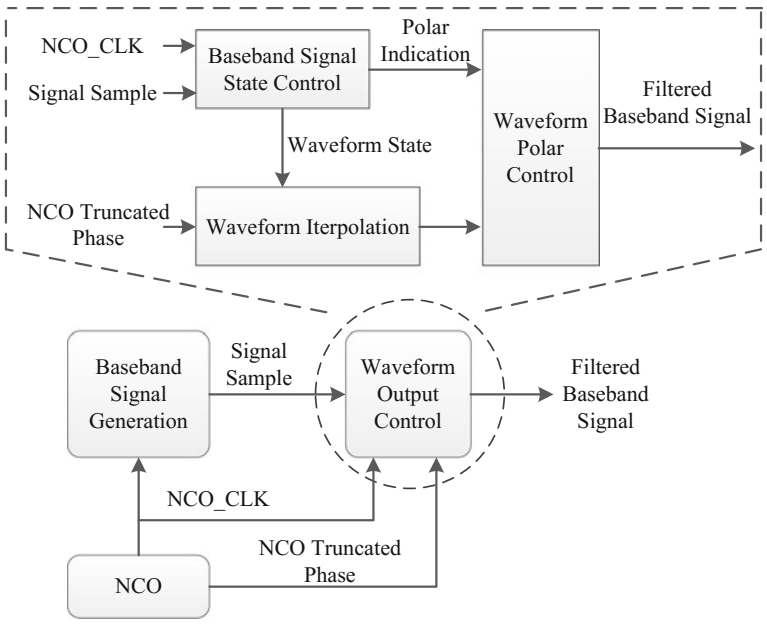

Fig. 4 NCO phase control high precision delay implementation structure

input to waveform output control module for generating signal waveform. The sampling point of the last one or more ideal baseband signal chips are latched in the waveform output control module when the input NCO clock valid, then uses them and the new input ideal baseband signal to generate the waveform state indication and waveform polarity indication signal. Signal waveform is generated using arbitrary waveform interpolation method at the waveform state indication, and finally output under the control of waveform polarity.

It is easy to know that the arbitrary waveform interpolation part consumes the most resource, and is the most important part in waveform output control module. A widely used arbitrary waveform interpolation methods at present is piecewise Chebyshev polynomial method [12], but it is difficult to eliminate the integral error when solving the interpolation coefficients, resulting in difficult to improve the accuracy of the waveform fitting. This report proposes an arbitrary waveform interpolation method based on piecewise third order Hermite interpolation, and the corresponding calculation equation for waveform interpolation can be expressed as

$$ff_k(\tau) \approx P_{H,k}(\tau) = a_{k0} + a_{k1}\tau + a_{k2}\tau^2 + a_{k3}\tau^3 \tag{4}$$

where

$$\begin{aligned} a_{k0} &= f(t_i) \\ a_{k1} &= f^{(1)}(t_i) \\ a_{k2} &= \frac{3f[t_i, t_{i+1}] - 2f^{(1)}(t_i) - f^{(1)}(t_{i+1})}{t_{i+1} - t_i} \\ a_{k3} &= \frac{f^{(1)}(t_i) - 2f[t_i, t_{i+1}] + f^{(1)}(t_{i+1})}{(t_{i+1} - t_i)^2} \end{aligned} \tag{5}$$

Furthermore, in order to efficiently implement the Hermite interpolation generation method, Eq. (4) can be rewritten as

$$ff_k(\tau) \approx P_{H,k}(\tau) = a_{k0} + \tau(a_{k1} + \tau(a_{k2} + \tau a_{k3})) \tag{6}$$

By Using Eq (6), the piecewise waveform interpolation structure can be illustrated as Fig. 5.

Obviously, there are only 3 MACs (Multiplier and Accumulator) need to be used when implementing waveform interpolation part, as well as a coefficient ROM. The storage capacity of coefficient ROM is determined by the number of interpolating piecewise segment. For facilitate the implementation, the number of piecewise are usually set to 2 m.

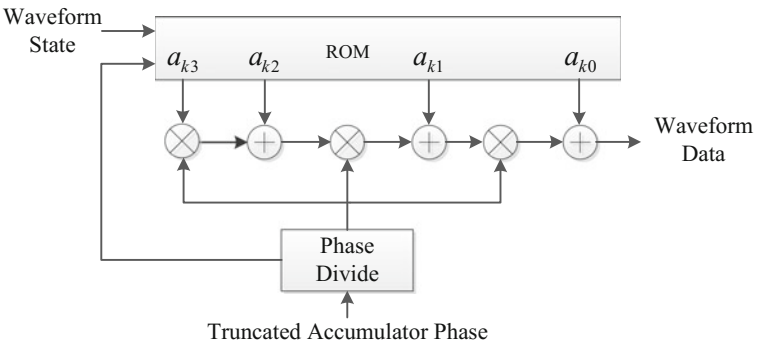

Fig. 5 The waveform interpolation structure

Table 1 Hardware resource consumption compares

Design method	MAC	RAM
Farrow structure VFD filter	420	0
Method proposed	36	$2^{10} \times 3$

4.2 Analyze of Hardware Resource Consumption

Taking B3I signal and the previous given design conditions for example, the simulation signal delay control error at different m can be simulated. The simulation results show that the delay measurement error of matching correlation method are always less than 10 ps when $m \geq 5$. Let $m = 5$, the coefficient ROM only needs to store $2 \times 32 \times 4$ interpolation coefficients, and the whole implement structure consumes just 3 MACs, While using Farrow structure VFD filter in [9] to achieve 0.1 ns delay resolution needs to consume at least 35 MACs.

The comparing results of hardware resource consumption between VFD filter method and the proposed method, when generates 12 channels simulation signal at the same time, is in Table 1.

Therefore, to achieve the same delay resolution by using the proposed method in this report, in addition to a small increase in combinational logic and memory resources consumption, the MAC resource consumption is reduced by about 91.4%.

5 Testing Results

The proposed method is applied to the design of satellite navigation signal simulator for generating the B3I signal. The design parameters are the same with the simulation parameters mentioned before. Figure 6 shows the observation result of high-speed digital oscilloscope after signal delay change of 1 ns.

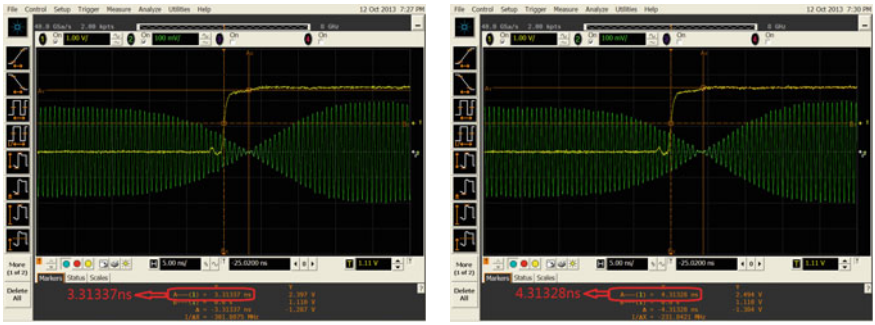

(a) Before 1ns delay *(b) After 1ns delay*

Fig. 6 1 ns delay observed by the oscilloscope

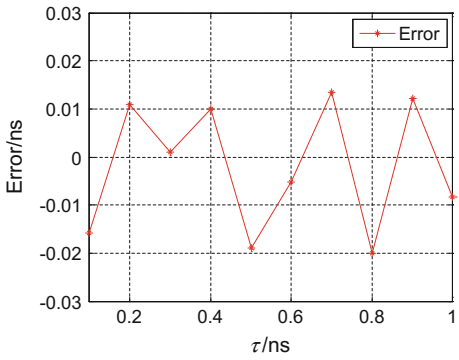

Fig. 7 Testing results with delay step 0.1 ns

Taking the simulator output 1PPS pulse signal as the oscilloscope trigger signal, delay variation of B3I RF signal can be observed by the delay variation of RF signal envelope minimum point relative to the rising edge of the 1PPS pulse. It is obvious that the signal delay controlled by the improved method can make the delay change less than 10 ns observed real time in time domain measurement. Furthermore, testing the delay precision using RF signal envelope measurement method mentioned in [8]. Set 0.1 ns be the delay control resolution, delay range is 0.1–1 ns, the testing results are shown in Fig. 7. Obviously, the delay control error is always less than 20 ps, which is a very high delay control precision.

6 Conclusions

In order to overcome the defects of the traditional high precision broadband direct-spread signal method, the NCO phase control waveform Hermite interpolation method is proposed in this report, which has the same delay control

performance as VFD method. But the proposed method is significantly better than the VFD filter method in resource consumption. When implementing the method using FPGA, only a small storage and combinational logic resource consumption increases compared with VFD filter method, and the hardware MAC consumption was reduced by 91.4%, which can effectively reduce the hardware cost of satellite navigation signal simulator.

Acknowledgements Acknowledge for the simulator development team of Satellite Navigation Engineering Research and Development Center, School of Electronic Science and Engineering, National University of Defense Technology. Thank them for verifying the proposed method.

References

1. Zhang X, Li CH, Huang YB et al (2014) Mixed-clock third-order DDS applied in signal Doppler Frequency Shift Simulation. J Natl Univ Def Technol 36(2):134–139
2. Sirbu M, Delfino E, Koivunen V (2004) A novel method for time delay acquisition in satellite navigation systems. In: IEEE eighth international symposium on spread spectrum techniques and applications, pp 726–730
3. Garrison JL, Liang L (2005) Numerical simulation of GNSS code tracking loops using Euler-Maruyama method. Electron Lett 41(15):868–869
4. Tierney J, Rader CM, Gold B (1971) A digital frequency synthesizer. IEEE Trans Audio Electroacoust 19(1):48–57
5. Zhang X (2004) Digital baseband signal processing and its VLSI implementation for spread spectrum communication. Science Press, Beijing
6. Meng FZ (2004) The research of the key technologies in the high dynamic GPS satellite signal simulator. Master's Degree Thesis of National University of Defense Technology
7. Kushner LJ, Ainsworth MT (1996) A spurious reduction technique for high-speed direct digital synthesizers. In: Proceedings of the 50th frequency control symposium, pp 920–927
8. Zhong X, Tang Z, Meng Z et al (2013) A study on high precision calibration of zero value for navigation signal simulator. In: China satellite navigation conference (CSNC) 2013 proceedings, pp 469–477
9. Yang J, Yun CJ, Zhong XP et al (2010) High precision delay satellite navigation signal generation theory and application in navigation satellite simulation test. In: The 1st China satellite navigation conference (CSNC) proceedings, Beijing
10. Chen ZY (2001) Research on the method of simulation navigation signals accurately based on BOC modulation. Master's Degree Thesis of National University of Defense Technology
11. Sha H, Chen HM, Lv ZC (2014) Dynamic delay generation method based on variable fractional delay filter. In: The proceeding of China satellite navigation conference, Nanjing
12. Ashrafi A, Adhami R, Joiner L et al (2004) Arbitrary waveform DDFS utilizing Chebyshev polynomials interpolation. IEEE Trans Circ Syst I Regul Pap 51(8):1468–1475

The Evaluation of Improvement of GPS Performance Combined with Quasi-Zenith Satellite System in Japan Area

Xuying Ma, Xiaping Ma, Chengpan Tang and Xingyu Wang

Abstract The Quasi-Zenith Satellite System is developed by SPRAC of Japan. It is a regional satellite navigation and augmentation system. In this contribution, we evaluated and analyzed the accuracy, availability and reliability of GPS aided with QZSS in Japan area from aspects of constellation structure and positioning performance based on measured data. The results show that: at different cut-off angle, the constellation structures of GPS aided with QZSS are better than that of GPS-only; meanwhile the positioning performance of GPS aided with QZSS is also better than that of GPS-only; furthermore, this advantage is more obvious under a high cut-off elevation angle condition. Japan is a country of dense buildings in the city and numerous mountains in the wild. The good performance of GPS aided with QZSS at higher cut-off angle overcomes the limitation of this observation environment. The mode of GPS aided with QZSS would improve the positioning accuracy, availability and reliability of satellite navigation systems dramatically in Japan area.

Keywords GPS · QZSS · Constellation structure improvement · Positioning performance improvement

X. Ma (✉)
University of Auckland, 23 Symonds Street, 1142 Auckland, New Zealand
e-mail: maxuying10086@163.com

X. Ma
Xi'an University of Science and Technology, No.58 YanTa Road, Xi'an 710054, China
e-mail: celiang0321@163.com

C. Tang
Shanghai Astronomy Observatory, Chinese Academy of Science, No.8 NanDan Road, Shanghai 200030, China
e-mail: cptang@shao.ac.cn

X. Wang
Xi'an Siyuan University, No.28 ShuiAn Road, Xi'an 710038, China
e-mail: 809914450@qq.com

J. Sun et al. (eds.), *China Satellite Navigation Conference (CSNC) 2017 Proceedings: Volume I*, Lecture Notes in Electrical Engineering 437,
DOI 10.1007/978-981-10-4588-2_45

1 Introduction

Satellite navigation and positioning technology has been developed rapidly in the past decades along with the progress of society and the development of technology. GPS, as the most advanced and mature GNSS system, has been widely used in control network layout, deformation monitoring, project surveying and other fields. In recent years, positioning technology based on Multi-GNSS systems will provide users with location services of higher accuracy and reliability with the maturity of GLONASS, BeiDou, Galileo and QZSS.

Quasi-Zenith Satellite System (QZSS) is developed by SPRAC of Japan. It is a regional satellite navigation and augmentation system. QZSS has high compatibility and interoperability with GPS and Galileo. QZSS cannot provide positioning and navigation services alone in the current stage due to few number of QZS satellites; however it can improve the accuracy and reliability of positioning in the Asia-Pacific region significantly when we use both GPS and QZSS systems [1]. Liao et al. [2] introduced orbit characteristics and navigation signal design of QZSS and also analysed its service area, availability and service performance. Nie et al. [3] carried out evaluation and analysis of SNR, multipath and IFB for QZSS based on the measured data of IGS stations. Li et al. [4] carried out simulation analysis on the augmentation of accuracy, integrity and availability of QZSS to GPS in Japan and eastern China area.

In this contribution, we evaluated and analyzed the accuracy, availability and reliability of GPS aided with QZSS in Japan area from aspects of constellation structure and positioning performance based on measured data. The results show that: at different cut-off angle, the constellation structures of GPS aided with QZSS are better than that of GPS-only; meanwhile the positioning performance of GPS aided with QZSS is also better than that of GPS-only; furthermore, this advantage is more obvious under a high cut-off elevation angle condition. Japan is a country of dense buildings in the city and numerous mountains in the wild. The good performance of GPS aided with QZSS at higher cut-off angle overcomes the limitation of this observation environment. The mode of GPS aided with QZSS would improve the positioning accuracy, availability and reliability of satellite navigation systems dramatically in Japan area.

2 The Overview of Quasi-Zenith Satellite System

QZSS is a new generation multi-task regional satellite navigation and augmentation system developed by SPRAC of Japan. Quasi-Zenith Satellite (QZS) provides users with not only location service through broadcasting traditional navigation signals but also improvement information for GPS and GLONASS systems through augmentation signals. This special function is similar to the current augmentation service provided by Satellite-Based Augmentation System (SBAS) [5]. In the following section of this paper, we mainly focused on the improvement of location service provided by traditional navigation signals of QZSS.

Since QZSS is initially designed as a regional navigation system, it is deliberately planned to meet the navigation demand of users in Japan area at the beginning of this project. Japan is a country of dense buildings in the city and numerous mountains in the wild, so the navigation signals are easily affected by obstacles when users carry out navigation and surveying. However, the influence of these obstacles will be greatly reduced if the navigation satellites can fly over Japan with high elevation [6]. Therefore, QZSS adopt a unique orbit design to meet this condition. According to the project plan, the navigation constellation of QZSS consists of three Inclined Geosynchronous Satellite Orbit (IGSO) satellites after the constellations are fully deployed. The three IGSO satellites will be deployed in three different large elliptical orbits; the semi-major axis is 42,164 km; the eccentricity is 0.099; the inclination is 45° and the difference of ascending node Ω between each satellite is 120°. This special orbit design guarantees that users in Japan area can receive signals from at least one QZSS satellite at any time. At present, Japan launched only one Quasi-Zenith satellite. Its PRN and code name are 193 and Michibiki respectively [7].

Figure 1 is the Footprints (left) and Skyplot of station chof (right) for QZSS J01 satellite. The ground track of QZSS J01 satellite looks like an asymmetric number '8', and this special orbit can prolong the fly time of navigation satellite over Japan area. We can learn from the Skyplot of station chof (right) that J01 satellite flies over Japan area with the elevation above 75° all the time. This will greatly improve the availability of QZSS.

In order to ensure high compatibility and interoperability with GPS in spatial and temporal reference, QZSS uses Japan Satellite Navigation Geodetic System (JGS) and Quasi-Zenith Satellite System Time (QZSST) as its coordinate system and time system respectively. The coordinate difference between JGS and WGS-84 of GPS is only 2 cm, users can ignore the tiny difference in ordinary navigation and pseudo-range positioning applications. The one second span of QZSS is the same as International Atomic Time TAI. QZSST is behind of TAI by 19 s, which is the same with GPST. In the aspect of interface with GPST, the satellite borne atomic clock of QZSS is controlled by GPST, which is the same with the satellite borne atomic clock of GPS [8].

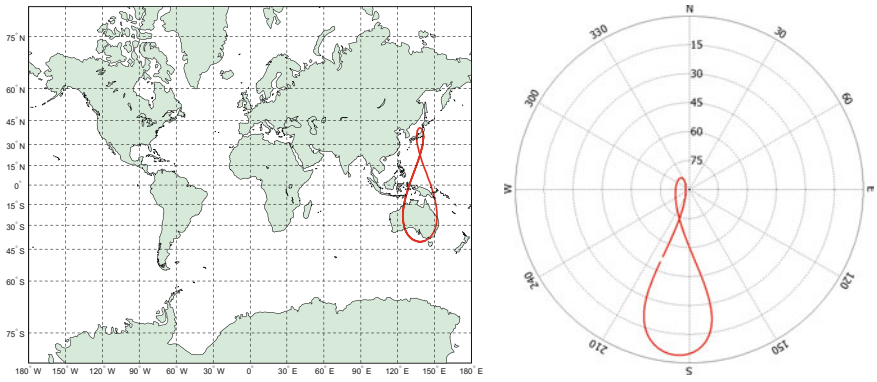

Fig. 1 Footprints (*left*) and Skyplot of station *chof* (*right*) for QZSS J01 satellite

3 The Improvement of GPS Aided with QZSS in the Aspect of Constellation Structure

We calculated the PDOP distribution of GPS-only and GPS/QZSS mode at different cut-off angle in Japan area to assess the improvement of constellation structure of GPS aided with QZSS by using GPS and QZSS broadcast ephemeris of April 9, 2016 (*doy*100) from MGEX (ftp://cddis.gsfc.nasa.gov).

Figure 2 is the comparison of PDOP distribution calculated by broadcast ephemeris between GPS-only and GPS/QZSS mode at different cut-off angle in Japan area. PDOP means position dilution of precision, which is a measure of X, Y, Z position geometry. Generally speaking, a better constellation structure it is, the smaller PDOP value it is. The left and right column show the PDOP distribution of

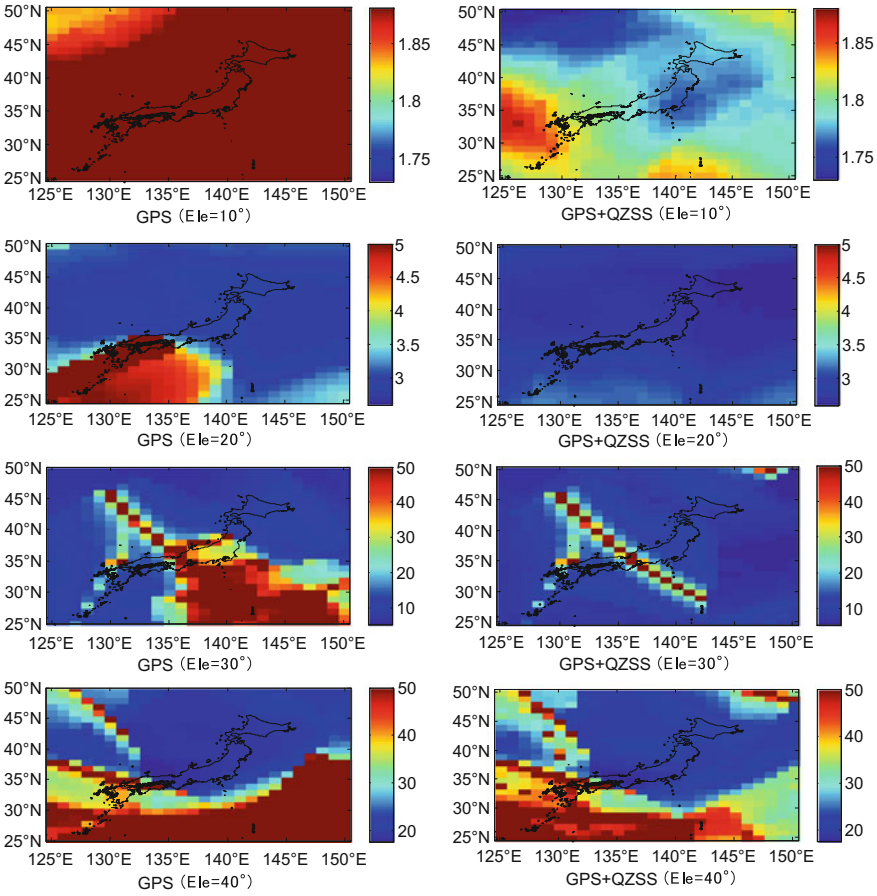

Fig. 2 The comparison of PDOP distribution calculated by broadcast ephemeris between GPS-only and GPS/QZSS mode at different cut-off angle in Japan area

GPS-only and GPS/QZSS mode at different cut-off angle in Japan area respectively. The cut-off angles are set 10°, 20°, 30° and 40° respectively from the top to bottom rows to simulate the different severity of signal block from obstacles. Note that we do not show the results of cut-off angle above 40° since results of both modes above 40° are so poor. Through the contrast and statistical analysis, it can be found that the PDOP values of GPS/QZSS mode at any cut-off angle in Japan area are generally smaller than that of GPS-only mode. It means that the GPS/QZSS mode can get a better constellation structure than GPS-only mode. Take the case of 10° cut-off angle as an example, the PDOP values of GPS-only mode in Japan area are around 1.85, while the PDOP values of GPS/QZSS mode in Japan area are about 1.75–1.80. Although there is only one QZS satellite J01 currently, the general PDOP values of GPS/QZSS mode decrease 2.70–5.41% compared with GPS-only mode. The GPS aided with QZSS improves the performance in the aspect of constellation structure greatly.

4 The Improvement of GPS Aided with QZSS in the Aspect of Positioning Performance

We assessed the improvement of positioning performance of GPS aided with QZSS by using measured data from MGEX (ftp://cddis.gsfc.nasa.gov). Currently, many MGEX stations can receive QZSS observation data. We selected stations of *chof* and *mizu* in Japan area to assess the positioning accuracy, availability and reliability of GPS aided with QZSS.

We carried out 24 h SPP solutions of *chof* and *mizu* in GPS-only and GPS/QZSS mode at different cut-off angle by using GPS and QZSS observation data of April 9, 2016 (doy100). The sampling interval of observation data is 30 s, the cut-off angles are set 10°, 20°, 30°, 40°, 50° and 60° respectively to simulate the different severity of signal block from obstacles. Figure 3 shows the positioning results of *chof* station, the red and blue dots represent GPS-only and GPS/QZSS model results respectively. Note that we only depicted the results of *chof* station since the space was limited and did not show results above 40° since both modes were so poor. The overall positioning results of *chof* and *mizu* are shown in Tables 1 and 2.

Take the results of station *chof* as an example: at 10° cut-off angle, the RMS of the coordinate biases time series in *N*, *E* and *U* direction of GPS-only mode are 1.40, 1.03 and 2.76 m respectively; the success rate of positioning is 100%, the RMS of the coordinate biases time series in *N*, *E* and *U* direction of GPS/QZSS mode are 1.26,1.01 and 2.51 m respectively; the success rate of positioning is 100%; the positioning accuracy in *N*, *E* and *U* direction and success rate of GPS/QZSS mode increase 10.00, 1.94, 9.06 and 0.00% respectively compared with GPS-only mode. At 20° cut-off angle, the positioning accuracy in *N*, *E* and *U* direction and success rate of GPS/QZSS mode increase 7.95, 4.00, 6.92 and 0.00% respectively compared with GPS-only mode. At 30° cut-off angle, the

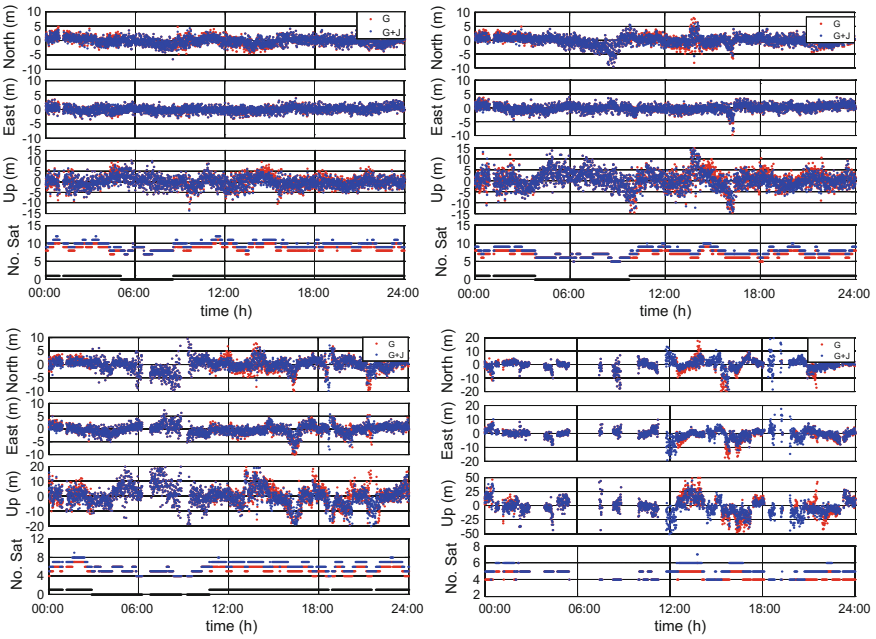

Fig. 3 SPP results comparison between mode of GPS-only and GPS/QZSS of station *chof* (cut-off angle set: *top left* 10°, *top right* 20°, *bottom left* 30°, *bottom right* 40°)

Table 1 Statistics of SPP solutions for *chof* station

SPP-mode	Direction	10°	20°	30°	40°	50°
GPS	N_RMS (m)	1.40	1.76	2.85	5.25	4.15
	E_RMS (m)	1.03	1.25	2.01	3.56	3. 85
	U_RMS (m)	2.76	4.19	8.51	15.15	30.24
	Success rate	100%	99.82%	93.65%	55.40%	7.82%
GPS + QZSS	N_RMS (m)	1.26	1.62	2.66	3.99	3.78
	E_RMS (m)	1.01	1.20	1.81	3.29	3. 21
	U_RMS (m)	2.51	3.90	7.22	13.51	21.62
	Success rate	100%	99.82%	95.51%	69.23%	21.51%

positioning accuracy in *N*, *E* and *U* direction and success rate of GPS/QZSS mode increase 6.67, 9.95, 15.16 and 1.99% respectively compared with GPS-only mode. At 40° cut-off angle, the positioning accuracy in *N*, *E* and *U* direction and success rate of GPS/QZSS mode increase 24.00, 7.58, 10.83 and 24.96% respectively compared with GPS-only mode. At 50° cut-off angle, the positioning accuracy in *N*, *E* and *U* direction and success rate of GPS/QZSS mode increase 8.92, 16.62, 28.51 and 175.06% respectively compared with GPS-only mode. At 60° cut-off angle, the GPS-only mode has been completely unable to provide location service, while the

Table 2 Statistics of SPP solutions for *mizu* station

SPP-mode	Direction	10°	20°	30°	40°	50°
GPS	N_RMS (m)	2.12	2.64	4.53	5.65	4.69
	E_RMS (m)	1.48	1.46	2.04	3.21	2.57
	U_RMS (m)	3.65	5.05	10.18	16.82	35.66
	Success rate	100%	100%	94.86%	53.09%	8.29%
GPS + QZSS	N_RMS (m)	1.95	2.56	4.37	5.11	3.94
	E_RMS (m)	1.46	1.44	1.92	3.62	3.59
	U_RMS (m)	3.54	5.02	9.33	15.65	26.40
	Success rate	100%	100%	96.18%	64.17%	22.15%

GPS/QZSS mode can still be able to provide location service of limited time and poor accuracy. Note that we do not show the SPP positioning statistical data at 60° cut-off angle in tables since the results are so poor. The results of station *mizu* are very similar to that of station *chof*. The mode of GPS aided with QZSS can improve the positioning accuracy, availability and reliability compared with GPS-only mode. Furthermore, this advantage is more obvious under a high cut-off elevation angle condition.

In summary, although GPS/QZSS mode has only one more satellite than GPS-only mode, the one more QZS J01 satellite makes great contribution to the improvement of the whole system due to its special orbit design. Japan is a country of dense buildings in the city and numerous mountains in the wild. The good performance of GPS aided with QZSS at higher cut-off angle overcomes the limitation of this observation environment. It can be expected that QZSS will play an important role in improving the positioning accuracy, availability and reliability of navigation system in Japan area after all three QZS are fully deployed.

5 Conclusion

QZSS is a new generation multi-task regional navigation and augmentation system developed by Japan. In this contribution, we evaluated and analyzed the accuracy, availability and reliability of GPS aided with QZSS in Japan area from aspects of constellation structure and positioning performance based on measured data. Currently we make some initial conclusions as follow:

1. The special constellation design of QZSS is highly targeted at users in Japan area, it can prolong the fly time of navigation satellite over Japan area and meanwhile the satellite flies over Japan with very high elevation;
2. The GPS aided with QZSS improves the performance in the aspect of constellation structure greatly compared with that of GPS-only mode;

3. The mode of GPS aided with QZSS can improve the positioning accuracy, availability and reliability compared with GPS-only mode. Furthermore, this advantage is more obvious under a high cut-off elevation angle condition;
4. Japan is a country of dense buildings in the city and numerous mountains in the wild. The good performance of GPS aided with QZSS at higher cut-off angle will overcome the limitation of this observation environment and play an important role in improving the positioning accuracy, availability and reliability of navigation system in Japan area.

References

1. Lou Y, Zheng F, Gong X et al (2016) Evaluation of QZSS system augmentation service performance in China region. Geomat Inf Sci Wuhan Univ 41(3):298–303
2. Liao N, Zhang Y, Qin B et al (2013) The signal and service performance of the QZSS navigation system. Geomat Spat Inf Technol 36(5):39–40
3. Nie X, Zheng F, Lou Y et al (2015) An analysis of the QZSS signal based on the data of IGS. In: China satellite navigation conference (CSNC) 2015 proceedings, vol II. Springer, Berlin, pp 325–335
4. Li Z, Hao J, Li J et al (2010) Analysis on QZSS augmentation on area performance of GPS. Geomat Inf Sci Wuhan Univ 35(1):17–20
5. Kogure S, Kishimoto M, Sawabe M et al (2007) Introduction of IS-QZSS (interface specification for quasi zenith satellite system). In: Proceedings of international technical meeting of the satellite division of the institute of navigation
6. Shao JN, Feng W, Shen JF (2009) QZSS and signal design. Sci Surv Mapp (s2):225–227
7. Hauschild A, Steigenberger P, Rodriguez-Solano C (2012) Signal, orbit and attitude analysis of Japan's first QZSS satellite Michibiki. GPS Solut 2012(16):127–133
8. Li Z, Chen F (2016) Improving availability and accuracy of GPS/BDS positioning using QZSS for single receiver. Acta Geodaetica Et Geophysica 1–15

Study on Test Consistency Which Based on the Record and Playback Instrument

Tian Wang, Wenbin Yang, Ming Peng, Shufeng Zhang, Qiang Chen and Weitao Wang

Abstract Navigation terminal testing technology has been getting more and more attention with the rapid development of satellite navigation industry. Traditional laboratory simulation test and actual signal test have advantages and disadvantages. Thus record and playback test has been created. It can effectively complete the actual use test of satellite navigation terminal through acquisition and storage of actual satellite navigation signal and playback under laboratory environment. This paper describes the acquisition, playback and calibration system in detail which based on the record and playback instrument. In the paper, u-blox multimode receiver is chosen as the reference receiver. It takes the capacious scene as an example and analyzes the positioning accuracy and speed accuracy from the angle of terminal test results. It makes a preliminary study on the consistency of playback test through assessing repeatability and stability of the record and playback system.

Keywords Record and playback · Repeatability · Stability

1 Introduction

The use of navigation terminal is growing expanding with the development of satellite navigation systems and constantly deepening on production and life applications. There are various types of navigation terminals. Its functions and uses vary. It is very important to test and verify its function and performance. So navigation terminal test technology is one of the core technologies of satellite

T. Wang (✉) · W. Yang · M. Peng · S. Zhang · Q. Chen · W. Wang
Beijing Orient Institute for Measurement & Test, Beijing 100086, China
e-mail: wangtian514@yeah.net

J. Sun et al. (eds.), *China Satellite Navigation Conference (CSNC) 2017 Proceedings: Volume I*, Lecture Notes in Electrical Engineering 437,
DOI 10.1007/978-981-10-4588-2_46

navigation application. It is a necessary means to develop the high-performance navigation terminal with independent intellectual property rights. It can effectively promote the navigation terminal standardization development with huge, long-term economic and social benefits [1].

The navigation terminal test can be divided into the indoor simulation test and the actual signal test according to the test implementation. The advantage of the indoor simulation test is that all kinds of error effects, signal levels and other factors can be accurately quantified. It can achieve a quantitative assessment of the terminal under test. But the indoor simulation test signal and the actual conditions of use are quite different. The indoor test results cannot fully reflect the actual use of results [2]. The actual signal test is to use the terminal to be tested to receive the actual satellite signal, and then evaluate its performance. The actual signal test has no model approximation and the test results are the actual performance of the receiving terminal. The actual signal results are closely related to the constellation state, ionosphere, multipath, receiver ambient environment and the atmospheric signal propagation environment of the test scene, so the test repeatability is poor and the test cost is high.

So the navigation signal record and playback test technology is produced. It can effectively complete the actual use of satellite navigation terminal performance testing through the record and storage of the actual satellite navigation signals, and in the laboratory environment for playback. It can not only avoid the actual field test satellite signal's uncertainty, and can also reduce the time and cost of field testing. It can solve the satellite navigation terminal indoor simulation environment and the real environment of the test inconsistency to a certain extent. The playback test process inevitably leads to test bias due to hardware mismatch and signal distortion because the electrical characteristics of the navigation signal are affected by the signal acquisition and playback device parameters. So verification of its consistency is required to ensure engineering availability. In this paper, the consistency of the playback test of the navigation signal record and playback instrument is studied preliminarily through data record and playback testing based on a subject.

2 Record, Playback and Calibration System

Navigation signal record is made by the record and playback instrument. During the acquisition, the navigation receiver is used to receive the position and velocity information at the same time, record and save, and then select the specific scene data after the acquisition to get the positioning result. Then in the laboratory, the same scene data is play backed. It verifies the consistency with the actual positioning information through using the navigation receiver to perform the playback test and to obtain the positioning result. In this paper, u-blox receiver is selected which is used as the transmission of record and playback signals and its positioning results are used to characterize the consistency of the playback.

2.1 Record and Playback Instrument

Navigation signal record and playback instrument is consist of signal record unit, storage control unit and the signal playback unit. The composition diagram is shown in Fig. 1.

(1) signal record unit

The signal record unit includes a broadband antenna, a radio frequency input module and a high-speed data acquisition module. It is used for receiving the GNSS satellite navigation signal to complete the RF signal preprocessing, down-converting and realize high-speed real-time sampling of the intermediate frequency signal, and sending the sampling result to the storage control unit for storage.

(2) storage control unit

The storage control unit is composed of a high-speed large-capacity disk array, a data flow management and control module and a user interface module. Data flow management and control module is used for capturing playback mode management, frequency selection, record/playback time and playback signal power strength control. The user interface module completes the human-machine interaction of the user.

(3) signal playback unit

The signal playback unit comprises a playback signal synthesizing module and a radio frequency output module. It is used for synthesizing the collected and stored

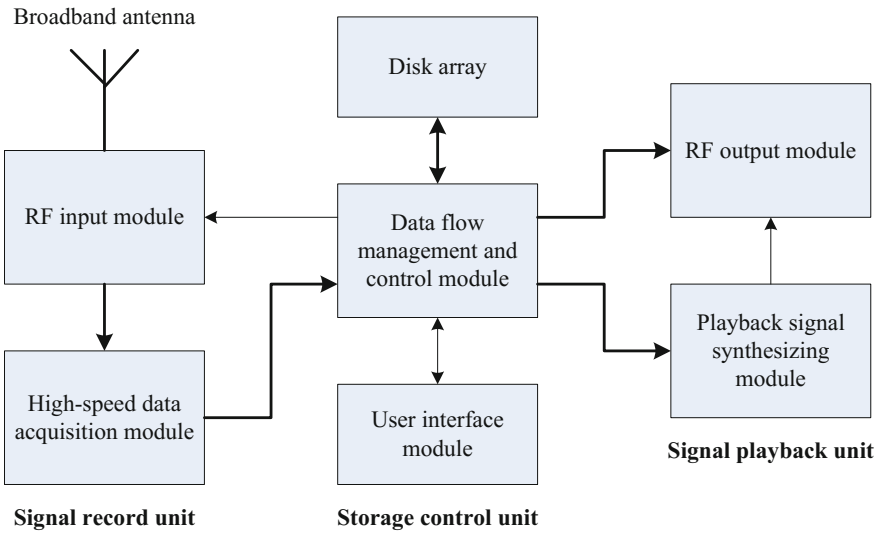

Fig. 1 Composition diagram of record and playback instrument

data into an intermediate frequency signal, converting the data to the navigation test signal required for the test and completing the power attenuation control of the output signal.

2.2 Dynamic Scene Calibration System

During the record of the navigation signal, it is necessary to acquire the accurate position, velocity and time information at the same time. This information is used as the baseline information in subsequent playback tests and is an important performance evaluation parameter. Data calibration is the basis for obtaining test metrics. The calibrated reference data should be more accurate than the measured data. Ideally, it should be an order of magnitude higher and triple relationship minimum.

We select NovAtel's GNSS/INS integrated navigation system SPAN/LCI as the dynamic scene calibration system. It includes the DL-V3 base station receiver, the SPAN-SE mobile station receiver, the IMU-LCI tactical inertial measurement unit and the Inertial Explorer (IE) post-processing software. The DL-V3 base station receiver generates a differential correction amount required for the post-RTK differential processing to the SPAN-SE receiver as a mobile station whose coordinates of the erect point are precisely known. The measurement data of the IMU-LCI tactical inertial measurement unit can be sent to the SPAN-SE mobile station receiver in real time. The receiver can provide the information of the position, velocity and attitude of the carrier through the deep coupling solution processing. The SPAN-SE mobile station receiver receives the difference correction amount provided by the base station receiver, eliminates most of the errors such as the ionospheric delay, and obtains more accurate position information with respect to the base station. The calibration system is shown in Fig. 2.

In the calibration system, the mobile station receiver, the reference u-blox receiver and the record and playback instrument simultaneously receive the actual satellite navigation signals and then play back in the laboratory. The actual acquisition schematic is shown in Fig. 3.

In the experiment, GPS L1 and BD B1 frequency navigation signals are collected and stored in real time, then the playback test is carried out in the laboratory environment.

3 Research on Consistency of Playback Test

After the satellite navigation signal is collected and replayed, the playback result of the tested receiver needs to be verified. The system composed of the receiver to be measured and the recorder is used as the object of study. The repeatability and

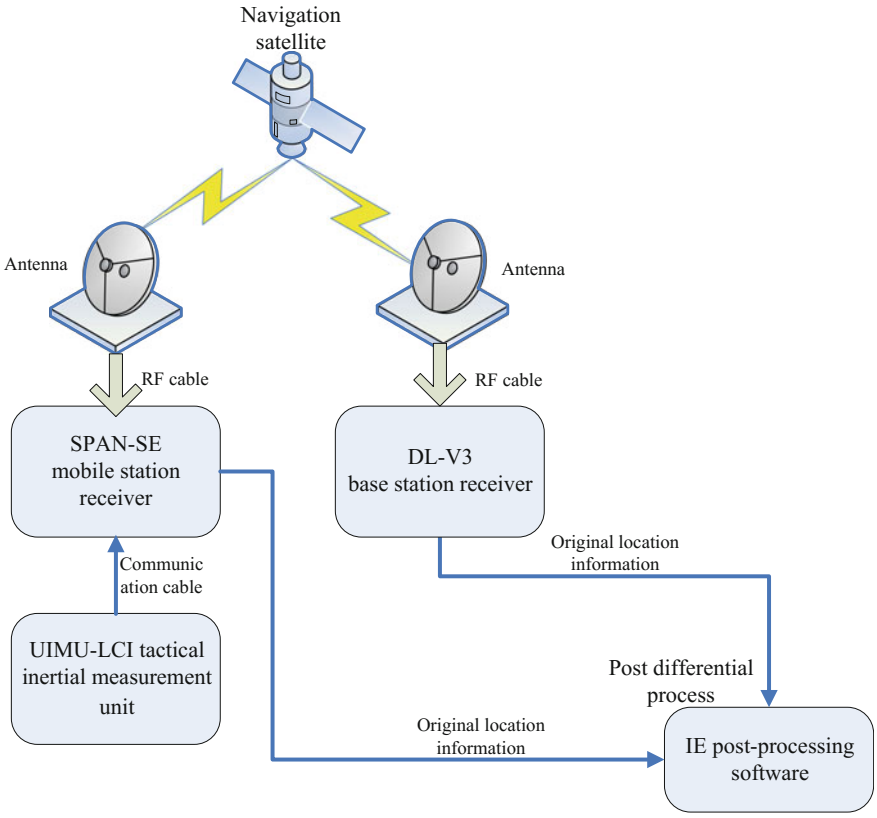

Fig. 2 Composition diagram of record and calibration system

stability of the system are analyzed from the perspective of the position of the measured receiver.

3.1 Repeatability

Reproducibility refers to the ability to repeat the same measurement over a short period of time under the same measurement conditions (including the same observer, at the same location, using the same measurement procedure), which provides the ability to display similar values. Reproducibility is a measure of the effect of random effects on the measurement results. The repeatability test is a measure of the degree of agreement between the measurement results [3].

In the specific implementation, we select a specific static or dynamic scene and play back six times continuously in a short time under the same laboratory

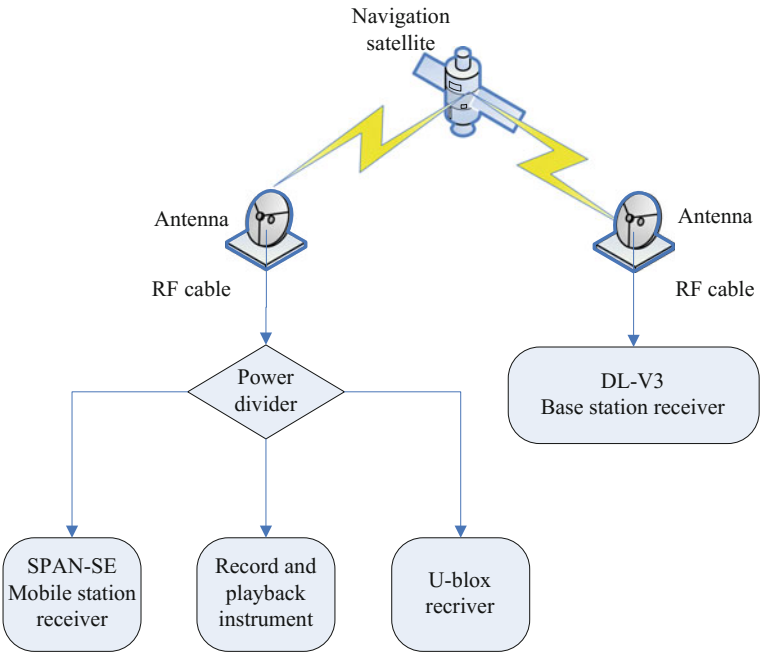

Fig. 3 Composition diagram of actual record

conditions and the playback environment with the same test method. The calculation formula is as follows.

$$S_r(x) = \sqrt{\frac{\sum_{i=1}^{n} (x_{r_i} - \bar{x}_r)^2}{n-1}} \tag{1}$$

where x_{r_i} represents the difference between the playback signal test result and the actual signal test result; $x_{r_i} = x_i - x_0$; x_i represents the playback signal test result; x_0 represents the actual signal test result; n represents the repeat playback times.

We select a dynamic open scene which surrounded by high-rise buildings and other buildings, wide field of vision, satellite signals can be direct. We select half an hour of data, continuous play back six times respectively and record each playback test data. The test results are as follows.

(1) the actual signal test results

In the dynamic open scene, the actual test results of the u-blox receiver are shown in Table 1.

Table 1 Actual test results of open scene signal

Receiver	Position accuracy (m)		Velocity accuracy (m/s)
	Level	Vertical	
u-blox	2.1504	6.2081	0.0976

Table 2 Playback test results

Results	Test items		
Playback numbers	Horizontal accuracy (m)	Vertical accuracy (m)	Velocity accuracy (m/s)
1	1.7803	6.2779	0.0987
2	1.7896	6.2721	0.0985
3	1.7832	6.2687	0.0986
4	1.7978	6.2658	0.0981
5	1.7991	6.2715	0.0978
6	1.7942	6.2693	0.0986
Average $\bar{x} = \frac{\sum_{i=1}^{n} x_i}{n}$	1.7907	6.2709	0.0984
Actual test result x_0	2.1504	6.2081	0.0976

(2) the playback signal test results

The results of six playback tests and repeatability analysis are shown in Tables 2 and 3 (Fig. 4).

The comparison between the actual signal test and the one-time playback signal test accuracy error is shown in Fig. 5.

Horizontal accuracy:
Repeatability $S_r(x) = 0.0077$ m

Table 3 Analytic results of repeatability

Difference	Test items		
Playback numbers	Horizontal accuracy (m)	Vertical accuracy (m)	Velocity accuracy (m/s)
1	0.3701	0.0698	0.0011
2	0.3608	0.064	0.0009
3	0.3672	0.0606	0.001
4	0.3526	0.0577	0.0005
5	0.3513	0.0634	0.0002
6	0.3562	0.0612	0.001
Average $\bar{x}_r = \frac{\sum_{i=1}^{n} x_{r_i}}{n}$	0.3597	0.0628	0.0008
Standard deviation $S_r(x) = \sqrt{\frac{\sum_{i=1}^{n} (x_{r_i} - \bar{x}_r)^2}{n-1}}$	0.0077	0.0041	0.0004

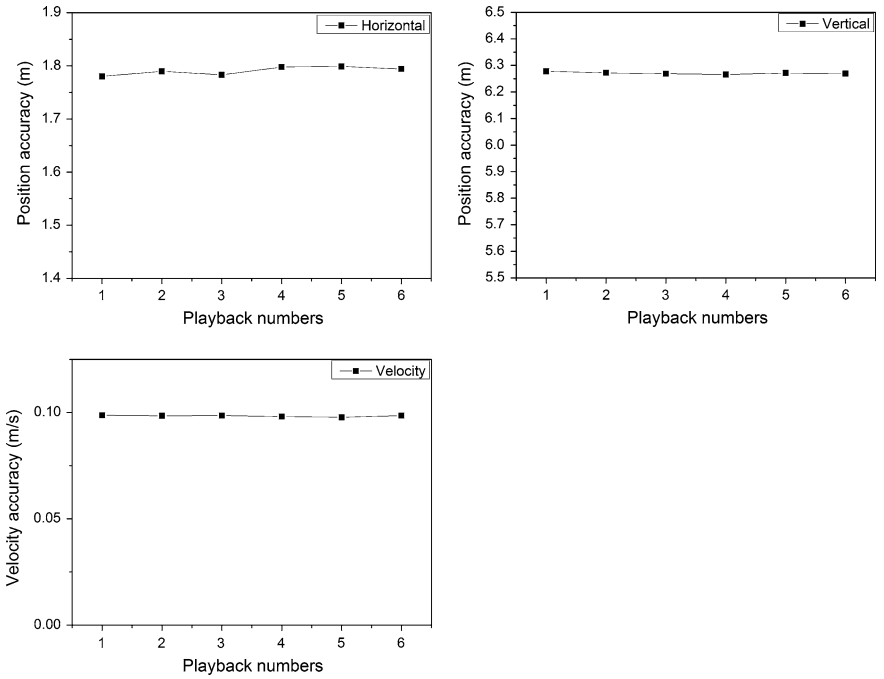

Fig. 4 Composition diagram of playback test results

Result error $\bar{x} - x_0 = (1.7907 - 2.1504)\,\mathrm{m} = -0.3597\,\mathrm{m}$
Vertical accuracy:
Repeatability $S_r(x) = 0.0041\,\mathrm{m}$
Result error $\bar{x} - x_0 = (6.2709 - 6.2081)\,\mathrm{m} = 0.0628\,\mathrm{m}$
Velocity accuracy:
Repeatability $S_r(x) = 0.0004\,\mathrm{m/s}$
Result error $\bar{x} - x_0 = (0.0984 - 0.0976)\,\mathrm{m/s} = 0.0008\,\mathrm{m/s}$

The main factors affecting the receiver's positioning accuracy are the number of visible satellites and the signal carrier-to-noise ratio. In the dynamic open scene, the number of available satellites and the carrier-to-noise ratio of the receiver in a playback signal and an actual signal test are analyzed, as shown in Figs. 6 and 7.

In the dynamic open scene due to the movement of the carrier and environmental changes, the multipath effect is unavoidable that the satellite navigation signal through the reflection or refraction of other objects to reach the receiver antenna. It has an impact on the pseudo-range and carrier phase with great chance. In addition, there is also signal diffraction that the linear distance between the satellite and the receiver antenna is obstructed by the obstacle to produce diffraction, and the diffraction signal arrives at the receiver antenna which also affects the code and phase measurement. It can be seen from Fig. 5. Vertical position error and velocity error curve coincidence is high, the actual and playback error results in a very small

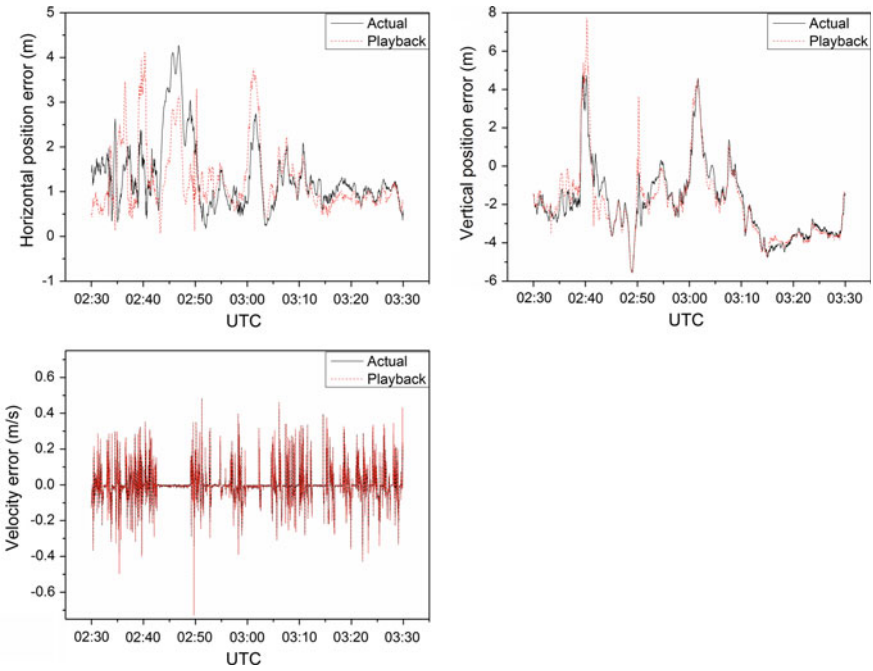

Fig. 5 Error contrast of position and velocity

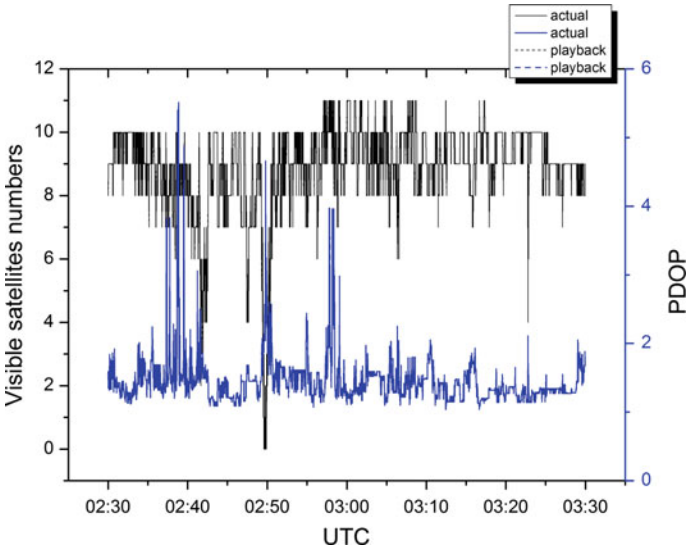

Fig. 6 Composition diagram of available satellite number and DOP

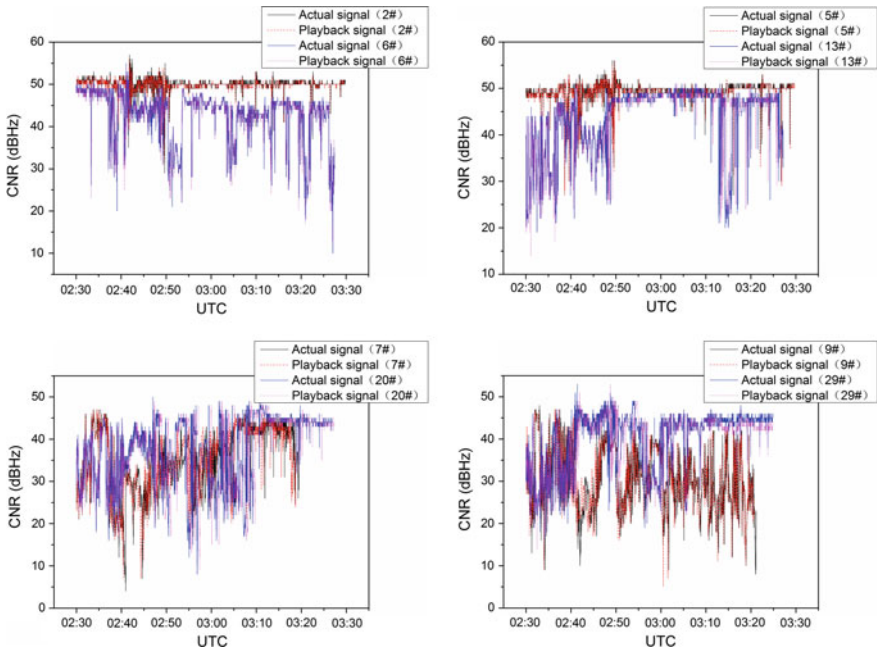

Fig. 7 Composition diagram of available satellite CNR

range. It can also been confirmed from the results of repeatability analysis. While the horizontal position error, in four different time periods there is a big shock. It may be due to the measured receiver itself caused by instability.

It can be seen from Figs. 6 and 7, the actual signal and the playback signal can be the same number of satellites, playback signal CNR of the actual signal to reduce the CNR of about 1–2 dB. Playback basically true reproduces the actual scene which is also confirmed from the test results analysis.

3.2 Stability

Stability refers to the degree of agreement between the measured results which are measured over the same measurement period (including the same observer, at the same location, using the same measurement procedure) over a defined period of time. Stability reflects the ability of the system characteristics to be constant over time.

In the specific implementation, we select a particular static or dynamic scene. Data are collected at different time intervals (1–2 days apart) (at least six times in the same scenario). Then we play back under the same laboratory conditions and the playback environment with the same test method. The calculation formula is as follows.

Table 4 Actual test results of open scene signal

Results	Test items		
Test numbers	Horizontal accuracy (m)	Vertical accuracy (m)	Velocity accuracy (m/s)
1	5.1715	5.9743	0.2554
2	3.909	5.5451	0.3401
3	4.9746	5.6607	0.2684
4	2.6474	3.091	0.1506
5	2.4838	2.9337	0.1393
6	3.439	3.2282	0.0894
Average $\bar{x}_0 = \frac{\sum_{i=1}^{n} x_i}{n}$	3.77088	4.4055	0.2072

Table 5 Record test results of open scene signal

Results	Test items		
Test numbers	Horizontal accuracy (m)	Vertical accuracy (m)	Velocity accuracy (m/s)
1	2.0432	3.2242	0.1191
2	2.0292	4.4042	0.3084
3	2.9331	4.1775	0.1967
4	2.2771	2.157	0.133
5	2.1043	2.6694	0.1335
6	1.0191	5.615	0.0881
Average $\bar{x}_0 = \frac{\sum_{i=1}^{n} x_i}{n}$	2.06767	3.70788	0.16313

$$S_m(x) = \bar{x}_m - \bar{x}_0 \tag{2}$$

where $\bar{x}_m$ represents the playback test results average; $\bar{x}_0$ represents the actual signal test result average.

In the open scene, we collect data six times at different time. The test results are shown in Tables 4 and 5.

Horizontal accuracy:
Stability $S_m(x) = \bar{x}_m - \bar{x}_0 = (2.06767 - 3.77088)\,\text{m} = -1.70321\,\text{m}$
Vertical accuracy:
Stability $S_m(x) = \bar{x}_m - \bar{x}_0 = (3.70788 - 4.4055)\,\text{m} = -0.69762\,\text{m}$
Velocity accuracy:
Stability $S_m(x) = \bar{x}_m - \bar{x}_0 = (0.16313 - 0.2072)\,\text{m/s} = -0.0441\,\text{m/s}$

In the stability analysis, the selected data is collected at different time intervals. As the constellation of different satellites in the navigation orbit by their respective movements at different times, the numbers of satellites at the same location are different and the spatial geometry of the layout is also different. It has a greater

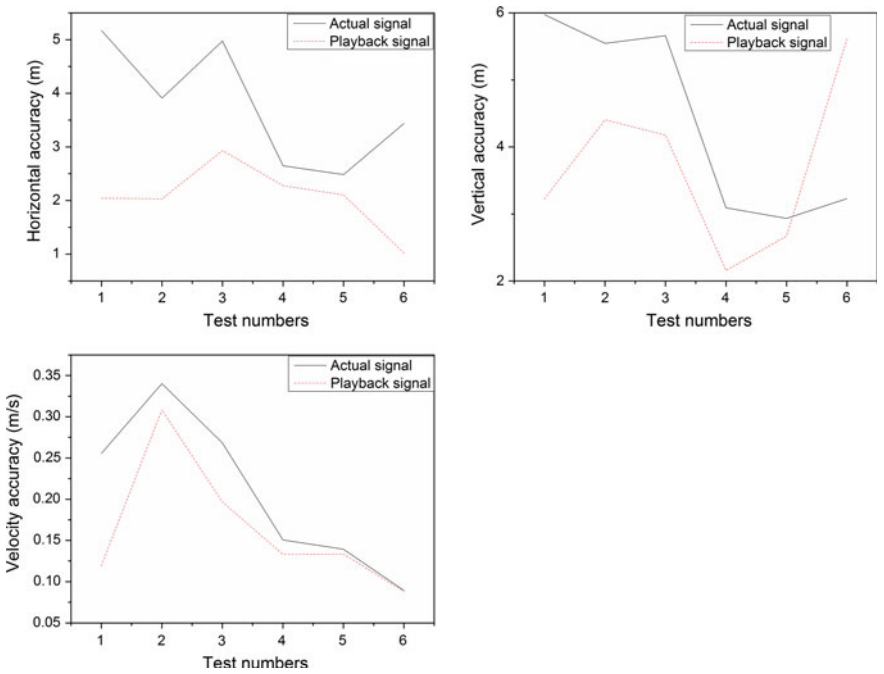

Fig. 8 Composition contrast diagram of test results

impact on the positioning performance. In addition, the weather conditions at different times are quite different; space environment error characteristics (including the ionosphere, the troposphere, etc.) are also different. These will have an impact on positioning. It can be seen from Fig. 8, the positioning accuracy is different at different time.

It can be seen from the above analysis of repeatability and stability that the playback signal test and the actual signal test results in the horizontal and vertical precision error is better than 0.5 m, the speed accuracy of the error is better than 0.1 m/s whether in a long or short time. The playback test results agree well with each other and the performance of the system is constant over time. Most of the selected time period the playback test and actual test results are within a very small error. It realizes the fidelity playback basically with the playback signal ensuring the actual constellation space configuration.

4 Summary

In this paper, It carried out the playback test based on the navigation signal record and playback instrument. The repeatability and stability of the playback system are analyzed from the perspective of the terminal receiver's test results. It uses the

concept of repeatability and stability in measurement. It only analyzes the open scene and can be transplanted to the diversity of other typical scenarios.

Through the preliminary verification and analysis, the record and playback technology is used to collect the navigation signals under certain typical scenes, and then it can be repeatedly played back under the laboratory conditions. It effectively reproduces the typical real scenes and realizes the high-fidelity playback.

5 Prospect

The depth and breadth of satellite navigation applications are greatly expanded with the Beidou satellite deployment gradually completed. The actual performance of the navigation terminal is closely related to the application scenario environment. At present, there are some problems in real signal testing, such as few samples, incomplete coverage and so on. Also there is still a lack of coverage of a wide range of navigation signal test data. It can be accumulated massive typical scene navigation data to facilitate the terminal test by using the navigation signal record and playback technology.

The construction of the standard public test data sets and sharing platform is the development trend of the current test field based on the typical scene data. It provides complete and efficient test conditions for navigation terminals in different industries by providing a unified standard scenario test data set to all developers worldwide. The navigation digital intermediate frequency signal is re-formed through the signal playback device to test the RF analog signal based on the test sharing platform. It will inevitably bring about signal distortion due to the mismatch of equipment, introduced during sample playback dual noise and other factors. So it's necessary to carry out playback of consistency verification to ensure the playback test and the real test results' consistent. It's the key of typical signal database data that can be applied to terminal test evaluation and popularization. Also it guarantees the accuracy of the test results. The proposed method in this paper can be used for this verification.

References

1. Wang T, Xia T, Zhang S (2015) Study on testing technology of navigation terminal. Metrol Meas Technol 35(4):6–9
2. Zhang Q (2012) Study on testing methods of Beidou-2 civil equipment. Odern Sci Technol Telecommun 15(3):78–80
3. JJF1033-2001, Rule for the examination of measurement standard

Multipath Effect Analysis of Beidou Satellite Pseudorange and Its Correction

Shengchao Wang, Xiaolin Jia, Guofeng Ji, Qingsong Ai, Meiqian Guan and Teng Peng

Abstract In this paper, we study the pseudorange multipath effect of Beidou satellite and analyze the correlation between multipath error and elevation angle of Beidou satellite. The method of quadratic polynomial fitting and wavelet transform are used to modify the pseudorange multipath. Experiments show that: Quadratic polynomial fitting method to correct the pseudorange multipath error, MP1, MP2 sequence standard deviation of a single satellite maximum reduction of 43.6 and 41.2%; Wavelet transform method to correct the pseudorange multipath error, MP1, MP2 sequence standard deviation of a single satellite maximum reduction of 57.3 and 57.9%.

Keywords Beidou navigation system · Multipath effect · Polynomial fitting · Wavelet transform

1 Introduction

China is building the Beidou navigation satellite system, since December 27, 2012, began to provide the Asia-Pacific region navigation, positioning and timing services. It currently consists of five geosynchronous orbit (GEO) satellites, five geosynchronous orbit (IGSO) satellites and five medium earth orbit (MEO) satellites [1, 2]. Beidou system broadcasts three frequencies of each satellite, including B1, B2 and B3 and three signal frequencies were 1561.098, 1207.140

S. Wang · G. Ji · Q. Ai · M. Guan · T. Peng
School of Geology Engineering and Surveying, Chang an University, No.126, Yanta Road, Xi an, Shanxi, China
e-mail: 364693662@qq.com

X. Jia (✉)
State Key Laboratory of Geo-Information Engineering, Xi'an, Shanxi, China
e-mail: 13891907401@139.com

X. Jia
Xi'an Research Institute of Surveying and Mapping, Xi'an, Shanxi, China

J. Sun et al. (eds.), *China Satellite Navigation Conference (CSNC) 2017 Proceedings: Volume I*, Lecture Notes in Electrical Engineering 437,
DOI 10.1007/978-981-10-4588-2_47

and 1268.520 MHz [3–6]. Multipath effect is an important source of error that affects GNSS applications. It is easy to be affected by the surrounding environment and can not be eliminated by differential modeling. In recent years, Beidou satellite multipath effect has been a hot research at home and abroad. In 2013, Nadarajah et al. first discovered the systematic deviation of the Beidou satellite, and made an in-depth study for it [7]. A recent study found that the Beidou MEO satellite and IGSO satellite, there is such a systematic error, but for the GPS, GLONASS and Galileo satellite does not exist [8]. Wang pointed out that the length of the orbital period of the GEO satellite and the length of the solar day are close, the systematic trend of GEO satellite multipath shows periodic repeats in units of days [9]. Wu et al. found that there are significant multipath effects in the pseudo range measurements of GEO and IGSO satellites and the method of using CNMC (Code Noise and Multipath Correction) to improve the pseudorange positioning accuracy is proposed [10]. Liu et al. [11] detailed comparative the study of GPS and Beidou satellite multipath effect. Zhao et al. [12] carried out a detailed study on the pseudorange multipath effect of the Beidou satellite and demonstrated that the systematic deviation of the Beidou satellite is independent of the station by using the single station difference, inter-satellite single difference and double difference analysis.

This paper analyzes the relationship between multipath effect of Beidou satellite pseudorange and elevation angle and signal to noise ratio, and the correlation between multipath error of MEO satellite and IGSO satellite and elevation angle is analyzed. The quadratic polynomial fitting method is adopted to correct the pseudorange multipath error of Beidou satellite. Since the quadratic polynomial fitting method can only correct the multipath error of MEO satellite and IGSO satellite, we use the wavelet transform method to correct the multipath errors of the three kinds of orbit satellites in the Beidou, so as to provide a better reference for Beidou satellite system.

2 Multipath Effect Analysis

Using the linear combination of carrier phase observations and pseudorange observations, the pseudorange multipath error can be derived as:

$$\mathrm{M}_{P_1} = P_1 - \frac{f_1^2 + f_2^2}{f_1^2 - f_2^2}\lambda_1\varphi_1 + \frac{2f_2^2}{f_1^2 - f_2^2}\lambda_2\varphi_2 + N_{P_1} \tag{1}$$

$$\mathrm{M}_{P_2} = P_2 - \frac{2f_1^2}{f_1^2 - f_2^2}\lambda_1\varphi_1 + \frac{f_1^2 + f_2^2}{f_1^2 - f_2^2}\lambda_2\varphi_2 + N_{P_2} \tag{2}$$

where M_{P_1} and M_{P_2} are multipath combination observations, P_1 and P_2 are pseudorange observations respectively, φ_1 and φ_2 are the carrier phase observations,

λ_1 and λ_2 are the wavelengths of the corresponding frequency of the carrier observation, f_1 and f_2 are the frequencies of the carrier phase observations, N_{P_1} and N_{P_2} are the sum of the constant part of the multipath effect and the carrier phase ambiguity parameter and the hardware delay. This combination eliminates the tropospheric delay,first order ionospheric delay term, the receiver clock and satellite clocks, and the distance term between the station and the satellite. In theory, the multipath error in the carrier phase observation does not exceed one-quarter of the carrier wavelength, much less than the multipath error in pseudo range measurement [13, 14]. At the same time, the carrier phase noise is far less than the noise of the pseudorange, so the impact of the carrier phase observations in the multipath effect can be ignored. N_{P_1} and N_{P_2} are a constant in the absence of cycle slips, N_{P_1} and N_{P_2} can be obtained by taking the mean value in a continuous arc segment, and then subtracted from the original combination to obtain the multipath effect error [15, 16].

2.1 *The Relationship Between Multipath Effect and Signal to Noise Ratio*

The signal to noise ratio of the observed satellites is the ratio of the signal power to the noise power, which can be used to evaluate the quality of the ranging signals and indirectly to reflect the accuracy of the carrier observations [2]. Figure 1 shows the relationship between the pseudorange multipath error and signal to noise ratio of GEO (C04), IGSO (C07) and MEO (C12) satellites with JFNG station sampling rate of 30 s on the 169th day in 2016. As can be seen from the figure, IGSO satellite with the signal to noise ratio decreases, multipath error range and the degree of variation becomes larger. With the increase of signal to noise ratio, the variation range and dispersion degree of the multipath error become smaller. And the multipath error fluctuation range is maximized when the signal to noise ratio is minimum. As for the MEO satellite of Beidou navigation system, the pseudorange multipath error presents a “V” shape, and as the signal to noise ratio increases, the pseudorange multipath error becomes smaller. As the signal to noise ratio decreases, the pseudorange multipath error becomes larger. For the GEO satellite,

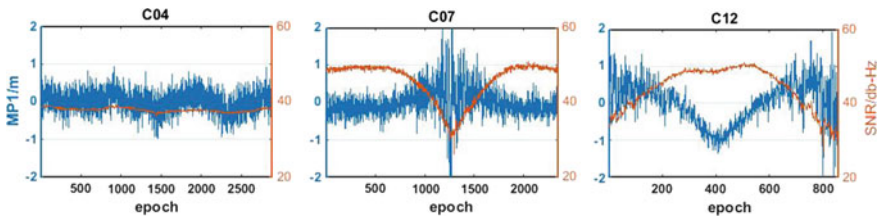

Fig. 1 The relationship between multipath error and signal to noise ratio

the signal to noise ratio exhibits a small change and the pseudorange multipath error exhibits a small fluctuation. Based on the analysis of other stations, it is found that the GEO satellite, IGSO satellite and MEO satellite pseudorange multipath error and signal to noise ratio show the above characteristics.

2.2 Relationship Between Multipath Error and Elevation Angle

In order to analyze the multipath error of Beidou satellite, the relationship between the multipath error and elevation angle of Beidou satellite is analyzed by using the above data. It can be seen from Fig. 2 that the multipath errors of MEO and IGSO satellites show certain correlation with the elevation angle: With the increase of elevation angle, the variation range and dispersion degree of pseudorange multipath error are obviously decreased, among which MEO satellite is the most obvious, followed by the IGSO satellite, and in low elevation angle, the multipath error of MEO satellite and IGSO satellite is larger. While the GEO satellites are located in a geostationary orbit with only a slow change in elevation [17]. As can be seen from the figure, GEO satellite multipath error with the change of the elevation angle, showing a certain cyclical changes.

2.3 Correlation Analysis of Multipath Error and Elevation Angle

Considering the relationship between the multipath error and elevation angle of Beidou MEO satellite and IGSO satellite, the Pearson correlation coefficient is used. For the validity of the data analysis results, we selected the four stations of BRUX, CUT0, FTNA, JFNG, 169 days to 186 days in 2016, the sampling interval is 30 s, for the same satellite to take its mean, as shown in Fig. 3. Among them, C13 satellite in October 2014 to stop the signal transmission. It can be seen from the figure that the multipath errors of the Beidou MEO satellite and the IGSO satellite

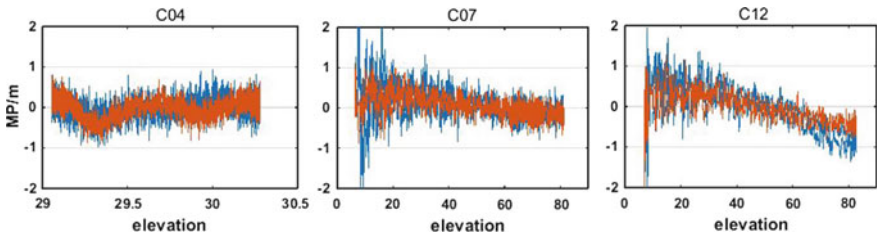

Fig. 2 The relationship between multipath error and elevation angle

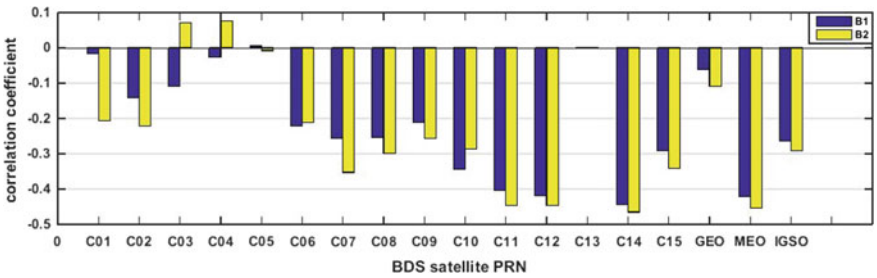

Fig. 3 Correlations of multipath errors with elevation angle

Table 1 Judgment criteria for correlation strength

Correlation coefficient (absolute value)	Relative intensity
0.8–1.0	Highly correlated
0.6–0.8	Strong correlation
0.4–0.6	Moderate correlation
0.2–0.4	Weak correlation

Coefficient range: −1 to 1 (A negative value indicates a negative correlation and a positive value indicates a positive correlation)

are negatively correlated with the elevation angle. Meanwhile, the correlation coefficient of MEO satellite multipath error with the elevation angle is larger than IGSO satellite. However, the correlation coefficient of GEO satellite multipath error with elevation angle has positive and negative values, and the correlation does not have a certain law. In general, the relative strength of the variables is determined by the values shown in Table 1 [18].

It is found that the average of the correlation coefficients of the multipath error with the elevation angle for all MEO satellites B1 and B2 at the four stations are −0.42 and −0.45 respectively. The mean values of the correlation coefficients of the multipath error with the elevation angle for IGSO satellites B1 and B2 at the four stations are −0.26 and −0.29, respectively. According to the criterion of Table 1, we can see that the multipath error of MEO satellite is highly correlated with the elevation angle, and the IGSO satellite has weak correlation.

3 Polynomial Fitting Method to Correct Multipath Error

3.1 Model Building

In view of the relationship between the multipath error and elevation angle of the Beidou MEO satellite and IGSO satellite, Wanninger proposed a piecewise linear

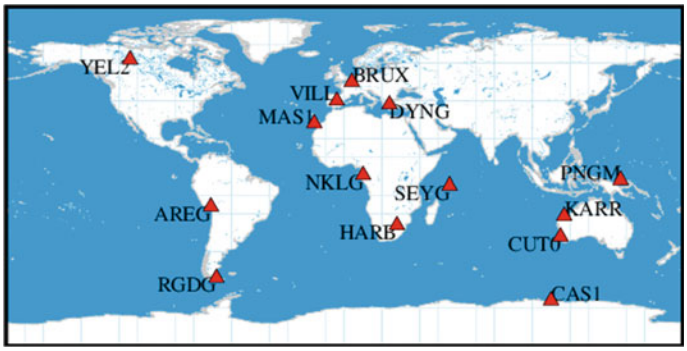

Fig. 4 Distribution of stations

Table 2 Quadratic polynomial equations

	Frequency	Quadratic polynomial equation
MEO	B1	$\mathcal{Y} = -0.0002473361\mathcal{X}^2 + 0.0070839932\mathcal{X} + 0.1583717072$
	B2	$\mathcal{Y} = -0.0001464664\mathcal{X}^2 + 0.0028278185\mathcal{X} + 0.1413055391$
IGSO	B1	$\mathcal{Y} = -0.0000365170\mathcal{X}^2 - 0.0029295726\mathcal{X} + 0.2007500572$
	B2	$\mathcal{Y} = -0.0000785455\mathcal{X}^2 + 0.0020413261\mathcal{X} + 0.0896812078$

interpolation method to correct pseudorange multipath errors. However, from the above analysis, we can see that the multipath error of Beidou satellite is not completely consistent with the elevation angle, so this paper uses quadratic polynomial fitting to correct the multipath error. The experimental data are from the 254th to the 284th days in 2016, 14 MGEX stations, sampling interval of 30 s, the station distribution shown in Fig. 4.

The quadratic polynomial coefficients are obtained by quadratic polynomial fitting of the corresponding multipath errors with the elevation angle of each satellite, and the quadratic polynomial coefficients of the MEO satellite and IGSO satellite are obtained by the mean values of the coefficients of the same satellite, The quadratic polynomial equation is given in Table 2. Figure 5 shows the trend of the MEO satellite and IGSO satellite multipath error correction values derived from the above 14 stations.

3.2 Experiment and Analysis

We use the data for 172 days in 2016, JFNG station, the sampling interval is 30 s. Figure 6 shows the comparison of the multipath errors of MEO (C11) and IGSO (C15) satellites before and after the model correction. As can be seen from the figure, the MEO satellite multipath error "V" trend term has been largely eliminated

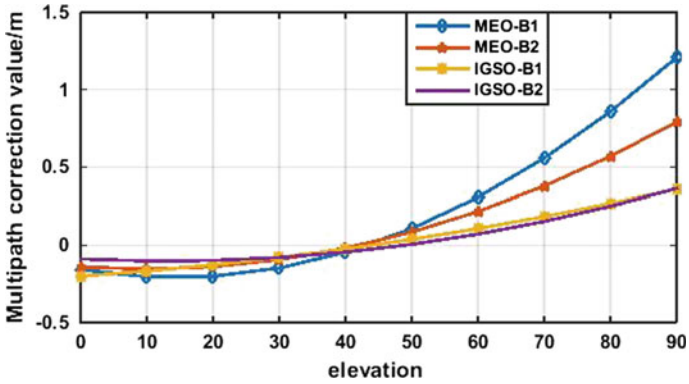

Fig. 5 Correction values of multipath error

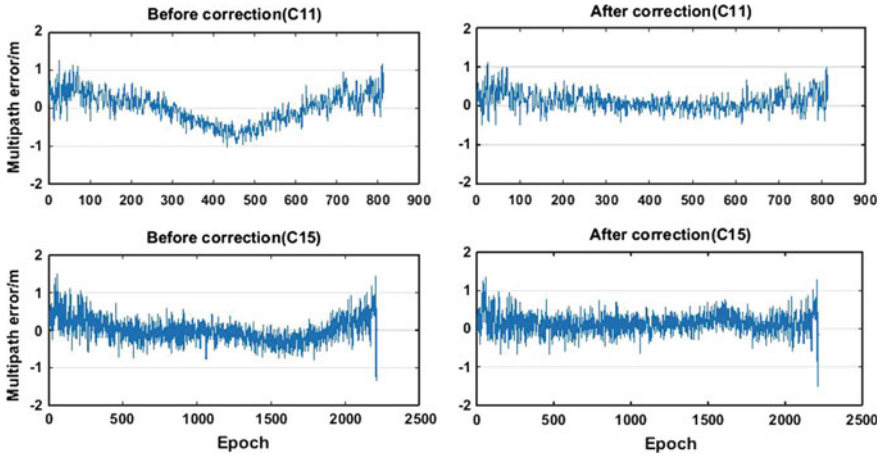

Fig. 6 Error correction of multipath by the quadratic polynomials

after model correction. The multipath error of the IGSO satellite has also been greatly improved.

The standard deviations of the multipath errors of MPI and MP2 sequences of the Beidou MEO (C11) and IGSO (C15) satellites before and after the quadratic polynomial model correction are shown in Fig. 7, respectively. It can be seen from the figure that the standard deviation of the MP1 and MP2 sequences of the MEO (C11) satellites are reduced by 38.6 and 41.2%, while the IGSO (C15) satellites are reduced by 10.9 and 22.5%, respectively. From the analysis results, it can be seen that the quadratic polynomial correction model has a good correction effect on Beidou satellite multipath error sequence.

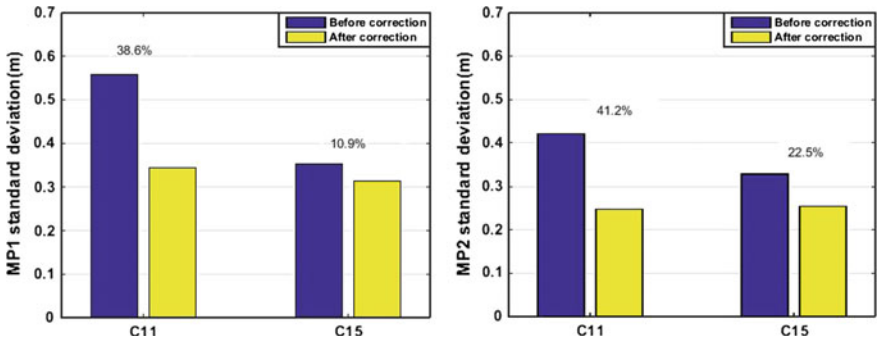

Fig. 7 Standard deviation of multipath error sequence

4 Wavelet Transform to Correct Multipath Error

The quadratic polynomial model can be used to correct the multipath errors of the Beidou MEO satellite and the IGSO satellite. However, the Beidou GEO satellite can not establish the model for effective correction. Therefore, this paper chooses the wavelet transform method to carry on the correct analysis to the multipath error of the three kinds of orbit satellites.

4.1 Fundamentals

The wavelet transform is the development of Fourier transform, it is a mathematical analysis method developed in recent years, which is has been widely used in the signal extraction and noise reduction [19]. The main steps of wavelet transform for noise reduction are as follows:

(1) Wavelet decomposition: under certain base wavelet and decomposition level, the wavelet decomposition of the signal with noise is carried out, and the corresponding wavelet decomposition coefficient is obtained.
(2) Threshold processing: there are 2 kinds of threshold processing methods for the wavelet coefficients of the high frequency part.
The first is the hard threshold: the wavelet coefficients whose absolute value is less than the given threshold is set to 0, while the absolute value of the wavelet coefficient is greater than the threshold value remain unchanged:

$$\omega_\lambda = \begin{cases} \omega, & |\omega| \geq \lambda; \\ 0, & |\omega| < \lambda. \end{cases} \tag{3}$$

The second is the soft threshold: the wavelet coefficient whose absolute value is smaller than a given threshold is set to 0 and a wavelet coefficient whose

absolute value is greater than the threshold value is subtracted from the threshold value:

$$\omega_\lambda = \begin{cases} sign(\omega)(|\omega| - \lambda), & |\omega| \geq \lambda; \\ 0, & |\omega|\lambda. \end{cases} \tag{4}$$

where ω is the wavelet coefficient, ω_λ is the wavelet coefficients after the action threshold, and λ is the threshold value.

(3) Wavelet reconstruction: the reconstructed wavelet coefficients after the threshold processing are used to get the denoised signal.

4.2 Experiment and Analysis

The multipath error of Beidou satellite includes random error and systematic error, in which the systematic deviation can be eliminated by the above process. In this experiment, the observation data of SEYG station at 254 days in 2016 are adopted, and the interval is 30 s. Using sym5 wavelet basis function, the decomposition layer is 2 layers. In the threshold processing, the hard threshold method is superior in the sense of mean square error, but the hard threshold function has a breakpoint at the threshold, the estimated signal will produce additional oscillations and will not have the same smoothness as the original signal so that the results are relatively rough. The soft threshold method does not generate the oscillation, the result is smoother. So we choose the soft threshold method.

Figure 8 shows the multipath error of the C03 satellite after wavelet decomposition, where s is the original signal sequence, a2 is the low frequency part of the

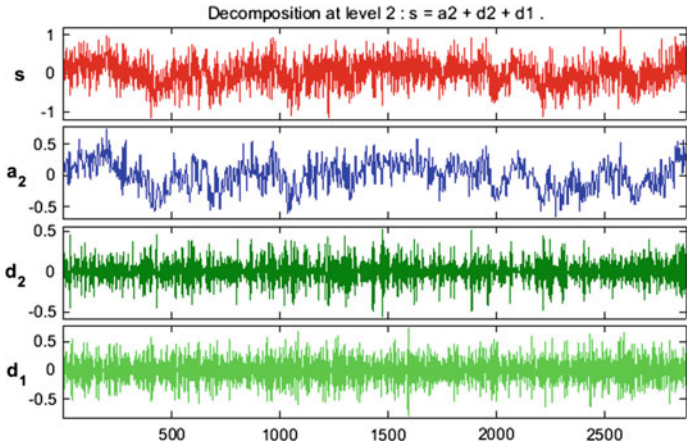

Fig. 8 Decompose multipath errors by wavelet transform

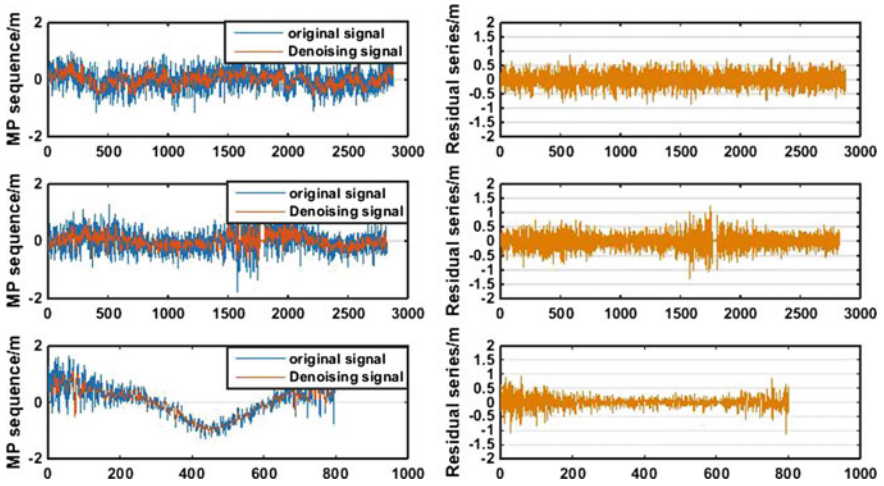

Fig. 9 Wavelet transform to correct multipath error

second layer, d1 and d2 are the high frequency components after wavelet decomposition. Only the low frequency part of each layer for further decomposition, and high frequency part is not considered [20]. Since the wavelet transform is a linear transformation, the original signal after wavelet decomposition can be expressed as s = a2 + d2 + d1.

The multipath error sequence of Beidou GEO satellite (C03), IGSO satellite (C09) and MEO satellite (C14) before and after wavelet transform is shown in Fig. 9. It can be seen that the multipath error is eliminated by the wavelet transform for Beidou satellite GEO satellite, IGSO satellite and MEO satellite, and the residual sequence of the noise is less than 0.5 m. Figure 10 shows the standard deviation of the MP1 and MP2 sequence of the three satellites before and after correction by wavelet transform. From the figure, it can be seen that after the wavelet transform processing, the MP1 sequence, the GEO satellite is reduced by 24.6%, the IGSO satellite is reduced by 25.3%, and the MEO satellite is reduced by 54.1%. The MP2 sequences, GEO satellites decreased by 32.7%, IGSO satellites decreased by 30.0%, MEO satellites decreased by 56.6%.

In order to carry out the comparative analysis of the above two methods, this paper uses the data of five stations 169th days in 2016, respectively, using the above two methods for Beidou MEO satellite and IGSO satellite pseudorange multipath error correction analysis, calculated standard deviation before and after correction of MP1 and MP2 sequence. Finally, the average deviation of the standard deviation before and after correction was analyzed, the statistical results shown in Fig. 11. It should be noted that B, C, F, J and S represent the BRUX station, the CUT0 station, the FTNA station, the JFNG station and the SEYG station respectively used in this experiment, and M represents Beidou MEO satellite, I represents the Beidou IGSO satellite. From the five station statistics, it is found that quadratic polynomial fitting

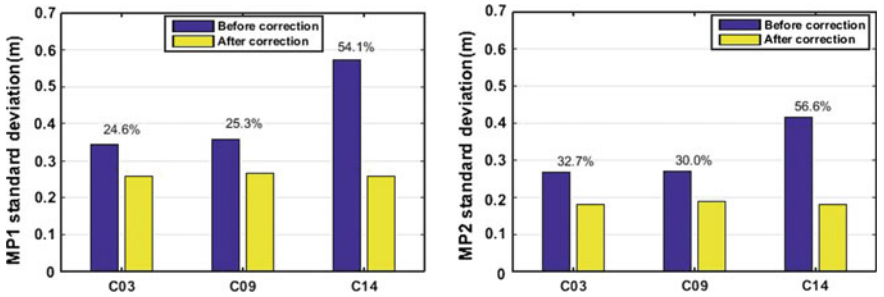

Fig. 10 Standard deviation of multipath error sequence

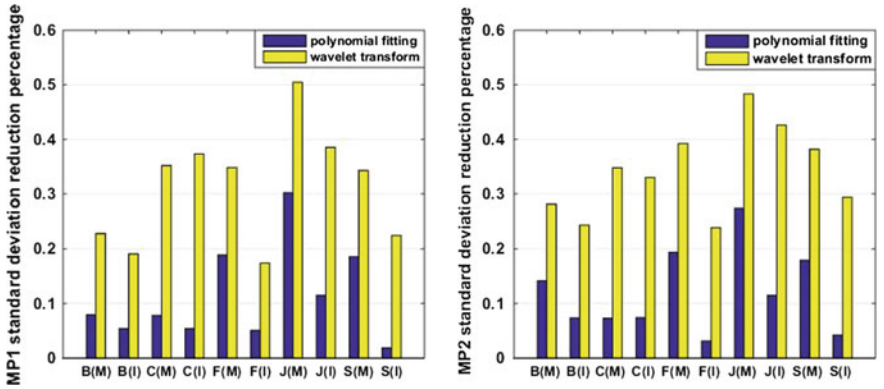

Fig. 11 Comparison of the quadratic polynomial fitting and wavelet transform

method to correct pseudorange multipath error, MP1 sequence standard deviation of a single satellite maximum reduction of 43.6%; MP2 sequence standard deviation of a single satellite maximum reduction of 41.2%. Correction of pseudorange multipath errors using wavelet transform the maximum reduction standard deviation of MP1 sequence is 57.3% for single satellite and 57.9% for single satellite with MP2 sequence standard deviation. According to Fig. 11, it is clear that the effect of multipath error correction by wavelet transform is better than that of quadratic polynomial fitting to correct multipath error.

5 Conclusion

This paper analyzes the relationship between multipath effect of Beidou satellite pseudorange and elevation angle and signal to noise ratio. Based on the correlation analysis between Beidou's elevation and multipath errors, the quadratic polynomial

fitting method is adopted to correct the multipath error for Beidou MEO satellite and IGSO satellite. In view of the quadratic polynomial fitting method can not effectively correct the Beidou GEO satellite, this paper uses wavelet transform to correct the Beidou three orbital satellite pseudorange multipath errors. The following conclusions can be drawn from the analysis:

(1) With the decrease of signal to noise ratio, the range and dispersion of the pseudorange multipath error of the Beidou IGSO satellite and MEO satellite become larger. With the increase of signal to noise ratio, the variation range and dispersion degree of the pseudorange multipath error become smaller. For the GEO satellite, the signal to noise ratio shows a slight change, and the pseudorange multipath error is also a small fluctuations.
(2) For the Beidou IGSO satellite and MEO satellite, with the increase of elevation angle, the pseudorange multipath error range and degree of dispersion were obviously decreased, the MEO satellite is the most obvious, followed by the IGSO satellite, and in low elevation angle, MEO satellite and IGSO satellite pseudorange multipath error range is larger. With the change of elevation angle, the multipath error of GEO satellite pseudorange shows a certain periodic variation.
(3) The correlation analysis shows that the multipath error of the Beidou MEO satellite is moderately correlated with the elevation angle, while the IGSO satellite is weakly correlated.
(4) Experiments show that polynomial fitting method and wavelet transform method have a good correction effect on Beidou satellite pseudorange multipath error sequence, in which wavelet transform method is more effective than Polynomial fitting method for Beidou satellite pseudorange multipath error. But the wavelet transform method can not forecast and correct multipath error, and polynomial fitting method can be.

Acknowledgements The authors would like to thanks iGMAS for their data support. This study is supported by the foundation of natural science of china (Grant No. 41604024).

References

1. Yang W, Tong H, Pan L et al (2016) Analysis and correction of BDS code multipath bias. In: China satellite navigation conference (CSNC) 2016 proceedings, vol III
2. Wang G, Zhao Q, Dai Z et al (2016) Characteristics analysis of BDS observations based on CMONOC data. Sci Surv Mapp 41(1):33–38
3. Shi C, Zhao Q, Hu Z et al (2013) Precise relative positioning using real tracking data from COMPASS GEO and IGSO satellites. GPS Solut 17(1):103–119
4. Han C, Yang Y, Cai Z (2011) Beidou navigation satellite system and its time scales. Metrologia 48(4):S213–S218(6)
5. Yang Y (2010) Progress, contribution and challenges of compass/Beidou satellite navigation system. Sci Surv Mapp 39(1):1–6

6. Dang Y, Mi J, Cheng Y (2007) Principles and applications of global navigation satellite system. Surveying and Mapping Publishing House
7. Nandakumaran N, Teunissen PJG, Noor R (2013) Beidou inter-satellite-type bias evaluation and calibration for mixed receiver attitude determination. Sensors 13(7):9435–9463
8. Wanninger L, Beer S (2015) BeiDou satellite-induced code pseudorange variations: diagnosis and therapy. GPS Solut 19(4):639–648
9. Wang M, Chai HZ, Liu M, Chen YL, Liu J (2016) A method of BDS relative positioning over long baseline considering the influence of multipath effect from GEO satellite. J Zhengzhou Inst Surv Mapp 33(2):1673–6338
10. Wu XL, Zhou JH, Gang W (2012) Multipath error detection and correction for GEO/IGSO satellites. Sci China Phys Mech Astron 55(7):1297–1306
11. Liu L, Feng H, Chen W et al (2016) Study of the comparison on GPS and BDS multipath effects. Urban Geotech Invest Surv 1:5–10
12. Zhao Q, Wang G, Liu Z et al (2015) Analysis of BeiDou satellite measurements with code multipath and geometry-free ionosphere-free combinations. Sensors 16(1)
13. Wang G, Jong KD, Zhao Q et al (2015) Multipath analysis of code measurements for BeiDou geostationary satellites. GPS Solut 19(1):129–139
14. Lambert W, Manja M (2001) Carrier phase multipath calibration of GPS reference stations. Navigation 48(2):112–124
15. Zhang XH, Ding LL (2013) Quality analysis of the second generation compass observables and stochastic model refining. Geomat Inf Sci Wuhan Univ 38(7):832–836
16. Guo F, Li X, Liu W (2016) Mitigating BeiDou satellite-induced code bias: taking into account the stochastic model of corrections. Sensors 16(6)
17. Zhang X, He X, Liu W (2016) Characteristics of systematic errors in the BDS Hatch–Melbourne–Wübbena combination and its influence on wide-lane ambiguity resolution. GPS Solut 1–13
18. Wang J, Wu X, Wang A (2014) The application of pearson correlation coefficient algorithm in searching for the users with abnormal watt-hour meters. Power Demand Side Manag 2:52–54
19. Xia L (2001) Theoretical study and numerical results of multipath effects in GPS observations. Wuhan University
20. Zhong P, Ding XL, Zheng DW et al (2008) Adaptive wavelet transform based on cross-validation method and its application to GPS multipath mitigation. GPS Solut 12(2):109–117

The Research on Time Series Modeling of ARMA and Medium/Long-Term Forecasting Method Using Global Ionospheric Harmonic Coefficient

Xiude Chen, Xiaolin Jia, Yongxing Zhu, Na Cheng, Shengyang Gao and Meiqian Guan

Abstract Regarding the ionospheric harmonic coefficients as the object to research, choosing the Box-Jenkins's method to order the auto-regressive moving average(ARMA) model to carry out ionospheric spherical harmonic coefficients modeling and medium/long-term (15 days or longer) forecasting [1, 2]. Because the ionospheric activity is affected by solar radiation, geomagnetic field and so on, it has a great relationship with the latitude. Therefore, this paper statistics forecast results of different zones of latitudes, also independently statistics the forecast results of region in China, and fully verifies the feasibility and validity of the model. The results shows the forecasting accuracy in the northern hemisphere is slightly better than that in the southern hemisphere; the forecasting precision is stable in the next 30 days, and 90% of root mean square (RMS) of forecasting results can reach 6 TECU; in the high latitudes, 90% of RMS of forecasting results can reach 3.5 TECU in the next 40 days; in China, 80% of RMS of forecasting results can reach 5 TECU in the next 40 days.

Keywords ARMA · Ionospheric spherical harmonic coefficients · Vertical total electron content · Modeling and forecasting

X. Chen (✉) · S. Gao · M. Guan
College of Geology Engineering and Geomantic, Chang'an University, Xi'an 710054, Shanxi, China
e-mail: 1425236262@qq.com

X. Jia (✉) · Y. Zhu
State Key Laboratory of Geo-information Engineering, Xi'an 710054, Shanxi, China
e-mail: 13891907401@139.com

X. Jia · Y. Zhu
Xi'an Research Institute of Surveying and Mapping, Xi'an 710054, Shanxi, China

N. Cheng
Shanghai Astronomical Observatory, Shanghai 200030, China

J. Sun et al. (eds.), *China Satellite Navigation Conference (CSNC) 2017 Proceedings: Volume I*, Lecture Notes in Electrical Engineering 437,
DOI 10.1007/978-981-10-4588-2_48

1 Introduction

Ionospheric activity will be affected by the solar radiation, geomagnetic field and other effects, so it brings great error to the satellite navigation applications. When GNSS signals through the ionosphere, the signal strength, frequency, polarization, phase and delay will be affected, these effects on satellite positioning, navigation, speed, timing and other applications will make effect [3]. The distance error caused by the ionosphere will be up to 15 m in the general day, up to 3 m at night, is currently the largest satellite navigation and positioning error. Therefore, the research on the forecasting work of ionospheric information is critical to GNSS navigation applications and the monitoring of the entire space environment.

At present, the forecasting methods of ionospheric information mainly include two categories, one is the traditional forecasting model based on mathematical methods and long-term observation data. Including the traditional empirical model and non-empirical model, the typical empirical model, Such as Klobuchar model, IRI model and so on; the non-empirical model, such as triangular series, polynomial, spherical harmonic function model and so on. The other one is the modern forecasting models, such as Ionospheric Computerized Tomography model, neural network model, grid model, time series model. The neural network model is used to predict the ionospheric information from 1 to 24 h in [4]. The ARMA model is used to predict the final ionospheric grid points of Center for Orbit Determination in Europe (CODE) with the resolution of 2.5 × 5 in [5, 6]. The ARMA model was used to predict the ionospheric information in the Antarctic area in [7]. The ARMA model is used to predict the ionospheric information and the characteristics of the forecasting result of the model was analyzed in [8]. The Auto-regressive (AR) model was used to modeling and the short-term ionospheric information forecast was carried out in [9]. The regional ionospheric modeling and the grid point prediction were carried out in [10]. The traditional forecast model is mainly used for short-term forecast of ionospheric information (usually within three days). At present, the ionospheric spherical harmonic modeling method was used to deal with the final ionospheric information adopted by the most ionospheric agency [11–13], this method is very popular for wide use (in both global and regional applications), and high-precision characteristics.

Considering the high accuracy of the ARMA time series model, in this paper, we used ARMA time series model to modeling and forecast the ionospheric information of medium and long-term. In addition, in order to statistic the forecasting results conveniently, we transform the forecast results into grids and statistic them in southern hemisphere region and northern hemisphere region.

2 ARMA Modeling and Forecasting

Based on the ionospheric information extracted from the observational data, we can modeling the ionospheric harmonic function [13], then, according to the least squares principle, estimate the spherical harmonic coefficients, and finally, obtain the ionospheric VTEC information. The mathematical expression of the spherical harmonic function is as follows:

$$VTEC(\varepsilon, \lambda) = \sum_{n=0}^{n_{\max}} \sum_{m=0}^{n} \tilde{P}_{nm}(\sin \varepsilon)(\tilde{C}_{nm} \cos(m\lambda) + \tilde{S}_{nm} \sin(m\lambda)) \quad (1)$$

In the formula, $VTEC(\varepsilon, \lambda)$ can be obtained from observational data of stations. ε is the geomagnetic latitude at Intersect Pierce Point (IPP). λ is the local time angle of sun-geomagnetic reference frame at IPP. $n_{\max}$ is the maximum order of spherical harmonic expansion (the maximum order of CODE is 15). $\tilde{P}_{nm}$ is the regularized Legendre function. $\tilde{C}_{nm}, \tilde{S}_{nm}$ is the spherical harmonics to be estimated.

Therefore, if we obtain the forecasting spherical harmonic coefficient in the next time (such as the ARMA modeling and forecasting method below), according to formula 1, we can calculate the VTEC information at IPP in the next time, finally get the forecasting ionosphere VTEC information.

2.1 Modeling Method of ARMA

The definition of ARMA is as follows [14],

$$x_t - \varphi_1 x_{t-1} - \varphi_2 x_{t-2} - \cdots - \varphi_p x_{t-p} = a_t - \theta_1 a_{t-1} - \theta_2 a_{t-2} - \cdots - \theta_q a_{t-q} \quad (2)$$

In the formula, p, q are the orders of the auto-regressive part and the moving average part. $\varphi_i(1, 2, \ldots p)$ and $\theta_i(1, 2, \ldots q)$ are the coefficients of the auto-regressive part and the moving average part. In addition, the time series should be stationary sequence when modeling ARMA. But in actual measurement, the time series often contain some non-stationary trend term and periodic term, and we usually use difference method to stable the time series. According to the characteristics and physical background of the spherical harmonic coefficients, we need not differing the time series of ionospheric spherical harmonic coefficients in this paper [8].

When the data is sufficient, there are no significant difference between two ordered method of Box-Jenkins and Pandit-Wu of modeling ARMA. In this paper, the time series of ionospheric spherical harmonic coefficients is relatively complete, so the ordered method of Box-Jenkins is only adopted.

The main steps of modeling ARMA time series based on spherical harmonic coefficients is as follows,

1. Data pre-processing. Firstly, the adjacent epoch values is differentiated, then the 1.3 times mode is regard as the basis for judging whether the data is missing or not, lastly the missing data is added used by interpolating of cubic equation and we can get the new time series.
2. Model identification. The truncation and trailing properties of the auto-correlation function and the partial correlation function of model are used to judge whether the model is an ARMA time series model or not.
3. The AIC minimum information criterion is used to determine the order of the model, find the most suitable p and q, and determine the auto-regressive and moving average coefficient using nonlinear least squares to estimate the parameters.
4. The adaptability test of the model. That is to test whether the remaining residual is white noise time series not.

2.2 The Forecasting Method of ARMA

In practice, the main purpose of modeling and analysis of time series is to forecast time series in the next time after determining the model of time series. The forecasting formula of ARMA model [14] is as follows,

$$\begin{aligned} x_{k+l} = \varphi_1 x_{k+l-1} + \varphi_2 x_{k+l-2} + \cdots + \varphi_p x_{k+l-p} + a_{k+l} \\ -\theta_1 a_{k+l-1} - \theta_2 a_{k+l-2} - \cdots - \theta_q a_{k+l-q} \end{aligned} \tag{3}$$

In the formula, use the data before the time of k to forecast l step, and the forecasting result is $\hat{x}_k(l)$, the true value is x_{k+l}, the forecasting errors are as follows,

$$\varepsilon(l) = x_{k+l} - \hat{x}_k(l) \tag{4}$$

In this paper, the linear minimum variance principle is used to determine the coefficients in Eq. (3), that is the variance of error is minimized. The formula is as follows,

$$D(\varepsilon_k(l)) = E[x_{k+l} - \hat{x}_k(l)]^2 = \min \tag{5}$$

2.3 The Statistical Methods of Forecasting Results

In order to test the accuracy of the prediction of the ionospheric spherical harmonic coefficients, we firstly bring the forecasting ionospheric spherical harmonic coefficients into the Eq. (1), and then calculate the global forecasting ionospheric grid,

such as xrig0200.16i. Lastly, compare the forecasting ionospheric grid results with the final ionospheric grid of CODE, such as codg0200.16i, and use the residual and RMS indicators to analysis the result. The residuals are calculated as follows,

$$V = VTEC_{xrig} - VTEC_{\text{codg}} \tag{6}$$

The RMS is calculated as follows,

$$RMS = \sqrt{V^T V/n} \tag{7}$$

In the formula, n is the amount of corresponding grid points.

In addition, there is a great relationship between forecasting ionospheric result and latitude, so we statistic the results according to different hemispheres and latitudes.

3 Examples of Analysis

In this paper, the ionospheric spherical harmonic coefficients of CODE center in the whole 2015 was used to be the original input time series. There are 25 sets of coefficients every day, and each coefficient is 15 × 15 order spherical harmonic coefficients, as follows (0, 0), (1, 0), (1, −1) … (15, −15). There are 25 × 256 coefficients. Here, we extract from the 25 sets of coefficients per day, according to a group per 2 h. There are 256 values per a group. Then we will carry out ARMA modeling and forecasting to the 256 values and the length of each value of 256 values is 12 × 365.

Using the method of 2.1 and 2.2, we carried out the ARMA modeling and forecasting to the 256 time series of ionospheric spherical harmonics coefficients respectively with the coefficients of the whole 2015. Then we forecast the spherical harmonic coefficients from January to March in 2016. The results of modeling and fitting of partial coefficients are shown in Sect. 3.1. In addition, we statistic the accuracy of the forecasting grid formed by the prediction coefficients according to latitudes and the northern and southern hemispheres, as shown in Sect. 3.2.

3.1 Modeling and Fitting Statistics

Considering the length of the article, p and q orders of ARMA for only some parameters are listed, as shown in the following Table 1.

The red data is the original data series, and blue is the fitting result sequence of ARMA model, and the green is the residual sequence from Figs. 1, 2, 3, 4, 5 and 6. Taking into account the length of the article, here, we only lists the first six

Table 1 The order of the model of partial coefficients

Coefficient	p	q
(0, 0)	14	15
(1, 0)	13	15
(1, 1)	11	14
(1, −1)	11	15
(2, 0)	13	15
(1, 2)	14	13
…	…	…

coefficients of the fitting results. The x-axis is the time series, and the length is 4380. The y-axis is the coefficient value of the corresponding order, and the unit is TECU.

Figures 1, 2, 3, 4, 5 and 6 are the spherical harmonic coefficient of the previously mentioned six coefficients modeled and fit. We can see that the fitting sequence is in good agreement with the original sequence. From the residuals, the fitting residuals belong to the white noise sequence. And the range of variation is within the range of 2TECU of 95%, and the partial coefficient is within 1TECU.

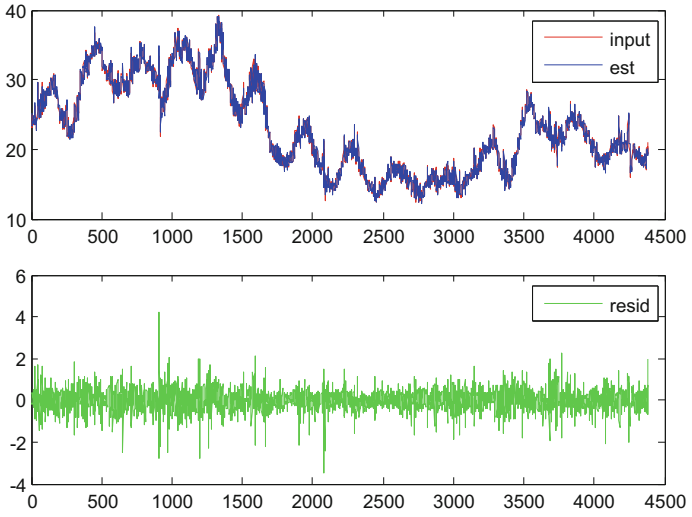

Fig. 1 Modeling fitting graphs of coefficients (0, 0)

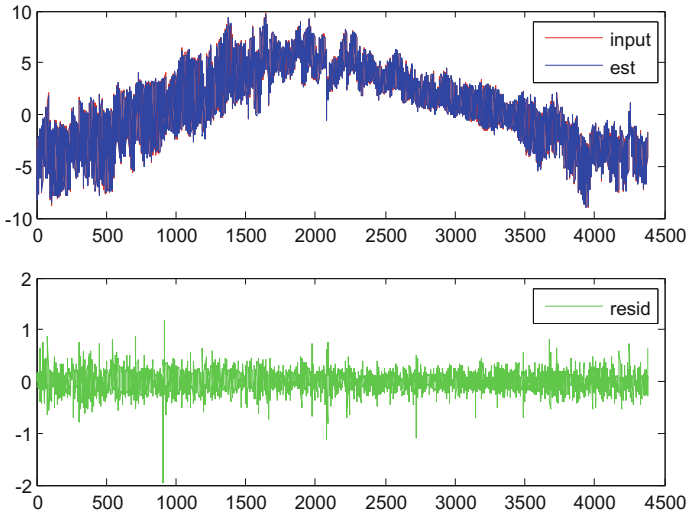

Fig. 2 Modeling fitting graphs of coefficients (1, 0)

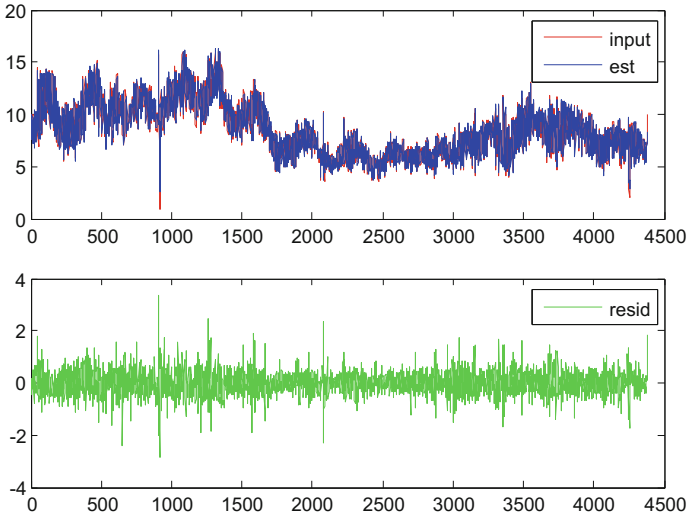

Fig. 3 Modeling fitting graphs of coefficients (1, 1)

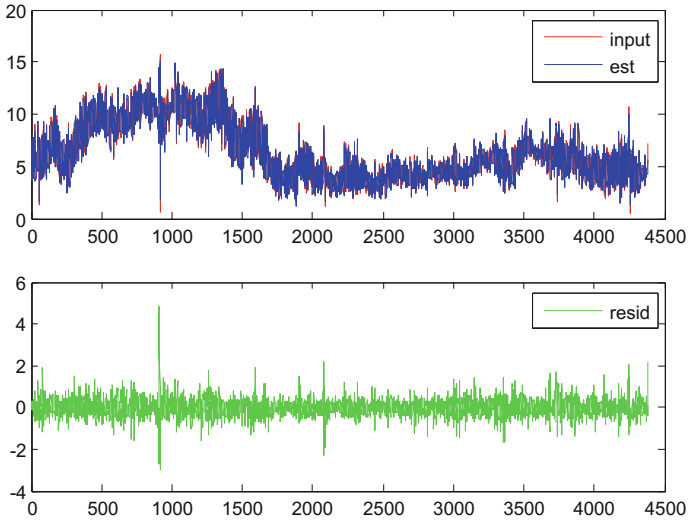

Fig. 4 Modeling fitting graphs of coefficients (1, −1)

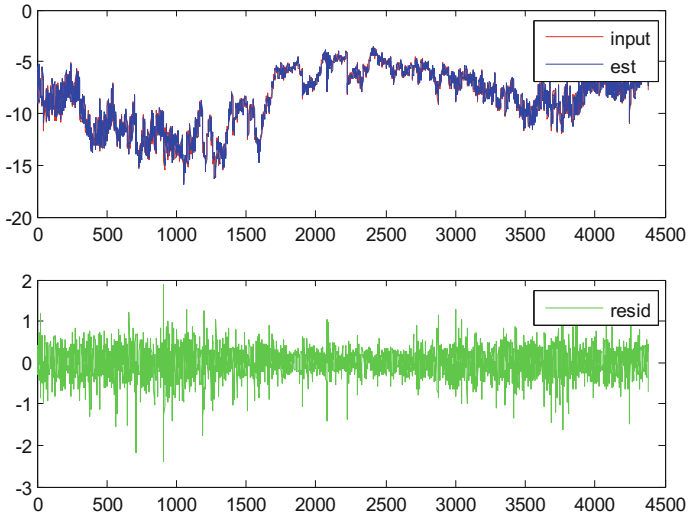

Fig. 5 Modeling fitting graphs of coefficients (2, 0)

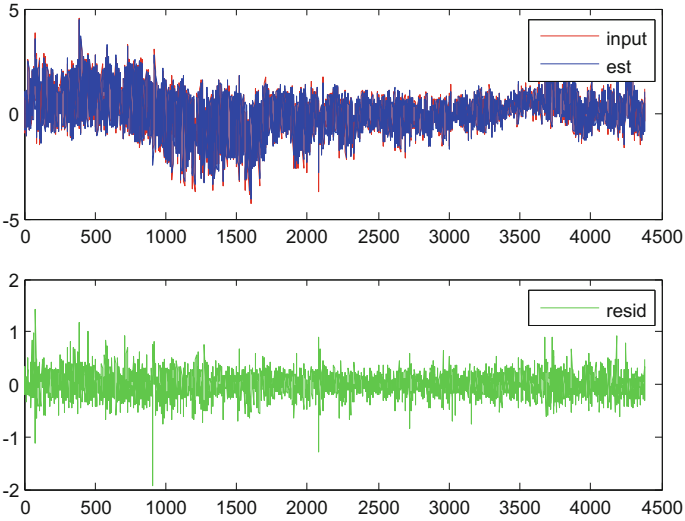

Fig. 6 Modeling fitting graphs of coefficients (2, 1)

3.2 Statistic Forecasting Results

We use the model of ARMA obtained from Sect. 3.1 to forecast the ionospheric spherical harmonic coefficients in the next 3 months (from January to March in 2016). Then we form the grids (from 180°W to 180°E and from 87.5°S to 87.5°N). And the resolution is 5 × 2.5. According to the statistical method in Sect. 2.3, comparing the forecasting ionospheric grids with the final ionospheric grids of CODE, we statistic and analysis the accuracy of forecasting ionospheric information. In order to make full use of the results of the forecast, we use two ways to statistic the forecasting result. One is to statistic the clock 0, 2, 4, …, 22, called all day. The other one is to statistic the clock of 8, 10, … 20, called daytime.

The red solid point is the RMS result of the whole day in Figs. 7, 8, 9, 10, 11, 12 and 13, and the green solid point is the RMS result of daytime in Figs. 7, 8, 9, 10, 11, 12 and 13. The statistical time is from January to March in 2016. Based on the ionospheric information extracted from the IGS stations distributed all over the world, the ionospheric spherical harmonics are modeled according to the spherical harmonic function and solved by the least squares criterion. So the distribution of IGS stations can affect the accuracy of the spherical harmonic coefficient itself. There is less land in southern hemisphere, so the station is relatively small. That caused that the forecasting accuracy is low in southern hemisphere (comparing with that in northern hemisphere).

Comparing Figs. 7, 8 and 9, the forecasting RMS accuracy in the whole day and daytime is consistent in the whole world, in southern hemisphere and in northern hemisphere. We can see that the 90% of RMS was within 5 TECU in the next

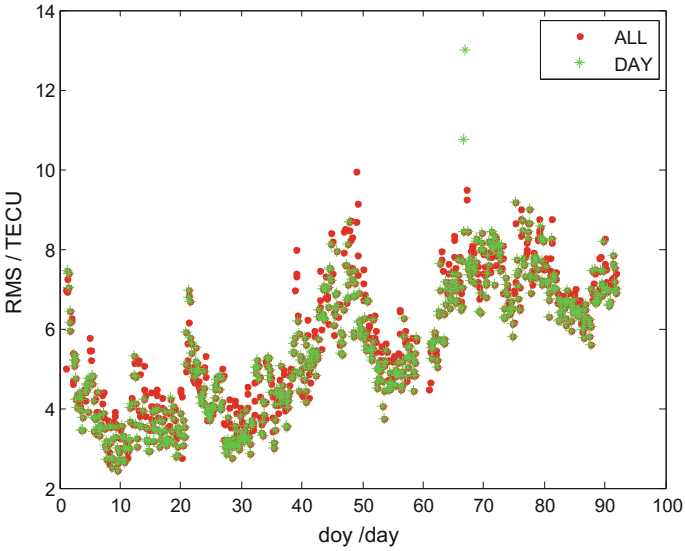

Fig. 7 Global full-day and daytime's forecasting grid's sequence of accuracy from Jan to Mar in 2016

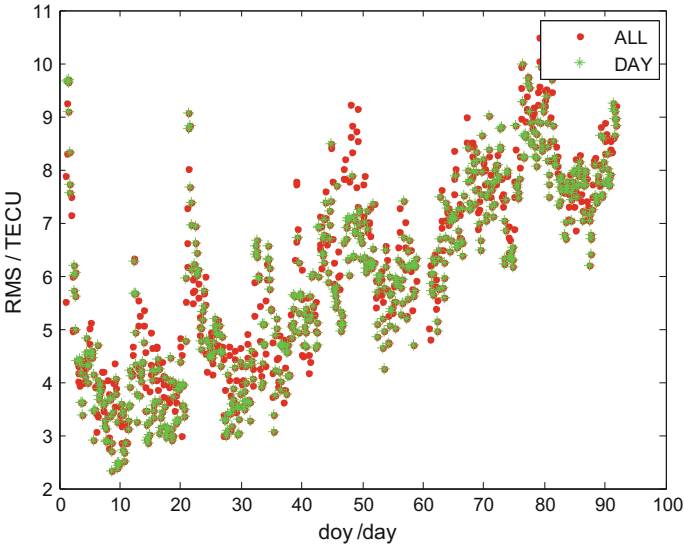

Fig. 8 Full-day and daytime's forecasting grid's sequence of accuracy in southern hemisphere from Jan to Mar in 2016

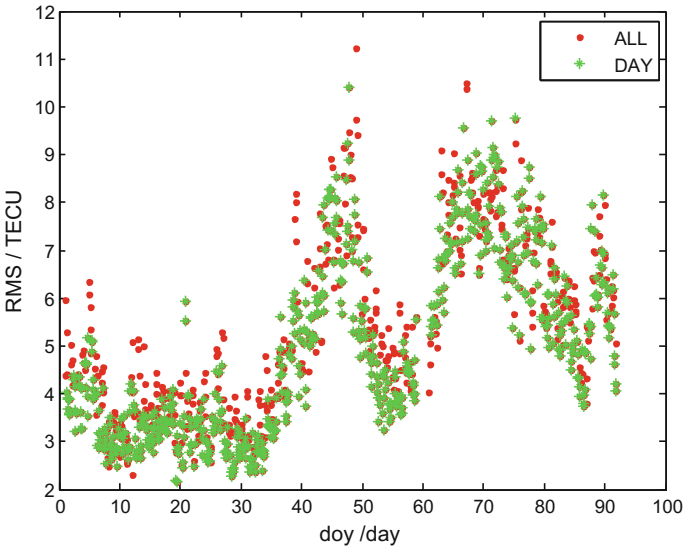

Fig. 9 Full-day and daytime's forecasting grid's sequence of accuracy in northern hemisphere from Jan to Mar in 2016

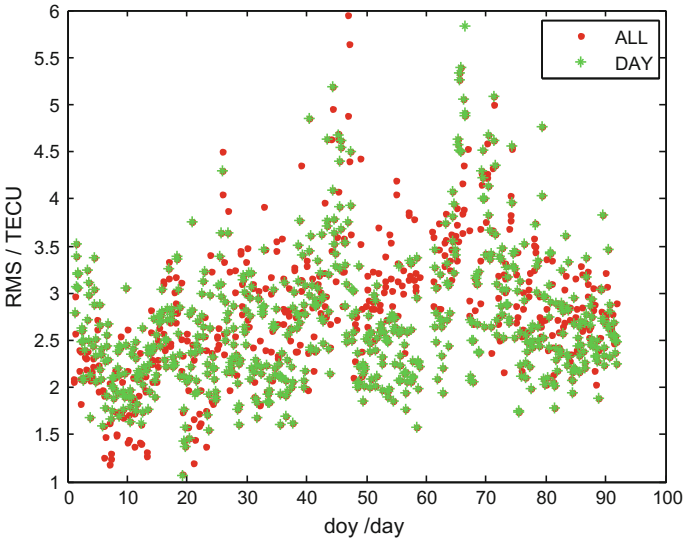

Fig. 10 Full-day and daytime's forecasting grid's sequence in the range of 60–85° latitude of northern hemisphere from Jan to Mar in 2016

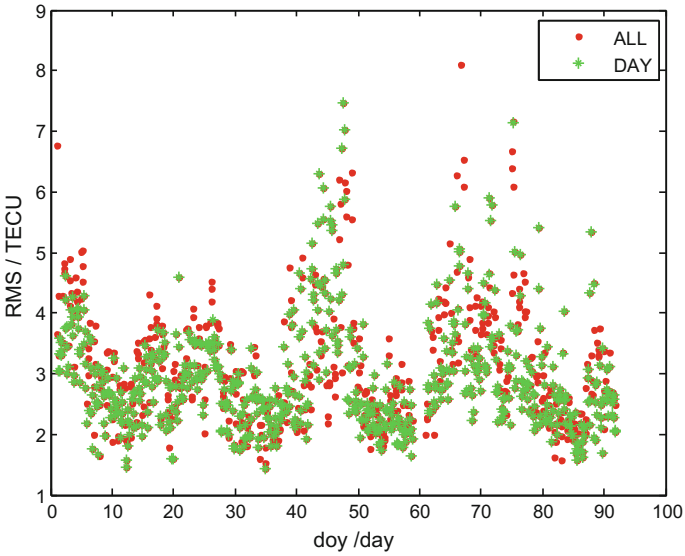

Fig. 11 Full-day and daytime's forecasting grid's sequence in the range of 45–55° latitude of northern hemisphere from Jan to Mar in 2016

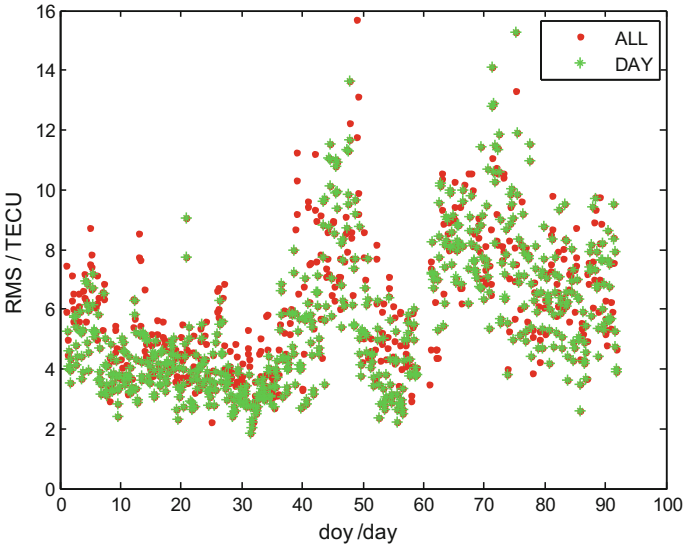

Fig. 12 Full-day and daytime's forecasting grid's sequence in the range of 20–35° latitude of northern hemisphere from Jan to Mar in 2016

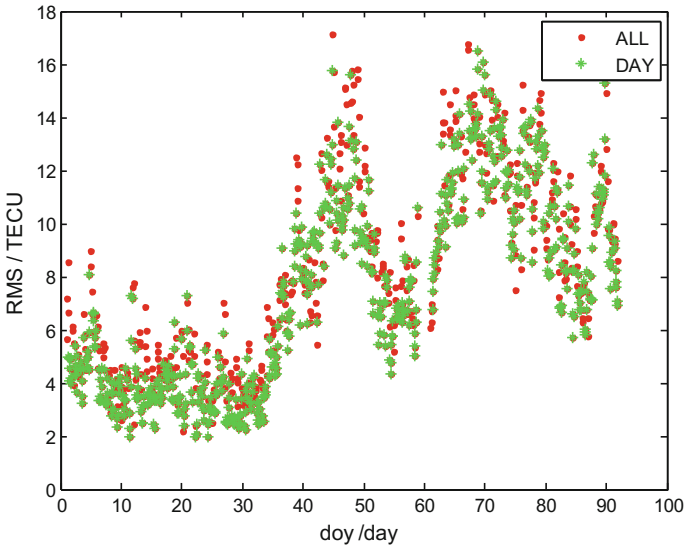

Fig. 13 Full-day and daytime's forecasting grid's sequence in the range of 0–15° latitude of northern hemisphere from Jan to Mar in 2016

30 days (from 1 to 31 in Jan of 2016), and 95% of RMS was within 9 TECU in the next 3 months (from Jan to Mar of 2016) in the whole world. With the time increasing, the RMS accuracy of forecasting result is obviously reduced, but 80% of RMS was within 5 TECU in the next 30 days in southern hemisphere. 80% of RMS was within 4 TECU in the next 30 days in northern hemisphere and accuracy was relatively stable, but the forecasting RMS in the next days (more than 30 days but less than 3 months) was unstable.

Comparing the forecasting RMS in southern hemisphere and in northern hemisphere, we can see the RMS accuracy of forecasting results in northern hemisphere was better than that in southern hemisphere whether in terms of magnitude or stability in the next 30 days, and there was a divergent trend for both in the next days (more than 30 days but less than 3 months).

The accuracy of original ionospheric spherical harmonic coefficients is limited, so the RMS accuracy of forecasting results is limited too. Considering that, we only discussed in detail the RMS of forecasting results in northern hemisphere.

Comparing the Figs. 10, 11, 12 and 13, we can see 90% of RMS was within 4 TECU in the next 30 days in high latitudes (from 60°N to 85°N and from 180°W to 180°E), and there was no significant change, but the stability of the accuracy was worse. 90% of RMS was within 5 TECU in the next 3 months in latitudes (from 40°N to 55°N and from 180°W to 180°E). 90% of RMS was within 6 TECU in the next 30 days in latitudes (from 20°N to 35°N and from 180°W to 180°E), and

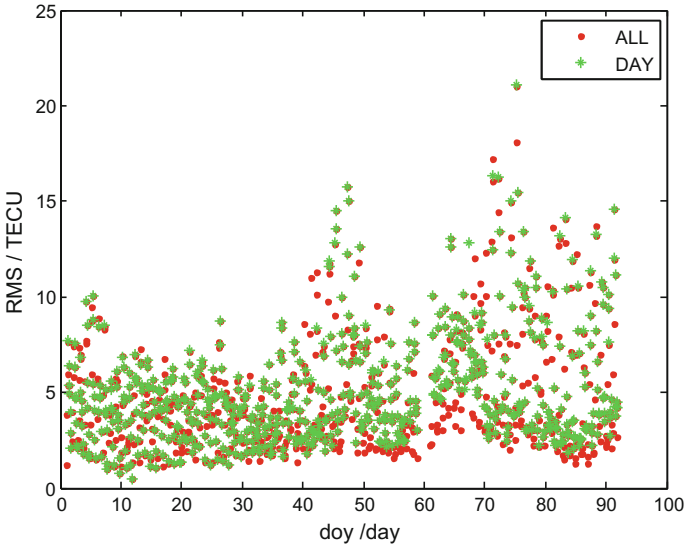

Fig. 14 Full-day and daytime's forecasting grid's sequence of the majority of China, (70, 130; 20, 55), from Jan to Mar in 2016

the stability of the accuracy was worse in the next days (more than 30 days but less than 3 months). 90% of RMS was within 6 TECU in the next 30 days in latitudes (from 0°N to 15°N and from 180°W to 180°E), and the accuracy and stability of the accuracy were obviously worse in the next days (more than 30 days but less than 3 months).

Comparing the Figs. 9, 10, 11, 12 and 13, we can get the stability of the accuracy was better in northern hemisphere than that in southern hemisphere in the next 30 days. The stability of the accuracy was worse in the next days (more than 30 days but less than 3 months), and as the latitude decreasing, this phenomenon became more and more obvious. There are two cycles in the RMS accuracy of forecasting results in the next days (more than 30 days but less than 3 months), and one cycle is about 25 days, the other one is about 35 days. In addition, as the latitude decreasing, these cycles became more and more obvious.

We can see 80% of RMS was within 5 TECU in the next 40 days in the most of China from Fig. 14, and the RMS accuracy was stable. The RMS accuracy was worse in the next days (more than 40 days but less than 3 months), but there were no obvious cycles.

4 Conclusion

Based on ionospheric spherical harmonic coefficients of CODE, we carried out ARMA modeling and forecasting the coefficients in the next 3 months. And we statistic the forecasting result, according to different latitudes and hemispheres. We can get preliminary conclusions, as the following,

1. The accuracy of forecasting result is better in northern hemisphere than that in southern hemisphere. The reason is the accuracy of the original ionospheric spherical harmonic coefficients of CODE is worse in southern hemisphere.
2. The accuracy of forecasting results is relatively stable in the next 30 days, as the latitude decreasing, the accuracy of forecasting results is worse, but 90% of RMS accuracy is within 6 TECU in northern hemisphere. The accuracy of forecasting results is worse in the next days (more than 30 days but less than 3 months), as the latitude decreasing, the accuracy of forecasting results is more worse and there are two small cycle (one is about 25 days, the other is about 35 days), and as the latitude decreasing, this phenomenon became more and more obvious.
3. 80% of RMS was within 5 TECU in the next 40 days in the most of China, and the accuracy of forecasting results is relatively stable. But the accuracy of forecasting results is obviously worse in the next days (more than 40 days but less than 3 months).
4. According to the relationship between the latitude, the accuracy and the arc of forecasting results, we can carry out forecasting of different arcs when the accuracy forecasting results and stability are guaranteed. Such as the arc can be set as 40 days or longer in high latitudes.

These conclusions provide important technical support for ionospheric anomalies (ionospheric disturbances, flicker, etc.) monitoring in the GNSS navigation and ionospheric research in the space environment.

We will carry out a more longer arc forecast in the next step and discuss the periodicity of the accuracy of forecasting results in detail.

Acknowledgements The authors would like to thank the center of International GNSS Monitoring and Assessment System (iGMAS) for its help with data and technical support.

References

1. Tian L et al (2011) Comparative analysis of studying on GPS station non-linear variation. Eng Surv Mapp 20(2):27–30
2. Tian L et al (2012) Study on ARMA model based on GPS station coordinate residual series [J]. J Geod Geodyn 32(2):124–127
3. Han WH (2012) The application of inequality constraints least squares in global ionospheric mapping with IGS ground based GNSS network. Wuhan University Press, Wuhan

4. Deng ZX (2012) Study on the ionospheric TEC storm and its forecasting method. Wuhan University Press, Wuhan
5. Liu J, Chai H, Liu X (2010) A predicting model of ionospheric based on ARIMA (p,1,1). J Geod Geodyn 30(3):79–82
6. Liu J (2011) Studying of ionosphere prediction model and discussion of pre-seism ionosphere anomalous. PLA Information Engineering University for the Degree of Master of Engineering
7. An JC et al (2015) Antarctic ionospheric prediction based on spherical cap harmonic analysis and time series analysis. Geomat Inf Sci Wuhan Univ 40(5):677–681
8. Zhou WL, Li SH, Jiang MX (2012) Ionospheric forecast based on spherical harmonic function model. J Geomat 37(3):3–5
9. Li X, Guo D (2010) Modeling and prediction of ionospheric total electron content by time series analysis. In: 2010 2nd international conference on advanced computer control (ICACC), vol 2. IEEE, pp 375–379
10. Jin SG, Zhang HP, Zhu WY (2004) Monitoring and predicting the real time ionospheric electron content by means of GPS. Acta Astronomica Sinica 45(2):213–219
11. Xu CD, Li HJ (2014) GNSS simulation principle of mathematical and system realization. China Astronautic Publishing House, Beijing
12. Liu Z, Skone S, Gao Y et al (2005) Ionospheric modeling using GPS data. GPS Solut 9(1):63–66
13. Li ZH, Zhang XH (2009) New techniques and precise data processing methods of satellite navigation and positioning. Wuhan University Press, Wuhan
14. Shen YZ, Tao BZ (2012) Practical methods for surveying data processing. Surveying and Mapping Press, Beijing

Comparison and Evaluation of Satellite Performance Based on Different Clock Products

Jie Zheng, Meijun Guo, Chao Xiong and Yun Xiao

Abstract Precision clock products because of the precision of different precision clock products lead to differences. In view of the problem that the clock difference products have different effects on the performance of the satellite, the performance evaluation and analysis of the in-orbit satellite is carried out. The frequency accuracy, stability and drift rate of GPS, BDS, Galileo and GLONASS satellites are calculated with the precision clock products provided by GBM, XRI, WUM and ISC. The result show that ISC and WUM provide clock difference products to assess the trend of the satellite clock indicators are fully consistent, while XRI and GBM evaluation of the performance of the satellite clock slightly worse. Clock performance evaluation of GNSS systems using optimal clock difference products provided by WUM. The frequency accuracy of BDS satellite is better than 4.5×10^{-11}, drift rate is better than 9×10^{-14}, the stability is 9×10^{-14}, the frequency accuracy of GPS, Galileo and GLONASS satellite is 10^{-12}–10^{-11}, drift rate is 10^{-15}–10^{-14}, the stability is 10^{-14}–10^{-13}.

Keywords Frequency accuracy · Drift rate · Stability · Performance evaluation

1 Introduction

Global satellite navigation system has been widely used in all walks of life. The performance evaluation of GNSS in orbit satellite atomic clock is of great significance for estimating the performance of navigation system, the integrity of monitoring system, the level and persistence of user positioning performance [1]. The performance evaluation of GNSS satellite clock is the use of GNSS service bureau and other organizations to provide precision satellite clock products to analysis the performance of atomic clock. Different precision clock products differ in accuracy,

J. Zheng (✉) · M. Guo · C. Xiong · Y. Xiao
Xi'an Aerors Data Technology Co., Ltd, Xi'an, Shaanxi, China
e-mail: 40735701@qq.com

J. Sun et al. (eds.), *China Satellite Navigation Conference (CSNC) 2017 Proceedings: Volume I*, Lecture Notes in Electrical Engineering 437,
DOI 10.1007/978-981-10-4588-2_49

delay, update rate and sampling rate [2], so do different precision clock difference products have an impact on the performance of satellite clocks evaluation results?

In this paper, the satellite clock performance of four navigation systems is evaluated for different clock products, a comprehensive analysis of 2016 GNSS satellite atomic clock performance. We compared the performance in four kind of clock products through the frequency accuracy, frequency drift rate, and frequency stability. At last, this paper evaluated the performance of different systems satellite atomic clock in detail analysis and evaluation using the best clock products.

2 Performance Evaluation of Satellite Clock

2.1 Frequency Accuracy

Frequency accuracy refers to consistency from the measured frequency (or calculation rate) and frequency definition, the formula is [3–5]:

$$\sigma_i' = (f_x - f_0)/f_0 \tag{1}$$

where σ_i' is the frequency accuracy, f_0 is the nominal frequency, f_x is the actual frequency value. In fact, the difference, between actual output frequency and its nominal frequency cannot measured directly, usually, the reference frequency marks as actual output frequency, so nominal frequency is usually required more than the actual frequency an order of magnitude. Moreover, Measurement frequency accuracy should choose a longer frequency measurement time as far as possible. If the frequency measurement time is too short, the short-term stability of frequency standard is relatively poor, the random fluctuation of frequency value will affect the accuracy of measurement error. Generally, the frequency accuracy can be calculated by the method of time difference, and the frequency accuracy can also be called the relative frequency deviation. Because of the high accuracy of the system, it can be considered that the relative frequency deviation is the frequency accuracy of the satellite atomic clock. The formula is,

$$\sigma_i' = -\Delta t/T = |(\hat{x}(t_2) - \hat{x}(t_1))/t_2 - t_1| = |(\hat{x}(t+\tau) - \hat{x}(t))/\tau| \tag{2}$$

where Δt is the time difference of the observed time intervals, T is the observing session length, $\hat{x}$ is the clock difference data.

There is a correction of the clock difference, there will be interval of the jump, which can be processed manually sampled time range extraction. Of course, the maximum frequency deviation caused by this large transition is eliminated during the 5-fold error, so there is no need to control the range of the calculation time deliberately.

2.2 Frequency Drift Rate

The frequency drift rate is a parameter that describes the variation of the atomic clock frequency. During the continuous orbit operation of the satellite, the output frequency of the atomic clock changes monotonously with the increase of orbit running time, due to its own and external various factors, which is called the frequency drift rate. In practical applications, we usually take the average value of multiple epoch frequency drift rates or obtain the optimal frequency drift by least-squares adjustment to evaluate the variation of atomic clock frequency. The least-squares solution of the frequency drift rate is [6]:

$$D = \sum_{i=1}^{N}(y_i - \bar{y})(t_i - \bar{t}) / \sum_{i=1}^{N}(t_i - \bar{t})^2 \tag{3}$$

where D is the frequency drift rate, $\bar{y}$ is the mean value of the relative frequency value y_i, t_i is the time to measure the relative frequency value, N is the number of samples, the formulas of $\bar{y}$ and $\bar{t}$ are

$$\bar{y} = 1/\mathrm{N}\sum_{i=1}^{N} y_i \tag{4}$$

$$\bar{t} = 1/\mathrm{N}\sum_{i=1}^{N} t_i \tag{5}$$

2.3 Frequency Stability

For frequency data, the standard Hadamard variance is defined as follows [7]:

$$H\sigma_y^2(\tau) = \frac{1}{6(M-2)\tau^2}\sum_{i=1}^{M-2}[y_{i+2} - 2\bar{y}_{i+1} + \bar{y}_i]^2 \tag{6}$$

For phase (time difference) data, it is defined as follows:

$$H\sigma_y^2(\tau) = \frac{1}{6\tau^2(N-3)}\sum_{i=1}^{N-3}[x_{i+3} - 3x_{i+2} + 3x_{i+1} - x_i]^2 \tag{7}$$

where N = M + 1 is the number of phase data named x_i, τ is the sampling interval. In this paper, the phase difference data is used to evaluate the stability of satellite clocks.

3 Data Processing Analysis and Evaluation

3.1 Performance Analysis and Comparison of Different Clock Difference Products

In this paper, the performance of GNSS satellite clocks is analyzed and compared in the precision clock difference products providing by GBM, ISC, WUM and XRI. Selecting the precision clock difference products with the GBM sampling rate of 30 s, ISC sampling rate of 300 s, WUM sampling rate of 300 s and XRI sampling rate of 30 s from January to September in 2016, the satellite clock data for each satellite is extracted as a unit to calculate the frequency accuracy, daily frequency drift and day stability of the BDS, GPS, GLONASS and Galileo respectively. The frequency accuracy and drift rate are taken as the average absolute value, the frequency stability is calculated using Hadamard variance.

3.1.1 Accuracy Analysis and Comparison

It can be seen from Fig. 1 that the frequency accuracy of GNSS in orbit atomic clock is in the order of 10^{-12}–10^{-11} from January to September of 2016. The frequency accuracy of BDS atomic clock is in the order of 10^{-11}, the frequency accuracy of C14 is lower, XRI results are better than other. The accuracy of GPS in orbit atomic clocks is in the order of 10^{-12}, ISC and WUM data calculation results is not much difference. The accuracy of GLONASS in orbit atomic clocks is in the order of 10^{-12}, ISC and WUM data calculation results are basically the same, the frequency accuracy of R09 and R15 satellite clocks is worse than other satellites. Accuracy of E11 and E19 satellites in Galileo system is better, the XRI data is better than the others. The results from the frequency accuracy assessment can be derived: Four kinds of data frequency accuracy trend of each star is basically the same from XRI, ISC and WUM, and the last two kinds are almost identical. The frequency accuracy of each star is the same trend of GBM evaluation for GPS and GLONASS, but the calculation accuracy will be poor.

3.1.2 Drift Rate Analysis and Comparison

It can be seen from Fig. 2 that the daily frequency drift of GNSS satellite atomic clock is at 10^{-15}–10^{-13} level. Among them, in addition to the GBM data calculated on the BDS atomic clock frequency drift rate in the order of 10^{-13}, the other clock products calculated daily frequency drift rate in the order of 10^{-14}. But C01, C05, C09 and C14 satellite clock frequency drift rate in the order of 10^{-13}, obviously higher than other satellite clock frequency drift rate. The daily frequency drift of GPS in orbit satellite clock is in the order of 10^{-15}–10^{-14}, most satellites are better than 10^{-15}, the accuracy of GBM data is poor. GLONASS in orbit satellite clock

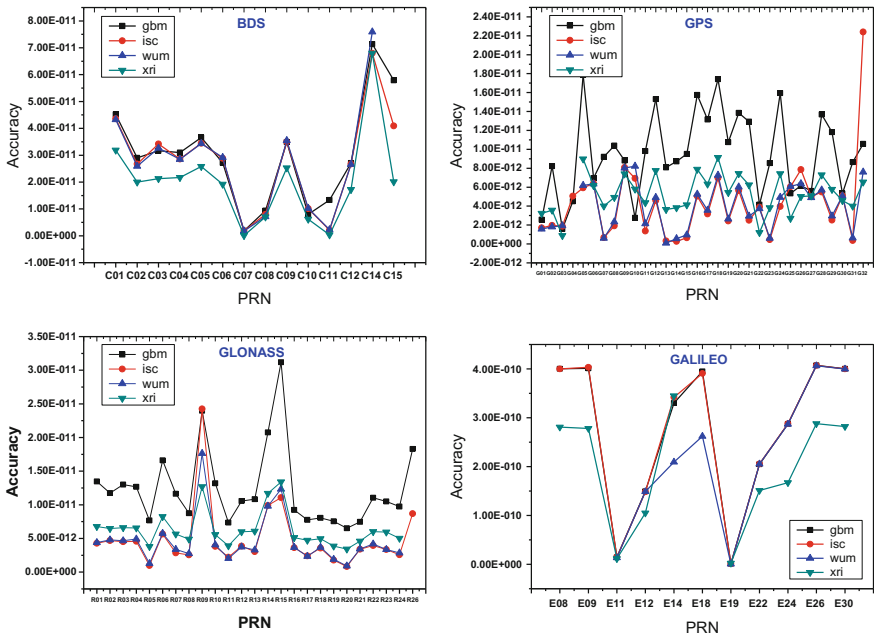

Fig. 1 Comparison of frequency accuracy of GNSS atomic clock with different clock difference products

drift rate in the order of 10^{-15}. Among them, it exist abnormal value of the individual satellite drift rate and the frequency drift jump. However, the average drift rate is better than GPS, This is mainly because the GLONASS satellite is equipped with cesium clock, the frequency drift characteristics are not obvious, the output frequency value is more stable than rubidium clock.

The results of drift rate comparison of the four systems with different clock difference products, GBM and XRI data are used to evaluate the frequency drift rate of the atomic clock in each system, which existing presence of outliers and frequency drift jumps. While the WUM and ISC precision clock difference of the GNSS atomic clock is more stable.

3.1.3 Stability Analysis and Comparison

It can be seen from Fig. 3 that the day stability of GNSS in orbit atomic clock is in the order of 10^{-14}–10^{-13}. The day stability of BDS atomic clock is in the order of 10^{-14} level, and the overall trend of the global stability of the four kinds of clock products is consistent. The day stability of GPS in orbit atomic clock in is in the order of 10^{-14}. The day stability of calculation of ISC clock products did not reach 7×10^{-14} level, day stability calculated by GBM and WUM clock difference is

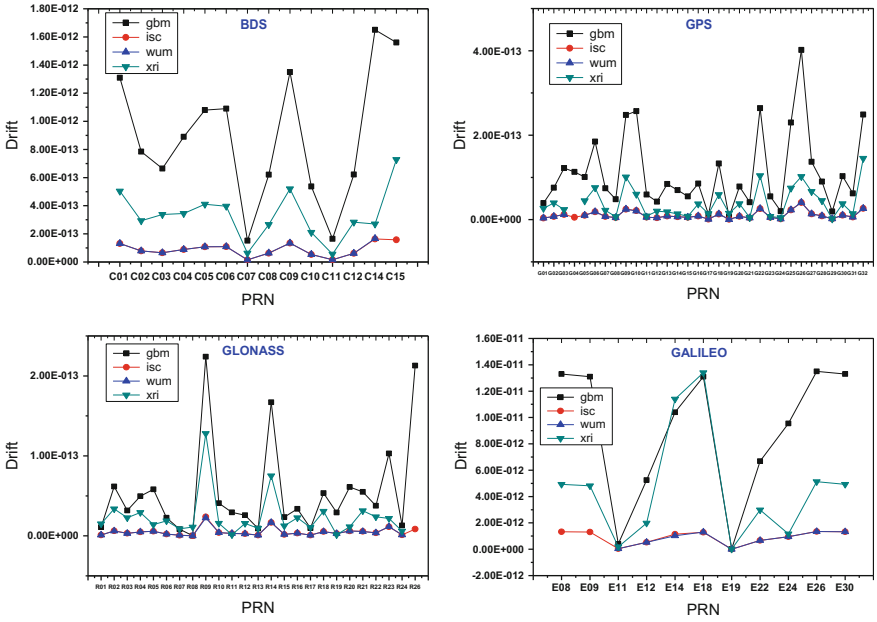

Fig. 2 Comparison of frequency drift rate of GNSS atomic clock with different clock difference products

better, indeed to 10^{-15} order. The stability trend of four kinds of products to calculate GLONASS atomic clocks in orbit is about consistent. In addition to the stability of the R15 satellite clock is poor, the rest of the satellite clock stability are in the order of $2 - 8\times10^{-14}$. The ISC data accurate is poor in evaluating the GPS and GALILEO satellite clocks.

The clock products provided by Wuhan University is the best in evaluating the frequency accuracy, frequency drift rate, frequency stability. Next, the detailed analysis and evaluation of the atomic clock of the system are carried out by using the WUM data.

3.2 WUM Precise Clock Difference Evaluation of Satellite Clock Performance

Following, the atomic clock performance of the four systems which using WUM sampling rate of 300 s of precision clock difference product from January to September in 2016 is analyzed. The estimated parameters are the frequency accuracy, daily frequency drift rate and day stability of each satellite. The frequency stability algorithm is the Hadamard variance.

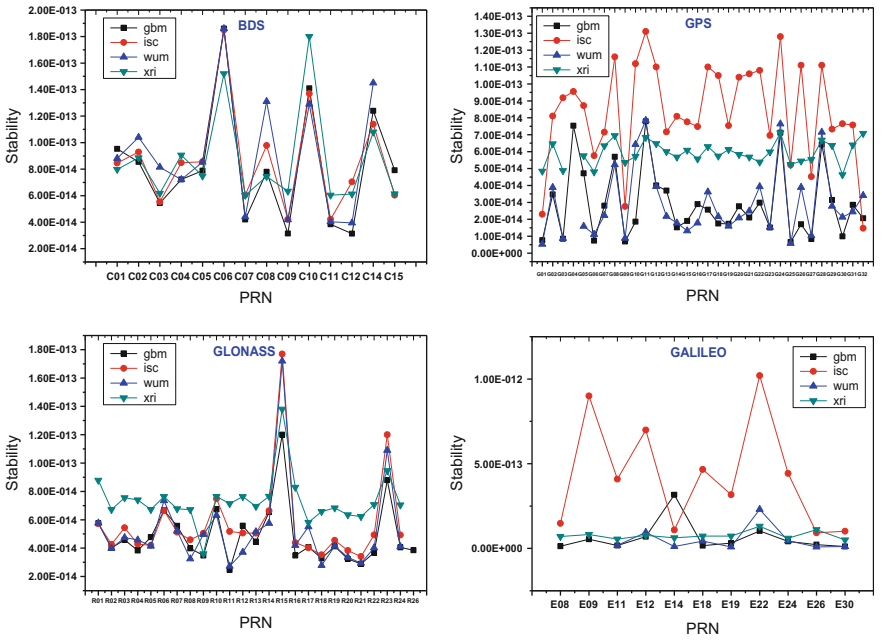

Fig. 3 Comparison of frequency stability of GNSS atomic clock with different clock difference products

3.2.1 Accuracy Assessment

It can be seen from Fig. 4 that the frequency accuracy of GNSS in orbit atomic clock in 2016 is in the order of 10^{-12}–10^{-10}. The frequency accuracy of BDS satellite clock is in order of 10^{-11}, the frequency accuracy of C14 satellite clock is poor in January to April, and jump in May, the accuracy returned to normal levels. In addition to C14 satellite frequency accuracy is low, the other satellite frequency accuracy is better than 4.5×10^{-11}. The frequency accuracy of GPS satellite clock is in order of 10^{-12}, the frequency accuracy of G26 satellite clock is low, about in the order of 10^{-11}, the frequency accuracy of the other satellite clock is better than 2×10^{-12}. The frequency accuracy of GLONASS in orbit atomic clock is in the same level as that of GPS, and its frequency accuracy is in order of 10^{-12}, except that the R15 satellite clock frequency is lower than 10^{-11}, the other satellite clocks are better than 1×10^{-11}. In addition to Galileo atomic clocks named E11 and E19 satellite clocks are in the order of 10^{-11} and 10^{-13}, and the other satellite frequencies are in order of 10^{-10}.

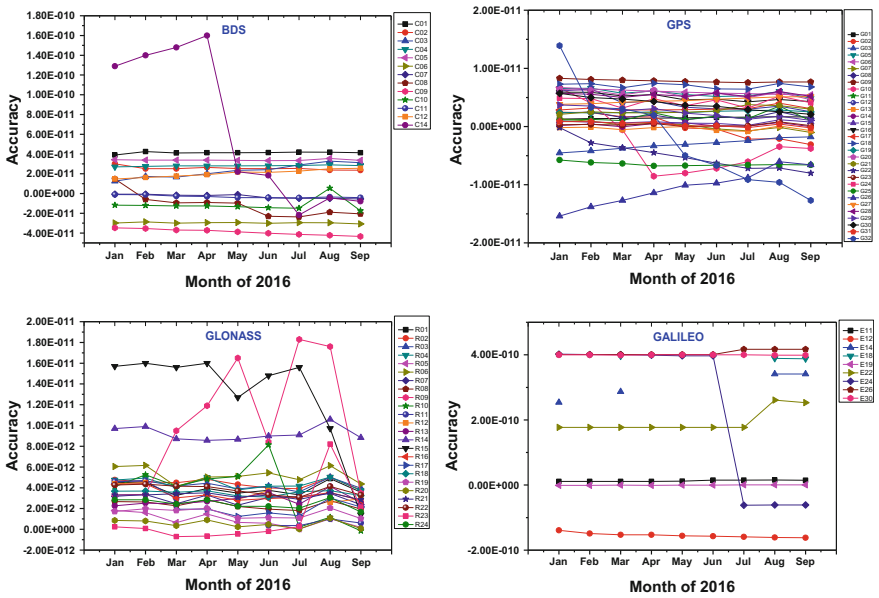

Fig. 4 Frequency accuracy of GNSS atomic clock

3.2.2 Drift Rate Assessment

It can be seen from Fig. 5 that the drift rate of GNSS satellite atomic clock is in order of 10^{-15}–10^{-14}. Among them, the daily frequency drift rate of the BDS in orbit atomic clock is in the order of 10^{-14}, but the frequency drift of C01, C05, C06 and C09 is in the order of 10^{-13}, which is obviously higher than the other satellite clocks. The daily frequency drift rate of GPS satellites is in the order of 10^{-15}–10^{-14}, most of the satellites are better than 10^{-15}. The daily drift rate of G09, G22, G26 and G32 is in the order of 10^{-14}, and in individual months there was a jump. The drift rate of GLONASS satellite in orbit on the whole in the order of 10^{-15}, in which the drift rate of R09 satellite has a jump, but the average drift rate is better than GPS. This is mainly because GLONASS satellites are carried by cesium clock, the frequency drift characteristics is not obvious, the output frequency value is more stable relative than rubidium clock. The daily frequency drift rate of E11 and E19 of Galileo system is in the order of 10^{-15}–10^{-14}, the frequency drift of E12 and E22 is in the order of 10^{-13}, the frequency drift of E26, E30 and E24 sate is poor that in the order of 10^{-13}, the frequency drift of E24 has jump.

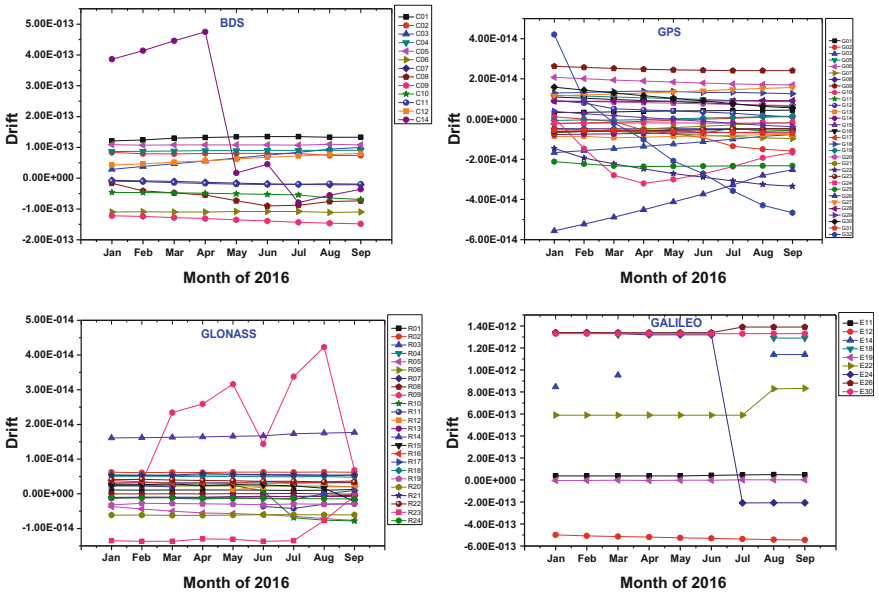

Fig. 5 Frequency drift rate of GNSS atomic clock

3.2.3 Stability Assessment

It can be seen from Fig. 6 that the day stability of GNSS in the orbital atomic clock is in the order of 10^{-14}–10^{-13}. The day stability of BDS atomic clock is generally in the order of 10^{-14}, but the day stability of the individual satellite clocks is poor. The day stability of the C14 satellites is in the order of 10^{-13} on January to April, the stability reached 10^{-14} after May. The day stability of C06 and C14 satellites is in the order of 10^{-13}, and the day stability of C10 satellite clock in August and September were greater volatility. The day stability of GPS satellite is in the order of 10^{-14}, and most of the satellite clock stability is better than 5×10^{-14}, the day stability of G11, G24, G28 and G32 is poor that in order of 10^{-14}–10^{-13}, and there are more jump. The stability of GLONASS in orbit atomic clock is consistent, with the exception of the stability of R15, and there is a jump for the stability of R09 and R23 satellite clock, the rest of the stability of satellite clock is in the order of $2 - 6 \times 10^{-14}$. The day stability of Galileo satellite clock is better than 5×10^{-14}, in addition to the day stability of E22 satellite clock jumped in August, the day stability of E24 satellite clock also appeared jump in March.

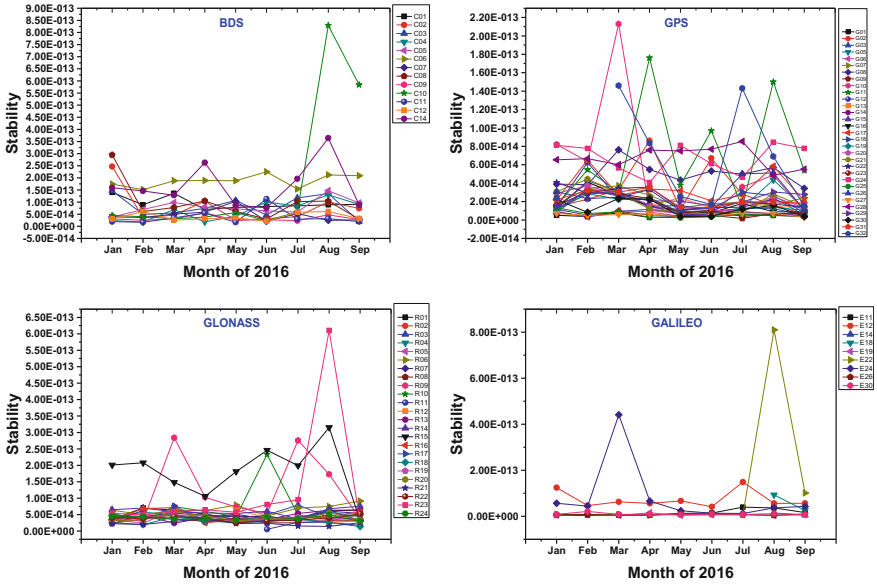

Fig. 6 Frequency stability of GNSS atomic clock

3.2.4 Performance Analysis of Satellite Atomic Clock

Next, it is demand for four systems at different time scales using the data of third quarter of 2016. As shown in the following Fig. 7.

It can be seen from Fig. 7 that the short-term stability of G01, G03, G06, G09, G25, G27 and G30 satellites of GPS is significantly higher than other satellites before 3000 s, all of these satellites are GPS BLOCK IIF satellite, we can see the BLOCK IIF satellites have excellent short-term stability.

The results show that the frequency accuracy of the BDS in orbit satellite clock is one order of magnitude lower than the other three systems, which is in the order of 10^{-11}, and the frequency accuracy of the GPS BLOCK IIF with rubidium clock and the Galileo E19 with hydrogen clock is the best. The frequency accuracy GLONASS with cesium clock is better. The frequency drift index of GLONASS with cesium clock is the best, and the performance of frequency drift of BDS with domestic rubidium clock is poor, but it is at same order of magnitude with the GPS rubidium clock. Comprehensive comparison, the latest generation BLOCK IIF of GPS equipped with rubidium clock and Galileo IOV satellite equipped with hydrogen clock with the optimal performance.

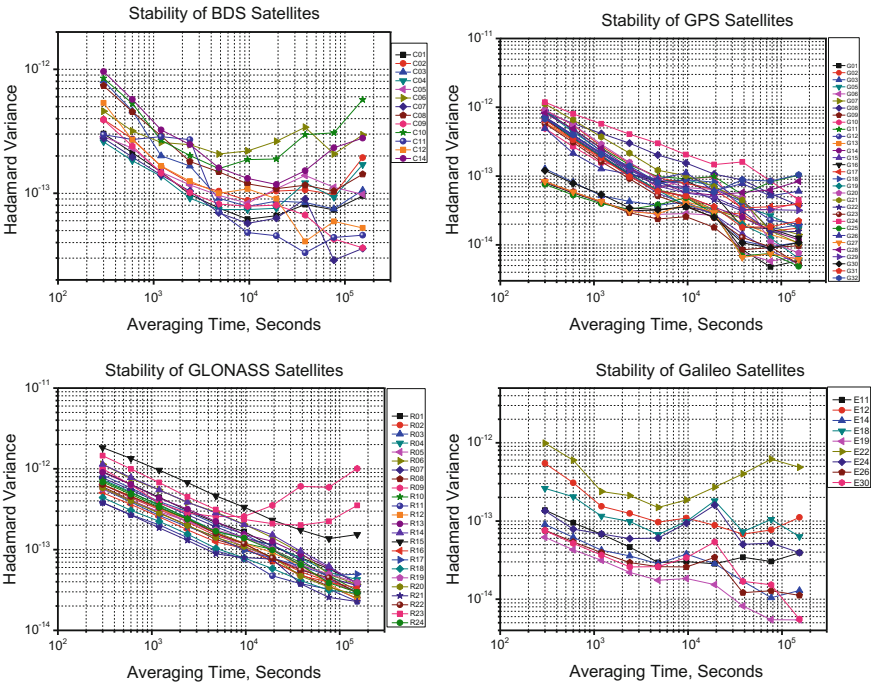

Fig. 7 Frequency accuracy waveform of GNSS atomic clock

Table 1 Synthesis results of BDS in-orbit satellite performance

	PRN	Accuracy	Drift	Day stability
	C01	4.1357E−11	1.3088E−13	9.5298E−14
	C02	2.5600E−11	7.9068E−14	7.8140E−14
	C03	2.3025E−11	6.5299E−14	8.3388E−14
	C04	2.8085E−11	8.9110E−14	6.3833E−14
	C05	3.3931E−11	1.0805E−13	8.0278E−14
GEO	Average	3.0400E−11	9.4483E−14	8.0188E−14
	C06	2.9669E−11	1.0932E−13	5.1878E−14
	C07	2.8244E−12	1.5093E−14	4.5743E−14
	C08	1.4974E−11	6.2199E−14	7.0210E−14
	C09	3.8909E−11	1.3505E−13	3.2587E−14
	C10	1.2657E−11	5.3298E−14	1.8953E−13
IGSO	Average	1.9807E−11	7.4992E−14	7.7989E−14
	C11	3.1157E−12	1.6632E−14	2.7288E−14
	C12	2.0494E−11	3.1796E−14	3.9495E−14
	C14	3.2258E−11	2.1701E−13	1.6756E−13
MEO	Average	1.8623E−11	8.8479E−14	7.8113E−14
Total average	All star	2.3608E−11	8.7909E−14	7.8863E−14

3.2.5 Comprehensive Analysis of GNSS Performance Evaluation

In order to analyze the on orbit clock performance of each system and compare it, using four system atomic clock nine months performance are averaged in absolute value respectively, which are listed in the following Table 1.

It can be seen from the statistical results, Among the 13 in-orbit satellites that can be served by BDS, the frequency accuracy and day drift rate of C01 satellite are poor, C10 satellite's day stability index is poor, three performance indicators of C14 satellite are poor, the other satellite are in the same order of magnitude, and the performance is better. In addition, the performance of GEO satellites is slightly worse than that of IGSO and MEO satellites. This phenomenon is related to the frequent change of GEO satellites. It is also related to the relatively low accuracy of clock difference calculation of GEO satellite orbit. Moreover, the current constellation of the BDS, GEO satellite is the first launch off, MEO satellite is later launched, and with the technology and experience of ascension, the later launched satellite performance is better than the previous launch of the satellite (Table 2).

GPS satellite systems exist many generations satellite, and the performance of each generation satellite clock is stratified. Also it is gradually improved. The latest generation of BLOCK IIF satellite clock performance is optimal, and its day stability is in the order of 10^{-15} (Table 3).

From the statistical results, we can see that the overall performance of the GLONASS system is stable, and the frequency drift rate reached 10^{-15} (Table 4).

The E12 and E19 of Galileo IOV satellite with a high-precision hydrogen clock, E11 with rubidium clock, E11 and E19 satellite clock frequency accuracy and frequency drift are better. The E22 of Galileo FOC satellite with rubidium clock, the rest with high-precision hydrogen clock, E22 satellite stability index is lower than other satellite, the day stability is in the order of 10^{-13}, other satellite day stability in the order of 10^{-14}.

Table 2 Synthesis results of GPS in-orbit satellite performance

	Accuracy	Drift	Day stability
BLOCK IIR	3.1463E−12	8.6816E−15	2.8386E−14
BLOCK IIR-M	2.4363E−12	5.2831E−15	2.2053E−14
BLOCK IIF	1.5022E−12	1.6809E−14	8.8767E−15

Table 3 Synthesis results of GLONASS in-orbit satellite performance

	Accuracy	Drift	Day stability
GLONASS	3.9334E−12	1.8912E−15	5.5408E−14

Table 4 Synthesis results of GALILEO in-orbit satellite performance

	PRN	Accuracy	Drift	Day stability
	E11	1.3075E−11	4.0847E−14	1.5537E−14
	E12	1.5437E−10	5.2419E−13	7.3374E−14
	E19	6.7266E−13	2.4838E−15	6.8291E−15
IOV	Average	5.6039E−11	1.8917E−13	3.1913E−14
	E14	1.3593E−10	4.5229E−13	9.9987E−15
	E18	1.3031E−10	4.3342E−13	5.9254E−14
	E22	1.9495E−10	6.4297E−13	1.0730E−13
	E24	2.8681E−10	9.5420E−13	8.2005E−14
	E26	4.0651E−10	1.3538E−12	7.9159E−15
	E30	3.9957E−10	1.3304E−12	1.0146E−14
FOC	Average	2.5901E−10	8.6118E−13	4.6103E−14
Total average	All	1.9136E−10	6.3718E−13	4.1373E−14

4 Conclusion

In this paper, GNSS in orbit satellite clock performance are analyzed provided by GBM, XRI, WUM and ISC. It is concluded that the accuracy of the clock difference products of the WUM is relatively high. The frequency accuracy, daily drift rate and day stability of the satellite clocks are calculated by using GNSS to evaluate the performance of better precision clock difference products. It is concluded that the clock difference products that provided by Wuhan University is superior to the performance analysis for four systems, and the comprehensive performance of GPS BLOCK IIF with rubidium clock and Galileo IOV with hydrogen clock is the best. The performance of BDS MEO satellite clock is better than GEO and IGSO satellite clock. The overall index of GLONASS satellite with cesium clock is better.

Acknowledgements Project supported by the National Natural Science Foundation of China (Grant No. 41304022)

References

1. Huang G, Zhang Q et al (2013) Quality variation of GPS satellite clocks on-orbit using IGS clock products. Adv Space Res 51(6):978–987
2. Li P, Shen Z, Wang M (2016) Error analysis of IGS precise ephemeris. J Geod Geodyn 26(3): P40–P45
3. Zhang Q (2014) Research on theory and method of GNSS monitoring and evaluation. The PLA Information Engineering University, pp 116–118
4. Huang G (2012) Research on algorithms of clock offset and quality evaluation of GNSS satellite clock. Chang'an University, pp 136–147
5. Jia X, Feng L, Mao Y, Yang H (2010) Performance evaluation of GPS on board clock. J Time Freq 33(2):P38–P39

6. Gou H (2006) Study on the analysis theories and algorithms of the time and frequency characterization for atomic clocks of navigation satellites. The PLA Information Engineering University
7. Li X et al (2010) Precise measurement of time frequency signal. Science Press, Beijing

Research on Monitoring and Evaluating Method of Beidou Monitoring Receiver Inter-frequency Bias

Gang Wang, Weigang Zhu and He Zhao

Abstract With the development of new global navigation satellite system applications, the demand of high accurate positioning navigation timing (PNT) service becomes urgent. For precise PNT, the hardware delay is regarded as an important parameter in the satellite navigation message. Instead of using the absolute receiver hardware delay, a method based on receiver inter-frequency bias (DCB, Differential code biases) calibration is presented to deal with the rank deficiency of a calculation matrix and to reduce jumps in DCB solutions in BDS. The current DCB estimation methods generally require the elimination or estimation of ionospheric delay error. Thus the error of modeling and mapping errors will influence the accuracy of DCB. In the paper, a method based on the difference of dual-frequency ionosphere-free code observations is proposed to monitor and evaluate the DCB of receiver, inter-frequency bias (IFB). Using it, the IFB of BDS can be computed. A one-year three-frequency BDS data set is processed to estimate the IFB. The results show that this algorithm can be used to estimate IFB effectively, the accuracy is better than 1 ns.

Keywords BeiDou navigation satellite system (BDS) · Receiver inter-frequency bias (IFB) · Accuracy evaluation · Ionosphere-free code observations

1 Introduction

The Global Navigation Satellite System (GNSS) is actually a radio system which measuring range by measuring time. As the signals at transmitter and receiver have inconsistent spatial and time references, Differential Code Bias (DCB) parameters are important part of GNSS navigation message to modify this bias. Because the

G. Wang (✉) · W. Zhu · H. Zhao
Beijing Satellite Navigation Center, Beijing 100094, China
e-mail: wggps126@126.com

J. Sun et al. (eds.), *China Satellite Navigation Conference (CSNC) 2017 Proceedings: Volume I*, Lecture Notes in Electrical Engineering 437,
DOI 10.1007/978-981-10-4588-2_50

satellite navigation system has more than two navigation frequencies, different frequencies of navigation signals within the satellite and receiver through a different path will have different hardware delay. In the GNSS data processing, the satellite and the receiver of hardware delay is a factor cannot be ignored. For example, when using Global Position System (GPS) observations to calculate ionosphere delay, we must considering DCB.

Yuan et al. carried out many researches about the calculation of DCB using the observations of GPS tracking stations [1–3]. Xie et al. [4] established a spherical harmonics ionospheric model, solving the ionosphere total electron content (TEC) while solving DCBs of GPS and GLONASS satellites and receivers. Zhang et al. [5] studied short term varying characteristics of receiver's DCB by zero baseline and short baseline data. Tang et al. [6] evaluated the DCB of receives by precise point positioning (PPP), and had an accuracy of 1 dm using the data of IGS. Fan [7] calculated DCB by solving PPP, and had an accuracy of 0.2 ns using the data of IGS stations in Europe.

After the operation of Beidou Satellite Navigation System (BDS), a large number of scholars have carried out research on the calculation of BDS satellite and receiver DCBs. The definition and calculation of BDS has been studied by Wu et al. [8, 9]. Fan [10] raised a new evaluation method of DCBs, using the tri-frequency data of BDS. The solutions of DCB between using GPS/BDS two systems and BDS single system have a difference about 0.1–0.227 ns [11]. GPS data combing with BDS data using low order spheric harmoics function to solve DCB had an accuracy about 0.3 ns [12].

The satellite hardware delay is related to the reference point of the satellite clock error parameter. Timing Group Delay (TGD) parameter provided by GPS is based on the reference point of P1/P2 ionosphere-free linear combination. TGD can be eliminated when the user is using an ionosphere-free combination. The DCB of receive is also related to the reference point of receive clock. GPS receive clock is usually referenced to C/A code, so DCB of C1 or P1 can be considered as zero. DCB of P2 have a bias to P1. GPS pseudo-range observation equation can be simplified as follows:

$$\begin{aligned} PR^{j}_{L1,i} &= \tilde{\rho} + I^{j}_{L1,i} + T^{j}_{gd} + E_{PR1} \\ PR^{j}_{L2,i} &= \tilde{\rho} + \gamma I^{j}_{L2,i} + \gamma T^{j}_{gd} + R_i + E_{PR2} \end{aligned} \tag{1}$$

$$\gamma = \left(\frac{L_1}{L_2}\right)^2$$

Where, $\tilde{\rho}$ contains geometric distance, tropospheric delay, satellite clock and the receiver clock and other frequency-free error, $I^{j}_{L1,i}$ is the ionosphere delay of L1 from receive i to satellite j, T^{j}_{gd} is TGD of satellite j, R_i is receiver's DCB of L2. E_{PR1} and E_{PR2} are observation error.

The dual-frequency pseudo-range can be used to obtain the ionosphere delay. From (1) we have:

$$I_{L1,i}^{j} = \frac{PR_{L2,i}^{j} - PR_{L1,i}^{j}}{\gamma - 1} = I_{L1,i} + \left(T_{gd}^{j} + \frac{R_i}{\gamma - 1} \right) + E_{PR12}$$

The ionospheric delay calculated by the dual-frequency pseudo-range contains a deviation associated with hardware delay. In [13] this bias is defined as inter frequency bias (IFB):

$$IFB_i^j = T_{gd1}^j + \frac{R_i}{\gamma - 1} \tag{2}$$

Obviously, the IFB contains the difference of hardware delay between the two frequencies between the satellite and the receiver, which is the differential-code deviation (DCB). Equation (2) is the ground-based formula for establishing the ionospheric model, as well as the basis for calculating the inter-code deviation between the satellite and the receiver.

Computing satellite and receiver DCBs using ground-based observations is basically a "extract-model-separate" approach. The main error in the extraction step is mainly "mapping error". In general, ionosphere shell model needs to project the slant TEC (STEC) to the vertical TEC (VTEC). The different between the height of shell models and the actual ionospheric F2 layer will cause "mapping error" [5]. Modeling step has two methods. Firstly, we can calculate the satellite and receiver's DCB in the establishment of the ionosphere model [1–4]. Secondly, we can use the known ionosphere model as the reference to calculate satellite and receive DCB [10]. Obviously, both the self-established model and the known ionosphere model, the model error will restrict DCB accuracy. In order to evaluate the IFB more effectively, this paper will use the characteristic of BDS triple-frequency to deviate the model and algorithm for calculating DCB of satellite and receive, so as to overcome the "mapping error" and "model error" on DCB calculation.

2 Mathematical Models

For a specific satellite-receiver link, simplified equations of the BDS triple-frequency range observations *PR* can be described as:

$$\begin{aligned} PR_{B1,i}^{j} &= \tilde{\rho} + I_{B1,i}^{j} + D_{B1}^{j} + D_{B1,i} + E_{PR,B1} \\ PR_{B2,i}^{j} &= \tilde{\rho} + \gamma_{1,2} I_{B1,i}^{j} + D_{B2}^{j} + D_{B2,i} + E_{PR,B2} \\ PR_{B3,i}^{j} &= \tilde{\rho} + \gamma_{1,3} I_{B1,i}^{j} + D_{B3}^{j} + D_{B3,i} + E_{PR,B3} \end{aligned} \tag{3}$$

Where $B1, B2, B3$ denote the triple-frequency signals of BDS; $\tilde{\rho}$ is the frequency-independent term including the true geometric range, the tropospheric delay, satellite clock error, receiver clock error; $I^j_{B1,i}$ denote the ionosphere delay of B1 frequency; D^j_{B1}, D^j_{B2}, and D^j_{B3} denote corresponding satellite hardware delays; $D_{B1,i}, D_{B2,i}$, and $D_{B3,i}$ denote corresponding receiver hardware delays; $E_{PR,B1}, E_{PR,B2}$ and $E_{PR,B3}$ denote corresponding measurement error; γ denote the frequency-dependent multiplier factors $(\gamma_{1,2} = B1^2/B2^2, \gamma_{1,3} = B1^2/B3^2)$.

We follow the standard approach and consider the geometry-free combination of the carrier phase-smoothed code measurements $(PR^j_{B2,i} - PR^j_{B1,i}, PR^j_{B3,i} - PR^j_{B1,i})$. This combination removes all common geometry-dependent errors. The only parameters remaining in the mathematical model are ionospheric delay, and satellite TGD and receiver IFB.

$$\begin{aligned} PR^j_{B2,i} - PR^j_{B1,i} = {} & (\gamma_{1,2} - 1) I^j_{B1,i} + (D^j_{B2} - D^j_{B1}) \\ & + (D_{B2,i} - D_{B1,i}) + E_{PR,B2B1} \end{aligned} \tag{4}$$

$$\begin{aligned} PR^j_{B3,i} - PR^j_{B1,i} = {} & (\gamma_{1,3} - 1) I^j_{B1,i} + (D^j_{B3} - D^j_{B1}) \\ & + (D_{B3,i} - D_{B1,i}) + E_{PR,B3B1} \end{aligned} \tag{5}$$

According to (4)–(5), the following equations can be obtained:

$$I^j_{B1,i} = \frac{(PR^j_{B2,i} - PR^j_{B1,i})}{(\gamma_{1,2} - 1)} - \frac{(D^j_{B2} - D^j_{B1}) + (D_{B2,i} - D_{B1,i})}{(\gamma_{1,2} - 1)} - \frac{E_{PR,B2B1}}{(\gamma_{1,2} - 1)} \tag{6}$$

$$I^j_{B1,i} = \frac{(PR^j_{B3,i} - PR^j_{B1,i})}{(\gamma_{1,3} - 1)} - \frac{(D^j_{B3} - D^j_{B1}) + (D_{B3,i} - D_{B1,i})}{(\gamma_{1,3} - 1)} - \frac{E_{PR,B3B1}}{(\gamma_{1,3} - 1)} \tag{7}$$

Substituting Eq. 6 in Eq. 6, we get the new equations expressed as:

$$\begin{aligned} & \frac{(PR^j_{B2,i} - PR^j_{B1,i})}{(\gamma_{1,2} - 1)} - \frac{(PR^j_{B3,i} - PR^j_{B1,i})}{(\gamma_{1,3} - 1)} = \frac{(D^j_{B2} - D^j_{B1}) + (D_{B2,i} - D_{B1,i})}{(\gamma_{1,2} - 1)} \\ & \quad - \frac{(D^j_{B3} - D^j_{B1}) + (D_{B3,i} - D_{B1,i})}{(\gamma_{1,3} - 1)} + E_{PR,B1B2B3} \\ & = 0.4565 D^j_{B1} + 1.4872 D^j_{B2} - 1.9437 D^j_{B3} + 0.4565 D_{B1,i} \\ & \quad + 1.4872 D_{B2,i} - 1.9437 D_{B3,i} + E_{PR,B1B2B3} \\ & = \tilde{D}^j_{CB} + \tilde{D}_{CB,i} + E_{PR,B1B2B3} \end{aligned} \tag{8}$$

Where $\tilde{D}^j_{CB} = 0.4565 D^j_{B1} + 1.4872 D^j_{B2} - 1.9437 D^j_{B3}$ and $\tilde{D}_{CB,i} = 0.4565 D_{B1,i} + 1.4872 D_{B2,i} - 1.9437 D_{B3,i}$, $\tilde{D}^j_{CB}$ denote the combinations of the different frequency satellite hardware delays, $\tilde{D}_{CB,i}$ denote the combinations of the

different frequency receiver hardware delays. In Eq. 8 the effects of receiver clock error, satellite clock error, tropospheric delay, ionosphere delay and topocentric satellite distance are eliminated, but due to the rank deficiency problem, the $\tilde{D}_{CB}^{j}$ and $\tilde{D}_{CB,i}$ were not separated. Additional information must be introduced to the least-squares solution (so-called constraints), to make separating of parameters. GPS DCB is computed by constraining the sum of DCB of all the satellites to zero. BDS DCB is computed by fixing of the one satellite DCB. By these methods, the problem of rank deficiency can be solved. $\tilde{D}_{CB}^{j}$ and $\tilde{D}_{CB,i}$ is computed by constraining the sum of $\tilde{D}_{CB}^{j}$ of five BDS GEO satellites to zero, according to the character of BDS constellation. The constraints are as follows:

$$\sum_{j=1}^{5} \tilde{D}_{CB}^{j} = 0 \tag{9}$$

This method not only overcomes the model error caused by the new ionospheric model or the known model, but also overcomes the mapping error caused by ionospheric observations projected in the observed direction as ionospheric delays in the vertical direction. The carrier phase-smoothed code measurements can be used to improve the calculation precision in practical calculation. The DCB of satellites and receivers are actually the combination of hardware delays. $\tilde{D}_{CB,i}$ calculated in this paper contains the hardware delays of three frequencies of the receiver. Its long-term variation can reflect the performance of the receiver, and can be used to evaluate the receiver Performance.

3 Data Processing

According to the theory provided above, the measured triple-frequency data of 66 Beidou monitoring receivers are calculated. Data using time is 2015. 01–2016. 04, about 66 weeks of data. The calculation is based on 1-h data for a calculation period, in which the single station uses The carrier phase-smoothed code measurements to calculate $\tilde{D}_{CB}^{j}$ and $\tilde{D}_{CB,i}$. The $\tilde{D}_{CB}^{j}$ and $\tilde{D}_{CB,i}$ are separated from each other by the integrated data processing. In order to improve the accuracy of $\tilde{D}_{CB}^{j}$ and $\tilde{D}_{CB,i}$ separation, the following constraints are used: each receiver has four or more satellites in the same epoch; each satellite is observed by more than 30 receivers simultaneously; and five GEO satellites are observed at the same time.

As can be seen from the calculation results, part of the Beidou monitoring receiver $\tilde{D}_{CB,i}$ has a jump (shown in Fig. 1), which is due to replace the receiver, the results will not serve as statistical content.

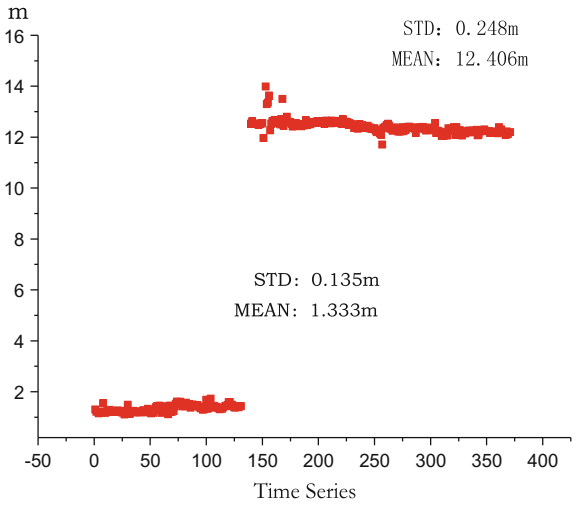

Fig. 1 DCB jump when the receiver was replaced

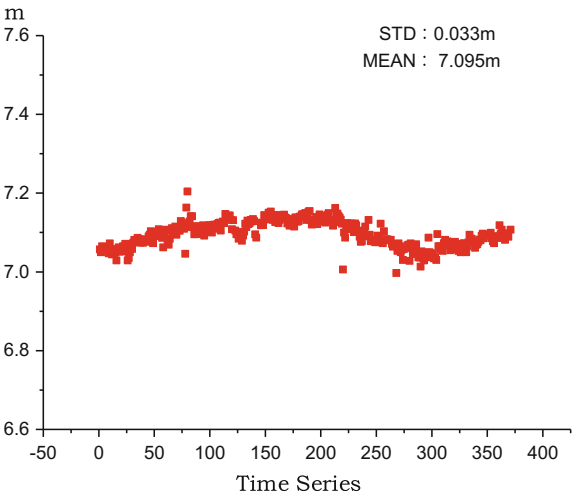

Fig. 2 The curve of one receiver's DCB

Under normal circumstances (no replacement receiver or receiver is not abnormal), $\tilde{D}_{CB,i}$ is a continuous curve (as shown in Figs. 2 and 3), can be used to monitor and evaluate the receiver hardware delay stability.

The statistical standard deviation (STD) of the data of the Beidou monitoring receiver is less than 1 ns (0.3 m) (shown in Fig. 4), which shows that the stability of the receiver hardware delay is less than 1 ns. Some receiver's stability of the delay is within 0.5 ns (as shown in Table 1).

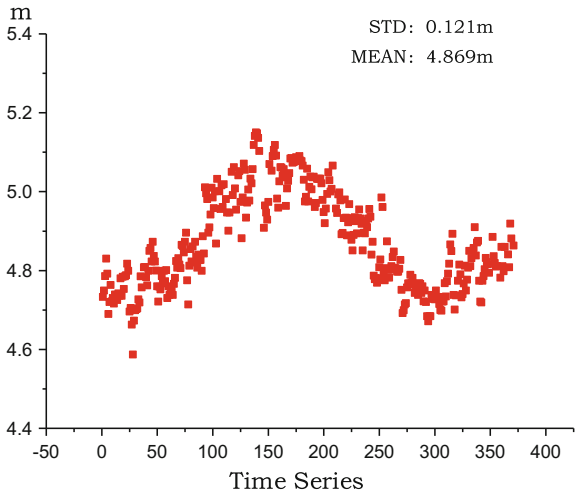

Fig. 3 The curve of one receiver's DCB

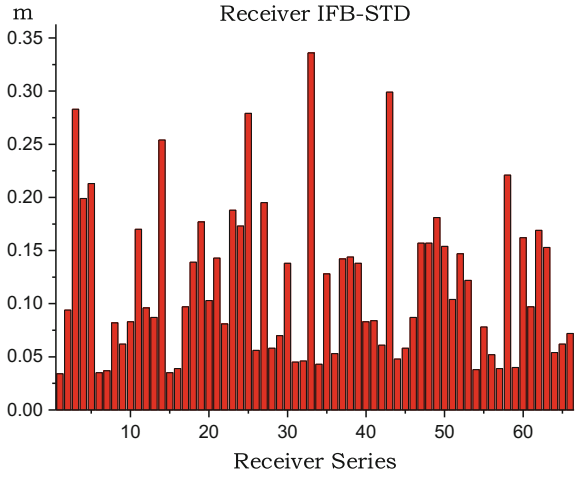

Fig. 4 Histogram of receivers' DCB

Table 1 Statistics of receivers' DCB

Receiver's DCB(STD) (m)	Number	Percent
0.0–0.1	35	53.0
0.1–0.2	24	36.3
0.2–0.3	6	9.2
>0.3	1	1.5

4 Conclusions and Discussion

Based on the characteristics of the BDS triple-frequency observation data, the combination of B1/B2/B3 code observation without ionospheric delay, tropospheric delay, and topocentric satellite distance is formed. Based on this triple-frequency combination observation, This method can effectively avoid the influence of ionospheric modeling error or mapping error. This method can be used to monitor the receiver's inter-frequency bias (IFB). According to the statistical results, the standard deviation of IFB between BDS monitoring receivers is less than 1 ns (0.3 m), and some receivers can reach the standard deviation of 0.5 ns, which shows that the stability of receiver hardware delay is good, the results show that the method can effectively monitor and evaluate the BDS monitoring receiver code error between the changes.

References

1. Yuan Y, Ou J (1999) The effects of instrumental bias in GPS observation on determining ionospheric delay and the methods of its calibration. Acta Geodaetica et Cartographic SINLGA 28(2):110–114
2. Song X, Yang X, Jiao W (2009) Determination of GPS receiver's DCB. J Geodesy Geodyn 29(1):127–131
3. Zhang W, Qiu W, Chang X (2013) Estimation of GPS differential code delay based on spherical harmonic function model. Bull Surveying Mapp 6:19–21
4. Xie Y, Wu J, Cheng J, Liu W (2014) Global ionospheric TEC modeling using measured GPS and GLONASS. Geomatics Inf Sci Wuhan Univ 39(8):930–934
5. Zhang B, Yuan Y, Ou J (2016) Short-term temporal variability of GPS receiver's differential code biases (DCB): retrieving and modeling. Chin J Geophys 59(1):101–115
6. Tang L, Lv C, Gao P, Lin X (2011) Receiver P1-P2 DCB estimate with PPP. J Geomatics 36(6):8–10
7. Fan L, Zhong S, Li Z, Ou J (2016) Effect of tracking station distribution the estimation of differential code biases by GPS satellites based on uncombined precise point positioning. Geomatics Inf Sci Wuhan Univ 41(3):316–321
8. Wu X, Liu L, Ping J, Dong E (2010) Separation methods of TGD and IFB for compass system. In: Proceeding of CSNC 2010, Beijing, pp 1451–1456
9. Wu X, Ping J, Liu L (2011) Hardware delay solution of regional satellite navigation system. Geomatics Inf Sci Wuhan Univ 36(10):1218–1221
10. Fan J, Wu X, Li Y, Wei G (2013) Compass satellite DCB parameter accuracy assessment based on tri-frequency data. Chin Space Sci Technol 2013(4):62–70
11. Xue J, Shuli S, Zhu W (2015) Global ionosphere model based on BDS/GPS dual-system observations. Scientia Sinica Physica Mechanica Astronomica 45:079505
12. Shu B, Liu H, Zhang M, Wu D (2016) Evaluation and analysis of BDS instrumental biases. Geomatics Inf Sci Wuhan Univ 41(2):279–284
13. Chao YC (1997) Real time implementation of the wide area augmentation system for the global positioning system with an emphasis on ionospheric modeling. Stanford University

BDS Multipath Real-Time Estimation Based on Generalized Regression Neural Network

Zongpeng Pan, Hongzhou Chai, Yang Chong, Yulong Kong and Rui Wang

Abstract Multipath is the main factor that affects the quality of the pseudo-range observation and the single point positioning. It is difficult to model and weaken the effect of multipath, due to its nonlinear and time-varying. This contribution presents a multipath real-time estimation method based on generalized regression neural network (GRNN). The real-time multipath is estimated using training samples based on sliding window data. Due to the nonlinear approximation property of GRNN, the BDS multipath is effectively reduced. Finally, the validity of real time multipath estimation based on GRNN is verified using MGEX data.

Keywords Multipath · BDS · Generalized regression neural network · GEO/IGSO/MEO

1 Introduction

The multipath (MP) is caused by the interference effect of the indirect satellite signal and the direct satellite signal. It can affect the quality of the pseudo-range observation and introduce bias in pseudo-range observation. Multipath is caused by the reflection satellite signal from ground objects, the satellite body reflection and scattering of atmosphere. Meanwhile, the reflection satellite signal from ground objects is the main source [1]. Multipath is the main factor that jeopardizes the quality of the pseudo-range observation and the single point positioning. Geng and Bock [2] showed that severe multipath can slow down the convergence of Precise Point Positioning (PPP) and the reliability of PPP ambiguity resolution.

In GNSS data processing, multipath error can be analyzed through a linear combination of pseudo-range and carrier phase observations [3], also called MP observation. With the development of Beidou satellite navigation system (BDS),

Z. Pan (✉) · H. Chai · Y. Chong · Y. Kong · R. Wang
Institute of Surveying and Mapping, Information Engineering University, Zhengzhou 450001, China
e-mail: panzongpeng@yeah.net

J. Sun et al. (eds.), *China Satellite Navigation Conference (CSNC) 2017 Proceedings: Volume I*, Lecture Notes in Electrical Engineering 437,
DOI 10.1007/978-981-10-4588-2_51

the characteristics of BDS pseudo-range measurement have been widely studied. Hauschild et al. [4], Montenbruck et al. [5, 6] and Wanninger et al. [7] analyzed the MP observations of BDS and demonstrated that BDS pseudo-range has code bias variations. BDS code bias variations are satellite, frequency and elevation-dependent, and it can introduce bias and variations in IGSO/MEO MP observations. Wanninger et al. [7] analyzed these code bias variations based on observation data of Multi-GNSS Experiment campaign (MGEX) and proposed two elevation-dependent piecewise linear models for IGSO and MEO satellites. However, there is no analysis on GEO satellites. Lou et al. [8] proposed a method for modeling the pseudo-range characteristics of GEO satellites based on geographically wide distribution of reference networks. Code bias variations of BDS satellites can be fitted by a third-order polynomial model [8]. After applying the code bias variations corrections, it can effectively improve the convergence of single frequency PPP and success rate of BDS long baseline ambiguity resolution. Shi et al. [3] analyzed multipath error of BDS GEO/IGSO, indicating that it is significantly larger than multipath of GPS satellites. Wang et al. [9] proposed using wavelet transform to extract the low-frequency part of GEO multipath error. By correcting the observations with low-frequency multipath of the previous day, it can improve the performance of BDS single point positioning [9]. Multipath extraction method mainly based on the characteristics of frequency and period of multipath, such as wavelet transform and sidereal filter. The carrier phase smoothing pseudo-range method can also use to weaken the multipath error.

It is difficult to model and weaken the effect of multipath, due to its nonlinear and time-varying. Therefore, this contribution proposes a multipath real-time estimation method based on generalized regression neural network (GRNN). The real-time multipath is estimated using training samples based on sliding window MP observations. Due to the nonlinear approximation property of GRNN [10–12], the BDS multipath is effectively reduced. The second part of this contribution is the construction of MP measurement and multipath real-time estimation method based on GRNN. The third part is the experimental and results analysis, and the final part gives the conclusion.

2 Mathematical Model

2.1 The Measurement of Multipath

Multipath error can be analyzed through a linear combination of pseudo-range and carrier phase observations, also called MP observation. For a satellite s observed by receiver r, considering hardware delays in code observations of receiver and satellite, the BDS pseudo-range and carrier phase measurements can be expressed as

$$P_{i,r}^{s} = \rho_{r}^{s} + I_{i,r}^{s} + b_{P_i,r} - b_{P_i}^{s} + MP_i + \varepsilon(P_{i,r}^{s}) \tag{1}$$

$$\lambda_i \varphi_{i,r}^{s} = \rho_{r}^{s} - I_{i,r}^{s} + \lambda_i N_{i,r}^{s} + \varepsilon(\varphi_{i,r}^{s}) \tag{2}$$

where $\varphi_{i,r}^{s}$ and $P_{i,r}^{s}$ are carrier phase and code observations of frequency i, the subscript r for station number, superscript s for any satellite, ρ_{r}^{s} is geometric component which include geometric distance between satellite and receiver, clock error of satellite and receiver, orbit error and tropospheric delay on the path. $b_{P_i,r}$ and $b_{P_i}^{s}$ are hardware delays in code observations of receiver and satellite. $I_{i,r}^{s}$ is ionosphere delay on the path, MP_i is the multipath of frequency l, $N_{i,r}^{s}$ is phase ambiguity which include initial phase bias. $\varepsilon(\varphi_{i,r}^{s})$ and $\varepsilon(P_{i,r}^{s})$ are carrier phase and code measurement noise and other un-modeled errors, λ_i is the wavelength of frequency i.

From Eq. (1), it must to eliminate the geometric and ionosphere delay in pseudo-range measurement in order to obtain multipath. Multipath error can be analyzed through a linear combination of pseudo-range and carrier phase observations, which can be expressed as

$$MP_i^{s} = P_{i,r}^{s} - \frac{f_i^2 + f_j^2}{f_i^2 - f_j^2}\lambda_i \varphi_{i,r}^{s} + \frac{2f_j^2}{f_i^2 - f_j^2}\lambda_i \varphi_{j,r}^{s} - B_{i,r}^{s} \tag{3}$$

$$B_{i,r}^{s} = -\frac{f_i^2 + f_j^2}{f_i^2 - f_j^2}\lambda_i N_{i,r}^{s} + \frac{2f_j^2}{f_i^2 - f_j^2}\lambda_i N_{j,r}^{s} + (b_{P_i,r} - b_{P_i}^{s}) \tag{4}$$

where, $B_{i,r}^{s}$ contains the linear combination of the phase ambiguities and the constant part of hardware delays. It can be obtained by averaging the whole arc data for the post data processing or by multi-epoch data smoothing for real-time data processing. The MP observations eliminate geometric distance between satellite and station, satellite and receiver clock error, orbit error, troposphere delay and ionosphere delay error, containing only code noise and multipath error. It must be noted that the MP observations also contain the carrier phase multipath effect. It can be ignored when compared with pseudo-range observation noise. Due to the maximum value of carrier phase multipath is less than a quarter of phase wavelength. Under normal circumstances, the pseudo-range noise is white noise. However, due to the influence of multipath error, the MP measurement shows slow change trend and correlation.

2.2 Generalized Regression Neural Network Model

Generalized regression neural network is based on mathematical statistics regression. It can generalize the nonlinear relation between the sample data. GRNN is

widely used in system modeling and prediction. In this contribution, GRNN is applied to estimate the BDS multipath error. GRNN is a nonlinear regression model. For nonlinear time series, the model can be expressed as [11]

$$Y_k = f(X_k) + \varepsilon_k \tag{5}$$

where, $f(\cdot)$ is regression function, ε_k for white noise. Given a set of training sample $\{(x_i, y_i)\}_{i=1}^{n}$, the regression function can be constructed by GRNN. The regression function can be expressed as a kernel function of multivariate normal distribution [11], as shown below

$$\hat{f}(X) = \sum_{i=1}^{n} y_i \exp\left(-\frac{(X - x_i)^2}{2\sigma^2}\right) \Big/ \sum_{i=1}^{n} \exp\left(-\frac{(X - x_i)^2}{2\sigma^2}\right) \tag{6}$$

where, σ is smoothing factor, which is the only adjustment parameter in GRNN. The model of GRNN includes input layer, mode layer, summation layer and output layer. For multipath real-time estimation, the process of GRNN is as follows

1. the training sample pairs $\{(y_{i-1}, y_i)\}_{i=k-1}^{k-n}$, which are from MP observations in the sliding window, are the input layer of the GRNN model. The current multipath error is as the output parameter, namely the output layer.
2. Based on the sample data of the input layer, the mode layer uses different smoothing factors to calculate the Gauss kernel function.
3. In summation layer, the weighted average of the Gauss kernel function is constructed based on Eq. (6).
4. Finally, output the estimation of current multipath error.

Multipath real-time estimation is based on the assumption that there has a nonlinear relationship between current multipath and MP observations in the sliding window. Then the GRNN is applied to construct this nonlinear relationship.

3 Experiments and Results Analysis

In order to validate the proposed GRNN multipath estimation method, the data of MRO1, in the 250th days of 2016, from MGEX is used to obtain MP observations of BDS GEO/IGSO/MEO satellites. The data sampling interval is 30 s, the satellite cut-off angle is 10°. Firstly, the multipath observation is constructed by using the linear combination of pseudo-range and carrier phase measurement, and the multipath error of BDS GEO/IGSO/MEO is analyzed. Secondly, the BDS code bias variations which are elevation-dependent. Its influence on BDS multipath is analyzed. Finally, the multipath error of BDS is estimated based on GRNN and the validity of GRNN multipath estimation method is verified.

3.1 BDS Multipath Characteristics Analysis

The multipath error time series and elevation of the BDS GEO/IGSO/MEO satellite in B1 frequency are shown in Fig. 1. Among Fig. 1, (a) is for GEO-C02, (b) is for IGSO-C07 and (c) is for MEO-C12 multipath time series, respectively.

It can be seen from Fig. 1, the elevation of GEO satellite has no significant variation, but the series of GEO multipath shows fluctuation. The influence of multipath on GEO code observation is obvious. The elevation of IGSO/MEO satellite has a significant variation and the multipath series have the corresponding change trend with the elevation. The reason for this phenomenon is that the code noise is large with low elevation of satellite. At the same time, there are obvious correlation and variations in BDS MP series. The characteristic of BDS multipath is not white noise. The variations of multipath are different with respect to different satellite. Therefore, the correlation analysis of multipath error of GEO/IGSO/MEO satellites is given. Figure 2 shows the autocorrelation of multipath error of BDS GEO/IGSO/MEO satellites.

As can be seen from Fig. 2, there are obvious correlation in multipath sequences of GEO/IGSO/MEO satellite. The correlation of MEO multipath is stronger than GEO and IGSO multipath, and the correlation decreases with the extension of lag time. The correlation of GEO and IGSO satellite multipath is consistent. With the extension of lag time, the correlation decreases gradually and tends to zero.

Wanninger et al. [7] demonstrated that the BDS multipath error has a variation, which is introduced by code bias variations in BDS pseudo-range. The code bias variations are elevation-dependent and can be corrected effectively by linear model

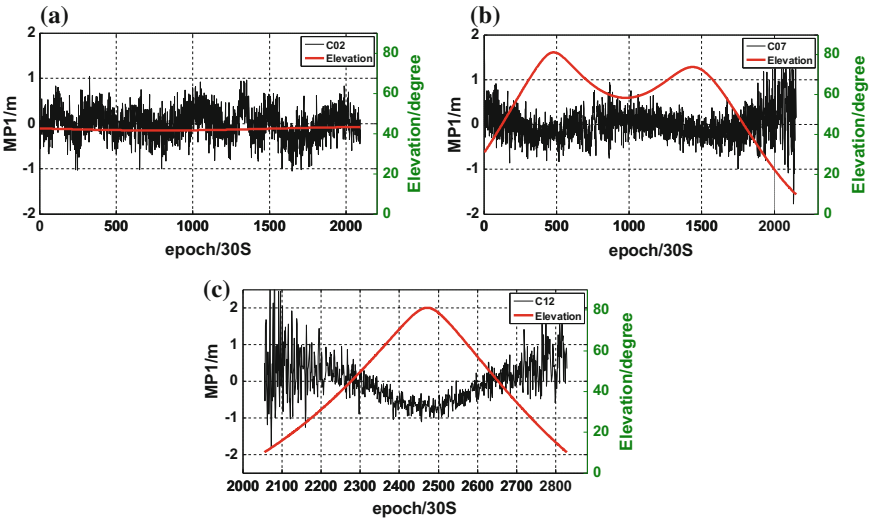

Fig. 1 BDS GEO/IGSO/MEO multipath time series

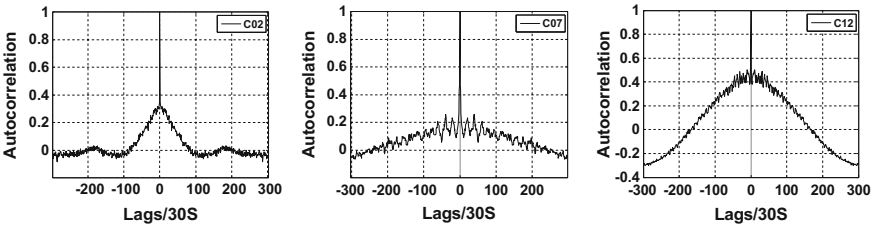

Fig. 2 Autocorrelation of BDS multipath error

or polynomial model [13]. However, the correction model is only for IGSO and MEO. Lou et al. [8] proposed a method for modeling the code bias variations based on geographically wide distribution of reference networks. Code bias variations of BDS satellites can be fitted by a third-order polynomial model.

3.2 Analyze the Influence of Code Variations on Multipath

BDS code bias variations are not constants and are satellite, frequency and elevation-dependent. A third-order polynomial is proposed to fit the code bias variations by Lou et al. [8]. The equation is as follows [8]

$$b_{P_i}^s = a_1 \cdot E + a_2 \cdot E^2 + a_3 \cdot E^3 \tag{13}$$

where, a_1, a_2, a_3 is polynomial coefficient, E is elevation in radians. The remaining symbols are consistent with the previous. As shown in Table 1, the polynomial coefficient of code bias variations is given by Lou et al. [8].

BDS code bias variations are satellite, frequency and elevation-dependent, and it can introduce bias and variations in multipath series. The BDS multipath series before and after correction of code bias variations are shown in Fig. 3.

It can be seen from Fig. 3, the polynomial model of code bias variations can reflect the multipath deviation, especially for the MEO and IGSO satellite. After the correction of code bias variations, the divergence in the MP sequence is significantly reduced. However, the value of GEO code bias variations has no significant variation. Due to the fluctuation of the elevation of GEO satellite is small. Table 2

Table 1 Correction coefficient of BDS code bias variations

Coefficient	GEO/IGSO				MEO		
	B1	B2	B3		B1	B2	B3
a1	−0.590	−0.257	−0.102		−0.946	−0.598	−0.177
a2	1.624	0.995	0.748		2.158	1.635	0.652
a3	−0.645	−0.381	−0.307		−0.642	−0.556	−0.178

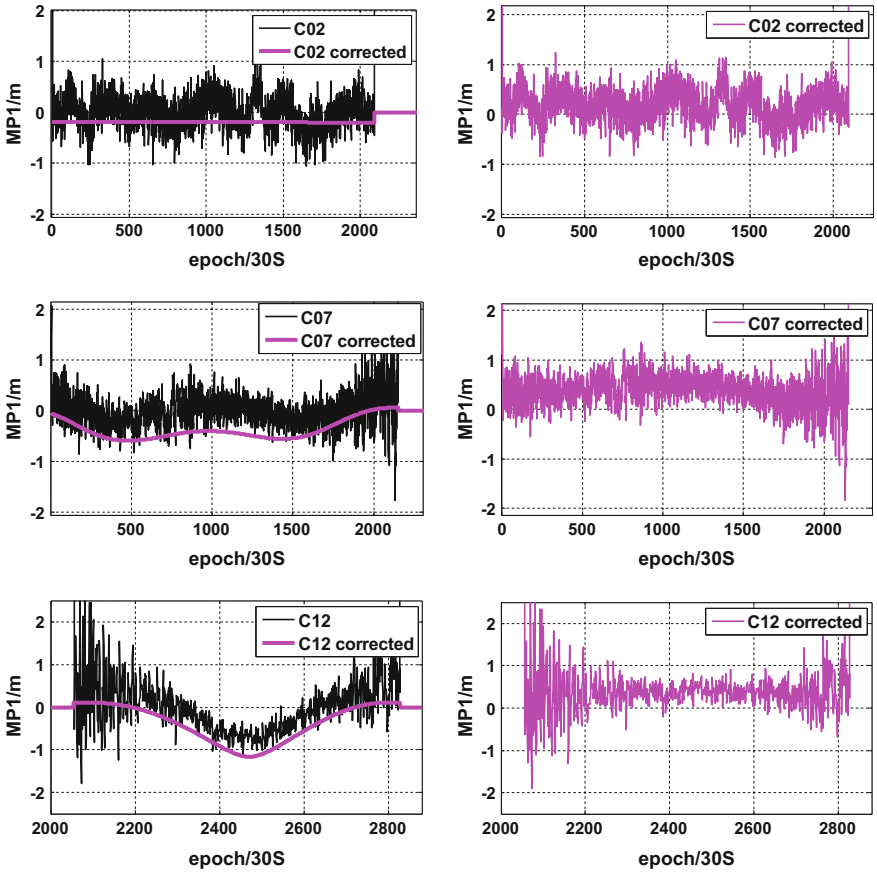

Fig. 3 GEO/IGSO/MEO multipath series before and after correction of code bias variations

gives the standard deviation (STD) statistics of multipath after correction of code bias variations.

From the statistical results in Table 2, we can see that the multipath error of MEO is reduced obviously after the correction of code bias variations. However, the reduced STD of GEO and IGSO multipath error is not significant.

Table 2 STD of multipath before and after correction of code bias variations (unit: m)

Satellite type	GEO(C02)	IGSO(C07)	MEO(C12)
Original MP	0.34	0.35	0.62
Correction of code bias variations	0.34	0.33	0.45

3.3 *Multipath Real Time Estimation Based on GRNN*

In order to validate the proposed GRNN multipath estimation method, the BDS multipath error is estimated using GRNN. The sliding window size is set to 20 epochs of multipath series. The detail steps to estimate multipath is described in Sect. 2.2. Figure 4 shows the multipath series of the BDS GEO/IGSO/MEO satellites before and after correction of GRNN multipath estimation.

As can be seen from Fig. 4, the GRNN multipath estimation method can effectively reflect the trend of multipath error of GEO/IGSO/MEO satellite. The statistical result from Table 3 shows that after correction of GRNN multipath estimation, the divergence in the MP sequence is significantly reduced. The STD of GEO/IGSO/MEO multipath error is decreasing significant after correction of GRNN multipath estimation, which verifies the feasibility of GRNN multipath estimation method.

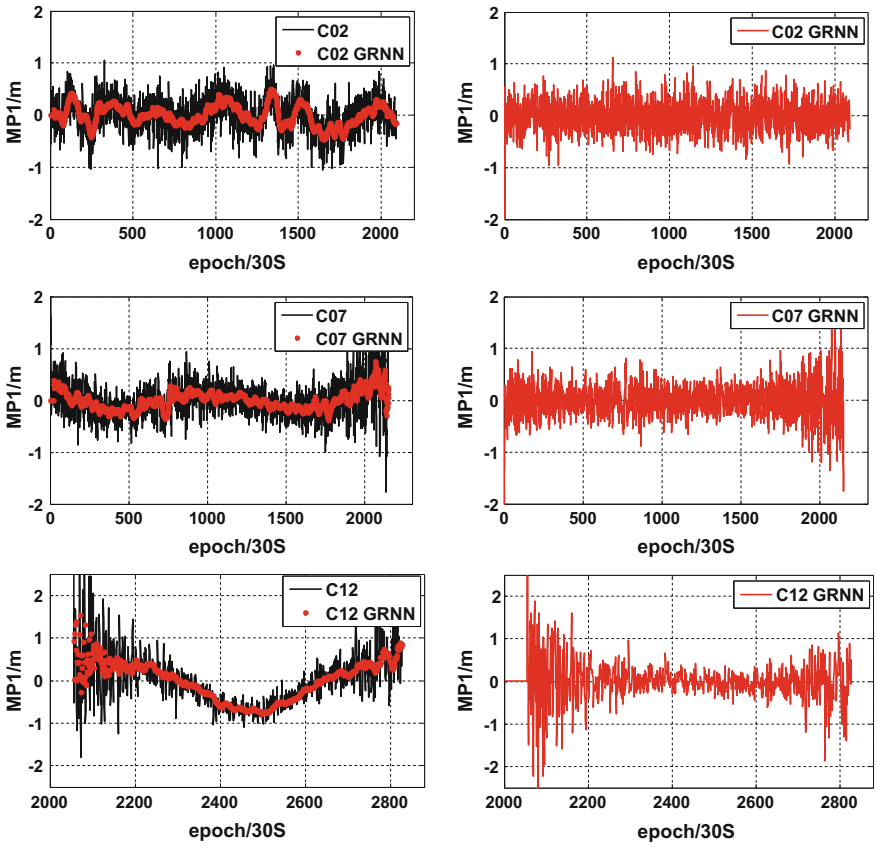

Fig. 4 GEO/IGSO/MEO multipath before and after correction of GRNN multipath estimation

Table 3 STD multipath error before and after correction of GRNN multipath estimation (unit: m)

Satellite type	GEO(C02)	IGSO(C07)	MEO(C12)
Original MP	0.34	0.35	0.62
correction of GRNN MP estimation	0.29	0.31	0.47

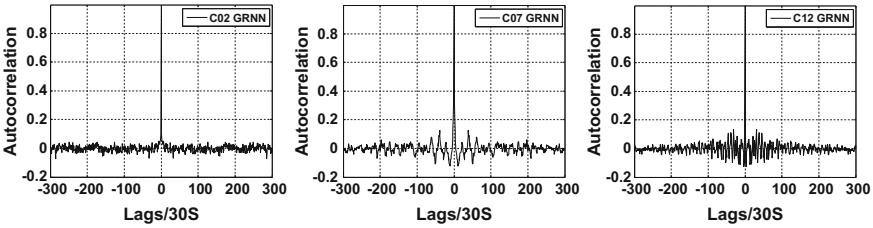

Fig. 5 Autocorrelation of multipath error after correction of GRNN multipath estimation

Meanwhile, the correlation of multipath sequences is also decreased after GRNN processing. Figure 5 shows the autocorrelation of multipath sequences after correction of GRNN multipath estimation. Compared with Fig. 2, the correlation of multipath error of GEO/IGSO/MEO is effectively reduced. This further verifies that GRNN can effectively approximate the local characteristics of multipath and reduce its correlation.

4 Conclusion

In this contribution, the multipath error of BDS GEO/IGSO/MEO satellites is analyzed. At the same time, BDS code bias variations are satellite, frequency and elevation-dependent, and it can introduce bias and variations in multipath series. The statistical characteristics of multipath before and after the correction of code bias variations are analyzed. The result shows that after the correction of code bias variations, the divergence in the MP sequence of IGSO/MEO is significantly reduced. However, GEO multipath has no significant variation after correction. Due to the fluctuation of the elevation of GEO satellite is small. It is difficult to model and weaken the effect of multipath, due to its nonlinear and time-varying. Therefore, this contribution investigates a multipath real-time estimation method based on generalized regression neural network. The experiment results show that the trend and correlation of multipath error can be effectively reduced after correction of GRNN multipath estimation, which verify the validity of the GRNN multipath estimation method.

Acknowledgements Thanks to the IGS MGEX for providing GNSS observations. This work was supported by National Natural Science Foundation of China (Grant No. 41274045, No. 41574010) and State Key Laboratory of Geo-information engineering (No. SKLGIE2015-Z-1-1).

References

1. Chen K (2012) Research on theory and methodology of GNSS multipath estimation. PLA Information Engineering University
2. Geng J, Bock Y (2014) Triple-frequency GPS precise point positioning with rapid ambiguity resolution. J Geod 87(1):449–460
3. Shi C, Zhao Q, Hu Z et al (2013) Precise relative positioning using real tracking data from COMPASS GEO and IGSO satellites. GPS Solut 17(1):103–119
4. Hauschild A, Montenbruck O, Sleewaegen JM et al (2012) Characterization of compass M-1 signals. GPS Solut 16(1):117–126
5. Montenbruck O, Hauschild A, Steigenberger P et al (2013) Initial assessment of the COMPASS/BeiDou-2 regional navigation satellite system. GPS Solut 17(2):211–222
6. Montenbruck O, Rizos C, Weber R et al (2013) Getting a grip on multi-GNSS-the international GNSS service MGEX campaign. GPS World 24:44–49 (2013-07)
7. Wanninger L, Beer S (2015) BeiDou satellite-induced code pseudorange variations: diagnosis and therapy. GPS Solut 19(4):639–648
8. Lou Y, Gong X, Gu S et al (2016) Assessment of code bias variations of BDS triple-frequency signals and their impacts on ambiguity resolution for long baselines. GPS Solut 1–10
9. Wang G, Jong K, Zhao Q et al (2015) Multipath analysis of code measurements for BeiDou geostationary satellites. GPS Solut 19(1):129–139
10. Wang W, Rong Z, Fan G (2011) Study on simulating method of navigation satellite clock error using generalized regression neural network. J Syst Simul 23(11):2339–2345
11. Fan G, Wang W, Xi X (2010) Modeling of ionosphere VTEC using generalized regression neural network. Acta Geodaetica Cartogr Sin 39(1):16–21
12. Lei Y, Zhao D (2013) Application of generalized regression neural network in short-time prediction for satellite clock error. J Astron Metrol Meas 33(4):39–44
13. Yang W, Tong H, Pan L et al (2016) Analysis and correction of BDS code multipath bias. In: China satellite navigation conference (CSNC) 2016 proceedings, vol III

Ephemeris Type B Fault Detection for BDS

Guanlong Wang, Xiaowei Cui, Yun Zhang and Liu He

Abstract An error of satellite position will therefore cause an error for user location. For a newly rise satellite, this paper proposes the method, called "EE-TE" to detect current broadcast ephemeris type B fault based on the previous pass validated ephemeris for BDS. Using an entire year of ephemeris data for all BDS satellites, the key parameters such as the position error covariance matrix inflation factor and the minimum detectable error are divided under the setting the probability of false detection and the probability of missing detection. Finally, the validity of the proposed method is verified by means of adding artificial ephemeris errors, and the MDE values is adequate to meet navigation availability requirements for LAAS.

Keywords BDS · Type B ephemeris fault · MDE · EE-TE

1 Introduction

Broadcast ephemerides is basic data to compute satellite locations and user position, together with ranging measurements. Difference technique was developed to eliminate the correlation ranging errors sources between a reference station receiver and user receivers. However, the satellite position error components orthogonal to the satellite line-of-sight (LOS) direction will could caused differential ranging error, which are significant with regard to the stringent alert limit requirements specified in LAAS with integrity risk of approximately 2e-7/approach [8].

Two basic types of orbit ephemeris threat are recognized [4], the second type also being subdivided into two cases:

G. Wang (✉) · X. Cui · Y. Zhang
Department of Electronic Engineering, Tsinghua University, Beijing 100084, China
e-mail: wgl14@mails.tsinghua.edu.cn

L. He
61773 Regiment, Wulumuqi 831400, China
e-mail: 1605343608@qq.com.cn

J. Sun et al. (eds.), *China Satellite Navigation Conference (CSNC) 2017 Proceedings: Volume I*, Lecture Notes in Electrical Engineering 437,
DOI 10.1007/978-981-10-4588-2_52

- Type A: The ephemeris data is erroneous following a satellite maneuver
- Type B: The ephemeris data is erroneous, but no satellite maneuver is involved.
  - Case I: The prior validated ephemeris is broadcast one hour ago, and both on one pass. In general, this case is similar for all orbit types of satellites.
  - Case II: For a newly rise satellites, the last available validated ephemeris received on the previous pass, it is necessary to study separately for different orbits types of satellite.

The likelihood of Type B failures is higher than Type A because orbit ephemeris uploads and broadcast ephemeris changeovers are frequent (once every one hour for BDS) whereas spacecraft maneuvers are rare [2]. So This paper focuses on the Type B ephemeris failures monitor. GPS proposed a method, called Yesterday's Ephemeris-Today's Ephemeris (YE-TE) to detect type B ephemeris fault with above case II. The minimum detectable error (MDE) derive from "YE-TE" is less than 3500 m [9]. Unlike the GPS, BDS constellation including GEO, IGSO and MEO satellites, therefore, the "YE-TE" method can't be suitable for the BDS.

Prior work is focused on post-ephemeris accuracy evaluation for BDS [5]. The ephemeris anomaly detection only checks the consistency of broadcast ephemeris and does not concern integrity risk generate by ephemeris fault [3]. In this paper, for the case II of type B ephemeris fault detect of BDS, the means of Ephemeris Extrapolate-Today's Ephemeris (EE-TE) is used to. Then, the key parameters such as the MDE and the inflation factor (IF) of satellite position covariation matrix are calculated under set the fault-free alarm probability (FFA) and the probability of missing detection (MD). Finally, the EE-TE is validated by adding known faults in the ephemeris data to verify that the MDE value satisfies the requirements of application integrity and availability.

This paper collects all the satellite broadcast ephemeris of BDS, which is provided by IGS Wuhan Data Center from 2014-08-21 to 2015-8-20.

2 Protection Levels and Minimum Detectable Error

For a navigation with LAAS, users continuously generate a vertical protection level (VPL) that takes into account the satellite position error [6]. Defining $\vec{x}$ to be the vector displacement between the user antenna and the reference antennas and $\delta\vec{e}_i$ as the error in the LOS unit vector to satellite i, it is shown that.

$$\delta\rho_i = \delta\vec{e}_i^{\,T}\vec{x} \tag{1}$$

and that $\delta\vec{e}_i$ can be expressed as a function of the satellite position error $\delta\vec{r}$.

$$\delta\vec{e}_i = \frac{\delta\vec{r}_i^T\left(I - \vec{e}_i\vec{e}_i^T\right)}{r_i}\vec{x} \tag{2}$$

where r_i is the scalar range to the satellite i, I is the 3 × 3 identity matrix. When this ephemeris error are projected into the user position domain, the resulting position estimate error for vertical direction will be:

$$\delta\vec{x}_{vert,i} = S_{vert,i}\frac{\delta\vec{r}_i^T\left(I - \vec{e}_i\vec{e}_i^T\right)}{r_i}\vec{x} + \sqrt{\sum_{j=1}^{n} S_{vert,j}^2\sigma_j^2} \tag{3}$$

where S is the weighted-least-squares projection matrix. *Svert, i* is the *i*th element of 3rd row of S. Then define a missed detection multiplier k_{MD} based on the assumed prior MD. write an upper bound on vertical position error, call $VPL(i)$ [8].

$$VPL(i) \le \frac{MDE}{r_i}\left|S_{vert,i}\right|\left\|\vec{x}\right\| + k_{MD}\sqrt{\sum_{j=1}^{n} S_{vert,j}^2\sigma_j^2} \tag{4}$$

At approach, the user computed max (VPL(i)), are compared with a predefined position error bound known as the vertical alert limit (VAL). For ensure navigation integrity, $VPL(i) < VAL$ must is. It is clear that the smaller the MDE value, the smaller the risk of ephemeris integrity for differential localization.

3 YE-TE Is not Suitable for BDS

GPS proposed YE-TE method to detect type B ephemeris fault in keep with the MEO satellite orbital period is about 24 h. According to the number of prior validated ephemeris, this means is divided into two classes: zero order hold (ZOH) and first order hold (FOH). Use the last validated ephemeris of the prior day, which is always 24 h old, the 15-element of ephemeris parameter vector can first be referenced to the toe corresponding to the current ephemeris by advancing the mean anomaly (M0), inclination (i0), and longitude of the ascending node (Ω0) by mean of executed using the rates for these parameters, that called ZOH. If there have two prior days of validated ephemeris data, the natural daily variations in the parameters can be partially captured using FOH [2]. Consider the YE-TE method for type B ephemeris fault detection for BDS IGSO satellite, that orbital period is also 24 h. Figure 1a, b illustrated the BDS IGSO-8 satellite position error distribution by ZOH and FOH.

From the Fig. 1a, b, it can be observed that the satellite position error of IGSO of BDS is obviously larger than that of GPS (BDS ZOH largest value is close to 6000 m, and exceed 10,000 m for FOH. GPS ZOH largest value is less than

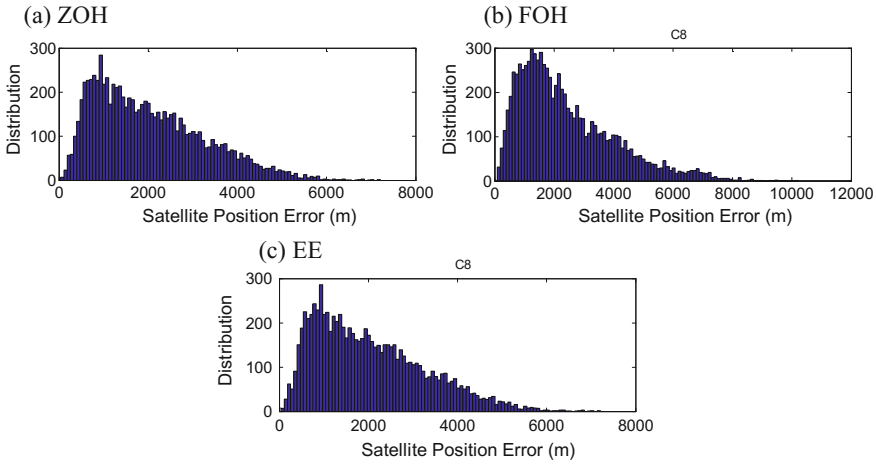

Fig. 1 IGSO-8 satellite position error distribution

2500 m, and FOH just 800 m). The reason can be explained by the sensitivity of satellite position error to variations of the broadcast ephemeris parameters.

Given the toe and Defined p = [p1, p2, …, p15] = [A, e, ω, Δn, M0, Ω0, Ωd, M0, i0, idot, Cuc, Cus, Crc, Crs, Cic, Cis], we can compute the sensitivity matrix for BDS satellite position error to variations of p.

$$\begin{bmatrix} \delta x(t) \\ \delta y(t) \\ \delta z(t) \end{bmatrix} = \begin{bmatrix} \frac{\partial f(p,\mathrm{toe},t)}{\partial p_1} \cdots \frac{\partial f(p,\mathrm{toe},t)}{\partial p_{15}} \\ \frac{\partial g(p,\mathrm{toe},t)}{\partial p_1} \cdots \frac{\partial g(p,\mathrm{toe},t)}{\partial p_{15}} \\ \frac{\partial h(p,\mathrm{toe},t)}{\partial p_1} \cdots \frac{\partial h(p,\mathrm{toe},t)}{\partial p_{15}} \end{bmatrix} \begin{bmatrix} \delta p_1 \\ \vdots \\ \delta p_{15} \end{bmatrix} \tag{5}$$

where f, g and h are nonlinear functions defined by the satellite position algorithms in BDS ICD-2013 [1]. In parallel to the sensitivity matrix computation, a full year of ephemerides from BDS IGSO-8 satellites was used to computed the standard deviations of the daily parameter variations for each ephemeris parameter ($\sigma p_{(i)}$). Using the sensitivity matrix and the $\sigma p_{(i)}$ it is possible to determine 1σ satellite position error variations due to nominal daily variations on the individual ephemeris parameters. Figure 2 shows IGSO-8 the 1σ satellite position error contribution due to the 1σ daily variation of each individual parameter.

The individual 1σ errors due to M0 and ω variations are not directly plotted in the figure, because daily variations in these parameters are not independent, but rather exhibit a strong negative correlation [6], but M0 + ω is plotted, and the order is about 500 m.

In Fig. 2, compare to GPS position sensitivity (Fig. 1 of [6]): the order of BDS satellite position error sensitivity to ephemeris parameters is larger than that of the

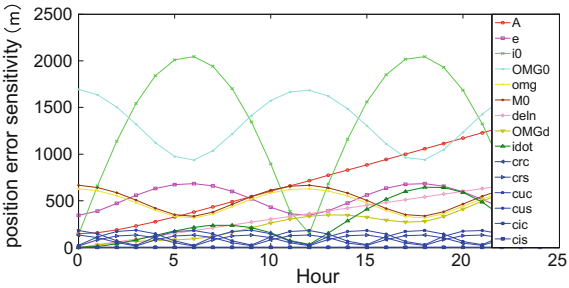

Fig. 2 Satellite position error sensitivity to parameter variations

GPS (the sensitivity error to i0 is about 6 times, to Ω0 Of the sensitive error is about 4 times, A sensitive error is about 3 times).

In conclusion, the YE-TE methods is not suitable for IGSO satellite of BDS, because the satellite orbit cycle error accumulation is larger more. And that, because the GEO satellite orbit cycle error accumulation is larger than that of the IGSO satellite and MEO satellite orbit revisit period is 7 days, so the YE-TE is not applicable to BDS ephemeris type B fault detection.

4 Detection of BDS Ephemeris Type B Fault

BDS GEO satellite has always been in view, the IGSO and MEO satellite out-view period is much smaller than the satellite orbit re-visit period, so that the case II of type B ephemeris fault detection method for BDS can be implement by EE-TE method. For a given current ephemeris and time epoch k (with k being the relative time with respect to toe: k = t − toe) we computed the satellite position vector $\vec{r}_k$, and also estimate the satellite position $\hat{r}_k$ by extrapolated using prior pass ephemeris, for the same time. The difference between the two will yield a position deviation vector $\delta\vec{r}_k$. Figure 1c uses the EE-TE method to BDS IGSO-8 satellite with 24 h interval. Compared with Fig. 1a, b, the maximum satellite position errors is approximately closed ZOH, and less than FOH.

The key of the BDS EE-TE method is to ascertain the period of prior pass ephemeris extrapolate. BDS GEO satellite prior ephemeris can select one hour before ephemeris. Figure 3a, b show the satellite elevation variations of the BDS IGSO-8 and MEO-11 satellites at three positions. In Fig. 3 it can be observed that BDS IGSO satellite out-view period are less than 8 h, MEO satellite orbital period of about 7 days, and its non-visible period are less than 20 h.

Based on the complete set of ephemerides $\delta\vec{r}_k$ data for all satellites for entire a year, we can generate fault-free empirical distributions and covariance matrices $\sum_{\delta r_k}$, and then define a normalized scalar test statistic as follows:

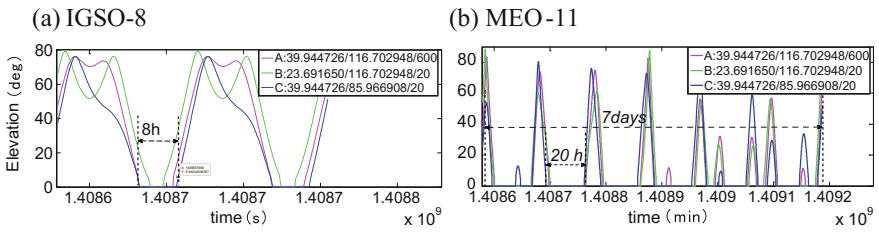

Fig. 3 IGSO-8 and MEO-11 invisible period

$$s_k = \delta\vec{r}_k^{\,T} \sum_{\delta\vec{r}_k}^{-1} \delta\vec{r}_k \tag{6}$$

The test statistic s_k is approximately chi-square distributed with three degrees of freedom. The s_k will compared with a threshold T to detect an anomalous ephemeris. The threshold T is defined as 19.763688, to ensure a probability of FFA (1.9e-4). Given an ephemeris anomaly, the test statistic will have a nearly non-central chi-square distribution. The minimum non-centrality parameter (λ) for such a distribution is 54.196099, that is consistent with the required probability of MD [6]. A satellite position error $\delta\vec{r}_e$ will be detectable if:

$$\lambda \leq \delta\vec{r}_e^{\,T} \sum_{\delta\vec{r}_k}^{-1} \delta\vec{r}_e \tag{7}$$

The maximum $\delta\vec{r}_e$ fails to satisfy this inequality defines the MDE:

$$MDE = \sqrt{\lambda \max(eig \sum_{\delta r_k})} \tag{8}$$

It is clear that small MDE values require that the $\sum_{\delta r_k}$ be small. A small covariance, in turn, can only be achieved by using a closest prior ephemeris. So that we set the BDS GEO satellite extrapolation period is 4 h, and IGSO satellite is 9 h, and MEO satellite is 20 h in this article. Using EE-TE method to one year ephemeris data, The distribution of fault-free satellite position error $\delta\vec{r}_k$ at toe is shown in Fig. 4, and the distributions of test statistic s_k is shown in Fig. 5, respectively corresponding to GEO, IGSO and MEO satellite of BDS.

For this data set, the allowable number of samples (Ns) whose values are larger than T are 8, 8, 4, respectively corresponding to GEO, IGSO and MEO satellite of BDS. But, in Fig. 5 it can be observed that the number of samples exceeding the T is bigger than Ns. To avoid this problem, the covariance matrices must be inflated (multiply by C) to reduce the number of FFAs below Ns. For the EE-TE method,

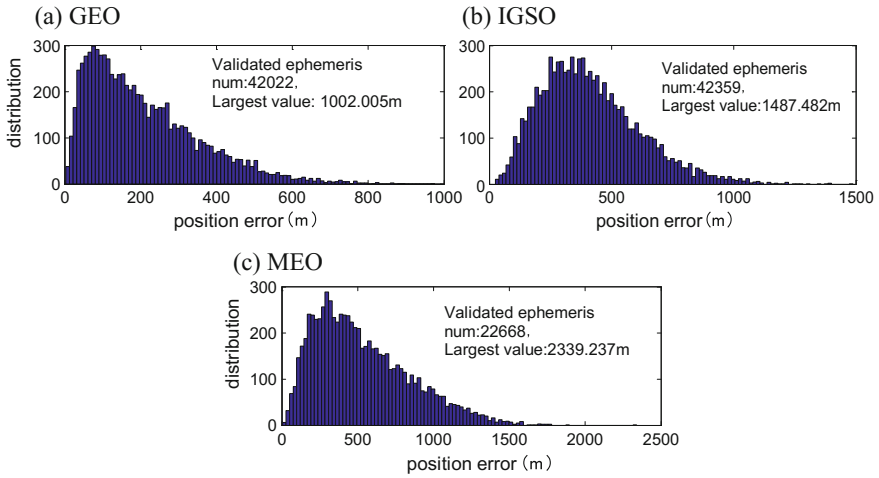

Fig. 4 Extrapolation satellite position error distribution

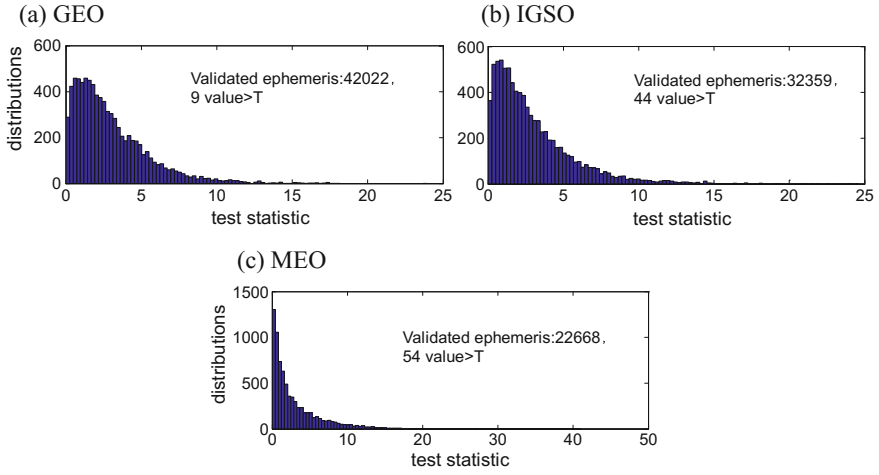

Fig. 5 Extrapolation error test statistics distribution

The C are 1.32, 1.28, 1.39, respectively corresponding to GEO, IGSO and MEO satellite of BDS.

To verify that the chi-square distribution is conservative for the adjusted test statistic, the cumulative distribution function (CDF) of the inflated test statistic data was compared with the theoretical chi-square CDF. And shown in Fig. 6. from which it can be observed that the probability, lower theoretical CDF surpasses the value of the upper empirical CDF, is 1e-4.It is possible now to compute the MDE using formula (8). The results, for individual satellites is shown in Fig. 7. From

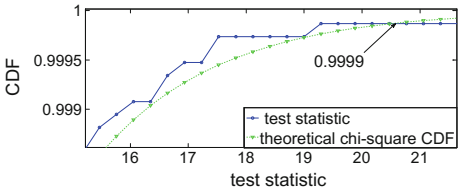

Fig. 6 Tail over-bounding of CDF for extrapolation

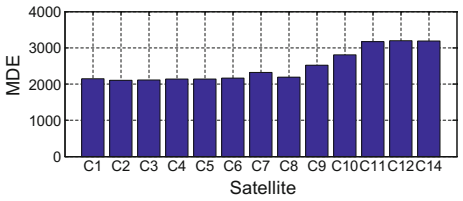

Fig. 7 MDEs for individual satellites

Fig. 7, the GEO and MEO satellites have smaller MDE variance (GEO satellite over 2100 m and MEO satellite over 3100 m), While the variance of MDE values of IGSO satellites is large, from 2100 to 2800 m.

5 Experimental Verification

Fault detection performance was also verified experimentally by deliberately injecting anomalous parameters in otherwise nominal ephemeris. For all ephemerides, position coordinates (r) were generated first with the fault-free parameters (p), and then again after introducing (one parameter at a time) an error δp to cause errors in the satellite position($r_{(fault)}$) of a magnitude similar to the derived MDE values. The true position error caused by the deliberately introduced parameter error was $\Delta r = r - r_{(fault)}$. An estimated position error was also computed $\Delta r_{(est)} = r_{(est)} - r_{(fault)}$,comparing the resulting value of s_k with the threshold T, it is determined whether or not the failure was detected.

Table 1 shows that the results of this empirical analysis agree with the analytically derived MDE values. For the GEO and IGSO satellite, there is no undetected error. For MEO satellite, the largest undetected error is 3388 m, beyond MDE value 185 m. The total number of undetected errors are 51 out of 63,712, the percentage is significantly below the allowed 1e-3 integrity constraint.

It is clear from Fig. 7 and Table 1, the BDS EE-TE is sufficient to ensure LAAS availability (max(MDE) = 3197 < 3500 m), and the EE-TE method used in this paper is effective to detect the type B ephemeris fault.

Table 1 Missed detection verification results

Satellite	Total error position generater	Error > MDE	Undetected error > MDE	Magnitude of maximum undetected error	MDE ±bin
GE0	630,330	301,769	0		
IGS0	635,385	268,378	0		
ME0-11	114,825	51,072	17	3351	18,762
ME0-12	111,165	44,690	29	3388	25,929
ME0-14	114,030	50,797	5	3377	19,021

6 Conclusions

For newly rise satellites, this paper explain YE-TE method, be used to detect type B ephemeris fault for GPS, is not suitable BDS by the sensitivity of the satellite position error to the variation of the ephemeris parameters. And then based satellite orbit re-visit period of BDS, proposed the EE-TE method to detect the current broadcast ephemeris type B fault. The simulation results show that the inflated factor of the satellite position error covariance matrix satisfies the requirement of the probability of MD. The calculated MDE can meet the requirement of LAAS CAT I availability for the fault detection of the ephemeris. It is shown that the EE-TE method for type B ephemeris fault detection is effective, which can provide reference for future ephemeris fault detection in the construction of LAAS system based on BDS.

References

1. Beidou Navigation Satellite System Signal in Space Interface Control Document Open Service Signal (ver.2.0). China Satellite Navigation Office
2. Gratton LR (2003) Orbit ephemeris monitors for category I local area augmentation of GPS. Illinois Institute of Technology
3. Liu C (2014) Real-time anomaly detection of BDS broadcast ephemeris. CSNC
4. Pullen S et al (2001) Ephemeris protection level equations and monitor algorithms for GBAS. In: Proceedings of Ion Gps Salt Lake City Ut, pp 11–14
5. Pan L, Cai C (2014) Accuracy assessment of BeiDou broadcast ephemeris. Bull Surv Mapp 9:16–18
6. Pervan B, Gratton L (2005) Orbit ephemeris monitors for local area differential GPS. IEEE Trans Aerosp Electron Syst 41(2):449–460
7. Pervan B, Chan F (2003) Detecting global positioning satellite orbit errors using short-baseline carrier-phase measurements. J Guid Control Dyn 26(1):122–131
8. Shively CA (2001) LAAS integrity risk due to satellite ephemeris faults
9. Shively CA (2001) Preliminary analysis of requirements for CAT IIIB LAAS. In: Proceedings of annual meeting of the institute of navigation

Radiation Pattern Measurement for Earth Station Antenna Based on UAV

Zheng Wang and Chunjie Qiao

Abstract Antenna pattern is an important performance parameter of antennas, which reflects the basic performance indexes and working condition. Antenna pattern measurement with high precision can be implemented by the anechoic chamber, but the environment of the anechoic chamber is not suitable for the large size ground station antenna. Given the impact of surrounding environment, it is necessary to measure the fixed antenna in open field. Since the antenna is fixed, the traditional on-site measurement schemes do not have high precision. As for the fixed ground station antenna, a solution is proposed to realize the high precision measurement by Unmanned Aerial Vehicle (UAV). UAV can flies along the orbit flexibly and conveniently to measure patterns in any plane. In order to reduce the influence of the positioning accuracy and flight leeway, the following improvements are implemented: (1) while the UAV flies, Real Time Kinematic (RTK) positioning based on Time Difference Of Arrival (TDOA) is applied to realize precise positioning; (2) Curve fitting method is used to decrease the angle deviation brought by flight leeway. The proposed method is verified by simulation. The simulation results show that the amplitude error, caused by positioning error and flight leeway, is reduced to 0.21 dB. The pointing angle deviation is 0.1°.

Keywords Antenna patterns · Measurement · Position · Curve fitting

Z. Wang (✉) · C. Qiao
College of Mechatronics Engineering and Automation, National University of Defense Technology, NUDT, Changsha, China
e-mail: zhengwang828@163.com

C. Qiao
e-mail: 13974998246@139.com

J. Sun et al. (eds.), *China Satellite Navigation Conference (CSNC) 2017 Proceedings: Volume I*, Lecture Notes in Electrical Engineering 437,
DOI 10.1007/978-981-10-4588-2_53

1 Introduction

Antenna pattern is an important performance parameter of the antenna, which reflects the basic performance indexes and working condition. High precision measurement of antenna pattern can be implemented in the anechoic chamber, but the environment of the anechoic chamber is not suitable for the large size ground station antenna. Given the impact of surrounding environment, it is necessary to measure the fixed antenna in open field. Reference [2] shows that the earth station antenna can be measured by using calibration tower, radio star or synchronous satellite, But these methods are aimed at the rotatable antenna. When the antenna is fixed, only the auxiliary antenna can be used to realize the measurement. For fixed earth station antenna, therefore, the way to ensure a flexible and convenient measurement to improve the measurement accuracy is significant.

The earth station antenna measurement can be implemented by satellites, radio star or aircraft carrying signal source that turns around the tested antenna [3–7]. In the reference [3], satellite is used to measure the earth station antenna pattern. Trajectories of the satellite or radio star is accurate, so the measuring precision is high. But it requires the antenna located in the orbit plane of the satellite or radio star, and the orbit cannot be changed, so only the patterns in the orbit plane can be measured. Different from the satellites or radio stars, the aircraft is flexible and controllable. Its flight trajectory can be adjusted according to the measurement requirements. But flight trajectory can't be controlled accurately, and positioning accuracy is not high by the traditional GPS positioning system. So the measurement error is bigger. In literature [5], the hot air balloon is used to realize the measurement of antenna pattern, the measurement accuracy is about 1 dB. In [6], amplitude error is about 3 dB, and angle error can be up to 5° by using aircraft.

With the development of the UAV, it can replace the airplane or hot air balloon for its flexible control method and low cost, as a new tool to the measurement of antenna pattern. To improve the accuracy of the measurement, a new measurement method by UAV is proposed. The RTK positioning is used to improve the positioning accuracy and reduce the measurement error, and curve fitting is used to reduce measuring angle offset.

2 Measurement Method

The measurement structure is shown in Fig. 1. The UAV carrying source antenna flies according to the preset orbit around the tested antenna. Positioning system is used to locate the UAV, and converts the position information to the angle information relativing to the tested antenna, and transmits it to the recorder. The tested antenna receives the signal of source antenna, and transmits it to the spectrum analyzer. When the frequency span of spectrum analyzer is set to zero, it can be used as a receiver to record the received signal power of tested antenna. The power

curve recorded by spectrum analyzer are transmitted to the recorder. According to the location information of UAV and the power curve, the antenna pattern can be drawn. At the same time, a standard reference antenna should be placed near the tested antenna. Therefore, the influence of transmission power, relative polarization and receiver sensitivity can be eliminated by normalization.

Measuring accuracy of antenna patterns is greatly influenced by GPS positioning error and angle offset caused by the yaw of UAV. In order to improve the accuracy of measurement, RTK positioning method is used to improve the positioning precision [8], and the curve fitting is used to reduce the measuring angle offset caused by the yaw of UAV.

2.1 The RTK Positioning Based on TDOA

The RTK positioning based on TDOA is shown in Fig. 2. Four receiving stations that the position is known exactly are placed in the ground. One is the master station, and the other three are auxiliary. The TDOA between the main and auxiliary station is used to realize the positioning of UAV. The position based on TDOA have higher clock synchronization accuracy compared to Global Positioning System (GPS). In addition, this method eliminate the positioning error caused by ephemeris error, influence of ionosphere and effect of troposphere. Meanwhile, RTK positioning is used to decrease the positioning error. The positioning error of the base station can be calculated according to the accuracy location of the base station. Then the position error of the UAV, especially the error caused by clock synchronization error, can be corrected by the positioning error of the base station. Therefore, the positioning accuracy can be improved effectively.

2.2 Curve Fitting

When the UAV flights according to the preset trajectory, the yaw will lead to angle deviation. In order to reduce the deviation, using the least square method, the

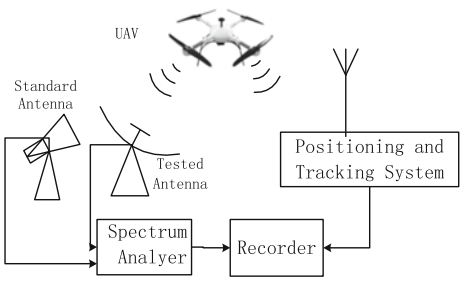

Fig. 1 Measuring principle diagram

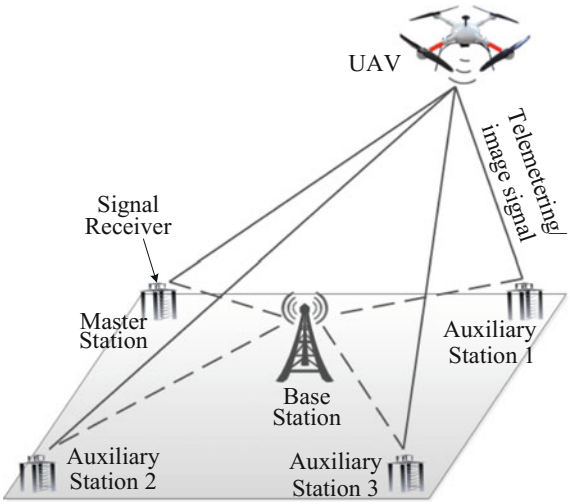

Fig. 2 RTK positioning principle diagram

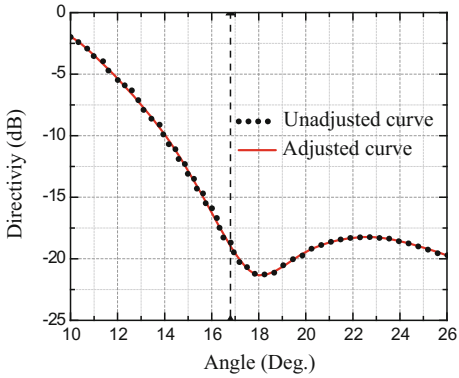

Fig. 3 Fragmented curve-fitting example

measurement deviation caused by yaw can be well improved through polynomial curve fitting and gaussian curve fitting.

In order to avoid error caused by steep and much sidelobes, different method of curve fitting is used according to the complexity of the received power curve. For instance, Fig. 3 shows a part of directional coefficient curve of an antenna. The curve is relatively steep in 16°–16.8°, polynomial curve fitting can be used. The curve in 16.8°–26° is relatively flat, gaussian curve fitting can be used. As shown in Fig. 3, the curve using fragmented fitting is more smooth, it can reduce the angle offset caused by yaw effectively.

In the process of measurement, the following points should be paid attention:

1. The distance between the UAV and the tested antenna R should conform to the far field measurement conditions:

$$R \geq \frac{2D^2}{\lambda} \tag{1}$$

where D is the aperture of the antenna in measurement, and λ is the operating wavelength of the antenna.

2. The source antenna carried by the UAV should be placed in the best installation location to avoid the change of the source antenna's performance caused by UAV.
3. The source antenna carried by the UAV should be omni-directional antenna, and the relative posture between the tested antenna and the source antenna should to keep unchanged.

3 Error Analysis and Simulation Results

3.1 Positioning Error

RTK positioning method can basically eliminate the positioning error caused by the clock synchronization error. Therefore, the positioning error is mainly caused by the signal noise and multipath. The influence of the multipath delay on pseudorange is negligible. The main influence of the multipath delay is that it decrease the received power. Consequently, the Signal to Noise Ratio (SNR) is decreased. Therefore, this part will analyse the positioning error caused by the SNR.

According to the signal link calculation formula, the dB value of received signal power is:

$$P_S = ERIP + G_r - 32.45 - 20\lg f(\text{MHz}) - 20\ \lg d(\text{km})\ - k \tag{2}$$

The G_r is the receiving antenna gain, f is the signal frequency, d is sending and receiving distance, k is the multiple path loss. The noise power is:

$$P_N = KT_iN_FB \tag{3}$$

where $K \approx 1.38 \times 10^{-23}\,\text{J/K}$, which is the boltzmann constant, T_i is the temperature of the thermal noise, NF is receiver noise factor, B is the signal bandwidth. SNR is defined as:

$$SNR = P_S/P_N \tag{4}$$

The maximum time delay error caused by the noise is [9]:

$$\sigma_t \leq \frac{\sqrt{8}}{GKMn \cdot \sqrt{SNR}\sqrt{N}} \sqrt{\ln\left(\frac{1}{1-P_0}\right)} \tag{5}$$

Among them, *GKMn* is relative value of global average sensitivity, N is the sample points used to capture, P_0 is confidence probability. The ranging error caused by delay is:

$$\sigma_R = c \cdot \sigma_t \tag{6}$$

where c is the speed of light.

In practical application, different ranging error can be obtained according to the different signal transceiver distance. The sum of two stations' ranging error is the time difference measurement error. The time difference error between i-th auxiliary station and master station is expressed as:

$$d\Delta R_i = \sigma_{ri} + \sigma_{r0} \tag{7}$$

Among them, σ_{ri} is the ranging error of the i-th auxiliary station, σ_{r0} is the ranging error of master station.

Setting the position of UAV is (x, y, z), the position of master station is (x_0, y_0, z_0), position of the auxiliary station is $(x_\mathrm{i}, y_\mathrm{i}, z_\mathrm{i})$, the equation can be established:

$$\begin{cases} \sqrt{(x-x_0)^2 + (y-y_0)^2 + (z-z_0)^2} = R_0 \\ \sqrt{(x-x_i)^2 + (y-y_i)^2 + (z-z_i)^2} = R_i \\ \Delta R_i = R_0 - R_i \end{cases} \tag{8}$$

Substitute the first two expressions into the third, and get the total differential equation:

$$d\Delta R = Gdr(\mathrm{n}) \tag{9}$$

where

$$G = \begin{Bmatrix} \frac{x-x_0}{R_0} - \frac{x-x_1}{R_1} & \frac{y-y_0}{R_0} - \frac{y-y_1}{R_1} & \frac{z-z_0}{R_0} - \frac{z-z_1}{R_1} \\ \frac{x-x_0}{R_0} - \frac{x-x_2}{R_2} & \frac{y-y_0}{R_0} - \frac{y-y_2}{R_2} & \frac{z-z_0}{R_0} - \frac{z-z_2}{R_2} \\ \frac{x-x_0}{R_0} - \frac{x-x_3}{R_3} & \frac{y-y_0}{R_0} - \frac{y-y_3}{R_3} & \frac{z-z_0}{R_0} - \frac{z-z_3}{R_3} \end{Bmatrix} \tag{10}$$

$d\Delta R$ is the time difference error and dr is the emitter positioning error, which can be expressed as follow respectively:

$$d\Delta R = \begin{Bmatrix} d\Delta R_1 \\ d\Delta R_2 \\ d\Delta R_3 \end{Bmatrix} \tag{11}$$

$$dr = \begin{Bmatrix} dx \\ dy \\ dz \end{Bmatrix} \tag{12}$$

By using the pseudo-inverse method, dr can be solved as:

$$dr = \left(G^{\mathrm{T}}G\right)^{-1}G^{\mathrm{T}}d\Delta R \tag{13}$$

Finally, the positioning error σ_R is:

$$\sigma_R = \sqrt{dx + dy + dz} \tag{14}$$

3.2 Pattern Measurement Error

Using the proposed method to measure the earth station antenna, the measurement error is mainly composed of positioning error, yaw of the UAV and ground reflections. According to the positioning error analysis method, when the distance between the UAV and the signal receiving station is less than 100 m, the positioning error is centimeter level, which can be ignored, relating to the distance between the UAV and the tested antenna,. When the distance between source antenna and tested antenna t is 50 m, and the yaw distance of UAV is 5 m, the yaw can cause the measuring angle offset up to 5°. If ignoring the measuring angle deviation, the direction diagram error can be up to 0.4–1 dB. Through curve fitting to smooth the measuring curve, the measuring error can be decreased by 0.2–0.8 dB. The error caused by yaw after curve fitting $\Delta\delta_1/\delta_1$ is about 0.2 dB. The error caused by ground reflection $\Delta\delta_2/\delta_2$ is about 0.15 dB. The RMS (root-mean-square) error of direction coefficient $\Delta D/D$ can be calculated by:

$$\frac{\Delta D}{D} = \sqrt{\left(\frac{\Delta\delta_1}{\delta_1}\right)^2 + \left(\frac{\Delta\delta_2}{\delta_2}\right)^2} \tag{15}$$

According to the expression (2), the RMS error is 0.25 dB.

In order to verify the feasibility of the proposed measuring method, simulation is carried out by the High Frequency Structure Simulater (HFSS) software of Ansoft company and Matlab tools of MathWorks company. Figure 4 shows the measurement results when the working frequency of the tested antenna is 1.5 GHz, the flight's radius of UAV is about 50 m, and the maximum distance of yaw is 5 m. Considering the complexity of the ground reflections, the simulation only introduced the positioning error and angular deviation caused the UAV's yaw. According to the simulation results, the deviation between the traditional measuring results (using common GPS positioning without curve fitting) and the ideal results is large. But the measuring results is improved well by using the RTK positioning

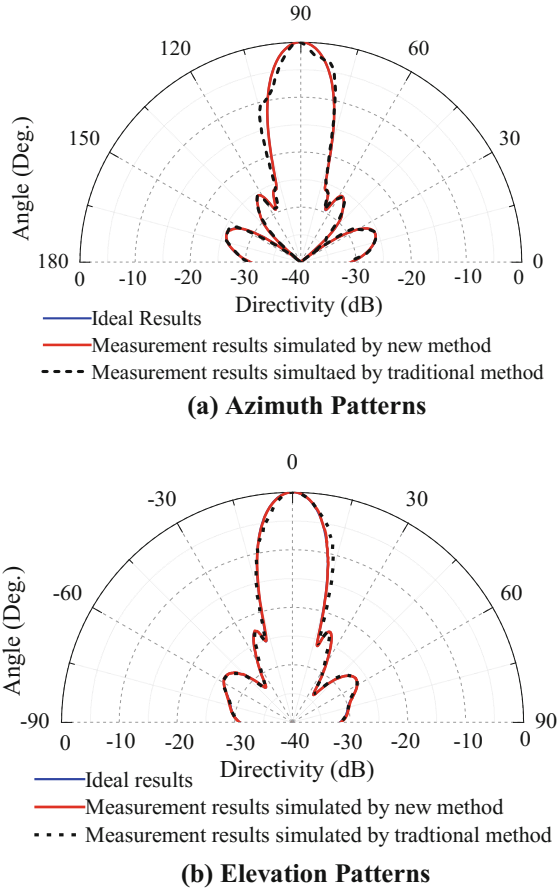

Fig. 4 Pattern measurement results simulated by HFSS and MATLAB

and curve fitting, which is basically coincide with the ideal result. The simulation shows that the amplitude RMS error is 0.21 dB. In the maximum radiation direction, the amplitude error is 0.02 dB and the angle error is 0.1°. According the simulation results, The simulation error of measurement agreed well with the theoretical estimates.

4 Conclusion

This paper proposed a method to measure the earth station antenna patterns by using UAV. The positioning accuracy can reach to centimeter level by using RTK position method. The angle offset caused by the yaw of UAV can be reduced by curve fitting. In order to verify the feasibility of this measuring method, the simulation is carried out. The simulation result shows that the method can make the

amplitude error decrease to 0.21 dB and pointing angle deviation to 0.1°. The measurement precision is high, which means the proposed measuring method can be widely applied to practical engineering measurement.

References

1. Picard D (2010) Antenna measurement. microwave and millimeter wave technologies modern UWB antennas and equipment, pp 193–214
2. Qin S,Xu D (2006) Satellite communication earth station antenna engineer measuring technology. People's Posts and Telecommunications Publishing Press, p 3
3. Brueckmann H (1963) Antenna pattern measurement by satellite. IEEE Trans Antennas Propag 143–147
4. Brueckmann H (1955) Helicopter measures antenna patterns. Electronics 28:P134–P136
5. Steele JG (1965) Measurement of antenna radiation patterns using tethered balloon. IEEE Trans Antennas Propag 179–180
6. Gliddon CW,. Carson CT (1973) Antenna radiation-pattern measurement using model aircraft. IEEE Trans Antennas Propag 700–702
7. Hutrado M (2001) An in-situ method to measure the radiation pattern of a GPS receiving antenna. IEEE Trans Instrum Meas 50(3):P846–P849
8. Li J (2010) The discuss to ensure the RTK positioning accuracy and the analysis of error sources. Modern Surv Mapp 33(1):P17–P19
9. Wang Y, Chen J (2012) Measuring principle. Tsinghua University Press

Research on Performance Evaluation of Beidou Be Enhanced by Pseudolites

Jingyang Fu, Guangyun Li, Tingsong Tang, Li Wang and Yanglin Zhou

Abstract Beidou ground-based pseudolites network is a ground-based augmentation system, it can provide service to the users for location and timing when the Beidou satellite signal be occlusion or interference. This paper introduces the composition, principle and key technology of Beidou ground-based pseudolites network, and then it using the real data from the experiments field to verify the assumptions. The experimental results show that the Beidou ground-based pseudolites network can provide good timing and positioning service for users, the single pseudolite timing accuracy is 2.06 ns. The static and dynamic positioning accuracy have a good performance when positioning by both Beidou and pseudolites observation, it is proved that the vertical direction accuracy of Beidou positioning is obviously be improved.

Keywords Beidou system · The ground-based augmentation system · Pseudolite · Test evaluation

1 Introduction

Beidou satellite navigation system is still in the development stage, at this stage, the system uses the mixed GEO + IGSO + MEO constellation [1, 2], the constellation makes part of the service area of the satellite visibility. In addition, Beidou Positioning System completely rely on the spread of the satellite signal, so in the

J. Fu (✉) · G. Li · L. Wang · Y. Zhou
College of Navigation and Aerospace Engineering, Information Engineering University, Zhengzhou 450001, China
e-mail: fjynoob@sina.com

J. Fu · T. Tang
Beijing Navigation Center, Beijing, China

J. Sun et al. (eds.), *China Satellite Navigation Conference (CSNC) 2017 Proceedings: Volume I*, Lecture Notes in Electrical Engineering 437,
DOI 10.1007/978-981-10-4588-2_54

city, such as mountain canyon and other buildings and special terrain, the positioning effect of Beidou system because the signal is blocked and reduced or is unable to locate. In addition, if in the special case of the Beidou satellite was completely disrupted, the Beidou system ground user equipment will not be used normally, by introducing the pseudolite technology can effectively solve the problems [3]. The concrete introduction way is to build the pseudolite foundation reinforcement network, which is composed of several pseudolites based on the time synchronization of the fiber. In order to validate the system of Beidou system and enhance the role, should evaluate timing and positioning test user terminal.

2 Beidou Ground Based Pseudolite Network

2.1 System Composition

Beidou satellite pseudolite network architecture consists of components and elements of participation. The main elements of pseudolite, pseudolite network management center, the pseudolite monitoring station, time synchronization system and Beidou navigation enhancement type foundation composed of positioning terminal, participation factors mainly include the Beidou satellite navigation system and the system of the ground control center, described later in this article the experiment is mainly related to the elements contained in part the network system.

2.2 Main Functions

The main functions of the various elements of the Beidou satellite network is the foundation of pseudo pseudolite navigation signal and ground responsible for broadcast message; pseudolite network management center (also known as pseudolite operation management center) information processing and task coordination is responsible for the foundation of the navigation system, convergence based navigation network, pseudolite monitoring stations and various data state, comprehensive treatment, instruction and data generation control; pseudolite monitoring station is responsible for the integrity monitoring of pseudolite signal, the monitoring information upload network management center; time synchronization system of Beidou navigation experiment system foundation and the two generation navigation system time synchronization, including the Beidou ground transportation control center and the pseudolite network management the center of time synchronization and pseudolite network management center and the pseudolite monitoring station, time synchronization; and finally by the Beidou ground The enhanced position location based navigation terminal positioning solution and timing.

2.3 Operation Mode

Beidou ground pseudolite network system work for the first through the pseudolite monitoring station on the coverage of all the regional pseudolite monitoring, the integrity and the time difference among pseudolite information through pseudolite control data network (fiber data channel) is transferred to the pseudolite network management center, completed in the pseudo time synchronization solution the satellite network management center, and will be in good condition and time synchronization information through the pseudolite control data network feedback to each pseudolite, thus forming a closed loop mode. The physical realization vector of the pseudolite synchronization control network is fiber, which can be realized by the existing commercial optical fiber line. Work as shown in Fig. 1:

3 Principle and Key Technology

3.1 Positioning and Timing Model

3.1.1 Positioning Algorithm

Because the pseudolite observation equations have the same principle, so from the observation equation of Beidou satellite, but due to the pseudolite in the earth, and in the process of communication through the Beidou satellite signal of the atmosphere is different, it can be improved as the observation equation:

$$P_i^{PL} = \rho + d_{trop} + c(dt^{PL} - dT) + d_{rtgdi} + d_{stgdi}^{PL} + \varepsilon_{p_i} \quad (1)$$

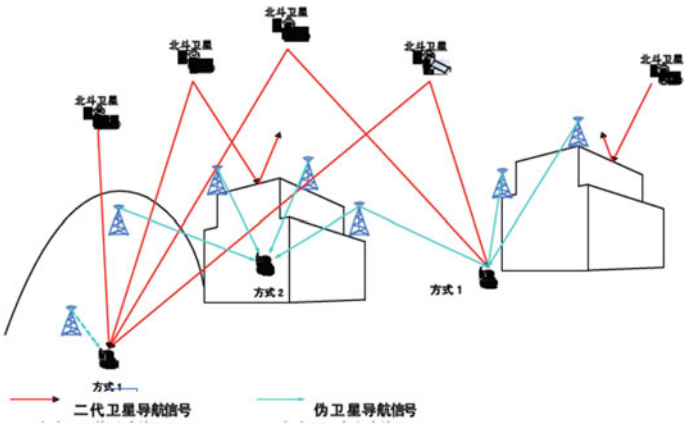

Fig. 1 Beidou pseudolite network operation mode

P_i^{PL} is pseudorange observation of PLs frequency B_i; ρ is free space geometric distance between the receiver and the pseudolites signal transmitting time signal time; d_{trop} is tropospheric delay error; dt^{PL} is the receiver clock error; dT is pseudolites clock error; d_{rtgdi} is receiver channel delay of frequency B_i; d_{stgdi}^{PL} is pseudolites channel delay of frequency B_i; ε_{p_i} is observation noise of PLs frequency B_i. In the pseudolite navigation message broadcast in the satellite ephemeris precise location coordinates through other traditional means of Surveying and mapping the measured pseudolite clock error, as mentioned by the optical fiber transfer to maintain, coordinate and clock receiver is the unknown parameters above observation equations are nonlinear model with unknown parameters. The first general by Taylor series linearization them after the solution, the Beidou satellite navigation system, satellite receiver distance, ignoring the two order and above the influence on the positioning accuracy for small, pseudolite measurements, ignoring the two order and above the error. So using Taylor series to expand the function $F(x)$ to the first order from x_0:

$$F(x) = F(x_0) + A\delta x + R \tag{2}$$

x_0 is the approximate estimate of x with the unknown quantity, $\delta x = x - x_0$; $A = \partial_x F(x_0)$ is the first partial derivative at x_0, R is the two order residual, and:

$$R = \frac{1}{2}\delta x^T \partial_{xx}^2 F(x_0 + t \cdot \delta x)\delta x \quad 0 < t < 1 \tag{3}$$

For geometric distances ρ, the following estimates can be obtained:

$$0 \le R \le \frac{\|\delta x\|^2}{2\rho} \tag{4}$$

So for the co-location of single epoch, the linear model of Beidou satellite, the pseudolite using a nonlinear model parameter estimation. For dynamic positioning can be multi epoch, using extended Kalman filtering to improve the estimation to correct a priori state estimation of linearization by iterating the linear observation equation. EKF algorithm for nonlinear function of nonlinear strength is strong, there is a large estimation error of the filter solution of problems, some scholars put forward the method of using UKF filter for positioning and navigation solution [4], the method is based on the basic principle of Kalman filter based on UT transform to linear Kalman filter frame, the deterministic sampling strategy nonlinear approximation method, the basic idea is from the nonlinear equation of mean and variance of the communication point of view, the basic idea of UKF is to be estimated by some special sample mean and variance of production (Sigma). These samples are weighted by state equation and observation equation to generate the mean and variance of state parameters. The research shows that the filtering method has a significant advantage in overcoming nonlinear error of nonlinear model.

3.1.2 Timing Algorithm

A known point timing by using the Beidou satellite, the position of the user is known for single satellite timing. GPS observation equations are as follows:

$$dTime = \left(P_i - (\rho + d_{trop} + d_{scal} + d_{rel} + c * dt + \frac{f_1^2}{f_i^2} d_{ion} + d_{rtgdi} + d_{stgdi} + \varepsilon_{p_i}) \right) / c \quad (5)$$

P_i is pseudorange observation of frequency B_i; ρ is free space geometric distance between the receiver and the satellite signal transmitting time signal time; d_{trop} is tropospheric delay error; d_{scal} is correction for the rotation of the earth; d_{rel} for relativistic corrections; dt is the receiver clock error; dT is satellite clock error; d_{ion} is the ionospheric delay of B_i, $f_1^2/f_i^2 d_{ion}$ is the of the ionospheric delay from double frequency difference; d_{rtgdi} is receiver channel delay of frequency B_i; d_{stgdi} is satellite channel delay of frequency B_i; ε_{p_i} is observation noise of frequency B_i, $dTime$ is the deviation of receiver clock error and the big dipper.

A known point timing by using pseudolite, user location is known, for single satellite timing. The following pseudo range of Beidou observation equation:

$$dTime = \left(P_i^{PL} - \left(\rho + d_{trop} + c * dt^{PL}) + d_{rtgdi} + d_{stgdi}^{PL} + \varepsilon_{p_i} \right) \right) / c \quad (6)$$

P_i^{PL} is the pseudorange observation of frequency
$dTime$ is obtained by the observation equations, it can be used in timing of the receiver.

3.2 Establishment of Relative Coordinate System

For the Beidou system users in many cases, the relative position of the role play a greater role than the absolute position, for example in the rescue and relief operations in command and control, a small range of precision work, and focus on the part of the target deformation monitoring and so on. Therefore, when the Beidou System in orbit satellites receive interference or destruction of the situation, in order to use the Beidou satellite pseudolite network as soon as possible independently of the existing Beidou users to provide location services. It needs to establish a set of relative coordinate system. Through this coordinate system, we can study the location of the user relative to the Beidou foundation satellite network system. When the absolute coordinates of the pseudolite in the Beidou pseudolite network are determined accurately, the cooperative positioning of Beidou satellite network and Beidou system can be further realized.

3.3 Time Synchronization Technology

Time synchronization between pseudolite and pseudolite with Beidou system is the key technology of Beidou satellite network application. Beidou ground pseudolite network using fiber frequency transmission technology [5–8] to establish and maintain the Beidou system and pseudo inter satellite time reference, 1–5 km from the pseudolite test site, and time-frequency source Beidou system optical fiber line distance is greater than 100 km (straight-line distance of about 40 km), scheduled time synchronization the precision is sub nanosecond to satisfy the application of decimeter level navigation. The time synchronization of the Beidou pseudolite network is shown in Fig. 2.

4 Experiment and Result Analysis

4.1 Experimental Environment and Equipment

The field selection in the eastern suburbs of Chengdu, Longquanyi area three mountains terrain side high-rise, the regional center for pond. Layout pseudo WeiXing Railway Station 5, pseudolite monitoring station 3, in addition to retaining the 1 pseudo WeiXing Railway Station backup. Among them, 4 pseudolite distribution in the junction of urban and mountain areas, the distal 1 pseudolite in the test area, around 3 stations are all located in the city and the mountains at the junction of the 4 pseudolite, and select the test area of the total area of not less than 10 km^2. The attenuation factor of horizontal precision in the experimental field is shown in Fig. 3:

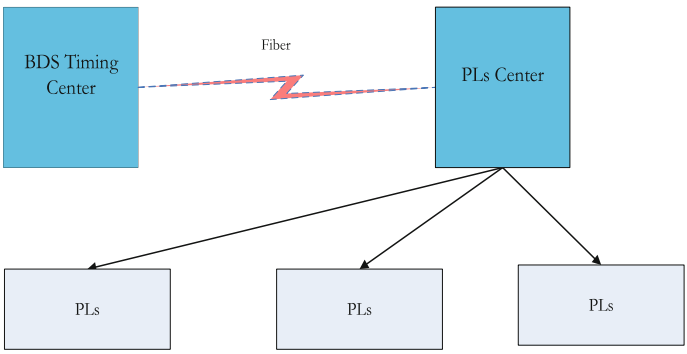

Fig. 2 Time synchronization of Beidou pseudolites network

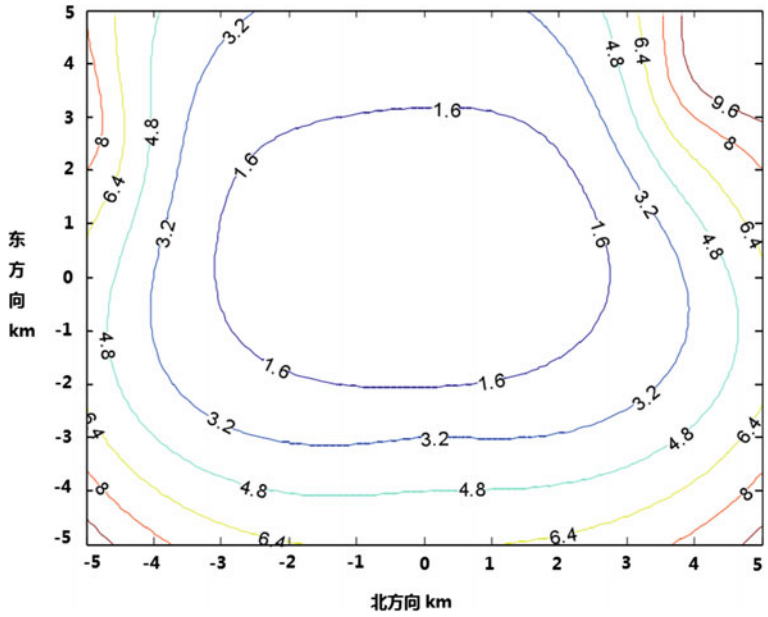

Fig. 3 HDOP of experimental area

The acquisition of experimental data is collected by Beidou pseudolite enhanced terminal and stored by notebook computer. Beidou pseudolite enhanced user terminal can receive the signal of each point of the Beidou satellite and the signal of each frequency point of the satellite through an antenna.

4.2 Pseudolite Timing Test

The base station placed 1 enhanced pseudolite positioning terminal, receiving single satellite signal and timing solution; 1PPS signal access time interval counter terminal 1PPS, transportation system output, measured between the two time, 1 h of continuous data acquisition, timing accuracy calculation on the ground user compass foundation pseudolite network.

The data source for the Beidou 519 weeks 103, 100–108,185 s to enhance data type of Beidou satellite positioning terminal and single pseudolite positioning terminal, placed in the transport system on the reference points. Test results are shown in Fig. 4.

From Fig. 4, test the timing precision of single satellite using single pseudolite data of 1 h, the test results for the 2.06 ns.

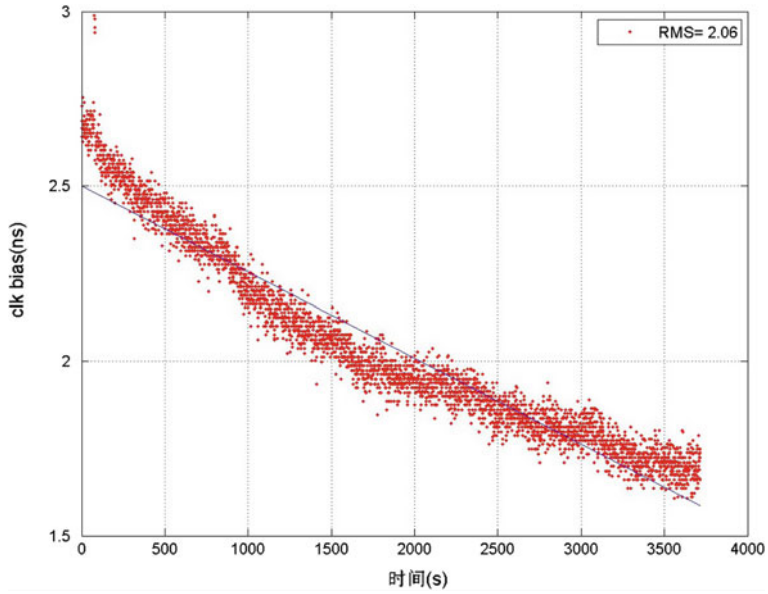

Fig. 4 Single pseudolite timing test results

4.3 Static Positioning Experiment

Enhanced positioning terminal works in the pseudolite independent positioning mode. The enhanced positioning terminal antenna is placed on the known points which coordinate has been precisely measured by other surveying and mapping means, and continuous data acquisition is carried out. By using the pseudo data of the pseudolite, the navigation message and other original observation data, the terminal positioning solution is calculated.

The data source for the Beidou 519 weeks 103, 100–108,185 s enhanced Beidou satellite positioning terminal and pseudolite data, positioning terminal placed in the transport system on the reference points. The post-processing method [9, 10] is used to compare the data processing results with known point coordinates. A total of 5 pseudolite observables are involved in the solution, as shown in Fig. 6.

From Fig. 5, the enhanced positioning terminal in the pseudolite independent working mode, the static positioning results for the horizontal accuracy of 1.322 m, elevation accuracy 1.297 m. The index is similar to the single dipper system for positioning the same level of indicators (Fig. 6).

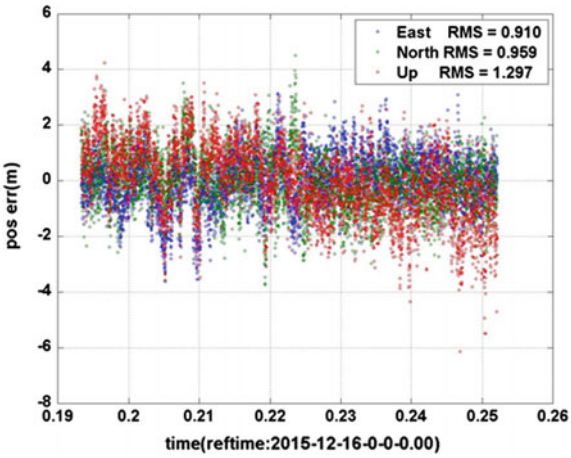

Fig. 5 *Curve* Static positioning results

4.4 Dynamic Positioning Experiment

In March 24, 2016, the test vehicle terminal dynamic positioning in the demonstration area, co-location model using the Beidou satellite and pseudolite, in base station set up dual band GPS base station equipment; in the demo car were set up and enhanced GPS receiver positioning terminal; according to the selected line, continuous testing; dynamic testing for a second sampling interval the original observation data, recording GPS, Beidou satellite, satellite pseudo base stations, demo car. Take into account the time reduction and coordinate conversion, the enhanced GPS receiver positioning terminal positioning results and the results of single point positioning in real time using a preliminary comparison test; base station and demonstration vehicle GPS data precision (relative positioning solution), and positioning results with enhanced positioning terminal positioning results are accurate by the time of reduction after the comparison test.

A total of five sets of experiments were conducted using data post-processing method [11, 12], measurement gives the Beidou and pseudolite positioning solution joint positioning results under the mode of evaluation of positioning accuracy of collaborative complex region. Specific results are as follows:

Five groups of test positioning accuracy statistical results are shown in Table 1.

As can be seen from the above table, in the 3 + 2 mode, the ground dynamic positioning accuracy for the horizontal direction 2.506 m, elevation direction 2.343 m. The experimental results show that the Beidou system can not provide users with positioning services when the introduction of pseudolite Beidou system can continue to normally serve the user.

In addition, in order to verify the contribution of the pseudolite to the positioning accuracy of the Beidou system, the positioning results of only the Beidou satellite positioning and the same number of Beidou satellite +2 pseudolite are analyzed and compared. Specific results are as follows (Fig. 7).

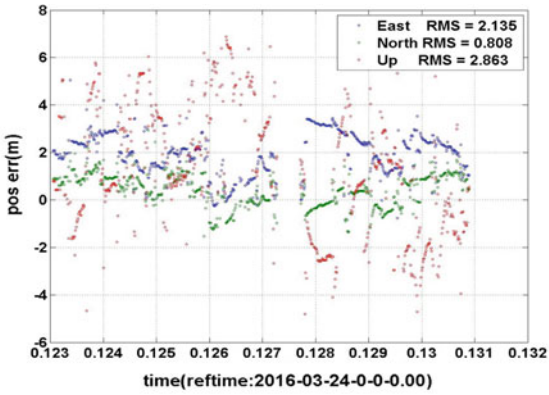

（a）3+2 positioning results round 1

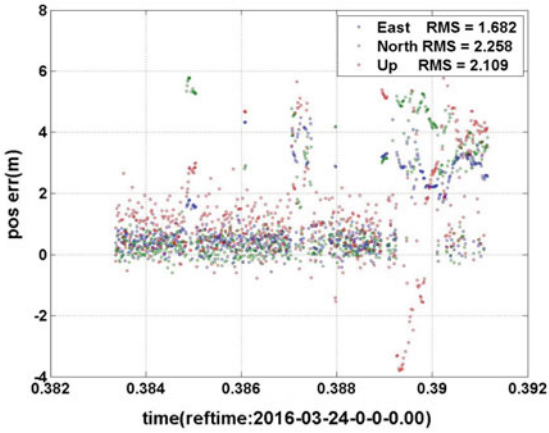

（b）3+2 positioning results round 2

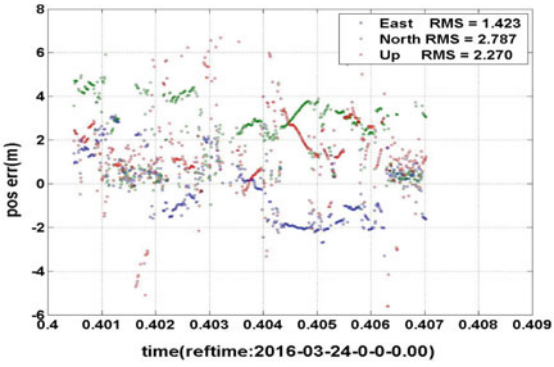

（c）3+2 positioning results round 3

Fig. 6 Dynamic positioning results in 3 + 2 mode

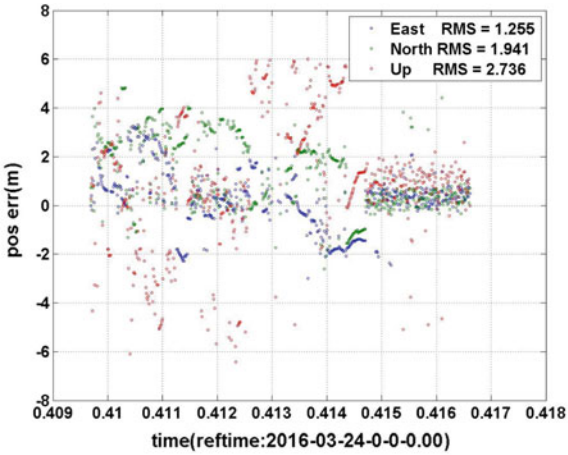

（d）3+2 positioning results round 4

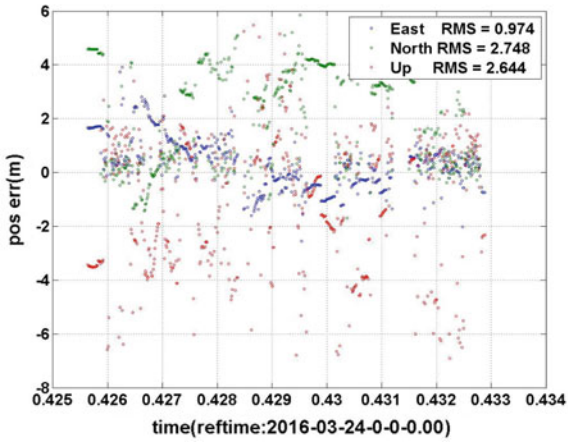

（e）3+2 positioning results round 5

Fig. 6 (continued)

Table 1 Statistical results of positioning accuracy in 3 + 2 mode (RMS, Unit: m)

Round	E	N	Horizon	Vertical
1	2.135	0.808	2.283	2.863
2	1.682	2.258	2.816	2.109
3	1.423	2.787	3.129	2.270
4	1.255	1.941	2.311	2.736
5	0.974	2.748	2.916	2.644
Avs	1.483	1.870	2.506	2.343

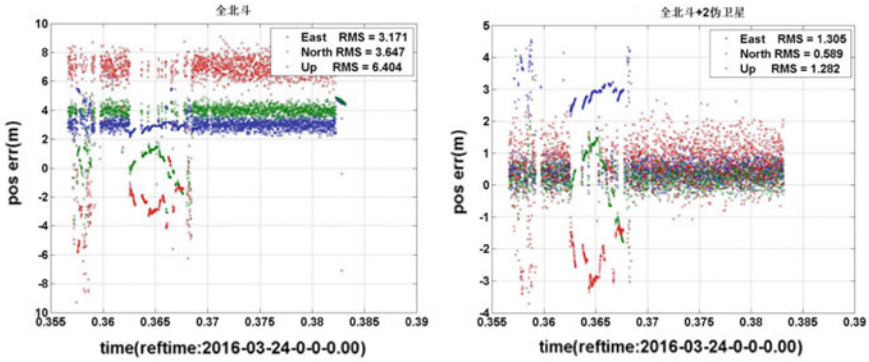

（a）Dynamic positioning results round 1

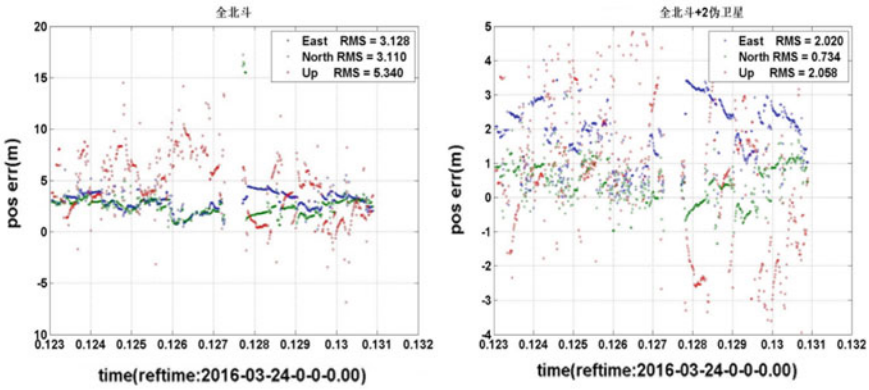

（b）Dynamic positioning results round 2

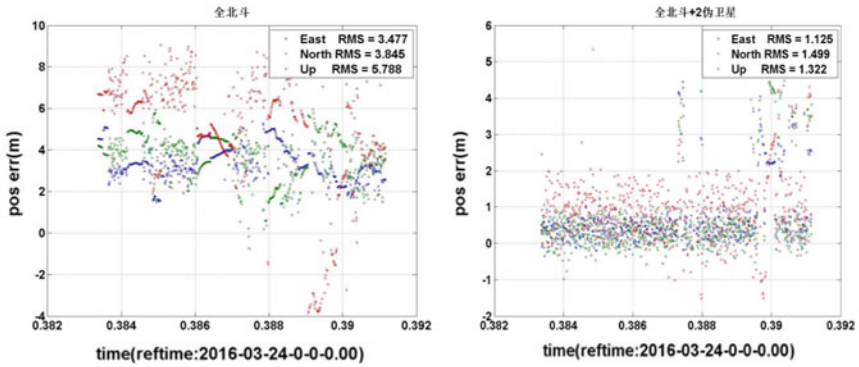

（c）Dynamic positioning results round 3

Fig. 7 Comparison of dynamic positioning results

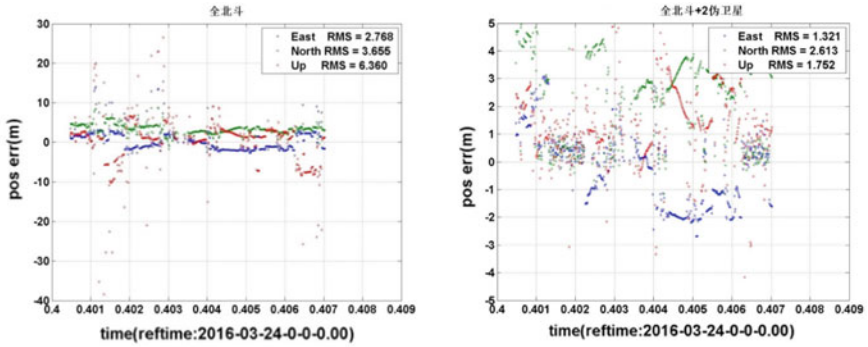

（d）Dynamic positioning results round 4

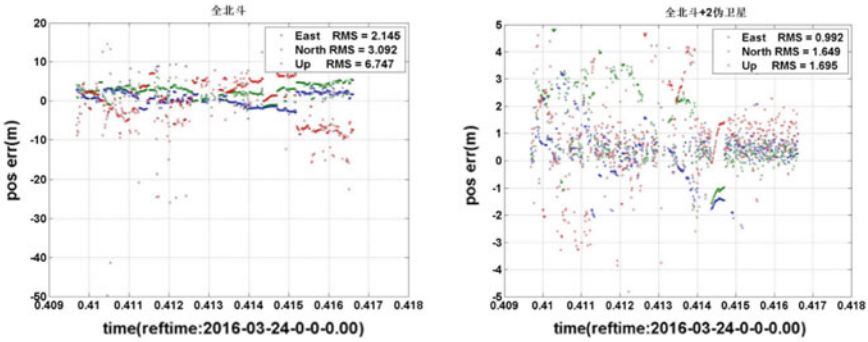

（e）Dynamic positioning results round 5

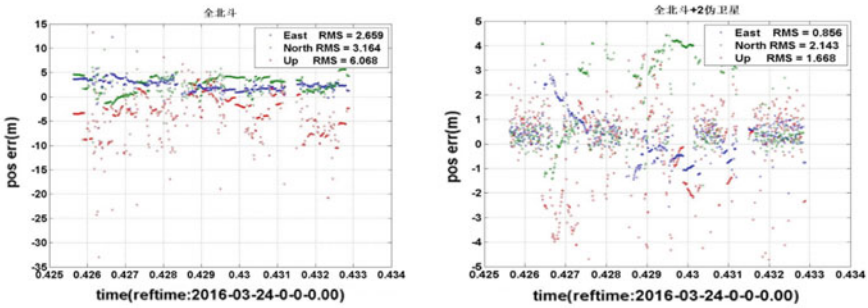

（f）Dynamic positioning results round 6

Fig. 7 (continued)

Table 2 shows, for ground users in 6 Beidou satellites working condition, the level of participation in the pseudolite positioning accuracy 2.382 m, elevation accuracy increased 4.488 m level and elevation accuracy has greatly improved, the elevation accuracy is improved more significantly.

Table 2 Comparison of positioning between 6 Beidou satellites and 6 + 2 mode (RMS, Unit: m)

Round	Horizon			Vertical		
	Beidou	Beidou + PLS	Difference	Beidou	Beidou + PLS	Difference
1	4.833	1.432	3.401	6.404	1.282	5.122
2	4.411	2.149	2.262	5.340	2.058	3.282
3	5.184	1.874	3.310	5.788	1.322	4.466
4	4.585	2.928	1.657	6.360	1.752	4.608
5	3.763	1.924	1.839	6.747	1.695	5.052
6	4.133	2.308	1.825	6.068	1.668	4.400
Avs	4.485	2.103	2.382	6.118	1.630	4.488

5 Conclusion

This paper introduces the Beidou ground pseudolite network, described in detail the principle and key technology of Pseudolite augmented Beidou system design, the pseudolite timing enhancement experiment, Beidou system static positioning and dynamic positioning experiment experiment. According to the data processing and analysis, we can get the following conclusions:

(1) For timing accuracy test using pseudolite satellite data, the result is 2.06 ns, that the pseudolite can provide better service for the user terminal in the timing of Beidou Beidou system to normal service;
(2) Pseudolite independent static positioning experiment shows that in the experimental field, the level of accuracy of pseudolite positioning has been quite independent and compass can basically meet the higher requirements, the user demand for static positioning;
(3) Several experimental results of Beidou + pseudolite dynamic positioning mode prove that the addition of pseudolite can significantly improve the geometry of satellite navigation and positioning

Improve the accuracy of user terminal positioning, especially for elevation accuracy improvement.

References

1. Zhou SS, Cao YL, Zhou JH, et al (2012) Positioning accuracy assessment for the 4GEO/5IGSO/2MEO constellation of COMPASS. Sci China (Phys Mech & Astrono), 55 (12):2290–2299
2. Li HN, Qian S et al (2014) The constellation stability promotion approaches for compass (beidou) regional navigation and positioning system. Sci China (Phy Mech & Astron), 44(6). (In Chinese)
3. Wang J, Gao J, LIU Chao et al (2010) High precision slope deformation monitoring model based on the GPS/Pseudolites technology in open-pit mine. Min Sci Technol 20(01):126–132

4. Wang Q (2010) The theory and application research of adaptive-robust UKF for satellite integrated navigation system. Huazhong University of Science and Technology, Wuhan. (In Chinese)
5. Chen X, Zhang J, Lu J, Lu X, Tian X, Liu B, Wu H, Tang T, Shi K, Zhang Z (2015) Feed-forward digital phase compensation for long distance precision frequency dissemination via fiber network. Opt Lett 40(3):371–374
6. Zhang Z (2011) Advances in high repetition rate femtosecond fiber lasers. Acta Optica Sinica 31(9). (In Chinese)
7. Xing CHEN, Zhang Jian, Jinlong Lu et al (2015) Feed-forward digital phase compensation for long-distance precise frequency dissemination via fiber network. Opt Lett 03:371–374
8. Zhang F, Hou D et al (2010) Timing delay jitter compensation of a fiber link with active delay compensation. Acta Optica Sinica 30(3). (In Chinese)
9. Wu XL, Zhou JH, Wang G (2012) Multipath error detection and correction for GEO/IGSO satellites. Sci China-Phys Mech Astron 55:1297–1306
10. Zhang YZ, Chen JP, Wu B et al (2014) GPS/GLONASS/COMPASS combined positioning based on CNMC, CSNC electronic proceedings
11. Chang ZQ, Hu XG, Guo R et al (2015) Comparison between CNMC and hatch filter & its precision analysis for BDS precise relative positioning (in Chinese). Sci Sin-Phys Mech Astron 45:079508 (In Chinese)
12. Cao YL, Hu XG, Wu B et al (2012) The wide-area difference system for the regional satellite navigation system of COMPASS. Sci China-Phys Mech Astron 55:1130–1138

Civil Avionic EMI Surrounding Impact Assessment and Testing on the Performance of Beidou B1I Signal

Pengfei Wang, Xiaofeng Shi, Taosheng Wang and Zhipeng Wang

Abstract The pseudo-range tracking accuracy of Beidou B1I receiver operating in civil avionic EMI surrounding is a key index of Beidou aviation application. The interference thresholds and the pseudo-range tracking accuracy of GPS and GLONASS receiver are defined in the standards of International civil aviation organization (ICAO). With the civil aviation application of Beidou satellite navigation, the anti-jamming performance of Beidou B1I navigation signal get more and more attention. This paper analyzed the civil avionic EMI surrounding, defined the interference thresholds of different interference type and conducted an anti-jamming testing in lab, which provide experimental basis for civil aviation standardization of Beidou B1I satellite signal.

Keywords Pseudo-range tracking accuracy · Interference threshold · Carrier-to-noise ratio

1 Introduction

The index of anti-interference performance of GNSS satellite navigation system for airborne equipment is an important chapter in the SARPs standard of the International Civil Aviation Organization (ICAO), which is the guide of civil

P. Wang (✉) · X. Shi · Z. Wang
Beihang University, Beijing 100191, China
e-mail: figo913@126.com

T. Wang
Beijing Institute of Tracking and Telecommunication Technology,
Beijing 100191, China
e-mail: wangts@beidou.gov.cn

J. Sun et al. (eds.), *China Satellite Navigation Conference (CSNC) 2017 Proceedings: Volume I*, Lecture Notes in Electrical Engineering 437,
DOI 10.1007/978-981-10-4588-2_55

aviation industry standards and Avionics manufacturers application standards. With the promotion of the civil aviation application plan of the Beidou B1I system, it is necessary to evaluate and test the accuracy of the Beidou B1I system in the civil aviation electromagnetic interference environment.

In this paper, accord to the requirements of GNSS navigation system in the ICAO standard, the electromagnetic interference environment of civil aviation is analysed; At the same time, combining with the characteristics of Beidou B1I signal, the electromagnetic interference tolerance of civil aviation for Beidou B1I airborne receiver is analysed, including continuous wave interference tolerance, limited bandwidth white noise interference and pulse interference tolerance, in this electromagnetic environment, the tracking accuracy of the Beidou B1I receiver is tested, which test results was submitted to the NSP meeting of the ICAO as an information paper.

2 Electromagnetic Environment of Civil Aviation

2.1 The Main Source of Electromagnetic Interference

In Organization ICAO SARPs standard, it is indicated that the source of interference is non-hostile interference, which can be classified as internal band interference and out of band interference, such as VHF, UHF, FM broadcast, TV radio, etc. Airborne avionics equipment is an important source of interference, such as airborne S interrogators and transponders, with emphasis on airborne satellite communication transceiver (SATCOM) which effects on GNSS receiver. The indications of the interference threshold levels are referenced to the antenna port. For the active antenna, the antenna port is a virtual point between the antenna oscillator and low noise amplifier; the passive antenna, the antenna port is RF output port actual passive antenna.

2.2 The Main Type of Electromagnetic Interference

Based on the above interference sources, the ICAO SARPs defines three types of interference, namely continuous wave interference, limited bandwidth white noise interference and pulse modulation interference. Continuous wave interference is a sweeping interference, which is a signal carrier interference; the limited bandwidth white noise is Gauss white noise interference, with the increasing of the interference bandwidth, the interference power also increases accordingly. The pulse modulation interference is mainly produced by the airborne DME interrogator and the S mode transponder, which is an important component of the L-band navigation equipment.

3 Theoretical Analysis of Interference Effects

3.1 Carrier to Noise Ratio (C/No) Without Interference

Without interference, carrier to noise ratio (C/No) formula is shown as follows:

$$C/N_0 = S_r + G_a - 10\log(kT_0) - N_f - L \tag{1}$$

S_r is the satellite signal power level received by BDS receiver. In accordance with BD ICD 2.0, the minimum user-received signal power level is specified to be −163 dBW for channel I, which is measured at the output of a 0 dB RHCP receiving antenna (located near ground), when the satellite's elevation angle is higher than 5° [1].

G_a is the antenna gain value (dB).

$10\log(kT_0)$ is the receiver noise density. k = $1.3806505 \times 10^{-23}$, T_0 = 298.5 K, so $10\log(kT_0) = -204$ dB/Hz

L is the processing loss of BDS receiver.

Assume that the antenna points to a satellite as a unit gain. Ga = 0, $N_f = 2$ dB, and L = 2 dB, so

$$C/N_0 = -163 + 0 - (-204) - 2 - 2 = 37 \text{ dB/Hz} \tag{2}$$

Without interference, the minimum value of carrier to noise is 37 dB/Hz. The estimated value of C/N_0 is derived here.

3.2 Carrier to Noise Ratio ($[C/No]_{eq}$) with Interference

With interference, the equivalent carrier to noise ratio formula is shown as follows:

$$[C/N_0]_{eq} = -10\,log\left[10^{-(C/N_0)/10} + \frac{10^{(J/S)/10}}{QR_C}\right] \tag{3}$$

Rc is the PRN chip rate of BDS B1I signal.

Q is the anti-interference quality factor. For narrow-band interference Q = 1, for broad-band interference Q = 1.5.

J/S is interference to signal ratio.

In accord to the analysis, the equivalent carrier to noise ratio for different kinds of interference can be derived.

Table 1 Q = 1, Equivalent carrier to noise ratio

J/S (dB)	0	5	10	15	20	25
$[C/N_0]_{eq}$ (dB/Hz)	35	34.98	34.93	34.79	34.38	33.27

Table 2 Q = 1.5, Equivalent carrier to noise ratio

J/S (dB)	0	5	10	15	20	25
$[C/N_0]_{eq}$ (dB/Hz)	35	34.98	34.96	34.86	34.57	33.78

For continuous wave interference, Q = 1(Table 1).
For limited band-width white noise interference, Q = 1.5 (Table 2).

3.3 Effect of Interference Signal on Pseudo Range Tracking Error

BDS receiver pseudo range tracking error formula is shown as follows:

$$\sigma_{pr}^2 \approx \Delta^2 \left[B_{DLL} 4d^2 (1-d) \right] / C/N_0 \tag{4}$$

From this formula, it can be found that σ_{pr} is a function of C/N_0. By measuring the C/N_0 of BDS receiver, the effect of interference signal on pseudo range tracking error can be estimated. The pseudo range tracking accuracy is affected by many factors, which is in the inverse proportional relationship carrier to noise ratio, so the deterioration of carrier to noise ratio can reflect the receiver pseudo range tracking accuracy deterioration.

4 The Definition of Airborne Electromagnetic Interference Environment for Beidou B1I Receiver

The definition of the electromagnetic interference environment of the B1I receiver is the assessment and determination of the electromagnetic interference environment. This interference tolerance not only requires the B1I Beidou receiver anti-jamming capability, but also limits the airborne electromagnetic interference environment, which has certain significance to protect the airborne Beidou B1I receiver working band. It should be noted that this interference tolerance does not represent the ultimate anti jamming capability of the B1I receiver.

4.1 The Criterion of Airborne Electromagnetic Interference Tolerance Definition

1. Principle 1, due to out-band interference from the same airborne transmitter, the section of out-band interference should be consistent with the out-band interference tolerance of GPS and GLONASS system.
2. Principle 2, because of the capability requirement for multipath rejection, the Beidou receiver of B1I pre-detection bandwidth is defined as ±10 MHz. In which band, it is based on J/S = 15 dB to define interference signal tolerance.
3. Principle 3, pulse modulation interference tolerance should be consistent with GPS, GLONASS system requirements.

4.2 Tolerance of Continuous Wave Interference

The definition of continuous wave interference tolerance is shown in Table 3, and the corresponding continuous wave interference tolerance figure is shown in Fig. 1.

4.3 Tolerance of Band-Limited Noise-Like Interference

After steady-state navigation has been established, Beidou B1I receivers used for the precision approach phase of flight or used on aircraft with on-board satellite communications shall meet the performance objectives with noise-like interfering

Table 3 Threshold of CW interference

Frequency range f_j of the interference signal	Interference thresholds for receivers
$f_j \leq 1315$ MHz	−4.5 dBW
1315 MHz < $f_j \leq$ 1525 MHz	−4.5 to −42 dBW
1525 MHz $\leq f_j \leq$ 1551.098 MHz	−42 to −148 dBW
1551.098 MHz $\leq f_j \leq$ 1571.098 MHz	−148 dBW
1571.098 MHz $\leq f_j \leq$ 1610 MHz	−148 to −60 dBW
1610 MHz < $f_j \leq$ 1618 MHz	−60 to −42 dBW[a]
1618 MHz < $f_j \leq$ 2000 MHz	−42 to −8.5 dBW[a]
1610 MHz $\leq f_j \leq$ 1626.5 MHz	−60 to −22 dBW[b]
1626.5 MHz $\leq f_j$ j $\leq$ 2000 MHz	−22 to −8.5 dBW[b]
$f_j \geq$ 2000 MHz	−8.5 dBW

[a]Applies to aircraft installations where there are no on-board satellite communications
[b]Applies to aircraft installations where there is on-board satellite communications

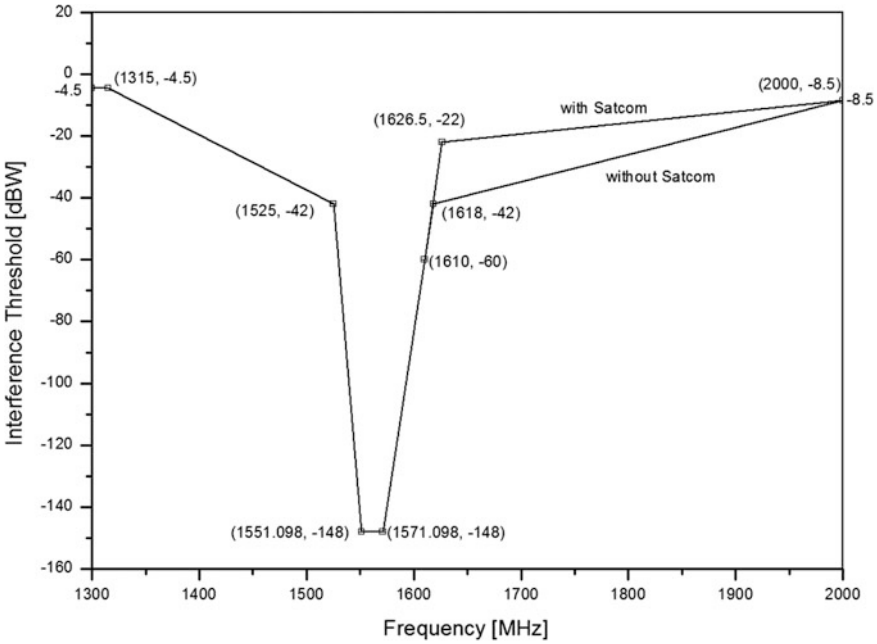

Fig. 1 CW interference threshold for BDS B1I receiver

Table 4 Threshold of band-limited noise-like interference

Interference bandwidth	Interference threshold[a]
0 Hz < Bwi ≤ 700 Hz	−148 dBW
700 Hz < Bwi ≤ 10 kHz	−148 + 6 log10(BW/700) dBW
10 kHz < Bwi ≤ 100 kHz	−141 + 3 log10(BW/10,000) dBW
100 kHz < Bwi ≤ 1 MHz	−138 dBW
1 MHz < Bwi ≤ 20 MHz	−138 to −125 dBW
20 MHz < Bwi ≤ 30 MHz	−125 to −118.6 dBW
30 MHz < Bwi ≤ 40 MHz	−118.6 to −117 dBW
40 MHz < Bwi	−117 dBW

[a]The interference threshold is not to exceed −138 dBW/MHz in the frequency range 1561.098 ± 10 MHz

signals present in the frequency range of 1561.098 MHz ± $B_{wi}/2$ and with power levels at the antenna port equal to the interference thresholds specified in Table 4 and Fig. 2 and with the desired signal level of −163 dBW at the antenna port.

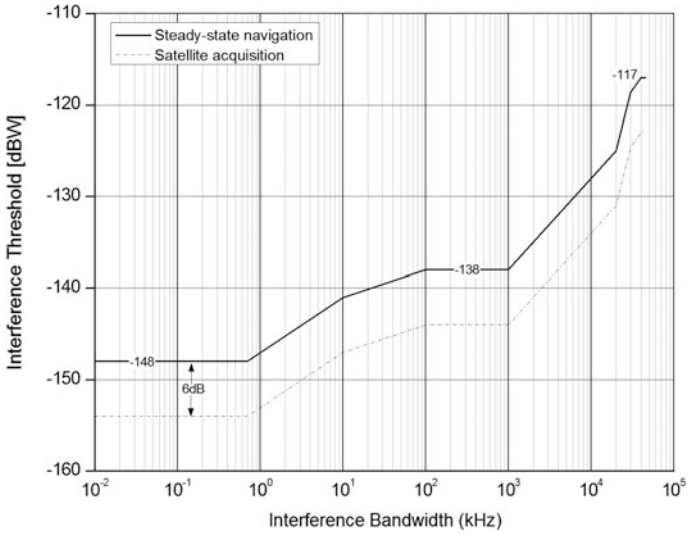

Fig. 2 AWGN interference threshold for BDS receiver

Table 5 Threshold of pulse modulation interference

Parameter	Value
Frequency range	1551.098 to 1571.098 MHz
Interference threshold (Pulse peak power)	−20 dBW
Pulse width	$\leq$ 125 μs
Pulse duty cycle	$\leq$ 1%
Signal bandwidth	$\geq$ 2 MHz

4.4 Tolerance of Pulse Modulation Interference

The definition of pulse modulation interference tolerance is shown in Table 5.

5 Pseudo Range Tracking Accuracy Testing of Receiver in Jamming Environment

5.1 Testing Purpose

Base on the investigation of civil aviation standards, the comparative analysis of GPS and Beidou system characteristics, the simulation of interference signal in GNSS receiver effect to noise ratio and the actual development of Beidou receiver hardware design process, the Beidou B1I system airborne electromagnetic

interference tolerance is defined. The experimental platform is built in the laboratory to reproduce the interference environment of three kinds of interference signals. The pseudo range tracking accuracy test of the Beidou receiver in the electromagnetic interference environment is completed.

5.2 *Testing Introduction*

Test Bench Introduction

As shown in Fig. 3, reference to RTCA Do-229D Appendix M in which a brief test set-up is demonstrated, our testing set-up is extended from it with supporting four receivers to do test synchronously [2]. A Beidou navigation simulator generates B1I signal same as receiving from its antenna. A low noise amplifier amplifies the B1I signal and suppresses out-band signals. A combiner mixes the interference signal and the B1I signal amplified by LNA. A divider has one input and four outputs, which divides input signal into four output signals and feeds those to four receivers. A data recording equipment is used to record four receiver data synchronously (Fig. 3).

The testing set-up intends to simulate a real airborne installation as possible, where satellites and the radiation pattern of the antenna are replaced by the BeiDou B1I simulator, the active portion of the antenna is replaced by a test amplifier with the same gain as the active antenna pre-amplifier [3, 4], and the loss block has the same total loss as a real one. The loss block is composed of the divider, the combiner, and associated cabling from the test amplifier output to the receiver port.

Solution for Generating Pulse Interference.

During the anti-interference testing, a commercial signal generator can be used to generate AWGN interference and CW interference. But for pulse interference, as the limited isolation value of commercial signal generator (70 dB), the pulse interference directly output by the generator can't satisfy anti-interference testing.

Because of the limited isolation value, when the maximum level of pulse interference is configured to −20 dBW, the minimum level of pulse interference

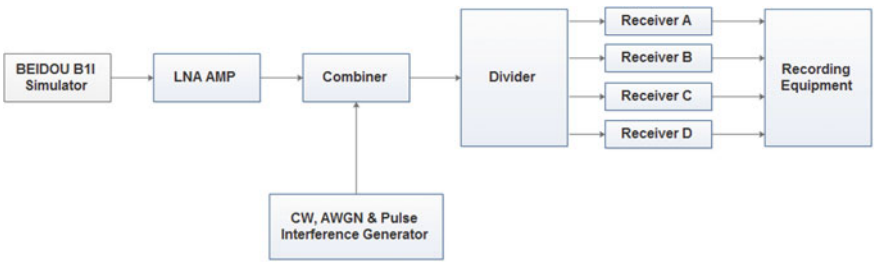

Fig. 3 Test bench for BDS B1I receiver

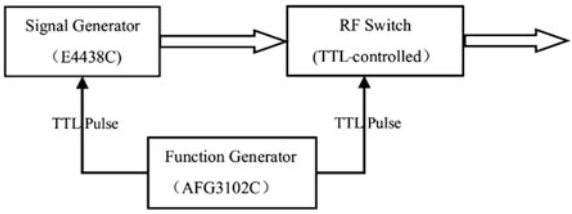

Fig. 4 Generating method for pulsed interference

Table 6 Performance of the BDS B1I receiver

Parameter	Value
Carrier smoothing pseudo range time	30 s
Pre-detection bandwidth	<20 MHz
Channel number	72
Tracking signal type	B1I

will be about −90 dBW. This kind of pulse interference is more likely a CW or AWGN interference. Receivers can't work in this interference environment.

Accord to the requirement of pulse interference generation, the isolation value of interference generator should be better than 120 dB. A new solution for pulse interference generation is explained in this paper. The solution is shown in Fig. 5.

In Fig. 4, Function Generator outputs TTL pulse in double channels synchronously. TTL pulse of channel one is fed to Signal Generator (E4438C) for pulse modulation base band signal. TTL pulse of channel two is fed to RF switch to control RF switch status. The isolation value of RF switch is about 60 dB, so the total isolation value of this solution is about 130 dB. It's better than 120dB that anti-interference testing required. The RF switch should be solid-state RF switch which has fast switch rate.

Beidou B1I Receiver Performance.

The performance of the Beidou B1I receiver during this test is shown in Table 6.

5.3 Test Results Analysis

In the process of testing, the RMS value of the pseudo range tracking accuracy is used to evaluate the performance of the Beidou B1I system under the airborne electromagnetic interference environment. The tracking accuracy of the pseudo range does not include the error of the satellite and the space segment, only the pseudo range tracking error caused by the thermal noise of the receiver is investigated. As shown in Fig. 5, it is the statistical distribution map for the Beidou receiver B1I measured pseudo range error, which satisfies the Gauss normal distribution, so the pseudo range tracking accuracy of RMS value could reveal the receiver pseudo range tracking performance [5].

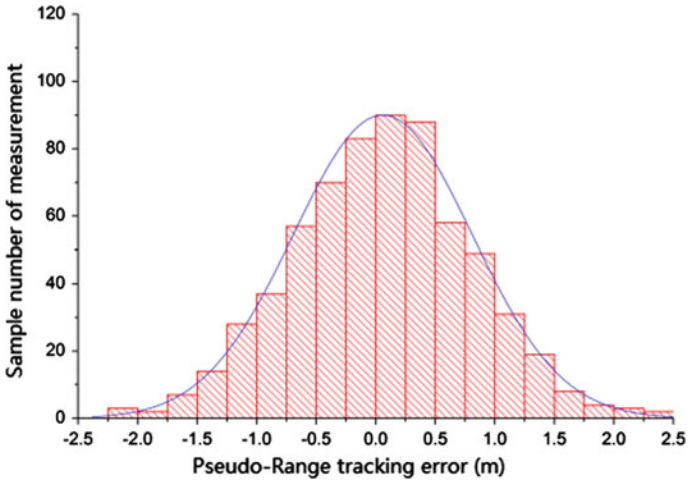

Fig. 5 Distribution of pseudo-range tracking error

The normalized RMS range error statistic, RMS_PR, is computed in accord to the following formula:

$$\mathrm{RMS\_PR(M)} = \sqrt{\frac{\sum_{j=1}^{M}\left\{\sum_{i=1}^{N_j}\frac{Z_{ij}^2}{N_j}\right\}}{M}} \tag{5}$$

where:

$$Z_{ij} = PR_{ij} - R_{ij} - (c\Delta t)_j$$

$$(c\Delta t)_j = \frac{1}{N_j}\sum_{i=1}^{N_j}\left(PR_{ij} - R_{ij}\right)$$

PR_{ij} smoothed pseudo-range, channel i, time j
R_{ij} true range, satellite i, time j
N_j number of satellites at time j
M number of sampling intervals

Pseudo Range Tracking Error during CW Interference Environment.

Every 5 min, the frequency of CWI interference is re-configured. CW interference frequency is scanning from 1315 to 2000 MHz. The output frequency of receiver observation data is 1 Hz, so there are 300 sample data at every CW carrier frequency configuration, those data can be used to process and get pseudo range tracking error (RMS).

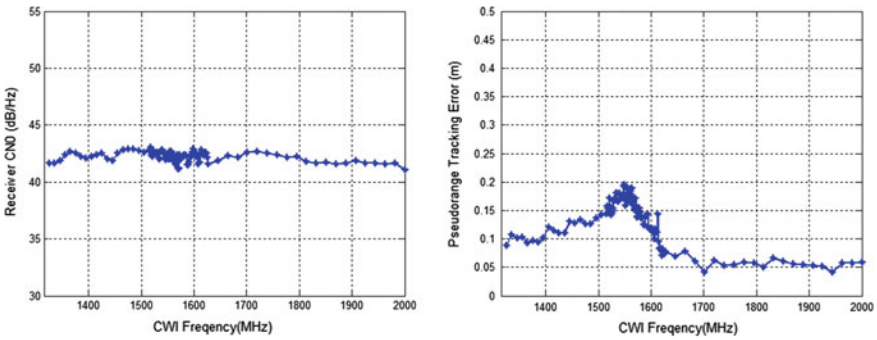

Fig. 6 C/N0 and pseudo-range tracking error RMS for CWI

As shown in Fig. 6, there are receiver pseudo range tracking errors during CWI interference. X-axis is CWI interference frequency from 1315 to 2000 MHz. he receiver pseudo range tracking error is better than 0.3 m.

Pseudo Range Tracking Error during Band-limited Noise-like Interference Environment.

Every 5 min, AWGN signal bandwidth is re-configured. AWGN signal bandwidth is limited between 50 kHz and 15 MHz because of the ability of the signal generator 4438C. The output rate of receiver observation data is 1 Hz, so there are 300 samples at every AWGN band width configuration, those data can be used to process and get pseudo range tracking error (RMS).

As shown in Fig. 7, the receiver carrier to noise ratio is worsen by AWGN interference. With AWGN interference, the carrier to noise ratio is about 40 dB/Hz. Without AWGN interference, the carrier to noise ratio is about 43 dB/Hz. there are receiver pseudo range tracking errors when receiver is affected by AWGN interference. X-axis is AWGN interference bandwidth. Just as shown in the figure, the receiver pseudo range tracking error is better than 0.2 m.

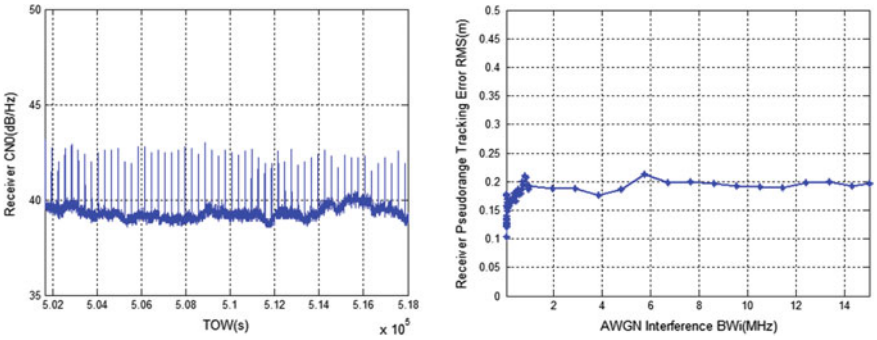

Fig. 7 C/N0 and pseudo-range tracking error RMS for band-limited noise-like interference

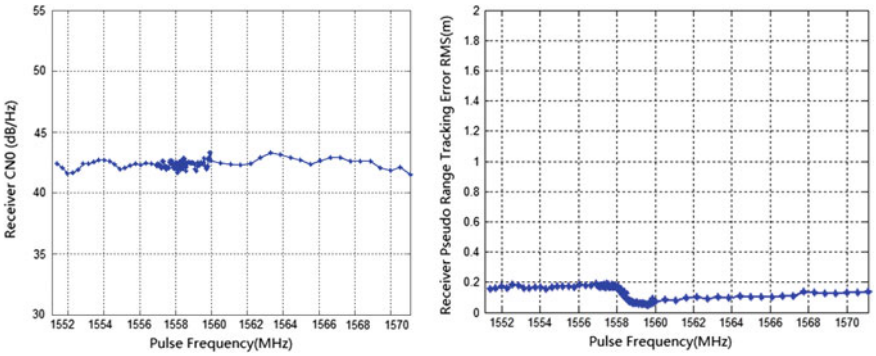

Fig. 8 C/N0 and pseudo-range tracking error RMS for pulse modulation interference

Pseudo Range Tracking Error during Pulse Modulation Interference Environment.

Every 5 min, the frequency of pulse modulation signal is re-configured. The output rate of receiver observation data is 1 Hz, so there are 300 samples at every AWGN band width configuration, those data can be used to process and get pseudo range tracking error (RMS).

Figure 8 shows the relationship between pulse frequency and receiver C/No. With pulse interference, the carrier to noise ratio is about 43 dB/Hz. In Fig. 9, there are receiver pseudo range tracking errors within pulse interference. The receiver pseudo range tracking error is better than 0.2 m.

6 Conclusion

The pseudo range tracking performance in the environment of airborne electromagnetic interference is an important index for the international civil aviation organization's application of GNSS system. With the promotion of the standardization of the Beidou, the pseudo range tracking performance of the Beidou B1I receiver in the interference environment becomes the focus of research. This paper analyzed the source of civil aviation electromagnetic interference signals and the classified typical interference signals, built civil aviation electromagnetic interference simulation environment in the laboratory, put forward a kind of high isolation pulse modulation interference pulse generation scheme and pseudo range tracking accuracy evaluation method. Beidou B1I receiver pseudo range tracking accuracy testing is accomplished in the lab. The test results are as follows:

(1) Scheme for generating high isolation pulse interference is put forward to meet the requirements of civil aviation pulse interference signal simulation, the pulse signal dynamic range is better than 120 dB, which provide necessary conditions for the anti-interference test.

(2) The probability distribution function of Beidou B1I receiver pseudo range error is Gaussian, tracking accuracy RMS value could evaluate the pseudo range tracking performance of the receiver.
(3) Under the condition of three types of electromagnetic interference, the RMS value of the pseudo range tracking accuracy of the B1I receiver is better than 0.3 m.

References

1. BeiDou Navigation Satellite System, Signal in Space, ICD. 2012
2. RTCA SC-159, Minimum operational performance standards for global position system/wide area augmentation system airborne equipment, RTCA document no. RTCA/DO-229D, 13 Dec 2006
3. Annex 10 to the Convention on International Civil Aviation, ICAO SARPs, 2006
4. RTCA SC-159, Minimum operational performance standards for GPS/local area augmentation airborne equipment, RTCA document no. RTCA/DO-253B, 26 June 2007
5. Betz JW (2001) Effect of partial-band interference on receiver estimation of C/N0. In: Proceedings of the ION NTM. Long Beach, CA, pp 817–828
6. Rao M, O'Driscoll C, Borio D, Fortuny J (2012) LightSquared effects on estimated C/N0, pseudoranges and positions. GPS Solutions

Research on Design and Implementation of the Test Support System Architecture for GNSS Ground Control Segment

Zhixue Zhang, Jinshi Xie, Na Zhao, Dongxia Wang and Xin Jie

Abstract Test systems of Global Navigation Satellite System (GNSS) ground control segment are important guarantees for system performance. A single test system cannot thoroughly support ground control segment tests both in the construction and operation phases. Based on this problem this paper proposes a test support system architecture, which could provide solutions for ground control segment tests. The paper firstly analyzes the test demands of the ground control segment in construction phase and operation maintenance phase. Then the architecture of test support systems is proposed. Moreover, implement and application of the architecture for different tests tasks in different phases are given. Analytical results demonstrate that the proposed system architecture which could fulfill the test demands of the whole ground control segment is practical, flexible and scalable. The results in this paper could provide references for the GNSS ground control segment tests and relative test system construction.

Keywords GNSS · Ground control segment · System test · System architecture

1 Introduction

GNSS is composed by the space segment (satellite constellation), ground control segment and application equipment segment. The main functions of satellite constellation include receiving navigation messages uploaded by the ground control segment and broadcast the messages to the user equipment. Ground control segment is mainly composed of master station, monitoring stations and upload/time synchronization stations. The master station is responsible for the navigation signal monitoring, time synchronization, navigation messages generation, task planning and scheduling, navigation constellation monitoring and control. Monitor stations using high performance monitoring receiver for continuous monitoring of multi

Z. Zhang (✉) · J. Xie · N. Zhao · D. Wang · X. Jie
Bejing Satellite Navigation Center, No. 22 Beiqing Road, Haidian District, Beijing, China
e-mail: zzx6057@sina.com

J. Sun et al. (eds.), *China Satellite Navigation Conference (CSNC) 2017 Proceedings: Volume I*, Lecture Notes in Electrical Engineering 437,
DOI 10.1007/978-981-10-4588-2_56

frequency satellite navigation signals and provides data for precise orbit determination, ionospheric correction and so on. Upload/time synchronization station work with the master station to upload navigation messages to the satellites. The user segment is mainly for receiving satellite navigation signal and provides positioning, speed testing and timing services for different users.

From the process of satellite navigation system construction and operation maintenance, ground control segment has different test demands and test methods at different stages. It is necessary for the ground control segment to establish a set of test systems for different test tasks. Until now there is little research on thorough demand analysis and corresponding test support system architecture of the ground Segment. From the construction reality this paper focuses on the demand analysis of the ground segment in the development stage of construction and operation and maintenance. The concept of ground control segment test support system construction is proposed for the first time, which could provide references for Beidou regional system and global system tests.

2 Current Status of Satellite Navigation System Test Techniques

An important direction of test technique of the satellite navigation system is the satellite navigation system simulation test, i.e., using computers to simulate, evaluate and verify the operations, construction, and maintenance of satellite navigation system. The simulation test of satellite navigation is an essential technique for system construction [2]. HFSS (High Fidelity System Simulator) is a set of high fidelity GPS simulation systems, which could be used for system operation training, and also could be used for system verification [3]. GSSF (Galileo System Simulation Facility), a simulation platform of Galileo system could verify the system framework design [4]. Most of the navigation system established dedicated satellite navigation system test fields for system performance evaluation and improvement, new signal and new service function verification. Foreign satellite navigation test fields include the construction in the development process of GPS system based on YPG (The test environment of GPS signal) and IGR system, GATE system in German (the equivalent to the combination of Yuma and IGR), GTR in Italy Rome (Galileo test field). In China, the major test field is the CGTR system (Galileo Chinese test field) [5]. Satellite navigation signal simulator which is essential for satellite navigation system construction and application is another typical product of satellite navigation simulation test technology.

Another important direction of satellite navigation system test is system performance evaluation. For example, the international global continuous monitoring and assessment system (iGMAS), use the GNSS high precision receiver and high gain antenna to monitor service performance and signal quality of GNSS, and

provides services for the majority of users around the world. The Beidou system has established a platform to monitor and evaluate open service space signal quality [6].

3 Demand Analysis for GNSS Ground Control Segment Test

All satellite navigation systems go through three stages of design, construction and operation and maintenance. From the practical construction point of view, the test demands of construction and operation and maintenance phases need more careful analysis. In real construction process, the construction phase could be divided into three parts of subsystem construction phase, integrated test phase and system test and evaluation phase. In the subsystem construction phase, the test environment of the subsystem is built up by the contractor. Thus, in this paper we focus on the test demands of the phases from integrated test to operation and maintenance.

3.1 Test Demand Analysis of Integrated Test Phase

Multi-band signal transceiver links are utilized for satellite time synchronization measurements and message injection, telemetry and telecontrol information transmission, data transmission between stations, and inter satellite measurement and data transmission, respectively. The test of each signal transceiver link focuses on satellite-ground signal connectivity, and the major transceiver indices.

During the system joint debugging, the implemented interfaces between satellites and ground stations, between systems in the master station, between the monitoring stations and master station should be tested very carefully.

During integrated test phase of the master control station, system businesses of time synchronization and satellite clock error prediction, precision orbit determination, wide area differential correction, ionospheric model parameter calculation and system integrity, message formulation, uplink message injection should be verified to ensure that the function and performance of the businesses could meet the system design requirements.

To ensure satellite tracking, ground control segment installs multiple large-diameter paraboloid antennas. After installation, electrical indices of antenna gain, polarization mode and electrical performance should be checked.

Ground control segment consists a number of monitoring stations, and each station installs 2–3 monitoring receivers. Before installation, monitoring receivers need parallel tests and manual test method has defects of low efficiency, human factors errors, etc. Therefore, an automatic batch receiver test system is highly needed to provide both wired and wireless test environments.

3.2 Test Demand Analysis of System Evaluation Phase

Before officially providing open services, function and performance index tests of the ground control segment should be carried out to check the actual state of the whole system, and guarantee that the status of the ground control segment fulfills the design requirement.

3.3 Test Demand Analysis of Operation Maintenance Phase

3.3.1 Business Troubleshooting Verification Test Requirements

During operation of the navigation system, fault positioning and recovery should be carried out immediately after failure occurs. For transceiver link troubleshooting and recovery, the test could be directly carried out based on the fault links. For system business processing troubleshooting, since the real-time online business cannot be interrupted, it is necessary to set up an independent troubleshooting verification environment.

3.3.2 System Performance Real-Time Monitoring Requirements

During operation, it is highly needed for service performance monitoring to detect anomalies in time and disposal afterwards. Service performance indices include spatial signal accuracy, positioning and timing accuracy, availability and continuity, etc.

4 Test Support System Design of Ground Control Segment

4.1 Test Support System Architecture Design

The test support system should include following functions.

1. Signal transceiver link test support, which could be applied in integrated test phase, system test and evaluation phase and operation and maintenance phase, assists test of all kinds of signal transmission link by developing various types of satellite simulator and equipped with universal testing instrument.
2. Interface test support, mainly used in the integration test phase, can also be used for interface verification after upgrading during the operation and maintenance phase.

3. System service test support, mainly used in the system integration test phase, especially based on simulation data. However, in the phase of system test evaluation and operation and maintenance, this function can be combined with system performance monitoring to provide real-time monitoring of system performance from both the internal and the user levels.
4. Large diameter parabolic antenna test support, which can be used in the integration testing phase, system testing and evaluation phase and operation and maintenance phase. By building the wireless far field test environment of the signal calibration tower, the main electrical performance and pointing indices test of the large diameter parabolic antenna can be assisted.
5. Monitoring receiver test support, which is mainly used in the integrated test phase, complete automatic batch test of the monitoring receiver before installation. This function can also be used during system operation and maintenance phase, for the monitoring receiver troubleshooting.
6. System service troubleshooting verification test support, which is mainly used in the operation and maintenance phase, build a test environment in full compliance with online business processing system, and support system business processing troubleshooting and verification.

4.2 Test Coverage Analysis of Test Support System Architecture

The corresponding relationship between the test demands and elements of the designed test support system architecture is shown in Table 1.

Table 1 Coverage analysis of ground control segment test support system

Element	Phase	Test demand
Signal transceiver link test support	Integrated test	Signal transceiver link test
	Operation and maintenance	Signal transceiver link troubleshooting
Interface test support	Integrated test	System interface test
System service test support	Integrated test	System service test
	Test and evaluation	System performance test
	Operation and maintenance	System performance real-time monitoring
Large diameter parabolic antenna test support	Integrated test	Large diameter parabolic antenna test
	Operation and maintenance	Large diameter parabolic antenna trouble
Monitoring receiver test support	Integrated test	Monitoring receiver test
	Operation and maintenance	Monitoring receiver troubleshooting
System service troubleshooting verification test support	Operation and Maintenance	System business troubleshooting verification

From Table 1, it can be readily seen that the test support architecture designed in this paper completely covers the test requirements of the ground control segment from the integrated test phase to operation and maintenance phase.

5 Implementation of Ground Control Segment Test Support System Architecture

5.1 Signal Transceiver Link Test Support

Transceiver link test scenario in the absence of the satellite link condition is shown in Fig. 1. The test devices (standard signal source, oscilloscope, spectrum analyzer and other universal test equipment) and satellite signal simulator (including the downlink navigation signal simulator, inter-station signal simulator, inter-satellite signal simulator, and telemetry signal simulator) are connected according to different test links and test items. Under the conditions of the actual satellites, receive link index test can directly use the orbiting satellites and the testing method is basically the same. Therefore, in order to guarantee the automatic test of the signal transceiver link, it is necessary to purchase the universal test instrument, develop the satellite signal simulator of different frequency band, different signal system and interface, develop the corresponding test and evaluation the software.

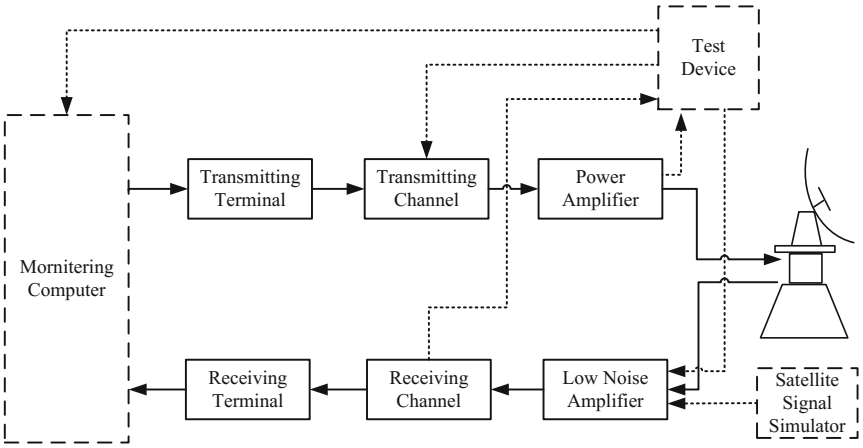

Fig. 1 The test of signal transceiver links based on satellite signal simulator

5.2 Interface Test Support

Interface test can be carried out in three phases. In the first stage, use satellite signal simulator connecting signal transceiver equipment to complete the information verification of the satellite interface. In the second stage, before each system is connected with each other, the interface test system can be used to interact with the system under test. The interface data is generated by emulation and sent to the system to be measured, and the interface data sent by the system under test is received. The system verifies the correctness of the interface by comparing the original binary interface information and the analytical information received by the system under test with the simulated data.

In the third stage, after each system is connected with each other, it can acquire the binary stream information of each system through the interception mode, and analyze the interface data of each system, and compare the information consistency among the systems.

5.3 System Business Test Support

In the absence of actual orbit satellite or constellation, or incomplete monitoring stations, simulation data could be used to test the system service process results (see Fig. 2). The service test system simulates the orbit and clock data of the whole constellation by data simulation unit, as well as the space environment parameter and the ground environment parameter, and further generates the simulation observation data and satellite telemetry data of each monitoring station. The data simulation unit sends the observation data and the telemetry data to the main control station service processing system, and the service processing system sends the generated navigation message to the upload station. The test evaluation unit obtains the navigation service processing result and the upload message generated by the service processing system through the internal network. By comparing the processing results of navigation business such as clock error, orbit, ionospheric model parameters and tropospheric model parameters with the original theoretical values in the simulation unit, the service process function and performance can be directly evaluated. By analyzing the injection message of the upload station and comparing with the result of the navigation service, the test and evaluation of the message formulation and upload service can be completed.

In the condition of complete constellation, the test system can also directly use the actual observation data for system service function and performance evaluation. The test and evaluation unit performs the UERE calculation directly using the navigation service processing result. In addition, we can compare the measurement data with the forecasting results of the service process center to realize the further evaluation of the business processing results.

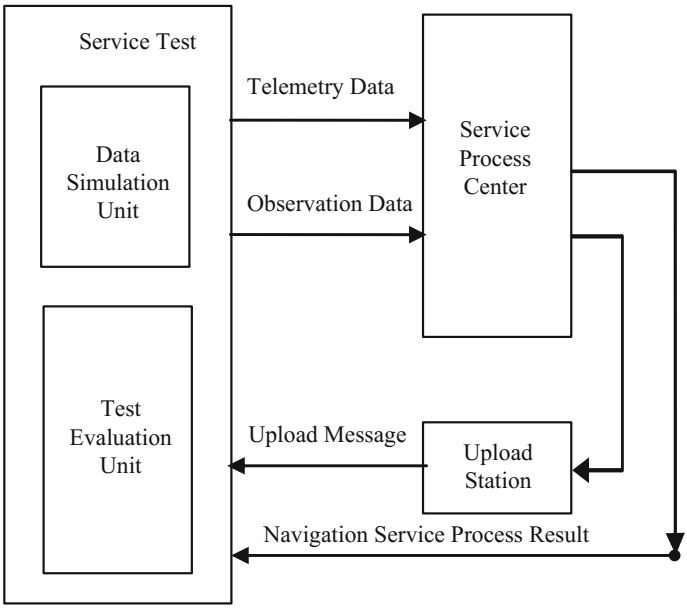

Fig. 2 The test of system business based on simulation data

5.4 *Large-Diameter Parabolic Antenna Test Support*

There are categories of antenna electrical index test methods including near-field, compact-field and far-field test methods. But limited by the antenna aperture and antenna field environment, generally we can only use far-field wireless test method which needs a signal calibration tower with certain distance, and set up a single carrier signal source on the top of the tower to send signals. By connecting the spectrum analyzer at the antenna coupling output port, the major electrical indices and pointing accuracy of the large aperture parabolic antenna can be tested (Fig. 3).

In addition, after the signal calibration tower is completed, through the establishment of different types of satellite signal simulator, it could be used for wireless test of transceiver links.

5.5 *Monitoring Receiver Test Support*

Cable test environment for monitoring receiver is shown in Fig. 4. Navigation signal simulator output RF navigation signal through the cable connection to the low noise amplifier of the receiver, to carry out major indices test including signal reception, signal acquisition, clock time and positioning accuracy, channel delay,

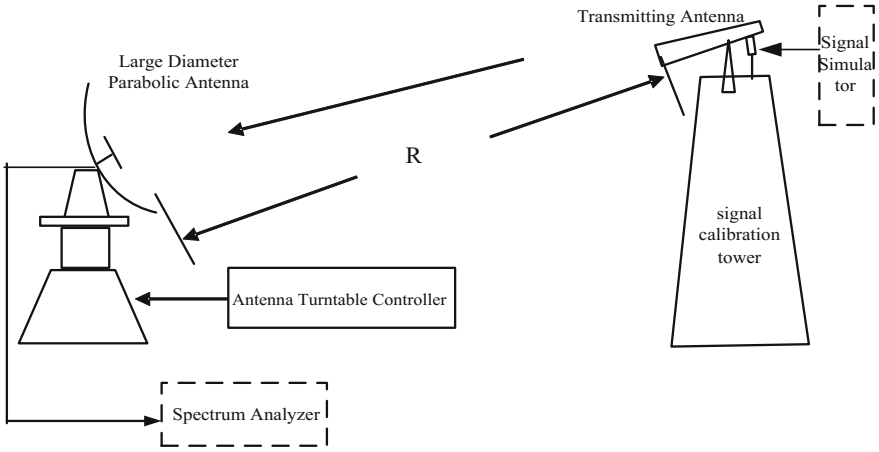

Fig. 3 Far field wireless test of parabolic antenna

device control and log query. The wired test environment supports simultaneous testing of multiple devices at the same time.

Wireless test environment for monitoring receiver is shown in Fig. 5. Monitoring Receiver test support system is mainly distributed in two areas, control room and microwave darkroom. The equipment in the microwave darkroom mainly includes transceiver antenna, interference antenna, turntable, serial server and program-controlled power lamp equipment, which are responsible for the establishment of system wireless test environment. The control room mainly includes equipment cabinet, console, which controls the test. Under wireless test conditions, some important performance indexes including error rate, measurement accuracy are tested.

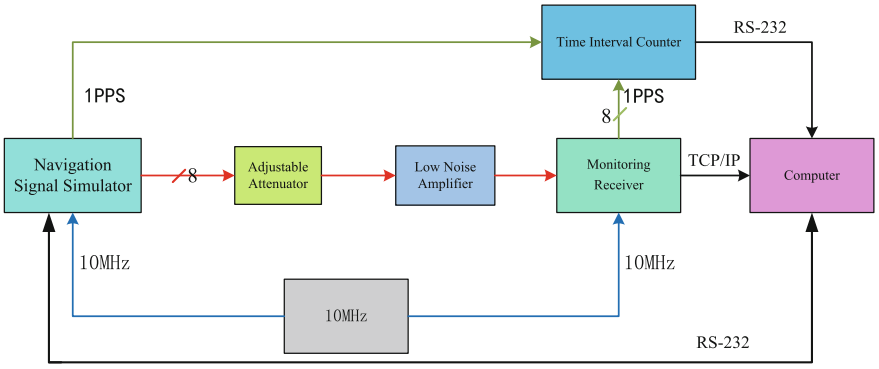

Fig. 4 The cable test of system monitoring receiver

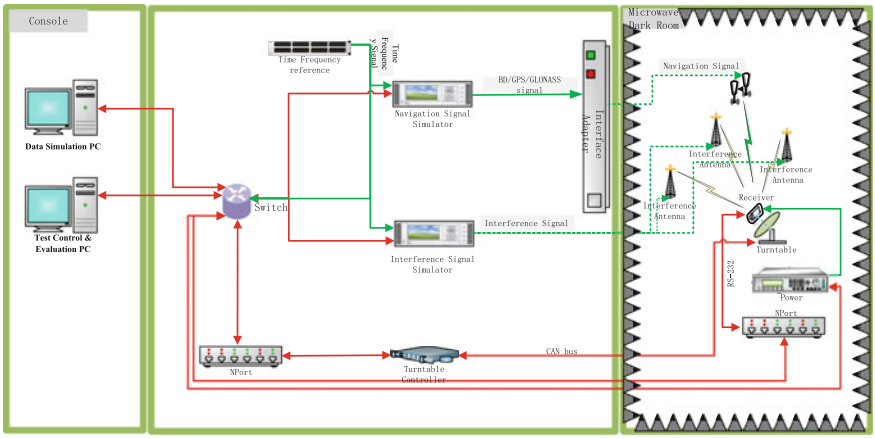

Fig. 5 The wireless-test of system monitoring receiver

5.6 *Test Support System Design of Test and Evaluation Phase*

For the troubleshooting of system services, it is necessary to deploy the same business software as the online system and configure the same hardware devices. The network security isolation device is used to support the security isolation between the platform and the online system. The system realizes the real-time data receiving, flow control, storage and extraction of the online system and the performance analysis and verification of the business processing software, and the troubleshooting and verification of the business process of the supporting system.

5.7 *Features of Testing Support System Architecture*

Through the realization of the designed test support system architecture,it can be seen that the test support system architecture has the following characteristics.

1. Utility: the test support system architecture could completely cover the system test requirements of the ground control segment and can be built up together with the ground control segment.
2. Flexibility: The functions of the test support architecture can be applied to different phase test of the ground control segment and some test support equipment can be used for multiple tests. For example, the signal calibration tower equipped with different signal sources can carry out large-diameter parabolic antenna test, various signal transceiver link test, respectively.

3. Scalability: The test security architecture designed in this paper can be extended according to the actual needs of the project. Moreover, a specific test function can also be extended for other test. For example, monitoring receiver test support system can be simply modified to support user terminal equipment testing.

6 Concluding Remarks

This paper analyzes the test requirements of the ground control segment from the integrated test phase to the test and evaluation phase and then to the operation and maintenance phase, and designs a test support system architecture. At the same time, the realization of the architecture is given. It can be seen from the analysis that the architecture completely covers the test requirements of the ground control segment, and has practical, flexible and scalable characteristics.

References

1. Elliott DK (2002) Understanding GPS principles and applications. Publishing House Of Electronics Industry, China
2. http://www.beidou.gov.cn. Accessed 20 Dec 2016
3. Driver T (1998) GPS high fidelity system simulator—a tool to benefit both the control and user segments. In: Proceedings of annual meeting of the institute of navigation
4. GSSF Operations Manual Volume 1, GSSFP2.OM.001, Issue 2 Rev. 1, September 2004
5. Yu B, Gan X, Li J (2010) Summarizing the test range of global satellite navigation system. In: The first china satellite navigation conference, Beijing
6. Jiao W, Ding Q, Li J et al (2011) Monitoring and assessment of GNSS open services. Sci Sinica (Physica, Mechanica & Astronomica) (05)

Analysis of Signal Quality and Navigation Performance for Beidou System

Shaohua Dou, Cuilin Kuang, Yaozong Zhou and Zhonghai Yi

Abstract With the rapid development of the Beidou satellite navigation system (BDS), assessment of its signal quality and navigation performance becomes more and more important. The pseudo-range multipath, carrier-phase signal-to-noise ratio (SNR) and accuracy of standard point positioning are usually taken as the indicators for assessment. In this research, we compared the signal quality and navigation performance of BDS with other three Global Navigation Satellite System (GPS, GLONASS, Galileo). The results of the Asia-Pacific region show that the pseudo-range multipath error for BDS is similar with GPS whereas the GLONASS code measurements exhibit a higher level. The level of carrier-phase signal-to-noise ratio for Galileo is largest, but similar for BDS, GPS and GLONASS. The standard point navigation and positioning performance of BDS is slightly lower than GPS, but it is better than GLONASS, and the accuracy of BDS, GPS and GLONASS standard point positioning is about 10 m. The pseudo-range multipath error of BDS increases as the satellites elevation decreases, but the carrier-phase signal-to-noise ratio is opposite. The variation of pseudo-range multipath error of BDS GEO satellites is small except for low satellites elevation, but the variation of signal-to-noise ratio of GEO satellites is relatively stable. The variation of multipath and signal-to-noise ratio of BDS IGSO and MEO satellites is relatively stable when the satellites elevation is larger than a certain value.

Keywords BDS · Signal quality · Navigation performance · Multipath error · Signal-to-noise ratio · Standard point positioning

S. Dou · C. Kuang (✉) · Y. Zhou · Z. Yi
School of Geosciences and Info-Physics, Central South University, Changsha, China
e-mail: cuilinkuang@163.com

J. Sun et al. (eds.), *China Satellite Navigation Conference (CSNC) 2017 Proceedings: Volume I*, Lecture Notes in Electrical Engineering 437,
DOI 10.1007/978-981-10-4588-2_57

1 Introduction

Following the Global Positioning System (GPS) of the United States and the Russia's GLONASS (GLO) navigation system, the third global navigation system, the Beidou satellite navigation system (BDS) has been developed by China. BDS was earlier referred to as COMPASS that used the active positioning method. The new generation of the BDS uses the passive positioning system similar to GPS. With the successful launch of the last geostationary orbit satellite on 25 October 2012, the regional BDS covering the Asia-Pacific region (latitude 55°, longitude 55° to 180°) was completed. And the constellation consists of 15 satellites, including 5 geostationary Earth orbit (GEO) satellites, 5 inclined geosynchronous orbit (IGSO) satellites, and 5 medium Earth orbit (MEO) satellites. This system provides positioning, navigation, timing and short message services for the Asia-Pacific region. The global BDS satellite constellation will be completed by 2020, which will include 5 GEO satellites, 3 IGSO satellites and 27 MEO satellites. At present, the regional BDS provides three navigation signals with frequencies of 1561.098 MHz (B1), 1207.14 MHz (B2), 1268.52 MHz (B3), and code rates of 2.046, 2.046 and 10.23cps, respectively.

In the past few years, some scholars have studied the navigation performance and signal characteristics of the BDS. Zhao et al. showed that with the same elevation, the carrier-to-noise ratio (CNR) of B1 observables is the lowest and that of B3 is the highest among the three BDS frequencies. And the multipath of BDS IGSO and MEO satellites are remarkably correlated with elevation angle [1]. Yang et al. concluded that the variation of BDS multipath error is related to the elevation angle, satellite orbit type and carrier frequency, but independent with the location of the receivers by analyzing the iGMAS data [2]. Wang et al. demonstrated that the GEO multipath error vary from <1 m to around 2 m [3]. Ma et al. [4] found that the multipath of GEO satellites presents low-frequency changes, but that of IGSO and MEO satellites exhibits high-frequency changes. Multipath correction will bring higher positioning accuracy, especially in the east-west direction. Cai et al. [5] showed that the code multipath error for GLONASS is the largest among the four global navigation systems, whereas the Galileo code measurements exhibit a low level code multipath error at frequency E5. Yang et al. [6] analyzed the navigation and positioning performance of BDS and got the results that its pseudo range and carrier measurement accuracy are at the same level with the GPS.

In this paper, with the selected GNSS data of MGEX and iGMAS stations, we analyzed the signal quality and the navigation performance of the second generation BDS by three specific indicators i.e., pseudo-range multipath error, signal-to–noise ratio and standard point positioning accuracy based on pseudo-range.

2 Data

In this research, the multi-GNSS data from 10th to 19th Feb 2016 were selected from 3 iGMAS and 11 MGEX stations distributed in the Asia-Pacific region (Fig. 1). Listed in Table 1 is the information of the 14 stations, ten of which are equipped with TRIMBLE NETR9 receivers. The GNSS data sampling interval was set as 30 s,and the format is above RINEX 3.0.

3 Signal Quality Analysis for Beidou System

3.1 The Indicator of Signal-to-Noise Ratio

Signal to noise ratio (SNR) is the ratio between the received carrier signal strength and the noise intensity, which is usually expressed as the carrier noise power density ratio (C/N0) with unit dB/Hz. The SNR is mainly affected by the antenna gain parameter, the state of the correlator in the receiver and the multipath error, which is good indicator of satellite signal quality. The SNR value changes with the multipath error. The higher the SNR, the better the signal quality and accuracy of the observation [7, 8]. As an important indicator of the quality of the observer carrier phase, SNR of each observation epoch of all satellites can be extracted directly from the RINEX file.

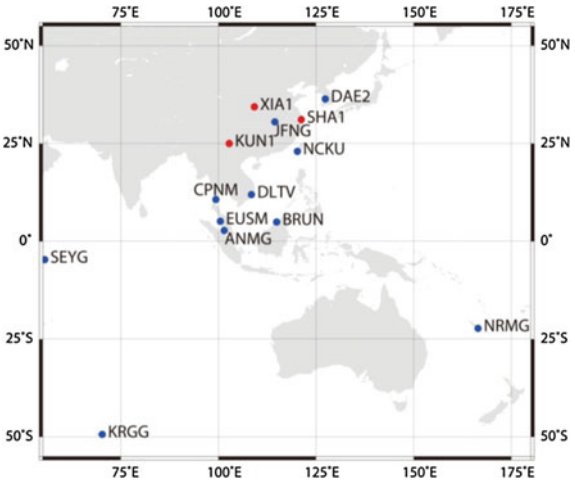

Fig. 1 Distribution of the selected GNSS stations. *Red dots* are iGMAS stations, and *blue dots* stand for MGEX stations (Color figure online)

Table 1 The information of selected stations

No.	Stations	Receiver types	Longitude (°)	Latitude (°)	Remarks
1	KUN1	UNICORE UB4B0I	102.80	25.03	iGMAS
2	SHA1	UNICORE UB4B0I	121.20	31.10	iGMAS
3	XIA1	gnss_ggr	109.22	34.37	iGMAS
4	ANMG	TRIMBLE NETR9	101.51	2.78	MGEX
5	BRUN	TRIMBLE NETR9	114.95	4.97	MGEX
6	CPNM	TRIMBLE NETR9	99.37	10.72	MGEX
7	DAE2	TRIMBLE NETR9	127.37	36.40	MGEX
8	DLTV	TRIMBLE NETR9	108.48	11.95	MGEX
9	EUSM	TRIMBLE NETR9	100.49	5.15	MGEX
10	JFNG	TRIMBLE NETR9	114.49	30.52	MGEX
11	KRGG	LEICA GR10	70.26	−49.35	MGEX
12	NCKU	TRIMBLE NETR9	120.22	23.00	MGEX
13	NRMG	TRIMBLE NETR9	166.48	−22.23	MGEX
14	SEYG	TRIMBLE NETR9	55.53	−4.68	MGEX

3.2 The Indicator of Pseudo-range Multipath Error

Because of the station observation environment and design of receiver itself, also some other reasons, the received data often contain reflected signals from surrounding objects such as surface buildings and water, which form the multipath errors interfering with the direct signals [4]. The magnitude of multipath errors is determined by the characteristics of the correlator and the tracking lock loop in the receiver. The multipath affects both the GNSS observations pseudo-ranges and carrier phases. The multipath of the former can be up to 0.5 code width, but of the latter is generally less than 1/4 wavelength, so the multipath of pseudo-range is mainly considered.

When dual-frequency data are available, the pseudo-range multipath error is estimated from the linear combination observation (MP), as shown in Formula (1), which eliminates the satellite-receiver geometry and all atmospheric effects. However, this combination observation does not eliminate ambiguities and any GPS error. While the latter is almost constant over time, this assumption is not always true for ambiguities due to a presence of cycle slips. The pre-processing (and optionally a cycle slip repair) is thus important for the multipath error estimation. This method is suitable for all frequencies, available signals and GNSS constellations providing dual-frequency observations at least.

$$MP_k = P_k - L_i - \beta(L_i - L_j) = P_k + \alpha L_i + \beta L_j \tag{1}$$

with

$$\alpha = -\frac{(f_j^2 + f_k^2) f_i^2}{(f_i^2 - f_j^2) f_k^2}, \quad \beta = \frac{(f_i^2 + f_k^2) f_j^2}{(f_i^2 - f_j^2) f_k^2} \tag{2}$$

where k, i and j are frequency (band) indexes, L is the measured carrier phase in meters observables, f is the carrier phase frequency in Hertz, and P is measured pseudo-range in meters. The multipath error statistics are then estimated as a standard deviation over a sequence of consecutive epochs [9, 10].

3.3 *Experimental Analysis for Beidou Signal Quality*

3.3.1 Comparison of SNR and Pseudo-rang Multipath in Different Systems

To analyze the signal quality of BDS, SNR and pseudo-range multipath of four different systems (GPS, BDS, GLONASS, Galileo) are compared. The results related to SNR are shown in Figs. 2 and 3, and the multipath error results are shown in Figs. 4 and 5. For Figs. 2 and 4, the relationships between multipath and SNR to elevation are based on the data of JFNG station on 10th Feb 2016. For Figs. 3 and 5, the mean of multipath and SNR are the processed results of continuous ten days data of JFNG station. The observation code tna (i.e. S1C, M1I, …) consists of three parts, t is observation type (i.e. S is SNR, M is multipath), n is frequency (i.e. 1, 2, 6, 7, …), and a is attribute, tracking mode or channel (i.e. I, C, W, …). The specific meaning of each encoding part (except for M is multipath) is based on RINEX version 3.02.

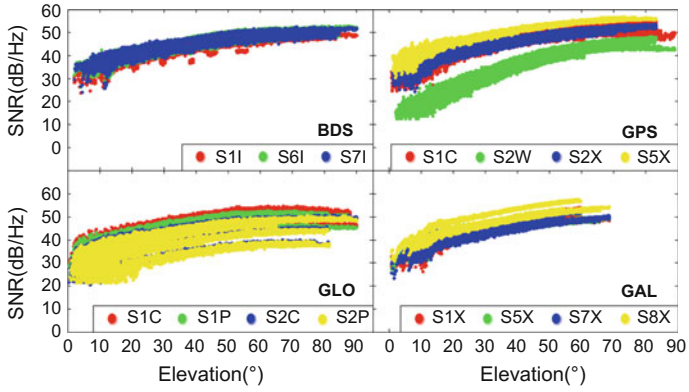

Fig. 2 The relationship between SNR and satellite elevation for BDS, GPS, GLONASS, and Galileo satellites at station JFNG

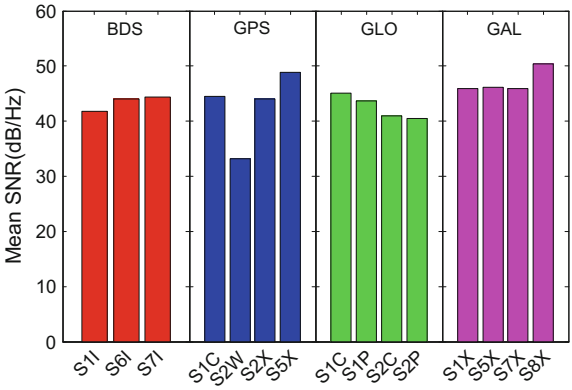

Fig. 3 The mean of SNR for BDS, GPS, GLONASS, and Galileo satellites at station JFNG

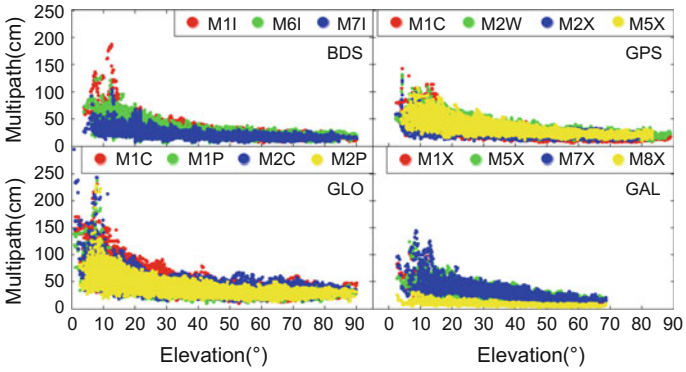

Fig. 4 The relationship between multipath and satellite elevation for BDS, GPS, GLONASS, and Galileo satellites at station JFNG

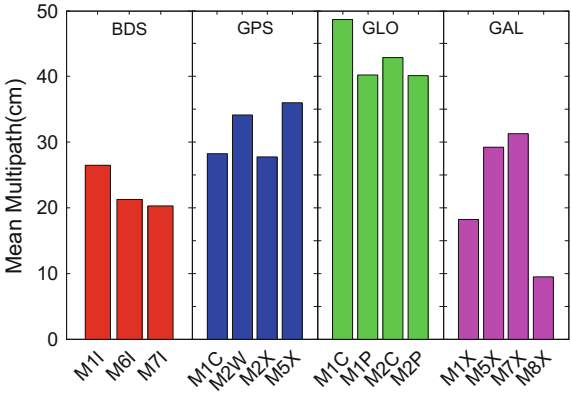

Fig. 5 The mean multipath for BDS, GPS, GLONASS, and Galileo satellites at station JFNG

Figures 2 and 3 show that the SNR of all system increase significantly with the growing elevations, and the SNR is lower when the elevation is low. The SNR of Galileo is the highest, and followed by that of BDS. The SNR of GLONASS and GPS 2 W signal are both affected by elevations, but the latter is more sensitive to elevation. And the mean SNR of GPS 2 W is the lowest. Among the three BDS signals, BDS 1I signal has the lowest SNR and BDS 7I has the highest SNR. When the elevations are about 20°, 30°, 40° and 50°, the SNR of 1I is much lower than that of 6I and 7I signals, this is because the 5 GEO satellites have lower SNR than other satellites at the same elevation.

As is shown in Figs. 4 and 5, the mean multipath error of BDS is smaller than that of GPS. And the multipath error on the 8X signal of Galileo has the smallest amplitude and dispersion, for which the multipath magnitude is below 0.5 m, even at low elevation angels. By contrast, GLONASS has the largest multipath magnitude. Remarkably, when the elevation angel is around 20°, the 7I signal of BDS has larger amplitude and dispersion, which may be caused by one GEO satellite. But the multipath error of the 7I signal is smaller when the elevation is below 20°. So we can infer that the multipath on the 7I signal of BDS GEO satellites is greatly influenced by the elevation angel. The smaller multipath error and larger SNR of the 7I signal of BDS MEO and IGSO satellites indicates that its anti-interference ability is the strongest.

3.3.2 Comparison of SNR and Pseudo-range Multipath with Different Frequencies for BDS

The satellite constellation of BDS, consisting of GEO, IGSO and MEO satellites, is different from that of GPS, GLONASS and Galileo. So it is necessary to analyze the SNR and pseudo-range multipath error characteristics of different types of BDS satellites. In this paper, BDS data collected from the 41st day of 2016 at the JFNG station were employed to analyse the difference, and the results are shown in Figs. 6 and 7.

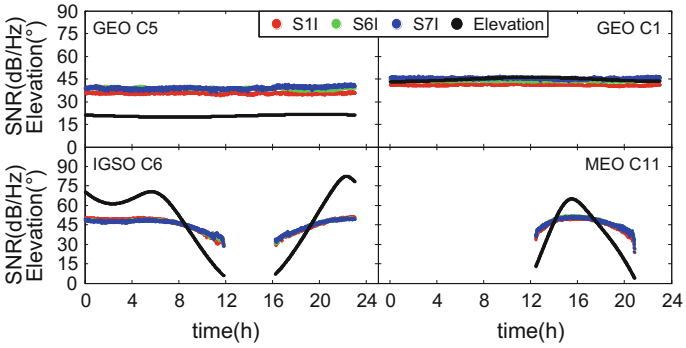

Fig. 6 The relationship between SNR and elevation angle for different BDS satellite types

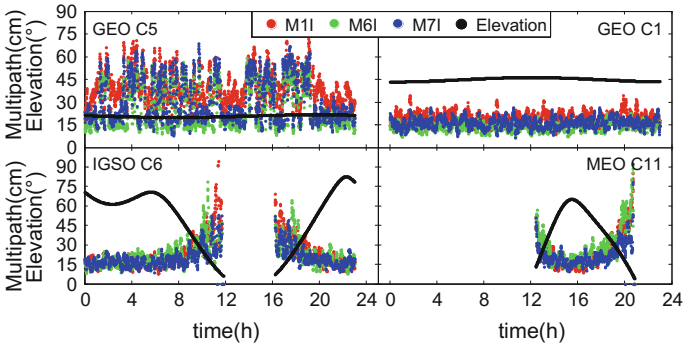

Fig. 7 The relationship between multipath and elevation angle for different BDS satellite types

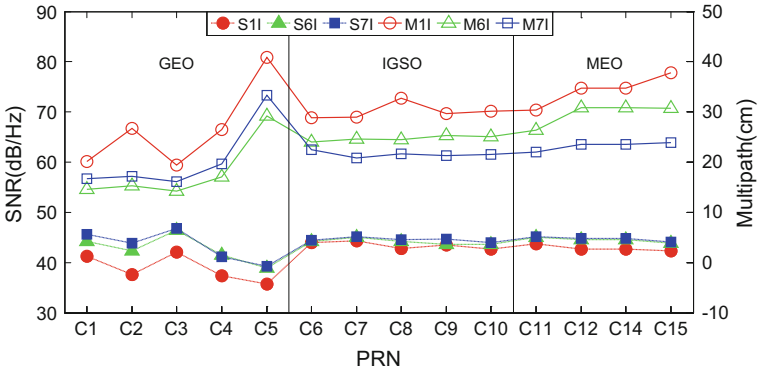

Fig. 8 The mean SNR and multipath of each BDS satellite

In Figs. 6 and 7, the SNR of BDS GEO satellites (i.e. C1, C5) are stable, but their multipath error is stable only when the elevation of satellites is high. For all satellites, the SNR increase significantly with the increasing elevations, and the trend of multipath is opposite. But the change of SNR and multipath is small when the elevation exceeds a certain value (i.e. 60°).

In order to compare the differences between different types of BDS satellites in detail, the mean SNR and multipath of each BDS satellite are shown in Fig. 8.

As Fig. 8 shows, BDS 1I signal has the smallest SNR but the largest multipath. For the BDS GEO satellites, the multipath on the 6I signal is the smallest, but for the BDS IGSO and MEO satellites, the multipath on 7I signal is the smallest. For the SNR on BDS 6I and 7I signal is similar. More experiments have shown that the above situation exists only in 'TRIMBLE NETR9' receiver.

4 Navigation Performance Evaluation for Beidou System

Pseudo-range standard point positioning has low economical cost, flexibility, convenience and fast speed, and can meet the requirements of real-time positioning very well, so it has been widely applied in various fields. In this paper, the BDS navigation performance evaluation is based on the standard point positioning of GNSS pseudo-range observation.

4.1 Pseudo-range Standard Point Positioning

Considering some important errors, the GNSS pseudo-range measurements can be written as:

$$\widetilde{\rho}^{j}(t) = \rho^{j}(t) + c \cdot \delta_{t_R}(t) - c \cdot \delta_{t^j}(t) + \Delta^{j}_{I_g}(t) + \Delta^{j}_{T}(t) + \varepsilon \tag{3}$$

where $\widetilde{\rho}^{j}(t)$ is the pseudo-range to the satellite receiver. $\rho^{j}(t)$ is the geometric distance to the satellite receiver. c is the speed of light, $\delta_{t_R}(t)$ is the receiver clock error. The satellite clock error $\delta_{t^j}(t)$ can be calculated by the clock error correction parameters in the navigation message. The ionosphere delay $\Delta^{j}_{I_g}(t)$ can be eliminated by dual-frequency combination. The troposphere delay $\Delta^{j}_{T}(t)$ can be calculated by the Saastamoinen model. And the pseudo-range measurements noise ε can be ignored. $\rho^{j}(t)$ contains the coordinate information of the receiver (x, y, z), so the formula contains four unknowns (x, y, z and $\delta_{t_R}(t)$). The receiver coordinates can be calculated by the linearization and Kalman filtering [11, 12].

4.2 Accuracy Evaluation for Standard Point Positioning

In the experiment, because the number of Galileo satellites is too small, the standard point positioning can't be calculated. The positioning residual RMS of BDS, GPS, GLONASS for each station shown in Fig. 9 is calculated with data of 10 days. Table 2 shows the positioning residual RMS for each system.

As is shown in Fig. 9, the pseudo-range standard point positioning results of iGMAS and MGEX station is similar. And BDS, except some station in the edge of BDS coverage, has similar results with GPS, significantly better than that of GLONASS. As is shown in Table 2, the accuracy of GPS is better than 3 m. The horizontal accuracy of BDS is better than 5 m, and the vertical accuracy is better than 10 m. For GLONASS, the accuracy of North (N) direction is better than East (E) direction, and E direction is better than Up (U) direction.

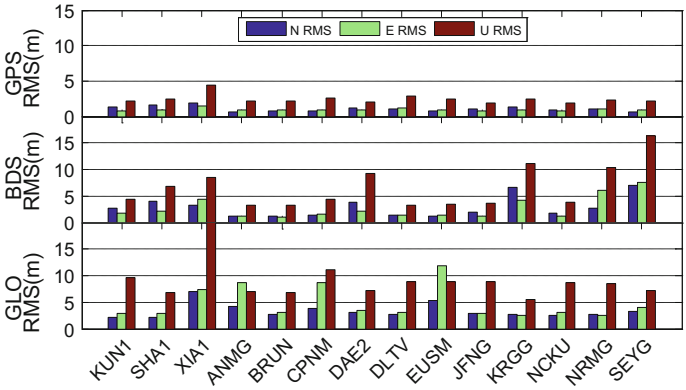

Fig. 9 RMS of standard point positioning residual for selected stations

Table 2 RMS of positioning residual for BDS, GPS, GLONASS standard point positioning

System	RMS (m)		
	N	E	U
BDS	3.42	3.34	7.63
GPS	1.14	0.96	2.50
GLO	3.63	5.62	9.74

5 Conclusions

In this paper, the GNSS data from 14 iGMAS and MGEX stations of the Asia-Pacific region were utilized to investigate the SNR, multipath error and pseudo-range standard point positioning accuracy of GPS, BDS, GLONASS and Galileo. Their characteristics with time and elevation were analyzed and compared for different system or different satellite types.

For the SNR and multipath error, BDS is similar to GPS, and the multipath error of GLONASS is the largest. For the accuracy of pseudo-range standard point positioning, the data from iGMAS get similar results with the data from MGEX. In the center area of BDS coverage, the positioning accuracy of BDS is similar with GPS, and better than GLONASS. The horizontal accuracy of BDS is better than 5 m, the vertical accuracy is better than 10 m. For GLONASS, the accuracy of N direction is better than E direction, and E direction is better than U direction.

The 1I signal of BDS has the lowest SNR but largest multipath. The 6I and 7I signal have similar SNR and multipath. With the same low elevation, the multipath on the 7I signal of GEO is larger than that of IGSO and MEO. With the same high elevation, the multipath on 7I signal of GEO is smaller than that of IGSO and MEO. For the data collected by the 'TRIMBLE NETR9' receiver, the multipath on 6I signal of BDS GEO satellites is the smallest, but that on 7I signal of BDS IGSO and MEO satellites is the smallest.

Acknowledgements The financial support from National Key Research and Development Plan (No. 2016YFb0501803) is greatly appreciated.

References

1. Zhao Q, Wang G, Liu Z et al (2015) Analysis of BeiDou satellite measurements with code multipath and geometry-free ionosphere-free combinations. Sensors 16(1)
2. Yang W, Tong H, Pan L et al (2016) Analysis and correction of BDS code multipath bias. In: China satellite navigation conference (CSNC) 2016 proceedings: volume III. Springer, Singapore
3. Wang G, Jong K, Zhao Q et al (2015) Multipath analysis of code measurements for BeiDou geostationary satellites. GPS Solutions 19(1):129–139
4. Ma X, Shen Y (2014) Multipath error analysis of COMPASS triple frequency observations. Positioning 05(1):12–21
5. Cai C, He C, Santerre R et al (2015) A comparative analysis of measurement noise and multipath for four constellations: GPS, BeiDou, GLONASS and Galileo. Survey Review 2015:1–9
6. Yang YX, Jinlong LI, Wang AB et al (2014) Preliminary assessment of the navigation and positioning performance of BeiDou regional navigation satellite system. Sci China Earth Sci 57(1):144–152
7. Axelrad P, Behre CP (1999) Satellite attitude determination based on GPS signal-to-noise ratio. Proc IEEE 87(1):133–144
8. Strode PRR, Groves PD (2016) GNSS multipath detection using three-frequency signal-to-noise measurements. GPS Solutions 20(3):399–412
9. Vaclavovic P, Dousa J (2015) G-Nut/anubis: open-source tool for multi-GNSS data monitoring with a multipath detection for new signals, frequencies and constellations. In: IAG 150 Years. Springer International Publishing, Switzerland, pp 1–8
10. Vaclavovic P (2013) G-nut software library—state of development and first results. Acta Geodynamica Et Geomaterialia 2013:431–436
11. Zhu Y, Jia X, Liang Y (2013) Analysis of positioning accuracy for COMPASS based on single/multi frequency pseudo-range. In: China satellite navigation conference (CSNC) 2013 proceedings. Springer, Berlin, pp 391–401
12. Mosavi MR, Azad MS, Emamgholipour I (2013) Position estimation in single-frequency GPS receivers using Kalman filter with pseudo-range and carrier phase measurements. Wireless Pers Commun 72(4):2563–2576

Influence of Space Environment on the Beidou Satellite and Its Countermeasures

Ailing Zhang, Xingyu Wang, Ting Wang, Wenjie Liang and Ni Kang

Abstract Space environment is the main factor that infects the operation and the safe of the satellites. The operation of the satellite components and electronic equipment may be destroyed because of various environmental factors, the performance of devices is decreased and damaged. The safety of the satellite in orbit is threatened. Since the running of the Beidou Navigation Constellation, a large number of satellite anomalies have been caused because of the space environment, the failure of the satellite components have been caused, the service of navigation and the safe of platform has been influenced. Several typical space environment effects and different influences on spacecraft are researched in this paper. The causes of faults which are associated with space environment are studied. The laws of generation of fault are analyzed. The disposal strategies of resolving these faults are presented. It is valuable for the Beidou satellite fault prediction and proposal. Meanwhile, it is helpful for the research department in the later designation.

Keywords Space environment · Fault · Countermeasure · Beidou satellite

1 Introduction

Space radiation is a major factor affecting the safe operation and operation of satellites. Various types of space radiation on the satellite have different types of effects, may undermine the satellite components and electronic equipment work, resulting in device performance degradation, or even damage, a serious threat to satellite security in orbit. It is estimated that the annual satellite radiation losses

X. Wang
Key Laboratory for Fault Diagnosis and Maintenance
of Spacecraft in Orbit, Xi'an 710043, China
e-mail: wxyyx_001@sina.com

A. Zhang (✉) · X. Wang · T. Wang · W. Liang · N. Kang
Xi'an Satellite Control Center, Xi'an 710043, China
e-mail: lmlzal@sina.com

J. Sun et al. (eds.), *China Satellite Navigation Conference (CSNC) 2017 Proceedings: Volume I*, Lecture Notes in Electrical Engineering 437,
DOI 10.1007/978-981-10-4588-2_58

caused by space radiation effects can reach several hundred million dollars. Since the Beidou navigation constellation has been in orbit, a large number of satellite anomalies have been caused by space radiation, leading to the failure of the satellite components, affecting the satellite navigation service performance and platform security. Therefore, it is very important and absolutely important to analyze the mechanism of the influence of space radiation on Beidou satellite and formulate the influence of Beidou satellite on space radiation, and to ensure the long life and high reliability operation of Beidou satellite.

2 Typical Space Radiation Effects and Hazards

Spacecraft operates in space outside the Earth's atmosphere, similar to the weather phenomenon on the surface of the Earth, where there are short-term changes in various spatial environmental states, and solar storms are one of the factors that cause changes in space weather. The solar eruption activity is a short-term, large-scale energy release phenomenon in the solar atmosphere. The matter and energy of the solar eruption activities can cause violent perturbations in the Earth's magnetosphere, ionosphere and the upper and middle atmosphere. When the sun burst out of the material and energy towards the Earth, it may cause the Earth's space environment disturbance, thereby affecting orbital spacecraft. Typical space radiation effects caused by solar storms are ionization total dose effect, displacement effect, single-particle effect, surface charge-discharge effect, internal charge effect, atmospheric drag effect and ionospheric disturbance effect.

2.1 Ionization Total Dose Effect

When the space charged particles collide with the components and materials that make up the spacecraft, some or all of the energy can be transferred to the components and materials through ionization to change their performance. This is called the "total ionization effect". Spacecraft components and materials in the space radiation environment, absorption of ionization after the transfer of energy components and materials will appear performance degradation parameters drift and other phenomena, affecting the normal operation of components [1].

2.2 Displacement Effect

High-energy particles are incident on the material, in addition to energy transfer through ionization, but also by atomic and non-elastic elastic collision (i.e., ionization), resulting in atomic displacement, and the formation of a stable defect, thus the performance of semiconductor devices. The effect is called the displacement

effect [2]. Displacement effect will make use of minority carriers of the work of the device signal to noise ratio variation, the output signal attenuation. For example, due to the displacement effect, CCD devices will appear on the image when the image of the device will affect the image quality, serious damage to the CCD device can not cause imaging.

2.3 Single Event Effect

When a single space energetic proton or heavy ion strikes the microelectronic device on the spacecraft, a large number of electron-hole pairs are generated by ionization in its moving path. The redistribution of these electron holes in the device, and sometimes cause data errors, confusion and even computer system computer system paralysis, causing satellite anomalies and failures in the orbit. This single event triggered by a single high-energy particle is a so-called single-event effect. Electronic devices are usually 0 and 1 two states, when a single high-energy particles were shot into the device, through ionization will produce a large number of electron-hole pairs. After redistribution of these electron holes inside the device, the state of the electronic device may change from the 0 state to the 1 state or from the 1 state to the 0 state. These electron-hole pairs are collected by the device electrodes, resulting in abnormal changes in the logic state of the device, or even cause device damage.

2.4 Surface Charge and Discharge Effect

The surface charge of a spacecraft means that the spacecraft immersed in the plasma environment is continually impacted by the charged particles, and the electrons of energy in the order of kilo electrons stay on the surface of the spacecraft. As a result, the surface of the spacecraft is negative with respect to the surrounding space Potential. Due to different parts of the surface of the spacecraft conductivity, design status and working conditions are different, there will be varying amounts of charged, so that the potential difference between the various parts of spacecraft. Surface charge and discharge effect will cause electrostatic discharge, electromagnetic pulse interference, high-voltage solar array secondary discharge effect, causing solar array power loss and physical damage to the surface material of spacecraft.

2.5 Charged Effect in Spacecraft

When a large radiation environment disturbance occurs, a large number of high-energy electrons can be injected into the geosynchronous orbit or even a low altitude orbit, making the Earth's radiation zone energy greater than 1 meV

increased significantly. These electrons will penetrate directly into the skin of the spacecraft, including the outer conductive surfaces and insulating materials, the spacecraft structures and instrumentation housings, deep-seated dielectrics such as circuit boards inside the spacecraft, wire insulation. Resulting in insulating media such as circuit boards, coaxial cable and other deep charge accumulation, resulting in deep dielectric charged, that is, the so-called internal charge effect. Electromagnetic pulse interference generated by internal discharge, usually through the internal wiring of the spacecraft, antenna and other coupled to the circuit, may cause the logic circuit flip, resulting in the wrong data reception and transmission. Electrostatic charge generated in the spacecraft can occur near the sensitive electronic circuit, so its harm to the spacecraft is relatively large.

2.6 Atmospheric Drag Effect

Spacecraft in the neutral atmosphere movement, and gas molecules collide momentum exchange force can be decomposed into lift, resistance and lateral force and other parts [3]. The resistance will have a hindrance to the movement of spacecraft, the size of the resistance is proportional to the speed of movement of spacecraft, the faster the greater the resistance. Atmospheric drag causes the spacecraft orbital to decay, and if there is not enough fuel to maintain orbital adjustment, atmospheric drag will cause the spacecraft orbital altitude to decay substantially, or even fall ahead of time.

2.7 Ionospheric Disturbance Effect

The change of the total electron content of the ionosphere caused by the solar storm will cause the navigation positioning error to increase [4]. During the ionospheric storm, the ionospheric refraction error of the electromagnetic signal will be greatly increased due to the intense fluctuation of the induced electron density, thus reducing the positioning accuracy. The effects of ionospheric storms on the satellite navigation system also show that the large ionospheric delay gradients caused by ionospheric storms will affect the realization of the differential technique in the satellite area or the enhancement system, which will affect the integrity of the satellite navigation system. electron density, thus reducing the positioning accuracy. The effects of ionospheric storms on the satellite navigation system also show that the large ionospheric delay gradients caused by ionospheric storms will affect the realization of the differential technique in the satellite area or the enhancement system, which will affect the integrity of the satellite navigation system.

3 Statistics and Analysis of Beidou Satellite Fault

3.1 Fault Statistics

Compass satellite from January 2015 to December a total of 256 failures. Statistical analysis of the annual data for 2015, for different months, we can see that the same month the same month, the overall distribution of satellite anomalies are basically the same trend. Each unit year is a solar return cycle, different years of the same month the sun light conditions change little, the satellite anomaly distribution also has annual cycle characteristics, see Fig. 1.

3.2 Fault Analysis

From January to December 2015, there were 256 satellite anomalies in Beidou, 248 caused by space radiation, accounting for 96.9% of all anomalies. See Table 1 for details (Figs. 2 and 3).

The statistical results show that the single-particle effect and the surface charge-discharge effect are the main causes of orbital anomalies caused by the space radiation environment.

Single particle flip is a single high-energy particles bombardment of large-scale, large scale integrated circuit chip produced. With the increasing complexity of spacecraft, high-performance microelectronic devices are widely used in spacecraft systems, single-particle flip is also increasingly frequent.

Electrostatic discharge on the surface of a spacecraft is a phenomenon in which the surface charges are quickly released and a transient pulse current is excited. Because the surface material of the spacecraft uses the high resistivity material, if the control improper will produce the static electricity discharge, disturbs the spacecraft the normal operation even to cause the damage.

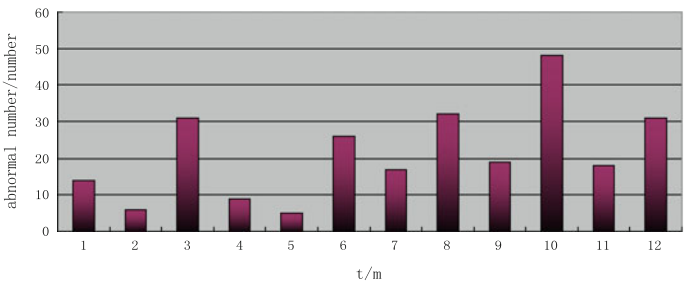

Fig. 1 Statistics of Beidou satellite abnormal situation in 2015

Table 1 Space radiation environment caused satellite abnormal

Serial number	Subsystem name	Description of anomalies	Number of occurrences of an exception	Exception location
1	Spread spectrum transponder	Spread spectrum transponder software exception	18	Space single-particle effect destroyed the FPGA device internal code caused a variety of equipment anomalies
2	Remote unit	Remote unit state transition	11	The remote unit is affected by the charge and discharge environment of the space surface, resulting in changes in the working state of components
3	Number of computers	The number of computer state transition	9	Single—particle effect causes the state transition of computer
4	Rubidium clock	Rubidium bell state transition	4	The anti-interference ability of the remote control circuit corresponding to the rubidium clock is relatively low, and it is easy to trigger under the influence of the space environment interference factor, resulting in misoperation, resulting in changes in the working state of rubidium clock. The analysis, can be considered to be caused by surface charge and discharge
5	Infrared earth sensor	Infrared earth sensor state transition	2	Single event effects on the transient state of infrared earth sensors
6	The navigation task processing unit	Navigation task processing unit exception	99	The single particle sensitive device in the navigation task processing unit is affected by the spatial single particle effect
7	Spread spectrum ranging receiver	Spread spectrum ranging receiver anomaly	105	Single-particle sensitive devices in spread-range ranging receivers are affected by single-particle space

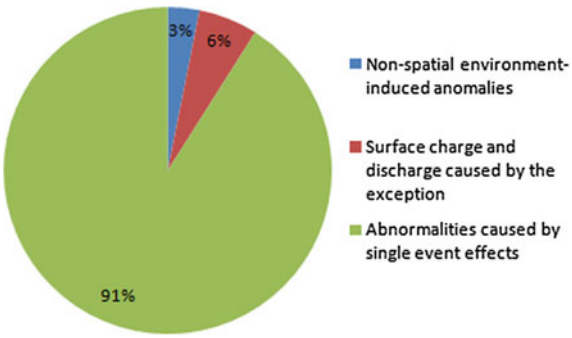

Fig. 2 Classification of satellite abnormal causes

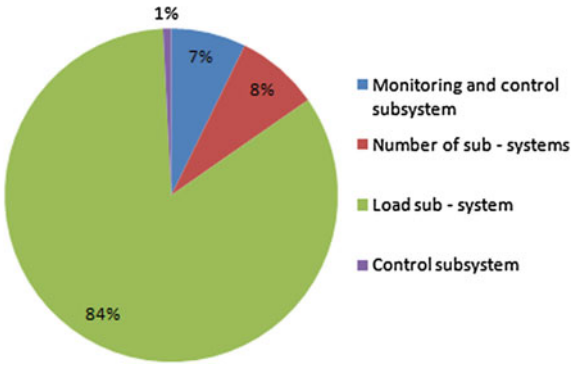

Fig. 3 Classification of satellite anomaly subsystems

4 Analysis of Abnormality and Spatial Environment

4.1 Space Environment

Space radiation environment has a certain influence on the satellite, its mode of action is reflected in a variety of space environmental effects, while a variety of spatial environmental parameters that describe the characteristics of environmental events. The conditions and explanations of the various environmental parameters are shown in Table 2.

Since 2010, the space environment has changed, the sun into a new cycle of activities, a variety of space environmental events increased significantly. Because of the different spatial and environmental conditions each year, the satellite anomalies related to the space environment are different each year. The sustained proton flux and electron flux have a certain influence on the navigation satellites. Generally, when the proton flux of 10 meV is higher than 8.6e+05, the proton flux reaches the level of energetic proton event, and the electron of 2 meV is greater than 1.0e+08. The level of electron enhancement event, the local magnetic Kp index greater than 4, to the level of geomagnetic storms. The occurrence of these alarm events, are associated with the sun's own activity.

Table 2 Common space environment parameters

Environmental parameters	Environmental data conditions	Description
Sun F 10.7 flow	≥ 120	Active level of solar activity
Proton > 10 meV Flux(/cm^2-day-sr)	$\geq 8.6e+05$	To achieve the level of high-energy proton events
Electronic >0.8 meV Flux(/cm^2-day-sr)	$\geq 1.0e+09$	To the level of high-energy electron enhancement events
Electronic > 2 meV Flux(/cm^2-day-sr)	$\geq 1.0e+08$	To the level of high-energy electron enhancement events
Kp index of geomagnetism	Kp $\geq$ 4	Reaching the level of geomagnetic storms

4.2 Satellite Anomaly

Based on the changes of space radiation environment from March to June in 2015, the abnormal occurrence of these three months was analyzed. The statistics are shown in Table 3 and Fig. 4.

As can be seen from Table 3, most of the anomalies occur, there is at least one space radiation environment alarm. At the same time, combined with Fig. 4 found that in March, June Beidou satellite abnormal frequency is more abnormal in March accounted for 12.1% of the proportion of anomalies in June accounted for 10.2%.

4.3 Correlation Analysis

According to the above data analysis, it can be concluded that the more and more frequent any of the three characterization quantities of the space radiation environment exceed the alarm threshold, the more frequent and more frequent alarm types occur, the more prone to on-orbit anomalies, and the frequency of occurrence of the abnormality is larger. Due to the high level of geomagnetic storms and high-energy electrons in March, anomalies occurred more frequently in March than in April and May, and because of the high levels of geomagnetic storms, high-energy electrons and high-energy protons in June. Frequency, and in three kinds of indicators should be higher than 4, 5 months, so the anomaly in June occurred more frequently and significantly more than 4, 5 months.

It can be concluded that the abnormity of orbiting spacecraft is greatly affected by the severity of the radiation environment alarm and the frequency of occurrence of the alarm, as well as the number of alarm types simultaneously. More than 90% of Beidou's anomalies are closely related to the space environment relationship; During the drastic change of the space environment, a high-energy electron storm occurred, and the high-energy electron flux increased greatly. The long and large magnetic storms and medium magnetic storms occurred on the geomagnetic field,

Table 3 Abnormalities and spatial radiation environment statistics in March–June

Serial number	The date the exception occurred	Kp (Kp index of geomagnetism)	Proton (the daily flux of high-energy protons in geosynchronous orbits greater than 10 meV)	Electron (geosynchronous orbit is greater than 2 meV daily flux of high-energy electrons)	Index analysis (measured data and alarm threshold)					
					Kp-4		Proton-8.6e+05		Electron-1.0e+08	
1	3-2	28	1.00E+04	1.10E+07	24	>0	−8.50E+05	<0	−8.90E+07	<0
2	3-3	11	1.10E+04	6.40E+07	7	>0	−8.49E+05	<0	−3.60E+07	<0
3	3-7	20	1.0E+04	4.7E+06	16	>0	−8.50E+05	<0	−9.53E+07	<0
4	3-8	11	1.10E+04	3.90E+07	7	>0	−8.49E+05	<0	−6.10E+07	<0
5	3-9	6	1.10E+04	5.30E+07	2	>0	−8.49E+05	<0	−4.70E+07	<0
6	3-10	5	1.10E+04	5.60E+07	1	>0	−8.49E+05	<0	−4.40E+07	<0
7	3-12	8	1.40E+04	3.90E+06	4	>0	−8.46E+05	<0	−9.61E+07	<0
8	3-20	24	1.00E+04	7.60E+08	20	>0	−8.50E+05	<0	6.60E+08	>0
9	3-21	14	1.0E+04	7.9E+08	10	>0	−8.50E+05	<0	6.90E+08	>0
10	3-22	24	1.0E+04	2.7E+08	20	>0	−8.50E+05	<0	1.70E+08	>0
11	3-23	21	9.7E+03	2.1E+08	17	>0	−8.50E+05	<0	1.10E+08	>0
12	3-24	12	2.0E+04	3.0E+08	8	>0	−8.40E+05	<0	2.00E+08	>0
13	3-27	9	1.30E+04	1.00E+08	5	>0	−8.47E+05	<0	0.00E+00	=0
14	3-30	5	1.10E+04	2.20E+06	1	>0	−8.49E+05	<0	−9.78E+07	<0
15	4-19	9	1.00E+04	2.30E+08	5	>0	−8.50E+05	<0	1.30E+08	>0
16	4-20	10	1.00E+04	7.00E+07	6	>0	−8.50E+05	<0	−3.00E+07	<0
17	4-21	22	1.00E+04	3.30E+07	18	>0	−8.50E+05	<0	−6.70E+07	<0
18	4-24	5	5.00E+04	5.10E+07	1	>0	−8.10E+05	<0	−4.90E+07	<0
19	4-25	4	3.30E+04	6.90E+07	−1	=0	−8.20E+05	<0	−2.40E+07	<0
20	4-28	6	1.40E+04	3.10E+06	2	>0	−8.46E+05	<0	−9.69E+07	<0
21	5-15	8	1.10E+04	2.90E+08	4	>0	−8.49E+05	<0	1.90E+08	>0

(continued)

Table 3 (continued)

Serial number	The date the exception occurred	Kp (Kp index of geomagnetism)	Proton (the daily flux of high-energy protons in geosynchronous orbits greater than 10 meV)	Electron (geosynchronous orbit is greater than 2 meV daily flux of high-energy electrons)	Index analysis (measured data and alarm threshold)					
					Kp-4		Proton-8.6e+05		Electron-1.0e+08	
22	5-16	6	1.10E+04	4.00E+08	2	>0	−8.49E+05	<0	3.00E+08	>0
23	5-20	7	1.00E+04	5.40E+06	3	>0	−8.50E+05	<0	−9.46E+07	<0
24	5-21	3	1.00E+04	7.80E+06	-1	<0	−8.50E+05	<0	−9.22E+07	<0
25	5-30	5	1.10E+04	2.20E+05	1	>0	−8.49E+05	<0	−9.98E+07	<0
26	6-2	3	1.10E+04	5.70E+05	-1	<0	−8.49E+05	<0	−9.94E+07	<0
27	6-8	33	1.20E+04	3.00E+05	29	>0	−8.48E+05	<0	−9.97E+07	<0
28	6-11	9	1.20E+04	2.10E+08	5	>0	−8.48E+05	<0	1.10E+08	>0
29	6-12	7	1.20E+04	2.50E+08	3	>0	−8.48E+05	<0	1.50E+08	>0
30	6-13	10	1.10E+04	1.40E+08	6	>0	−8.49E+05	<0	4.00E+07	>0
31	6-14	20	1.10E+04	3.10E+07	16	>0	−8.49E+05	<0	−6.90E+07	<0
32	6-15	14	1.00E+04	6.40E+07	10	>0	−8.50E+05	<0	−3.60E+07	<0
33	6-16	11	1.20E+04	7.30E+07	7	>0	−8.48E+05	<0	−2.70E+07	<0
34	6-18	7	7.30E+05	4.90E+07	3	>0	−1.30E+05	<0	−5.10E+07	<0
35	6-19	5	5.10E+05	5.60E+07	1	>0	−3.50E+05	<0	−4.40E+07	<0
36	6-21	8	1.90E+07	8.00E+07	4	>0	1.81E+07	>0	−2.00E+07	<0
37	6-22	55	2.70E+06	2.70E+07	51	>0	1.84E+06	>0	−7.30E+07	<0
38	6-24	17	3.20E+05	7.10E+07	13	>0	−5.40E+05	<0	−2.90E+07	<0
39	6-25	33	1.10E+06	1.10E+08	29	>0	2.40E+05	>0	1.00E+07	>0
40	6-26	10	7.20E+05	2.70E+08	6	>0	−1.40E+05	<0	1.70E+08	>0

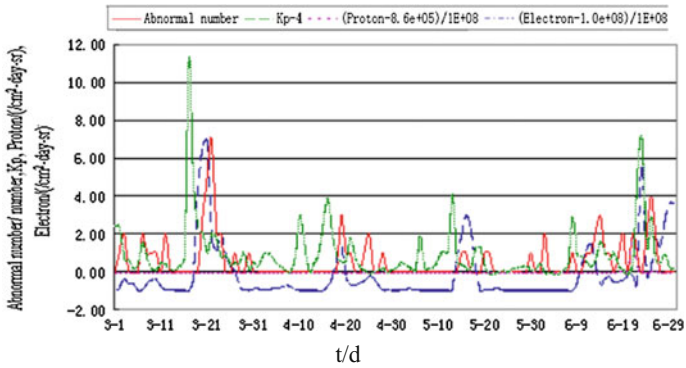

Fig. 4 Abnormal distribution and spatial radiation environment changes in March–June

which accords with the typical charge-discharge effect. Since the charge and discharge takes a certain amount of time to accumulate, its effect generally needs to be delayed after the performance in the event of a large magnetic storm, usually abnormal in the following days which broke out.

According to the data analysis in Table 3, we can get the correspondences of the radiation environment of different space when the anomaly occurs. The details are shown in Table 4.

As can be seen from Table 4, 95.8% of the anomalies occurred when the geomagnetic storm alarm, 49.3% of the abnormal high-energy electronic alarm occurs, 9.9% of the abnormal high-energy proton alarm. Of the anomalies, 81.7% were load abnormalities and 18.3% were platform anomalies. It can be concluded that when the magnetic storms, high-energy electron storm events or high-energy electron fluxes increase in the space environment (high-energy electron fluxes greater than 2 meV will maintain a small high-energy electron storm level or a high level of electron flux) occurrence of satellite anomalies. In the anomaly classification statistics, the load anomaly is obviously more than the satellite platform anomaly.

5 Countermeasure of Satellite Abnormity Caused by Space Radiation Environment

5.1 The Prediction of Satellite Anomaly Based on Spatial Environment Data Is Made

Taking July–October 2015 as an example, the spatial radiation environment in July–October is shown in Fig. 5:

By analyzing the spatial radiation environment data:From July to October, geomagnetic storms, high-energy protons, and high-energy electrons all exceeded

Table 4 Classification of Abnormal Space Radiation Environment and Distribution of Abnormal Months

Serial number	Kp-4	Proton-8.6e +05	Electron-1.0e +08	Abnormal frequency and month distribution	Frequency of occurrence of abnormality
The first sort	≥ 0	<0	<0	A total of 30 times (March 11 times, April 6 times, May 2 times, June 11 times)	Load abnormalities 25 times, Platform exception 5 times
The second category	>0	<0	≥ 0	A total of 31 times (March 20 times, April 3 times, May 2 times, June 6 times)	Load abnormalities 24 times, Platform exception 7 times
The third category	<0	<0	<0	A total of 3 times (May 1 times, June 2 times)	Load abnormalities 2 times, Platform exception 1 times
The fourth category	>0	>0	<0	A total of 3 times (June 3 times)	Load abnormalities 3 times
The fifth category	>0	>0	>0	A total of 4 times (June 4 times)	Load abnormalities 4 times

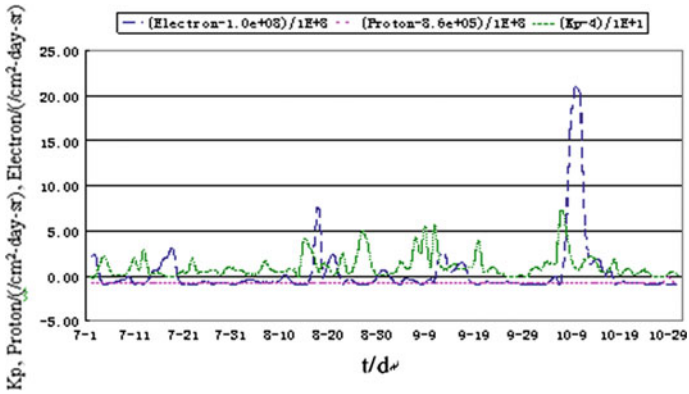

Fig. 5 July–october space radiation environment changes

the alarm value. It can be predicted that anomalies and frequent occurrences occurred in these three months. Secondly, according to the level of geomagnetic storm, high-energy proton and high-energy electron exceeding the threshold level, the probability of occurrence of anomaly in August, September and October is predicted to be higher, and the occurrence frequency is more frequent. At the same time, in October, for example, according to October space radiation environment statistics, as shown in Table 5, according to the previously summarized spatial radiation environmental impact classification of abnormal species can be obtained by the distribution of abnormal phenomena.

According to the correlation analysis of satellite anomaly and space environment, the data of space radiation environment in October are analyzed (as shown in Table 5), which can be used to predict the occurrence of satellite anomalies due to space environment in October) (Table 6).

5.2 *Ground Disposal According to the Predicted Results*

In the ground monitoring and control work, according to the predictive results of the control of the ground disposal, can make the load system to restore ground controllability stronger. The ground observation and control system can negotiate with the transportation control system, select the satellite control system to carry on the on-orbit operation, restores the load system function when the transportation control system influence is small. The specific operation is to Beidou satellite spread spectrum transponder, navigation task processing unit, spread spectrum ranging receiver and other parts susceptible to space environment in order to reset the operation, so you can restore the device to flip the logic state or sensitive electronic components and component misuse, recovery of satellite load

Table 5 Statistics of space radiation environment in October

Date	Kp (Kp index of geomagnetism)	Proton (the daily flux of high-energy protons in geosynchronous orbits greater than 10 meV)	Electron (geosynchronous orbit is greater than 2 meV daily flux of high-energy electrons)	Index analysis (measured data—standard value)			Abnormal phenomena may occur code
				Kp-4	Proton-8.6e+05	Electron-1.0e+08	
10-1	11	3.30E+04	6.70E+06	>0	<0	<0	The first sort
10-2	14	1.30E+04	1.30E+06	>0	<0	<0	
10-3	11	1.10E+04	7.60E+05	>0	<0	<0	
10-4	20	1.10E+04	1.90E+06	>0	<0	<0	
10-5	18	1.10E+04	5.60E+07	>0	<0	<0	
10-6	19	1.10E+04	9.40E+07	>0	<0	<0	
10-7	77	1.10E+04	4.10E+06	>0	<0	<0	
10-8	56	1.10E+04	4.80E+08	>0	<0	<0	The second category
10-9	26	1.10E+04	1.70E+09	>0	<0	<0	
10-10	12	1.20E+04	2.20E+09	>0	<0	<0	
10-11	12	1.10E+04	2.10E+09	>0	<0	<0	
10-12	22	1.10E+04	6.20E+08	>0	<0	<0	
10-13	25	1.10E+04	2.40E+08	>0	<0	<0	
10-14	23	1.10E+04	2.70E+08	>0	<0	<0	
10-15	10	1.10E+04	2.70E+08	>0	<0	<0	
10-16	8	1.10E+04	7.90E+07	>0	<0	<0	The first sort
10-17	11	1.10E+04	1.80E+08	>0	<0	<0	The second category
10-18	22	1.20E+04	1.70E+07	>0	<0	<0	The first sort
10-19	5	1.10E+04	1.40E+07	>0	<0	<0	
10-20	9	1.20E+04	3.40E+07	>0	<0	<0	

(continued)

Table 5 (continued)

Date	Kp (Kp index of geomagnetism)	Proton (the daily flux of high-energy protons in geosynchronous orbits greater than 10 meV)	Electron (geosynchronous orbit is greater than 2 meV daily flux of high-energy electrons)	Index analysis (measured data—standard value)			Abnormal phenomena may occur code
				Kp-4	Proton-8.6e+05	Electron-1.0e+08	
	12	1.10E+04	1.30E+07	>0	<0	<0	
10-22	6	2.00E+04	1.40E+07	>0	<0	<0	
10-23	7	2.10E+04	1.10E+07	>0	<0	<0	
10-24	11	1.20E+04	1.10E+07	>0	<0	<0	
10-25	8	1.20E+04	2.70E+06	>0	<0	<0	
10-26	3	1.10E+04	2.10E+06	<0	<0	<0	The third category
10-27	4	1.20E+04	8.20E+06	>0	<0	<0	The first sort
10-28	3	1.10E+04	1.40E+07	<0	<0	<0	The third category
10-29	5	7.90E+05	5.60E+06	>0	<0	<0	the first sort
10-30	9	1.50E+05	1.40E+06	>0	<0	<0	
10-31	6	3.00E+04	5.60E+05	>0	<0	<0	

Table 6 October abnormal forecast

Date	Abnormal types may occur	An abnormal condition may occur
10-1 to10-7, 10-16, 10-18 to10-25, 10-27, 10-29 to10-31	The first sort	Abnormal load, Platform exception
10-8 to10-15, 10-17	The second category	Abnormal load, Platform exception
10-26, 10-28	The third category	Abnormal load, Platform exception

applications, reducing the single event on the satellite security and the impact of the application and improve the viability of orbiting satellites.

6 Verification

Through the statistics of the actual occurrence of satellite anomalies from July to October, and compared with the changes of space radiation environment in the same period, the comparison is shown in Fig. 6:

In July, 2015, 17 anomalies occurred, and 32 anomalies occurred in August, 19 anomalies occurred in September, and 48 anomalies occurred in October. Among them, the proportion of anomalies in July was 14.7%, the proportion of abnormal anomalies in August was 27.6%, the abnormal proportion in September was 16.4%, the abnormal proportion in October was 41.1%.

The anomalies occurred in October were compared with those in Table 6, and the results of the comparison are shown in Table 7:

By comparing the actual situation of the anomaly with the previous forecasting results, it can be concluded that the spatial radiation environment changed dramatically in October, the three kinds of alarm were frequent and the alarm value

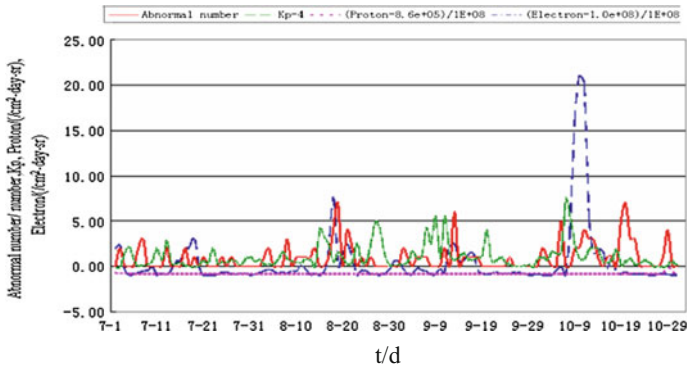

Fig. 6 Abnormal frequency, distribution and spatial radiation environment change from July to October

Table 7 Classification of abnormal space radiation environment and comparison of abnormal situation

Date	Abnormal situation	Possible abnormal species	Compare the results
10-2	Load abnormalities	The first sort	√
10-3	Load abnormalities	The first sort	√
10-6	Load abnormalities	The first sort	√
10-9	Load abnormalities	The second category	√
10-10	Load abnormalities	The second category	√
10-11	Load abnormalities	The second category	√
10-12	Load abnormalities	The second category	√
10-13	Platform exception	The second category	√
10-14	Load abnormalities	The second category	√
10-16	Load abnormalities	The first sort	√
10-17	Load abnormalities	The second category	√
10-19	Load abnormalities	The first sort	√
10-20	Load abnormalities	The first sort	√
10-21	Load abnormalities	The first sort	√
10-22	Load abnormalities	The first sort	√
10-28	Load abnormalities	The third category	√
10-29	Load abnormalities	The first sort	√

exceeded the threshold level. The actual anomaly was in accordance with the predicted result.

7 Conclusion

Since the Beidou satellites in orbit since the operation, the data show that: space radiation environment changes will Beidou satellite safe and stable operation of the associated impact, especially for Beidou satellite load, directly related to the navigation performance and continuous. Space radiation environment changes are complex, the need to further master the spatial environment of the law of particle changes, so that the satellite itself and the daily manipulation to adapt to the space radiation environment. In the operation and management of the satellite, as far as possible accurate according to the spatial radiation environment data to accurately predict the occurrence time and type of anomaly, for the cumulative effect of the abnormal use of power, reset and other means, early to resist the possible impact. To resist the abnormal type, try to avoid the high incidence in the exception of an important manipulation. In order to make better use of Beidou satellite navigation performance and provide background information for the safe operation of satellites, it is necessary to accumulate on-orbit satellites data and corresponding space radiation environment data for the follow-up better management satellites.

References

1. Cao Z et al (2013) The space radiation environment induced by single particle effect. Vaccum Low Temp 19(3):125–129
2. Du H et al (1996) Space environment manual for low - orbit spacecraft. National Defense Industry Press, Beijing
3. http://www.be-radiation-safe.com/ionizing-radiation.html
4. Jin X (2004) Space environment and on-orbit failure of spacecrafts. Spacecraft Environ Eng 21 (3):1–6

VPL Optimization Method with Multi-objective Program

Xueen Zheng, Chengdong Xu, Fei Niu and Anjin Li

Abstract As a promising fault detection algorithm, Advanced Receiver Autonomous Integrity Monitoring (ARAIM) was widely researched by European Space Agency (ESA) and the Federal Aviation Administration (FAA). To meet the requirement of precision approach based on vertical navigation and to improve the availability of the ARAIM algorithm, the vertical protection limit (VPL) needed to be optimized. The false detection probability and the missed detection probability were the optimization parameters, and the VPL optimization problem was transformed into double-objective program problem, so the VPL model was established. For verifying the effectiveness of the optimization algorithm, GPS navigation data acquired by two observation stations were used to optimize the VPL. The results show that the optimal VPL is positively correlated with the number of visible stars, and the optimization efficiency is 10%.

Keywords GNSS · ARAIM · Multi-objective optimization · The LPV-200 service

X. Zheng (✉) · C. Xu
School of Aerospace Engineering, Beijing Institude of Technology, Beijing, China
e-mail: zxe2017@163.com

C. Xu
e-mail: xucd@bit.edu.cn

F. Niu
Beijing Satellite Navigation Center, Beijing, China
e-mail: niufei009@sina.com

A. Li
Shandong Entry—Exit Inspection and Quarantine Bureau, Qingdao, China
e-mail: ykanjin@163.com

J. Sun et al. (eds.), *China Satellite Navigation Conference (CSNC) 2017 Proceedings: Volume I*, Lecture Notes in Electrical Engineering 437,
DOI 10.1007/978-981-10-4588-2_59

1 Introduction

As BeiDou Navigation Satellite System (BDS) is constructed in China, users could observed more than 10 satellites navigation. But the frequency of satellite failures will increase as much as the number of satellite. Receiver Autonomous Integrity Monitoring (RAIM) as a failure detection algorithms is useful. Its characteristic is that could apply in the receiver and is real-time detection. It use extra pseudo-range to check the failure, that is based a statistical method to judge whether to have failure, and could identify the failure satellite. Applying RAIM could reduce the dependence of the ground monitoring. EU and USA are researching the Advanced RAIM (ARAIM) [1] to use for vertical guidance service for aircraft in the worldwide. In the future, LPV-200 can provide a 200-foot navigation service for aircraft in the vertical direction [2, 3].

Vertical error inevitably will be greater than the level due to the geometric positioning approach of navigation constellation, so vertical guidance is more difficult than level guidance. In spite of Wide Area Augmentation System (WAAS) based on ground could advance the position accuracy. When it use two-frequency signal (L1 and L5), the position accuracy is enhanced to 1 m, but it have a defect that the time interval between two signal uploading is longer than 6 s. When the aircraft fly at an altitude of 200 ft, 6 s is too long to not confirm the position, and the fail will make the flier mistake that they are falling too fast. And RAIM is real-time to detect the failure of satellite, so it is more effective.

2 Basic Theory of ARAIM

RAIM algorithm is based on the hypothesis testing [4]. Use the redundancy to detect the integrity of system. And the RAIM can identify the fault satellites. Traditional RAIM can be used for the navigation satellite fault detection and identification. For precision approach of vertical navigation service, it is necessary to improve the usability of RAIM algorithm for meeting the service requirements.

In the development of RAIM algorithm, RAIM algorithm for single-satellite fault detection is based on least squares method or parity vector [5]. Especially the RAIM algorithm based parity vector, avoid a large number of matrix calculations, so that it has been applied in engineering.

Nowadays, due to the development of GNSS, because the number of satellites in orbit increased, the probability of multi-star fault is increased. and the multi-constellation fault detection algorithm has become the main direction of RAIM algorithm development. In multi-constellation fault detection, the main question is double satellites fault detection, but the fault detection above two satellites, usually is ignored because probability is considered too small.

$$P_F = P_1 + P_2 + P_{\geq 3} \tag{2.1}$$

$$P_1 = C_1^n P_{sat}(1 - P_{sat})^{n-1} \tag{2.2}$$

$$P_2 = C_2^n P_{sat}^2(1 - P_{sat})^{n-2} \tag{2.3}$$

$$P_{\geq 3} = \sum_{k=3}^{n} C_k^n P_{a\_priori}^k (1 - P_{sat})^{n-k} \tag{2.4}$$

P_F represents the probability of satellite failure, P_1 represents the probability of single-satellite failure, P_2 represents the probability of double-satellite failure, $P_{\geq 3}$ represents the probability of more than two satellite failure. C_1^n is a binomial coefficient, P_{a_priori} is a single satellite fault prior probability, suppose it is 10^{-5}, and they are independent of each other. If in the vision field, the number of satellites are 16, $P_{\geq 3} \leq 10^{-9}$. the probability of satellite failure can be expressed as:

$$\hat{P}_F = P_1 + P_2 \approx P_F \tag{2.5}$$

3 LPV-200 Service and ARAIM Algorithm

Traditional RAIM algorithm could not meet the requirement of LPV-200, ARAIM is still under development. In the future, it may meet this requirement.

In October 2006, the Federal Aviation Administration (FAA) announced that it will provide global guidance service of LPV-200 levels for civil aircraft in 2020–2050 [6].

The LPV-200 service directs the aircraft to a height of 200 ft (60 m) from the ground. It meet a required navigation performance (RNP).Compared to the Class I precision approach, the performance of the LPV-200 has improved. According to the International Civil Aviation Organization (ICAO) standards, LPV-200 standards are as follows [6]:

1. For Probability of Hazardously Misleading Information (PHMI) LPV-200 and ICAO are the same. PHMI of ICAO is that the horizontal and vertical integrity risks do not exceed 2×10^{-7}/approach, and the LPV-200 presents that the vertical hazardously misleading information is $\Pr\{HMI\} \leq 10^{-7}$/approach. That is equivalent to ICAO.
2. The protection value must be less than the alarm value: the vertical protection level (VPL) must be less than the vertical alert limit (VAL), VPL < VAL = 35 m; horizontal protection level, HPL) is less than the horizontal alert limit (HAL), HPL < HAL = 40 m. This requirement is the most important in the LPV-200. The main contribution of this paper is optimize VPL value.

3. Required accuracy: vertical navigation system error (VNSE) (95%) $\leq$ 4 m, and when there is no failure in the satellites, the probability that VNSE is not less to 10 m does not exceed 10^{-7}.
4. The probability of false alarm in LPV-200 is derived from the continuity risk requirement of ICAO, and its value is half of the ICAO standard, $P_{fa} \leq 4 \times 10^{-6}/15$.
5. the alarm time: $TTA \leq 6$ s. One of the advantages of using the ARAIM approach for integrity monitoring on the LPV-200 approach is that it does not need to meet the 6 s alarm time requirement. Because the ARAIM algorithm differs from the Wide Area Augmentation System (WAAS) the ARAIM is real-time approach. Moreover, ARAIM has a prediction function, before flying, you can do of the integrity prediction of the whole flight phase.

ARAIM algorithm is the enhance of RAIM algorithm that computes the VPL. The following is the mathematical expression of VPL:

$$VPL_k = K_{fa,k} \times \sigma_{dV,k} + K_{md,k} \times \sigma_{V,k} + E_k \tag{3.1}$$

$$E_k = \sum_{i=1}^{N} |\Delta S_k(3,i)| \times B_{norm}(i) + \sum_{i=1}^{N} |S_k(3,i)| \times B_{\max}(i) \tag{3.2}$$

4 Optimization Algorithm

In this section, VPL optimization method will be introduced, that is the main innovation content of this article. As described previously, VPL value includes false alarm probability and missed probabilities and other information. The VPL for the system is determined by the maximum of VPL_k values [7–9]. In the traditional method, parameters $K_{fa,k}$, $K_{md,0}$ and $K_{md,k}$, are calculated by the following formula.

$$K_{fa,k} = -Q^{-1}\left(\frac{Total\_P_{fa}}{2 \times N}\right) \tag{4.1}$$

$$K_{md,0} = -Q^{-1}\left(\frac{\Pr\{HMI\}}{2 \times (N+1)}\right) \tag{4.2}$$

$$K_{md,k} = -Q^{-1}\left(\frac{\Pr\{HMI\}}{P_{a\_priori}(N+1)}\right) \tag{4.3}$$

The equation of VPL is rewritten as:

$$VPL = \mathrm{MAX}\left(VPL_k(P_{fa,k}, PHMI_k)\right) \tag{4.4}$$

So the VPL value could be minimized by assigning the misjudgment probability and the missed detection probability properly. The following parameters are defined.

$$\begin{aligned}
a_i &= K_{fa,k}, \\
b_i &= K_{md,k}, \\
c_i &= \sigma_{dv,k}, \\
E_i &= \sum_{j=1}^{N} |\Delta S_i(3,j)| \times B_{norm}(j) + \sum_{j=1}^{N} |S_0(3,j)| \times B_{\max}(j), \\
d_i &= \sigma_{v,k}, \\
g_i &= P_{priori}(i), \\
A &= P_{af}/2, \\
B &= PHMI.
\end{aligned}$$

The original function is transformed into the following:

$$\begin{aligned}
\min \quad & Z = \max(a_i \times c_i + b_i \times d_i + E_i) \\
\text{s.t.} \quad & \sum_{k=0}^{N} Q(-a_i) \le A \\
& \sum_{k=0}^{N} Q(-b_i) g_i \le B
\end{aligned} \tag{4.5}$$

After measuring pseudo-range, parameter c_i, b_i, E, could put into the optimization equation. And parameter g_i is known. After a previous analysis, one optimization objective equation and two constraints are derived. But this is not enough, it is necessary to transform function for improve the readability of the optimization. The equivalent function of the optimization equation is shown as follow:

$$\begin{aligned}
z_i &= a_i \times c_i + b_i \times d_i + E_i \\
R &= \sum_{i=1}^{N} z_i \\
L &= \sum_{j=1}^{N-1} (z_1 - z_2)^2 + (z_n - z_1)^2
\end{aligned} \tag{4.6}$$

When the function R takes a minimum value and L takes a zero value, the optimization equation takes the minimum value. In this case, the objective function is transformed into the following:

$$
\begin{aligned}
&\min \quad R \\
&\min \quad L \\
&\text{s.t.} \quad R = \sum_{i=1}^{N} z_i \\
&\qquad L = \sum_{j=1}^{N-1} (z_1 - z_2)^2 + (z_n - z_1)^2 \\
&\qquad z_i = a_i \times c_i + b_i \times d_i + E_i \\
&\qquad \sum_{k=0}^{N} Q(-a_i) \le A \\
&\qquad \sum_{k=0}^{N} Q(-b_i) g_i \le B
\end{aligned}
\tag{4.7}
$$

Obviously this is a multi-objective optimization problem. There are two objective functions R and L, and we will use the objective programming method to solve this problem.

First, provided the expected value of the objective: $R = 35 \times N$ and $L = 0$, they have the same level of optimization. Assumed that e_1^-, e_1^+ are positive and negative deviation of the function R, and e_2^+, e_2^- are positive and negative deviation of the function L. Their weights are 1, objective function rewritten as follows:

$$
\begin{aligned}
&\min \quad U = e_1^+ + e_2^+ + e_2^- \\
&\text{s.t.} \quad \sum_{i=1}^{N} z_i + e_1^- - e_1^+ = 35 \times N \\
&\qquad \sum_{j=1}^{N-1} (z_1 - z_2)^2 + (z_n - z_1)^2 + e_2^- + e_2^+ = 0 \\
&\qquad z_i = a_i \times c_i + b_i \times d_i + E_i \\
&\qquad \sum_{k=0}^{N} Q(-a_i) \le A \\
&\qquad \sum_{k=0}^{N} Q(-b_i) g_i \le B \\
&\qquad e_1^+, e_1^-, e_2^+, e_2^- \ge 0
\end{aligned}
\tag{4.8}
$$

The remaining question is mathematical problem. The luck is that nonlinear optimization algorithm could be solved by computer program. After obtain LPV-200 parameter, and the optimized VPL value is solved by the optimization algorithm.

5 Application of Optimization Method

The simulation environment was set up under the background of LPV-200 service. Continuity risk $\leq 4 \times 10^{-6}$, integrity risk $\leq 10^{-7}$, these two parameters are constraints of optimization. The probability of the single satellite fault is 10^{-5}, this value for the VPL is a important parameter. The probability of the single satellite fault is as smaller as the optimized VPL. The probability of the satellite failure is a systematic attribute, which could not be optimized. If navigation systems is different, the probability of satellite fault will be different. Fortunately, the level of satellite manufacturing are able to meet that the probability of failure is 10^{-5}, so it will not fact the optimization result.

In order to prove that the optimization algorithm is universal, the real data of two observation which are recorded in Table 1 is used to verify universality in this paper.

The data includes azimuth and elevation angles of observable GPS single satellites in the 86,400 epochs. Take 300 s as a time interval, 288 epochs are extracted.

Figure 1 describes the VPL values for 288 epochs. Figures 1a and 2a describes the VPL values with no-optimization, and Figs. 1b and 2b describes the VPL values with optimization. they show that the fluctuation value of VPL is very large. The data of statistical analysis is in Table 2. When the probability of satellite failure is 10^{-5}, average value of VPL is under 35 m. but 8.86–14.58% VPL exceeds 35 m. That does not meet the requirement for ARAIM continuous availability.

It causes azimuth and elevation angles and the number of visible satellite. It also shows that the number of satellites of the single constellation is difficult to meet the requirement of vertical navigation.

Figure 2 shows the number of visible satellites. At the observation point (30.51, 114.49, 71.32), 12 satellites could be visible, and at least 5 satellites could be observed. The number of visible satellite has a significant effect on the VPL value. The data in the Figs. 1 and 2 is able to match.

Figure 3 shows the number of satellites visible throughout the day. At the JFGN tracking station, the elevation angles of visible satellite are greater than 11°, and we collect 5–12 satellites. And at the BJFS tracking station, the elevation angles of visible satellite are greater than 5°, and we collect 4–11 satellites. The insufficient number of visible satellites is also the one reason that GPS constellation is difficult to be used for satellite fault detection in China.

Table 1 Basic information of the observation station

Name	ECEF coordinate	Time
JFNG	(−2,279,828.8292, 5,004,706.5483, 3,219,777.4684)	The 342th day in 2014
BJFS	(−2,148,744.713, 4,426,640.854, 4,044,655.92)	The 1th day in 2015

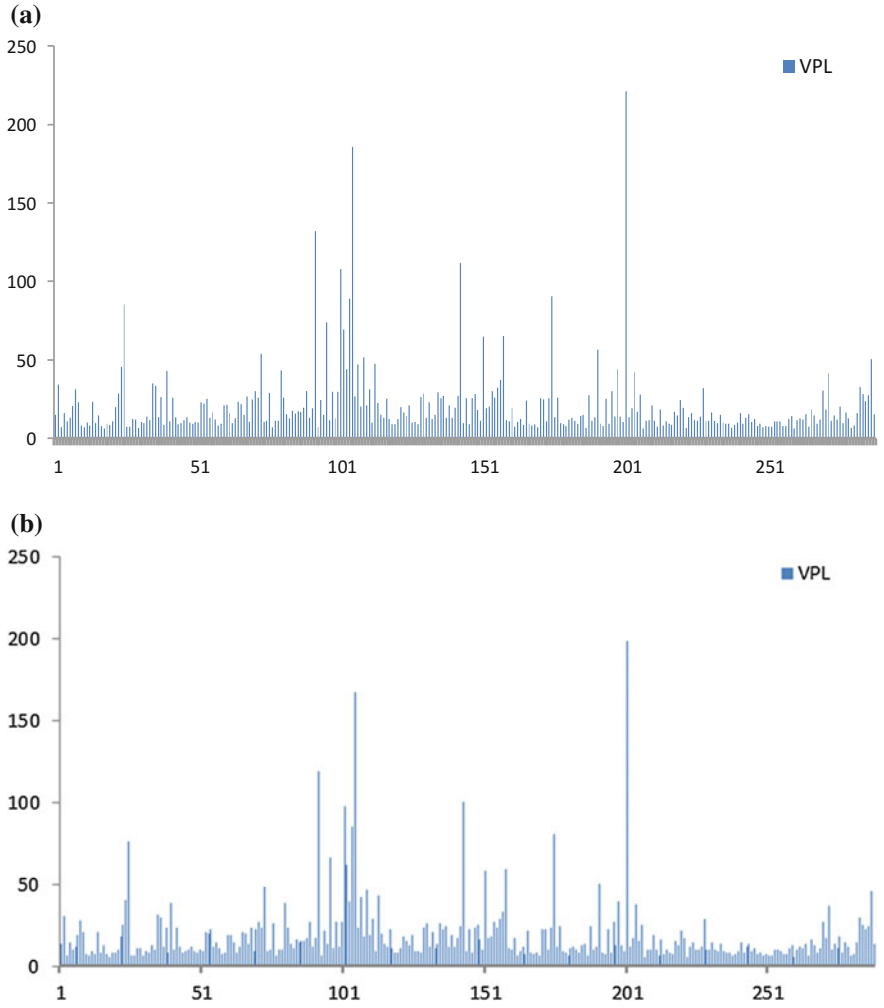

Fig. 1 VPL in JFNG station

Because the RAIM algorithm for single-satellite fault detection requires more than four visible satellites, double-satellites fault detection requires more than five visible satellites. In China, the continuity of ARAIM could not be met. A decrease in the number of visible stars could also affect VPL. This data in Fig. 3 is consistent with the data in Figs. 1 and 2.

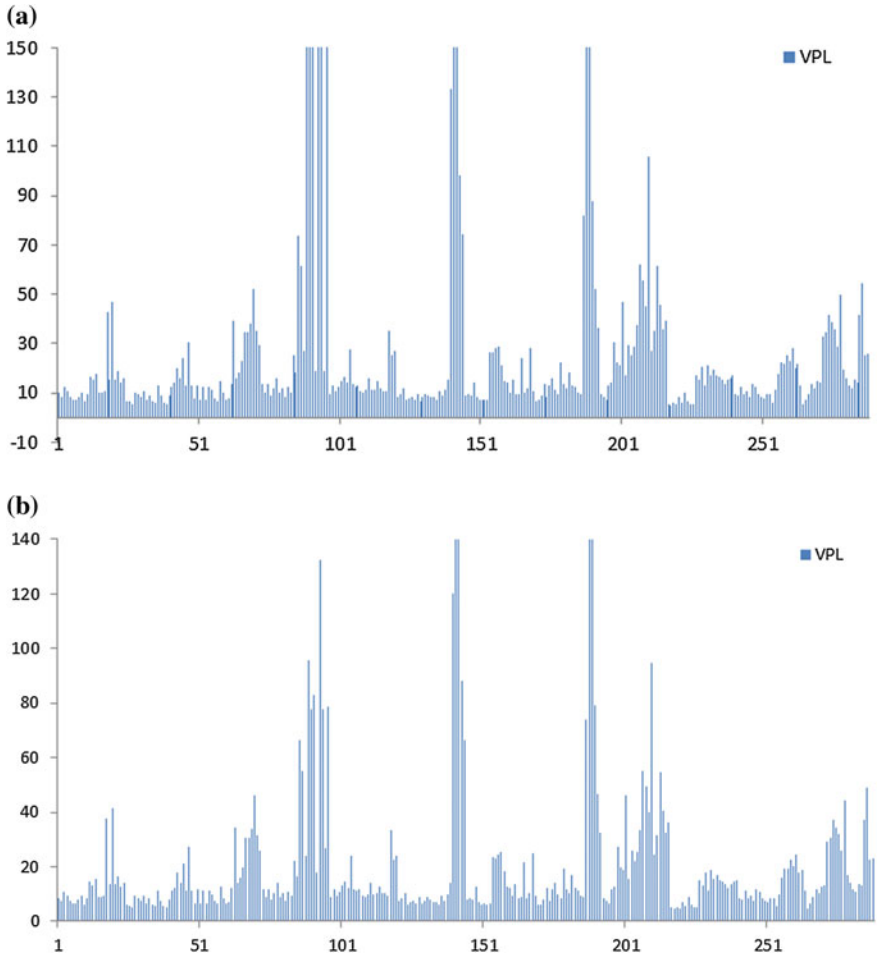

Fig. 2 VPL in BJFS station

Table 2 Data contrast between optimization and norm

		Equal allocation	Optimal VPL	Optimal ratio
JFNG	Average 99.5% VPL	20.8126	18.6859	0.1026
	Variance	22.7884	20.5091	
BJFS	Average 99.5% VPL	23.2746	19.8706	0.1089
	Variance	30.0169	23.3676	

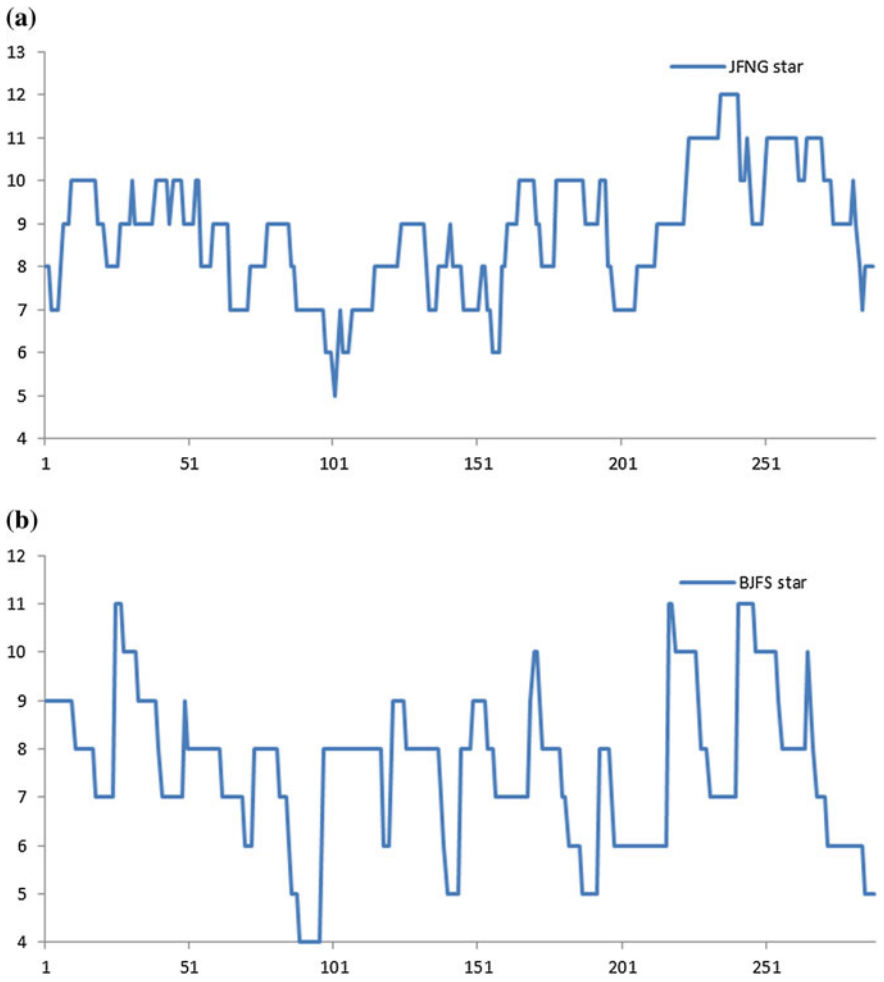

Fig. 3 Number of visibility of satellites

Figure. 4 show that the comparison between no-optimal VPL and optimal VPL. The dotted line represents no-optimal vertical protection limit, it is called VPL_1. The solid line represents optimal vertical protection limit, it is called VPL_2. In the 20 epochs, the optimization method has a very obvious effect, when the VPL_1 is larger, the amplitude value $VPL_1 - VPL_2$ is greater, and the optimization rate $(VPL_1 - VPL_2)/VPL_1$ is also greater. It could shows that the optimization method proposed in this paper is more effective when VPL_1 is larger.

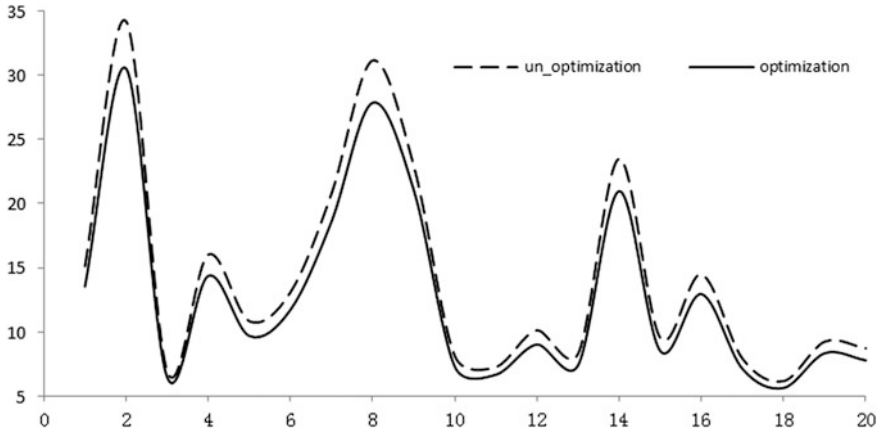

Fig. 4 VPL contrast between optimization and norm

6 Conclusion

The VPL optimization algorithm proposed in this paper has certain optimization effect, and the optimization rate is about 10%. The experiment shows that the VPL value limited to the number of GPS satellites could not meet the requirement of instantaneous vertical guidance service. In view of the development of BDS in recent years, it is feasible to provide the vertical guidance service for the aircraft with multiple navigation systems. The optimized VPL value may meet the requirement of instantaneous vertical navigation service [10].

Acknowledgements Acknowledge the National Natural Science Foundation of China (No. 61502257, No. 41304031).

References

1. Lee YC (1999) Analysis of range and position comparison methods as a means to provide GPS integrity in the user receiver. In: The user receiver US Institute of Navigation annual meeting, pp 1–4
2. Shuai J et al (2012) Exploration of advanced RAIM to provide LPV-200 service. Measure Control Technol 11:75–79
3. Lee YC, McLaughlin MP (2007) Feasibility analysis of RAIM to provide LPL-200 approaches with future GPS. In: Proceedings of ION GNSS-2077, Fort Worth, TX, pp 2898–2910
4. Joerger M, Chan F-C, Boris P (2014) Solution separation versus residual-based RAIM. Navig J Inst Navig 4:273–291
5. Joerger M, Chan FC, Langel S et al (2012) RAIM detector and estimator design to minimize the integrity risk. In: 25th International technical meeting of the satellite-division of the Institute-of-Navigation, pp 2785–2807

6. FAA (2010) Phase II of the GNS S evolutionary architecture study
7. Mathieu Joerger et al (2016) Integrity risk minimisation in RAIM part 1: optimal detector design. J Navig 3:449–467
8. Blanch J, Walter T, Enge P et al (2010) RAIM with optimal integrity and continuity allocations under multiple failures. IEEE Trans Aerosp Electron Syst 3:1235–1247
9. Blanch J, Walter T, Enge P (2013) Optimal positioning for advanced RAIM. Navig J Inst Navig 4:279–289
10. Blanch J, Walter T, Enge P et al (2011) A proposal for multi-constellation advanced RAIM for vertical guidance. In: 24th international technical meeting of the satellite division of the Institute of Navigation (ION GNSS), pp 2665–2680

Multi-station Combined Evaluation Method for Navigation Signal Tracking Error Based on Optimization Weight

Jianlei Yang, Qinan Zhi, Song Xie and Xiaonan Li

Abstract In operation and control system of BeiDou Navigation Satellite System (BDS) and international GNSS Monitoring and Assessment System (iGMAS), the single-station evaluation method of navigation signal is susceptible to environmental of the site area, so the reliability is poor. And the traditional multi-objective/multi-attribute comprehensive evaluation method has strong subjective randomness and lacks quantitative analysis. Aimed at above problem, a multi-station combined evaluation method for navigation signal tracking accuracy based on optimization weight was proposed. In the proposed method, the optimal comprehensive evaluation equation was establishing, and the optimized weights were calculated by solving equation. And last, the comprehensive evaluation result was obtained by using the optimized weights. Experimental and simulation results show that the proposed method is more robust than the single-station evaluation method and multi-objective/multi-attribute comprehensive evaluation method. And the proposed method can provide more objective, reliable and accurate evaluation results. The proposed method can provide effective theoretical guidance for the evaluation of tracking precision of Beidou operation and control system and iGMAS.

Keywords BDS · Multi-station combined evaluation · Operation and control system · iGMAS · Single-station evaluation method · Multi-objective/multi-attribute comprehensive evaluation method

J. Yang (✉) · Q. Zhi · S. Xie · X. Li
State Key Laboratory of Satellite Navigation System and Equipment Technology, Shijiazhuang, China
e-mail: yangjianlei555@126.com

J. Yang · Q. Zhi · S. Xie · X. Li
The 54th Research Institute of CETC, Shijiazhuang, China

J. Sun et al. (eds.), *China Satellite Navigation Conference (CSNC) 2017 Proceedings: Volume I*, Lecture Notes in Electrical Engineering 437,
DOI 10.1007/978-981-10-4588-2_60

1 Introduction

In the navigation system, due to the existence of various interference factors, sudden state and some design defects, one can provide high-performance positioning, navigation and timing services, not only need to study the signal system and other principle issues, establish a comprehensive signal monitoring, analysis and evaluation system, such as Department of Defense (DoD) monitoring network of Global Positioning System (GPS), Global Differential GPS (GDGPS) System, International GPS Service (IGS), Information Analysis Center (IAC) of Glonass, Galileo Experimental Sensor Stations (GESS). In addition, there are a number of universities and research institutions [1–4], such as Stanford University, Ohio University, Japan Electronic Navigation Research Institute (ENRI) of Japan,the German Aerospace Center (DLR), Chilboten Observatory of UK, European Space Agency (ESA) and Thales Alenia Aerospace Corporation (TAS), and so on.

The BeiDou Navigation Satellite System (BDS) is designed to provide global coverage around 2020, so the establishment of a global monitoring system becomes inevitable. China's satellite navigation signal quality monitoring started late, but the development is rapid. There are many established high-gain navigation signal monitoring antenna, such as 7.3 m antenna of National Time Service Center, 18 m antenna of China Electronics Technology Group Corporation 54th Institute (CETC 54), 25 m antenna of the Xinjiang Observatory Nanshan station, 40 m antenna of Luonan county and 7.3 m of Lintong District, and so on. In order to further improve the reliability of Global Navigation Satellite Systems (GNSS), China proposed the concept of the International GNSS Monitoring and Assessment System (iGMAS) in March 2011. This system is one of the major special experiments of BDS. It is and information product platform to monitor the operation status and evaluate the main performance indexes of GNSS, to generate high precision precision ephemeris and satellite clock error, earth orientation parameter, tracking station coordinate, global ionization Layer delay. IGMAS was originally designed to consist of about 30 globally distributed tracking stations, three data centers, seven analysis centers, a monitoring and evaluation center, a product integration and service center, an operational management control center and a communications network [5].

Single-station signal performance evaluation methods, such as pseudo-range, carrier phase, Doppler and carrier-to-noise ratio, are subject to many uncertainties factors of local environment, such as electromagnetic interference, multipath interference and ionospheric flicker. Therefore, the Single-station evaluation results are inevitably affect by uncertainties factors. Therefore, in order to reduce the use of risk, single-station signal quality evaluation have to be extended to multi-station combined evaluation, thereby enhancing the reliability and accuracy of the evaluation system. Multi-objective/multi-attribute decision-making method has been widely used in many fields and has achieved good results, such as military, health, transportation, water conservancy, mining and other fields. And it is also be applied to the navigation signal synthesis performance evaluation, such as radar charting, expert scoring, linear weighting, weighted TOPSIS and multi-attribute group

decision making, and so on [6]. These methods, however, need to be improved due to their inefficiency of dealing with subjectivity, lack of consideration of correlations among the attributes, or lack of quantitative analysis [7].

Aiming at this problem, this paper proposed multi-station combined evaluation method for navigation signal tracking accuracy based on optimization weight. The theoretical expression of this method is given. The correctness of the proposed theoretical model is verified by Monte Carlo simulation. Compared with the single-station evaluation method and the equal-weight linear weighting method, the effectiveness of the method is verified.

2 The Traditional Method

For the traditional comprehensive evaluation methods, such as radar chart, expert scoring method, linear weighting method, weighted TOPSIS method, etc., need to be involved in the decision of weight and the index system level, so the subjective is large, and lack of quantitative analysis. The single station evaluation method is to collect the observation data of the single-station monitoring receiver, and then evaluate the performance of the navigation signal. The commonly used evaluation indexes are signal power, code tracking accuracy, carrier tracking accuracy, anti-interference and anti-multipath. The code tracking error of non-coherent early-late power (NELP) discriminators affected by white Gaussian noise (WGN) can be expressed as follows [8]

$$\begin{aligned}\sigma^2_{\mathrm{DLL,NELP,WGN}} &= \frac{B_{\mathrm{DLL}}(1-0.5B_{\mathrm{DLL}}T_{\mathrm{Int}})\left(\int_{-B_r/2}^{B_r/2} G_S(f)\sin^2(\pi f\Delta)df\right)}{(2\pi)^2\frac{P_S}{N_0}\left(\int_{-B_r/2}^{B_r/2} fG_S(f)\sin^2(\pi f\Delta)df\right)^2} \\ &\times\left(1+\frac{\int_{-B_r/2}^{B_r/2} G_S(f)cos^2(\pi f\Delta)df}{\frac{P_S}{N_0}T_{\mathrm{Int}}\left(\int_{-B_r/2}^{B_r/2} G_S(f)cos(\pi f\Delta)df\right)^2}\right)\end{aligned} \tag{1}$$

where B_{DLL} is the loop bandwidth of phase lock loop (PLL), Δ is the early-late spacing, $G_S(f)$ is the power spectrum density (PSD) of navigation signal, P_S/N_0 is the carrier to noise ratio, B_r is the two-sided bandwidth of pre-correlation filter, T_{Int} is the coherent integration time.

In phase lock loop (PLL) of data channel, the carrier tracking error of the dot product (DP) and coherent (Coh) affected by WGN can be modeled as [9]

$$\sigma^2_{\mathrm{PLL,DP,WGN}} = \frac{B_{\mathrm{PLL}}(1-0.5B_{\mathrm{PLL}}T_{\mathrm{Int}})}{\frac{P_{\mathrm{S}}}{N_0}\int_{-B_{\mathrm{r}}/2}^{B_{\mathrm{r}}/2} G_{\mathrm{S}}(f)df}\left(1+\frac{1}{2\frac{P_{\mathrm{S}}}{N_0}T_{\mathrm{Int}}\int_{-B_{\mathrm{r}}/2}^{B_{\mathrm{r}}/2} G_{\mathrm{S}}(f)df}\right) \tag{2}$$

$$\sigma^2_{\mathrm{PLL,Coh,WGN}} = \frac{B_{\mathrm{PLL}}(1-0.5B_{\mathrm{PLL}}T_{\mathrm{Int}})}{\frac{P_{\mathrm{S}}}{N_0}\int_{-B_{\mathrm{r}}/2}^{B_{\mathrm{r}}/2} G_{\mathrm{S}}(f)df} \tag{3}$$

where B_{PLL} is the loop bandwidth of PLL.

The effect of the interference on the code tracking performance can be measured by the code tracking standard deviation, the code tracking error of CELP and NELP affected by broadband interference can be shown as follows [3]

$$\sigma^2_{\mathrm{DLL,CELP,Trad}} = \frac{B_{\mathrm{DLL}}(1-0.5B_{\mathrm{DLL}}T_{\mathrm{Int}})}{4\pi^2}\left[\frac{\int_{-B_{\mathrm{r}}/2}^{B_{\mathrm{r}}/2} G_{\mathrm{S}}(f)\sin^2(\pi f\Delta)df}{\frac{P_{\mathrm{S}}}{N_0}\left(\int_{-B_{\mathrm{r}}/2}^{B_{\mathrm{r}}/2} fG_{\mathrm{S}}(f)\sin(\pi f\Delta)df\right)^2}+\frac{\int_{-B_{\mathrm{r}}/2}^{B_{\mathrm{r}}/2} G_{\mathrm{I}}(f)G_{\mathrm{S}}(f)\sin^2(\pi f\Delta)df}{\frac{P_{\mathrm{S}}}{P_{\mathrm{I}}}\left(\int_{-B_{\mathrm{r}}/2}^{B_{\mathrm{r}}/2} fG_{\mathrm{S}}(f)\sin(\pi f\Delta)df\right)^2}\right] \tag{4}$$

$$\sigma^2_{\mathrm{DLL,NELP,Trad}} = \sigma^2_{\mathrm{DLL,CELP,Trad}}\left[1+\frac{\int_{-B_{\mathrm{r}}/2}^{B_{\mathrm{r}}/2} G_{\mathrm{S}}(f)\cos^2(\pi f\Delta)df}{T_{\mathrm{Int}}\frac{P_{\mathrm{S}}}{N_0}\left(\int_{-B_{\mathrm{r}}/2}^{B_{\mathrm{r}}/2} G_{\mathrm{S}}(f)\cos(\pi f\Delta)df\right)^2}+\frac{\int_{-B_{\mathrm{r}}/2}^{B_{\mathrm{r}}/2} G_{\mathrm{I}}(f)G_{\mathrm{S}}(f)\cos^2(\pi f\Delta)df}{T_{\mathrm{Int}}\frac{P_{\mathrm{S}}}{P_{\mathrm{I}}}\left(\int_{-B_{\mathrm{r}}/2}^{B_{\mathrm{r}}/2} G_{\mathrm{S}}(f)\cos(\pi f\Delta)df\right)^2}\right] \tag{5}$$

where P_{I} and P_{S} are the power of signal and interference.

The effective carrier-to-noise ratio in the presence of interference can be expressed as

$$(P_{\mathrm{S}}/N_0)_{\mathrm{Eff,Trad}} = \frac{1}{\frac{1}{P_{\mathrm{S}}/N_0}+\frac{P_I}{P_{\mathrm{S}}}\frac{1}{Qf_{\mathrm{PRN}}}} = \frac{P_{\mathrm{S}}}{N_0}\left[1+\frac{P_{\mathrm{I}}}{N_0}\frac{\int_{-B_{\mathrm{r}}/2}^{B_{\mathrm{r}}/2} G_{\mathrm{I}}(f)G_{\mathrm{S}}(f)df}{\int_{-B_{\mathrm{r}}/2}^{B_{\mathrm{r}}/2} G_{\mathrm{S}}(f)df}\right]^{-1} \tag{6}$$

where f_{PRN} denotes the rate of the pseudo-random noise (PRN) code, Q is the anti - interference quality factor, and can be defined as follows

$$Q = \frac{\int_{-\infty}^{\infty}|H_{\mathrm{R}}(f)|^2G_{\mathrm{S}}(f)df}{f_{\mathrm{PRN}}\int_{-\infty}^{\infty}|H_{\mathrm{R}}(f)|^2G_{\mathrm{I}}(f)G_{\mathrm{S}}(f)df} = \frac{\int_{-\infty}^{\infty}|H_{\mathrm{R}}(f)|^2G_{\mathrm{S}}(f)df}{f_{\mathrm{PRN}}\kappa_{\mathrm{IS}}} \tag{7}$$

where $H_{\mathrm{R}}(f)$ is the receiver transfer function, and its maximum amplitude is 1; κ_{IS} called spectral separation coefficient (Spectral Separation Coefficient, SSC), and its definition is as follows

$$\kappa_{\mathrm{IS}} = \int_{-\infty}^{\infty} |H_{\mathrm{R}}(f)|^2 G_{\mathrm{I}}(f) G_{\mathrm{S}}(f) df \tag{8}$$

Substitute (6) into (4) and (5) respectively, carrier tracking error of DP and Coh can be derived.

3 The Proposed Method

The proposed method can used to comprehensive analysis of navigation signals for iGMAS data analysis center, monitoring and evaluation center and Beidou main control station, the tasks that can be realized are shown in the red line area. Some pictures in Fig. 1 are referenced Ref. [10].

In Ref. [11], an optimal weighted combined acquisition scheme was given, and it is proved that combined acquisition of GPS L1using L1 L1C Data channel, Pilot channel and L1 C /A channel can improve the robustness of the acquisition algorithm. This paper applies this idea, and using the idea in multi-station combined assessment to improve the reliability of evaluation results.

$$X_i \sim N\left(\mu_i, \sigma_i^2\right) \quad i = 1, 2, \ldots, N \tag{9}$$

where subscript i denotes the i-th tracking station, $N\left(\mu_i, \sigma_i^2\right)$ means Gaussian distribution with mean μ_i and variance σ_i^2.

The codes and carrier phase combined evaluation outputs of the i-th and $i+1$-th tracking station can be shown below as follows

$$X_{c,i+1} = w_i X_i + w_{i+1} X_{i+1} = w_i X_i + (1 - w_i) X_{i+1} \tag{10}$$

where w_i represents the weights, and $X_{c,i+1}$ represents the combined output evaluation value after linear weighting.

For the variance σ_i^2 and σ_{i+1}^2, the output after combined is as follows

$$\sigma_{c,i+1}^2 = w_i^2 \sigma_i^2 + (1 - w_i)^2 \sigma_{i+1}^2 \tag{11}$$

The optimal can be obtained, when the code and carrier tracking variance $\sigma_{c,i+1}^2$ is the minimal, thus

$$\min\left(\sigma_{c,i+1}^2\right) = \frac{d\sigma_{c,i+1}^2}{dw_i} = 0 \tag{12}$$

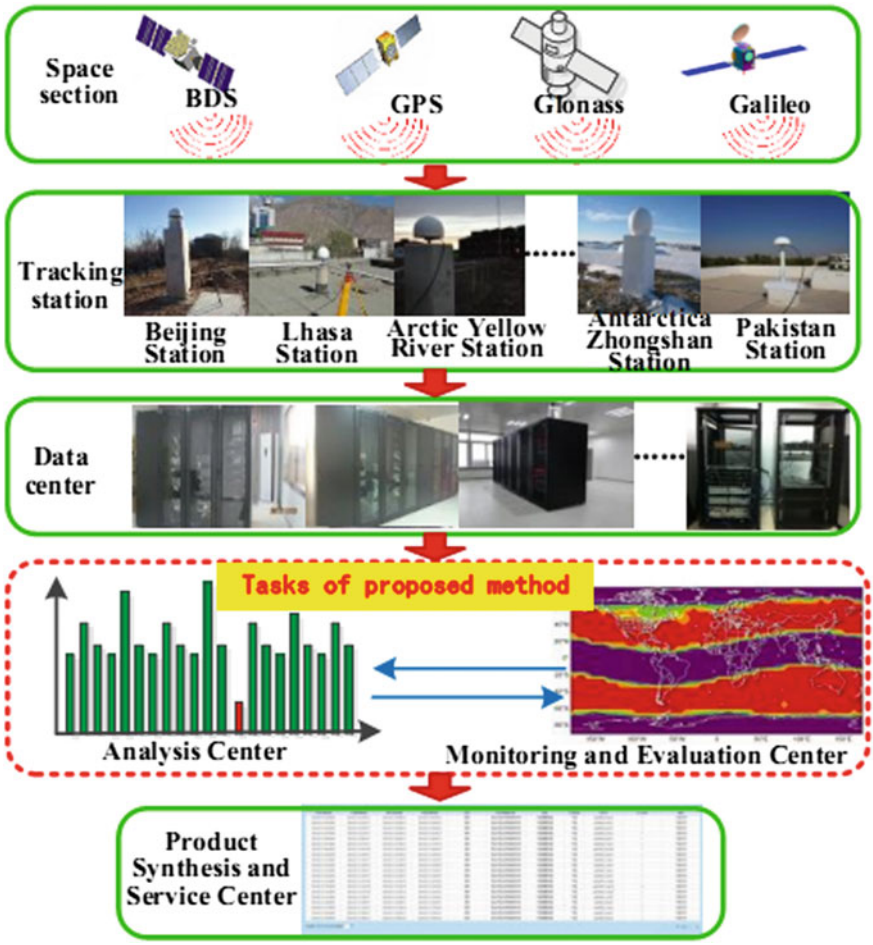

Fig. 1 The diagram of proposed method tasks

Solving Eq. (12), the optimal w_i can be obtained as follows

$$w_i = \frac{\sigma_i^2 \sigma_{i+1}^2}{\sigma_i^2 + \sigma_{i+1}^2} \tag{13}$$

Substitute (13) into (11), the optimal combined evaluation of tracking error can be obtained for the i-th and $(i+1)$-th tracking station as follows

$$\sigma_{c,i+1}^2 = \frac{\sigma_i^2 \sigma_{i+1}^2}{\sigma_i^2 + \sigma_{i+1}^2} \tag{14}$$

In a similar derived process from (11) to (14), the tracking error of N tracking stations combined can be derived as follow:

$$\begin{aligned}\sigma_{c,N}^2 &= \frac{\sigma_1^2\sigma_2^2\ldots\sigma_N^2}{\sigma_1^2\sigma_2^2\ldots\sigma_{N-2}^2\sigma_{N-1}^2+\sigma_1^2\sigma_2^2\ldots\sigma_{N-2}^2\sigma_N^2+\cdots+\sigma_2^2\sigma_3^2\cdots\sigma_{N-1}^2\sigma_N^2} \\ &= \frac{\prod_{i=1}^{N}\sigma_i^2}{\sum_{j=1}^{N}\left(\prod_{k=N-1,k\neq j}^{1}\sigma_k^2\right)}\end{aligned} \tag{15}$$

4 Experiment and Analysis

In this section, the correctness and anti-interference of the proposed method was verified. In experiments, the BOC(1,1) was used with $T_{\text{Int}} = 10$ ms, $B_{\text{DLL}} = 2$ Hz $B_{\text{PLL}} = 10$ Hz, $B_{\text{r}} = 4.092$ MHz, $\Delta = 0.2$ chip. The five tracking stations $T_1, T_2, \ldots, T_5$ are used, and the noise-to-noise ratio of each tracking station is 26–35 dB-Hz, 36–45 dB-Hz, 33–42 dB-Hz, 36–45 dB-Hz, 41–50 dB-Hz, respectively.

4.1 The Correctness Analysis of Proposed Method

In this paper, Monte Carlo simulation is used to verify the validity of the proposed comprehensive evaluation model. Figure 2 shows the results of a comprehensive evaluation of the code and carrier tracking accuracy of the five tracking stations, where the abscissa is the carrier-to-noise ratio of the tracking station T_2.

From Fig. 2, we can see that the theoretical curve is consistent with the simulation curve, which proves the correctness of the proposed mathematical model ().

4.2 Anti-interference Analysis of Proposed Method

In order to verify the anti-interference of the proposed method, the wideband interference is added in tracking station T_1 and T_2, with 15 dB equivalent carrier-to-noise ratio reduced in these two tracking stations. The anti-interference performance of proposed method was compared with single-station evaluation method and equal weight linear weighting method. Figures 3 and 4 are the code and carrier tracking error evaluation results of different methods in the presence of the wideband interference.

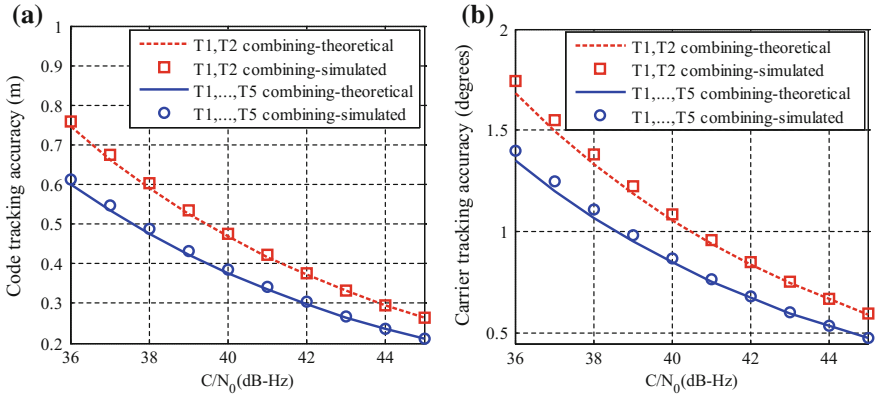

Fig. 2 The multi-station combined evaluation of code and carrier tracking error. **a** Evaluation of code tracking error. **b** Evaluation of carrier tracking error

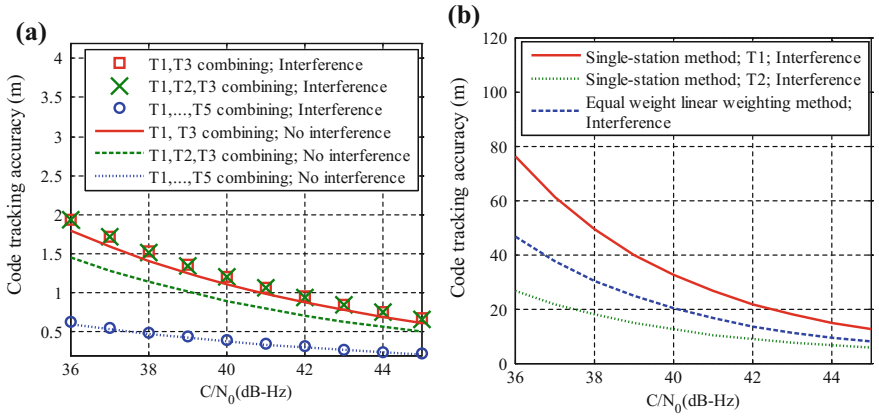

Fig. 3 The evaluation performance comparison of code tracking error among three methods with interference existing. **a** The influence of interference on the proposed method. **b** The influence of interference on single-station evaluation method and equal weight linear weighting method

From Figs. 3a and 4a, it can be seen that the accuracy of the combination evaluation for T_1, T_2 and T_3 is reduced by 2, 0.5–0.8 dB for combination evaluation for T_1 and T_3, nd no deteriorate when combination evaluation for $T_1, T_2, \ldots, T_5$.

From Figs. 3b and 4b, it can be found that Single-station evaluation method and equal-weight linear weighting method are affected by the interference, and the large code tracking accuracy is evaluated. These two methods will have a great impact on the comprehensive evaluation. From the above analysis we can see that the reliability of this method is high, and is less affected by interference.

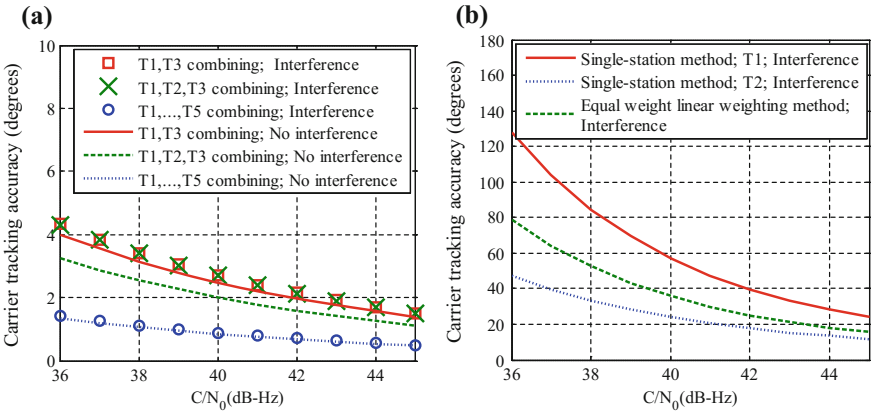

Fig. 4 The evaluation performance comparison of carrier tracking error among three methods with interference existing. **a** The influence of interference on the proposed method. **b** The influence of interference on single-station evaluation method and equal weight linear weighting method

5 Conclusion

In this paper, a multi-station combined evaluation method for navigation signal tracking accuracy based on optimization weight was proposed. In the proposed method, the optimized weights were calculated by solving established equation, and then the comprehensive evaluation result was obtained by using the optimized weights. Experimental and simulation results show that the proposed method is more robust than the single-station evaluation method and multi-objective/multi-attribute comprehensive evaluation method. And the proposed method can provide more objective, reliable and accurate evaluation results.

Some limitations in this paper and future work should be pointed out here: (1) The multi-station combined evaluation method for more indicators should be researched, such as signal power, phase consistency, bit error rate, and so on; (2) The combined evaluation method of single-station or multi-station for different Attribute indicators is also worth exploring; (3) Experiments should be carried out using real data from different tracking stations.

Acknowledgements This work was supported by National High Technology Research and Development Program of China (Grant No. 2015AA124001).

References

1. Phelts RE, Gao GX, Wong G et al (2010) New GPS signals evaluation grade chips off the block IIF. Inside GNSS 7(8):36–45
2. Gatti G, Falconde M, Alpe V et al (2008) Glove-B chilbolton in-orbit test. Inside GNSS 9 (10):30–35
3. Tiberius C, Marel HVD, Sleewaegen JM et al (2008) Analyzing a Glove-A/B double difference. Inside GNSS 9(10):40–44
4. Wang H, Liu C (2009) Measuring system for satellite navigation signal quality. GNSS World China 6:60–63
5. Jiao W (2011) Monitoring and evaluation of GNSS open services. In: The 2nd China Satellite Navigation Academic annual conference, Shanghai, China
6. Ma X (2013) The research of comprehensive evaluation method for navigation signal waveforms performance. Huazhong University of Science and Technology
7. Liu Q, Kou Y, Huang ZA (2016) Comprehensive evaluation approach of navigation signal performance based on multi-attribute group decision making. In: China Satellite Navigation conference (CSNC), vol II. Springer, Singapore
8. Betz JW, Kolodziejski KR (2009) Generalized theory of code tracking with an early-late discriminator part II: noncoherent processing and numerical results. IEEE Trans Aerosp Electron Syst 45(4):1557–1564
9. Julien O (2005) Design of Galileo L1F receiver tracking loops. University of Calgary
10. Jiao W (2016) New Progress in the international GNSS monitoring and evaluation system (iGMAS). In: The 2nd China Geodesy and Geophysics Society conference, Nanjing
11. Macchi F (2010) Development and testing of an L1 combined GPS-Galileo software receiver. University of Calgary, Calgary

Test and Evaluation on Timing Performance of BeiDou IGSO-6 Satellite

Dan-dan Li, Feng Zhu, Long-xia Xu, Bo Li and Xiao-hui Li

Abstract In March 2016, China launched IGSO-6 satellite. To obtain actual test values of the performance indexes, test and evaluation works need to be done before IGSO-6 satellite provides services formally, which provide promise for the network running and service performance. From users' view, the paper uses the method of testing the bias between UTC broadcast by the satellites and actual UTC, carries out the test works on single satellite timing and multiple satellites timing and evaluates the timing performance of IGSO-6 satellite. The evaluation results show that the timing errors with grid point ionospheric model are less than that with Klobuchar model regardless of at B1 or B3 frequency point. The timing error of IGSO-6 satellite is about −7 ns at B1 frequency point and its standard deviation is better than 9 ns. The B3 timing error is about −11 ns and its standard deviation is better than 9 ns, which is worse than that of B1. The B1 + B2 and B1 + B3 timing accuracy are the same of 1 ns. After adding IGSO-6 satellite, the multiple satellites timing accuracy at B1 and B3 frequency point improve by about 0.6 ns and that of B1 + B2 and B1 + B3 are 0.5 and 0.4 ns respectively. The multiple satellites timing accuracy have a certain improvement at different modes when adding IGSO-6 and it meets the network conditions.

Keywords IGSO-6 · UTC · Test and evaluation method · Timing performance

D. Li (✉) · F. Zhu · L. Xu · B. Li · X. Li
National Time Service Center, CAS, Xi'an, China
e-mail: leedanvip@163.com

D. Li · F. Zhu · L. Xu · B. Li · X. Li
Key Laboratory of Precision Navigation Positioning and Timing, CAS, Xi'an, China

D. Li · B. Li
University of Chinese Academy of Sciences, Beijing, China

J. Sun et al. (eds.), *China Satellite Navigation Conference (CSNC) 2017 Proceedings: Volume I*, Lecture Notes in Electrical Engineering 437,
DOI 10.1007/978-981-10-4588-2_61

1 Introduction

The IGSO-6 satellite is the twenty-second BeiDou navigation satellite launched by China and its number is 15. It is the first in-orbit backup satellite launched after the successful operation of BeiDou regional satellite navigation system. IGSO-6 satellite provides services for users together with other in-orbit satellites after completing in-orbit test. This improves the system reliability and advances the system constellation robustness. The performance of BeiDou navigation satellite system (BDS) is improved. Before adding satellite health signs, single satellite timing performance is evaluated firstly and then the multiple satellites timing performance and these promise the timing accuracy in the BDS service specification.

The time broadcast by BeiDou satellite is UTC and UTC is calculated by BIPM and published monthly through BIPM circular T. Zhu [1] proposed the method to test the bias between UTC broadcast by the satellites and actual UTC. The paper developments test and evaluation research on the timing performance of new-generation navigation satellites utilizing the method and the standard time and frequency resource of UTC (NTSC). Firstly, the basic principle of timing performance test evaluation is introduced. Then the evaluation indexes of timing performance and their calculation methods are introduced. The timing accuracy of BeiDou IGSO-6 satellite is evaluated and multiple satellites timing accuracy is evaluated through integrated multiple satellites test. Then the timing accuracy of BeiDou IGSO-6 satellite and improvement of multiple satellites timing accuracy when considering IGSO-6 is given.

2 Basic Principle of Timing Performance Test and Evaluation

With the 10 MHz frequency signal and 1PPS time signal generated and maintained by National Time Service Center of the Chinese Academy of Sciences (NTSC) as the reference, the bias between UTC broadcast by the satellites and actual UTC is tested through placing BeiDou timing receiver in NTSC and timing performance of BeiDou satellites in the various modes is evaluated through integrated comprehensive calculation. The basic principle of timing performance test and evaluation is showed in Fig. 1.

1. Zero-value calibration of the BeiDou timing receiver is realized so that the receiver time is completely synchronized with UTC (NTSC).
2. Calculate bias between BeiDou satellite broadcasting system time and UTC (NTSC) by pseudo-range modification [2, 3]:

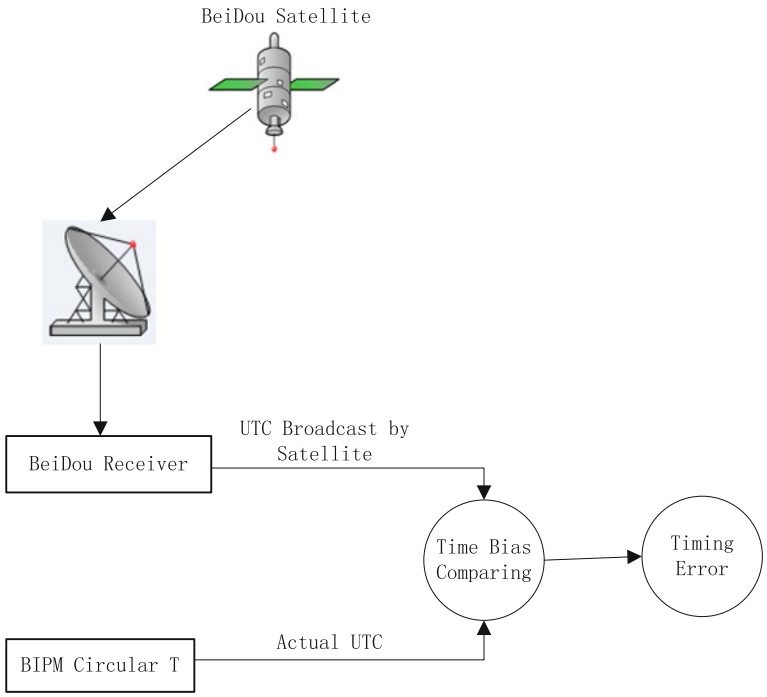

Fig. 1 Test and evaluation principle of timing performance

$$\begin{aligned}\delta t_{NTSC,S}(i,\mathrm{j}) &= UTC(NTSC) - SvBDT(i) \\ &= \rho/c - r/c + \delta t_{clk} - \delta t_{ion} - \delta t_{trop} - \delta t_{sagnac} - \delta t_{other}\end{aligned} \tag{1}$$

ρ is the pseudo-range from satellite to receiver, r is the geometry path from satellite to receiver, δt_{clk} is the satellite clock bias, δt_{ion} and δt_{trop} are relatively the ionosphere delay and troposphere delay, δt_{sagnac} is the sagnac modification, δt_{other} is the other delay, j is the mode.

3. Calculate the UTC time broadcast by BeiDou satellite i in the mode j:

$$\delta t_{S,UTC}(i,j) = UTC - UTC(NTSC) = \delta t_{trace} - \delta t_{\mathrm{NTSC},S}(i,j) \tag{2}$$

δt_{trace} is the traceability data from navigation message [4, 5].
Calculate the UTC time broadcast by BeiDou satellites in the mode j.

$$\delta t_{\mathrm{S},UTC}(j) = \frac{\sum_{i=1}^{n} p_i \cdot \delta t_{S,UTC}(i,j)}{\sum_{i=1}^{n} p_i} \tag{3}$$

n is the number of visible satellites at the current epoch and p_i is the weighted value corresponding to the satellite i.

4. Obtain the actual UTC time from BIPM Circular T:

$$\delta t_{BIPM} = UTC - UTC(NTSC) \tag{4}$$

5. Calculate the timing error of BeiDou satellite i in mode j:

$$\sigma_{S,UTC}(i,j) = \delta t_{S,UTC}(i,j) - \delta t_{BIPM} \tag{5}$$

Calculate the multiple satellites timing error in mode j:

$$\sigma_{\mathrm{S},UTC}(j) = \delta t_{S,UTC}(j) - \delta t_{BIPM} \tag{6}$$

In conclusion, the UTC time broadcast by BeiDou satellites is obtained through pseudo-range modification and the bias between satellites broadcasting UTC time and actual UTC time is calculated by using the actual UTC time from BIPM Circular T. This is the actual timing error received by users and then the timing accuracy of BDS is evaluated.

3 Evaluation Indexes and Their Calculation Methods

3.1 Evaluation Indexes

- Single satellite timing accuracy
  During the evaluation period, bias between satellite broadcasting UTC time and actual UTC time is the single satellite timing accuracy and the actual UTC time is issued periodically by BIPM through Circular T.
- Multiple satellites timing accuracy
  Multiple satellites timing accuracy is the statistic of bias between satellite broadcasting UTC time and actual UTC time which is the weighted average of biases of all visible satellites at the same epoch during the evaluation period. Multiple satellites timing accuracies are compared according to whether adding IGSO-6 satellite.

3.2 Calculation Methods

BeiDou satellites timing accuracy assessment is mainly performance characterized by the average and standard deviation. The average characterizes the accuracy of satellite broadcasting UTC time, which can be regarded as uncertainty B and reflects the timing accuracy of navigation system. The standard deviation

characterizes the dispersion degree of satellite broadcasting UTC time, which can be regarded as uncertainty A and reflects the distribution of timing error. Their expressions are shown as:

$$\text{Average: } \mu = \frac{\sum_{i=1}^{n} \Delta_i}{n} \tag{7}$$

$$\text{Standard Deviation: } \sigma = \sqrt{\frac{\sum_{i=1}^{n} (\Delta_i - \mu)^2}{n-1}} \tag{8}$$

n is the number of sampling points, Δ_i is the value of the ith sampling point, and μ is the average of the values of n sampling points.

The improvement of multiple satellites timing accuracy is calculated as follows.

$$\phi = \mu_2 - \mu_1 \tag{9}$$

μ_2 is the multiple satellites timing accuracy when considering IGSO-6 satellite, μ_1 is the multiple satellites timing accuracy without considering IGSO-6 satellite.

4 Timing Performance Evaluation Results

Based on the observation data of BeiDou timing receiver from June 1 to July 10, 2016, the satellite broadcasting UTC time is calculated. Combining the actual UTC time in the same period, the time accuracy of BeiDou IGSO satellites, multiple satellites timing accuracy and improvement of multiple satellites timing accuracy when considering IGSO-6 is analyzed.

4.1 Single Satellite Timing Accuracy

4.1.1 B1 Timing Accuracy

B1 timing accuracy is calculated by using B1 single-frequency ionospheric delay for correction. Figure 2 shows the B1 timing errors of the BeiDou IGSO-6 satellite when using the K8 model [6, 7] and the grid point [8, 9] ionospheric delay.

The statistics of B1 timing error of IGSO satellites when using K8 model and grid point ionospheric delay for correction are shown in Table 1.

As can be seen from Table 1, the B1 single satellite timing error is smaller when using grid point ionospheric delay for correction than using K8 model. And with the average as the evaluation results, the B1 timing error of IGSO-6 satellite is

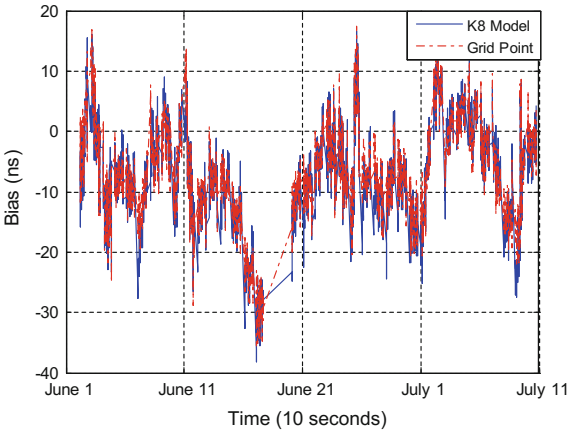

Fig. 2 B1 timing error of BeiDou IGSO-6 satellite

about −7 ns and standard deviation is better than 9 ns which is better than the results of the other IGSO satellites.

4.1.2 B3 Timing Accuracy

B3 timing accuracy is calculated by using B3 single-frequency ionospheric delay for correction. Figure 3 shows the B3 timing errors of the BeiDou IGSO-6 satellite when using the K8 model and the grid point ionospheric delay.

The statistics of B3 timing error of IGSO satellites when using K8 model and grid point ionospheric delay for correction are shown in Table 2.

It can be seen from Table 2 that the B3 single satellite timing error is smaller when using grid point ionospheric delay for correction than using K8 model. And with the average as the evaluation results, the B3 timing error of IGSO-6 satellite is about −10 ns and standard deviation is better than 9 ns which is better than the results of the other IGSO satellites.

4.1.3 B1 + B2 Timing Accuracy

B1 + B2 timing accuracy is obtained by using B1/B2 dual-frequency ionospheric delay for correction. The B1 + B2 timing accuracy of BeiDou IGSO-6 satellite is shown in Fig. 4.

As shown in Table 3, with the average as evaluation result, the B1 + B2 timing error of IGSO-6 satellite is 1.2 ns and standard deviation is better than 9 ns. And there are deviations from the results of the other five IGSO satellites.

Table 1 The statistics of the IGSO satellites B1 timing error (unit: ns)

Prn	K8 model				Grid point			
	Average	Standard deviation	Maximum	Minimum	Average	Standard deviation	Maximum	Minimum
6	−10.12	9.18	19.95	−49.88	−9.30	8.77	22.97	−46.78
7	−12.71	8.57	14.89	−49.87	−12.61	8.23	13.11	−50.49
8	−13.44	8.67	27.80	−60.22	−12.86	8.39	28.10	−52.71
9	−9.67	8.43	20.86	−46.02	−9.08	8.15	18.62	−45.71
10	−13.78	8.29	30.01	−45.19	−13.18	8.21	29.40	−45.40
IGSO-6	−7.25	8.32	16.74	−38.12	−6.98	7.90	17.40	−35.59

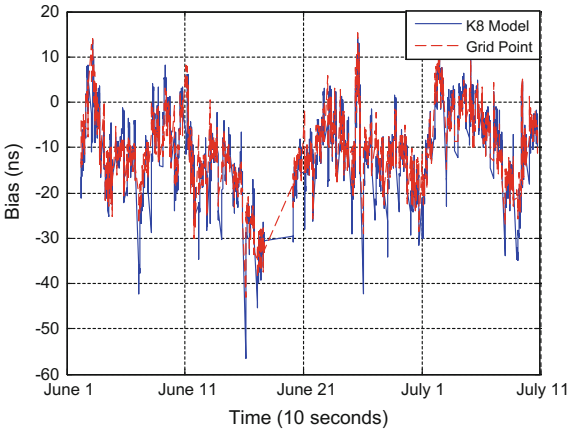

Fig. 3 B3 timing error of BeiDou IGSO-6 satellite

4.1.4 B1 + B3 Timing Accuracy

B1 + B3 timing accuracy is obtained by using B1/B3 dual-frequency ionospheric delay for correction. The B1 + B3 timing accuracy of BeiDou IGSO-6 satellite is shown in Fig. 5.

As shown in Table 4, with the average as evaluation result, the B1 + B3 timing error of IGSO-6 satellite is 1 ns and standard deviation is better than 9 ns. And there are some deviations from the results of the other five IGSO satellites.

4.1.5 Conclusion of Single Satellite Timing Performance

With dividing the 40 days test time into four periods, the timing error of IGSO-6 satellite in each period is calculated, and the timing errors of IGSO-6 satellite in different time periods are compared. The average and standard deviation of IGSO-6 satellite in different modes are shown in Figs. 6 and 7.

As shown in Figs. 6 and 7, in the four periods, the B1 timing error of IGSO-6 satellite is less than that of B3 and the dual-frequency timing error is less than single-frequency timing error which difference is about 10 ns and the standard deviations of timing error in different modes are better than 9 ns.

4.2 Multiple Satellites Timing Accuracy

4.2.1 B1 Timing Accuracy

Figure 8 shows the B1 multiple satellites timing error using K8 model and grid point ionospheric delay for correction.

Table 2 The statistics of the IGSO satellites B3 timing error (unit: ns)

Prn	K8 model				Grid point			
	Average	Standard deviation	Maximum	Minimum	Average	Standard deviation	Maximum	Minimum
6	−13.83	10.26	30.47	−66.21	−12.57	9.11	35.01	−53.77
7	−16.19	9.46	18.28	−60.49	−16.04	8.70	13.49	−60.82
8	−15.85	9.45	25.64	−68.39	−14.98	8.68	26.09	−57.00
9	−12.03	9.21	29.19	−51.03	−11.14	8.44	25.38	−50.56
10	−16.42	8.77	28.03	−52.45	−15.51	8.53	27.11	−52.03
IGSO-6	−10.54	9.06	14.21	−56.60	−10.14	8.08	15.20	−42.99

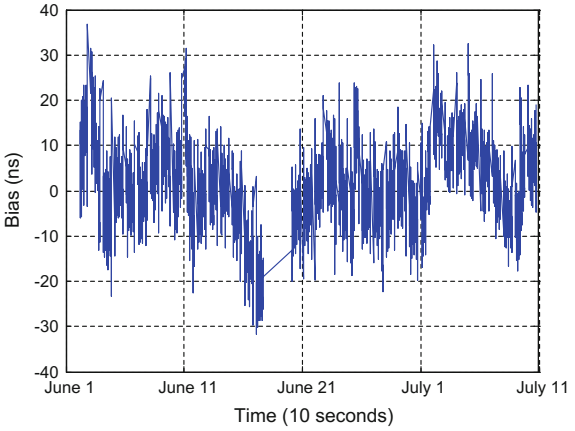

Fig. 4 B1 + B2 timing error of BeiDou IGSO-6 satellite

Table 3 Statistics of IGSO satellites B1 + B2 timing error (unit: ns)

Prn	Average	Standard deviation	Maximum	Minimum
6	0.42	9.00	38.05	−49.07
7	−2.75	8.14	48.67	−42.39
8	−4.49	8.46	36.57	−46.71
9	−0.42	8.32	32.15	−48.35
10	−4.91	8.21	39.93	−49.32
IGSO-6	1.23	8.33	36.88	−31.72

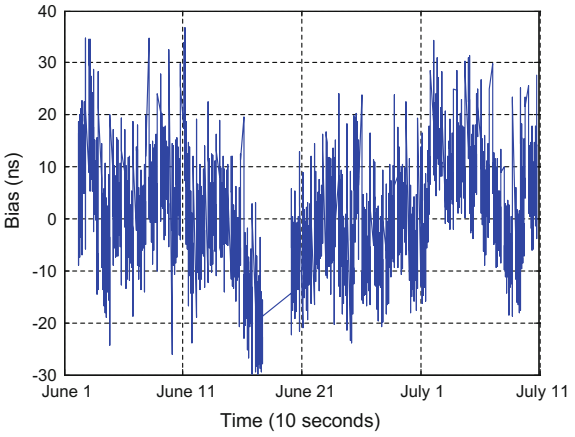

Fig. 5 B1 + B3 timing error of BeiDou IGSO-6 satellite

It can be seen from Table 5 that the B1 multiple satellites timing error is smaller when using grid point ionospheric delay for correction than using K8 model, and the improvement of B1 multiple satellites timing accuracy is about 0.6 ns when adding IGSO-6 satellite.

Table 4 Statistics of IGSO satellites B1 + B3 timing error (unit: ns)

Prn	Average	Standard deviation	Maximum	Minimum
6	1.19	9.15	44.63	−41.92
7	−2.21	8.27	58.62	−39.78
8	−4.93	8.66	42.35	−45.28
9	−0.29	8.80	35.40	−48.46
10	−4.94	8.32	62.87	−46.90
IGSO-6	1.05	8.80	36.72	−29.91

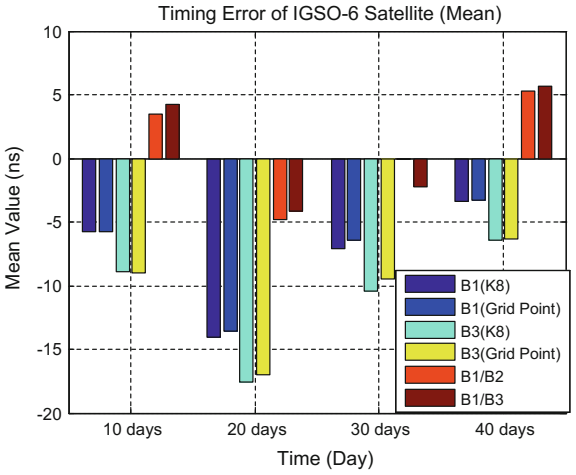

Fig. 6 The average of IGSO-6 satellite timing error

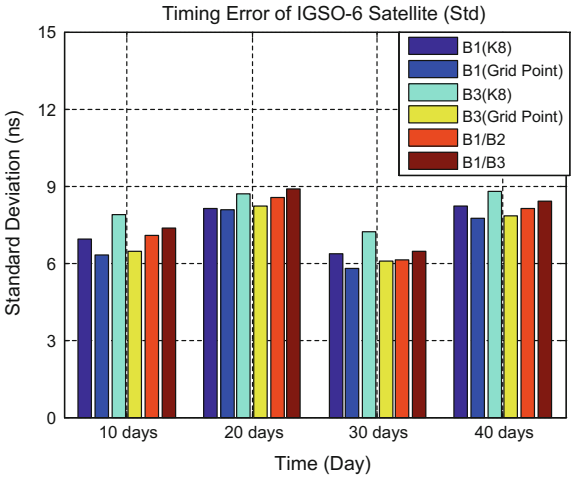

Fig. 7 The standard deviation of IGSO-6 satellite timing error

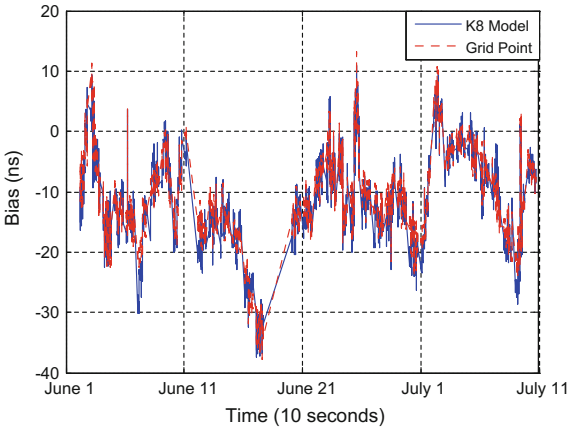

Fig. 8 B1 timing error of BeiDou IGSO satellites

Table 5 Effect of IGSO-6 on B1 timing error (unit: ns)

Correction model	Without IGSO-6	With IGSO-6	Improvement
K8	−12.13	−11.52	0.61
Grid point	−11.61	−11.04	0.57

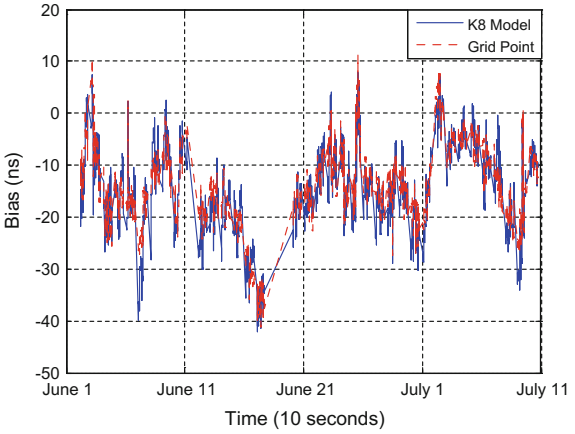

Fig. 9 B3 timing error of BeiDou IGSO satellites

4.2.2 B3 Timing Accuracy

Figure 9 shows the B3 multiple satellites timing error when using K8 model and grid point ionospheric delay for correction.

As can be seen from Table 6, the B3 multiple satellites timing error when using grid point ionospheric delay for correction is smaller than that of using K8 model, and the B3 multiple satellites timing accuracy is improved when adding IGSO-6 satellite.

Table 6 Effect of IGSO-6 on B3 timing error (unit: ns)

Correction model	Without IGSO-6	With IGSO-6	Improvement
K8	−15.20	−14.61	0.59
Grid point	−14.42	−13.88	0.54

4.2.3 B1 + B2 Timing Accuracy

With the average as evaluation result, the influence of IGSO-6 satellite on B1 + B2 multiple satellites timing error is analyzed. The results are shown in Table 7.

As can be seen from Table 7, the B1 + B2 multiple satellites timing accuracy is improved by 0.5 ns after adding IGSO-6 satellite.

4.2.4 B1 + B3 Timing Accuracy

With the average as evaluation result, the influence of IGSO-6 satellite on B1 + B3 multiple satellites timing error is analyzed. The results are shown in Table 8.

It can be seen from Table 8 that the B1 + B3 multiple satellites timing accuracy is improved by 0.37 ns when adding IGSO-6 satellite.

4.2.5 Conclusion of Multiple Satellites Timing Performance

Figure 10 shows the improvement of multiple satellites timing accuracy when adding IGSO-6 satellite in different periods.

As can be seen from Fig. 10, in the third period, the B1 + B3 multiple satellites timing accuracy is reduced by about 0.1 ns when adding IGSO-6 satellite and the multiple satellites timing accuracy is improved by 0.2–0.8 ns in other periods.

Table 7 Effect of IGSO-6 on B1 + B2 timing error (unit: ns)

Without IGSO-6	With IGSO-6	Improvement
−2.83	−2.33	0.50

Table 8 Effect of IGSO-6 on B1 + B3 timing error (unit: ns)

Without IGSO-6	With IGSO-6	Improvement
−2.02	−1.65	0.37

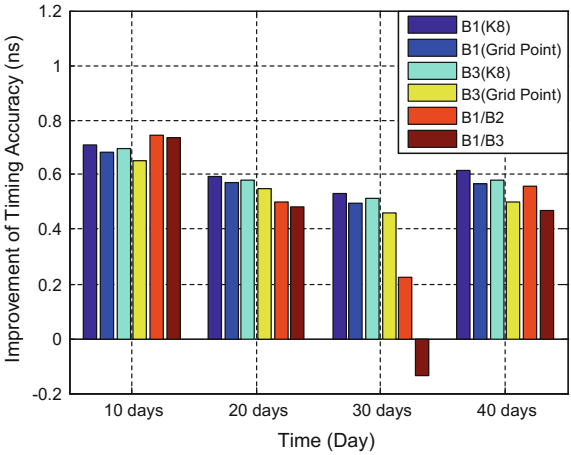

Fig. 10 The improvement of timing accuracy with IGSO-6

5 Conclusion

The B1 and B3 timing accuracy of IGSO-6 satellite are better than that of the other five BeiDou IGSO satellites and the B1 + B2 and B1 + B3 timing accuracy have some differences from that of the other five BeiDou IGSO satellites. After adding IGSO-6 satellite, the multiple satellites timing accuracy is improved. Therefore, IGSO-6 satellite meet networking conditions. At August 5, 2016, BeiDou official website released that the test evaluation work of the twenty-second BeiDou navigation satellite had completed and it provides services to users officially and the satellite number is varies from 15 to 13 [10].

The timing performance evaluation of GEO-7 satellite is conducting, and then the new launched BeiDou satellites and the new signal system BOC and S-band signals.

Acknowledgements Funded by National Natural Science Foundation of China (Grant No. 11503030) and National Defense Innovation Foundation of China (Grant No. CXJJ-16M205).

References

1. Zhu F, Li X, Zhang H et al (2016) Study on integrated testing and evaluation method of GNSS timing performance. In: China satellite navigation conference (CSNC) 2016, vol I. Springer, Singapore
2. Xu L (2012) A new common-view based timing method. Chinese Academy of Sciences (National Time Service Center)
3. Zhu F (2015) The time parameter of satellite navigation and its test method. University of Chinese Academy of Sciences
4. Sun G, Lu H, Shen L et al (2016) Evaluation and monitoring on traceability model based on the BDS, GPS and GLONASS. In: China Satellite Navigation Conference (CSNC)

5. Dong S, Wu H, Li X et al (2008) The compass and its time reference system. Metrologia 45 (6):S47–S50
6. Zhang F, Yang Z, Cheng P et al (2014) Comparision of ionospheric delay accuracy between GPS and Beidou. Comput Eng Sci 36(2):270–274
7. Sun M, Yu J, Hu Y et al (2015) Correction accuracy analysis on ionospheric model of beidou system. J Geomatics Sci Technol 32(1):27–31
8. Li J, Wang D, Zeng G et al (2016) Refraction correction for range data using iGMAS ionosphere harmonic-sphere grids. In: China Satellite Navigation Conference (CSNC)
9. Cui Y, Meng Z, Jia W et al (2014) The research and application of wide area differential grid ionospheric model in BD2 system. Aerosp Control 32(6):12–15
10. http://www.beidou.gov.cn/2016/08/05/20160805be35373a002d45788fc4b8e4b798750c.html. Accessed 5 Aug 2016

Research of Navigation Terminal Test Method Based on Real Playback Signal

Xiaoxi Jin, Yuze Wang and Rendong Ying

Abstract With the continuous promotion of Beidou satellite navigation applications, the pace of city market accelerate, and how to improve the navigation terminal performance is a hot issue under city environment because of its wide application and complex signal propagation. Based on received Beidou satellite signal power shadowing under different environments in city application, the paper proposed a statistical Markov model with three states: line-of-sight (LOS)-shadow-block, and using a combination of mixture Gaussian functions to approximate the distribution to describe signal variations to represent environment parameter variations. Channel parameters are evaluated from the experimental data in shanghai and utilized to verify a simulated model. Results presented in the form of signal waveforms, probability density functions show close agreement with measurements.

Keywords Playback test system · Test scene design · Performance indicators

1 Introduction

In the past ten years, Beidou navigation terminal technology to flourish, Beidou terminal applications were blowout, such as urban vehicle navigation, auxiliary communication and navigation, indoor navigation. With the deepening of navigation applications, navigation terminals and chip manufacturers increasingly rely on the navigation terminal industry-standard test to ensure the terminal performance of qualified.

X. Jin (✉)
Beijing Satellite Navigation Center, Beijing 100094, China
e-mail: 838617547@qq.com

Y. Wang · R. Ying
China Key Lab of Navigation and Location-Based Services,
Shanghai Jiao Tong University, Shanghai 200240, China

J. Sun et al. (eds.), *China Satellite Navigation Conference (CSNC) 2017 Proceedings: Volume I*, Lecture Notes in Electrical Engineering 437,
DOI 10.1007/978-981-10-4588-2_62

At present, the navigation terminal test methods are divided into two categories: based on analog signal test and real signal test. The test method of terminal performance based on analog signal is to provide a stable, accurate, reliable and easy-to-use test environment for the development and testing of the navigation terminal by setting different test parameters and scenes to simulate the real navigation satellite signals. The test method has the advantage of full control of the test scene, the test can be repeated, various types of error, signal level and other factors can be accurately quantified, but the test method has obvious limitations, the real signal user environment section has a variety of The simulation results show that the performance of the analog signal environment is different from that of the real signal receiving environment, and the simulation results show that the simulated signal can not simulate the real signal completely. The test method based on the real signal is to receive the real satellite signal with the terminal to be measured. The test result is the actual performance of the receiving terminal. However, the real signal changes with time. The constellation state, ionosphere, multipath, receiver environment and the atmospheric signal propagation environment of the scene are changing, so the test method is less reproducible and the test cost is higher.

Therefore, combining the advantages of simulator test and real signal test, it is necessary to establish the real-time signal acquisition and playback test. At present, the R&D in the collection of playback devices, the domestic unit has carried out a number of related research work, such as Hunan Matrix Electronic Technology Co., Ltd., a power company, Xiamen University Hercynian Engineering Engineering Technology Center. The full-frequency navigation signal acquisition and playback instrument of Hunan Matrix Electronics supports simultaneous recording and playback of four channels of BD-2, GPS, GLONASS, Galileo multi-system. The sampling bandwidth can be expanded up to 4bit, different scenes can be selected during playback. But also controllable, the signal can be output through the RF cable or antenna. Foreign collection and playback equipment Spirent, Rohde Schwartz as the representative. The combination of FSW spectrum analyzer, IQR high-speed signal storage instrument and R & S SFBW signal playback device can be used to collect sampling frequency 150 MSPS, sampling bandwidth 60 MHz, sampling bit width 16 bit, signal sampling range covers 1–5 GHZ range Within any of the navigation frequency signal, on behalf of the current international performance of the highest signal acquisition and playback equipment.

From the device point of view, the existing technical indicators to achieve the navigation signal sampling requirements, but the lack of playback-based test methods, error correction methods and other research work. This paper is on the acquisition and playback system based on the test scenarios, test indicators for research. This paper is divided into four parts. Section 1 is introduction. Section 2 is composed of the test platform. Section 3 is the design of the test scene. Section 4 is a typical test scenario. Section 5 is conclusion.

2 Playback Test Platform

The design of this paper is based on the collection and playback test platform built by Shanghai Key Laboratory of Positional Service and Satellite Navigation. The acquisition and playback test platform consists of acquisition and calibration subsystem, scene database subsystem, playback test subsystem, analysis subsystem, The composition of the control center is shown in Fig. 1.

The Beidou navigation terminal test platform based on the collection and playback has the characteristics of high sampling rate, large storage capacity, wide storage mode and wide application scene. It can fully meet the requirements of terminal manufacturers to collect, replay and analyze the experimental data of typical application scenarios. Parameters of the test platform are as follows:

- Scenes include Shanghai, Beijing and Xi'an. The scene types include urban canyons, woodlands, suburbs, open areas, elevated roads, tunnels, water and industrial areas. Vehicles are vehicles with speeds of 0–120 km/h.
- Acquisition indicators, the signal contains B1/L1, sampling rate of 62 MSPS, sampling accuracy of 8 bit, front-end bandwidth of 24 M, signal strength −128 to −168 dBm.

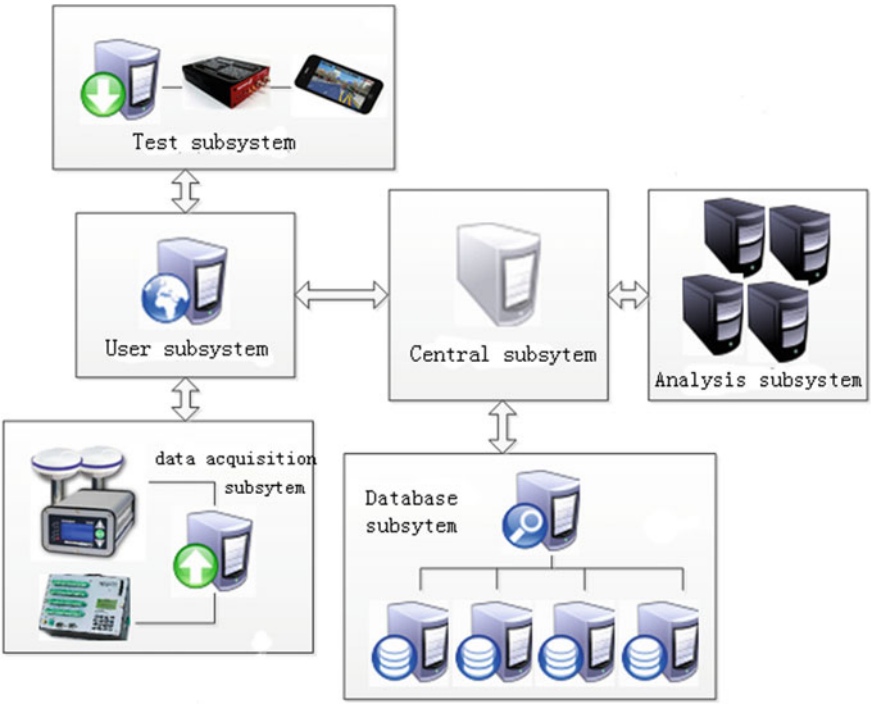

Fig. 1 Test system based on real BDS signal data

- calibration indicators, positioning accuracy better than 0.1 m, speed accuracy better than 0.01 km/h.
- playback indicators, playback signal power error is less than 0.5 dB, playback signal carrier frequency accuracy $\pm 5 \times 10^{-10}$. Playback test error (positioning accuracy, dynamic characteristics) differences of less than 10%.

The above parameters have been tested through the test, this part is not the focus of this article, so do not repeat them.

3 Test Scene Design

The main task of the test scenario design is to provide a description of the different scenes of the database. In order to facilitate the user to test the equipment, the developer can carry out the detailed analysis based on the scene features. When the scene design is done, the influence of satellite constellation, user trajectory and occlusion environmental parameters on the performance of the navigation terminal is considered, and the parameters characterizing the scene characteristic are extracted by the model analysis of the scene data.

3.1 Definition of Scene Parameters

The velocity factor characterizes the motion characteristics of the user. According to the user's speed, the user can be divided into quasi-static carrier (≤ 20 km/h), low-speed carrier (20–60 km/h), medium-speed carrier (60–100 km/h). The velocity characteristics include the uphill, turn, straight line and other movement characteristics of the carrier.

The number of visible satellites is the number of satellites that the user can receive signals at a certain moment. The number of visible satellites is the most direct characterization of the constellation character.

3.2 Markov Parameter Model Based on Mixed Gaussian

These observations clearly suggest that classical distributions used radio propagation cannot be used directly to characterize the channel. Rather, a combination of distribution is required, the overall pdf follows the general expression given in [1]

$$f_{overall} = P_{los} f_{shadow} + P_{shadow} f_{block} + P_{block} f_{block} \tag{1}$$

where

f_{los} pdf of the signal variations in LOS conditions;
f_{shadow} pdf of the signal variations in shadowed conditions;
f_{block} pdf of the signal variations in blocked conditions;
P_{los} probability that the link is in LOS conditions;
P_{shadow} probability that the link is in shadowed conditions;
P_{block} probability that the link is in blocked conditions;

P is described by two matrices:

- State probability matrix-[W]
- State transition probability matrix-[P].

Each element in matrix[P], P_{ij} represents the probability of change from state I to state j. the overall probability for each state is contained in matix[W] where each element, W_i,represents the total probability of being in state I. the matrix elements W_i, and P_{ij} can be defined as follows:

$$P_{ij} = N_{ij}/N_i \tag{2}$$

$$W_i = N_i/N \tag{3}$$

where N_i is the number of the minimum state length corresponding to state I and N is the total number of the state, N_{ij} is the number of the transitions from state I to state j.

So, we proposed three-state-model defined:

- S1: LOS conditions;
- S2: Shadow conditions;
- S3: Block conditions;
- [P]: State probability matrix;
- [W]: State transition probability matrix (Fig. 2).

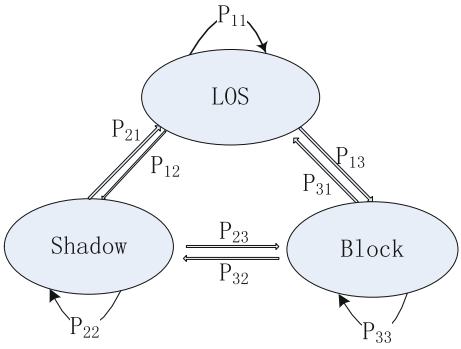

Fig. 2 Three-state channel model of BDS signal

The distribution of the three state are described by mix Gaussian distribution:

$$f \sim \sum_{i=1}^{k} w_i \mathrm{N}(\mu_i, \Sigma_i) \tag{4}$$

So, the GM-HMM model parameter:

$$\lambda = (P, W, \mu, \Sigma) \tag{5}$$

4 Typical Test Scenarios

Correlation coefficients for typical scenes parameters estimated are shown in Figs. 3, 4, 5 and Table 1.

Fig. 3

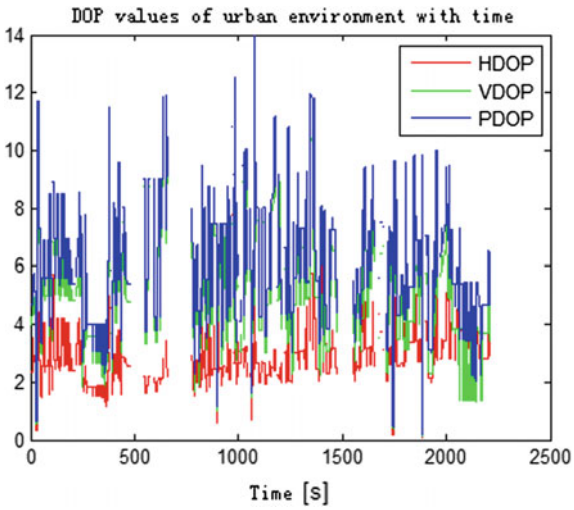

Fig. 4

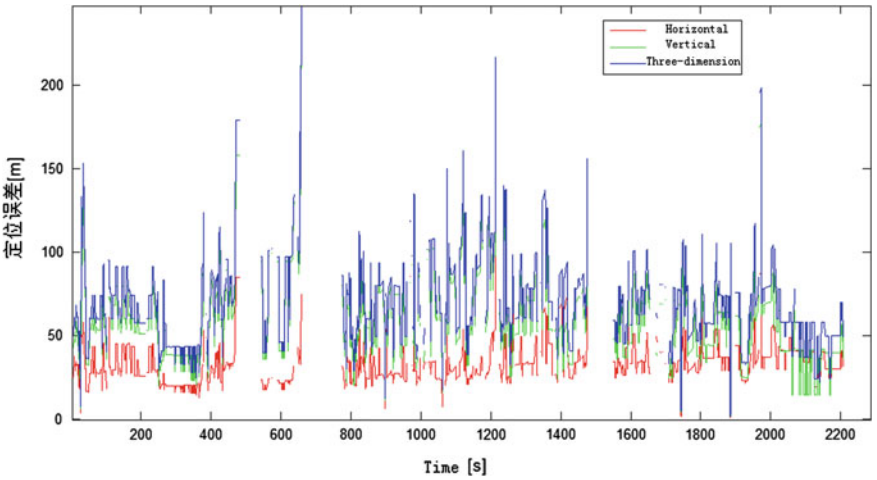

Fig. 5

Table 1 Characteristic factor and positioning accuracy values for urban environment (confidence: 95%)

Urban scene	Value
Velocity (km/h)	36
Number of visible satellites	5
PDOP	6.9
Shielding factor	56, 12, 32%
Signal intensity factor (dB Hz)	35.2
Signal fluctuation	0.78
Horizontal positioning accuracy (m)	54.75
Elevation Positioning Accuracy (m)	101.78

$$P = \begin{bmatrix} 0.7131 & 0.137 & 0.1199 \\ 0.1148 & 0.8261 & 0.0291 \\ 0.0417 & 0.0115 & 0.9468 \end{bmatrix} \quad W = \begin{bmatrix} 56\% \\ 12\% \\ 32\% \end{bmatrix} \quad \mu = \begin{bmatrix} 41.1 \\ 18 \\ 3 \end{bmatrix} \quad \Sigma = \begin{bmatrix} 1.9 \\ 21 \\ 2 \end{bmatrix}$$

4.1 Open-Space Scene

See Figs. 6, 7, 8 and Table 2.

$$P = \begin{bmatrix} 0.9714 & 0.0286 \\ 0.2179 & 0.7821 \end{bmatrix} \quad W = \begin{bmatrix} 87\% \\ 13\% \end{bmatrix} \quad \mu = \begin{bmatrix} 47.3 \\ 44.8 \end{bmatrix} \quad \Sigma = \begin{bmatrix} 0.66 \\ 2.1 \end{bmatrix}$$

Fig. 6 Route of open-space scene (highway Shanghai)

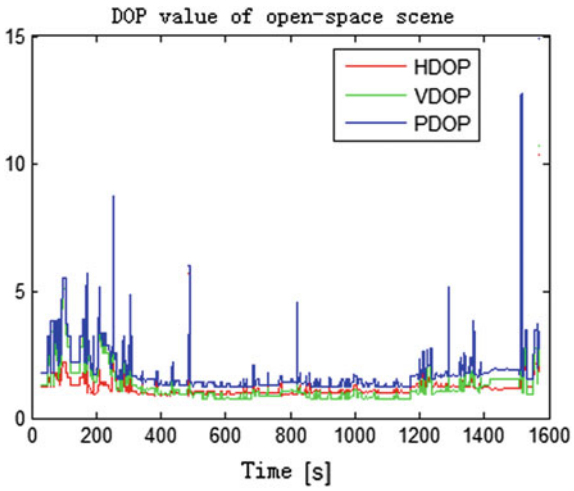

Fig. 7 DOP value of open-space scene

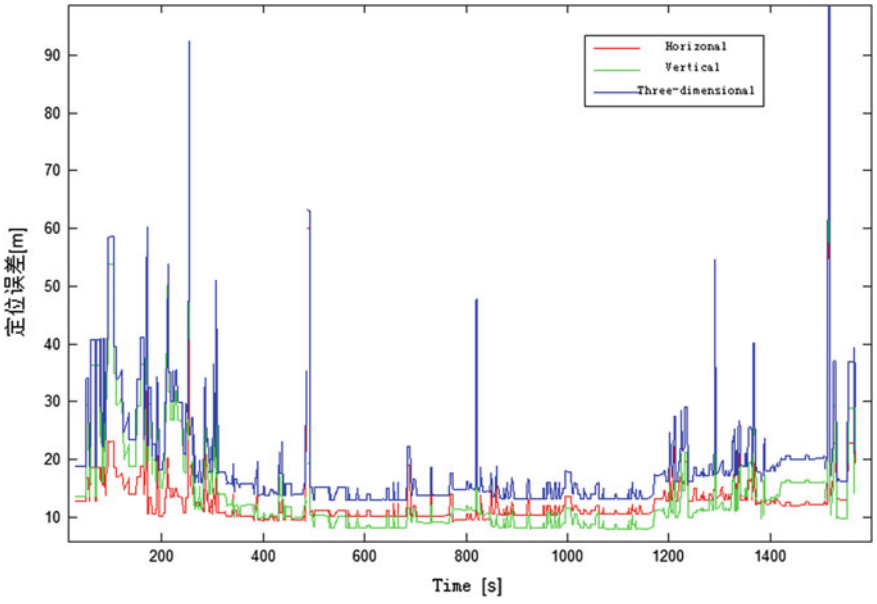

Fig. 8 Simulated positioning accuracy value of open-space scene

Table 2 Characteristic factor and positioning accuracy values for open-space environment (confidence: 95%)

Open-space	Value
Velocity (km/h)	76
Number of visible satellites	8
PDOP	1.8
Shielding factor	87, 13%
Signal intensity factor (dB Hz)	46.9
Signal fluctuation	0.95
Horizontal positioning accuracy (m)	18.50
Elevation positioning accuracy (m)	30.91

5 Conclusion

In this paper, based on the platform of the test platform, the testing scene and test index of the real mining signal are given. In this paper, six scene feature factors such as velocity factor, satellite visible number, DOP, occlusion factor, signal strength factor and signal fluctuation are defined, and the Gaussian Markov model is given, and the localization accuracy index Of the theoretical formula. At the end of this paper, the actual mining signals of two kinds of environment (urban canyon, open area) are analyzed, and the characteristics of the two typical scenes and the theoretical value of positioning precision are given. These studies provide a more complete research idea for the typical scene scenario and index definition based on the acquisition and playback test system. Other typical scenarios can be analyzed by this research method.

References

1. Fontán FP, Vázquez-Castro M, Cabado CE et al (2001) Statistical modeling of the LMS channel. IEEE Trans Veh Technol 50(6):1549–1567
2. Gang X (2009) Principles of GPS and receiver design. Publishing House of Electronics Industry, Beijing
3. Fuyuan F (2009) GPS signal simulation source test technology research and implementation. Beijing University of Post and Telecommunications, Beijing
4. Brisco C, Alonso JI (1998) Statistical and empirical models for LMSC fading based on GPS measurement. First international workshop on radiowave propagation modelling for SatCom services at Ku-Band and above, ESTEC, Noordwijk, The Netherlands, Oct 1998. http://www.estec.esa.nl/xewww/cost255/ws/98c08/98c08pgm.html
5. Akturan R, Vogel WJ (1997) Path diversity for LEO satellite-PCS in the urban environment. IEEE Trans Antennas Propag 45(7):1107–1116
6. Yao T (1992) Digital speech processing. Huazhong University of Science and Technology Press, Huazhong

7. Alasseur C, Scalise S, Husson L et al (2008) A novel approach to model the land mobile satellite channel through reversible jump Markov chain Monte Carlo technique. Wireless Commun IEEE Trans on 7(2):532–542
8. Scalise S, Ernst H, Harles G (2008) Measurement and modeling of the land mobile satellite channel at Ku-Band. IEEE Trans Veh Technol 57(2):693–703
9. Chen L, Zhu Q (2003) Random process and its applications. Higher Education Press, Beijing

Part IV
User Terminal Technology

Space-borne BDS and GPS Receiver of LING QIAO: Results over Two Years In-orbit Operation

Sihao Zhao, Xi Chen, Sen Yuan, Linling Kuang and Mingquan Lu

Abstract China's first low earth orbit (LEO) communication experimental satellite —LING QIAO satellite, jointly developed by Tsinghua University and Xinwei Group Co., Ltd., was launched on September 4th, 2014 and has been in operation in orbit for over two years. A BeiDou Navigation Satellite System (BDS) + Global Positioning System (GPS) dual-mode navigation receiver, developed by the Space Center and the Position Navigation and Timing (PNT) Center of Tsinghua University, is employed for positioning and timing for the onboard mobile communication base station payload. In this paper, the general missions of the satellite are reviewed, and then the BDS + GPS receiver design is introduced. The in-orbit operation data are collected and analyzed, based on which the numbers of the tracked navigation satellites, the position and velocity results, and the influence of the space environments on the receiver are presented. All of those will play a guiding role in the next generation space-borne global navigation satellite system (GNSS) receiver design and development.

Keywords LING QIAO satellite · Space-borne GNSS receiver · BeiDou Navigation Satellite System (BDS) · Global Positioning System (GPS) · Positioning · Timing · In-orbit data

1 Introduction

Global Navigation Satellite System (GNSS) receivers are adopted for positioning, velocity measurement and timing by modern low earth orbit (LEO) artificial satellites, among which LEO mobile communication satellites witnesses a fast development in recent years. Iridium Communications Inc. is developing

S. Zhao (✉) · M. Lu
Department of Electronic Engineering, Tsinghua University, Beijing, China
e-mail: zsh_thu@tsinghua.edu.cn

X. Chen · S. Yuan · L. Kuang
Space Center, Tsinghua University, Beijing, China

J. Sun et al. (eds.), *China Satellite Navigation Conference (CSNC) 2017 Proceedings: Volume I*, Lecture Notes in Electrical Engineering 437,
DOI 10.1007/978-981-10-4588-2_63

Iridium NEXT satellites to update its aging first-generation constellation. An augmentation of Global Positioning System (GPS) is achieved by Iridium and Boeing [1]. Cooperation between Iridium and Stanford University is being conducted to improve the integrity and broaden the service area of GPS [2]. A satellite network company—OneWeb, also announced its plan for a 648-satellite LEO communication constellation [3].

China's first LEO communication experimental satellite, named LING QIAO (International code: 2014-051A), developed by Tsinghua University and Xinwei Telecom Group was launched on September 4th, 2014. Multimedia telecommunication and experiments of other payloads onboard will be carried out in orbit [4]. Up to now, LING QIAO has been in operation in space for over two years. Unlike Iridium satellites that are equipped with a fixed mobile communication system, LING QIAO adopted a user fixed mobile communication system in which wireless communication beams get realtime adjustment to the user orientation. Such an adaptive communication system maximizes the usage of the limited wireless spectrum, however, it also highly relies on GNSS to obtain a precise space and time reference under rapid relative movement between LING QIAO and the users. The challenges therein for such GNSS receivers are achieving robust positioning and precise timing under a space vehicle movement with a speed of about 7.5 km/s at 800 km altitude.

In this work, the missions and overall design of LING QIAO satellite is firstly reviewed. The satellite navigation subsystem with BeiDou Navigation Satellite System (BDS) and GPS receivers is then introduced. The two-year in-orbit data of the space-borne BDS and GPS receivers are collected and analyzed to offer a summary of their performance. The findings and lessons from the space-borne receivers will be a guidance for future satellite-based BDS and GPS receiver design and development.

2 Brief Overview of LING QIAO Missions

The project of LING QIAO started from October, 2010. The design and development of the satellite was jointly conducted by Tsinghua University and Xinwei Group. The satellite flight model was completed in December, 2012. On September 4th, 2014, it was launched by CZ-2D rocket from Jiuquan, China. The missions of this satellite include: (1) Verification of multimedia trunking communications based on smart satellite antenna—fast beam adaptation for specific areas, mobile and trunking communication service for handheld and vehicle mounted user end, and networking applications for ground users. (2) Verification of global electromagnetic spectrum scanning. (3) Demonstration of positioning and timing ability using space-borne BDS and GPS receivers.

LING QIAO satellite has a volume of 720 mm × 660 mm × 760 mm, and a weight of about 135 kg. It operates on a sun synchronous orbit with an altitude of about 800 km above the earth surface. Figure 1 shows the appearance of the satellite and some of its components. The satellite upper side in the figure faces the earth during its flight and the bottom side in the figure points to the azimuth. On the earth side, several telecommunication antennas including mobile communication antenna, electromagnetic spectrum antenna, telemetry and track and command (TT&C) antenna are installed, while on the azimuth side, the BDS and GPS antennas are placed inside the separating ring which connects the rocket.

The payloads of the satellites function as follows.

(1) Fifteen smart point beams that can be adjusted independently can be formed by the mobile communication payload. A maximum data rate of 56 kbps that supports 7 concurrent 8 kbps full-duplex speech communications for handheld devices can be achieved within a ground area of 1200 km^2. Maximum 1 Mbps data distribution and video transfer are available for ground vehicle or airborne user devices.
(2) The spectrum scanning payload works on 2–4 GHz frequency band, covering a ground area of 2000 km^2. The receiver sensitivity is better than −95 dBm (20 MHz), the scanning frequency step is 20 MHz and the dwell time at each point is 100 ms. The scanned data can be real-time processed, stored onboard or transferred down to the ground database.
(3) The satellite navigation subsystem provides positioning, velocity measurement and timing services. The 3-dimensional position error (root mean square error—RMSE) is required to be better than 15 m, the velocity RMSE better than 1 m/s and the timing pulse RMSE better than 100 ns. All GNSS measurement data can be transferred to the ground for post processing such as precise orbit determination.

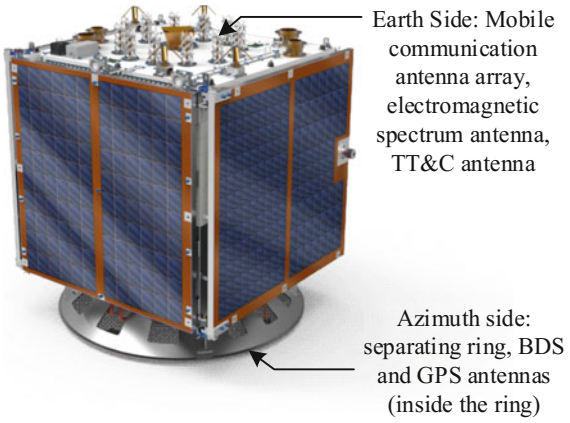

Fig. 1 Exterior of LING QIAO satellite

3 Design of the Navigation Subsystem of LING QIAO

The navigation subsystem is one of the most important subsystems onboard, which supplies accurate timing, position and velocity information for other subsystems such as the mobile communication payload. The subsystem receives GPS L1 and BDS B1 civilian signals, and outputs the satellite position, velocity, time and a precise pulse per second (1PPS). The position, velocity and universal time coordinated (UTC) information is broadcast via the satellite bus for other subsystems, and the 1PPS is transferred to the mobile communication subsystem through a multipoint low voltage differential signaling (MLVDS) bus.

The subsystem contains two GPS receivers and one BDS payload as depicted in Fig. 2. One of the GPS receivers works as the main device and the other as the backup. The BDS receiver shares antennas with the GPS receivers via two splitters. The BDS and GPS signal firstly enters a surface acoustic wave (SAW) filter to suppress the out-band electromagnetic interference. Then the signal is amplified by a low noise amplifier (LNA) and split for the GPS and BDS receivers, respectively. The BDS baseband module selects one of the two signal inputs according to the ground instruction [5].

The hardware of the LING QIAO BDS and GPS receivers are shown in Fig. 3. The GPS main and backup receivers share one printed circuit board (PCB) while the BDS receiver occupies another PCB. The three receivers are all connected to the satellite bus. The power supply converters are placed on the side of the devices for better heat control. The BDS receiver processes the B1 signal based on a field programmable gate array (FPGA) and generates the position, velocity and time information using the range measurements and the broadcast ephemeris data [6].

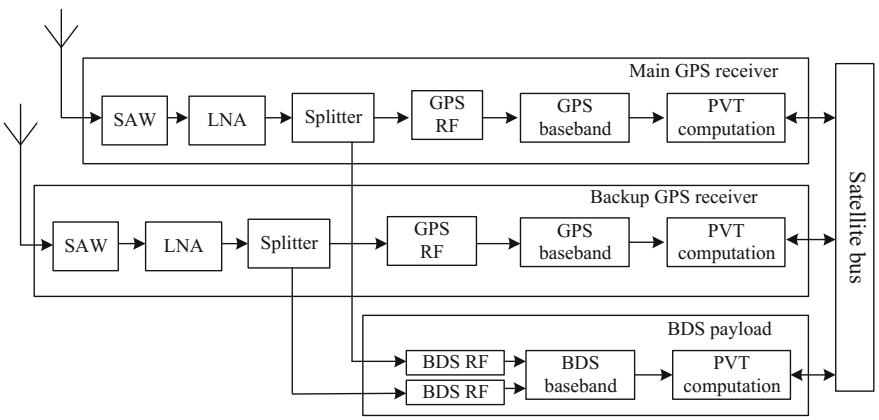

Fig. 2 GNSS navigation subsystem of LING QIAO

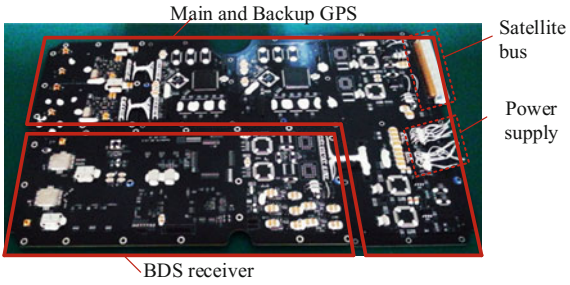

Fig. 3 Photo of the LING QIAO BDS + GPS receiver hardware

4 In-orbit Performance of the Space-borne GNSS Receivers

4.1 Number of Tracked BDS and GPS Satellites

The availability of the navigation satellites depends on the coverage of the navigation constellation. GPS covers the entire globe while BDS is still a regional system so far. The coverage of BDS over the entire earth lacks verification through real data, and we collected 48-h in-orbit data from LING QIAO which recorded the tracked number of BDS satellites as given by Fig. 4. As can be seen from the figure, the maximum number of visible BDS satellites is 9, the minimum is 1, and the average is 5.7. Furthermore, the time percentage when no fewer than 4 satellites are

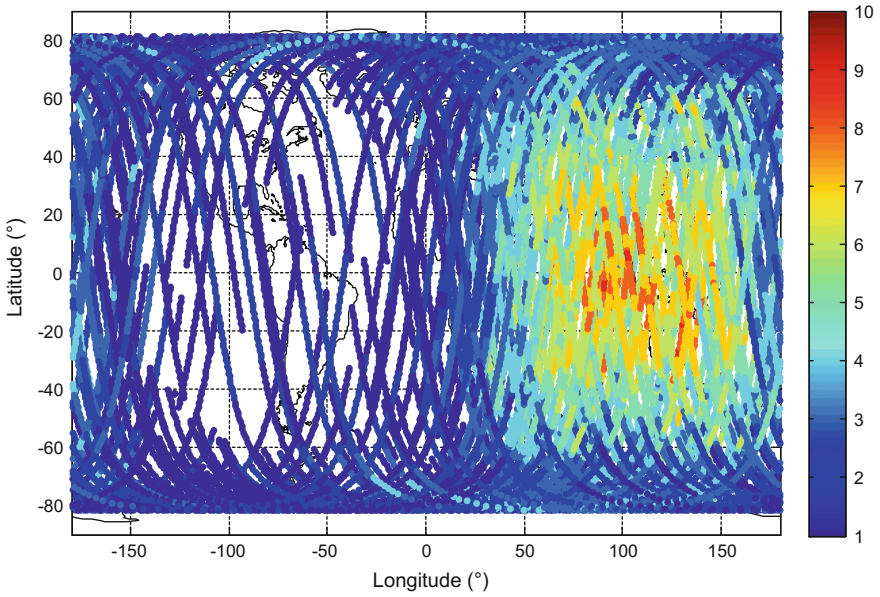

Fig. 4 BDS satellites tracked by LING QIAO BDS receiver

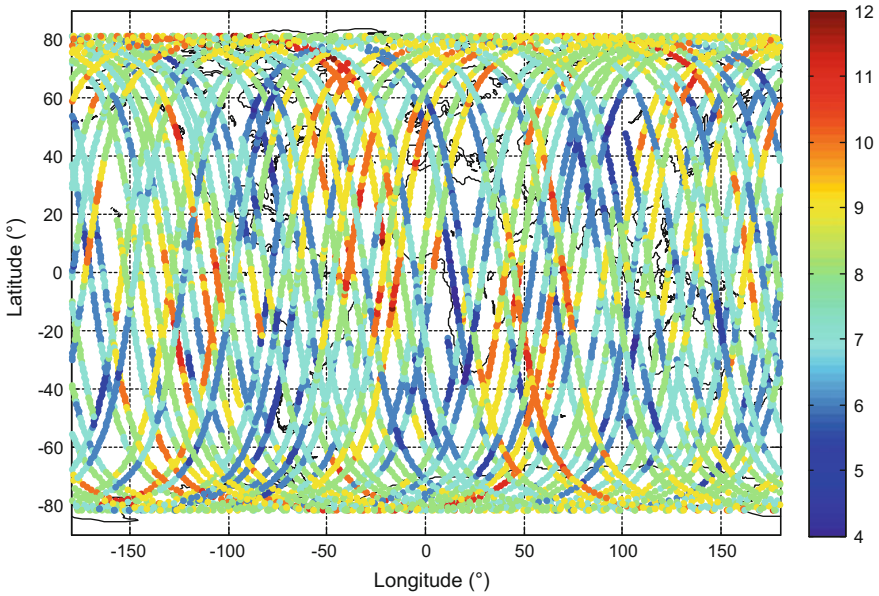

Fig. 5 GPS satellites tracked by LING QIAO GPS receiver

tracked is 94.4%. Inside the area from 55°N to 55°S and 70°E to 150°E, the tracked number of satellites is not fewer than 4, which is in accordance with the regional BDS service area announced in [7]. It is noteworthy that the actual BDS system coverage is better than this. The limited in-orbit performance is mainly caused by the design drawbacks of the BDS receiver such as the extra signal loss in SAW filter at B1 frequency and lack of a fast acquisition module which will be improved in future design. In other areas, the BDS receiver cannot track sufficient satellites to position. In order to evaluate the BDS coverage inside its service area, the number of tracked BDS satellites is recorded from UTC 09:20 to 09:50, May-6, 2015, when LING QIAO was flying over Beijing. During this period, the maximum number of tracked satellites is 9, minimum is 2, and average is 5.1.

Another 48-h GPS dataset is recorded and the number of tracked satellites over the globe is given by Fig. 5. The number of tracked GPS satellites ranges from 4 to 12 with an average of 7.6.

4.2 Comparison of Tracked Satellites on Earth and in Space

Generally, the number of tracked satellites decreases if the receiver is further away from the ground given the same view angle of the antenna and the receiver. Meanwhile, the space vehicle flies at a much higher speed than a ground user which also causes a different variation pattern of the tracked satellites. Therefore, the

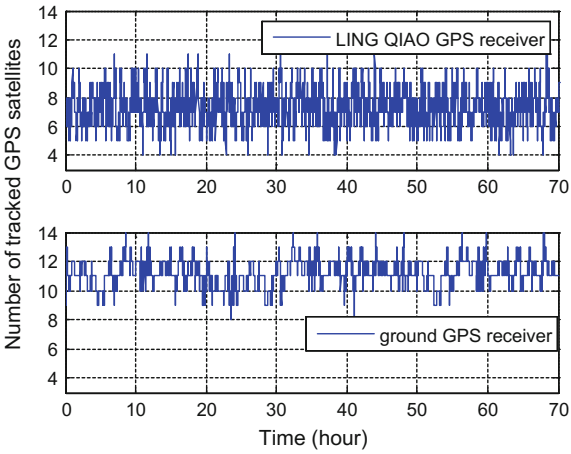

Fig. 6 Number of tracked GPS satellites by LING QIAO GPS receiver (*top*) and a ground receiver (*bottom*)

number of tracked satellites in space will largely differ from that on the ground. Figure 6 demonstrates the number of tracked GPS satellites by the LING QIAO GPS receiver in orbit and a commercial receiver on the ground during two 70-h periods. It can be observed that the average number of tracked satellites by LING QIAO is 7.5 compared with 11 for the ground receiver. Besides, the variation of the number of tracked satellites by the space-borne GPS receiver is more severe and faster than the ground receiver.

4.3 In-orbit Position and Velocity Results

BDS and GPS in-orbit data during the same period when LING QIAO flew over China are collected and analyzed. Compared with the orbit determination results from the GPS positioning solutions, the BDS position RMSE is 13 m and velocity RMSE is 20 cm/s, while the GPS position RMSE is 1 m and velocity RMSE 1.1 cm/s [5] which all satisfy the mission requirement. The BDS receiver's position and velocity results show larger error than the GPS receiver which is caused by the drawbacks in the receiver design mentioned above. Software update to optimize signal acquisition and tracking, and hardware improvement such as SAW filter replacement are necessary in the future work.

5 Space Environmental Impact on GNSS Receivers

Thermal vacuum and space radiations are among the major concerns for space receiver design. The former requires a proper working temperature for the devices and the latter should be combated with radioresistance measures and high reliability design.

5.1 Receiver Status Under Temperature Variation

The temperature inside the satellite should remain in a benign range for electronic devices through proper heat control design. The temperature data of the GPS receiver during December 1–3, 2015 are recorded and illustrated in Fig. 7. The daily average temperature is 24.09, 24.14 and 24.26 °C, respectively. The temperature fluctuation period is approximately 5400 s which matches the orbit period. The sunlight condition causes the variation of temperature, i.e., the temperature drops when the satellite is under the earth shadow and rises under sunlight.

The daily average temperature over one year is shown in Fig. 8. The highest reaches 26 °C and the lowest falls to 14 °C. The temperature curve jumped at the end of March, 2016, which was caused by a single event upset (SEU) as described in next sub-section and resulted in an increase in electric current. Overall, the heat control design works effectively and guarantees a proper temperature for GNSS receivers.

5.2 Influence from Space Radiations

Space radiations mainly include total dose effects and single event effects (SEE). The total dose effects have marginal influence on the age of LEO satellites, so SEE is the major concern in the design phase. Typical SEEs contains SEU, single event latchup (SEL) and single event functional interruption (SEFI) which may cause malfunctions or even damage to the receivers. The LING QIAO GPS receiver is implemented on application-specific integrated circuit (ASIC) while the BDS receiver is based on the configurable logic blocks of a static random access memory (SRAM) FPGA which is more vulnerable to space radiations.

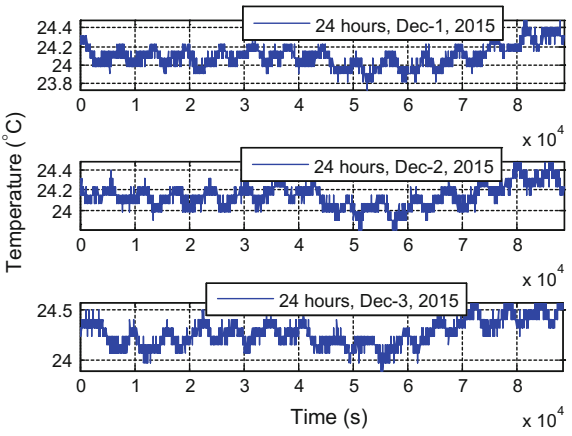

Fig. 7 Daily temperature variation curve

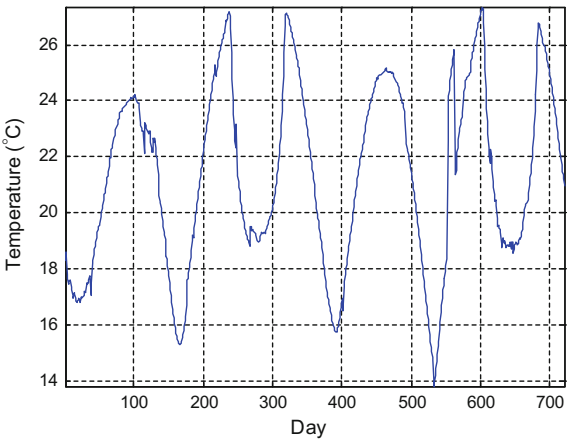

Fig. 8 Yearly temperature variation curve

The BDS and GPS receivers underwent three SEEs during the two-year in-orbit operation as listed below.

(1) On UTC 17:04:25, January-28, 2015, at the spot of (−9.87°S, −41.94°E) over the South Atlantic Ocean, the current rose from 0.32 to 1.21 A. The BDS receiver automatically powered off due to the overrun of the power management module. It is considered to be a SEL because the 3.3 V circuit was observed to experience a current surge beyond its limitation.
(2) On UTC 21:42:10, May-19, 2015, at (−49.86°S, −12.03°E) over South America, GPS broadcast stopped, and the number of tracked satellites dropped to zero. It lasted 1 h 2 min and was confirmed to be an automatic reset caused by SEU.
(3) On UTC March-22, 2016, the controller area network (CAN) interface of the GPS receiver failed and the 5.5 V current increased by 0.35 A. The GPS receiver was manually restarted on March-28 and the system recovered. It was confirmed that the 5 V circuit of the micro-controller for CAN interface suffered from a SEL.

In order to combat these SEEs, some protections were implemented during the design phase as follows. These measures are proved to be necessary and effective over the two-year flight.

(1) Automatic overcurrent shutdown is implemented to prevent any detrimental damage caused by SEE.
(2) Watchdogs and important variables in software are also protected by triple modular redundancy (TMR).
(3) Basic working states such as position results are monitored by software. When an unrecoverable exception occurs, the software automatically restarts the whole system.
(4) Warm functional backup of the satellite bus interfaces is implemented.

6 Conclusion and Future Work

The main tasks of LING QIAO communication experimental satellite are reviewed. Its overall design especially the GNSS subsystem design is introduced. In-orbit data from the LING QIAO BDS and GPS receivers over the two-year flight are collected and analyzed. The working status of the receivers including the numbers of tracked BDS and GPS satellites, the position and velocity solutions and the impact of the satellite temperature and space radiations is summarized.

In the future, based on the experiment data and lessons learned from the two-year flight of LING QIAO, the space-borne GNSS receivers will be modified and improved to enhance their performance.

Acknowledgements This work is funded by Natural Science Foundation of China (No. 61671264).

References

1. Jewell D (2016) Iridium and GPS revisited: a new PNT solution on the horizon? GPS World. Available: http://gpsworld.com/iridium-and-gps-revisited-a-new-pnt-solution-on-the-horizon/
2. Gao GX, Heng L, Walter T et al (2011) Breaking the ice—navigation in the Arctic. In: InsideGNSS, pp 60–64
3. Foust J (2015) The return of the satellite constellations. Available: http://www.thespacereview.com/article/2716/1
4. Jin J, Kuang L, Yan J et al (2015) Smart communication satellite (SCS)-an application oriented micro-satellite for communication. In: Proceedings of AIAA Space and Astronaut Forum and Exposition(SPACE), 2015, pp SSC15-V-2
5. Chen X, Zhao S, Wang M et al (2015) Space-borne BDS receiver for LING QIAO satellite: design, implementation and preliminary in-orbit experiment results. GPS Solutions
6. Wang J, Chen X, Huang Z et al (2016) Performance analysis on delay-multiply acquisition for space-borne GNSS receivers. In: Proceedings of IEEE 83rd vehicular technical conference (VTC Spring), Nanjing, China, pp 1–5
7. BeiDou Navigation Satellite System Open Service Performance Standard, China Satellite Navigation Office (2013)

Modeling and Simulation of Receiver-Spoofer Attacking Process in Tracking Stage

Meng Zhou, Hong Li, Peng Liu and Mingquan Lu

Abstract Since the Global Navigation Satellite System (GNSS) has been constructed and normally operated, it has been widely applied in aviation, aerospace, navigation, power grid monitoring and communication. However, two factors determine its inherent vulnerability: (1) the navigation signal is prone to be jammed due to the very weak signal strength; (2) The fake signal could be easily generated because the navigation system Interface Control Documents (ICD) is open for the world. Therefore, GNSS receiver is often to be an important spoofing and jamming target for malicious attacks. Hence, when the receivers are once attacked, it can cause huge economic losses; moreover, it could also lead to serious safety problems for users. For the attacking of the receiver-spoofer in tracking stage (receiver-spoofer for short), it can take control of the target virtually without causing the target receiver unlocked, so it could make great hazards and destruction because of the high concealment. To analysis the technique of the receiver-spoofer, it discusses the principle when the attack takes over the control of receiver code loop in tracking stage in this paper. In order to model the spoofing process, the formulas of the key parameters in spoofing process were deduced and the simulation was achieved. Ultimately, the results, using a software receiver, verify the correctness of the simulation algorithm. Using the result in this paper, it cannot only provide a theoretical guide for the subsequent receiver-spoofer attack, but it can also provide a reference for the anti-attacking technique against the receiver-spoofer.

Keywords Receiver-Spoofer · Spoofing signal ratio · Modeling · Simulation

M. Zhou (✉) · H. Li · P. Liu · M. Lu
Department of Electronic Engineering, Tsinghua University,
Beijing 100084, China
e-mail: Maggice-sun@163.com

J. Sun et al. (eds.), *China Satellite Navigation Conference (CSNC) 2017 Proceedings: Volume I*, Lecture Notes in Electrical Engineering 437,
DOI 10.1007/978-981-10-4588-2_64

1 Introduction

1.1 Vulnerability of GNSS

The GPS system of US is the first global satellite navigation system (GNSS), which can provide real-time, all-weather, continuous, global coverage of positioning, navigation, time service. Thereafter, Russia's GLONASS system and EU's GALILEO system, as well as China's CAMPASS system join the GNSS community, which greatly improved the completeness, positioning and timing accuracy of GNSS system, more and more applications to aerospace, aviation, mobile communications, power grid monitoring and other civilian infrastructures. However, GNSS signal power is very weak, usually below −160 dBW, and most of the signal interface format is open and transparent, which makes some hostile individuals and organizations easy to attack GNSS system, so GNSS user cannot receive the correct navigation messages or only receive the wrong navigation information. This can cause deviation from the correct navigation route, or produce the wrong time synchronization results, resulting in huge economic losses, and even a threat to personal safety [1, 2].

There are usually two kinds of GNSS attacks, one is called interference, generally by sending high-power RF signal to suppress the real navigation signal, making the receiver does not work; the other called spoofing, which by transmitting a fake signal similar to the real navigation signal, the receiver to receive the wrong navigation information, thus affecting or even control the positioning and timing results. In comparison, the spoofing is more difficult to be detected, and can be used to targeted attacks, so at present it becomes the focus of GNSS attack research.

1.2 Receiver-Spoofer

Receiver-Spoofer is very difficult to be found, as shown in Fig. 1, it is generally composed of a navigation signal receiving device, a spoofing signal generating device and a spoofing signal transmitting device. At first the Receiver-Spoofer collects the GNSS navigation signal to calculates the carrier frequency, carrier phase, code frequency, code phase and navigation message, etc. Then, based on the information and its relative position with the target receiver, a counterfeit navigation signal is generated. When this generated navigation signal reaches the target, its carrier frequency, carrier phase, code frequency, code phase, navigation message and other information will be as same as the actual navigation signal, which makes it possible to not interrupt the target receiver on the navigation signal tracking, and secretly into the receiver code loop, to change the phase identification results, and ultimately capture the control of the target receiver [3].

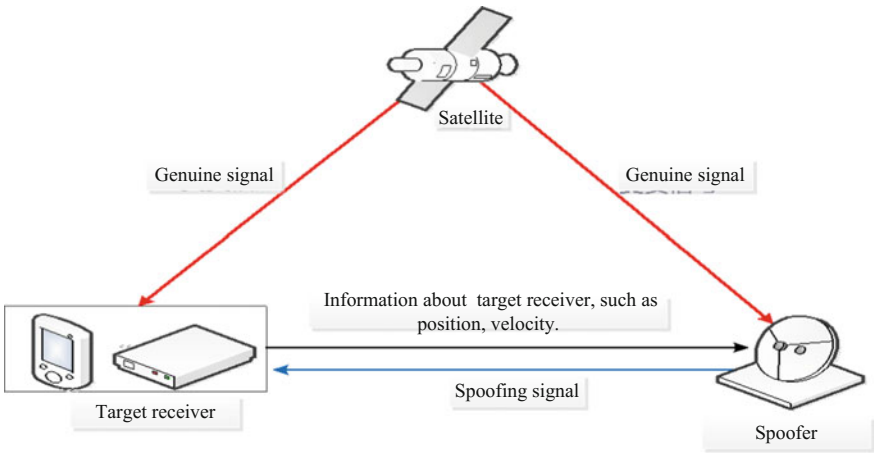

Fig. 1 Principle of receiver-spoofer

In 2008, T.E. Humphreys et al., in the University of Texas, pioneered the implementation of the receiver-spoofer platform in a laboratory environment, as shown in Fig. 3 [4]. Using the platform, they tested four commercial receivers, such as ordinary commercial receiver, power grid monitoring timing receiver, mobile base station timing receiver and marine GPS receiver, and the results showed that the typical commercial receivers do not have the ability to detect the spoof [5, 6]. These objects lost the control of the code loop and locked in the spoofing signal in the condition of without giving any alarm signal. The principle of receiver-spoofer to take the control of code loop is shown in Fig. 2.

When the fake signal enter the code loop, it can influence the output of the advance and delay correlator, so it can change the code phase in the local receiver and the fake signal is locked. In this paper, it analyzes in detail the process of capturing the loop control by spoofing signal, and study its mechanism, moreover, to determine which parameters will influence the process, and provide the advice for anti-spoofing technology.

2 Analysis of Spoofing Process

2.1 Model of Spoofing Signal

The structure of spoofing signal and genuine signal is same, so the received signal by receiver can be expressed as follows:

$$S(t) = \sqrt{2P}(x(t)D(t))\sin(2\pi ft + \theta) \tag{1}$$

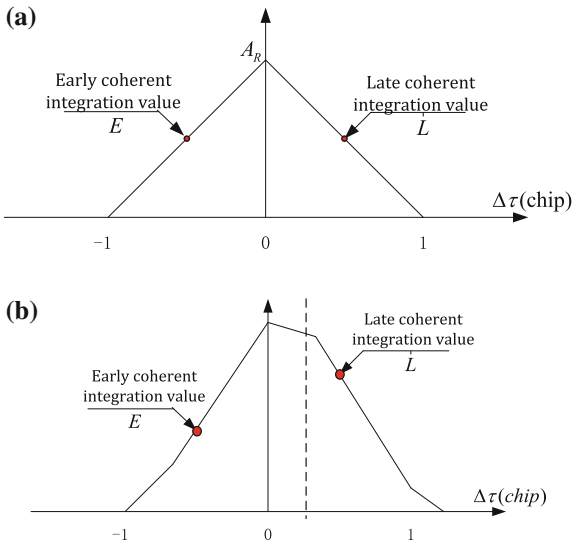

Fig. 2 **a** Correlator output before the fake signal enters the code loop. **b** Correlator output after the fake signal out of the code loop

where

P Average power of signal;
$x(t)$ Level of PN code generated by satellite;
$D(t)$ Level of data generated by satellite;
f Carrier frequency of spoofing signal;
θ Carrier phase of spoofing signal

Receiver-spoofer can get the navigation message via receiving the genuine navigation signal, and the frequency of this message is much lower than that of PN code, so it can be considered in the process of spoofing that the data $D(t)$ is always aligned with the genuine signal. In this paper, the focus will be put on the effect of other four parameters, that are P, $x(t)$, f, and θ.

2.2 *Modeling of Spoofing Process*

When receiver processes the navigation signal, a sinusoidal carrier signal with coincident phase and frequency with received carrier will be generated in carrier loop, and a local code with coincident phase and frequency with received code will generated in code loop. The key to the local code alignment with the navigation signal is the phase detector and the Numerically Controlled Oscillator (NCO). The phase detector calculates the phase difference between the local code and the navigation signal, and then adjusts the frequency of the local code through the NCO to make the two coincide.

According to the introduction in Sect. 1.2, we know that the spoofing signal will slowly align the genuine signal, and then gradually deviate from it when the spoofing occurs. According to the tracking principle of code and carrier loop [7], it is known that when the spoofing signal enters the tracking range of the discriminator, the value of the integrator will be changed to break the balance of discriminator, so as to readjust the NCO, and the early correlation value of the local code is again equal to the late value. Taking the code loop as an example to illustrate this process, the discriminator of the code loop uses the triangular symmetry of the PN code autocorrelation function to achieve the phase alignment of the local code and the received code. It will calculate the advance correlation value and the late correlation value of the local code and the received signal, if the two values are equal, then alignment is reached between the local code and received code. The commonly used calculation formula of discriminator is shown in Eq. (2).

$$\delta_{cp} = (1 - d)\frac{E - L}{E + L} \tag{2}$$

where

δ_{cp} is the output of discriminator
d is the correlator spacing, i.e. the chips of early or late of early minus late discriminator
E, L is the correlation output of early and late integrator respectively.

Consider that from change of spoofing signal's phase to adjust of discriminator, then to the balance again of discriminator as a cycle, thus at the end of each cycle, Eq. (3) is hold.

$$\begin{cases} E(n) - L(n) = 0 \\ \tau_S(n) + \tau_R(n) = \Delta t(n) \end{cases} \tag{3}$$

Here, $E(n)$, $L(n)$ is the output of early and late correlation integrator after nth cycles finished, respectively.

$\tau_S(n)$, $\tau_R(n)$ is the phase difference between spoofing or genuine code with local code after nth cycles finished, respectively.

$\Delta t(n)$ is the phase difference between spoofing and genuine signal in nth cycles, which changes at the beginning of each cycle, but as constant during each cycle, until the next cycle begin.

According Eq. (3), due to the change of $\Delta t(n)$, the value of $\tau_S(n)$ and $\tau_R(n)$ is different at the end of each cycle completion. Once one of them exceeds the tracking range ($1 + d$ chips) of the discriminator, it no longer affects the calculation of the local code phase, and the control is entirely on the other side. The whole process is shown in Fig. 3.

Assume that the receiver is in a stable tracking of the genuine signal while the spoofing occurs, now, the replica of code is aligned with received code, $\tau_R(0) = 0$,

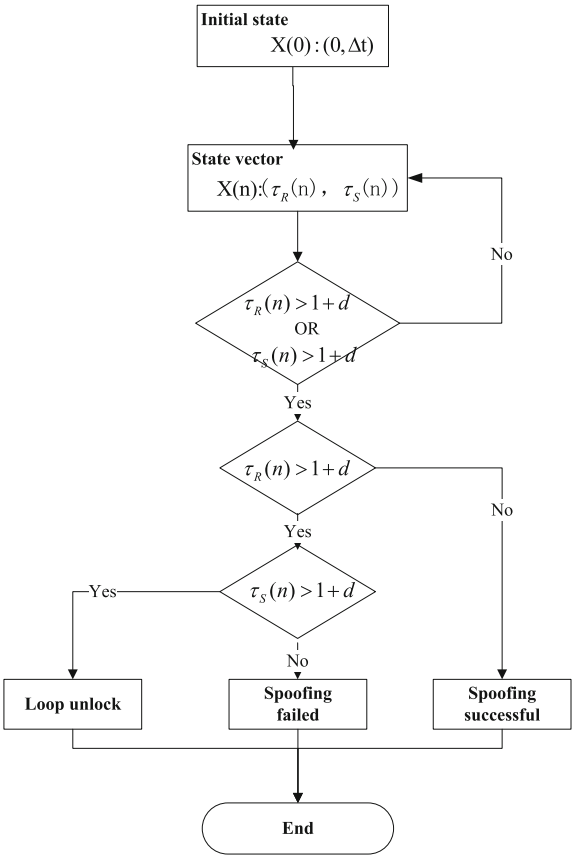

Fig. 3 The flow chart of spoofing process

$\tau_S(0) = \Delta t(0)$. When the spoofing signal enters the traction range of discriminator, the output is changed by the influence of the spoofing signal. The phase of the local code is also changed. The value of $\tau_R(\mathrm{n})$, $\tau_S(\mathrm{n})$ is updated until one of them exceeds the traction range of the discriminator. If $\tau_R(\mathrm{n})$ exceeded, the loop is captured by spoofing signal, however, if $\tau_S(\mathrm{n})$ exceeded, the loop is still controlled by the genuine signal, if both exceeded, then the loop lost lock. If loop noise is not taken into account, this iterative process will be definite, each group parameters will correspond to a definite final state; on the contrary, it is a stochastic process, the final state is the probability combinations of three cases.

2.3 *Calculation of Vector* $(\tau_S(n), \tau_R(n))$

In terms of the analysis of Sect. 2.2, we can find that the value of vector $(\tau_S(n), \tau_R(n))$ plays a decisive role in the process of spoofing. From Eq. (3), if the

value of E, L is known, then the value of $(\tau_S(n), \tau_R(n))$ can be obtained. In Ref. [8], the formula is given as Eq. (4)

$$S_K = A \cdot R(\tau_K)|\sin c(f_e T_{coh})|, \quad K = E, L \tag{4}$$

where

A is the correlation amplitude
$R(\tau_K)$ is the normalized autocorrelation function
f_e is the frequency difference between received signal and local code
T_{coh} is the period of correlation integrate

When genuine and spoofing signal are received at the same time, E, L can be calculated from Eq. (5)

$$\begin{aligned} S_K &= \sqrt{(I_K + I'_K)^2 + (Q_K + Q'_K)^2} \\ &= \sqrt{\begin{array}{c}(A \cdot R(\tau_K)|\sin c(f_e T_{coh})|)^2 + \left(\eta A \cdot R(\tau'_K)\left|\sin c(f'_e T_{coh})\right|\right)^2 \\ + 2\eta A^2 R(\tau_K) R(\tau'_K)|\sin c(f_e T_{coh})|\left|\sin c(f'_e T_{coh})\right| \cos(\phi - \phi')\end{array}} \\ K &= E, L \end{aligned} \tag{5}$$

where

η is the ratio of amplitude of spoofing signal and genuine signal, i.e. spoofing-to-signal ratio (SSR)
$\phi - \phi'$ is the difference of carrier phase between spoofing and genuine signal

For simplicity, given the carrier phase of spoofing and genuine signal are aligned, that is, $f_e = f'_e = 0$ and $\phi - \phi' = 0$, Eq. (5) becomes

$$\begin{aligned} E &= E_R + E_S \\ L &= L_R + L_S \end{aligned} \tag{6}$$

2.3.1 Discriminator Spacing Less or Equal than 0.5 Chips

When the discriminator spacing is less or equal than $d \leq 0.5$ chips, for each signal in the range of discriminator, in terms of Eq. (6) and the correlation function R of PN code, the value of E_R, E_S, L_R and L_S can be obtained according to Eq. (7)

$$\begin{cases} E(\tau) = 0, & L(\tau) = A(1 + d + \tau), & -1 - d \leq \tau < -d \\ E(\tau) = A(1 + d - \tau), & L(\tau) = 0, & d \leq \tau < d + 1 \\ E(\tau) = A(1 - d + \tau), & L(\tau) = A(1 - d - \tau), & -d \leq \tau \leq d \\ E(\tau) = 0, & L(\tau) = 0, & \text{other} \end{cases} \tag{7}$$

So, there are nine states according to the different value of $\tau_R(n-1)$, $\tau_S(n-1)$ and the formula for calculating $(\tau_S(n), \tau_R(n))$ in different cases are as follows:

- State 1

$$\begin{aligned} \tau_R(n) &= \frac{2\eta t(n) - (1+d)}{2\eta - 1} \\ \tau_S(n) &= \frac{(1+d) - t(n)}{2\eta - 1} \end{aligned} \tag{8}$$

- State 2

$$\begin{aligned} \tau_R(n) &= \frac{\eta t(n) - d}{\eta} \\ \tau_S(n) &= \frac{d}{\eta} \end{aligned} \tag{9}$$

- State 3

$$\begin{aligned} \tau_R(n) &= \frac{\eta t(n)}{\eta + 1} \\ \tau_S(n) &= \frac{t(n)}{\eta + 1} \end{aligned} \tag{10}$$

- State 4

$$\begin{aligned} \tau_R(n) &= 1 + d - 2d\eta \\ \tau_S(n) &= t(n) - (1 + d - 2d\eta) \end{aligned} \tag{11}$$

- State 5

$$\begin{aligned} \tau_R(n) &= 0 \\ \tau_S(n) &= t(n) \end{aligned} \tag{12}$$

- State 6

$$\begin{aligned} \tau_R(n) &= d\eta \\ \tau_S(n) &= t(n) - d\eta \end{aligned} \tag{13}$$

- State 7

$$\begin{aligned}\tau_R(n) &= \frac{\eta t(n) - (1+d)(\eta-1)}{\eta+1} \\ \tau_S(n) &= \frac{t(n) + (1+d)(\eta-1)}{\eta+1}\end{aligned} \tag{14}$$

- State 8

$$\begin{aligned}\tau_R(n) &= \frac{2d - \eta(1+d) + \eta t(n)}{\eta} \\ \tau_S(n) &= \frac{2d - \eta(1+d)}{\eta}\end{aligned} \tag{15}$$

- State 9

$$\begin{aligned}\tau_R(n) &= \frac{\eta(1+d-t(n))}{2-\eta} \\ \tau_S(n) &= \frac{2t(n) - \eta(1+d)}{2-\eta}\end{aligned} \tag{16}$$

2.3.2 Discriminator Spacing Larger than 0.5 Chips

When the discriminator spacing is $d > 0.5$ chips, the output of early correlator E and late correlator L can be get from following formula (17)

$$\begin{cases} E_s = 0, & L_s = A_s(1+d+\tau), & -1-d \le \tau < -d \\ E_s = 0, & L_s = A_s(1-d-\tau), & -d \le \tau < d-1 \\ E_s = A_s(1-d+\tau), & L_s = A_s(1-d-\tau), & d-1 \le \tau \le 1-d \\ E_s = A_s(1-d+\tau), & L_s = 0, & 1-d < \tau \le d \\ E_s = A_s(1+d-\tau), & L_s = 0, & d < \tau \le 1+d \\ E_s = 0, & L_s = 0, & \text{other} \end{cases} \tag{17}$$

In terms of Eq. (17), there are 9 states for different $\tau_R(n-1)$ and $\tau_S(n-1)$, the $\tau_R(n)$, $\tau_S(n)$ are calculated for these 9 states as follows:

(1) State 1

$$\begin{aligned}\tau_R(n) &= \frac{2\eta t(n) - (1+d)}{2\eta - 1} \\ \tau_S(n) &= \frac{(1+d) - t(n)}{2\eta - 1}\end{aligned} \tag{18}$$

(2) State 2

$$\begin{aligned}\tau_R(n) &= \frac{2\eta t(n) + d - 1}{2\eta + 1} \\ \tau_S(n) &= \frac{t(n) - d + 1}{2\eta + 1}\end{aligned} \tag{19}$$

(3) State 3

$$\begin{aligned}\tau_R(n) &= \frac{\eta t(n)}{\eta + 1} \\ \tau_S(n) &= \frac{t(n)}{\eta + 1}\end{aligned} \tag{20}$$

(4) State 4

$$\begin{aligned}\tau_R(n) &= \frac{\eta t(n) + \eta(1-d) - (1+d)}{\eta - 1} \\ \tau_S(n) &= \frac{-\eta(1-d) + (1+d) - t(n)}{\eta - 1}\end{aligned} \tag{21}$$

(5) State 5

$$\begin{aligned}\tau_R(n) &= \frac{\eta t(n) + \eta(1-d) - (1-d)}{\eta + 1} \\ \tau_S(n) &= \frac{-\eta(1-d) + (1-d) + t(n)}{\eta + 1}\end{aligned} \tag{22}$$

(6) State 6

$$\begin{aligned}\tau_R(n) &= \frac{\eta(1-d) + \eta t(n)}{2 + \eta} \\ \tau_S(n) &= \frac{2t(n) - \eta(1-d)}{2 + \eta}\end{aligned} \tag{23}$$

(7) State 7

$$\begin{aligned}\tau_R(n) &= \frac{\eta t(n) + (1+d)(1-\eta)}{\eta+1} \\ \tau_S(n) &= \frac{t(n) - (1+d)(1-\eta)}{\eta+1}\end{aligned} \tag{24}$$

(8) State 8

$$\begin{aligned}\tau_R(n) &= \frac{(1-d) - \eta(1+d) + \eta t(n)}{\eta-1} \\ \tau_S(n) &= \frac{-(1-d) + \eta(1+d) - t(n)}{\eta-1}\end{aligned} \tag{25}$$

(9) State 9

$$\begin{aligned}\tau_R(n) &= \frac{\eta(1+d-t(n))}{2-\eta} \\ \tau_S(n) &= \frac{2t(n) - \eta(1+d)}{2-\eta}\end{aligned} \tag{26}$$

When correlator spacing $d < 0.5$ chips, there have similar results.

2.4 Simulation of Spoofing Process

Based on the analysis and derivation of Sect. 2, and assuming that the phase of the spoofing signal changes uniformly, we can realize a complete simulation of spoofing attack process as follows.

Simulation input: spoofing-to-signal ratio η, genuine and spoofing signal phase difference $t(0)$, spoofing signal movement rate v, discriminator spacing d.

Simulation output: phase difference between genuine signal and local code $\tau_R(\mathrm{n})$; phase difference between spoofing signal and local code $\tau_S(\mathrm{n})$.

Spoofing results (success, failure, or loss of lock).

Simulation steps:

(1) Let the initial value of the vector $(\tau_S(n), \tau_R(n))$ is $(0, t(0))$, $n = 0$;
(2) In terms of d to select the corresponding update calculation formula of $(\tau_S(n), \tau_R(n))$, $n = n + 1$, calculate $(\tau_S(n), \tau_R(n))$, $t(n)$;
(3) Decide $\tau_S(n)$ or $\tau_R(n)$ whether or not greater than $1 + d$, if yes, then go to Step 4, else, go to Step 2 again;
(4) If the value $\tau_S(n)$ is greater than $1 + d$, the result of the spoofing is set to as failure. If $\tau_R(n)$ is greater than $1 + d$, the result of the spoofing is set to as

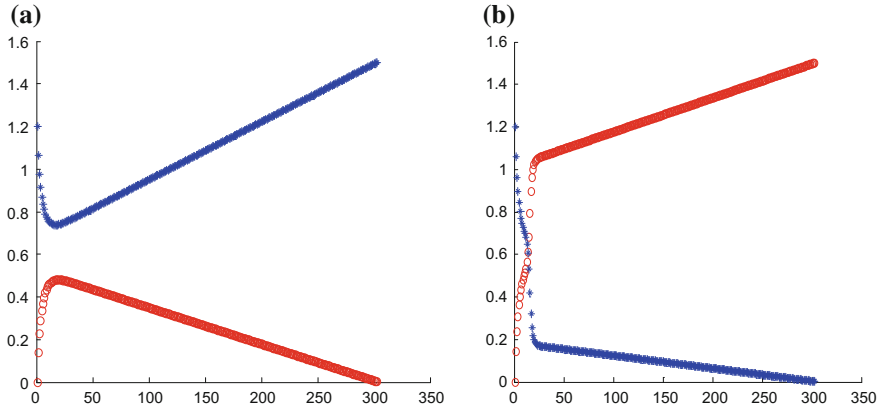

Fig. 4 Simulation results of spoofing process

success. If the value of $\tau_S(n)$ and $\tau_R(n)$ are all greater than $1+d$, the result of the spoofing is set to as unlock. The simulation ends.

The above simulation algorithm is realized by using matlab. Figure 4 shows the results of $(\tau_S(n), \tau_R(n))$ when different value of η, $t(0)$, v are input into the simulation program.

The red circle in Fig. 4 represents the change trajectory of $\tau_R(n)$, and the blue circle represents the change trajectory of $\tau_S(n)$. In Fig. 4a, the simulation ends in the condition $\tau_S(n) > 1+d$, which means the spoofing is failed. In Fig. 4b, the simulation ends in the condition $\tau_R(n) > 1+d$, which means the spoofing is successful.

3 Experiment and Verification

Using GPS signal simulator to generate two signals A and B, where A as genuine signal, B as spoofing signal, the amplitude ratio of B and A acts as SSR η, A and B have same carrier frequency and phase, the code phase difference of these two signal is $t(0)$, The PN code of the signal B approaches signal A with the velocity v and then moves away. We sample the two signals at a rate of 60 MHz, and stores the data. Matlab software receiver reads the samples of these two signals, and records the phase difference $(\tau_S(n), \tau_R(n))$ between local code and these two signal's PN code in whole process, and compared with the simulation results. Change η, $t(0)$ and v, repeat the experiment. The comparison results are shown in Fig. 5. Since the moving rate of spoofing signal does not affect the simulation result of error comparison, there is no consideration of the moving rate v in the experiment.

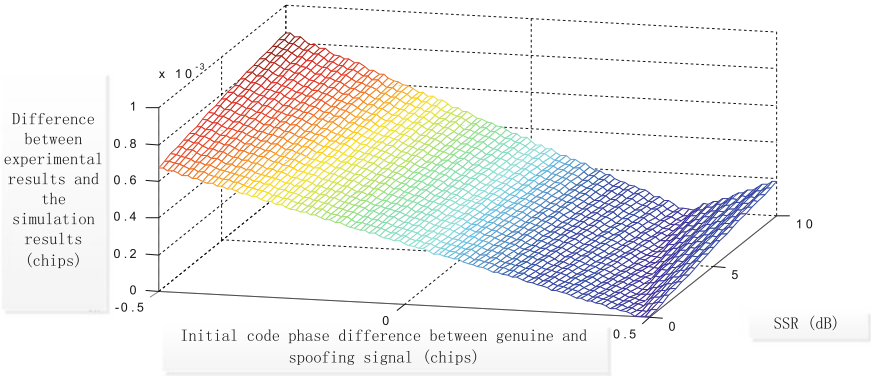

Fig. 5 The comparison of experimental results and simulation results

The calculation error of $\tau_R(n)$ is shown in Fig. 5, we can find that the results calculated by software receiver are very close to that of simulation, thus the correctness of previous spoofing process analysis and simulation program is verified.

4 Conclusions

In this paper, the spoofing signal and spoofing process are modeled in terms of the analysis of receiver-spoofer technology, and the formula for calculating $(\tau_S(n), \tau_R(n))$ that is the key parameter vector during spoofing process is obtained, and simulation of spoofing process is realized using Matlab software. Finally, a series of experiments proved the validity of the process model and the simulation program. In future, we will further consider the influence of noise on the spoofing process, and add this factor into the simulation process. These analyzes can provide the theoretical guidance and research platform for future research of GNSS spoofing and anti-spoofing technology.

Acknowledgements This work was supported by the National Natural Science Foundation of China (Grant No. 61571255).

References

1. Vulnerability assessment of the transportation infrastructure relying on the Global Positioning System (2001). Technical report, John A. Volpe National Transportation Systems Center
2. Warner JS, Johnston RG (2002) A simple demonstration that the global positioning system (GPS) is vulnerable to spoofing. J Secur Adm 25:19–27

3. Humphreys TE, Ledvina BM, Psiaki ML, Hanlon BWO, Kintner Jr PM (2008) Assessing the spoofing threat: development of a portable GPS civilian spoofer. In: Proceedings of the ION GNSS international technical meeting of the satellite division, p. 56
4. Humphreys T, Kintner P, Psiaki Jr M, Ledvina B, O'Hanlon B (2009) Assessing the spoofing threat. GPS world, Jan 2009
5. Humphreys TE, Ledvina BM, Psiaki ML, Hanlon BWO, Kintner PM (2008) Assessing the spoofing threat: development of a portable GPS civilian spoofer. In: Institute of Navigation GNSS (ION GNSS 2008), Savanna, GA, Sept 2008, pp 16-19
6. Shepard D, Humphreys T (2011) Characterization of receiver response to a spoofing attack. In: Proceedings of ION GNSS 2011, Portland, OR, Sept 2011
7. Kaplan E (2006) Understanding GPS: principles and applications, Second Edition, Artech House, Inc.
8. Zarlink Semiconductor (1999) GPS2000: GPS Receiver Hardware Design, Application Note 855, Issue 2.0, October 1999

Low Power Consumption Control Method for Navigation Receiver with Multi-stage Bandwidth

Daowei Chen, Hong Lei Lin and De-hui Xu

Abstract With the rapid development of global satellite navigation technology and the progress of the mass consumer level user terminal equipment has been a large-scale popularization and application of energy limited mobile terminal equipment to reduce power consumption is of great significance. In order to achieve the goal of reducing the power consumption of the receiver, the receiver can quickly and stably track the convergence and reduce the convergence time by adjusting the bandwidth of the control loop. By analyzing the simulation results, the design of multilevel bandwidth adjustment can effectively reduce the convergence time and significantly reduce the power consumption of the receiver.

Keywords Navigation receiver · Power control · Multi level bandwidth

1 Introduction

The continuous construction and development of the global satellite navigation system has greatly promoted the application and popularization of the satellite navigation and positioning technology in the social production and life, especially the terminal products represented by the satellite navigation receivers and their embedded positioning devices. In the smart phones, Watches, tablet PCs, car navigation, trackers and other mass consumer electronics has been widely used. To prolong the time for the electronic equipment is always one of the goals of the engineer, and reduce the power consumption of the navigation module is the key to achieving this trend [1]. Although the battery technology continues to progress, but its capacity growth is very limited, the capacity of the battery in recent years, only

D. Chen (✉) · D. Xu
College of National Defense Information Science, Wuhan 430010, China
e-mail: daoweic@qq.com

H.L. Lin
College of Electronic Science and Engineering, National University of Defense Technology, Changsha 410073, China

J. Sun et al. (eds.), *China Satellite Navigation Conference (CSNC) 2017 Proceedings: Volume I*, Lecture Notes in Electrical Engineering 437,
DOI 10.1007/978-981-10-4588-2_65

increased 2–4 times [2], but this is far cannot meet the demand, the lower the power consumption of the navigation receiver to extend the carrier of the working time, improve the availability of equipment, it is of great significance for the user. It is very important to implement low-power control for receivers, especially for mobile phones, PNDs, watches, tablet computers, etc. which are particularly strict in power consumption and are used in a large amount.

2 The Method of Receiver Power Consumption Saving

2.1 Basic Method of Power Consumption Control

The technology of controlling Navigation receiver power is currently mainly using a variety of low-power mode, divided into a fixed duty cycle mode and the non-fixed cycle mode of operation [3], the former is to periodically turn off the receiver components, While the latter is non-periodic. The fixed cycle mode is also called the power saving mode, as shown in Fig. 1, the method is to make the receiver in the standby state (various state definitions shown in Table 1) standby time length shown in the figure for 540 ms, track the signal time 300 ms, and spend 160 ms time to solve the position, and finally to maintain cyclical 1 s/time output positioning results, this approach to avoid the traditional receiver continuous tracking of the extra power overhead, while ensuring reliable results output. Further considering the problem of signal variation, the power saving mode can be improved to the adaptive power saving mode, and the adaptive power saving mode is switched to the continuous operation state when the signal strength is lower than a certain threshold, such as 26 dB-Hz. Also, in order to reduce power dissipation in

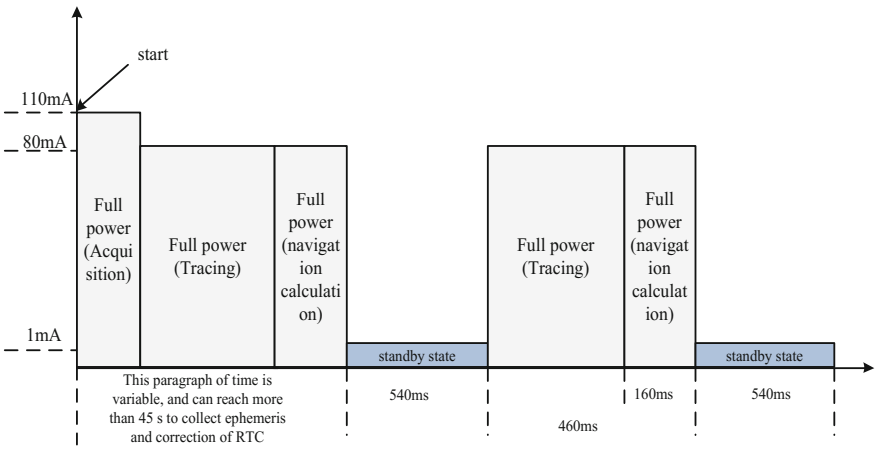

Fig. 1 Power saving mode

Table 1 Various state definition

Receiver state	Switch state	Power consumption
Full power state	Power supply for all parts	High
CPU state	In addition to the CPU, TCXO and synchronizer, the rest is turned off	Medium
Standby state	RF, baseband clock is powered down, only the internal core registers, RTC and RAM power supply	Low
Sleep state	RF, the baseband is powered down, keeping RTC and RAM running	Extremely low

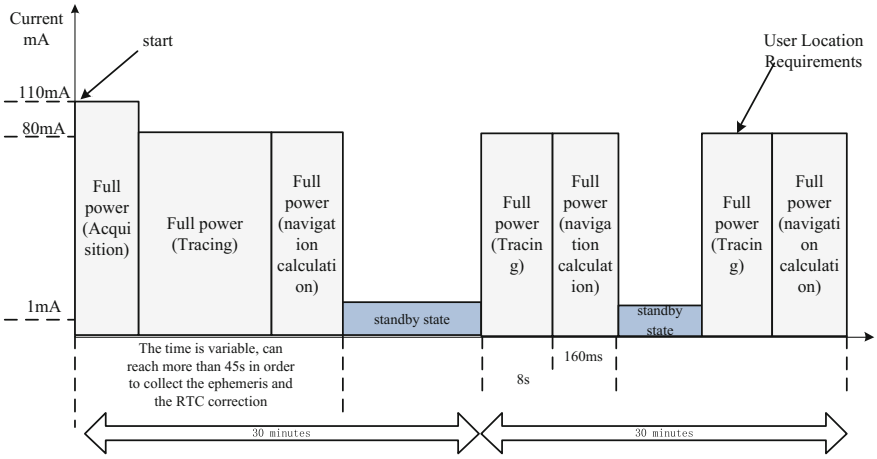

Fig. 2 Compulsory positioning mode

a greater degree, the receiver can be updated in a longer cycle, as shown in Fig. 2, for a period of 8 s 160 ms, which can be forced when rapid repositioning is required, For compulsory positioning mode [3], the compulsory positioning mode allows the receiver in the sleep process to resume operation and output positioning results.

2.2 Power Consumption Control Principle Analysis

At present, the power-saving mode is mainly used to control the power consumption of the navigation chip. That is to say, the receiver is in the standby and working state regularly in one positioning period. For example, supposing the positioning result update period is 1 s, To keep track of the solution, the remaining 0.8 s receiver in standby mode, this method by periodically turning off the receiver

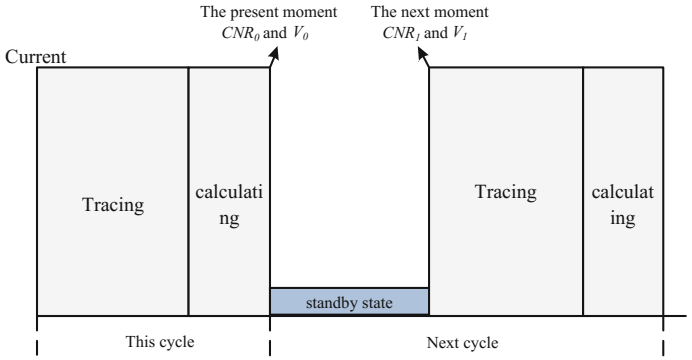

Fig. 3 State transition diagram during Standby state

most of the devices, can effectively reduce the receiver power, the principle is shown in Fig. 3.

Under the premise of satisfying the tracking performance of the navigation receiver, the longer the standby time, the greater the proportion of power consumption. Since the receiver decoding time is fixed, it is necessary to shorten the convergence time of the tracking loop in order to increase the power consumption control effect. The shorter convergence time means that the power control ratio can be higher, but can not shorten the convergence Time, because the premise is not to affect the loop tracking performance. How to shorten the convergence time of the receiver loop after restart, in order to obtain the maximum standby time, thus increasing the power consumption ratio is the focus of this paper.

3 The Method of Adjusting the Power of Consumption Multistage Bandwidth Control

Because the bandwidth is directly related to the convergence speed of the loop, a method is proposed to shorten the convergence time by using the multi-level bandwidth dynamic adjustment to stabilize the convergence of the receiver loop.

The higher the bandwidth of the receiver tracking loop, the shorter the convergence time of the phase error and the frequency error, but the worse the tracking accuracy. The longer the convergence time is, the higher the tracking accuracy is. Therefore, in order to achieve fast loop convergence while ensuring that the tracking accuracy does not decline, we can use multi-level loop bandwidth adjustment method, that is, the receiver from standby to cut into continuous working condition, the larger the loop bandwidth to initial Error, and then use the smaller loop bandwidth to stabilize the tracking convergence. This method can speed up the loop convergence and ensure the tracking accuracy is not reduced,

compared to the previous single-stage bandwidth can save unnecessary convergence time, indirectly reduce power consumption.

The key problem of the above method lies in: first, all levels of the loop bandwidth parameter value, how to select the second, bandwidth at all levels should be run how long, can guarantee the tracking performance and convergence time is the shortest, which has the largest power consumption control. For the above problem, this paper first complete theoretical analysis model is established, and then through the simplification and simulation analysis method to determine the optimal selection of the parameters.

3.1 Theoretical Analysis

For the fast convergence of the loop phase error, theoretically we can establish the model of the convergence of the n-level bandwidth, that is, the theoretical n-level loop bandwidth $B_1 \ldots B_n$ makes the total convergence time to be minimized. As shown in Fig. 4.

The objective of the optimization is to find the minimum convergence time T and its corresponding bandwidth B_i and t_i so that they satisfy the requirements of Eq. 3.1:

$$\sum_{i \in 1 \ldots n} t_i \geq T \tag{3.1}$$

The convergence time of each bandwidth is not only related to the loop bandwidth B_i, but also with the initial phase of the input $\Delta\theta$ is closely related, as to the mathematical model shown in Fig. 5:

$$t_i = f(B_i, \Delta\theta) \tag{3.2}$$

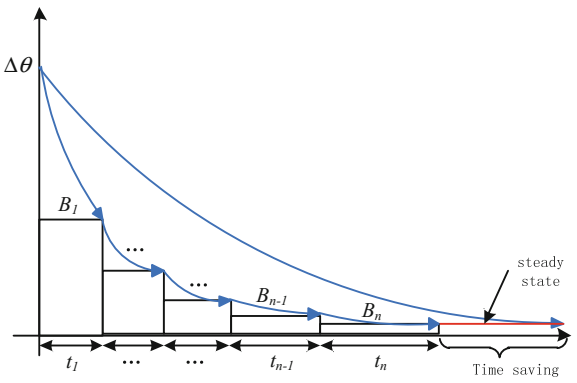

Fig. 4 n-level bandwidth loop tracking convergence diagram

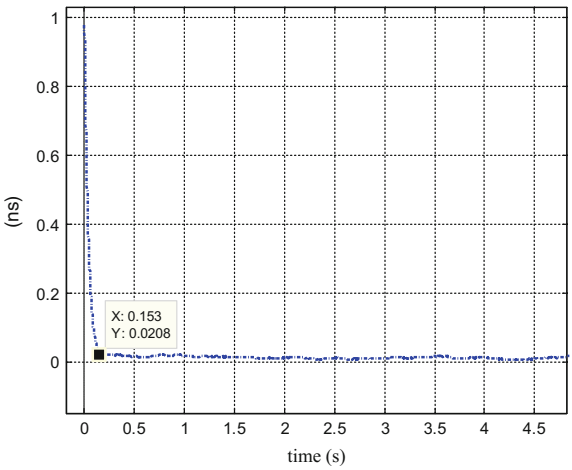

Fig. 5 The receiver loop convergence time

For the function f in 3.2, there is no accurate analytic expression, the literature [4] pointed out that the phase-locked loop phase acquisition time is affected by the initial phase difference is very difficult to accurately calculate. the sine phase detector with the largest second-order ring The fast acquisition time can be calculated as follows:

$$T_{\max} \approx \frac{10\tau_1}{K\tau_2} = \frac{5}{\zeta w_n} \tag{3.3}$$

Among them, ζ is the damping coefficient, ω_n is the characteristic frequency, K is the loop gain. And the convergence time T_L of the receiver code ring can be approximated by the following Eq. 3.4, B_n is the loop bandwidth.

$$T_L \approx \frac{2\pi}{\omega_n} = \frac{\pi\left(4\zeta^2 + 1\right)}{4\zeta B_n} \tag{3.4}$$

However, this equation is independent of the initial phase $\Delta\theta$ of the input and is obviously meaningless for the solution. In fact, this equation defines the steady-state of the tracking as the initial phase of the input decreases to a certain percentage and the falling time is defined as the convergence time. So we cannot use the exact mathematical expression, according to the input of the initial phase $\Delta\theta$ and bandwidth B_i, to solve the exact convergence time t_i.

In order to achieve optimal bandwidth design, we must solve the approximate form of 3.2, otherwise we can not find the optimal loop parameters. Aiming at this problem, this paper adopts the method of actual simulation and theoretical formula

derivation to solve the approximate formula of loop convergence time, and finally obtains the optimal loop bandwidth parameter.

1. Derivation of convergence time formula

First of all, in [5], an approximate estimation formula for the lock-in time is given for PLL synthesizer:

$$t_{Lock} = \frac{2}{w_{LPF}} \ln \frac{\Delta f}{(f_1 + \Delta f)|\alpha|} \tag{3.5}$$

w_{LPF}, Which is the loop bandwidth, α the stability of tracking into the lock after the accuracy, Δf the input frequency difference. The literature [6] gives a relatively complex approximation formula for the lock-in time of the third-order charge pump phase-locked loop, as shown below:

$$t_{locking} = \frac{\ln[2(a-1)\frac{f_{tol}}{N\Delta f}]}{k_c(a - \overline{a^2 - 1})} \tag{3.6}$$

f_{tol} The frequency tolerance, a is a coefficient, k_c which is a bandwidth-dependent quantity.

Therefore, by the above formula with the loop transfer function for Laplace inverse transform can be approximated to derive the receiver phase-locked loop convergence time approximation formula as follows:

$$t \approx \frac{k}{B_n} \ln\left(\frac{\Delta\theta}{\theta_e}\right) \tag{3.7}$$

Among them, $\Delta\theta$ is the initial phase, B_n is the loop bandwidth, θ_e is the steady-state tracking error. For the coefficient k in the formula, the value of k is determined by the actual simulation of the multi-loop of the receiver.

Simulation parameter and conditions Settings:

Setting $\Delta\theta$ is 1 ns; Setting B_n is 4 Hz; Convergence to the steady state $\theta_e = 0.02$ ns; For the analysis under the theory of performance, set to no noise environment, simulation platform with a standard of the GNSS software receiver simulation program [7], Intermediate frequency carrier frequency 31.25 MHz, Spread spectrum code bit rate 10.23 MHz;

1000 simulations to determine the average convergence time t is 0.1536 s, as shown in Fig. 3. So determine the coefficient of k is 0.1571, so the convergence time formula 3.7 modified as follows:

$$t \approx \frac{0.1571}{B_n} \ln(\frac{\Delta\theta}{\theta_e}) \tag{3.8}$$

3.2 The Shortest Search Time

The steady-state tracking variance formula for the convergence time according to the above-mentioned formula 3.8 and the following Eq. 3.9 is obtained.

$$\sigma_D = \sqrt{\frac{B_n \cdot \mathrm{D}}{2 \cdot C/N_0}\left(1 + \frac{1}{T \cdot C/N_0}\right)} \tag{3.9}$$

The theoretical minimum convergence time and the corresponding bandwidth value of the multi-level bandwidth can be solved by the exhaustive search method. The search algorithm is implemented as follows:

First, given the initial phase deviation $\Delta\theta$, according to 3.6 to calculate the convergence rate of the first stage of different bandwidth, according to 3.9 to determine the first-class bandwidth corresponding to the steady-state tracking standard deviation σ, and then 3σ as the next level of the entrance Phase deviation, the same in accordance with 3.6 to calculate the convergence rate of the second stage of different bandwidth, and then determine the second-order bandwidth of the steady-state tracking standard deviation, so repeated, can be n-band bandwidth of the convergence time and the corresponding bandwidth value, Find the minimum total convergence time and its corresponding bandwidth value at all levels, then it is the desired target solution. The following Table 2 shows the two-level bandwidth search algorithm.

In order to ensure the final loop tracking accuracy, the final bandwidth value can be set to a small value such as 0.2 Hz, in order to ensure tracking performance.

Table 2 Convergence time search algorithm

Optimal bandwidth and time search algorithm
• Set the carrier-to-noise ratio, integration time, steady-state tracking variance
• For (N_1 = 1: The maximum bandwidth value)
– According to the Eq. 3.8 to calculate the first level of bandwidth N_1 Corresponding to the convergence time; – According to Eq. 3.8 to calculate the bandwidth N_1 Corresponding to the steady-state tracking standard deviation σ, Then 3 σ is taken as the inlet bias of the second stage; – for (N_2 = 1: The maximum bandwidth value) – According to the Eq. 3.8 to calculate the second level of bandwidth N_2 Corresponding to the convergence time; end for • end for – The minimum value of the sum of two-stage convergence time and its corresponding bandwidth value are searched • return

4 Simulation Verification and Results

Taking into account the short standby time of the receiver and the Doppler can predict the frequency deviation and the loop has a certain tolerance, and measurement accuracy mainly associated with the code ring, so we mainly simulate the code ring phase deviation.

4.1 Analysis on Two Levels of Bandwidth

1. Simulation analysis is carried out under noiseless conditions

Condition setting:

The initial phase deviation $\Delta\theta$ is 1 ns, and the chip interval D is set to 1;

Integration time T = 0.001 s; second-level bandwidth is fixed to 0.2 Hz;

Simulation platform is still using the aforementioned GNSS software receiver, the same parameter settings.

First of all, according to 3.1 in the search algorithm to get the results shown in Table 3.

The maximum bandwidth of the search is set to 200 Hz, that is, the bandwidth search range is 1–200 Hz. This is because the additional bandwidth above 200 Hz has little effect on the convergence time, As shown in Fig. 6.

Put the value of Table 1 into the simulation program to observe the loop convergence performance.

Simulation analysis and conclusion:

1. As can be seen from Fig. 7, the optimal two-stage bandwidth is not significantly different from the first-order bandwidth in convergence time, but the tracking accuracy is significantly better.
2. As can be seen from Fig. 8, the optimal two-level bandwidth is significantly faster than the first-order small bandwidth and the non-optimal two-stage bandwidth of 1–0.2 Hz, but the final stable tracking accuracy There was no drop. Therefore, it can be concluded that the convergence of the two-stage bandwidth is better than that of the single-stage bandwidth, and the convergence time is the shortest.

Table 3 Two-stage bandwidth and convergence time for optimal search results

Bandwidth series	Optimal parameter	
	Bandwidth (Hz)	Convergence time (s)
First level	2	0.3016
Second level	0.2	0.3126
Total		0.6141

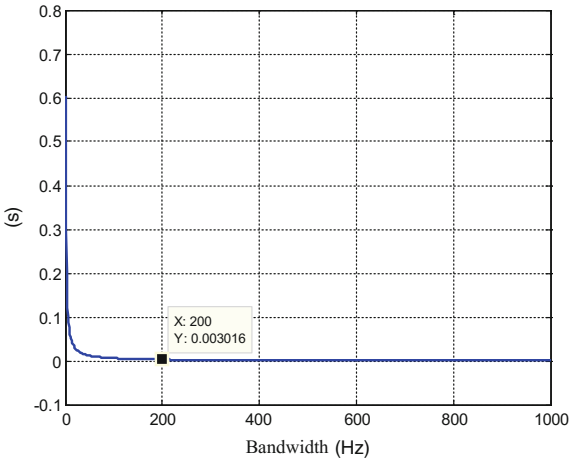

Fig. 6 Loop convergence time for different bandwidths

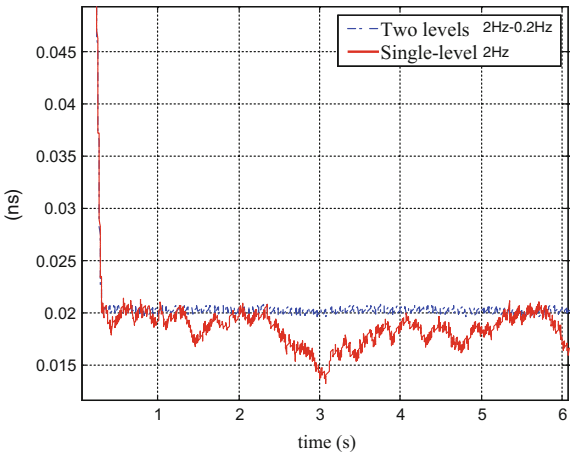

Fig. 7 Comparison between Two-level bandwidth and the first-class large-bandwidth

3. From the power control point of view, single-stage 0.2 Hz convergence time is 3.171 s, while the optimal two-level bandwidth only need 0.6141 s, tracking convergence time shortening means that can reduce tracking power consumption, in the ideal case tracking The proportion of lower power consumption up to (3.171 − 0.6141)/3.171 = 80.63%.
2. Simulation is performed at 40 dB-Hz:

The condition setting is the same as in simulation 1, except that the carrier-to-noise ratio is set to 40 dB-Hz.

The search results of the following Table 4.3 are also obtained according to the aforementioned search algorithm:

The above search value is substituted into the convergence of the loop, as shown in Fig. 9.

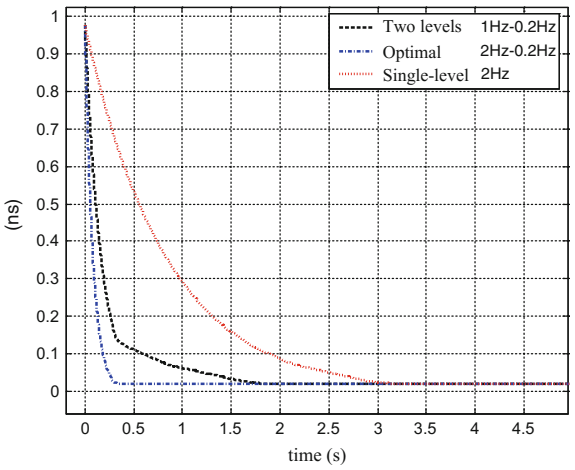

Fig. 8 Optimal two-level bandwidth compared with other bandwidths

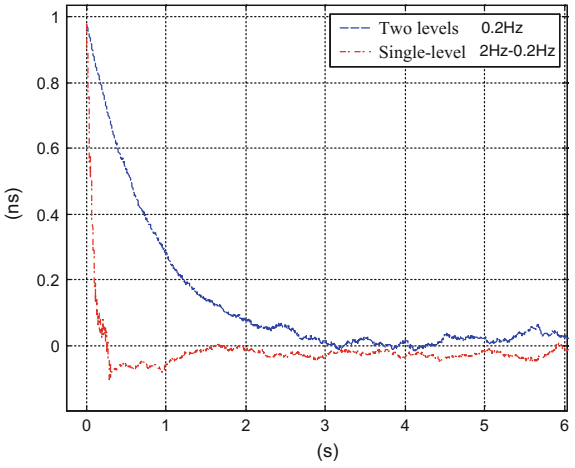

Fig. 9 Two-level bandwidth and single-stage small-bandwidth loop convergence comparison

Simulation analysis and conclusion:

1. From Figs. 9 and 10, it can be seen that, similar to the simulation results under noiseless conditions, the two-stage bandwidth is not lost in accuracy compared with single-stage bandwidth, but the convergence time is longer.
2. As can be seen from Tables 3 and 4, the convergence time at different carrier to noise ratio is different, this is because the 3.9 type is related to the input carrier to noise ratio, in fact, 3.8 type of calculation should be in the approximate without noise under the high carrier noise ratio. Otherwise, it will appear the unreasonable phenomenon of that the time value of searching exceeds single-level bandwidth convergence time.

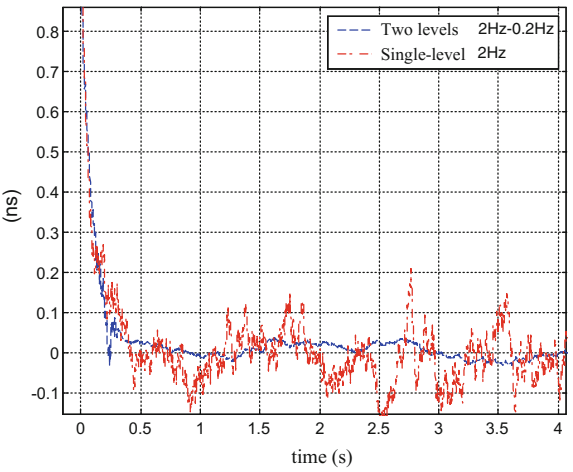

Fig. 10 Two-stage bandwidth and single-stage large-bandwidth loop convergence comparison

Table 4 Two-stage bandwidth and convergence time for optimal search results

Bandwidth series	Optimal parameter	
	Bandwidth (Hz)	Convergence time (s)
First level	2	0.3016
Second level	0.2	3.8633
Total		4.1649

5 Conclusions

The above analysis shows that multi-level bandwidth can effectively accelerate the convergence time, thus increasing the standby time, indicating that multi-level bandwidth can be significantly compressed convergence time, which is to save tracking power consumption is extremely beneficial. The convergence of the two levels is analyzed, and the convergence time is better optimized for more bandwidths of level 3 and level 4, but the optimization proportion is obviously smaller and smaller. In addition to be sure that the increase in the number of bandwidth, the receiver will bring scheduling and implementation complexity. So the actual project should be based on the need to select more two or three bandwidth adjustment.

References

1. Li Y, Qiu Z (2008) Navigation and positioning, 2nd edn. National Defense Industry Press, Beijing, pp 481–483
2. Cui Y (2008) Application of low power technology in backend design. Fudan University Master Thesis, pp 1–30

3. Paek J, Kim J, Govindan R (2010) Energy-efficient-rate-adaptive GPS-based positioning for smartphones. MobiSys'10, 15–18 June 2010, San Francisco, California, USA. Copyright 2010 ACM 978-1-60558-985-5/10/06
4. JiYu Z, JueSheng Z, Xin Ping W (2012) Phase-locked technology, 2nd edn. Xi'an University of Electronic Science and Technology Press, Xi'an
5. Chen MH, Li JX, Shi X (2012) Phase locked loop frequency synthesizer based on lock—in time analysis. J Microw 28(1):57–61
6. Li Z, Kui WH, Zhi ZR (2004) Study on the lock time of the third order charge pump phase locked loop. Prog Solid Electr 24(2):196–199
7. Borre K, Akos DM, Bertelsen N (2009) Software-defined GPS and Galileo receivers. National Defense Industry Press, Beijing

A Vector and Scalar Hybrid Tracking Loop for New Generation Composite GNSS Signal

Honglei Lin, Shengqiang Lou, Xiaomei Tang, Bo Xu and Gang Ou

Abstract To the new generation composite GNSS signal, a DU-HTL (Dual Update-rate Hybrid Tracking Loop) of SPLL (Scalar Phase Lock Loop) and VFLL (Vector Frequency Lock Loop) based on a DUKF (Dual Update-rate Kalman Filter) is proposed. Analysis and simulation show, in the DU-HTL, the additional VFLL has litter performance improvement in carrier phase tracking accuracy, but the tracking robustness is improved larger with the help of VFLL especially in the signal shielding environment. When the update-rate of VFLL is low as 0.1 s, DU-HTL also has better performance of signal reacquisition.

Keywords Composite GNSS signal · Vector tracking loop · Scalar tracking loop · Hybrid tracking loop

1 Introduction

With the development of GNSS (Global Navigation Satellite System), such as the modernization of GPS (Global Positioning System) and the globalization of BDS (BeiDou System), new generation GNSS signal will be broadcast, and a salient feature of the new signal is the addition of pilot signal where no navigation messages is modulated on it [1–3]. To tracking this composite signal, the method of OLC PLL (Optimal Linear Combination Phase Lock Loop) based on combined discriminator is studied by many researches [4–6], such as pilot and data coherent combined, non-coherent combined discriminator and so on. All those discriminators can make full use of pilot signal and data signal, but the coherent of two types of signal must be the same. In fact the coherent time of pilot signal can be designed flexibly. Yao et al. [7] proposed a structure of DUKF (Dual Update-rate Kalman Filter), one of its characteristic is the coherent of the pilot and data signal are different, furthermore, a method of dual update-rate PLL and FLL is studied by [8]

H. Lin · S. Lou · X. Tang · B. Xu · G. Ou (✉)
National University of Defense Technology, Deya. 109, Changsha 410073, China
e-mail: ougang_nnc@163.com

J. Sun et al. (eds.), *China Satellite Navigation Conference (CSNC) 2017 Proceedings: Volume I*, Lecture Notes in Electrical Engineering 437,
DOI 10.1007/978-981-10-4588-2_66

and [9]. In fact, these methods can be treated as a more generic DU-STL (Dual Update-rate Scalar Tracking Loop) based on DUKF (Dual Update-rate Kalman Filter).

In recent years, the attention on VTL (Vector Tracking Loop) is paid more and more. The current results show that VTL has a better tracking performance in sensitivity, signal reacquisition, usability and so on [10]. The VFDLL (Vector Frequency and Delay Lock Loop) is studied in detail [11] and its tracking threshold and dynamic are analyzed and verified by simulations [12]. The performance and valid of VTL are studied in different environments, such as fade channel city and canyon [13]. In [14], a method call called VPLL (Vector Phase Lock Loop) is proposed and analysis, VPLL can track all view satellite signals carrier phase in one tracking loop. Furthermore the error factors of signal carrier phase in VPLL are subdivided into position error, clock error, atmospheric transmission error and others. These errors are then filtered by a set of orthogonal projection filter [15]. Simulations show that this method has a better performance in tracking accuracy. In general, VPLL method needs much more computational resource, to overcome the shortcomings [16], gives a continuous and stable tracking method by adding a local phase tracking filter in each channel based on the structure of VFLL, and further compares the performance of three different kinds of local phase filters. Based on the structure of the scalar FLL assisted PLL [17], regards the VFLL as a special frequency discriminator and directly uses its result fed back to the PLL in each channel. Compared with the VPLL method, the above two methods can reduce the implementation complexity, but the update-rate of the VTL is still high.

In this paper, a DU-HTL (Dual Update-rate Hybrid Tracking Loop) of SPLL and VFLL based on the DUKF model is designed for new generation of pilot and data composite signal. The VFLL tracking technology is used for the pilot branch to prolong the signal integration time, which can also reduce the computation cost while improving the integration gain. The SPLL tracking technology is adopted for the data branch, and the integration time is designed according to the message rate, which can demodulates the navigation data while get the continuously and stably carrier phase measurements. Combine the different update-rate VFLL and SPLL to form a hybrid tracking loop based on the DUKF model, this structure can also achieve the performance of vector loop assisted the scalar loop. Analysis and simulation results show that though the tracking accuracy of this DU-HTL is almost the same as the DU-STL, the robustness of DU-HTL is better than DU-STL. DU-HTL can track the transient loss-lock or occluded signal continuously. Compare with sole VFLL which needs higher update-rate, the VFLL in DU-HTL can work as a low update-rate as sub-second, the computational burden is reduced greatly. If using the MUKF model given in [18], this DU-HTL can easily extend to three different loops, the data branch SPLL, the pilot branch SPLL, and the pilot branch VFLL. Due to the MUKF technology is not published up to now, the DUKF model is used as an example to analyze the this DU-HTL method.

The remainder of this paper is organized as follows, firstly, based on the DUKF technology and the VFLL model, the DU-HTL of VFLL and SPLL based on DUKF model is designed. Then the carrier tracking accuracy of DU-HTL and DU-STL is

compared and analyzed, the results of numerical calculation show that these two methods are almost the same on the equal conditions, furthermore the re-acquisition performance simulation of DU-HTL is also implemented. Finally the conclusion is achieved.

2 Hybrid Structure of Vector and Scalar Tracking Loop

2.1 Dual Update-Rate Scalar Tracking Loop

Figure 1 shows a scalar tracking loop based on DUKF model, in which the pilot branch using FLL, data branch using PLL, the coherent integration time of pilot branch is longer than the data branch. The algorithm model is described as follows.

The signal model of the pilot and data composite signal can be simplified as

$$\begin{aligned} r(t) = &\sqrt{\mu_d \cdot C} \cdot D(t-\tau) \cdot c_d(t-\tau) \cdot \cos[2\pi \cdot f(t) \cdot t + \theta(t)] \\ &+ \sqrt{\mu_p \cdot C} \cdot c_p(t-\tau) \cdot \sin[2\pi \cdot f(t) \cdot t + \theta(t)] + n(t) \end{aligned} \tag{1}$$

where μ_d and μ_p are the ratio of the pilot and the data branch to the total signal power, and there is $\mu_d + \mu_p = 1$, C is the signal power, $D(t)$ is the navigation message on the data channel. $c_d(t)$ and $c_p(t)$ are the pseudo-random code on pilot and data signal. $f(t)$ and $\theta(t)$ are the signal Doppler and carrier phase respectively, τ is the signal delay, $n(t)$ is the band-limited Gaussian noise, and its power spectral density is N_0.

To ith channel satellite signal, after the orthogonal transformation and coherent integration, the correlation value I_p^i, I_d^i, Q_p^i, Q_d^i are obtained, where the superscript i denotes the channel ith signal, the subscripts p and d denote the pilot and data branches respectively, and their the expression are as follows

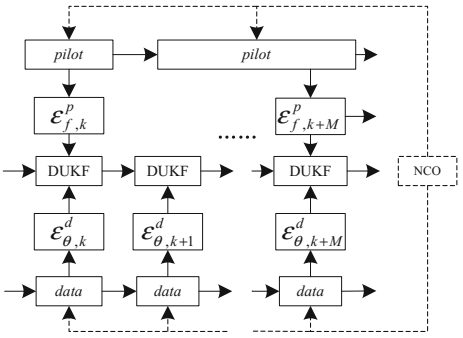

Fig. 1 The processing frame of DU-STL

$$\begin{cases} I_p^i \approx \sqrt{\mu_p} \cdot a_k^i \cdot \cos(\pi \cdot \Delta f_k^i \cdot T_c + 2\pi \cdot \Delta\theta_k^i) + n_{p,I} \\ Q_p^i \approx \sqrt{\mu_p} \cdot a_k^i \cdot \sin(\pi \cdot \Delta f_k^i \cdot T_c + 2\pi \cdot \Delta\theta_k^i) + n_{p,Q} \\ I_d^i \approx \sqrt{\mu_d} \cdot a_k^i \cdot d_d \cdot \cos(\pi \cdot \Delta f_k^i \cdot T_c + 2\pi \cdot \Delta\theta_k^i) + n_{d,I} \\ Q_d^i \approx \sqrt{\mu_d} \cdot a_k^i \cdot d_d \cdot \sin(\pi \cdot \Delta f_k^i \cdot T_c + 2\pi \cdot \Delta\theta_k^i) + n_{d,Q} \end{cases} \tag{2}$$

Regardless of tracking error of pseudo-random code, a_k^i meets

$$a_k^i = \sqrt{C^i/N_0 \cdot T_c} \cdot \sin c\left(\pi \cdot \Delta f_k^i \cdot T_c\right) \tag{3}$$

where C^i/N_0 is the carrier to noise ratio of the input signal, T_c is for coherent integration time, Δf_k^i is the residual Doppler, $\Delta\theta_k^i$ is the residual carrier phase, $n_{p,I}$, $n_{p,Q}$, $n_{d,I}$ and $n_{d,Q} \sim N(0, 1)$.

In the DU-STL based on DUKF model, there are two different update-rate Kalman filtering process, respectively T_c and $M \cdot T_c$, the following will use DU-STL (T_c, $M \cdot T_c$) to identify this method, where T_c is the integration time of data signal and $M \cdot T_c$ is the integration time of pilot signal.

The dynamic equation of DUKF is

$$X_{k+1}^i = \Phi \cdot X_k^i + w_k \tag{4}$$

where $X_k^i = [\theta_k^i, f_k^i, \alpha_k^i]^T$, θ_k^i, f_k^i, α_k^i are the signal carrier phase, Doppler, and change of Doppler in cycles, Hz and Hz/s, $w_k = [\omega_{rf} \cdot w_b, \omega_{rf} \cdot w_d, (\omega_{rf}/c) \cdot w_a]^T$ is the dynamic noise, w_b and w_d are the phase noise and frequency noise caused by the crystal oscillator, w_a is the accelerating noise in the direction of the satellite and user's line of sight. ω_{rf} is the signal Carrier frequency. c is the light in the vacuum propagation velocity, about 3×10^8m/s. Φ is the state transition matrix, and it is given by

$$\Phi = \begin{bmatrix} 1 & T_c & T_c^2/2 \\ 0 & 1 & T_c \\ 0 & 0 & 1 \end{bmatrix} \tag{5}$$

Q is the covariance matrix of w_k, specifically

$$\begin{aligned} Q = \left(\frac{\omega_{rf}}{c}\right)^2 \cdot q_a \cdot \begin{bmatrix} T_c^5/20 & T_c^4/8 & T_c^3/6 \\ T_c^4/8 & T_c^3/6 & T_c^2/2 \\ T_c^3/6 & T_c^2/2 & T_c \end{bmatrix} \\ + \omega_{rf}^2 \cdot q_f \cdot \begin{bmatrix} T_c^3/3 & T_c^2/2 & 0 \\ T_c^2/2 & T_c & 0 \\ 0 & 0 & 0 \end{bmatrix} + \omega_{rf}^2 \cdot q_p \cdot \begin{bmatrix} T_c & 0 & 0 \\ 0 & 0 & 0 \\ 0 & 0 & 0 \end{bmatrix} \end{aligned} \tag{6}$$

Table 1 Allan parameters of TCXO and OCXO

Oscillator type	h_0/s	h_{-2}/Hz
TCXO	2×10^{19}	3×10^{-20}
OCXO	2×10^{-25}	6×10^{-25}

where q_a is the acceleration noise spectral density of the receiver in the LOS (Line of Sigh) direction. q_p and q_f are the power spectral density of the phase noise and the frequency noise respectively, they all satisfy the relation $q_p = h_0/2$, $q_f = 2\pi^2 \cdot h_{-2}$ with Allan variance parameters h_0, h_{-2} of the oscillator. Typical crystal parameters are show in Table 1.

The measurement equation of the DUKF model can be described as

$$\Delta Y_k^i = A_k \cdot \Delta X_k^i + v_k^i \tag{7}$$

where ΔY_k^i is the measurement information, that is, the result $\varepsilon_{f,k}^i$ or $\varepsilon_{\theta,k}^i$ of the discriminator output, H_k is the measurement matrix, v_k^i is the measurement noise, and the covariance matrix satisfies

$$\sum_k^i = E\left[v_k^i \cdot v_k^{iT}\right] \approx \sigma_{\varepsilon,k}^2 \tag{8}$$

$\sigma_{\varepsilon,k}^i$ is the standard deviation of the discriminator output, $\sigma_{\varepsilon,k}^i = \sigma_{f,k}^i$ for the discriminator, $\sigma_{\varepsilon,k}^i = \sigma_{\theta,k}^i$ for the phase detector, where $\sigma_{f,k}^i$ and $\sigma_{\theta,k}^i$ are given by the empirical formula [12], in particular

$$\sigma_{f,k}^i = \frac{1}{2\pi \cdot MT_c} \cdot \sqrt{\frac{1}{2MT_cC^i/N_0}\left(1 + \frac{1}{2MT_cC^i/N_0}\right)} \tag{9}$$

$$\sigma_{\theta,k}^i = \frac{1}{2\pi} \cdot \sqrt{\frac{1}{2T_cC^i/N_0}\left(1 + \frac{1}{2T_cC^i/N_0}\right)} \tag{10}$$

In the DUKF-based DU-STL model, A_θ is for the data branch phase detector, and A_f is for the pilot branch discriminator, respectively,

$$\begin{aligned} A_\theta &= \begin{bmatrix} 1 & -T_c/2 & 0 \end{bmatrix} \\ A_f &= \begin{bmatrix} 0 & 1 & -\frac{(M-2)\cdot T_c}{2} \end{bmatrix} \end{aligned} \tag{11}$$

The different selections of ΔY_k^i, A_k and $\sum_k^i$ at different update epochs are different. When only the data branch phase detector is valid, the parameters in the measurement equation are

$$\begin{cases} \Delta Y_k^i = \varepsilon_{\theta,k}^i \\ A_k = A_\theta \\ \sum_k^i = \sigma_{\theta,k}^{i2} \end{cases} \tag{12}$$

When the discriminator results of both the data branch and the pilot branch are valid, the parameters are

$$\begin{cases} \Delta Y_k^i = \left[\varepsilon_{\theta,k}^i; \varepsilon_{f,k}^i\right] \\ A_k = \left[A_\theta; A_f\right] \\ \sum_k^i \approx diag\left(\left[\sigma_{\theta,k}^{i2}; \sigma_{f,k}^{i2}\right]\right) \end{cases} \tag{13}$$

Therefore, the DUKF-based DU-STL processing steps can be described as follows

Step 1, State Prediction

$$X_{k|k-1}^i = \Phi \cdot X_{k-1}^i \tag{14}$$

Step 2, Forecast covariance matrix

$$P_{k|k-1}^i = \Phi \cdot P_{k-1}^i \cdot \Phi^T + Q \tag{15}$$

Step 3, Kalman gain matrix calculation:

$$G_k^i = P_{k|k-1}^i \cdot A_k^T \cdot \left(\sum_k^i + A_k \cdot P_{k|k-1}^i \cdot A_k^T\right)^{-1} \tag{16}$$

Step 4, State update

$$X_k^i = X_{k|k-1}^i + G_k^i \cdot \Delta Y_k^i \tag{17}$$

Step 5, Covariance matrix update

$$P_k^i = P_{k|k-1}^i - G_k^i \cdot A_k \cdot P_{k|k-1}^i \tag{18}$$

2.2 Vector Frequency Lock Loop

In STL method, each satellite signal is tracked alone, while in VTL, all the satellite signals are tracking in one loop, and an EKF navigation solution filter is also included in the VTL model. The dynamic model of EKF is

$$\Delta X_k^V = \Phi_V \cdot \Delta X_{k-1}^V + \omega_k \tag{19}$$

where $\Delta X_k^V = [\Delta v_x, \Delta a_x, \Delta v_y, \Delta a_y, \Delta v_z, \Delta a_z, \delta f]$ is the state vector of receiver, v_x, v_y, v_z are the three-dimensional velocities in the ECEF (Earth Centered Earth Fixed) coordinate system, a_x, a_y, a_z are the three-dimensional accelerations, $\Delta(\ )_k$ is the state error, δf is the receiver clock drift. The update interval of the vector tracking loop is T_v. Φ_V state transition matrix, it is given by

$$\Phi_V = \begin{bmatrix} 1 & T_v & 0 & 0 & 0 & 0 & 0 \\ 0 & 1 & 0 & 0 & 0 & 0 & 0 \\ 0 & 0 & 1 & T_v & 0 & 0 & 0 \\ 0 & 0 & 0 & 1 & 0 & 0 & 0 \\ 0 & 0 & 0 & 0 & 1 & T_v & 0 \\ 0 & 0 & 0 & 0 & 0 & 1 & 0 \\ 0 & 0 & 0 & 0 & 0 & 0 & 1 \end{bmatrix}_{7\times 7} \tag{20}$$

ω_k is the process noise, and its covariance matrix Q_V is

$$Q_V = \begin{bmatrix} Q_x & 0 & 0 & 0 \\ 0 & Q_y & 0 & 0 \\ 0 & 0 & Q_z & 0 \\ 0 & 0 & 0 & Q_f \end{bmatrix}_{7\times 7} \tag{21}$$

where

$$\begin{aligned} Q_x = Q_y = Q_z &= q_a \begin{bmatrix} T_v^3/3 & T_v^2/2 \\ T_v^2/2 & T_v \end{bmatrix} \\ Q_f &= q_f \cdot T_v \end{aligned} \tag{22}$$

The measurement equation of VFLL is

$$\Delta Z_k = H_k \cdot \Delta X_k^V + \xi_k \tag{23}$$

where $\Delta Z_k = [\varepsilon_{f,k}^1, \varepsilon_{f,k}^2, \ldots, \varepsilon_{f,k}^N]^T$, $\varepsilon_{f,k}^i$ is the signal frequency increment of the ith satellite in k epoch, N is the number of satellites, H_k is the observation matrix, The error covariance matrix of ΔZ_k is R_k, where the value of each element is determined by (9). ΔZ_k is used as the measurement of VFLL and the final frequency error $\Delta \widehat{Z}_k$ is also estimated. The process flow is shown below

Step 1, Receiver motion state and covariance prediction

$$\begin{aligned} \Delta X_{k|k-1}^V &= \Phi_V \cdot \Delta X_{k-1}^V \\ P_{V,k|k-1} &= \Phi_V \cdot P_{V,k-1} \cdot \Phi_V^T + Q_V \end{aligned} \tag{24}$$

Step 2, Kalman gain matrix calculation,

$$K_k = P_{V,k|k-1} \cdot H_k^T \left(H_k \cdot P_{V,k|k-1} \cdot H_k^T + R_k\right)^{-1} \tag{25}$$

Step 3, Receiver state and covariance matrix update

$$\begin{aligned} \Delta X_k^V &= \Delta X_{k|k-1}^V + K_k \cdot \left(\Delta Z_k - H_k \cdot \Delta X_{k|k-1}^V\right) \\ P_{V,k} &= (I - K_k \cdot H) \cdot P_{V,k|k-1} \end{aligned} \tag{26}$$

Step 4, Final frequency error estimation and estimated covariance

$$\Delta \widehat{Z}_k = H_k \cdot \Delta X_k^V \tag{27}$$

$$P_{Z,k} = H_k \cdot P_{V,k} \cdot H_k^T \tag{28}$$

2.3 Dual Update-Rate Hybrid Tracking Loop

The traditional VTL has high computational burden and the tracking error is also easy to propagate between the channels. The scalar tracking loop is independent of each other and does not need to rely on the navigation filter and its computational burden is lower. A DU-HTL of vector and scalar is designed to maximize the advantages of two different tracking methods. The tracking structure is shown in Fig. 2.

In DU-HTL method, the SPLL is used for the data branch, the integration time is T_c, and the VFLL is used for the pilot branch with the integration time $M \cdot T_c$. These two different tracking loops are combined together by a DUKF filter, which is used to control the local channel carrier NCO. The above method can be represented as DU-HTL (T_c, $M \cdot T_c$).

In the DU-HTL (T_c, $M \cdot T_c$) model, the discriminator results on the pilot branch are not directly fed back to the DUKF, they are filtered by VFLL and then participate in the DUKF, that is, to ith satellite, when both the data branch and the pilot branch of the discriminator results are valid, DUKF filter model parameters are given by

$$\begin{cases} \Delta Y_k^i = \left[\varepsilon_{\theta,k}^i; \Delta \widehat{Z}_k(i)\right] \\ A_k = \left[A_\theta; A_f\right] \\ \sum_k^i = diag\left(\left[\sigma_{\theta,k}^{i2}; P_{Z,k}(i,i)\right]\right) \end{cases} \tag{29}$$

where $\Delta \widehat{Z}_k(i)$ is the ith element of the vector $\Delta \widehat{Z}_k$, and $P_{Z,k}(i, i)$ is the ith row and ith column of the matrix $P_{Z,k}$. $\Delta \widehat{Z}_k$ and $P_{Z,k}$ are given by (27) and (28).

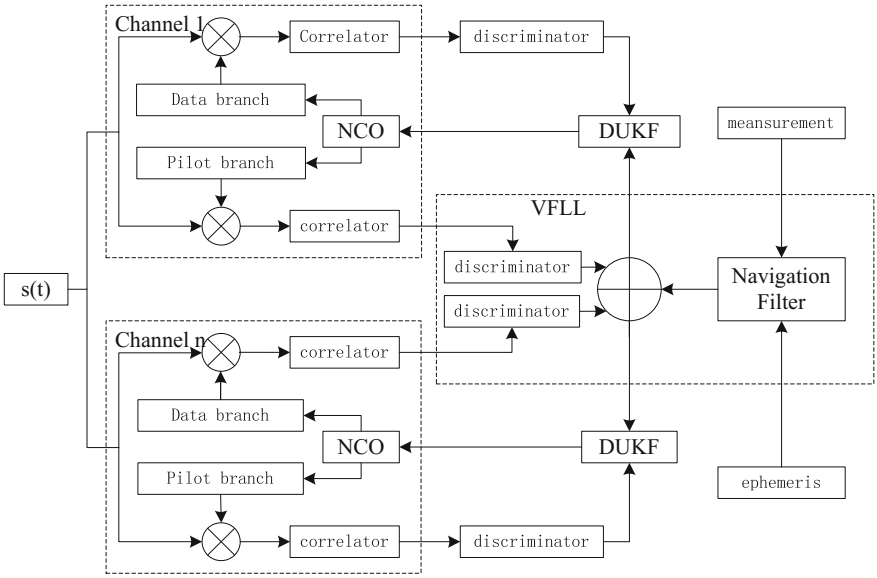

Fig. 2 A vector and scalar hybrid tracking loop structure

In the DU-HTL(T_c, $M \cdot T_c$) model, compared with the DU-STL tracking method, since the results of the VFLL participate in the DUKF filter, different channels can mutual aid each other, and in extreme conditions, DU-HTL can track the transient lost lock signal continuously. Compared with the traditional VFLL method, the scalar carrier tracking loop is added to the DU-HTL model, which can reduce the update-rate of VFLL while providing the robust carrier phase tracking result.

3 Performance Analysis and Simulation

In this section, based on the tracking accuracy of DU-STL and VFLL, the carrier phase tracking accuracy of DU-HTL model is analyzed theoretically and the results are simulated numerically. Furthermore, the GPS constellation is taken as an example to compare DU-HTL and DU-STL Performance.

3.1 Tracking Performance Analysis

For the DU-STL method given in Sect. 2.1, the carrier phase tracking accuracy can be obtained from the covariance matrix P_k^i of the state parameter X_k^i and the iterative solving equation of P_k^i is

$$P_k^i = \left(I - G_k^i \cdot A_k\right) \cdot \left(\Phi \cdot P_{k-1}^i \cdot \Phi^T + Q\right) \tag{30}$$

where G_k^i is the Kalman gain determined by (16), A_k and $\sum_k^i$ may take different values at different epochs. Taking into account the periodicity of DUKF, the steady-state condition is the covariance matrix P_k^i is maintained after one cycle of iteration unchanged

$$P_{k+M}^i = P_k^i \tag{31}$$

Solving (30) and (31), can be obtained state parameter X_k^i of steady-state estimation accuracy P_s^i, so the carrier phase tracking accuracy is

$$\sigma_{\theta,STL}^i = 360^\circ \cdot \sqrt{P_s^i(1,1)} \tag{32}$$

For the VFLL method given in Sect. 2.2, the steady-state tracking accuracy is satisfied

$$\Phi_V \cdot P_V^- \cdot \Phi_V^T - \Phi_V \cdot P_V^- \cdot H_s^T \cdot \left(H_s \cdot P_V^- \cdot H_s^T + R\right)^{-1} H_s \cdot P_V^- \cdot \Phi_V^T + Q_V - P_V^- = 0 \tag{33}$$

where P_V^- is the forward prediction result of P_V, so there is

$$P_V = P_V^- - P_V^- \cdot H_s^T \left(H_s \cdot P_V^- \cdot H_s^T + R\right)^{-1} \cdot H_s \cdot P_V^- \tag{34}$$

Substituting the results of the above equation into (28), the tracking accuracy covariance matrix P_Z can be obtained.

To solve the tracking accuracy of the DU-HTL model, the accuracy of the SPLL and VFLL needs to be solved simultaneously. According to the DUKF filter parameters given in (29) according to the Eqs. (30), (31) and (28), (33), (34), the final value of P_s^i can be obtain, recorded it as $P_{HTL,s}^i$, so the final carrier phase tracking accuracy of

$$\sigma_{\theta,HTL}^i = 360^\circ \cdot \sqrt{P_{HTL,s}^i(1,1)} \tag{35}$$

Figure 3 shows a GPS constellation, and the tracking precision of the 18th satellite is numerically calculated according to the above analysis method to compare the DU-HTL and DU-STL carrier phase tracking accuracy. The results are shown in Fig. 4. Where the coherent integration time of the data branch is 1 ms and the coherent integration time of the pilot branch is 20, 50 and 100 ms respectively.

According to the above analysis, it can be seen that the carrier phase tracking accuracy of DU-HTL and DU-STL is almost the same, only when the pilot branch

coherent integration time is relatively long, DU-STL accuracy will be slightly better than the DU-HTL, but the difference is relatively small.

3.2 Simulation Results

To verify the correctness of the above analysis, the following simulation method will be used to compare the performance of DU-STL and DU-HTL model, a GPS constellation is shown in Fig. 3, a total of eight visible satellites, satellite motion parameters generated by the STK software, the data sampling rate is 100 Hz. The receiver motion trajectory is shown below and the duration is 100 s, the following will focus on the tracking accuracy and signal re-acquisition performance.

3.2.1 Carrier Phase Tracking Accuracy

The carrier-to-noise ratio in the simulation is 35 dBHz, the data branch coherent integration time is 10 ms, and the pilot branch coherent integration time is set 20, 50 and 100 ms, respectively. The statistics of all satellite's carrier phase tracking accuracy are shown in Table 2, where the unit is degrees.

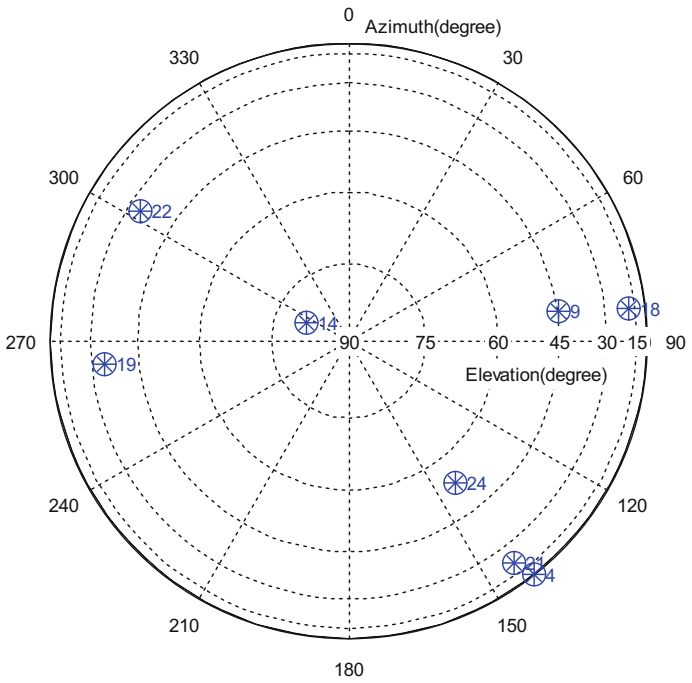

Fig. 3 GPS constellation in simulation

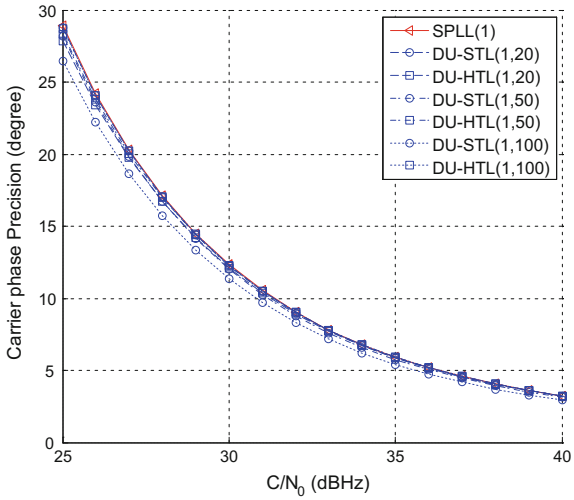

Fig. 4 Carrier phase accuracy with the signal C/N_0

Table 2 Carrier phase accuracy in different tracking methods

PRN	SPLL (10)	DU-STL			DU-HTL		
		(10, 20)	(10, 50)	(10, 100)	(10, 20)	(10, 50)	(10, 100)
4	3.0051	3.0031	2.9487	2.8083	3.1354	2.8557	2.9939
9	3.1723	2.9829	3.0753	2.8811	3.0503	2.9510	2.9810
14	3.1406	3.1576	2.9193	3.0551	3.0796	2.8437	3.0191
18	3.0797	3.0987	3.0005	2.7514	2.9715	2.9376	3.0803
19	2.9608	2.9084	2.9052	3.0122	3.1495	2.9871	3.0156
21	3.2643	3.2344	3.0767	2.8676	3.0005	2.9771	2.9611
22	3.0053	3.1230	3.0966	2.7763	2.9023	3.0351	3.0660
24	3.0928	3.1186	2.9974	2.8278	3.1865	3.0822	3.0030

According to the above statistical results, to the DU-STL method, prolong the coherence integration time of the pilot branch is longer can slightly improve the tracking accuracy. To the DU-HTL method, the accuracy is slightly worse than DU-STL especially when the coherent integration time of pilot branch is long, but their difference is not significant.

3.2.2 Signal Re-acquisition Performance

In the DU-HTL model, the additional VFLL can improve its performance of signal re-acquisition compared to DU-STL, this simulation scene is set as all signal strength is 35 dBHz at the beginning, and then from 20 to 60 s, the signal intensity

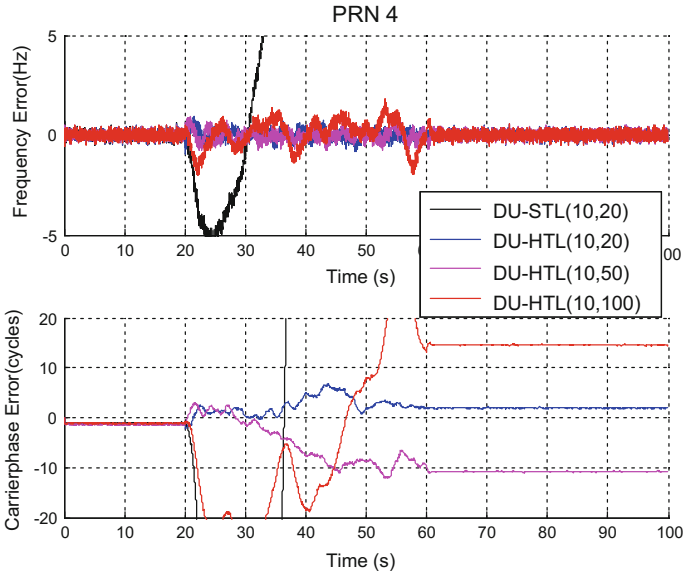

Fig. 5 Carrier tracking error of PRN = 4

of satellite 4 and 9 dropped to 5 dBHz and resumed to 35 dBHz after 60 s. The signal intensity of satellite 14 and 18 was reduced to 5 dBHz from 40 to 80 s, and resumed to 35 dBHz after 80 s. Figures 5 and 6 are the carrier frequency and phase tracking error results of satellite 4 and 18 using DU-HTL and DU-STL respectively.

As Figs. 5 and 6 shown, to the DU-STL methods, when the C/N_0 drops to 5 dBHz, the carrier frequency and phase errors increase large quickly and finally the signal lost. To the DU-HTL method, when the C/N_0 drops to 5 dBHz, the frequency errors can keep a small scope and the signal can be tracked by other satellites' assisted provided by VFLL and when its C/N_0 increases to 35 dBHz, DU-HTL can re-track signal quickly, but DU-STL methods could not. The VFLL in DU-HTL can keep the signal frequency locked in the weak signal environments or transient loss, so that the carrier phase can be relocked quickly when the signal strength returns to normal. Comparing the DU-HTL method of different update-rate of VFLL, it is shown that the longer update interval of VFLL, the frequency tracking errors are greater during signal loss.

4 Conclusion

A scalar and vector hybrid tracking loop based on the DUKF for the new generation GNSS signal is studied, where the VFLL is used for pilot channels with long coherent integration time and the SPLL is used for data channel with the short

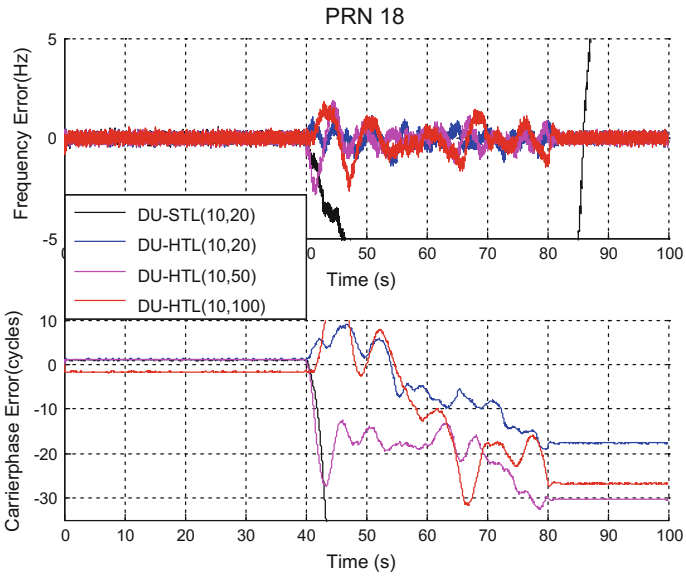

Fig. 6 Carrier tracking error of PRN = 18

coherent integration time correspondence with the message rate on it. The simulation and analysis results show that traditional dual update-rate STL method, the carrier phase tracking accuracy of DU-HTL is litter higher, but the tracking robustness is better than DU-STL especially in the signal shielding environment. Compared with the traditional sole VFLL structure, the VFLL in DU-HTL can work as a low update-rate as sub-second, so the computational burden can be reduced significantly.

References

1. BeiDou Navigation Satellite System Signal In Space Interface Control Document Open Service Signal, Version 2.0. (2013) China Satellite Navigation Office
2. IS-GPS-705-A (2010) Global positioning system wing systems engineering &integration interface specification IS-GPS-705, Rev A. Navstar GPS Space Segment/User Segment L5 Interfaces
3. OS SIS ICD Issue 1 (2010) European GNSS (Galileo) open service signal in space interface control document
4. Jovanovic A, Mongredien C, Tawk Y et al (2011) Implementation and optimization of a Galileo E1 two-step tracking algorithm using data/pilot combining and extended integration time. ION ITM 2011, Institute of Navigation, Portland OR, pp 3756–3766
5. Muthuraman K (2010) Adaptive data pilot carrier phase tracking for modernized GNSS signals. ION ITM 2010, The Institute of Navigation, San Diego, CA, pp 736–749
6. Shen Y, Zhang L, Fu Z (2012) The research on the combination of discriminators in Galileo L1F signal carrier tracking loop. J Astronaut 33(3):380–386

7. Yao Z, Cui X, Lu M (2009) Dual update-rate carrier tracking technique for new generation global navigation satellite system signals in dynamic environments. IET Radar Sonar Navig 3 (3):203–213
8. Li J, Yao Z, Cui X (2011) Dual Update-rate FLL-assisted phase lock loop of novel robust receivers for new generation global navigation satellite signals. ION ITM 2011, Institute of Navigation, Portland OR, pp 3652–3659
9. Lv P, Lu M, Yao Z (2013) Dual update-rate INS aided carrier phase lock loop for new generation global navigation satellite signals. CSNC 2013, Wuhan, pp 715–724
10. Lashley M, Bevly D, Petovello M (2009) What are vector tracking loops and what are their benefits and drawbacks. GNSS Solut Column Inside GNSS 4(3):16–21
11. Lashley M, Bevly D (2009) Vector delay/frequency lock loop implementation and analysis. ION ITM 2009, Institute of Navigation, Anaheim, CA, pp 1073–1086
12. Lashley M, Bevly D (2009) Performance analysis of vector tracking algorithms for weak GPS signals in high dynamics. IEEE J Sel Topics Signal Process 3(4):661–673
13. Won J, Eissfeller B (2010) Effectiveness analysis of vector-tracking-loop in signal fading environment. In: Proceedings NAVITEC2011, ESTEC, Noordwijk, The Netherlands, pp 1–12
14. Zhodzishsky M, Yudanov S, Ashjaee J (1998) Co-op tracking for carrier phase. ION GPS-98, Nashville, TN, pp 653–664
15. Henkel P, Giger K, Gvnther C (2009) Multifrequency, multisatellite vector phase-locked loop for robust carrier tracking. IEEE J Sel Topics signal Process 3(4):674–681
16. Petovello M, Lachapelle G (2006) Comparison of vector-based software receiver implementations with application to ultra-tight GPS/INS integration. ION GNSS 2006, Institute of Navigation, Fort Worth, pp 1790–1799
17. Stefan K, Christian A, Daniel G et al (2008) GNSS receiver with vector based FLL-assisted PLL carrier tracking loop. ION GNSS 2008, Institute of Navigation, Savannah, CA, pp 197–203
18. Lin H, Huang Y, Tang X, Xiao Z, Ou G Robust multiple update-rate Kalman filter for new generation GNSS signals carrier tracking. GPS solution, Submission to publish

A Kinematic GNSS Positioning Method Based on Unscented Kalman Filter

Chunhua Li, Guofu Pan, Chenglin Cai, Chenggang Li and Xiaoyu Shi

Abstract When satellite signal is keep out seriously, the number of satellites is insufficient, multipath effect heavily affected, kalman filter positioning will appear filtering divergence and the least-squares positioning easily arise large deviation, this paper put forward a kinematic GNSS positioning method based on unscented kalman filter (UKF) with single and double difference at a time among adjacent coordinates to smooth the positioning results in order to modifying the calculated every epoch coordinate. Multi-group experiments results showed that this method can eliminate positioning deviation points and realize the continuity and validity of the positioning. At present the method has been successfully applied to wearable device in Hi-Target Surveying Instrument Co. Ltd, which offered wearable device sufficient insurance on the continuity and validity of positioning.

Keywords Kinematic positioning · The first difference · The second difference · Unscented kalman filter

1 Introduction

Kinematic GNSS positioning technology is been widely used in all kinds of life, so both its accuracy and reliability of positioning precision are required to be higher. However, cycle slip and data interruption can always occur due to the loss of satellite signal and serious lack of satellites, kalman filter positioning will appear filtering divergence and the least-squares positioning easily arise large deviation. In order to overcome this issue and improve the positioning precision, the laws of the moving object is modeled as an specific equation such as uniform motion model,

C. Li (✉) · G. Pan · C. Li · X. Shi
Hi-Target Surveying Instrument Co. Ltd, Guangzhou 511400, China
e-mail: chunlihua@126.com

C. Cai
Institute of Information and Communication, Guilin University of Electronic Technology, Guilin 541004, China

J. Sun et al. (eds.), *China Satellite Navigation Conference (CSNC) 2017 Proceedings: Volume I*, Lecture Notes in Electrical Engineering 437,
DOI 10.1007/978-981-10-4588-2_67

accelerated motion model, linear approximation model, and curve approximation model [1–4]. Simultaneously, a kinematic GNSS positioning method based on unscented kalman filter (UKF) with single and double difference at a time among adjacent coordinates to smooth the positioning results in order to modifying the calculated every epoch coordinate. Multi-group experiments results showed that this method can eliminate positioning deviation points and realize the continuity and validity of the positioning. At present the method has been successfully applied to wearable device in Hi-Target Surveying Instrument Co. Ltd, which offered wearable device sufficient insurance on the continuity and validity of positioning.

2 The Principle of This Algorithm

The principle of this method is that we used the least square algorithm [5–7] or kalman filter method [8, 9] to calculate the coordinates in a fixed period at first, then these coordinates can be made single difference and double difference at a time, finally the UKF is been used to smooth the coordinates, where the first difference at a time among the coordinates is velocity and the second difference at a time among the coordinates is acceleration. The coordinates of X direction, Y direction, and Z direction have been smoothed separately in the method, and the detailed procedures are listed as follows:

Step one: the single difference at a time among the coordinates.

We can get $(x_2 - x_1, y_2 - y_1, z_2 - z_1)$, $(x_3 - x_2, y_3 - y_2, z_3 - z_2)$ $(x_4 - x_3, y_4 - y_3, z_4 - z_3), \ldots, (x_n - x_{n-1}, y_n - y_{n-1}, z_n - z_{n-1})$ by making single difference at a time among the coordinates: (x_1, y_1, z_1), (x_2, y_2, z_2), (x_3, y_3, z_3), (x_n, y_n, z_n), we set $X_1 = [x_2 - x_1, x_3 - x_2, x_4 - x_3, \ldots, x_n - x_{n-1}]$, $Y_1 = [y_2 - y_1, y_3 - y_2, y_4 - y_3, \ldots, y_n - y_{n-1}]$, $Z_1 = [z_2 - z_1, z_3 - z_2, z_4 - z_3, \ldots, z_n - z_{n-1}]$ for a very convenient representation in this paper.

Step two: the double difference at a time among the coordinates.

Making single difference at a time again among these coordinates: $(x_2 - x_1, y_2 - y_1, z_2 - z_1), (x_3 - x_2, y_3 - y_2, z_3 - z_2), (x_4 - x_3, y_4 - y_3, z_4 - z_3), \ldots, (x_n - x_{n-1}, y_n - y_{n-1}, z_n - z_{n-1})$, get $X_{11} = [(x_3 - x_2) - (x_2 - x_1), (x_4 - x_3) - (x_3 - x_2), (x_5 - x_4) - (x_4 - x_3), \ldots, (x_n - x_{n-1}) - (x_{n-1} - x_{n-2})]$ $Y_{11} = [(y_3 - y_2) - (y_2 - y_1), (y_4 - y_3) - (y_3 - y_2), (y_5 - y_4) - (y_4 - y_3), \ldots, (y_n - y_{n-1}) - (y_{n-1} - y_{n-2})]$, $Z_{11} = [(z_3 - z_2) - (z_2 - z_1), (z_4 - z_3) - (z_3 - z_2), (z_5 - z_4) - (z_4 - z_3), \ldots, (z_n - z_{n-1}) - (z_{n-1} - z_{n-2})]$.

Step three: constructing a matrix.

In order to avoid redundancy, this paper described the procedures of X direction coordinates in details. As for X direction coordinates, we treat $[x_3, x_4, \ldots, x_n]$ as the first row of the matrix, and treat $[x_3 - x_2, x_4 - x_3, \ldots, x_n - x_{n-1}]$ as the second row

of the matrix,then treat $[(x_3 - x_2) - (x_2 - x_1), (x_4 - x_3) - (x_3 - x_2), \ldots, (x_n - x_{n-1}) - (x_{n-1} - x_{n-2})]$ as the third row of the matrix, so we can construct a matrix $X = \begin{bmatrix} x_2 & \cdots & x_{n-1} \\ x_3 - x_2 & \cdots & x_n - x_{n-1} \\ (x_3 - x_2) - (x_2 - x_1) & \cdots & (z_n - z_{n-1}) - (z_{n-1} - z_{n-2}) \end{bmatrix}$, the procedures to deal with Y direction coordinates and Z direction coordinates are the same to X direction coordinates, we can construct a matrix $Y = \begin{bmatrix} y_2 & \cdots & y_{n-1} \\ y_3 - y_2 & \cdots & y_n - y_{n-1} \\ (y_3 - y_2) - (y_2 - y_1) & \cdots & (y_n - y_{n-1}) - (y_{n-1} - y_{n-2}) \end{bmatrix}$,
$Z = \begin{bmatrix} z_2 & \cdots & z_{n-1} \\ z_3 - z_2 & \cdots & z_n - z_{n-1} \\ (z_3 - z_2) - (z_2 - z_1) & \cdots & (z_n - z_{n-1}) - (z_{n-1} - z_{n-2}) \end{bmatrix}$.

Step four: Calculating square-error and constructing square-error matrix.

As for X direction coordinates, the element p can be got by calculating the variance in the first row of matrix X, p_1 can be obtained using the second row of matrix X, and p_{11} is calculated by using the third row of matrix X. we construct a matrix P as follows:

$$P = \begin{bmatrix} p & 0 & 0 \\ 0 & p_1 & 0 \\ 0 & 0 & p_{11} \end{bmatrix} \tag{1}$$

Step five: Using UKF filter method to process.

We hope to directly process the observation value $(x_1, x_2, x_3, \ldots, x_n)$, because of the use of single difference and double difference at a time, x_1 and x_2 did not be processed, we just smooth $x_3, \ldots, x_n$, we set $X = [\chi_3, \chi_4, \ldots, \chi_n]$, where $\chi_3 = [\, x_2, x_3 - x_2, (x_3 - x_2) - (x_2 - x_1)]^T$, $, \ldots, \chi_n = [\, x_{n-1}, x_n - x_{n-1}, (x_n - x_{n-1}) - (x_{n-1} - x_{n-2})]^T$, the detailed filter procedures are listed as follows:

(a) Produce 2n + 1 Sigma point.

$$X_{k,0} = \overline{X_k} = \chi_3 \tag{2}$$

$$X_{k,i} = \begin{cases} \overline{X_k} + (\sqrt{(m+\lambda)\sum \overline{X_k}})_{i-1} \quad (i = 1, \ldots, m) \\ \overline{X_k} - (\sqrt{(m+\lambda)\sum \overline{X_k}})_{i-m-1} \quad (i = m+1, \ldots, 2m) \;\; W_0^m = \lambda/(m+\lambda) \end{cases} \tag{3}$$

$$W_0^c = \lambda/(m+\lambda) + (1 - \alpha^2 + \beta) \tag{4}$$

$$W_i^m = W_i^c = 0.5/(m+\lambda) \quad (i = 1, \ldots, 2m) \tag{5}$$

where m (m = 3) is the number of state parameters, $\lambda = \alpha^2(m+\kappa) - m$ is the scaling factor; α represents the distance between Sigma and $\overline{X_k}$, and usually setting $10^{-4} \leq \alpha \leq 1$, κ is the constant, setting to 0 or (3-m); β is used to integrate the prior information of prediction vector, setting $\beta = 2$ is optimal while considering Gaussian distribution; $(\sqrt{(m+\lambda)\sum \overline{X_k}})_i$ is the i-th column elements of the matrix's square root which can be obtained by Cholesky decomposition method.

(b) Using the process model to transform sigma points, and that is making unscented transformations of state variables.

$$\chi_i[k+1/k] = f[\chi_i(k/k)] \quad (i = k = 3, 4, 5, \ldots, n) \tag{6}$$

where $f[.]$ is the state shift function of the unscented transformation.

(c) Calculating predict estimate value.

$$\widehat{X}(k+1/k) = \sum_{i=0}^{2n} W_i^{(m)} \chi_i(k+1/k) \tag{7}$$

(d) Calculating predicted covariance.

$$P(k+1/k) = \sum_{i=0}^{2n} W_i^{(c)} [\chi_i(k+1/k) - \widehat{X}(k+1/k)]^T \tag{8}$$

(e) Calculating measurements with measuring equations.

$$Z_i(k+1/k) = h[\widehat{X}(k+1/k)] \tag{9}$$

where $h[.]$ is observation function of the unscented transformation.

(f) Calculating the predicted measuring values

$$\widehat{Z}(k+1/k) = \sum_{i=0}^{2n} W_i^{(m)} Z_i(k+1/k) \tag{10}$$

(g) Calculating the variance of the information.

$$P_{zz}(k+1/k) = \sum_{i=0}^{2n} W_i^{(c)} [Z_i(k+1/k) - \widehat{Z}(k+1/k)][Z_i(k+1/k) - \widehat{Z}(k+1/k)]^T \tag{11}$$

(h) Calculating the covariance P_{xz} between $\widehat{X}(k+1/k)$ and $\widehat{Z}(k+1/k)$

$$P_{xz}(k+1/k) = \sum_{i=0}^{2n} W_i^{(c)}[\chi_i(k+1/k) - \widehat{X}(k+1/k)][Z_i(k+1/k) - \widehat{Z}(k+1/k)]^T \tag{12}$$

(i) Calculating kalman gains.

$$K(k+1) = P_{xz}P_{zz}^{-1} \tag{13}$$

(j) Updating error covariance.

$$P(k+1/k) = P(k+1/k)] - k(k+1)P_{xz}k^T(k+1) \tag{14}$$

(k) Updating the state.

$$\widehat{X}(k+1/k+1) = \widehat{X}(k+1/k) + K(k+1)[Z(k+1) - \widehat{Z}(k+1/k)] \tag{15}$$

Step six: RTS (Real-time smooth) process.

In order to make positioning curve get smoother, we use the RTS method to smooth the point results after processed by UKF method.

Initial value is define as follows:

$$X_N^s = \widehat{X}_{N/N} \tag{16}$$

$$P_N^s = P_{N/N} \tag{17}$$

when $k = N-1, \ldots, 1, 0$, process coordinates according to the following equation:

$$Z_{f,k+1} = (P_{k+1/k})^{-1} \tag{18}$$

$$K_k = P_{k/k}A^T Z_{f,k+1} \tag{19}$$

$$P_k^s = P_{k/k} - K_k(P_{k+1/k} - P_{k+1}^s)K_k^T \tag{20}$$

$$x_k^s = \widehat{X}_{k/k} + K_k(x_{k+1}^s - \widehat{X}_{k+1/k}) \tag{21}$$

The X direction coordinates can be smoothed in this way, the results in present epoch can be obtained by using the present and the former epoch positioning results. Moreover, this means we can check the present epoch result by comparing the result smoothed before and after. Thus, the procedures to deal with the Y direction coordinates and Z direction coordinates are the same to X direction coordinates.

Essentially, UKF is a method to estimate the state of parameters, where the estimation of the parameters of the system realized in a joint estimation manner.

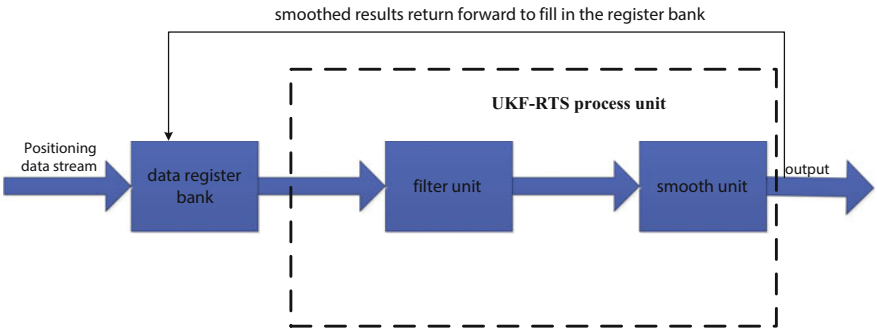

Fig. 1 UKF-RTS real-time process flow

This joint estimation is a simple method, only adding the parameters to the end of the state variables to consist of an augmented state matrix. The most important point of UKF is how to determine the number of sigma points, the positions of sigma points, and its weigh. At present, the 2n + 1 Sigma point strategy is more popular, these sigma points generated by using the present estimation value and the volume of matrix $\pm(n+k)P$ are a symmetrical distribution on X direction coordinates and have the same means and variance of state variables. This paper adopted the sliding window mechanism to reach the aim of smoothing and checking the result. By this way, the present epoch and former epochs can be used to smooth the present positioning result. The UKF-RTS Real-time Process flow chart is shown in Fig. 1.

3 Numerical Examples Validate This Algorithm

The suitability and practicability of this method are proved through examples with static data and dynamic data. Static data was collected on known points and measured by self-developed receiver called iRTK2 in our company, iRTK2 is shown in Fig. 2, the built-in motherboard of iRTK2 is Trimble motherboard, dynamic data was collected in Tian'an technology park in Panyu of Guangzhou city using self-developed wearable devices in our company, wearable device is shown in Fig. 3, the built-in motherboard of wearable device is ublox high-precision module.

3.1 Numerical Examples Validate This Algorithm with Static Data

In view of static data, we decode the raw data into Rinex 3.02 data format at first, in order to validate this algorithm we employ two kinds of schemes: least-square method is adopted for the pseudo-range single point positioning in view of the

Fig. 2 Measurement receiver iRTK2

Fig. 3 Wearable device

GPS/BDS in scheme one; standard kalman filtering method is adopted for the pseudo-range single point positioning in view of the GPS/BDS in scheme two; the method put forward in this paper is adopted for the pseudo-range single point positioning in view of the GPS/BDS in scheme three. Experiments results are shown in Figs. 4 and 5.

From Figs. 4 and 5, we can see that compared with the least squares method, the positioning curve of kalman filter method is more smooth, but the tracking

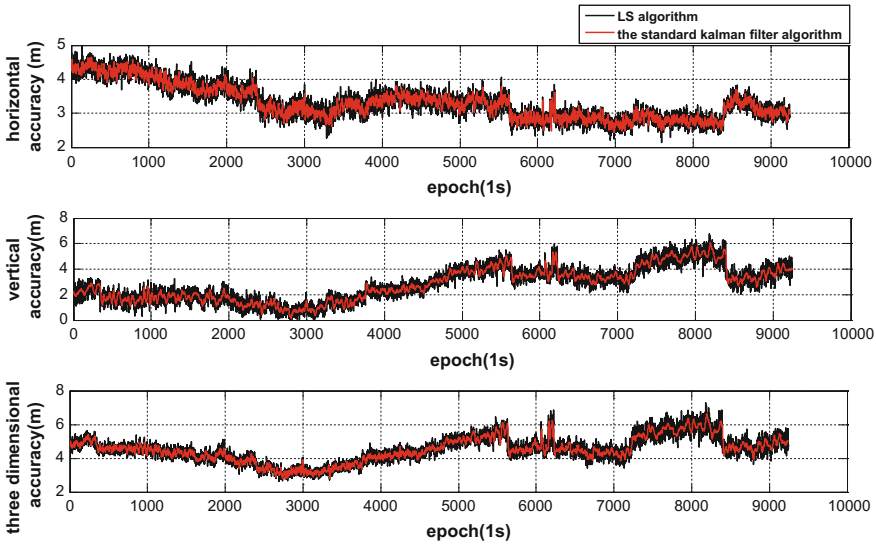

Fig. 4 Positioning results comparison between standard kalman filter algorithm and LS algorithm in static data

trajectory of the method put forward in this paper is the most smooth in all methods, not large hops any all, The reasons is that the algorithm used single and double difference at a time among coordinates of the positioning results a short time ago to obtain the velocity and acceleration information of vehicle, then combined with the current calculated point coordinates to get the final point coordinates. Figures 4 and 5 indicate that this algorithm is very effective to the static positioning, so it has certain reference significance on deformation monitoring.

3.2 Numerical Examples Validate This Algorithm with Dynamic Data

We adopt the post-processing method to validate this algorithm by using satellite raw data received by ublox module, we employ three kinds of schemes: the first scheme, wearable module output single point positioning solution of the least squares method only, compared the results of the least squares method with that combined with the algorithm in this paper; the second scheme, wearable module output RTD, (Real-time pseudo-range difference, RTD) [10] only, compared the results of RTD with that combined with the algorithm in this paper; the third scheme, wearable module output RTK (Real-time kinematic difference, RTK) solution only [10], compared the results of RTK with that combined with the algorithm in this paper. RTK solutions including fixed and float solutions, because

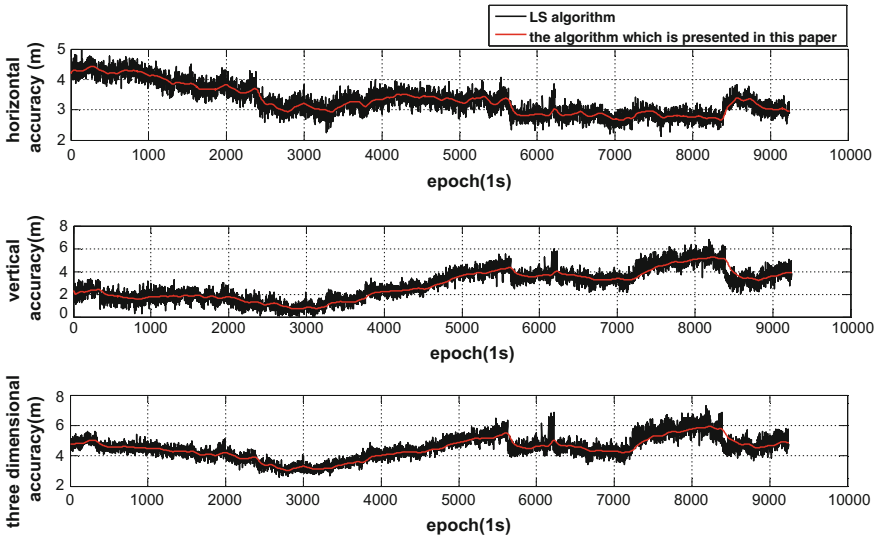

Fig. 5 Positioning results comparison between the algorithm which is presented in this paper and LS algorithm in static data

of the high precision of itself, the algorithm of this paper is just to do check the results, when the difference between the RTK solution combined with the algorithm presented in this paper and the RTK solutions is more than two meters, we just put the RTK solution with the algorithm presented in this paper as the final results; the reasons to select the three solutions are that the single point positioning and RTD solutions is served for the class of meter level navigation; RTD and RTK solutions is served for the class of sub-meter and centimeter level navigation. We choose technology park where our company located for dynamic testing to validate this algorithm, the park has many tall buildings, the verification results were shown in Figs. 6, 7 and 8.

From Figs. 6, 7 and 8, we could draw the following conclusion:

Figures 6 and 7 indicate that the single point positioning solution and RTD solution becomes smoother and there will be no big hops after joining algorithm in this paper;

From Fig. 8, we can see that the algorithm presented in this paper has very good judgment ability for RTK solution which is in the abnormal situation, and which can effectively eliminate abnormal situation.

Through the comparative analysis of dynamic data and static data, this algorithm makes wearable equipment can effectively guarantee the continuity and reliability of positioning in poor park environment.

Fig. 6 Positioning results of the first scheme (position results of single point positioning is *red*, while position results of improved single point positioning combined with the algorithm which is presented in this paper is *green*)

Fig. 7 Positioning results of the second scheme (position results of pseudo-range difference positioning is *red*, while position results of improved pseudo-range difference positioning combined with the algorithm which is presented in this paper is *green*)

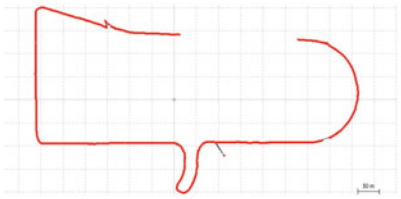

RTK solutions

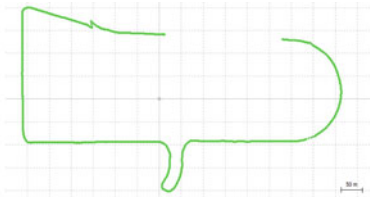

RTK solutions combined with the algorithm which is presented in this paper

Fig. 8 Positioning results of the third scheme (position results of real-time kinematic positioning is *red*, while position results of improved real-time kinematic positioning combined with the algorithm which is presented in this paper is *green*) (color figure online)

3.3 Experiments Validate the Integrity of This Algorithm

We choose the harsh environment to validate the integrity of this algorithm in the park where our company located. Put the RTK positioning results of self-developed measuring receiver as a benchmark, using self-developed two wearable device which tied to measuring receiver for test, as shown in Fig. 9, one adopted the algorithm presented in this paper, the other is not using the algorithm of this paper, two sets of wearable devices output RTD solutions. we make comparison between real-time results of the wearable devices and real-time RTK results of the measuring receiver, the statistical results about the proportion of horizon precision which is less than 0.5, 1.0, 1.5 m as shown in Table 1.

Table 1 indicates that the positioning accuracy of wearable device which adopted this algorithm is higher, these results show us that this algorithm also play a role in harsh environment and it has a good reliability.

4 Conclusions

The proposed method in this paper could smooth the positioning results in order to modifying the calculated coordinates among epochs combined UKF filter with single and double difference at a time in coordinates. Through multiple sets of tests of the static and dynamic data, the experimental results show that this algorithm can eliminate positioning deviation points and realize the continuity and validity of the positioning. Therefore, it has a certain reference value for real-time navigation

Fig. 9 Test fixture

Table 1 The comparison between real-time positioning results of two wearable devices and that of measuring receiver

Horizon precision (m)	<0.5	<1.0	<1.5
Use this algorithm (%)	22.01	66	89.7
Not use this algorithm (%)	18.20	43	64.6

module and unmanned aerial vehicle (uav) navigation module, also have certain reference significance in deformation monitoring at the same time.

Acknowledgements The authors are grateful to *Hi-Target Surveying Instrument Co. Ltd for supporting a good technology* platform. This research is supported by the National Natural Science Foundation (61263028), Science and Technology Plan Project of Guangzhou city (201604010075), "Collaborative Precision Positioning" Project of National Key Research Program of China (2016YFB0501900).

References

1. Li B, Shen Y, Zhou Z (2010) Approximation models with moving window in the pseudo-range kinematic GPS positioning. J Geod Geodyn 143–180
2. Jiexian Wang, Shanbiao Ji, Dajie Liu (1999) Calculation model for GPS pseudorange positioning. J Tongji Univ 27(5):530–535
3. Yang Y, He H, Xu T (2001) Adaptive robust filtering for kinematic GPS positioning. Acta Geodaetica et Cartographica Sinica 30(4):293–298
4. Yang Y, Xu T (2003) An adaptive kalman filter combining variance component estimation with covariance matrix estimation based on moving window. Geomat Inf Sci Wuhan Univ 28 (6):714–718
5. Li C, Cai C, Liang Y, Xu L (2015) A high-precision weighted least squares algorithm for BDS pseudo-range single point positioning. Sci Surv Mapp 40(9):33–38
6. Kaplan ED, Hegarty CJ (2007) Understanding GPS: principles and applications, 2nd edn (trans: Kou Y). Publishing House of Electrical Industry, Beijing, pp 36–42
7. Li C, Cai C, Deng K et al (2014) A fast pseudo-range single point positioning algorithm for the Beidou navigation system based on weighted least squares. J Chongqing Univ Posts Telecommun (Natural Science Edition) 26(4):466–472
8. Yang Y (2006) Adaptive kinematic navigation positioning. Surveying and Mapping Press, Beijing
9. Zhao Q (2013) The research and implementation of kalman filter in GPS positioning system. University of Electronic Science and Technology of China, pp 33–49
10. Li Z, Huan J (2010) GPS surveying and data processing. Wuhan University Press

Analysis of Cross-Correlation Peak Distortion Caused by Antenna Array Space-Time Adaptive Processing

Xinzhi Dai, Junwei Nie, Baiyu Li, Zukun Lu and Gang Ou

Abstract Space-time adaptive processing (STAP) combines information available from both spatial and temporal domains, which can effectively enhance the GNSS receivers' performance of interference suppression. But STAP has the potential to distort cross-correlation peak, which would deteriorate acquisition and tracking performance. In this paper, the cross-correlation peak distortion under space-time power inversion (PI) criterion and minimum variance distortionless response (MVDR) criterion are analyzed by theoretical analysis and simulations. Analysis and simulation show that the spatial correlation coefficient between interference and desired signal, taps number of Tapped Delay Line (TDL) and taps delay can directly affect the cross-correlation peak. The conclusions can be used to optimize the antenna array design and space-time adaptive algorithm for reducing cross-correlation peak distortion caused by STAP.

Keywords Antenna array · Space-time adaptive processing · Cross-correlation peak

1 Introduction

The Globe Navigation Satellite System (GNSS) can provide users with high-precision time and position information [1]. At present, GNSS is widely used in civilian and military field. GNSS signals received on the ground are very weak, so they are vulnerable to intentional and unintentional interference.

In order to maintain the integrity and functionality of GNSS receivers in environments with strong interference, antenna arrays are widely utilized in the GNSS receivers for anti-jamming. STAP is one of the applications of antenna array.

X. Dai · J. Nie (✉) · B. Li · Z. Lu · G. Ou
Satellite Navigation Research and Development Center,
National University of Defense Technology, Changsha, China
e-mail: njw1004@126.com

J. Sun et al. (eds.), *China Satellite Navigation Conference (CSNC) 2017 Proceedings: Volume I*, Lecture Notes in Electrical Engineering 437,
DOI 10.1007/978-981-10-4588-2_68

STAP can combine the information available from both spatial and temporal domains, which can significantly improve GNSS receivers' anti-jamming performance. But at the same time, STAP would distort cross-correlation peak [3, 4]. The position errors caused by STAP can be several meters and even increase to hundreds meters. So the distortion of the cross-correlation peak must be mitigated for the high accuracy GNSS applications. At present, there are many studies on how to compensate the cross-correlation peak distortion caused by STAP [5–7]. While a few of those analyzes the causes of cross-correlation peak distortion. In reference [8], simulation is used to analyze the affection of STAP on the cross-correlation peak. In reference [9], [10], the theoretical model of cross-correlation peak distortion is analyzed, but the theoretical analysis is not sufficient. In short, the recent researches about the affection of STAP on cross-correlation peak are mainly based on simulation and lack of sufficient theoretical analysis. Studying the cross-correlation peak distortion caused by STAP can help mitigate the distortion and is useful for high accuracy GNSS applications.

In this paper, the theoretical model of cross-correlation peak distortion is analysed under space-time PI criterion and space-time MVDR criterion. And the theoretical model is verified by simulations.

2 Signal Model

An arbitrary antenna array with N elements and TDLs with M taps is considered. For the sake of simplicity and without loss of generality, only one GNSS signal and interfering signal are considered. The received signal vector, $\boldsymbol{x}(t)$, at the antenna array can be expressed as

$$\boldsymbol{x}(t) = \boldsymbol{a}_s s(t) + \boldsymbol{a}_J J(t) + \boldsymbol{n}(t) \tag{1}$$

where $s(t)$ is the GNSS signal, $J(t)$ is the interference, $\boldsymbol{n}(t)$ is complex white Gaussian noise vector, $\boldsymbol{a}_s$ is the steering vector of the GNSS signal and $\boldsymbol{a}_J$ is the signal steering vector of interference.

In a STAP processor, the output signal, $y_{out}(t)$, can be expressed as

$$y_{out}(t) = \boldsymbol{w}^H \boldsymbol{x}'(t) \tag{2}$$

where $\vec{\boldsymbol{x}}(t) = [\boldsymbol{x}^T(t), \boldsymbol{x}^T(t - T_s), \cdots, \boldsymbol{x}^T(t - (M-1)T_s)]^T$ and T denotes transpose, T_s is the tap delay which is usually the sampling duration, $\boldsymbol{w}$ is space-time weight vector, H denotes conjugate transpose.

The weight vector in STAP is determined by the weighting criterion. In this paper, the space-time PI criterion and space-time MVDR criterion are chosen for analysis. The weight vector of the space-time PI criterion can be expressed as

$$\boldsymbol{w} = \mu \boldsymbol{R}_{xx}^{-1} \boldsymbol{b} \tag{3}$$

where μ is a constant, $\boldsymbol{R}_{xx}$ is the space-time correlation matrix, $\boldsymbol{b} = [0, \cdots, 1, \cdots, 0]_{1\times MN}^{T}$ and the position of 1 is determined by the reference tap. The weight vector of the space-time MVDR criterion can be expressed as

$$\boldsymbol{w} = \mu \boldsymbol{R}_{xx}^{-1} \boldsymbol{a} \tag{4}$$

where μ is also a constant, $\boldsymbol{a} = \left[0, 0, \cdots, \boldsymbol{a}_s^T, \cdots, 0, 0\right]_{1\times MN}^{T}$ and the position of $\boldsymbol{a}_s$ is determined by the reference taps.

3 Analysis of Cross-Correlation Peak Distortion

According to reference [11], the output of the desired signal can be expressed as

$$y_s = \sum_{m=1}^{M} \boldsymbol{w}_m^H \boldsymbol{a}_s s(t - (m-1)T_s) \tag{5}$$

where $\boldsymbol{w}_m = \left[w_{1,m}, w_{2,m}, \cdots, w_{N,m}\right]^T$, $(m = 1, 2, \cdots M)$ represents the weight vector at the m th tap of TDLs. The cross-correlation function (CCF) of the desired signal can be obtained by correlating the output signal with the local signal replicas. It can be expressed as

$$C(\tau) = \sum_{m=1}^{M} h(m) R(\tau - (m-1)T_s) \tag{6}$$

where $h(m) = \boldsymbol{w}_m^H \boldsymbol{a}_s, (m = 1, 2, \cdots, M)$ is the transfer coefficient of CCF, $R(\tau)$ is the ideal CCF. The main focus here is on the distortion of the cross-correlation peak, CCF will be just referred to as cross-correlation peak in the sequel.

It can be seen from Eq. (6) that the signal steering vector, weight vector, tap delay and the taps number will directly affect the cross-correlation peak. But the results getting from Eq. (6) are not very satisfactory, because the impact of these parameters on the cross-correlation peak is not clear. In this paper, we will further analyze Eq. (6) under specific criteria.

3.1 Analysis of Cross-Correlation Peak Distortion Under Space-Time PI Criterion

Without loss of generality, we assume that the first tap of the first antenna element is the reference tap, so $\boldsymbol{b} = [1, 0, \cdots, 0]^T_{1\times MN}$. The inversion of the space-time covariance matrix is derived in Appendix A. By substituting Eq. (22) and $\boldsymbol{b}$ into Eq. (3), the weight vector of space-time PI criterion can be obtained as

$$\boldsymbol{w} = \frac{\mu}{\delta_n^2}\left[\boldsymbol{b} - \sum_{i=1}^{M}\frac{\lambda_i}{N\lambda_i + \delta_n^2}\boldsymbol{u}_{i,1}^*(\boldsymbol{u}_i \otimes \boldsymbol{a}_J)\right] \tag{7}$$

where $\boldsymbol{u}_{i,1}$ is the first element of $\boldsymbol{u}_i$. The transfer vector, $\boldsymbol{h}$, formed by the transfer coefficients can be calculated as

$$\begin{aligned}\boldsymbol{h} &= [\,h(1) \quad h(2) \quad \cdots \quad h(M)\,]^T \\ &= \left[\boldsymbol{I}_{M\times M} \otimes \boldsymbol{a}_s^T\right]\boldsymbol{w}^* \\ &= \frac{\mu}{\delta_n^2}\left[\left[\boldsymbol{I}_{M\times M} \otimes \boldsymbol{a}_s^H\right]\boldsymbol{b} - \sum_{i=1}^{M}\frac{\lambda_i \boldsymbol{a}_s^T \boldsymbol{a}_J^*}{N\lambda_i + \delta_n^2}\boldsymbol{u}_{i,1}\boldsymbol{u}_i^*\right]\end{aligned} \tag{8}$$

Suppose that $J(t) = b(t)e^{jwt}$ is a narrow-band interference, where $b(t)$ is the baseband signal and $b(t - mT_s) \approx b(t), (m = 1, \cdots M-1)$, e^{jwt} is the intermediate frequency (IF) carrier. The temporal correlation matrix of interference can be expressed as

$$\boldsymbol{R}_J = P_J\begin{bmatrix} 1 & e^{jwT_s} & \cdots & e^{jw(M-1)T_s} \\ e^{-jwT_s} & 1 & \cdots & e^{jw(M-2)T_s} \\ \vdots & \vdots & \ddots & \vdots \\ e^{-jw(M-1)T_s} & e^{-jw(M-2)T_s} & \cdots & 1 \end{bmatrix} \tag{9}$$

where P_J is the interference power. The only nonzero eigen value of $\boldsymbol{R}_J$ is MP_J and the corresponding normalized eigen vector is $\boldsymbol{u} = \left[\frac{1}{\sqrt{M}} \quad \frac{1}{\sqrt{M}}e^{-jwT_s} \quad \cdots \quad \frac{1}{\sqrt{M}}e^{-jw(M-1)T_s}\right]^T$. The spatial correlation coefficient between interference and the desired signal is $\rho = \boldsymbol{a}_s^T\boldsymbol{a}_J^*/N$ [12]. Hence, Eq. (8) can be rewritten as

$$\boldsymbol{h} = \frac{\mu}{\delta_n^2}\left\{[\,1 \quad 0 \quad \cdots \quad 0\,]^T - \frac{MNP_J\rho}{MNP_J + \delta_n^2}\left[\,\frac{1}{M} \quad \frac{1}{M}e^{jwT_s} \quad \cdots \quad \frac{1}{M}e^{jw(M-1)T_s}\,\right]^T\right\} \tag{10}$$

In practice, the interference power is much higher than the noise power, so we get $MNP_J/\left(NMP_J+\delta_n^2\right)\approx 1$. Hence, one gets

$$\boldsymbol{h}=\frac{\mu}{\delta_n^2}\left[1-\frac{\rho}{M}\quad -\frac{\rho}{M}e^{jwT_s}\quad \cdots \quad -\frac{\rho}{M}e^{jw(M-1)T_s}\right]^T \tag{11}$$

The cross-correlation peak under space-time PI criterion can be obtained as

$$\begin{aligned} C(\tau)&=\sum_{m=1}^{M}h(m)R(\tau-(m-1)T_s)\\ &=\frac{\mu}{\delta_n^2}\left[\left(1-\frac{\rho}{M}\right)R(\tau)-\frac{\rho}{M}\sum_{m=1}^{M-1}e^{jwmT_s}R(\tau-mT_s)\right] \end{aligned} \tag{12}$$

From Eq. (12), we can get that, (1) the actual cross-correlation peak $C(\tau)$ is formed by an ideal cross-correlation peak and $(M-1)$ delayed cross-correlation peaks, (2) the delayed cross-correlation peaks are attenuated by ρ/M and the ideal cross-correlation peak is attenuated by $1-\rho/M$. The following conclusions can be drawn: first, when the spatial correlation coefficient is small ($\rho\approx 0$), the actual cross-correlation peak is almost the same as the ideal peak; second, when the spatial correlation coefficient is large, the actual cross-correlation peak will be obviously distorted and the peak position is related to taps number and delay time. The analysis above is based on the assumption that the first tap of the first antenna element is the reference tap. When kth tap is selected as the reference tap, the general expression of Eq. (12) is

$$C(\tau)=\frac{\mu}{\delta_n^2}\left(1-\frac{\rho}{M}\right)R(\tau-(k-1)T_s)-\frac{\mu}{\delta_n^2}\frac{\rho}{M}\sum_{m=0,m\neq k}^{M-1}e^{jw(m-(k-1))T_s}R(\tau-mT_s) \tag{13}$$

3.2 Analysis of Cross-Correlation Peak Distortion Under Space-Time MVDR Criterion

Without loss of generality, we assume that the first taps of TDLs are selected as the reference taps, so we get $\boldsymbol{a}=\left[\boldsymbol{a}_s^T,0,\cdots,0,0\right]_{1\times MN}^T$. According to Eq. (4) and (22), the weight vector of space-time MVDR criterion can be obtained as

$$\boldsymbol{w}=\frac{\mu}{\delta_n^2}\left[\boldsymbol{a}-\sum_{i=1}^{M}\frac{\lambda_i N}{N\lambda_i+\delta_n^2}\rho\boldsymbol{u}_{i,1}^*(\boldsymbol{u}_i\otimes\boldsymbol{a}_J)\right] \tag{14}$$

then the transfer vector can be obtained as

$$\boldsymbol{h} = \frac{\mu N}{\delta_n^2}\left[1 - \frac{|\rho|^2}{M} \quad -\frac{|\rho|^2}{M}e^{jwT_s} \quad \cdots \quad -\frac{|\rho|^2}{M}e^{jw(M-1)T_s}\right]^T \tag{15}$$

where $|\cdot|$ denotes absolute value. The cross-correlation peak can be obtained as

$$\begin{aligned} C(\tau) &= \sum_{m=1}^{M} h(m)R(\tau - (m-1)T_s) \\ &= \frac{\mu N}{\delta_n^2}\left[\left(1 - \frac{|\rho|^2}{M}\right)R(\tau) - \frac{|\rho|^2}{M}\sum_{m=1}^{M-1} e^{jwmT_s}R(\tau - mT_s)\right] \end{aligned} \tag{16}$$

From Eq. (16), we can get that, (1) the actual cross-correlation peak is formed by an ideal cross-correlation peak and $(M-1)$ delayed cross-correlation peaks, (2) the delayed cross-correlation peaks are attenuated by ρ^2/M, (3) the actual cross-correlation peak has a gain of N times. Because the absolute value of ρ^2/M is smaller than that of ρ/M, It can be concluded that the distortion of cross-correlation peak under space-time MVDR criterion is smaller than that under space-time PI criterion when the interference is the same.

4 Simulation

In order to verify the theoretical model, a software-defined receiver is used for simulation. The simulation parameters are set as follows, the carrier frequency is 1268.52 MHz, IF is 46.52 MHz, the signal code rate is 10.23 MHz, the sampling rate is 62 MHz. The interference is a continuous wave (CW) interference and the center frequency is the same as the carrier frequency. The signal-to-noise ratio (SNR) is −25 dB, and the jamming-to-signal ratio (JNR) is 80 dB. The antenna array is a 4-element uniform circular array with a half wavelength.

The space-time PI criterion is simulated firstly. The taps number of TDL is 5 and the first tap of TDL is chosen as the reference tap. The cross-correlation peaks under four scenarios are simulated. The parameters of the four scenarios are shown in Table 1 and the simulation results are shown in Fig. 1.

It can be seen from Fig. 1 that when the spatial correlation coefficient is small (scenario 1 and scenario 2), the actual cross-correlation peak is almost the same as the ideal peak. When it becomes larger (scenario 3 and scenario 4), actual cross-correlation peak is obviously distorted and the peak position is shifted. The simulation results agree with the theoretical model.

The scenario 1 is simulated again under space-time PI criterion, but different taps of the first antenna element is chosen as the reference tap. And the corresponding cross-correlation peaks are shown in Fig. 2

Table 1 Parameters of four simulation scenarios

Scenarios	DOA of desired signal	DOA of interference	Spatial correlation coefficient
1.	Azimuth = 50, Elevation = 45	Azimuth = 300, Elevation = 2	0.002
2.	Azimuth = 11, Elevation = 24	Azimuth = 300, Elevation = 2	0.001
3.	Azimuth = 135, Elevation = 11	Azimuth = 300, Elevation = 2	0.9
4.	Azimuth = 285, Elevation = 20	Azimuth = 300, Elevation = 2	0.91

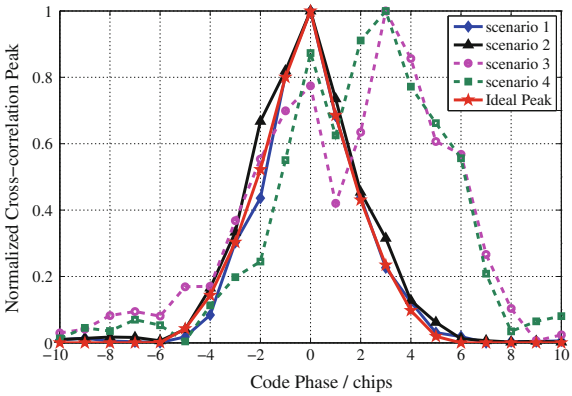

Fig. 1 Cross-correlation peaks under space-time PI criterion

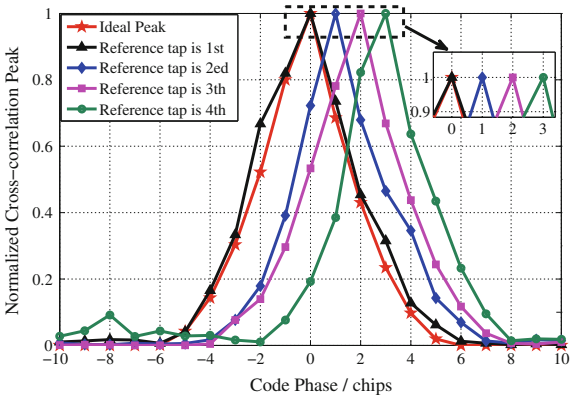

Fig. 2 cross-correlation peaks under different reference taps

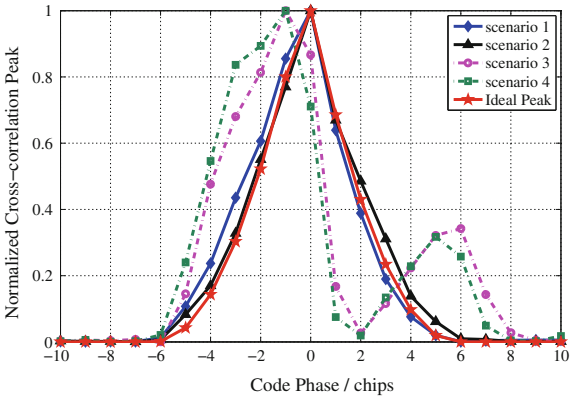

Fig. 3 Cross-correlation under space-time MVDR criterion

As can be seen from Fig. 2, when the spatial correlation coefficient is small enough, the reference tap position will affect the position of the actual cross-correlation peak. The simulation results verify the conclusion in Eq. (14).

The space-time MVDR criterion is simulated and the simulation scenarios are the same as the scenarios in Table 1. The first taps of TDLs are chosen as the reference taps. The results are shown in Fig. 3.

The conclusions drawn from Fig. 3 are similar to that drawn from Fig. 1. What's more, it can be found that when the spatial correlation coefficient is large (scenario 3 and scenario 4), the cross-correlation peak distrotion under space-time MVDR criterion is smaller than the case under space-time PI criterion. This result suggests that the space-time MVDR criterion can reduce the cross-correlation peak distortion comparing with the space-time PI criterion when the interference is the same. This conclusion also agrees with the theoretical model.

The scenario 1 is simulated under space-time MVDR criterion, and different taps of TDLs are chosen as the reference taps. The corresponding cross-correlation peaks are shown in Fig. 4.

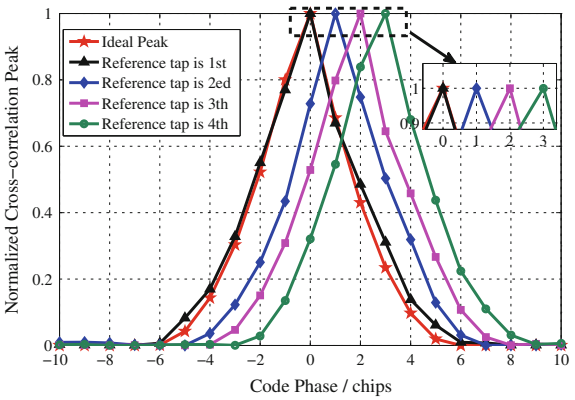

Fig. 4 Cross-correlation peaks under different reference taps

It can be seen from Fig. 4 that when the correlation coefficient is small enough, the position of the cross-correlation peak is determined by the position of reference taps, and it is similar to the case under space-time PI criterion.

5 Conclusion

The theoretical model of cross-correlation peak under space-time PI criterion and space-time MVDR criterion is established and verified by simulations. Analysis and simulation show that after STAP the actual cross-correlation peak is formed by M cross-correlation peaks and that is the main cause of cross-correlation peak distortion. The spatial correlation coefficient of the desired signal and interference is an important index that affects the cross-correlation peak. A small spatial correlation coefficient means a small distortion. The position of the reference tap is also an important index that affects the peak position of cross-correlation peak. When the correlation coefficient is small enough, the position of reference tap will directly determine the peak position of cross-correlation peak.

The above conclusion can provide the following guidance for reducing the cross-correlation peak distortion caused by STAP. Firstly, choose the antenna array with small spatial correlation coefficient. Because the spatial correlation coefficient is related to the array geometry, choosing the antenna array with small correlation coefficient can help reduce the cross-correlation peak distortion. Secondly, compensate the cross-correlation peak offset. Because the position of the reference tap may cause the peak position offset (unless the first tap of TDL is chosen as the reference tap), the signal processing after STAP must compensate the offset.

Appendix A

The space-time correlation matrix of the input signal, $\boldsymbol{x}'(t)$, can be written as

$$\boldsymbol{R}_{xx} = E\left[\boldsymbol{x}'(t)(\boldsymbol{x}'(t))^H\right] \tag{17}$$

In practice, interference power and noise power are much higher than the desired signal power, so the desired signal can be ignored in Eq. (17). Assuming the interference and the noise are not related. One gets

$$\boldsymbol{R}_{xx} = \boldsymbol{R}_{jj} + \delta_n^2 \boldsymbol{I} \tag{18}$$

where $\boldsymbol{R}_{jj}$ is the space-time correlation matrix of interference, δ_n^2 denotes the noise variance, $\boldsymbol{I}$ is a $MN \times MN$ unit matrix. Under narrowband assumption, the interference space-time correlation matrix can be written as

$$\boldsymbol{R}_{jj} = \boldsymbol{R}_J \otimes \left(\boldsymbol{a}_J \boldsymbol{a}_J^H\right) \tag{19}$$

where $\boldsymbol{R}_J$ represents the temporal correlation matrix, $\otimes$ denotes the Kronecker tensor product.

Because $\boldsymbol{R}_J$ is a Hermite matrix, its eigen value decomposition can be expressed as

$$\boldsymbol{R}_J = \sum_{i=1}^{M} \lambda_i u_i u_i^H \qquad (i = 1, 2, \cdots, M) \tag{20}$$

where λ_i is the eigen value, u_i is the corresponding eigen vector. $\boldsymbol{a}_J \boldsymbol{a}_J^H$ is also a Hermite matrix with only one nonzero eigen value which is N. According to the property of Hermite matrix, the nonzero eigen values of $\boldsymbol{R}_{jj}$ are $N\lambda_i$ and the corresponding eigen vectors are $\xi_i = \boldsymbol{u}_i \otimes \frac{\boldsymbol{a}_J}{\sqrt{N}}, (i = 1, 2, \cdots, M)$. According to Schmidt orthogonalization, the eigen vectors $\xi_i = \boldsymbol{u}_i \otimes \frac{\boldsymbol{a}_J}{\sqrt{N}}, (i = 1, 2, \cdots, M)$ can be extended to MN standard orthogonal eigen vectors. Hence, the eigen value decomposition of $\boldsymbol{R}_{xx}$ can be written as

$$\begin{aligned} \boldsymbol{R}_{xx} &= \sum_{i=1}^{M} N\lambda_i \left(\xi_i \xi_i^H\right) + \delta_n^2 \sum_{i=1}^{MN} \left(\xi_i \xi_i^H\right) \\ &= \sum_{i=1}^{M} \left(N\lambda_i + \delta_n^2\right)\left(\xi_i \xi_i^H\right) + \delta_n^2 \sum_{i=M+1}^{MN} \left(\xi_i \xi_i^H\right) \end{aligned} \tag{21}$$

The inverse of $\boldsymbol{R}_{xx}$ can be obtained as

$$\begin{aligned} \boldsymbol{R}_{xx}^{-1} &= \sum_{i=1}^{M} \frac{1}{N\lambda_i + \delta_n^2} \left(\xi_i \xi_i^H\right) + \frac{1}{\delta_n^2} \sum_{i=M+1}^{MN} \left(\xi_i \xi_i^H\right) \\ &= \frac{1}{\delta_n^2} \sum_{i=1}^{MN} \left(\xi_i \xi_i^H\right) - \frac{1}{\delta_n^2} \sum_{i=1}^{M} \frac{N\lambda_i}{N\lambda_i + \delta_n^2} \left(\xi_i \xi_i^H\right) \\ &= \frac{1}{\delta_n^2} \left[\boldsymbol{I} - \sum_{i=1}^{M} \frac{\lambda_i}{N\lambda_i + \delta_n^2} (\boldsymbol{u}_i \otimes \boldsymbol{a}_J)(\boldsymbol{u}_i \otimes \boldsymbol{a}_J)^H \right] \end{aligned} \tag{22}$$

References

1. Guoqiang Gan, Zhihe Qiu (2000) Navigation and position—the big dipper of modern war. National Defense Industry Press, Beijing (in Chinese)
2. Kaplan ED, Hegarty CJ (2006) Understanding GPS: principles and applications. 2nd edition, Artech House, Boston, p 80

3. Church CM (2009) Estimation of adaptive antenna induced phase biases in globe navigation satellite systems receiver measurements. Master thesis, Ohio State University, Ohio
4. Marathe T, Daneshmand S, Lachapelle G (2015) Characterizing signal distortion due to space-time processing of interference impacted GNSS signals. In: Proceedings of the 28th international technical meeting of the ION satellite division, p 3084–3093
5. O'Brien AJ, Gupta IJ (2011) Mitigation of adaptive antenna induced bias errors in GNSS receivers. IEEE Trans Aerosp Electron Syst 47:524–538
6. Daneshmand S, Jahromi AJ, Broumandan A, et al (2015) GNSS space-time interference mitigation and attitude determination in the presence of interference signals. Sensors 15:12180–12204
7. Gupta IJ, Church CM, O'Brien AJ, et al (2007) Prediction of antenna and antenna electronics induced biases in GNSS receivers. In: Proceedings of ION GNSS conference, p 650–656
8. Fante RL, Fitzgibbons MP, McDonald KF (2004) Effect of adaptive array processing on GPS signal crosscorrelation. In: Proceedings of the 17th international technical meeting of the satellite division of ION, p 579–583
9. Wenfei G, Jiansheng Z, Tisheng Z, et al (2011) Analysis method for satellite signal cross-correlation peak bias in space-time adaptive processing. Geomatics Info Sci Wuhan University 36:1077–1080 (in Chinese)
10. Marathe T, Daneshmand S, Lachapella G (2016) Assessment of measurement distortions in GNSS antenna array space-time processing. Int J Antennas and Propag, p 1–17
11. Feiqiang C, Junwei N, Baiyu L, et al (2015) Distortionless space-time adaptive processor for global navigation satellite system receiver. Electron Lett 51:2138–2139
12. Hengcheng L (1982) Spatial correlations in adaptive arrays. IEEE Trans Antenna Propag 30:212–223

Joint Implementation of Interference Suppression and Signal Acquisition for GNSS Antenna Array Receivers

Feiqiang Chen, Junwei Nie, Guozhu Zhang, Zhengrong Li and Feixue Wang

Abstract It is well known that, signal acquisition has the lowest sensitivity of the whole GNSS (Global Navigation Satellite System) receiver operation. Signal acquisition could fail due to insufficiency of interference mitigation and signal attenuation during interference suppression and thus it has become the performance bottleneck in the presence of interference. When a GNSS receiver works at acquisition stage, for traditional array processing methods, it is difficult to enhance the satellite signal through array gain due to the lack of essential priori knowledge. In this paper, a novel anti-jamming algorithm is proposed. Compared with the traditional methods, which perform interference suppression and signal acquisition in sequence, the proposed method combines these two processes into a single algorithm. The main advantage is that, it is capable of providing array gain to enhance the desired signal at signal acquisition stage. Theoretical and experiment results show that, the proposed method could increase the signal-to-noise-ratio (SNR) N times at acquisition stage for a N elements antenna array, and thus improve the availability of the receivers significantly in harsh interference environment.

Keywords Satellite navigation · Beamforming · Antenna array · Anti-jamming · Signal acquisition

1 Introduction

The surprising evolution of global navigation satellite system (GNSS) in military and aviation applications has led to growing concerns for its safety. It is well known that GNSS receivers are vulnerable to interference due to the weak power of

F. Chen · J. Nie (✉) · G. Zhang · Z. Li · F. Wang
National University of Defense Technology, Changsha 410072, China
e-mail: njw1004@126.com

J. Sun et al. (eds.), *China Satellite Navigation Conference (CSNC) 2017 Proceedings: Volume I*, Lecture Notes in Electrical Engineering 437,
DOI 10.1007/978-981-10-4588-2_69

received satellite signals (typically about 20–30 dB below noise). Interference could degrade the signal-to-noise-ratio (SNR) which leads to accuracy degradation, and even denial-of-service. A promising solution to the interference problem is use of adaptive antenna array [1–4]. It allows the receiver to operate in the spatial domain in addition to the time/frequency domain and hence offers improved interference suppression (IS) capabilities.

For GNSS receivers, signal acquisition (SA) is known to be the weakest part of the whole receiver operation [2]. This is mainly reflected in two aspects, first, the acquisition sensitivity is generally smaller than the tracking sensitivity of 10 dB or more [5], the signal may be normally tracked but failed to be acquired under a given SNR condition. Second, since the signal tracking process is initialized by the results of SA, once SA failed, the follow-up signal tracking, data demodulation and position solution are difficult to work normally. Therefore, SA has become the performance bottleneck of anti-jamming GNSS receivers in harsh interference environments.

In order to improve the SA capabilities of GNSS receivers, on one hand, the interference should be mitigated sufficiently to minimize interference residue, on the other hand, the antenna array should offer processing gain to enhance the signal and thus increase the SNR. There are a number of array processing techniques which are able to provide gain by forming a beam in the satellite direction while perform IS. However, their capability is usually applied to the signal tracking rather than SA operation. For example, the minimum variance distortionless response (MVDR) method [6, 7] requires the direction of arrival (DOA) of the desired signal, the minimum mean square error (MMSE) method [8] need to extract synchronization parameters from tracking results to construct a reference waveform. These prior knowledge are difficult to be obtained at acquisition stage, especially for cold acquisition. Therefore, these techniques have no advantage with respect to SA performance over simple null-steering methods such as power inversion (PI) algorithm [9].

To overcome the above problem, a blind IS method based on spectral self-coherent restoral (SCORE) was developed in [10, 11], it can form main beams towards satellites at SA stage, but the algorithm is effective for only one satellite signal. In fact, at least 4 satellites are required for positioning and timing. Against this background, a novel method is proposed to protect the SA stage of receivers. Compared with the above methods mentioned, which perform IS and SA in sequence, the proposed method combines these two processes into a single algorithm. The main advantage is that, its IS capability could be applied to the SA operation. What's more, it could enhance the desired signal and thus improve the SA performance significantly.

2 Signal Model and Problem Statement

Considering the reception of one satellite signal due to the very low cross-correlation of the pseudorandom spreading codes, adopting the complex envelop notation, the received signal vector by an arbitrary N-element antenna array can be expressed as

$$\boldsymbol{x}(t) = \boldsymbol{a}s(t) + \boldsymbol{n}(t) \tag{1}$$

where $\boldsymbol{x}(t) = [\,x_1(t) \quad x_2(t) \quad \cdots \quad x_N(t)\,]^T \in \boldsymbol{C}^{N\times 1}$ is the array baseband snapshot, each row corresponding to one antenna, $(\cdot)^T$ denotes transpose. $\boldsymbol{a} \in \boldsymbol{C}^{N\times 1}$ is the steering vector of the satellite signal which is determined by signal DOA and array attitude. $s(t) = A_0 p(t-\tau_0)\mathrm{e}^{j2\pi f_d t}$ is the satellite signal, where $p(t)$ is the pseudo-random spreading code, A_0 is the amplitude, τ_0 and f_d are the code phase and doppler frequency respectively, which are also known as the synchronization parameters to be estimated by a GNSS receiver. Note that, the navigation data is not included in the expression because all the processing is considered within the same symbol. $n(t) \in C^{N\times 1}\boldsymbol{n}(t) \in \boldsymbol{C}^{N\times 1}$ is the signal not of interest (SNOI), including interfering signals and additive white Gaussian noise.

Assume that, K snapshots are used for SA, then, the input data matrix could be expressed as

$$\boldsymbol{X}(t) = [\boldsymbol{x}(t-(K-1)T_s), \ldots, \boldsymbol{x}(t-T_s), \boldsymbol{x}(t)] \tag{2}$$

where $\boldsymbol{X}(t) \in \boldsymbol{C}^{N\times K}$ and T_s is the sampling period.

The array output after interference mitigation is represented by the sum of the input data snapshot multiplied by the weight vector

$$\boldsymbol{y} = \boldsymbol{w}^H \boldsymbol{X} \in \boldsymbol{C}^{1\times K} \tag{3}$$

where $\boldsymbol{w} \in \boldsymbol{C}^{N\times 1}$ is the weight vector which depends on the corresponding interference mitigation algorithm. The weight vector of MVDR and MMSE could be expressed as [6, 8]

$$\boldsymbol{w}_{MVDR} = \frac{\boldsymbol{R}_{xx}^{-1}\boldsymbol{a}}{\boldsymbol{a}^H \boldsymbol{R}_{xx}^{-1}\boldsymbol{a}} \tag{4}$$

$$\boldsymbol{w}_{MMSE} = \boldsymbol{R}_{xx}^{-1}\boldsymbol{r}_{xd} \tag{5}$$

where $\boldsymbol{R}_{xx} = E[\boldsymbol{x}(t)\boldsymbol{x}^H(t)]$ is the spatial auto-correlation matrix of the array snapshots, $\boldsymbol{r}_{xd} = E[\boldsymbol{x}(t)d^H(t)]$ is the cross-correlation vector between the array snapshots and a reference waveform, $d(t)$ is the reference waveform which are correlate with the satellite signal. An ideal reference waveform is the satellite signal itself, i.e. $d(t) = p(t-\tau_0)e^{j2\pi f_d t}$.

The above two algorithms have been proved to be optimum in the sense of maximizing the array output signal-to-interference-plus-noise-ratio (SINR), they are able to provide gain by forming a beam in the satellite direction while perform IS. However, at SA stage, due to the extremely low power of the received signal, prior knowledge including steering vector $\boldsymbol{a}$, code phase τ_0 and doppler frequency f_d are difficult to obtain. Thus, the two algorithms degenerate into simple null-steering mode (PI algorithm) under this condition, the weight vector of which is represented as

$$\boldsymbol{w}_{PI} = \frac{\boldsymbol{R}_{xx}^{-1}\boldsymbol{c}}{\boldsymbol{c}^H\boldsymbol{R}_{xx}^{-1}\boldsymbol{c}} \tag{6}$$

where $\boldsymbol{c} = [1, 0, \ldots, 0]^T \in \boldsymbol{C}^{N\times 1}$ is a constraint vector.

PI approach only performs IS and does not provide gain by forming a beam in the satellite direction. After IS, the array output is used to perform SA. As can be seen from the above derivation, conventional array processing techniques are not able to enhance the SNR by beamforming at SA stage due to the lack of a priori information. This is especially true when the receiver is required to be operational at "cold" start.

3 Proposed Technique

As we all known, the purpose of SA is to obtain rough estimate of synchronization parameters of those visible satellites, and to help the receiver to initialize its tracking loops. Estimation of synchronization parameters, i.e. τ_0 and f_d, is accomplished by an exhaustive grid search in the entire parameter space. We try to use the grid search process to form a reference waveform that is needed for MMSE method. The steps are as follows:

Firstly, for any given code phase τ and doppler frequency f, we can construct a corresponding reference signal, i.e. $\tilde{d}(t,f,\tau) = p(t-\tau)\mathrm{e}^{j2\pi ft}$. According to the principle of the MMSE algorithm and Eq. (5), we could obtain the corresponding weight vector:

$$\boldsymbol{w}(f,\tau) = \hat{\boldsymbol{R}}_{xx}^{-1}\hat{\boldsymbol{r}}_{x\tilde{d}}(f,\tau) \tag{7}$$

where, $\hat{\boldsymbol{R}}_{xx} = \boldsymbol{X}\boldsymbol{X}^H/K$ is the estimation of the auto-correlation matrix of the snapshots, $\hat{\boldsymbol{r}}_{x\tilde{d}}(f,\tau) = \boldsymbol{X}\tilde{\boldsymbol{d}}(t,f,\tau)^H/K$ is the estimation of the cross-correlation vector between the array snapshots and the constructed reference signal, where $\tilde{\boldsymbol{d}}(t,f,\tau) = [\tilde{d}(t-(K-1)T_s,f,\tau),\ldots,\tilde{d}(t-T_s,f,\tau),\tilde{d}(t,f,\tau)]$ is the constructed reference signal vector composed by K snapshots.

Note that, because the synchronization parameters are unknown, the weight vector in (7) is different with that of MMSE algorithm, $\boldsymbol{w}(f,\tau)$ is the function of doppler frequency f and code phase τ. Then, the array output can be obtained by weighting the array input data matrix by the array weight vector:

$$\boldsymbol{y}(f,\tau) = \boldsymbol{w}^H(f,\tau)\boldsymbol{X} = \hat{\boldsymbol{r}}_{xd}^H(f,\tau)\hat{\boldsymbol{R}}_{xx}^{-1}\boldsymbol{X} \tag{8}$$

It can be seen from (8) that, the array output is still the function of doppler frequency f and code phase τ, only when the values of these two parameters are close to their true value, i.e. τ_0 and f_d, the constructed signal has a great relevance with the desired signal, and beamforming is able to be performed.

Then, the array output will be used for SA. According to the principle of Generalized Likelihood Ratio Test (GLRT), the detector could be expressed as

$$\begin{aligned} T(\boldsymbol{y}) &= \max_{f,\tau}\left\{ \left|\hat{r}_{y\tilde{d}}(f,\tau)\right|^2 \Big/ \hat{R}_{yy}(f,\tau) \right\} \\ &= \max_{f,\tau}\left\{ \hat{\boldsymbol{r}}_{x\tilde{d}}^H(f,\tau)\hat{\boldsymbol{R}}_{xx}^{-1}\hat{\boldsymbol{r}}_{x\tilde{d}}(f,\tau) \right\} \geq \gamma \end{aligned} \tag{9}$$

where, $\hat{r}_{y\tilde{d}}(f,\tau) = \boldsymbol{y}(f,\tau)\tilde{\boldsymbol{d}}(t,f,\tau)^H/K$ is the estimation of the cross-correlation vector between the array output and the constructed reference signal, $\hat{R}_{yy}(f,\tau) = \boldsymbol{y}(f,\tau)\boldsymbol{y}(f,\tau)^H/K$ is the estimation of the auto-correlation matrix of the array output, γ is the detection threshold, which could be calculated from a given false alarm probability.

From the above derivation, it can be see that the grid search process of synchronization parameters is shared by both IS and SA. In other words, instead of performing IS and SA in sequence, the proposed method performs these two processes simultaneously. On the other hand, because the interference mitigation method is based on MMSE criterion, the proposed algorithm could maximize the array output SINR and thus outperform PI algorithm in protecting the SA operation.

The implementation schematic of the proposed algorithm is present in Fig. 1. The array signal received by the antenna array is then processed by frond-end and A/D converter, the input data matrix $\boldsymbol{X}$ is used to calculate the test statistic $T(\boldsymbol{y})$. If $T(\boldsymbol{y}) \leq \gamma$, then the test determines the absence of the satellite signal, otherwise, the test determines the presence of the satellite signal, at the same time, the doppler frequency $\hat{f}_d$ and code phase $\hat{\tau}_0$ that maximizing $T(\boldsymbol{y})$ are taken as the estimate of synchronization parameters. The array output is obtained according to (8) after the synchronization parameters are estimated. Finally, the array output and synchronization parameters are sent to the signal tracking module for subsequent processing.

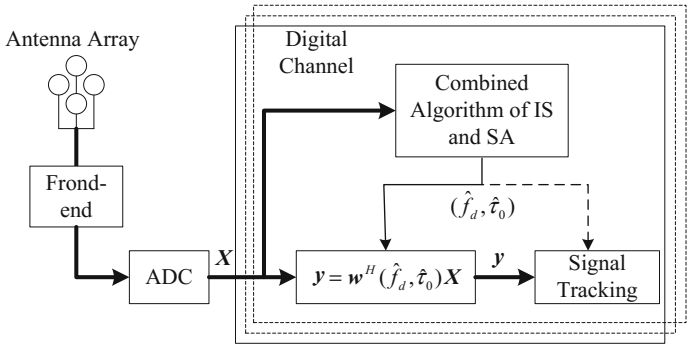

Fig. 1 Implementation schematic of the proposed algorithm

4 Experimental Results

In the simulations, the array consists of four omnidirectional antennas with one element at the centre of a circle and the other three elements uniformly distributed on the perimeter of the aperture. The radius of the circular array is half a wavelength. The desired signal is GPS civil signal at L1 band with a chip rate of 1.023 Mcps. The sampling frequency is 2.048 MHz and the acquisition time is set to 1 ms (K = 2048). The receiver used in the simulation performs cold acquisition, the doppler search step is 500 Hz and code phase search step is one sampling period.

4.1 Results in the Presence of a Single Satellite Signal

In the experiment, the elevation angle and azimuth angle of the satellite signal are 75° and 45° respectively. One interfering signal with uniformly distributed random DOA and different INR (interference-to-noise ratio) is considered. Detection probability is used as performance metric, detection here is defined as the synchronization parameters are estimated correctly (the error is within one search grid).

Figure 2a, b show the acquisition performance in terms of detection probability versus C/N_0 (carrier-to-noise density ratio) when a 2 MHz wideband interference and a CW (Continuous Wave) interference is present respectively. The data in these plots is obtained by averaging over 1000 independent trials. As shown, the performance of the proposed method outperforms the PI method significantly both in low-power and high-power interference conditions. Figure 2a, b, we could find that the interference rejection capability of the proposed method is more sensitive to interference bandwidth rather than interference power, it degrades slightly when the CW is replaced by wideband interference. Primary reason should be take into

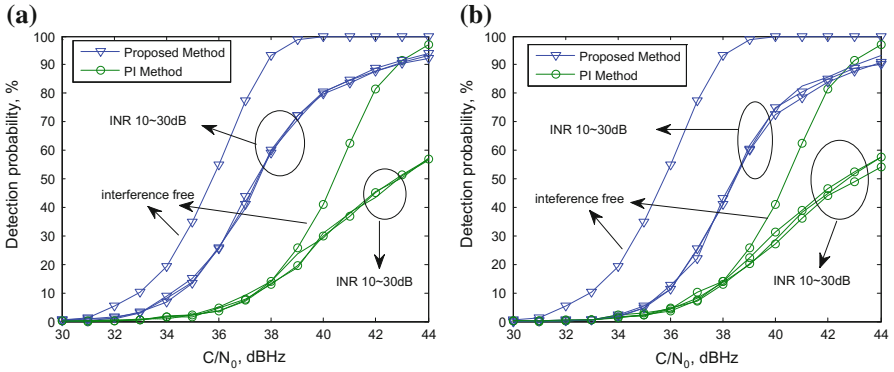

Fig. 2 Detection probability versus C/N_0: **a** Detector performance in the presence of a wideband interference and **b** detector performance in the presence of a CW interference

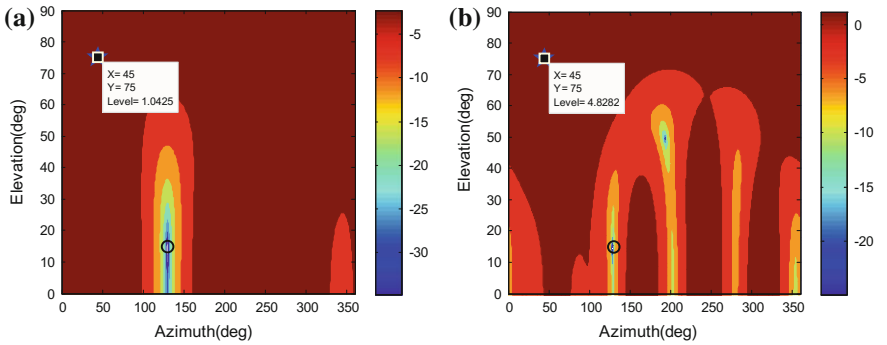

Fig. 3 Antenna pattern of the proposed algorithm: **a** PI algorithm and **b** the proposed algorithm

account is the level of correlation between interference with different bandwidths and the satellite signal.

Furthermore, in the experiment, we fixed a set of signal/interference scenario to observe the antenna pattern to verify the beamforming ability while suppressing interference. Figure 3a, b show the antenna pattern of PI algorithm and the proposed algorithm in the presence of a wideband interference respectively, the incident direction of the wideband interference are 15° for elevation and 130° for azimuth, and the INR is 30 dB.

It can be seen from Fig. 3 that, both the PI algorithm and the proposed algorithm form a deep null in the direction of the interference (marked with "○" in the figure). For PI algorithm, the array gain in the direction of satellite signal (marked with "★" in the figure) is about 1.0 dB, since the algorithm does not constrain the response of the signal direction, antenna gain in the direction of the signal can not be controlled. As for the proposed algorithm, the array gain in the direction of satellite signal is about 4.8 dB, which indicates that the signal is enhanced successfully. On the other

hand, the array gain is still small than the theoretical upper limit (10 * lg4 = 6.02 dB), which is mainly caused by the estimate error of the synchronization parameters. Reducing the step of synchronization parameters search may increase the array gain, while it will also increase the acquisition time of the receiver.

4.2 Results in the Presence of Multiple Satellite Signals

To validate the algorithm performance in the presence of multiple-GPS signals as well as multiple wideband interferences, in the experiment, the spatial distribution of the satellites are set according to Ref. [12], where the number of visible satellites are eight, and carrier to noise ratio are 44 dBHz, all interfering signals incident from low elevations, the INR are 30 dB. The sky plot of all the satellites and interference sources is shown in Fig. 4a. The acquisition performance is shown in Fig. 4b–d. Acquisition metric, which is the ratio of maximized correlation value to second maximized correlation value, is used to evaluate the acquisition performance. From Fig. 4, we could conclude that:

(1) Under interference free condition, the two algorithm are both able to acquire all satellite signals successfully, while the acquisition metric for the proposed algorithm is significantly higher than that of PI algorithm. The benefit is that, you could obtain better detection performance for a given false alarm probability.
(2) When J1 is switched on, since satellite PRN7 incidents from the close direction with J1, the two algorithms both are unable to acquire the satellite signal. This is caused by the inherent shortcomings of antenna array based anti-jamming method, and increasing the array aperture could obtain a certain degree of improvement.
(3) Compared with interference free scenario, the performance of the two algorithms both degrade when interference is switched on, while the proposed algorithm outperforms PI algorithm, this phenomenon is more obvious when J1 and J2 are switched on at the same time. A reasonable explanation for this is that, PI algorithm forming nulls in the direction of interference at the same time, other direction of the incident signals have a certain attenuation, because the proposed algorithm have beamforming capability, this phenomenon could be improved to some extent.

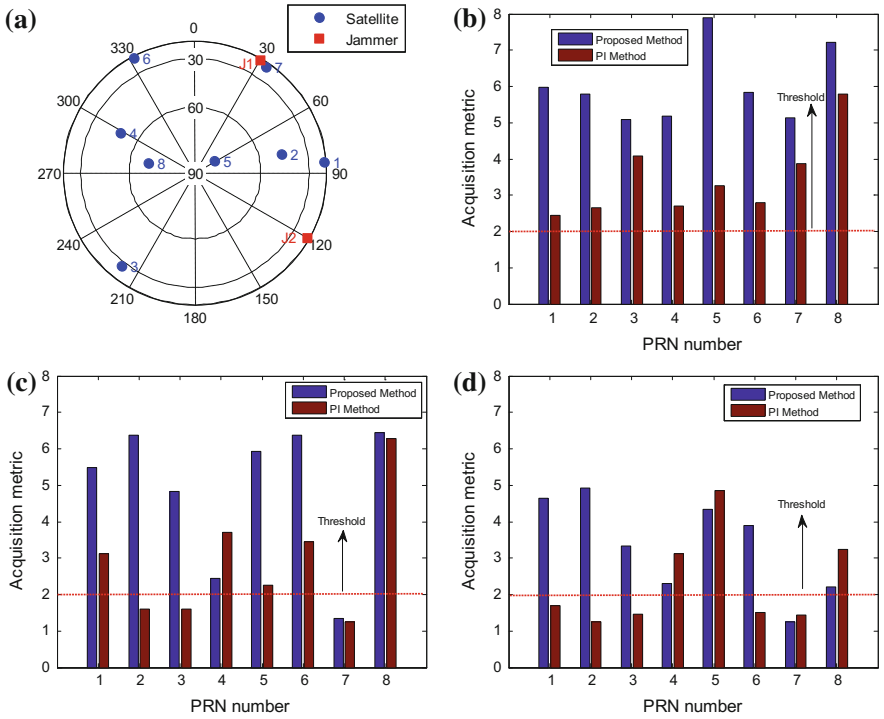

Fig. 4 Acquisition results in the presence of multiple interferences: **a** sky plot **b** interference free **c** J1 is switched on **d** both J1 and J2 are switched on

5 Conclusions

Signal acquisition has become the performance bottleneck of GNSS receivers in harsh interference environments due to its low sensitivity. In this paper, a novel anti-jamming algorithm based on the MMSE criterion is proposed to protecting the acquisition stage. Experimental results show that the proposed algorithm could obtain array signal processing gain to enhance the satellite signals while mitigating the interference, and thus improve the signal acquisition performance of the receiver. For a N elements antenna array, the proposed algorithm could enhance the SNR N times theoretically, the real performance may degrade slightly due to the estimate error of synchronization parameters. We will analyze the impact of estimate error of synchronization parameters on algorithm performance in our further work.

References

1. O'Brien AJ (2009) Adaptive antenna arrays for precision GNSS receivers. The Ohio State University, Columbus
2. Arribas J, Fernandez-Prades C, Closas P (2013) Antenna array based GNSS signal acquisition for interference mitigation. IEEE Trans Aerosp Electron Syst 49(1):223–243
3. Li M, Dempster AG, Balaei AT et al (2011) Swichable beam steering/null Steering algorithm for CW interference mitigation in GPS C/A code receivers. IEEE Trans Areosp Electron Syst 47(3):1564–1579
4. Li M, Wang FX, Balaei AT et al (2008) A GNSS software receiver beamforming architecture. Proceedings of international symposium on GPS/GNSS. Tokyo, Japan, pp 904–909
5. Instruments National (2003) GPS receiver testing. National Instruments GPS Receiver Testing Tutorial, Austin
6. Applebaum SP (1976) Adaptive arrays. IEEE Trans Antennas Propag 24(5):585–598
7. Zhang YD, Amin MG (2012) Anti-Jamming GPS receiver with reduced phase distortions. IEEE Signal Process Lett 19(10):635–638
8. O'Brien AJ, Gupta IJ (2011) Optimum adaptive filtering for GNSS antenna arrays. In: Proceedings of the 27th international technical meeting of the institute of navigation, Savannah, GA, USA, pp 2796–2805
9. Compton RT (1979) The power-inversion adaptive array: concept and performance. IEEE Trans Aerosp Electron Syst 15(6):803–813
10. Amin MG, Sun W (2005) A novel interference suppression scheme for global navigation satellite systems using antenna array. IEEE J Sel Areas Commun 23(5):999–1012
11. Sun W, Amin MG (2005) A self-coherence anti-jamming GPS receiver. IEEE Trans Signal Process 53(10):3910–3915
12. Marathe T, Daneshmand S, Lachapelle G (2015) Characterizing signal distortion due to space-time processing of interference impacted GNSS signals. In: Proceedings of the 28th international technical meeting of the ION satellite division, ION GNSS+ 2015, Tampa, Florida, USA, pp 3084–3093
13. Lu D, Wu R, Liu H (2013) Global positioning system anti-jamming algorithm based on period repetitive CLEAN. IET Radar Sonar Navigation 7(2):164–169

GNSS Spoofing Detection Based on Power Monitoring of Two-Antenna

Fei Wang, Hong Li and Mingquan Lu

Abstract GNSS spoofing attack is threatening GNSS services which are widely used in both civil and military applications. Spatial processing countermeasure is one kind of spoofing detection techniques. It consists of multi-antenna based and moving antenna based methods. Existing multi-antenna methods require multi-antenna measurements which are highly synchronized, and the moving antenna methods cannot work when the receiver is static. In this paper, two spoofing detection metrics based on two-antenna signal-plus-noise power are proposed. Correlation coefficient can be applied when the antennas are static, and normalized differential power ratio can be applied regardless of the motion of the receiver. Experimental results show that the proposed method can detect the spoofing signals effectively. The proposed metrics don't require highly synchronized measurements and can be obtained in the tracking stage of the receiver, which can guarantee a quick spoofing detection.

Keywords GNSS · Spoofing detection · Power monitoring · Two-antenna · Correlation coefficient · Normalized differential power ratio

1 Introduction

Global navigation satellite system (GNSS) has been widely applied in transportation, power grid, financial market, safety of life, and military affairs. But GNSS signals are vulnerable to in-band interferences. A jammer hinders a receiver from processing GNSS signals by sending high-power evil signals, and a spoofer can falsify a receiver's navigation solution by sending simulated or replayed GNSS signals. GNSS spoofing is more threatening since a conventional receiver can hardly find itself being affected by spoofing signals [1].

F. Wang · H. Li (✉) · M. Lu
Department of Electronic Engineering, Tsinghua University, Beijing 100084, China
e-mail: lihongee@tsinghua.edu.cn

J. Sun et al. (eds.), *China Satellite Navigation Conference (CSNC) 2017 Proceedings: Volume I*, Lecture Notes in Electrical Engineering 437,
DOI 10.1007/978-981-10-4588-2_70

Many GNSS anti-spoofing techniques have been developed in recent years [2, 3]. One of the most robust spoofing detection techniques is the spatial processing countermeasure, which consists of multi-antenna based and moving antenna based methods. Most spatial processing techniques assume that the spoofing signals come from a common transmitting antenna. It is reasonable because a spoofer with multi-radiator is complex, expensive and hard to implement. In multi-antenna based methods, [4] detects a spoofing attack by comparing the positioning results of multi-receiver. References [5, 6] detect a spoofing attack by monitoring differential pseudorange and carrier phase, respectively. Reference [7] detects a spoofing attack by comparing carrier to noise ratio (C/N_0) of signals received from two antennas with different gain patterns. In a receiver with a moving antenna, the powers of different spoofing signals change with similar patterns since the propagation paths of all the spoofing signals are the same. Therefore, a spoofing attack can be detected by calculating the correlation coefficients of powers of different signals. Correlation coefficients close to 1 indicate that there are pairwise spoofing signals [8]. Another moving antenna based method is proposed in [9]. It acquires and tracks all the spoofing and authentic signals at the same time and distinguishes them by calculating the correlation coefficients of Doppler frequency shifts of different signals.

In this paper, we propose a spoofing detection method based on power measurements of two-antenna. It is also assumed that the spoofing signals come from a common source. The fundamental principle of the proposed method is that the propagation paths and incident angles of authentic signals from satellites to the receiving antennas are different and time-varying, and the gain patterns of the antennas are anisotropic. Therefore, the two-antenna powers of authentic signals change differently, and the power ratios between two antennas are also different for different satellites. But the propagation paths and incident angles of spoofing signals are constant. Therefore, the two-antenna powers of spoofing signals change with the same pattern and the two-antenna power ratios are similar. The main contributions of the paper are listed as follows.

- We propose two metrics to detect GNSS spoofing attacks, namely two-antenna power correlation coefficient and two-antenna normalized differential power ratio.
- We perform experiments with a real-time GNSS receiver in normal conditions and under replaying spoofing attacks, respectively. Results show that the metrics perform well in distinguishing spoofing signals from authentic ones.
- We analyze the advantages of the proposed method. The proposed metrics can be obtained in the tracking stage. Therefore, they can detect a spoofing attack quickly. In addition, the power measurements do not need to be highly synchronized as the power measurements usually change continuously and slowly. Hence, the proposed method can be applied when multiple receivers are not synchronized strictly.

The remainder of the paper is organized as follows. Section 2 introduces the configuration of a multi-antenna GNSS spoofing detection system. Section 3

presents the experiments for testing the proposed metrics with different configurations of receiving antennas. Finally, conclusions are given in Sect. 4.

2 Spoofing Detection Based on Power Measurements

A spoofing detection system based on multi-antenna is given in Fig. 1. Different processing units can either be independent receivers connected by communication links or parallel processing modules embedded in one receiver. Existing multi-antenna based methods detect spoofing attacks by comparing the positioning results, C/N_0, pseudoranges or carrier phases of different processing units. In this paper, we apply the signal-plus-noise power in each tracking module to detect the spoofing signals. The power measurements can be obtained in the tracking modules. Therefore, a spoofing attack can be detected as early as possible.

In order to avoid estimating the noise floor which may introduce additional error, we apply the signal-plus-nose power instead of C/N_0 in spoofing detection. The measurement of total power in $1/T_{coh}$ noise bandwidth is given by [10]

$$P_{wb}(k) = \sum_{n=kL_0+1}^{kL_0+L_0} [I_P^2(n) + Q_P^2(n)] \tag{1}$$

where L_0 is the number of non-coherent integration. I_P and Q_P are prompt in-phase and quadrature coherent integration results in T_{coh} and can be expressed as

$$\begin{aligned} I_P(n) &= aD(n)\mathrm{sinc}(f_e T_{coh})R(\tau_P)\cos\Delta\phi + \omega_{IP} \\ Q_P(n) &= aD(n)\mathrm{sinc}(f_e T_{coh})R(\tau_P)\sin\Delta\phi + \omega_{QP} \end{aligned} \tag{2}$$

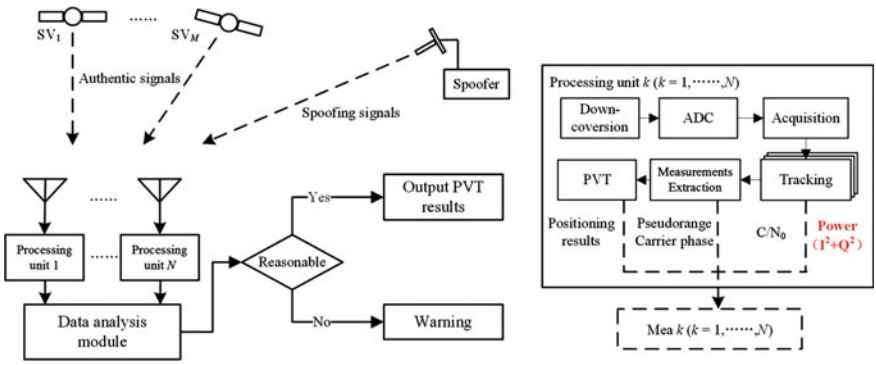

Fig. 1 Configuration of a multi-antenna GNSS spoofing detection system

where a is the amplitude of signal, $D(n)$ is the modulated navigation data, f_e is the frequency tracking error, $R(.)$ represents the autocorrelation function of the pseudorange code, τ_P is the time difference between the prompt local C/A code and the receiving signal, $\Delta\phi$ is the carrier phase tracking error, and ω_{IP} and ω_{QP} are noises of in-phase and quadrature channels.

In order to mitigate the disturbance of the noise, average value of P_{wb} during L_1 epochs is employed, which can be expressed as

$$P = \frac{1}{L_1}\sum_{k=1}^{L_1} P_{wb}(k) \tag{3}$$

2.1 Two-Antenna Power Correlation Coefficient

By arranging the power measurements in a period of time, signal-plus-noise power of the jth antenna can be written as the following matrix form

$$\boldsymbol{P}^{(j)} = \begin{bmatrix} \boldsymbol{p}_1^{(j)} \\ \boldsymbol{p}_2^{(j)} \\ \vdots \\ \boldsymbol{p}_M^{(j)} \end{bmatrix} = \begin{bmatrix} P_1^{(j)}(1) & P_1^{(j)}(2) & \cdots & P_1^{(j)}(K) \\ P_2^{(j)}(1) & P_2^{(j)}(2) & \cdots & P_1^{(j)}(K) \\ \vdots & \vdots & \ddots & \vdots \\ P_M^{(j)}(1) & P_M^{(j)}(2) & \cdots & P_M^{(j)}(K) \end{bmatrix} \tag{4}$$

where $P_i^{(j)}(k)$ represents the average power of the ith signal in the kth processing interval. Since two-antenna model can be easily extended to multi-antenna case, in the following paper, a two-antenna model is adopted for simplification.

When an antenna receives authentic signals, the angles of arrival (AOAs) and the propagation paths of the signals change due to the motion of the satellites. The changes are different for different antennas. Therefore, the correlation between the powers of different antennas is low in a period of time. However, when the receiving antennas are static, the AOAs and propagation paths of different spoofing signals are constant. Therefore, the changing patterns of powers of different antennas are determined by the power changes of the spoofing signals, and they will be very similar, resulting in very high correlation coefficients. Based on the above analysis, the correlation coefficients of two-antenna powers can be applied for spoofing detection. The correlation coefficient between two-antenna powers corresponding to the ith satellite is given by

$$\rho_i = \frac{E\left\{[\boldsymbol{p}_i^{(1)} - E(\boldsymbol{p}_i^{(1)})][\boldsymbol{p}_i^{(2)} - E(\boldsymbol{p}_i^{(2)})]\right\}}{\sqrt{D(\boldsymbol{p}_i^{(1)})D(\boldsymbol{p}_i^{(2)})}} \tag{5}$$

where $E(\cdot)$ is the symbol of expectation and $D(\cdot)$ is the symbol of variance. In practical applications, the average value of ρ_i of all satellites can be applied as the statistic of spoofing detection.

2.2 Two-Antenna Normalized Differential Power Ratio

In this section, another spoofing detection metric is proposed. First, we define the *i*th satellite's power ratio between two antennas in the *k*th time interval as follows

$$PR_i(k) = P_i^{(2)}(k)/P_i^{(1)}(k) \tag{6}$$

The propagation paths from different satellites to one receiving antenna are different, but the propagation paths of different spoofing signals from a spoofer to one receiving antenna are all the same. Hence, the power ratios of different authentic signals are different, but the power ratios of different spoofing signals are approximately equal. Based on the above analysis, the following metric named normalized differential power ratio is presented for spoofing detection.

$$R_i(k) = [PR_i(k) - PR_{ref}(k)]/PR_{ref}(k) \tag{7}$$

where $PR_{ref}(k)$ is the power ratio reference which is used for normalization. $PR_{ref}(k)$ is defined as follows

$$PR_{ref}(k) = \frac{1}{M}\sum_{i=1}^{M} PR_i(k) \tag{8}$$

where M is the total number of satellites. Small $R_i(k)$ indicates that the signals come from the same direction. Different from the two-antenna power correlation coefficients, the normalized differential power ratios can detect a spoofing attack regardless of the motion of the receiving antennas.

3 Experiments

In this section, experimental results are presented to show the spoofing detection performance of the proposed metrics. GPS L1 C/A signals are applied in the experiments. The signal processing parameters are set as follows. The coherent integration time is 1 ms. L_0 and L_1 in Eqs. (1) and (3) are set to 10 and 100, respectively. Therefore, the processing interval is 1 ms $\times$ 10 $\times$ 100 = 1 s. In order to reduce the effects of noise, the power measurements are further smoothed every 10 points. The length of the power vector $p_i^{(j)}$ is 300 s.

3.1 Configurations of Experiments

The configurations of experiments with different two-antenna geometries are shown in Fig. 2. The receiving antenna of the spoofer receives GNSS signals in L1 band and sends them to the replaying module. Then, the signals are delayed and sent to the transmitting antenna. After that, the spoofing signals are transmitted to the receiving antennas of the victim receiver. There are two different configurations, namely S1, S2, respectively. In S1, both the antennas are static. In S2, one of the antennas is static and the other one is moved randomly.

3.2 Experimental Results

Experimental results of S1 and S2 are presented and compared in this subsection, respectively.

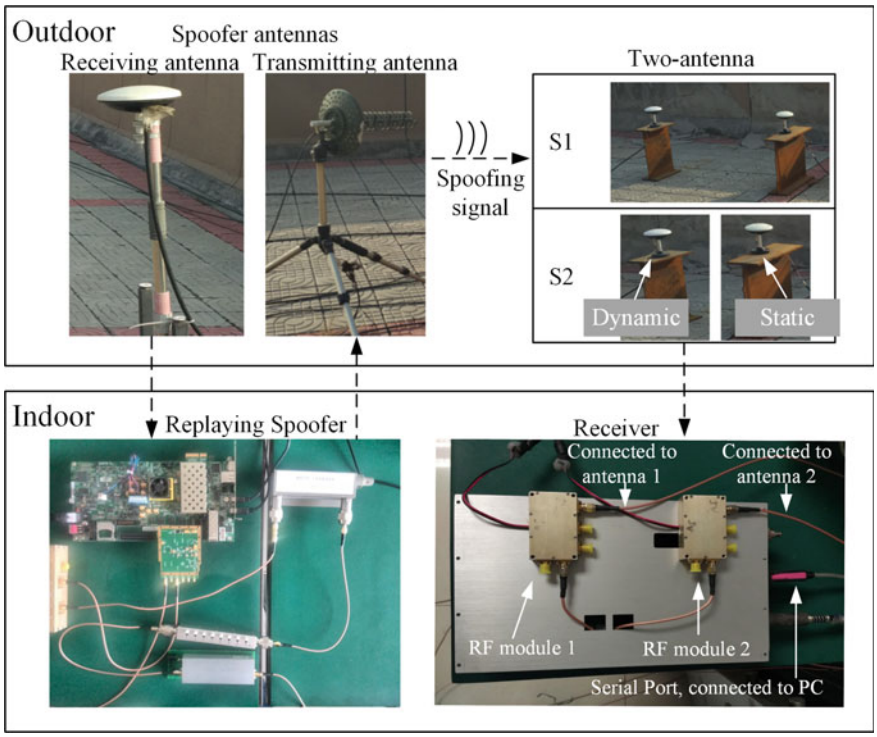

Fig. 2 Configurations of GNSS spoofing experiments

3.2.1 Results of S1

Figure 3 shows the two-antenna power correlation coefficients of different satellites in S1. Figure 3a, b show the correlation coefficients of authentic and spoofing signals, respectively. It can be seen that the correlation coefficients of the authentic signals change randomly, but those of the spoofing ones are all larger than 0.97.

The average correlation coefficients of authentic and spoofing signals are shown in Fig. 3c. The metrics of authentic signals are between −0.3 and 0.3, indicating that the two-antenna powers of authentic signals are not correlated. However, the metrics of the spoofing ones are very close to 1, indicating that the two-antenna powers of spoofing signals are highly correlated, thus the signals can be recognized as spoofing ones.

Figure 4 shows the two-antenna power ratios and normalized differential power ratios in S1. Figure 4a, b show the power ratios of authentic and spoofing signals, respectively. It can be seen that the power ratios of different authentic signals are quite different, but those of the spoofing ones are approximately equal. Therefore, normalized differential power ratios of the authentic signals are different, but those of the spoofing ones are very close to 0, as shown in Fig. 4c, d.

3.2.2 Results of S2

Figure 5 shows the two-antenna power correlation coefficients of different satellites in S2. Similar to Fig. 3, the correlation coefficients of authentic signals change

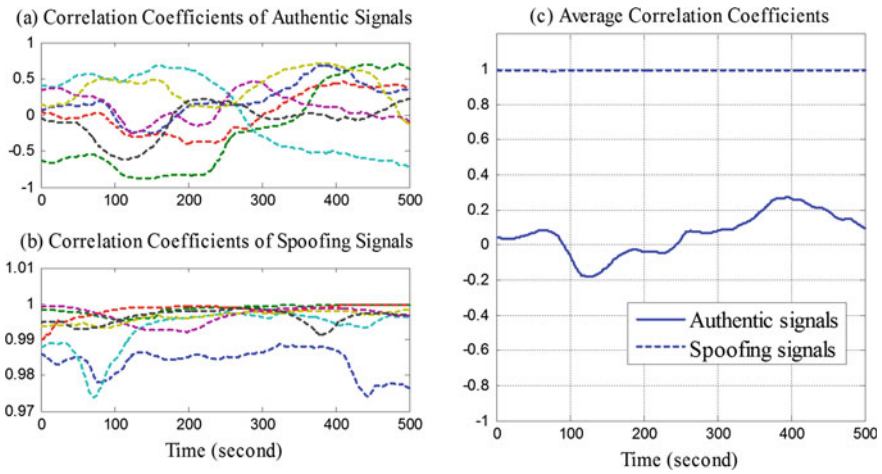

Fig. 3 **a** Correlation coefficients between two-antenna powers of authentic signals; **b** correlation coefficients between two-antenna powers of spoofing signals; **c** average correlation coefficients between two-antenna powers. The *solid* and *dotted lines* correspond to the authentic and spoofing signals, respectively. In S1, both the antennas are static

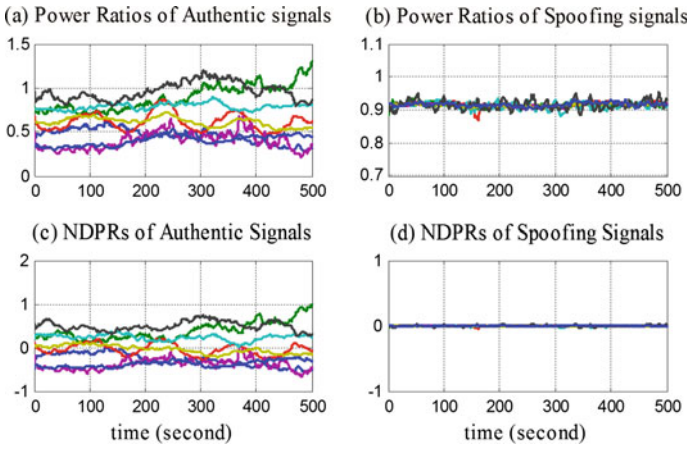

Fig. 4 **a** Power ratios of authentic signals; **b** power ratios of spoofing signals; **c** normalized differential power ratios (NDPRs) of authentic signals; **d** normalized differential power ratios (NDPRs) of spoofing signals. In S1, both the antennas are static

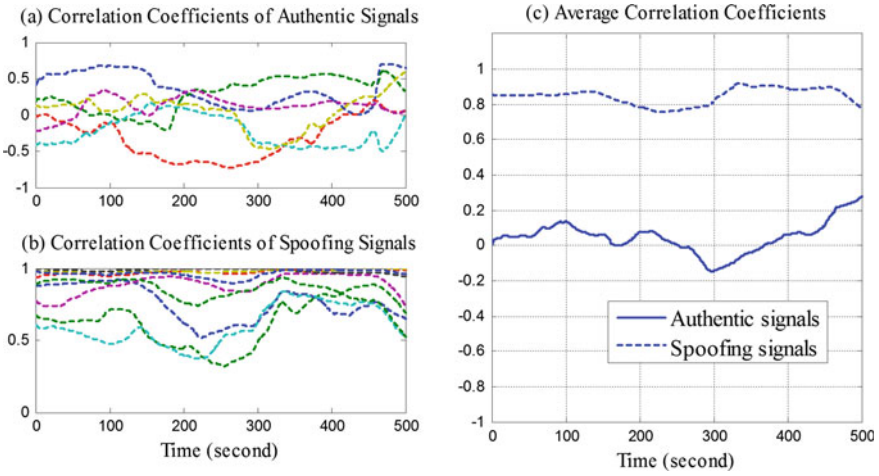

Fig. 5 **a** Correlation coefficients between two-antenna powers of authentic signals; **b** correlation coefficients between two-antenna powers of spoofing signals; **c** average correlation coefficients between two-antenna powers. The *solid* and *dotted lines* correspond to the authentic and spoofing signals, respectively. In S2, one antenna is dynamic and the other one is static

randomly in the experiments. But the results of the spoofing signals decrease dramatically. However, the correlation coefficients of spoofing signals are still higher than those of the authentic ones since the motion of receiver is mild.

The average correlation coefficients of authentic and spoofing signals are shown in Fig. 5c. Results of spoofing signals are still higher than those of the authentic

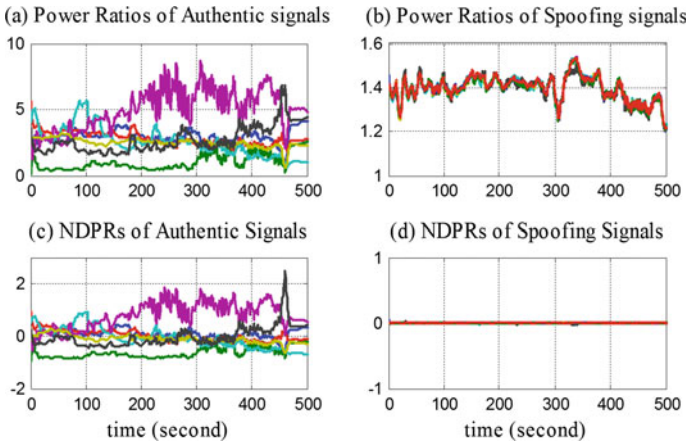

Fig. 6 **a** Power ratios of authentic signals; **b** power ratios of spoofing signals; **c** normalized differential power ratios (NDPRs) of authentic signals; **d** normalized differential power ratios (NDPRs) of spoofing signals. In S2, one antenna is dynamic and the other one is static

ones, but it can be inferred that the correlation coefficients of spoofing signals will further decrease when the velocity of the antenna is higher. Then, the metric may fail to detect a spoofing attack.

Figure 6 shows the two-antenna power ratios and normalized differential power ratios in S3. Compared with Fig. 4, the power changes of authentic signals are more intense, and the power ratios of spoofing signals are no longer constant due to the motion of the antenna. Nevertheless, the normalized differential power ratios of spoofing signals are still very close to 0, which means that the metric can still be applied to detect a spoofing attack.

4 Conclusions

In this paper, two metrics are proposed based on two-antenna signal-plus-noise power, namely correlation coefficient and normalized differential power ratio. Since the propagation paths of authentic signals are different, while it is assumed that the spoofing signals come from a common source, the proposed metrics show different characteristics when the receiver processes authentic and spoofing signals. When authentic signals are processed, the correlation coefficients of different signals will be randomly distributed, their average values will be small, and the normalized differential power ratios will be non-zero. When spoofing signals are processed, the correlation coefficients will be close to one and the normalized differential power ratios will be very close to zero. Therefore, a spoofing attack can be detected with the proposed metrics. Furthermore, the power measurements do not need to be

highly synchronized as the powers change continuously and slowly, and they can be obtained in the tracking stage, thus the alert-time of spoofing attacks can be shortened.

Acknowledgements This work was supported by the National Natural Science Foundation of China (Grant No. 61571255).

References

1. Humphreys TE, Ledvina BM, Psiaki ML, O'Hanlon BW, Kintner PM Jr (2008) Assessing the spoofing threat: development of a portable GPS civilian spoofer. In: Proceedings of the ION GNSS international technical meeting of the satellite division, vol 55, p 56
2. Psiaki ML, Humphreys TE (2016) GNSS spoofing and detection. Proc IEEE 104(6): 1258–1270
3. Broumandan A, Jafarnia-Jahromi A, Daneshmand S et al (2016) Overview of spatial processing approaches for GNSS structural interference detection and mitigation. Proc IEEE 104(6):1246–1257
4. Swaszek PF, Hartnett RJ (2013) Spoof detection using multiple COTS receivers in safety critical applications. In: Proceeding of ION GNSS+ 2013, Nashville TN
5. Zhang Z, Zhan X (2016) GNSS spoofing network monitoring based on differential pseudorange. Sensors 16(10)
6. Psiaki ML, O'Hanlon BW, Powell SP, Bhatti JA, Wesson KD, Humphreys TE, Schofield A (2014) GNSS spoofing detection using two-antenna differential carrier phase. In: Proceedings of ION GNSS+. Tampa, FL
7. Zhang Z, Trinkle M, Qian L et al (2012) Quickest detection of GPS spoofing attack. In: IEEE military communications conference, pp 1–6
8. Nielsen J, Broumandan A, Lachapelle G (2011) GNSS spoofing detection for single antenna handheld receivers. Navigation 58(4):335–344
9. Broumandan A, Jafarnia-Jahromi A, Lachapelle G (2015) Spoofing detection, classification and cancelation (SDCC) receiver architecture for a moving GNSS receiver. GPS Solutions 19 (3):475–487
10. Groves PD (2005) GPS signal to noise measurement in weak signal and high interference environments. Navigation 52(2):83–94

Application Strategy and Receiver Verification for the New Generation of BeiDou Navigation Satellites

Bin Tang, Jinlong Li, Qian Wang and Jiazheng Fu

Abstract Since March 30, 2015, BeiDou satellite navigation system (hereinafter referred to as the BDS) has launched five new generation of satellites and two BDS-2 satellites, which means BDS is expanding from regional to global. The new generation of Beidou navigation satellites are the 17th to 21st BDS satellites. They will be used for the verification of new navigation signal, inter-satellite links and other for the BeiDou global satellite navigation system. For the two BDS-2 satellites, which are the 22nd and 23rd BDS satellites, and how to replace the current satellites? The application strategy of the five new generation of BeiDou navigation satellites and two BDS-2 satellites from the view of application, then which will be verified by BDS receiver. The conclusion will be used to support BDS smooth transition from regional to global.

Keywords BDS · The new generation of satellites · Application strategy · Receiver verification

1 Introduction

Since 2000, China started to build BeiDou satellite navigation system, and gradually formulated a three-step strategy of development: to complete BDS-1 by the end of 2000; to complete BDS-2 and provide services for the area of Asia-Pacific by the end of 2012, and the space constellation of BDS-2 was consisted of 14 satellites—5 Geostationary Earth Orbit (GEO) satellites, 5 Inclined Geosynchronous Satellite Orbit (IGSO) satellites and 4 Medium Earth Orbit (MEO) satellites; and to complete the construction of the BeiDou global system around 2020 [1].

B. Tang (✉) · J. Li · Q. Wang · J. Fu
Beijing Satellite Navigation Center, 5136 Box, Beijing 100094, China
e-mail: donaldgnss@126.com

J. Sun et al. (eds.), *China Satellite Navigation Conference (CSNC) 2017 Proceedings: Volume I*, Lecture Notes in Electrical Engineering 437,
DOI 10.1007/978-981-10-4588-2_71

BDS-2 satellites were launched from 2009 to 2012, and the GEO satellites and IGSO satellites were first launched, which have the larger contribution to the services of positioning than MEO satellites. From now to 2020, when the BeiDou global system provides services, the BDS-2 satellites will gradually to be failure. If there is no smooth application strategy of the satellites, the BDS services for the existed users will be affected. In the expanding process from BDS-2 to BeiDou global, China has launched five new generation of satellites and two BDS-2 satellites from March 30, 2015 to the end of 2016. The new generation of BeiDou navigation satellites are the 17th to 21st BDS satellites, which are two IGSO satellites and three MEO satellite. Two BDS-2 satellites are the 22nd and 23rd BDS satellites, which are a IGSO satellite and a GEO satellite [2].

The new generation of BeiDou navigation satellites will be used for the verification of the new navigation signal, inter-satellite links and other validation work for the BeiDou global system [3]. For the two BDS satellites, how to replace the current satellites? The impact of the BDS-2 satellites failure will be studied before 2020, then the corresponding application strategies of the five new-generation BeiDou navigation satellites and the two BDS-2 satellites will be put forward based on the view of application. These application strategies will be verified by BDS receiver, and the conclusion of validation will be used to support BDS smooth transition from regional to global.

2 The State of BeiDou Satellites

According to the Beidou official website, before the end of 2014, the state of BeiDou satellite is listed in Table 1 [4].

Table 1 The state of BeiDou satellite

BeiDou satellite	Date	Orbit	State
1st	2007.04.14	MEO	Test
2nd	2009.04.15	GEO	Failure
3rd	2010.01.17	GEO	Available
4th	2010.06.02	GEO	Available
5th	2010.08.01	IGSO	Available
6th	2010.11.01	GEO	Available
7th	2010.12.18	IGSO	Available
8th	2011.04.10	IGSO	Available
9th	2011.07.27	IGSO	Available
10th	2011.12.02	IGSO	Available
11th	2012.02.25	GEO	Available
12th, 13th	2012.04.30	MEO	Available
14th, 15th	2012.09.19	MEO	Available
16th	2012.10.25	GEO	Available

As can be seen from Table 1, the 1st satellite of the BDS is a test satellite, the 2nd satellite has been disabled. By the end of 2012, when the BDS-2 was completed, there were fourteen satellites for the BDS-2, including five GEO, five IGSO and four MEO satellites. From 2015, the 17th to 21st satellites, which are the new generation of BeiDou navigation satellites. A new dedicated platform a number of new technologies were used in these satellites for the verification of inter-satellite links, satellite atomic clock and downlink navigation signal [5]. The 22nd satellite and 23rd satellite will be in service with other satellites in orbit after completion of the on-orbit test, which will further enhance the stability of the system constellation and strengthen the service of BDS-2 [6]. The 22nd satellite and 23rd satellite are called the backup satellites of BDS-2 [7].

3 Application Strategy for the New Generation of BeiDou Navigation Satellites

3.1 The Impact of the BDS-2 Satellites Failure

The life of BeiDou satellite in orbit is generally 8 years. By the end of 2018, there will be five BDS-2 satellites to be end of life, including three GEO and two IGSO satellites. By the end of 2019, three IGSO satellites will be end of life. By the end of 2020, all the remaining satellites of BDS-2 will be end of life. From the current to 2020, when BeiDou global system can provide services, if there is no corresponding smooth application strategy of satellite, the existed users of BeiDou will inevitably affected.

According to the construction plan of BeiDou global system, the goal is to provide basic services to the countries along the Belt and Road and in neighboring regions by 2018, and to complete the constellation deployment with the launching of 35 satellites by 2020 to provide services to global users [1]. In November 2016, the latest release of BeiDou Satellite System Signal In Space Interface Control Document Open Service Signal (Version 2.1) (hereinafter referred to as the BeiDou ICD) was published, the open service signals B1I and B2I was defined. B2I signal will be gradually replaced by the better performance signal [8]. In other words, the current B1I will be retained for at least a certain period of time, which will be broadcast through the global satellite to ensure a smooth transition for the existed BDS-2 users.

3.2 The Application Strategy for the New Launching Satellites

Because of the launch schedule of BeiDou global satellites is uncertainty, it is very necessary to make full use of five new generation of satellites and two BDS-2 backup satellites. The service capabilities of BDS will be ensured, and the existed users will not be affected.

3.2.1 The Application Strategy for the New Generation of Satellites

BDS-2 has been a continuous and stable system. The new launching satellites and the later satellites of global system, which are controlled by different ground systems. How to get satellite services from different ground control system at the same time. The ground control system of the new generation of satellites is also independent of the BDS-2, which can be just to carry out the relevant test for BeiDou global system.

Because of the ground system the new generation of satellites is only for the test, the operating state can not meet the reliability requirements of the online operating system, these satellites will be put into the BDS-2 to operate. In summary, the application strategies of five new generation of satellites are as follows:

1. Because of the new generation satellites and the BDS-2 satellites belong to different ground systems, the positioning test based on these satellites will be carried out to provide feasibility validation. By adjusting the clock difference parameter a0 of the new generation satellite, the UERE of new-generation satellite and the BDS satellites will be consistent, which ensures that the positioning accuracy from the two types of satellites is not degraded. At last, the common BDS receiver is used to receive the signals from two types of satellites at the same time, the satellite UERE and the positioning accuracy of receiver is studied to support for the smooth transition service of BDS.
2. After the ground control system of BDS-2 is updated, the five new generation of satellites will be controlled by BDS-2. It is completely feasible in technology, not to go into details in this paper. It is necessary to consider the application of the existed user.

    - According to the BeiDou ICD (version 1.0) released in 2012 and the BeiDou ICD (version 2.0) released in 2013, the space section of BDS-2 are composed of five GEO satellites, five IGSO satellites and four MEO satellites [9, 10]. The PRN of these satellites are numbered 1–14. So some BeiDou receivers are designed to receive the signals only from PRN 1 to 14 satellites. In order to ensure the use of these receivers, the new generation of satellites should be priority to use PRN 1–14. This is also true for the global system satellites which will participate in a smooth transition.

- The rate of D2 navigation message in B1I signal broadcast by GEO satellites, is 500 bps, while the B1I signal broadcast by IGSO and MEO satellites, whose message rate is 50 bps. The demodulation method of the receiver is different for the two types of messages. The PRN of GEO satellites are 1–5, and the new generation of satellites are non-GEO satellites, so the PRN 1–5 can not be used when the new generation satellite numbers are reconstructed to within 14.

3.2.2 The Application Strategy for the Backup Satellites of BDS-2

The 22nd and 23rd satellites are the IGSO satellites and GEO satellites, respectively. As the backup satellites can be operated by the ground control system of BDS-2 directly, the UERE is also consistent with the current BDS-2 satellites. The PRN of satellite is only considered.

The application strategy of the backup satellites will be same as the new generation of satellites. The PRN of satellites will be within 14, and the numbers 1–5 will not be used by the non-GEO satellites. The detailed application strategies are as follows:

1. As the current satellite of PRN 13 has been failure, the 22nd satellites can use PRN 13 to provide services. This replacement strategy has been recognized by the official website of BeiDou [11].
2. The 23rd satellite is a GEO satellite, which will not be replaced until the current GEO satellites are failure. If this GEO satellite need to be used currently, the BeiDou ICD will be revised to avoid using error for the receiver.
3. If there are backup satellite of BDS-2 in the follow, which will obey the above application strategy.

4 Receiver Verification

The feasibility of the application strategy needs to be verified by the user receiver. The new generation of satellites are operated by BDS-2, and the ground control system of BDS-2 will be updated adaptively, there is no technical problem. So only the feasibility of the positioning services from the satellites which are belong to different ground control system need to be verified. Positioning accuracy is determined by the UERE and DOP of the satellites. The new generation of satellites are added into BDS-2, the visible of satellites will be increased, so the DOP value will generally be decreased, then the impact of positioning accuracy will be only UERE. In the process of re verification, the signal from BDS-2 satellites and new

generation of satellites are received to analyze UERE by the receiver at the same time. The observation equation of the satellite signal received by the receiver can be approximately described as:

$$P_i^j = \rho_i^j + c(dt - dt^j) + Trop^j + ion_i^j + M_i^j + \varepsilon_i^j \tag{1.1}$$

where P_i^j is the observation of pseudo-range, ρ_i^j is the distance between satellite and earth (including the orbit error of satellite, the error of receiver position), c is the speed of light, dt is the clock error of receiver, dt^j is the clock error of satellite, $Trop^j$ is tropospheric error, Ion_i^j is ionospheric error, M_i^j is multipath error, ε_i^j is the error in addition to the above-mentioned error, including noise, i is the frequency, and j is the number of the satellite. The coordinate of the receiver is known, so there is only the error of satellite orbit included in ρ_i^j. The coordinate of receiver, tropospheric model correction, and ionospheric model correction are put into (1.1), then the linearized residuals of observation can be obtained. The residuals of the multiple satellites can be averaged to eliminate the influence of the clock error of receiver, at last the UERE of each satellite can be counted. In this paper, the B1I signal of the new generation of satellites and the BDS-2 satellites were continuously received from August 26 to September 2, 2016. The statistical results of UERE are shown in Fig. 1.

In Fig. 1, C01 to C14 are the satellites of BDS-2, C15 is the 22nd satellite, B31 to B34 are the new generation of satellites. In August 30th, the clock difference parameter a0 of the new generation satellites was adjusted, and the UERE of the new generation of satellites is consistent with the satellites of BDS-2. The positioning accuracy of the receiver with B1I is shown in Table 2.

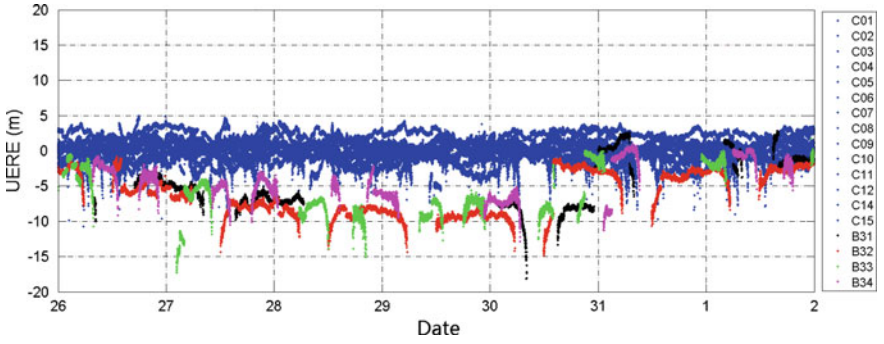

Fig. 1 The statistical results of UERE

Table 2 The statistical results of position accuracy with B1I (95%)

Date	Only BDS-2 satellites		BDS-2+ the new generation satellites	
	Horizontal	Elevation	Horizontal	Elevation
8.26	3.89	5.07	4.83	6.07
8.27	3.28	4.71	6.79	6.55
8.28	3.30	5.25	7.53	8.47
8.29	2.76	5.97	7.24	9.74
8.30	3.23	3.77	5.50	10.67
8.31	3.62	4.54	3.17	4.34
9.1	3.30	4.12	3.07	3.85

5 Conclusion

The result of receiver verification indicates that the new generation satellites can provide the service together with the BDS-2 satellites, and only the clock difference parameter a0 need to be adjusted, so that the two kinds of satellite UERE will be consistent. When the UERE of these satellites are consistent, the positioning accuracy of BDS-2+ the new generation satellites will be improved than positioning with BDS-2 satellites alone. By this verification, it is further explained that the new generation of satellites can be incorporated into the BDS-2. The same method can also be used for the following BeiDou global satellites to provide smooth transition for the users of BDS-2.

Acknowledgements This paper is supported by national natural science fund (41474027).

References

1. The State Council Information Office of the People's Republic of China (2016) China's BeiDou navigation satellite system. Foreign Languages Press, Beijing
2. BeiDou official website (2016) The launch records of BeiDou satellite. http://www.beidou.gov.cn/xtjs.html. Cited 12 June 2016
3. Xinhua News Agency (2015) China successfully launched the first new generation of BeiDou navigation satellite. http://news.xinhuanet.com/tech/2015-03/31/c_1114813366.htm. Cited 1 Mar 2015
4. BeiDou official website (2014) The satellite status of BeiDou navigation system. http://www.beidou.gov.cn/2015/10/20/201510208de633655fd64d1198fae37d56583543.html. Cited 27 Sept 2014
5. Linlin W, Yifang H (2016) The new generation of BeiDou navigation "key satellite" is successfully launched. Xinhua News Agency. http://news.xinhuanet.com/2016-02/01/c_1117960936.htm. Cited 1 Feb 2016
6. Xinhua News Agency (2016) China successfully launched the 23rd BeiDou navigation satellite. http://news.xinhuanet.com/2016-06/13/c_129054934.htm. Cited 13 June 2016
7. Zhe S (2016) The first 22 satellites of BeiDou satellite navigation system is backup for BDS-2. The Journal of China Aerospace. http://www.spacechina.com/n25/n144/n206/n216/c1232638/content.html. Cited 1 Apr 2016

8. China Satellite Navigation Office (2016) BeiDou Satellite system signal in space interface control document open service signal (Version 2.1)
9. China Satellite Navigation Office (2012) BeiDou Satellite System Signal In Space Interface Control Document Open Service Signal (Version 1.0)
10. China Satellite Navigation Office (2013) BeiDou satellite system signal in space interface control document open service signal (Version 2.0)
11. BeiDou official website (2016) The 22nd BeiDou navigation satellite is to provide services. http://www.beidou.gov.cn/2016/08/05/20160805be35373a002d45788fc4b8e4b798750c.html. Cited 5 Aug 2016

A Polarization Anti-jamming Algorithm Based on Space-Frequency Constraints

Yongxiang Zheng, Chao Ren and Gang Hu

Abstract Polarization sensitive array (PSA) is an array system composed of polarization sensitive elements which consist of electromagnetic vector sensor. Compared with the conventional array, the PSA not only can obtain the spatial information of the signal, but also can perceive the polarization state information of the signal. As a result the anti-jamming processing in the polarization domain can increase the anti-jamming degree of freedom, as well as improve the anti-jamming performance. Based on the PSA, this paper extends the existing spatial and polarization domain filtering model to the spatial, spectral and polarization domain for wideband signal processing. A polarization anti-jamming algorithm based on space-frequency constraint is proposed. The algorithm transforms the received signal into the frequency domain, constraining the polarization domain and spatial domain on every frequency bin of interest with polarization-spatial domain steering vector by the linearly constrained minimum variance (LCMV) criterion. While suppressing the interferences, the processing loss of the desired signal can be reduced, enhancing the anti-jamming ability. The simulation results show that the proposed algorithm can effectively suppress the interference and fully validates the effectiveness of the proposed algorithm. The algorithm can be widely used in satellite navigation anti-jamming receiver, significantly improving the availability and sensitivity of the receiver in a complex environment.

Keywords PSA · Anti-jamming · Space-frequency · Constraint · LCMV

Y. Zheng (✉) · C. Ren · G. Hu
Unicore Communications, Inc., Fengxiandonglu Road,
Haidian District, Beijing 100081, China
e-mail: yongxiangzheng@navchina.com

J. Sun et al. (eds.), *China Satellite Navigation Conference (CSNC) 2017 Proceedings: Volume I*, Lecture Notes in Electrical Engineering 437,
DOI 10.1007/978-981-10-4588-2_72

1 Introduction

As we know, in the satellite navigation system, the landing signals are extremely weak after making a long journey from satellites, which are vulnerable to interferences, so anti-jamming technology has always been an important issue in the field of satellite navigation. Many classical algorithms have been developed to eliminate interferences, processing the signals in time domain, frequency domain and space domain [1]. Algorithm in polarization domain which is based on the PSA is another effective approach [2]. Comparing with the ordinary antenna array, the PSA obtains not only the spatial information of the signal, but also the polarization information. Thus, anti-jamming algorithms carried out in the polarization domain increase the degree of freedom and anti-jamming performance. Over the past decades, researchers have conducted an in-depth study and made a lot of achievements in the field of PSA [3, 4]. Applications of the PSA in anti-jamming processing has been analysed in detail in [5, 6], where desired signals and interferences cannot be separated in space domain, the interference can be effectively suppressed in the polarization domain [7]. An adaptive polarization filter is proposed, and the relationship between the theoretical performance of the adaptive polarization filter and the signal-to-noise ratio (SNR) is deduced in [8]. A joint polarization and space domain anti-jamming method is proposed for satellite navigation signals in [9, 10] respectively, which can effectively suppress the interference and enhance the desired signal. A new method of interference detection and suppression is proposed from the view of polarization diversity in [11].

After reviewing the signal model of PSA, the polarization anti-jamming model is described in Sect. 2. A new polarization anti-jamming algorithm based on space-frequency constraint is proposed in Sect. 3. Results obtained from computer simulations of the new algorithm are presented in Sect. 4. Finally, in Sect. 5, we conclude the paper.

2 Polarization Anti-jamming

2.1 Signal Model for PSA

Assuming there is a polarization sensitive array centered at the origin of the coordinates, which is a uniform circular array (UCA) of biorthogonal electric dipoles as shown in Fig. 1. In order to simplify the analysis, we make the ideal hypothesis on the electromagnetic signal, the propagation medium, the array state and the environment.

There is the incident electromagnetic waves coming from (θ, φ), of which the polarization parameter is (γ, η), then the polarization vector can be expressed as

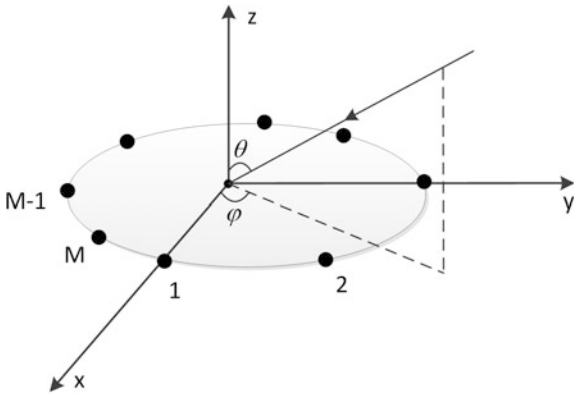

Fig. 1 Electromagnetic wave reception of a uniform circle array

$$s_p = \begin{bmatrix} \boldsymbol{E}_x \\ \boldsymbol{E}_y \end{bmatrix} = \begin{bmatrix} -\sin\varphi & \cos\theta\cos\varphi \\ \cos\varphi & \cos\theta\sin\varphi \end{bmatrix} \begin{bmatrix} \cos\gamma \\ \sin\gamma e^{j\eta} \end{bmatrix} \tag{2.1}$$

where $\boldsymbol{E}_x$ and $\boldsymbol{E}_y$ denote the polarization component of the direction x and y, respectively.

Let the radius of the uniform circular array be $R = \lambda/2$, where λ is the wavelength of the carrier. According to the phase relation of each element to the coordinate origin, the spatial steering vector of array is

$$s_a = \left[e^{j\xi\cos(\varphi - r_0)}, e^{j\xi\cos(\varphi - r_1)}, \ldots, e^{j\xi\cos(\varphi - r_m)} \right]^T \tag{2.2}$$

where $\xi = \frac{2\pi R}{\lambda}\sin\theta = 2\pi\sin\theta$ and $r_n = \frac{2\pi}{M}m$, $(m = 1, 2, \ldots, M)$.

Assuming that the incident signal is $s(t)$, then the signal received by the whole polarization sensitive array can be expressed as

$$\boldsymbol{X}(t) = \boldsymbol{S}s(t) + \boldsymbol{N}(t) \tag{2.3}$$

where $\boldsymbol{N}(t)$ represents the Gaussian white noise and $\boldsymbol{S} = \boldsymbol{s}_p \otimes \boldsymbol{s}_a$ is defined as the polarization-space joint steering vector, where $\otimes$ denotes the Kronecker product of the matrix.

2.2 Polarization Anti-jamming Model

Assuming that there are H desired signal and L jamming signal arrive at the polarization sensitive array simultaneously

$$\boldsymbol{S}(t) = [s_1(t), s_2(t), \ldots, s_H(t)] \tag{2.4}$$

$$\boldsymbol{J}(t) = [j_1(t), j_2(t), \ldots, j_L(t)] \tag{2.5}$$

The received signal of the array is

$$\boldsymbol{X}(t) = \boldsymbol{S}_s\mathbf{S}(t) + \boldsymbol{S}_j\boldsymbol{J}(t) + \boldsymbol{N}(t) \tag{2.6}$$

where $\boldsymbol{S}_s$ and $\boldsymbol{S}_j$ are the steering vectors of the desired signals and the interfering signals respectively.

The array output signal $\boldsymbol{Y}(t)$ is the sum of the array received signal vector $\boldsymbol{X}(t)$, shown as

$$\boldsymbol{Y}(t) = \boldsymbol{W}^H\boldsymbol{X}(t) \tag{2.7}$$

where W is the weight of the polarization and space domain filtering.

The optimal weight under the LCMV criterion can be obtained by

$$\min_{W} \boldsymbol{W}^H\boldsymbol{R}_{XX}\boldsymbol{W} \quad \text{s.t.} \quad \boldsymbol{C}^H\boldsymbol{W} = f \tag{2.8}$$

where $\boldsymbol{R}_{XX} = \boldsymbol{X}(t)\boldsymbol{X}^{\mathrm{H}}(t)$ is the correlation matrix of the received signal, and C is the steering vector of the constrained signal and f is a constant, usually 1 or 0.

Using the Lagrangian algorithm, the optimal weight can be expressed as

$$\boldsymbol{W}_{opt} = \boldsymbol{R}_{xx}^{-1}\boldsymbol{C}(\boldsymbol{C}^H\boldsymbol{R}_{xx}^{-1}\boldsymbol{C})^{-1}f \tag{2.9}$$

3 Polarization Anti-jamming Model Based on Space Frequency Constraints

Since the satellite navigation signal usually has a certain bandwidth, the conventional polarization and space domain algorithm focus only on the frequency of the carrier, while ignoring the influence of other frequency points in the bandwidth. By Fourier transforming the received signal into the frequency domain, polarization and space domain algorithm is carried out on every frequency bin of the desired signal band which can improve anti-jamming capability and have less SNR lost.

Performing a discrete Fourier transform on signals received by the array described in the Eq. (2.6), we obtain a wideband model as follows

$$\boldsymbol{X}(f_k) = \boldsymbol{S}_s(f_k)\boldsymbol{S}(f_k) + \boldsymbol{S}_j(f_k)\boldsymbol{J}(f_k) + \boldsymbol{N}(f_k), \quad k = 1, 2, \ldots, K \tag{3.1}$$

where $\boldsymbol{X}(f_k)$ is the received signals on frequency bin f_k, $\boldsymbol{S}(f_k)$, $\boldsymbol{J}(f_k)$ and $\boldsymbol{N}(f_k)$ are Fourier transformed desired signal, interference and noise respectively.

The frequency domain steering vector of desired signal and interference is $\boldsymbol{S}_s(f_k)$ and $\boldsymbol{S}_j(f_k)$ respectively, expressed as follows:

$$\boldsymbol{S}_s(f_k) = [\boldsymbol{s}_{s1}(f_k), \boldsymbol{s}_{s2}(f_k), \ldots, \boldsymbol{s}_{sH}(f_k)] \tag{3.2}$$

$$\boldsymbol{S}_j(f_k) = [\boldsymbol{s}_{j1}(f_k), \boldsymbol{s}_{j2}(f_k), \ldots, \boldsymbol{s}_{jL}(f_k)] \tag{3.3}$$

where $\boldsymbol{s}_{sh}(f_k) = \boldsymbol{s}_{ph}(f_k) \otimes \boldsymbol{s}_{ah}(f_k)$ $(h = 1, 2, \ldots H)$ is defined as the joint polarization and space domain steering vector of the desired signal of the f_k frequency bin, $\mathbf{s}_{jl}(f_k) = \mathbf{s}_{pl}(f_k) \otimes \mathbf{s}_{al}(f_k)$ $(l = 1, 2, \ldots L)$ is defined as the joint polarization and space domain steering vector of the interference of the f_k frequency bin.

The array filter output in frequency domain on f_k frequency bin is

$$\boldsymbol{Y}(f_k) = \boldsymbol{W}^H(f_k)\boldsymbol{X}(f_k) \tag{3.4}$$

where $\boldsymbol{W}(f_k)$ is the weight of the polarization and space domain on the f_k frequency bin. Finally, the time domain output of the array can be obtained by performing the inverse discrete Fourier transform.

The same method can be used in Eq. (2.8) to obtain the $\boldsymbol{W}(f_k)$. Without loss of generality, we choose the joint polarization and space domain steering vector of the first desired signal as the constraint steering vector $\mathbf{C}$, where

$$\boldsymbol{C} = [\boldsymbol{s}_{s1}(f_1), \boldsymbol{s}_{s1}(f_2), \ldots, \boldsymbol{s}_{s1}(f_K)] \tag{3.5}$$

The optimal weight based on the space-frequency constraint can be obtained by introducing the formula (1.14) into (1.9) as

$$\boldsymbol{W}_{JFPS}(f_k) = \boldsymbol{R}_{xx}^{-1}(f_k)\boldsymbol{C}(\boldsymbol{C}^H\boldsymbol{R}_{xx}^{-1}(f_k)\boldsymbol{C})^{-1}f \tag{3.6}$$

where $f = [1, 1, \ldots, 1]$, which means the amplitude of first desired signal are all set to 1.

4 Computer Simulations

The following two computer simulations are going to test the proposed anti-jamming algorithm in the case of single interference and three interferences respectively. The experiment is based on the array structure shown in Fig. 1, and the desired signal and wideband interferences are of the same frequency. The bandwidth is 20 MHz, sampling rate is 62 MHz, and FFT point is 1024.

Example 1: Single Interference Example The spatial and polarization parameters of the desired signal and interference is $\theta_s = 20°$, $\phi_s = 40°$, $\gamma_s = 30°$, $\eta_s = 80°$ and $\theta_i = 20°$, $\phi_i = 40°$, $\gamma_i = 70°$, $\eta_i = 40°$. Obviously, the direction of arrival of the desired signal and interference are the same and the polarization parameters are

different. Figure 2 shows the polarization domain array pattern on center frequency bin of band, since the other frequency bins have the similar results. There forms a null in the polarization domain direction of interference, and the gain of desired signal has almost no loss. Figure 3 shows the space domain array pattern at the direction of interfering, which forms a deep null. Figure 4 is the space domain array pattern at the direction of signal, which has no loss. In short, the interference both in the polarization domain or space domain, have been nulled, and desired signal always remain the same because of the constraint.

Example 2: Three Interferences Example The polarization and space domain parameters of the desired signal are the same as described in Example 1. The number of interference sets to three, and the parameters are defined as: interference 1:$\theta_s = 20°$, $\phi_s = 80°$, $\gamma_s = 70°$, $\eta_s = 40°$, interference 2: $\theta_s = 80°$, $\phi_s = 150°$, $\gamma_s = 30°$, $\eta_s = 70°$, interference 3: $\theta_s = 50°$, $\phi_s = 270°$, $\gamma_s = 10°$, $\eta_s = 20°$. Figure 5 shows the polarization domain array pattern. The corresponding apace domain array pattern is shown in Fig. 6. As can be seen from the figure, the three interferences have been deeply nulled in both polarization and space domain.

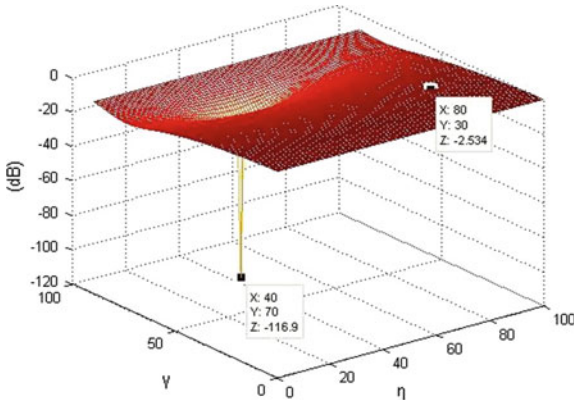

Fig. 2 Polarized domain array pattern

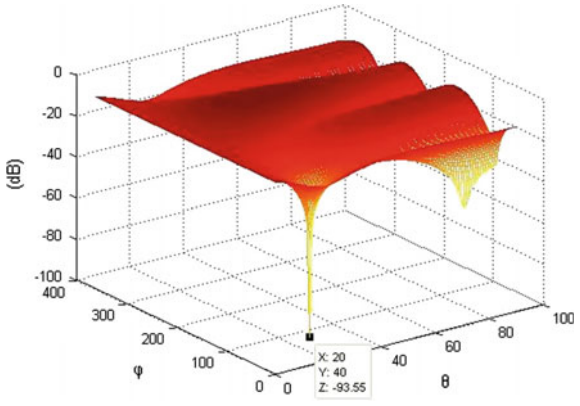

Fig. 3 Space domain array pattern for interference

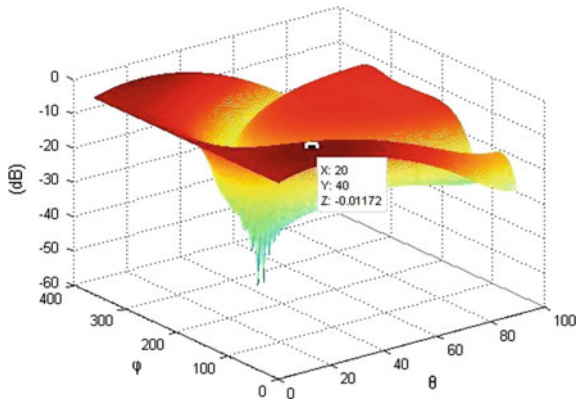

Fig. 4 Space domain array pattern for desired signal

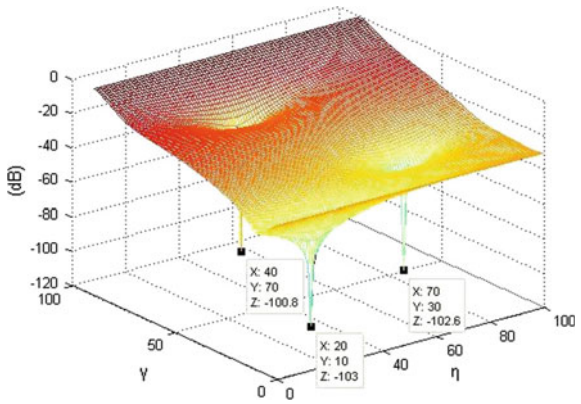

Fig. 5 Polarization domain array pattern

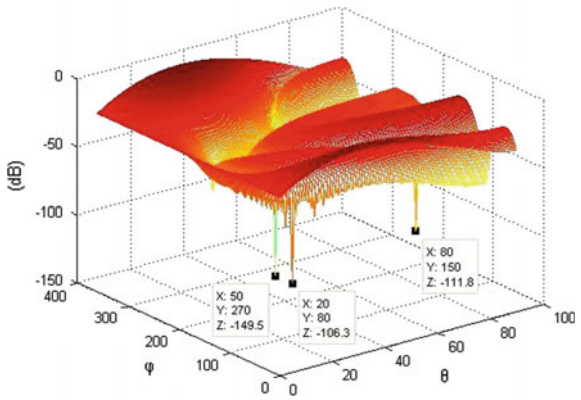

Fig. 6 Space domain array pattern

5 Conclusions

In this paper, a polarization anti-jamming algorithm based on space-frequency constraints is proposed. The key of the algorithm is to utilize the information of the polarization, space and frequency domain of the wideband signal at the same time. The polarization and space domain steering vector is constrained to all frequency bins of the desired signal band by the LCMV criterion. With constraining the desired signal gain to be 1, desired signal has almost no loss while eliminating the interference. Finally, several simulation examples demonstrate the effectiveness of the algorithm.

References

1. Wang Y, Ding Q (2009) Adaptive array processing. Tsinghua University Press, Beijing
2. Zhuang Z (2005) Signal processing of polarization sensitive array. National Defence Industry Press, Beijing
3. Compton RT Jr (1981) On the performance of a polarization sensitive adaptive array. IEEE Trans Antennas Propag 29(5):718–725
4. Compton RT Jr (1981) The tri-pole antenna: an adaptive array with full polarization flexibility. IEEE Trans Antennas Propag 29(6):944–952
5. Zhang X, Shi Y, Xu D (2008) Novel blind joint direction of arrival and polarization estimation for polarization-sensitive uniform circular array. Prog Electromagn Res 86(1): 19–24
6. Fante L, Vaccaro JJ (2000) Wideband cancellation of interference in a GPS receive array. IEEE Trans Aerospace Electron Syst 36(2):551
7. Dai HY, Wang XS, Li YZ (2012) Main-lobe jamming suppression method of using spatial polarization characteristics of antennas. IEEE Trans Aerosp Electron Syst 48(3):2167–2179
8. Xu Z, Wang X, Xiao S (2002) Adaptive recursive filtering in polarization domain. Chin J Electron 30(4):608–610
9. Zhang M, Wang L, Xu SB (2011) GPS signal anti-jamming based on dual-polarized antenna array. In: IEEE International Conference on Signal Processing, Communications and Computing (ICSPCC), pp 1–4
10. Zheng W, Wang L (2013) Joint polarized and spatial domain anti-jamming method for GNSS. In: IEEE international conference on signal processing, communication and computing (ICSPCC), pp 1–5
11. Sun L, Jing BG, Cheng Y (2015) Jamming monitoring and anti-jamming by polarization diversity reception in the satellite navigation system. In: 8th international congress on image and signal processing (CISP), pp 1303–1307

Navigation Terminal Test Decision Scheme Design and Verification

Zhiheng Zhang, Weiwei Qiu and Zi Wang

Abstract This paper conducts some essential theoretical research on navigation terminal test. Technical details are studied including model set up, project design and simulation verification. Moreover, based on the technical details navigation terminal test methods are studied.

Keywords Test · Project design · Simulation verification

1 Introduction

A GNSS navigation terminal, in general, is an electronic device that receives and digitally processes the signals from a GNSS satellite constellation in order to provide position, velocity and time (of the receiver) [1]. Various Navigation terminals are widely used in GNSS ground control systems and used by the users. Thus, navigation terminal test is vital for the function of the terminal [2]. Especially the batch test, which could test several terminals in parallel, can improve test efficiency dramatically. This paper conducts some essential theoretical research on navigation terminal test and carries on the study and verification of batch test theory

2 Design of Test Batch Decision

According to the classification of batch decision making, the decision problem of batch testing of navigation terminals can be considered as a multi-objective decision problem.

Z. Zhang (✉) · W. Qiu · Z. Wang
Beijing Satellite Navigation Center, Beijing, China
e-mail: zhangzh44@sina.com

J. Sun et al. (eds.), *China Satellite Navigation Conference (CSNC) 2017 Proceedings: Volume I*, Lecture Notes in Electrical Engineering 437,
DOI 10.1007/978-981-10-4588-2_73

2.1 Target Type and Attribute Value Normalization Mode

Assuming there are m targets $G_1, G_2, \ldots, G_m$ and n decision plan $A_1, A_2, \ldots, A_n$. Under the target $G_j\,(i = 1, 2, \ldots, m)$ the attribute of plan $A_j (j = 1, 2, \ldots, n)$ is a_{ij}, then the decision matrix is $A = \left(a_{ij}\right)_{m\times n}$. Marked as $M = (1, 2, \ldots, m)$, $N = (1, 2, \ldots, n)$. The target types can be divided into the benefit type goal, the cost type goal, the fixed type goal, the deviation type goal, the interval type goal generally, deviate the interval type goal. Cost-type goal is the goal of the smaller the better goal; fixed target is the target value which is better closer to a fixed value α_i; deviation type target is the target value deviates from a fixed value β_i; interval-type goal is the target value is closer to a fixed interval $\left[q_1^i, q_2^i\right]$ (Including falling into the interval); deviation from the target interval is the target value deviates from a fixed interval $\left[q_1^i, q_2^i\right]$.

Let $I = \cup_{i=1}^{6} I_l$, I_l represent profit type, cost type, fixed type, deviation type, interval type, deviation from the interval of the target set of subscripts respectively.

In order to eliminate the influence of different physical dimensions on the decision results, the decision matrix $A = \left(a_{ij}\right)_{m\times n}$ can be transformed into normalized matrix $R = \left(r_{ij}\right)_{m\times n}$, where

$$r_{ij} = (a_{ij} - \min_j a_{ij})/(\max_j a_{ij} - \min_j a_{ij}),\ i \in I_1, j \in N \tag{1}$$

$$r_{ij} = (\max_j a_{ij} - a_{ij})/(\max_j a_{ij} - \min_j a_{ij}),\ i \in I_2, j \in N \tag{2}$$

$$r_{ij} = 1 - a_{ij} - \alpha_i/\max_j a_{ij} - a_i,\ i \in I_3, j \in N \tag{3}$$

$$r_{ij} = (a_{ij} - \beta_i - \min_j a_{ij} - \beta_i)/(\max_j a_{ij} - \beta_i - \min_j a_{ij} - \beta_i),\ i \in I_4, j \in N \tag{4}$$

$$r_{ij} = \begin{cases} 1 - \dfrac{\max\{q_1^i - a_{ij}, a_{ij} - q_2^i\}}{\max\{q_1^i - \min\limits_j a_{ij}, \max\limits_j a_{ij} - q_2^i\}}, a_{ij} \notin [q_1^i, q_2^i] \\ 1, a_{ij} \in [q_1^i, q_2^i] \end{cases},\ i \in I_5, j \in N\,\mathrm{v} \tag{5}$$

$$r_{ij} = \begin{cases} \dfrac{\max\{q_1^i - a_{ij}, a_{ij} - q_2^i\}}{\max\{q_1^i - \min\limits_j a_{ij}, \max\limits_j a_{ij} - q_2^i\}}, a_{ij} \notin [q_1^i, q_2^i] \\ 0, a_{ij} \in [q_1^i, q_2^i] \end{cases},\ i \in I_6, j \in N \tag{6}$$

2.2 Decision—Making Process

Due to the complexity of objective things and the vagueness of human thinking, it is often difficult to give a clear target weight, but only to provide its possible range

of changes. We can set the weight vector of the target as $\omega = (\omega_1, \omega_2, \ldots, \omega_m)^T$, $0 \le a_i \le \omega_i \le b_i, i \in M, \sum_{i=1}^{m} \omega_i = 1$, where b_i, a_i are upper limit and lower bound of ω_i. The overall attribute value of A_j is

$$z_j = \sum_{i=1}^{m} \omega_i r_{ij}, \quad j = 1, 2, \ldots, n \tag{7}$$

The multi-objective decision-making of a finite number of schemes is essentially a comparison of the ranking of these schemes. Obviously, the greater the overall attribute value, then its corresponding program A_j becomes more excellent.

First look at the individual properties of A_j $(j = 1, 2, \ldots, n)$, the overall program to take the optimal value, the corresponding weight of each target. To this end, the following single-objective decision-making model is established by

$$\begin{aligned} &\max \sum_{i=1}^{m} \omega_i r_{ij} \\ &0 \le a_i \le \omega_i \le b_i, i \in N \\ &\sum_{i=1}^{m} \omega_i = 1 \end{aligned}$$

Solution of this model, will be optimal target weight vector $\omega^{(j)} = \left(\omega_1^{(j)}, \omega_2^{(j)}, \ldots, \omega_m^{(j)}\right)^T$ of each plan $A_j (j = 1, 2, \ldots, n)$ corresponding to the program. Then we use normalized matrix $R = \left(r_{ij}\right)_{m \times n}$ and weight vector $\omega^{(j)}$ $(j = 1, 2, \ldots, n)$ to find the optimal coordination weight vector of the target. Let the weight vector $\omega^{(j)}$ $(j = 1, 2, \ldots, n)$ make up as matrix

$$W = \begin{bmatrix} \omega_1^{(1)} & \omega_1^{(2)} & \cdots & \omega_1^{(n)} \\ \omega_2^{(1)} & \omega_2^{(2)} & \cdots & \omega_2^{(n)} \\ \cdots & \cdots & \cdots & \cdots \\ \omega_n^{(1)} & \omega_n^{(2)} & \cdots & \omega_n^{(n)} \end{bmatrix}$$

Then the weight vector is obtained by linear combination of n weight vectors as

$$\omega = W \cdot w \tag{8}$$

$\omega = \left(\omega_1, \omega_2, \ldots, \omega_m\right)^T$ is the combination of weight vector, w is a $n \times 1$ column vector to be determined and meet the constrain condition

$$w^T w = 1 \tag{9}$$

Let $r_j = \left(r_{1j}, r_{2j}, \ldots, r_{mj}\right)^T (j = 1, 2, \ldots, n)$, then $R = (r_1, r_2, \ldots, r_n)^T$ from (7) and (8) we can get

$$z_j = \sum_{i=1}^{m} \omega_i r_{ij} = \omega^T r_j = (Ww)^T r_j \tag{10}$$

We should choose weight vector $\omega = (\omega_1, \omega_2, \ldots, \omega_m)^T$ So that the overall attribute values of all schemes are as large as possible. To this end, the following multi-objective decision model is constructed

$$\begin{aligned} &(\text{MOD} \quad max\{z_1, z_2, \ldots, z_n,\} \\ &\text{s.t.} \quad w^T w = 1 \end{aligned}$$

Since there is no prior preference relationship for each attribute, the above multi-objective decision-making model can be transformed into equal-weight single-objective decision problem:

$$\begin{aligned} &(\text{SOD2})\, max = Z^T Z \\ &\quad \text{s.t.} \quad w^T w = 1 \\ &z = (z_1, z_2, \ldots, z_n,)^T \end{aligned}$$

Let $f(w) = Z^T Z$, from (10) we know

$$f(w) = z^T z = w^T (R^T W)^T (R^T W) w \tag{11}$$

According to matrix theory, $f(w)$ has the max value, which is maximum eigenvalue λ_{max} of $(R^T W)^T (R^T W)$, w is the corresponding eigenvectors. Because the matrix $(R^T W)^T (R^T W)$ is symmetrical non-negative, According to the Perron-Frobenius theorem of non-negative irreducible matrices: λ_{max} is single root, eigenvector $w > 0$. So, from (8) we can get Combining weight vector (best coordination weight vector), and get the comprehensive attribute value of each scheme, and sort them out.

To sum up, we get the following decision-making algorithm as follows.

(1) There are m targets $G_1, G_2, \ldots, G_m$ in the targer-decision problem and n decision plans $A_1, A_2, \ldots, A_n$. The attribute value of Plan $A_j\,(j = 1, 2, \ldots, n)$ under the condition $G_i\,(i = 1, 2, \ldots, m)$ is a_{ij}, so we get the decision matrix $A = \left(A_{ij}\right)_{m \times n}$;

(2) According to (1)–(6) we transform matrix A into matrix $R = \left(r_{ij}\right)_{m \times n}$;

(3) By experts (or by other means, such as the Analytic Hierarchy Process) target weight range of possible changes;

(4) From single-goal decision model

$$(\text{SOD1})\ \max \sum_{i=1}^{m} \omega_i r_{ij}$$
$$\text{s.t.}\quad 0 \le a_i \le \omega_i \le b_i, i \in N \quad \sum_{i=1}^{m} \omega_i = 1$$

To get the optimal target weight vector $\omega^{(j)} = \left(\omega_1^{(j)}, \omega_2^{(j)}, \ldots, \omega_m^{(j)}\right)^T$ $(j = 1, 2, \ldots, n)$

(5) n weight vectors $\omega^{(j)}(j = 1, 2, \ldots, n)$ make up the matrix $W = \left(\omega_i^j\right)_{m \times n}$, calculate the maximum eigenvalue λ_{max} and feature vector W of $(R^T W)^T (R^T W)$;

(6) To find combined weight vector (the optimal coordination weight vector) and carry on normalization processing, and then from (7) to get the comprehensive attribute value $Z_j\,(j = 1, 2, \ldots, n)$ of each scheme;

(7) Sort the order of $Z_j\,(j = 1, 2, \ldots, n)$ from large to small to find the order of $A_j\,(j = 1, 2, \ldots, n)$;

(8) End.

3 Simulation Test Validation

Mainly to the GPS navigation terminal receiver batch test as an example, analysis of navigation terminals on the test batch decision-making problems.

Examples include: GPS signal simulation generator 1, cost about 10 million; Assuming that the computer used in each test value of 5000 yuan; for each batch test in the test station value of 2000 yuan. At the same time assume that each computer can handle up to 8 terminal test results (taking into account the serial data transfer rate is limited).

Here consider the following five test programs, namely, 1, 4, 1, 1, 8, 1, 1, 12, 16, 16, and 1 min 32 of the batch test program. Respectively, as A1, A2, A3, A4, A5. The attribute values for the individual scenarios are listed in the following table.

In the target concentration, the test cost and the signal attenuation belong to the cost type goal, the single test quantity is the benefit goal, uses the above design method to carry on the decision-making, the concrete step as follows:

(1) Established by the decision matrix data in Table 1.

$$A = \begin{bmatrix} 11.3 & 12.1 & 13.4 & 14.2 & 18.4 \\ 4 & 8 & 12 & 16 & 32 \\ 6 & 9 & 10.8 & 12 & 15 \end{bmatrix}$$

Table 1 Scenario properties table

Aims	Program				
	A1	A2	A3	A4	A5
Testing cost (ten thousand yuan)	11.3	12.1	13.4	14.2	18.4
Single test	4	8	12	16	32
Signal attenuation (dB)	6	9	10.8	12	15

(2) Converting the decision matrix into a normalized decision matrix according to the normalization criteria:

$$R = \begin{bmatrix} 1 & 0.887 & 0.704 & 0.592 & 0 \\ 0 & 0.143 & 0.286 & 0.429 & 1 \\ 1 & 0.667 & 0.467 & 0.333 & 0 \end{bmatrix}$$

(3) Assuming the weight range of the target is:

$$0.1 \le w_1 \le 0.6, \quad 0.2 \le w_2 \le 0.5, \quad 0.01 \le w_3 \le 0.3$$

(4) For the decision-making program A2, the goal decision model is established by

$$\begin{gathered} \max\{0.887w_1 + 0.143w_2 + 0.667w_3\} \\ \text{s.t. } 0.1 \le w_1 \le 0.6, \quad 0.2 \le w_2 \le 0.5, \quad 0.01 \le w_3 \le 0.3 \\ w_1 + w_2 + w_3 = 1 \end{gathered}$$

The optimal target weight vector corresponding to the scheme can be solved $w(2) = (0.6\ 0.2\ 0.2)^T$.

Similarly, using the same method, find the optimal target weight vector corresponding to other schemes:

$$\begin{aligned} w^{(1)} &= (0.5,\ 0.2,\ 0.3)^T \\ w^{(3)} &= (0.6,\ 0.2,\ 0.2)^T \\ w^{(4)} &= (0.6,\ 0.39,\ 0.01)^T \\ w^{(5)} &= (0.2,\ 0.5,\ 0.3)^T \end{aligned}$$

(5) Vector $w^{(j)}\ (j = 1, 2, 3, 4, 5)$ make up the matrix

$$W = \begin{bmatrix} 0.5 & 0.6 & 0.6 & 0.6 & 0.2 \\ 0.2 & 0.2 & 0.2 & 0.39 & 0.5 \\ 0.3 & 0.2 & 0.2 & 0.01 & 0.3 \end{bmatrix}$$

calculate matrix $(R^T W)^T (R^T W)$, we get

$$(R^T W)^T (R^T W) = \begin{bmatrix} 1.6656 & 1.7059 & 1.7059 & 1.5149 & 1.2431 \\ 1.7059 & 1.7479 & 1.7479 & 1.5543 & 1.2743 \\ 1.7059 & 1.7479 & 1.7479 & 1.5543 & 1.2743 \\ 1.5149 & 1.5543 & 1.5543 & 1.4444 & 1.2229 \\ 1.2431 & 1.2743 & 1.2743 & 1.2229 & 1.0686 \end{bmatrix}$$

which has maximum eigenvalue λ_{max} and its corresponding feature vector

$$\lambda_{max} = 7.5282, \omega = (0.4684,\ 0.48,\ 0.48,\ 0.4346,\ 0.36418)^T$$

(6) From (8) we get combined weight vector (best coordinating vector) and normalized to

$$w = (0.8272,\ 0.4602,\ 0.3223)^T$$

then from (7) to get the comprehensive attribute value of each scheme:

$$Z_1 = 1.1495, Z_2 = 1.0145, Z_3 = 0.8645, Z_4 = 0.7945, Z_5 = 0.4602$$

(7) $Z_1 > Z_2 > Z_3 > Z_4 > Z_5$

At this point, you can get in the test conditions under the decision-making results. It should be noted that in practical applications, there are two parameters that need to be set by specific application specific, one is the original property values for each program, the need for accurate test of the actual cost of such statistics; its Second, the weight range under different objectives, the need to test the specific needs of the task set. Here only for example.

4 Conclusions

This paper built up a multi-objective decision for the batch test of navigation terminals and proposed a heuristic solution for this problem. Moreover, Simulation verification was conducted to demonstrate the feasibility for the model and test scheme given in this paper. The batch test scheme could be applied in real navigation terminal test.

References

1. Tan S (2010) The engineering of satellite navigation and positioning, 2nd edn. National Defence Industry Press, Changsha
2. Elliott DK 2002(Ch) Understanding GPS principles and applications. Publishing House of Electronics Industry

Study on Identification Parameters and Updating Mechanism of Beidou Navigation Message

Hailing Wu, Hui Liu, Rufei Zhang, Cheng Liu, Hang Ruan and Jun Mo

Abstract In the application of high-precision satellite navigation and positioning, differential GNSS positioning technology is used to eliminate the influence of various errors in order to improve the performance of positioning accuracy. The mathematical physics of differential GNSS positioning technology is based on the same space-time datum (the same orbit and difference parameters). Thus, in the RTCM/RTCA differential protocol, an IOD field is constructed based on the parameters of the GNSS navigation message parameters. The base station transmits the IOD parameter to the rover and compare it with the IOD parameters that formed by rover itself, then it can determine whether they are using the same ephemeris and clock difference parameters. The IOD field in the differential protocol is generally constructed based on a unique parameter in the GNSS navigation message for a certain period of time. There is no special field used to identify the parameter group in the BeiDou navigation message. Therefore, it is necessary to analyze the parameters of the existing navigation message, discuss the mechanism of parameter formation and constrain the broadcasting mechanism of the message so as to solve the obstacles in the scale application of BeiDou high precision differential. In this paper, the technical background of BeiDou RTCM IOD is discussed, the solution is studied and the experimental results show that it is feasible and effective to construct BDS RTCM IOD parameters based on Toe.

Keywords BeiDou · ICD · IODE · IODC · RTCM

H. Wu (✉)
National University of Defense Technology, Changsha, China
e-mail: wuhl@beidou.gov.cn

H. Wu · C. Liu · H. Ruan
Beijing Institute of Tracking and Communication Technology, Beijing, China

H. Liu · R. Zhang
GNSS Research Center, Wuhan University, Wuhan, China

J. Mo
Wuhan Nav&LBS, INC, Wuhan, China

J. Sun et al. (eds.), *China Satellite Navigation Conference (CSNC) 2017 Proceedings: Volume I*, Lecture Notes in Electrical Engineering 437,
DOI 10.1007/978-981-10-4588-2_74

1 Overview

As important parameters of GNSS, ephemeris and clock error broadcasting in navigation data are received by user for satellite position and time solution. Further, user position and time can be solved with satellites' ranges. Due to the constant change of satellite's positions and time, the ephemeris and clock error both have their own timelines. They are usually updated every hour. In the differential technologies such as RTK (Real-Time Kinematic) and CORS (Continuously Operating Reference System), infrastructures such as base stations and users such as moving stations receive satellite navigation signals respectively for solution. And the differential information is transformed from base station to moving station for differential technology applications. The differential technology requires the same set of ephemeris and clock error for solution, so parameter identifies the timeliness and consistency of ephemeris and clock error need designed. It's the foundation of the application of differential technologies such as RTK and CORS. Currently, the international universal differential data format is RTCM (Radio Technical Commission for Maritime Service) SC-104. It limits the IOD parameter with 8 bits to identify the timeliness and consistency of ephemeris and clock error of GNSS. The BeiDou workgroup was founded since 2013 to research specialized about BeiDou joining RTCM format. The IOD parameter issue has already become the main block of BeiDou standardization work.

GPS designed IODE (Issues of Data, Ephemeris) and IODC (Issues of Data, Clock) respectively in its navigation data, and made convention that the same set of the ephemeris's IODE is always the same with the IODC's last 8 bits in its ICD document. On the other hand, RTCM SC-104 generate GPS IOD (Issues of Data) according to IODE and IODC to identify the uniqueness ephemeris and clock error. Similar measures with slightly difference were adopted in GLONASS (Global Navigation Satellite System) and Galileo.

BDS (BeiDou Navigation Satellite System) navigation data has no specialized parameter to identify navigation data sets, but AODE (Age of Data Ephemeris)/Toe (time of ephemeris) and AODC (Age of Data Clock)/Toc (time of clock) are designed instead. However, regarding currently system status, this two sets of parameters can either identify or distinguish a specific set of ephemeris parameters. And it is a puzzle that the 8 bits IOD parameter which identifies timeliness and consistency of ephemeris and clock error must be based on the parameters above. To solve this problem, currently navigation data should be analyzed and the parameter generation mechanism should be discussed, and the navigation data broadcasting mechanism should be ordered in system operating and controlling phase. Thus the optimum scheme could be found with sufficient test and verify.

2 Ephemeris and Clock Error Analysis of Other GNSSs Navigation Message

2.1 IOD Field of GPS Navigation Message

In order to insure the smooth and correct processing of navigation signals, GPS identities specific constraints of navigation message uploading and update strategy in IS-GPS200H, and identities the update mechanism and comovement relation of the main parameters. The GPS IOD field in RTCM is also defined by the parameters such as IODE, IODC, Toe and Toc of ICD. The constraint mechanisms of ephemeris and clock error of GPS are stated in following:

(1) Constraint to IODC: the IODC parameter occupies 10 bits, providing in sub frame 1, and provides convenient method to detection clock error parameter status. The broadcasting IODC value will not repeat in 7 days.
(2) Constraint to IODE: the IODE parameter occupies 8 bits, providing in sub frame 2 and sub frame 3, any changing of sub frame 2 and sub frame 3 will cause the IODE's changing at the same time. It provides a convenient method to detection ephemeris parameter status. The broadcasting IODE value will not repeat in 6 days.
(3) Relationship of IODC and IODE: IODE in frame 2 and sub frame 3 should be accordance with IODC's low 8 bits in sub frame 1. Mismatch of them indicates updating of data set, and the new message needs to be collection.
(4) About message's normally updating: In the beginning of a new GPS week, no matter which message is broadcasted at last week end, subframe 1–5 will start from subframe 1 and 25 circulation pages of subframe 4, 5 will start from 1st page. When the message broadcasted by subframe 1–3 needs to be updated, new message always starts from the edge (GPS time is the integral multiples of 30 s); when the message of subframe 4–5 need to be updated, new message may broadcast from any page. Generally, broadcast gap of subframe 1–3 is 2 h and correspondingly, matching gap is 4 h.
(5) About message uploading update (including failure recovery): besides newly updated 1st group of message dataset, updating of new message dataset only happens around one hour. Newly updated 1st group of message dataset broadcasts from frontier of the frame, but also may update at any time among the one hour so that the gap may shorter than one hour. Ground operation and control make sure that the Toe value of newly uploading 1st dataset is different form that before updating. During the updating, ground operation and control will introduce slight change in Toe so that there will be gap between Toe and one hour border and the Toe value will broadcast in the 1st dataset by satellite. 2nd dataset after 1st dataset may also show the same gap. When there is gap before uploading, ground operation and control will introduce additional

difference during uploading. Difference of Toe value can indicate the difference of data concentrated value. If Toe is not integral point, it means there is new uploading during last four hours.

Under above restriction mechanism, in RTCM standard format, GPS system generates data issue field IOD according to its IODE and IODC parameters (8 bit, same with IODE).

2.2 GLONASS Satellite Ephemeris Identify Parameter

Similarly, GLONASS designs Ephemeris time (8 bit) in its satellite navigation message that can use tb to identify satellite ephemeris. Tb is time gap based on UTC (SU) +3 h. In RTCM standard format, IOD of this system generates, 8 bit among which 0–6 bit is the least significant bat constituted by tb and 7 bit is set to be zero, ignore. In difference application, user can compare difference message with tb of GLONASS satellite message to decide if user equipment and reference station correction are based on same group of satellite orbit determination [6–9].

2.3 Galileo Satellite Data Age

Similar to GPS, Galileo has designed IODnav field identify satellite ephemeris and IOD identify almanac parameters. RTCM difference agreement plan adopts 10 bit IODnav identify satellite ephemeris. Because IOD data field in difference agreement is only 8 bits, Galileo system IOD is constituted by top digit 0 and 7 least significant bits of IODnav. In practical application, there may be 7 least significant bits of two border epoch IOD are equal, at this moment Galileo IOD top digit value is 1 [6, 7, 9, 10].

So, different ephemeris data correspond to different IOD fields. When satellite ephemeris parameters change, identify fields will change accordingly. When base station and used generate satellite ephemeris IOD according to the same regulation and base station sends IOD fields to users, uses will compare it with their own IOD fields to know whether both sides use the same satellite ephemeris data.

3 Analysis on Identity Parameter of Ephemeris and Clock Error of BDS Navigation Data

The navigation message design of China's BDS is different with GPS and GLONASS. There is no identify field of ephemeris parameter such as GPS IODE and GLONSS tb in BDS, and parameter sets of AODE (5 bits) and Toe (17 bits),

AODC (5 bits) and Toc (17 bits) instead. Toe is the ephemeris reference moment, and AODE is the latest observation moment of Toe and the calculated ephemeris parameter. Toc is the clock error reference moment, and AODC is the latest observation moment of Toc and the calculated clock error parameter. However, according to currently system, these two sets of parameters might not be changed with the ephemeris and clock error parameters. Thus cannot be used to identify a specific ephemeris parameter set.

In this regard, BDS navigation data changes every hour, and it starts from the beginning moment of the first sub frame. The same ephemeris and Toe parameters will be broadcasted in the same hour, with Toe is generally on time, and other set of ephemeris parameters will be updated and broadcasted after an hour, pointing to the next Toe on time. Due to the updating of GEO and entering MEO/IGSO every hour, the AODE value of the domestic BDS satellites is always 1, so the AODE parameter cannot be used to identify a specific ephemeris parameter set. The off-time update will happen when the satellite fast recoveries form fault, and it may cause the situation that ephemeris parameter has already been calculated anew but the Toe parameter corresponding is still ancient. In this case, whether individual Toe and AODE or their combination can not be used to identify a specific ephemeris parameter set. AODC and Toc parameters have the same issue.

According to reference 11 and experiment data analysis of this paper, the discipline of BDS AODE and AODC parameters updating is described as below.

(1) BDS AODE and AODC have no specific relationship, and the difference of them is less than 1 in most cases.
(2) The values change of BDS AODE of GEOs are very small and are equal to 1 and less than 4 in most cases.
(3) The values change of BDS AODE of IGSOs present a law with 1 h cycle, and the values are equal to 1 and less than 8 in most cases.
(4) The values range of BDS AODE of MEOs are 0–31, with large value changing and inconspicuous law.

Through the study of phenomenon above, because of the relative rest of BDS GEOs and earth, the continuous communication of satellites and control center could be maintained. The difference of reference moment and latest moment is always less than 1, presenting as the AODE value is equal to 1 in most cases [12]. Currently, BDS control centers distributed in all of the world are uneven—mainly focus on Chinese mainland, so the difference of reference moment and latest moment will reduce and value of AODE will reduce relevantly while IGSOs and MEOs are gradually close to Chinese mainland. Otherwise, value of AODE will increase.

4 Construct BDS RTCM IOD Parameters Based on Toc

1. The appropriate constraints are put forward for the parameters generation mechanism of the control system

Normally, the navigation message is updated at the whole point and the corresponding Toe and Toc values are changed at the same time when the navigation message is updated (the current Compass ICD document only marked the AODE and AODC are updated at the whole point in BDT).

In the case of a navigation message needs to be re-injected due to some reason such as a satellite failure recovery:

(1) In case of recalculate and update satellite navigation message, be insure to change the Toe and Toc values at the same time. That is in the case of the update is not at the whole point, ensure the Toe and Toc of the first ephemeris not taken whole point and return to normal whole point update at next whole point;
(2) The satellite navigation message is updated at the beginning of a main frame. The purpose is to ensure that different groups of ephemeris parameters will not be broadcast in a main frame;
(3) Toe and Toc align with the start time of a main frame. That is the value corresponds to the start time of sub-frame 1 of the D1 navigation message or the start time of the page 1 of the sub-frame 1 that belongs to the D2 navigation message.

2. Generate BDS RTCM IOD field based on Toe and Toc

After the Compass Toe and Toc parameters (17 bits, scale factor is 8 s) are generated according to the constraint mechanism described above, an 8 bit BDS RTCM IOD field can be constructed and used for the differential protocol between the infrastructure and the user to uniquely identify a group ephemeris and satellite clock parameter changes, to ensure the Beidou system differential application services in the RTCM standard.

A possible construction is:

$$\text{BDS RTCM IODE} = \text{mod}(\text{Toe}, 28, 800)/120;$$
$$\text{BDS RTCM IODC} = \text{mod}(\text{Toc}, 28, 800)/120;$$

In this definition, it can guarantee the IOD field will not be repeated for up to 8 h. This is sufficient to provide normal differential application service within the Beidou observable arc, since the observable arc of the Beidou satellite is less than 8 h.

3. In the follow-up ICD file upgrade of Beidou system, the update mechanism of Toe and Toc will be supplemented and explained.

5 Relevant Test Verification

5.1 BDS IOD Test Verification Based on Toe

In order to verify the Beidou navigation message identification parameters, this paper collected 10 days of GPS and Beiou navigation message data, and the IOD problems of two systems were tested respectively. For the sake of simplicity, this paper only analyzes the GPS 3 satellite, Beidou 3 (GEO satellite), 7 (IGSO satellite), and 11 (MEO satellite) satellite. The results are as follows:

As can be seen from Fig. 1, GPS satellite IODE and IODC are changed every two hours. Both IODE and IODC are incremental over one week time and fully synchronized.

As can be seen from Figs. 2, 3 and 4, the AODE values change of Beidou GEO satellite are very small and most of time is 1 and generally not more than 4; the AODE values of Beidou IGSO show a 1d change rule, most of time the value is 1 and the upper limit is 8; the AODE values of Beidou MEO satellite vary greatly, and the regularity is not obvious but the value has a certain range from 0 to 31.

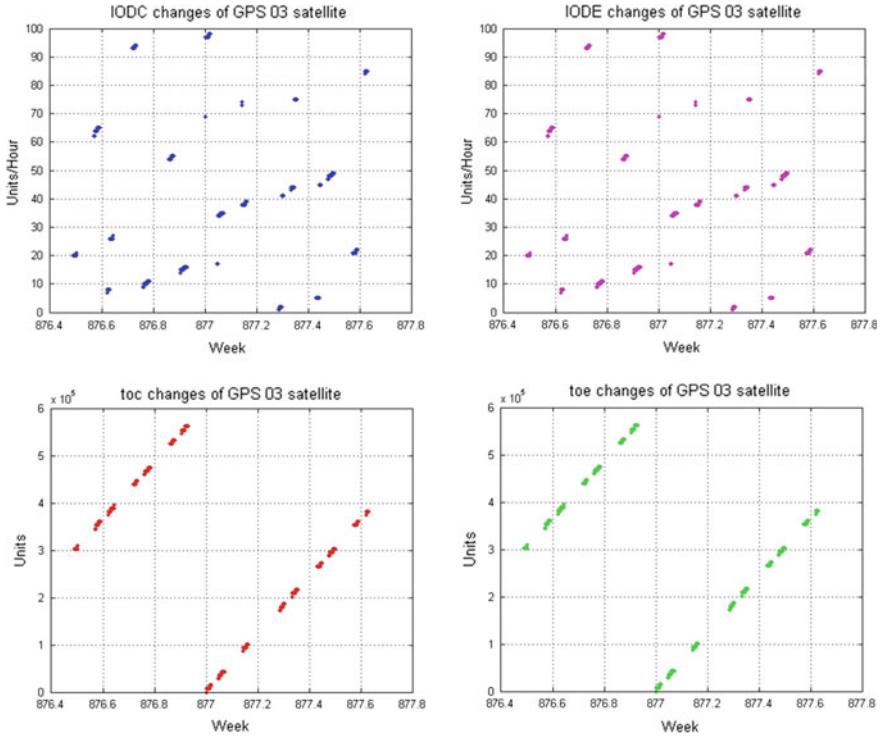

Fig. 1 GPS 3 satellite experimental results

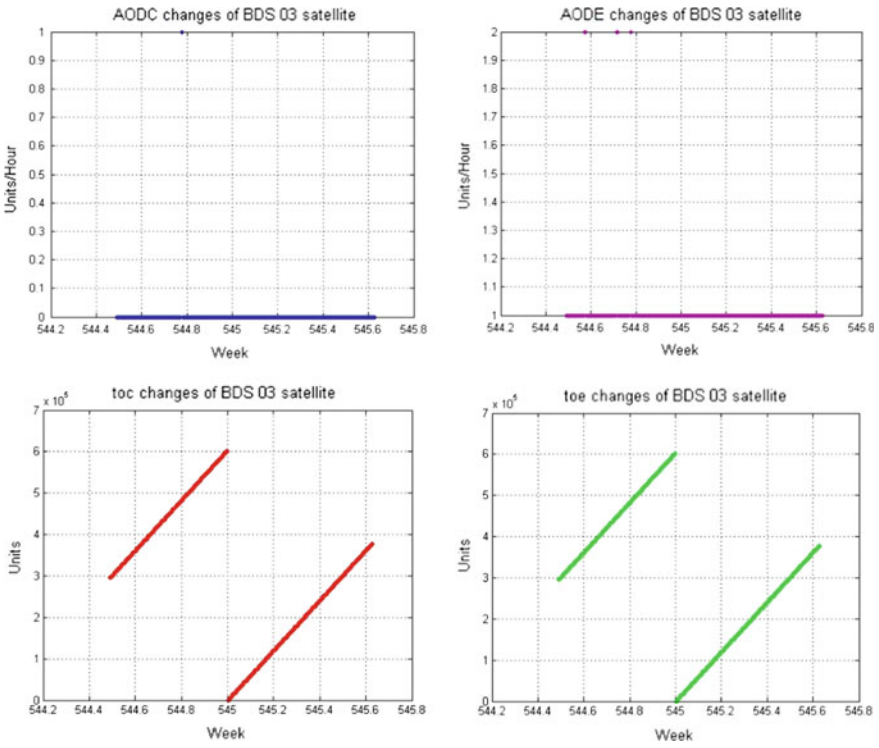

Fig. 2 BDS 3 (GEO satellite) satellite experimental results

The experimental results of GPS and BDS system are coincided with the content described in Chap. 2.

5.2 *BDS Broadcast Ephemeris Update Monitoring After BDS-SIS-ICD2.1 Released*

After BDS-SIS-ICD 2.1released, the changes of Toc/Toe/AODC/AODE was tested when the BDS navigation message was updated. The observation period of the date used in experiment is from 08:24:51 on July 8, 2017 to 02:50:00 on July 14, 2017. The results are as follows:

As can be seen from Fig. 5 that the Toe changes of five GEO satellite are generally gentle and updated at the whole point. However, the corresponding Toe of satellite 1, 2, 4 and 5 appears non-integral update at 151,227 epoch because the ephermeris updated at non-integral. So, it is feasible and effective to construct BDS RTCM IOD parameters based on Toe.

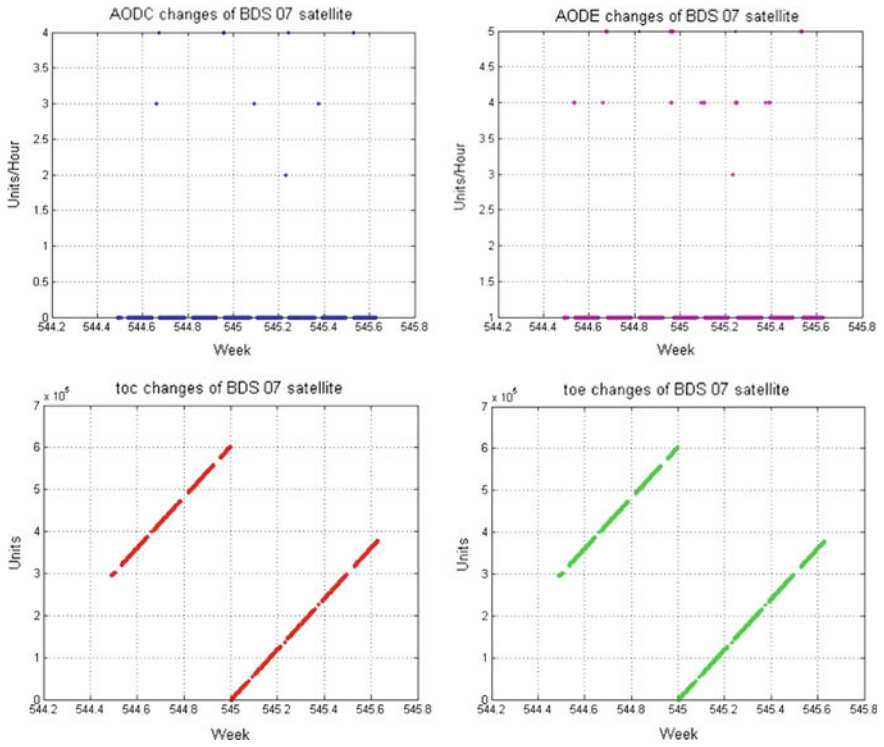

Fig. 3 BDS 7 (IGSO satellite) satellite experimental results

6 Conclusion

GNSS systems need to design fields that indicate the timeliness and consistency of ephemeris and satellite clock parameters to ensure that the user uses the correct ephemeris and satellite clock data for resolution. Beidou satellite navigation system does not design ephemeris parameter identification field such as GPS IODE, but AODE and Toe, AODC and Toc two sets of parameters were designed. But, for the current system state, these two sets of parameters cannot absolutely identify a group of ephemeris parameters. This brought new difficulties for Beidou high-precision applications and also become the primary obstacle for Beidou join the RTCM international standard.

Since the beginning of 2014, Beidou Receiver International General Data Standards Working Group has organized domestic and foreign experts and institutions study on this issue for several times. Finally, after the discussion of Beidou Receiver International General Data Standards Working Group, the Beidou Engineering General and the relevant departments, the adjustment program of the Beidou message identification parameters and update mechanism was proposed according to the existing Beidou ICD file, and the technical feasibility evaluation

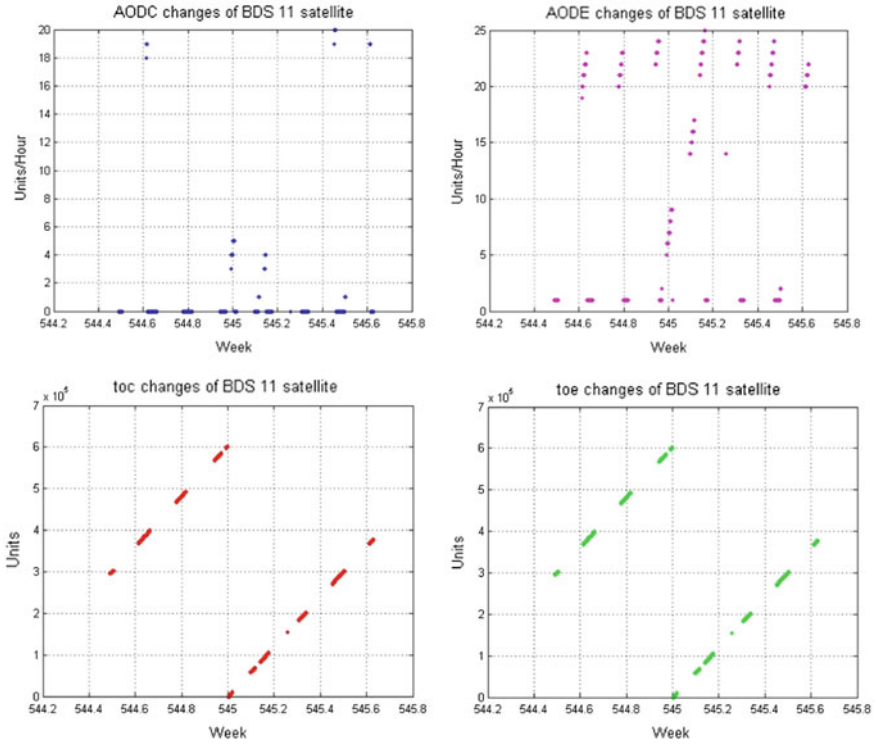

Fig. 4 BDS 11 (MEO satellite) satellite experimental results

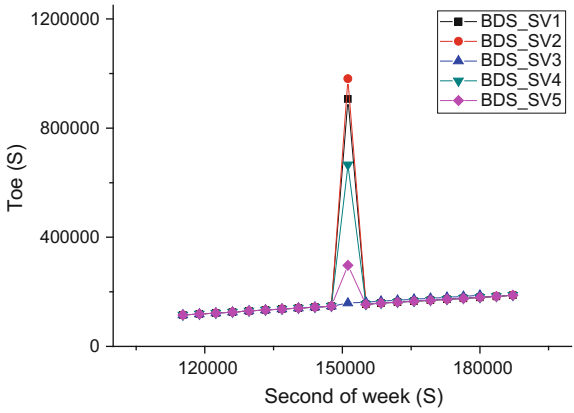

Fig. 5 Toe changes of BDS GEO satellites after BDS-SIS-ICD2.1 released

were carried. The experimental results show that it is feasible and effective to construct BDS RTCM IOD parameters based on Toe. Research suggests that the method is feasible and can meet the urgent need of the application of the Beidou differential system. It also provides useful references for the more comprehensive and in-depth international standards and application of the Beidou system.

References

1. Global Positioning System Wing (2014) Interface Specification IS-GPS-200H
2. China Satellite Navigation Office (2016) BeiDou Navigation satellite system signal in space interface control document (v2.0)
3. GLONASS Interface Control Document (2008) (5.1 edn)
4. European GNSS (Galileo) (2010) Open service signal in space interface control document (Issue 1.1)
5. RTCM Special Committee No. 104 (2007) RTCM standard GNSS (global navigation satellite systems) Services—Version 3
6. RTCM Special Committee. Committee Draft for Vote RTCM 10402. 4: Differential GNSS (Global Navigation Satellite Systems) Services, Version 2[S]. [S. l.]: SC,2013
7. RTCM Special Committee (2001) RTCM Recommended standards for differential GNSS (global navigation satellite systems) service, Version 2.3[S] [S.l.]: SC
8. Coordinate Scientific Information Center (2002) GLONASS ICD (Version, 2002, 5)
9. Radio Technical Commission for Maritime Service (2013) RTCM standard 10403. 2: differential GNSS (global navigation satellite systems) service, Version 3[S]
10. European GNSS Supervisory Authority (2010) Galileo O S. SISICD: Galileo open service, signal in space interface control document draft 1. 1[S]
11. Zheng H, Liu H, Qiao C (2015) Study on generating methods of BDS IODE. Bull Surv Mapp 5:24–29
12. Montenbruck O, Steigenberger P (2013) The BeiDou navigation message. J Global Position Syst 12(1):1–12

Research on Multipath Interference Suppression Algorithm Based on Blind Equalization

Dengao Li, Chong Han, Jumin Zhao, Xiaofang Zhao and Doudou Deng

Abstract Multipath interference is the main source of error in the urban environment. In order to effectively suppress multipath interference and improve the continue tracking performance. So, in this paper, the blind equalization algorithm is introduced in the tracking loop to meet the design requirements of high precision receiver. In harsh environment, multipath interference can cause large position error. The decision feedback blind equalization (CMA-DFE) algorithm is used to recover the original signal, which can reduce the impact of multipath interference on the position accuracy. Therefore, the algorithm can improved the performance of the mitigation multipath effect. Firstly, the signal model is established and the effect of multipath interference on tracking loop is analyzed. Then, the tracking loop based on decision feedback blind equalization is proposed. Finally, according to experimental results, the algorithm could effectively suppress multipath interference and improve position accuracy.

Keywords Multipath interference · Blind equalization · Tracking loop

1 Introduction

In the urban environment, serious multipath interference is one of the main sources of error, which may cause phase and navigation data distortion. The multipath signals increase the measurement error of the receiver, such as code phase, carrier frequency, Doppler shift, thus affecting the positioning accuracy of the receiver. Therefore, it is necessary to reduce the multipath affect by using the suppression algorithm.

D. Li (✉) · C. Han · J. Zhao · X. Zhao · D. Deng
Taiyuan University of Technology, Shanxi, Taiyuan, China
e-mail: lidengao@tyut.edu.cn

J. Sun et al. (eds.), *China Satellite Navigation Conference (CSNC) 2017 Proceedings: Volume I*, Lecture Notes in Electrical Engineering 437,
DOI 10.1007/978-981-10-4588-2_75

As the study of multipath signal estimation and suppression had been proposed for a long time, the narrow correlation technology [1] and multipath estimation delay locked loop (MEDLL) has good performance of multipath suppression. The narrow correlator [2] has good performance in suppressing multipath signals by reducing the delay correlator space. But it can only suppress the long delayed multipath signals [3] together with the degradation of dynamic performance [4]. While the MEDLL [5] uses the estimation algorithm in the tracking loop to estimate and eliminate multipath signal parameters, such as genetic estimation algorithm [6], maximum likelihood estimation algorithm [7] and particle filter based on Bayesian criterion [8], which can improve the estimation accuracy of the multipath parameters. However, it only has good performance in the case of changing multipath signal slowly. Jiang'an et al. [9] proposed a multipath approximation method based on genetic algorithm aiming at solving the short delay problem. It transforms the multipath signal estimation problem to the optimal fitting problem. The genetic algorithm is used to optimize the approximation, and the suppressions of the direct and multipath signals are established respectively. Cheng et al. [10] established a model of the pseudo-range of NLOS signals to measure the influence on the GNSS pseudorange data, and used the edge likelihood ratio detection algorithm to identify and estimate the deviation caused by NLOS signals and then to improve the GNSS receiver navigation and position accuracy. Zhao et al. [11] estimated signal delay by using the prior information of multipath signals and the posterior probability density function of the multipath signals obtained by particle filter. Dong et al. [12] used novel neural network algorithm to suppress multipath signals, and a full function of neural network is embedded into the GNSS navigation receiver to suppress the influence of multipath signals.

In order to effectively suppress multipath signals, the blind equalization algorithm is introduced into the tracking loop to compensate the received signal distortion. The decision feedback blind equalization algorithm is used to recover the original signal, which can effectively reduce the positioning error. In this paper, the influence of multipath interference on the tracking loop is analyzed and the multipath signal model is established. Then the tracking loop based on blind equalizer is proposed. Finally, the experimental results show that the proposed algorithm can effectively suppress multipath interference and improve the positioning accuracy.

2 Multipath Interference Suppression Algorithm

2.1 Multipath Signal Model

In the urban canyon environment, due to the reflection and scattering, multipath effect is very obvious. The effect of scattering on the pseudorange measurement precision is not obvious, so the scattering signals can be regarded as additional low frequency noise. The propagation path of multipath signals is longer than direct

signals, so the multipath signals always delay. Generally, the amplitude of multipath signal is less than direct signal, and will cause the power attenuation when the signal is reflected. The IF signal can be shown as (1) when the multipath signals is N.

$$S_N(t) = A_0 c(t-\tau_0)\cos[\omega_c(t-\tau_0)] + \sum_{i=1}^{N} \alpha_i A_i c(t-\tau_i)\cos[\omega_c(t-\tau_i)+\theta_i] + n(t) \tag{1}$$

where A_i is the amplitude of the received signals, $c(t)$ is the pseudo-random code, ω_c is the angular frequency of carrier, τ_i is the delay of the multipath signals, θ_i is the ith carrier phase, $n(t)$ is the noise.

The code-related interval of early-late correlator is d, the multipath signals $S_N(t)$ and local carrier is demodulated as baseband signal, then through integral accumulation with the local code, the obtained advanced, instant and lag correlation value is:

$$I_P = \frac{A_0}{2}R(\hat{\tau}) + \sum_{i=1}^{N}\frac{A_i}{2}R(\hat{\tau}-\tau_i)\cos(\theta_i) \tag{2}$$

$$I_E = \frac{A_0}{2}R\left(\hat{\tau}+\frac{d}{2}\right) + \sum_{i=1}^{N}\frac{A_i}{2}R\left(\hat{\tau}-\tau_i+\frac{d}{2}\right)\cos(\theta_i) \tag{3}$$

$$I_L = \frac{A_0}{2}R\left(\hat{\tau}-\frac{d}{2}\right) + \sum_{i=1}^{N}\frac{A_i}{2}R\left(\hat{\tau}-\tau_i-\frac{d}{2}\right)\cos(\theta_i) \tag{4}$$

$$Q_P = \frac{A_0}{2}R(\hat{\tau}) + \sum_{i=1}^{N}\frac{A_i}{2}R(\hat{\tau}-\tau_i)\sin(\theta_i) \tag{5}$$

$$Q_E = \frac{A_0}{2}R\left(\hat{\tau}+\frac{d}{2}\right) + \sum_{i=1}^{N}\frac{A_i}{2}R\left(\hat{\tau}-\tau_i+\frac{d}{2}\right)\sin(\theta_i) \tag{6}$$

$$Q_L = \frac{A_0}{2}R\left(\hat{\tau}-\frac{d}{2}\right) + \sum_{i=1}^{N}\frac{A_i}{2}R\left(\hat{\tau}-\tau_i-\frac{d}{2}\right)\sin(\theta_i) \tag{7}$$

where $\hat{\tau} = \dot{\tau} - \tau_0$ is code error of tracking loop, τ_i and θ_i is code delay and carrier phase error respectively, $R(\tau)$ is pseudo-code autocorrelation function. Because of the influence on the multipath interference for carrier is far less than influence on code loop, so the carrier is totally removed.

2.2 The Influence of Multipath Interference for Tracking Loop

2.2.1 The Influence of Multipath Interference for Code Loop

Using the early late envelopment discriminator to analysis the influence of multipath interference on DLL phase function, the phase function is:

$$F=\sqrt{I_E^2+Q_E^2}-\sqrt{I_L^2+Q_L^2} \tag{8}$$

For calculation convenience, usually assume that the received signal contains a direct signal and a multipath signal, the formulas (3), (4), (6) and (7) can be put into (8) to obtain the phase function:

$$\begin{aligned} F=&\frac{A_0}{2}\left[R\left(\hat{\tau}+\frac{d}{2}\right)-R\left(\hat{\tau}-\frac{d}{2}\right)\right] \\ &+\frac{A_1}{2}\left[R\left(\hat{\tau}-\tau_1+\frac{d}{2}\right)-R\left(\hat{\tau}-\tau_1-\frac{d}{2}\right)\right] \end{aligned} \tag{9}$$

where $\hat{\tau}=\dot{\tau}-\tau_0$ is code error in the tracking loop under the influence of the multipath interference, $\tau_e=\dot{\tau}_0-\tau_0$ is the code delay error, c is the code element width, $\tau=\tau_1-\tau_0$ is the code relative delay during multipath signals and direct signals. $F = 0$ in (9), the code phase tracking error can be as:

$$\tau_e=\begin{cases} \frac{A_1\tau}{A_0+A_1} & 0\le\tau\le\frac{A_0+A_1}{2A_0}d \\ \frac{A_1}{2A_0}c & \frac{A_0+A_1}{2A_0}d<\tau\le c-\frac{A_0-A_1}{2A_0}d \\ \frac{A_1}{2A_0-A_1}\left(c+\frac{d}{2}-\tau\right) & c-\frac{A_0-A_1}{2A_0}d\le\tau\le c+\frac{d}{2} \\ 0 & \tau>c+\frac{d}{2} \end{cases} \tag{10}$$

According to Eq. (10), it is known that code-related interval; M/D (the amplitude ratio of the multipath signal and direct signal) and multipath signal code delay all have some influence on the code tracking error. Therefore, this paper proposed a tracking loop based on blind equalizer to eliminate the effect of multipath signal on the tracking loop and reduce the code tracking error.

2.2.2 The Influence of Multipath Interference on Carrier Loop

When the receiver works in the environment of multipath interference, the phase of the local carrier generated by the phase locked loop is locked in the offset phase of

the composite signal, and there is an offset compared to the phase of the direct signal. The function of discriminator of carrier loop is expressed as:

$$V = \arctan\left(\frac{Q_P}{I_P}\right) \tag{11}$$

The Eq. (12) can be obtained by substituting (2), (5) into the above (11):

$$V(\theta) = \arctan\left(\frac{\frac{A_0}{2}R(\hat{\tau}) + \sum_{i=1}^{N}\frac{A_i}{2}R(\hat{\tau}-\tau_i)\sin(\theta_i)}{\frac{A_0}{2}R(\hat{\tau}) + \sum_{i=1}^{N}\frac{A_i}{2}R(\hat{\tau}-\tau_i)\cos(\theta_i)}\right) \tag{12}$$

where θ is the difference between the phase of the composite signal and the phase of the direct signal. The phase-locked loop pulls the V value near to zero, let $V(\theta) = 0$, then we can get:

$$\theta = \arctan\left(\frac{A_1 R(\hat{\tau}-\tau_i)\sin(\theta_1)}{A_0 R(\hat{\tau}) + A_1 R(\hat{\tau}-\tau_i)\cos(\theta_1)}\right) \tag{13}$$

The tracking error is related to the multipath delay, amplitude ratio of multipath signal to direct signal, the phase of the reflected signal. The maximum phase tracking error is analyzed according to calculate the maximum value of (13).

2.3 The Tracking Loop Based on Blind Equalizer

Equalization method is one of the most effective methods to suppress multipath interference. In order to recover the distortion of the received signal caused by multipath interference and eliminate the multipath error, a feedback blind equalizer algorithm is introduced in the tracking loop, the structure of the proposed method is show as Fig. 1. The satellite signal is converted to the intermediate frequency signal $S_N(t)$ by the receiver RF front-end and down-conversion. Then the baseband signal is correlated with the local C/A code to obtain the correlation function, and the correlation function is used as the input of the equalizer. The complex representation of the correlation function of the I/Q is shown in Eq. (14). The output of the decision feedback blind equalizer is, and it is used as the input of the carrier and code loops.

$$r(n) = r_I(n) + jr_Q(n) \tag{14}$$

The length of the forward feedback filter for the decision feedback blind equalizer is N_A, tap coefficient vector is $\omega_f(n)$, the input of the forward feedback filter is $r(n)$,

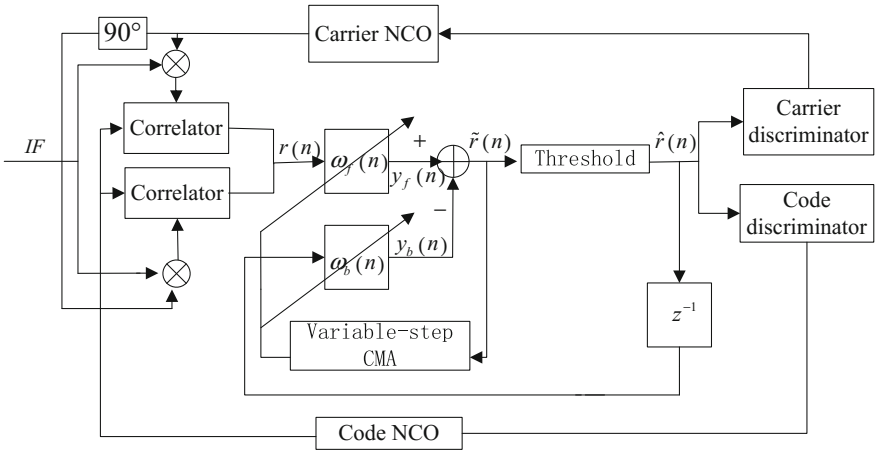

Fig. 1 Tracking loop based on blind equalization

the length of the forward feedback filter is N_B, tap coefficient vector is $\omega_b(n)$, from Fig. 1 we can obtained $\hat{r}(n)$ is the decision output at time n, the chip interval signal in the feedback filter is $[\hat{r}(n-1), \cdots, \hat{r}(n-N_B+1)]$, therefore, the current time signal is estimated as follows:

$$\tilde{r}(n) = y_f(n) - y_b(n) \tag{15}$$

The CMA algorithm is used in the proposed method, the error function is $e(n) = |\hat{r}(n)| - R^2$, cost function of decision feedback blind equalizer is $J = \frac{1}{2}E[e^2(n)]$, and then the tap coefficient can be updated as Eq. (16):

$$\omega(n+1) = \omega(n) + \mu\Delta J \tag{16}$$

where, R^2 is the modulus of high-order statistical characteristic, which can be show as $R^2 = \frac{E\{|r(n)|^4\}}{E\{|r(n)|^2\}}$, $\Delta J = \frac{\partial \Delta J}{\partial \omega}$, μ is the step size of CMA algorithm, and it is show as Eq. (17):

$$\mu(n) = \mu(n-1) - \nabla \tag{17}$$

where, $\nabla = E\left[(\tilde{r}(n) - r(n))^2\right]$.

When the receiver works in the environment of serious multipath interference, the blind equalizer is used to feedback the distortion caused by multipath interference. In the early stage of the algorithm, a larger step size is adopted, and then ∇ is used to adjust the step size, which can effectively improve the convergence speed of the equalizer and reduce the injustice. It can eliminate the influence of multipath

interference on the correlation, recover the symmetry characteristic of the correlation peak, reduce the tracking error, and improve the positioning accuracy.

3 Simulation Experiment

The data is collected by GNSS IF signal sampler and used to simulate and analyse via the software MATLAB receiver. The paper shows the suppress effecting of the algorithm mainly on two sides: carrier phase error and positioning accuracy.

The effectiveness of the proposed algorithm is verified by comparing the performance of the traditional tracking loop and the improved tracking loop. As shown in Fig. 2, a large code tracking error is caused by multipath interference. The code phase average error of the traditional tracking loop is about 0.65 chips, and the error of the tracking Loop Based on Blind Equalizer is about 0.5 chips. In order to better illustrate the performance of the improved tracking loop to suppress multipath signals, the difference between the improved algorithm and the traditional algorithm is shown in Fig. 3. Compared with the traditional algorithm, the code tracking error is reduced by 0.15 chips.

In addition, the carrier phase error of the traditional tracking loop and the improved tracking loop are analyzed. As shown in Fig. 4, when the M/D is 5 dB, the traditional algorithm, narrow correlation algorithm and strobe correlation structure are compared. When the multipath delay is less than 10/16 chips, the proposed algorithm has better performance.

The code tracking error and the carrier phase error are analysed in Figs. 2 and 4. In the condition of serious multipath interference, the tracking loop based on blind

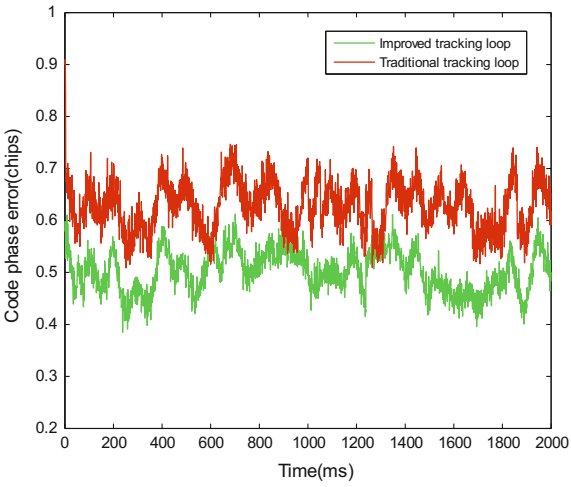

Fig. 2 Code tracking error

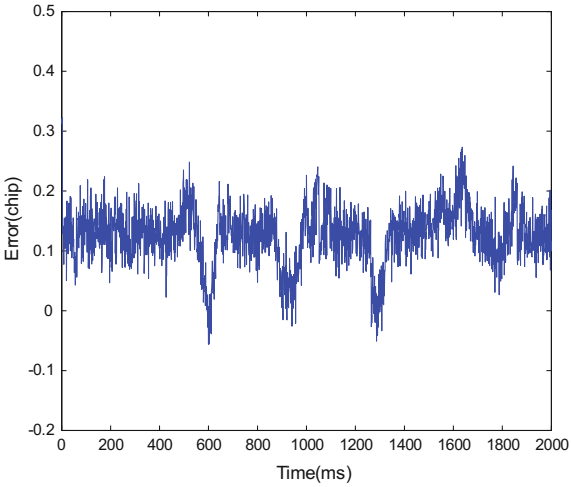

Fig. 3 Comparison of code phase error

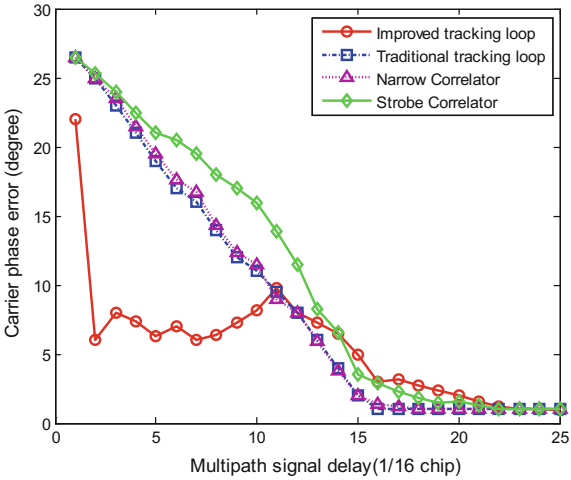

Fig. 4 Carrier phase error

equalizer is to improve the accuracy of pseudorange and pseudorange rate, and increase the positioning accuracy of the receiver, as shown in Fig. 5. As can be seen from Fig. 5, the proposed algorithm reduces the positioning error compared to the strobe correlation structure and the narrow correlation algorithm. Based on the above analysis, the tracking loop based on blind equalizer can effectively suppress multipath signals.

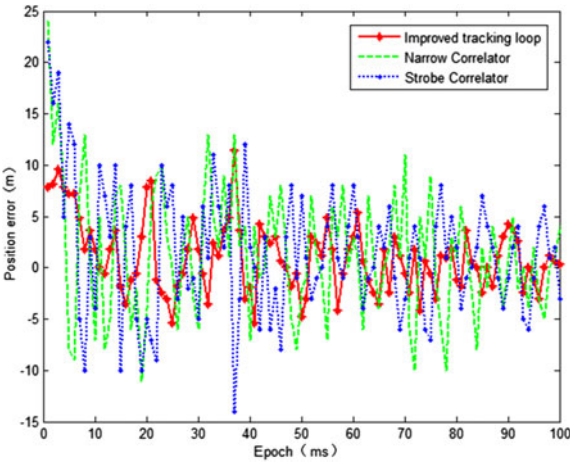

Fig. 5 Positioning error analysis

4 Conclusion

In this paper, the blind equalizer is introduced in the tracking loop, which can effectively compensate the distortion of the channel, and solve the problem of low accuracy in the serious multipath interference. The blind equalizer reduces the effect of multipath interference on the tracking loop and ensures the positioning accuracy of the receiver. The experimental results show that the new algorithm can effectively suppress the multipath interference and improve the positioning accuracy.

References

1. Wu J, Dempster AG (2012) Code tracking variance analysis for GNSS receivers with "strobe correlators". IEEE Trans Aerosp Electron Syst 48(3):2760–2782
2. Dierendonck VA, Fenton P, Ford T (1992) Theory and performance of narrow correlator spacing in a GPS receiver. Navigation 39(3):265–283
3. Jardak N, Samama N (2010) Short multipath insensitive code loop discriminator. IEEE Trans Aerosp Electron Syst 46(1):278–295
4. Irsigler M, Eissfeller B (2003) Comparison of multipath mitigation techniques with consideration of future signal structures. In: Proceedings of ION-GPS
5. van Nee RD, Siereveld J, Fenton PC, Townsend BR (1994) The multipath estimating delay lock loop: approaching theoretical accuracy limits. In: Position location and navigation symposium. IEEE, pp 246–251
6. Wang J et al (2009) Study of optimum fitting using the genetic algorithm for multipath mitigation in GPS receivers. J Xidian Univ 1044–1048
7. Blanco-Delgado N, Nunes FD (2012) Multipath estimation in multicorrelator GNSS receivers using the maximum likelihood principle. IEEE Trans Aerosp Electron Syst 48(4):3222–3233
8. Liu X, Closas P, Liu J, Hu X (2010) Particle filtering and its application for multipath mitigation with GNSS receivers. In: Position location and navigation symposium plans, vol 298(16). IEEE, pp 1168–1173

9. Wang JA, Zhuang YQ, Di LI, Zhao J (2009) Study of optimum fitting using the genetic algorithm for multipath mitigation in gps receivers. J Xidian Univ 36(6):1044–1048
10. Cheng C, Tourneret JY, Pan Q, Calmettes V (2016) Detecting, estimating and correcting multipath biases affecting GNSS signals using a marginalized likelihood ratio-based method. Sig Process 118(C):221–234
11. Zhao Y, Xue X, Zhang T (2013) A modified particle filter for dynamic multipath mitigation in GPS receivers. In: Proceedings of the 2012 international conference on information technology and software engineering. Springer, Berlin
12. Dong D, Wang M, Chen W, Zeng Z, Song L, Zhang Q et al (2016) Mitigation of multipath effect in GNSS short baseline positioning by the multipath hemispherical map. J Geodesy 90 (3):255–262

A Fundamental Architecture of Anti-spoofing GNSS Receiver

Li He, Hong Li and Mingquan Lu

Abstract Spoofing attack is growing into a great potential menace to future GNSS systems and related applications, featured by its stealth. Spoofing signal can deceive victim receivers by changing ranging observables covertly, leading to wrong positioning or timing solutions. It is reasonable to keep the power of spoofing signal similar to the power of authentic signal, in addition to its signal structure and navigational data. Therefore, there still are chances to track authentic signal along with received signal. Changing transmit time observables is essential to a successful spoofing attack. Based on this fact, we propose an acquisition and tracking framework in which transmit time plays a core role. This framework combines several algorithms, namely multi-peak acquisition algorithm, multiple tracking algorithm and repetitive signal cancelation regime. A receiver, equipped with the proposed framework, can continuously acquire all existing signals and then tracks them, regardless of their authenticity. Moreover, experiments on GPS simulator attack and meaconing spoofing signal are shown.

Keywords Software receiver · Anti-spoofing · Multiple peak acquisition · Multiple peak tracking

1 Introduction

GPS system and its vast application have achieved such a great success that almost every sector of today's society relies on its functionality. Therefore, criminals would be more motivated to sabotage it. Recent years have witnessed a rapid rise of

L. He (✉) · H. Li · M. Lu
Department of Electronic Engineering, Tsinghua University,
100084 Beijing, China
e-mail: heliosthu@163.com

H. Li
e-mail: lihongee@mail.tsinghua.edu.cn

M. Lu
e-mail: lumq@mail.tsinghua.edu.cn

J. Sun et al. (eds.), *China Satellite Navigation Conference (CSNC) 2017 Proceedings: Volume I*, Lecture Notes in Electrical Engineering 437,
DOI 10.1007/978-981-10-4588-2_76

incidents caused by GPS interference both unintentionally and intentionally. Amongst these interferences, a method named spoofing has drawn large attention because of stealth and dangerous potential. Spoofing is able to covertly coerce a GPS receiver to output incorrect timing and positioning solution. Spoofing device transmits signals that resemble true GPS signal in vicinity of intended victim, in order to disturb victim's tracking of authentic signal, finally capture its tracking loop.

No concern on GPS security was spent during construction, especially the C/A signal on GPS L1 frequency. Most civilian receivers have no precautions against spoofing. They would utilize any signal available to estimate observables in purpose of positioning. This straightforward but fragile logic leaves a backdoor to various spoofing and interference.

Many methods have been proposed to tackle with malicious interference and spoofing against GPS. Some of them need modification to hardware of existing receivers, such as adding AGC monitor [2] (to monitor signal power), or adding more antenna or cooperation between receiver [3] (to estimate direction of arrival). However, the expense makes updating hardware of existing receivers impossible. Some papers propose single-antenna receiver defence method based on baseband signal processing, requiring no modification to hardware of receivers and signal regime.

Reference [4] proposes that, anomaly occurred during the capture of tracking loop can be detected by monitoring the symmetry of triangular-shaped correlation function of ranging code. This method has high false alarm rate in strong multipath environment, and its transient nature easily confuses with false alarm. Reference [6] points out that monitoring abnormal changes in carrier to noise ratio (C/N_0) has potential to detect spoofing. Meanwhile, reference [6] also points out this method is limited without hardware modification. Reference [7] uses cross-correlation of in-phase component of correlation value to discriminate whether the received signals are transmitted from one antenna. But this requires receiver moving in a shading-variation scenario. Reference [1] intensively reviews this type of defence methods.

In summary, methods based on signal feature are somewhat flawed, leading to limited effectiveness in actual use. Considering these facts, this paper proposes a fundamental framework supported by a novel running logic. This framework converts extra computation capability in a receiver into the ability of anti-spoofing. By acquiring and tracking all signals regardless of authenticity, this framework enables defence against various spoofing methods (including simulator attack, meaconing attack and intermediate spoofing attack) after knowing signal characteristics.

This rest part is arranged as follow. The second section characterizes the assumptions and features of spoofing signal, and roughly analyses viable defence. The third and fourth sections introduce the proposed mechanism for the acquisition and tracking of spoofing signal. The fifth section shows experimental results on over-the-air GPS signal. The sixth section comprises conclusion and discussion.

2 Analysis of Spoofing Attack

2.1 Assumptions and Premises

According to their nature, attacks on GPS receivers can be roughly categorized into two types, i.e., jamming and spoofing. Jamming refers to attack in which transmission of interference signal disrupts tracking or acquisition of satellite signal. Some jamming signal suppresses the amplifier of victim receiver into non-linear state, blocking receiver baseband processing away from true signal. Some jamming triggers loss of lock in tracking loop. Nonetheless, this type of attack will raise alarm by disrupting normal working of receiver, thus preventing further damage. On the contrary, spoofing signal needs infiltration into baseband and capture of tracking loop. This precludes extremely large signal power. Spoofing signal with power larger than true signal can be detected by power monitoring [2].

All spoofing methods mentioned above are coarse and primitive, especially compared to the novel and inexpensive spoofing method proposed by [5]. The most advantage of this method is stealth. It does not cause any loss of lock and cannot be detected by power monitoring. Concerning its characteristic, we make several assumptions as follow:

1. The low noise amplifier (LNA) of receiver still works in linear state;
2. Spoofing signal has similar power with authentic signal;
3. No nulling or shading of true signal transmitted from GPS satellites.

The assumptions of spoofing signal are reasonable. We only focus on advanced and cost-limited spoofing approaches, not those can be defeated by simple defense methods such as power monitoring. Therefore, these assumptions agree with the capability of existing spoofing techniques, and suffice to circumvent simple anti-spoofing methods.

2.2 Characteristics of Spoofing Signals

Several premises about spoofing and authentic signal have been previously assumed. In this section, characteristics of the signal under assumptions above will be analyzed:

Assumption 1 guarantees that the receiver still is able to receive and acquire GPS signal (no matter of the authenticity);

Assumption 2 ensures that spoofing signal neither does not simply suppress true signal under noise floor, nor the inter-address interference is large enough to prevent acquiring the true ones;

Assumption 3 guarantees the availability of true signal, which means true signal still can be acquired.

With these assumptions, the received signal is the mixture of spoofing signals and authentic ones, and both can be acquired and tracked steadily. As we can see from Sect. 1, most spoofing techniques (ranging from simplest simulator attack to sophisticated spoofing) aiming at civilian receivers need "drag" the timing and positioning solution of a victim from its real time-space point, while a GPS receiver resolves by measuring the transmit time of present signal. Consequently, most spoofing attempts necessarily deviate from true signal in transmit time observables.

This mixed signal appears more than one recognizable peak in the correlation domain used in acquisition. This phenomenon differentiates itself from the single peak scene under normal circumstance. Therefore, this mixed signal could be named as "multi-peak signal". In next section we propose an acquisition algorithm in purpose of acquiring multi-peak signal.

3 Multi-peak Acquisition

From the analysis of the characteristic in previous section, it could be seen that the multi-peak signal can be discriminated by the multiple peaks in the correlation domain.

3.1 Recognition and Acquisition of Multi-peak Signal

In the discrete code phase-Doppler frequency domain used in acquisition stage, a correlation peak comprises several relatively large values on adjacent grids. True signal only contains one correlation peak, if no strong multipath or spoofing signal imposed. Whereas the mixed signal shows multiple correlation peaks (when transmit time or Doppler frequency differs from each other), meaning that there would be several areas containing relatively large correlation values in the mentioned domain.

The acquisition algorithm of a normal receiver often searches for the maximum of correlation values and corresponding code phase and Doppler frequency, or find the correlation value larger than a preset threshold in a sequential search. The naivety of this strategy incapacitates acquiring all correlation peaks stemming from mixed signal. Thus, some modifications to the traditional acquisition strategy are necessary. Existing acquisition algorithm can be modified to output information about multiple correlation peaks rather than only one peak. Maximum search method should be changed into multiple maxima search method; threshold method should find all correlation points exceeding the threshold as output. Thus, multi-peak acquisition algorithm outputs several code phase and Doppler frequency pairs that can initialize tracking channels.

However, one correlation peak always causes several relatively large correlation values (or larger than preset threshold) on code phase-Doppler frequency grids.

Hence, if these acquisition results are directly utilized to initialize tracking channels, there would be a great waste in computation resources. By analyzing the structure of correlation peak, we could cluster these raw results to reduce computing consumption.

Correlation peak clustering exploits the structure of correlation peak, and these raw results originated from a single correlation peak are contiguous. This fact facilitates the clustering and recognition algorithm based on comparing the code phases and Doppler frequencies of raw results. The procedure can be listed as:

(1) Clustering the raw results according to their code phases and Doppler frequencies. Ensures that within same correlation peak set the range of code phase does not exceed one code chip, and the range of Doppler frequency does not exceed coherence bandwidth;
(2) The number of points accumulated in a correlation peak set is marked as "support" of the correlation peak set;
(3) In high C/N0 scenario, delete all the correlation peak set with support of 1, and the rest is remained as initial values for tracking channels, which would reduce computation burden largely. In low C/N0 scenario, all the raw results are needed to prevent missing any potential signal (Fig. 1).

3.2 *Parameters and Performance*

For multi-maxima method, the only configurable parameter is the number of multi-maximum. Since one correlation peak causes several maxima according to the configuration of acquisition, and the number of correlation peaks have linear impact on the multiplicity of maxima as long as the overlapping of different correlation peak is limited. Therefore, to set the number of maxima, parameters of acquisition and the expected number of correlation peaks have to be taken into

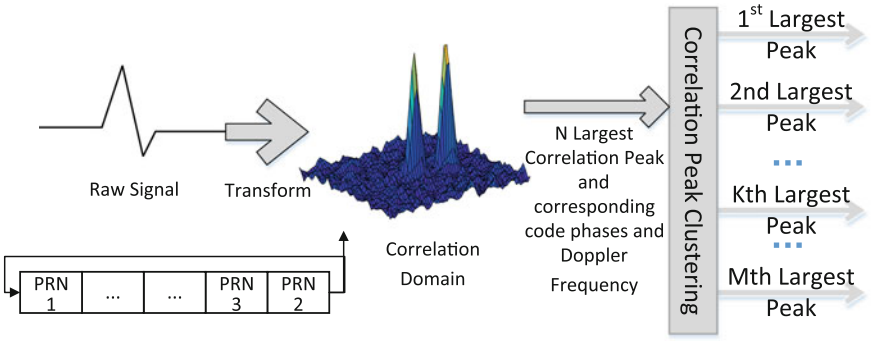

Fig. 1 Acquisition of multi-peak signal

consideration. If the parameter N is set too low, there probably would be miss detection of possible correlation peaks; if too large, it would aggravate computation burden.

The threshold decision method only relies on the threshold itself. If the threshold is set too low, there would more false alarm due to the increased noise; if too high, there would be more miss detection.

Usually, in complex signal environment, any fixed parameter has its failure area. In fact, the optimal parameter setting is to change it dynamically considering signal environment fluctuation. Unlike normal acquisition, the mathematics behind multi-peak acquisition is a ternary hypothesis test, which requires further analysis. Further mathematical derivation is omitted for the brevity of this paper.

4 Multiple Tracking Strategy

Multi-peak signal acquisition can only detect the presence of spoofing signals, but what is more desirable is the ability to distinguish the authenticity of the signal. The foundation of further discrimination and mitigation of spoofing signal is the tracking of all possible signals.

4.1 Logic and Procedure of Tracking

The computation resource of civilian GNSS receiver is structured as channels, and the identification of a specific channel is the PRN code it tracks. In premise of multi-peak signal, however, PRN number does not suffice to identify different channels clearly. Consequently, the tracking logic and procedure of receiver call for modification.

First of all, how to uniquely identify different signals. As previously analysed, the transmit time of spoofing signal should deviate from the authentic ones, then the PRN and transmit time pair is sufficient to uniquely identify the signal being tracked. Therefore, the channel-based architecture still works, only with little change of identifying channels by the mentioned pair.

The most resource consumed in multi-peak tracking is computation capacity. So, a receiver with multi-peak tracking ability inevitably requires more computation capacity, leading to more power consumption. Thus receivers with configurable channels are more suitable for multi-peak signal tracking (Fig. 2).

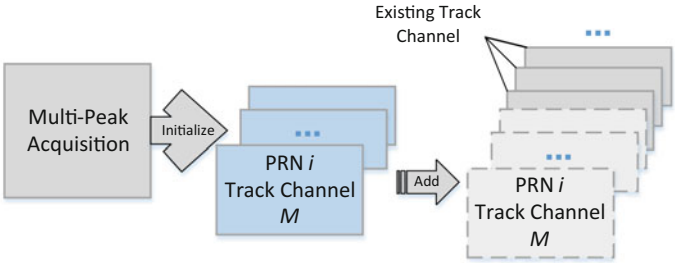

Fig. 2 Tracking of multi-peak signal

4.2 Repeating Acquisition and Duplicate Signal Cancellation

The acquisition strategy of normal civilian receiver only tries to acquire the PRN that is not under tracking, rather than those already under tracking. The reason behind is that receiver has no prior knowledge of emerging satellite (because of satellite position and signal fading environment), while those already in tracking require no more acquisition attempts.

Similarly, we possess no prior knowledge about when spoofing begins, when the spoofing signal captures tracking loop, or when the transmit time of spoofing signal deviates. In a word, we have no idea about when the normal signal becomes multi-peak signal. Consequently, existing acquisition strategy cannot timely counter spoofing signal in long-term operation.

Accordingly, to detect spoofing signal in time, multi-peak acquisition process needs to be repeated for all PRN codes (whether or not a channel is assigned for it). However, this repetition will certainly cause re-acquisition of same signal and its redundant tracking as a consequence. It is obviously not reasonable to assign two channel to track one replica of same signal, while missing an existing signal is more undesirable.

The "PRN-Transmit Time" pair can uniquely determine the signal represented by a single correlation peak in multi-peak signal. Therefore, by comparing the transmit times with same PRN, if the difference of transmit times is smaller than the error performance of tracking loop (typical tracking error performance is around 10 ns), they can be identified as signal represented by a single correlation peak; if the transmit time difference exceeds the error of tracking loop, then we believe that the signals compared originate from different correlation peaks.

But the repeating acquisition leads to re-entry of the signal from the same correlation peak, then there would certainly be two channels with transmit time difference less than tracking error. The extra channels tracking same correlation peak need to be cancelled in purpose of saving resources. To avoid the confusion about cancelling which channel, another feature is necessary for discriminating the channels. The duplicate channels tracking same correlation peak can only stem

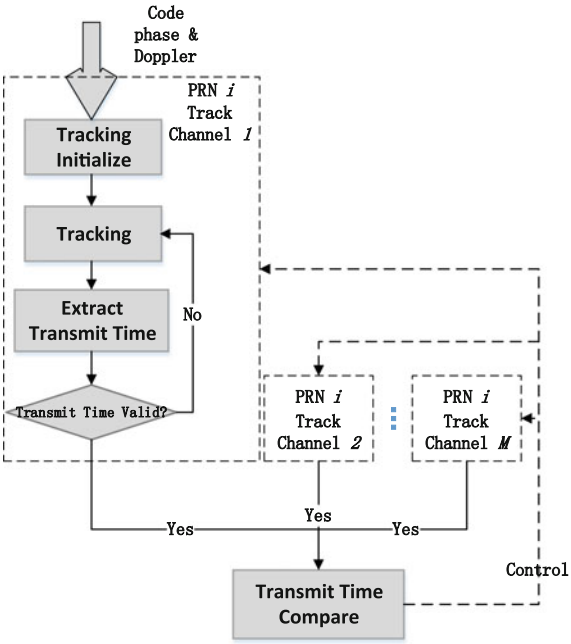

Fig. 3 Recursive acquisition and cancellation of multi-peak signal

from successive multi-peak acquisitions, because of correlation peak clustering. Thus the channel of which the tracking duration is longer should outlive the others. Then through comparing PRN number, transmit time and tracking duration of channels, the repeating multi-peak acquisition can work along with the multi-peak tracking. This mechanism satisfies both the purpose of saving computation resource and missing no possible signal (Fig. 3).

5 Experimental Results

After establishing experimental platform, we have conducted experiments both on GPS simulator signal and receiver-spoofer meaconing live signal. The configuration of platform is depicted in Fig. 4. To test the function of the proposed architecture, we can send spoofing signal (at similar power as true signal) into the receiver by adjusting the attenuator.

Figures 5 and 6 shows actual results on the multi-peak signal formed by true signal and spoofing signal transmitted from simulator and receiver-spoofer, respectively.

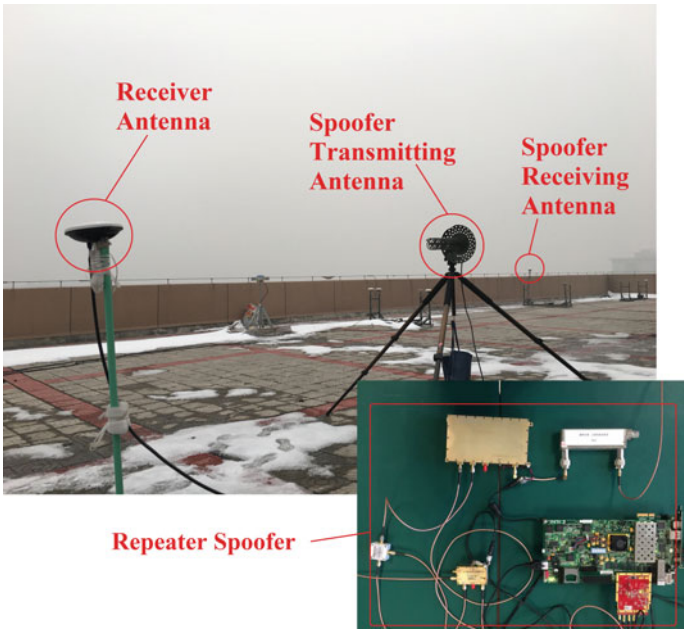

Fig. 4 Meaconing spoofing platform

```
**********************************GPS L1_Power:4.058842**********************************
S01
1       20      CCBFTP  0  S01  0.92    40.69   -1125.41673025   90989.94898950  1068408 18280   1068564.37
2       27      CCBFTP  0  S01  0.93    41.23   767.35718391     90989.95775123  1090451 326096  1138166.06
9       28      CCBFTP  0  S01  0.93    41.26   4787.43866693    90989.94937093  1052591 69956   1054913.10
12      4       CCBFTP  0  S01  0.94    42.21   1069.10084757    90989.95355592  1224503 315012  1264373.42
20      25      CCBFTP  0  S01  0.92    40.54   -819.28327754    90989.95351263  719578  208839  749270.46
21      23      CCBFTP  0  S01  0.92    40.77   552.13644422     90989.95049877  847861  115487  855690.09
22      13      CCBFTP  0  S01  0.95    42.58   1209.81716976    90989.95428680  1297396 187727  1310907.25
25      8       CCBFTP  0  S01  0.93    41.42   2823.04023148    90989.95717634  751920  576806  947675.50
S02
0       29      CCBFTP  0  S02  0.96    43.79   -2369.04815021   474893.65598582 1682164 518518  1760266.07
3       24      CCBFTP  0  S02  0.96    44.06   4119.15711521    474893.65287865 1244597 253091  1270069.58
4       2       CCBFTP  0  S02  0.94    41.81   -3116.51200282   474893.65220716 1356287 197862  1370643.57
6       21      CCBFTP  0  S02  0.97    44.43   2847.57482885    474893.65705140 1267300 52978   1268406.86
14      5       CCBFTP  0  S02  0.98    47.40   -1631.41236444   474893.65893093 1903103 101449  1905805.06
23      15      CCBFTP  0  S02  1.00    53.34   1205.24800533    474893.66488625 3447290 322114  3462306.42
26      20      CCBFTP  0  S02  0.99    49.30   1181.77056168    474893.66479228 3043870 19383   3043931.71
29      13      CCBFTP  0  S02  0.99    51.77   -773.79472714    474893.66397579 3382441 115436  3384410.23

elapsedTime= 120.00
```

Fig. 5 Result on GPS simulator attack

In Fig. 5, the simulator-generated signal is readily separated by transmit time clustering algorithm (in the upper part). There are 8 replayed satellites in Fig. 6 that are discriminated from their authentic counterparts. In summary, the receiver equipped with the proposed architecture can readily defence the spoofing attacks with reasonable power that is launched by simulator and receiver-spoofer.

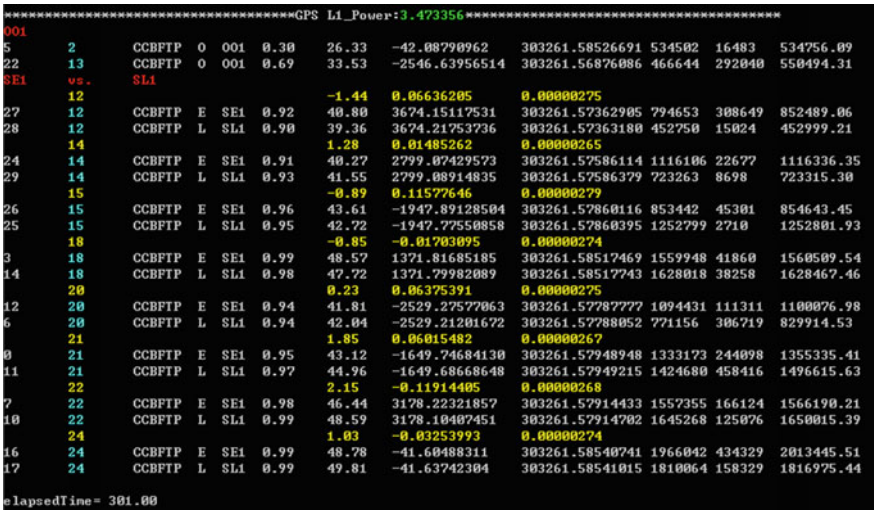

Fig. 6 Result on meaconing attack

6 Conclusions

In this paper, we propose a fundamental receiver architecture and its supporting algorithms. This architecture can be utilized to acquire and track the multi-peak signal that is often encountered in spoofing scenario. The proposed architecture exploits the extra computation resource, and has no requirements of modifying existing RF frontend or IF device.

It is worth mentioning that the proposed architecture cannot discriminate and mitigate spoofing signal. However, the capability of acquiring and tracking multi-peak signal endowed by this architecture lays a cornerstone for further discrimination, mitigation and localization of spoofing signal.

The comparison of signal features enables discrimination of spoofing signal from the true one. For example, the transmit times of signal from GPS simulator always cluster in a small range, while separated from the transmit times of true signal. Meaconing signal does also show a strong pattern. The transmit time extracted from meaconing signal is earlier than true signal, and the differences equal over all satellites. On a receiver in motion, the time history of signal features (such as carrier Doppler frequency and carrier phase) can lend a hand in discrimination.

After distinguishing the spoofing signal, their observables will be excluded from position calculation. This mitigates the impact of spoofing signal, boosts the robustness of receiver. Conversely, the feature and observable of spoofing signal facilitate the localization of spoofer.

In summary, the architecture proposed in this paper exchange extra computation resource for capability of acquiring and tracking multi-peak signal. This architecture lays foundation for detection, discrimination, mitigation and localization of spoofing signal.

Acknowledgements This work was supported by the National Natural Science Foundation of China (Grant No. 61571255).

References

1. Jafarnia-Jahromi A, Broumandan A, Nielsen J, Lachapelle G (2012) GPS vulnerability to spoofing threats and a review of antispoofing techniques. Int J Navig Obs
2. Akos DM (2012) Who's afraid of the spoofer? GPS/GNSS spoofing detection via automatic gain control (AGC). Navigation 59(4):281–290
3. Borio D, Gioia C (2016) A sum-of-squares approach to GNSS spoofing detection. IEEE Trans Aerosp Electron Syst 52(4):1756–1768
4. Manfredini EG, Motella B, Dovis F (2015) Signal quality monitoring for discrimination between spoofing and environmental effects, based on multidimensional ratio metric tests. Proc ION GNSS+, Tampa, FL
5. Humphreys TE, Ledvina, BM, Psiaki ML, O'Hanlon BW, Kintner Jr PM (2008, September) Assessing the spoofing threat: development of a portable GPS civilian spoofer. In: Proceedings of the ION GNSS international technical meeting of the satellite division, vol 55, p 56
6. Jafarnia Jahromi A, Broumandan A, Nielsen J, Lachapelle G (2012) GPS spoofer countermeasure effectiveness based on signal strength, noise power, and C/N0 measurements. Int J Satell Commun Network 30(4):181–191
7. Nielsen J, Broumandan A, Lachapelle G (2011) GNSS spoofing detection for single antenna handheld receivers. Navigation 58(4):335–344

Performance Analysis on High Dynamic Signal Acquisition of INS-Aided BDS Receiver

Xiaqing Tang, Shulei Chen, Xuwei Cheng, Junqiang Gao and Zepeng Sun

Abstract Improving the dynamic performance and signal acquisition performance of BDS receiver aided by INS is the hot spot of the current navigation research. Through the comparison between fundamentals of traditional acquisition algorithm and the acquisition algorithm aided by INS, this paper analyzes the effect of INS velocity errors on doppler errors of BDS receiver. By simulating the carrier trajectory in high dynamic state and assisting the acquisition of BDS by INS in different accuracy grades, the accuracy grades suiting the needs will be chosen according to the results of acquisition performance. The experiment results illustrate that the signal acquisition sensibility of INS-aided BDS receiver is improved and the selected equipment has a very high cost performance. Besides, according to specific application conditions, inertial sensors in different accuracy grades are needed to be chosen. The results can serve as good instruction for the choice of integrated navigation sensors and models.

Keywords BDS · INS-aided · Signal acquisition · High dynamic state · Performance analysis

1 Introduction

The emergence of the Beidou Navigation Satellite System (BDS) is conducive to break the monopoly of GPS of the US in the global navigation business, it also provides a reliable approach for the national-defense and civil satellite navigation

X. Tang · S. Chen (✉) · X. Cheng · J. Gao · Z. Sun
Department of Control Engineer, Academy of Armored Force Engineering, Beijing 100072, China
e-mail: chenshulei@vip.qq.com; 362731142@qq.com

X. Tang
e-mail: tangxiaqing_001@163.com

J. Sun et al. (eds.), *China Satellite Navigation Conference (CSNC) 2017 Proceedings: Volume I*, Lecture Notes in Electrical Engineering 437,
DOI 10.1007/978-981-10-4588-2_77

application in China. The receiver's research is one of the hot spots for current national-defense science and technology development and how to improve the rapidity and accuracy of the satellite signal acquisition of receiver is the key point of the research as well. Satellite signal strength will be greatly weakened in the complex battlefield environment, the BDS receiver needs higher performance to acquire satellite signals in high dynamic and high interference environments [1].

The problems of satellite signal acquisition and tracing can be solved by two means. On the one hand, the method of hardware upgrade can be taken; on the other hand, the multi-sensor such as inertial navigation system can be taken to integrate information so as to support the work of BDS receiver. As for the former, massive man power and material resources are required to research and develop, which is used to upgrade the receiver antenna and other hard wares. The latter, even if the sensor with the lower accuracy can also get a larger receiver performance improvement. At present, the navigation and positioning of the integrated navigation system of the inertial navigation system aided satellite receiver is adopted.

In this paper, a serial sliding correlation acquisition algorithm is used to capture the Beidou satellite signal and add INS and ephemeris information to assist Beidou satellite receiver, Although a lot of research on integrated navigation, there are little analysis of which INS accuracy can be achieved greater performance and can get the maximum cost performance in the high dynamic conditions. Firstly we analyze the principle of INS aided receiver acquisition. Then, the relationship between the velocity position error of INS and the Doppler error and the code phase error is calculated. By emulating carrier's movement under high dynamic date, acquisition auxiliary signals with the INS of various accuracy s. Finally analyze the results, structure the ascending curve of carrier's acquisition performances to different INS under specific dynamic condition, and select the INS with optimal cost performance. This research is embodied with guiding significance for the inertial sensor in integrated navigation area.

2 Principle of Signal Acquisition with the Aid of INS

2.1 Serial Sliding Correlation Search Method

The satellite signal transmitted by the Beidou satellite can generate the Doppler frequency shift and the code phase shift by the relative motion between the satellite and the ground receiver, so it is necessary to determine a satellite signal from two dimensions of frequency and code phase. Serial sliding correlation acquisition method will reduce the search range by changing the frequency and code phase of the local signal and acquire the signal finally [2] Fig. 1 is the serial sliding correlation search view.

When the serial sliding correlation acquisition method is used, the uncertain frequency range and the uncertain codes range are assumed to be f_{unc} and t_{unc} [3].

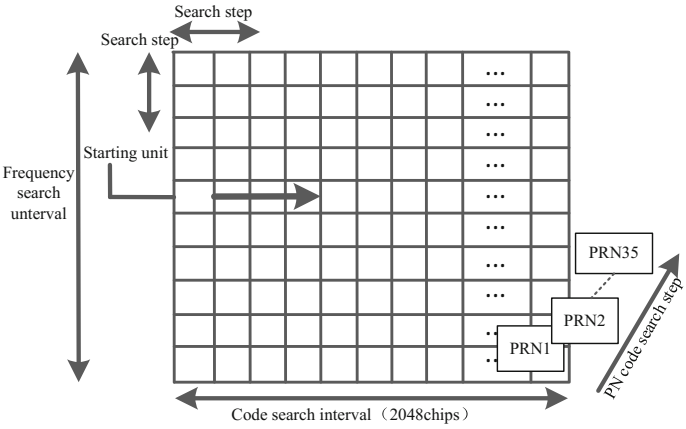

Fig. 1 Serial sliding correlation search

Frequency search step and code search step are f_{bin} and t_{bin}. The total number of search units is

$$N_{cell} = \frac{2f_{unc}t_{unc}}{f_{bin}t_{bin}} \tag{1}$$

The Beidou satellite navigation system has three kinds of satellite constellations, which are GEO, IGSO and MEO. According to the maximum satellite velocity, the maximum value of the satellite Doppler shift is

$$f_{GEO} = V_{GEO}\frac{f_{B1}}{c} \approx 70 \cdot 8\,\text{Hz} \tag{2}$$

$$f_{IGSO} = V_{IGSO}\frac{f_{B1}}{c} \approx 2207 \cdot 4\,\text{Hz} \tag{3}$$

$$f_{MEO} = V_{MEO}\frac{f_{B1}}{c} \approx 4496 \cdot 5\,\text{Hz} \tag{4}$$

The error of RF front-end receiver of satellite clock oscillators can not be ignored and 1 ppm RF crystal deviation will make B1 frequency 1.56 kHz frequency deviation, what's more, environmental impact and other factors also affect the Doppler frequency shift, High speed carrier Doppler frequency shift range is [−10, +10 kHz]. The number of Beidou navigation satellite chips in one cycle is 2046 and when the frequency of the search step is 500 Hz and code phase of the search step is 0.5 chip. The total number of search units is

$$N_{cell} = \frac{2 * 10,000 * 2046}{500 * 0.5} = 163,680 \tag{5}$$

The time of a search step is T_{dwell}, detection probability is P_d, loss factor is k_p and k_p=1, false alarm probability is P_{fa}, integral time is T, there is the following formula

$$T_{dwell} = \left(\frac{2 - P_d}{P_d}\right)\left(\mathrm{k}_p P_{fa} + 1\right) T \tag{6}$$

So the total search time is

$$T = T_{dwell} N_{cell} \tag{7}$$

In the case that the search step size is determined, the less the search scope is, the less time is needed. Use INS and ephemeris almanac information to assist receiver, then estimate the motion information of the satellite and the carrier in this paper, finally reduce the Doppler range and the code phase range. If the ephemeris almanac information is accurate, then the influence factor og the receiver acquisition performance is mainly the accuracy of INS [4].

2.2 The Analysis of INS-Aided

Speed and position information of the INS with ephemeris information are sent to the BDS receiver and estimate Doppler frequency shift, then narrow the two-dimensional search range of the signal.

$$f = \pm f_s + f_{rev} \pm \Delta f_s + \Delta f_{rev} \tag{8}$$

where, the Doppler shift generated by satellite motion is f_s, the Doppler shift generated by the motion of the carrier is f_{rev}, the frequency drift caused by the clock error of the Beidou satellite is Δf_s, the frequency drift of satellite receiver clock error is Δf_{rev}. If the main consideration is the Doppler frequency shift of the relative motion [5]. The formula (8) can be simplified as follows

$$f \approx f_{rev} \pm f_s = \frac{(V_{rev} - V_s)\overrightarrow{e}}{\lambda} \tag{9}$$

The movement speed V_s of the satellite can be obtained by satellite ephemeris solution, the movement speed V_{rev} of the carrier is estimated by INS, the unit vector $\vec{e}$ can be got from the relative position of the carrier and the satellite, and carrier wave length is λ.

The performance of receiver is closely related to Doppler error and code phase error, and the satellite speed can be accurately given by ephemeris information, so the Doppler error is mainly related to the carrier velocity error of the INS solution.

We can get the formula by partial derivation of formula (9)

$$\sigma_f = \sqrt{\frac{\vec{e} \cdot E(\delta V_{rev}(\delta V_{rev})^T) \cdot \vec{e}^T}{\lambda^2}} \tag{10}$$

where, receiver velocity error is δV_{rev}, the code phase offset generated by the relative motion can be expressed as follows

$$\Delta\tau_{dyn}(t_n) = \frac{\Delta R_{LOS}(t_n)}{c} = \frac{1}{c}\int_{t_0}^{t_n} a_{rx} \cdot \vec{e} dt = \frac{\overline{V_{rx}} \cdot \vec{e}}{c} \tag{11}$$

where, the distance from the satellite to the receiver over a period of time in the line of sight (LOS) is $\Delta R_{LOS}(t_n)$, carrier mean velocity is $\overline{V_{rx}}$, So the code phase shift error is

$$\sigma_{\Delta\tau} = \sqrt{\frac{\vec{e} \cdot E(\delta V_{rev}(\delta V_{rev})^T) \cdot \vec{e}^T}{c^2}} \tag{12}$$

3 Experimental Design

The satellite receiver will receive the signal into IF signal, the IF signal is mixed with the local sinusoidal signal and cosine signal, the two signals are integrated and get the decision variable, and then detect whether there is a corresponding satellite signal, if the corresponding satellite signal does not exist, the frequency and code phase of the local signal will be changed, and then continue judgment. INS and ephemeris almanac information can make sure the scope of the search, then greatly reduce the number of code and frequency search, the acquisition with the aid of INS structure is shown as follows (Fig. 2).

Assuming the carrier does high speed movement to a BeiDou satellite and the initial speed is 340 m/s, the attitude angle is 0, the average acceleration is 2 m/s^2 and run 280 s. The starting point is the star that you can see from the figure, the motion trajectory is as follows (Fig. 3).

The receiver uses 10 sets of different accuracy INS to assist signal acquisition, the 10 sets of INS cover the MENS level, tactical level and navigation level. Their gyro accuracy and accelerometer accuracy are as follows (Table 1).

Because of the different accuracy of INS, the Doppler shift error and the code phase error are different in acquisition. So the detection probability is different.

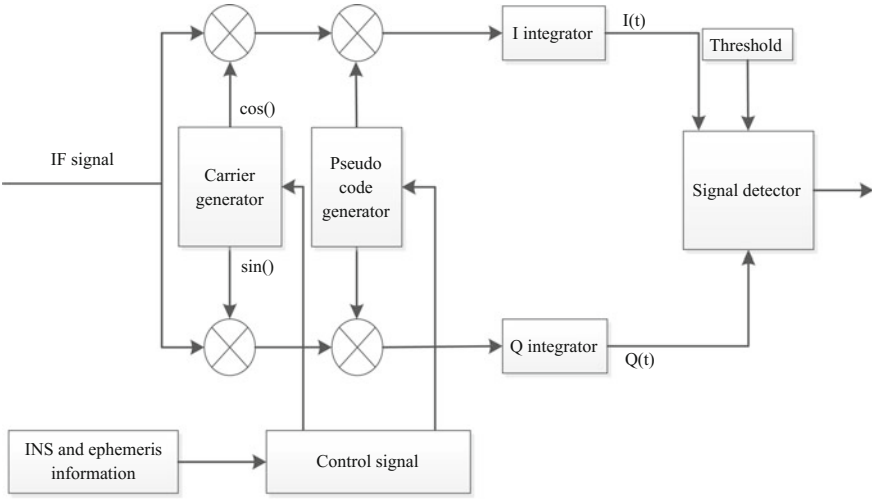

Fig. 2 Acquisition with the aid of INS structure

Fig. 3 Carrier trajectory

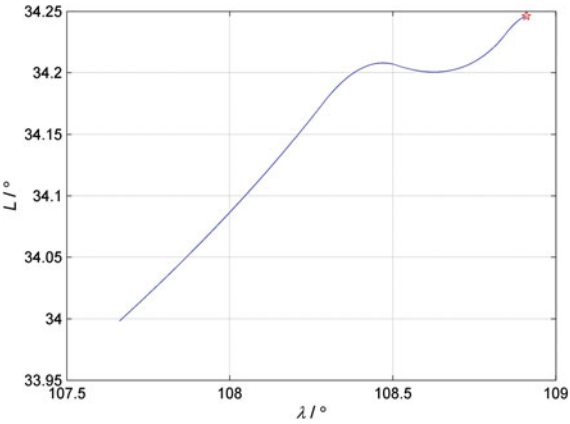

Table 1 The accuracy of different equipments

Group number	01	02	03	04	05	06	07	08	09	10
Gyro accuracy (deg/h)	100	100	100	50	50	10	10	1	1	1
Accelerometer accuracy (mg)	10	1	0.1	10	1	1	0.1	10	1	0.01

We use the detection probability in different carrier to noise ratio as the most important index to reflect the performance of the receiver. For non coherent integration, the decision variable Z is

$$Z = \frac{1}{K}\sum_{K=1}^{K}\sqrt{I_K^2 + Q_K^2} \tag{13}$$

When the signal to be acquired does not exist, the decision variable Z is in the Rayleigh distribution, so false alarm probability is as follows

$$P_{fa} = \int_{V_t}^{\infty} p(z|H_0)\mathrm{dz} = e^{-\frac{V_t^2}{2\sigma_n^2}} \tag{14}$$

If threshold value for detection is V_t, noise power is σ_n^2, So the threshold value can be detected as follows [6]

$$V_t = \sigma_n\sqrt{-2\ln P_{fa}} \tag{15}$$

If there is a signal that can be acquired, detection probability is as follows

$$P_d(B) = Q_1\left(\frac{\sqrt{\lambda}}{\sigma_n}, \frac{\sqrt{\beta}}{\sigma_n}\right) \approx Q_1\left(\frac{\sqrt{CN}}{N_0 f_s}, \frac{\sqrt{N\beta}}{N_0 f_s}\right) \tag{16}$$

where, $Q_1(\cdot,\cdot)$ is 1st order Marcum'Q-Function, it is as follows

$$Q_K(\mathrm{a},\mathrm{b}) = \frac{1}{a^{K-1}}\int_b^{+\infty} x^K e^{-\left(\frac{x^2+a^2}{2}\right)} I_{K-1}(\mathrm{ax})\mathrm{dx} \tag{17}$$

where, I_{K-1} is K−1 order bessel function, so the detection probability is expressed as follows

$$P_D(B) = \frac{1 - \left[1 - e^{-\left(\frac{B}{2\sigma_n^2}\right)}\right]^N}{N \cdot e^{-\left(\frac{B}{2\sigma_n^2}\right)}} \cdot Q_1\left(\frac{A}{\sigma_n}, \frac{\sqrt{B}}{\sigma_n}\right) \tag{18}$$

The influence diagram of Doppler error on detection probability when the code phase error is 0.5 and the influence code phase error on detection probability when Doppler error is 100 Hz are as follows (Fig. 4).

When the detection threshold is 0.95, Doppler error is less than 200 Hz and the code phase error is less than 1/4 chip, the sensitivity of receiver is high.

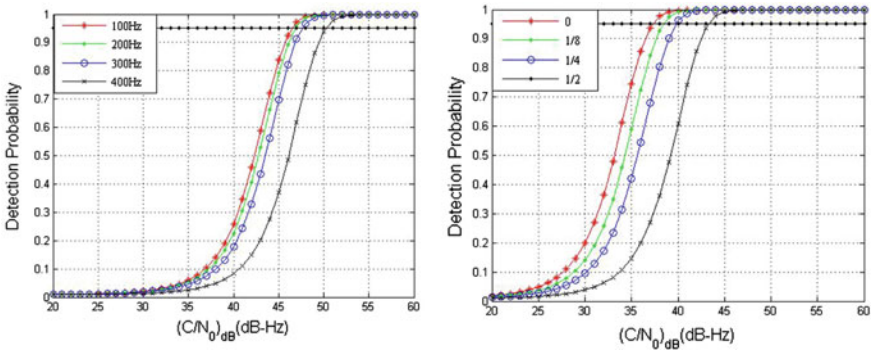

Fig. 4 The influence of Doppler frequency shift error and chip error on the acquisition sensitivity

4 Experimental Result Analysis

The carrier frequency of B1 is 1561.095 MHz, 1 ms contains 2046 chips of code. In the simulation process, we use the velocity error and position error at 150 s. And the speed error and position error can be got, finally Doppler shift error and code phase shift error are calculated, Table 2 is the simulation data table.

According to the above formula, the Doppler shift error and code phase shift error can be got, then we can get 10 groups of the detection probability with different INS aids when the time is 150 s. Thus the acquisition sensitivity of the receiver can be got as follows (Table 3).

Though the above data, we can use 2D interpolation of simulation software to construct the relationship view between the acquisition sensitivity with different INS aids. Where the X axis is the gyro constant drift, the Y axis is accelerometer constant drift, the Z axis for capture sensitivity. The relationship view is as (Fig. 5).

Table 2 Simulation data

Group number	Speed error (m/s)	Position error (m)	Doppler shift error (Hz)	Code phase shift error
01	75	4924.43	393.38	0.512
02	74.33	4272.01	389.87	0.508
03	74	4121.04	388.14	0.505
04	36.24	2469.82	190.05	0.248
05	35.11	2404.16	184.18	0.239
06	7.57	400	39.69	0.052
07	7.28	400	38.18	0.049
08	1.81	136.38	6.92	0.012
09	1.32	130.62	9.46	0.009
10	0.83	125.39	4.39	0.006

Table 3 Acquisition sensitivity of different devices

Group number	01	02	03	04	05	06	07	08	09	10
Acquisition sensitivity (deg/h)	55.8	55.2	55	42.2	39.8	37.0	36.5	36.2	36.1	36.0

We can know that when the detection threshold is 0.95, Doppler error computation is less than 200 Hz and the code phase error is less than 1/4 chip according the above, acquisition sensitivity is very high. If we use the research method in this paper, we can get that, if use the INS composed of 55 deg/h accuracy gyros and 10 mg accuracy accelerometer to assist receiver, the acquisition performance can be better and the cost performance is high. By the simulation, use this precision INS for assistance, we could have a comparison with no aid of INS on acquisition sensitivity as follows (Fig. 6).

If use the clock whose sampling frequency is 4.092 MHz, there will be a sampling point on a code chip, the number of points calculated on the code phase is 4092, so n = 4092.

The data is always dispersed in receiver operating process. $I(\tau)$ and $Q(\tau)$ can be dispersed as I_K and $Q(k)$ (k = 0, 1, …, n−1). If we adopt regular serial acquisition method, every change in the value of k would require n times of multiplication and addition operations. Because there are n values of k, n^2 times of multiplication and addition operations are required in a carrier frequency. For M times of frequency searches, Mn^2 times of calculation are needed. Thus, we can make calculation analysis based on the changes of the acquisition scope. If Use this INS with low accuracy as mentioned above to assist, the Doppler frequency shift search range can be reduced to [−200, +200 kHz] in a short time, this range is smaller than the

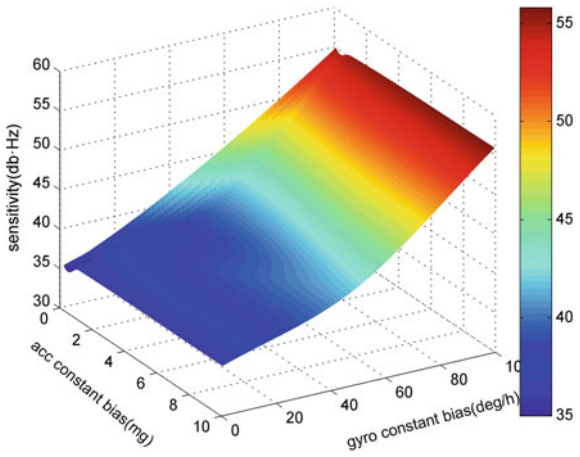

Fig. 5 Acquisition sensitivity of diffierent INS

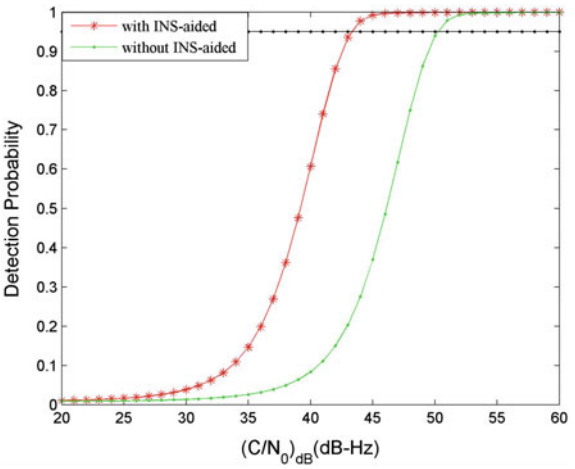

Fig. 6 Acquisition sensitivity contrast with or without the aid of INS

Table 4 Calculation analysis

Acquisition mode	With or without INS aid	Search scope	Number of search units	Calculation
Serial acquisition	Without	[− 10 kHz, 10 kHz]	163680	670,433,280
Serial acquisition	With	[− 200 Hz, 200 Hz]	<10	40,960

frequency search step. In summary, we can List the calculated quantities with or without INS assistance as follows (Table 4).

With the aid of INS and ephemeris, the calculation of acquisition can be reduced a lot. So the acquisition time will be much shorter.

If the detection probability P_d of Beidou receiver is 0.95, the false alarm probability P_{fa} is 0.01, the time domain integration time of acquisition is 2 ms, the receiver clock frequency is 5.714 MHz [7], so the acquisition time without the aid of INS is

$$T = T_{dwell}\frac{2f_{unc}t_{unc}}{f_{bin}t_{bin}} = 362\,s \tag{19}$$

The acquisition time with the aid of INS is

$$T_{INS} = T_{dwell}\frac{2f_{unc}t_{unc}}{f_{bin}t_{bin}} < 2\,s \tag{20}$$

So the acquisition time can be reduced greatly by the aid of INS. In this paper, the Doppler error and the chip error are mainly caused by the INS error, So the acquisition performance of the receiver is mainly affected by INS, If the satellite

signal acquisition method and the signal sampling rate are changed, the selection method of inertial sensor will still have good effect.

5 Conclusion

In order to improve the performance of satellite receiver under high dynamic state And consider the price and technology and other factors. In this paper, use many groups of INS whose accuracy is different assist the receiver to acquire the signal. Through analysis, choose the right INS equipment. The results show that, if use the INS what's chosen to assist receiver under setting conditions, the calculation of acquisition will be reduced greatly, what's more, the acquisition time will be shortened and the acquisition sensitivity of receiver will be enhanced, it is important that the equipment selected has an absolute advantage in price.

This paper provides reference for the selection of INS in high dynamic navigation. It has guiding significances to design integrated navigation system with lower price and higher accuracy.

References

1. Liu JY, Zeng QH (2010) Navigation system theory and application. Nwupress, Xi'an, pp 152–154
2. Lashley M, Bevly DM (2013) Performance comparison of deep integration and tight coupling. Navigation 60(3):159–178
3. Shan T (2014) IMU-Aided GPS signal acquisition under high dynamic environment. Inf Control 43(1):45–48
4. Zhang GL, Zeng J (2008) Principle and technology of integrated navigation. Xi'an Jiantong University Press, Xi'an, pp 31–46
5. Lu Y (2016) BDS/GPS dual mode software receiver. Electronic Industry Press, Beijing, pp 134–136
6. He XF (2011) Performance analysis on high dynamic signal acquisition aided by SINS for GNSS satellites. J Chin Inertial Technol 19(4):446–451
7. Li KB (2014) Research and simulation realization of high dynamic GPS signal capture algorithm. Harbin University of Science and Technology, Harbin

The Real-Time Realization and Performance Analysis of BDS Vector Receiver

Cailun Wu, Song Xie, Jianwei Zhang and Yachuan Li

Abstract In this paper, the principle of vector receiver is introduced in details. According to the characteristics of real-time receiver, the real-time vector receiver architecture and real-time implementation flow are given. The vector receiver was successfully run on the hardware platform and evaluated the positioning accuracy, computational complexity and sensitivity performance. In this paper, the effect of clock drift and integration time on the tracking performance of vector receiver is given, which provides a good reference value for different series of crystal selection. Finally, for different application areas, this paper evaluates the vector receiver performance with the loop NCO update rates and the different measurement update rates, thus laying a good foundation for the subsequent implementation of GNSS/INS deep combination hardware.

Keywords Vector receiver · Real-time · Weak signal · High dynamic · Vector loop

1 Introduction

With the application of Beidou satellite navigation system more and more popular, satellite navigation receivers for different applications have become more diverse. Compared with the conventional receiver, the vector receiver has excellent performance in aspects of the high sensitivity, anti-jamming, high dynamic and so on. Especially, the system combined with INS is one of the trends of future integrated

C. Wu (✉) · S. Xie · J. Zhang
State Key Laboratory of Satellite Navigation System and Equipment Technology, Shijiazhuang, China
e-mail: wucailun123@sina.com

Y. Li
The 54th Research Institute of CETC, Shijiazhuang, China

J. Sun et al. (eds.), *China Satellite Navigation Conference (CSNC) 2017 Proceedings: Volume I*, Lecture Notes in Electrical Engineering 437,
DOI 10.1007/978-981-10-4588-2_78

navigation system. Therefore, the vector receiver has always been a hotspot of the development of GNSS receiver technology. So far, the domestic truly-realized real-time vector receiver is rare. The essence of the vector receiver is the idea of utilizing the joint tracking of multiple channels to get the benefit in signal processing, which have obvious advantages especially in some critical applications like weak signal tracking and re-acquisition of loss lock.

In addition to independent vector receivers, and the combination system with inertial navigation systems is also the main direction of development. The introduction of inertial navigation makes the Kalman filter of integration filtering more simple in dynamic model estimation and can obtain more advantages in dynamic performance. Therefore, the deep-integration navigation system based on vector architecture becomes a hot research direction. In essence, the vector receiver is the core of the deep-integration navigation system, so in order to achieve deep-integration system, it is necessary to understand the principle of vector receivers, especially real-time vector receiver. Zhao Sihao of Tsinghua University gives the vector receiver architecture, simulation results and the performance analysis of vector receivers from different Q matrix and R matrix [1]. Zhu Zhen-Zhen of National University of Defense Technology (NUDT) has also studied the overall architecture of the vector receiver and presented the implementation framework of VDLL and VFLL [2]. Zhang Xin of Shanghai Jiaotong University also independently completed simulation work of the vector receiver, mainly for high-dynamic scenes, which have no detailed reports of specific results [3]. So far, domestic real-time vector receivers have not appeared in mature products or models. With the increasing demand of GNSS/INS deep integrated navigation systems, the research of real-time vector receivers has reached the point that must be solved.

2 The Principle of the Vector Receiver

Traditional receivers use a single channel to complete independent tracking, the channel does not affect each other. Compared with traditional receivers, the idea of vector receiver is to use the position and speed of the receiver and combine the satellite's position and velocity calculation code and carrier Doppler frequency to close the loop instead of directly using phase detector and loop filter. And the processing gain of the vector receiver is about 10–15 dB. The main difference is that the coherent phase-discriminator or the non-coherent phase-discriminator [1].

2.1 The Basic Principle

In traditional satellite navigation receivers, correlation operation between the AD samples and the local carrier and pseudo-codes is necessary in order to achieve

stable tracking of satellite signals. The correlation values are processed in the code and carrier frequency discriminators and the corresponding loop filter to obtain the code frequency and the carrier frequency error. Then, the receiver uses the code frequency and carrier frequency error to update the code NCO and carrier NCO. The receiver will adjust the local code and carrier output until it is perfectly aligned with the pseudo code and carrier of the input signal. While the vector receiver uses the co-processing of all channels and uses position/velocity information and clock skew to close the receiver loop. Therefore, finding the relationship between position error and code phase error is the primary problem of vector receivers.

Figure 1 presented the relationship between the receiver position and the code phase. Assumed that the estimated position of the receiver is rather close to the true position, the light-of-sight direction of them is approximately parallel, since both are far away from the satellite.

Projecting the position error in the line-of-sight direction, the distance error in the line-of-sight direction is obtained. The error term embodies the impact of the code phase error and clock error. And the relationship between the code phase error and the position error can be expressed as follows.

$$\Delta\rho_j = \delta P * a_j + t_b + \varepsilon_j \tag{1}$$

In which the subscript j represents the satellite number; δP is the receiver position error; t_b is receiver's clock error; a_j is normalized vector of the line-of-sight direction; ε is the un-modeled error. Based on the same assumption, the relationship between the carrier frequency error and the receiver speed error can be expressed as following.

$$\Delta\phi_j = \delta V * a_j + t_d + \eta_j \tag{1.2}$$

In the above equation, t_d is the clock drift; δV is the receiver velocity error; η_j is the un-modeled error. Through derivation of the two above equations, the direct relationship between the position and velocity information and loop tracking has been established, thus overcome the constraints of the traditional two-level structure of loop processing and positioning solution.

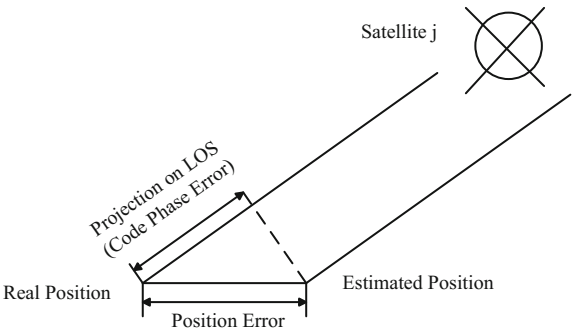

Fig. 1 The relationship between receiver position and code phase

2.2 The Model Analysis

The previous section gives the basic idea of the vector receivers, the following section will focus on the derivation of the implement of the vector receiver architecture. The vector receiver omits the traditional loop, and uses the Kalman filter to realize the joint processing of tracking and positioning directly. The state transition model is used to predict the position and velocity at time $k + 1$. Then position and velocity information can be obtained as follows.

$$P_{k+1} = P_{k+1} + \Delta t * V_k \tag{3}$$

$$\hat{V}_{k+1} = V_k \tag{4}$$

In which, "∧" represents the predicted value of the corresponding variable; Δt is the time interval between time k and k + 1. It is assumed that the receiver already get the code frequency/phase ($\varphi_{j,k}$/$f_{code,j,k}$), the carrier frequency ($f_{j,k}$), the signal transmission time t, the clock deviation (t_b), and the clock drift (t_d) of the j-th satellite signal accurately at time k, as well as the position (P_k) and velocity (V_k) of the receiver. With the position and velocity information at time $k + 1$, the code phase/frequency and carrier frequency of the received signal at time $k + 1$ can be predicted from the calculation of satellite position and velocity according to ephemeris. The code phase/frequency and carrier frequency predictions for the j-th satellite are calculated as follows

$$\hat{\varphi}_{j,k+1} = \varphi_{j,k} + (\Delta P_{j,k,k+1} - \Delta t * V_k)^T a_{j,k+1} + \Delta t * c \tag{5}$$

$$\hat{f}_{code,j,k+1} = [1 + t_{d,k} + (V_{j,k} - V_k)^T a_{j,k+1}] * f_{co}/c \tag{6}$$

$$\hat{f}_{j,k+1} = [1 + t_{d,k} + (V_{j,k} - V_k)^T a_{j,k+1}] * f_n/c \tag{7}$$

where $\Delta P_{j,k,k+1}$ is the displacement vector of the j-th satellite between time k and k + 1; $V_{j,k}$ is the velocity vector of the satellite j at time k; f_{code} and f_n are the nominal frequency of the pseudo-code and the carrier, respectively (For B1, $f_{code} =$ 2.046 MHz and $f_n = 1561.098$ MHz); c is the speed of light. By using the above formulation the loop NCO can be updated the loop can be closed.

The vector receiver can reproduce the local code and carrier based on the calculated pseudo-code and carrier NCO. The code phase error ($\Delta\rho$) and the carrier frequency error ($\Delta\phi$) can be obtained by processing the correlation values using the code and carrier discriminators.

The carrier frequency discriminator is used rather than a phase discriminator in a vector receiver, mainly due to the lack of linearity of the phase discrimination and the fact that the velocity change in a larger dynamic can't be fully reflected in the phase change. Due to the existence of clock error and clock drift in the real-time receiver, it is necessary to fully consider the influence of clock error and clock drift

in closed-loop receiver. From time k to k + 1, the deviation of clock is entirely determined by the clock frequency error within the present and previous period, and the clock frequency error can usually be considered to change relatively slowly.

After clarifying how to update the loop, the following describes the relevant variables for the Kalman filter in the vector receiver. The vector receiver uses the Kalman filter to estimate the position and velocity information of the receiver for the correction of the predicted value. Therefore, the position error, the velocity error and the total error are selected as the Kalman filter states. If using in the deep integration, the states will contain the inertial error, the dimension of states will increases. In the early development stage, the state transition models can be used constant velocity model, so the state transition matrix is extremely simple, not repeat them here.

After description of the states and the state transition matrices, the rest is the observation and observation matrix. The observed quantity is the code phase discriminator error and the carrier frequency discriminator error, then the observation is as follows:

$$Z_k = HX_k + V_k = [\, z_{co,1,k} \quad z_{ca,1,k} \quad \cdots \quad z_{co,n,k} \quad z_{ca,n,k} \,]^T_{1\times 2n} \tag{8}$$

The observation matrix represents the correspondence between the discriminator error and the states error, expressed by the direction cosine matrix H, and the formula is:

$$H = \begin{bmatrix} a_{jx,k} & a_{jy,k} & a_{jz,k} & 0 & 0 & 0 & 1 & 0 \\ 0 & 0 & 0 & a_{jx,k} & a_{jy,k} & a_{jz,k} & 0 & 1 \end{bmatrix} \tag{1.9}$$

where $a_{jx,k}, a_{jy,k}, a_{jz,k}$ are the three components of the unit line-of-sight direction vector from the receiver to the j-th satellite at time k. Through the above analysis, the states, the state transition matrix, the observations and the observation matrix are obtained. The overall architecture of the Kalman filter of the whole vector receiver is basically formed.

3 The Real-Time Realization of Vector Receiver

After completing the above theoretical analysis, the entire system can be used to build in hardware. The real-time vector receiver using FPGA + DSP architecture, the FPGA is similar with the conventional receiver, which completes the capture function and correlator parts. Given the resources to consider, the FPGA chip selection is the Altera's CycloneV series A9 chips, which the resources is about 300 K LEs, to meet the operational requirements of vector receivers; the DSP chip is the TI's 6748 chip, and embedded double-precision floating-point multiplier to improve floating point computing ability. The block diagram of the whole process is shown in Fig. 2.

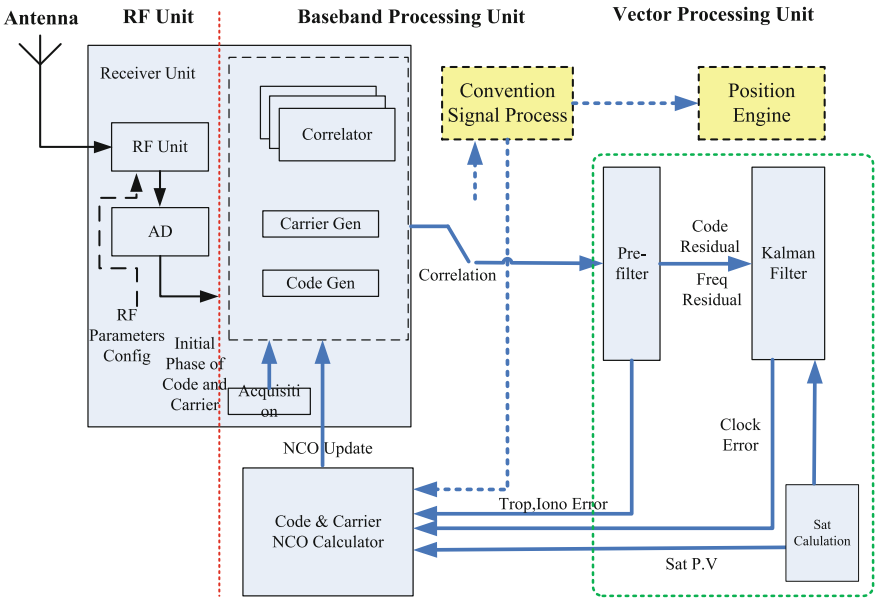

Fig. 2 The architecture of real-time vector receiver

It can be seen from Fig. 2, the biggest difference between the conventional receiver and the vector receiver is addition of vector processing unit. The traditional receiver architecture still exist, including the antenna, RF and correlators and baseband signals and information processing part. In addition to this, the baseband signal pre-filtering process and the Kalman filter process and the calculation section of the code and carrier NCO control module are added.

The whole real-time vector receiver processing flow is as follows:

1. The traditional receiver starts and completes the positioning;
2. Initialize the vector receiver according to the positioning information, including opening the pseudo-code generator, initializing the loop NCO (if necessary, closing the traditional receiver);
3. Initialize the correlator to start correlation;
4. Complete phase detection and output phase error;
5. Pre-filter processing is performed and the pseudo-range residual and pseudo-range residual are output;
6. Implementation of Kalman filter processing, the output of the new navigation solution and clock error and clock drift;
7. Calculate satellite position and calculate LOS and NCO control volume;
8. Update the loop NCO;
9. Repeat steps 4–8.

From the above process can be seen, compared with the conventional receiver, the vector receiver cancel the traditional loop processing. The use of pre-filter to get

pseudo-range residual and pseudo-range rate residuals, and send into the Kalman filter, and finally the Kalman output used to completing the entire loop update. The update rate of the Kalman filter and the NCO update rate can be set differently depending on the application and the hardware performance level.

4 Performance Analysis

The main performance evaluation of real-time vector receiver includes positioning accuracy, computational complexity and weak signal tracking ability evaluation. In order to realize the positioning accuracy evaluation, the traditional receiver and the vector receiver both are used in the realization process at the same time. The whole receiver uses BDS B1 signal to verify, the vector receiver works in the normal receiver and the vector receiver mode at the same time, and outputs the positioning result synchronously.

It can be seen from Fig. 3, the position accuracy of the two receivers are basically the same. But the short-term error jitter of the vector receiver using Kalman filter is less than the conventional receiver.

The vector receiver uses many matrix inversion and other operations, therefore its real-time processing capability determines whether the vector receiver can run in real-time. This receiver uses TI's 6748 chip to complete the calculation of the vector computation part. To facilitate the evaluation, TI's BIOS operating system was used to analyze CPU load changes.

As can be seen from Table 1, with the Kalman filter update rate increases its computational complexity varies greatly. The increase of the processing channel will not result in the increasion of the computational complexity, nor will the change of the update rate lead to an increase in the computational complexity.

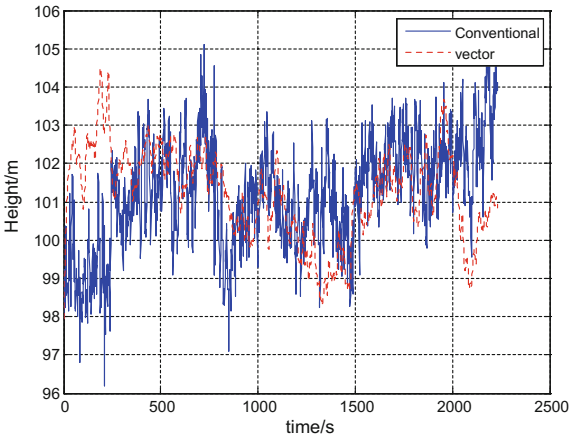

Fig. 3 The position results of vector receiver and conventional recevier

Table 1 The computational load of real-time vector receiver

Process mode	KF update (Hz)	Loop update (Hz)	Channels	CPU load (%)
1	1	100	6	24
2	1	100	8	28
3	2	50	6	31
4	2	100	8	36
5	5	50	6	43
6	5	50	8	45
7	10	100	6	52
8	10	100	8	56

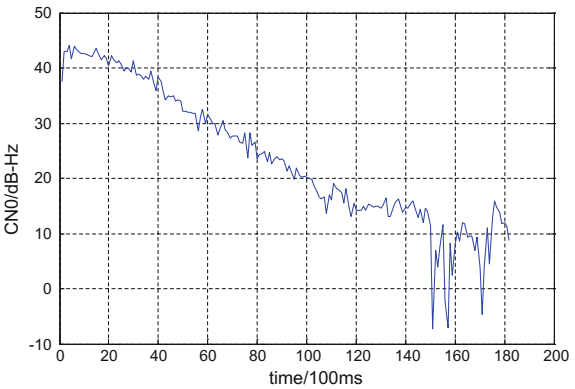

Fig. 4 CN0 evaluation of the vector receiver

Finally, the tracking performance of the vector receiver is evaluated. In this paper, we only use 1 ms coherent integration time to estimate the weak signal tracking ability. When the signal power level is reduced to −150 dBm, the receiver can still output the positioning solution by gradually reducing the power level of the simulator. The carrier to noise ratio changes as shown below:

As can be seen from Fig. 4, the vector receiver has a strong tracking ability, only 1 ms coherent integration of the track sensitivity can reach 22 dB-Hz. Note, however, that increasing the correlation integration time does not result in a linear increase in sensitivity.

5 Conclusion

Through the research of this paper, it solves the architecture and realization problem of the BDS real-time vector receiver. The performance is satisfactory, and further analysis and optimization are needed. In addition, if there is an abnormal channel, how to ensure the robustness of the vector receiver problems to be further studied.

In the future, the inertial system will be introduced into the structure based on the vector receiver, and the GNSS/INS deep integrated navigation system will be realized, and the high dynamic performance of the vector receiver will be solved.

References

1. Wang X, Li Y, Ji X (2015) SINS/GPS integrated navigation technique. Beihang University Press, Beijing, pp 1–3
2. Xie G (2009) GPS principles and receiver engineering. Publishing House of Electronics Industry, Beijing, pp 183–186
3. Zhao S (2011) GNSS/INS integrated navigation: research on key technologies and working performances, Tsinghua University
4. Zhu Z (2011) Research on key techniques of vector tracking for satellite navigation, National Universtiy of Defense Technology
5. Zhang X (2013) Research on realtime GNSS vector tracking technology, Shanghai Jiaotong University

Parameters Design Method of Kalman Filter-Based Tracking Loop in GNSS/INS Deep Integration

Bing Li, Wenfei Guo, Xiaoji Niu, Nesreen I. Ziedan and Jingnan Liu

Abstract This paper proposes a parameter design method of a second-order KF tracking loop in the deep integration architecture according to inertial sensor errors and receiver oscillator errors. Firstly, the effects of INS aiding on the state-driven and measurement noises of KF tracking loop are analyzed. Secondly, through coordinate frame transformation and LOS projection, the variances of the two accelerometer noises in the Earth-centered Earth-fixed (ECEF) frame and LOS direction are obtained. Lastly, the performance of KF-based tracking loop in the deep integration architecture is tested through the data collected from the GNSS/INS hardware simulator, and is compared with the conventional tracking loop in the deep integration architecture. The test results show that the proposed parameter design method makes the channel KF in the deep integration share the comparable performance to the conventional tracking loop in the deep integration. The test results illustrate the correctness and effectiveness of the parameter design method proposed in the paper. Since each parameter is set according to its physical meaning in the paper, the empirical and tentative trials in the parameter optimization process are avoided.

Keywords Kalman filter · Parameter design · State driven noise · Accelerometer noise

B. Li (✉) · W. Guo · X. Niu · J. Liu
GNSS Reasearch Center, Wuhan University, Wuhan, China
e-mail: wehappy_8888@whu.edu.cn

N.I. Ziedan
Computer and Systems Engineering Department,
Zagazig University, Zagazig, Egypt
e-mail: ziedan@ieee.org

J. Sun et al. (eds.), *China Satellite Navigation Conference (CSNC) 2017 Proceedings: Volume I*, Lecture Notes in Electrical Engineering 437,
DOI 10.1007/978-981-10-4588-2_79

1 Introduction

In the GNSS/INS deep integration architecture, the inertial navigation system (INS) provides Doppler aiding information for GNSS receiver tracking loops, which substantially improve receiver's tracking and navigation performance. Therefore, GNSS/INS deep integration technology has been widely used under various challenging environments, such as high dynamics, weak signals and anti-interference.

For conventional carrier phase tracking loops, parameters including loop order, bandwidth and coherent integration time need to be designed. In conventional receivers without INS aiding, the effects of noise performance and dynamic response should be taken into consideration in the tracking loop design [1]. While in the deep integration architecture, the INS aiding guarantees the dynamic response of the tracking loop, but brings about the INS aiding error which influences the loop tracking performance and should be considered consequently [2]. For a KF-based tracking loop, measurement noise covariance matrix R, state-driven noise covariance matrix Q and state estimation error covariance matrix P should be designed. The parameter design method of KF-based tracking loop without INS aiding has been widely investigated. In Won [3], the measurement noise covariance R was set according to the real time estimates of carrier-to-noise ratio (C/N_0), while the state-driven noise covariance Q was chosen to make the resulting equivalent bandwidth swing within an empirically feasible range. Thus, the tracking loop automatically adjusted its bandwidth under different GNSS signal strengths to maintain accurate carrier phase tracking performance. In Won [4], the structural equivalence of conventional and KF-based tracking loop, as well as the relationship between the loop bandwidth and the covariance matrix P, Q, R were analysed, based on which it was proposed that the covariance matrix of KF should be set according to the empirical or priori knowledge and the bandwidth of conventional tracking loop. In Sun [5], the noise covariance was set according to its physical meaning. The measurement of KF-based tracking loop was taken from the carrier phase discriminator output. Therefore, the measurement noise covariance R should be calculated through the formula of the discriminator output variance. Moreover, it was analysed that the state-driven noises are comprised of the receiver oscillator noise and line-of-sight (LOS) dynamic change. The characteristic of the receiver oscillator noise was determined by the oscillator type, while the LOS dynamic change was caused by the motion of both satellites and receiver. With the assumption that the receiver was static, the corresponding state-driven noise variance was set by calculating the maximum acceleration of the satellite motion in the LOS direction.

In GNSS/INS deep integration architecture, the signal tracking loop only needs to track the residual dynamics because of the INS aiding. Therefore, the KF-based tracking loops need to adjust its noise covariance parameters to maintain the best tracking performance. However, the parameter design method of KF-based tracking loop in the deep integration architecture was not given in details in many works.

Based on previous research, we analyse the effects of INS aiding on the state-driven and measurement noises of KF-based tracking loop. Moreover, a parameter design method of a second-order KF carrier phase tracking loop in the deep integration architecture according to inertial sensor errors and receiver oscillator errors is proposed and verified through simulation tests.

2 Model of KF-Based Carrier Phase Tracking Loop

In conventional GNSS receivers without INS aiding, the state vector of a 2nd order KF-based carrier phase tracking loop is comprised of the carrier phase error between the incoming and local signals x_φ in unit of radian, and the carrier Doppler frequency of the incoming signal x_ω in unit of rad/s. The system measurement is the carrier phase discriminator output $\Delta\overline{\varphi}_{k+1}$ in unit of radian. The state transition equation and the measurement equation are expressed as:

$$\begin{cases} \begin{bmatrix} x_\varphi \\ x_\omega \end{bmatrix}_{k+1} = \begin{bmatrix} 1 & T \\ 0 & 1 \end{bmatrix} \begin{bmatrix} x_\varphi \\ x_\omega \end{bmatrix}_k - \begin{bmatrix} T \\ 0 \end{bmatrix} w_{NCO,k} + \begin{bmatrix} 1 & 0 & 0 \\ 0 & 1 & 1 \end{bmatrix} \begin{bmatrix} w_b \\ w_d \\ w_a \end{bmatrix} \\ \Delta\overline{\varphi}_{k+1} = \begin{bmatrix} 1 & T/2 \end{bmatrix} \begin{bmatrix} x_\varphi \\ x_\omega \end{bmatrix}_k - \frac{T}{2} w_{NCO,k} + v_{k+1} \end{cases} \quad (1)$$

where T is the coherent integration time in unit of second, $w_{NCO,k}$ is the carrier Doppler frequency of local signal in unit of rad/s, v_{k+1} is the system measurement noise. w_b is the driven white noise of the receiver oscillator clock error with power spectra density (PSD) q_b in unit of $(\text{rad/s})^2/\text{Hz}$. w_d is the driven white noise of the receiver oscillator clock drift with PSD q_d in unit of $(\text{rad/s}^2)^2/\text{Hz}$. w_a is the driven white noise of the LOS velocity random walk with PSD q_b in unit of $(\text{rad/s})^2/\text{Hz}$. The state-driven noise covariance matrix can be expressed as:

$$Q = q_b \begin{bmatrix} T & 0 \\ 0 & 0 \end{bmatrix} + q_d \begin{bmatrix} \frac{T^3}{3} & \frac{T^2}{2} \\ \frac{T^2}{2} & T \end{bmatrix} + q_a \begin{bmatrix} \frac{T^3}{3} & \frac{T^2}{2} \\ \frac{T^2}{2} & T \end{bmatrix} \quad (2)$$

In a conventional receiver, a KF-based tracking loop needs to track all the signal dynamic changes caused by the motion of satellite and receiver, and the oscillator errors. While in the deep integration architecture, the majority dynamics of the receiver is tracked by INS. Combined with the estimate of the satellite dynamics through the ephemeris data, the INS aiding information to the GNSS tracking loop already includes the relative motion between the satellite and the receiver in the LOS direction. Moreover, the receiver oscillator errors can be estimated by PVT algorithm or loosely-coupled algorithm. Therefore, the signal tracking loop only needs to track the residual LOS relative motion and residual oscillator errors. In other words, the tracking loop works in the quasi-static mode due to the INS aiding,

which means that the noise covariance parameters of KF-based tracking loop should be re-designed.

3 Parameters Design Method of KF-Based Carrier Phase Tracking Loop in Deep Integration Architecture

In the deep integration architecture, the measurement of KF-based tracking loop is still the carrier phase discriminator output. Therefore, the measurement noise variance R is set in the same way as in the conventional receiver, i.e. through the formula of the discriminator output variance as expressed in the following [3, 6]:

$$R = \frac{1}{2T * C/N_0}\left(1 + \frac{1}{2T * C/N_0}\right)(rad^2) \tag{3}$$

where $C/N_0 = 10^{cn0/10}$. $cn0$ is the carrier to noise ratio in unit of dB-Hz.

The driven noise characteristics of receiver oscillator errors are determined by the oscillator type itself. Although the oscillator errors can be estimated by PVT algorithm and loosely-coupled algorithm and are compensated to the INS aiding information, the stochastic characteristics of the oscillator errors do not change, neither does the design method of the oscillator driven noise variance. Given the oscillator H parameters, the clock noise spectra densities are given by [7]:

$$q_b = h_0/2 \tag{4}$$

$$q_d = 2\pi^2 h_{-2} \tag{5}$$

In the deep integration architecture, w_a denotes the driven noise of the residual dynamics in the LOS direction caused by the calculation error of INS mechanization and ephemeris data. In [8] the accuracy of the satellite position and velocity solutions derived from broadcast ephemeris was assessed with the solutions derived from precise ephemeris taken as the reference true value. The results showed that the satellite position error of broadcast ephemeris was within 2 m, and the satellite velocity error was within 1 mm/s. In the GNSS/INS deep integration architecture, INS mechanization results are corrected by GNSS single point positioning (SPP) measurements through loosely-coupled integration. Therefore, the long-term accuracy of INS mechanization in the deep integration architecture depends on the accuracy of GNSS measurements. In general, the GNSS position error is at the meters level, and the velocity error at the centimeters or decimeters level. The meter-level position error has very little effect on the calculation of LOS unit vector, while the GNSS receiver velocity error is obviously much larger than the satellite velocity error. Therefore, compared to the INS mechanization error, the calculation error of broadcast ephemeris can be neglected.

Since w_a is a driven noise at the Doppler rate (acceleration) level, it can be assumed that the INS mechanization error comes from the inertial sensor errors, which will be discussed in the following subsections.

3.1 Sensor Errors of Gyroscope

The white noise and bias instability in the gyroscope output cause the calculation error of attitude update in the INS mechanization, which results in inaccurate gravity compensation and the consequent horizontal acceleration errors, velocity and position update errors as well. In the deep integration architecture, INS mechanization is periodically corrected by GNSS measurements and the systematic part of the inertial sensor errors are compensated as well. Therefore, it's necessary to assess the gravity compensation error in horizontal acceleration caused by the gyroscope white noise and bias instability during consecutive two GNSS corrections.

It is assumed that the PSD of gyroscope white noise is P_{w_g} in unit of $(deg/\sqrt{h})^2$. The bias instability is modeled as a 1st order Guassian-Markov process with root mean square σ_{b_g} in unit of deg/h. The gravity compensation error caused by the gyroscope white noise during GNSS correction period T (unit: s) is approximated as:

$$\Delta a_{w_g} = \sqrt{P_{w_g}} * \sqrt{T} * g \tag{6}$$

where g is the gravitational acceleration which is taken as 9.8 m/s^2 in the paper. The gravity compensation error caused by the gyroscope bias instability is approximated as:

$$\Delta a_{b_g} = \sigma_{b_g} * T * g \tag{7}$$

The MEMS grade MTi-G and tactical grade FSAS are taken as example in the later analyses, and the corresponding inertial sensor errors are summarized in Table 1. Generally the longest GNSS correction period T is one second. For FSAS the maximum acceleration error caused by the gyroscope bias instability and white

Table 1 Parameters of typical IMU sensor errors

	Gyroscope	Accelerometer
MTi-G (MEMS grade)	Bias instability: 100 deg/h	Bias instability: 2000 mGal
	White noise: $3\ ^\circ/\sqrt{h}$	White noise: $0.12\ m/s/\sqrt{h}$
FSAS (tactical grade)	Bias instability: 0.1 deg/h	Bias instability: 1000 mGal
	White noise: $0.1\ ^\circ/\sqrt{h}$	White noise: $0.03\ m/s/\sqrt{h}$

noise is 4.75×10^{-6} and 2.85×10^{-4} m/s^2, respectively. Compared to the standard deviation (STD) of the accelerometer bias instability 0.01 m/s^2, it can be concluded that the acceleration error caused by FSAS gyroscopes during one second is much smaller than that caused by accelerometer bias instability. For MTi-G the maximum acceleration error caused by the gyroscope bias instability and white noise is 4.75×10^{-3} and 8.55×10^{-3} m/s^2, respectively. Compared to the STD of the accelerometer bias instability 0.02 m/s^2, the same conclusion can be drawn that the acceleration error caused by MTi-G gyroscopes can be neglected.

Based on the analyses above, it can be seen that during one second GNSS correction period, the acceleration error caused by the gyroscopes in the MEMS and tactical grade INS can be neglected compared to that caused by the accelerometers. Moreover, shorter GNSS correction period leads to smaller acceleration error caused by gyroscopes. But the acceleration error caused by accelerometers remains the same. Therefore, the sensor errors of gyroscope is not considered in the paper when setting the noise variance of w_a.

3.2 White Noise of Accelerometer

In general, a triad of accelerometers in an inertial measurement unit (IMU) share the same model and white noise characteristics. Since the accelerometer output is in the body frame, it should be transformed into the ECEF frame and then projected onto the LOS direction to obtain the white noise variance of the triad of accelerometers for one GNSS receiver channel. The white noise covariance matrix of the triad of accelerometers in the body frame can be expressed as:

$$P_b = E\left[\vec{w}_{acc}\vec{w}_{acc}^T\right] = \begin{bmatrix} \sigma^2 & 0 & 0 \\ 0 & \sigma^2 & 0 \\ 0 & 0 & \sigma^2 \end{bmatrix} \tag{8}$$

where $\vec{w}_{acc}$ is the white noise vector of the triad of accelerometers, σ^2 is the white noise variance of one accelerometer. Therefore, the white noise covariance matrix of the triad of accelerometers in the ECEF frame can be expressed as:

$$P_e = C_b^e P_b C_e^b = C_n^e C_b^n \begin{bmatrix} \sigma^2 & 0 & 0 \\ 0 & \sigma^2 & 0 \\ 0 & 0 & \sigma^2 \end{bmatrix} (C_n^e C_b^n)^T \tag{9}$$

where C_b^e, C_n^e, C_b^n are all coordinate frame transformation matrices. b denotes the body frame, e denotes the ECEF frame, and n denotes the local level frame. Assuming that $\vec{u}$ (1 * 3 dimensions) is the LOS unit vector for one GNSS tracking channel, the white noise variance value of the triad of accelerometers in the LOS direction can be expressed as:

$$\sigma_{LOS}^2 = \vec{u} P_e \vec{u}^T \tag{10}$$

3.3 Bias Instability of Accelerometer

The bias instability discussed here in the paper refers to the residual part after the error compensation of accelerometers. It can be seen from the estimation error covariance matrix P that each accelerometer has a different estimation error variance of bias instability. Therefore, it's necessary to take coordinate frame transformation and LOS projection to obtain the final noise variance for one signal tracking loop.

The bias instability is usually modelled as a 1st order Gaussian-Markov process, while the state-driven noise of a KF is required to be a Gaussian white noise. To deal with the residual bias instability the following three approaches are considered:

(1) The residual bias instability is simplified as a state-driven white noise, and its variance in the body frame is directly taken from the corresponding elements of P matrix representing the bias instability estimation error variance. Referring to the expressions (8–10), the subsequent coordinate frame transformation and LOS projection is given by:

$$\sigma_{b,LOS}^2 = \vec{u} C_n^e C_b^n \begin{bmatrix} \sigma_x^2 & 0 & 0 \\ 0 & \sigma_y^2 & 0 \\ 0 & 0 & \sigma_z^2 \end{bmatrix} (C_n^e C_b^n)^T \vec{u}^T \tag{11}$$

where σ_x, σ_y and σ_z are the STDs of bias instability estimation errors from P matrix.

(2) The residual bias instability is added to the KF-based tracking loop model as an external input. However, the real value of the residual bias instability is not available, since P matrix only gives its variance. Therefore, this approach is unfeasible.

(3) The residual instability is modelled as a 1st order Gaussian-Markov process and is estimated as a state of KF-based tracking loop. In this case, the 2nd order KF is extended to a 3rd order filter. Obviously it increases the complexity of each tracking loop. Moreover, the residual bias instability is estimated by KF only using the measurements from each channel itself, which undermines its estimation accuracy.

Therefore, the first approach is taken to deal with the residual instability in the paper. Based on the analyses of this section, it can be concluded that the measurement noise variance and the driven noise variances of receiver oscillator errors do not change in the deep integration architecture. During one second GNSS correction period, the calculation errors of ephemeris data and the sensor errors of gyroscopes can be neglected. The state-driven noise w_a mainly consists of the white

noise and bias instability of accelerometers. Since these two sensor noises are independent and uncorrelated, the variance of w_a should be the geometric summation of the variances of the accelerometer white noise and bias instability.

4 Simulation Test Results

The GPS and IMU data used in the simulation tests are generated by the hardware simulator from US Corporation NavLabs and are collected by the hardware receiver platform developed by GNSS Research Center of Wuhan University. The data are stored in a binary file for post-processing through a deep integration software receiver. The receiver remains static at the beginning and then experiences several low dynamic motions, including accelerations, decelerations and turns.

The deep integration architectures based on 2^{nd} order conventional and KF-based tracking loops are tested in the paper. The IMU adopted is FSAS of tactical grade. The coherent integration time of carrier phase tracking loop, the period of GNSS PVT algorithm and the update period of loosely-coupled integration are all set as 10 ms. The receiver oscillator type is OCXO. The noise variances in Q and R matrices of KF-based tracking loop are set according to the parameter design method proposed in the paper. Then according to [7] the equivalent bandwidth of KF is calculated as 6 Hz. Based on the analyses in [9], the optimal bandwidth of a FSAS-aided second order conventional carrier phase tracking loop at the 40 dB-Hz carrier-to-noise ratio and 1 g dynamic is within 3–5 Hz. And 5 Hz is chosen here in the paper for the conventional tracking loop.

Figure 1 demonstrats the carrier phase discriminator outputs and Doppler frequency error of one tracking channel (PRN 3). It can be seen that the discriminator outputs and Doppler frequency errors of KF-based tracking loop and conventional tracking loop are almost the same, which shows that the two tracking loops share the comparable carrier phase and Doppler frequency tracking performance in the deep integration architecture.

Figures 2 and 3 demonstrates the position and velocity errors of the receiver PVT algorithm. Obviously the deep integration architectures with KF-based and conventional tracking loops share the same navigation performance.

The above simulation test results clearly show that the KF-based tracking loop which adopts the parameter design method proposed in the paper share almost the same tracking performance with the conventional tracking loop with the opitimal bandwidth. It is proven that the proposed method is correct and feasible in the parameter design of INS-aided KF-based tacking loops, and is also beneficial for conventional tracking loops choosing the optimal bandwidth in the deep integration architecture.

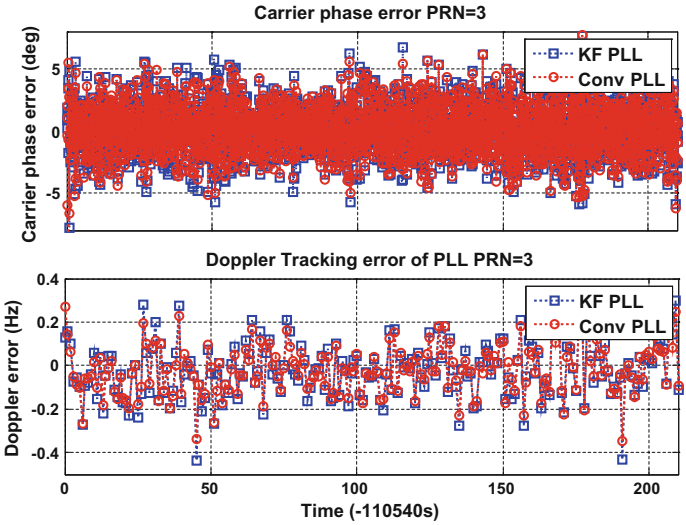

Fig. 1 Carrier phase and Doppler frequency tracking errors (PRN3) of KF-based/conventional PLL in deep integration

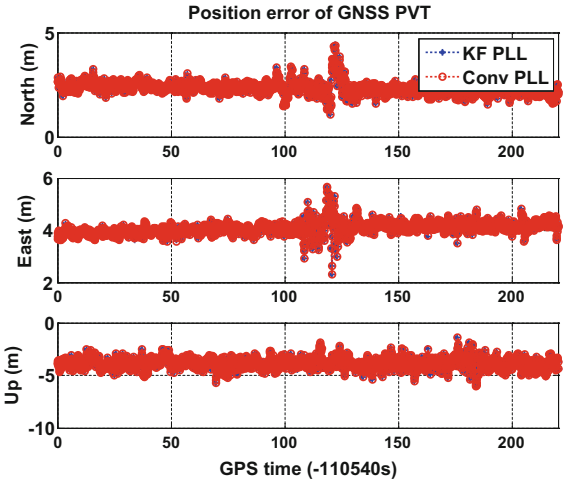

Fig. 2 PVT position error of deep integration receiver with KF-based/conventional PLL

5 Conclusion

This paper analyses the differences between the 2nd order KF-based tracking loops with or without INS aiding, and then proposes a parameter design method for KF tracking loop in the deep integration architecture according to the inertial sensor

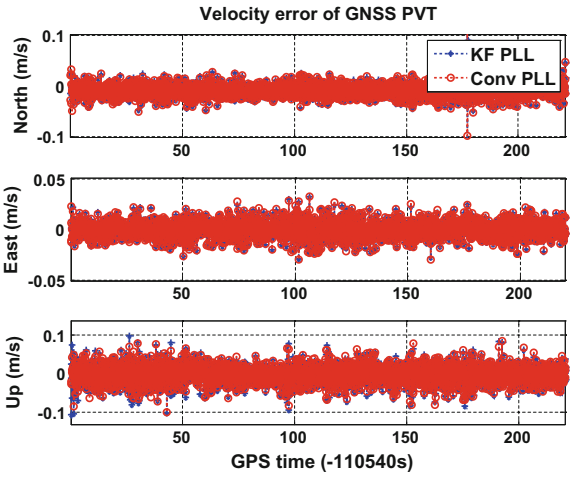

Fig. 3 PVT velocity error of deep integration receiver with KF-based/conventional PLL

errors and receiver oscillator errors. The simulation test results illustrate the correctness and effectiveness of the parameter design method proposed in the paper. Since each parameter is set according to its physical meaning, the empirical and tentative trials in the KF parameter optimization process are avoided. Moreover, the proposed parameter design method also provides a reference for the conventional tracking loop choosing the optimal bandwidth in the deep integration architecture since these two types of tracking loops share the equivalent structures.

Acknowledgements This work was supported by the National Key Research and Development Program of China (2016YFB0501804), the National Natural Science Foundation of China (41604021).

References

1. Ebinuma T, Kato T (2012) Dynamic characteristics of very-high-rate GPS observations for seismology. Earth Planets Space 369–377
2. Ban Y (2016) Research on the high dynamic tracking technology of GNSS/INS deep integration. Doctoral dissertation, Wuhan University, pp 103–104
3. Won J-H, Eissfeller B (2013) A tuning method based on signal-to-noise power ratio for adaptive PLL and its relationship with equivalent noise bandwidth. IEEE Commun Lett 17 (2):393–396
4. Won J-H, Pany T, Eissfeller B (2012) Characteristics of Kalman filters for GNSS signal tracking loops. IEEE Trans Aerospace Electron Syst 48(4):3671–3681
5. Sun X, Qin H, Niu J (2013) Comparison and analysis of GNSS signal tracking performance based on kalman filter and traditional loop. WSEAS Trans Signal Process 9(3):99–108
6. Tang X, Gianluca F, Emanuela F, Letizia L (2015) Theoretical analysis and tuning criteria of the Kalman filter-based tracking loop. GPS Solutions 19(3):489–503
7. O'Driscoll C, Petovello MG, Lachapelle G (2011) Choosing the coherent integration time for Kalman filter-based carrier-phase tracking of GNSS signals. GPS Solutions 15(4):345–356

8. Liu W, Hao J, Li Z (2010) Solution method and accuracy analysis of satellite position and velocity from broadcast ephemeris. J Geodesy Geodyn 30(2):144–147
9. Zhang T (2013) Research of scalar tracking technologies based on GNSS/INS deep integration and prototype system verification. Doctoral dissertation, Wuhan University, pp 100–104

Optimal Carrier Tracking PLL in the Presence of Phase Noise in GNSS Receiver

Shenhui Xue, Xinming Huang, Zengjun Liu, Xiangwei Zhu and Guangfu Sun

Abstract Carrier tracking phase lock loop (PLL) applied extensively in GNSS receivers and high-precision time transfer systems. The PLL is one of the important structures for carrier phase tracking in receivers. Generally, carrier phase noise can be degraded by local frequency references. However, this modification induces phase jitter, so that the accuracy of carrier phase in PLL will be reduced. On this basis, the characteristic of phase noise in carrier tracking is analyzed under the classic power law model and the variance of carrier phase jitter is calculated in the conventional second-order carrier PLL. Optimization is analyzed to obtain the optimal design of loop bandwidth, damping factor and coherent integration time (CIT) under the influence of phase noise in GNSS receivers. As a result, it is useful for carrier tracking to improve the performance of carrier PLL in the presence of phase noise and to reduce the variance of carrier phase jitter.

Keywords Phase noise · Power law model · PLL · Loop bandwidth · Damping factor · Coherent integration time

1 Introduction

The process of carrier phase tracking is vulnerable to the phase noise of local frequency references, resulting in phase jitter and tracking error of carrier phase, even loss of lock for input signal. In most consumer-grade GNSS receivers, frequency references often do not satisfy the requirement of very high frequency stability and may become the main source of phase noise. Thus the PLL in GNSS receivers must be optimized for the performance of local frequency references.

S. Xue · X. Huang · Z. Liu · X. Zhu · G. Sun (✉)
Satellite Navigation R&D Center, School of Electronic Science and Engineering, National University of Defense Technology, Changsha 410073, China
e-mail: gfsunmail@163.com

J. Sun et al. (eds.), *China Satellite Navigation Conference (CSNC) 2017 Proceedings: Volume I*, Lecture Notes in Electrical Engineering 437,
DOI 10.1007/978-981-10-4588-2_80

So far, the traditional analysis of PLL has been in the frequency domain and it has developed a general method which is deriving the PLL transfer function including discriminator, loop filter and numerically controlled oscillator (NCO), and obtaining the output power spectrum of phase noise. In [1], calculations of variance of phase jitter induced by phase noise are performed based on digital PLL, and the relationship between phase jitter and the combination of loop bandwidth and coherent integration time is given. However, there are not any optimal loop parameters for PLL design. Reference [2] analyses the mathematical model of phase noise and gives the variance of phase jitter induced by propagation for received signals. However, the phase noise induced by local frequency references is not taken into account. In [3], local oscillator is introduced into noise sources and the transfer function of digital PLL is derived under discrete model. Though the work of [3] gives analysis of carrier phase jitter and optimization of loop parameters, it has ignored the influence of flicker frequency noise in the model.

The work of this paper is to introduce the characteristic of phase noise, which includes flicker frequency noise, induced by local frequency references, and to explain the influence on second-order carrier tracking PLL under power law model and give the optimization method for stationary GNSS receiver. Furthermore, the optimization is introduced in the presence of phase noise and thermal noise in second-order PLL and the optimal parameters of designing PLL are given for reducing the tracking carrier phase jitter.

2 Carrier Tracking Phase Lock Loop

2.1 Modeling of Phase Noise

2.1.1 Definition of Phase Noise

The frequency stability of local oscillator refers to the changes of frequency accuracy within a certain time interval, reflecting its ability to maintain a constant frequency [4]. Usually short term frequency stability refers to frequency or phase changes within the time interval in seconds and the frequency accuracy fluctuation generated by them. One of the random fluctuations is mainly caused by the internal noise of frequency reference, random in nature, characterized and processed by mathematical statistic methods. This frequency random fluctuation is defined as phase noise [4].

Without the effect of random amplitude fluctuation in practical, the output of oscillators can be expressed as

$$V(t) = V_0 \sin[2\pi v_0 t + \varphi(t)] \tag{1}$$

where V_0 and v_0 are the nominal amplitude and frequency, $\varphi(t)$ is randomized phase generated by the internal noise modulation (PM or FM) in frequency references, which is phase noise [5].

2.1.2 Description in Frequency Domain—Power Law Model

Phase noise is characterized by various kinds of power spectrum in frequency domain. The relative frequency spectral density $S_y(f)$ is defined as the mean square value of relative frequency fluctuation, at f deviated from the center frequency within unit bandwidth, whose unit is Hz^{-1} [5].

Considering phase noise is non-stationary process, the most widely used description is the power law model. This model assumes that the relative frequency spectral density can be taken as a sum of series of frequency items with different integer exponent [6], that is $S_y(f) = \sum_{\alpha=-2}^{2} h_\alpha f^\alpha, f_l < f < f_h$, where f_h is the effective noise bandwidth, h_α is the noise factor. Table 1 lists the noise factor reference values of several common oscillators.

In practice phase noise mainly consists of five independent common noise which is shown as follows

$$S_y(f) = h_2 f^2 + h_1 f^1 + h_0 f^0 + h_{-1} f^{-1} + h_{-2} f^{-2} \tag{2}$$

Here in the Eq. (2) index h are white phase noise ($\alpha = 2$), flicker phase noise ($\alpha = 1$), white frequency noise ($\alpha = 0$), flicker frequency noise ($\alpha = -1$) and random walk frequency noise ($\alpha = -2$). The phase spectral density of flicker phase noise and white phase noise is relatively lower than the others, which has less impact on phase jitter [1], so they are negligible and this paper mainly considers random walk frequency noise, flicker frequency noise and white frequency noise.

Since the phase spectral density $S_\varphi(f)$ is associated with $S_y(f)$, it can be shown as

$$S_\varphi(f) = \frac{v_0^2}{f^2} S_y(f) = \frac{v_0^2}{f^2} \sum_{\alpha=-2}^{2} h_\alpha f^\alpha, \quad f_l < f < f_h \tag{3}$$

where v_0 is the center frequency. Phase spectral density can also be characterized by power law model.

Table 1 Parameters of different clock model

Oscillator	h_{-2}	h_{-1}	h_0
TCXO	2.00×10^{-20}	1.00×10^{-20}	1.00×10^{-21}
OCXO	2.51×10^{-22}	2.51×10^{-23}	2.51×10^{-26}
Ru	1.30×10^{-26}	1.00×10^{-22}	1.00×10^{-23}
Cs	4.00×10^{-29}	7.00×10^{-23}	2.00×10^{-20}

2.1.3 Description in Time Domain—Allan Deviation

Phase noise is characterized by all kinds of phase jitter deviation in time domain. One of the most commonly used models is Allan deviation. Because the practical relative instantaneous frequency deviation cannot be achieved in actual measurement, smoothing time is considered instead. What Allan deviation describes is the fluctuation of adjacent frequency difference. Its convergence solves the problems of divergence and characterization uncertainty for standard deviation [4].

Description of phase noise in frequency and time domain can be converted to both sides. When the relative frequency spectral density is known, Allan deviation can be expressed as

$$\sigma_y^2(\tau) = \int_0^\infty S_y(f) \frac{2\ \sin^4(\pi f \tau)}{(\pi f \tau)^2} df \tag{4}$$

2.2 *Modeling of Phase Tracking Loop*

Typical carrier tracking PLL in GNSS receivers is shown in Fig. 1, which includes mixers, accumulators, discriminator, loop filter and NCO.

Input signals of carrier tracking PLL can be expressed as [3]

$$r[k] = \sqrt{2} c[k] d[k] \sin(2\pi f k T_s + \theta[k] + \psi[k]) + n[k] \tag{5}$$

where k is the index, T_s is the sampling period, $c[k]$ is the spreading code sequence, $d[k]$ is data, $\theta[k]$ is the phase error due to satellite Doppler and Doppler shift, $\psi[k]$ is the phase error due to local oscillators.

After correlated with local replica code, and mixing of input signal with local in-phase and quadrature signals, output signals can be represented as [1]

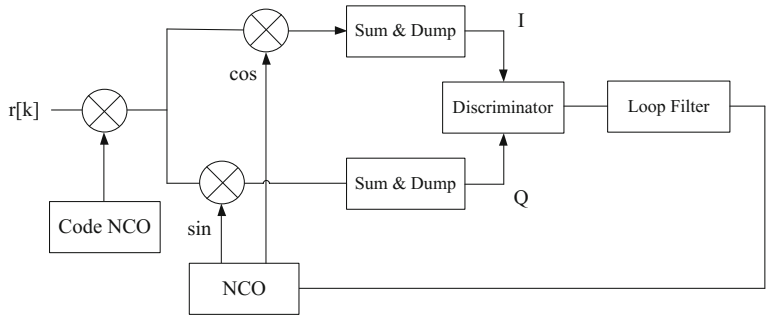

Fig. 1 Block diagram of GNSS PLL

$$I[k] = d[k]R(\tau[k])\,\mathrm{sinc}\left(\frac{\delta\omega[k]T_{coh}}{2}\right)\cos\delta\theta + n_i[k] \tag{6}$$

$$Q[k] = d[k]R(\tau[k])\,\mathrm{sinc}\left(\frac{\delta\omega[k]T_{coh}}{2}\right)\sin\delta\theta + n_q[k] \tag{7}$$

where $R(\tau[k])$ is the autocorrelation function of spreading code, $\delta\omega[k]$ is carrier frequency error, T_{coh} is coherent integration time, $\delta\theta$ is phase tracking error and $n[k]$ is zero-mean Gaussian white noise. Without considering the effect of code phase error and frequency error, $R(\tau[k])\,\mathrm{sinc}(\delta\omega[k]T_{coh}/2) \approx 1$. Signals of I and Q channel are input to discriminator for phase detection. The arctangent discriminator is mostly used which has the maximum linear phase range.

The equivalent linear model of PLL under the steady-state is shown in Fig. 2 [9]. Gain of discriminator $K_D = 1$ is normalized. θ_i is the input phase. $\widehat{\theta}$ is estimation of carrier phase, so that the estimation of phase error is expressed as

$$\delta\theta = \theta_i - \widehat{\theta} = \delta\varphi + n_\theta \tag{8}$$

where $\delta\theta$ is phase tracking error, $\delta\varphi$ is phase noise introduced by local oscillators. n_θ is thermal noise. These two uncorrelated noise can be analyzed independently for linear loop model. Using the loop transfer function, further analysis of phase noise can be made.

3 Effects of Phase Noise on PLL

3.1 Theoretical Analysis

3.1.1 Transfer Function of Phase Lock Loop

From linear model of the loop, closed-loop transfer function and transfer function between phase tracking error and phase noise and thermal noise are given as follows for second-order PLL.

$$H(\omega) = \frac{\omega_n^2 + ja_2\omega_n\omega}{\omega_n^2 - \omega^2 + ja_2\omega_n\omega} \tag{9}$$

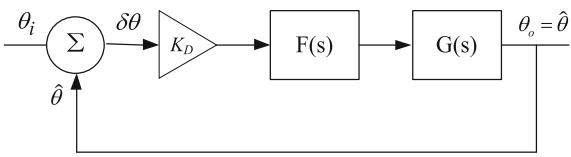

Fig. 2 Linearized PLL model

Error transfer function is expressed as

$$H_e(\omega) = 1 - H(\omega) = \frac{\omega^2}{\omega^2 - \omega_n^2 - ja_2\omega_n\omega} \tag{10}$$

The relationship between a_2 and second-order loop damping factor ξ is $a_2 = 2\xi$. Thus a_2 is the same as damping factor. ω_n is the nature frequency of second-order PLL, and is associated with loop noise bandwidth as [10]

$$B_L = \frac{1 + a_2^2}{4a_2}\omega_n \tag{11}$$

3.1.2 Tracking Loop Error

Effect on PLL phase tracking error can be analysed by phase jitter. Relationship between variance of phase jitter and output phase spectral density is expressed as

$$\sigma_\varphi^2 = \frac{1}{2\pi}\int_0^\infty S_{\varphi_o}(\omega)d\omega \tag{12}$$

Using power law model of phase noise, phase spectral density can also be expressed as

$$S_\varphi(\omega) = \frac{(2\pi v_0)^2}{\omega^2}S_y(\omega), \quad 0 < \omega < \omega_h \tag{13}$$

Variance of phase jitter induced by phase noise goes as [11]

$$\sigma_\varphi^2 = 2\pi f_0^2 \int_0^{2\pi f_h} \left[\frac{4\pi^2 h_{-2}}{\omega^4} + \frac{2\pi h_{-1}}{\omega^3} + \frac{h_0}{\omega^2} + \frac{h_1}{2\pi\omega} + \frac{h_2}{4\pi^2}\right] \cdot \frac{\omega^4}{\omega^4 + \left(a_2^2 - 2\right)\omega\omega_n + \omega_n^4} d\omega \tag{14}$$

where f_0 is the center frequency, f_h is the effective noise bandwidth given by $f_h = 1/2T_{coh}$ [12]. Expressions between phase jitter and loop bandwidth can be inferred with Eq. (12).

3.2 *Numerical Analysis*

GPS L1 signal is adopted for theoretical and numerical analysis. Carrier frequency is 1575.42 MHz and reference values of noise factors under power law model are given in Table 1.

3.2.1 Loop Phase Jitter

For second-order PLL, temperature compensated crystal oscillator (TCXO) in Table 1 is used. Factor a_2 ranges from 0.2 to 4 with an interval of 0.1. The corresponding damping factor ranges from 0.1 to 2. Loop noise bandwidth B_L ranges from 3 to 50 Hz with an interval of 1 Hz. Output phase jitter caused by phase noise is shown in Fig. 3.

From Eq. (16), phase jitter is related with loop noise bandwidth, loop filter and coherent integration time. From Fig. 3, phase noise has great impact on PLL phase jitter. It is likely to cause lost lock of the loop when bad loop parameters are selected. Hence, it is necessary to find out the effect for different loop parameters.

3.2.2 Effect of Loop Parameters

Effect of loop noise bandwidth Four kinds of frequency reference in Table 1 are analysed respectively. a_2 is set to a common value of 1.414 [10] and coherent integration time is 10 ms. Curves of phase jitter versus loop noise bandwidth are shown in Fig. 4.

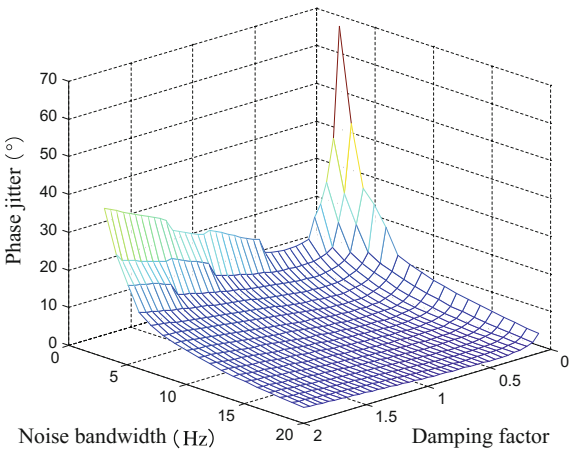

Fig. 3 Phase jitter induced by phase-noise

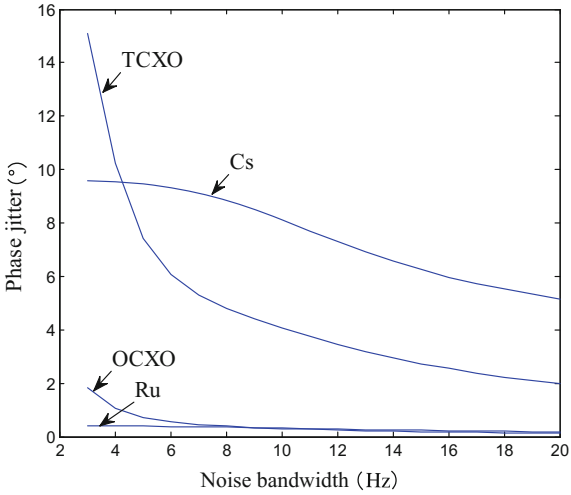

Fig. 4 Phase jitter depended on B_L

The curves show that, for different oscillators, phase jitter decreases with loop noise bandwidth. Therefore, it is a useful way of increasing loop noise bandwidth to reduce phase jitter induced by phase noise.

Effect of damping factor From Fig. 3 it can be seen that phase jitter is related with damping factor. Under the condition of noise bandwidth 10 Hz and coherent integration time 10 ms, relationship between phase jitter and damping factor is shown in Fig. 5.

Parameter a_2 is associated with loop noise bandwidth. It can be seen from Fig. 5 that for different frequency references, damping factor is 0.5 when output phase

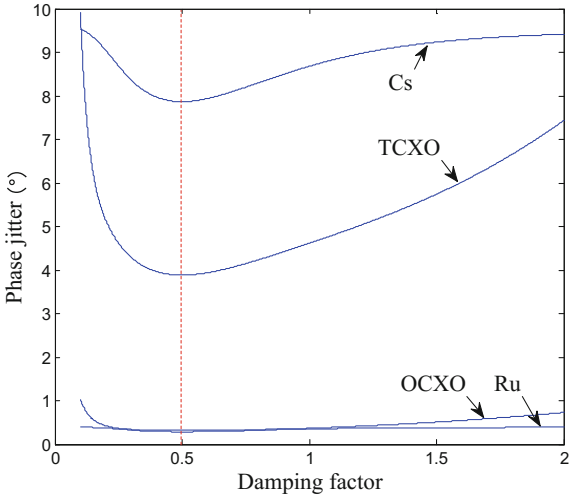

Fig. 5 Phase jitter depended on damping factor

jitter achieves the minimum and $a_2 = 1$ corresponds to the smallest loop noise bandwidth. Therefore it is the best value of ξ without dynamic stress of PLL.

Effect of coherent integration time Coherent integration time is very important in design of PLL. From Sect. 2.1.3, Allan deviation and relative frequency spectral density can be converted between time and frequency domain, which shows how the integral factor $\sin^4(\pi f\tau)/(\pi f\tau)^2$ affects Allan deviation in time domain. It varies as sin c function with the change of time. Figure 6 shows the curves of phase jitter versus coherent integration time.

It shows that longer CIT results in better noise filtering with smaller passband bandwidth of integral filter. But for phase noise, Fig. 6 shows that in the case of small noise bandwidth, phase jitter will fluctuate with the change of CIT. Thus, coherent integration time should be set to a higher value and dodge these values which make phase jitter significantly increased.

4 Optimization of Phase Lock Loop

4.1 Loop Tracking Error in the Presence of Phase Noise and Thermal Noise

It is inevitable to consider the effects of thermal noise in receivers. Optimization of PLL in the case of phase noise and thermal noise is also necessary because characteristics of thermal noise and phase noise are different. Phase jitter variance induced by thermal noise gives as [10]

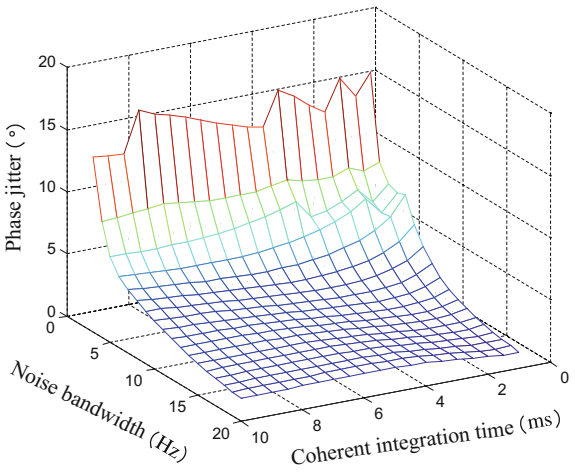

Fig. 6 Phase jitter depended on CIT

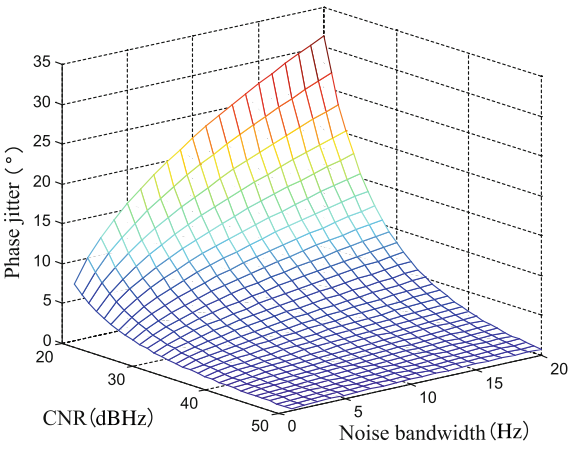

Fig. 7 Phase jitter induced by thermal noise

$$\sigma_n^2 = \frac{B_L}{C/N_0}\left(1 + \frac{1}{2T_{coh} \cdot C/N_0}\right) \tag{15}$$

where C/N_0 is the carrier to noise ratio (CNR) for input signals, B_L is loop noise bandwidth, T_{coh} is coherent integration time. Figure 7 shows the thermal noise-induced phase jitter versus CNR and loop noise bandwidth.

In contrast with Fig. 3, for thermal noise, phase jitter decreases with CNR. However, loop noise bandwidth controls the noise energy getting into PLL. Phase jitter induced by thermal noise increases with loop noise bandwidth. This runs totally contrary to the phase jitter induced by phase noise. Therefore, it is important to find the optimal value.

In the presence of phase noise and thermal noise, output phase jitter variance can be expressed as

$$\sigma_\varphi^2 = 2\pi f_0^2 \int_0^{2\pi f_h} \left[\frac{4\pi^2 h_{-2}}{\omega^4} + \frac{2\pi h_{-1}}{\omega^3} + \frac{h_0}{\omega^2} + \frac{h_1}{2\pi\omega} + \frac{h_2}{4\pi^2}\right] \cdot \frac{\omega^4}{\omega^4 + \left(a_2^2 - 2\right)\omega\omega_n + \omega_n^4} d\omega + \frac{B_L}{C/N_0}\left(1 + \frac{1}{2T_{coh} \cdot C/N_0}\right) \tag{16}$$

The total phase jitter is shown in Fig. 8. From the diagram, it can be inferred that higher CNR results in lower noise power and smaller phase jitter. However, in the case of narrow noise bandwidth, thermal noise can be rejected so that phase jitter is mainly caused by phase noise, and no longer decreased with CNR rapidly.

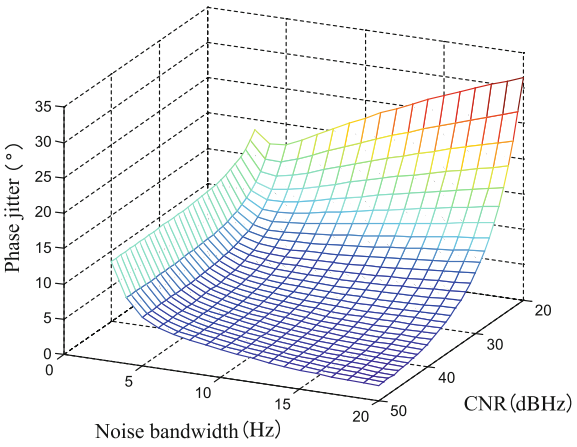

Fig. 8 Phase jitter induced by phase noise and thermal noise

Total phase jitter is not always monotonous with loop noise bandwidth, but associated with CNR of input signal. Thus further optimization of loop parameters in the presence of phase noise and thermal noise can be made to reduce the tracking error of PLL.

4.2 Optimal Loop Parameters

In light of total phase jitter variance, phase jitter is mainly related with CNR, loop noise bandwidth, damping factor and coherent integration time, which can be further optimized respectively.

4.2.1 Optimal Loop Noise Bandwidth

Curves of total phase jitter with noise bandwidth are shown in Figs. 8 and 9 under the condition of different CNR. When CNR is low, output phase jitter decreases firstly and then increases with noise bandwidth. Theoretically there is an optimal noise bandwidth minimizing output phase jitter, and the optimal value increases with CNR. When CNR is high, phase jitter decreases monotonically with noise bandwidth.

From Sect. 4.1, phase jitter caused by phase noise and thermal noise changes oppositely with loop noise bandwidth. When CNR is low, thermal noise power is strong and has obvious effect on phase jitter. So the optimal noise bandwidth can be found which gets the minimum phase jitter. At the same time, the optimal noise bandwidth value increases with CNR.

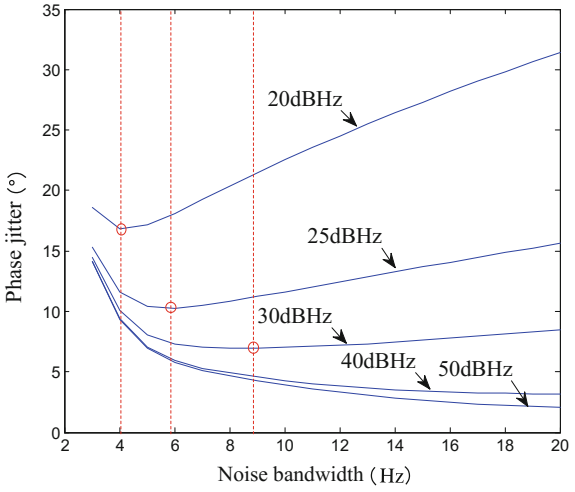

Fig. 9 Phase jitter depended on B_L versus C/N_0

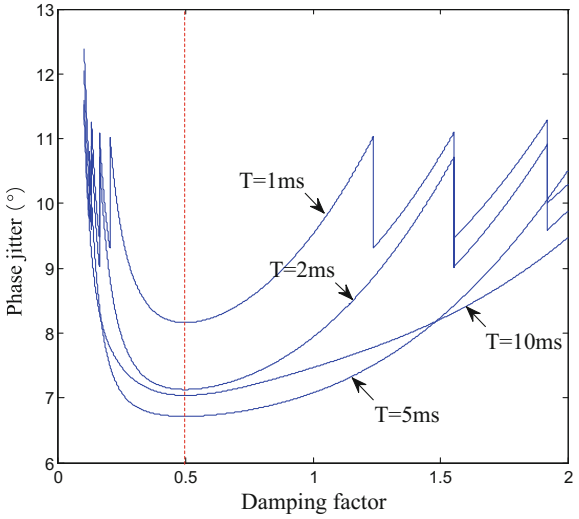

Fig. 10 Phase jitter depended on damping factor versus CIT

4.2.2 Optimal Damping Factor

From Sect. 3.2.2, there is the best value of damping factor in the case of phase noise. Since phase jitter caused by thermal noise has no direct relationship with damping factor, taking thermal noise into account does not affect the optimal value of damping factor. Figure 10 shows that the optimal damping factor does not change with coherent integration time at different CNRs.

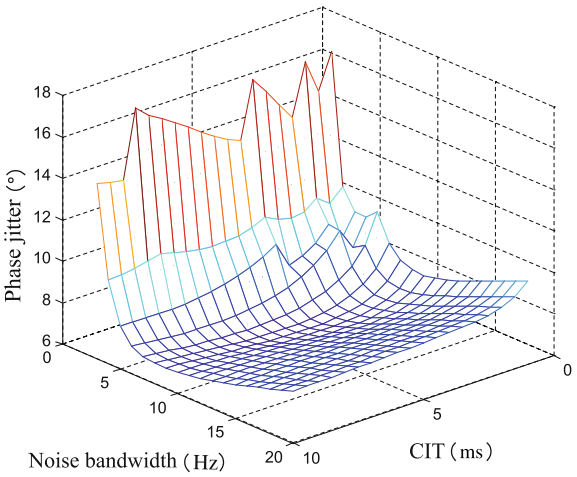

Fig. 11 Phase jitter depended on CIT and B_L

4.2.3 Optimal Coherent Integration Time

In Sect. 3.2.2 phase jitter does not change monotonically with CIT but fluctuates in the case of phase noise. Figure 11 shows the output phase jitter curves with CIT at 30 dB Hz CNR when thermal noise is introduced.

The diagram shows that given small noise bandwidth, phase jitter, mainly caused by phase noise, still has fluctuation with the change of CIT. Under the condition of large noise bandwidth, phase jitter is increased with the decrease of CIT, where phase jitter is mainly caused by thermal noise and extending integration time is good for noise filtering.

Influences of CNR on CIT mainly reflect on the phase jitter caused by thermal noise. When CNR is low, thermal noise power dominates so that phase jitter decreases with CIT increasing. When CNR is high, phase jitter caused by phase noise dominates and total phase jitter will be shown as Fig. 6.

In all, CIT should be as big as possible to reduce the impact of noise. However, under the condition of low CNR, the choice of CIT should avoid some peak values of phase jitter fluctuation.

5 Conclusion

This paper analyzes the second-order carrier tracking PLL under the influence of phase noise, deduces phase jitter variance caused by phase noise of frequency references including flicker frequency noise. Furthermore, performance of second-order PLL is examined through theoretical and numerical analysis in the presence of phase noise and thermal noise. The results are given as follows:

(1) Large loop noise bandwidth is the optimal since it has good effect on suppression of phase noise. In the case of low CNR, there is an optimum loop noise bandwidth which increases with CNR.
(2) The optimum value of damping factor is $\xi = 0.5$ in the presence of phase noise and thermal noise. Only in this way the PLL can be optimized.
(3) Long coherent integration time is an optimal for phase noise rejection. Under the condition of low CNR, choice of time value should be careful to avoid some peak values of phase jitter fluctuation.

References

1. Wu XY, Gong H, Zhu XW, Ou G (2012) Impact of oscillator phase noise on carrier DPLL tracking performance in GNSS receiver. J Natl Univ Defense Technol 34(1):127–131
2. Song ZQ, Liu D, Zhang B (2011) Effects of the deterioration of downlink navigation signal phase noise on ranging error. In: The 2nd China satellite navigation conference, vol 37(2), pp 195–197
3. Curran JT, Lachapelle G, Murphy CC (2012) Digital GNSS PLL design conditioned on thermal and oscillator phase noise. IEEE Trans Aerosp Electron Syst 48(1):180–196
4. Liu ZY (2013) The research and implement of phase noise extraction technology, XIDIAN University
5. Liu ZJ (2013) Research on the characteristics of phase noise in high-precision receiver RF Front-end, National University of Defense Technology
6. Yang WK (2008) The study of phase noise analysis and identification. National University of Defense Technology
7. Zhu XW, Sun GF, Yong SW (2010) The impact of phase noise to GPS carrier ranging. In: The 1st China Satellite Navigation Conference 2010
8. Rebeyrol E, Macabian C et al (2006) Phase noise in GNSS transmission/reception system. In: ION NTM, Monterey, CA, pp 698–708
9. Rozavi A, Gebre-Egziabher D, Akos DM (2008) Carrier loop architectures for tracking weak gps signals. IEEE Trans Aerosp Electron Syst 44(2):699–710
10. Kaplan ED (2006) Understanding GPS principles and application, 2nd edn. Artech House, Inc., London
11. Irsigler M, Eissfeller B (2002) PLL tracking performance in the presence of oscillator phase noise. GPS Solutions 5(4):45–57
12. Zhu XW, Sun GF, Yong SW (2007) A practical phase noise simulation and verification method. In: 2007 China time and frequency symposium, pp 419–425

A GNSS Spoofing Detection Technique Based on Signal Spatial Correlation

Zhenglin Geng, Junwei Nie, Zhibin Xiao, Xiangwei Zhu and Feixue Wang

Abstract The gain of a GNSS receiving antenna is a function of signal arrival angle which consists of azimuth and elevation. Thus, the antenna direction changing would make impact on the gain of the received signals, which would be reflected on the signal CNR estimated results. Since the spoofing signals are generally transmitted from a single source, they always have the same arrival angles. Therefore, the CNR variations of spoofing signals have high correlativity as the receiving antenna direction changing, which could be used to differentiate the authentic and spoofing signals. In this paper, the influence of receiving antenna direction changing on CNR estimations for authentic signals and spoofing signals is analyzed, and the relativity of CNR variations is studied to differentiate the authentic signals and the spoofing signals. Furthermore, the effectiveness of the spoofing detection technique is verified by a series of experiments, in which the CNR estimations with a rotating antenna are monitored and utilized to distinguish the spoofing signals.

Keywords GNSS · Spoofing detection · Spatial correlation

1 Introduction

GNSS signals are vulnerable to the jamming and spoofing signals [1]. A spoofing attack is more menacing than jamming since the target receiver is not aware of the threat. Several anti-spoofing techniques have been proposed in the open literature recently. Such as amplitude discrimination, time of arrival (TOA) discrimination, consistency of navigation inertial measurement unit (IMU) cross check, polarization discrimination, angle of arrival (AOA) discrimination, cryptographic authentication [2, 3] and AGC monitoring [4].

Z. Geng (✉) · J. Nie · Z. Xiao · X. Zhu · F. Wang
College of Electronic Science and Engineering, National University of Defense Technology, Changsha 410073, China
e-mail: oliver8812@163.com

J. Sun et al. (eds.), *China Satellite Navigation Conference (CSNC) 2017 Proceedings: Volume I*, Lecture Notes in Electrical Engineering 437,
DOI 10.1007/978-981-10-4588-2_81

Moreover, a spoofing detection technique that comparing the theoretical phase differences and the practical phase differences observed by two fixed GNSS antennas in order to discriminate the spoofing threat is proposed [5, 6]. However, this technique needs to know the orientation of the antenna array and the azimuth and elevation of each satellite, and it takes a long time (about 1 h) to discriminate against the spoofing signals.

In order to present a credible navigation solution to the receiver, a spoofer is required to transmit at least 4 GNSS signals simultaneously. However, utilizing a set of spoofers to transmit each different GNSS signal separately is not deemed practical [6], as different spoofing transmitters should be synchronized precisely. Generally, it is assumed that the spoofing signals are transmitted from a single source. Figure 1 shows the signal receiving scenario.

Based on the assuming, a synthetic array spoofing discrimination method [7] based on signal amplitude spatial relativity is proposed. This method requires receiver to move a long distance to construct a synthetic array, so, the signal amplitude could have a detectable variety.

In this paper, a spoofing detection technique based on signal spatial correlation is proposed, which could avoid the receiver to move a long distance by utilizing the gain directivity of the receiving antenna.

2 Signal Receiving Model

Considering the GPS L1 C/A code, the received signal subjected to a spoofing attack can be modeled as,

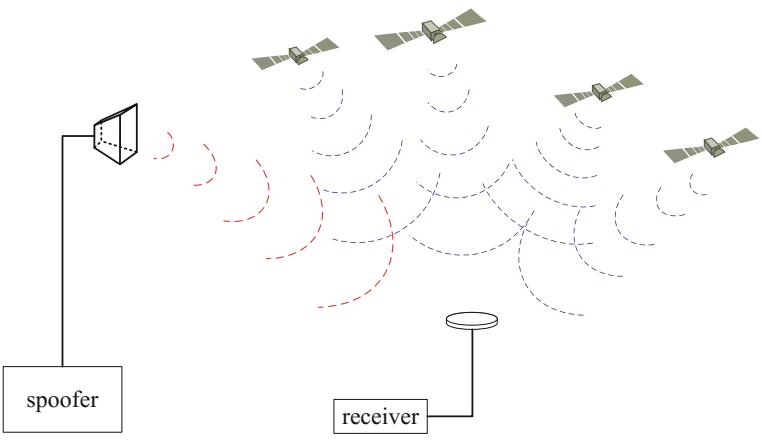

Fig. 1 The signal receiving scenario

$$r(t) = \sum_{m=1}^{N_a} G_R(\theta_m, \phi_m)\sqrt{p_m^a}F_m^a(t) + \sum_{q=1}^{N_s} G_R\left(\theta_q, \phi_q\right)\sqrt{p_q^s}F_q^s(t) + \eta(t) \quad (1)$$

where,

$$F_m^a(t) = d_m^a\left(t - \tau_m^a\right)c_m^a\left(t - \tau_m^a\right)e^{j\phi_m^a + j2\pi f_{ms}^a t} \quad (2)$$

$$F_q^s(t) = d_q^s\left(t - \tau_q^s\right)c_q^s\left(t - \tau_q^s\right)e^{j\phi_q^s + j2\pi f_q^s t} \quad (3)$$

where t is time, N_a and N_s is the number of authentic signals and spoofing signals respectively. ϕ, f and τ are the phase, Doppler frequency and code delay of the received signals respectively. p is the receiving signal power on the antenna aperture, the superscripts a and s represent the authentic and spoofing signals, and the subscripts m and q represent the $m-$th authentic and $q-$th spoofing signal respectively. $\eta(t)$ is the complex additive white Gaussian noise with variance σ^2.

In this model, $d(t)$ and $c(t)$ represent the navigation data bits and the PRN code. Considering the directivity of antenna gain, $G_R(\theta_m, \phi_m)$ represents the gain on the direction of azimuth angle ϕ_m, elevation angle θ_m, and $G_R\left(\theta_q, \phi_q\right)$ represents the gain on the direction of azimuth angle ϕ_q and elevation angle θ_q. As the different distributions of satellites, authentic signals have different azimuth angles ϕ_m and elevation angles θ_m, namely, $\theta_m \neq \theta_n$, $\phi_m \neq \phi_n$, $m, n \in \boldsymbol{J}^a, m \neq n$, thus, their gains $G_R(\theta_m, \phi_m)$ are different generally. However, the azimuth angle ϕ_q and elevation angle θ_q of the spoofing signals are the same, namely, $\theta_p = \theta_q$, $\phi_p = \phi_q$, $p, q \in \boldsymbol{J}^s, p \neq q$, so the gains of spoofing signals $G_R\left(\theta_q, \phi_q\right)$ are all the same, where $\boldsymbol{J}^a$ and $\boldsymbol{J}^s$ are the sets of authentic and spoofing signals.

According to the Friis formula [8]

$$P_R = P_T\frac{G_T G_R \lambda^2}{(4\pi D)^2} \quad (4)$$

where P_R is the received signal power, P_T is the transmitted power, G_T and G_R represent the gains of transmitting antenna and receiving antenna, respectively. λ is the wave length, D is the propagation distance from the transmitting antenna to the receiving antenna. Then, the signal power on the receiving antenna aperture could be expressed as Eq. (5).

$$p = P_T\frac{G_T \lambda^2}{(4\pi D)^2} \quad (5)$$

When the receiving antenna rotates only, P_T and G_T nearly remain unchanged in a period of time, and the changes of λ and D are relatively slow. So, the p in Eq. (5) could be regarded as a constant. And the CNR could be calculated as,

$$CNR = \frac{P_R}{N_0} = \frac{G_R(\theta, \phi)p}{N_0} \tag{6}$$

where N_0 is the noise power spectrum density, and $G_R(\theta, \phi)$ is the antenna gain on the direction of azimuth angle ϕ and elevation angle θ. Here, the superscript and subscript of p, ϕ and θ are omitted.

It is obvious that a signal's AOA determines the gain of the receiving antenna for the signal, further, the CNR is determined. So, the antenna direction change would result in the variation of the AOA and CNR.

For the spoofing signals, the AOAs change uniformly, so the CNR variation trends of spoofing signals are approximately the same, but the CNRs of the authentic signals vary respectively because the authentic signals have different AOAs. Consequently, the spoofing signals could be detected according to the correlation coefficients of CNR variations.

For a typical GNSS receiving antenna, the difference in antenna gain at high and low elevation angles is approximately 8 dB [9], and the CNR difference is 8 dB correspondingly. It determines the CNR variation range while receiving antenna rotates. Figure 2 shows the gain pattern of the microstrip antenna in use.

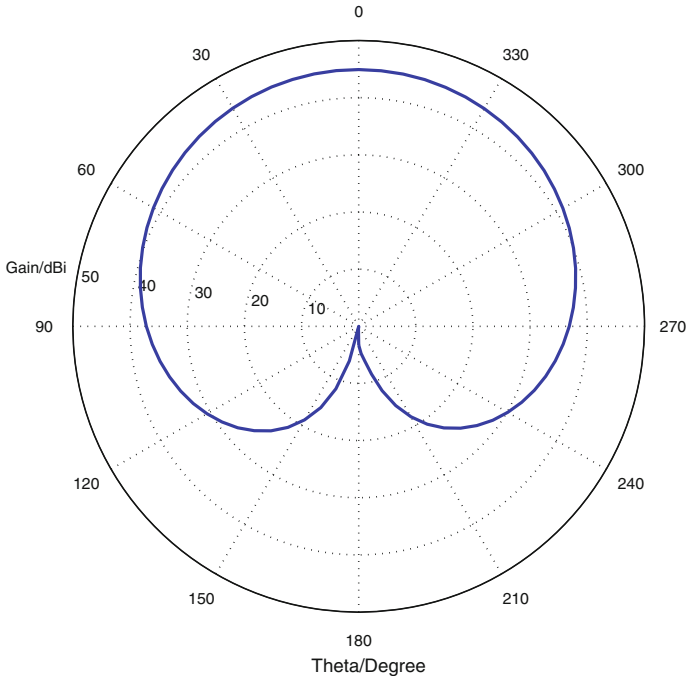

Fig. 2 Gain pattern of the microstrip antenna in use

Assume that the receiving antenna rotates randomly, T_s represents the time interval, the arrival angles of the $m-$th authentic and the $q-$th spoofing signal at nT_s could be represented as $\left(\theta_m^a(nT_s), \phi_m^a(nT_s)\right)$ and $\left(\theta_q^s(nT_s), \phi_q^s(nT_s)\right)$ respectively. $\boldsymbol{G}_m^a$ and $\boldsymbol{G}_q^s$ are the gain vectors on N different directions respectively.

$$\boldsymbol{G}_m^a = \begin{bmatrix} G_R\left(\theta_m^a(T_s), \phi_m^a(T_s)\right) \\ G_R\left(\theta_m^a(2T_s), \phi_m^a(2T_s)\right) \\ \vdots \\ G_R\left(\theta_m^a(nT_s), \phi_m^a(nT_s)\right) \end{bmatrix} \tag{7}$$

$$\boldsymbol{G}_q^s = \begin{bmatrix} G_R\left(\theta_q^s(T_s), \phi_q^s(T_s)\right) \\ G_R\left(\theta_q^s(2T_s), \phi_q^s(2T_s)\right) \\ \vdots \\ G_R\left(\theta_q^s(nT_s), \phi_q^s(nT_s)\right) \end{bmatrix} \tag{8}$$

Correspondingly, $c_m^a(nT_s)$ and $c_q^s(nT_s)$ are the estimated CNR of $m-$th authentic signal and $q-$th spoofing signal at nT_s respectively. $\mathbf{C}_m^a$ and $\mathbf{C}_q^s$ are the CNR vectors of authentic and spoofing signals on N different directions respectively.

$$\boldsymbol{C}_m^a = \left[c_m^a(T_s), c_m^a(2T_s), \ldots, c_m^a(NT_s)\right]^T \tag{9}$$

$$\boldsymbol{C}_q^s = \left[c_q^s(T_s), c_q^s(2T_s), \ldots, c_q^s(NT_s)\right]^T \tag{10}$$

where,

$$c_m^a(nT_s) = \frac{P_R}{N_0} = \frac{G_R\left(\theta_m^a(nT_s), \phi_m^a(nT_s)\right)p_m^a(nT_s)}{N_0} \tag{11}$$

$$c_q^s(nT_s) = \frac{P_R}{N_0} = \frac{G_R\left(\theta_q^s(nT_s), \phi_q^s(nT_s)\right)p_q^s(nT_s)}{N_0} \tag{12}$$

In a logarithmic way, Eqs. (9) and (10) could be expressed as

$$\boldsymbol{C}_m^a = \boldsymbol{G}_m^a + \boldsymbol{p}_m^a - \boldsymbol{N}_0 \tag{13}$$

$$\boldsymbol{C}_q^s = \boldsymbol{G}_q^s + \boldsymbol{p}_q^s - \boldsymbol{N}_0 \tag{14}$$

where, $\boldsymbol{p}_m^a$, $\boldsymbol{p}_q^s$ and $\boldsymbol{N}_0$ denotes the vectors $\left[p_m^a(T_s), p_m^a(2T_s), \ldots, p_m^a(NT_s)\right]^T$, $\left[p_q^s(T_s), p_q^s(2T_s), \ldots, p_q^s(NT_s)\right]^T$ and $[N_0, N_0, \ldots, N_0]^T$ in a logarithmic way, respectively.

Generally, the authentic signals' CNRs are between 38.5 and 46.5 dBHz [9], and the spoofing signals' are higher. Because the p in Eq. (5) is different for each signal, the average of CNRs could be different for each signal, so observation $\boldsymbol{X}_m^a$ and $\boldsymbol{X}_q^s$ are proposed to present the changes of CNRs.

$$\boldsymbol{X}_m^a = \boldsymbol{C}_m^a - E\left(\boldsymbol{C}_m^a\right) \tag{15}$$

$$\boldsymbol{X}_q^s = \boldsymbol{C}_q^s - E\left(\boldsymbol{C}_q^s\right) \tag{16}$$

$E(\cdot)$ denotes an expected value operator, as assumed before, the p and N_0 could be regarded as constants in a short period of time. Then,

$$E\left(\boldsymbol{C}_m^a\right) = E\left(\boldsymbol{G}_m^a + \boldsymbol{p}_m^a - \boldsymbol{N}_0\right) = E\left(\boldsymbol{G}_m^a\right) + \boldsymbol{p}_m^a - \boldsymbol{N}_0 \tag{17}$$

$$E\left(\boldsymbol{C}_q^s\right) = E\left(\boldsymbol{G}_q^s + \boldsymbol{p}_q^s - \boldsymbol{N}_0\right) = E\left(\boldsymbol{G}_q^s\right) + \boldsymbol{p}_q^s - \boldsymbol{N}_0 \tag{18}$$

Bring Eqs. (13), (14), (17) and (18) into Eqs. (15) and (16),

$$\boldsymbol{X}_m^a = \boldsymbol{G}_m^a - E\left(\boldsymbol{G}_m^a\right) \tag{19}$$

$$\boldsymbol{X}_q^s = \boldsymbol{G}_q^s - E\left(\boldsymbol{G}_q^s\right) \tag{20}$$

Finally, the variations of gains could be got. Herein a correlation coefficient is utilized to measure the correlation between different PRNs. The correlation coefficient between i-th and j-th signal is defined as

$$\rho_{ij} = \frac{\boldsymbol{X}_i^H \boldsymbol{X}_j}{\sqrt{\boldsymbol{X}_i^H \boldsymbol{X}_i}\sqrt{\boldsymbol{X}_j^H \boldsymbol{X}_j}} \tag{21}$$

where i and j indicate the index of the GNSS signals. If $i = j$, $\rho_{ij} = 1$, when $i \neq j$, the ρ_{ij} decreases along with the correlation weakening between $\boldsymbol{X}_i$ and $\boldsymbol{X}_j$, the spoofing signals could be discriminated with correlation coefficients.

3 Spoofing Detection Technique

The proposed GNSS spoofing detection methodology process is shown in Fig. 3.

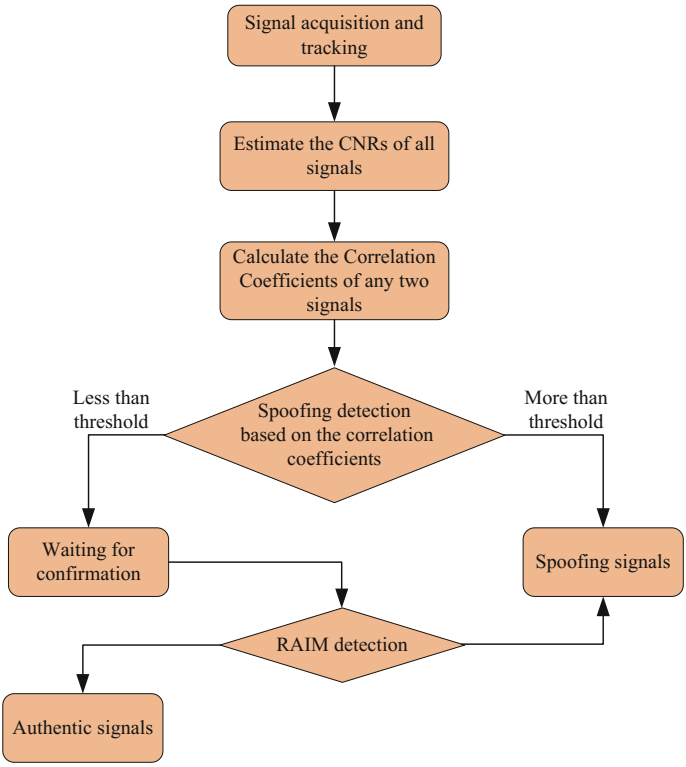

Fig. 3 Process of the proposed GNSS spoofing detection methodology

It could be summarised as follows,

(1) The receiver tracks all received signals after signal acquisition.
(2) Estimate and record the CNRs of all the received signals while the receiving antenna rotates. Note that the rotation rate should not be too slow, otherwise the CNR variations would be unobvious and the gap of correlation coefficients between authentic case and spoofing case would be too small to differentiate.
(3) Calculate the correlation coefficients of every two signals based on the recorded CNR data.
(4) Compare the correlation coefficients with the threshold, then, classify the signals into two groups, the spoofing group and the authentic group. However, the spoofing signal is probably mistakenly sorted into the authentic group when just only one spoofing signal exists, so the signals in the authentic group need to be confirmed ulteriorly. And the receiver autonomous integrity monitoring (RAIM) method could be used here due to its effectiveness for the case that there is only one spoofing signal [10].
(5) Utilize the RAIM to detect the spoofing signal which is mistakenly sorted in the authentic group.

4 Experimental Results

The experimental results of this single antenna spoofing detection technique are provided in this section.

In these experiments, all the experimental measurements are based on the BDs signals. A signal source which could receive and regenerate BDs signals are used for spoofing generation, and a BDs receiver is fixed on a platform which could rotate in azimuth and elevation. During the experiments, the CNRs estimated results of authentic and spoofing signals are estimated and recorded while the platform rotates randomly. Then, the recorded data are used for spoofing detection.

Figure 4 shows the CNR variations for different PRNs in spoofing scenario. As evident, the signal CNR variations are highly correlated in the spoofing case.

Figure 5 shows the measured correlation coefficients of signal CNR variations shown in Fig. 4. It is could be seen that the correlation coefficients under spoofing scenario are all approximately to 1.

Figure 6 shows the CNR variations for different PRNs for authentic signal case. In the authentic signal case shown in Fig. 6, the signal CNR variations are changing independently.

Figure 7 shows the measured correlation coefficients of signal CNR variations shown in Fig. 6.

As shown, the pairwise correlation coefficients in the case of authentic signals are much smaller compared with the spoofing signals case.

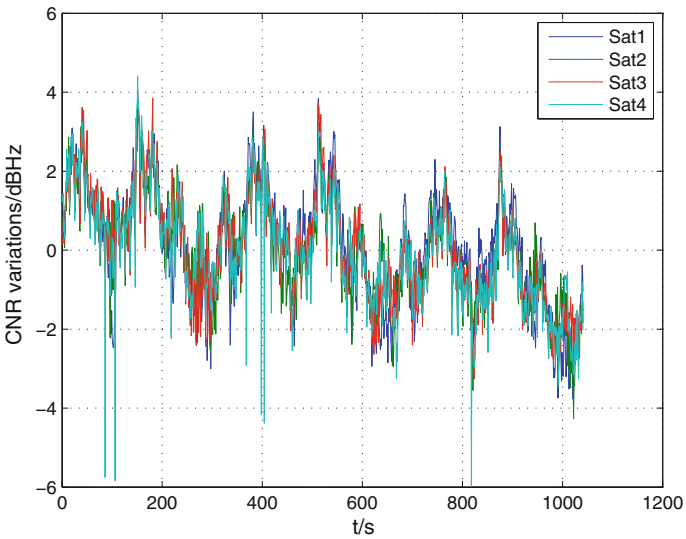

Fig. 4 CNR variations for different PRNs in spoofing scenario

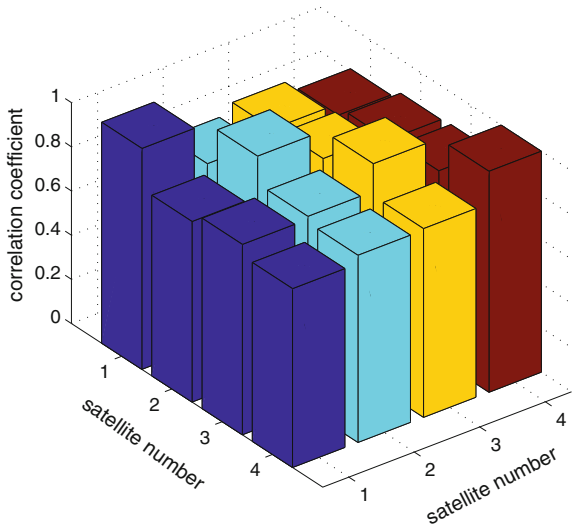

Fig. 5 Correlation coefficient values of the signal CNR variations in spoofing scenario

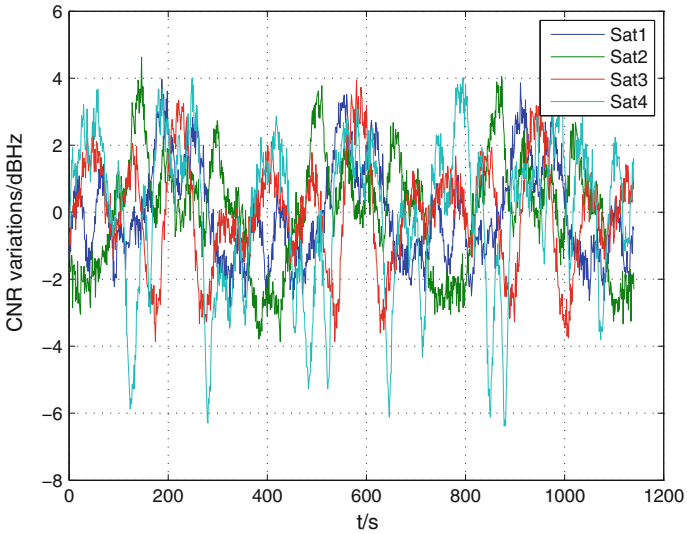

Fig. 6 CNR variations for different PRNs in authentic scenario

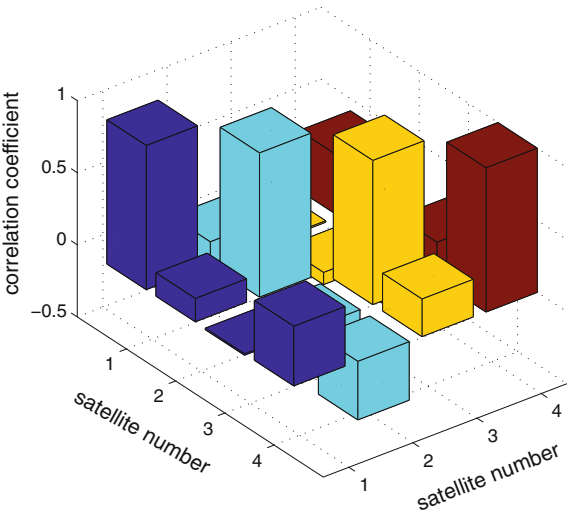

Fig. 7 Correlation coefficient values of the signal CNR variations in authentic scenario

5 Conclusion

A spoofing detection method based on signal spatial correlation is investigated in this paper. Experimental results show that spoofing signals transmitted from a single source can be detected effectively based on the CNR correlation coefficients while the receiving antenna direction changes.

This technique is easily equipped on common GNSS receivers because it is not necessary to redesign the hardware of the receiver, and furthermore, the CNR estimation is an fundamental function for the receivers, so, it could be used directly for spoofing detection and needs little modifying in software.

References

1. John A (2001) Vulnerability assessment of the transportation infrastructure relying on the global positioning system. Technical Report, Volpe National Transportation Systems Center
2. Key EL (1995) Techniques to counter GPS spoofing internal memorandum. The MITRE Corporation, Bedford, Massachusetts, USA
3. Wen H, Huang PY-R, Dyer J, Archinal A, Fagan J (2005) Countermeasures for GPS signal spoofing. In: Proceedings of the 18th international technical meeting of the satellite division of the institute of navigation (ION GNSS 2005)
4. Akos DM Who's afraid of the spoofer? GPS/GNSS spoofing detection via automatic gain control (AGC). J Navig 59(4):281–290
5. Broumandan. A et al (2007) Direction of arrival estimation of GNSS signals based on synthetic antenna array, ION GNSS, 2007
6. Montgomery PY, Humphreys TE, Ledvina BM (2009) Receiver-autonomous spoofing detection: experimental results of a Multi-antenna receiver defense against a portable civil GPS spoofer. In: Proceedings of ION ITM. Anaheim, CA, pp 124–130, 26–28 Jan 2009

7. Broumandan A, Jafarnia-Jahromi A, Dehghanian V, Nielsen J, Lachapelle G (2012) GNSS spoofing detection in handheld receivers based on signal spatial correlation. In: Proceedings of IEEE/ION PLANS 2012, Myrtle Beach, South Carolina, pp 479–487, 24–26 Apr 2012
8. Xie G (2009) Principles of GPS and receiver design. Publishing House of Electronics Industry, Beijing, p 7
9. Misra P, Enge P (2008) Global position system signal, measurement, and performance (2nd edn). Publishing House of Electronics Industry, Beijing, p 4
10. Jafarnia-Jahromi A, Broumandan A, Nielsen J, Lachapelle G (2012) GPS Vulnerability to spoofing threats and a review of antispoofing techniques. Int J Navig Obs 2012:16

A Multi-mode Multi-channel C Band CAPS Terminal Transceiver Chip Design

Siyuan He, Wei Liu, Xiangwei Wang, Chaoxian Zhu, Gong Zhang, Sijing Hu, Changhong Zhang, Fangfang Zhang, Yu Zheng, Dongchun Wang, Qiangyu Hao, Weifeng Zhang, Mingzhao Wang, Hongyin He, Xiaolan Wang and Guanyi Ma

Abstract For modern wireless transceiver terminal, more and more modes are integrated on the same chip. All the frequency spectrum of transceiver channels coexist on the single chip, beside increasing isolation, how to plan and reduce the implementation difficulty to avoid spectrum interference has become a new problem, especially for high frequency broadband system. Transponding type of Chinese Area Positioning System (CAPS) using the transponder on the active orbit communication satellite as the relay, sending the ranging codes and navigation message data which were produced by the ground control station to the user to realize the navigation. At the same time with the satellite transponder is rich in resources, developing navigation and two-way communication transceiver terminal, can make the system achieve navigation and communication integration. Based on the above background, this paper shows an RF transceiver chip design to meet the requirements of the performance of CAPS terminal. Propose a novel spectrum allocation scheme, which employ two-step-up/down conversion architecture in frequency spectrum shifting, reuse the PLL synthesizers in TX first-step-up, through the calculation of each non-overlap spectrum conditions, thus only four PLLs can cover all three broadband channels. So the communication receiver, navigation receiver and communication transmitter, the three channels can work at the same time without interference with each other, but also solve the problem of image rejection and side-band suppression. And combined with the Power Amplifier (PA), Low Noise Amplifier (LNA) and other off-chip components, the composition of the RF terminal system can meet the needs of the miniaturization of communication and navigation integration.

S. He (✉) · W. Liu · X. Wang · C. Zhu · G. Zhang · S. Hu · C. Zhang · F. Zhang · Y. Zheng · D. Wang · Q. Hao · W. Zhang · M. Wang · H. He
Guangzhou Runxin Information Technology Co. Ltd, Guangzhou, China
e-mail: hesiyuan118@126.com

X. Wang · G. Ma
National Astronomical Observatories, Chinese Academy of Sciences, Beijing, China

J. Sun et al. (eds.), *China Satellite Navigation Conference (CSNC) 2017 Proceedings: Volume I*, Lecture Notes in Electrical Engineering 437,
DOI 10.1007/978-981-10-4588-2_82

Keywords Chinese area positioning system (CAPS) · Communication and navigation integration · Transceiver chip · Spectrum allocation · Phase error

1 Issues Proposal

Transponding type of Chinese Area Positioning System (CAPS) using the transponder on the active orbit communication satellite as the relay, sending the ranging codes and navigation message data which were produced by the ground control station to the user to realize the navigation [1]. At the same time in view of high-frequency and broadband, it can also achieve a total capacity of 1 million units of voice communications (which is not available in Beidou RDSS [2]), more than 10 million short message service. This system has variable frequency, variable coding and strong anti-interference ability. So the trend of Radio Frequency (RF) chip design for purpose of communication and navigation integration terminal is a must.

For modern wireless transceiver terminal, more and more modes are integrated on the same chip. All the spectrum of transceiver channels coexist on the single chip, besides strengthening the isolation at the same time, how to plan and reduce the implementation difficulty to avoid spectrum interference has become a new problem, especially for terminal systems such as CAPS which utilize high frequency and broadband.

CAPS by virtue of the communications satellite using the C band spectrum, as shown in Table 1.

For the CAPS terminal, in uplink side, the baseband only provides single-ended IF analog signal and requires single carrier output with suppressed side-band. For the uplink side, not providing quadrature IF means it cannot construct quadrature upconverter to suppress the side-band signal, and even provide quadrature intermediate frequency signal, the quadrature LO (Local Oscillator) signal is also needed to construct quadrature mixer, which is relying on the two times of the LO frequency of the oscillator to obtain. For an RF signal frequency is as high as 6.5 GHz, the corresponding frequency of oscillator which produce quadrature LO will be nearly 13 GHz, but in the current integrated circuit manufacturing process is almost impossible. Generally speaking with non-zero IF, the downlink frequency

Table 1 C-band spectrum for CAPS

C band spectrum	Radio frequency (MHz)	Intermediate frequency (MHz)
Navigation downlink spectrum	3624–4200/5020	21 ± 13
Communication downlink spectrum	3624–4200	5 ± 3
Communication uplink spectrum	5849–6423	15 ± 3 (single-ended analog input)

band also needs to suppress image signal, which is also need to build into the quadrature signal to obtain. Two receiver and one transmitter all work in the near each 600 MHz bandwidth without interfering with each other, but also to achieve a reasonable image (in receiver side) rejection/side-band (in transmitter side) suppression >30 dB requirements. This puts forward the requirements for single chip spectrum allocation.

2 Implementation Scheme

2.1 Solutions [3]

Because the frequency of the uplink is higher than the downlink, the spectrum allocation for a single chip integration should give priority to uplink spectrum shifting. For the uplink side, using the two-step-up conversion architecture in frequency spectrum shifting, can meet the side-band suppression requirement on the one hand, and on the other hand, the difficulty of frequency synthesizer to realize high frequency is reduced. Specifically, as shown in Figs. 1 and 2, firstly, IF signal mixes with a fixed LO namely TX1_LO, double side-band output two signals namely TX1_LO + IF and TX1_LO-IF, select one as high IF signal namely TX_HIF, the other band is the side-band (SB), then selecting an external SAW (Surface Acoustic Wave) filter can easily to achieve suppression of side-band more than 30 dB, then the high IF signal mixes with the variable frequency LO namely second TX2_LO, which cover the uplink bandwidth, upper side-band output, and the lower side-band spectrum can be filtered by an off-chip filter, the final output spectrum would be TX_HIF + TX2_LO. So the variable frequency of this

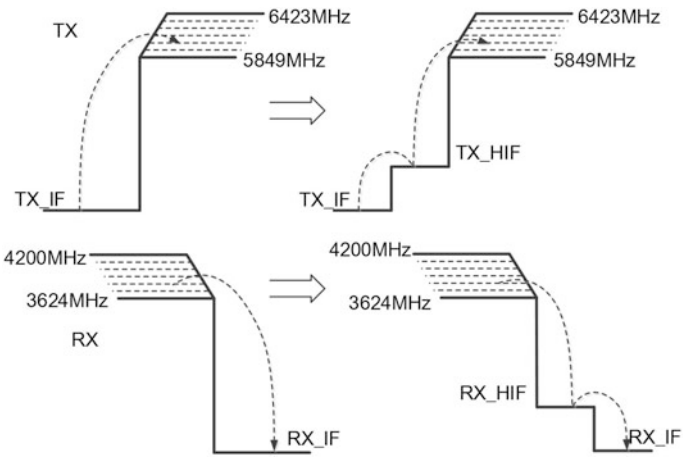

Fig. 1 The diagram of two-step-up/down TRX

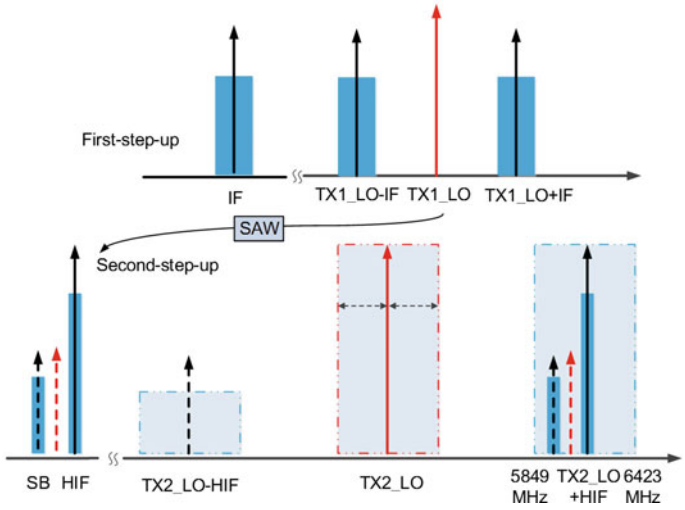

Fig. 2 The spectrum diagram of two-step-up TX

second-step-up conversion LO is the uplink spectrum frequency minus the high IF frequency, which reduces the two-step-up of the LO frequency.

On the downlink side, using the two-step-down conversion architecture can also simplify frequency spectrum shifting process. The frequency synthesizer which generates the first LO frequency TX1_LO can be reused, and the orthogonal RX2_LO of the receiver second-step-down frequency conversion can be generated by the frequency divider to realize the rejection of the receiver image signal. Specifically, as shown in Fig. 1, firstly the receiver downlink spectrum RX mixes with the variable frequency RX1_LO to generate a high fixed frequency high IF namely (RX_HIF), the coverage of the variable RX1_LO would be the downlink bandwidth, and RX_HIF mixes with the second orthogonal LO to the final intermediate frequency (IF), using poly-phase or complex filter can easily achieve the image signal rejection more than 30 dB. The selection of lower LO mode in the first-step-down process (i.e., the LO frequency is lower than the receiver frequency) can reduce the LO frequency. In the first-step-down it will also need an image signal rejection, which the spectrum frequency and the downlink spectrum frequency is far apart, can be easily filtered by an off-chip filter.

Due to the same frequency of the downlink receiver spectrum of navigation and communication, the radio frequency circuits of the two receiving channels can be reused. Simple but also brings the problem, is when the two channels of the input frequency are close, how to ensure normal work without mutual interference. Due to the adoption of the two-step-down conversion architecture, the RX spectrum is made up of RX1_LO plus RX2_LO (IF is ignored), where RX1_LO is variable frequency, the coverage for the downlink bandwidth, and RX2_LO frequency is generated by the divider which frequency is produced by the first-step-up TX

synthesizer. Then we can put it into two situations: No. 1, when the two receiver downlink frequency is far apart (for example, >50 MHz), the two paths produce the first LO frequency RX1_LO of the RX_VCO in different frequency, the final receiver IF would be not affected. No. 2, when the two receiver downlink frequency is relatively close (for example, <50 MHz), resulting in RX1_LO frequency is closer to RX_VCO and may cause frequency pulling mutual interference. Clarify its mechanism then how to set up regulations to avoid this possibility would be easy. In the 2nd situation, to change the frequency of one path RX2_LO while the other path remains, the corresponding frequency of its RX1_LO will also be changed, so that the phenomenon of frequency pulling can be avoided. Specifically, as shown in Fig. 3, the frequency of RX2_LO can be designed is formed by TX1_LO divide by two or three in frequency, when the two receiver spectrum are close, one of the second-step-down LO remains for the divide by two mode means RX2_LO = (1/2) *TX1_LO, then switching the other path to divider by three model means RX2_LO = (1/3)*TX1_LO, close spectrum can be determined by baseband detection, so as to generate two RX_VCO the frequency of the first variable LO becoming far and not be disturbed. The divide by two or three mode can be easily implemented in the circuit.

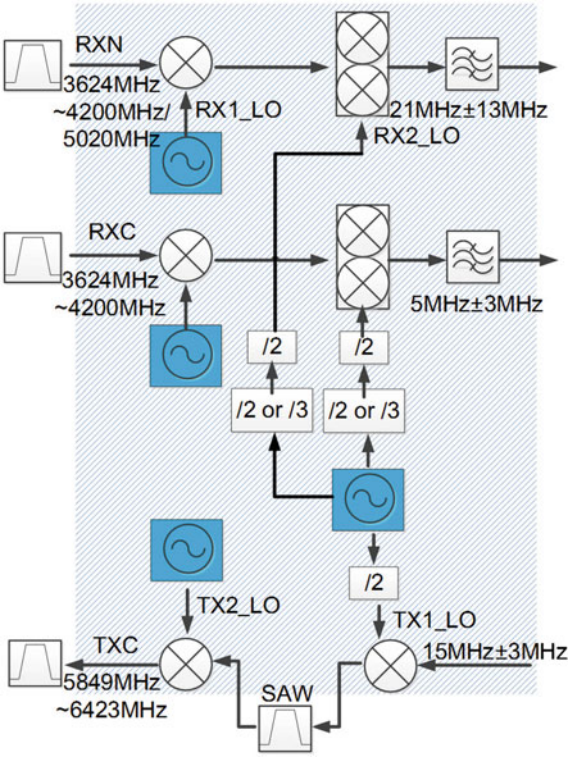

Fig. 3 The spectrum allocation on single chip for CAPS

2.2 Implementation Steps

The scheme includes the following steps:

1. Firstly, determining the LO frequency of first-step-up conversion which is a fixed frequency, and can be used as a two RX channel second-step-down frequency conversion LO after the frequency divider. Therefore, the frequency synthesizer can be reused, which can simultaneously provide the LO signal for the three channels, which directly determines the allocation of the LO spectrum of each channel. In order to meet the requirements of the three channels of the CAPS terminal all working at the same time, and considering the requirements of the image rejection and side-band suppression, the spectrum of each channel is not overlapped after the allocation, which is restricted by the following conditions:

Condition 1: after the first-step-up conversion, the frequency of TX_HIF as intermediate frequency must satisfy its high product does not fall into the variable LO spectrum range of second-step-up conversion. Because the signal strength of the TX is generally large, and the harmonics due to nonlinear (usually an odd number, even number can be suppression by the differential mode) interfere the variable frequency TX2_LO (the LO is directly produced by VCO, also belong to the large signal). Specifically, the influence of the 3rd harmonic which is the maximum does not fall into the variable spectrum. For the first-step-up TX1_LO (MHz), the second-step-up TX2_LO (MHz), uplink output spectrum of 5849–6423 MHz, then 3*TX_LO1 (3rd harmonic signal) > 6423-TX1_LO (the highest frequency of the variable frequency spectrum), or 3*TX_LO1 (the 3rd harmonic signal) < 5849-TX1_LO (the lowest frequency of the variable frequency spectrum). Thus calculated TX1_LO > 1605, or TX1_LO < 1460.

Condition 2: the LO spectrum of the second-step-up does not fall into the receiver input spectrum. When the receiver and transmitter channels both work at the same time, the large signal of the second-step-up LO may cause interfere to the receiver spectrum, for 3624–4200 MHz of the downlink spectrum, 5849-TX1_LO (the lowest frequency of the LO spectrum) > 4200 (the highest frequency of receiver spectrum), then calculated TX1_LO < 1650.

Condition 3: The side-band spectrum of the second-step-up conversion does not fall into the receiver input spectrum. The same condition as No. 2, when receiver and transmitter both work at the same time, during the second-step-up conversion two signals will be generated, one, the upper side-band (the sum frequency) as output signal and the other, the lower side-band (the differ frequency) as the side-band signal, the lower frequency as the lower side-band signal, may cause interfere to the receiver spectrum, for receiver spectrum 3624–4200 MHz, 6423-2*TX1_LO (the highest frequency of the side-band spectrum) < 3624 (the lowest frequency of receiver spectrum), thus calculated TX1_LO > 1400.

Condition 4: the VCO frequency which generate the first-step-up conversion LO does not fall into the receiver of the first-step-down variable LO spectrum. Because the VCO's output as large signal, falling into the LO spectrum, it may cause the same frequency mutual interference. The first-step-up synthesizer of the LO frequency is divider by two as the second-step-down LO frequency, namely 0.5*TX1_LO, 2*TX1_LO (the VCO frequency) > 4200-0.5*TX1_LO (the highest frequency of the fist-step-down LO spectrum), or 2*TX1_LO (the VCO frequency) < 3624-0.5*TX1_LO (the lowest frequency of the fist-step-down LO spectrum), then calculated TX1_LO < 1450, or TX1_LO > 1680.

In summary, at the same time to meet the above conditions is 1400 < TX1_LO < 1450.

2. After determining the frequency of TX1_LO, then the frequency synthesizers frequency spectrum of each channel should be determined. Choose a suitable SAW filter in frequency after the first-step-up conversion, then choose the USB (Upper Side Band) or LSB (Lower Side Band) as in the pass band, and the other side would be arranged at the stop band, the 30 dB suppression can be easily satisfied; in the choice of an off-chip filter, meet the uplink spectrum frequency offset 2*TX1_LO which the lower side-band spectrum (i.e. uplink spectrum-2*TX1_LO) more than 30 dB suppression, the specification can be easy to achieve; in the choice of an off-chip filter at the front of the receiver, meet the image spectrum of downlink spectrum frequency offset at TX1_LO (i.e.downlink spectrum-TX1_LO) 30 dB rejection, the specification can be easy to achieve. This can both meet the requirements of image rejection and side-band suppression.

3. In order to meet the two receiver channels when two frequency closing can still work without interference, the frequency divider by two or three switching mode can be designed to avoid possibility of the two VCO with the same frequency. When the two receiver frequency are close, which can be detected by the baseband chip firstly, given the two RX IF were 21 ± 13 and 5 ± 3 MHz respectively, can be set when the two downlink frequency interval is less than <50 MHz, start the switch mode, one will switch to the divider by three mode, the other will keep constant mode divide by two. Given the different second-step-down LO frequency (more than hundreds of MHz interval), thus the first-step-down VCO frequency which generate LO will have hundreds of MHz intervals without interference.

3 Implementation Effect and Conclusions

By using the above spectrum allocation scheme, through the two-step-up/down conversion architecture, communication uplink spectrum 5849–6423 MHz communication downlink spectrum 3624–4200 MHz and navigation downlink

spectrum 3624–4200/5020 MHz can work at the same time without interference with each other in a single chip to achieve spectrum coverage. The chip integrates LNA, Mixer, ADC, AGC, a complex filter, a temperature sensor, a sigma delta fractional-N PLL and capless LDO circuits, using the 130 nm CMOS process, the measurement results show that: the output phase noise in-band integral degree of less than 2°, adjacent channel suppression of more than 30 dB, the output power of the chip temperature stability is less than 1 dB, 3rd order inter-modulation is less than −30 dBc, side-band suppression more than 35 dBc, the phase error is less than 3°; the receiver AD output Spurious Free Dynamic Range(SFDR) is more than 35 dB, the equivalent number of bits is greater than 3.5, image rejection is more than 35 dBc, the automatic gain control range is more than 50 dB; and the module which add the off-chip LNA and PA together to achieve the output power of more than 33 dBm, and the noise figure is less than 2 dB. Meet the requirements of CAPS radio frequency terminal.

Measurement results: as shown in Fig. 4, add the IF frequency 15 MHz, −15 dBm analog signal, output spectrum by spectrum analyzer: point 1 for the output of the main tone signal, point 2 for the frequency offset of 15 MHz carrier

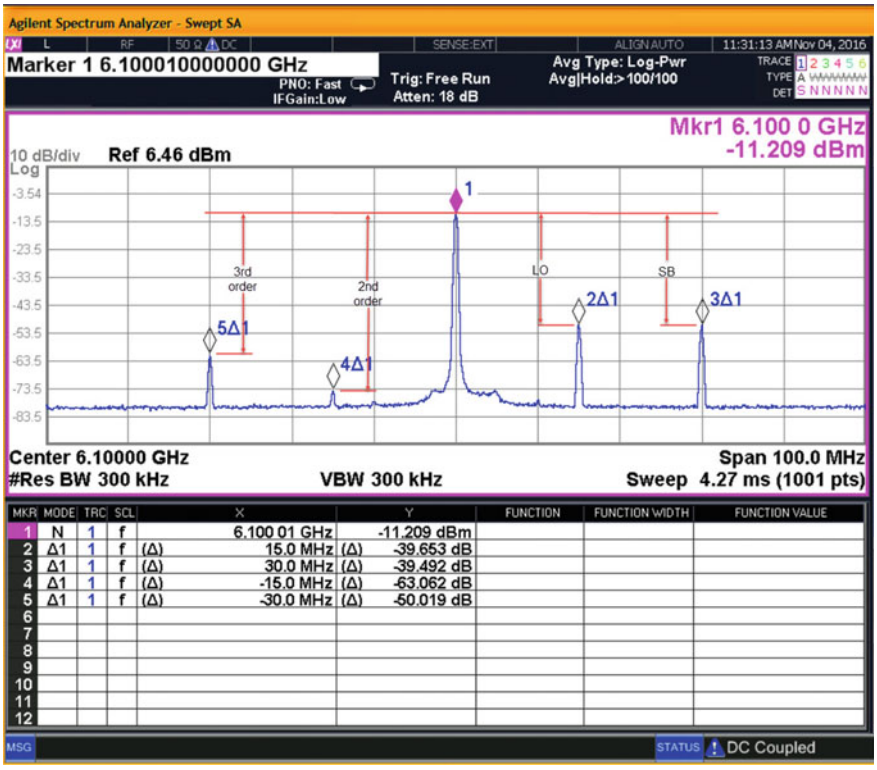

Fig. 4 TX SSB output spectrum

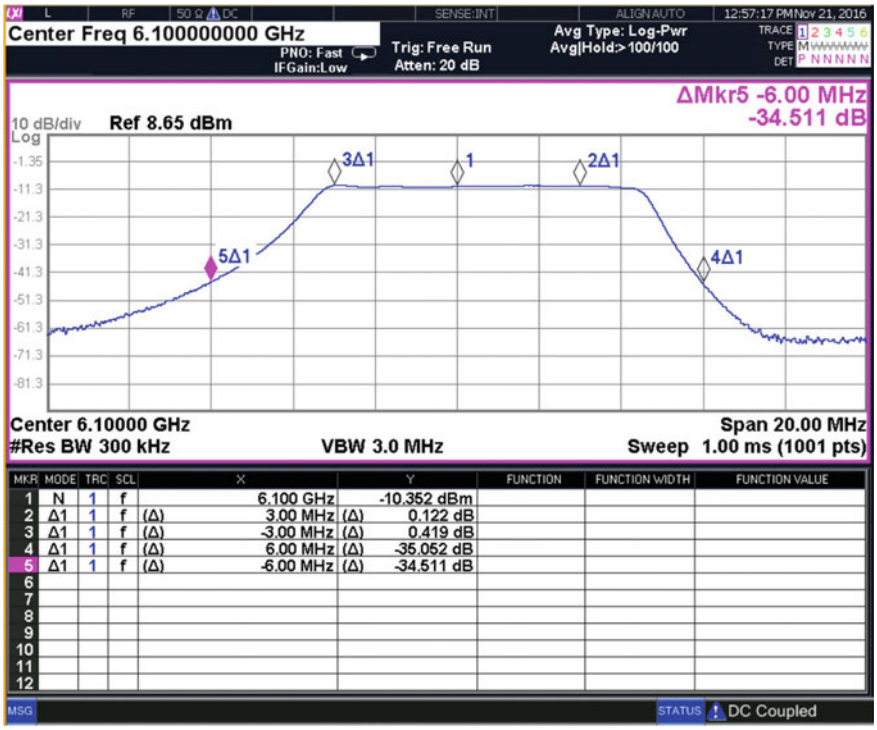

Fig. 5 Filter characteristics of TX output

leakage, and point 3 for the carrier frequency offset 15 MHz side-band suppression, point 4 for the 2nd harmonic, point 5 for the 3rd harmonic. This ratio with the main tone, the carrier leakage suppression is −39 dBc, side-band suppression is −39 dBc, 2nd harmonic suppression is −63 dBc, the 3rd harmonic suppression is −50 dBc.

As shown in Fig. 5, sweep the TX IF frequency to get the output filter characteristics. Its band (+3 MHz) flatness is less than 0.5 dB, adjacent channel suppression (±6 MHz) 34.5 dB.

As shown in Fig. 6, the output phase noise in-band is less than 2°.

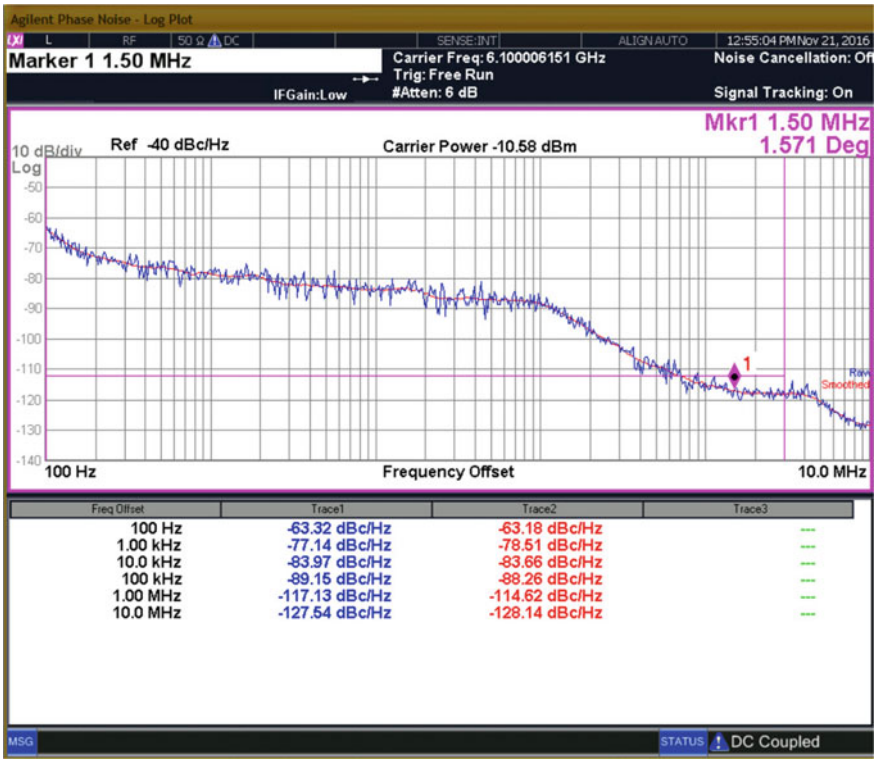

Fig. 6 Phase noise performance of TX output

As shown in Fig. 7, transmit input 1 MHz offset two-tone signal, output 3rd order intermodulation, OIP3 is 12 dBm, the 3rd order intermodulation is less than −45 dBc.

As shown in Fig. 8, TXIF add 15 MHz, −15 dBm, BPSK as the symbol rate of 4.2996 Msps modulation signal generated by the vector signal generator, transmitter output through the spectrum analyzer 89601 vector signal analysis software to calculate the phase error is less than 3°.

In Fig. 9, the image rejection test of navigation receiver channel and the communication receiver channel. Adding two tones with the same amplitude one is the useful radio frequency signal, the other is the image radio frequency signal, the

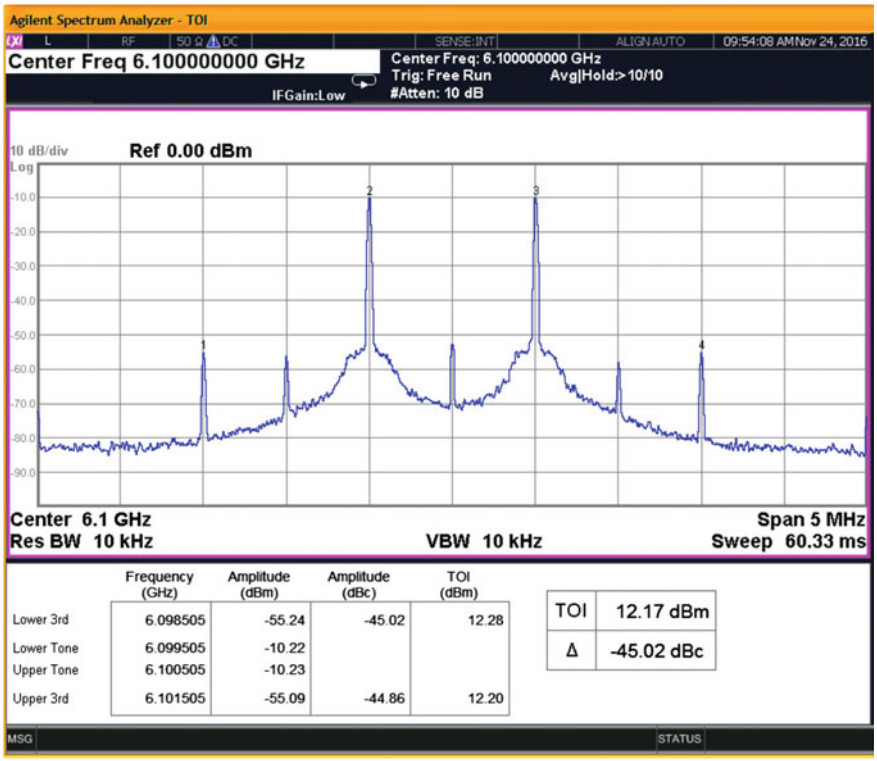

Fig. 7 3rd Intermodulation performance of TX output

navigation IF analog output at 21 MHz is the useful signal, and at the 1 MHz frequency offset is the image signal, the image rejection is 45.2 dBc. Similarly, the image rejection is 45.4 dBc in communication receiver channel.

As shown in Fig. 10, the digital output performance of the navigation channel and communication channel. Two sets of 4 bits ADC are integrated in two receiver channels, through the logic analyzer analysis software, it reads that SFDR were 36.4, 37 dB, the equivalent bits were 3.7, 3.8 bit respectively.

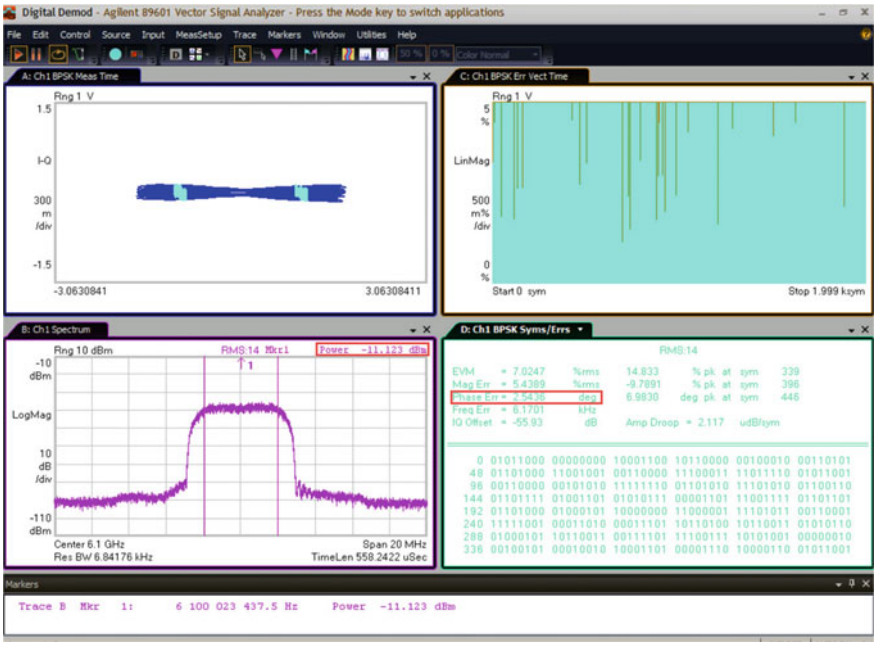

Fig. 8 EVM performance of TX output

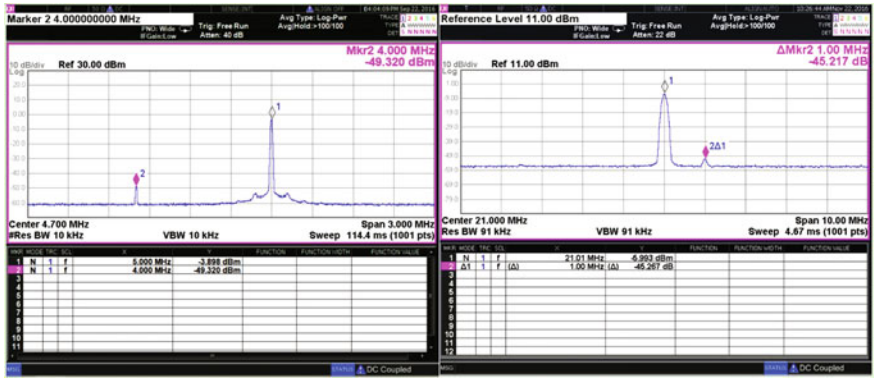

Fig. 9 Image rejection performance of RXN&RXC

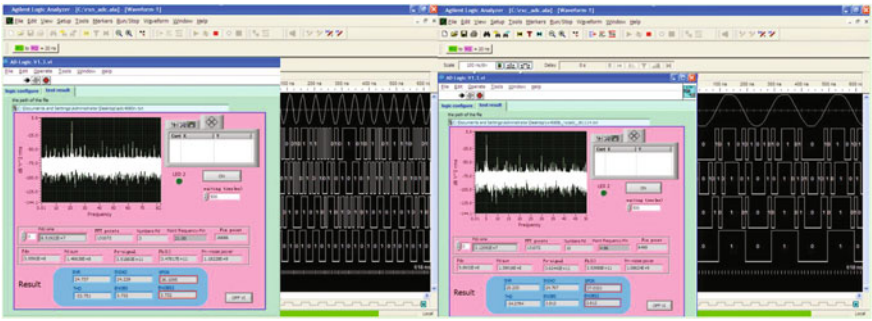

Fig. 10 Digital output performance of RXN&RXC

References

1. Shi H (2009) Principles of transponding satellite navigation. Science Press, Beijing
2. He S, Qu Y (2014) A radio transmitter for RDSS terminal. In: 5th CSNC2014, nanjing
3. He S (2016) Frequency spectrum allocation apparatus and method for a single chip in multi-mode. Chinese Patent 2016109523494, Guangzhou Runxin Information Technology Co. Ltd, 27 Oct 2016

Parameters Estimation Method for LFM Interference to GNSS Uplink Injection

Shuren Guo, Hang Ruan and Hailing Wu

Abstract Satellite navigation system has been widely used in military and civilian realms in the world. As applications of satellite communication and radar increases, the electromagnetic environment becomes more and more complex. For middle and high orbit navigation satellites, various intentional or (and) unintentional interferences exist in the same frequency band of the uplink injection, which may reduce the quality of the uplink data, increase the error rate, and further, if in severe condition, affect the operation of satellite navigation system. Currently, radar signal is a main type of unintentional interference for the uplink injection of the navigation satellite. In this paper, the interference signal power level from ground radar to uplink injection is analyzed. For the typical linear frequency modulated (LFM) radar signal, a method based on fractional Fourier transform (FrFT) is proposed to estimate the signal parameters, and simulation experiment is performed to demonstrate the validation of the method. The results of this paper could be used for reference for the space electromagnetic environment monitoring for satellite navigation system.

Keywords GNSS · Uplink injection · Linear frequency modulated (LFM) · Parameters estimation · Fractional fourier transform (FrFT)

1 Introduction

Global Navigation Satellite System can be divided into space, ground and user segments. Among them, ground segment mainly consists of master control station, monitor station and uplink injection station. Under the control of master control

S. Guo · H. Wu
National University of Defense Technology, Changsa, China

S. Guo · H. Ruan (✉) · H. Wu
Beijing Institute of Tracking and Telecommunication Technology, Beijing, China
e-mail: ruanhang@beidou.gov.cn

J. Sun et al. (eds.), *China Satellite Navigation Conference (CSNC) 2017 Proceedings: Volume I*, Lecture Notes in Electrical Engineering 437,
DOI 10.1007/978-981-10-4588-2_83

station, uplink injection station mainly aims to send information about navigation data, massage and control instruction to orbit satellites, it can also be used for distance measuring and time synchronization between space and ground, which is the key point to operate satellite navigation system and provide serves of precise position and time synchronization. Uplink injection link includes injection station on the ground and the receiver equipment of uplink injection on the satellite. Once some interferences exist in the receiver, it may reduce the quality of the uplink data, increase the error rate, and further, if in severe condition, navigation data and massage even may be failed to inject, which may affect the stable operation of the whole satellite navigation system. Comparing to the interferences exist in the receiver of down-link of the user segment, its influence is always global.

With the development of technology, the quantity and types of the ground communication and radar equipment are increasing, the working frequency band is being various, which contributes to a more and more complex electromagnetic environment that GNSS has to face. The distribution of radar's working frequency band is 1215–1400 MHz [1], determined by International Telecommunication Union (ITU), overlap with GNSS uplink injection working frequency band, 1300–1350 MHz. Because of the pulse and the high peak power characteristics of most radar signals, when the radar operates, due to its similar frequency of radiation with uplink injection, it will bring some interferences to uplink injection receiver, and influence the receiver's normal reception of uplink injection information. For all this, this paper will firstly analyze the interference from ground radar to uplink injection in terms of signal power level. For the typical linear frequency modulated (LFM) radar signal, a method based on fractional Fourier transfer (FrFT) is proposed to estimate the signal parameters, and simulation experiment is performed to demonstrate the validation of the method. In the end of this paper, come up with the conclusion that satellite navigation system should have the ability to monitor the space electromagnetic environment, to avoid interference in the case of interference with some uplink injection strategies. The results of this paper could be used for reference for the space electromagnetic environment monitoring for satellite navigation system.

2 Analysis About the Interference Signal Power from Radar to Uplink Injection

Uplinks of satellite navigation system usually adopt the Direct Sequence Spread Spectrum technology (DSSS), which has a wide signal spectrum, and has some characteristics like safe and hidden, the signal system itself has some ability to against interference. But, as applications of various of ground radars increases, especially the continuous development of L-Band large power pulse radar technology, satellite navigation system's uplinks are facing such more and more serious unintentional interference. When there is a stringent duty cycle of pulse signal of

large power radar, its high peak power will increase the AGC setting time of uplink injection receivers of satellite navigation system, and increase the error rate of uplink injection signals in short time, it will be a threat to uplink injection security. On the other side, when the duty cycle is large, it will continuous influence the error rate, which brings worse harms [2].

Supposing equipment on the ground uplink inject signals have the power P_z, the wavelength λ, the transmitting antenna gain G_z, the distance between ground injection station and satellite is R_z, the spaceborne uplink injection receiver's antenna gain is G_{rz}, combined loss L_z, so the power of uplink injection signal received by star based receiver is:

$$P_{rz} = \frac{P_z G_z G_{rz} \lambda^2}{(4\pi R_z)^2 L_z} \tag{1}$$

Power of the spaceborne uplink injection receiver's noise is:

$$N = kTB_z \tag{2}$$

Among them, $k = 1.38 \times 10^{-23}$ J/K is Boltzmann constant, T is noise temperature, in Kelvin (K), B_z is noise bandwidth, usually, its value comes from uplink injection signal before despreading.

Supposing radar signal has the transmitting power P_s, bandwidth B_s, the transmitting antenna gain G_s, the distance between ground radar and satellite is R_s, the spaceborne uplink injection receiver's antenna gain in the direction of radar is $G_{rz}(\theta)$, combined loss is L_s, so the radar signal power received by the spaceborne uplink injection receiver in the similar frequency is:

$$P_{rs} = \begin{cases} \frac{P_s G_s G_{rz}(\theta) \lambda^2 B_z}{(4\pi R_s)^2 B_s L_s}, & B_z \le B_s \\ \frac{P_s G_s G_{rz}(\theta) \lambda^2}{(4\pi R_s)^2 L_s}, & B_z > B_s \end{cases} \tag{3}$$

Among them, if the signal bandwidth from radar is wider than its from uplink injection station, what really influence the spaceborne uplink injection receiver is the signal power which exist within the receiver bandwidth, the rest of signal will be filtered.

In this case, the power ratio of radar signal and uplink injection signal received by the spaceborne uplink injection receiver is:

$$\frac{P_{rs}}{P_{rz}} = \begin{cases} \frac{P_s G_s G_{rz}(\theta) B_z R_z^2 L_z}{P_z G_z G_{rz} B_s R_s^2 L_s}, & B_z \le B_s \\ \frac{P_s G_s G_{rz}(\theta) R_z^2 L_z}{P_z G_z G_{rz} R_s^2 L_s}, & B_z > B_s \end{cases} \tag{4}$$

Supposing the effective isotropic radiated power (EIRP) of uplink injected signal is 44 dBW, bandwidth is 10.23 MHz, the effective noise temperature of the spaceborne uplink injection receiver is 350 K, in this case the noise power can be

calculated, which is about −133 dBW. For middle orbit navigation satellite, it is estimated that the uplink injected signal power received by the spaceborne uplink injection receiver is about −142 dBW, carrier-to-noise ratio is about 61 dBHz, which meets the carrier-to-noise ratio range for the measured result that from the spaceborne uplink injection receiver [3]. According to the estimate result, uplink injected signal adopt the DSSS should have smaller power than noise power, so that uplink injected signal could be hidden in the noise, and will be equipped with stronger disguise and better performance of anti-interception.

As for L-Band ground radar, whose working range is more than hundreds of kilometers, its typical peak power is about hundreds of KW magnitude. While such as large early warning radar, COBRA DANE, its typical peak power reaches to 15.4 MW, its average power is 0.92 MW [4]. To consider it without losing generality, we suppose that radar peak power is 100 kW, antenna gain is 39.5 dB (with a 10 m effective aperture), so EIRP of the radar is 89.5 dBW, supposing the transmission loss from radar to satellite is 5 dB more than that from uplink injection station to satellite, and 20% bandwidth of radar signal exist in the bandwidth of the spaceborne receiver, considering that the uplink injection receiver antenna is always ball beam, star based receiver antenna has the same gain between radar direction and uplink injection station direction, so that we can calculate the radar signal power what spaceborne uplink injection receiver receive, it is about −109 dBW, this is 33 dB higher than uplink injected signal, even if the spread spectrum gain is 25 dB, radar signal is still 8 dB stronger than uplink injected signal, which will influence the acquisition and tracking of uplink injected signal seriously.

3 Method to Estimate the LFM Radar Signal Parameters

From the previous analysis, we know that L-Band ground radar signal has some interferences to uplinks of satellite navigation system, which will influence the reception of uplink injected signal by satellite, and will have an impact on system operation. Therefore, it has important significance for navigation satellite to have some ability to monitor electromagnetic environment in the working frequency bands. Using spaceborne electromagnetic environment monitoring equipment on navigation satellite to identify various intentional or (and) unintentional interferences, is an important part to avoid influences caused by interferences, so it will be particularly important to estimate signal parameters. Currently, pulse compression technique has been widely used in the field of radars to realize the strong detection capability as wide-pulse radar and the high range resolution as narrow-pulse radar synchronously. LFM is a kind of widely used signal in pulse compression technique. Here, this section will discuss the method to estimate the LFM radar signal parameters in spaceborne monitoring of electromagnetic environment.

3.1 Parameter Estimation Method for Single LFM Signal

Generally, using short time Fourier transform, we can estimate LFM signal parameters quickly, but short time Fourier transform has limited time or frequency resolution, thus we can only get some rough estimated parameters.

Currently, the fractional Fourier transform (FrFT) has been used in the estimation of LFM signal parameters. The fractional Fourier transform to signal $x(t)$ can be defined as [5]:

$$X_\alpha(u) = \int_{-\infty}^{+\infty} x(t) K_\alpha(u,t) \mathrm{d}t \tag{5}$$

$$K_\alpha(u,t) = \begin{cases} \sqrt{1 - \mathrm{j}\cot\alpha}\exp(\mathrm{j}\pi((t^2+u^2)\cot\alpha - 2ut\csc\alpha)), \\ \quad \alpha \neq n\pi; \\ \delta(u-t), \alpha = 2n\pi; \\ \delta(u+t), \alpha = (2n \pm 1)\pi. \end{cases} \tag{6}$$

Among them, $n = 1, 2, \ldots$; $K_\alpha(u,t)$ is the kernal of FrFT, α is rotation angle. When rotation angle $\alpha = \pi/2$, FrFT changes into traditional Fourier transform.

Traditional Fourier transform can be regarded as a transform spin from time-axis to frequency-axis anticlockwise at angle $\pi/2$, while FrFT can spin at any angle, so that FrFT can be regarded as a kind of generalized Fourier transform. As for FrFT, if we choose suitable rotation angle α, we can highly gather the energy of LFM signal in FrFT domain, which is shown in Fig. 1:

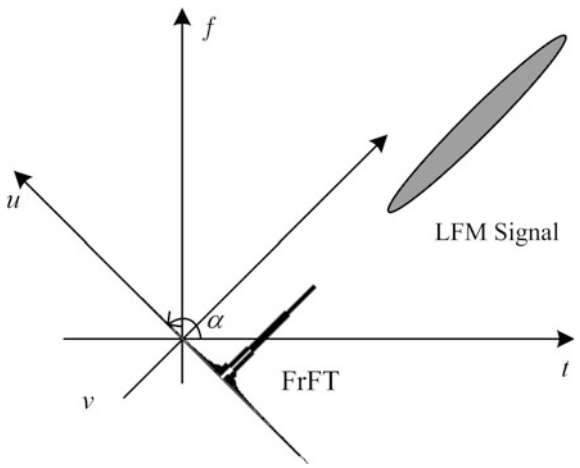

Fig. 1 FrFT schematic

Supposing LFM radar signal can be expressed as:

$$s(t) = A\ \exp[j2\pi(f_0 t + \frac{1}{2}\gamma t^2)] \tag{7}$$

Among them, A is amplitude, f_s is center frequency, γ is frequency modulation slope.

The method to estimate LFM signal parameters using FrFT is: calculate the value of FrFT at different rotation angles, searching the maximum absolute value we get at all rotation angles, and find the angle α_0 and the frequency u_0 under the condition of maximum absolute value, the frequency modulation slope and the initial frequency can be calculated using:

$$\begin{cases} \gamma = -\cot(\alpha_0) \\ f_0 = u_0 \csc(\alpha_0) \end{cases} \tag{8}$$

Considering the dimensional normalization in discrete Fourier transform (DFT) calculating, the real frequency modulation slope and the initial frequency should be calculated as formula (9):

$$\begin{cases} \gamma = -(\cot\alpha_0) \cdot f_s/T \\ f_0 = u_0 \csc\alpha/T \end{cases} \tag{9}$$

Among them, T is sampling time while f_s is sampling frequency.

To obtain the best rotation angle with high precision, the small rotation angle search step length will be necessary, but at the same time, the computational cost increases, the efficiency decreases. So that we can use the hierarchical search to estimate the best rotation angle, while, we can start with a big step length to find a rough value, and then we can search precisely around the range whose center is the rough value, the specific steps are:

Step 1 According to the initial search scope $[0, \pi)$, determine the initial search step $\Delta\alpha_0$ and the end search step $\Delta\alpha_{\text{end}}$, while $\Delta\alpha_0$ values a little bigger. (such as 0.1π).

Step 2 Obtain the peak value S_i after FrFT when step is $\Delta\alpha_0$, and its corresponding best rotation angle α_i.

Step 3 Take α_i in step 2 as the initial search step, doing the following update process:

$$\begin{cases} \alpha_{i+1,\min} = \alpha_i - \Delta\alpha_i \\ \alpha_{i+1,\max} = \alpha_i + \Delta\alpha_i \\ \Delta\alpha_{i+1} = \Delta\alpha_i/10 \end{cases} \tag{10}$$

Among them, $[\alpha_{i+1,\min}, \alpha_{i+1,\max}]$ is the search range for the $i+1$ times search, $\Delta\alpha_{i+1}$ is the search step for the $i+1$ times search, while $\Delta\alpha_i$ is the search step for the i times search.

Step 4 When $\Delta\alpha_{i+1} \geq \Delta\alpha_{\text{end}}$, search as step 2 with a step $\Delta\alpha_{i+1}$ and obtain its peak value S_{i+1}, otherwise, finish the search, and take $\Delta\alpha_i$ as the final best rotation angle.

3.2 Parameter Estimation Method for Multiple LFM Signals

In reality, there may be multiple LFM signals with different strength, which can be expressed as:

$$s_i(t) = A_i \exp[j2\pi(f_{0,i}t + \frac{1}{2}\gamma_i t^2)], i = 1, 2, \ldots, n \tag{11}$$

In this case, using the method to estimate FrFT parameters directly will brings the problem that the strong signal components will cover up the weak signal components, which causes a large error to the weak signal components' detection and estimation. Therefore, on the basis of analysis to single LFM signal parameters estimation, we can combine CLEAN technology to realize the separation between strong and weak signal components and the parameters estimation from large to small in FrFT domain [5], the specific steps are:

Step 1 When estimating the i th component, do FrFT to echo sequences and modulus them with step $\Delta\alpha$ at different rotation angles, forming a two-dimensional distribution $S_i(\alpha, u)$ in the FrFT distribution plane (α, u).

Step 2 Search the peak value in the two-dimensional distribution plane (α, u), obtain the corresponding rotation angle α_i and frequency u_i of the peak value, using formula (9) to calculate the initial frequency and the frequency modulation slope of the i th component.

Step 3 Construct a narrow-band filter $w_i(u)$ with a center frequency u_i, do band-stop filtering processing in the FrFT distribution plane of the ith component, do FrFT at the rotation angle $-\alpha_i$ to the parts outside the filter band, which will be taken as the original signal of next signal separation parameters estimation, while:

$$s_{i+1}(t) = \int_{-\infty}^{+\infty} S_i(\alpha_i, u)(1 - w_i(u))K_{-\alpha_i}(u, t)\boldsymbol{d}u \tag{12}$$

Step 4 Replace i with i + 1, repeat the above steps, until the LFM components with sharp peak value can not be detected.

4 Simulation Experiment

To demonstrate the validation of the method, simulation experiment is performed here, which demonstrates the parameters estimation performance of single LFM signal and multiple LFM signals separately.

4.1 Parameter Estimation Method for Single LFM Signal

The simulation parameters are: LFM signal initial frequency 15 MHz, frequency modulation slope 2×10^{12} GHz/s, initial search range for best rotation angle is [0, π), initial search step 0.1 π, end search step 0.0005 π.

Figure 2 is the time-frequency domain distribution of single LFM signal (using short time Fourier transform), Fig. 3 is the distribution of the signal in the FrFT distribution plane after the fractional Fourier transform. According to calculate the position of the peak point, the best rotation angle can be calculated, which is 111.6°, while the position of peak point is 140. It can be obtained by calculation that the frequency modulation slope is 2.0232×10^{12} GHz/s, the center frequency is 15.057 MHz. Thus it can be seen that the estimated values and the actual values are very closed, the parameter estimation method for single LFM signal is effective in this paper.

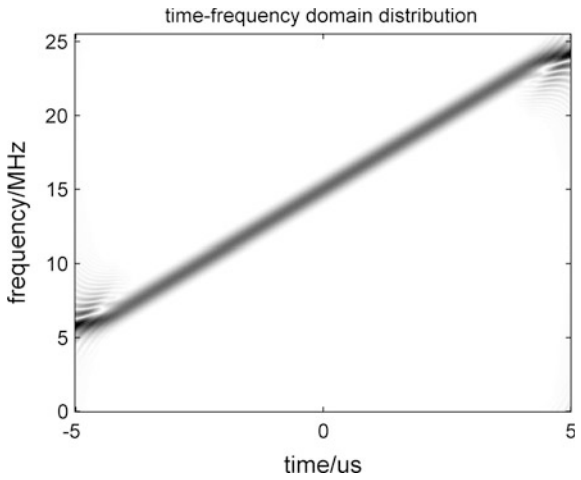

Fig. 2 Time-frequency domain distribution

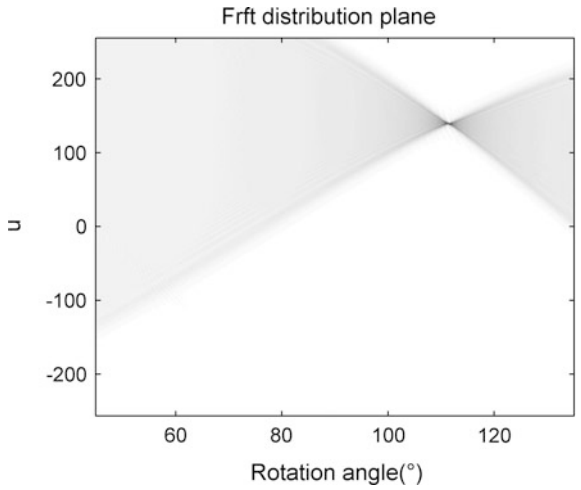

Fig. 3 FrFT plane distribution

4.2 Parameter Estimation Method for Multiple LFM Signals

The simulation parameters are: 3 initial frequencies of LFM signal are 15, 10 and 15 MHz, frequency modulation slopes are 2×10^{12}, 1.5×10^{12} and -2×10^{12} GHz/s, amplitudes are 10, 10 and 5. Initial search range for best rotation angle is [0, π), initial search step 0.1 π, end search step 0.0005 π.

Figure 4 is the time-frequency domain distribution of single LFM signal (using short time Fourier transform), Fig. 5 is the distribution of the signal in the FrFT distribution plane after the fractional Fourier transform. The estimated values of best rotation angle are 111.6°, 106.38°and 68.58°, the positions of peak values are 140, 97,

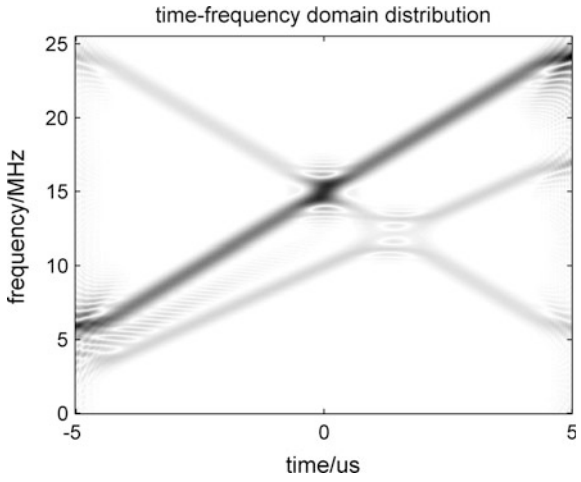

Fig. 4 Time-frequency domain distribution

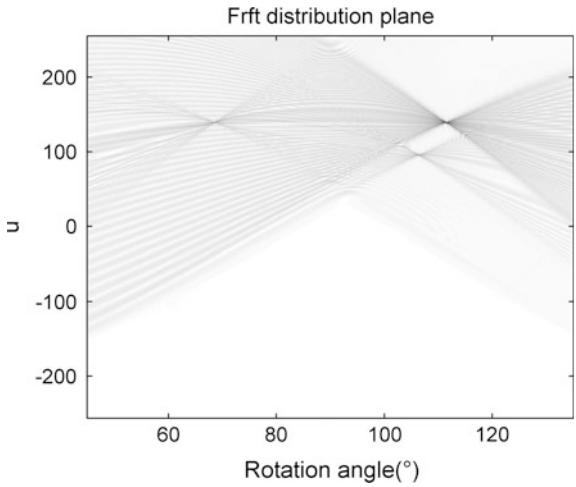

Fig. 5 FrFT plane distribution

140. The frequency modulation slopes which the above parameters corresponding are 2.0232×10^{12}, 1.502×10^{12} and -2.0046×10^{12} GHz/s, whose center frequencies are 15.057, 10.11 and 15.039 MHz. Thus it can be seen that the parameter estimation method for multiple LFM signals is effective in this paper.

5 Summary

Considering the spectrum interferences to satellite navigation uplink injection receiver from increasing huge power ground electronic equipments, we suggest that navigation satellites should have the ability to monitor the electromagnetic environment in working band. Thus, after identify and positioning the interference sources, influence will be avoid to a certain extent by changing the configurations and the strategies of ground uplink injection, which ensures the security of the uplink injection of navigation system, and improves the system reliability.

References

1. Ding L, Geng F (2005) Radar principle. Xidian University Press House, Xi'an, pp 7–8 (in Chinese)
2. Guo S, Hu Z (2013) Forecast and simulation for effect of electromagnetic environment to the up-link receiving end of the satellite navigation system. In: The 4th China satellite navigation conference, Wuhan, China, 2013 (in Chinese)

3. Liu X (2013) Study on key techniques of spaceborne DSSS receiver for satellite based navigation system. National University of Defense Technology, 2013 (in Chinese)
4. Wang X (2009) Performance analysis of the upgraded Cobra Dane radar system based on STK. Mod Radar 31(1):4–8 (in Chinese)
5. Ruan H, Wu Y, Ye W (2013) Inverse synthetic aperture Ladar imaging algorithm for maneuvering target based on FRFT-CLEAN. J Electron Inf Technol 35(7):1540–1546 (in Chinese)

Analysis of Threshold Setting for Eigenvalue Ratio Based Interference Detection Under Constant Missed Detection Probability

Gangqiang Guan, Deyong Xian, Liu Shi, Jia Mu and Xinshu Zhao

Abstract Interference detection is very important for high reliability applications with array-based GNSS receivers in complex electromagnetic environments, such as shipping positioning in sensitive waters, electromagnetic environment monitoring around the GNSS ground reference stations, etc. According to the common hypothesis that the power of the interference is far greater than the received GNSS signal, the interference can be detected using the ratio of the maximum eigenvalue and the minimum eigenvalue of the sample covariance matrix. However, the probability distribution function of the eigenvalue ratio is complex, it is difficult to compute the optimized threshold and analyze the detection performance. To solve these problems, the Tracy-Widom distribution is accurately approximated by using the Gaussian distribution with suitable parameters, and the analytical formulas for threshold setting are given under the constant probability of missed detection condition for the first time, then threshold setting and detection performance under different parameters are analyzed by simulation.

Keywords Interference detection · Eigenvalue ratio · Threshold setting · GNSS

1 Introduction

GNSS receiver is vulnerable to various intentional or unintentional interference, it is necessary to detect the interference that may appeared in the antenna received data, so as to take appropriate interference mitigation method in subsequent processing

G. Guan (✉) · D. Xian · J. Mu · X. Zhao
Beijing Satellite Navigation Center, Beijing, China
e-mail: closetoqiang@163.com

L. Shi
Beijing Institute of Remote Sensing Information Technology, Beijing, China
e-mail: wxdwyyg@163.com

J. Sun et al. (eds.), *China Satellite Navigation Conference (CSNC) 2017 Proceedings: Volume I*, Lecture Notes in Electrical Engineering 437,
DOI 10.1007/978-981-10-4588-2_84

[1]. By the way of power estimation of the received data, such as energy detector, interference detection can be achieved traditionally [2–4]. However, the probability density function of detection metrics is related to the channel noise power, which can significantly affect the detector performance. In recent years, with the rapid development of spectrum sensing technology in cognitive radio, the presence or the absence of a primary signal can be inferred based on the ratio of the largest and the smallest eigenvalue of the received signal's covariance matrix [5–7]. But because the probability distribution function of eigenvalue ratio is complex, it is difficult to analyze the threshold setting and the corresponding performance. According to the existing related research literature, the analytic formula of the threshold setting under the condition of constant false alarm probability is deduced in [8] when the pdf of the maximum eigenvalue and the minimum eigenvalue are all approximated to Gaussian distribution, but no more analysis under the constant missed detection probability. In the literature [9], the interference detection metric is directly approximated as Gaussian distribution, but the reason of this approximation is not provided. Based on this, the analytic formula of the detection threshold is deduced under the condition of constant missed detection probability, and the performance of interference detection is simulated and analyzed under different parameter settings.

2 Eigenvalue Based Interference Detection

2.1 Signal Model

Interference detection is used for inferring whether the intentional or unintentional interference source is presented or not in the GNSS receiver operation environment. Such signal detection problem can be summarized as a binary hypothesis testing model [6, 9]

$$\begin{aligned} H_0&: \boldsymbol{x}(t) = \boldsymbol{n}(t) \\ H_1&: \boldsymbol{x}(t) = \boldsymbol{H}(\theta, \phi)\boldsymbol{s}(t) + \boldsymbol{n}(t) \end{aligned} \tag{1}$$

where H_0 and H_1 represent the two hypothesis: the absence and presence of interference signal, $\boldsymbol{x}(t)$ is the signal vector received by the antenna array, $\boldsymbol{s}(t)$ is the interference signal waveform vector, $\boldsymbol{H}(\theta,\varphi)$ is the steering matrix, θ and φ are the azimuth and elevation angle of the incident signal, respectively, $\boldsymbol{n}(t)$ is the noise vector.

Suppose that N antenna elements receive the plane wave signal incident from the far field, and collect K data sampling snapshots within a specified period, the overall receiving data can be arranged by N × K matrix, which can be denoted as

$$\boldsymbol{X} = \begin{pmatrix} x_{1,1} & x_{1,2} & \cdots & x_{1,K} \\ x_{2,1} & x_{2,2} & \cdots & x_{2,K} \\ \vdots & \vdots & \vdots & \vdots \\ x_{N,1} & x_{N,2} & \cdots & x_{N,K} \end{pmatrix} \tag{2}$$

where $x_{i,k}$ is the k-th snapshot received by the i-th antenna element. The sampling covariance matrix of the received data can be written as

$$\boldsymbol{R}_x = \boldsymbol{X}\boldsymbol{X}^{\mathrm{H}} \tag{3}$$

The eigenvalue decomposition of data covariance matrix can be written as

$$\boldsymbol{R}_x = [\boldsymbol{u}_1, \ldots, \boldsymbol{u}_N] \begin{bmatrix} \lambda_1 & & & \\ & \lambda_2 & & \\ & & \ddots & \\ & & & \lambda_N \end{bmatrix} [\boldsymbol{u}_1, \ldots, \boldsymbol{u}_N]^{\mathrm{H}} \tag{4}$$

where $\lambda_k (k = 1, \ldots, N)$ is the k-th eigenvalue of the array covariance matrix. And then

$$\lambda_1 \geq \lambda_2 \geq \cdots \geq \lambda_P > \lambda_{P+1} = \cdots = \lambda_N = \sigma^2 \tag{5}$$

where $\boldsymbol{u}_k$ is the eigenvector corresponding to eigenvalue λ_k.

According to the assumption that the interference power received by the receiver antenna in a complex electromagnetic environment is much greater than the GNSS signal, the large P eigenvalues of the covariance matrix correspond to the sum of the interference energy and the noise energy, while the remaining N-P small eigenvalues correspond to the noise energy. Therefore, the ratio of the largest eigenvalue and the minimum eigenvalue can be used to infer whether the interference appears or not.

Then the detection metric can be defined as

$$\mathrm{T} = \frac{\lambda_1}{\lambda_N} \tag{6}$$

Assume the detection threshold is γ, when $\mathrm{T} < \gamma$, then H_0 holds, which means no interference appears. While $\mathrm{T} \geq \gamma$, H_1 is judged to be true, which means that at least one interference signal appear. Since the covariance matrix of the received data is an approximate estimation of the statistical covariance matrix by a finite number of data snapshots, the fluctuations of the eigenvalues of covariance matrix will be random. Therefore the random matrix theory is used to analyze the detection performance of the eigenvalue-based detector [10, 11].

2.2 Probability Density Function Under H_1

Under the hypothesis H_1, to ensure the interference can be judged correctly by the eigenvalue-based detector the interference-to-noise ratio needs to satisfy [6, 7]

$$\rho > \frac{1}{\sqrt{KN}} \tag{7}$$

where ρ is the interference-to-noise ratio. Now we define

$$t_1 = N\rho + 1 \tag{8}$$

$$\mu_s(t_1, N, K) = t_1\left(1 + \frac{N/K}{t_1 - 1}\right) \tag{9}$$

$$\upsilon_s(t_1, N, K) = t_1\left(1 - \frac{N/K}{(t_1 - 1)^2}\right)^{1/2} \tag{10}$$

$$\mu'_{\_}(N, K) = \left(\sqrt{\frac{N-1}{K}} - 1\right)^2 \tag{11}$$

$$\upsilon'_{\_}(N, K) = \left(\sqrt{\frac{N-1}{K}} - 1\right)\left(\sqrt{\frac{K}{N-1}} - 1\right)^{1/3} \tag{12}$$

In this case, the probability distribution of the largest eigenvalue and the smallest eigenvalue will be satisfied that

$$L_{1|H_1} = K^{1/2}\frac{\lambda_1 - \sigma^2\mu_s(t_1, N, K)}{\sigma^2\upsilon_s(t_1, N, K)} \sim N(0, 1) \tag{13}$$

$$L_{N|H_1} = K^{2/3}\frac{\lambda_N - \sigma^2\mu'_{\_}(N, K)}{\sigma^2\upsilon'_{\_}(N, K)} \sim f_{W_2}(z) \tag{14}$$

It means that when $N, K \to \infty$, $L_{1|H_1}$ will converge to the standard normal distribution and $L_{N|H_1}$ will converge to the second-order Tracy-Widow distribution.

Then the detection metric T under H_1 can be rewritten as

$$\mathrm{T} = \frac{\lambda_1}{\lambda_N} = \frac{K^{-1/2}\mu_s(t_1, N, K)L_{1|H_1} + \mu_s(t_1, N, K)}{K^{-2/3}\upsilon'_{\_}(N, K)L_{N|H_1} + \mu'_{\_}(N, K)} \tag{15}$$

Then the probability density functions of the numerator and denominator of T are

$$f'_{L_{1|H_1}}(z)=\frac{(K/2\pi)^{2/3}}{\upsilon_s(t_1,N,K)}\exp\left(-\frac{K}{2\upsilon_s^2(t_1,N,K)}(z-\mu_s(t_1,N,K))^2\right) \tag{16}$$

$$f'_{L_{N|H_1}}(z)=\frac{K^{2/3}}{|\upsilon_-(N,K)|}f_{W_2}\left(\frac{K^{2/3}}{|\upsilon_-(N,K)|}\left(\mu_+(N,K)-z\right)\right) \tag{17}$$

The probability density function of T can be denoted by

$$f_{T|H_1}(t)=\begin{cases}\int_0^{+\infty} xf'_{L_{1|H_1}}(tx)f'_{L_{N|H_1}}(x)dx, & t>1\\ 0, & t\le 1\end{cases} \tag{18}$$

Although the probability density function of the interference detection metric T based on the ratio of largest eigenvalue and the smallest eigenvalue is obtained while the elements number N and the data snapshots K are all infinite, according to the existing numerical analysis results, the probability density function represented by Eq. (18) is also suitable when N and K are finite.

2.3 Threshold Setting Under Constant Missed Detection Probability

According to the signal model of the binary hypothesis test, the false alarm probability and the missed detection probability of a detector can be defined as

$$P_{fa}=\mathrm{P}_r(T\ge\gamma|H_0)=1-F_{T|H_0}(\gamma) \tag{19}$$

$$P_{md}=\mathrm{P}_r(T<\gamma|H_1)=F_{T|H_1}(\gamma) \tag{20}$$

where $F_{T|H_0}(t)$ and $F_{T|H_1}(t)$ are the cumulative distribution function of the detection metric under the assumptions H_0 and H_1 respectively. $f_{T|H_0}(t)$ and $f_{T|H_1}(t)$ are the corresponding probability density function.

According to Eq. (20), when the probability of missing detection $\mathrm{P_{md}}$ is given the threshold may be set as

$$\gamma(P_{md})=F^{-1}_{T|H_1}(P_{md}) \tag{21}$$

In order to obtain the analytic expression of the threshold setting when the missed detection probability is constant, it is necessary to make a suitable approximation and analyze the eigenvalue distribution under H_1 condition.

Since the distribution function of the detection metric under H_1 is independent of the noise power, we can suppose the noise power is 1, which cannot affect the analysis result. According to Eq. (13), the maximum eigenvalue λ_1 can be written as

$$\lambda_1 = K^{-1/2}\mu_s(t_1, N, K)L_{1|H_1} + \mu_s(t_1, N, K) \tag{22}$$

Since it follows the Gaussian distribution, its mean and variance are

$$\mu_1 = E[\lambda_1] = \mu_s(t_1, N, K) \tag{23}$$

$$\sigma_1^2 = Var[\lambda_1] = K^{-1}\upsilon_s^2(t_1, N, K) \tag{24}$$

Likewise, according to Eq. (14), the minimum eigenvalue L_N can be written as

$$\lambda_N = K^{-2/3}\upsilon'_-(N, K)L_{N|H_1} + \mu'_-(N, K) \tag{25}$$

Since at the time $N, K \to \infty$ $L_{1|H_1}$ and $L_{N|H_1}$ converge to the Gaussian distribution and the second-order Tracy-Widow distribution respectively, λ_1 and λ_N will converge to the Gaussian distribution and second-order Tracy-Widow distribution, too. In order to obtain an analytic threshold setting equation, the second-order Tracy-Widow distribution can be approximated as a Gaussian distribution while the corresponding mean and variance are

$$\mu_N = E[\lambda_N] = -1.771K^{-2/3}\upsilon'_-(N, K) + \mu'_-(N, K) \tag{26}$$

$$\sigma_N^2 = Var[\lambda_N] = 0.813K^{-4/3}\upsilon'^2_-(N, K) \tag{27}$$

According to the analysis in [8], the accumulation distribution function of the detection metric T_0 under H_1 condition can be approximated as

$$F_{T|H_1}(t) = \Phi\left(\frac{\mu_N t - \mu_1}{\sqrt{\sigma_N^2 t^2 + \sigma_1^2}}\right) \tag{28}$$

Therefore, the detection threshold at constant detection probability P_{md} can be written as

$$\gamma(P_{md}) = \frac{\mu_1\mu_N + \eta\sqrt{\sigma_1^2\mu_N^2 + \sigma_N^2\mu_1^2 - \eta^2\sigma_1^2\sigma_N^2}}{\mu_N^2 - \eta\sigma_N^2} \tag{29}$$

where $\eta = \Phi^{-1}(P_{md})$.

3 Simulation Results

The probability density function and the cumulative distribution function of the two-order Tracy-Widow distribution and the Gaussian distribution are contrasted in Figs. 1 and 2, respectively. As can be seen, the second-order Tracy-Widow is accurately approximated to the Gaussian distribution $N(-1.771, 0.813)$. Therefore, it is reasonable to use the Gaussian distribution to get the analytical formula of detection threshold for simplifying the calculation process of the detection threshold setting under constant missed detection probability.

Figures 3, 4 and 5 are the curves between the detection threshold and missed detection probability, interference-to-noise ratio, the elements number N, respectively. It can be seen from these figures that under the condition of constant missed detection probability the threshold will be larger as the increase of the number of elements and the interference-to-noise ratio, while the interference-to-noise ratio has the greatest effect on the threshold setting. This is because the interference signal energy basically determines the expected distribution of the detector metrics, which is also consistent with traditional experience. Moreover, it can be seen from Eqs. (15) and (29) that the probability distribution function under the condition H_1 and the threshold setting under the constant missed detection probability are also independent of the noise power.

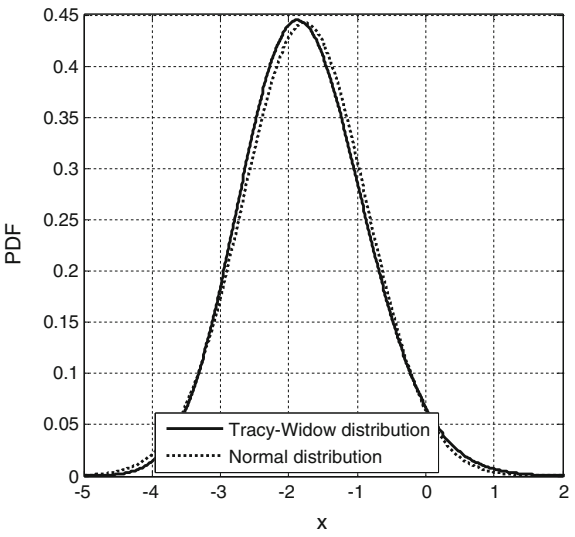

Fig. 1 Probability density function of Tracy-Widow distribution versus normal distribution pdf

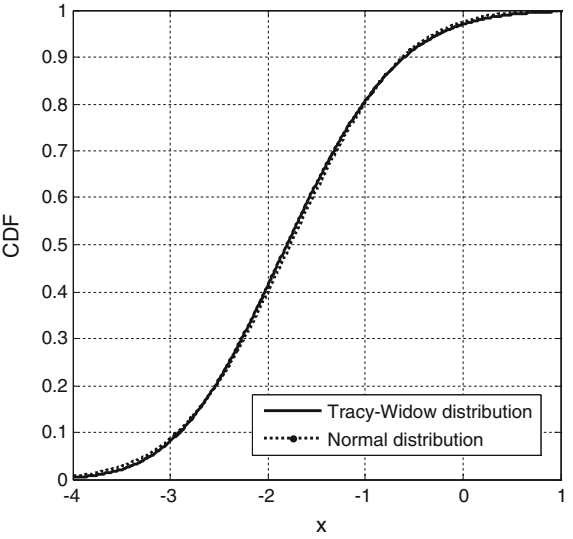

Fig. 2 Cumulative density function of Tracy-Widow versus normal distribution

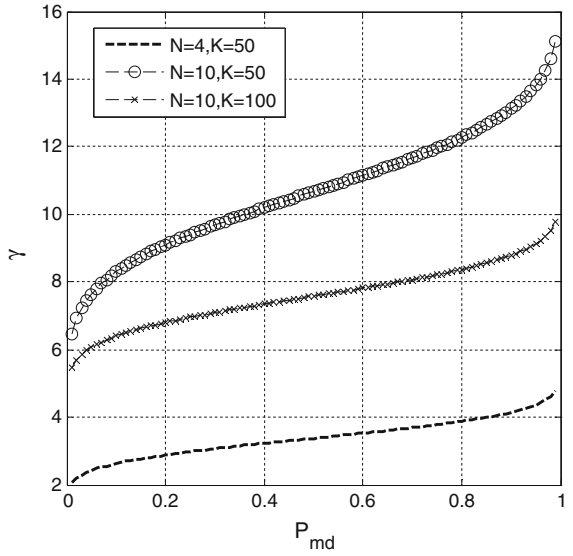

Fig. 3 Threshold setting under different miss detection probability ($\rho = -5$ dB)

4 Analysis of Detection Performance

The detection performance is usually expressed by the receiver operating characteristic (ROC) curve, which is the relationship curve between the false alarm probability and the missed detection probability, as

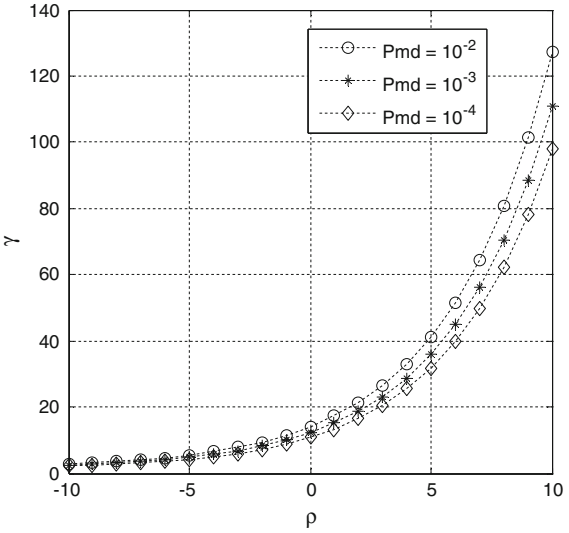

Fig. 4 Relations between threshold setting and interference-noise-ratio under different miss detection probability (N = 10, K = 100)

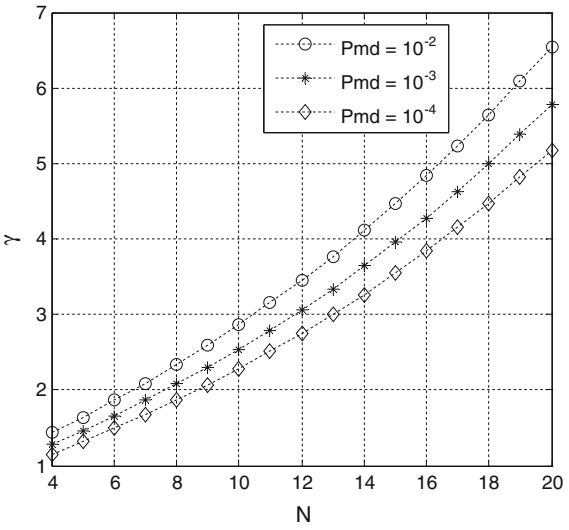

Fig. 5 Relations between threshold setting and antenna number under different miss detection probability (ρ = −10 dB, K = 100)

$$P_{md}\left(P_{fa}\right) = F_{T|H_1}\left(F^{-1}_{T|H_0}\left(1 - P_{fa}\right)\right) \tag{30}$$

The ROC curves under different parameter settings are shown in Figs. 6 and 7. It can be seen from the figures that the detection performance will be severely degraded when the elements number N and data snapshot K are too small. Therefore, to ensure the performance of the interference detector based on the ratio of the maximum eigenvalue and minimum eigenvalue, N and K should be compromised between implementation complexity and detection performance.

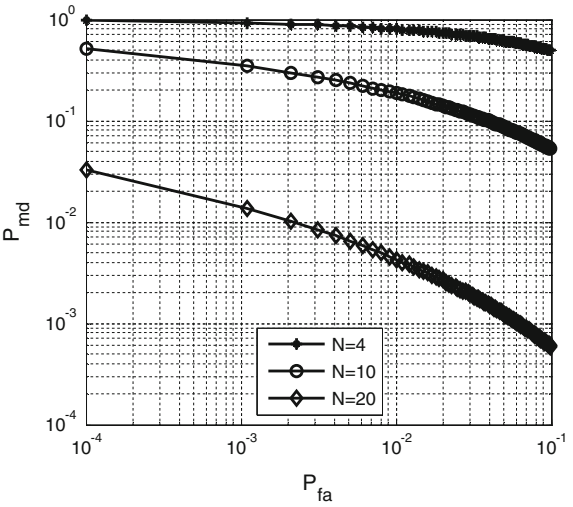

Fig. 6 ROC curve with different antenna number (K = 100, ρ = −10 dB)

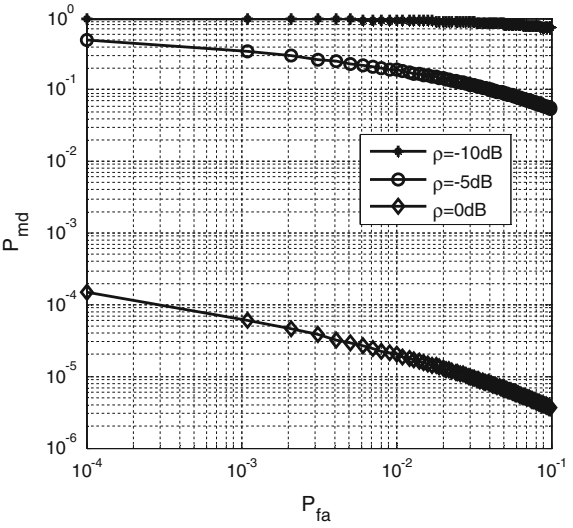

Fig. 7 ROC curve with different JNR (N = 4, K = 50)

5 Conclusion

Interference detection by using the ratio of the largest eigenvalue and the smallest eigenvalue of the received signal's covariance matrix has the advantage of being independent of the noise power. In order to simply the computation complexity of the threshold setting under constant missed detected probability, the second-order Tracy-Widow distribution to which the eigenvalues obey is approximated to Gaussian distribution with appropriate parameters. In this paper, the analytic expression of the detection threshold setting under the condition of constant missed detection probability is deduced respectively under the Gaussian distribution approximation, which can provide a theoretical basis for performance analysis of the eigenvalue based detection method.

References

1. Bhatti JA, Humphreys TE, Ledvina BM (2012) Development and demonstration of a TDOA-based GNSS interference signal localization system, vol 116, no 9, pp 455–469
2. Atapattu S, Tellambura C, Jiang H (2011) Energy detection based cooperative spectrum sensing in cognitive radio networks. IEEE Trans Wireless Commun 10(4):1232–1241
3. Pillay N, Xu HJ (2012) Blind eigenvalue-based spectrum sensing for cognitive radio networks. IET Commun 6(11):1388–1396
4. Nadler B, Penna F, Garello R (2011) Performance of eigenvalue-based signal detectors with known and unknown noise level 57(4):1–5
5. Zeng Y, Liang YC (2008) Eigenvalue based spectrum sensing algorithms for cognitive radio. IEEE Trans Commun 57(6):1784–1793
6. Penna F, Garello R (2009) Theoretical performance analysis of eigenvalue-based detection. Mathematics
7. Penna F, Garello R, Spirito MA (2009) Probability of missed detection in eigenvalue ratio spectrum sensing. In: IEEE international conference on wireless and mobile computing, networking and communications, pp 117–122
8. Wei L, Tirkkonen O (2010) Spectrum sensing with Gaussian approximated eigenvalue ratio based detection. IEEE Int Symp Wirel Commun Syst, 961–965
9. Egea D, Lopez-Salcedo JA, Seco-Granados G (2014) Interference and multipath sequential tests for signal integrity in multi-antenna GNSS receivers. In: IEEE sensor array and multichannel signal processing workshop, pp 117–120
10. Arts M, Bollig A, Mathar R (2015) Quickest eigenvalue-based spectrum sensing using random matrix theory. Comput Sci
11. Bornemann F (2010) On the numerical evaluation of distributions in random matrix theory: a review. Markov Processes & Relat Fields 16(2):803–866

Ranging Performance Analysis and Discriminator Parameters Optimization for Double Estimator Technology

Yang Gao, Henglin Chu, Zheng Yao and Xiaowei Cui

Abstract Double Estimator Technology (DET) uses subcarrier tracking loop and code tracking loop to track the Binary Offset Carrier modulated satellite navigation signal, the two loops couple with each other, which causes difficulties for ranging accuracy analyzing and discriminating parameters optimizing. While current research never considered the couple characteristics of the two loops. In this paper, a ranging performance analyzing method for DET is proposed, which considers both the code and the subcarrier discriminating functions to describe the influence of the couple characteristics. By using this analyzing method and taking Sine-BOC signal for example, the influence of the code discriminating space on the ranging accuracy was analyzed, and some special influencing features were first shown and explained. The analyzing shows that, due to the couple characteristics and the special two-dimension correlation function features, the influence of the code discriminating space should not be ignored: when the code discriminating space equals odd times of subcarrier square, the ranging accuracy is high and near to the BOC signal theory accuracy, while the code discriminating space equals even times of subcarrier square, the ranging accuracy degrades seriously, which can be 6–8 dB lower than that for odd. These results can be reference for the discriminating parameter selection and optimization for satellite navigation receivers.

Keywords Satellite navigation · Double estimator technology · Ranging accuracy · Couple characteristics · Code discriminator space

Y. Gao (✉) · H. Chu
Beijing Satellite Navigation Center, Beijing 100094, China
e-mail: bikong_001@aliyun.com

Z. Yao · X. Cui
Department of Electronic Engineering, Tsinghua University, Beijing, China

J. Sun et al. (eds.), *China Satellite Navigation Conference (CSNC) 2017 Proceedings: Volume I*, Lecture Notes in Electrical Engineering 437,
DOI 10.1007/978-981-10-4588-2_85

1 Introduction

Double Estimator Technology (DET) proposed in these years is suitable for processing Binary Offset Carrier modulated (BOC) signals in Global Navigation Satellite System (GNSS) [1–3], it can solve the ambiguity problem at the expense of little signal performance loss and with low implementation complexity, thus has a good application prospect in the BOC signal, especially for high order BOC signal receiving and processing [4]. Currently, many improved technologies based on the DET idea have been proposed and wide used in GNSS receiver, which can further enhance the ranging precision [5] or reduce the complexity [6, 7].

Ranging accuracy is one key performance of the GNSS receiver. Ranging accuracy usually relates to the parameters the technique uses, for example, for the traditional C/A signal receiving, reducing the early-late discriminating space can improve the actual ranging accuracy effectively [8]. DET uses code tracking loop and subcarrier tracking loop to track the BOC signal, whose discriminating parameters are more than that of the traditional method, thus it necessary to analyze the relationship between the ranging accuracy and the discriminating parameters in DET, which is help to optimize the parameters to get the optimal ranging performance.

Current research on DET ranging often assumes that the code tracking loop and the subcarrier tracking loop are independent from each other [2, 4], so the analysis only focuses on the subcarrier loop. However, the code tracking loop and subcarrier tracking loop couple with each other in fact [5], which means that the code discriminating parameter also influences the final ranging performance. So the code tracking loop parameters should also be considered when analyzing the DET performance.

DET ranging performance and parameter optimization are investigated in this paper based on considering the couple characteristic of the two loops. A general method for analyzing the ranging performance of two coupled loops was proposed, and the expression of "two-dimension correlation function" is also provided as the key part of the analyzing method. By using the proposed method, the influence of code discriminator space on DET ranging performance was analyzed for Sine-phased BOC signal, based on which, code discriminator space optimization choice is given. The analysis results show that: for finite bandwidth Sine-phased BOC signal, when the code discriminator space is an odd number of the subcarrier square width, the DET ranging performance is almost the same with the traditional matching receiving method, when the code discriminator space is an even number of the subcarrier square width, the DET ranging performance degrade seriously. Thus, to get high ranging performance, an odd number of subcarrier square should be preferred to an even number for DET code discriminator space choosing.

2 DET and Couple Characteristic

2.1 DET Math Model

The baseband BOC signal model can be expressed as [9–11]

$$x(t) = \sqrt{2C_s} \cdot c(t - t_0) \cdot s(t - t_0) e^{j\theta} + n(t) \tag{1}$$

where C_s is signal power, $c(t - t_0)$ is the pseudo noise (PN) code waveform whose chip width is T_c, $s(t - t_0)$ is the subcarrier waveform whose square width is T_s (the period of subcarrier is $2T_s$), t_0 is the path delay, θ is the carrier phase, and $n(t)$ is complex Gaussian white noise with spectrum density N_0.

DET uses both code tracking loop and subcarrier tracking loop to track the baseband signal (carrier tracking loop is not discussed here). Considering the coherent discriminator method, the discriminating function of the code tracking loop and subcarrier tracking loop can be expressed as

$$e_c = \Re\left\{ \frac{1}{T} \int_0^T x(t) \cdot \left[c\left(t - t_{0c} - \frac{\Delta_c}{2}\right) - c\left(t - t_{0c} + \frac{\Delta_c}{2}\right) \right] s(t - t_{0s}) \cdot e^{-j\hat{\theta}} \cdot dt \right\} \tag{2}$$

$$e_s = \Re\left\{ \frac{1}{T} \int_0^T x(t) \cdot c(t - t_{0c}) \left[s\left(t - t_{0s} - \frac{\Delta_s}{2}\right) - s\left(t - t_{0s} + \frac{\Delta_s}{2}\right) \right] \cdot e^{-j\hat{\theta}} \cdot dt \right\} \tag{3}$$

where e_c is the code discriminator error, $\Re\{\cdot\}$ is real part operation, T is the integration time, Δ_c is the code discriminator space, t_{0c} is the local code delay, t_{0s} is the local subcarrier delay, $\hat{\theta}$ is the estimate of the carrier phase, e_s is the subcarrier discriminator error and Δ_s is the subcarrier discriminator space.

Based on these discriminating methods, an unambiguity and low precision ranging measurement can be got from the code tracking loop, an ambiguity and high precision ranging measurement can be got from the subcarrier loop, and the final unambiguity and high precision ranging measurement can be got through a nonlinearly combination of the two measurements, the final precision is determined by the subcarrier loop [1–3].

2.2 Couple Characteristic

Ignoring the error of carrier phase estimate $\hat{\theta}$, (2) and (3) can be written as:

$$e_c = \sqrt{2C_s} \cdot \left[R\left(\tau_c - \frac{\Delta_c}{2}, \tau_s\right) - R\left(\tau_c + \frac{\Delta_c}{2}, \tau_s\right) \right] + N_c \tag{4}$$

$$e_s = \sqrt{2C_s} \cdot \left[R\left(\tau_c, \tau_s - \frac{\Delta_s}{2}\right) - R\left(\tau_c, \tau_s + \frac{\Delta_s}{2}\right) \right] + N_s \tag{5}$$

where $\tau_c = t_0 - t_{0c}$ is the relative delay between the received signal and the local PN code, $\tau_s = t_0 - t_{0s}$ is the relative delay between the received signal and local subcarrier, N_c is the real part of the code discriminator complex noise, N_s is the real part of the subcarrier discriminator complex noise, $R(\tau_c, \tau_s)$ is the normalized 2 dimension cross correlation function of the received signal and the local signal, which is calculated as:

$$R(\tau_c, \tau_s) = \frac{1}{T} \int_0^T c(t)s(t) \cdot c(t - \tau_c) \cdot s(t - \tau_s) \cdot \mathrm{d}t \tag{6}$$

Because of the complexity of $R(\tau_c, \tau_s)$, the two discriminators is not independent from each other, which means that e_c does not only relate to τ_c but also to τ_s, and e_s is also influenced by both τ_c and τ_s. This couple characteristic can be shown through the discriminator curves, as Figs. 1 and 2 show.

Figures 1 and 2 show the discriminator curves for PN code and subcarrier respectively, where $BOC_s(4,1)$ signal, $\Delta_c = 0.4\,T_c$ and $\Delta_s = 0.4\,T_s$ is taken for example. As these figures show, when there is a non-zero bias in one dimension, the zero-crossing point of the curve in other dimension leaves away from the center. Obviously, this characteristic may influence the tracking precision, which should be considered in performance analysis and parameter optimization.

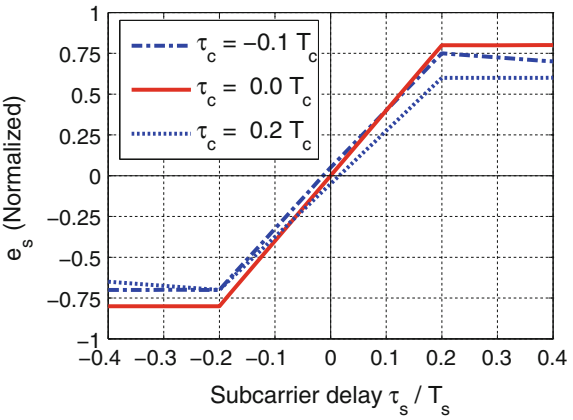

Fig. 1 The influence of the code error on subcarrier discriminating curve

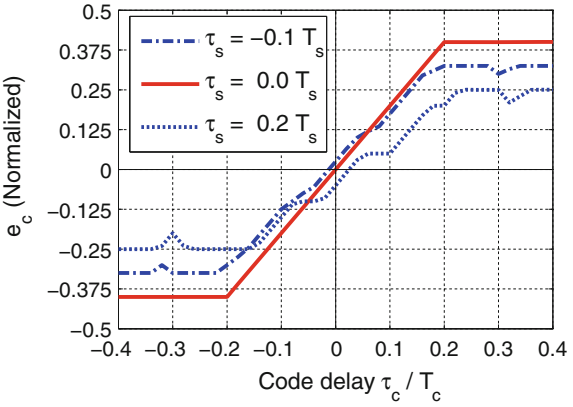

Fig. 2 The influence of the subcarrier error on code discriminating curve

3 Noise Performance Analysing Method

3.1 Analysing Method for Couple Discriminator

The two-dimension couple discriminating functions can be written in a general form as

$$\begin{cases} e_c = K_c(\tau_c, \tau_s) + N_c \\ e_s = K_s(\tau_c, \tau_s) + N_s \end{cases} \tag{7}$$

where $K_c(\tau_c, \tau_s)$ is the function that map two delay errors τ_c and τ_s to code discriminator output error, $K_s(\tau_c, \tau_s)$ is the function that map two delay errors τ_c and τ_s to subcarrier discriminator output error. The specific expressions of $K_c(\tau_c, \tau_s)$ and $K_c(\tau_c, \tau_s)$ are determined by both $R(\tau_c, \tau_s)$ and the discriminating methods, and to meet non-bias tracking constraints, $K_c(0, 0) = 0$ and $K_s(0, 0) = 0$ must be satisfied, N_c and N_s are discriminator noise which usually assumed as White Gaussian Noise.

In steady tracking state, τ_c and τ_s are both very small, thus (7) can be written as a linear expansion

$$\begin{cases} e_c \approx \kappa_{cc} \cdot \tau_c + \kappa_{cs} \cdot \tau_s + N_c \\ e_s \approx \kappa_{sc} \cdot \tau_c + \kappa_{ss} \cdot \tau_s + N_s \end{cases} \tag{8}$$

where

$$\begin{cases} \kappa_{cc} = \frac{\partial K_c(\tau_c, \tau_s)}{\partial \tau_c}\big|_{\tau_c=\tau_s=0} \\ \kappa_{cs} = \frac{\partial K_c(\tau_c, \tau_s)}{\partial \tau_s}\big|_{\tau_c=\tau_s=0} \\ \kappa_{sc} = \frac{\partial K_s(\tau_c, \tau_s)}{\partial \tau_c}\big|_{\tau_c=\tau_s=0} \\ \kappa_{ss} = \frac{\partial K_s(\tau_c, \tau_s)}{\partial \tau_s}\big|_{\tau_c=\tau_s=0} \end{cases} \tag{9}$$

Considering the non-bias tracking constraints, the two delay estimates can be written as

$$\begin{bmatrix} \hat{\tau}_c \\ \hat{\tau}_s \end{bmatrix} = \boldsymbol{\kappa}^{-1} \begin{bmatrix} e_c \\ e_s \end{bmatrix} = \begin{bmatrix} \tau_c \\ \tau_s \end{bmatrix} + \boldsymbol{\kappa}^{-1} \begin{bmatrix} N_c \\ N_s \end{bmatrix} \tag{10}$$

Thus, the variance can be calculated as

$$\begin{bmatrix} \mathrm{var}(\hat{\tau}_c) & \mathrm{var}(\hat{\tau}_c, \hat{\tau}_s) \\ \mathrm{var}(\hat{\tau}_s, \hat{\tau}_c) & \mathrm{var}(\hat{\tau}_s) \end{bmatrix} = \boldsymbol{\kappa}^{-1} \cdot \mathbf{q} \cdot \left[\boldsymbol{\kappa}^{-1}\right]^T \tag{11}$$

where $\mathrm{var}(\cdot)$ is the variance operation, $\boldsymbol{\kappa}$ is called slope matrix, $\mathbf{q}$ is called noise variance matrix, the two can be calculated as:

$$\boldsymbol{\kappa} = \begin{bmatrix} \kappa_{cc} & \kappa_{cs} \\ \kappa_{sc} & \kappa_{ss} \end{bmatrix} \tag{12}$$

$$\mathbf{q} = \begin{bmatrix} \mathrm{E}(N_c^2) & \mathrm{E}(N_c \cdot N_s) \\ \mathrm{E}(N_c \cdot N_s) & \mathrm{E}(N_s^2) \end{bmatrix} \tag{13}$$

where $\mathrm{E}(\cdot)$ is expectation operation. As the ranging precision is determined by the subcarrier loop, considering the loop filter influence [9], the final ranging variance is

$$\sigma_{\tau_s}^2 = \mathrm{var}(\hat{\tau}_s) \cdot 2B_L T \cdot (1 - 0.5B_L T) \tag{14}$$

where B_L is the loop bandwidth, and T is the integration time.

3.2 Key Part Calculation Method

The tracking precision calculation method for coupled loops is given, where slop matrix $\boldsymbol{\kappa}$ and noise matrix $\mathbf{q}$ are keys for calculation. For some specific discriminating method, $\boldsymbol{\kappa}$ and $\mathbf{q}$ are both determined by $R(\tau_c, \tau_s)$, thus the latter gives $R(\tau_c, \tau_s)$ calculation method for finite bandwidth signal.

Considering the ideal self-correlation feature of PN code, (6) can be written as

$$R(\tau_c, \tau_s) = \frac{1}{T_c} \int_0^{T_c} u(t)s(t) \cdot [u(t - \tau_c)s(t - \tau_s)] \cdot \mathrm{d}t \tag{15}$$

where is the $u(t)$ unit square wave with chip width T_c. According to the transformation between time and frequency domain in [9], (15) can be written as

$$R(\tau_c, \tau_s) = \frac{1}{T_c} \int_{-\beta_r/2}^{\beta_r/2} G_{BOC}(f) \cdot \left[G_{BOC}^{(\tau_s - \tau_c)}(f) \cdot \mathrm{e}^{-j2\pi f \cdot \tau_c} \right]^* \cdot \mathrm{d}f \tag{16}$$

where β_r is the signal band width, $G_{BOC}(f)$ and $G_{BOC}^{(\tau_s-\tau_c)}(f)$ are the Fourier transformation of the received signal and the local signal, respectively, as (17) and (18) show.

$$G_{BOC}(f) = \int_0^{T_c} u(t) \cdot s(t) \cdot \mathrm{e}^{-j2\pi f \cdot t} \cdot \mathrm{d}t \tag{17}$$

$$G_{BOC}^{(\tau_s-\tau_c)}(f) = \int_0^{T_c} u(t) \cdot s[t - (\tau_s - \tau_c)] \cdot \mathrm{e}^{-j2\pi f \cdot t} \cdot \mathrm{d}t \tag{18}$$

When giving specific BOC signal and the discriminating methods, the expression of $R(\tau_c, \tau_s)$, $K_c(\tau_c, \tau_s)$ and $K_s(\tau_c, \tau_s)$ can be got based on above method and the ranging performance can be calculated further.

4 Noise Performance Analysis and Parameter Optimization

4.1 Noise Performance Analysis

Using the proposed method and taking Sine-phased BOC signal for example, the tracking performance of the DET will be analyzed in this section. As the couple characteristic is focused, the key part is the influence of the PN code discriminator space on the ranging performance.

Specifically, take $BOC_s(2,1)$ and $BOC_s(6,1)$ for instance, and the coherent E-L discriminating method shown in (4) and (5) are used, the DET ranging precision curves under different PN code space are shown in Figs. 3 and 4.

In Figs. 3 and 4, the subcarrier discriminator space Δ_s is $0.5T_s$, the integration time is 1 ms, and loop bandwidth B_L is 1 Hz, the signal bandwidth is set to including the two main lobes of BOC signal, that is 6 MHz for $BOC_s(2,1)$ and 14 MHz for $BOC_s(6,1)$. The traditional matching receiving method with coherent E-L discriminating function is also given for comparison, which is calculated according to [9, 10]. As the two figures show.

(1) DET is not a strict full precision tracking method; the precision is loss comparing with the matching receiving, and the loss relates to the PN code space.

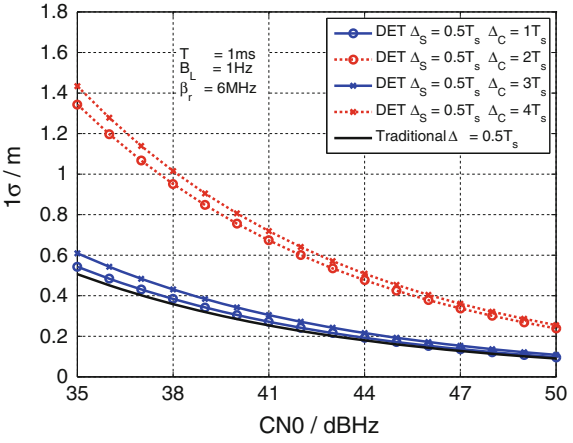

Fig. 3 The tracking precision of DET for BOCs(2, 1) signal

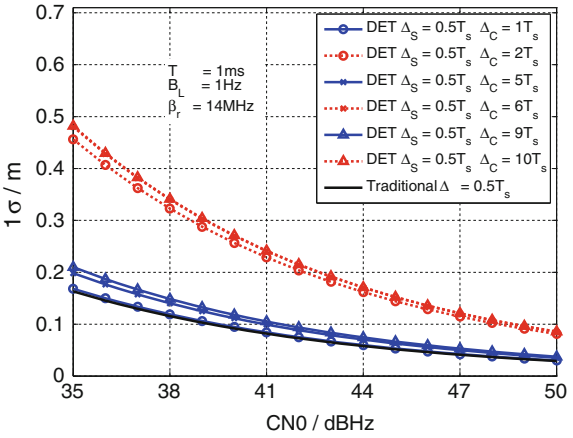

Fig. 4 The tracking precision of DET for BOCs(6, 1) signal

(2) The DET tracking precision can be seriously influenced by the PN code space, and the influence can be divided into two groups: when Δ_c is an odd number of T_s, the tracking precision is relatively high; when Δ_c is an even number of T_s, the tracking precision is relatively low. The difference between the two groups can be 6–8 dB.
(3) In each group, the tracking precision rises with Δ_c degrades, and the difference is around 1 dB.

The above features, especially feature (2) is first obtained, which is opposite to the intuitive understanding. To test and verify this phenomenon, take $BOC_s(2,1)$ for instance, under the same conditions with Fig. 3, simulations were made for comparison; the results are shown in Fig. 5.

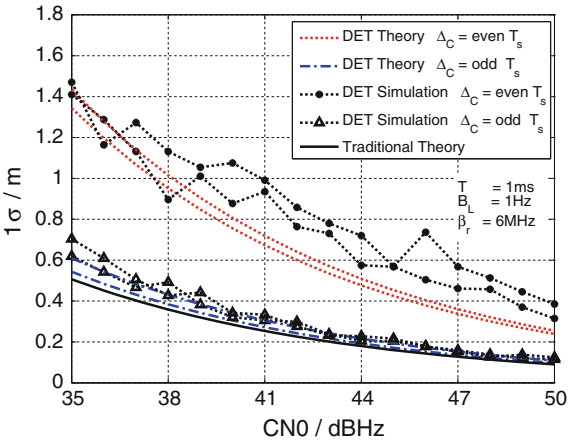

Fig. 5 The comparison of the theory and the simulation results for DET tracking precision for BOCs(2, 1) signal

As Fig. 5 shows, when Δ_c is an odd number of T_s, the simulation results coincide well with the theory results, when Δ_c is an even number of T_s, the simulation result is a little different from the theory results, which is due to the approximation in theory analysis. However, the "group feature" in simulation results coincide well with that in theory results: the noise variance when Δ_c is an even number of T_s is much higher than that when Δ_c is an odd number of T_s.

This phenomenon can be explained by Fig. 6.

Figure 6 shows the PN code delay dimension shape of $R(\tau_c, \tau_s)$ for finite bandwidth $BOC_s(2,1)$ signal, and the subcarrier delay $\tau_s = 0$ here. As can be seen in Fig. 6, when the $\Delta_c = 2T_s$ or other even number of T_s, the slope of the correlation function is very low, thus the code discriminator is not sensitivity to the code delay error, which results in high jitters in code tracking loop, and because of the couple characteristics, this high jitter influences the subcarrier tracking loop, which final causes the bad ranging performance. While when $\Delta_c = 3T_s$ or other odd number of T_s, the slope of the correlation function is relative high, the jitter in code tracking loop will be much smaller, which can make the final ranging performance much better. Numerical analysis shows that, the slope difference between the two situations can be as large as 10 times, which can fully result in 6–8 dB in ranging precision.

4.2 *Parameters Optimization for BOCs Signal*

Selecting several $BOC_s(kn, n)$ signals to see the PN code delay dimension shape of $R(\tau_c, \tau_s)$, as Fig. 7 shows.

In Fig. 7, four kinds of modulation orders of BOCs signals are taken for reference, the signal bandwidths are set to include the two main lobes, and the Y axis are added some offsets to show clearer. As Fig. 7 shows, all the shapes show the

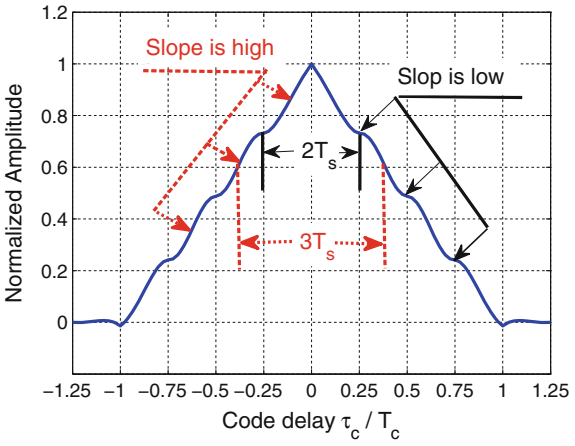

Fig. 6 The code dimension shape of the cross correlation function for finite bandwidth BOCs(2, 1) signal

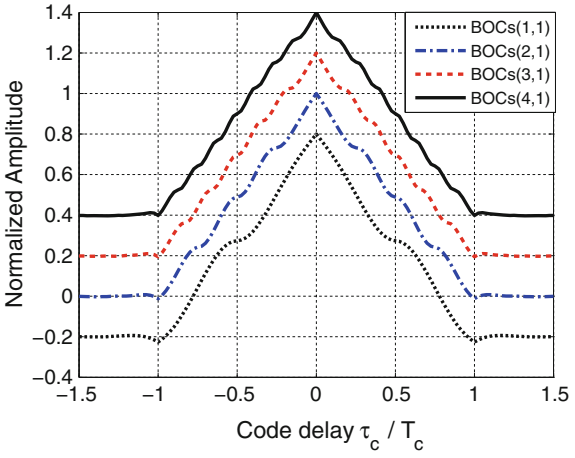

Fig. 7 The code dimension shape of the cross correlation function for finite bandwidth BOCs signal

similar features, that is "high slop when Δ_c is odd number of T_s and low slop when Δ_c is even number of T_s". These common features indicate that, the relationship between slop and Δ_c is general in bandwidth limited $BOC_s(kn, n)$ signals, thus, when using DET to processing $BOC_s(kn, n)$ signals, an odd number of T_s should be preferred by Δ_c to an even number.

5 Summary

For the couple characteristic between the code tracking loop discriminator and the subcarrier tracking loop discriminator in DET, a tracking precision analyzing method as well as some key parts calculation method are proposed in this paper.

Based on these methods and take Sine-phase BOC signal for instance, the tracking performance of DET is analyzed, the special way that the code discriminator space influence on ranging performance is first obtained and explained. The research shows that, PN code discriminator space can affect DET ranging seriously, for Sine-phase BOC signals, when PN code space is an odd number of subcarrier square wave width, the ranging performance is relatively high, near to the full precision; when PN code space is an even number of subcarrier square wave width, the ranging performance degrades 6–8 dB comparing with that in odd. Thus, using DET to receive sine-phased BOC signal, PN code space with an odd number of subcarrier square should be preferred. For Cosine-phased BOC signal, DET performance can also be analyzed through the ways provided in this paper.

References

1. Hodgart MS, Blunt PD (2007) A dual estimate receiver of binary offset carrier (BOC) modulated signals for global navigation satellite systems. Electron Lett 43(16):877–878
2. Hodgart MS, Blunt PD (2008) A receiver of binary offset carrier (BOC) modulated signals. World Patent, WO2008017860A1 [P], pp 2–14
3. Hodgart MS, Blunt PD, Unwin M (2008) Double estimator a new receiver principle for tracking BOC signals. InsideGNSS 3(3):26–36
4. Blunt P, Weiler R, Hodgart S (2007) Demonstration of BOC(15, 2.5) acquisition and tracking with a prototype hardware receiver. Proceedings of the European navigation conference, Geneva, Switzerland, May 2007
5. Gao Y, Yao Z, Zhu Y, Lu M (2014) A two-dimension tracking based multipath mitigation method for BOC signals. Proceedings of the 2014 international technical meeting of the institute of navigation, San Diego, California, US, pp 876–883
6. Ji Ren, Jia W, Chen H et al (2012) Unambiguous tracking method for alternative binary offset carrier modulated signals based on dual estimate loop. IEEE Commun Lett 16(11):1737–1740
7. Yang Z, Huang Z, Geng S (2011) Novel tracking loop of BOC signal based on subcarrier tracking. J Beijing Univ Aeronaut Astronaut 37(2):245–248
8. Van DAJ, Fenton P, Ford T (1992) Theory and performance of narrow correlator spacing in a GPS receiver. Navigation 39(3):265–284
9. Betz JW, Kolodziejski KR (2009) Generalized theory of code tracking with an early-late discriminator part I: lower bound and coherent processing. IEEE Trans Aerosp Electron Syst 45(4):1538–1550
10. Betz JW, Kolodziejski KR (2009) Generalized theory of code tracking with an early-late discriminator part II: noncoherent processing and numerical results. IEEE Trans Aerosp Electron Syst 45(4):1551–1564
11. Betz JW (2001) Binary offset carrier modulations for radio navigation. J Navig 48(4):227–246